

AD-A272 788



N00014-91-J-1993

Fifth Symposium on

13

# NUMERICAL AND PHYSICAL ASPECTS OF AERODYNAMIC FLOWS

13-15 January 1992

CALIFORNIA STATE UNIVERSITY  
LONG BEACH, CALIFORNIA

**S** DTIC  
ELECTE  
NOV 17 1993  
**A**

This document has been approved  
for public release and sale; its  
distribution is unlimited.



93-26511



93 11 1 103

**Best  
Available  
Copy**

Fifth Symposium on

# NUMERICAL AND PHYSICAL ASPECTS OF AERODYNAMIC FLOWS

13-15 January 1992

CALIFORNIA STATE UNIVERSITY  
LONG BEACH, CALIFORNIA

INFO QUALITY INSPECTED 8



Accession For	
NTIS	CRA&I <input checked="" type="checkbox"/>
DTIC	TAS <input type="checkbox"/>
Unannounced <input type="checkbox"/>	
Justification	
By	
Distribution/	
Availability Codes	
Dist	Avail and/or Special
A-1	

# **Fifth Symposium on**

## **NUMERICAL AND PHYSICAL ASPECTS OF AERODYNAMIC FLOWS**

### **Preface**

This volume contains the papers presented at the Fifth Symposium on Numerical and Physical Aspects of Aerodynamic Flows, held at the California State University, Long Beach, from 13 to 15 January 1992. The symposium, like its immediate predecessors, considers the calculation of flows of relevance to aircraft, ships and missiles with emphasis on the solution of two-dimensional unsteady and three-dimensional equations.

The general format of the symposium and of this proceedings volume is similar to that of the Third and Fourth Symposium. There are 44 papers and the Stewartson Memorial Lecture given by Professor Peter Bradshaw. The first two sessions deal with transition and turbulence modelling. These are followed by two sessions on aircraft icing. Sessions 5 and 6 report recent advances in high-lift research and describe computational methods using solutions of Navier-Stokes equations and

inviscid and viscous flow equations with experimental work to guide the development of the calculation methods. Unsteady flows are addressed in Sessions 7 and 8. The remaining four sessions deal with two- and three-dimensional steady flows and describe calculational methods based on the Navier-Stokes equations and their reduced forms. This volume will be of value to researchers, engineers and designers and, in particular, will provide a better understanding of aerodynamic flows and the development of calculational methods.

This symposium was made possible by financial support from the California State University, the Office of Naval Research, the NASA Ames Research Center, and the Army Research Center, and with the cooperation of authors, session chairs, participants and colleagues at the University and at the Douglas Aircraft Company.

Tuncer Cebeci  
January 1992



## CONTENTS

### Stewartson Memorial Lecture

P. Bradshaw, "Turbulence: The Chief Outstanding Difficulty of Our Subject."

### SESSION 1: Transition and Turbulence Modelling, 1

\*\* Lead Speaker: D. Bushnell, "Supersonic Laminar Flow Control."

T. A. Zang, C. L. Chang and L. L. Ng, "The Transition Prediction Toolkit: LST, SIT, PSE, DNS, and LES."

\* U. Dallmann, T. M. Fischer, W. Koch and H. Bippes, "On the Role of Secondary Instabilities in Laminar-Turbulent Transition of 2D and 3D Boundary Layers."

R. Niethammer, D. Arnal, V. de Latharpe, H. H. Chen and T. Cebeci, "Three-Dimensional Compressible Stability-Transition Calculations Using the Spatial Theory."

### SESSION 2: Transition and Turbulence Modelling, 2

D. C. Wilcox, "The Remarkable Ability of Turbulence Model Equations to Describe Transition."

R.M.C. So, H. S. Zhang and Y. G. Lai, "A Compressible Near-Wall Turbulence Model for Boundary-Layer Calculations."

S. K. Kim, M. K. Chung and J. R. Cho, "Analysis of the Effect of Initial Conditions on the Initial Development of a Turbulent Jet."

\* S. Ellil and C. P. van Dam, "The Influence of Bulges on Boundary Layer Instability."

M. Morzynski and F. Thiele, "Stability Investigations of Airfoil Flow by Global Analysis."

### SESSION 3: Aircraft Icing, 1

\*\* Lead Speaker: J. J. Reinmann, "NASA'S Aircraft Icing Technology Program."

M. B. Bragg, A. Khodadoust and M. Kerho, "Aerodynamics of a Finite Wing with Simulated Ice."

K. M. Al-Khalil, T. G. Keith, Jr. and K. J. De Witt, "Numerical Modeling of Runback Water on Ice Protected Aircraft Surfaces."

### SESSION 4: Aircraft Icing, 2

H. Hefazi and L. T. Chen, "A Composite Structured/Unstructured-Mesh Euler Method for Complex Airfoil Shapes."

J. Shin and T. H. Bond, "Experimental and Computational Ice Shapes and Resulting Drag Increase for a NACA 0012 Airfoil."

T. Cebeci, H. H. Chen, K. Kaups and S. Schimke, "Recent Progress in the Analysis of Iced Wings."

### SESSION 5: High Lift, 1

\* Lead Speaker: L. Olson, "High-Lift Aerodynamics: Prospects and Plans."

S. E. Rogers, N. L. Wiltberger and D. Kwak, "Efficient Simulation of Incompressible Viscous Flow Over Multi-Element Airfoils."

D. J. Mavriplis, "Unstructured Mesh Algorithms for Aerodynamic Calculations."

T. Cebeci, "An Interactive Boundary-Layer Approach to Multielement Airfoils at High Lift."

### SESSION 6: High Lift, 2

W. O. Valarezo, C. J. Dominik and R. J. McGhee, "Reynolds and Mach Number Effects on Multielement Airfoils."

G. W. Brune, "Quantitative Three-Dimensional Low Speed Wake Surveys"

- \* P.M.V.H. Vijgen, J. Hardin and L. Yip, "Flow Predictions Over a Transport Multi-Element High Lift System and Comparison with Flight Measurements."

R. Balasubramanian, K. M. Jones and E. G. Waggoner, "Assessment of Computational Issues Associated with Analysis of High-Lift Systems"

#### SESSION 7: Unsteady Flows, 1

P. F. Lorber and F. O. Carta, "Unsteady Transition Measurements on a Pitching Three-Dimensional Wing."

- \* K. N. Ghia, U. Ghia and G. A. Osswald, "Investigation of Forced Unsteady Separated Flows Using Velocity-Vorticity Form of Navier-Stokes Equations."

S. Aso and M. Hayashi, "Numerical Simulations of Dynamic Stall Phenomena by Discrete Vortex Method and Viscous Flow Calculation."

W. J. McCroskey, "Some Recent Applications of Navier-Stokes Codes to Rotorcraft."

#### SESSION 8, Unsteady Flows, 2

M. F. Platzer, M.S. Chandrasekhara, J. A. Ekaterinaris and L. W. Carr, "Dynamic Airfoil Stall Investigations."

- \* T. T. Huang, D. J. Fry, H.-L. Liu, J. Katz and T. C. Fu, "Simultaneous Mapping of the Unsteady Flow-fields by Particle Displacement Velocimetry (PDV)."

- \* J. C. LeBalleur and P. Girodroux-Lavigne, "Calculations of Fully Three-Dimensional Separated Flows with an Unsteady Viscous-Inviscid Interaction Method."

#### SESSION 9: Two- and Three-Dimensional Flows, 1

- \*\* Lead Speaker: F. T. Lynch, "Practical Aerodynamics For Subsonic Transport Design."

D. H. Choi, C. H. Sohn and C. S. Oh, "Prediction of Airfoil Stall Using Navier-Stokes Equations in Streamline Coordinates."

H. J. Sung, J. W. Rhim and M. Kiya, "Discrete-Vortex Simulation of Pulsating Flow on a Turbulent Leading-Edge Separation Bubble."

M. Hafez, M. Soliman and S. White, "A Unified Approach for Numerical Simulation of Viscous Compressible and Incompressible Flows Over Adiabatic and Isothermal Walls."

#### SESSION 10: Two- and Three-Dimensional Flows, 2

S. Agrawal, B. A. Robinson and R. M. Barnett, "Improved Numerical Predictions of Vortex Breakdown on a Delta Wing."

P. Atcliff, D. Kumar and J. L. Stollery, "Plume Effects on the Flow Around a Blunted Cone at Hypersonic Speeds."

C. G. Yam and H. A. Dwyer, "Combined Forced and Free Convection in a Curved Duct."

J. P. Brazier, B. Aupoix and J. Cousteix, "Investigations of Entropy Layer Along Hypersonic Hyperboloids Using a Defect Boundary Layer."

#### SESSION 11: Two- and Three-Dimensional Flows, 3

Lead Speaker: S. G. Rubin and K. Srinivasan, "Adaptive Multigrid Domain Decomposition Solutions for Viscous Interacting Flows."

P. V. Luong, J. F. Thompson, B. Gatlin, C. W. Mastin and H. J. Kim, "Adaptive Eagle Dynamic Solution Adaptation and Grid Quality Enhancement."

A. J. van der Wees and J. Van Muijden, "A Robust Quasi-Simultaneous Interaction Method for a Full Potential Flow with a Boundary Layer with Application to Wing/Body Configurations."

SESSION 12: Two- and Three-Dimensional Flows, 4

Lead Speaker: V. C. Patel and L. Larsson, "Ship Viscous Flow: A Report on the 1990 SSPA-CTH-11HR Workshop."

R. Houdeville, "Three-Dimensional Boundary-Layer Calculation by a Characteristic Method."

W. H. Jou, L. B. Wigton, S. R. Allmaras, P. R. Spalart and N. J. Yu, "Towards Industrial-Strength Navier-Stokes Codes."

---

\*Abstract only.

\*\*Paper not available at time of printing.

1088c

**STEWARTSON MEMORIAL LECTURE**

# Stewartson Memorial Lecture

## TURBULENCE: THE CHIEF OUTSTANDING DIFFICULTY OF OUR SUBJECT

Peter Bradshaw  
Mechanical Engineering Dept., Stanford University  
Stanford, CA 94305

### Abstract

A review of interesting current topics in turbulence research is decorated with examples of popular fallacies about the behaviour of turbulence. Topics include the status of the Law of the Wall, especially in compressible flow; analogies between the effects of Reynolds number, pressure gradient, unsteadiness and roughness change; the status of Kolmogorov's universal equilibrium theory and local isotropy of the small eddies; turbulence modelling, with reference to universality, pressure-strain modelling and the dissipation equation; and chaos. Fallacies include the mixing-length concept; the effect of pressure gradient on Reynolds shear stress; the separability of time and space derivatives; models of the dissipation equation; and chaos.

### 1. Introduction

I first met Keith Stewartson in the early 1960's, when he was a young member of the British Aeronautical Research Council's Fluid Motion Subcommittee and I was its (very) young secretary. Even in those days, I dimly sensed that Keith was not particularly fond of turbulence. It is, therefore, a matter of double regret that I should be giving, so soon, a lecture in his memory, and should be forced to choose the subject of turbulence as being my only area of aerodynamic competence.

Those who knew Keith will recall that his strongest term of scientific condemnation was "unrigorous". I'm sure he regarded the whole phenomenon of turbulence as being unrigorous and probably invented by the Devil on the seventh day of Creation (when the Good Lord wasn't looking); I am inclined to agree. Keith would certainly have approved of the rigour of Horace Lamb's "Hydrodynamics" (Cambridge University Press) - what the reviewer of a later book once called his "awful correctness". Lamb, after discussing all the branches of hydrodynamics known to him, finally had to deal with turbulence and remarked, in Article 365, p. 651 of the 1916 edition, "It remains to call attention to the chief outstanding difficulty of our subject." Seventy-odd years have come and gone; difficulties in hydrodynamics have come and gone; but turbulence still remains as the "chief outstanding difficulty of our subject". Another dead friend, Jack Nielsen, Chief Scientist of NASA Ames, said a few years ago that turbulence modeling was the "pacing item" in the use of the NAS computer complex, and I think his comment, like Lamb's, is still true.

In the last ten years or so we have become able to solve the complete time-dependent Navier-Stokes equations for turbulent flow. However, the Reynolds numbers at which

we can get numerically-accurate complete solutions are usually only about three or four times the lowest at which turbulence can exist, and are considerably lower than the Reynolds numbers obtainable in laboratory experiments, let alone those found in real life. Therefore, although turbulence is starting to become accessible to computers, there is no immediate prospect of the subject going the same way as stress analysis and succumbing almost entirely to computation: unlike elasticity, turbulence is a non-linear (strictly, quasi-linear) phenomenon and, at least at high Reynolds numbers, is at present accessible only to experiment. Thus, experimental fluid dynamics will last for many years (hopefully, for my working lifetime).

Of course, turbulence would merely be a laboratory curiosity or a computational playground if it were not for its extreme importance in real life and in all the scientific and engineering disciplines represented here today:- in meteorology, aeronautical aerodynamics, shipbuilding, oceanography, in all forms of pipeline design and manufacture, in combustion, in any form of mixing of contaminant, whether of heat or concentration or pollutant - in other words in almost all forms of "interesting" fluid motion except those on an extremely small scale. The cream poured into a cup of coffee goes turbulent, and the flow patterns look very cloud-like. (The poem on the letter "H" will be quoted in the oral lecture.)

I propose to use this Memorial Lecture to try to inject a certain amount of rigour into the study of turbulence, specifically by using the occasion to review some popular fallacies about turbulence and the way in which turbulent flows behave. Some of these fallacies or illogicalities are propagated by popular but outdated textbooks, but some are at a deeper level of incomprehension, including the preconceptions of workers in statistical mechanics who think that turbulence must be easy. Naturally, parts of the material that I will produce are controversial, in the sense that some of my professional colleagues may disagree with me. However, I hope that even the controversial sections of the paper will be of interest and may stimulate clarifying discussion, either at this meeting or after it. It is of course difficult to group illogicalities into any logical order, so I have imbedded them into a study of the more popular topics of turbulence "theory". I hope the result is neither a rag-bag nor a grab-bag. The oral lecture will be less specialised than this written version.

My favorite definition of turbulence is that it is the general solution of the Navier-Stokes equations. This is the perfect answer by a government servant to an inquiry by a Congressman or Member of Parliament: it is brief, it is entirely true, and it adds nothing to what was known

already. Nearly everybody believes, of course, that the Navier-Stokes equations are an adequately exact description of turbulence, or indeed of any other nonrelativistic motion of a Newtonian fluid. Even the smallest eddies in turbulence in ordinary liquids and gases at earth-bound temperatures and pressures are large compared to the mean free path between molecular collisions, so the constitutive equation of the fluid is not in doubt. However, Sec. 4 of the present paper deals with the influence of fluctuating dilatation *divu* on turbulence in compressible gas flow, and in this case the uncertain value of the bulk viscosity  $\beta$  (Goldstein<sup>1</sup>) may matter.

Fortunately for professional educators, it is generally accepted that the basic phenomena of turbulence are the same at any Mach number – except for some special effects to be discussed in Sec. 4 – so unless stated otherwise I will assume the density to be constant.

## 2. The Law of the Wall

One of the main building blocks, or even foundation stones, of the engineering study of turbulence is the "Law of the Wall". It derives from the hypothesis / assumption that, sufficiently close to a solid wall (meaning, for example, a distance from the wall an order of magnitude less than the diameter of a pipe or the thickness of a boundary layer) the flow depends only on the distance from the wall, on the shear stress at the wall  $\tau_w$ , and on fluid properties. The characteristics of the outer part of the flow do not matter except that they determine  $\tau_w$ . (In the discussion below, the term "shear stress" will sometimes be used to mean "shear stress / density", for short.)

Let us consider a boundary layer for simplicity. The characteristics of the outer part of the flow to be considered include the free-stream velocity  $U_e$  and the boundary layer thickness  $\delta$ . The irrelevance of  $U_e$ , as such, is a consequence of Galilean (translational) invariance and does not need much discussion. The irrelevance of  $\delta$  is more crucial, as it depends on the assumption that the flow close to the surface consists of eddies whose length scales (in all directions) are proportional to  $y$ , with negligible contributions from eddies whose length scales (in any direction) depend on  $\delta$ : if this is so, the boundary layer thickness should not appear in any scaling of the inner-layer eddies. We shall see in Sec. 5 that this hopeful view is not quite correct, but it is certainly acceptable to first order.

The consequence of these arguments is, of course, that the mean velocity and turbulence near the surface should scale on the "friction velocity"  $u_\tau \equiv (\tau_w/\rho)^{1/2}$ , on the distance from the surface,  $y$ , and on the kinematic viscosity  $\nu$ . One of the several dimensionally-correct ways of writing this relationship is

$$U/u_\tau = f_1(u_\tau y/\nu). \quad (1)$$

Another is obtained by differentiating Eq. (1) and hiding a factor of  $u_\tau y/\nu$  inside the function  $f_2$ , as

$$\partial U/\partial y = (u_\tau/y) f_2(u_\tau y/\nu). \quad (2)$$

Here  $u_\tau y/\nu$  is an eddy Reynolds number based on the eddy velocity and length scales, i.e. the friction velocity and the distance from the surface. At large values of this Reynolds number we expect the effects of viscosity on the turbulence to be negligible and therefore Eq. (2) reduces to

$$\partial U/\partial y = u_\tau/(\kappa y) \quad (3)$$

where  $\kappa \approx 0.41$  is a constant – Von Karman's constant, of course. The integral of this relationship is the logarithmic law, the additive constant  $C \approx 5$  being a constant of integration depending on the velocity difference between the wall and the point at which Eq. (3) becomes valid.

The advantages of the above analysis over the traditional "overlap" demonstration are (i) that the only assumption made about the outer layer is that it doesn't matter, and (ii) that a simple physical argument can be used to simplify Eq. (2) to the so-called mixing-length formula, Eq. (3).

The constant of integration  $C$  is equal to 5 only on smooth walls: on rough walls, it becomes a function of the roughness Reynolds number  $u_\tau k/\nu$  and of the roughness geometry; the uncertainty of the effective origin of  $y$  on rough walls is a further complication. The constant  $\kappa$ , on the other hand, is supposedly universal: it is the same in flows of water and of air on all geometries involving smooth surfaces, and indeed on all geometries involving only small roughness; it is the same in the atmospheric boundary layer, in the depths of the ocean and on the sands of Mars. Alas  $\kappa$  and  $C$  are not constant within the turbulence modelling community – a remarkably wide range of values is in use. Those quoted are from the painstaking data analysis of Coles<sup>2</sup>.

Now there are still textbooks – and even living people – that regard the log law as a deduction from the mixing-length formula, Eq. (3), (which it is) and also regard the mixing-length formula for the inner layer as correct (which it is) and also regard Prandtl's original derivation of the mixing-length formula by analogy with molecular motion as correct (which it certainly is not). As the Roman Catholic Church quite properly pointed out to Galileo, the success of deductions from a hypothesis does not prove its truth. Philosophers call this the fallacy *post hoc, ergo propter hoc* ("after that, therefore because of that") and it is the basis of witch-doctoring (last time we slaughtered a white cow, it rained; there is a drought: therefore...).

Quite apart from philosophical questions of falsifiability, it is clear that if a result can be derived by dimensional analysis alone, like Eq. (3), then it can be derived by almost any theory, right or wrong, which is dimensionally correct and uses the right variables. There is a strong suspicion that Prandtl got the idea of the lumps of fluid ("Flüssigkeitsballen") of mixing-length theory from visual studies of turbulent open-channel flows with particles sprinkled on the surface to show up the motion. Unfortunately the boundary condition at a free surface permits

only motion tangential to the surface and not normal to it, so the surface becomes a plane of symmetry with the vorticity vector everywhere normal to it. The only motions that can remain are what sailors, but not landlubberly turbulence researchers, call "eddies". Try it, and you will see what Prandtl saw.

### 3. Extensions to the law of the wall

The law of the wall derived in Sec. 2 is valid, or is supposed to be valid, for a shear stress equal to the wall shear stress and a density equal to the wall density. There is some support for an extended version of Eq. (3), still for  $u_* y/\nu > 30$  approx., in conditions where either the shear stress  $\tau \equiv -\rho \bar{u}v$  or the density  $\rho$  varies with distance from the surface. If  $u_*$  is replaced by  $(\tau/\rho)^{1/2}$ , we get

$$\partial U/\partial y = (\tau/\rho)^{1/2}/(\kappa y) \quad (4)$$

The hand-waving argument for Eq. (4) is that, in the original analysis leading to Eq. (3),  $u_*$  is really being used as the scale at height  $y$ , and not as a true surface parameter: if  $\tau$  varies with  $y$  then the local value, rather than the wall value, is the correct one to use in formulating an eddy velocity scale. This would be a rigorous argument only if the typical eddy size were small compared with  $y$ , so that the local shear stress would be closely equal to the right basis for a velocity scale, namely some kind of weighted-average shear stress over a  $y$  distance equal to a typical eddy size. Unfortunately, of course, the eddy size is of the same order as  $y$ .

All we can claim is that local shear stress gives the best easily-available velocity scale. Therefore, the extension of Eq. (3) to Eq. (4) requires an extension of faith in the inner-layer hypothesis which by no means all research workers possess. Nevertheless the application of Eq. (4) to flows with suction or injection, where the shear stress varies with distance from the surface according to  $\tau = \tau_w + \rho U V_w$  is quite well supported by experiment. An operational difficulty is that in typical flows with suction or injection the surface is porous, on a length scale  $h$ , say, which is usually not small compared with the viscous scale  $\nu/u_*$ , so that the "roughness" or "porosity" Reynolds number  $u_* h/\nu$  is important, implying that the additive constant in any integral of Eq. (4) will depend on the surface conditions as well as on the transpiration parameter  $V_w/u_*$ .

### 4. Compressible flow

In the inner layer of a boundary layer in compressible flow, the shear stress is approximately equal to the surface value, but the density varies quite rapidly with distance from the surface (increasing as the temperature decreases with distance from the hot wall). The "Van Driest transformation" transforms inner-layer velocity profiles to fit the incompressible log. law. The transformation is, in effect, an integral of Eq. (4) with  $\rho$  as a function of  $y$ . Here  $T$  and hence  $\rho$  come from the assumption of a constant turbulent Prandtl number: details will not be given here, but can be found in Ref. 3 and elsewhere. The Van Driest skin-friction formula is derived from the Van Driest transformation. Predictions of skin friction in compressible

boundary layers (on flat plates in zero pressure gradient, say) are currently a subject of controversy, but there are certainly no experimental data that reliably invalidate the Van Driest skin-friction formula or the Van Driest transformation. This is probably the best justification for the extension of the law-of-the-wall analysis discussed in Sec. 3, but doubtless does little for the confidence of the determinedly subsonic.

In low-speed flow, the mean (streamwise) pressure gradient, as such, has almost no effect on turbulence (see Sec. 6). In compressible flow, streamwise pressure gradients change the density of fluid elements and can produce large changes in turbulence quantities, especially, of course, in flows through shock waves (e.g. Selig et al.<sup>4</sup>). Moreover, even pressure fluctuations which are not small compared with the mean pressure can affect turbulence. Specifically, if the Mach number based upon a typical fluctuating velocity and the local speed of sound is no longer small compared to unity, there may be significant dissipation of turbulent energy via dilatation fluctuations  $\text{div} u$ , and significant correlations between fluctuations of pressure and of dilatation<sup>5,6</sup>. Measurements correlated by Birch & Eggers<sup>7</sup> show that the rate of spread of a turbulent mixing layer (in zero mean pressure gradient) starts to depend significantly on Mach number at Mach numbers close to unity. The more recent data of Papamoschou & Roshko<sup>8</sup> show even larger Mach-number dependence. This apparently contradicts the well-known finding that the behavior of compressible boundary layers can be quite well predicted by turbulence models that ignore compressibility effects (except of course that the right mean density must be used), at least for Mach numbers up to about 5. However, the typical turbulence intensity of a mixing layer is about five times that in a boundary layer, which implies that a mixing layer at  $M=1$ , where  $M$  is based on the mean velocity difference across the layer, has the same ratio of velocity fluctuation to speed of sound (a.k.a. fluctuating Mach number) as a boundary layer at roughly  $M=5$ . There is great current interest, stemming from the NASP and SCRAMJET projects, in prediction of mixing layers as the only shock-free turbulent flow for which the data show obvious effects of compressibility.

### 5. "Inactive" motion

The log-law analysis relies on the first-order hypothesis that  $u_*$ ,  $v$  and  $\nu$  are the only relevant variables, which cannot be exactly and perfectly true. If the arguments that lead to Eq. (3) are applied to the turbulent motion they lead to results for the log-law region like  $\overline{u^2}/u_*^2 = \text{constant}$ , whereas any boundary-layer experiment shows a decrease with increasing  $y$ , starting as close to the wall as  $u_* y/\nu = 17$  at typical small laboratory Reynolds numbers. This has led some people to regard the whole law-of-the-wall concept of local scaling as fallacious and its apparent success for the mean motion as fortuitous. Fortunately, this apparent discrepancy in the log-law analysis can be used to rescue the basic assumptions, by taking note of the so-called "inactive" motion<sup>9,10</sup>. The concept is simple: the motion near the surface, even though it results mainly from eddies actually generated near the surface,

is necessarily affected by eddies in the outer part of the flow (i.e. those whose length scale is of the order of  $\delta$ ). Because the pressure fluctuation at a given point in a turbulent flow is derived from an integral of the governing Poisson equation over the whole of the flow, it follows that the eddies in the outer part of the boundary layer or pipe flow can produce pressure fluctuations which extend towards the surface and cause nominally-irrotational motion in the surface layer. An equivalent, alternative, explanation is the "splat" mechanism (the origin of the term will be explained in the oral lecture) in which the large eddies in the outer flow are supposed to move towards the surface, to be reduced to rest by the normal-component "impermeability" condition at the wall, and to release their normal-component energy into the two tangential components  $u$  and  $w$ .

The "splat effect" motions, and the pressure fluctuations generated in the outer layer, have very long wavelengths in the  $x$  and  $z$  directions compared to the motions generated close to the surface. It follows from the continuity equation that the  $v$ -component velocity produced near the surface by outer-layer pressure fluctuations or large-eddy intrusions is of the order of  $y/\lambda$  times the  $u$ - or  $w$ -component velocity, where  $\lambda$  is the  $x$ - or  $z$ -component wavelength. Therefore the contribution of the "inactive" motion to the shear stress  $-\rho\bar{u}v$  is small, of the order of  $y/\lambda$  - hence the name "inactive". Note that the "inactive" fluctuations are not entirely irrotational: the boundary condition  $u = 0, v = 0$  at the surface results in the generation of a Stokes layer (see Sec. 6 on "slip velocity"). Even though "inactive"  $u$ -component fluctuations contribute significantly to  $\bar{u}^2$ , producing the anomalous  $y$ -dependence of  $\bar{u}^2$  mentioned above, the effect on the mean law of the wall is very small. (A logarithm is a slowly changing function, so that fluctuations in  $u_\tau$  have very little effect on the term  $\ln(u_\tau y/\nu)$  in the log. law, and, therefore, the time-average velocity closely follows the log. law written with time-average  $u_\tau$ .) The same arguments can be used to support the use of the log. law in unsteady-flow calculations at not-too-high amplitudes. The unsteady log. law must also be limited to not-too-high frequencies of unsteadiness: one would expect it to break down, at given  $y$ , at a frequency which was not small compared to the typical turbulence frequency  $u_\tau/y$ . Very few unsteady-flow experiments reach frequencies high enough to disturb the log. law - which is a criticism of unsteady-flow experiments in general.

The contribution of the "inactive" fluctuations to the power spectra of  $u$  and  $w$  at low wave numbers (low frequencies: wave number =  $2\pi/[\text{wavelength}]$ ) is considerable, resulting in very large differences between the measured spectra in typical turbulent flows and those predicted by inner-layer analysis. The latter predicts that the wave-number spectral density should scale on  $u_\tau$  and  $y$ , and that the wave number  $k$  should appear as  $ky$  (since we have neglected  $\nu$ , this applies only for  $u_\tau y/\nu > 30$  and at wave numbers small compared with the viscous limit, but neither restriction concerns us here). In practice, there is an apparent Reynolds-number effect at given  $u_\tau y/\nu$ : strictly it is a  $y/\delta$  effect, but  $y/\delta \equiv (u_\tau y/\nu)/(u_\tau \delta/\nu)$ .

In the atmospheric boundary layer, which is of the order of 1 km thick, the inactive-motion effects on spectra measured at the standard height of 10 m are very large, and in particular the  $u$ -component spectrum follows a  $-5/3$  power law down to very low wave numbers. This phenomenon, which is present, but less spectacular, in laboratory boundary layers, has been the cause of a large amount of confusion, controversy and difficulty, because the classical Kolmogorov scaling indicates that the spectrum should vary as  $k^{-5/3}$  only for wave numbers large compared to those of the energy-containing eddies. In the context of the atmospheric boundary layer at a height of 10 m this means wavelengths much smaller than 10 m. The fact that the experimentally-observed spectrum follows the  $-5/3$  law down to wave numbers far lower than could be expected from the arguments of inner-layer scaling and the Kolmogorov universal-equilibrium hypothesis is one of the most difficult "fallacies" in turbulent flow: it is of course a case of *post hoc ergo propter hoc*.

In summary, the qualitative idea of "inactive motion" explains both the apparent failure of inner-layer scaling and the unexpected success of the  $-5/3$  law.

## 6. "Slip velocity"

Several difficulties or misconceptions about turbulent flows over walls can be cleared up if we recall that the very thin viscous wall region  $u_\tau y/\nu < 30$  really produces what might be called a "slip velocity" between the fully-turbulent flow and the surface. As well as the obvious example of Reynolds-number (and Peclet-number) effects, they include the effects of pressure gradient, unsteadiness and change of surface roughness.

### 6.1 Effects of Reynolds number and Peclet number (viscosity and conductivity)

If the Reynolds number of a turbulent flow - based on total thickness and, say, the square root of the maximum shear stress or turbulent energy - is large, classical (e.g. Kolmogorov) theory suggests that the details of the turbulent motion should be independent of Reynolds number, except for the very smallest eddies which are responsible for viscous dissipation of turbulent kinetic energy into thermal internal energy. In this respect at least, classical theory seems to be correct, and there is no significant evidence to refute it. If the Reynolds number of a given turbulent eddy, made with its typical velocity fluctuation and its typical length scale, is large, there is no reason why viscous effects on the eddy should be significant. (This statement should strictly be phrased in statistical terms!) In a pipe flow, half the mean-square  $u$ -component intensity near the centre-line comes from wavelengths larger than the pipe diameter, so the "eddy Reynolds number" of the main energy-containing eddies is of the same order as the mean Reynolds number defined at the start of the paragraph, and we can use the former for simplicity. The "energy cascade" process of Kolmogorov theory, attributable to random vortex stretching, implies that turbulent energy is transferred from energetic eddies of low wave number (i.e. large Reynolds number) to weak eddies of high wave number (small Reynolds number), and



although back-scatter transfer from small eddies to large can occur intermittently, the time-average transfer of energy is from the large eddies to the small and there seems to be no significant "back scatter" of viscous effects.

Near a solid surface ( $y^+ > 30$ ) the largest eddies, whose wavelength is roughly equal to  $y$ , are no longer very large compared to the smallest eddies (the smallest-eddy scale, Kolmogorov's  $\eta$  or  $l_\eta$ , is about  $0.06y$  at  $y^+ = 30$ ), so the energy-containing eddies - which also carry the shear stress - start to depend on viscosity. (Also, and slightly differently, the mean velocity gradient becomes so large that viscous shear stress is a significant fraction of the total shear stress.) Therefore, viewed from the outer part of the flow, there is a viscosity-dependent region near the wall and so the velocity difference between the surface and, say,  $y/\delta = 0.1$ , depends on Reynolds number. Viewed from the outer part of the flow, there is a Reynolds-number-dependent "slip velocity" at (strictly near) the surface.

In a free shear layer (wake, jet, mixing layer...) there is no true viscous effect unless the Reynolds number is so low that turbulence can only just exist. However, free shear layers can be quite strongly dependent on the initial conditions, for long distances downstream, and since the initial conditions frequently do depend on Reynolds number there is a "pseudo-viscous" effect.

A corollary of the negligibility of viscosity as part of turbulent transport of momentum is the negligibility of conductivity in the transport of heat or mass by turbulence. Briefly (again) the "turbulent Prandtl number" is independent of the molecular Prandtl number unless the Reynolds number based on eddy velocity scale and eddy length scale, i.e.  $u_\tau y/\nu$  is small.

## 6.2 Effect of pressure gradient

Another of the standard incomprehensions about turbulent flow is the effect of (streamwise) mean pressure gradient on the turbulence as such: recall that we are considering only incompressible flow. It arises partly because experimenters tend to normalize their turbulence measurements by the local mean velocity. In adverse pressure gradient, say, the mean velocity decreases with increasing  $x$  so the normalized turbulence intensities, shear stress etc. increase. However it can easily be shown that absolute turbulence properties on a given streamline are only slightly affected by pressure gradient.

The Reynolds-stress transport equations do not contain the mean pressure (they contain correlations between the pressure fluctuation and instantaneous rate of strain, but pressure fluctuations have no connection whatsoever with the mean pressure). Also, the  $z$ -component mean vorticity  $\partial V/\partial x - \partial U/\partial y$  is unaffected by pressure gradient, and if we assume that the boundary layer approximation is valid this means that  $\partial U/\partial y$  is unaffected, even though the pressure change leads to a change in velocity all through the shear layer and thus may change  $\delta$  significantly. Alternatively, recall that a static-pressure gradient does not affect the total pressure  $P$  (on a given streamline) directly. In the simple case of two-dimensional

flow, therefore,  $\partial P/\partial \psi$ , where  $\psi$  is the stream function, is unaffected, and if  $\partial p/\partial y$  is negligible, as required by the boundary-layer approximation, a little algebra shows that  $\partial U/\partial y$  is unaffected. At the surface, where the total pressure is equal to the static pressure, there is a change in  $P$  and  $\partial U/\partial y$ , produced of course by viscous stresses. The "internal layer", in which the total pressure and mean vorticity rise to their unaffected profiles, gradually spreads out from the surface, but outside this the static-pressure gradient has no effect except to reduce the mean velocity and thus thicken the boundary layer. This result applies to laminar or turbulent boundary layers (or other wall flows such as those in tapered ducts). In summary, the initial effect of pressure gradient is confined to the "slip velocity" at the wall.

Mean pressure gradients do have some effects on the turbulent motion. Adverse pressure gradient stretches eddies in the  $y$  direction, because the shear layer thickens: however, the area, in side view, of a given eddy or fluid element is unaltered, and so if we suppose that the length scale of an eddy is just the square root of its area in side view, or the cube root of its volume, the length scale is unaltered. (This is admittedly a crude argument.) Of the terms in the Reynolds-stress transport equations, the only ones directly affected are the  $y$ -component diffusion terms, which are the derivatives of various triple products, etc., with respect to  $y$ . If the triple product on a given streamline is unaffected but the streamlines diverge in the  $x - y$  plane because of the adverse pressure gradient, the  $y$ -wise derivative is reduced.

## 6.3 Unsteadiness

The effect of unsteadiness can be understood in the same way as that of pressure gradient - of course, unsteadiness is usually forced by a streamwise pressure gradient. In the case of unsteady laminar flow the internal layer is called a Stokes layer. There are close correspondences in laminar flow between an infinite oscillating plate in still air and flow over an infinite stationary surface driven by an oscillating pressure gradient, and the qualitative correspondence carries over to turbulent flow. If the pressure gradient is strong enough to cause separation (however defined), the internal layer is carried into the outer part of the flow and the "slip velocity" concept breaks down, as it would in steady separation.

## 6.4 Change of roughness

Another occasion where a change of boundary condition affects the flow only in an "internal layer" is the flow downstream of a change in surface roughness. This is comparatively rare in aerodynamics but an important case in meteorology where, for example, air can flow from the "smooth" ocean to the land and undergo a change of apparent surface roughness. Indeed, the internal-layer concept was first proposed to describe this case. As the surface boundary condition changes, the additive constant  $C$  in the logarithmic law for a smooth surface is replaced by the appropriate value for a rough surface. The effect of this change in surface boundary condition spreads outward from the surface at an angle of the order of  $\text{rms } u/U$ , i.e.

of the order c. 3 %, so that the rate of contamination of outer-layer turbulence by inner-layer changes is no greater than about 1 or 2 degrees. Since the pressure gradient is nominally zero there is no streamline divergence above the internal layer, although the change in velocity in the internal layer produces a vertical displacement of the outer flow (upwards, in the case of a smooth-to-rough change where the flow in the internal layer is retarded).

## 7. Spectra and convection velocity

Classical turbulence theory aims to predict all the statistical properties, not simply the Reynolds stresses. In particular it deals with the statistical distribution of eddy sizes. It is usually formulated in terms of wave-number spectra, wave number being a vector with the direction of wavelength and the magnitude of  $2\pi/\text{wavelength}$ . (The alternative is two-point spatial correlations, which are less convenient mathematically.) Wave-number spectra are the Fourier transforms of the two-point correlations, but a full description requires correlations for all magnitudes and directions of the distance between the two points, or spectra for all magnitudes and directions of the wave number). In most experiments only frequency spectra, and a few correlations along the coordinate axes, are measured.

This is the best place to comment on the definition of "frequency" in turbulence. The frequency seen by an observer moving with the mean flow is (velocity scale of turbulence) / (length scale of turbulence) – for example  $u_*/y$  in the inner layer – but the frequency seen by a fixed observer is approximately (MEAN velocity) / (length scale of turbulence) and is usually much larger. The reciprocal of the moving-observer frequency is sometimes called the "eddy turnover time": this is of course an order-of-magnitude concept. A related difficulty is the status of time derivatives: all transport equations in fluid flow, including the Navier-Stokes equations, have the operator

$$\frac{\partial}{\partial t} + u_i \frac{\partial}{\partial x_i} \quad (5)$$

on the left-hand side. It is called the substantial derivative, or the transport operator, and it is the rate of change with time seen by a fluid element. The relative size of the temporal and spatial derivatives depends on the velocity of the observer but the sum of the derivatives does not.

The fixed-observer frequency is used to deduce  $x$ -component wave-number spectra from frequency spectra, using Taylor's hypothesis that the speed at which the turbulence pattern moves downstream (its "convection velocity") is closely equal to the mean velocity. It is qualitatively obvious that this will only work well if the mean velocity is large compared to the velocity scale of turbulence, so that an eddy is carried past the measurement point in a time very much less than its turnover time. A more precise analysis is possible.

There are various definitions of the actual "convection velocity" of turbulence: most are in effect phase velocities and therefore not ideal for considering convection of turbulent kinetic energy or Reynolds stress. A plausible

definition of a group (energy-transport) velocity comes from considering the streamwise (say,  $x$ -wise) "diffusion" of turbulent energy (transport of the turbulent energy by the turbulence): the energy flux rate, whose  $x$  derivative appears in the turbulent energy equation, is  $\overline{p'u/\rho} + (\overline{u^3} + \overline{uv^2} + \overline{uw^2})/2$ . Rates of energy flux due to pressure fluctuations seem to be small – except perhaps near the free-stream edge of a turbulent flow where pressure fluctuations drive an "irrotational" motion which extends outside the vortical region – and are certainly not measurable, which is some justification for neglecting them. Doing this, and writing  $\overline{q^2}$  for  $\overline{u^2} + \overline{v^2} + \overline{w^2}$ , (so that the turbulent kinetic energy is  $\overline{q^2}/2$ ), the above energy flux rate can be written as  $(\overline{u^3} + \overline{uv^2} + \overline{uw^2})/\overline{q^2}$ . We can define the transport velocity of turbulent energy as this flux rate divided by the turbulent energy. The largest contribution to the numerator is  $\overline{u^3}/2$  – though the others are not negligible – so the transport velocity is of order  $\sqrt{(\overline{q^2})} \times S_u$ , where  $S_u$  is the skewness of  $u$ . Now  $S_u$  lies in the range  $\pm 1$  approx. over most of a boundary layer, so we can finally say that the  $x$ -component transport velocity of turbulent energy is not more than a few times  $\sqrt{(\overline{q^2})}$ . Since this is the difference between the group velocity of the turbulence and the mean velocity, we see that the difference is a small percentage of the mean velocity in flows with low turbulence intensity, such as boundary layers. This quantitatively justifies the use of Taylor's hypothesis in such flows and of course allows an estimate of its inaccuracy in highly-turbulent flows.

Differences between convection velocity and mean velocity are large near the free-stream edges of mixing layers and jets. In these regions the irrotational motion, induced by pressure fluctuations generated in the high-intensity region of the flow near the inflexion point(s) in the velocity profile, is strong compared to the true (vorticity-carrying) turbulence, and its convection velocity is necessarily close to the mean velocity in the high-intensity region. The rotational motion (vorticity pattern) seems to travel at a speed close to the local mean velocity, as predicted by the above analysis (intensities near the outer edge of a jet are not large). In terms of the above analysis, the streamwise transport velocity of the vorticity pattern is still dominated by the triple-product terms, while  $\overline{p'u/\rho}$  determines the transport velocity of irrotational motion.

The de Havilland Comet I jet airliner had four engines, buried in the wing roots. The designers carefully arranged that the jets themselves would clear the fuselage, but forgot the "near field" pressure fluctuations – far more intense than the jet noise – that drive the irrotational motion. The pressure patterns, travelling at the above-mentioned convection velocity, produced fluctuating stresses at the fixed-observer frequency in the aircraft skin, which led to fatigue of the aluminium.

Later marks of Comet had the engines toed out.

Misconceptions about turbulence can be expensive!

## 8. The microscale and the Kolmogorov theory

Frequently, the Taylor "microscale" is used as a length scale in discussions of wave-number (or frequency) spectra.

The microscale  $\lambda$  is a hybrid scale of turbulence. It is usually defined by

$$\lambda^2 = \overline{u^2} / (\partial \overline{u} / \partial x)^2 \quad (6)$$

(other definitions with different choices of velocity component or gradient direction occasionally appear). This is an equation whose numerator is a property of the energy-containing turbulence, but whose denominator is a property of the dissipating eddies (if the dissipating eddies are statistically isotropic the dissipation rate is  $15\nu(\partial \overline{u} / \partial x)^2$ ). For this reason it is a misconception to regard the microscale as the length scale of any particular group of eddies: it actually lies closer to the length scale of the dissipating eddies than that of the energy-containing eddies. The Reynolds number based on the microscale and the root-mean-square turbulence intensity,  $(\overline{u^2})^{1/2}/\nu$ , however, has a more understandable meaning. If the Reynolds number is high enough for the dissipation to be equated to the isotropic formula, the microscale Reynolds number is proportional to the square root of an "eddy" Reynolds number for the energy-containing motion, based on the rms turbulence intensity and the dissipation length scale  $L \equiv (\overline{u^2})^{3/2}/\epsilon$ . Of course, this does not give the microscale the status of Eddy Length Scale *post hoc*.

It is important to notice that the "dissipation" in the definition of  $L$  is in fact the rate of transfer of turbulent kinetic energy from the large eddies to the smallest eddies which is, by all prevailing turbulence theories, supposed to be a property of the large eddies rather than the smallest eddies. The smallest eddies simply rearrange themselves to dissipate the energy handed down to them. If the turbulence is changing slowly with time (or streamwise distance) then, of course, the rate of transfer from the large eddies to the smallest eddies is equal to the rate at which energy is being dissipated by the smallest eddies, but this is not formally an equality because the "cascade" process is not instantaneous. In rapidly-changing turbulent flows the "equilibrium" arguments fail, and the rate of transfer from the energy-containing eddies to the dissipating eddies is not equal to the rate at which energy is being transferred from the dissipating eddies to heat.

This restriction on Kolmogorov's "universal equilibrium" theory, which we used in Sec. 6.1, is too often forgotten.

Another restriction of the Kolmogorov theory is that, of course, energy which is transported in the  $y$  direction by turbulent "diffusion" will be generated at small  $y$ , but dissipated at large  $y$  where the statistical properties are different. In particular, in flows with a free-stream boundary, energy is generated in regions of large mean shear and then transported in the positive  $y$  direction to regions of zero or negligible mean shear before being dissipated. The energy transfer through the inertial subrange at the second location is likely to be intermediate between the dissipation rates at the two locations.

Nevertheless results from a large number of experiments on turbulent shear layers have recently been analysed<sup>11</sup> to show that Kolmogorov scaling works remark-

ably well when adjusted for the intermittency factor  $\gamma$  (the fraction of time for which the flow at a given location is turbulent). In an intermittent region, the average of any turbulence quantity within the turbulent part of the flow is  $1/\gamma$  times the conventional average over all time. For example the conventional-average spectral density and the dissipation  $\epsilon$  must both be multiplied by  $1/\gamma$ . However the Kolmogorov "-5/3" law for the spectral density in the so-called inertial subrange contains  $\epsilon^{2/3}$  so that, formally, there is a spare factor of  $\gamma^{1/3}$  and we certainly do not expect the Kolmogorov law to hold if written with conventional-average quantities. The data analysis of Ref. 11 shows that the Kolmogorov formula still works for a wide range of intermittent flows when written for the turbulent part of the flow, i.e. taking account of the "spare factor", and using the dissipation rate at the local value of  $y$ . Since the formula strictly applies only to nearly-homogeneous turbulence, and an intermittent region, almost by definition, contains only one large eddy at a time, this result is a surprising testimonial to the robustness of the Kolmogorov theory. Needless to say, the usual cautions about *post hoc* apply.

## 9. Turbulence modelling

### 9.1 Normal pressure gradients

An incomprehension entirely unrelated to turbulence, which nevertheless causes confusion in tests of turbulence models, is the effect of normal pressure gradient on boundary layers and other shear layers. If the shear layer obeys the boundary layer approximation then, by definition, the pressure gradient in the  $y$  direction is negligibly small. However, if in a real flow the normal pressure gradient is not negligible, there will be a velocity gradient  $\partial U / \partial y$  even in the external stream (where the total pressure is constant) and this velocity gradient will, in principle, lead to extra production of turbulence via the product of mean velocity gradient and turbulent shear stress. Of course, the same effects would be found within the shear layer  $y < \delta$ , but would be less easily identified. Therefore, even if a turbulence model produces exactly correct predictions of the shear stress - given the mean velocity profile as input - it will not give acceptable results in the case where normal pressure gradients affect the mean velocity gradient. (Recall that the boundary-layer momentum equation can be written as  $dP/dx = d\tau/dy$ .) This is probably a much more important reason for inaccuracy of predictions based on the boundary layer approximation in rapidly-growing flows near separation than the often-quoted presence of significant normal-stress gradients.

### 9.2 Universality

Perhaps the biggest fallacy about turbulence is that it can be reliably described (statistically) by a system of equations which is far easier to solve than the full time-dependent three-dimensional Navier-Stokes equations. Of course the question is what is meant by "reliably", and even if one makes generous estimates of required engineering accuracy and requires predictions only of the Reynolds stresses, the likelihood is that a simplified model of tur-

bulence will be significantly less accurate, or significantly less widely applicable, than the Navier-Stokes equations themselves – i.e. it will not be “universal”.

Irrespective of the use to which a model will be put, lack of universality may interfere with the calibration of a model. For example, it is customary to fix one of the coefficients in the model dissipation-transport equation so that the model reproduces the decay of grid turbulence accurately. This involves the assumption that the model is valid in grid turbulence as well as in the flows for which it is intended – presumably shear layers, which have a very different structure from grid turbulence.

It is becoming more and more probable that really reliable turbulence models are likely to be so long in development that large-eddy simulations (from which, of course, all required statistics can be derived) will arrive at their maturity first. (The late Stan Corrsin once described the process of turbulence modelling as a “trek to determinacy”.) Certainly, over the last twenty years the rate of progress in turbulence modelling has been pretty small compared to the rate of progress in development of digital computers, and the consequent increase in Reynolds-number range and geometrical complexity attainable by simulations. Until recently, most work has concentrated on “complete” simulations, covering the whole range of eddy sizes, while large-eddy simulations, which alone offer the prospect of predictions at high Reynolds numbers, have been somewhat neglected.

### 9.3 Eddy viscosity and gradient transport

Turbulence models which invoke an eddy viscosity (of whatever type) necessarily produce pseudo-laminar solutions with the stresses closely linked to the mean-flow gradients: they may be well-behaved but they are not usually very accurate away from the flows for which they have been calibrated. Turbulence models based on term-by-term modelling of the Reynolds-stress transport equations produce solutions which may be accurate in some cases, but are liable to fail rather badly in other cases: that is, they are “ill-behaved” in a way that eddy-viscosity methods are not.

It may be this “reliable inaccuracy”, rather than the larger computer resources needed for Reynolds-stress transport models, which has led to two-equation (e.g.  $k, \epsilon$ ) or even one-equation methods being the industry standard. With all goodwill to my friends Barrett Baldwin and Harv. Lomax, the one-equation Baldwin-Lomax turbulence model has been extended – by others – far beyond its intended domain, simply because it has the virtue of almost never breaking down computationally!

It has, of course, often been said that it is just as unreliable and unrealistic to define an eddy viscosity entirely in terms of turbulence properties (as in the  $k, \epsilon$  method) as to define it entirely in terms of mean-flow properties as in the Baldwin-Lomax method. Eddy viscosity is the ratio of a turbulence quantity (i.e. a Reynolds-stress) to a mean-flow quantity (i.e. a rate of strain or velocity gradient), so, like the microscale, it is a hybrid quantity.

Minor fallacies in turbulence modelling abound, but misuse of gradient-transport hypotheses is probably responsible for more than its fair share. One of the most spectacular was the use many years ago, by authors I will not identify, of the gradient-transport approximation for diffusion of turbulent energy by pressure fluctuations. In terms of classical physics, anything less likely than pressure diffusion to obey a gradient-transport approximation could scarcely be imagined. A fallacy which has, in charity, to be regarded as a deliberate approximation, is the use – even in Reynolds-stress transport models – of the eddy-diffusivity (gradient-transport) approximation for the turbulent transport terms. It appears that most of the turbulent transport of Reynolds stress is provided by triple products of velocity fluctuations, rather than by the pressure diffusion just mentioned, and therefore a gradient-transport approximation is not so obviously unphysical.

### 9.4 The dissipation-transport equation

Most turbulence models, whether relying on an eddy viscosity or on the Reynolds-stress transport equations, use the dissipation-transport equation to provide a length scale or time scale of the turbulent flow. Strictly, the length scale or time scale required is that of the energy-containing Reynolds-stress-bearing eddies, not that associated with the dissipating eddies as such, and so two questions arise. One is whether the rate of dissipation is adequately equal to the rate of energy transfer from the large eddies (which clearly, is the quantity that we really want to model); the other is whether, if we really pretend to be using the dissipation transport equation – all of whose terms depend on the statistics of the *smallest* eddies – we can logically model those terms by using the scales of the larger, energy-containing eddies. I think it is inescapable that current models of the so-called dissipation transport equation, which certainly do parameterize the terms as functions of the large-eddy scales, start out with the dissipation-transport equation as such and end up with a totally-empirical transport equation for the energy transfer rate. In other words, the relation between the “dissipation” transport models and the exact transport equation for turbulent energy dissipation is so tenuous as not to need consideration. Unfortunately, even Reynolds-stress transport models usually employ this suspect dissipation-transport equation to provide a length scale, and this is undoubtedly one of the reasons why Reynolds-stress transport models have not outstripped two-equation models. A less-used alternative to the  $\epsilon$  equation is the  $\omega$  equation (admitted to be totally empirical).  $\omega$  is nominally proportional to  $\epsilon/k$  where  $k$  is the turbulent kinetic energy, but conversion from one to the other (in either direction) produces the interesting result that the turbulent transport terms in the transport equation for the first quantity (the integral of transport terms over the flow volume being by definition zero) convert to a transport term plus a “source” term in the equation for the second quantity. There is increasing evidence that using  $\omega$  to provide a length scale gives better results than using  $\epsilon$ : if there is a reason other than more judicious choices of empirical coefficients, it must lie in the above-mentioned source term.

## 9.5 Invariance

One of the customary requirements of a turbulence model is that it should be "invariant" (with respect to translation or rotation of axes). The boundary layer (thin-shear layer) equations are not invariant: it is therefore quite unrealistic to expect a shear-layer model to be totally invariant, and it is perfectly realistic to suppose that the direction normal to the shear-layer ( $y$ ) is a special direction. There seems to be no reason why a turbulence model should not, given an identifiable "special direction" in a shear-layer use that special direction for orientation of its empirical constants and functions. Even though equations (such as the Navier-Stokes equations or the time-average Reynolds equations) may be invariant, the boundary conditions for which they are to be satisfied certainly are not invariant (almost by definition). Therefore, the solutions of the exact, or approximate, equations of motion of turbulent flow cannot be expected to be invariant with respect to translation or rotation. From this it is a rather small step to argue that the empirical constants or functions in these model equations should, again, be released from invariance requirements.

## 9.6 Local modelling of pressure-fluctuation terms

The mean products of fluctuating pressure and fluctuating rates of strain that act as redistribution terms in the Reynolds-stress transport equations represent, very crudely speaking, the effect of eddy collisions in making the principal Reynolds stresses more nearly equal – that is, making the turbulence more nearly isotropic (statistically). The shear stress in isotropic turbulence is zero, so the effect of the pressure-strain terms on the shear stress, and their modelling, is of great interest.

Pressure fluctuations within a turbulent flow are one of the Great Unmeasurables: they are of the order of  $\rho u^2$  and so, unfortunately, are the pressure fluctuations induced on a static-pressure probe by the velocity field. That is, the signal-to-noise ratio is of the order of one. To say that signals cannot be deduced even with  $S/N = O(1)$  is itself a fallacy, but in this case the attempts made to do so have not met with general acceptance. Pressure fluctuations can be extracted from simulations, but these are confined to low Reynolds number.

An equation for the pressure (mean and fluctuating) can be obtained by taking the divergence of the Navier-Stokes equations. It is a Poisson equation, and it is necessary in turbulence modelling to consider the different terms on the right-hand side separately, by writing a Poisson equation for each and adding the solutions to get the pressure. One such is the equation for the "rapid" pressure, which for a two-dimensional boundary-layer flow is

$$\frac{\nabla^2 p}{\rho} = -2 \frac{\partial U}{\partial y} \frac{\partial v}{\partial x} \quad (7)$$

The "rapid" pressure is so called because it responds immediately to a change in the mean flow, as represented by  $\partial U / \partial y$ . To regard this apparently-surprising fact as physically meaningful is a misconception: it is just a result of

the way we take averages, and, obviously, the turbulence at a given instant does not know what the mean flow is. A highly symbolic solution of the equation is

$$\frac{p'}{\rho} = -2 \nabla^{-2} \frac{\partial U}{\partial y} \frac{\partial v}{\partial x} \quad (8)$$

where  $\nabla^{-2}$  is a weighted integral over the whole flow volume. In other words, the "rapid" pressure at a given point, and its contribution to the pressure-strain terms at that point, depend on conditions for a distance of several typical eddy length scales around that point – i.e. they are "non-local". The same non-locality accounts for the presence of irrotational velocity fluctuations outside the turbulent motion.

Almost all current stress-transport turbulence models, with the exception of that of Durbin<sup>12</sup>, model the pressure-strain terms and other pressure-velocity correlations entirely as functions of local quantities. (All the other terms in the Reynolds-stress transport equations are genuinely local quantities.) This is equivalent to replacing Eq. (8) by

$$\frac{p'^B}{\rho} = -2 \frac{\partial U}{\partial y} \nabla^{-2} \frac{\partial v}{\partial x} \quad (9)$$

– that is, evaluating  $\partial U / \partial y$  at the position where  $p'$  is required and volume-integrating only  $\partial v / \partial x$ .

In Ref. 13, the behavior of existing models for the pressure-strain terms was analyzed, using simulation data in a duct flow to evaluate the terms directly. The results, surprisingly, suggest that the difference between the exact pressure-strain terms, using  $p'$  from Eq. (8), and the approximate results, using  $p'^B$  from Eq. (9), is negligibly small (or, at least, small enough to be hidden in the empirical coefficient in the pressure-strain model) except in the viscous wall region. Within the viscous wall region, the difference between the true pressure fluctuation  $p'$  and the approximate pressure fluctuation  $p'^B$  is not only very large but eccentrically behaved. It is not suggested that viscous effects, arising from the  $v = 0$  boundary condition at the surface, are directly to blame: it is much more likely that the effects of the  $v = 0$  boundary condition are mainly responsible, but it is surprising that these effects should be small outside the viscous wall region. A final possibility is that the changes in turbulence structure with  $u_\tau y / \nu$  in the viscous wall region are so large as to invalidate local models.

This suggests not only that standard pressure-strain models are grossly inaccurate in the viscous wall region, but also that any extension of a standard turbulence model into the viscous wall region will be similarly inaccurate. This inaccuracy can be camouflaged by the insertion of "low-Reynolds-number" functions, nominally functions of the wall distance  $u_\tau y / \nu$ . Obviously, if the real flow scales with  $u_\tau y / \nu$ , this simple procedure suffices, but if the flow approaches, or goes beyond, separation then inner-layer scaling – and presumably "low-Reynolds-number" models – break down, even if  $u_\tau y / \nu$  is replaced by the guaranteed-real quantity  $k^{1/2} y / \nu$ .

## 10. Chaos

"What kept you?" you may ask. Chaos has been one of the buzzwords in applied mathematics in recent years, and turbulence is often cited as the supreme example. The complication of turbulent motion, with its broad spectrum of wavelengths, is far greater than that of the "chaotic" solutions of some low-order systems of coupled ordinary differential equations. Analysis of simulation data<sup>14</sup> suggests that the dimension of the turbulence attractor (roughly, the number of modes or "degrees of freedom" needed to represent the turbulent motion) is several hundreds at least, even at the lowest Reynolds number at which turbulence can exist. The upper bound on the dimension is, roughly, the number of totally-arbitrary modes (say, Fourier modes or finite-difference formulae) needed to represent the motion. Now since direct-simulation calculations need, typically,  $128^3 \approx 2 \times 10^6$  Fourier or finite-difference points for flows at a very modest laboratory-scale Reynolds number, we can take the upper bound of the attractor dimension as being of this order: for the barely-turbulent flow of Ref. 13,  $32^3 \approx 30000$  might do. Large-eddy simulations need fewer points:  $128^3$  might do for any Reynolds number, at least if the viscous wall region did not have to be resolved. These are all impracticably large estimates of the attractor dimension.

However, several authors have based their work on the classically incorrect syllogism "Solutions of some equations with few degrees of freedom yield complicated behavior: turbulence has complicated behavior: therefore turbulence may be represented by the solution of equations with few degrees of freedom". The last hypothesis of course stood by itself for many years B.C. (before chaos), and a great deal of brain power has been applied to prove it - i.e. to produce a usable small set of modes to describe turbulence - but without great success: the most ambitious efforts require an amount of computing time which is not much less than that of a large-eddy simulation.

The concepts of chaos theory may of course be qualitatively useful in turbulence studies. One is the concept of predictability. Qualitative arguments about the non-linear Navier-Stokes equations suggest that if two almost identical turbulence fields with the same boundary conditions are set up at time  $t = 0$ , then the two instantaneous velocity and pressure fields will become more and more different at time goes on, even though the statistical properties of the two fields will still be (nearly) equal. To a worker in turbulence, particularly an experimenter, this does not seem odd - but the issue of instantaneous versus statistical predictability has attracted a lot of attention in chaos studies, and perhaps our intuition about the Navier-Stokes equations may be put on a firmer footing. Deissler<sup>15</sup> reviews applications of chaos studies in fluid dynamics; for a popular introduction to chaos studies in general, see the book by Gleick<sup>16</sup>; and see also, of course, the new interdisciplinary journal "Chaos".

## 11. Conclusions

In this paper, we have gone all the way from very basic

questions of turbulence theory to the important practical question of the reliability of turbulence models, and then ended in chaos. The fallacies that we have discussed do not necessarily form a coherent story, but I think it can be said that most of them fall into the general category of wishful thinking - the hope of finding simple solutions to a difficult problem. I will end with one of my favorite quotations, from H. L. Mencken, "to every difficult question there is a simple answer - which is wrong".

## References

- <sup>1</sup> Goldstein, S., "The Navier-Stokes Equations and the Bulk Viscosity of Simple Gases", *J. Math. and Phys. Sci., University of Madras*, vol. 6, 1972, pp. 225-261.
- <sup>2</sup> Coles, D., "The Young Person's Guide to the Data", *Computation of Turbulent Boundary Layers - 1968 AFOSR-IFP-Stanford Conference*, vol. II (D.E. Coles and E.A. Hirst, Eds.), Thermosciences Division, Stanford University, 1969, pp. 1-45.
- <sup>3</sup> Bradshaw, P., and Cebeci, T., *Physical and Computational Aspects of Aerodynamic Flows*, Springer-Verlag, New York, 1984.
- <sup>4</sup> Selig, M., Andreopoulos, J., Muck, K., Dussauge, J. and Smits, A.J., "Turbulence Structure in a Shock Wave/Turbulent Boundary Layer Interaction", *AIAA J.*, Vol. 27, 1989, pp. 862-869.
- <sup>5</sup> Sarkar, S., Erlebacher, G., Hussaini, M.Y., and Kreiss, H.O., "The Analysis and Modeling of Dilatational Terms in Compressible Turbulence", *J. Fluid Mech.*, Vol. 227, 1991, pp. 473-493.
- <sup>6</sup> Zeman, O., "Dilatation Dissipation - the Concept and Application in Modeling Compressible Mixing Layers", *Phys. Fluids A*, Vol. 2, 1990, pp. 178-188.
- <sup>7</sup> Birch, S.F., and Eggers, J.M., "A Critical Review of the Experimental Data for Developed Free Turbulent Shear Layers", *NASA SP-321*, 1973, pp. 11-37.
- <sup>8</sup> Papamoschou, D., and Roshko, A., "The Compressible Turbulent Shear Layer - an Experimental Study", *J. Fluid Mech.*, Vol. 197, 1989, pp. 453-477.
- <sup>9</sup> Townsend, A.A., "Equilibrium Layers and Wall Turbulence", *J. Fluid Mech.*, Vol. 11, 1961, pp. 97-116.
- <sup>10</sup> Bradshaw, P., "Inactive Motion and Pressure Fluctuations in Turbulent Boundary Layers", *J. Fluid Mech.*, Vol. 30, 1967, pp. 241-258.
- <sup>11</sup> Kuznetsov, V.R., Praskovsky, A.A., and Sabelnikov, V.A., "Intermittency and Fine-Scale Turbulence Structure in Shear Flows", presented at *Eighth Symposium on Turbulent Shear Flows*, Munchen, 1991.
- <sup>12</sup> Durbin, P.A., "Near Wall Turbulence Closure Modeling Without 'Damping Functions'", *NASA Ames-Stanford Center for Turbulence Research Manuscript 112*, 1990.
- <sup>13</sup> Bradshaw, P., Mansour, N.N., and Piomelli, U., "On

Local Approximations of the Pressure-Strain Term in Turbulence Models", *Proceedings of the Summer Program 1987, NASA Ames-Stanford Center for Turbulence Research, 1987*, pp. 159-164.

- <sup>14</sup> Keefe, L., "Connecting Coherent Structures and Strange Attractors", *Near-Wall Turbulence - 1988 Zaric Memo-*

*rial Conference* (S.J. Kline and N.H. Afgan, Eds.), Hemisphere, Washington, 1990.

- <sup>15</sup> Deissler, R.G., "On the Nature of Navier-Stokes Turbulence", *NASA Tech. Memo.* 109183, 1989.  
<sup>16</sup> Gleick, J., *Chaos: Making a New Science*, Penguin Books, New York, 1988.

### 364-365] *Damping of Vibrations in a Spherical Vessel* 651

It is to be noticed that the ratio of (8) to (12) is of the order  $\sqrt{(ac/v)}$ , numerical factors being omitted. In all cases to which our approximations apply this ratio is large, so that the radial vibrations are much more slowly extinguished, so far as viscosity alone is concerned, than those which correspond to values of  $n$  greater than 0. This is readily accounted for. In the latter modes the condition that there is to be no slipping of the fluid in contact with the vessel implies a relatively greater amount of distortion of the fluid elements, and consequent dissipation of energy, in the superficial layers of the gas.

The method of the dissipation function, which was applied in Art. 346 to the case of water waves, might be used to obtain the result (12) for the radial vibrations, but would lead to an erroneous result for  $n > 0$ , since the underlying assumption that the motion is only slightly modified by the friction is violated at the boundary.

In the gravest radial vibration we have  $ka = 4.493$ , whence

$$\tau = -0.743 \frac{a^2}{\nu}.$$

In the case of air at 0° C. this makes  $\tau = .56\text{sec}^*$ .

#### *Turbulent Motion.*

365. It remains to call attention to the chief outstanding difficulty of our subject.

It has already been pointed out that the neglect of the terms of the second order ( $u\partial u/\partial z$ , &c.) seriously limits the application of many of the preceding results to fluids possessed of ordinary degrees of mobility. Unless the velocities, or the linear dimensions involved, be very small the actual motion in such cases, so far as it admits of being observed, is found to be very different from that represented by our formulae. For example, when a solid of 'easy' shape moves through a liquid, an irregular eddying motion is produced in a layer of the fluid next to the solid, and a trail of eddies is left behind, whilst the motion at a distance laterally is comparatively smooth and uniform.

The mathematical disability above pointed out does not apply to cases of *rectilinear* flow, such as have been discussed in Arts. 330, 331; but even here observation shews that the types of motion investigated, though always theoretically possible, become under certain conditions practically unstable.

The case of flow through a pipe of circular section was made the subject of a careful experimental study by Reynolds†, by means of filaments of coloured fluid introduced into the stream. So long as the mean velocity ( $w_0$ ) over the cross-section falls below a certain limit depending on the radius of the pipe and the nature of the fluid, the flow is smooth and in accordance

\* This Art. is derived with slight alteration from a paper cited on p. 636.

† "An Experimental Investigation of the Circumstances which determine whether the Motion of Water shall be Direct or Sinuous, and of the Law of Resistance in Parallel Channels." *Phil. Trans.* t. cxxxv. p. 935 (1883) [*Papers*, t. ii p. 51]. For a historical account of the researches and partial anticipations of other writers, see Knibbe, *Proc. Roy. Soc. N.S.W.* t. xxxi. p. 314 (1897). Reference is made in particular to Hagen, *Berl. Abh.* 1854, n. 17.

**TRANSITION AND TURBULENCE MODELLING, 1**  
**SESSION 1**



# The Transition Prediction Toolkit: LST, SIT, PSE, DNS and LES

Thomas A. Zang\*

NASA Langley Research Center, Hampton, VA

Chau-Lyan Chang,<sup>†</sup>

High Technology Corporation, Hampton, VA

and

Lian L. Ng,<sup>‡</sup>

Analytical Services & Materials Inc., Hampton, VA

## Abstract

The  $\epsilon^N$  method for predicting transition onset is an *amplitude ratio* criterion that is on the verge of full maturation for three-dimensional, compressible, real gas flows. Many of the components for a more sophisticated, *absolute amplitude* criterion are now emerging: receptivity theory, secondary instability theory, parabolized stability equations approaches, direct numerical simulation and large-eddy simulation. This paper will provide a description of each of these new theoretical tools and provide indications of their current status.

## 1 Introduction

Robust tools for predicting the location of the onset of transition in boundary layers on aerospace vehicles have obvious technological importance. For practical engineering purposes one desires a prediction tool which is quantitatively and not just qualitatively correct: the issue is not *whether* transition occurs but *where*. At present transition prediction tends to be based on simple correlations, such as crossflow Reynolds number or  $Re_\theta/M$ ; modified one- or two-equation turbulence models which seek to translate the freestream turbulence level into computations of laminar-transitional-turbulent flow; and linear stability theory.

The pioneering work of Smith & Gamberoni [1] and Van Ingen [2] introduced an empirical method for estimating the location of transition onset based on an *amplitude ratio* criterion. This tool has come to be known as the  $\epsilon^N$

method or the  $N$ -factor method. The next level of transition prediction methodology is likely to involve an *absolute amplitude* criterion. In order to achieve this goal, many more physical effects must be taken into account and more analysis tools must be utilized.

The seeds of transition are the disturbance environment in which the vehicle operates. Transition is born by the receptivity process in which the background disturbances are incorporated within the boundary layer as linear instability waves. It is nurtured by a relatively long region of linear instability growth. Once secondary instability effects develop, they induce rapid growth, and at a sufficiently high amplitude the nonlinear regimes are entered and transition commences, as signified by, say, the skin friction or heat transfer rise.

Characterization of the disturbance background is a prerequisite for an absolute amplitude criterion. Both amplitude and spectral information are required. This is necessarily an experimental task and will not be addressed further in this paper.

The theoretical and computational tools which can now be brought to bear on the transition problem include Receptivity Theory, Linear Stability Theory (LST), Secondary Instability Theory (SIT), Parabolized Stability Equations approaches (PSE), Direct Numerical Simulation (DNS), and Large-Eddy Simulation (LES).

Receptivity theory is a very active area of current research. The essential problem is that the freestream disturbances often have much longer length scales than the instability waves in boundary layers. Therefore, the incorporation of background disturbances into boundary-layer instability waves requires a wavelength conversion mechanism. A variety of linear and asymptotic techniques have been applied to this problem. We refer the reader to [3]-[8] for some recent work in this field. The latter two articles are particularly concerned with compressible flow.

This paper furnishes a brief description of the remainder

\*Senior Research Scientist

<sup>†</sup>Research Scientist.

<sup>‡</sup>Research Scientist. Present Address: Boeing Commercial Airplane Group, Seattle, Washington.

This paper is declared a work of the U.S. Government and is not subject to copyright protection in the United States.

of these tools and provides examples of recent work. We shall limit ourselves to illustrating these methods for supersonic flows, and shall highlight some recent results from the theoretical and computational transition program at the NASA Langley Research Center.

## 2 Governing Equations

The starting point for these analysis tools is, of course, the compressible Navier-Stokes equations. In dimensionless form the equations for a thermally and calorically perfect gas are

$$\begin{aligned} \frac{\partial \rho}{\partial t} + \frac{\partial(\rho u_k)}{\partial x_k} &= 0 \\ \frac{\partial u_k}{\partial t} + \frac{\partial(u_k u_l)}{\partial x_l} &= -\frac{1}{\rho} \frac{\partial p}{\partial x_k} + \frac{1}{\rho Re} \frac{\partial \sigma_{kl}}{\partial x_l} \\ \frac{\partial p}{\partial t} + u_k \frac{\partial p}{\partial x_k} + \gamma p \frac{\partial u_k}{\partial x_k} &= \frac{1}{M_e^2 Pr Re} \frac{\partial q_k}{\partial x_k} + \frac{\gamma - 1}{Re} \Phi \\ \gamma M_e^2 p &= \rho T. \end{aligned} \quad (1)$$

where

$$\sigma_{kl} = -\frac{2}{3} \mu \frac{\partial u_m}{\partial x_m} \delta_{kl} + \mu \left( \frac{\partial u_k}{\partial x_l} + \frac{\partial u_l}{\partial x_k} \right) \quad (2)$$

is the viscous stress tensor,

$$q_k = \kappa \frac{\partial T}{\partial x_k} \quad (3)$$

is the heat flux, and

$$\Phi = \frac{\partial u_k}{\partial x_l} \sigma_{kl} \quad (4)$$

is the viscous dissipation. The Reynolds number is denoted by  $Re$ , the Prandtl number by  $Pr$ , the Mach number at the boundary-layer edge by  $M_e$ , and the ratio of specific heats by  $\gamma$ . (For all the examples in this paper  $\gamma = 1.4$ .) In these equations  $\rho$  is the density,  $\mathbf{u} \equiv (u_1, u_2, u_3) = (u, v, w)$  the velocity,  $p$  the pressure, and  $T$  the temperature. We shall denote the solution vector by  $\mathbf{q} = (\rho, u, v, w, p)$ . The coordinate system is chosen so that  $\mathbf{x} \equiv (x_1, x_2, x_3) = (x, y, z)$ , where  $x$ ,  $y$ , and  $z$  are the streamwise, spanwise, and wall-normal coordinate directions, respectively.

In this paper, most dependent variables are normalized with respect to their boundary-layer edge values;  $p$  is scaled by  $\rho_e^* u_e^{*2}$ . Distances are scaled by the variable  $L^* = (\nu_e^* x^*/u_e^*)^{1/2}$ . The superscript  $*$  characterizes a dimensional quantity, the subscript  $e$  indicates a value at the edge of a boundary layer,  $u$  is the streamwise velocity, and  $\nu$  is the kinematic viscosity. The viscosity,  $\mu^*$ , is assumed to be given by the Sutherland formula.

Although results will be presented here for flat plates, cylinders and cones, the equations and notation will be given just for the flat plate. See [9] for the appropriate equations for the more general situation.

## 3 Linear Stability Theory

The techniques of compressible linear stability theory are quite well known; see, for example, [10]. The starting point is a laminar mean flow,  $\mathbf{q}_0$ . In most cases an approximate mean flow is utilized, e.g., a quasi-parallel solution of the boundary-layer equations. One must then imagine that an appropriate forcing term has been added to Eq. (1). See [11] for a recent discussion. The total flow field,  $\mathbf{q}(\mathbf{x}, t)$ , is written as

$$\mathbf{q}(\mathbf{x}, t) = \mathbf{q}_0(z) + A(\mathbf{q}_1(z) e^{i(\alpha x + \beta y - \omega t)} + \text{c. c.}) \quad (5)$$

The streamwise and spanwise wave numbers are denoted by  $\alpha$  and  $\beta$ , respectively, and  $\omega$  is the (temporal) frequency. The complex amplitude function,  $\mathbf{q}_1(z)$ , determines the structure in the wall-normal direction. The compressible Navier-Stokes equations are then linearized about the mean flow to first-order in the amplitude  $A$ . When combined with appropriate boundary conditions, an eigenvalue problem results.

The spanwise wavenumber is invariably taken to be real. In temporal theory,  $\alpha$  is real and  $\omega$  is the (complex) eigenvalue, with  $\omega$  the spatial growth rate. In the spatial concept,  $\omega$  is real and  $\alpha$  is the eigenvalue, with  $-\alpha_i$  the spatial growth rate. In many cases the simpler temporal theory is applied, and the spatial growth rate approximated by  $-\alpha_i = \omega_i/c_g$ , where  $c_g$  is the group velocity of the wave. The linear instability is referred to as the *primary* instability.

Some recent developments for compressible flow include incorporation of non-parallel effects through multiple-scale techniques [12], real gas effects [13], proper shock-wave boundary conditions [14], and clarification of some issues regarding propagation of three-dimensional waves [15].

The  $N$ -factor method is applied by first computing the laminar mean flow past the body of interest and then applying LST to that flow. For a given frequency,  $\omega$ , the streamwise location at which a wave first becomes unstable,  $x_0$ , is identified and then the spatial growth rate is integrated downstream to produce the  $N$ -factor:  $N(\omega) = \int_{x_0}^x (-\alpha_i) dx'$ . (Note that if the amplitude of the instability at  $x_0$  is denoted by  $A_0$ , then the amplitude at  $x$  is given by  $A/A_0 = e^{N(\omega)}$ ; thus,  $e^{N(\omega)}$  measures the amplitude ratio.) This calculation is performed for a range of frequencies, and for each  $x$ , the maximum over  $\omega$ , denoted

by just  $N$ , is taken.

The estimate of transition onset is based upon an empirical correlation between  $N$  and the location of transition. The  $N$ -factor method has had a surprising degree of success, even considering its limitations, such as inapplicability to flows in a high disturbance background for which the linear instability regime is "by-passed". The  $N$ -factor method has matured to the point at which an analysis capability is imminent for transition estimation across the speed range (including real gas effects) and for arbitrary steady three-dimensional mean flows.

The computer requirements for solving a single LST eigenvalue problem are inconsequential. Even application of the  $N$ -factor method to a three-dimensional mean flow requires only on the order of an hour of supercomputer time. However, a non-trivial related task is computation of an accurate mean flow. LST requires accurate (and oscillation-free) mean flows and this is a far more stringent requirement than is customary in conventional steady-state CFD. This can take many tens of supercomputer hours for a three-dimensional configuration.

## 4 Secondary Instability Theory

Secondary instability theory picks up where LST leaves off. In SIT one includes some weakly nonlinear (and three-dimensional) effects. One considers the linear stability with respect to secondary disturbances of a base flow comprised of a laminar mean flow (assumed locally parallel) modulated by a small (but finite) amplitude primary disturbance. SIT is now well-established for incompressible flow. See Herbert [16] for a thorough review of the subject. In recent years it has been extended and applied to compressible boundary layers in [17], [18], [19], and [20]. Here we review some of the developments discussed in [20].

The frequency, wavelength, and shape of the primary disturbance are obtained using LST. The primary wave is assumed to have no growth during the evolution of the secondary disturbance. In a Galilean frame,  $x^+ = x - c_r t$ , moving with the phase velocity,  $c_r$ , of the primary wave, the total flow variable,  $q$ , can be written in the Floquet form

$$q = q_b + \epsilon \Re \left\{ e^{\sigma t} \epsilon^{\gamma x^+} e^{i\beta_2 y} e^{ih \frac{\alpha_1}{2} x^+} \sum_{j=-\infty}^{\infty} q_{2,j}(z) e^{ij\alpha_1 x^+} \right\}, \quad (6)$$

where  $q_b$  is given by Eq. (5). Hereafter, the subscripts 0, b, 1, and 2 refer, respectively, to the laminar mean flow, the modulated base flow, the primary disturbance, and the secondary disturbance. The primary wave amplitude,  $A$ ,

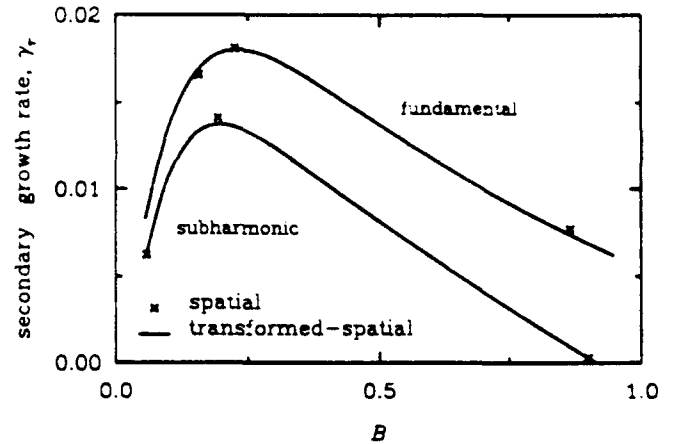


Figure 1: Variation of  $\gamma_r$  with  $B$  when  $M_e = 1.6$ . Fundamental at  $A = 2.9\%$ . Subharmonic at  $A = 1.5\%$ .

is defined so that it corresponds to the maximum value of the perturbation mass flux. The equations governing the secondary disturbance are obtained by linearizing Eq. (1) about the modulated base flow. The discretized disturbance equations are converted into a complex algebraic eigenvalue problem for  $\sigma$  or  $\gamma$  and their associated eigenfunctions. In temporal theory,  $\gamma = 0$  and  $\sigma \neq 0$  is the complex eigenvalue to be determined. In the spatial concept, we write  $\sigma = \gamma c_r$  in Eq. (6) and solve for  $\gamma$  as the eigenvalue [16]. The temporal and spatial growth rates are given by the real parts of  $\sigma$  and  $\gamma$ , respectively. The detuning parameter,  $h$ , defines the type of secondary instability. The subharmonic modes are given by  $h = 1$ , while the fundamental modes correspond to  $h = 0$ . In practice the sum in Eq. (6) includes from 2 to 5 modes.

As one example, consider the boundary layer over an insulated flat plate at Mach number  $M_e = 1.6$ , Reynolds number  $Re = 1050$ , Prandtl number  $Pr = 0.72$ , and temperature  $T_e = 216^\circ$  Rankine. The primary wave is slightly damped, and is located near branch two of the neutral stability curve with  $\alpha_1 = 0.1471$  and  $F \equiv 10^6 \times \omega_1 / Re = 82.6$ . For clarity, the secondary growth rate obtained from the temporal theory, which has been converted to a spatial growth rate by using the transformation  $\gamma_r = \sigma_r / c_r$ , is termed the "transformed-spatial" growth rate. In many cases of interest both the dominant fundamental and subharmonic travel synchronously with the primary, i.e.,  $\gamma_i = 0$ .

In Fig. 1, the secondary growth rate is plotted as a function of the normalized spanwise wavenumber  $B \equiv 10^3 \times \beta_2 / Re$ . (For constant boundary-layer edge conditions, the parameter  $B$  signifies a wave of fixed spanwise wavelength as it propagates downstream.) The "transformed-spatial" growth rate agrees well with the (true) spatial growth rate. The most amplified subhar-

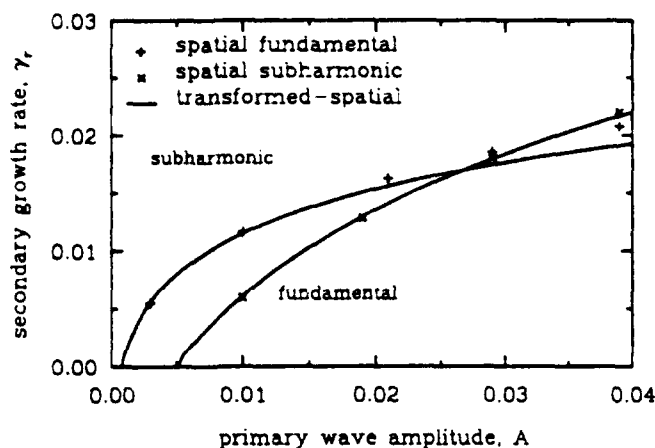


Figure 2: Variation of  $\gamma_r$  with  $A$  when  $M_e = 1.6$ .

monic disturbance consists of a pair of oblique waves traveling at equal and opposite angles at about  $70^\circ$  to the mean-flow direction. The most unstable fundamental disturbance is comprised of a stationary mode, which represents a spanwise periodic distortion of the mean flow, and a pair of oblique waves propagating in opposite directions at about  $57^\circ$  to the mean-flow direction.

Figure 2 depicts the typical catalytic effect of the primary amplitude on the growth rates of the secondary disturbances. The spanwise wavenumbers,  $B$ , of the subharmonic and the fundamental are 0.19 and 0.22, respectively; these particular values of  $B$  correspond roughly to the most amplified secondary disturbances. The subharmonic instability prevails over the fundamental instability in an environment with a primary amplitude,  $A$ , of less than about 2.8%, while the converse is true for higher values of  $A$ . The transformed-spatial growth rates of the subharmonic modes are almost identical to the spatial rates for small  $A$  — the former increasingly underpredicts the latter as  $A$  increases from 1.5%.

The preceding behavior is expected, since the use of temporal data to approximate spatial growth becomes less accurate when the growth rate is relatively high. Still, the transformation of temporal data to approximate the spatial growth rates of fundamental resonance modes is surprisingly accurate even for a primary amplitude as high as 4%.

The second example, given in Fig. 3, corresponds to a laminar boundary layer on an insulated 7-degree half-angle sharp cone at  $M_e = 6.8$ . The parameters are  $Re = 1939$ ,  $T_e = 128^\circ$  Rankine,  $Pr = 0.70$ . The primary disturbance is axisymmetric and is of the "second mode" type with  $\alpha_1 = 0.2788$  and  $F = 135$ . The two sets of calculations also serve to contrast the secondary instability

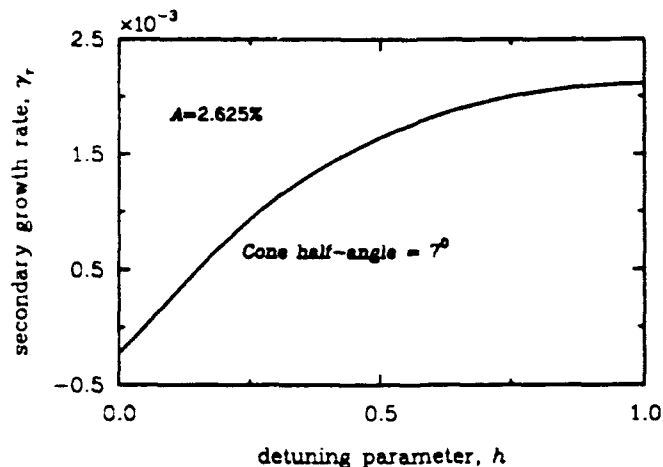


Figure 3: Effect of the detuning parameter on  $\gamma_r$ .  $M_e = 6.8$  and  $B = 0.135$ .

arising from a first-mode primary (at  $M_e = 1.6$ ) with that arising from a second-mode primary (at  $M_e = 6.8$ ). Over a range of Mach numbers up to at least 6.8, subharmonic secondary instability ( $h = 1$ ) is found to prevail in a low primary-disturbance environment. This is especially true for high-speed flows. In particular, as illustrated in Fig. 3, no fundamental instability ( $h = 0$ ) for  $M_e = 6.8$  exists even for a primary amplitude of 2.625%. In fact, both the first- and second-mode primary waves associated with high-speed flows have been found ineffective in catalyzing unstable fundamental resonance modes.

Recent developments in SIT include incorporation of non-parallel effects (but only for the evolution of the primary wave) [17]. Ng & Erlebacher [19] have developed a fairly general capability which allows for oblique primary waves (important at low supersonic Mach number, where the most unstable primary is oblique).

SIT has greater computational requirements than LST — the matrix eigenvalue problems which must be solved are larger than in LST. Nevertheless, a solution can be obtained in minutes on a supercomputer.

## 5 Parabolized Stability Equations

As a consequence of the rapid growth of the secondary wave, many harmonic waves, including the mean flow correction mode, are excited to large amplitudes, and eventually strongly nonlinear effects ensue; the flow then becomes transitional. Although SIT furnishes a guide to mechanisms that may be present near transition onset, it does not at present account for many non-parallel effects, and it incorporates only the lowest level non-linearity.

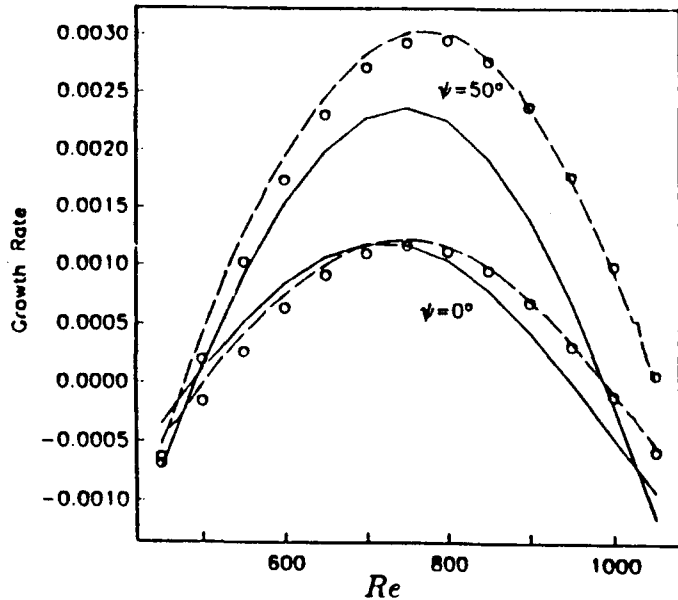


Figure 4: PSE computation of the effect of non-parallel mean flows for both 2-D and 3-D disturbances of a  $M_e = 1.6$  flow at  $F = 40$ . (Solid lines are from parallel LST, dashed lines from PSE calculations, and symbols are from multiple-scales analysis [12].)

One efficient method which does incorporate both non-parallel and non-linear effects is the parabolized stability equations approach, first suggested by Herbert and Bertolotti [21], [22]. The PSE method facilitates the solution of the full partial differential equations for the disturbances by employing a partial parabolization along the dominant flow direction. In this approach, the disturbance is decomposed into a wave part and a shape function part. The elliptic terms are retained for the wave part, whereas the governing equations for the shape function are parabolized in the streamwise direction. The parabolized equations for the shape function are then solved numerically by a marching procedure. The wave properties are extracted from a local analysis. Nonlinear terms are formulated as forcing functions for the corresponding linear equations. Because the equation set contains non-parallel as well as nonlinear terms, the PSE method governs the spatial evolution of disturbances from the linear stage up to the transitional stage.

The PSE approach has been successfully applied to the stability of supersonic two-dimensional boundary layers by Bertolotti & Herbert [23] and Chang *et al.* [24]. In the linear regime, the method provides a means to include non-parallel effects due to the growth of the boundary layer, which is ignored in traditional LST. Furthermore, non-

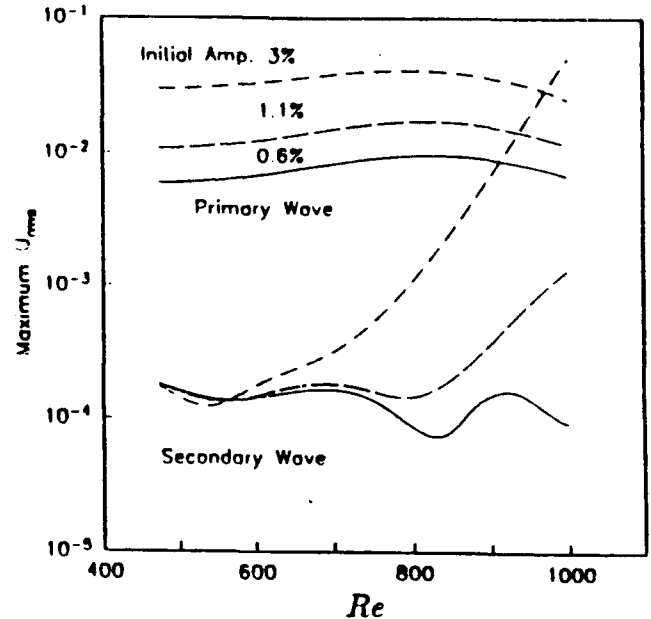


Figure 5: PSE amplitude evolution of the primary and subharmonic waves at  $M_e = 1.6$ ,  $F = 50$ , and  $B = 0.053$ .

linear effects such as wave/wave interaction or secondary instability can be simulated by the non-linear PSE.

To demonstrate the applicability of the PSE approach, we present some of the results given in [24]. Linear PSE calculations were performed for a Mach 1.6 flat-plate boundary layer previously studied by El-Hady [12]. The frequency of the disturbances is  $F = 40$ . Calculations were performed for both 2-D and 3-D linear disturbances; the wave angle for the oblique, 3-D waves was about  $50^\circ$ . The growth rate of the mass flow fluctuations from the PSE calculations together with the multiple-scales results are plotted along with the growth rates obtained by quasi-parallel LST in Fig. 4. PSE results agree quite well with those obtained from the multiple-scales approach. The results also indicate that for the first mode disturbance at Mach 1.6, flow non-parallelism has more effect on three-dimensional disturbances than on two-dimensional ones. The non-parallel effect on oblique waves is qualitatively very similar to that in incompressible flows, as found by Bertolotti [21].

Compressible non-linear PSE computations for secondary instability mechanisms and the subsequent start of laminar breakdown have also been demonstrated. The flow is again a Mach 1.6 flat-plate boundary layer with a primary disturbance frequency of  $F = 50$ . The free-stream temperature is  $540^\circ$  Rankine and the Prandtl number is  $Pr = 0.71$ . Figure 5 shows the evolution of primary and subharmonic disturbances for various initial amplitudes of

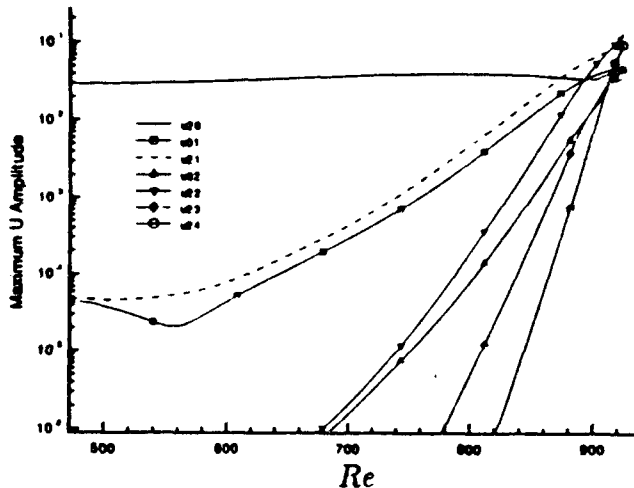


Figure 6: PSE amplitude evolution of various Fourier modes for a  $M_e = 1.6$  fundamental breakdown

the primary waves (the subharmonic amplitudes are the same for all three cases). The spanwise wave number of the subharmonic mode is fixed at  $B = 0.053$ , which corresponds to an oblique wave angle of  $45^\circ$ . As can be seen, a 1.1% initial amplitude for the primary mode is enough to trigger the secondary growth.

Non-linear PSE calculations were also performed for the same Mach 1.6 case but for a fundamental-type secondary resonance. The initial amplitude of the primary wave is again 3% and that of the secondary is taken to be 0.005%. The spanwise wave number is  $B = .152$  (oblique wave angle of  $60^\circ$  for the secondary wave) and the primary wave frequency is again  $F = 50$ . The non-linear evolution of the maximum rms amplitude of  $u'$  (a prime is used to denote the fluctuating part of a variable) is shown in Figure 6. Clearly, the presence of the primary 2-D and secondary 3-D disturbances results in wave resonance and strong secondary growth of the oblique wave. When the secondary disturbance is amplified to about the same amplitude of the primary wave, all harmonics are excited and the flow becomes transitional. This is confirmed by plotting the average wall shear in Figure 7. The computed wall shear is only slightly above the laminar value for most of the computational domain. (The PSE wall shear lies above the laminar value right from the beginning because of the relatively high initial amplitude of the 2-D primary disturbance.) Eventually the wall shear departs sharply from the laminar value, indicative of transition onset. Thus, the PSE computation captures the skin friction rise, which is one of the criteria for transition onset; accurate prediction of its location is a prime goal of transition prediction methods.

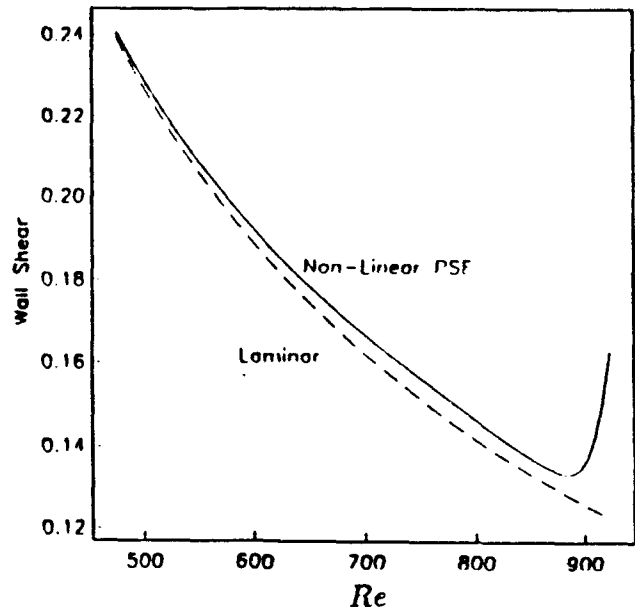


Figure 7: PSE wall shear of laminar and perturbed flows for a  $M_e = 1.6$  fundamental breakdown.

Linear PSE computations (equivalent to non-parallel LST) are quite cheap. Nonlinear PSE can compute up to the skin friction rise in no more than an hour of supercomputer time. However, current numerical techniques for nonlinear PSE have computational requirements which scale quadratically with both the number of spanwise Fourier components and the number of temporal frequencies retained in the approximation. This means that PSE computations for the later stages of transition and for random inflow and/or freestream conditions are exceedingly expensive.

The SIT and PSE tools that have been described up to this point are oriented towards *forced* transition, i.e., transition characterized by sharply defined frequencies as might occur from specific forcing. The technologically interesting problem is that of *natural* transition, for which a broad range of frequencies is present. To capture the nonlinear interaction between a wide range of frequencies, DNS and LES are currently the most appropriate tools.

## 6 Direct Numerical Simulation

Direct numerical simulation solves the time-dependent, three-dimensional, nonlinear, Navier-Stokes equations subject to prescribed initial and boundary conditions without recourse to empirical models. A thorough review of this approach has been given by Kleiser & Zang [25].

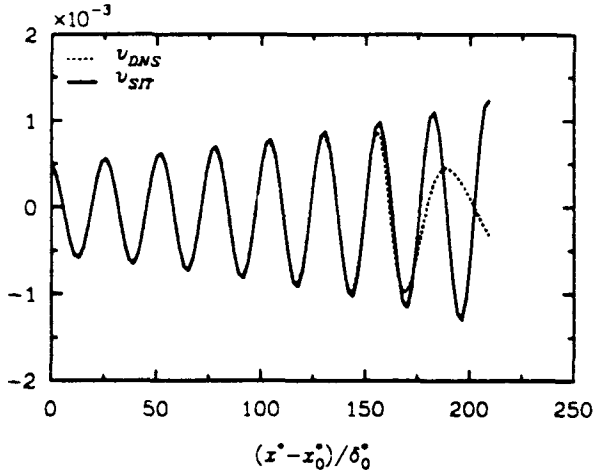


Figure 8: Spatial SIT vs. DNS for a  $M_e = 1.6$  fundamental instability.

When attacked as the total boundary-layer transition problem – from receptivity through fully-developed turbulence – the non-parallel, spatial formulation is certainly more appropriate than the temporal approximation. However, DNS for the complete transition process is an exceedingly expensive tool even for the low Reynolds numbers to which it is of necessity restricted. Gilbert & Kleiser [26] performed the first well-resolved simulation of the complete transition to turbulence and this took several hundred supercomputer hours for a temporal computation of forced incompressible transition. With somewhat relaxed resolution requirements Rai & Moin [27] have recently computed bypass transition for low-speed flow past a flat plate. This required many hundreds of supercomputer hours and it remains to be seen what the requirements are for a well-resolved computation for this problem. For the foreseeable future, both temporal and spatial DNS have a role, but this tool ought to be applied selectively.

One role for DNS is the corroboration of simpler tools, such as SIT and PSE. For compressible flows it has been used to verify temporal SIT [19], [9], spatial SIT [20], and some aspects of nonlinear PSE [24]. Given the algebraic complexity of SIT and PSE, particularly for oblique primaries, this role is a needed one to establish confidence in them. (It also furnishes a stringent calibration of DNS.)

One comparison between spatial (but quasi-parallel) SIT and DNS by Ng & Zang [20] was performed for a fundamental type instability at  $M_e = 1.6$ ,  $Re = 613$ ,  $Pr = 0.70$ , and  $T_e = 520^\circ$  Rankine. The primary wave is a 2-D first mode with frequency  $F = 73$ . The subharmonic secondary wave has spanwise wavenumber  $B = 0.1465$ . The amplitude of the primary is chosen to be 6%, while that of the secondary is 0.1%. Although the spatial DNS code is designed for non-parallel flow, for comparison with

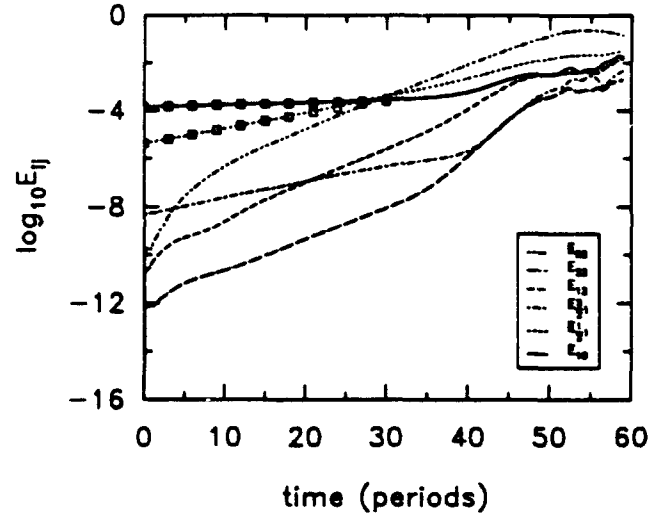


Figure 9: Evolution of selected harmonics from DNS of  $M_e = 4.5$  cylinder subharmonic transition.

the quasi-parallel SIT theory the mean flow was constrained to be parallel by using a forcing function. The initial conditions consisted solely of the laminar mean flow. At the inflow boundary,  $x^* = x_0^* = u_e^* L^{*-2} / \nu_e^*$ , the flow consisted of the mean flow plus the appropriate contributions from the linear and secondary eigenfunctions. The physical domain consisted of 8 wavelengths of the primary wave, with “buffer domain” modifications [28] to the Navier-Stokes equations in the last 2 wavelengths used to ameliorate potential difficulties with the outflow boundary conditions. (See [20] for details.) Figure 8 shows the spanwise velocity component,  $v$ , at  $z = 0.26^*$ , where  $\delta^*$  is the displacement thickness, and  $\beta_2 y = \pi/2$  after 10 periods of forcing; this component is due solely to the secondary instability. The agreement between the DNS and SIT results is excellent, except, of course, in the buffer domain.

This computation utilized 12 points per streamwise wavelength. For transition in high-speed flows the growth rates of both primary and secondary disturbances are lower than for incompressible flow. As a consequence on the order of  $10^2$  wavelengths would be needed to follow the primary/secondary stages from about the 1% level to the skin friction rise. This is a prohibitive expense and argues strongly for the use of simpler methods such as SIT and especially PSE for routine application to the early stages of transition.

The unique niche for DNS is the highly nonlinear, laminar breakdown stage and the subsequent transition to turbulence; for this the non-parallel effects appear to be less significant than they are for the rather lengthy primary and secondary instability stages. These early stages are nowadays treated far more efficiently by SIT and PSE ap-

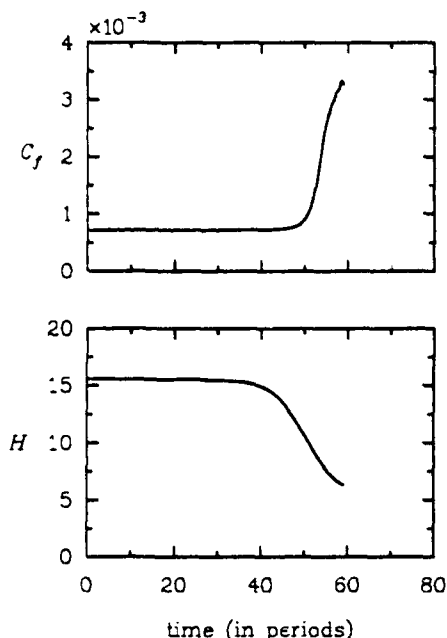


Figure 10: Skin friction and shape factor from DNS of  $M_e = 4.5$  cylinder subharmonic transition.

proaches than by DNS. Indeed, the simpler theories can well be used to set the stage for the DNS: LST selects the dominant primary instability (and determines the relevant streamwise scales); SIT and/or PSE select the dominant spanwise scales and can be used to “jump start” the DNS at fairly high disturbance levels.

This is the approach that was taken by Pruett & Zang [29] in their temporal DNS of transition in Mach 4.5 flow past a cylinder. The primary disturbance was a second mode and the secondary disturbance was of subharmonic type. Due to the periodicity assumptions in the streamwise ( $x$ ) and spanwise ( $y$ ) directions, the dependent variables have Fourier series representations in these directions. A useful measure of the strength of a given Fourier harmonic is

$$E_{k_x, k_y}(t) = d_{k_x} d_{k_y} \int_0^\infty \rho_0(z) |\hat{\mathbf{u}}_{k_x, k_y}(z, t)|^2 dz, \quad (7)$$

where  $\hat{\mathbf{u}}_{k_x, k_y}$  is the Fourier coefficient of the velocity corresponding to wavenumbers  $k_x$  and  $k_y$  (with respect to  $\alpha_1$  and  $\beta_2$ , respectively);

$$d_k = 2 - \delta_{k0} \quad (8)$$

accounts for some of the symmetries in the problem. The quantity  $E_{k_x, k_y}$  is approximately the kinetic energy of the  $(k_x, k_y)$  mode.

Figure 9, taken from [29], summarizes the time evolution of the principal modes for the Mach 4.5 cylinder sim-

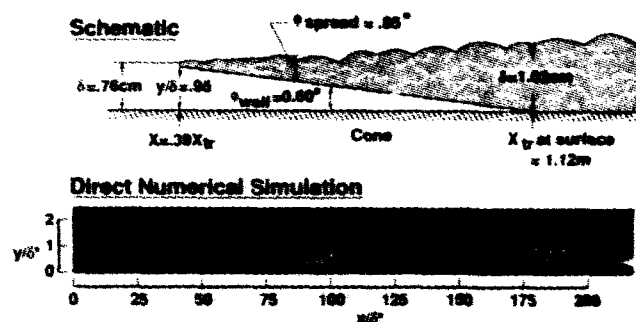


Figure 11: Cartoon of the precursor transition effect (top) [30] and its manifestation in the spatially-reconstructed Reynolds stress from DNS of  $M_e = 6.8$  cone subharmonic transition (bottom).

ulation. (Time is reckoned in units of the period of the primary wave.) The DNS proceeded through the stages of primary/secondary instability then underwent weakly nonlinear and strongly nonlinear stages, and finally commenced laminar breakdown. The stages cited above last from 0-15, 15-35, 35-45 and 45-60, respectively. The symbols on the figure are the predictions from LST and SIT for the growth of the primary and secondary disturbances. They are in good agreement with the DNS. One interesting feature of this simulation is the prominence that the  $(0, 2)$  mode assumes in the latter stages of transition. This mode is not present in the initial conditions (nor in SIT) and is generated by nonlinear effects. Additional DNS have revealed that this mode plays an essential role in the final laminar breakdown.

Figure 10 shows the evolution of the skin friction,  $C_f$ , and the shape factor,  $H$ , for the Mach 4.5 cylinder transition. This simulation was stopped at about 60 periods because of strong gradients that even its million grid points could not resolve. Indeed, the judgment of Pruett & Zang [29] was that the resolution became questionable after 55 periods. This resolution problem intensifies as Mach number increases, and in a particular computation may eventually manifest itself in negative values of some of the thermodynamic quantities. This particular difficulty does not arise for low-speed DNS. For compressible flow the dilemma is that highly-accurate central-difference schemes do not have sufficient artificial viscosity to resolve strong gradients at high Reynolds number, whereas conventional upwind CFD schemes are so dissipative that they corrupt the delicate physics of transition. An encouraging recent development is the work of Atkins [30], which demonstrated good results for a compressible free shear layer transition using a fifth-order ENO scheme.

The shape factor plot suggests that the simulation



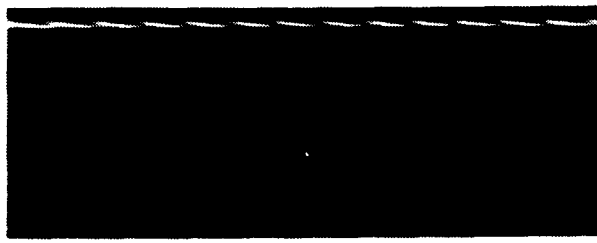
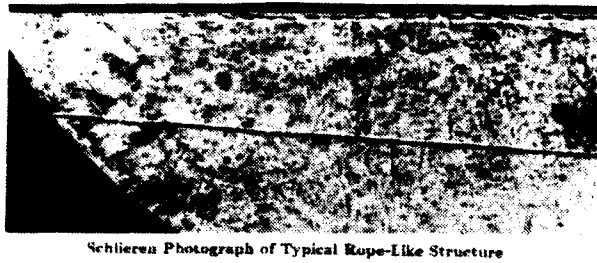


Figure 12: Experimental (top) [32] and DNS (bottom) [25] visualizations of the rope-like structures in supersonic transition.

has proceeded almost completely through the transition process. Figure 11 presents the spatially-reconstructed streamwise velocity fluctuations, as represented by the Reynolds-stress component  $\tau_{11} = -\overline{\rho u' u'}$ , from a Mach 6.8 cone simulation [29]. These exhibit the so-called “precursor transition effect”, sketched in the cartoon in the top part of the figure, whereby the transition originates near the boundary-layer edge and gradually propagates toward the wall. This same effect is present in the DNS. Flow-field visualizations presented in Fig. 12 demonstrate the presence in the Mach 4.5 cylinder DNS of the “rope-like structures” that have been observed in numerous experiments ([31],[32],[33]). One of the more significant conclusions of [29] was that the rope-like structures are actually manifestations of SIT and not LST, as had long been suspected.

A last sample of results from this DNS is presented in Fig. 13. It illustrates the evolution of the turbulent kinetic energy,  $k$ , and the turbulent dissipation,  $\epsilon$ , through the transition region. This kind of information, supplemented by detailed information on the key terms in the evolution equations for these quantities, has the potential to lead to substantial improvements in two-equation models for transitional flow. However, DNS (particularly spatial DNS) is so computationally intensive that a less drastic, but still effective, tool for exploring the later stages of transition would be quite desirable. The following section describes

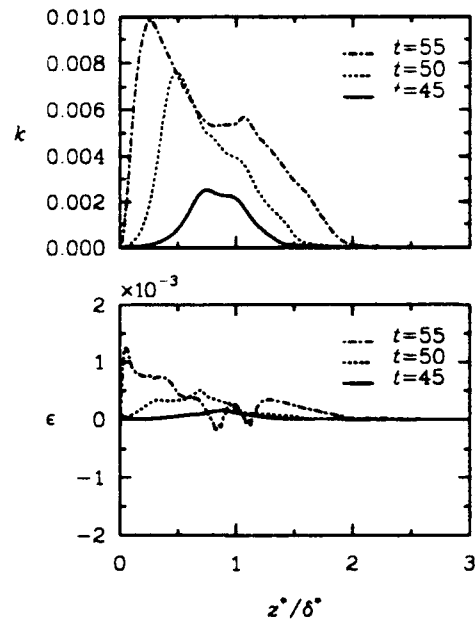


Figure 13: Evolution of turbulent kinetic energy and dissipation for  $M_e = 4.5$  cylinder subharmonic transition.

a promising candidate.

## 7 Large-Eddy Simulation

In large-eddy simulation the small *scales* of the flow are modeled in terms of the large-scale flow. The Reynolds-averaged Navier-Stokes equations, in contrast, model the higher-order *moments* in terms of the lower-order moments. In LES the flow variables are decomposed into a large-scale (resolvable) component and a small-scale (subgrid-scale) component. LES was originally developed for turbulent flow (see [34] for a survey of the state-of-the-art in LES), and, at least with the more established subgrid-scale (SGS) models, some refinements have proven necessary to handle transitional flow properly. In the transitional case one not only wants to have a model which works well for the final turbulent state, but also one which captures the primary, secondary and nonlinear stages correctly (without, for example, exerting excessive damping of the instability waves), predicts well the location of transition onset, and makes good predictions from transition onset through the transitional zone to the fully turbulent state. Piomelli and co-workers ([35], [36], [37], [38]) have led the effort to utilize DNS of transition to calibrate and refine SGS models for this process. This work has to date been confined to incompressible flow. In this section we describe some recent developments for compressible transition modeling via LES.

The large-scale field is defined by the filtering operation:

$$\bar{\mathcal{F}}(\mathbf{x}) = \int G(\mathbf{x}, \mathbf{x}') \mathcal{F}(\mathbf{x}') d\mathbf{x}'. \quad (9)$$

where the integral is extended over the entire spatial domain and  $G = \bar{G}_1 \bar{G}_2 \bar{G}_3$ , where  $\bar{G}_i(x_i)$  is the filter function in the  $i$ th direction. For the velocity and temperature, Favre filtering is utilized:  $\mathcal{F} = \bar{\mathcal{F}} + \mathcal{F}'$ , where  $\mathcal{F}'$  is the SGS part of  $\mathcal{F}$  and the Favre filter is defined by  $\bar{\mathcal{F}} = \overline{\rho \mathcal{F}} / \bar{\rho}$ . The sharp Fourier cutoff filter is chosen for this work because of previous experience with this filter in LES of incompressible transition ([35]).

The dimensionless governing equations for compressible LES are

$$\begin{aligned} \frac{\partial \bar{\rho}}{\partial t} + \frac{\partial(\bar{\rho} \bar{u}_k)}{\partial x_k} &= 0 \\ \frac{\partial(\bar{\rho} \bar{u}_k)}{\partial t} + \frac{\partial(\bar{\rho} \bar{u}_k \bar{u}_l)}{\partial x_l} &= -\frac{\partial \bar{p}}{\partial x_k} + \frac{\partial \bar{\sigma}_{kl}}{\partial x_l} + \frac{\partial \tau_{kl}}{\partial x_l} \\ \frac{\partial \bar{p}}{\partial t} + \bar{u}_k \frac{\partial \bar{p}}{\partial x_k} + \gamma \bar{p} \frac{\partial \bar{u}_k}{\partial x_k} &= \frac{1}{M_e^2 Pr Re} \frac{\partial \bar{q}_k}{\partial x_k} \\ + \frac{\gamma-1}{Re} \bar{\Phi} + \frac{1}{M_e^2} \frac{\partial Q_k}{\partial x_k} + (\gamma-1) \bar{u}_k \frac{\partial \bar{p}}{\partial x_k} &- (\gamma-1) \bar{u}_k \frac{\partial \bar{p}}{\partial x_k} \\ \gamma M_e^2 \bar{p} &= \bar{\rho} \bar{T}. \end{aligned} \quad (10)$$

The SGS stress tensor  $\tau_{kl}$  and the SGS heat flux  $Q_k$  are defined by  $\tau_{kl} = -\bar{\rho}(\bar{u}_k \bar{u}_l - \bar{u}_k \bar{u}_l + \bar{u}_k' \bar{u}_l' + \bar{u}_l' \bar{u}_k' + \bar{u}_k' \bar{u}_l')$  and  $Q_k = -\bar{\rho}(\bar{u}_k \bar{T} - \bar{u}_k \bar{T} + \bar{u}_k' \bar{T}' + \bar{u}_k' \bar{T}')$ .

There have been a number of SGS models proposed for compressible LES ([39], [40], [41], [42]). Two of these models have been applied to the Mach 4.5 transition problem discussed in the preceding section.

The first SGS model considered is the SEZHu model derived by Speziale *et al.* [40] for compressible isotropic turbulence. This model has been chosen because there are now available some extensive *a posteriori* comparisons of its performance on compressible, isotropic turbulence ([44], [45]). Following the work of Piomelli *et al.* [46], only the Smagorinsky portion of the SEZHu model is used with the Fourier cutoff filter. (This filter is applied in  $x$  and  $y$ ; no filtering is applied in the inhomogeneous  $z$  direction.) Hence, the SGS stress model is of the form

$$\tau_{kl} = 2 C_R \mathcal{D} \Gamma \bar{\rho} \Delta^2 II_{\bar{S}}^{1/2} \left( \bar{S}_{kl} - \frac{1}{3} \bar{S}_{mm} \delta_{kl} \right), \quad (11)$$

and the SGS heat flux is given by

$$Q_k = -\frac{C_R \mathcal{D} \Gamma \bar{\rho}}{Pr_T} \Delta^2 II_{\bar{S}}^{1/2} \frac{\partial \bar{T}}{\partial x_k}, \quad (12)$$

where

$$\mathcal{D} = \left( 1 - e^{-z^+/25} \right)^2, \quad (13)$$

$\bar{S}_{kl} = (\partial \bar{u}_k / \partial x_l + \partial \bar{u}_l / \partial x_k) / 2$  is the Favre-filtered rate-of-strain tensor and  $II_{\bar{S}} = \bar{S}_{mn} \bar{S}_{mn}$  is its second invariant.  $C_R$  is the compressible Smagorinsky constant.  $Pr_T$  is the turbulent Prandtl number, and  $\Delta = (\Delta x \Delta y \Delta z)^{1/3}$ . The function  $\Gamma$  is an intermittency-like term that turns itself on slowly in the transitional zone [35]. Eq. (13) represents a Van Driest wall damping and  $z^+$  indicates a wall-normal distance made dimensionless by the wall shear velocity and kinematic viscosity.

The second SGS model considered here is the structure function model [43], which is based on a physical space implementation of the concept of spectral eddy viscosity. Some results for this model have been reported for a spatial LES of a Mach 5 boundary layer [41]. The structure function model is of the following form for the SGS shear stress and heat flux:

$$\tau_{kl} = C_R \mathcal{D} \Gamma \bar{\rho} \Delta x \sqrt{\bar{F}_2(\mathbf{x}, \Delta x, \Delta y, t)} \times \left( \bar{S}_{kl} - \frac{1}{3} \bar{S}_{mm} \delta_{kl} \right) \quad (14)$$

$$Q_k = -\frac{C_R \mathcal{D} \Gamma \bar{\rho} \Delta x}{Pr_T} \sqrt{\bar{F}_2(\mathbf{x}, \Delta x, \Delta y, t)} \frac{\partial \bar{T}}{\partial x_k}, \quad (15)$$

where

$$\begin{aligned} \bar{F}_2 = & \frac{1}{4} (||\mathbf{u}(\mathbf{x} + \Delta \mathbf{x}, y, z, t) - \mathbf{u}(\mathbf{x}, y, z, t)||^2 \\ & + ||\mathbf{u}(\mathbf{x}, y, z, t) - \mathbf{u}(\mathbf{x} - \Delta \mathbf{x}, y, z, t)||^2 \\ & + \frac{\Delta x}{\Delta y} (||\mathbf{u}(\mathbf{x}, y + \Delta y, z, t) - \mathbf{u}(\mathbf{x}, y, z, t)||^2 \\ & + ||\mathbf{u}(\mathbf{x}, y, z, t) - \mathbf{u}(\mathbf{x}, y - \Delta y, z, t)||^2)) \end{aligned} \quad (16)$$

Although neither Van Driest wall damping nor the intermittency term were in the structure function model as used in [41], they were added here as they seem to furnish better results.

The structure-function SGS model was tested *a posteriori* both with and without the "intermittency" function, and a comparison is given in Fig. 14 for the primary and secondary components. (In the latter case  $\Gamma = 1$ .) The coefficients for these runs were  $C_R = 0.06$ , which is the value recommended in [41], and  $Pr_T = 0.70$ . The LES used  $10^4$  grid points, two orders of magnitude fewer than the DNS. The original structure function model is clearly far too dissipative in the early stages, whereas the modified model agrees very well with the high-resolution DNS. In this respect these results are similar to those reported in [35] for the original and modified Smagorinsky model when applied to incompressible transition. The integral properties are in quite good agreement with those of the high-resolution DNS up to  $T = 55$ ; they are summarized

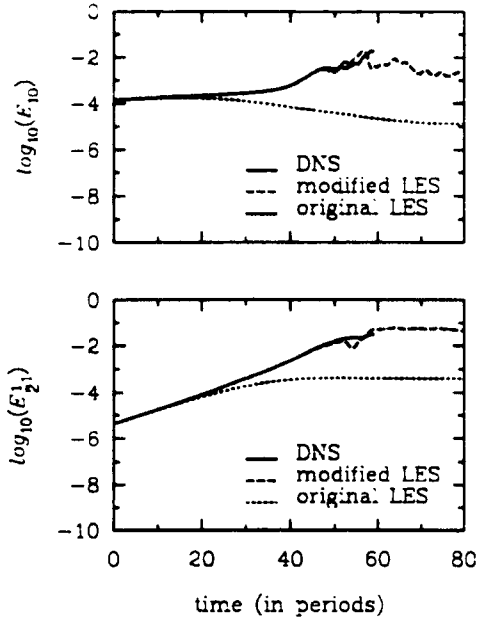


Figure 14: Comparison of unmodified and modified structure function for LES of  $M_e = 4.5$  cylinder transition.

in Figure 15. Note that the computation reaches the fully turbulent regime.

For the SEZHu model the nominal coefficient is  $C_R = 0.011$  [44]. However, on the same grid as was used for the previous LES computations this had to be increased to  $C_R = 0.50$  in order to compute all the way through to turbulence. The reason for this is not entirely clear at present. It might be that the larger value of the Smagorinsky constant serves to provide artificial viscosity needed to stabilize the computation, or it might be due to the much smaller length scales involved in second mode transition. The later stages of the DNS suggest that for the turbulent state the computational box, in wall units, was 240 in  $x$  and 150 in  $y$ , as opposed to typical values from incompressible flow of 2000 and 1000, respectively.

Kral & Zang [47] have performed some LES of a Mach 4.5 turbulent boundary layer with computational domains closer to the standard incompressible sizes. Here they found that reasonable results could be obtained with the constants  $C_R$  closer to the accepted incompressible values. It appears that application of the dynamic eddy viscosity concept [37] to this problem would be quite fruitful.

The potential of LES for transition is that it permits computations through the transitional zone at an order of magnitude or more lesser expense than for DNS. A discussion of what sort of information can be reliably provided by LES and DNS is given in [48]. For incompressible flow, demonstrations are needed for spatial transition; for com-

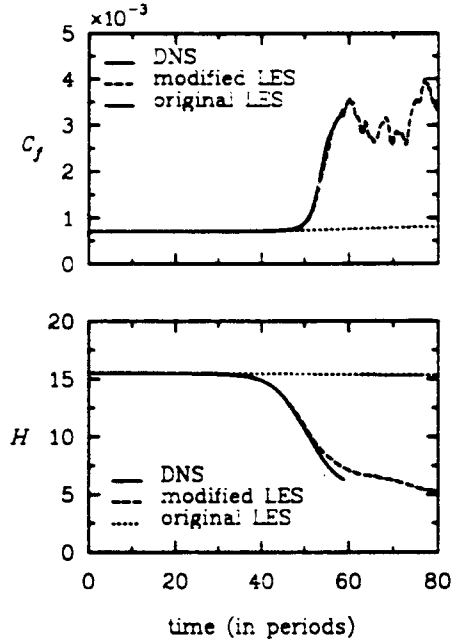


Figure 15: Evolution of skin friction and shape factor for LES of  $M_e = 4.5$  cylinder transition.

pressible flow, the role of the SGS viscosity needs clarification: To what extent is it furnishing artificial viscosity rather than serving its intended purpose of modeling the physics?

## 8 Prospects

The past several years have witnessed many exciting developments in transition research, particularly for compressible flow, that make an absolute amplitude criterion for prediction of transition onset a tantalizing prospect. Many of the components of such a methodology have been discussed in this paper. LST technology is virtually complete for real configurations. SIT is likely to be absorbed within PSE. The scope of PSE needs to be vastly increased and it would greatly benefit from a firmer mathematical foundation. DNS will no doubt undergo algorithmic improvements and take advantage of increased computational power. LES will likely evolve through several generations of SGS model improvements.

The philosophy, not only for transition prediction, but also for basic research into transition physics, ought to be to apply to each stage of transition or to each physical problem the most economical and revealing method in the transition prediction toolkit.

## Acknowledgments

The authors would like to thank their many colleagues in the Theoretical Flow Physics Branch and at I.C.A.S.E. for their contributions to this work. The bulk of the SIT, PSE, DNS and LES results shown here were obtained during a 1990-91 special project on the NASA Ames Numerical Aerodynamic Simulation system. Special thanks go to Beyong Kim for the graphical illustration of the rope-like structures shown in Figure 12. The second and third authors were supported by NASA Langley Research Center under contracts NAS1-18240 and NAS1-18599, respectively.

## References

- [1] Smith, A. M. O.; and Gamberoni, A. H.: Transition, Pressure Gradient and Stability Theory. Report ES26388, Douglas Aircraft Co., 1956.
- [2] Van Ingen, J. L.: A Suggested Semi-Empirical Method for the Calculation of the Boundary Layer Transition Region. Report VTH-74, Tech. Univ. Delft, Dept. of Aeronautics, 1956.
- [3] Nishioka, M.; and Morkovin, M. V.: Boundary-layer receptivity to unsteady pressure gradients: experiments and overview. *J. Fluid Mech.* **171**:219-261, 1986.
- [4] Goldstein, M. E.; and Hultgren, L. S.: Boundary-layer receptivity to long-wave free-stream disturbances. *Ann. Rev. Fluid Mech* **21**:137-166, 1989.
- [5] Kerschen, E. G.: Boundary layer receptivity theory. *Appl. Mech. Rev.* **43**(5):S152-S157, 1990.
- [6] Choudhari, M.; and Streett, C. L.: A Finite Reynolds Number Approach for the Prediction of Boundary Layer Receptivity in Localized Regions. NASA TM 102781, 1991.
- [7] Choudhari, M.; and Streett, C.: Boundary Layer Receptivity Phenomena in Three-Dimensional and High-Speed Boundary Layers. *AIAA Paper No. 90-5258*, 1990.
- [8] Choudhari, M., Ng, L.; and Streett, C. L.: A general approach for the prediction of localized instability generation in boundary layer flows. In *Proc. of the Boundary Layer Transition and Control Conference*, Cambridge, UK, April 9-12, 1991.
- [9] Pruett, C. D., Ng, L., and Erlebacher, G.: On the nonlinear stability of a high-speed, axisymmetric boundary layer. *Phys. Fluids A* **3**, 1991, in press.
- [10] Mack, L. M.: Boundary-layer linear stability theory. In *Special Course on Stability and Transition of Laminar Flow*, ed. R. Michel. AGARD Report No. 709, pp. 3.1-3.81, 1984.
- [11] Pruett, C. D., Ng, L., and Erlebacher, G.: On the non-uniqueness of the parallel-flow approximation. In *Proc. of the ICASE/LaRC Workshop on Transition and Turbulence*, ed. M. Y. Hussaini. New York: Springer, 1992.
- [12] El-Hady, N. M.: Nonparallel instability of supersonic and hypersonic boundary layers. *Phys. Fluids A* **3**(9):2164-2178, 1991.
- [13] Malik, M. R.: Prediction and control of transition in supersonic and hypersonic boundary layers. *AIAA J.* **27**(11):1487-1493, 1989.
- [14] Chang, C.-L.; Malik, M. R.; and Hussaini, M. Y.: Effects of Shock on the Stability of Hypersonic Boundary Layers. *AIAA Paper No. 90-1448*, 1990.
- [15] Balakumar, M.; and Malik, M. R.: Waves Produced From a Harmonic Point Source in a Supersonic Boundary Layer. *AIAA Paper No. 91-1646*, 1991.
- [16] Herbert, Th.: Secondary instability of boundary layers. *Ann. Rev. Fluid Mech.* **20**:487-526, 1988.
- [17] El-Hady, N. M.: Spatial three-dimensional secondary instability of compressible boundary layer flows. *AIAA J.* **29**(5):688-696, 1991.
- [18] Masad, J. A.; and Nayfeh, A. H.: Subharmonic instability of compressible boundary layers. *Phys. Fluids A* **2**(8):1380-1392, 1990.
- [19] Ng, L.; and Erlebacher, G.: Secondary instabilities in compressible boundary layers. *Phys. Fluids A* **4**, 1992, in press.
- [20] Ng, L. L.; and Zang, T. A.: Secondary Instability Mechanisms in Compressible, Axisymmetric Boundary Layers. *AIAA Paper No. 92-0743*, 1992.
- [21] Bertolotti, F. P.: Linear and Nonlinear Stability of Boundary Layers with Streamwise Varying Properties. Ph.D. Dissertation, Ohio State University, 1990.
- [22] Herbert, Th.: Boundary-Layer Transition - Analysis and Prediction Revisited. *AIAA Paper No. 91-0737*, 1991.
- [23] Bertolotti, F.; and Herbert, Th.: Analysis of the linear stability of compressible boundary layers using the PSE. *Theor. Comput. Fluid Dyn.* **3**:117-124, 1991.

- [24] Chang, C.-L.; Malik, M. R.; Erlebacher, G.; and Hussaini, M. Y.: Compressible Stability of Growing Boundary Layers Using Parabolized Stability Equations. *AIAA Paper No. 91-1636*, 1991.
- [25] Kleiser, L.; and Zang, T. A.: Numerical simulation of transition in wall-bounded shear flows. *Ann. Rev. Fluid Mech.* **23**:495-537, 1991.
- [26] Gilbert, N.; and Kleiser, L.: Near-wall phenomena in transition to turbulence. In *Near-Wall Turbulence: 1988 Zoran Zaric Memorial Conference*, ed. S.J. Kline & N.H. Afgan, pp. 7-28. Washington: Hemisphere, 1989.
- [27] Rai, M. M.; and Moin, P.: Direct Numerical Simulation of Transition and Turbulence in a Spatially Evolving Boundary Layer. *AIAA Paper No. 91-1607*, 1991.
- [28] Macaraeg, M. G.: Stability of nonsimilar shear layers. *Int. J. Numer. Meth. Heat & Fluid Flow*, 1992, in press.
- [29] Pruett, C. D.; and Zang, T. A.: Direct Numerical Simulation of Laminar Breakdown in High-Speed, Axisymmetric Boundary Layers. *AIAA Paper No. 92-0742*, 1992.
- [30] Atkins, H. L.: High-Order ENO Methods for the Unsteady Compressible Navier-Stokes Equations. *AIAA Paper No. 91-1557*.
- [31] Fischer, M.; and Weinstein, L.: Cone transitional boundary-layer structure at  $M_e = 14$ . *AIAA J.* **10**:699-701, 1972.
- [32] Kendall, J. M.: Wind tunnel experiments relating to supersonic and hypersonic boundary-layer transition. *AIAA J.* **13**:290-299, 1975.
- [33] Demetriades, A.: Hypersonic Viscous Flow Over a Slender Cone. Part III: Laminar Instability and Transition. *AIAA Paper No. 74-535*, 1974.
- [34] Galperin, B.; and Orszag, S. A. (eds.): *Large Eddy Simulation of Complex Engineering and Geophysical Flows*. Cambridge, UK: Cambridge Univ. Press, 1992, in press.
- [35] Piomelli, U.; Zang, T. A.; Speziale, C. G.; and Hussaini, M. Y.: On the large eddy simulation of transitional wall-bounded flows. *Phys. Fluids A* **2**(2):257-265, 1990.
- [36] Piomelli, U.; and Zang, T. A.: Large-eddy simulation of transitional channel flow. *Comput. Phys. Comm.* **65**:224-230, 1991.
- [37] Germano, M.; Piomelli, U.; Moin, P.; and Cabot, W. H.: A dynamic subgrid-scale eddy viscosity model. *Phys. Fluids A* **3**(7):1760-1765, 1991.
- [38] Zang, T. A.; and Piomelli, U.: Large-eddy simulation of transitional flow. In *Large Eddy Simulation of Complex Engineering and Geophysical Flows*, ed. B. Galperin and S. A. Orszag. Cambridge, UK: Cambridge Univ. Press, 1992, in press.
- [39] Yoshizawa, A.: Statistical theory for compressible turbulent shear flows, with the application to subgrid modeling. *Phys. Fluids* **29**:2152-2164, 1986.
- [40] Speziale, C. G.; Erlebacher, G.; Zang, T. A.; and Hussaini, M. Y.: The subgrid-scale modeling of compressible turbulence. *Phys. Fluids* **31**(4):940-942, 1988.
- [41] Lesieur, M.; Comte, P.; and Normand, X.: Direct and Large-Eddy Simulations of Transitioning and Turbulent Shear Flows. *AIAA Paper No. 91-0335*, 1991.
- [42] Moin, P.; Squires, K.; Cabot, W.; and Lee, S.: A Dynamic Subgrid-Scale Model for Compressible Turbulence and Scalar Transport, CTR Manuscript 124, 1991.
- [43] Comte, P.; Lee, S.; and Cabot, W. H.: A subgrid-scale model based on the second-order velocity structure function. In *Proc. of the Summer Program 1990*, Center for Turbulence Research, pp. 31-45. Stanford University, 1990.
- [44] Zang, T. A.; Dahlburg, R. B. and Dahlburg, J. P.: Direct and large-eddy simulations of three-dimensional compressible Navier-Stokes turbulence. *Phys. Fluids A* **4**(1), 1992, in press.
- [45] Erlebacher, G.; Hussaini, M. Y.; Speziale, C. G.; and Zang, T. A.: Toward the large-eddy simulation of compressible turbulent flows. *J. Fluid Mech.*, 1992, in press.
- [46] Piomelli, U.; Moin, P.; and Ferziger, J. H.: Model consistency in large-eddy simulation of turbulent channel flows. *Phys. Fluids* **31**:1884-1891, 1988.
- [47] Kral, L. D.; and Zang, T. A.: Large-eddy simulation of supersonic, wall-bounded, turbulent flows In *Proc. of the ICASE/LaRC Workshop on Transition and Turbulence*, ed. M. Y. Hussaini. New York: Springer, 1992.
- [48] Zang, T. A.: Numerical simulation of the dynamics of turbulent boundary layers: perspectives of a transition simulator. *Phil. Trans. R. Soc. Lond. A* **336**:95-102, 1991.

ON THE ROLE OF SECONDARY INSTABILITIES IN LAMINAR-TURBULENT TRANSITION  
OF 2D AND 3D BOUNDARY LAYERS

by

Uwe Dallmann, Thomas M. Fischer, Werner Koch  
DLR Institute for Theoretical Fluid Mechanics  
Bunsenstrasse 10, D-3400 Göttingen, Germany

and

Hans Bippes  
DLR Institute for Experimental Fluid Mechanics  
Bunsenstrasse 10, D-3400 Göttingen, Germany

Abstract

The accurate prediction of laminar/turbulent transition is one of the fundamental problems in engineering fluid mechanics. There is almost unanimous consent that such a transition criterion should come from stability theory. Linear primary stability theory describes the initial stage of transition, but falls short of predicting transition. Only in conjunction with empirical correlations, the widely used  $e^n$  method is obtained, which, however, lacks a solid physical base. Three-dimensional secondary instabilities are known to play an important role in the transition process. However, no use has been made so far of secondary instabilities, instability interactions or wave resonances to define a "transition location."

The paper summarizes new attempts to identify certain interaction and resonance phenomena within the laminar-turbulent transition regime in two- and three-dimensional boundary layers which are associated with rapid structural and temporal changes of fluctuations beyond their exponential growths.

At first, a numerical bifurcation analysis for Blasius boundary-layer flow on a flat plate will be presented. Using the parallel-flow approximation, two-dimensional, wave-like finite amplitude solutions have been computed. This resulted in the neutral surface of two-dimensional nonlinear Tollmien-Schlichting waves. The computation of three-dimensional secondary instabilities for this two-dimensional neutral surface led to an exciting discovery: a direct 1:1 internal resonance between amplified, phase-locked secondary instability modes is possible. This implies a  $t \cdot \exp(\sigma t)$  behavior

for temporal amplification ( $\sigma$  being the temporal amplification rate). Varying the Reynolds number, the amplification rate of this resonance point changes from being damped ( $\sigma < 0$ ) to being amplified ( $\sigma > 0$ ). The Reynolds number corresponding to the cross-over point appears to be related to the experimentally observed transition Reynolds number in a low-disturbance flow. Therefore, this resonance would not only explain the explosive start of transition but also a physically satisfactory criterion for transition prediction without recourse to empirically determined constants.

On the other hand, for three-dimensional boundary layers, the dominating role of crossflow vortices is well-known. Nevertheless, very little is known about their interaction with fluctuations giving rise to spatial distributions of their rms-values. Such theoretical investigations of possible secondary instabilities of a three-dimensional boundary layer accompany a basic transition experiment, which is being performed at the DLR in Göttingen. Primary stationary and secondary non-stationary disturbances are used to model the mean flow and the fluctuations of a measured (quasi-) saturation state. The analysis is based on a Falkner-Skan-Cooke approximation of the undisturbed flow. A secondary stability approach selects the proper waves amongst the spectrum of amplified disturbances in order to model the dominating interactions. Good agreement of the secondary stability model with this experiment is obtained, especially concerning the spatial distribution of the rms fluctuation. However, so far a striking change of the vortex pattern due to secondary instability has not been observed for three-dimensional boundary layers.

# THREE-DIMENSIONAL COMPRESSIBLE STABILITY- TRANSITION CALCULATIONS USING THE SPATIAL THEORY

by

R. Niethammer\* and D. Arnal\*\*  
ONERA/CERT, Toulouse, France

and

V. de Laharpe†, H. H. Chen†† and T. Cebeci†††  
California State University, Long Beach

## Abstract

The  $e^n$ -method is employed with the spatial amplification theory to compute the onset of transition on a swept wing tested in transonic cryogenic flow conditions. Two separate eigenvalue formulations are used. One uses the saddle-point method and the other assumes that the amplification vector is normal to the leading edge. Comparisons of calculated results with experimental data show that both formulations give similar results and indicate that the wall temperature has a rather strong effect on the value of the  $n$  factor.

## 1. Introduction

In the absence of leading-edge contamination and Görtler instability, it is well known that transition on swept wings may occur either due to streamwise instability (related to the properties of the streamwise velocity profile  $u$ ) or cross-flow instability (related to the properties of the cross-flow velocity profile  $w$ ). Since the  $u$ -profiles look like Falkner-Skan profiles, the streamwise instability is similar to that of a two-dimensional flow and leads to turbulence in flows with positive pressure gradient. On the other hand, the development of a cross-flow profile is characterized by an inflectional instability that can induce transition in flows with a negative pressure gradient.

In order to design new aircraft wings, one must be able to predict transition on swept wings. The most popular method for predicting transition is the  $e^n$ -method, which was initially developed for two-dimensional flows<sup>1,2</sup>. This method is based on the solution of the Orr-Sommerfeld equation using either temporal or spatial amplification theory. In either approach the integrated amplification rates  $A/A_0$  of the unstable frequencies are determined, and transition is computed on the assumption that it occurs when the ratio  $A/A_0$  of the locally most unstable wave reaches a critical value  $e^n$ , with  $n$  between 8 and 10 for a low disturbance environment.

In the extension of this method to three-dimensional flows, both temporal and spatial amplification theories can again be used. In the former case, the eigenvalue problem involves five scalars  $\alpha$ ,  $\beta$ ,  $\omega_r$ ,  $\omega_i$  and  $R$  and in the latter case it involves six scalars  $\alpha_r$ ,  $\alpha_i$ ,  $\beta_r$ ,  $\beta_i$ ,  $\omega$  and  $R$ . In both approaches, the solution procedure is considerably more difficult than its counterpart in two-dimensional flows because the nontrivial solution of the linear stability equations in three-dimensional flows provides only two relations

between the eigenvalues  $\alpha$ ,  $\beta$ ,  $\omega$  and  $R$ . To predict transition for example, in spatial amplification theory,  $\omega$  and  $R$  are prescribed, so two new relations between  $\alpha$  and  $\beta$  are required before the solution of the linear stability equations can be obtained.

To date, most problems of the three-dimensional transition problems employing linear stability theory have been treated by using the temporal theory. When  $R$  and  $\omega_r$  are specified, the values of  $\alpha$  and  $\omega_i$  are not unique, since they both are functions of  $\beta$  [ $\alpha = \alpha(\beta)$  and  $\omega_i = \omega_i(\beta)$ ]. A possible solution is to determine the wave number direction  $\psi = \tan^{-1}(\beta/\alpha)$  for which  $\omega_i$  is maximum and integrate  $\omega_i$  along the group velocity direction according to Gaster's transformation<sup>3</sup>. This "envelope method" is one of the approaches used in the COSAL code developed by Malik.<sup>4</sup>

In spatial theory, the introduction of an additional scalar in the dispersion relation makes the problem more difficult: the amplification rate vector  $\hat{A}$  is no longer a scalar; it is a function of both  $\alpha_i$  and  $\beta_i$ . As a result, a new relation is needed in the eigenvalue formulation.

In this paper we consider two completely different eigenvalue formulations and compare their predictions with measurements. The first formulation is based on the wave packet theory (saddle-point method) and the second is based on the assumption that the amplification vector  $\hat{A}$  is normal to the wing leading edge. The experimental data correspond to measurements obtained at ONERA/CERT for a transonic swept wing. The tests have been conducted in a cryogenic wind tunnel at very low stagnation temperatures.

The following section describes the calculation method employing both eigenvalue formulations. Results are presented in the third section and the predictions of both methods are compared with measurements. The paper ends with a summary of the more important conclusions.

## 2.0 Description of the Computational Methods

The compressible stability equations and their boundary conditions are well known and are given in several references, see for example Ref. 4. With the parallel flow approximation, they can be written in the following dimensionless form:

Continuity:

$$1(\alpha u + \beta w - \omega)\hat{\rho} + \rho \left[ \frac{d\hat{v}}{dy} + 1(\alpha \hat{u} + \beta \hat{w}) \right] + \frac{d\rho}{dy} \hat{v} = 0 \quad (1)$$

\*Visiting research student from München University, Germany

\*\*Research engineer

†Visiting Research student from ENSAE, Toulouse, France

††Associate Professor

†††Professor and Chairman

### x-Momentum

$$\begin{aligned}
 \rho[1(\alpha u + \beta w - \omega)(\alpha \hat{u} + \beta \hat{w}) + (\alpha \frac{du}{dy} + \beta \frac{dw}{dy})\hat{v}] \\
 = -1(\alpha^2 + \beta^2) \frac{\hat{p}}{\gamma M_e^2} + \frac{\mu}{R} \{ (\alpha \frac{d^2 \hat{u}}{dy^2} + \beta \frac{d^2 \hat{w}}{dy^2}) \\
 + (\alpha^2 + \beta^2) [1 \frac{d\hat{v}}{dy} - 2(\alpha \hat{u} + \beta \hat{w})] \\
 + \frac{2}{3} \frac{\lambda - \mu}{R} (\alpha^2 + \beta^2) [1 \frac{d\hat{v}}{dy} - (\alpha \hat{u} + \beta \hat{w})] \\
 + \frac{1}{R} \frac{d\mu}{dT} (\alpha \frac{d^2 \hat{u}}{dy^2} + \beta \frac{d^2 \hat{w}}{dy^2}) \hat{T} \\
 + \frac{1}{R} [(\frac{d\mu}{dT} \frac{d\hat{T}}{dy} + \frac{d^2 \mu}{dT^2} \frac{d\hat{T}}{dy} \hat{T}) (\alpha \frac{du}{dy} + \beta \frac{dw}{dy})] \\
 + \frac{1}{R} \frac{d\mu}{dT} \frac{dT}{dy} [(\alpha \frac{du}{dy} + \beta \frac{dw}{dy}) + 1(\alpha^2 + \beta^2) \hat{v}] \quad (2)
 \end{aligned}$$

### z-Momentum

$$\begin{aligned}
 \rho[1(\alpha u + \beta w - \omega)(\alpha \hat{w} - \beta \hat{u}) + (\alpha \frac{dw}{dy} - \beta \frac{du}{dy})\hat{v}] \\
 = \frac{\mu}{R} [(\alpha \frac{d^2 \hat{w}}{dy^2} - \beta \frac{d^2 \hat{u}}{dy^2}) - (\alpha^2 + \beta^2)(\alpha \hat{w} - \beta \hat{u})] \\
 + \frac{1}{R} [\frac{d\mu}{dT} \frac{dT}{dy} (\alpha \frac{d\hat{w}}{dy} - \beta \frac{d\hat{u}}{dy}) + \frac{d\mu}{dT} (\alpha \frac{d^2 \hat{w}}{dy^2} - \beta \frac{d^2 \hat{u}}{dy^2}) \hat{T} \\
 + (\frac{d\mu}{dT} \frac{d\hat{T}}{dy} + \frac{d^2 \mu}{dT^2} \frac{d\hat{T}}{dy} \hat{T}) (\alpha \frac{dw}{dy} - \beta \frac{du}{dy})] \quad (3)
 \end{aligned}$$

### y-Momentum

$$\begin{aligned}
 1\rho(\alpha u + \beta w - \omega)\hat{v} = -\frac{1}{\gamma M_e^2} \frac{d\hat{p}}{dy} + \frac{\mu}{R} [2 \frac{d^2 \hat{v}}{dy^2} \\
 + 1(\alpha \frac{du}{dy} + \beta \frac{dw}{dy}) - (\alpha^2 + \beta^2) \hat{v}] \\
 + \frac{2}{3} \frac{\lambda - \mu}{R} \{ \frac{d^2 \hat{v}}{dy^2} + 1(\alpha \frac{du}{dy} + \beta \frac{dw}{dy}) \} \\
 + \frac{1}{R} \{ 1 \frac{d\mu}{dT} (\alpha \frac{du}{dy} + \beta \frac{dw}{dy}) \hat{T} + 2 \frac{d\mu}{dT} \frac{dT}{dy} \frac{d\hat{v}}{dy} \\
 + \frac{2}{3} \frac{d}{dT} (\lambda - \mu) \frac{dT}{dy} [\frac{d\hat{v}}{dy} + 1(\alpha \hat{u} + \beta \hat{w})] \} \quad (4)
 \end{aligned}$$

### Energy

$$\begin{aligned}
 \rho[1(\alpha u + \beta w - \omega)\hat{T} + \frac{dT}{dy} \hat{v}] = -(\gamma - 1) [\frac{d\hat{v}}{dy} \\
 + 1(\alpha \hat{u} + \beta \hat{w})] + \frac{\gamma \mu}{PrR} (\frac{d^2 \hat{T}}{dy^2} - (\alpha^2 + \beta^2) \hat{T} \\
 + \frac{1}{k} [\frac{dk}{dT} \frac{d^2 \hat{T}}{dy^2} + \frac{d^2 k}{dT^2} (\frac{dT}{dy})^2] \hat{T} + \frac{2}{k} \frac{dk}{dT} \frac{dT}{dy} \frac{d\hat{T}}{dy} \\
 + \gamma \frac{(\gamma - 1)}{R} M_e^2 \{ 21\mu(\alpha \frac{du}{dy} + \beta \frac{dw}{dy}) \hat{v} \\
 + \frac{d\mu}{dT} (\frac{d^2 \hat{u}}{dy^2} + \frac{d^2 \hat{w}}{dy^2}) \hat{T} \\
 + \frac{2\mu}{\alpha^2 + \beta^2} [(\alpha \frac{du}{dy} + \beta \frac{dw}{dy})(\alpha \frac{du}{dy} + \beta \frac{dw}{dy}) \\
 + (\alpha \frac{dw}{dy} - \beta \frac{du}{dy})(\alpha \frac{dw}{dy} - \beta \frac{du}{dy})] \} \quad (5)
 \end{aligned}$$

$$y = 0, \quad \hat{u} = \hat{v} = \hat{w} = \hat{T} = 0 \quad (6a)$$

$$y \rightarrow \infty, \quad \hat{u}, \hat{v}, \hat{w}, \hat{T} \rightarrow 0 \quad (6b)$$

The above equations can be expressed as a first-order system by defining the following new variables with primes denoting differentiation with respect to  $y$ ,

$$\begin{aligned}
 z_1 = \alpha \hat{u} + \beta \hat{w}, \quad z_2 = \alpha \hat{u}' + \beta \hat{w}', \quad z_3 = \hat{v}, \quad z_4 = \frac{\hat{p}}{\gamma M_e^2} \\
 z_5 = \hat{T}, \quad z_6 = \hat{T}', \quad z_7 = \alpha \hat{w} - \beta \hat{u}, \quad z_8 = \alpha \hat{w}' - \beta \hat{u}' \quad (7)
 \end{aligned}$$

In terms of these new variables, Eqs. (1) to (6), for a three-dimensional compressible flow can be written as

$$z' = Bz \quad (8)$$

where  $z = (z_1, z_2, \dots, z_8)^T$  and  $B$  is a  $8 \times 8$  coefficient matrix defined by

$$B = \begin{bmatrix} 0 & 1 & 0 & 0 & 0 & 0 & 0 & 0 \\ b_{21} & b_{22} & b_{23} & b_{24} & b_{25} & b_{26} & 0 & 0 \\ b_{31} & 0 & b_{33} & b_{34} & b_{35} & 0 & 0 & 0 \\ b_{41} & b_{42} & b_{43} & b_{44} & b_{45} & b_{46} & 0 & 0 \\ 0 & 0 & 0 & 0 & 0 & 1 & 0 & 0 \\ 0 & b_{62} & b_{63} & b_{64} & b_{65} & b_{66} & 0 & b_{68} \\ 0 & 0 & 0 & 0 & 0 & 0 & 0 & 1 \\ 0 & 0 & b_{83} & 0 & b_{85} & b_{86} & b_{87} & b_{88} \end{bmatrix} \quad (9)$$

with its nonzero elements given in Appendix 1.



The solution of Eq. (8) subject to the boundary conditions given by

$$y = 0, \quad z_1 = z_3 = z_5 = z_7 = 0 \quad (10)$$

$$y \rightarrow \infty, \quad z_1, z_3, z_5, z_7 \rightarrow 0$$

can be obtained with two separate eigenvalue formulations as described in the following two subsections, 2.1 and 2.2.

## 2.1 Eigenvalue Formulation Based on the Direction of the Amplification Vector (ONERA/CERT Method)

The basic assumption of this method, first proposed by Mack,<sup>7</sup> is that on a wing with  $x$  and  $z$  denoting the coordinates normal to the leading edge and spanwise direction, amplification only occurs in the  $x$ -direction and not in the spanwise direction; that is,

$$\beta_1 = 0 \quad (11)$$

This assumption, formulated for an infinite swept wing, reduces the number of unknown eigenvalues in the spatial theory from six to five. With  $\omega$  and  $R$  given in the transition prediction problem, the unknown eigenvalues correspond to  $\alpha_1$ ,  $\alpha_r$  and  $\beta_r$ . For an assumed  $\beta_r$ , the wave number  $\alpha$  is then calculated so that the amplification rate  $\alpha_1$  can be determined. Additional calculations are then performed for different values of  $\beta_r$  in order to determine the maximum amplification rate. This procedure, as in the saddle-point method, is repeated for each  $x$ -station and the  $n$ -factor in the  $e^n$ -method is calculated from

$$n = - \int_{x_0}^x (\alpha_1)_{\max} dx \quad (12)$$

for different specified frequencies. Here  $x_0$  corresponds to the  $x$ -station where the stability calculations are initiated. Transition is assumed to occur for the frequency for which the locally most unstable disturbance reaches a value of  $n$  between 8 and 10.

## 2.2 Eigenvalue Formulation Based on the Saddle-Point Method (CSC Method)

The Cebeci-Stewartson-Chen (CSC) method was first proposed and used by Cebeci and Stewartson

and is described in some detail in Ref. 7. In this method the relationship between the two wave numbers  $\alpha$  and  $\beta$  is not assumed but computed from the requirement that  $\partial\alpha/\partial\beta$  is real. According to this requirement, the wave orientation and growth direction of the disturbance are given by

$$\left(\frac{\partial\alpha}{\partial\beta}\right)\omega, R = -\tan\gamma = -\frac{z}{x} \quad (13)$$

where  $\gamma$  denotes the angle that the disturbance makes with the  $x$ -axis,  $\alpha$  and  $\beta$  are related by Eq. (13) and the disturbance propagating along the ray is given by the two terms on the right-hand side of Eq. (13). The disturbances are damped if the amplification rate  $\Gamma$  defined by

$$\Gamma = \alpha_1 - \beta_1 \left(\frac{\partial\alpha}{\partial\beta}\right)\omega, R \quad (14)$$

is  $> 0$ , neutral if  $\Gamma = 0$ , and amplified if  $\Gamma < 0$ . Once  $\alpha$  and  $\beta$  are computed with the constraints of Eq. (13), the amplification rate is obtained from Eq. (14); additional calculations are then made for different values of  $\partial\alpha/\partial\beta$  so that new values of  $\alpha$  and  $\beta$  are calculated to determine the maximum value of  $\Gamma$ . Further details of the solution procedure are given in Ref. 8.

## 3.0 Results and Discussion

### 3.1 Experimental Conditions

The experimental data used in our studies correspond to laminar flow on a 15-degree swept tapered wing. The chord is 0.228m at the root and 0.145m at the tip. The wing has a span of 0.39m with an AS409 cross-section and a trailing-edge sweep angle of three degrees. The height of the hollows on the wing is less than 0.05 mm (from peak to valley) for a chordwise extent of about 2 cm. In order to avoid the need to perform full three-dimensional stability/transition calculations, the measurements discussed in Ref. 9 and summarized in Ref. 10, were carried out under infinite swept conditions with the wing having a mean sweep angle of 12 degrees at an angle of attack of 0.3 degrees. The computations were made at a mean chord of 0.186m.

Figure 1 shows the Mach number distributions measured at different Reynolds numbers for a free-stream Mach number of 0.74 at two stagnation pressures. As can be seen, the Mach number distribution has "bumps" around  $x/c \approx 0.3$  and 0.47 caused

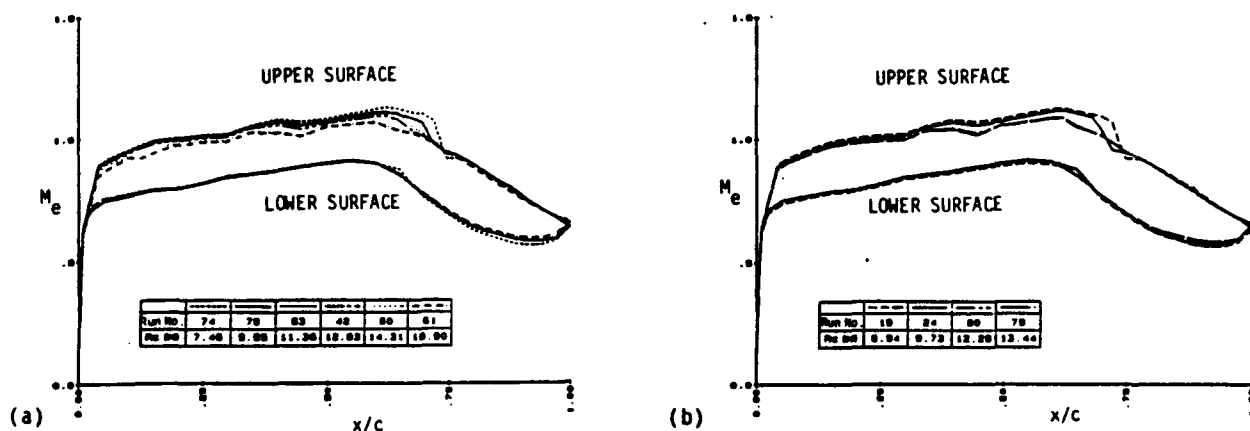


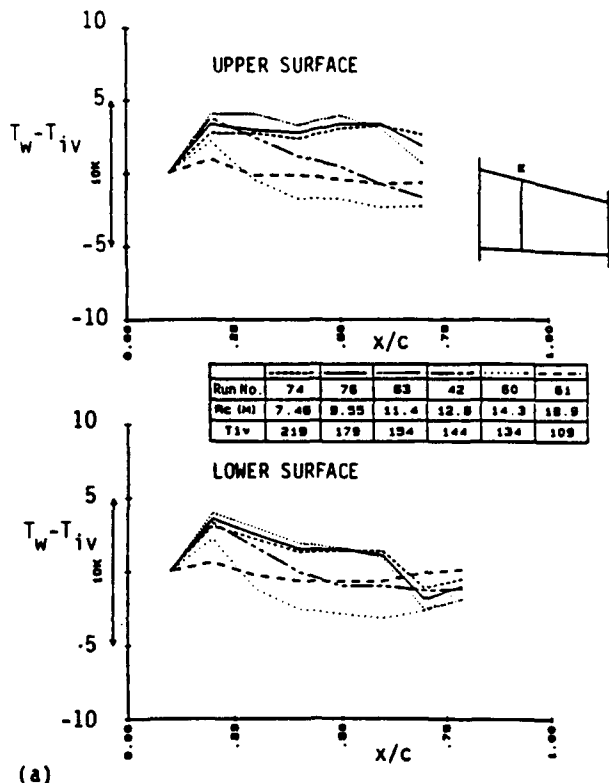
Fig. 1. Mach number distributions for  $M_\infty = 0.74$ ,  $\alpha = 0.3$ , and  $p_1 = (a) 2.0 \text{ bar}$ , (b)  $2.5 \text{ bar}$ .

by small hollows in the model. On the lower surface, a smooth bend around  $x/c = 0.20$  is visible. These discontinuities are common for all experiments and their effects on transition were part of the investigation conducted and discussed in detail in Ref. 10.

Figure 2 shows the variation of the experimental wall temperature distributions along the chord. Each distribution is referenced to its temperature,  $T_{iv}$ , measured at the first thermocouple in the flow direction. The maximum relative difference between the wall and freestream temperature is 5 degrees, which indicates that the influence of a nonadiabatic wall on transition must be considered. This includes the relative undulation as well as the absolute wall temperature.

Figure 3 shows the variation of the drag coefficient with Reynolds numbers at three stagnation pressures and several stagnation temperatures. Since the drag coefficient increases significantly for a turbulent boundary layer, it can be used as an indicator of transition. The evolution of  $C_d$  was measured in the cryogenic, transonic wind tunnel, T2, at ONERA/CERT for different stagnation pressures (1.7 to 2.5 bars) and different stagnation temperatures (between 165 and 109K). The values of  $C_d$  were obtained from wake measurements.

In the present study we consider two runs corresponding to 42 and 79, with Run 42 having a stagnation temperature of 145K and a stagnation pressure of 2.0 bar. The influence of higher temperature at a higher pressure is examined with run 79, which has a stagnation temperature of 165K and a stagnation pressure of 2.5 bar. In both cases we calculate only the upper surface of the wing.



(a)

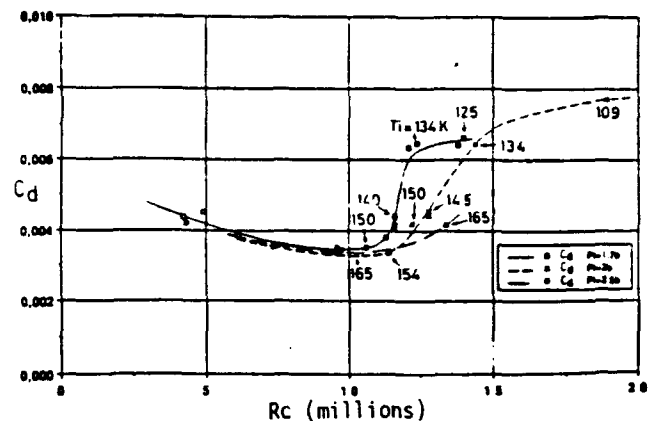
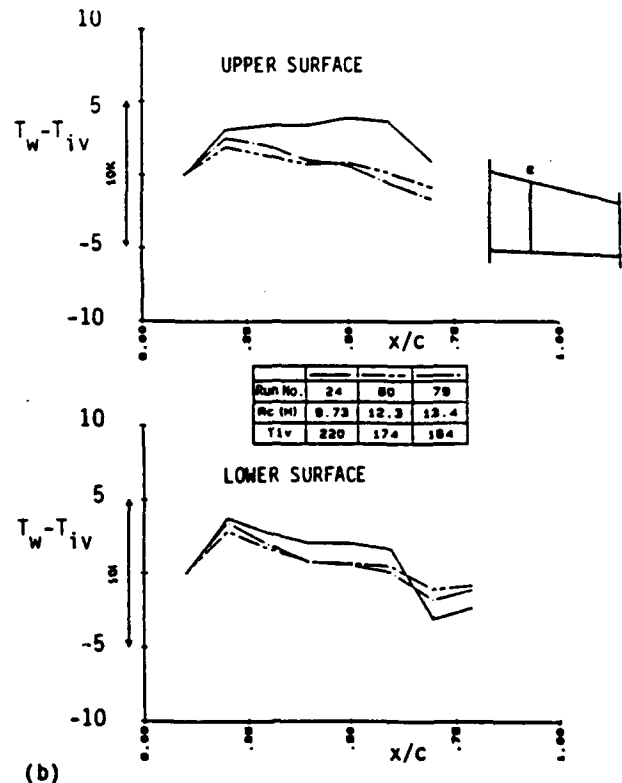


Fig. 3. Variation of the drag coefficient  $C_d$  with stagnation temperature  $T_1$  and pressure  $p_1$  as a function of Reynolds number  $R_c$ .

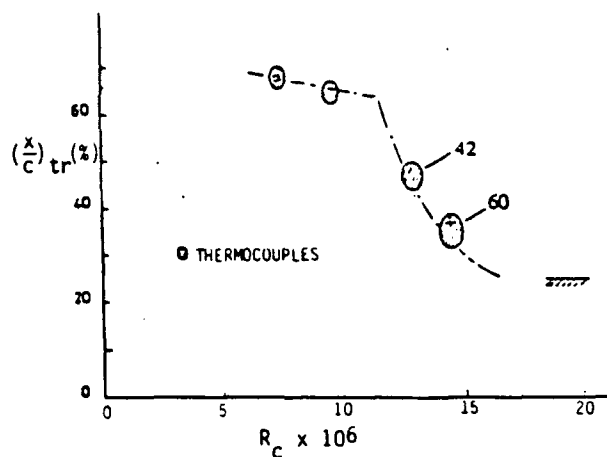
Additional studies are in progress for run 60, which has a stagnation temperature of 134K, and a stagnation pressure of 2.0 bar. These studies will be reported separately.

Figure 4 shows the experimental transition locations for runs 42 and 60. The location of transition was determined from the change of the wall temperature measured by thermocouples, along the chord, resulting from the different heat fluxes for laminar and turbulent flow. For run 79, the location of transition was assumed to be the same as that of run 42 because of the similar drag coefficient and Reynolds number (Fig. 3).

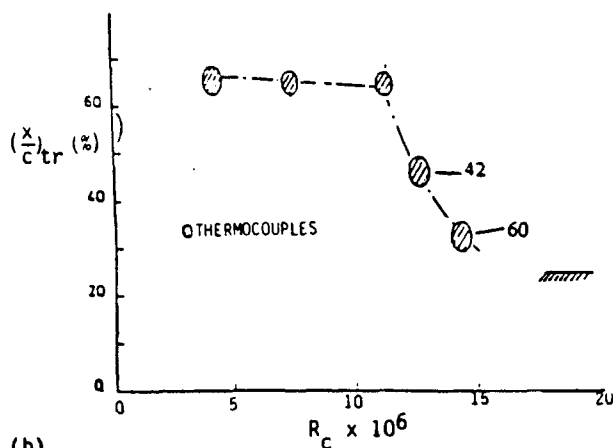


(b)

Fig. 2. Difference between the wall and freestream temperature,  $M_\infty = 0.74$ ,  $\alpha = 0.3$ ,  $p_1 =$  (a) 2.0 bar, (b) 2.5 bar.



(a)



(b)

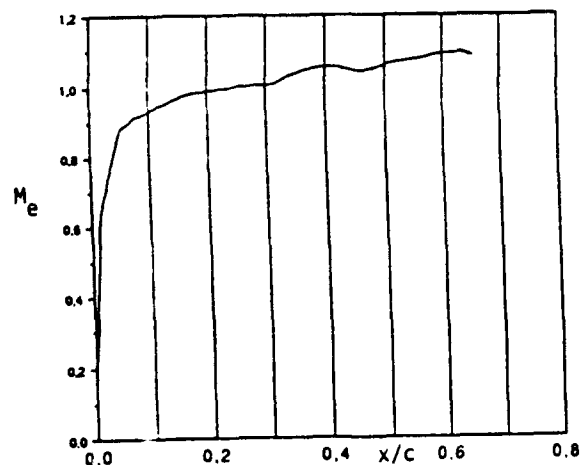
Fig. 4. Transition locations for runs 42 and 60, (a) upper surface, (b) lower surface.

### 3.2 Calculations with the ONERA/CERT Method

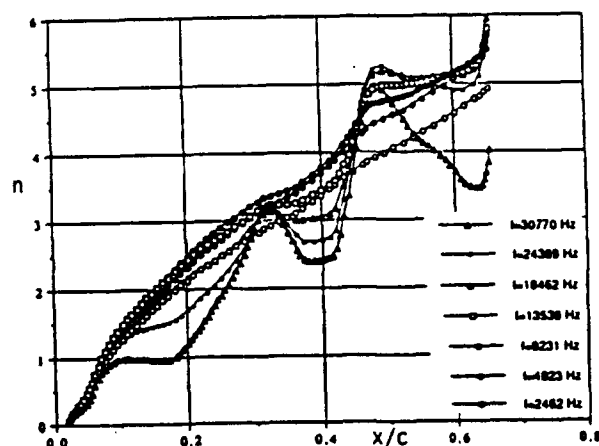
A detailed discussion of the calculations for the experimental work described in the previous subsection is presented in Ref. 10. In this subsection we present results for runs 42 and 79 for Mach number distributions containing "bumps" around  $x/c \approx 0.3$  and  $0.47$  caused by small hollows in the model and compare them with the calculations employing the CSULB method in subsection 3.3. Studies are in progress for Mach number distributions without bumps and will be reported separately.

The boundary-layer and stability calculations for run 42 were performed for an adiabatic wall and specified wall temperature distributions at a Reynolds number of  $12.8 \times 10^6$ . Figure 5 shows the predictions of the ONERA/CERT method for the adiabatic wall case together with the measured Mach number distribution (Fig. 5a) used in the boundary-layer calculations for a stagnation temperature of  $145K$  and a stagnation pressure of  $2.0$  bar. According to Fig. 4, the location of transition corresponds to  $x/c \approx 0.47$ .

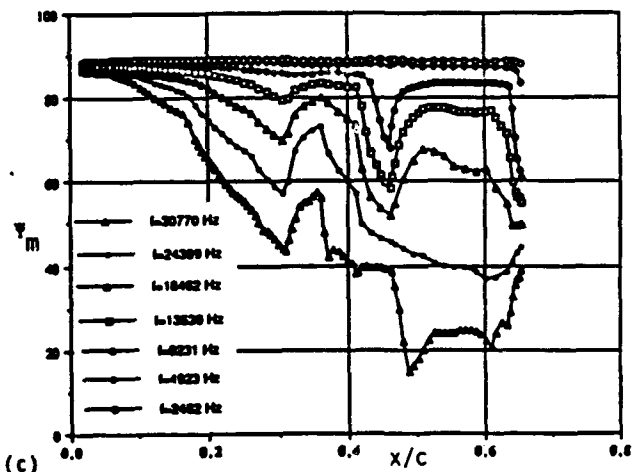
The calculated  $n$ -factors shown in Fig. 5b were obtained for seven frequencies which can be classified in three groups: (1) the high ones from



(a)



(b)



(c)

Fig. 5. Distributions of (a) Mach number, (b) computed  $n$  factors, and (c) the most unstable direction  $\phi_m$  of the disturbances for the adiabatic wall temperature distribution in Run 42 for the upper surface.

15 to 30 kHz, (2) the range from 9 to 15 kHz, and (3) the low ones from 2 to 9 kHz. Beginning with high frequencies, the calculations indicate rather strong undulations of  $n$  and of the wave directions  $\psi_m$  (Fig. 5c) along the chord. The undulations of  $n$  increase with frequency and show a strong dependence on the pressure gradient. Excluding the region of high rise of  $M_e$  ( $x/c = 0$  to 0.06, the following mechanism can be observed. A relative low pressure gradient has a stabilizing effect, whereas a higher, even positive pressure gradient is destabilizing. This effect becomes more and more distinct with increasing  $x/c$ . Looking, for example, at the  $n$ -curve with frequency 30770 Hz, we can see that the relative low pressure gradient between  $x/c = 0.06$  and 0.2 leads to an almost constant  $n$ . The increase of  $dp/dx$  between 0.2 and 0.3 leads to a strong rise of  $n$ . The steeper Mach number distribution from  $x/c = 0.3$  to 0.41 leads to a restabilization. The process is repeated as the pressure gradient changes again significantly at  $x/c = 0.41$  and 0.47.

Figure 6 shows the variation of the computed  $n$  values obtained for seven frequencies at the measured transition location of  $x/c = 0.47$ . The maximum value of  $n$  is around 4.8 for a frequency of approximately 25 kHz. The computed value of  $n$  for transition is much lower than the value of  $n$  for this cryogenic wind tunnel T2 of CERT which has a freestream turbulence level of about 0.2% and a transition value of  $n$  between 7 and 8 based on experiments performed at ambient flow conditions.

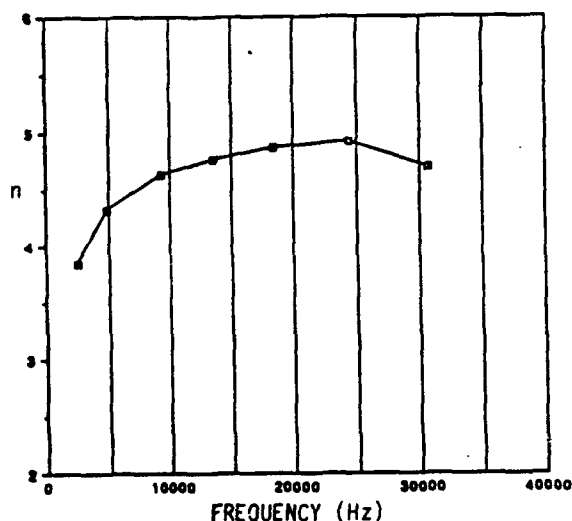


Fig. 6. Variation of  $n$  as a function of frequency at the transition point  $x/c = 0.47$ .

To investigate the influence of wall temperature on the stability calculations, the following studies were conducted for specified wall temperature distributions. Figure 7 shows that the experimental wall temperature is higher than the adiabatic wall temperature and varies more along the chord. Since a higher wall temperature makes the boundary layer more unstable, it is plausible to assume that the stability calculations will yield higher values of  $n$  than those corresponding to adiabatic wall temperatures.

Figure 8 shows the computed results for the same two high and low frequencies studies previously. The characteristic shape of the curves has

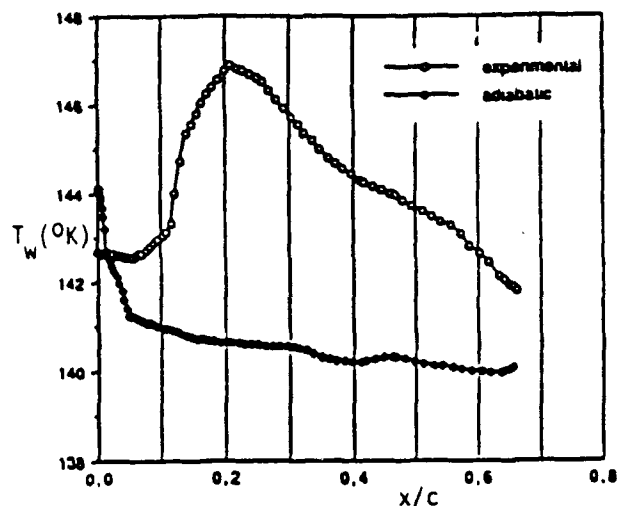
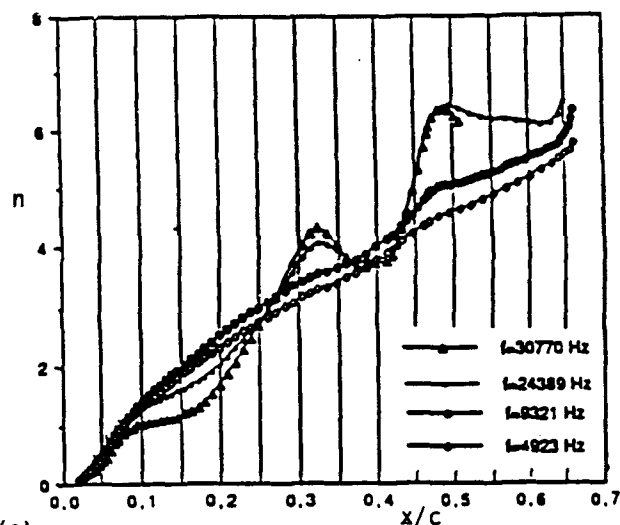
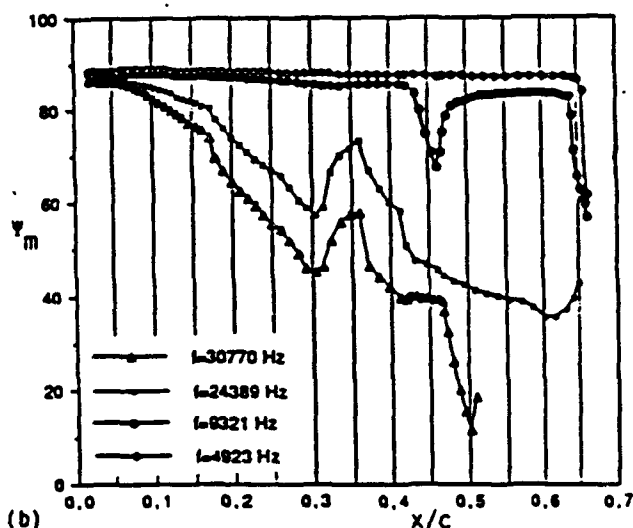


Fig. 7. Comparison of measured and adiabatic wall temperature distributions along  $x/c$ .



(a)



(b)

Fig. 8. Distributions of (a) computed  $n$  factors and (b) the most unstable direction  $\psi_m$  of the disturbances for the experimental wall temperature distribution in run 42.

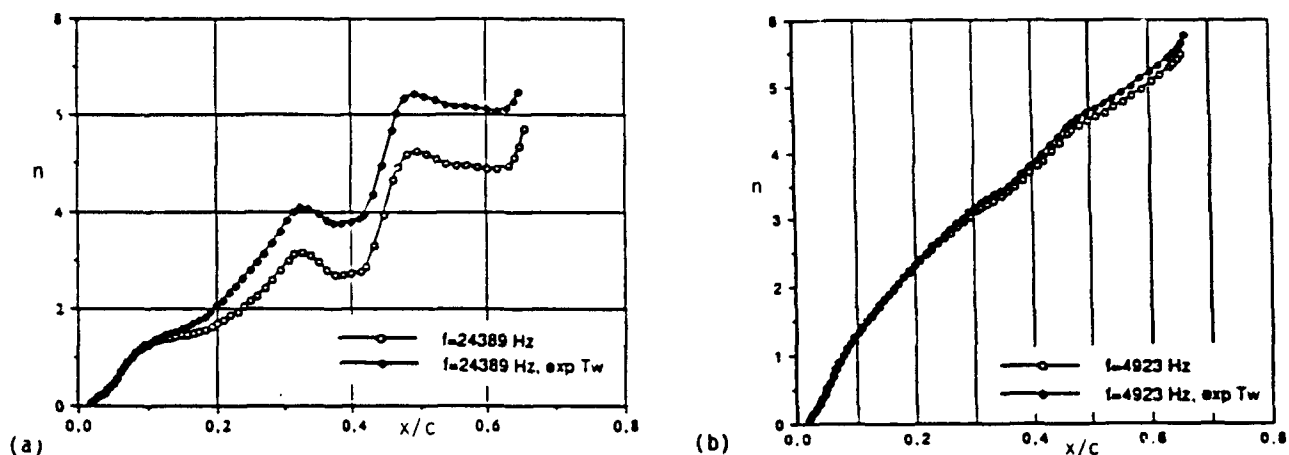


Fig. 9. Comparison of  $n$ -factor distributions for adiabatic and experimental wall temperature distributions in run 42, (a) high frequency case, (b) low frequency case.

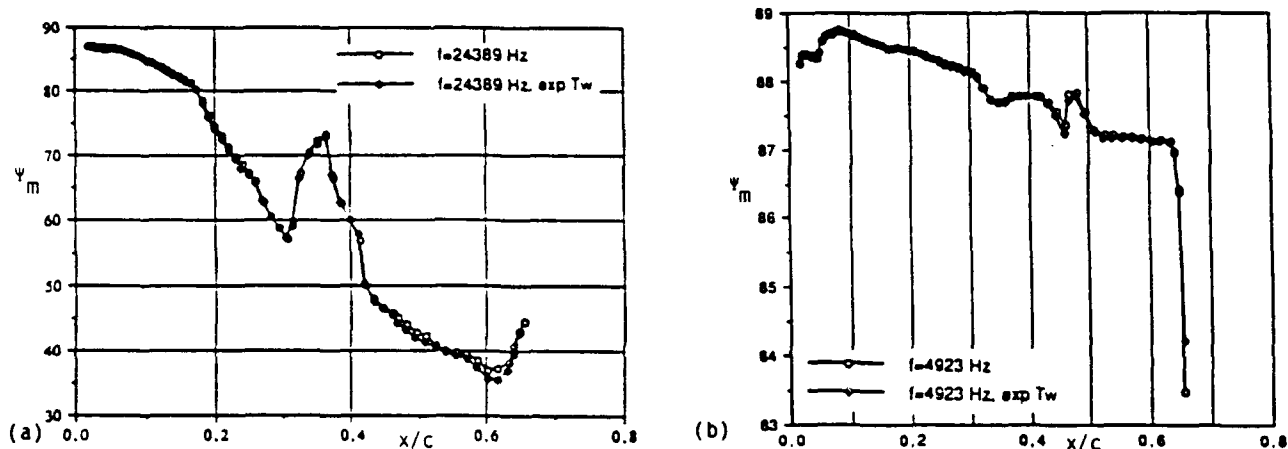


Fig. 10. Comparison of  $\psi_m$  distributions for adiabatic and experimental wall temperature distributions in run 42, (a) high frequency case, (b) low frequency case.

not changed and the previously discussed mechanisms for the adiabatic wall temperature calculations are still valid. However, in direct comparison with the adiabatic case, it can be observed that the results with high frequency (Fig. 9a) show a remarkably higher  $n$  distribution for  $x/c$  greater than 0.17 for the case of the experimental temperature distribution while the  $n$  curves for the lower frequencies are almost similar (see Fig. 9b). The  $\psi_m$  distributions for either case (see Fig. 10) show that the most unstable directions are independent of the wall temperature.

Figures 11 to 13 show the results for run 79 at a chord Reynolds number of  $13.4 \times 10^6$ . This case essentially has the same drag coefficient and Reynolds number as run 42. For this reason we assume the location of transition to be at  $x/c \approx 0.47$ .

Figure 11 shows the calculated  $n$ -factor distribution for an adiabatic wall temperature distribution and Fig. 12 shows the comparison of the  $n$ -factor distributions for adiabatic and experimental wall temperature distributions. As shown in Fig. 13, the temperature differences between adiabatic and measured wall temperatures for this run is weaker than for run 42. As a result, the distribution of  $n$  factors for both cases do not differ much from each other although, as in run

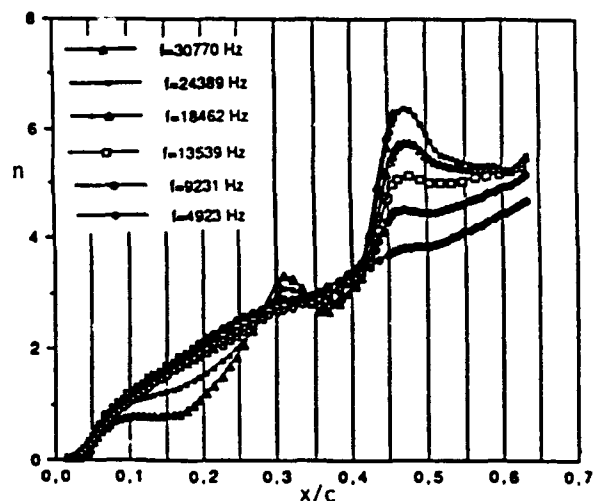


Fig. 11. Distribution of computed  $n$  factors for adiabatic wall conditions in run 79.

42, the measured wall temperatures lead to higher values of  $n$  than those obtained with adiabatic wall conditions. It can also be seen that, while the value of  $n$  at transition location,  $x/c = 0.47$ , is slightly over 7 for calculations performed with a measured wall temperature distribution, it is around 6.3 for adiabatic wall conditions.

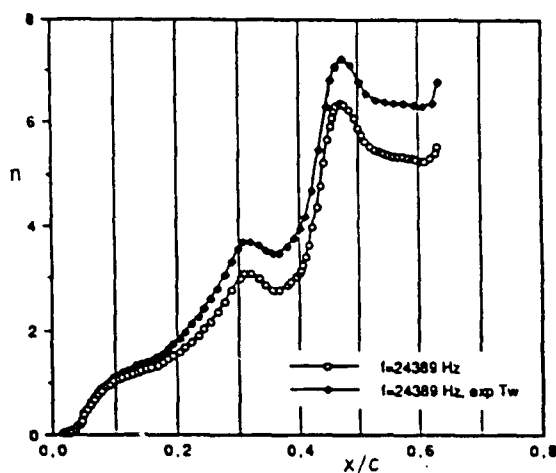


Fig. 12. Comparison of computed  $n$  factors for adiabatic and measured wall temperature distributions in run 79.

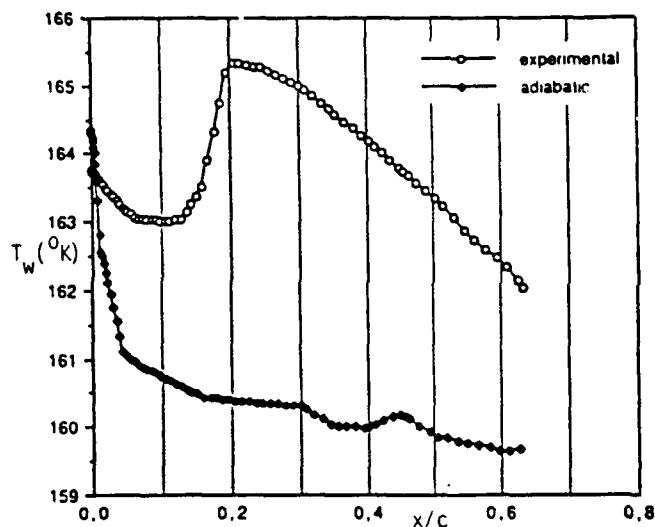


Fig. 13. Difference of real and adiabatic wall temperature distributions along  $x/c$ .

We note from the above results that near the leading edge ( $x/c < 0.10$ ), all the unstable frequencies are of the crossflow type. Further downstream, the most unstable direction of the high frequencies decreases, leading to a more or less streamwise instability. It is interesting to note that this streamwise instability is very sensitive to small Mach number variations (hollows) as well as to the wall temperature. By contrast, the most unstable direction of the low frequencies remains close to  $90^\circ$ : they correspond to a crossflow instability which does not "see" the hollows (the evolution of the  $n$ -factor is monotonic). This instability is also not sensitive to the wall temperature variations. This is due to the fact that it is an "inflectional" instability governed by an inflection point located near the outer edge of the boundary layer.

### 3.3 Calculations with the CSC Method

A detailed description of the stability calculations for runs 42 and 79 are given in the previous section for the upper surface of the AS 409

wing. Similar detailed calculations have also been performed for the same runs, including run 60, using the CSC method described in subsection 2.2 and will be reported separately. In this subsection we shall present a summary of the predictions of the saddle-point method of Cebeci and Stewartson for the same runs, 42 and 79, by showing the distribution of  $n$  factors at several frequencies. We shall also present and discuss the procedure of determining the frequencies used in the calculation of amplification rates, which is different than any other method which employs a combination of linear stability theory and  $e^n$ -method to predict transition. In fact, the studies conducted with this method for incompressible flows on wings and bodies of revolution and recent studies in compressible flows over modern transport and military wings show that the calculation of the critical frequencies is the most important aspect of the transition prediction procedure using stability theory. The critical frequencies originate in a very narrow regions and require care and patience to compute their magnitudes and locations.

The frequencies needed in transition calculations are computed from zarfs recommended by Cebeci and Stewartson.<sup>7</sup> They essentially correspond to neutral stability curves in three-dimensional flows and have the following properties,

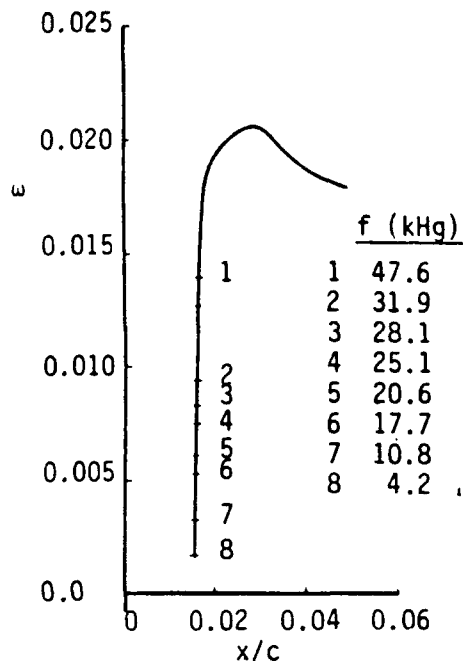
$$\alpha_1 = \beta_1 = 0, \quad \frac{\partial \alpha}{\partial \beta} = \text{real} \quad (15)$$

In the saddle-point method, for given velocity profiles obtained with the infinite-swept boundary-layer method of Cebeci, the stability calculations begin on the zarf where, with  $R$  known and  $\alpha_1, \beta_1$  zero, the eigenvalue problem consists of calculating  $\alpha_r, \beta_r$  and  $\omega$  with the requirement given by Eq. (13). With the eigenvalues and disturbance angle  $\gamma$  of the zarf known at a specified  $x/c$ -location and with dimensional frequency specified, the calculations at the following  $x/c$ -station are performed to obtain  $\alpha$  and  $\beta$  again with the requirement that  $\partial \alpha / \partial \beta$  is real. This eigenvalue procedure is then repeated for different values of  $\partial \alpha / \partial \beta$  or  $\gamma$  to find the value of  $\gamma$  for which  $r$  is maximum at each  $x/c$ -station. This process is repeated for each  $x/c$ -station, and  $n$  is calculated by evaluating the integral

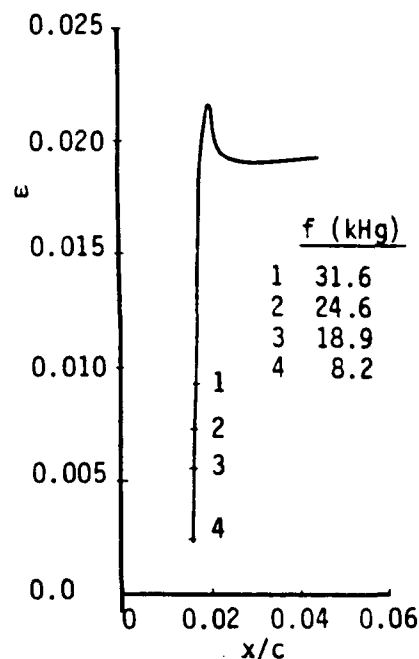
$$n = - \int_{x_0}^x r dx \quad (16)$$

Figure 14 shows the zarfs for run 42 for an adiabatic wall and measured wall temperature distributions. As can be seen, the frequencies originate at nearly the same location (on a vertical line) and vary drastically one from another. Their calculation requires care and patience. A paper in preparation will discuss our procedure for generating them.

Figure 15 shows the computed  $n$  factors for the zarfs of Fig. 14. The results show that for adiabatic wall conditions, the maximum value of  $n$  for experimental transition location is around 6.3; the corresponding value for the measured wall temperature is 7.3. What is more important, however, is the fact that in the latter case, the computed transition location agrees very well with the observed location considering that the  $n$ -value for transition in this tunnel lies between 7 and 8.

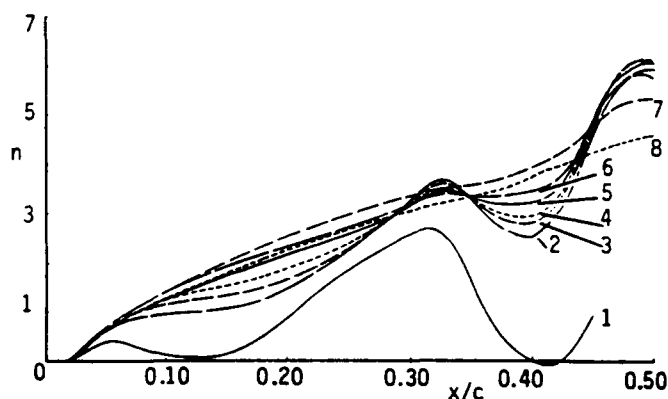


(a)

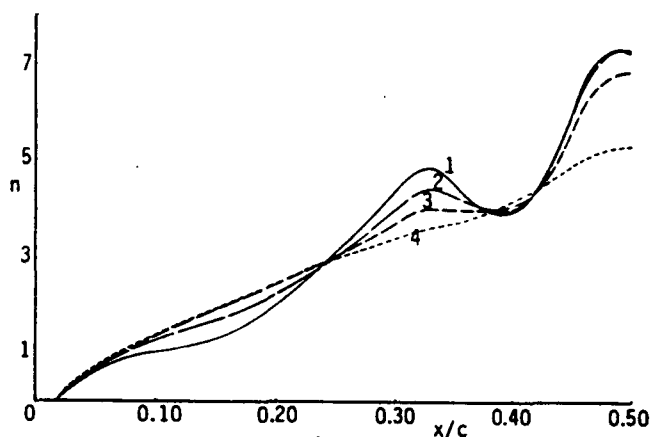


(b)

Fig. 14. Zarfs for run 42 for (a) adiabatic and (b) measured wall temperature distributions.



(a)



(b)

Fig. 15. Computed n-factors for run 42 for (a) adiabatic and (b) measured wall temperature distributions.

Figure 16 shows the zarfs for run 79 with wall conditions corresponding to adiabatic temperature and Fig. 17 shows a comparison between the zarfs obtained under adiabatic and measured wall temperature conditions. Again the steep rise in frequencies at almost one  $x/c$ -location is noted. The zarf calculations were performed for a very fine  $x/c$ -grid, since most of the frequencies start their amplification in an interval of  $1/1000^{\text{th}}$  of chord around 0.015. Figure 16 also shows zarfs away from the leading edge. These zarfs have low values of  $\beta_r$  around  $10^{-2}$ , occur in an almost zero pressure gradient region and do not lead to amplification rates that grow significantly.

Figure 18 shows the computed n factors for run 79 with stability calculations performed for zarfs

in Fig. 17 under adiabatic and measured wall temperature conditions. For this flow, the n-value is much higher than those in run 42. For an adiabatic wall, it reaches a maximum value of around 8 and a value of around 9 for the measured wall temperature case. If we take the n value to be 7.5, a mid-n value of the expected n-value range for this wind tunnel, then transition occurs at  $x/c = 0.46$  for adiabatic wall conditions and  $x/c = 0.47$  for measured wall temperature conditions. This compares well with inferred transition location of  $x/c = 0.47$ .

Figures 19 and 20 show a comparison between the calculated n-factors obtained with both methods, with results of CSC corresponding only to the disturbance that leads to transition. As can be

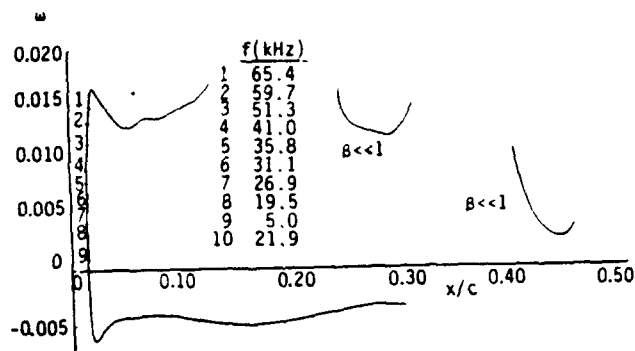


Fig. 16. Zarfs for run 79 for adiabatic wall temperature distribution.

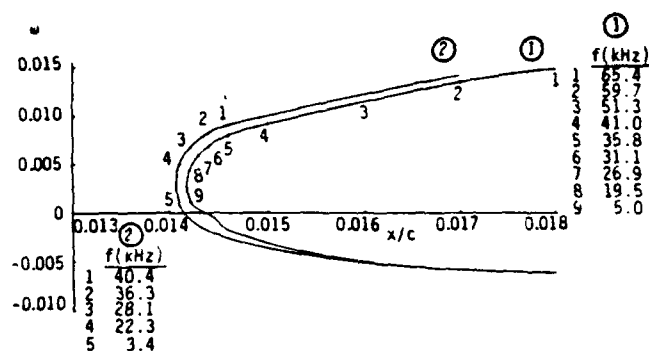


Fig. 17. Comparison between zarfs of run 79 for (1) adiabatic and (2) measured wall temperature distributions.

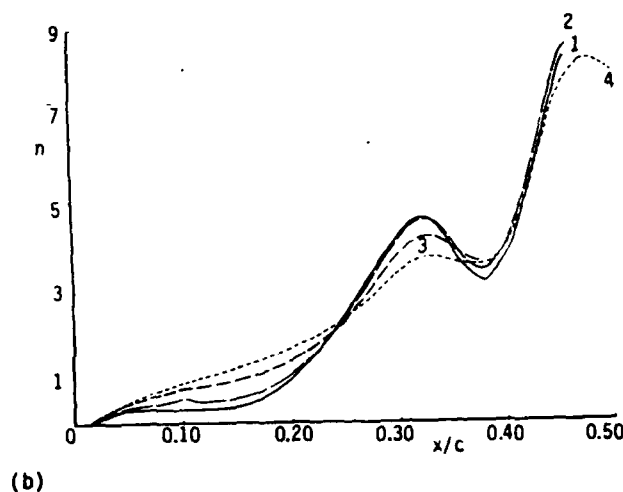
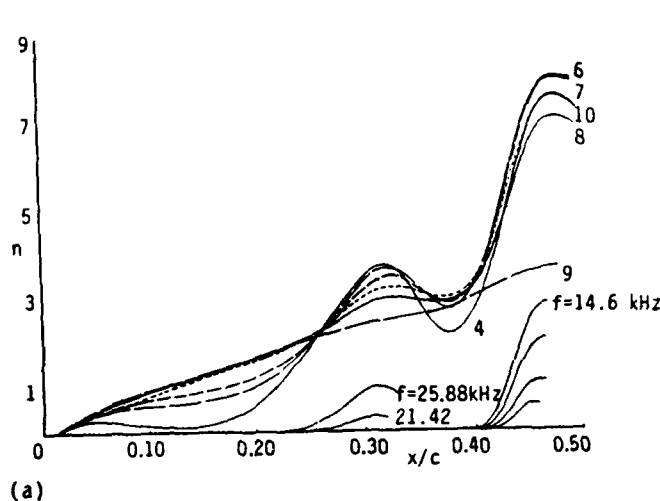


Fig. 18. Computed n-factors for run 79 for (a) adiabatic and (b) measured wall temperature distributions.

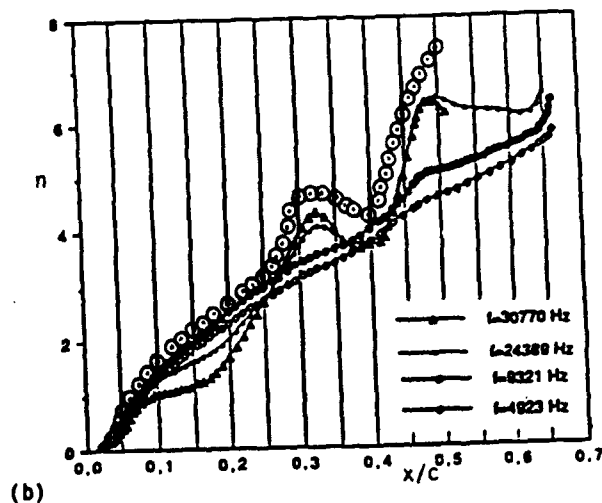
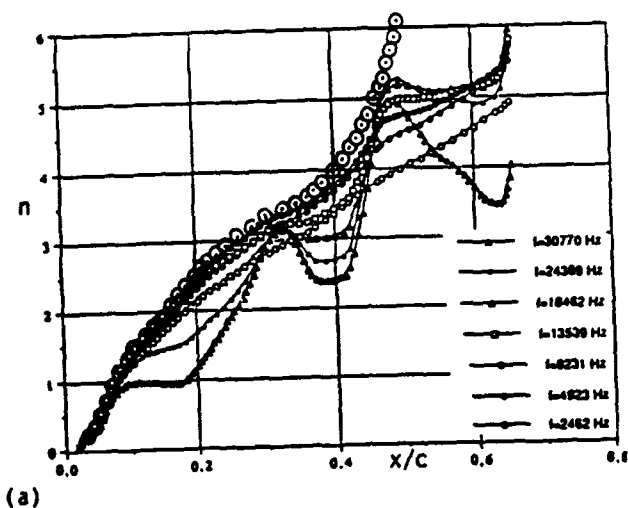


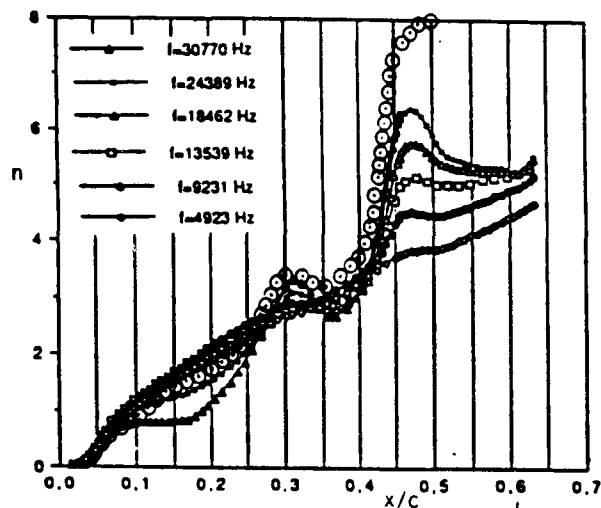
Fig. 19. Comparison between the predictions of CSC (denoted by circles ⊙) and ONERA/CERT methods for (a) adiabatic, and (b) measured wall temperature distributions in run 42.

seen, for  $x/c$  around 0.45, the calculations with the CSC method indicate higher values of the n-factor. The calculations with the ONERA/CERT method correlate the data with  $n$  between 6.5 and 7 while those of CSC with  $n$  between 7 and 8.

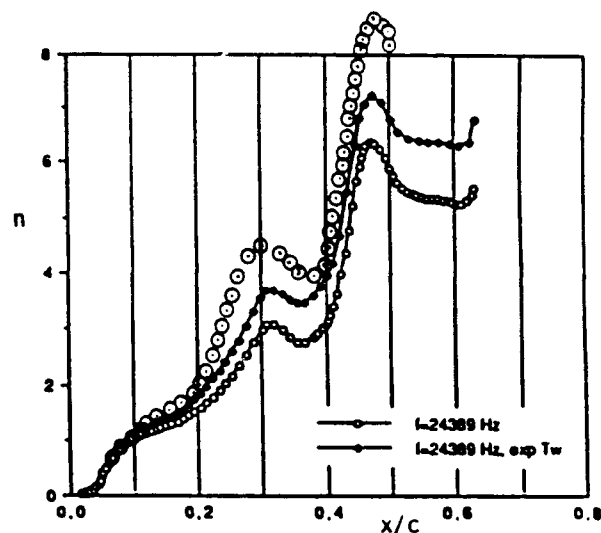
#### 4.0 Concluding Remarks

Based on the studies reported here and in Refs. 9 and 10, the following two comments can be made. First, rather crude assumptions have been made in





(a)



(b)

Fig. 20. Comparisons between the predictions of CSC (denoted by circles  $\odot$ ) and ONERA/CERT methods for (a) ablatitic, and (b) measured wall temperature distributions in run 79.

the computations (infinite swept wing assumption with a mean sweep angle and a mean chord). Second, it is possible that cryogenic conditions (temperature fluctuations) degrade the flow quality. This could explain the reason why the ONERA/CERT method calculates  $n$ -factors somewhat lower than those computed for ambient temperature with the same stability code. For stagnation temperatures lower than those considered in the paper, ice crystals appear on the model and trigger transition.

**Acknowledgement:** The authors are grateful to Dr. Y. Vigneron of Aerospatiale Toulouse (AS Toulouse) for giving them permission to publish the experimental data shown in Figures 1 to 4.

## 5.0 References

- Smith, A.M.O. and Gamberoni, N., "Transition, Pressure Gradient, and Stability Theory," Proc. Int. Congress Appl. Mech., Vol. 9, Brussels, Vol. 4, p. 234, 1956.
- Van Ingen, J.L., "A Suggested Semi-Empirical Method for the Calculation of the Boundary-Layer Region," Rept. No. VTH71, VTH74, Delft, Holland, 1956.
- Gaster, M., "A Note on the Relation Between Temporally Increasing and Spatially Increasing Disturbances in Hydrodynamic Stability," J. Fluid Mech., Vol. 14, pp. 222-224, 1962.
- Malik, M.R., "COSAL - A Black Box Compressible Stability Analysis Code for Transition Prediction in Three-Dimensional Boundary Layers," NASA CR 165 925, 1982.
- Mack, L.M., "Boundary-Layer Stability Theory," AGARD Rept. No. 709, 1984.
- Mack, L.M., "Stability of Three-Dimensional Boundary Layers on Swept Wings at Transonic Speeds," IUTAM Symposium, Transsonicum III, Göttingen, May 1988.
- Cebeci, T. and Stewartson, K., "Stability and Transition in Three-Dimensional Flows," AIAA J., Vol. 18, pp. 398-405, 1980.
- Cebeci, T., Chen, H.H., Arnal, D. and Huang, T.T., "A Three-Dimensional Linear Stability Approach to Transition on Wings and Bodies of Revolution at Incidence," to be published in AIAA J., December 1991.
- Séraudie, A., Archambaud, J.P. and Payry, M.J., "Etude de la laminarité sur l'aile AS409 jusqu'à des nombres de Reynolds de l'ordre de 14 millions dans la soufflerie T2," ONERA/CERT Internal Report No. 33/5006-19, June 1989.
- Niethammer, R., "Boundary-Layer Stability Computations Related to Laminar Flow Experiments at Low Temperatures," Projet de fin d'études. Département d'études et de recherches en aerothermodynamique, Toulouse Cedex, July 1991.

## Appendix 1. Nonzero Elements of Matrix B.

$$\gamma_1 = \alpha u + \beta w - \omega, \quad \gamma_2 = \alpha^2 + \beta^2, \quad d = \frac{\lambda}{\mu}$$

$$\gamma_3 = \alpha \frac{du}{dy} + \beta \frac{dw}{dy}, \quad \gamma_4 = \alpha \frac{dw}{dy} - \beta \frac{du}{dy}$$

$$b_{21} = \frac{1R}{\mu T} \gamma_1 + \gamma_2, \quad b_{22} = -\frac{1}{\mu} \frac{du}{dT} \frac{dT}{dy}$$

$$b_{23} = \frac{R\gamma_3}{\mu T} - \gamma_2 \frac{1}{\mu} \frac{du}{dT} \frac{dT}{dy} - \frac{1+2d}{3} \gamma_2 \frac{1}{T} \frac{dT}{dy}$$

$$b_{24} = \frac{1R}{\mu} \gamma_2 - \frac{1+2d}{3} \gamma_2^2 \gamma_1$$

$$b_{25} = \frac{1+2d}{3T} \gamma_1 \gamma_2 - \frac{1}{\mu} \frac{du}{dT} \left( \alpha \frac{d^2 u}{dy^2} + \beta \frac{d^2 w}{dy^2} \right)$$

$$- \frac{1}{\mu} \frac{d^2 w}{dT^2} \frac{dT}{dy} \gamma_3$$

$$b_{26} = -\frac{1}{\mu} \frac{d\mu}{dT} \gamma_3, \quad b_{31} = -1, \quad b_{33} = \frac{1}{T} \frac{dT}{dy}$$

$$b_{34} = -1 \gamma M_e^2 \gamma_1.$$

$$b_{35} = \frac{1}{T} \gamma_1, \quad E = \frac{R}{\mu} + \frac{2}{3} 1(2+d) \gamma M_e^2 \gamma_1$$

$$b_{41} = -\frac{1}{E} [-2b_{22} + \frac{2}{3} (2+d)b_{33}], \quad b_{42} = -\frac{1}{E}$$

$$b_{43} = \frac{1}{E} [-\gamma_2 + \frac{2(2+d)}{3\mu T} \frac{d\mu}{dT} (\frac{dT}{dy})^2 \\ + \frac{2(2+d)}{3T} \frac{d^2 T}{dy^2} - \frac{1R}{\mu T} \gamma_1]$$

$$b_{44} = -\frac{21}{3E} (2+d) \gamma M_e^2 (-\gamma_1 b_{22} + \gamma_3 + b_{22} \gamma_1)$$

$$b_{45} = \frac{1}{E} [\frac{1}{\mu} \frac{d\mu}{dT} \gamma_3 + \frac{2(2+d)}{3T} (-b_{22} \gamma_1 + \gamma_3)]$$

$$b_{46} = \frac{21}{3ET} (2+d) \gamma_1$$

$$b_{62} = -2(\gamma - 1) \text{Pr} M_e^2 (\frac{\gamma_3}{\gamma_2})$$

$$b_{63} = \frac{\text{Pr} R}{\mu} b_{33} - 21(\gamma - 1) \text{Pr} M_e^2 \gamma_3$$

$$b_{64} = -\frac{1}{\mu} (\gamma - 1) \text{Pr} M_e^2 \gamma_1$$

$$b_{65} = 1 \frac{\text{Pr} R}{\mu T} \gamma_1 + \gamma_2 - \frac{1}{k} \frac{dk}{dT} \frac{d^2 T}{dy^2} - \frac{1}{k} \frac{d^2 k}{dT^2} (\frac{dT}{dy})^2 \\ - (\gamma - 1) \text{Pr} M_e^2 \frac{1}{\mu} \frac{d\mu}{dT} (\frac{d^2 u}{dy^2} + \frac{d^2 w}{dy^2})$$

$$b_{66} = -\frac{2}{k} \frac{dk}{dT} \frac{dT}{dy},$$

$$b_{68} = -\frac{2(\gamma - 1)}{\gamma_2} \text{Pr} M_e^2 \gamma_4$$

$$b_{83} = \frac{R}{\mu T} \gamma_4.$$

$$b_{85} = -\frac{1}{\mu} \frac{d\mu}{dT} (\alpha \frac{d^2 w}{dy^2} - \beta \frac{d^2 u}{dy^2}) - \frac{1}{\mu} \frac{d^2 \mu}{dT^2} \frac{dT}{dy} \gamma_4$$

$$b_{86} = -\frac{1}{\mu} \frac{d\mu}{dT} \gamma_4, \quad b_{87} = \frac{1R}{\mu T} \gamma_1 + \gamma_2, \quad b_{88} = b_{22}$$

**TRANSITION AND TURBULENCE MODELLING, 2**  
**SESSION 2**



# THE REMARKABLE ABILITY OF TURBULENCE MODEL EQUATIONS TO DESCRIBE TRANSITION

13-15 JANUARY 1992

by

David C. Wilcox  
DCW Industries, Inc.  
La Cañada, California

## Abstract

This paper demonstrates how well the  $k$ - $\omega$  turbulence model describes the nonlinear growth of flow instabilities from laminar flow into the turbulent flow regime. Viscous modifications are proposed for the  $k$ - $\omega$  model that yield close agreement with measurements and with Direct Numerical Simulation results for channel and pipe flow. These modifications permit prediction of subtle sublayer details such as maximum dissipation at the surface,  $k \sim y^2$  as  $y \rightarrow 0$ , and the sharp peak value of  $k$  near the surface. With two transition specific closure coefficients, the model equations accurately predict transition for an incompressible flat-plate boundary layer. The analysis also shows why the  $k$ - $\epsilon$  model is so difficult to use for predicting transition.

## 1. Introduction

There has been renewed interest in development of methods for predicting boundary-layer transition. Current interest in vehicles such as the National Aerospace Plane (NASP), for example, provides the impetus for developing accurate transition prediction tools. Furthermore, because hypersonic boundary layers rarely achieve momentum-thickness Reynolds numbers large enough to sustain fully-developed turbulence, even the post-transition region generally exhibits nontrivial viscous effects. Consequently, accurate low-Reynolds-number turbulence models are also needed.

The standard approach is to view development of a transition model and a low-Reynolds-number turbulence model as two separate issues. The strongest argument in favor of this approach is simply that all spectral effects are lost in the time-averaging process used by turbulence models. Tollmien-Schlichting waves, for example, cannot be distinguished by a turbulence-model. Since a given boundary layer is unstable to perturbations that fall in a specific range of frequencies, conventional turbulence models, which distinguish only magnitude and an average frequency, can never be certain if a given perturbation will actually cause transition. However, if we implement two separate models, one for the transition region and another for the developing turbulent region, achieving a smooth joining of the two models' predictions presents an additional complication.

This complication can be avoided if we view both issues as low-Reynolds-number phenomena that can be addressed in the context of a single model. The strongest argument for this approach is that we can use the same model to describe a smooth transition from laminar to fully turbulent flow, including the transitional region. This approach is plausible provided we restrict our applications to broadband transition-triggering disturbances.

The research of Wilcox, et al.<sup>1-6</sup> provides a great deal of support for the latter approach. Using a  $k$ - $\omega^2$  turbulence model and transition-specific, low-Reynolds-number modifications, Wilcox simulated boundary-layer transition for a wide range of Mach numbers including pressure gradient, surface roughness, surface heating and cooling, and surface

mass transfer. The purpose of this paper is to build upon the work of Wilcox, et al. taking advantage of recent Direct Numerical Simulation (DNS) results in developing appropriate viscous modifications for the Wilcox'  $k$ - $\omega$  model. The scope of this paper is confined to incompressible flows.

For incompressible turbulent fluid flow, the complete set of equations that constitute the Wilcox  $k$ - $\omega$  two-equation model are as follows.

$$\frac{\partial u_i}{\partial x_i} = 0 \quad (1)$$

$$\frac{\partial}{\partial t}(\rho u_i) + \frac{\partial}{\partial x_j}(\rho u_j u_i) = \frac{\partial}{\partial x_j}[-p\delta_{ij} + \hat{\tau}_{ij}] \quad (2)$$

$$\begin{aligned} \frac{\partial}{\partial t}(\rho k) + \frac{\partial}{\partial x_j}(\rho u_j k) &= \tau_{ij} \frac{\partial u_i}{\partial x_j} - \beta^* \rho \omega k \\ &+ \frac{\partial}{\partial x_j}[(\mu + \sigma^* \mu_T) \frac{\partial k}{\partial x_j}] \end{aligned} \quad (3)$$

$$\begin{aligned} \frac{\partial}{\partial t}(\rho \omega) + \frac{\partial}{\partial x_j}(\rho u_j \omega) &= \alpha \frac{\omega}{k} \tau_{ij} \frac{\partial u_i}{\partial x_j} - \beta \rho \omega^2 \\ &+ \frac{\partial}{\partial x_j}[(\mu + \sigma \mu_T) \frac{\partial \omega}{\partial x_j}] \end{aligned} \quad (4)$$

$$\hat{\tau}_{ij} = 2\mu S_{ij} + \tau_{ij} \quad (5)$$

$$\tau_{ij} = 2\mu_T S_{ij} - \frac{2}{3}\rho k \delta_{ij} \quad (6)$$

$$\mu_T = \alpha^* \rho k / \omega \quad (7)$$

$$S_{ij} = \frac{1}{2} \left[ \frac{\partial u_i}{\partial x_j} + \frac{\partial u_j}{\partial x_i} \right] \quad (8)$$

In Equations (1-8),  $t$  is time,  $x_i$  is position vector,  $u_i$  is velocity,  $\rho$  is density,  $p$  is pressure,  $\mu$  is molecular viscosity, and  $\hat{\tau}_{ij}$  is the sum of molecular and Reynolds stress tensors. Also,  $\delta_{ij}$  is the Kronecker delta,  $k$  is the turbulence kinetic energy,  $\omega$  is specific dissipation rate,  $\tau_{ij}$  is Reynolds stress tensor, and  $\mu_T$  is eddy viscosity. The six parameters  $\alpha$ ,  $\alpha^*$ ,  $\beta$ ,  $\beta^*$ ,  $\sigma$  and  $\sigma^*$  are closure coefficients whose values are given below.

$$\alpha^* = \frac{\alpha_o^* + Re_T/R_k}{1 + Re_T/R_k} \quad (9)$$

$$\alpha = \frac{5}{9} \cdot \frac{\alpha_o + Re_T/R_\omega}{1 + Re_T/R_\omega} \cdot (\alpha^*)^{-1} \quad (10)$$

$$\beta^* = \frac{9}{100} \cdot \frac{5/18 + (Re_T/R_g)^4}{1 + (Re_T/R_g)^4} \quad (11)$$

$$\beta = 3/40, \quad \sigma^* = \sigma = 1/2 \quad (12)$$

$$\alpha_0^* = \beta/3, \quad \alpha_0 = 1/10 \quad (13)$$

$$R_g = 8, \quad R_k = 6, \quad R_\omega = 2.7 \quad (14)$$

where  $Re_T$  is turbulence Reynolds number defined by

$$Re_T = \rho k / (\omega \mu) \quad (15)$$

Section II explains in detail how the turbulence model simulates transition, and justifies the form of the viscous modifications. Section III explains why the most popular low-Reynolds-number  $k-\epsilon$  models are unsuitable for predicting transition. Section IV demonstrates how well the model performs for low-Reynolds-number channel flow and for pipe flow. Section V includes transition predictions for an incompressible flat-plate boundary layer. Section VI presents a summary of and conclusions drawn from the study.

## II. Simulating Transition with Turbulence Model Equations

Turbulence model equations can be used to predict transition from laminar to turbulent flow, although most models predict transition to turbulence at Reynolds numbers that are at least an order of magnitude too low. To understand why and how the  $k-\omega$  model predicts transition, consider the flat-plate boundary layer. For the  $k-\omega$  model, the incompressible, two-dimensional boundary-layer form of the equations for  $k$  and  $\omega$  is as follows.

$$u \frac{\partial u}{\partial x} + v \frac{\partial u}{\partial y} = \frac{\partial}{\partial y} \left[ (\nu + \nu_T) \frac{\partial u}{\partial y} \right] \quad (16)$$

$$u \frac{\partial k}{\partial x} + v \frac{\partial k}{\partial y} = \nu_T \left( \frac{\partial u}{\partial y} \right)^2 - \beta^* \omega k + \frac{\partial}{\partial y} \left[ (\nu + \sigma^* \nu_T) \frac{\partial k}{\partial y} \right] \quad (17)$$

$$u \frac{\partial \omega}{\partial x} + v \frac{\partial \omega}{\partial y} = \alpha \frac{\omega}{k} \nu_T \left( \frac{\partial u}{\partial y} \right)^2 - \beta \omega^2 + \frac{\partial}{\partial y} \left[ (\nu + \sigma \nu_T) \frac{\partial \omega}{\partial y} \right] \quad (18)$$

$$\nu_T = \alpha^* k / \omega \quad (19)$$

where  $u$  and  $v$  are velocity components in the streamwise ( $x$ ) and normal ( $y$ ) directions, respectively,  $\nu$  is kinematic molecular viscosity, and  $\nu_T$  is kinematic eddy viscosity. We can most clearly illustrate how the model equations predict transition by rearranging terms in Equations (17) and (18) as follows.

$$u \frac{\partial k}{\partial x} + v \frac{\partial k}{\partial y} = P_k \beta^* \omega k + \frac{\partial}{\partial y} \left[ (\nu + \sigma^* \nu_T) \frac{\partial k}{\partial y} \right] \quad (20)$$

$$u \frac{\partial \omega}{\partial x} + v \frac{\partial \omega}{\partial y} = P_\omega \beta \omega^2 + \frac{\partial}{\partial y} \left[ (\nu + \sigma \nu_T) \frac{\partial \omega}{\partial y} \right] \quad (21)$$

The *net production per unit dissipation* for the two equations,  $P_k$  and  $P_\omega$ , are defined by:

$$P_k = \frac{\alpha^*}{\beta^*} \left( \frac{\partial u / \partial y}{\omega} \right)^2 - 1 \quad (22)$$

$$P_\omega = \frac{\alpha \alpha^*}{\beta} \left( \frac{\partial u / \partial y}{\omega} \right)^2 - 1 \quad (23)$$

There are two important observations worthy of mention at this point. *First*, if the turbulence energy is zero, Equation (21) has a well-behaved solution. That is, when  $k = 0$ , the eddy viscosity vanishes and the  $\omega$  equation uncouples from the  $k$  equation. Consequently, the  $k-\omega$  model has a nontrivial laminar-flow solution for  $\omega$ . *Second*, the signs of  $P_k$  and  $P_\omega$  determine whether  $k$  and  $\omega$  are amplified or reduced in magnitude. However, it is not obvious by inspection of Equations (22) and (23) how the signs of these terms vary with Reynolds number as we move from the plate leading edge to points downstream. We can make the variation obvious by rewriting Equations (22) and (23) in terms of the Blasius transformation.

Before we introduce the Blasius transformation, we must determine the appropriate scaling for  $\omega$ . To do this, we note that close to the surface of a flat plate boundary layer, the specific dissipation rate behaves according to<sup>7</sup>

$$\omega \rightarrow \frac{6\nu}{\beta y^2} \quad \text{as } y \rightarrow 0 \quad (24)$$

In terms of the Blasius similarity variable,  $\eta$ , defined by

$$\eta = y / (\nu x / U_\infty)^{1/2} \quad (25)$$

where  $U_\infty$  is freestream velocity, the asymptotic behavior of  $\omega$  approaching the surface is

$$\omega \rightarrow \frac{6 U_\infty}{\beta x} \frac{1}{\eta^2} \quad \text{as } \eta \rightarrow 0 \quad (26)$$

Consequently, we conclude that the appropriate scaling for  $\omega$  in the Blasius boundary layer is given by

$$\omega = \frac{U_\infty}{x} W(x, \eta) \quad (27)$$

where  $W(x, \eta)$  is a dimensionless function to be determined as part of the solution. Hence, if we write the velocity in terms of dimensionless velocity,  $F(x, \eta)$ , i.e.,

$$u = U_\infty F(x, \eta) \quad (28)$$

the *net production per unit dissipation* terms become

$$P_k = \frac{\alpha^*}{\beta^*} Re_x \left( \frac{\partial F / \partial \eta}{W} \right)^2 - 1 \quad (29)$$

$$P_\omega = \frac{\alpha \alpha^*}{\beta} Re_x \left( \frac{\partial F / \partial \eta}{W} \right)^2 - 1 \quad (30)$$

Thus, both  $P_k$  and  $P_\omega$  increase linearly with Reynolds number,  $Re_x$ . From the exact laminar solution for  $F(\eta)$  and  $W(\eta)$  [the  $x$  dependence vanishes for the Blasius boundary layer], the maximum value of the ratio of  $\partial F / \partial \eta$  to  $W$  is given by

$$\left( \frac{\partial F / \partial \eta}{W} \right)_{\max} \approx \frac{1}{300} \quad (31)$$

Hence, as long as the eddy viscosity remains small compared to the molecular viscosity, we can specify the precise points where  $P_k$  and  $P_\omega$  change sign. In general, using Equation (31), we conclude that the sign changes occur at the following Reynolds numbers.

$$(Re_x)_k = 9 \cdot 10^4 \frac{\beta^*}{\alpha^*} \quad (32)$$

$$(Re_x)_\omega = 9 \cdot 10^4 \frac{\beta}{\alpha \alpha^*} \quad (33)$$

With no viscous modifications, the closure coefficients  $\alpha$ ,  $\alpha^*$ ,  $\beta$  and  $\beta^*$  are 5/9, 1, 3/40 and 9/100, respectively. These values correspond to the limiting form of Equations (9-14) as  $Re_T \rightarrow \infty$ . Using these *fully turbulent* values, we find  $(Re_x)_k = 8,100$  and  $(Re_x)_\omega = 12,150$ . Thus, starting from laminar flow at the leading edge of a flat plate, the following sequence of events occurs.

- (1) The computation starts in a laminar region with  $k = 0$  in the boundary layer and a small freestream value of  $k$ .
- (2) Initially, because  $P_k < 0$  and  $P_\omega < 0$ , dissipation of both  $k$  and  $\omega$  exceeds production. Turbulence energy is entrained from the freestream and spreads through the boundary layer by molecular diffusion. Neither  $k$  nor  $\omega$  is amplified and the boundary layer remains laminar.
- (3) At the *critical Reynolds number*,  $Re_{xc} = 8,100$ , production catches dissipation in the  $k$  equation. Downstream of  $x_c$ ,  $k$  production exceeds  $k$  dissipation and turbulence energy is amplified. At some point in this process, the eddy viscosity grows rapidly and this corresponds to the transition point.
- (4)  $k$  continues to be amplified and, beyond  $Re_x = 12,150$  production catches dissipation in the  $\omega$  equation.  $\omega$  is now amplified and continues growing until a balance between production and dissipation is achieved in the  $k$  equation. When this balance is achieved, transition from laminar to turbulent flow is complete.

Consistent with experimental measurements, the entire process is very sensitive to the freestream value of  $k$ . There is also a sensitivity to the freestream value of  $\omega$ , although the sensitivity is more difficult to quantify.

Three key points are immediately obvious. *First*,  $k$  begins growing at a Reynolds number of 8,100. By contrast, linear-stability theory tells us that Tollmien-Schlichting waves begin forming in the Blasius boundary layer at a Reynolds number of 90,000. This is known as the *minimum critical Reynolds number*. Correspondingly, we find that the model predicts transition at much too low a Reynolds number. *Second*, inspection of Equations (32) and (33) shows that the width of the transition region is controlled by the ratio of  $\beta$  to  $\alpha \alpha^*$ . *Third*, transition will never occur if  $P_\omega$  reaches zero earlier than  $P_k$ . Thus, occurrence of transition requires

$$\alpha \alpha^* < \alpha^* \beta / \beta^* \quad \text{as } Re_T \rightarrow 0 \quad (34)$$

This fact must be preserved in any viscous modification to the model. The viscous modifications in Equations (9-14), i.e., the dependence of  $\alpha$ ,  $\alpha^*$  and  $\beta^*$  upon  $Re_T$ , are designed to accomplish two objectives. The most important

objective is to match the *minimum critical Reynolds number*. Reference to Equation (32) shows that we must require

$$\beta^* / \alpha^* \rightarrow 1 \quad \text{as } Re_T \rightarrow 0 \quad (35)$$

A secondary objective is to achieve *asymptotic consistency* with the exact behavior of  $k$  and dissipation,  $\epsilon = \beta^* k \omega$ , approaching a solid boundary. That is, we would like to have

$$k/y^2 \rightarrow \text{constant}, \quad \epsilon/k \rightarrow 2\nu/y^2 \quad \text{as } y \rightarrow 0 \quad (36)$$

Close to a solid boundary, Wilcox<sup>7</sup> shows that the dissipation and molecular diffusion terms balance in both the  $k$  and  $\omega$  equations. The very-near-wall solution for  $\omega$  is given by Equation (24). The solution for  $k$  is of the form

$$k/y^n \rightarrow \text{constant} \quad \text{as } y \rightarrow 0 \quad (37)$$

where  $n$  is given by

$$n = \frac{1}{2} [1 + (1 + 24\beta^*/\beta)^{1/2}] \quad (38)$$

Noting that dissipation is related to  $k$  and  $\omega$  by

$$\epsilon = \beta^* k \omega \quad (39)$$

we can achieve the desired asymptotic behavior of Equation (36) by requiring

$$\beta^* / \beta \rightarrow 1/3 \quad \text{as } Re_T \rightarrow 0 \quad (40)$$

Requiring this limiting behavior as  $Re_T \rightarrow 0$  is sufficient to achieve the desired asymptotic behavior as  $y \rightarrow 0$  since the eddy viscosity, and hence,  $Re_T$  vanish at a solid boundary.

If we choose to have  $\beta$  constant for all values of  $Re_T$ , Equations (34), (35) and (40) are sufficient to determine the limiting values of  $\alpha^*$  and  $\beta^*$  and an upper bound for  $\alpha \alpha^*$  as turbulence Reynolds number becomes vanishingly small. Specifically, we find

$$\left. \begin{array}{l} \alpha \alpha^* < \beta \\ \alpha^* \rightarrow \beta/3 \\ \beta^* \rightarrow \beta/3 \end{array} \right\} \quad \text{as } Re_T \rightarrow 0 \quad (41)$$

Wilcox, et al.<sup>14</sup> make the equivalent of  $\alpha \alpha^*$  and  $\alpha^*$  in their  $k-\omega^2$  models approach the same limiting value and obtain excellent agreement with measured transition width for incompressible boundary layers. Numerical experimentation with the  $k-\omega$  model indicates the optimum choice for incompressible boundary layers is  $\alpha \alpha^* \rightarrow 0.74\beta$ , or

$$\alpha \alpha^* \rightarrow 1/18 \quad \text{as } Re_T \rightarrow 0 \quad (42)$$

Equations (9-14) postulate functional dependencies upon  $Re_T$  that guarantee the limiting values in Equations (41) and (42), as well as the original *fully turbulent* values for  $Re_T \rightarrow \infty$ .

The three coefficients  $R_k$ ,  $R_k$  and  $R_\omega$  control the rate at which the closure coefficients approach their fully turbulent values. As in previous analyses based on the  $k-\omega$  model,<sup>7,8,9</sup> we can determine their values by using perturbation methods to analyze the viscous sublayer. Using the well established procedure, we can solve for the constant in the law of the wall,  $B$ , by solving the sublayer equations and evaluating the following limit.

$$B = \lim_{y \rightarrow 0} \left[ u^+ - \frac{1}{\kappa} \ln y^+ \right] \quad (43)$$

where  $u^* = u/u_*$  and  $v^* = u_*y/\nu$  are standard sublayer scaled coordinates. Also,  $\kappa = 0.41$  is Kármán's constant. For a given value of  $R_\delta$  and  $R_\kappa$ , there is a unique value of  $R_w$  that yields a constant in the law of the wall of 5.0. For small values of  $R_\delta$  the peak value of  $k$  near the surface is close to the value achieved without viscous corrections, viz.  $u_*^2/(\delta^*)^2$ . As  $R_\delta$  increases, the maximum value of  $k$  near the surface increases. Comparison of computed sublayer structure with Direct Numerical Simulation (DNS) results of Mansour, et al<sup>10</sup> indicates the optimum choice for these three coefficients is as indicated in Equation (14). Section IV presents a complete comparison of computed channel flow properties with the Mansour, et al DNS results.

The only flaw in the model's asymptotic consistency occurs in the Reynolds shear stress,  $\tau_{xy}$ . While the exact asymptotic behavior is  $\tau_{xy} \sim v^3$ , the model as formulated predicts  $\tau_{xy} \sim y^4$ . This discrepancy could easily be removed with another viscous modification. However, results obtained to date indicate this is of no significant consequence. It has no obvious bearing on either the model's ability to predict transition or properties of interest in turbulent boundary layers. The additional complexity and uncertainty involved in achieving this subtle feature of the very-near-wall behavior of  $\tau_{xy}$  does not appear to be justified.

### III. Difficulties Attending Use of the k- $\epsilon$ Model

Given the information developed in Section II, it is a simple matter to explain why little progress has been made in predicting transition with the k- $\epsilon$  model.<sup>11</sup> The primary difficulties can be easily demonstrated by focusing upon incompressible boundary layers. If we use the standard form of the k- $\epsilon$  model, Equations (17-19) are replaced by

$$u \frac{\partial k}{\partial x} + v \frac{\partial k}{\partial y} = \nu_T \left( \frac{\partial u}{\partial y} \right)^2 - \epsilon + \frac{\partial}{\partial y} \left[ (\nu + \nu_T / \sigma_k) \frac{\partial k}{\partial y} \right] \quad (44)$$

$$u \frac{\partial \epsilon}{\partial x} + v \frac{\partial \epsilon}{\partial y} = C_{\epsilon 1} \frac{\epsilon}{k} \nu_T \left( \frac{\partial u}{\partial y} \right)^2 - C_{\epsilon 2} \frac{\epsilon^2}{k} + \frac{\partial}{\partial y} \left[ (\nu + \nu_T / \sigma_\epsilon) \frac{\partial \epsilon}{\partial y} \right] \quad (45)$$

$$\nu_T = C_\mu f_\mu k^2 / \epsilon \quad (46)$$

Values of the closure coefficients/functions  $C_{\epsilon 1}$ ,  $C_{\epsilon 2}$ ,  $C_\mu$ ,  $f_\mu$ ,  $\sigma_k$  and  $\sigma_\epsilon$  differ amongst the various versions of this model. In the absence of viscous modifications, the standard values used are  $C_{\epsilon 1} = 1.44$ ,  $C_{\epsilon 2} = 1.92$ ,  $C_\mu = .09$ ,  $f_\mu = 1$ ,  $\sigma_k = 1$  and  $\sigma_\epsilon = .769$ .

One critical difference from the k- $\omega$  model is obvious by inspection of Equations (44-46). Specifically, if the turbulence energy is zero,  $\epsilon$  must also be zero. We cannot simply drop the eddy viscosity in the  $\epsilon$  equation because of the presence of  $k$  in the denominator of the  $\epsilon$  equation's dissipation term. The model does possess a laminar-flow solution for the ratio of  $\epsilon$  to  $k$ . That is, if we make the formal change of variables

$$\epsilon = C_\omega k \omega \quad (47)$$

and assume  $\nu_T < \nu$ , the following laminar-flow equation for  $\omega$  results.

$$u \frac{\partial \omega}{\partial x} + v \frac{\partial \omega}{\partial y} = (C_{\epsilon 1} - 1) f_\mu \left( \frac{\partial u}{\partial y} \right)^2 - (C_{\epsilon 2} - 1) C_\mu \omega^2 + \nu \frac{\partial^2 \omega}{\partial y^2} + \frac{2\nu}{k} \frac{\partial k}{\partial y} \frac{\partial \omega}{\partial y} \quad (48)$$

Equation (48) is nearly identical to the limiting form of Equation (1) for  $\nu_T/\nu \rightarrow 0$ . The only significant difference is the last term on the right-hand side of Equation (48). Except close to the surface where  $k$  must be exactly zero, this term is unlikely to have a significant effect on the solution for small nonzero values of  $k$ . However, in a numerical solution, products of dependent-variable gradients are generally destabilizing, and the problem can only be aggravated by having a coefficient inversely proportional to  $k$ . This is not an insurmountable problem. However, establishing starting conditions is clearly more difficult with the k- $\epsilon$  model than with the k- $\omega$  model.

Given the diverse nature of viscous modifications that have been proposed for the k- $\epsilon$  model,<sup>12</sup> it is impossible to make any universal statements about why a specific model fails to predict realistic transition Reynolds numbers. Perhaps the strongest statement that can be made is, *no one has approached the problem from the transition point of view*. Most researchers have sought only to achieve asymptotic consistency and attempted transition predictions only as an afterthought. We can gain some insight by examining the net production per unit dissipation terms for the  $k$  and  $\epsilon$  equations that are analogous to Equations (29) and (30), viz.

$$P_k = \frac{f_\mu}{C_\mu} Re_\tau \left( \frac{\partial F / \partial \eta}{W} \right)^2 - 1 \quad (49)$$

$$P_\epsilon = \frac{C_{\epsilon 1} f_\mu}{C_{\epsilon 2} C_\mu} Re_\tau \left( \frac{\partial F / \partial \eta}{W} \right)^2 - 1 \quad (50)$$

*On the one hand*, without viscous damping, if we assume Equation (31) is valid, we find  $(Re_\tau)_k = 8,100$  and  $(Re_\tau)_\epsilon = 10,800$ . Consequently, like the high-Reynolds-number version of the k- $\omega$  model, transition will occur at too low a Reynolds number.

*On the other hand*, because  $f_\mu$ ,  $C_{\epsilon 2}$  and sometimes  $C_{\epsilon 1}$  are often permitted to be functions of distance from the surface and/or functions of  $Re_\tau$ , we cannot simply use Equation (31). Furthermore, some modelers add terms to the  $k$  and  $\epsilon$  equations in addition to damping the closure coefficients. Each set of values for the closure coefficients and additional terms must be used in solving Equation (48) to determine the laminar-flow solution for  $\epsilon/k$ . While it is clearly impossible to make a quantitative evaluation of all variants of the k- $\epsilon$  model, we can nevertheless make some general observations.

From the analysis of the k- $\omega$  model, it is obvious that having  $f_\mu < 1$  will tend to delay transition. Virtually all modelers implement an  $f_\mu$  that will accomplish this end. However, the modifications of Jones and Launder,<sup>11</sup> Chien,<sup>13</sup> and Lam and Bremhorst,<sup>14</sup> for example, damp  $C_{\epsilon 2}$  to the extent that  $(Re_\tau)_\epsilon$  is smaller than  $(Re_\tau)_k$ . This is the opposite of what is needed and will have an undesirable effect on both the onset of and the extent of the transition region.

This discussion is not intended as an exhaustive survey of the numerous low-Reynolds-number versions of the k- $\epsilon$  model. Rather, it is intended to illustrate how difficult it is to apply the model to the transition problem. Given enough additional closure coefficients and damping functions, the k- $\epsilon$  model can probably be modified to permit satisfactory transition predictions. However, even if this is done, establishing starting conditions will ultimately require a solution to Equation (48). That is, to initialize the computation, we must effectively transform to the k- $\omega$  model. Since this is the natural starting point, it seems illogical to perform subsequent computations in terms of  $k$  and  $\epsilon$ .

## IV. Turbulent Flow Applications

To achieve a complete description of the transition from laminar to turbulent flow, we must be able to accurately describe the flow in the turbulent regime. This is, after all, the primary advantage of using turbulence model equations to describe transition. In this section, we examine channel and pipe flow to demonstrate how well the low-Reynolds-number form of the  $k-\omega$  model predicts properties of turbulent flows.

Figures 1 and 2 compare computed channel-flow skin friction,  $c_f$ , with the Halleen and Johnston<sup>15</sup> correlation for Reynolds number based on channel height,  $H$ , and average velocity ranging from  $10^3$  to  $10^5$ . The correlation is

$$c_f = 0.0706 Re_H^{-1/2} \quad (51)$$

As shown, computed  $c_f$  differs from the correlation by less than 3% except at the lowest Reynolds number shown where the correlation probably is inaccurate. Figure 3 compares computed pipe flow  $c_f$  with Prandtl's universal law of friction, viz.

$$c_f^{-1/2} = 4 \log_{10}(2 Re_D c_f^{1/2}) - 1.6 \quad (52)$$

Reynolds number based on pipe diameter,  $D$ , and average velocity varies from  $10^3$  to  $10^6$ . As with channel flow, computed  $c_f$  falls within 5% of the correlation except at the lowest Reynolds number indicated where the correlation is likely to be in error.

For more detailed comparisons, we consider two low-Reynolds-number channel-flow cases corresponding to the DNS results of Mansour, et al<sup>10</sup> and one high-Reynolds-number pipe flow case corresponding to measurements of Laufer<sup>16</sup>.

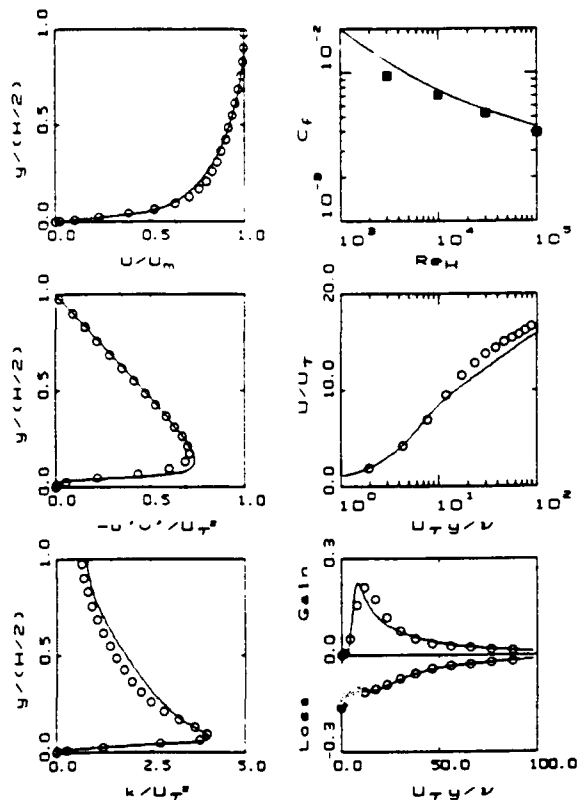


Figure 1. Incompressible channel flow with  $Re_\tau = 180$ ,  $Re_H = 5,590$ ; o Mansour, et al; ■ Johnston Formula.

For purposes of identification, the three cases are referred to in terms of the parameter

$$Re_\tau = u_\tau R / \nu \quad (53)$$

where  $u_\tau$  is friction velocity and  $R$  is either channel half height or pipe radius. Figures 1 and 2 compare various computed profiles with the Mansour, et al DNS results for  $Re_\tau = 180$  and 395, respectively.

Six different comparisons are shown in each figure, including mean velocity, skin friction, Reynolds shear stress, turbulence kinetic energy, turbulence energy production and dissipation rate. For both cases, velocity, Reynolds shear stress, and turbulence kinetic energy profiles differ by less than 7%. Most notably, for both Reynolds numbers, the model predicts the peak value of  $k$  near the channel wall to within 4% of the DNS value. Additionally, approaching the surface, the turbulence-energy production,  $\tau_{xy} \partial U / \partial y$ , and dissipation,  $\epsilon$ , are within 10% of the DNS results except very close to the surface.

Figure 3 compares  $k-\omega$  model pipe flow results with Laufer's<sup>16</sup> measurements at a Reynolds number based on pipe diameter and average velocity of 40,000. As shown, computed and measured velocity and Reynolds shear stress profiles differ by less than 8%. As with channel flow, computed and measured turbulence kinetic energy differ by about 5% including close to the surface where the sharp peak occurs. Note that, at this high a Reynolds number, the  $k$  profile has a sharp spike near  $y = 0$  and this feature is captured in the computations. Except very close to the surface, computed turbulence energy production and dissipation differ from measured values by less than 10%. This may actually be a desirable result. That is, some controversy exists about the accuracy of Laufer's dissipation measurements close to the surface.

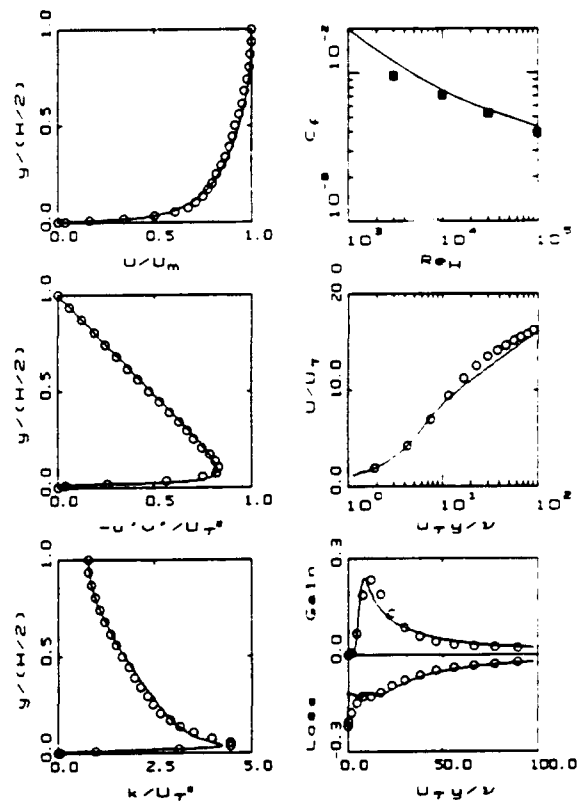


Figure 2. Incompressible channel flow with  $Re_\tau = 395$ ,  $Re_H = 13,750$ ; o Mansour, et al; ■ Johnston Formula.



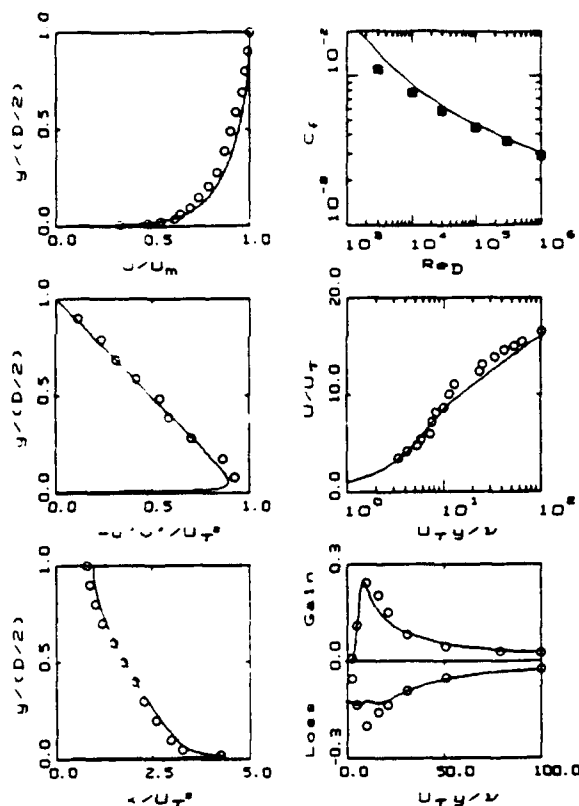


Figure 3. Incompressible pipe flow with  $Re_\tau = 1058$ ,  $Re_H = 40,000$ ;  $\circ$  Laufer;  $\bullet$  Prandtl Formula.

## V. Transition Applications

Figure 4 compares computed and measured transition Reynolds number,  $Re_{\theta_t}$ , for an incompressible flat-plate boundary layer. We define the transition Reynolds number as the point where the skin friction achieves its minimum value. Results are displayed as a function of freestream turbulence intensity,  $T$ , defined by

$$T = 100 \left( \frac{2}{3} \frac{k_e}{U_e^2} \right)^{1/2} \quad (54)$$

where subscript  $e$  denotes the value at the boundary-layer edge. As shown, consistent with the data compiled by Dryden,<sup>17</sup>  $Re_{\theta_t}$  increases as the freestream intensity decreases. Because  $\omega$  can be thought of as an averaged frequency of the freestream turbulence, it is reasonable to expect the predictions to be sensitive to the freestream value of  $\omega$ . To assess the effect, the freestream value of the turbulence length scale defined by  $\lambda = k^{1/2}/\omega$  has been varied from .0016 to .1006 where  $\delta$  is boundary layer thickness. As shown, computed  $Re_{\theta_t}$  values bracket virtually all of the data. These predictions are markedly superior to the preliminary efforts of Wilcox<sup>18</sup> in developing low-Reynolds-number modifications for the  $k-\omega$  model.

Figure 5 compares computed width of the transition region with measurements of Dhawan and Narasimha.<sup>19</sup> We define transition width,  $\Delta x_t$ , as the distance between minimum and maximum skin-friction points. The computed width falls within experimental data scatter for  $Re_{x_t} < 10^6$ , and lies a bit above the data for larger values.  $\Delta x_t$  is unaffected by the freestream value of  $\omega$ .

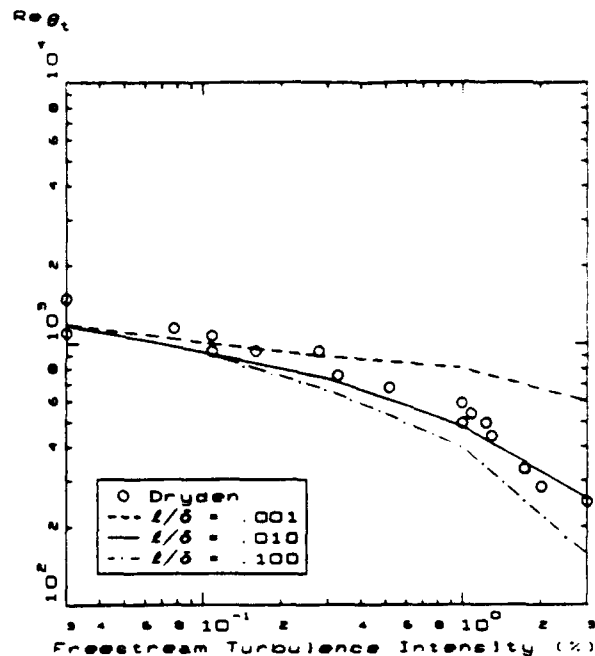


Figure 4. Comparison of computed and measured variation of transition Reynolds number with freestream turbulence intensity; incompressible flat-plate boundary layer.

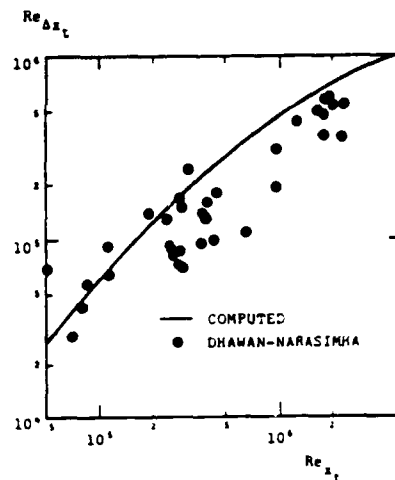


Figure 5. Comparison of computed and measured width of the transition region for an incompressible flat-plate boundary layer.

## VI. Summary and Conclusions

The primary objective of this paper has been to illustrate how two-equation turbulence models, most notably the  $k-\omega$  model, predict transition. While the long-term goal of this research is to develop a transition model for all Mach numbers, this paper has focused on the case about which we know the most, viz, incompressible flow. The low-Reynolds-number modifications proposed not only facilitate accurate transition predictions, but also yield reasonably close agreement with DNS results for low-Reynolds-number channel flow.

The degeneracy of the  $\epsilon$  equation in the  $k-\epsilon$  model is a major stumbling block that impedes successful application

to the transition problem. By transforming the model to an equivalent  $k-\omega$  model, it would be possible to remove some of the difficulties. After making such a transformation however, there is little reason to transform back.

The applications presented in Sections IV and V indicate we have formed a solid foundation for future low-Reynolds-number and transition research.

## VII. Acknowledgements

Research was supported by the U. S. Army Research Office and the NASA Langley Research Center under Contract DAAL03-89-C-0032 with Dr. Thomas Doligalski, Dr. Julius Harris and Dr. Thomas Zang as Contract Monitors.

## References

- <sup>1</sup>Wilcox, D. C., "Turbulence-Model Transition Predictions," *AIAA Journal*, Vol. 13, No. 2, pp. 241-243 (1975).
- <sup>2</sup>Wilcox, D. C., "Turbulence Model Transition Predictions: Effects of Surface Roughness and Pressure Gradient," *AIAA Paper 75-857*, Hartford, CT (1975).
- <sup>3</sup>Wilcox, D. C. and Chambers, T. L., "Application of the Turbulence-Model Transition-Prediction Method to Flight Test Vehicles," *Turbulence in Internal Flows*, S.N.B. Murthy, pp. 233-247 (1976).
- <sup>4</sup>Wilcox, D. C., "A Model for Transitional Flows," *AIAA Paper 77-126*, Los Angeles, CA (1977).
- <sup>5</sup>Wilcox, D. C., "Alternative to the  $\epsilon^3$  Procedure for Predicting Boundary-Layer Transition," *AIAA Journal*, Vol. 19, No. 1, pp. 56-64 (1981).
- <sup>6</sup>Wilcox, D. C. and Marvin, J. G., "Combined Effects of Freestream Turbulence and Mass Addition on Blunt-Body Heating and Transition," *Proceedings of the 2nd ASME/JSME Joint Thermal Engineering Conference*, Honolulu, HI (1987).
- <sup>7</sup>Wilcox, D. C., "Reassessment of the Scale Determining Equation for Advanced Turbulence Models," *AIAA Journal*, Vol. 26, No. 11, pp. 1299-1310 (1988).
- <sup>8</sup>Wilcox, D. C. and Traci, R. M., "A Complete Model of Turbulence," *AIAA Paper 76-351*, San Diego, CA (1976).
- <sup>9</sup>Wilcox, D. C. and Rubesin, M. W., "Progress in Turbulence Modeling for Complex Flow Fields Including Effects of Compressibility," *NASA TP 1517* (1980).
- <sup>10</sup>Mansour, N. N., Kim, J. and Moin, P., "Reynolds Stress and Dissipation Rate Budgets in Turbulent Channel Flow," *JFM*, Vol. 194, pp. 15-44 (1988).
- <sup>11</sup>Jones, W. P. and Launder, B. E., "The Prediction of Laminarization with a Two-Equation Model of Turbulence," *International Journal of Heat and Mass Transfer*, Vol. 15, pp. 301-314 (1972).
- <sup>12</sup>Patel, V. C., Rodi, W. and Scheuerer, G., "Turbulence Models for Near-Wall and Low Reynolds Number Flows: A Review," *AIAA Journal*, Vol. 23, pp. 1308-1319 (1985).
- <sup>13</sup>Chien, K-Y., "Predictions of Channel and Boundary-Layer Flows with a Low-Reynolds-Number Turbulence Model," *AIAA Journal*, Vol. 20, pp. 33-38 (1982).
- <sup>14</sup>Lam, C. K. G. and Bremhorst, K. A., "Modified Form of the  $k-\epsilon$  Model for Predicting Wall Turbulence," *Journal of Fluids Engineering*, Vol. 103, pp. 456-460 (1981).
- <sup>15</sup>Halleen, R. M. and Johnston, J. P., "The Influence of Rotation on Flow in a Long Rectangular Channel - An Experimental Study," *Report MD-18*, Mechanical Engineering Dept., Stanford University (1967).
- <sup>16</sup>Laufer, J., "The Structure of Turbulence in Fully Developed Pipe Flow," *NACA 1174* (1952).
- <sup>17</sup>Dryden, H. L., *Aerodynamics and Jet Propulsion*, Vol. V, University Press, Princeton, NJ (1959).
- <sup>18</sup>Wilcox, D. C., "Progress in Hypersonic Turbulence Modeling," *AIAA Paper 91-1785*, Honolulu, HI (1991).
- <sup>19</sup>Dhawan, S. and Narasimha, R., "Some Properties of Boundary Layer Flow During the Transition from Laminar to Turbulent Motion," *JFM*, Vol. 3, pp. 418-436 (1958).

# A Compressible Near-Wall Turbulence Model for Boundary Layer Calculations

R. M. C. So, H. S. Zhang and Y. G. Lai\*  
Mechanical and Aerospace Engineering  
Arizona State University  
Tempe, AZ 85287-6106, USA

## Abstract

A compressible near-wall two-equation model is derived by relaxing the assumption of dynamical field similarity between compressible and incompressible flows. This requires justifications for extending the incompressible models to compressible flows and the formulation of the turbulent kinetic energy equation in a form similar to its incompressible counterpart. As a result, the compressible dissipation function has to be split into a solenoidal part, which is not sensitive to changes of compressibility indicators, and a dilatational part, which is directly affected by these changes. This approach isolates terms with explicit dependence on compressibility so that they can be modeled accordingly. An equation that governs the transport of the solenoidal dissipation rate with additional terms that are explicitly dependent on compressibility effects is derived similarly. A model with an explicit dependence on the turbulent Mach number is proposed for the dilatational dissipation rate. Thus formulated, all near-wall incompressible flow models could be expressed in terms of the solenoidal dissipation rate and straight-forwardly extended to compressible flows. Therefore, the incompressible equations are recovered correctly in the limit of constant density. The two-equation model and the assumption of constant turbulent Prandtl number are used to calculate compressible boundary layers on a flat plate with different wall thermal boundary conditions and free-stream Mach numbers. The calculated results, including the near-wall distributions of turbulence statistics and their limiting behavior, are in good agreement with measurements. In particular, the near-wall asymptotic properties are found to be consistent with incompressible behavior; thus suggesting that turbulent flows in the viscous sublayer are not much affected by compressibility effects.

## 1. Introduction

Density variation in a turbulent flow can come from different sources. Some of these are: (i) isothermal mixing of gases of different density, (ii) strong temperature gradient in a homogeneous fluid, (iii) reactive flows and (iv) compressibility effects in high speed flows. Each of these sources gives rise to specific aspects that require modeling if the governing equations are to be solved. This study makes an attempt to address the last source; that is, the modeling of high speed compressible turbulent flows.

Most studies on compressible turbulent flow modeling [1-9] invoke the Morkovin postulate [10] to justify the direct extension of the incompressible models to compressible flows. The postulate was formulated based on early experiments on compressible boundary layers along adiabatic walls and compressible wakes, and essentially suggested that the dynamical field in a compressible flow behaves like an incompressible one. This postulate was used by numerous researchers to assure that compressibility effects can be accounted for directly by the variable mean density in the governing equations alone. In other words, the influences of fluctuating density on turbulence mixing are essentially assumed to be negligible. The validity and extent of Morkovin's postulate were reviewed by Bradshaw [2] and he noted that the postulate is appropriate for flows where density fluctuations are moderate. Therefore, the postulate is not valid for hypersonic boundary

Therefore, the postulate is not valid for hypersonic boundary layers, where the Mach number is five or greater, and for flows with strong pressure gradient effects, such as shock-turbulent-boundary-layer interactions. The latter point was confirmed by the studies of Wilcox and Alber [1] and Bradshaw [11] and led to proposals to have the effects of pressure-dilatation correlation modeled in the governing equations [12]. A more recent study where density fluctuations are also considered has been given by Speziale and Sarkar [13]. Besides these modifications, all turbulent compressible flow modeling rely on incompressible models.

Two sources of difficulties arise when incompressible turbulence models are extended to compressible flows. One is due to compressibility itself and another is associated with the turbulence phenomena. In compressible flows, the governing equations are coupled and temperature cannot be considered as a passive scalar. As a result, all other thermodynamic variables adopt new roles. Therefore, mathematically, compressible flows cannot be considered as straightforward extension of incompressible flows. Furthermore, pressure is only a force term in incompressible flows and all disturbances propagate at infinite speed. On the other hand, pressure also supports finite velocity propagation of disturbances in compressible flows. Other complications come from the variable mean density, which contributes to increased non-linearity of the governing equations, and the fluctuating density, which causes the closure problem to become more difficult.

The second source of difficulties has to do with turbulence mixing. Here, even for incompressible flows, many problems remain to be resolved [14-17], especially when the flow is unsteady and/or three-dimensional [18]. However, among the many problems associated with turbulence modeling, one stands out as most fundamental and urgently needs attention. This is the treatment of the near-wall flow [17]. Conventional approach is to invoke the wall function assumptions; thus implying that near-wall turbulence is in local equilibrium. Even for simple wall shear flows, the assumption is not quite valid because near-wall turbulence is not in local equilibrium. Consequently, a low-Reynolds-number treatment is necessary in order to obtain results that agree with measurements in the near-wall region [17, 19-21]. The need for near-wall treatment of flows with heat and mass transfer has also been pointed out [22-25]. This problem is expected to be more acute in compressible flow modeling [13] where the non-linearity of the governing equations are further compounded by the variable mean density.

The present objective is to model near-wall compressible turbulent flows where the coupling between velocity and temperature cannot be ignored. As a first attempt, only the modeling of the turbulent kinetic energy and its dissipation-rate equations is considered. With the assumption of gradient transport, the two-equation model could be used to effect closure of the mean flow equations. Since the transport equations for the heat fluxes and the temperature dissipation rate are not modeled and solved, a constant turbulent Prandtl number is invoked to relate the heat fluxes to the momentum fluxes. In view of this assumption, the present approach only addresses the issue of compressibility effects on turbulent mixing and not on heat transfer and its interaction with turbulence. An attempt

\* Present address: CFD Research Corporation, 3325 Triana Blvd., Huntsville, AL 35805

on this latter problem will be made after the present model has been validated.

## 2. Proposed Modeling Approach

With the availability of near-wall models for temperature variance and its dissipation rate [24], heat fluxes [25], Reynolds-stresses [26] and the dissipation rate of the turbulent kinetic energy [27], the time is now ripe for their extension to compressible flows. In order to consider the effects of variable mean density and its fluctuation on turbulence mixing, it is necessary to analyse the exact equations and propose appropriate models to effect closure. Two approaches are available. One is to propose totally new models for the terms in the compressible equations, while another is to attempt to extend the incompressible models to compressible flows in a credible way. Both approaches involve assumptions that could or could not be verified experimentally. Since the present knowledge of incompressible flow modeling is quite mature, as a first attempt, it is expedient to extend these models to compressible flows. This can be accomplished by recasting the compressible equations in forms similar to their incompressible counterparts so that terms with explicit dependence on compressibility effects can be isolated separately, and the incompressible limit can be recovered in a straight forward and correct manner.

Since the turbulent kinetic energy equation or  $k$ -equation is obtained by contracting the Reynolds-stress equations, this means that the recasting of the Reynolds-stress equations should be attempted first. In other words, the viscous diffusion and dissipation terms in the Reynolds-stress equations have to be similarly defined as their incompressible counterparts. This suggests splitting the viscous dissipation function into a solenoidal part, which is not sensitive to changes of compressibility indicators, and a dilatational part, which is directly affected by these changes<sup>28</sup>. When the Reynolds-stress equations are written in this form, three additional terms that depend explicitly on compressibility effects are present. The  $k$ -equation is then obtained by contracting the Reynolds-stress equations and its incompressible counterpart is recovered correctly when density becomes constant and the additional terms vanish identically. An equation that governs the transport of the solenoidal dissipation rate ( $\epsilon$ ) of the turbulent kinetic energy ( $k$ ) is derived and modeled along the line suggested above. Again, additional terms that depend explicitly on compressibility effects appear in the equation. This equation also reduces correctly to its modeled incompressible counterpart because the additional terms vanish for constant density flows. All models proposed for the  $k$  and  $\epsilon$  equations are expressed in terms of this solenoidal dissipation rate. A model with explicit dependence on the turbulent Mach number proposed by Sarkar et al. [28] for the dilatational dissipation is adopted. Thus formulated, the two-equation model is valid for compressible flows and approaches its incompressible limit in a straight forward and correct manner.

The systematic approach described above, if proven successful, could be used to extend incompressible near-wall models for heat-fluxes, temperature variance and its dissipation rate to compressible flows. A set of equations governing the transport of incompressible heat fluxes has been proposed and validated against simple flows with heat transfer [25], while a similar set of equations for the temperature variance and its dissipation rate [24] has also been validated against boundary-layer flows. This means that near-wall heat transfer models could also be extended to compressible flows using the approach proposed above. However, before this extension is undertaken, the asymptotic consistency of these models has to be verified. Until such time, the assumption of a constant turbulent Prandtl number for near-wall compressible flow is inevitable.

In the following, the compressible equations are first

derived, then the near-wall modeling of the  $k$  and  $\epsilon$  equations are discussed. In section 6, the two-equation model is used to calculate compressible boundary layers on a flat plate assuming a constant turbulent Prandtl number. Comparisons with measurements [9, 29-31] and other calculations, such as those obtained using the  $k$ - $\omega$  model of Wilcox [8], are carried out to assess the importance of density fluctuations on the calculated results and, hence, the validity and extent of Morkovin's hypothesis.

## 3. Mean Flow Equations

The compressible mean flow equations are obtained by applying Favre averaging to the instantaneous Navier-Stokes equations which for Newtonian fluids can be written as:

$$\frac{\partial \rho}{\partial t} + \frac{\partial}{\partial x_i} (\rho u_i) = 0 \quad (1)$$

$$\frac{\partial (\rho u_i)}{\partial t} + \frac{\partial}{\partial x_j} (\rho u_i u_j) = - \frac{\partial p}{\partial x_i} + \frac{\partial \tau_{ij}}{\partial x_j} \quad (2)$$

$$\begin{aligned} \frac{\partial (\rho C_p T)}{\partial t} + \frac{\partial}{\partial x_i} (\rho C_p T u_i) &= \frac{\partial p}{\partial t} + u_i \frac{\partial p}{\partial x_i} \\ &+ \frac{\partial}{\partial x_i} \left( \kappa \frac{\partial T}{\partial x_i} \right) + \tau_{ij} \frac{\partial u_i}{\partial x_j} \end{aligned} \quad (3)$$

$$\text{where } \tau_{ij} = \mu \left( \frac{\partial u_i}{\partial x_j} + \frac{\partial u_j}{\partial x_i} \right) - \frac{2}{3} \mu \frac{\partial u_k}{\partial x_k} \delta_{ij} \quad (4)$$

$u_i$  is the  $i$ th component of the velocity vector,  $x_i$  is the  $i$ th component of the coordinates and  $p$ ,  $T$ ,  $\rho$ ,  $\mu$ ,  $\kappa$ ,  $C_p$  are pressure, temperature, density, viscosity, thermal conductivity and specific heat at constant pressure, respectively. Favre decomposition is applied to all variables except  $p$  and  $\rho$  where conventional Reynolds decomposition is assumed. In other words

$$u_i = \langle U_i \rangle + u_i' \quad (5)$$

$$T = \langle \Theta \rangle + \theta'' \quad (6)$$

$$p = \bar{P} + p' \quad (7)$$

$$\rho = \bar{\rho} + \rho' \quad (8)$$

where  $u_i'$  and  $\theta''$  are the Favre fluctuations and  $p'$  and  $\rho'$  are the Reynolds fluctuations. If  $\langle \rangle$  is used to denote Favre-averaged quantities and the overbar the Reynolds-averaged quantities, then the mean equations for compressible flows can be obtained as follows. The above decompositions (5)-(8) are substituted into (1)-(4) and the resultant equations are averaged over time. If the turbulent flow is further assumed to be stationary and the mean momentum equation and the Reynolds-stress and turbulent kinetic energy,  $k = \frac{1}{2} \langle u_i u_i \rangle$ , equations to be derived later are used to simplify the thermal energy equation, the turbulent mean flow equations become

$$\frac{\partial}{\partial x_i} (\bar{\rho} \langle U_i \rangle) = 0 \quad (9)$$

$$\begin{aligned} \frac{\partial}{\partial x_j} (\bar{\rho} \langle U_i \rangle \langle U_j \rangle) &= - \frac{\partial \bar{P}}{\partial x_i} + \frac{\partial \langle \tau_{ij} \rangle}{\partial x_j} - \frac{\partial}{\partial x_j} \\ &(\bar{\rho} \langle u_i' \rangle \langle u_j' \rangle) + \frac{\partial \tau_{ij}}{\partial x_j} \end{aligned} \quad (10)$$

$$\begin{aligned}
& \frac{\partial}{\partial x_i} \left( \bar{p} \langle U_i \rangle \left[ \bar{C}_p \langle \Theta \rangle + \frac{1}{2} \langle U_k \rangle \langle U_k \rangle + k \right] \right) \\
&= \frac{\partial}{\partial x_i} \left( \bar{\kappa} \frac{\partial \langle \Theta \rangle}{\partial x_i} \right) + \frac{\partial}{\partial x_j} \left( \bar{\tau}_{ij} \langle U_j \rangle \right) - \frac{\partial}{\partial x_i} \left( \bar{p} \bar{C}_p \langle \theta'' u_i'' \rangle \right) \\
&- \frac{\partial}{\partial x_i} \left( \bar{p} \langle u_i'' u_j'' \rangle \langle U_j \rangle \right) + \frac{\partial}{\partial x_i} \left( \bar{\tau}_{ij} \langle U_j \rangle \right) - \frac{\partial}{\partial x_i} \left( \bar{p} \langle k u_i'' \rangle \right) \\
&+ \frac{\partial}{\partial x_i} \left( \bar{u}_j'' \bar{\tau}_{ij} \right) + \frac{\partial}{\partial x_i} \left( \bar{u}_j'' \langle \tau_{ij} \rangle \right) + \frac{\partial}{\partial x_i} \left( \bar{\kappa} \frac{\partial \bar{\theta}''}{\partial x_i} \right) \quad (11)
\end{aligned}$$

In these equations,  $\mu = \bar{\mu}$ ,  $\kappa = \bar{\kappa}$  and  $C_p = \bar{C}_p$  have been substituted and the mean and fluctuating stresses are given by

$$\begin{aligned}
\langle \tau_{ij} \rangle &= \bar{\mu} \left( \frac{\partial \langle U_i \rangle}{\partial x_j} + \frac{\partial \langle U_j \rangle}{\partial x_i} \right) - \frac{2}{3} \bar{\mu} \delta_{ij} \frac{\partial \langle U_k \rangle}{\partial x_k} \\
\bar{\tau}_{ij} &= \bar{\mu} \left( \frac{\partial \bar{u}_i''}{\partial x_j} + \frac{\partial \bar{u}_j''}{\partial x_i} \right) - \frac{2}{3} \bar{\mu} \delta_{ij} \frac{\partial \bar{u}_k''}{\partial x_k}
\end{aligned}$$

The quantity,  $\bar{C}_p \langle \Theta \rangle + \frac{1}{2} \langle U_k \rangle \langle U_k \rangle + k$ , is the mean total enthalpy  $\langle H \rangle$ . Thus written, (9)-(11) reduce to their incompressible counterparts exactly when density becomes constant.

An order-of-magnitude analysis is carried out on (9) - (11). The result shows that the underlined terms are of smaller order and, as a first approximation, could be neglected compared to the terms retained. Thus formulated, the compressible equations are identical to the incompressible equations and the additional unknowns are the turbulent momentum and heat fluxes, just as in the incompressible case. The present approach proposes to close these equations assuming gradient transport. As a first attempt, a near-wall two-equation  $k$ - $\epsilon$  model is used to determine the turbulent viscosity and a constant turbulent Prandtl number is invoked to relate turbulent momentum and heat fluxes. Therefore, the present model cannot fully account for the effects of density fluctuation on turbulent heat transfer.

#### 4. Modeling of the Turbulent Kinetic Energy Equation

The Favre-averaged transport equation for the Reynolds stresses  $\bar{p} \langle u_i'' u_j'' \rangle$  could be similarly derived as in the

incompressible case [16]. That is, the  $i$ th fluctuating velocity equation is obtained by subtracting the mean momentum equation from the instantaneous equation. Repeat the same procedure to obtain the  $j$ th fluctuating velocity equation. The  $i$ th fluctuating velocity equation is then multiplied by the  $j$ th fluctuation velocity and vice versa and the two equations are added together and averaged over time. Omitting all the algebra, the final exact equation is:

$$\begin{aligned}
& \frac{\partial}{\partial t} \left[ \bar{p} \langle u_i'' u_j'' \rangle \right] + \frac{\partial}{\partial x_k} \left[ \bar{p} \langle U_k \rangle \langle u_i'' u_j'' \rangle \right] = - \frac{\partial}{\partial x_k} \left[ \bar{p} \langle u_i'' u_j'' u_k'' \rangle \right] \\
&+ \frac{\partial}{\partial x_k} \left[ \bar{u}_i'' \bar{\tau}_{jk} + \bar{u}_j'' \bar{\tau}_{ik} \right] - \left[ \bar{\tau}_{ik} \frac{\partial \bar{u}_j''}{\partial x_k} + \bar{\tau}_{jk} \frac{\partial \bar{u}_i''}{\partial x_k} \right] \\
&- \left[ \bar{u}_i'' \frac{\partial \bar{p}'}{\partial x_j} + \bar{u}_j'' \frac{\partial \bar{p}'}{\partial x_i} \right] - \left[ \bar{p} \langle u_i'' u_k'' \rangle \frac{\partial \langle U_j \rangle}{\partial x_k} + \bar{p} \langle u_j'' u_k'' \rangle \frac{\partial \langle U_i \rangle}{\partial x_k} \right] \quad (12)
\end{aligned}$$

$$- \left[ \bar{u}_i'' \frac{\partial \bar{p}}{\partial x_j} + \bar{u}_j'' \frac{\partial \bar{p}}{\partial x_i} \right] + \left[ \bar{u}_i'' \frac{\partial \langle \tau_{ik} \rangle}{\partial x_k} + \bar{u}_j'' \frac{\partial \langle \tau_{jk} \rangle}{\partial x_k} \right]$$

Symbolically, the above equation can be written as

$$C_{ij} = D_{ij}^T + D_{ij}^{*v} - \bar{p} \epsilon_{ij}^* + \Phi_{ij} + P_{ij} + G_{ij} + T_{ij} \quad (13)$$

With the exception of  $G_{ij}$  and  $T_{ij}$ , (13) is similar to its incompressible counterpart [26]. For an incompressible flow,  $u_i'' = 0$ , and  $G_{ij} = T_{ij} = 0$ . Even under this condition, (13) fails to reduce properly to the incompressible equation given in Ref. 26. The reason lies in the grouping of the terms  $(D_{ij}^{*v} - \bar{p} \epsilon_{ij}^* + \Phi_{ij})$ . In order to achieve this incompressible limit

correctly, a re-arranging of the terms in  $(D_{ij}^{*v} - \bar{p} \epsilon_{ij}^* + \Phi_{ij})$  is necessary. If viscous diffusion and dissipation in compressible flows are again defined similarly to their incompressible counterparts, or

$$D_{ij}^{*v} = \frac{\partial}{\partial x_k} \left( \bar{\mu} \frac{\partial \bar{u}_i'' \bar{u}_j''}{\partial x_k} \right) \quad (14)$$

$$\epsilon_{ij} = 2\bar{\nu} \frac{\partial \bar{u}_i'' \partial \bar{u}_j''}{\partial x_k \partial x_k} \quad (15)$$

then the terms  $(D_{ij}^{*v} - \bar{p} \epsilon_{ij}^* + \Phi_{ij})$  can be re-arranged to give

$$D_{ij}^{*v} - \bar{p} \epsilon_{ij}^* + \Phi_{ij} = D_{ij}^v - \bar{p} \epsilon_{ij} - \bar{p} \epsilon_{ij}^c + \Phi_{ij}^* \quad (16)$$

$$\text{where } \epsilon_{ij}^c = \frac{\bar{\nu}}{3} \left( \frac{\partial \bar{u}_i''}{\partial x_j} \frac{\partial \bar{u}_k''}{\partial x_k} + \frac{\partial \bar{u}_j''}{\partial x_i} \frac{\partial \bar{u}_k''}{\partial x_k} \right) \quad (17a)$$

$$\begin{aligned}
\Phi_{ij}^* &= - \left[ \bar{u}_i'' \frac{\partial \bar{p}'}{\partial x_j} + \bar{u}_j'' \frac{\partial \bar{p}'}{\partial x_i} \right] + \frac{\bar{\mu}}{3} \left[ \frac{\partial}{\partial x_j} \left( \bar{u}_i'' \frac{\partial \bar{u}_k''}{\partial x_k} \right) \right. \\
&+ \frac{\partial}{\partial x_i} \left( \bar{u}_j'' \frac{\partial \bar{u}_k''}{\partial x_k} \right) \left. \right] + \frac{\partial \bar{\mu}}{\partial x_k} \left( \bar{u}_i'' \frac{\partial \bar{u}_k''}{\partial x_j} + \bar{u}_j'' \frac{\partial \bar{u}_k''}{\partial x_i} \right) \\
&- \frac{2}{3} \left[ \frac{\partial \bar{\mu}}{\partial x_j} \bar{u}_i'' \frac{\partial \bar{u}_k''}{\partial x_k} + \frac{\partial \bar{\mu}}{\partial x_i} \bar{u}_j'' \frac{\partial \bar{u}_k''}{\partial x_k} \right] \quad (17b)
\end{aligned}$$

Note that (16) reduces to its incompressible counterpart exactly when constant fluid properties are assumed. For compressible flows, an extra term  $\bar{p} \epsilon_{ij}^c$  appears in (16). In addition, three additional terms are found in  $\Phi_{ij}^*$ . The term  $\bar{p} \epsilon_{ij}^c$  is a dilatational term and could be interpreted as compressible or dilatational dissipation. This term is only important for compressible flows.

It should be pointed out that  $\Phi_{ij}^*$  is given by (17b) and, as a result of this particular partitioning, there are several extra terms resulted from compressibility and variable viscosity. However, at high Reynolds number, dimensional arguments reveal that these extra contributions are not important. If pressure diffusion is further neglected, then  $D_{ij}^v$ ,  $\bar{p} \epsilon_{ij}$  and  $\Phi_{ij}$  would assume the same form as their incompressible counterparts. Therefore, the high-Reynolds-number incompressible models proposed for these terms [16, 32] could be straight-forwardly extended to compressible flows. However, a model for the compressible dissipation term  $\bar{p} \epsilon_{ij}^c$  is

required to complete closure. For high-Reynolds-number flows, this compressible dissipation could be assumed to be isotropic. As a result, the following model is proposed:

$$\epsilon_{ij}^c = \frac{2}{3} \delta_{ij} \epsilon^c \quad (18)$$

$$\text{where } \epsilon^c = \frac{\bar{u}}{3} \left( \frac{\partial \bar{u}_k}{\partial x_k} \right)^2$$

The modeling of  $\epsilon^c$  has been attempted by Sarkar et al. [28]. They are the first to realize that the contribution of the dilatational dissipation term is important for supersonic shear flows. A simple algebraic model, which is based on an asymptotic analysis and a direct numerical simulation of the simplified governing equations, has been proposed for  $\epsilon^c$ . Their proposal could be modified to become

$$\epsilon^c = \alpha_1 M_t^2 \bar{\epsilon} \quad (19)$$

where  $\alpha_1$  is a model constant,  $M_t^2 = 2k/\bar{c}^2$ ,  $\bar{\epsilon} = \bar{\mu} \left( \frac{\partial \bar{u}_k}{\partial x_k} \right)^2$  is the

dissipation of  $k$  and  $\bar{c}$  is the local mean speed of sound. Therefore,  $M_t$  is the local turbulent Mach number. It should be pointed out that Sarkar et al.'s [28] definition of  $\epsilon^c$  is four times larger than the definition given in (19) as a result of a different splitting of the terms in (16). Consequently,  $\alpha_1$  should take on a value equal to 1/4 of that suggested in Ref. 28. Based on an analysis of decay of compressible isotropic turbulence, Sarkar et al. [28] suggested a value of one for their constant. In other words,  $\alpha_1 = 0.25$ . If  $\alpha_1$  is evaluated based on compressible shear flows, its value would be 0.15. The present study adopts  $\alpha_1 = 0.15$  for the analyses of boundary-layer flows.

The  $k$ -equation is obtained by contracting (12) and making use of (16) and (18) to simplify the resulting equation which can be written as:

$$\begin{aligned} \frac{D(\bar{\rho}k)}{Dt} = & D_k^v + D_k^T + \frac{1}{2}P_{ii} + \frac{1}{2}\Phi_{ii}^* - \frac{1}{2}\bar{\rho}\epsilon_{ii} - \frac{1}{2}\bar{\rho}\epsilon_{ii}^c \\ & + \frac{1}{2}G_{ii} + \frac{1}{2}T_{ii} \end{aligned} \quad (20)$$

It can be seen that the terms,  $D_k^T$ ,  $\Phi_{ii}^*$  and  $\bar{\rho}\epsilon_{ii}$ , and the coefficient,  $u_i$ , appearing in  $G_{ii}$  and  $T_{ii}$  require modeling. Furthermore, when  $\bar{\rho}$  is assumed to be constant and  $u_i = 0$ , the last three terms in (20) are identically zero and the incompressible equation is recovered exactly. The modeling of  $D_k^T$ ,  $\Phi_{ii}^*$  and  $\bar{\rho}\epsilon_{ii}$  could be accomplished by drawing parallels with their incompressible counterparts [26, 27]. However, this requires knowledge of their behavior in the near-wall region.

The near-wall behavior of (20) can be analysed by assuming Taylor series expansions about the wall for the fluctuating quantities. This analysis is similar to the incompressible case [26] except that expansions also have to be assumed for  $\rho'$  and  $\theta'$ . The proposed expansions are:

$$\begin{aligned} u'' &= a_1 y + a_2 y^2 + \dots \\ v'' &= b_1 y + b_2 y^2 + \dots \\ w'' &= c_1 y + c_2 y^2 + \dots \\ \theta'' &= d_1 y + d_2 y^2 + \dots \\ \rho' &= e_1 y + e_2 y^2 + \dots \end{aligned} \quad (21)$$

It should be cautioned that, although the velocity and temperature expansions are physically correct, the expansion for density is an assumption. As pointed out by Bradshaw [11], the fluctuating temperature and density could not go to zero simultaneously at the wall. Otherwise, it would lead to a zero wall  $\rho'$ . In general, temperature fluctuation is assumed to be zero at the wall, while  $\rho'$  is not. Here, the assumption is made that  $\rho'$  also goes to zero at the wall, however, its value away from the wall is finite. Since  $\rho'$  is taken to be essentially zero over the whole field in Morkovin's hypothesis [10], the present approach could be viewed as a partial relaxation of that assumption. Consequently, the proposed model would not be valid for all free-stream Mach number and wall thermal boundary conditions. Therefore, one of the present objective is to analyse the validity and extent of the proposed two-equation model.

For incompressible flows,  $b_1 = 0$  is obtained by imposing the incompressibility condition and becomes a crucial condition in near-wall analysis. This important condition holds the key to the present extension of the near-wall incompressible models to compressible flows. In order to show that  $b_1$  indeed vanishes under these conditions, the continuity equation for  $\rho'$  is first derived, or

$$\frac{\partial \rho'}{\partial t} + \frac{\partial}{\partial x_k} (\bar{\rho} u_k' + \rho' \langle U_k \rangle + \rho' u_k') = 0. \quad (22)$$

Expansions (21) are then substituted into the above equation. If  $\langle U_k \rangle = 0$  at the wall is used, it can be easily verified that, under the assumption of (21),  $b_1 = 0$  is still a valid condition for compressible flows, irrespective of the thermal boundary condition. Therefore, the assumed  $\rho'$  expansion facilitates the modeling of compressible flows, because all terms in (20) have similar forms as their incompressible counterparts except the extra  $\epsilon_{ii}^c$  term which needs to be analyzed.

Using definition (18) for  $\epsilon_{ii}^c$ , it is easily verified that  $\epsilon_{ii}^c$  is of order  $y^2$ . The high-Reynolds-number model (19) also has similar behavior near a wall. Therefore, it is proposed to extend (19) to near-wall flow without modification, while the near-wall balance provided by the exact  $\epsilon_{ii}^c$  is taken into consideration by combining it with the  $\Phi_{ii}^*$  term. As for  $\bar{\rho}\epsilon_{ii}$ , it could be modeled by following the arguments presented in Refs. 26 and 27 for incompressible flows. In essence, Refs. 26 and 27 argue that the incompressible  $\epsilon_{ii}$  can be set equal to  $2\epsilon$  and the near-wall corrections proposed for  $\epsilon_{ii}$  have little or no effects on the behavior of  $\epsilon_{ii}$  in the region near a wall. This means that  $\epsilon_{ii}$  can be approximated by  $2\epsilon$  in the whole field. In view of this, the model for  $\bar{\rho}\epsilon_{ii}$  can be assumed to be given by  $2\bar{\rho}\epsilon$ . Based on this model, equation (15) and expansions (21), it can be easily shown that the leading term of  $\epsilon$  in the near-wall region is a constant equal to its wall value  $\epsilon_w$ . Again, the behavior is similar to its incompressible counterpart.

Near-wall analysis again shows that turbulent diffusion is a higher order term and its high-Reynolds-number model could be adopted because it does not affect near-wall balance of the  $k$ -equation. Consistent with the assumption of gradient transport for two-equation models, the incompressible model for turbulent diffusion of  $k$  is extended to compressible flows by writing  $D_k^T = \partial((\bar{\mu}/\sigma_k)\partial k/\partial x_i)/\partial x_i$ , where  $\sigma_k$  is a constant and  $\bar{\mu}_t$  is the turbulent viscosity defined by  $\bar{\mu}_t = C_\mu f_\mu \bar{\rho} k^2/\epsilon$ . In this definition,  $C_\mu$  is a model constant while  $f_\mu$  is a damping function to be defined later. Based on (21), the leading order term of  $k$  in the near-wall region is  $y^2$ . Since  $\epsilon = \epsilon_w$  in this region,  $k^2/\epsilon$  has to be of order  $y^4$ . If the shear stress is defined with respect to  $\bar{\mu}_t$ , then it can be shown that the leading order term of the shear stress has to be of order  $y^3$  in the near-wall region. Therefore, it follows that  $\nabla_t = \bar{\mu}_t/\bar{\rho}$  is also of order  $y^3$  near a wall and this,

in turn, leads to a similar behavior for the modeled  $D_k^T$  term in the near-wall region. This behavior is consistent with the behavior of the exact term  $D_k^T$  appearing in (20). In other words, the modeled  $D_k^T$  does not affect the near-wall balance of (20).

According to (18),  $\epsilon_{ii}^c = 2\epsilon^c$ . As such, the near-wall behavior of the exact  $\epsilon_{ii}^c$  is not properly accounted for by the proposed model. In the above discussion, it is argued that the near-wall behavior of  $\epsilon_{ii}^c$  could be modeled together with the term  $\Phi_{ii}$ . In order to analyse the near-wall behavior of the combined term  $(\Phi_{ii} + \bar{\rho}\epsilon_{ii}^c)$ , the behavior of  $G_{ii}$  and  $T_{ii}$  near a wall has to be studied. The appearance of mean pressure in  $G_{ii}$  makes the analysis slightly more difficult. However, the difficulty could be circumvented by making use of the mean momentum equation (10). The final analysis shows that the combined  $(G_{ii} + T_{ii})$  term has the following near-wall behavior; namely,

$$\begin{aligned} G_{11} + T_{11} &\rightarrow O(y^2); G_{33} + T_{33} \rightarrow O(y^2); \\ G_{22} + T_{22} &\rightarrow O(y^3). \end{aligned} \quad (23)$$

This means that, to the lowest order, the near-wall behavior of  $(\Phi_{ii} + \bar{\rho}\epsilon_{ii}^c)$  is similar to its incompressible counterpart [26]. For incompressible flows, the term,  $\Phi_{ii}$ , can be written into a pressure diffusion part and a pressure redistribution part. Pressure redistribution is identically zero and since pressure diffusion is relatively small, it is usually neglected. Such is not the case for compressible flows. The term,  $\Phi_{ii}$ , can again be partitioned into a pressure diffusion part, which could be neglected, and a term involving pressure-velocity-gradient correlation. This latter term does not vanish because fluid volume changes as a result of density variation. Therefore, an argument could be made to model the term,  $(\Phi_{ii} + \bar{\rho}\epsilon_{ii}^c)$ , to account for dilatational effects only. In view of this, the following model is proposed, or

$$(\Phi_{ii} + \bar{\rho}\epsilon_{ii}^c) = -\gamma\bar{\rho}k\left(\frac{\partial\langle U_i \rangle}{\partial x_i}\right), \quad (24)$$

where  $\gamma$  is a model constant.

The proposed models still fail to close the k-equation because of the presence of  $\bar{u}_i$  in  $T_{ii}$  and  $G_{ii}$ . Therefore, it is necessary to shed some light on the modeling of  $\bar{u}_i$ , which is identically zero for incompressible flows. Using Favre averaging, it can be shown that  $-\rho'u_i = \bar{\rho}\bar{u}_i$ . In other words,  $\bar{u}_i = -\rho'u_i/\bar{\rho}$ . Previous proposals for  $-\rho'u_i$  are based on the gradient transport assumption; namely,

$$-\rho'u_i = \frac{\bar{\rho}}{\sigma_p} \frac{\partial \bar{p}}{\partial x_i}, \quad (25)$$

where  $\sigma_p$  is a model constant. However, a more elaborate way to model the term is to adopt the proposal,

$$\bar{u}_i = -\frac{\bar{\rho}'u_i}{\bar{\rho}} = C_p \frac{k}{\bar{\rho}\epsilon} \langle u_i u_j \rangle \frac{\partial \bar{p}}{\partial x_j}, \quad (26)$$

where  $C_p$  is a model constant. Alternatively, the term can also be modeled by

$$\bar{u}_i = \beta \frac{\bar{u}_i \bar{\theta}}{\langle \theta \rangle}, \quad \text{with } \beta = -\left(\frac{\partial \bar{p}}{\partial \langle \theta \rangle}\right)_p \frac{\langle \theta \rangle}{\bar{\rho}}, \quad (27)$$

where  $\beta$  equals to unity for an ideal gas.

The near-wall behavior of the modeled k-equation can now be analysed using expansions (21). It can be easily shown that in the region very near a wall, the modeled k-equation is in balance up to order  $y$ . Consequently, it does not need further modifications to achieve a consistent asymptotic behavior near a wall.

## 5. Modelling of the Dissipation-Rate Equation

The exact transport equation for the solenoidal dissipation rate  $(\bar{\rho}\epsilon)$  can be derived as in the Reynolds-stress equation (12). It has been pointed out that the  $\epsilon$ -equation is the most difficult to model even for incompressible flows [13, 16, 17, 26, 27, 32]. The reason being that many of the terms in the exact equation are either not known or could not be measured accurately at present. Consequently, the incompressible  $\epsilon$ -equation is modeled in an ad hoc manner to resemble the k-equation in form so that the right hand side of the  $\epsilon$ -equation again consists of four terms; namely, viscous diffusion, turbulent diffusion, production and destruction of  $\epsilon$ . The equation is further modified for near-wall flows by adding an extra destruction term  $\xi$  so that the modeled equation remains balance as a wall is approached. There is a lack of measurements in compressible flows, therefore, a rigorous modeling of the compressible  $\epsilon$ -equation is not possible at present. An alternative is to extend the high-Reynolds-number incompressible models to compressible flows and then seek a near-wall correction to the modeled  $\epsilon$ -equation along the line suggested in Ref. 27. In view of this, the exact transport equation for the dissipation rate is not in a convenient form to work with. The proposal of Speziale and Sarkar [13] with the dilatational effects explicitly written out will be more appropriate.

Following Speziale and Sarkar [13], the modeled transport equation for  $\epsilon$  with near-wall correction is written in the simplified form; namely

$$\frac{D\bar{\rho}\epsilon}{Dt} = \frac{\partial}{\partial x_i} \left( \mu \frac{\partial \epsilon}{\partial x_i} \right) + D_\epsilon^t + P_\epsilon - \Delta_\epsilon - \frac{4}{3} \bar{\rho} \epsilon \frac{\partial \langle U_i \rangle}{\partial x_i} + \xi, \quad (28)$$

where  $D_\epsilon^t$  is the turbulent transport of  $\epsilon$ ,  $P_\epsilon$  is the production of  $\epsilon$  due to deviatoric strains,  $\Delta_\epsilon$  is the destruction of  $\epsilon$  and  $\xi$  is a near-wall correction for compressible flows. The second last term on the right hand side of (28) is exact and results from the writing of the exact  $\epsilon$ -equation into the form of (28). When the dissipation-rate equation is formulated in this form, it is reducible exactly to its incompressible counterpart and, therefore, the terms  $D_\epsilon^t$ ,  $P_\epsilon$  and  $\Delta_\epsilon$  can be modeled by a variable density extension of their incompressible models. Following the suggestions of Refs. 13 and 27, the models proposed for  $D_\epsilon^t$ ,  $P_\epsilon$  and  $\Delta_\epsilon$  are:

$$D_\epsilon^t = \frac{\partial}{\partial x_i} \left( \frac{\mu_t}{\sigma_\epsilon} \frac{\partial \epsilon}{\partial x_i} \right), \quad (29a)$$

$$P_\epsilon = -C_{\epsilon 1} \bar{\rho} \epsilon \left( \langle u_i u_j \rangle \left( \frac{\partial \langle U_i \rangle}{\partial x_j} + \frac{1}{3} \frac{\partial \langle U_k \rangle}{\partial x_k} \delta_{ij} \right) \right), \quad (29b)$$

$$\Delta_\epsilon = C_{\epsilon 2} \bar{\rho} \frac{\bar{\rho}'\epsilon}{k}, \quad (29c)$$

where the model constants  $C_{\epsilon 1}$  and  $C_{\epsilon 2}$  are the same as those given in Ref. 27 for incompressible flows and  $\tilde{\epsilon} = \epsilon - \epsilon_w$ . It should be noted that the mean dilatational effects are accounted for exactly by (29b) for compressible flows and that these models reduce exactly to their incompressible counterparts when the flow Mach number becomes very small. In addition, the ordering of these model terms is similar to their incompressible counterparts. Therefore, the near-wall function  $\xi$  can be determined in a manner similar to that proposed in Ref. 27.

The incompressible form of (28) with model terms given in (29) is identical to that proposed in Refs. 26 and 27. In these studies, the coincidence condition suggested by Shima [21] was used to determine  $\xi$ . This is equivalent to requiring the modeled  $\epsilon$ -equation to achieve balance behavior in the near-wall region at least up to order  $y$ . The approach used to deduce  $\xi$  is to assumed a functional form for  $\xi$  with two undetermined model constants. One of the constant can be determined from near-wall analysis, while the other is evaluated using computer optimization. The  $\xi$  function thus determined has been used in Ref. 27 to calculate flat plate boundary-layer flows and in Ref. 26 to calculate fully-developed channel and pipe flows. These calculations were carried out over a wide range of flow Reynolds number. The results were compared with direct simulation data as well as measurements. Very good agreement has been found for both the limiting behavior of the turbulence quantities and  $\epsilon$  when compared to direct simulation data [33-35]. Furthermore, the two-equation model calculations of Ref. 27 are found to give better results than those obtained by Speziale et al. [36]. In view of this success, the same approach can be used to determine  $\xi$  for compressible flows.

The functional form assumed in Ref. 27 is adopted here, or

$$\xi = f_{w,2} \bar{\rho} \left[ -N \frac{\epsilon \tilde{\epsilon}}{k} + M \frac{\epsilon^{*2}}{k} \right], \quad (30)$$

where  $f_{w,2}$  is a damping function that goes to one at the wall and zero far away from the wall. It is defined in Ref. 27 as  $f_{w,2} = e^{-(R_t/64)^2}$ , where  $R_t = k^2/\nu \epsilon$  is the turbulent Reynolds number. The function  $\epsilon^*$  is defined as  $\epsilon^* = \epsilon - 2\nu k/y^2$  by generalizing the incompressible definition used in Ref. 27. Similarly,  $\tilde{\epsilon}$  is defined with  $\epsilon_w$  given by  $\epsilon_w = 2\nu (\partial k/\partial x_j)_w$ . Once  $\xi$  is postulated, the near-wall behavior of (28) and the modeled terms of (29) can be analysed using expansions (21). If the modeled equation is again required to be in balance up to order  $y$ , then it can be easily shown that  $N = 2 - C_{\epsilon 2}$  because the mean dilatational terms are of order  $y$ . Therefore, to order  $y^0$  they do not contribute to  $\xi$ . In Ref. 27, the part involving  $C_{\epsilon 2}$  in  $N$  is grouped together with  $M$  to give  $M_1 = (C_{\epsilon 2} \epsilon \tilde{\epsilon}/\epsilon^{*2} + M)$  and its value is determined through computer optimization studies. Again, the same procedure is followed in the present study to determine  $M_1$ .

Finally, to complete closure of the governing equations, gradient transport is assumed for the Reynolds stresses and the relation is given by

$$-\bar{\rho} \langle u_i u_j \rangle = \bar{\mu}_t \left[ \frac{\partial \langle U_i \rangle}{\partial x_j} + \frac{\partial \langle U_j \rangle}{\partial x_i} - \frac{2}{3} \delta_{ij} \frac{\partial \langle U_m \rangle}{\partial x_m} \right] - \frac{2}{3} \delta_{ij} \bar{\rho} k. \quad (31)$$

In addition, a constant turbulent Prandtl number is assumed so that heat and momentum diffusivity can be related by  $Pr_t = \bar{\nu}/\bar{\alpha}_t$ , where  $\bar{\alpha}_t$  is the turbulent thermal diffusivity. The damping function  $f_{\mu}$  appearing in the definition of  $\bar{\mu}_t$  can now be defined. In view of the similarity of the present  $k$  and  $\epsilon$  equations with those for incompressible flows, the  $f_{\mu}$  used in Ref. 27 is adopted here. It is defined as

$$f_{\mu} = (1 + 3.45/\sqrt{R_t}) \tanh(y^*/115). \quad (32)$$

where  $y^* = y u_{\tau}/\nu$  is the wall coordinate and  $u_{\tau}(x)$  is the friction velocity. In this definition,  $y$  is taken to be the normal coordinate and  $x$  the stream coordinate.

## 6. Model Validation

A first step to validate the two-equation model for compressible flows is to apply it to calculate flat plate boundary-layer flows with different wall boundary conditions and free-stream Mach numbers. In this initial attempt, heat flux is not modeled separately. Instead, it is related to momentum flux via the assumption of a constant turbulent Prandtl number. The rationale for doing this is to carefully assess the assumption made in (21) concerning the expansion for  $\rho'$ , whose validity affects the near-wall analysis used to justify the direct extension of the incompressible near-wall function  $\xi$  to compressible flows. By choosing the simplest type of compressible flows to validate the model, a careful analysis of the validity and extent of the expansion for  $\rho'$  can be carried out. A second objective of this validation is to determine, if possible, the validity and extent of Morkovin's hypothesis. In other words, it is hoped to evaluate the Mach number range and the type of wall thermal boundary conditions in which the effects of fluctuating density can be neglected in the modeling of the governing equations. Therefore, the experimental data chosen for comparisons are selected from three different groups; one with adiabatic wall boundary condition and varying free-stream Mach number, another with constant wall temperature and varying free-stream Mach number, and finally the variations of skin friction with free-stream Mach number and wall temperature as prescribed by the van Driest II formulae given in Ref. 9. The data for the first two groups are selected from Ref. 31. Only one case with constant wall temperature is selected. The reasons being that the other cases reported in Ref. 31 are either not accurate as far as the measured skin friction is concerned or the measured mean velocity and temperature are doubtful. In the following, the governing equations for compressible flat plate boundary-layer flows are first presented. Then the calculations and comparisons with data are examined and the validity of the two-equation model is studied in detail. Finally, the model performance and its proposed improvement are discussed.

### 6.1 Governing Equations

Two-dimensional, steady compressible boundary layers on a flat plate are considered. If the usual boundary-layer approximations are made, then equations (9) - (11), (20) and (28) can be substantially simplified. For the sake of completeness, the boundary-layer equations in Cartesian  $x$ - $y$  coordinates are listed here as:

$$\frac{\partial}{\partial x} (\bar{\rho} \langle U \rangle) + \frac{\partial}{\partial y} (\bar{\rho} \langle V \rangle) = 0, \quad (33)$$

$$\bar{\rho} \langle U \rangle \frac{\partial \langle U \rangle}{\partial x} + \bar{\rho} \langle V \rangle \frac{\partial \langle U \rangle}{\partial y} = \frac{\partial}{\partial y} \left[ \left( \bar{\mu} + \bar{\mu}_t \right) \frac{\partial \langle U \rangle}{\partial y} \right], \quad (34)$$

$$\bar{\rho} \langle U \rangle \frac{\partial \langle H \rangle}{\partial x} + \bar{\rho} \langle V \rangle \frac{\partial \langle H \rangle}{\partial y} = \frac{\partial}{\partial y} \left[ \left( \frac{\bar{\mu}}{Pr} + \frac{\bar{\mu}_t}{Pr_t} \right) \frac{\partial \langle H \rangle}{\partial y} \right], \quad (35)$$

$$\frac{\partial \langle H \rangle}{\partial y} + \bar{\mu} \left( 1 - \frac{1}{Pr} \right) \left( 1 + \frac{Pr(1-Pr_t)\bar{\mu}_t}{Pr_t(1-Pr)\bar{\mu}} \right)$$

$$\langle U \rangle \frac{\partial \langle U \rangle}{\partial y} - \left( \frac{\bar{\mu}}{Pr} + \frac{\bar{\mu}_t}{Pr_t} \right) \frac{\partial k}{\partial y}.$$



$$\bar{\rho} \langle U \rangle \frac{\partial k}{\partial x} + \bar{\rho} \langle V \rangle \frac{\partial k}{\partial y} = \frac{\partial}{\partial y} \left[ \left( \bar{\mu} + \frac{\bar{\mu}_t}{\sigma_k} \right) \frac{\partial k}{\partial y} \right] + \bar{\mu}_t \left( \frac{\partial \langle U \rangle}{\partial y} \right)^2 - \frac{2}{3} \bar{\mu}_t \left( \frac{\partial \langle U \rangle}{\partial x} + \frac{\partial \langle V \rangle}{\partial y} \right)^2 - \frac{2}{3} \bar{\rho} k \left( \frac{\partial \langle U \rangle}{\partial x} + \frac{\partial \langle V \rangle}{\partial y} \right) - \bar{\rho} (\epsilon + \epsilon^c) - \gamma \bar{\rho} k \left( \frac{\partial \langle U \rangle}{\partial x} + \frac{\partial \langle V \rangle}{\partial y} \right) + \bar{u}'' \frac{\partial}{\partial y} \left( \bar{\mu} \frac{\partial \langle U \rangle}{\partial y} \right) \quad (36)$$

$$\bar{\rho} \langle U \rangle \frac{\partial \epsilon}{\partial x} + \bar{\rho} \langle V \rangle \frac{\partial \epsilon}{\partial y} = \frac{\partial}{\partial y} \left[ \left( \bar{\mu} + \frac{\bar{\mu}_t}{\sigma_\epsilon} \right) \frac{\partial \epsilon}{\partial y} \right] + C_{\epsilon 1} \frac{\epsilon}{k} \bar{\mu}_t \left( \frac{\partial \langle U \rangle}{\partial y} \right)^2 - C_{\epsilon 2} \bar{\rho} \frac{\epsilon}{k} - \frac{4}{3} \bar{\rho} \epsilon \left( \frac{\partial \langle U \rangle}{\partial x} + \frac{\partial \langle V \rangle}{\partial y} \right) + \xi \quad (37)$$

In writing down these equations, (33) has been used to relate the shear stress to the mean velocity gradient. It is also noted that  $G_{ij}$  is zero for flat plate boundary-layer flows while the only term of importance in  $T_{ij}$  is that given by  $u''$ . If (25) is used to evaluate  $u''$ , then  $T_{ij}$  is of order  $y^2$  and is not important in the near-wall region, which according to So et al. [27] is bounded by  $0 \leq y^+ \leq 5$ . The model constants are taken from Refs. 27 and 32 and are given by:  $C_{\mu} = 0.096$ ,  $C_{\epsilon 1} = 1.5$ ,  $C_{\epsilon 2} = 1.83$ ,  $\sigma_k = 0.75$ ,  $\sigma_\epsilon = 1.45$ ,  $\alpha_1 = 0.15$ ,  $\sigma_p = 0.5$  and  $\gamma = 0.182$ . The turbulent Prandtl number  $Pr_t$  is specified as 0.9, while  $Pr$  is assumed constant and taken to be 0.74. Sutherland and power laws are used to evaluate fluid viscosity at an appropriate reference temperature. The constants  $\sigma_p$  and  $\alpha_1$  are determined by calibrating the calculated results against some classic experiments such as those provided in Refs. 29 and 30. Once determined, they are kept constant for all other calculations. In fact, the cases to be compared in the next section are different from the cases used to calibrate  $\sigma_p$  and  $\alpha_1$ . As for  $N$  and  $M_1$ , the final choice of values adopted are 2 and 1.5, respectively, just as in Ref. 27.

The boundary conditions are no slip at the wall for mean velocities and  $k$ , and zero heat flux or constant wall temperature at the wall for enthalpy. As for  $\epsilon$ , its value at the wall is given by  $2\bar{v} (\partial \bar{k} / \partial y)_w^2$ . At the edge of the boundary layer, free-stream conditions are specified for both mean stream velocity and enthalpy. In principle,  $k$  and  $\epsilon$  should be zero in the free stream. However, in practice, they are assumed to take on some very small values, of the order of  $10^{-7}$ , in the free stream. Thus formulated, the above equations and the appropriate boundary conditions can be solved numerically using the boundary-layer code developed by Anderson and Lewis [30] and modified by So et al. [27].

All measurements used to validate the near-wall two-equation model are drawn from Ref. 31. The calculations are carried out over the range,  $0 < M_\infty < 10$ , for adiabatic wall boundary condition and over the range,  $0 < \Theta_w / \Theta_r < 1$ , for constant wall temperature condition. Here,  $\Theta_w$  is the wall temperature and  $\Theta_r$  is the recovery temperature for adiabatic wall boundary condition and is the adiabatic wall temperature for constant wall temperature. It should be pointed out that  $\Theta_w / \Theta_r = 1.0$  corresponds to adiabatic wall boundary condition while  $\Theta_w / \Theta_r < 1$  indicates that the wall is cooled. Since only mean flow properties are available from Ref. 31, comparisons are made with these measurements and another set of calculations using the  $k$ - $\omega$  model of Wilcox [8]. All comparisons are made at the same momentum thickness Reynolds number ( $R_\theta$ ) as the measurements. Four sets of data are chosen and these are cases 55010504, 53011302 and 73050504 with adiabatic wall boundary condition and case 59020105 with constant wall

temperature. The free-stream Mach number ( $M_\infty$ ) for these cases are 2.244, 4.544, 10.31 and 5.29, respectively, while the corresponding  $R_\theta$ 's are 20,797, 5,532, 15,074 and 3,939. Therefore, the data cover a wide range of  $R_\theta$  and  $M_\infty$ . The variations of skin friction with  $M_\infty$  and  $\Theta_w / \Theta_r$  are compared with the van Driest II formulae reported for a fixed  $R_\theta$  as specified in Ref. 9. Finally, an assessment of compressibility effects on near-wall flows is attempted by comparing the calculated turbulence statistics for the different cases investigated.

## 6.2 Comparisons with Data

The results are organized in the following manner for presentation. Mean stream velocities are normalized by  $u_\tau$  to give  $u^+$  and they are plotted versus  $\ln y_w^+$  (Fig. 1), where  $y_w^+$  is defined as  $u_\tau y / \bar{v}_w$ . A direct plot of the mean velocities is also given in Fig. 2 where  $\langle U \rangle / U_\infty$  versus  $y / \delta$  is shown. Here,  $\delta$  is the boundary layer thickness defined as the location of  $y$  in which  $\langle U \rangle / U_\infty = 1.0$  as specified by the measurements and  $U_\infty$  is the free-stream velocity. On the other hand, mean temperatures are normalized by  $\Theta_\infty$ , the free-stream temperature, and are shown versus  $y / \delta$  (Fig. 3). Plots for the properties,  $k^+ = k / u_\tau^2$ ,  $\epsilon^+ = \epsilon \bar{v} / u_\tau^3$ ,  $-\overline{uv}^+ = -\overline{uv} / u_\tau^2$  and  $-\overline{\theta v}^+ = -\overline{\theta v} / U_\infty \Theta_\infty$ , are presented in terms of  $y_w^+$  and  $y / \delta$ . Near-wall behavior of  $k^+$ ,  $\epsilon^+$ ,  $-\overline{uv}^+$  and  $-\overline{\theta v}^+$  (Figs. 4 - 7) are discussed first, then the distributions of  $k^+$  and  $-\overline{uv}^+$  in the outer region are examined (Figs. 8 and 9). In Figs 8 and 9,  $\delta$  is not interpreted from measurements; rather it is evaluated at the  $y$  location where  $\langle U \rangle / U_\infty = 0.9974$ . Only the budget of  $k$  in the near-wall region for case 73050504 ( $M_\infty = 10.31$  and  $\Theta_w / \Theta_r = 1.0$ ) is presented (Fig. 10) because the  $k$  budgets for the other cases are essentially similar to that shown in Fig. 10. The effects of Mach number on the asymptotic behavior of  $k$  are examined by plotting  $a_k$  versus  $M_\infty$  (Fig. 11), where  $a_k$  is the leading coefficient in the expansion of  $k^+$  in terms of  $y_w^+$ . According to Ref. 27,  $\epsilon_\infty^+ = 2a_k$ . Therefore, by examining  $a_k$  versus  $M_\infty$ , the variation of  $\epsilon_\infty^+$  with Mach number is also evident. Other asymptotic properties are tabulated in Table 1 for comparison. The variations of skin friction coefficient,  $C_f = 2\tau_w / \bar{\rho} U_\infty^2$ , with  $M_\infty$  and  $\Theta_w / \Theta_r$  are compared with van Driest II results [9] in Fig. 12. Finally, the mean velocity plots in terms of the compressible  $u^+$  defined as  $u^+ = (\int (\bar{\rho} / \rho_w) d\langle U \rangle) / u_\tau$  for two different  $M_\infty$  are shown in Fig. 13. This figure is provided to illustrate the deviation or lack thereof from the van Driest law of the wall for compressible flows [37, 38].

Two versions of the present  $k$ - $\epsilon$  model are used to calculate boundary-layer flows. One designated  $k$ - $\epsilon$  model/1 solves the  $k$  and  $\epsilon$  transport equations as given in (38) and (39). The second designated  $k$ - $\epsilon$  model/2 solves (38) and (39) with all additional compressible terms neglected and the  $\partial k / \partial y$  term omitted in (37). In other words, the two-equation model for  $k$ - $\epsilon$  model/2 is a direct variable density extension of the two-equation incompressible model of Ref. 27. These calculations can be used to evaluate the validity and extent of Morkovin's hypothesis and the importance of having an asymptotically consistent near-wall correction for two-equation models.

Four sets of  $u^+$  results are shown in Fig. 1. In the figure, the calculated and measured  $C_f$  and the  $C_f$  determined from the van Driest II formula of Ref. 9 are listed for comparison. The log-law shown is used to demonstrate the existence of a log region in the calculated and measured flows, while the von Karman constant  $\kappa$  is taken to be 0.41. It is recognized that the intercept is a function of Mach number; however, in this figure, the intercept is taken to be 4.7. The actual value used is not important because the purpose here is to illustrate the slope of the log-law. It can be seen that a log region indeed exists for all calculated and measured flows. The slope is fairly constant for the three adiabatic wall cases tested and the  $\kappa$  thus determined is approximately 0.41. For the cooled wall case, the  $k$ - $\epsilon$  model predicted slopes are slightly different from that calculated by  $k$ - $\omega$  model. None of these slopes yields a von Karman constant of 0.41 though.  $C_f$  is predicted correctly by all three models with a

maximum error of less than 5%. For the cooled wall case, the measured  $C_f$  is substantially higher than the van Driest II value and, according to Ref. 31, is not as accurate as the measured  $C_f$  for the other cases studied. The model calculations are in good agreement with the van Driest II values for all cases examined.

Calculated  $u^+$  profiles correlate well with measurements. At high Mach numbers, there seems to be substantial difference between model predictions and measurements in the outer region of the boundary layer. Such a difference is also noted when the plots are given in terms of  $\langle U \rangle / U_\infty$  versus  $y/\delta$  in Fig. 2. From these plots, it can be seen that k- $\epsilon$  model predictions of  $\langle U \rangle / U_\infty$  are in better agreement with data than k- $\omega$  calculations (Fig. 2). The agreement between k- $\epsilon$  model predictions and measurements is good up to  $M_\infty = 10.31$ . On the other hand, the discrepancy between calculations and measurements deteriorates as  $M_\infty$  increases for the k- $\omega$  model. Therefore, the proposed k- $\epsilon$  models represent improvements over existing models whose predictions are correct only for  $M_\infty \leq 5$  (see e.g. Ref. 39). Since most existing models do not have an asymptotically consistent near-wall correction and are direct extensions of their incompressible counterparts, the discrepancies display by these

models for  $M_\infty > 5$  are understandable. Present results show that, if the near-wall flow is modeled in an asymptotically correct and consistent manner, the incompressible models can be straight-forwardly extended to compressible flows with a free-stream Mach number as high as 10. It should be pointed out that the k- $\omega$  model is not an asymptotically consistent near-wall model. Therefore, its prediction of  $\langle U \rangle / U_\infty$ , in particular that for the cooled wall case, is not as good as k- $\epsilon$  model calculations. One reason could be the fairly low  $R_\theta$  (3,939) for this case. Since the results of k- $\epsilon$  model/2 are also in good agreement with measurements (Figs. 1 and 2), the comparisons suggest that the additional compressible terms in (38) and (39) are not too important. However, an examination of the mean temperature results tends not to support this conclusion (Fig. 3).

The mean temperature profile comparisons are shown in Fig. 3. Predictions by the k- $\omega$  model show substantial discrepancies compared to the k- $\epsilon$  model calculations and measurements; particularly for the cooled wall case (Fig. 2a). Discrepancies between measurements and k- $\omega$  predictions increase as  $M_\infty$  increases and as  $\Theta_w/\Theta_r$  decreases. On the other hand, the agreement between k- $\epsilon$  model/1 predictions and data improves as  $M_\infty$  increases for adiabatic wall boundary condition. This is not true for k- $\epsilon$  model/2 where the disagreement with data is quite substantial at  $M_\infty = 10.31$  (Fig. 2b). The predictions of the cooled wall case (Fig. 2a) tell a different story. It seems that k- $\epsilon$  model/2 gives as good a prediction of the cooled wall case as that of k- $\epsilon$  model/1 (Figs. 1a and 2a). The following three reasons could be put forward to explain this behavior. Firstly, the  $\rho'$  expansion may not be totally valid for constant wall temperature boundary condition. Secondly, the proposed compressible models may be more applicable for adiabatic wall boundary condition. Thirdly, the assumption of a constant turbulent Prandtl number may not be appropriate.

The near-wall distributions of  $k^+$  for the four cases are shown in Fig. 4. Only the predictions of k- $\epsilon$  model/1 and k- $\omega$  model are compared. The calculations of k- $\epsilon$  model/2 are not shown; instead, the limiting behavior of  $k^+$ ,  $-\overline{uv}^+$  and  $-\theta v^+$  is tabulated in Table 1 for comparison. In general, the predictions of k- $\omega$  model are substantially lowered than those of k- $\epsilon$  model/1. The peaks are about 40% lower than those predicted by k- $\epsilon$  model/1 and the locations where the peaks occur are calculated to be further away from the wall than k- $\epsilon$  model/1 predictions. According to k- $\epsilon$  model/1, the peak of  $k^+$  decreases as  $M_\infty$  increases. The decrease is more than 20% over a Mach number range of 10. On the other hand, a slight cooling of the wall at  $M_\infty = 5.29$  causes the peak of  $k^+$  to decrease to the same level as that for the case of adiabatic wall with  $M_\infty = 10.31$ . These results suggest that wall cooling has more influence on reducing turbulent mixing compared to compressibility effects. Overall, compressibility reduces turbulent mixing and the

reduction increases with  $M_\infty$ . The near-wall distributions of  $\epsilon^+$  as calculated by k- $\epsilon$  model/1 are plotted in Fig. 5. It can be seen that the distributions are very similar to those shown in Ref. 27 for incompressible flows. The variations of  $\epsilon^+$  with  $M_\infty$  and  $\Theta_w/\Theta_r$  are very similar to those of  $k^+$ . Again, maximum  $\epsilon^+$  occurs at the wall and a plateau in  $\epsilon^+$  is found in the range,  $7 \leq y_w^+ \leq 13$ . This means that compressibility has little or no effects on the near-wall behavior of  $\epsilon^+$ . The exception is that increases in compressibility and wall cooling tend to decrease  $\epsilon_w^+$ .

In general, k- $\omega$  model gives a very accurate prediction of  $-\overline{uv}^+$  near a wall. Its predictions are as good as those given by k- $\epsilon$  model/1 (Fig. 6). From this set of predictions, the following observations can be made. Firstly, the peak of  $-\overline{uv}^+$  decreases with increasing  $M_\infty$  and decreasing  $\Theta_w/\Theta_r$ . Secondly, as  $M_\infty$  increases and  $\Theta_w/\Theta_r$  decreases, the location of the peak moves towards the wall. Thirdly, the rate of decrease of  $-\overline{uv}^+$  in the range,  $30 \leq y_w^+ \leq 100$ , increases as  $M_\infty$  increases. Finally, the asymptotic near-wall behavior of  $-\overline{uv}^+$  is listed in Table 1 for comparison. Much the same behavior is also true for  $-\theta v^+$  whose distributions in the near-wall region are shown in Fig. 7.

If the distributions of  $\overline{\theta v^+}$  are plotted instead of  $-\overline{\theta v^+}$ , the curves will have the same shape as those shown for  $-\overline{uv}^+$ . Therefore, the observations drawn for  $-\overline{uv}^+$  are also valid for  $\overline{\theta v^+}$ .

The distributions of  $k^+$  and  $-\overline{uv}^+$  across the boundary layer are compared in Figs. 8 and 9, respectively. In all cases shown, k- $\omega$  model over-predicts  $k^+$  and  $-\overline{uv}^+$  in the outer part of the boundary layer compared to the calculations of k- $\epsilon$  model/1. The over-prediction extends across the range,  $0.2 \leq y/\delta \leq 1.0$ . Reduction of turbulence activities in the outer part of the boundary layer is clearly evident when either compressibility or wall cooling effects are present. The reduction increases as  $M_\infty$  increases and  $\Theta_w/\Theta_r$  decreases. Therefore, it is expected that turbulence activities will be substantially reduced in a flow where the free-stream Mach number is large and the wall is highly cooled.

The near-wall k budget for case 73050504 is plotted in Fig. 10. Other budget plots are not shown because they are essentially similar to that given in Fig. 10. It can be seen that the k budget bears a lot of similarity with that calculated for incompressible flows (see e.g. Ref. 27). The additional compressible terms have negligible effect on the near-wall k budget. Therefore, the assumptions made to derive the near-wall function  $\xi$  in the dissipation-rate equation are justified. Again, viscous diffusion balances dissipation at the wall. This balance extends to about  $y_w^+ = 4$  where turbulent diffusion and production become important. In the region,  $4 \leq y_w^+ \leq 15$ , viscous and turbulent diffusion, production and dissipation are equally important. Beyond  $y_w^+ = 15$ , production and dissipation are in balance, just as in the case of incompressible flows. Consequently, the near-wall k behavior is very similar for both incompressible and compressible flows.

According to Refs. 25 and 27, Taylor series expansions about  $y_w^+ = 0$  can be assumed for  $k^+$ ,  $-\overline{uv}^+$  and  $-\theta v^+$ . For incompressible flows, the expansions are valid up to about  $y_w^+ = 7$ . This range may not be applicable for compressible flows. Nevertheless, such expansions for small  $y_w^+$  can still be assumed. With the help of (21) these expansions can be written as:

$$k^+ = a_k(y_w^+)^2 + b_k(y_w^+)^3 + \dots \quad (40a)$$

$$-\overline{uv}^+ = a_{uv}(y_w^+)^3 + b_{uv}(y_w^+)^4 + \dots \quad (40b)$$

$$-\overline{\theta v^+} = a_{\theta v}(y_w^+)^3 + b_{\theta v}(y_w^+)^4 + \dots \quad (40c)$$

where the  $a$ 's and  $b$ 's are time-average coefficients that are functions of  $x$ . A similar expansion can be deduced for  $\epsilon^+$ . Again, using (21), the definition of  $\epsilon$  and its wall boundary condition, the expansion for  $\epsilon^+$  can be written as:

$$\epsilon^+ = 2a_k + 4b_k y_w^+ + \dots \quad (41)$$

From these expansions, it can be easily deduced that  $k^{+2}/\epsilon^+(y_w^+)^2 = 0.5$ . Therefore, the asymptotic behavior of  $k^{+2}/\epsilon^+(y_w^+)^2$  is 0.5 and is independent of  $M_\infty$  and wall thermal boundary conditions. The accuracy in which a model can predict this quantity is a reflection of the asymptotic consistency of the model. Table 1 shows that  $k$ - $\epsilon$  model/1 is indeed asymptotically consistent while  $k$ - $\epsilon$  model/2 is not as good. As

for the  $k$ - $\omega$  model, its prediction of this limiting value is poor, therefore, it is not listed in Table 1.

The " $a$ " coefficients can be determined from the calculations and their values are also listed in Table 1 for comparison. It can be seen that  $a_k$  varies with free-stream Mach number. A plot of  $a_k$  versus  $M_\infty$  for adiabatic wall boundary condition is shown in Fig. 11. The value of  $a_k$  for the incompressible case is taken from Ref. 27 and is plotted at  $M_\infty = 0$ . Clearly, the trend is to approach an asymptotic value for  $a_k$  at high  $M_\infty$ . This decrease in  $a_k$  is one of the reasons why  $k$  decreases for high Mach number flows (Figs 4 and 8). The physical reason is that compressibility tends to hinder turbulence mixing. As a result, both turbulent shear stress and kinetic energy decrease significantly as  $M_\infty$  increases (Figs. 4, 6, 8 and 9). Since  $\epsilon_k^+ = 2a_k$  according to (41), dissipation at the wall is also dependent on  $M_\infty$ . There is no clear trend for  $a_{uv}$  and  $a_{v\theta}$ . However, the values of  $a_{uv}$  are consistent with those calculated for incompressible flows [27] and direct simulation data [35]. The value of  $a_{v\theta}$  is essentially zero. Since there is no data available, its correctness cannot be verified.

Finally, the ability of the  $k$ - $\epsilon$  models to predict skin friction coefficient over a range of  $M_\infty$  and wall temperatures is illustrated in Fig. 12. In Fig. 12a, the variation of  $C_f/(C_f)_i$  with  $M_\infty$  for the case of adiabatic wall boundary condition is shown. Here,  $(C_f)_i$  is the skin friction coefficient for an incompressible flow evaluated at  $R_\theta = 10^4$  and is determined to be  $2.73 \times 10^{-3}$ . The figure shows a comparison of the calculations of  $k$ - $\epsilon$  model/1 and  $k$ - $\epsilon$  model/2 with the van Driest II distribution. Below  $M_\infty = 5$ , the calculated variations of  $C_f/(C_f)_i$  with  $M_\infty$  are slightly lower than the van Driest II distribution but they are slightly higher beyond  $M_\infty = 5$ . Essentially, there is no difference between the predictions of  $k$ - $\epsilon$  model/1 and  $k$ - $\epsilon$  model/2. This means that both versions of the  $k$ - $\epsilon$  model give a correct prediction of the  $C_f/(C_f)_i$  variation with  $M_\infty$  for adiabatic wall boundary condition. The predictions for the cooled wall case are not as good, especially at low temperature ratio (Fig. 12b). Three sets of calculations are presented. These are  $k$ - $\epsilon$  model/1,  $k$ - $\epsilon$  model/2 and a third version of  $k$ - $\epsilon$  model/1 with the  $\partial k/\partial y$  term in (37) neglected. Calculations for this case are carried out at  $M_\infty = 5$ ,  $R_\theta = 10^4$  and the incompressible  $C_f$  is again determined to be  $2.73 \times 10^{-3}$ . It can be seen that error of 5% or larger starts to accumulate at approximately  $\Theta_w/\Theta_f = 0.4$  for  $k$ - $\epsilon$  model/1. This trend is contrary to previous calculations [8]. An examination of the governing equations solved by other researchers revealed that, besides differences noted in the turbulence model equations, the mean energy equation solved by these researchers does not include the term  $\partial k/\partial y$  in the right hand side of (37). Indeed, when the  $\partial k/\partial y$  term is neglected, an overall improvement is obtained. The predicted  $C_f$  at  $\Theta_w/\Theta_f = 0.2$  is increased by about 6%, thus giving a better agreement with the van Driest II formula. If the additional compressible terms in the  $k$ - $\epsilon$  equations are further neglected ( $k$ - $\epsilon$  model/2), the calculated  $C_f$  is only improved by about 3%. The remaining disagreement could be attributed to the assumption of a constant

turbulent Prandtl number. When  $Pr_t = 0.7$  is assumed, the calculations are in even better agreement with data. The reason could be due to a further reduction of turbulent mixing as a result of the wall being cooled. However, this effect has not been appropriately accounted for in the models, particularly their near-wall behavior. In other words, if highly cooled-wall flows are to be predicted correctly, heat fluxes should be modeled separately rather than linking to momentum fluxes via a constant turbulent Prandtl number.

### 6.3 Discussion

In the past, velocity profiles in wall coordinate were invariably plotted in terms of  $u^+$  to illustrate the existence of the log-law and the constancy of  $\kappa$  in compressible boundary-layer flows. The proposal was first suggested by van Driest [37] and later confirmed by Maisie and McDonald [38] when they analysed ten sets of data in the Mach number range of 0 - 5.

Since then, the compressible law of the wall is taken to be given by  $u_c^+$  rather than by  $u^+$  and  $\kappa$  is considered to be about 0.41 and constant over the Mach number range of 0 - 5. The calculated and measured velocity plots given in Fig. 1 show support for the compressible law of the wall when it is written in terms of  $u^+$  rather than  $u_c^+$ . Furthermore,  $\kappa$  is determined to be approximately 0.41 and is relatively constant over the Mach number range of 0 - 10. These results seem to conflict with the proposal of van Driest [37]. In order to resolve this seeming contradiction, the velocity plots of  $u_c^+$  versus  $\ln y_w^+$  for cases 55010504 ( $M_\infty = 2.244$ ,  $\Theta_w/\Theta_f = 1$ ) and 53011302 ( $M_\infty = 4.544$ ,  $\Theta_w/\Theta_f = 1$ ) are shown in Fig. 13. In addition, the compressible law of the wall as given in Ref. 38 is shown for comparison. It can be seen that a line that is parallel to the compressible law of the wall can be drawn through a few of the data points spanning over a narrow range of  $y_w^+$ . On the other hand, the calculated profiles are in agreement with data over a wider range of  $y_w^+$ . The slopes of the calculated profiles are roughly parallel and are slightly larger than the slope of the compressible law of the wall shown. Therefore, irrespective of how the velocity profiles are plotted, the calculations are in good agreement with data. However, the slope of the log-law is given by  $1/0.41$  only when the profiles are plotted in terms of  $u^+$ .

### 7. Conclusions

The  $k$  and  $\epsilon$  equations for compressible flows are derived by assuming that there is no dynamical similarity between the compressible and incompressible fields. Therefore, the influences of fluctuating density on the mean and turbulence fields have to be accounted for in the modeled equations. This can be accomplished by first re-casting the exact  $k$  and  $\epsilon$  equations into forms that are similar to their incompressible counterparts. In other words, the viscous diffusion and dissipation functions have to be defined exactly like their incompressible terms. This procedure gives rise to additional terms in the  $k$  and  $\epsilon$  equations. These terms depend explicitly on compressibility and vanish when the fluid density becomes constant. One extra term in the  $k$ -equation is related to fluid dilatation and can be interpreted as compressible dissipation. The others are production terms that depend on the gradients of the mean pressure and mean viscous shears. All additional terms are found to be relatively unimportant in the near-wall region, or  $0 \leq y_w^+ \leq 50$ . This realization, therefore, allows the near-wall incompressible models to be extended directly to compressible flows without modifications, while still maintaining the balance of the modeled equations as a wall is approached. Models are proposed for the additional terms in the  $k$  and  $\epsilon$  equations. The constants introduced by the new models are determined by calibrating the calculations against measurements in compressible flows.

The near-wall two-equation model is used to calculate compressible flat plate boundary-layer flows with different wall thermal boundary conditions and free-stream Mach numbers.

Comparisons are made with various mean flow measurements and with calculations of the  $k-\omega$  model. Good agreement is obtained between the present calculations and measurements. In particular, the log-law for compressible flows is recovered and the slope of the log-law is found to be fairly independent of free-stream Mach number for the range,  $0 \leq M_\infty \leq 10$ , tested. Even though  $k-\omega$  model gives a correct prediction of  $u^+$  versus  $\ln y_w^+$ , their velocity comparison in terms of  $\langle U \rangle / U_\infty$  versus  $y/\delta$  shows substantial discrepancy with data. The discrepancy increases with increasing Mach number and can be attributed to a near-wall behavior that is not asymptotically correct.

The following conclusions can also be drawn from the above analysis. Firstly, Morkovin's hypothesis is valid up to a free-stream Mach number of about 5 for flat plate boundary-layer flows with adiabatic wall boundary condition. This means that the effects of fluctuating density are becoming more and more important as  $M_\infty$  increases beyond 5. Secondly, the assumption of a constant turbulent Prandtl number is not appropriate for cooled wall thermal boundary condition. The reason is further reduction in turbulent mixing due to a cooled wall and this effect is not correctly accounted for in a constant turbulent Prandtl number approach. Most likely a heat flux model is required if the characteristics of cooled-wall compressible boundary-layer flows are to be predicted correctly. Thirdly, it is important to model the near-wall flow correctly if the overall boundary-layer characteristics are to be predicted with confidence. This point is substantiated by the  $k-\epsilon$  model calculations where all additional compressible terms in the turbulence equations are neglected. These results are in good agreement with measurements even though they differ slightly from the predictions of  $k-\epsilon$  model/1 where all the additional terms are retained. In other words, an asymptotically consistent near-wall model is more important to the prediction of compressible boundary-layer flows than the inclusion of fluctuating density effects in the modeled equations. Fourthly, the predicted near-wall characteristics are very similar to those calculated for incompressible flows. In the range of free-stream Mach number tested, the calculated near-wall characteristics are essentially independent of Mach number and wall thermal boundary condition. Very near the wall, viscous diffusion of  $k$  is balanced by the dissipation of  $k$ . Beyond  $y_w^+ = 15$ , dissipation is balanced by mean shear production of  $k$ . In between these two regions, viscous and turbulent diffusion of  $k$ , production of  $k$  and dissipation of  $k$  are of importance in the budget of  $k$ . The additional compressible terms in the  $k$ -equation are essentially negligible in the near-wall region up to  $y_w^+ = 50$ . This is the reason why the model also performs well when the additional compressible terms are neglected in the equations. Finally, the term  $\partial k / \partial y$  in the mean energy equation makes a significant contribution to the calculated  $C_f$  in the highly cooled wall case. Traditionally, this term is neglected. However, present analyses show that even though it is relatively unimportant in flows with adiabatic wall boundary condition, it cannot be neglected in flows with a highly cooled wall. The inclusion of this term degrades the prediction of  $C_f$ . It is believed that the degradation is a result of an incorrect modeling of turbulent heat flux. Therefore, improvements should be directed at the relaxation of the constant turbulent Prandtl number assumption.

#### Acknowledgement

This work was supported by NASA Langley Research Center, Hampton, Virginia 23665, under Grant No. NAG-1-1080.

#### References

- [1] Wilcox, D.C. and Alber, I.E., "A turbulence model for high speed flows," Proc. of the 1972 Heat Transfer and Fluid Mechanics Institute, Stanford University Press, 1972, pp. 231-252.
- [2] Bradshaw, P., "Compressible turbulent shear layers," Annual Review of Fluid Mechanics 9, 1977, pp. 33-64.
- [3] Rubesin, M.W., "A one-equation model of turbulence for use with the compressible Navier-Stokes equations," NASA TM-X-73-128, 1976.
- [4] Viegas, J.R., and Horstman, C.C., "Comparison of multiequation on turbulence models for several shock boundary layer interaction flows," AIAA Journal 17, 1979, pp. 811-820.
- [5] Vandromme, D., Ha Minh, H., Viegas, J.R., Rubesin, M.W. and Kollman, W., "Second order closure for the calculation of compressible wall bounded flows with an implicit Navier-Stokes solver," 4th Turbulent Shear Flows Conferences, Karlsruhe, 1983, pp. 1.1-1.6c.
- [6] Saffman, P. G. and Wilcox, D. C., "Turbulence-Model Predictions for Turbulent Boundary Layers," AIAA Journal, 12, 1974, pp. 541-546.
- [7] Coakley, T. J., "Turbulence modeling methods for the compressible Navier-Stokes equations," AIAA Paper 83-1693, 1983.
- [8] Wilcox, D. C., "Reassessment of the scale-determining equation for advanced turbulence models," AIAA Journal, 26, 1988, pp. 1299-1310.
- [9] Kline, S. J., Cantwell, B. J. and Lilley, G. M. (eds.), *Proceedings of the 1980-81 AFOSR-HTTM-Stanford Conference on Complex Turbulent Flows*, Stanford University Press, Stanford, CA, 1981.
- [10] Morkovin, M., "Effects of compressibility on turbulent flows," *Mecanique de la turbulence*, C.N.R.S., edited by A.Favre, 1962, pp. 367-380.
- [11] Bradshaw, P., "The effect of mean compression or dilatation on the turbulence structure of supersonic boundary layers," Journal of Fluid Mechanics 63, 1974, pp. 449-458.
- [12] Oh, Y.H., "Analysis of two-dimensional free turbulent mixing," AIAA Paper No. 74594, 1974.
- [13] Speziale, C. G. and Sarkar, S., "Second-Order Closure Models for Supersonic Turbulent Flows," AIAA Paper No. 91-0217, 1991.
- [14] Rodi, W., "Recent developments in turbulence modeling," Proc. 3rd Int. Symp. on Refined Flow Modelling and Turbulence Measurements, Tokyo, July 26-28, 1988.
- [15] Launder, B.E. and Tselepidakis, D.P., "Contribution to the second-moment modeling of sublayer turbulent transport," Proc. Zoric Memorial International Seminar on Wall Turbulence, Dubrovnik, Yugoslavia, 1988.
- [16] Speziale, C. G., "Analytical methods for the development of Reynolds-stress closures in turbulence," Annual Review of Fluid Mechanics, 23, 1991, pp. 107-157.
- [17] So, R. M. C., Lai, Y. G., Zhang, H. S. and Hwang, B. C., "Near-wall second-order turbulence closures: a review," AIAA Journal, 1991, to appear.
- [18] Cousteix, J., "Three-dimensional and unsteady boundary layer computation," Annual Review of Fluid Mechanics 18, 1986, pp. 173-196.

- [19] Hanjalic, K. and Launder, B.E., "Contribution towards a Reynolds-stress closure for low-Reynolds-number turbulence," *Journal of Fluid Mechanics* 74, 1976, pp. 593-610.
- [20] So, R.M.C. and Yoo, G.J., "Low-Reynolds-number modeling of turbulent flows with and without wall transpiration," *AIAA Journal* 25, 1987, pp. 1556-1564.
- [21] Shima, N., "A Reynolds-stress model for near-wall and low-Reynolds-number regions," *Journal of Fluids Engineering* 110, 1988, pp. 38-44.
- [22] Yoo, G.J. and So, R.M.C., "Variable density effects on axisymmetric sudden-expansion flows," *International Journal of Heat and Mass Transfer* 32, 1989, pp. 105-120.
- [23] Launder, B.E., "On the computation of convective heat transfer in complex turbulent flows," *Journal of Heat Transfer* 110, 1988, pp. 1112-1128.
- [24] Nagano, Y. and Kim, C., "A two-equation model for heat transport in wall turbulent shear flow," *Journal of Heat Transfer* 110, 1988, pp. 583-589.
- [25] Lai, Y.G. and So, R.M.C., "Near-wall modeling of turbulent heat fluxes," *International Journal of Heat and Mass Transfer*, 33, 1990, pp. 1429-1440.
- [26] Lai, Y.G. and So, R.M.C., "On near-wall turbulent flow modeling," *Journal of Fluid Mechanics*, 221, 1990, pp. 641-673.
- [27] So, R.M.C., Zhang, H.S. and Speziale, C.G., "Near-wall modeling of the dissipation-rate equation," *AIAA Journal*, 1991, to appear.
- [28] Sarkar, L., Erlebacker, G., Hussaini, M.Y. and Kreiss, H.O., "The analysis and modeling of dilatational terms in compressible turbulence," *NASA CR-181959*, 1989.
- [29] Coles, D., "Measurements of turbulent friction on a smooth flat plate in supersonic flow," *Journal of Aeronautical Sciences* 21, 1954, pp. 433-448.
- [30] Anderson, E. C. and Lewis, C. H., "Laminar or turbulent boundary-layer flows of perfect gases or reacting gas mixtures in chemical equilibrium," *NASA CR-1893*, 1971.
- [31] Fernholz, H. H. and Finley, P. J., "A critical compilation of compressible turbulent boundary layer data," *AGARDograph* No. 223, 1977.
- [32] Jones, W.P., "Models for turbulent flows with variable density and combustion," *Prediction Method for Turbulent Flows*, (Edited by W. Kollenann), Hemisphere, London, 1980, pp. 379-422.
- [33] Mansour, N.N., Kim, J. and Moin, P., "Reynolds-stress and dissipation-rate budgets in a turbulent channel flow," *Journal of Fluid Mechanics*, 194, 1988, pp. 15-44.
- [34] Mansour, N.N., Kim, J. and Moin, P., "Near-wall k- $\epsilon$  turbulence modeling," *AIAA Journal*, 27, 1989, pp. 1068-1073.
- [35] Spalart, P.R., "Direct simulation of a turbulent boundary layer up to  $Re_\theta = 1410$ ," *Journal of Fluid Mechanics*, 187, 1988, pp. 61-98.
- [36] Speziale, C. G., Abid, R. and Anderson, E. C., "A critical evaluation of two-equation models for near-wall turbulence," *AIAA Paper* No. 90-1481, 1990.
- [37] Driest, E. R. van, "Turbulent Boundary Layer in Compressible Fluids," *Journal of Aeronautical Sciences*, 18, 1951, pp.145-160 and 216.
- [38] Maise, G. and McDonald, H., "Mixing Length and Kinematic Eddy Viscosity in a Compressible Boundary Layer," *AIAA Journal*, 6, 1968, pp. 73-80.
- [39] Bradshaw, P., Launder, B. E. and Lumley, J. L., "Collaborative Testing of Turbulence Models," *Journal of Fluids Engineering*, 113, 1991, pp.3-4.

Case	$M_\infty$	$\Theta_w/\Theta_r$	Model	$a_k$	$a_{uv} \times 10^4$	$a_{v\theta} \times 10^7$	$k^+/\epsilon^+(y_w^+)^2$
55010504	2.244	1.0	k- $\epsilon$ model/1	0.0987	7.167	-0.465	0.50
55010504	2.244	1.0	k- $\epsilon$ model/2	0.0992	7.198	-0.998	0.50
53011302	4.544	1.0	k- $\epsilon$ model/1	0.0824	6.700	-6.44	0.50
53011302	4.544	1.0	k- $\epsilon$ model/2	0.0836	6.760	-11.79	0.50
73050504	10.31	1.0	k- $\epsilon$ model/1	0.0741	6.630	89.5	0.50
73050504	10.31	1.0	k- $\epsilon$ model/2	0.0771	6.740	-131.0	0.51
59020105	5.29	0.92	k- $\epsilon$ model/1	0.0784	6.120	11.1	0.50
59020105	5.29	0.92	k- $\epsilon$ model/2	0.0788	6.140	-5.88	0.50

Table 1. Asymptotic near-wall behavior of the turbulence properties.

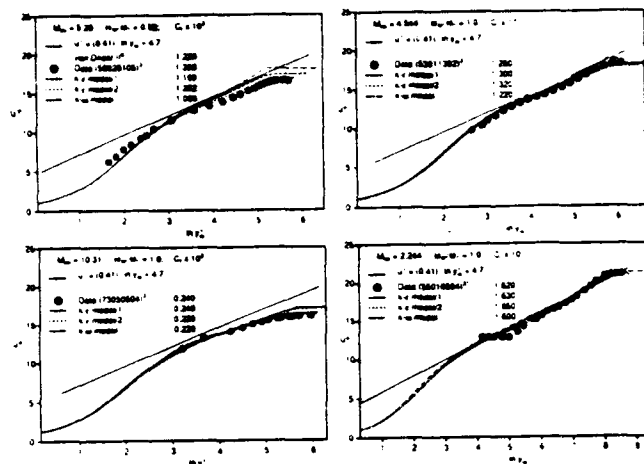


Figure 1. Comparison of calculated  $u^+$  with measurements.

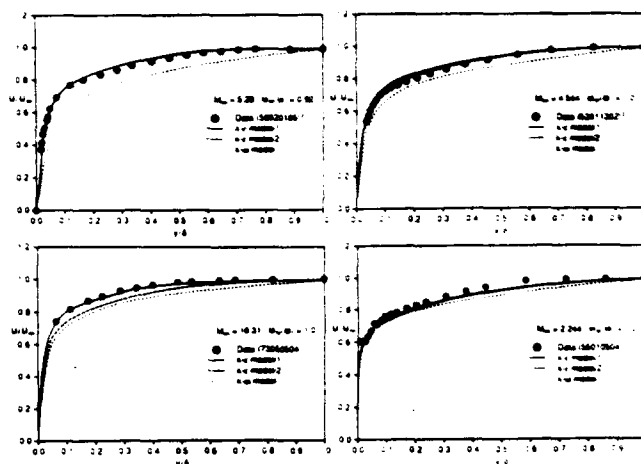


Figure 2. Comparison of calculated  $\langle U \rangle / U_\infty$  with measurements.

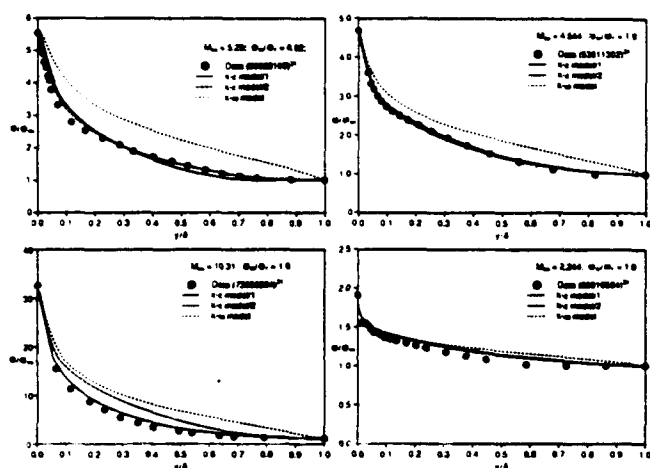


Figure 3. Comparison of calculated mean temperatures with measurements.

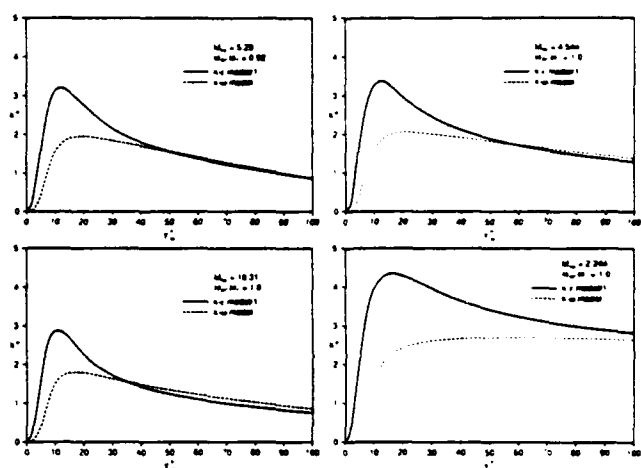


Figure 4. Near-wall distributions of turbulent kinetic energy.

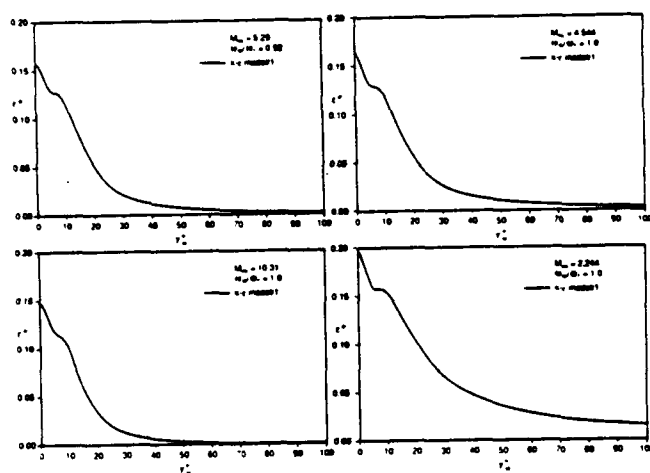


Figure 5. Near-wall distributions of the solenoidal dissipation rate of the turbulent kinetic energy.

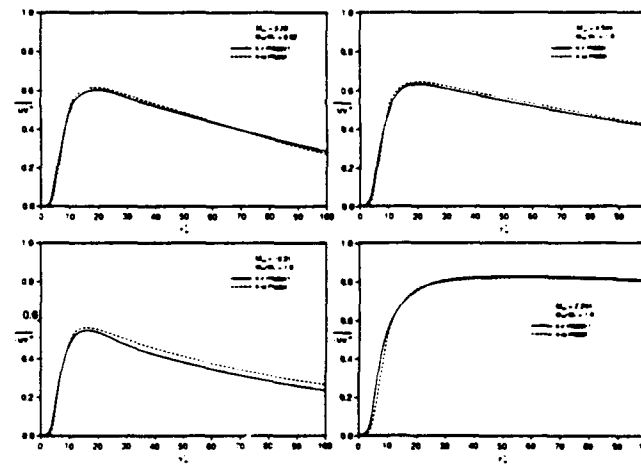


Figure 6. Near-wall distributions of Reynolds shear stress.

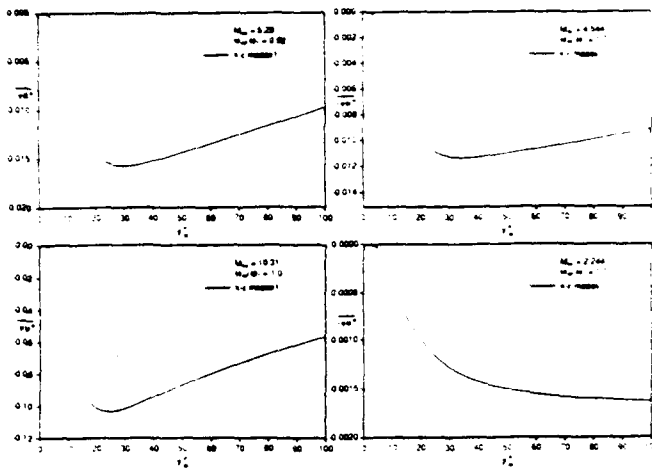


Figure 7. Near-wall distributions of Reynolds heat flux.

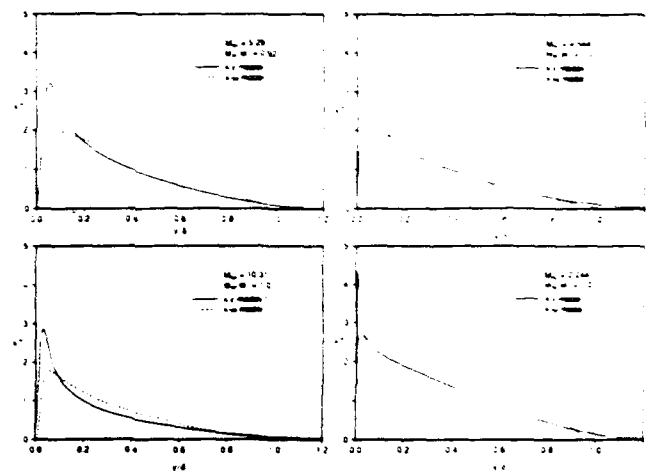


Figure 8. Turbulent kinetic energy distributions across the boundary layer.

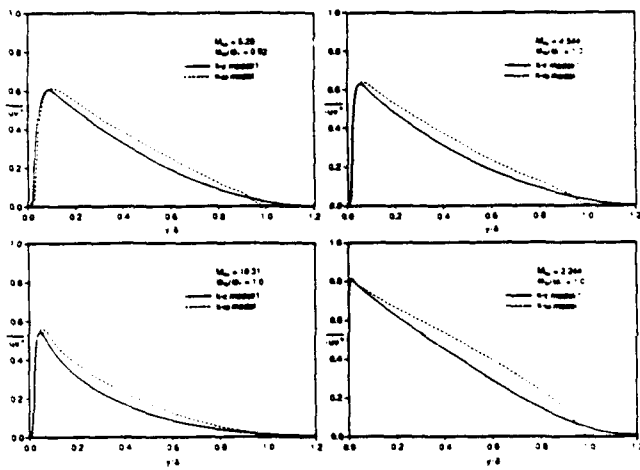


Figure 9. Reynolds shear stress distributions across the boundary layer.

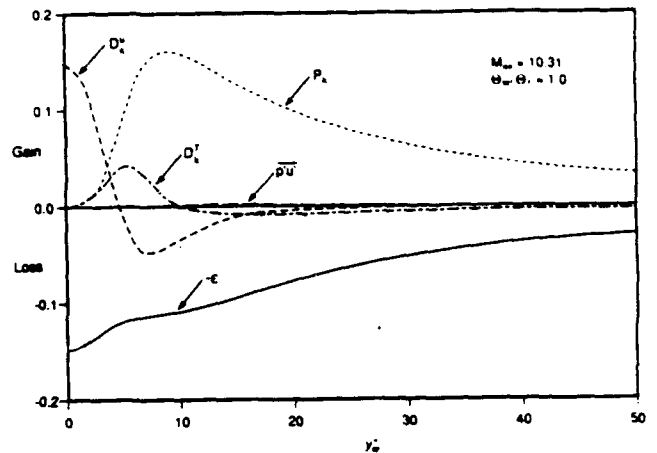


Figure 10. Near-wall  $k$  budget for the case with  $M_{\infty} = 10.31$  and adiabatic wall boundary condition.

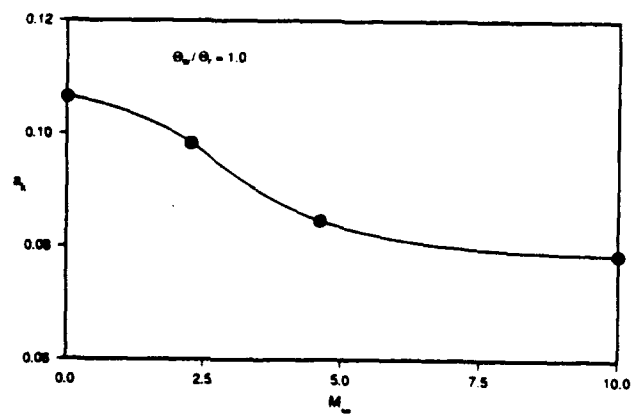


Figure 11. Variation of the slope of  $k^+$  at the wall with  $M_{\infty}$ .

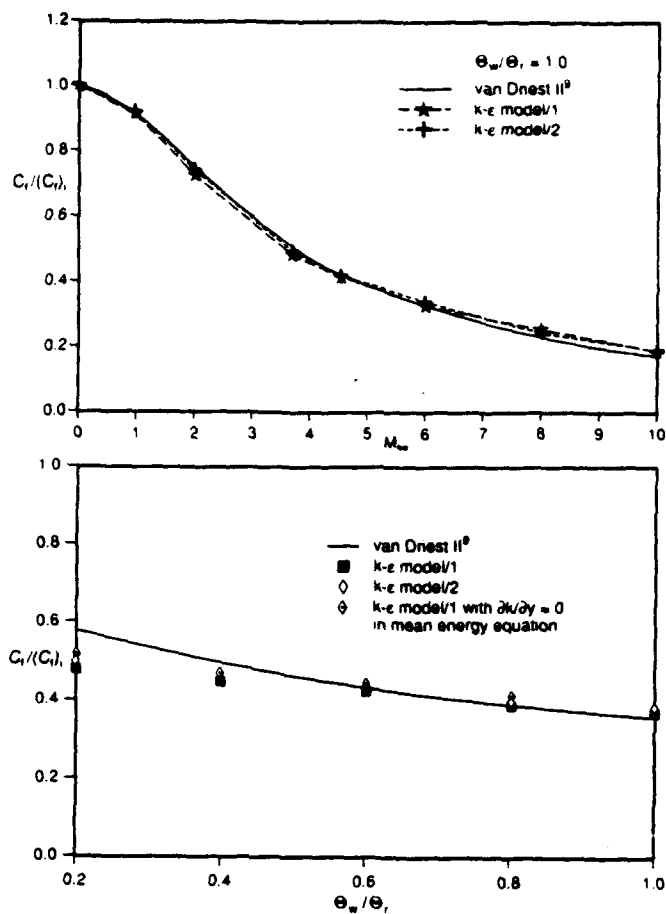


Figure 12. Skin friction coefficient variations with  $M_\infty$  and  $\theta_w/\theta_r$ .

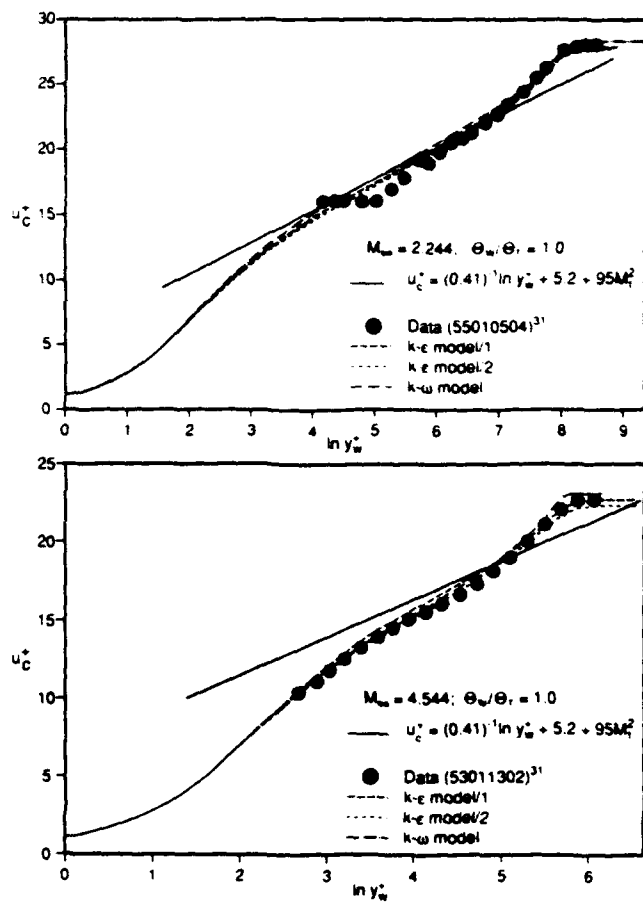


Figure 13. Mean velocity plots in terms of van Driest variable  $u_c^+$  for cases 55010504 and 53011302.



# ANALYSIS OF THE EFFECT OF INITIAL CONDITIONS ON THE INITIAL DEVELOPMENT OF A TURBULENT JET

Soong Ki Kim,\* Myung Kyoong Chung,\*\* and Ji Ryong Cho\*  
Korea Advanced Institute of Science and Technology, Seoul, Korea

The effect of the initial condition at the jet exit on the downstream evolution, particularly within the potential core length, were numerically investigated as well as with available experimental data. In order to select most dependable computational model for the present numerical experiment, a comparative study has been performed with different turbulence models at  $k$ - $\epsilon$  level, and it was found that the  $k$ - $\epsilon$ - $\gamma$  model yields superior prediction accuracy over other conventional models. The calculated results show that the potential core length and the spreading rate of the initial mixing layer are dependent on the initial length scale as well as the turbulent kinetic energy at the jet exit. Such effect of the initial length scale increases with higher initial turbulence level. An empirical parameter has been devised to collapse the calculated data of the potential core length and the spreading rate with various initial conditions onto a single curve.

## Introduction

It is well known that the potential core length, the spreading rate and the asymptotic peak turbulence intensity vary widely from experiment to experiment in the jet initial region.<sup>1,2</sup> Husain and Hussain<sup>3</sup> showed experimentally that the boundary layer state, laminar or turbulent, the momentum thickness and the fluctuation level in the initial boundary layer at the jet exit were important factors which govern the downstream jet development. Gutmark and Ho<sup>4</sup> found that such scatter of the experimental data stems from spatially coherent disturbances in individual facilities. They considered the initial instability frequency as one of the important initial conditions affecting the jet evolution.

In addition to the condition of the initial boundary layer, however, since the jet exit flow field is composed of the boundary layer near the inner wall and the core flow in the central region, the turbulent state of the initial jet core must also affect the downstream jet evolution process. Turbulent intensity in a laboratory jet is typically 0.5% or less, while those in practical turbojet and turbofan engines have been reported to be between 3% and 15%.<sup>5</sup> Thus, in the initial region of the jet flow, the mixing layer and the turbulent core should interact with each other. If the level of the initial core turbulence is low, the effect of the interaction may be small or negligible. However, if it is sufficiently high, the flow field in the initial region should be regarded as a complex flow according to Bradshaw's category.<sup>6</sup>

Vlasov et al.<sup>7</sup> reported that the potential core length significantly decreases with increasing initial core turbulence. More elaborate experiment was performed by Raman et al.<sup>8</sup> who kept the exit mean velocity profile and the boundary layer state nearly the same, but varied the core turbulent intensity between 0.15% and 5% by using various turbulence generating grids. From the variation of the mean velocity along the jet centerline, they concluded that the turbulent intensity in the initial core has only small effect on the jet evolution. However, considering that the freestream length scale is an important parameter for the development of the turbulent boundary layer, which has been vividly demonstrated by Hancock and Bradshaw<sup>9</sup>, the length scale of the core turbulence should be considered as an additional controlling parameter for the downstream jet development. Unfortunately, however, experimental data of the initial length scale or dissipation rate are almost unavailable from published reports. Therefore, in the present study, a computational analysis is carried out to systematically investigate the effects of the turbulent intensity and the length scale in the initial core region on the initial development of a turbulent jet flow.

Since most previous computational studies have been concentrated on the flow field in the self-preserving region, those on the jet initial region are only scarcely found in open literatures. Islam and Tucker<sup>9</sup> computed the turbulent flow of a jet initial region by a revised mixing length model. Meanwhile, computational turbulence models such as  $k$ - $\epsilon$  and Reynolds stress models have serious "anomaly problems" when they are applied to compute turbulent free shear flows: "round-jet / plane-jet anomaly"<sup>10</sup> and "plane-wake / plane-jet anomaly"<sup>11</sup>. Recently, Cho and Chung<sup>12</sup> developed a new  $k$ - $\epsilon$ - $\gamma$  model and made considerable improvement in the prediction accuracy for free shear flows in their similarity regions.

In the present study, firstly, three variants of  $k$ - $\epsilon$  model and the new  $k$ - $\epsilon$ - $\gamma$  model were applied to the initial region of the round and plane jets to prove that the  $k$ - $\epsilon$ - $\gamma$  model is more reliable than other models. Secondly, using the  $k$ - $\epsilon$ - $\gamma$  model the effects of the initial core turbulence, i.e. the turbulent kinetic energy, and the dissipation rate or length scale are systematically investigated, and the results are compared with available experimental data in the initial jet region.

## Computational Models

In order to numerically examine the initial jet evolution process which exhibits quite complex nature of turbulence, a dependable computational model must be employed. As is well known, the  $k$ - $\epsilon$  model has a number of variant forms which has been formulated to remedy the vulnerable model coefficients of the standard  $k$ - $\epsilon$  model under certain circumstances. One of such weaknesses in computation of free shear flows has been expressed by a term "round-jet / plane-jet anomaly"<sup>10</sup>. Specifically, the predictions of a round jet and a plane jet with the same model constants show inconsistent results: If the model constants are adjusted with reference to the spreading rate of the plane jet, the computed spreading rate of the round jet is higher than that of the plane jet by as much as 25% whereas most experimental data demonstrate that the round jet spreads slower than the plane jet by about 15%.

Pope<sup>10</sup> attributed the anomaly to the neglect of the mean vortex stretching effect in the source term of the dissipation equation, and introduced a vortex stretching invariant term  $\chi \equiv (k/\epsilon)^{1/2} \Omega_{ij} \Omega_{ji} S_{ij}$ , where  $\Omega_{ij}$  and  $S_{ij}$  are the rate of mean rotation and rate of mean strain tensors, respectively. Note that the invariant  $\chi$  has a positive value in the round jet whereas it vanishes in the plane jet. Thus, the modified form of  $k$ - $\epsilon$  model suggested by Pope is as follows:

\* Graduate student, Department of Mechanical Engineering.

\*\* Professor, Department of Mechanical Engineering.

+ Present affiliation: Research Engineer, Korea Institute of Machinery and Metals.

$$\frac{Dk}{Dt} = \frac{\partial}{\partial x_j} \left[ \frac{v_i}{\sigma_k} \frac{\partial k}{\partial x_j} \right] + P - \epsilon \quad (1)$$

$$\frac{D\epsilon}{Dt} = \frac{\partial}{\partial x_j} \left[ \frac{v_i}{\sigma_\epsilon} \frac{\partial \epsilon}{\partial x_j} \right] + \frac{\epsilon^2}{k} \left[ C_{\epsilon 1} \frac{P}{\epsilon} - C_{\epsilon 2} + C_{\epsilon 3} \chi \right] \quad (2)$$

$$v_i = c_\mu \frac{k^2}{\epsilon} \quad P = -\overline{u_i u_j} \frac{\partial U_i}{\partial x_j}$$

Here the model constants are ;  $C_\mu=0.09$ ,  $\sigma_k=1.0$ ,  $\sigma_\epsilon=1.3$ ,  $C_{\epsilon 1}=1.45$ ,  $C_{\epsilon 2}=1.90$ ,  $C_{\epsilon 3}=0.79$ .

Hanjalic and Launder<sup>13</sup> found that the rate of spectral energy transfer across the wave number space, which is nearly equal to the dissipation rate, is significantly promoted by irrotational deformation which is associated with normal strains. They also noted that the irrotational deformation has larger value in the round jet than in the plane jet, which stimulated them to propose the following variant of the  $k$ - $\epsilon$  model to solve the "round-jet / plane-jet anomaly" problem.

$$\frac{Dk}{Dt} = \frac{\partial}{\partial x_j} \left[ \frac{v_i}{\sigma_k} \frac{\partial k}{\partial x_j} \right] + P_{k,s} + P_{k,n} - \epsilon \quad (3)$$

$$\frac{D\epsilon}{Dt} = \frac{\partial}{\partial x_j} \left[ \frac{v_i}{\sigma_\epsilon} \frac{\partial \epsilon}{\partial x_j} \right] + \frac{\epsilon^2}{k} \left[ C_{\epsilon 1} \frac{P_{k,s}}{\epsilon} - C_{\epsilon 2} + C_{\epsilon 3} \frac{P_{k,n}}{\epsilon} \right] \quad (4)$$

$$P_{k,s} = -\overline{u_i u_j} \frac{\partial U_i}{\partial x_j} \quad (i \neq j), \quad P_{k,n} = -\overline{u_i u_j} \frac{\partial U_i}{\partial x_j} \quad (i=j)$$

$$\overline{u^2} - \overline{v^2} = c_{uv} k, \quad v_i = c_\mu \frac{k^2}{\epsilon}$$

where  $C_\mu=0.09$ ,  $\sigma_k=1.0$ ,  $\sigma_\epsilon=1.0$ ,  $C_{\epsilon 1}=1.44$ ,  $C_{\epsilon 2}=1.90$ ,  $C_{\epsilon 3}=4.44$ ,  $C_{uv}=0.33$ .

Quite recently, Cho and Chung<sup>12</sup> showed that, although the above two variants improve the consistency in predicting the plane jet and round jet with varying degree of accuracy, such modifications do not yield any better solution to the "plane-jet / plane-wake anomaly problem" which was raised as another computational anomaly through AFOSR-HTTM-Stanford Conference on Complex Turbulent Flows in 1980.<sup>11</sup> With a lengthy discussion about the role of intermittency in the mixing layer between the shear flow in the core region and the ambient potential flow outside the jet boundary, they proposed a new  $k$ - $\epsilon$ - $\gamma$  equation model as follows ( See Cho and Chung<sup>12</sup> for details ) :

$$\frac{Dk}{Dt} = \frac{\partial}{\partial x_j} \left[ \frac{v_i}{\sigma_k} \frac{\partial k}{\partial x_j} \right] + P_{k,s} + P_{k,n} - \epsilon \quad (5)$$

$$\frac{D\epsilon}{Dt} = \frac{\partial}{\partial x_j} \left[ \frac{v_i}{\sigma_\epsilon} \frac{\partial \epsilon}{\partial x_j} \right] + \frac{\epsilon^2}{k} \left[ C_{\epsilon 1} \frac{P_{k,s} + 3P_{k,n}}{\epsilon} - C_{\epsilon 2} + C_{\epsilon 3} \chi + C_{\epsilon 4} \Gamma \right] \quad (6)$$

$$\frac{D\gamma}{Dt} = \frac{\partial}{\partial x_j} \left[ (1-\gamma) \frac{v_i}{\sigma_\gamma} \frac{\partial \gamma}{\partial x_j} \right] + c_{\gamma 1} \gamma (1-\gamma) \frac{P_{k,s} + P_{k,n}}{k} + c_{\gamma 2} \frac{k^2}{\epsilon} \frac{\partial \gamma}{\partial x_j} \frac{\partial \gamma}{\partial x_j} - c_{\gamma 3} \gamma (1-\gamma) \frac{\epsilon}{k} \Gamma \quad (7)$$

$$v_i = c_\mu \left( 1 + C_{\mu 2} \frac{k^3}{\epsilon^2} \frac{1-\gamma}{\gamma^3} \frac{\partial \gamma}{\partial x_k} \frac{\partial \gamma}{\partial x_k} \right) \frac{k^2}{\epsilon}$$

$$\Gamma = \frac{k^{2.5}}{\epsilon^2} \frac{U_i}{(U_k U_k)^{0.5}} \frac{\partial U_i}{\partial x_j} \frac{\partial \gamma}{\partial x_j}$$

Proposed model constants are;  $C_\mu=0.09$ ,  $C_{\mu 2}=0.1$ ,  $\sigma_k=\sigma_\epsilon=1.0$ ,  $C_{\epsilon 1}=1.44$ ,  $C_{\epsilon 2}=1.92$ ,  $C_{\epsilon 3}=0.30$ ,  $C_{\epsilon 4}=0.10$ ,  $C_{\gamma 1}=1.6$ ,  $C_{\gamma 2}=0.15$ ,  $C_{\gamma 3}=0.16$ .

For more detail computation, the Reynolds stress model may be utilized. However, it has been widely demonstrated that when it comes to compute the simple free shear flows, the Reynolds stress model yields similar prediction accuracy as the  $k$ - $\epsilon$  model<sup>14</sup>, and no attempt has been made at modifying the Reynolds stress model to solve the anomaly problem. For this reason, it was not included in the present numerical investigation

### Initial Conditions and Computational Method

It is assumed that the velocity profile at the exit consists of two regions: a boundary layer near the inner wall and the core layer in the central region. The initial boundary layer is further assumed to be in a fully developed turbulent state. Thus, all turbulent parameters in that region can be estimated by those of a fully developed turbulent boundary layer over a flat plate. In practice, Husain and Hussain showed that the mean velocity and the turbulent intensity profiles in the initial boundary layer at the jet exit are close to the flat plate data. Therefore, we picked up the mean velocity profile and the turbulent kinetic energy profile from Klebanoff's experiment on a flat plate. And the dissipation rate data were calculated by assuming a local equilibrium. There have been a large number of jet experiments, however, unfortunately, we can not find any experiment which measured the initial levels of the turbulent kinetic energy and the dissipation rate in the core region, simultaneously. Therefore, we are managed to assume them within a physically reasonable range.

In the core region at the jet exit, the mean velocity, the turbulent kinetic energy and the dissipation rate were assumed uniform, but with their magnitudes being different for different cases. In order to specify the relative magnitude between the turbulent kinetic energy and the dissipation rate, i.e. the initial eddy viscosity level  $k^2/\epsilon$ , in a physically realistic range, the data from a grid-generated turbulence were adopted. Comte-Bellot and Corrsin<sup>15</sup> presented various data set of the energy decay of the grid turbulence. Fig.1 represents the relations between the length scale and the intensity of turbulence for three cases in Comte-Bellot and Corrsin. From these relations, a total of 20 pairs of data were used to specify the initial turbulent kinetic energy and the dissipation rate in the core region at the jet exit. Since the boundary layer profiles are nearly invariant within 50% of the boundary layer thickness,  $\delta$ , the initial profiles of the mean velocity, the turbulent kinetic energy and the dissipation rate are smoothly connected in the region  $0.5\delta$ - $\delta$ .

The upwind finite-difference procedure<sup>16</sup> was used to solve the system of the governing equations. Predictions of the jet flow reported below were obtained by using 200 cross-stream nodes, 50 uniform nodes inside the jet exit diameter and 150 stretched nodes outward. The jet exit mean velocity  $U_e$  was 20 m/sec and jet exit diameter  $D$  or width  $H$  was 10 cm, hence, Reynolds number based on  $D$  or  $H$  was about  $1.3 \times 10^5$ . Initial boundary layer thickness and the momentum thickness were assumed 6mm and 1mm, respectively. The turbulent kinetic

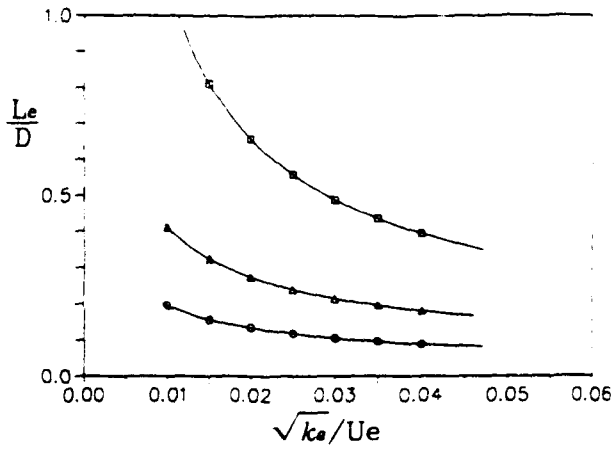


Fig.1 The initial conditions of the jet exit core region selected from Comte-Bellot and Corrsin:  $\circ$  ;  $R_M=3.4 \times 10^4$ ,  $\Delta$  ;  $R_M=6.8 \times 10^4$ ,  $\square$  ;  $R_M=13.5 \times 10^4$ .

energy and the dissipation rate were estimated by assuming  $u^* = 1.0$  m/sec.

### Results and Discussion

#### Performance Tests of Computational Models

In the present investigation, the standard  $k-\epsilon$  model<sup>14</sup>, modified  $k-\epsilon$  models by Pope, and Hanjalic and Launder, and the  $k-\epsilon-\gamma$  model were applied to compute the initial flow field of a plane jet and a round jet for a case with  $\sqrt{k_e}/U_e = 0.01$ ,  $Le/D=0.2$  in Fig.1. Table.1 represents the predicted potential core lengths and spreading rates. The spreading rate can be

defined in various ways. The shear layer width at a certain downstream location  $x$  is determined by either  $B_1=y_{0.1}-y_{0.9}$ , or  $B_2=y_{0.1}-y_{0.95}$ , and the vorticity thickness  $\delta_w$  defined by  $=U_e/(\partial U/\partial y)_{max}$ , where  $y_{0.1}$ ,  $y_{0.9}$ , and  $y_{0.95}$  indicate cross-stream locations from the jet centerline where the local mean velocity is 10%, 90% and 95% of the centerline mean velocity, respectively. The symbol  $x_p$  represents the potential core length.

By comparing the predicted values in Table.1, it is concluded that the  $k-\epsilon-\gamma$  model provides the most reasonable predictions for all jet parameters. Specifically, the prediction of the potential core length is remarkably improved, which can also be appreciated from Fig.2 and 3. In Fig.3, the experimental data show that the turbulent kinetic energy at the jet centerline increases monotonically in the potential core region. However, all models failed to reproduce such increase. From the exact turbulent kinetic energy equation, it can be seen that, since there is no mean shear in the potential core, the turbulent kinetic energy should simply decay. Thus, it is likely that either a certain unknown mechanism exist in the core region or the real flow had some initial shear at the jet exit. Hussain and Husain<sup>20</sup> explained that this occurs because the core potential fluid is exposed to a 'massaging' effect of motions in the mixing layer all around of, which argument however cannot be supported by the governing field equation. Nevertheless, the  $k-\epsilon-\gamma$  model predicts very fairly the variation of the turbulent kinetic energy along the centerline except in the potential core region.

Fig.4 represents the mean velocity profile in similarity coordinate at about the end of the potential core region. Before the end of the potential core region, the initial mixing layer attains similarity. This can be further clarified by the fact that the shear layer thickness varies linearly<sup>3</sup>. In all computations of the mean velocity, the turbulent shear stress

Table 1 Potential core lengths and initial spreading rates of jet flows

(  $\sqrt{k_e}/U_e = 0.01$ ,  $Le/D = Le/H = 0.2$  )

Flow	Model and experiment	$x_p$	$\frac{dB_1}{dx}$	$\frac{dB_2}{dx}$	$\frac{d\delta_w}{dx}$
round jet	$k-\epsilon-\gamma$	4.57 D	0.163	0.175	0.141
	Hanjalic and Launder's $k-\epsilon$	8.33 D	0.154	0.158	0.076
	Pope's $k-\epsilon$	7.89 D	0.146	0.152	0.112
	Standard $k-\epsilon$	7.21 D	0.155	0.162	0.128
	experiment	4.90 D <sup>18</sup>	0.16 - 0.165 <sup>1</sup>	0.158 - 0.202 <sup>2</sup>	0.112 - 0.175 <sup>4</sup>
plane jet	$k-\epsilon-\gamma$	4.80 H	0.163	0.177	0.155
	Hanjalic and Launder's $k-\epsilon$	10.10 H	0.163	0.168	0.110
	Standard $k-\epsilon$	8.74 H	0.151	0.159	0.136
	experiment	4.50 H <sup>19</sup>	0.155 - 0.180 <sup>1</sup>	-	0.155 - 0.179 <sup>1</sup>

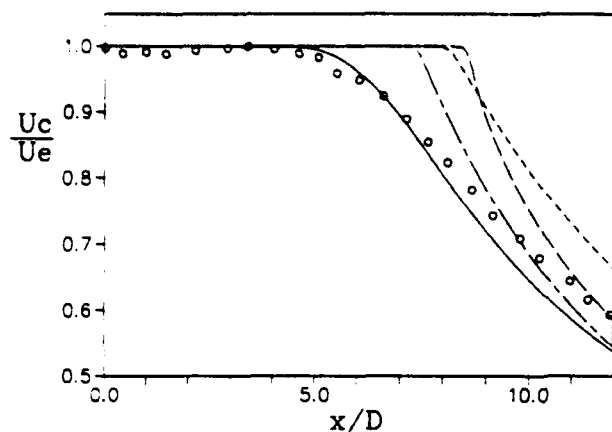


Fig.2 The comparison of model on the variation of the streamwise mean velocity along the centerline in a roundjet : experimental data :  $\circ$  ; Raman et al. : predictions for  $\sqrt{k_e}/U_e = 0.01$ ,  $L_e/D = 0.2$ : predictions : — ;  $k-\epsilon-\gamma$  model of Cho and Chung ; — — ;  $k-\epsilon$  model of Hanjalic and Launder, - - - - ;  $k-\epsilon$  model of Pope, - - - - ; standard  $k-\epsilon$  model.

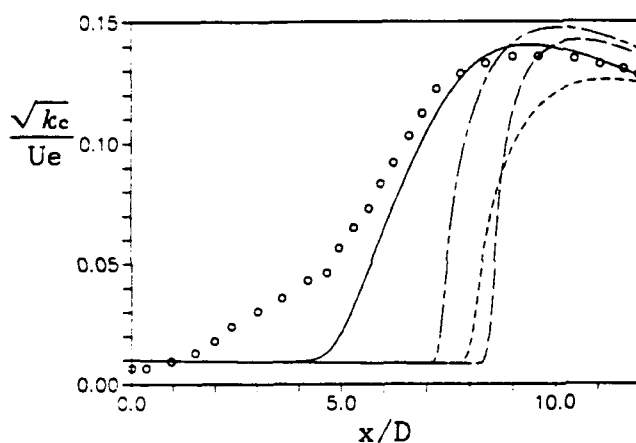


Fig.3 The comparison of models on the variation of the turbulent kinetic energy along the centerline in a roundjet : experimental data :  $\circ$  ; Raman et al. for  $u'/U_e = 0.5\%$ , assume  $v' = w' = 0.6u'$  : predictions for  $\sqrt{k_e}/U_e = 0.01$ ,  $L_e/D = 0.2$ , lines the same as Fig.2.

and the turbulent kinetic energy, the  $k-\epsilon-\gamma$  model outperforms over the  $k-\epsilon$  models as can be seen in Figs.4,5 and 6. The better performance of  $k-\epsilon-\gamma$  model in the core region ( $(y-y_{0.5})/(y_{0.1}-y_{0.9}) < 0$ ) may be attributed to the correct representation of the interaction between the mean velocity gradient and the intermittency gradient by the  $k-\epsilon-\gamma$  model (see, for details, Cho and Chung).

#### Effects of the Initial Conditions on the Downstream Evolution

In order to investigate the effects of the initial conditions on the jet downstream development, the  $k-\epsilon-\gamma$  model was utilized. The initial conditions for the present computation were

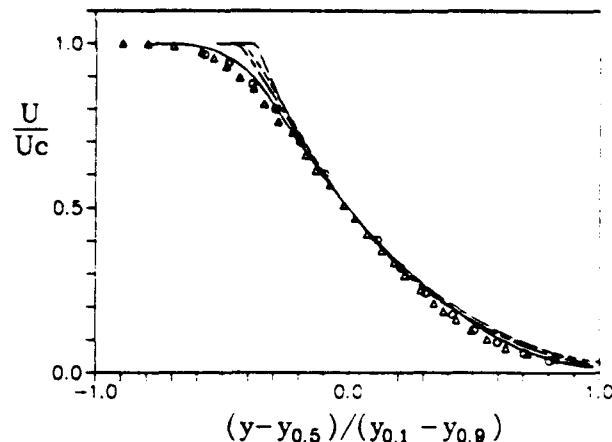


Fig.4 The streamwise mean velocity profiles in the initial similarity region of a round jet : experimental data :  $\circ$  ; Bradshaw et al.,  $\Delta$  ; Husain and Hussain : predictions : — ;  $k-\epsilon-\gamma$  model of Cho and Chung ; — — ;  $k-\epsilon$  model of Hanjalic and Launder, - - - - ;  $k-\epsilon$  model of Pope, - - - - ; standard  $k-\epsilon$  model.

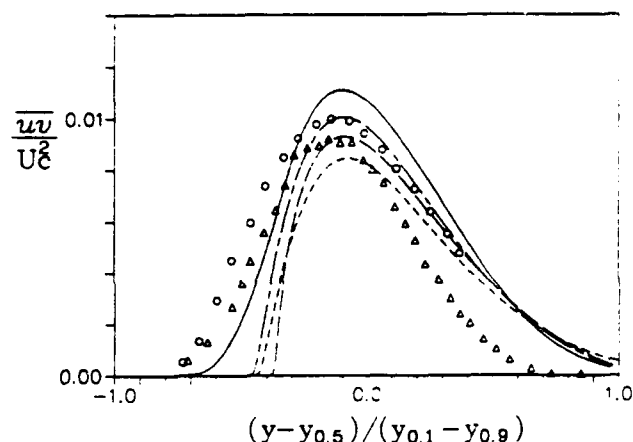


Fig.5 The Reynolds shear stress profiles in the initial similarity region of a round jet : symbols and lines the same as Fig.4.

selected from Fig.1 as discussed previously. Fig.7 reveals that the potential core length is smaller for higher initial turbulence level, but that the centerline mean velocity decay rates after the core region are nearly the same for all cases. Computed  $k$  variations along the centerline in Fig.8 agree well with experimental data only after the core region. For initially high turbulence level, experimental data of the turbulent kinetic energy decay near the exit and then increase monotonically, but the computed one decays continuously in the potential core. The discrepancy between these two observations is not yet understood.

The variations of the potential core length and the spreading rate with different initial conditions are represented in Fig.9. If the level of the initial turbulent kinetic energy is increased, the potential core length is reduced and the

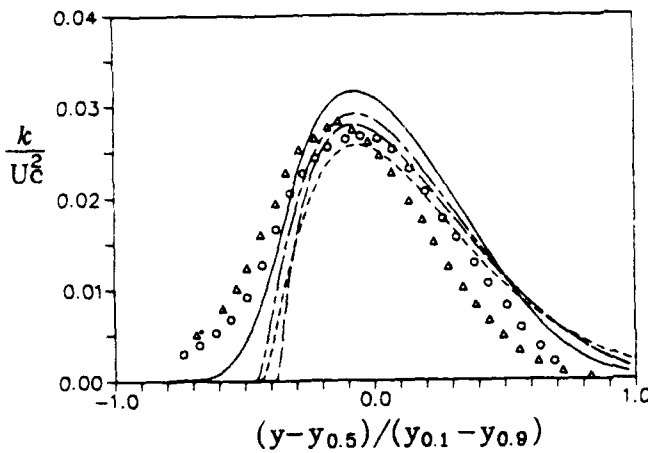


Fig. 6 The turbulent kinetic energy profiles in the initial similarity region of a round jet : symbols and lines the same as Fig. 4.

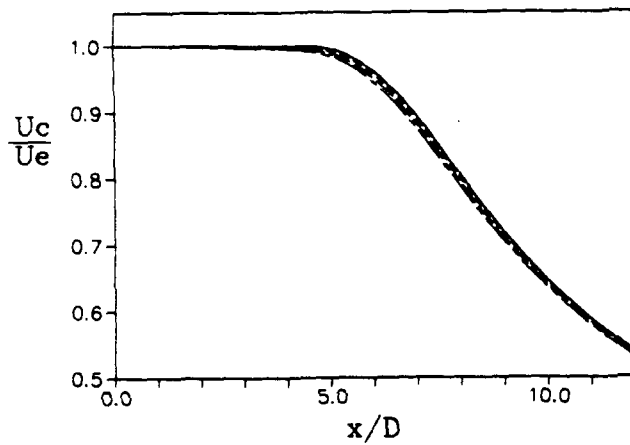


Fig. 7 The variation of the streamwise mean velocity along the centerline in a round jet with the kinetic energy of the exit core turbulence for  $R_M = 3.4 \times 10^4$  in Fig. 1 :  $\circ$  ;  $\sqrt{k_c}/U_e = 0.01$ ,  $\Delta$  ;  $\sqrt{k_c}/U_e = 0.02$ ,  $\square$  ;  $\sqrt{k_c}/U_e = 0.03$ ,  $\diamond$  ;  $\sqrt{k_c}/U_e = 0.04$ .

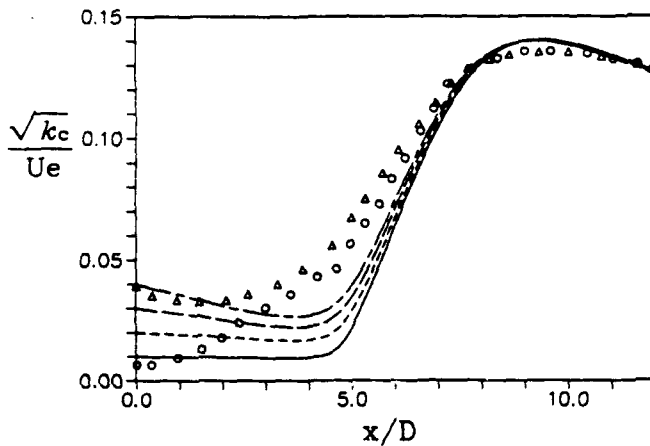


Fig. 8 The variation of the turbulent kinetic energy along the centerline in a round jet with the kinetic energy of the exit core turbulence : experimental data from Raman et al. :  $\circ$  ;  $u'/U_e = 0.5\%$ ,  $\Delta$  ;  $u'/U_e = 5.0\%$  : prediction for  $R_M = 3.4 \times 10^4$  in Fig. 1, lines the same as Fig. 7.

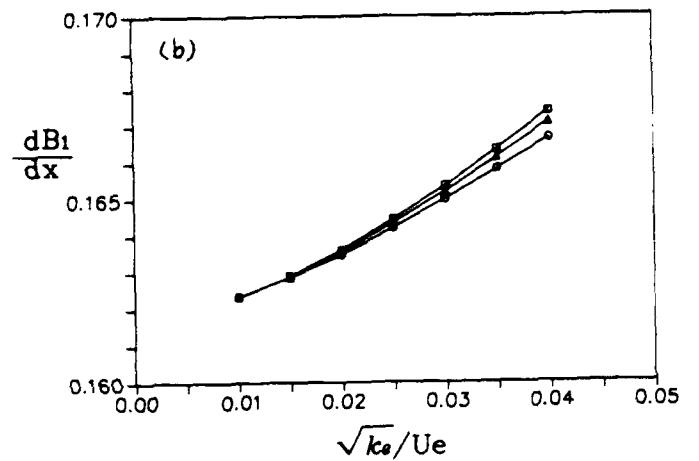
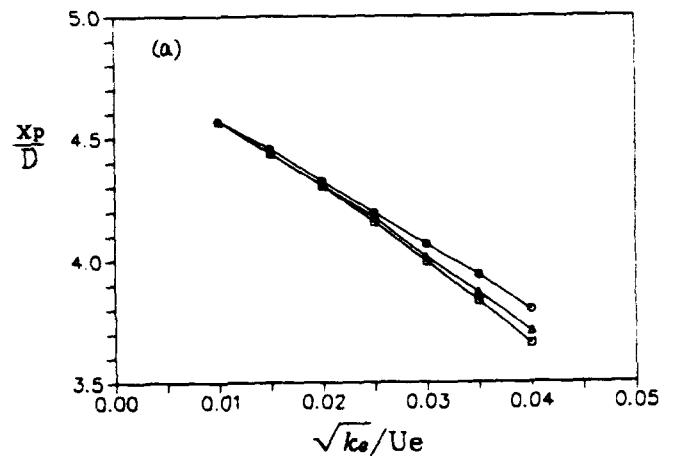


Fig. 9 The variation of the predicted potential core length and the spreading rate in a round jet with initial conditions as a function of initial turbulence level :  $\circ$  ;  $R_M = 3.4 \times 10^4$ ,  $\Delta$  ;  $R_M = 6.8 \times 10^4$ ,  $\square$  ;  $R_M = 13.5 \times 10^4$  : (a) the potential core length ; (b) the spreading rate.

spreading rate becomes large. Also, it can be seen that the effect of the initial length scale is such that increasing initial length scale shortens the potential core length and augments the spreading rate. Moreover, such effect of the initial length scale is magnified at increased initial turbulence level. Consequently, the mixing is promoted by increasing both the initial turbulent kinetic energy and the initial length scale. This is because larger core length scales penetrate further into the mixing layer. Similar conclusion can be drawn from the experiment of Hancock and Bradshaw<sup>1</sup>, who carried out an experiment of the effects of freestream turbulence on a flat plate boundary layer.

Finally, an attempt is made at devising by trial-and-error to collapse the calculated data into a single correlation. The parameter found in this way is shown in Figs. 10(a) and (b), where the number 80 is an empirically determined constant. All data nicely fall on a single curve as can be seen in figures. This parameter was found to correlate the plane jet data too (not shown in this paper).

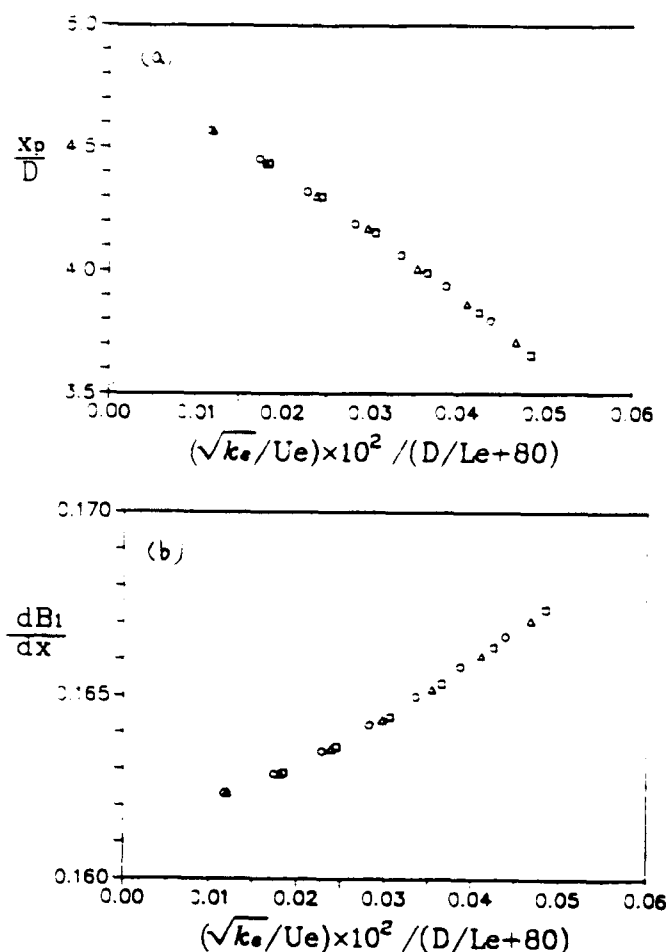


Fig.10 The variation of the predicted potential core length and the spreading rate in the initial region of a round jet with initial condition as a function of a nondimensional parameter : symbols the same as Fig.9 : (a) the potential core length ; (b) the spreading rate.

### Conclusions

The effects of initial conditions at the jet exit have been numerically investigated. As a most reliable computational model, the  $k-\epsilon-\gamma$  turbulence model has been selected by comparing the prediction accuracies of various turbulence models at  $k-\epsilon$  level. It was found that the standard form and a couple of variants of the  $k-\epsilon$  model yield too lengthy potential core and lower spreading rate, whereas the  $k-\epsilon-\gamma$  model reproduce faithfully the turbulent flow field in the jet initial region.

The calculated results show that the potential core length and the spreading rate in the initial mixing layer are dependent on the initial length scale as well as on the turbulent kinetic energy at the jet exit. Such effect of the initial length scale increases with higher initial turbulence level. An empirical parameter has been devised to collapse the calculated data of the potential core length and the spreading rate with various initial conditions onto a single correlation curve.

### References

- <sup>1</sup> Rodi, W., "A Review of Experimental Data of Uniform Density Free Turbulent Boundary Layers," *Studies in Convection*, edited by B.E. Launder, Vol. 1, 1975, pp. 79-165.
- <sup>2</sup> Hussain, A.K.M.F. and Zedan, M.F., "Effect of the Initial Condition on the Axisymmetric Free Shear Layer: Effect of the Initial Momentum Thickness," *Phys. Fluids*, Vol. 21, July 1978, pp. 1100-1112.
- <sup>3</sup> Hussain, Z.D. and Hussain, A.K.M.F., "Axisymmetric Mixing Layer : Influence of the Initial and Boundary Conditions," *AIAA Journal*, Vol. 17, June 1979, pp.48-55.
- <sup>4</sup> Gutmark, E. and Ho, C., "Preferred Modes and the Spreading rates of Jets," *Phys. Fluids*, Vol. 26, October 1983, pp. 2932-2938.
- <sup>5</sup> Raman, G., Zaman, K.B.M.Q. and Rice, E.J., "Initial Turbulence Effect on jet Evolution with and without Tonal Excitation," *Phys. Fluids A*, Vol. 1, July 1989, pp. 1240-1248.
- <sup>6</sup> Bradshaw, P., "Review - Complex Turbulent Flows," *Trans. ASME, J. Fluids Engng*, Vol. 97, June 1975, pp. 146-154.
- <sup>7</sup> Vlasov, E.V., Ginevskii, A.S. and Karavosov, R.K., "Investigation of the Wave Structure of a Jet Entry - Zone Flow at Various Level of Initial Turbulence," *Fluid Mech. Sov. Res.*, Vol. 7, 1978, pp. 65-73.
- <sup>8</sup> Hancock, P.E. and Bradshaw, P., "Turbulence Structure of a Boundary Layer beneath a Turbulent Free Stream," *J. Fluid Mech.*, Vol. 205, 1989, pp. 45-76.
- <sup>9</sup> Islam, S.M.N. and Tucker, H.J., "Flow in the Initial Region of Axisymmetric Turbulent jets," *Trans. ASME, J. Fluids Engng*, Vol. 102, March 1980, pp. 85-91.
- <sup>10</sup> Pope, S.B., "An Explanation of the Turbulent Round-Jet / Plane-Jet Anomaly," *AIAA Journal*, Vol. 16, March 1978, pp. 279-281.
- <sup>11</sup> Kline, S.J., Cantwell, B. and Lilley, G.K. (eds), "1981/82 Comparison of Computation and Experiment," *Proc. 1980-81 AFOSR-HTTM-Stanford Conference on Complex Turbulent Flows*, Stanford.
- <sup>12</sup> Cho, J.R. and Chung, M.K., "A proposal of  $k-\epsilon-\gamma$  Equation Turbulence Model," submitted for publication in the *Journal of Fluid Mechanics*, 1991.
- <sup>13</sup> Hajalic, K. and Launder, B.E., "Sensitizing the Dissipation Equation to Irrotational Strains," *Trans. ASME, J. Fluids Engng*, Vol. 102, March 1980, pp. 34-40.
- <sup>14</sup> Launder, B.E., Reece, G.J. and Rodi, W., "Progress on the Development of a Reynolds-stress Turbulence Models," NASA SP 321.
- <sup>15</sup> Comte-Bellot, G. and Corrsin, S., "The Use of a Contraction to Improve the Isotropy of Grid-generated Turbulence," *J. Fluid Mech.*, Vol. 25, 1966, pp. 657-682.
- <sup>16</sup> Anderson, D.A., Tannehill, J.C. and Pletcher, R.H., *Computational Fluid Mechanics and Heat Transfer*, McGraw-Hill, New York, 1984, p.344.
- <sup>17</sup> Launder, B.E. and Spalding, D.B., "The Numerical Computation of turbulent Flows," *Computer Methods in Applied Mechanics and Engineering* 3, 1974, pp. 269-289.
- <sup>18</sup> Rajaratnam, N., "Turbulent Jets," Elsevier Scientific Publishing Company, 1976.
- <sup>19</sup> Hussain, A.K.M.F. and Clark, A.R., "Upstream Influence on the Near Field of a Plane Turbulent jet," *Phys. Fluids*, Vol. 20, September 1977, pp. 1416-1426.
- <sup>20</sup> Hussain, A.K.M.F. and Hussain, Z.D., "Turbulence Structure in the Axisymmetric Free Mixing Layer," *AIAA Journal*, Vol. 18, December 1980, pp. 1462-1469.
- <sup>21</sup> Bradshaw, P., Ferriss, D.H. and Johnson, R.F., "Turbulence in the Noise-producing Region of a Circular Jet," *J. Fluid Mech.*, Vol. 19, 1964, pp. 591-624.

# THE INFLUENCE OF BULGES ON BOUNDARY-LAYER INSTABILITY

By

S. Elli and C. P. van Dam

Dept. of Mechanical, Aeronautical and Materials Engr.  
University of California, Davis, CA

## Abstract

Local disturbances caused by a spanwise surface corrugation affect the position of the boundary-layer transition, and so the drag, of an object. This premature transition from laminar to turbulent flow is often associated with a separation of the laminar boundary-layer from its surface (Fage, 1943). Also the roughness-induced separation bubble provides an important link between the pressure and velocity fluctuations in the environment and the development of the disturbance in the laminar boundary-layer, i.e., the receptivity problem (Morkovin, 1990; Bodonyi et al., 1989).

To investigate the influence of a laminar separation bubble on boundary-layer instability, a separated flow generated by a velocity gradient over a flat plate was analyzed by direct numerical simulation using finite-difference solutions of the Navier-Stokes equations. The bubble acts as a strong amplifier of the instability waves and a highly nonlinear flow field is shown to develop downstream of the bubble (fig. 1). Consequently, the results of the direct numerical simulation differ noticeably from those of the classical linear stability theory proving the fact that the nonparallel effects together with the nonlinear interactions are crucial to this flow development (Fig. 2).

In the present paper, the effect of physical perturbations such as humps and hollows on boundary-layer instability is analyzed. This problem has been considered theoretically by several researchers (e.g., Nayfeh et al., 1987 and 1990; Cebeci et al., 1988). They used linear stability theory in their approach which does not include the nonparallel nor the nonlinear effects. Therefore, to account for these important effects in studying flow over humps and hollows the direct simulation technique is being implemented in generalized coordinates.

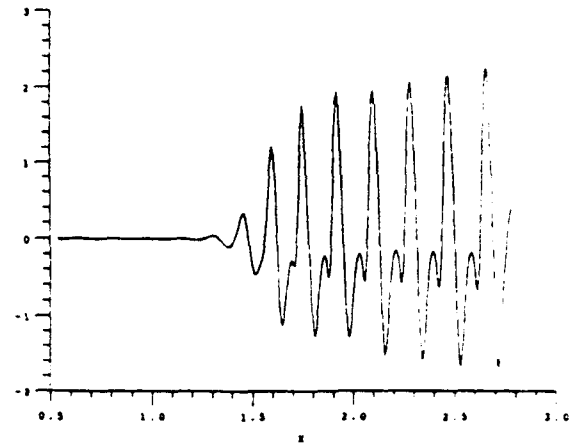


Figure 1. Normal velocity perturbation  $v'$  at  $y = 3\Delta y$ ;  $Re = 10^5$

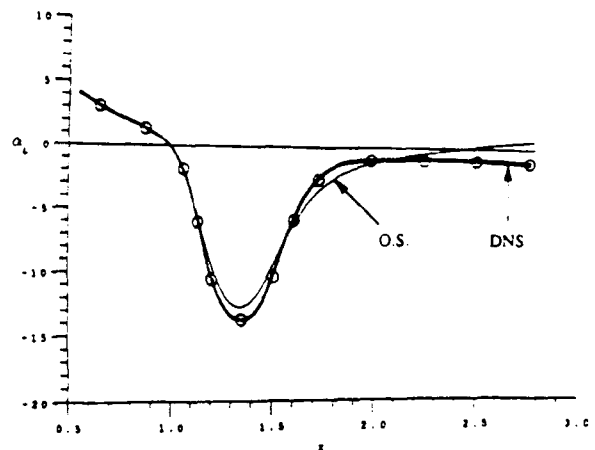


Figure 2. Spatial amplification rate  $\alpha_i$  for separated flow problem obtained from direct numerical simulation;  $F = 1.4 \times 10^4$

# STABILITY INVESTIGATIONS OF AIRFOIL FLOW BY GLOBAL ANALYSIS

Marek Morzyński

Hermann Föttinger-Institut  
Technische Universität, Berlin

Frank Thiele

Abteilung Turbulenzforschung  
DLR, Berlin

## Abstract

As the result of global, non-parallel flow stability analysis the single value of the disturbance growth-rate and respective frequency is obtained. This complex value characterizes the stability of the whole flow configuration and is not referred to any particular flow pattern. The global analysis assures that all the flow elements (wake, boundary and shear layer) are taken into account. The physical phenomena connected with the wake instability are properly reproduced by the global analysis. This enhances the investigations of instability of any 2-D flows, including ones in which the boundary layer instability effects are known to be of dominating importance. Assuming fully 2-D disturbance form, the global linear stability problem is formulated. The system of partial differential equations is solved for the eigenvalues and eigenvectors. The equations, written in the pure stream function formulation, are discretized via FDM using a curvilinear coordinate system. The complex eigenvalues and corresponding eigenvectors are evaluated by an iterative method. The investigations performed for various Reynolds numbers emphasize that the wake instability develops into the Karman vortex street. This phenomenon is shown to be connected with the first mode obtained from the non-parallel flow stability analysis. The higher modes are reflecting different physical phenomena as for example Tollmien-Schlichting waves, originating in the boundary layer and having the tendency to emerge as instabilities for the growing Reynolds number. The investigations are carried out for a circular cylinder, oblong ellipsis and airfoil. It is shown that the onset of the wake instability, the waves in the boundary layer, the shear layer instability are different solutions of the same eigenvalue problem, formulated using the non-parallel theory. The analysis offers large potential possibilities as the generalization of methods used till now for the stability analysis.

## Introduction

The boundary layer stability analysis based on the solution of the Orr-Sommerfeld equation is a useful tool for practical analysis of the laminar-turbulent transition. The only competing method is based on purely empirical formulas, characterized most often by the shape parameter.

It is widely accepted that infinitely small disturbances, although amplified according to linear stability theory are not able to onset the laminar-turbulent transition unless the amplification reaches some value so a factor has to be introduced to correct the results of the analysis. The  $e^N$  method has been developed to match the results of the empirical and theoretical investigations.

The laminar-turbulent transition is usually preceded by the Tollmien-Schlichting waves. Several receptivity experiments (Morkovin [4]) were provided to understand the phe-

nomena of the Tollmien-Schlichting waves generation. It is commonly accepted that Tollmien-Schlichting waves are generated by an external source of disturbance (as for example acoustic excitation) and that the non-parallel or non-uniform effects enhance the feedback between the wave and the excitation. These non-parallel and non-uniform effects are the viscous boundary layer growth, the change of the surface curvature and variation of the surface static pressure. The growth of the boundary layer is evident near the leading edge of the blunt body, change of the surface curvature causes the non-parallelity of the flow, surface static pressure changes significantly in the separation region. It is characteristic that these three problems were studied separately. Goldstein [1] solved analytically the problem of evolution of Tollmien-Schlichting waves near the leading edge. The influence of sudden change of the geometry was investigated by Goldstein [2] and Ruban [3].

These investigations have one common feature - the assumption of slow variation of the flow in the streamwise direction as necessary condition for weakly non-parallel analysis.

Elliptic nature of the Navier-Stokes equation describing the flow suggest that the phenomena in all these regions are not independent and influence each other. The question arises if interactions of the leading edge geometry, boundary layer and wake can be described by a single theory. The natural choice is to drop the parallel flow assumption and to treat the flow in all these regions as a whole. The consequence is the attempt to use the non-parallel flow, global stability analysis. The non-parallel theory was successfully used to study the wake instability [10, 9, 8, 7, 12]. There are no theoretical limitations to apply this analysis also to various geometries, as for example the airfoil. Because the assumptions of the non-parallel theory is a generalization of the classical parallel flow analysis, one can expect that this method is adequate not only for determination of the wake instability. The instability of the boundary and shear layer must be reflected in the eigenvalue solutions of the problem.

## Governing equations

Linear stability theory is concerned with the development in time and space of infinitesimal perturbations around a given basic flow. If this basic flow is assumed to be parallel, the classical theory of parallel shear flow stability can be applied. This method has been also successfully used for nearly parallel flows for which the multiple-scale method, adopting the concept of "slow" variation of flow parameters in one direction, is valid. In general, non-parallel case only the two-dimensional theory taking into account the non-parallel effects is adequate. The equations of this theory are briefly presented here.

The problem was solved in the pure (Lagrangian) stream function finite difference formulation. This formulation, not



very common in the Navier-Stokes equations solvers, offers certain advantages for the eigenvalue analysis. The primitive variables formulation ([9]) results in much larger matrices. Although the eigenvalues are equal for velocities and pressure one has to deal with the full system. This difference in size is even more evident because the matrix entries are complex for the eigenvalue analysis.

The unsteady incompressible Navier-Stokes equations written in the stream function formulation take the form:

$$\left[ \frac{\partial}{\partial t} + (\nabla \times \vec{\psi}) \cdot \nabla - \frac{1}{Re} \Delta \right] \Delta \vec{\psi} = 0 \quad (1)$$

$$\vec{\psi} = \psi \vec{e}_3 \quad (2)$$

We assume that the stream function  $\vec{\psi}(x, y, t)$  is a sum of a steady part  $\bar{\psi}(x, y)$  and the unsteady disturbance  $\tilde{\psi}'(x, y, t)$ :

$$\vec{\psi}(x, y, t) = \bar{\psi}(x, y) + \tilde{\psi}'(x, y, t) \quad (3)$$

The disturbance value is assumed to be small compared to the stream function value. Introducing equation (3) into (1) we obtain the nonlinear equation:

$$\left[ \frac{\partial}{\partial t} + (\nabla \times \bar{\psi}) \cdot \nabla - \frac{1}{Re} \Delta \right] \Delta \tilde{\psi}' + (\nabla \times \tilde{\psi}') \cdot \nabla (\Delta \bar{\psi} + \Delta \tilde{\psi}') = 0 \quad (4)$$

Assuming a small disturbance allows the linearization of the equation (4) i.e. we ignore the terms containing  $(\tilde{\psi}')^2$ . In the disturbance equation we separate the time and space dependence:

$$\tilde{\psi}'(x, y, t) = \tilde{\varphi}(x, y) e^{-\lambda t} \quad (5)$$

where

$$\lambda = \pi(St + i\sigma) \quad (6)$$

Introducing the above relationship into (4) results in the linear partial differential equation:

$$i\lambda \Delta \tilde{\varphi} - (\nabla \times \bar{\psi}) \cdot \nabla \Delta \tilde{\varphi} - (\nabla \times \tilde{\varphi}) \cdot \nabla \Delta \bar{\psi} + \frac{1}{Re} \Delta^2 \tilde{\varphi} = 0 \quad (7)$$

The fundamental difference between this equation and the Orr-Sommerfeld one, which is derived in similar manner assuming the disturbance form as:

$$\tilde{\psi}'(x, y, t) = \tilde{\varphi}(y) e^{i(\alpha x - \beta t)} \quad (8)$$

is that, while Orr-Sommerfeld equation is an ordinary differential equation, equation (5) is a partial differential equation. This means different methods of solution and numerical problems encountered for the two cases.

To solve the problem for an arbitrary flow geometry the curvilinear body fitted coordinate system should be used for the solution of the equation (1) and (7). For orthogonal metric the following relations are valid:

$$g_{ij} = 0, \quad g^{ij} = 0, \quad i \neq j \quad (9)$$

hence equations (1) and (7) can be written as:

$$g'' \left[ \frac{\partial}{\partial t} \psi|_{ii} + \epsilon^{mn3} \psi|_n \psi|_{m} - \frac{1}{Re} g^{jj} \psi|_{ijj} \right] = 0 \quad (10)$$

$$g'' \left[ i\lambda \psi|_{ii} - \epsilon^{mn3} (\psi|_n \varphi|_{m} + \varphi|_n \psi|_{m} + \frac{1}{Re} g^{jj} \psi|_{ijj}) \right] = 0 \quad (11)$$

The symbol  $|$  denotes the covariant derivative of the function. For further specialized metric tensor coefficients

$$\begin{aligned} g_{11} &= \alpha^2(\xi) g(\xi, \eta) \\ g_{22} &= \beta^2(\eta) g(\xi, \eta) \end{aligned} \quad (12)$$

only  $g(\xi, \eta)$  and its first order derivatives  $g_{,\xi}$  and  $g_{,\eta}$  have to be calculated for any transformation.

Reynolds number  $Re$  and Strouhal number  $St$  are expressed as:

$$Re := \frac{dU_\infty}{\nu}, \quad St := \frac{df}{U_\infty} \quad (13)$$

Discretized, equation (11) can be written as:

$$(A - \lambda B)\varphi = 0 \quad (14)$$

and represents the generalized eigenvalue problem.

For the eigenvalue calculations complex numbers can be split into real and imaginary parts so that only the real arithmetic has to be applied. Then the two parts of equation (2.10) may be written:

$$\begin{aligned} A\varphi_r - \lambda_r B\varphi_r + \lambda_i B\varphi_i &= 0 \\ A\varphi_i - \lambda_i B\varphi_r + \lambda_r B\varphi_i &= 0 \end{aligned} \quad (15)$$

### Solution

#### Numerical discretization and meshes

The discretization of the Navier-Stokes equations (11) and disturbance equation (12) is accomplished using the finite difference method. In both cases the thirteen-point stencil was used. The accuracy of the derivatives for such a stencil is maximum  $O(h^2)$  for the fourth order terms. The unsteady version contains implicit stepping in time.

For all the calculations the orthogonal O-type mesh obtained by the conformal mapping is applied. The Karman-Trefftz transformation was used for the airfoil calculations. The metric coefficients (13) are expressed analytically by means of symbolic manipulation program to assure the maximum accuracy.

#### Boundary Conditions

For the steady Navier-Stokes equation solution the following boundary conditions are used:

$$\psi = 0, \quad \psi_{,n} = 0 \quad \text{on the body} \quad (16)$$

$$\frac{D\omega}{Dt} = 0, \quad \psi_{,n} = \psi_{pot,n} \quad \text{in the farfield} \quad (17)$$

The collocation of the vorticity transport equation is made only for the outflow. For the inflow the Dirichlet boundary condition with the value of the potential flow solution is taken. The boundary conditions for the disturbance equation (12) are:

$$\varphi = 0, \quad \varphi_{,n} = 0 \quad \text{on the body} \quad (18)$$

$$\frac{D\omega}{Dt} = 0, \quad \frac{D\varphi}{Dt} = 0 \quad \text{in the farfield} \quad (19)$$

The Dirichlet boundary condition (zero disturbance) is introduced for the inflow. The introduction of the convective boundary conditions appears to be an important factor of improving the numerical accuracy, especially for the steady and unsteady flow calculations.

#### Solution of the eigenvalue problem

In any eigenvalue problem the question arises whether all the eigenvalues are sought or whether determination of only one or few is satisfactory. Solving similar problem Zebib and Kim et al. [10,11] applied the QZ type decomposition from the standard libraries. The advantage of finding all of the eigenvalues is that no guess values have to be made. For relatively small matrix size, resulting from the use of the spectral method or crude FDM meshes this procedure is acceptable and was used in our earlier investigations [7]. Jackson applied for the unsymmetrical, complex generalized eigenvalue problem, appearing in the non-parallel flow stability theory the inverse iteration method [9]. This concept is also adopted in our present investigations. The eigenvalue, closest to the guess value and the related eigenvector are both determined at the same time. Till now it is the only realistic method for very large equation systems.

The following equations explain the principle steps of this method. Applying the Newton-Raphson method to equation (14) we obtain

$$(A - \lambda^{(n)}B)(\varphi^{(n)} + d\varphi^{(n)}) - d\lambda^{(n)}B\varphi^{(n)} = 0 \quad (20)$$

which can be written as:

$$(A - \lambda^{(n)}B)\eta^{(n+1)} = B\varphi^{(n)} \quad (21)$$

where the normalization is performed as follows:

$$\varphi^{(n+1)} = \varphi^{(n)} + d\varphi^{(n)} \quad (22)$$

and

$$(e^r)_i = \delta_{ir} \quad (23)$$

denotes a unit vector. The correction of  $d\lambda^{(n)}$  is calculated from:

$$d\lambda^{(n+1)} = \frac{1}{(e^r)^T \eta^{(n+1)}} \quad (24)$$

The iteration process involves the repeated solution of the equation (21), normalization of the eigenvector and correction of the eigenvalue. This process continues until convergence of the eigenvector and eigenvalue is achieved. The procedure, which consists of LU decomposition at each step with a quadratic rate of convergence, was replaced by a method using only one LU decomposition. The convergence is then only linear but the back-substitution time is significantly reduced compared to the decomposition time, justifying many iteration steps:

$$(A - \lambda_0 B)^{-1} B\varphi^{(n)} = \eta^{(n+1)} \quad (25)$$

The scheme is found to be convergent to the eigenvalue closest to  $\lambda_0$  and to produce the appropriate eigenvector.

#### Numerical results

The linear stability analysis consist of two steps. First the steady solution of the Navier-Stokes equations has to be found. In practice both, the steady and unsteady solution of

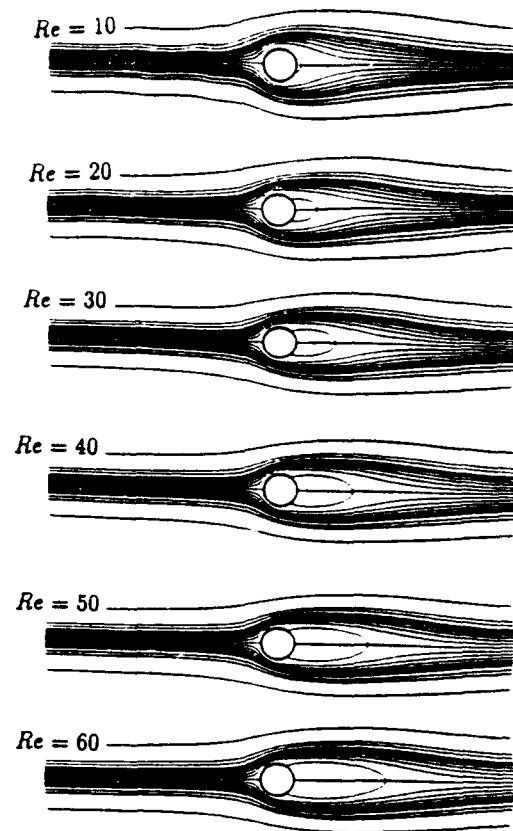


Figure 1: Steady flow solutions for the circular cylinder flow

the Navier-Stokes equations was performed. The unsteady one served as the reference data for the comparison to the results of eigenvalue analysis. It is characteristic that obtaining of the unsteady solution near the critical Reynolds number is difficult. For symmetrical flow some external forcing has to be introduced. The response of the flow field is dependent on the way the disturbance is introduced. The nearly neutral stability of the flow caused that the influence of the disturbance dominates the flow even after a long time. In this case the purely numerical aspects of the computation are of much greater significance. Also unsymmetrical flows near the critical Reynolds number requires a lot of CPU time to become fully unstable. The flow patterns of initial periods are different from the "fully developed" unsteady ones (Fig.12). Near the critical Reynolds number such patterns can persist over a long time requiring significant amount of CPU time to obtain the real periodic state. Some codes fail to carry out the calculations long enough in time and due to unphysical boundary conditions the solution breaks down when the vorticity reaches the outflow boundary. The unsteady simulation for the Reynolds number higher than the critical one is easier. For this reason always the higher Reynolds number unsteady solutions were taken for the comparison with the stability analysis.

In the linear stability theory the Navier-Stokes equations are linearized about a steady flow. The quality of the steady solution has then the direct influence on the eigenvalue analysis. The accuracy of the solution is the best for the circular cylinder flow and is decreasing for the ellipsis

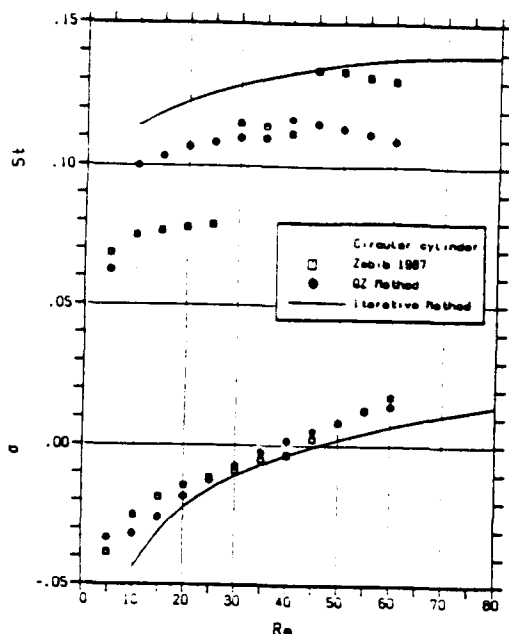


Figure 2: The growth-rate and the Strouhal number for the circular cylinder flow.

and airfoil flow where leading and trailing edge can cause numerical problems even for meshes generated by the conformal mapping. In case of limited computer resources it is satisfactory for the numerical simulation of the flow to use relatively crude mesh spacing on central, upper and lower parts of the airfoil. In this case the gradients of the quantities along the boundary layer are not very large. For the eigenvalue analysis however, also the fine discretization in this direction is very important. The attempt to detect the Tollmien-Schlichting waves necessities at least several tenth of points for one period preserving also the fine discretization in the radial direction. The compromise for these two contradictory requirements was partly obtained by calculation of the steady solution on one mesh and interpolation of the result on another mesh, more suitable for the stability calculations.

The eigenvalue solution was calculated for the external flow around the circular cylinder, ellipsis and an airfoil. The circular cylinder served as the source of reference data, for the validation of the program because a lot of numerical and experimental results is available. The only existing results for non-parallel analysis are the circular cylinder results [10, 9]. The flow around the ellipsis was investigated to analyze different eigenmodes. The modes characterized by higher frequency are clearly appearing for high Reynolds numbers. Because of the extremely long wake for  $Re > 200$ , causing several numerical difficulties such an analysis could not be carried out for the circular cylinder. Finally the NACA 4412 airfoil flow for  $\alpha = 0^\circ$  and  $\alpha = 15^\circ$  was shown to examine the potential possibilities connected with the eigenvalue analysis of this geometry.

#### Circular cylinder results

For the symmetrical flow around cylinders it is always,

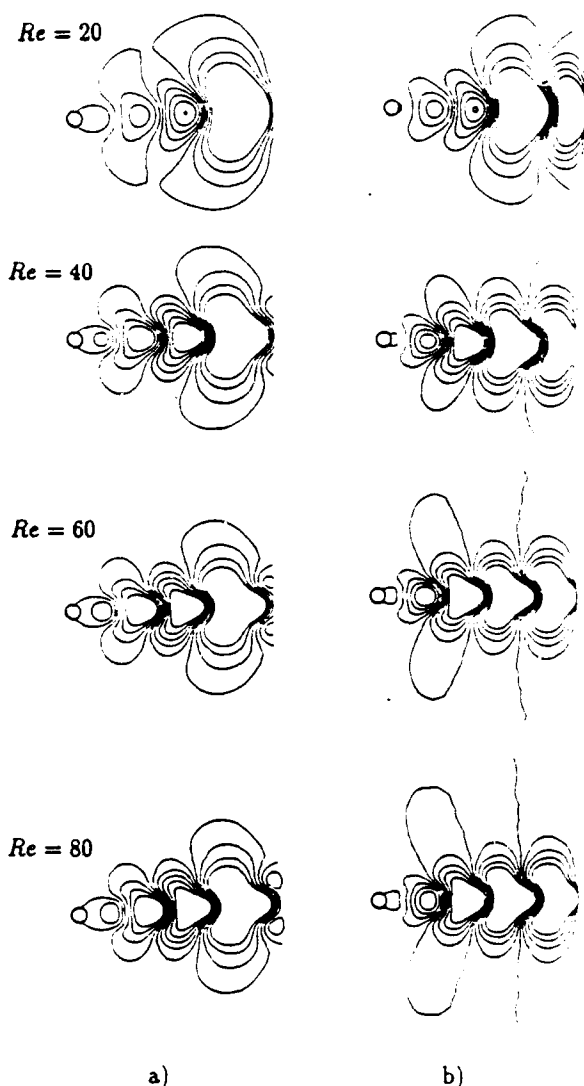


Figure 3: Real (a) and imaginary (b) part of the eigenvector.

theoretically, possible to obtain a steady-state solution, even above the critical Reynolds number. The streamlines patterns obtained for the steady flow around a circular cylinder are shown in Fig.1. These results served as the input data for the eigenvalue analysis. The guess value for the Strouhal number is 0.12 and the growth-rate 0. The result of the calculation consist of the complex eigenvalue for each Reynolds number together with a complex eigenvector. The growth-rate and the corresponding frequency as the function of the Reynolds number is shown in Fig.2. Some results of our previous investigations using the QZ method are also plotted. The results of these calculations are compared with those obtained by Zebib [10], which uses the non-parallel analysis in the spectral stream function formulation together with a full-matrix eigenvalue solver of a QZ-type. For the inverse iteration method, used in our computations, the critical values are  $Re_c = 46.23$  and  $St_c = 0.1345$ .

The real and imaginary part of an eigenvector for the increasing Reynolds number is depicted in Fig.3. Over a wide

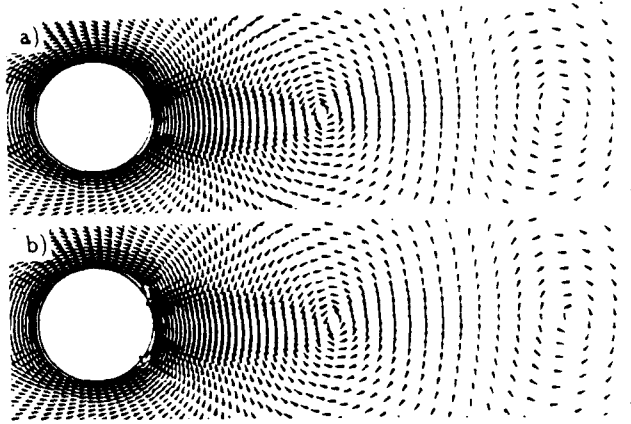


Figure 4: Eigenvector velocities (imaginary part): (a) below  $Re_c$  ( $Re = 40$ ) (b) above  $Re_c$  ( $Re = 50$ ).

range of Reynolds numbers the eigenvector (disturbance) patterns are very similar, showing the physical aspects of the phenomena to be already present in flows of fairly small Reynolds number. The increase in Reynolds number allows these modes to cross the zero-growth-rate line and emerge as instabilities. The problem arises if there is any difference in eigenvector patterns below and above the critical Reynolds number. It is known from the parallel flow stability analysis that the wake stability is governed by its characteristics in the vicinity of the rear stagnation point. Careful study of the eigenvector values near the cylinder shows (Fig.4) the difference in the disturbance patterns above the  $Re_c$ . This enhances the onset of the Karman vortex street.

To evaluate how realistic are the obtained eigenvalue solutions the disturbance is summed with the steady-state solution for  $Re = 90$ . As the reference the unsteady flow simulation for  $Re=100$  is taken (Fig.5). The same periodic patterns are present in both pictures. This proves that for the cylinder flow instability the non-linear effects are not significant.

#### Ellipsis flow

Following the approach for the circular cylinder flow the elliptic cylinder was analyzed. It is known from experiments and non-parallel flow stability analysis of Jackson, performed for the bodies with different cross-sections that the proper scaling of Strouhal number is based on the dimension perpendicular to the main flow direction. For such a scaling its value is not much different for various shape of the cylinder. The critical Reynolds number reflects also the overall shape of the body. The relation between the axis ratio of the ellipsis and the critical Reynolds number was studied earlier [8]. For the oblong ellipsis situated parallel to the flow direction the critical Reynolds number is increasing while the slope of the growth-rate curve becomes smaller, comparing to the circular cylinder results. As can be expected the Karman vortex street mode results differ only slightly from ones obtained for the circular cylinder. The eigenvector patterns, growth-rate and frequency relations for increasing Reynolds numbers are similar to the circular cylinder ones. The interesting results are obtained also for the Reynolds number higher than the critical one. We assume that the steady flow solution coincides with the real one in the boundary layer and

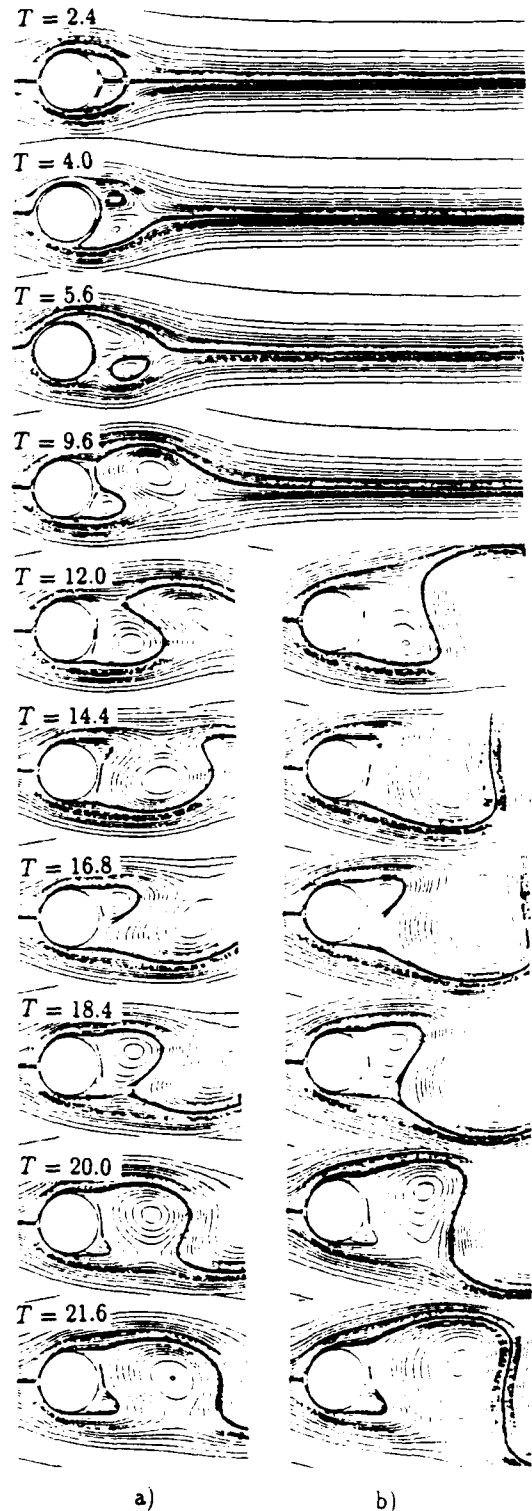


Figure 5: Karman vortex street (a) superposition of the disturbance and steady solution,  $Re = 90$  (b) unsteady simulation,  $Re = 100$

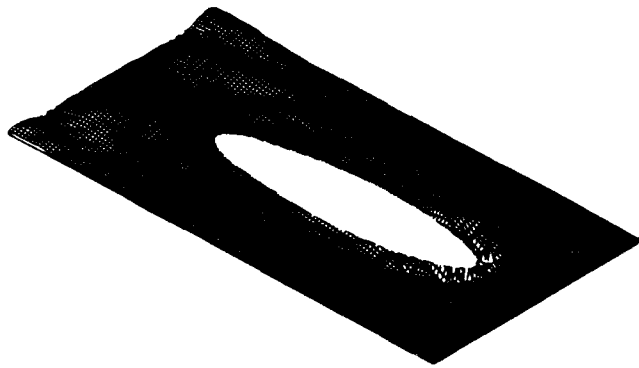


Figure 6: Higher mode eigenvector (real part) for the 1:5 ellipsis flow,  $Re = 200$

the shear layer near the body, even for the Reynolds number higher than the critical one. The justification for such an assumption are the experimental investigations of Kourta et al. [13] and Unai and Rockwell [14] in the higher Reynolds number range the Karman vortices are formed not directly behind the cylinder. Between the cylinder and the vortex street a dead fluid zone is found, bounded by two nearly parallel shear layers. As the Reynolds number increases the length of the dead-fluid zone decreases and the location of the first instability waves in the shear layer moves upstream. According to the results of the parallel flow stability analysis the unsteady behavior of the fluid is governed by the flow in direct neighborhood of the body. This conclusion allows us to cut the steady solution and limit the computational domain. The fact that the length of the wake, obtained as the steady-state solution of the Navier-Stokes equations exceeds the assumed "infinity" distance (the wake end is outside the computational domain) is in context of the eigenvalue analysis not relevant.

This steady flow solution is used as the base for the eigenvalue analysis. The assumed guess frequency is higher than for the Karman vortex mode. The result of the higher mode analysis is depicted in Fig. 7 and 8. The growth-rate is a function of both Reynolds number and mode, so that different modes are preferentially amplified as the Reynolds number increases. In Fig. 7 the growth-rate and the Strouhal number for higher mode is depicted together with the first one for the ellipsis having the axis ratio 1:5. The temporal evolution of the waves is shown in Fig. 8. The amplitude of the wave is raising in the direction of the separation. The waves on the upper and lower surface of the ellipsis are shifted in phase as the result of superposition of the symmetric pattern of disturbances and antisymmetric stream function. The characteristic patterns for all higher modes investigated are the family of branches of disturbance streamlines having sequentially positive and negative values. Each branch is ended with a cell located in the vicinity of the maximum velocity gradients in the boundary or shear layer. The eigenvector patterns should be analyzed in connection with the steady flow solution. The disturbance is added to it to obtain the unsteady flow. In the steady solution two regions can be distinguished - "soft" part where the stream function

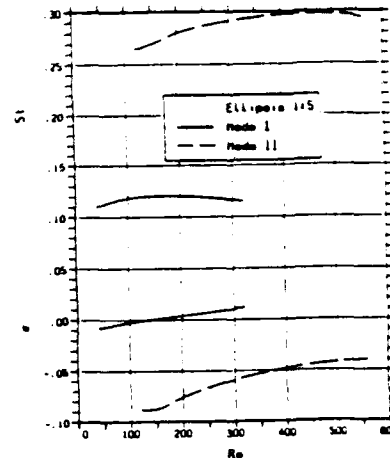


Figure 7: The growth-rate and the Strouhal number for the 1:5 ellipsis flow

values are small, containing the boundary layer, separation and wake region and the "stiff" part where the stream function values are large in comparison to the disturbance. It is obvious that when adding the disturbance and steady state solution only the "soft" part is "modulated" while the "stiff" one is practically not influenced (Fig. 8). For this reason the considerations concerning the eigenvector patterns outside the "soft" region have very limited practical meaning. This conclusion is confirmed by numerical calculations, showing that the "soft" regions of the eigenvector are related to the growth-rate and frequency value. The rest of the field is more likely influenced by numerical aspects of the computations.

For the Blasius profile instability the Tollmien-Schlichting wave length is approximately six times larger than the boundary layer thickness. Since the boundary layer on the ellipsis is relatively thick for the range of the Reynolds numbers applied in the calculations the detected Tollmien-Schlichting waves are also long. The shorter ones, for higher Reynolds numbers require much finer meshes, especially in the circumferential direction. The eigenvector cells, located on the ellipsis surface near the leading edge are shorter (in the circumferential direction) than the ones in the separation region. For a given constant frequency which is the same for the whole field it can mean only that the wave propagates slower near the leading edge and faster in the separation region. The propagation along the shear layer of the wake has approximately constant velocity. All the found eigenvalues for the Tollmien-Schlichting mode were damped ones. The question arises if the Tollmien-Schlichting wave, considered globally, in the boundary layer and propagating further along shear layer can become amplified without external excitation. The growth-rate is raising with the increasing Reynolds number and one can expect that the higher mode wave will become only slightly damped or even amplified for the high enough Reynolds number.

For any flow around the cylinder exist many eigenmodes. In practice near any given frequency exist an eigenvalue, mostly with such a low growth-rate that it is unlikely that

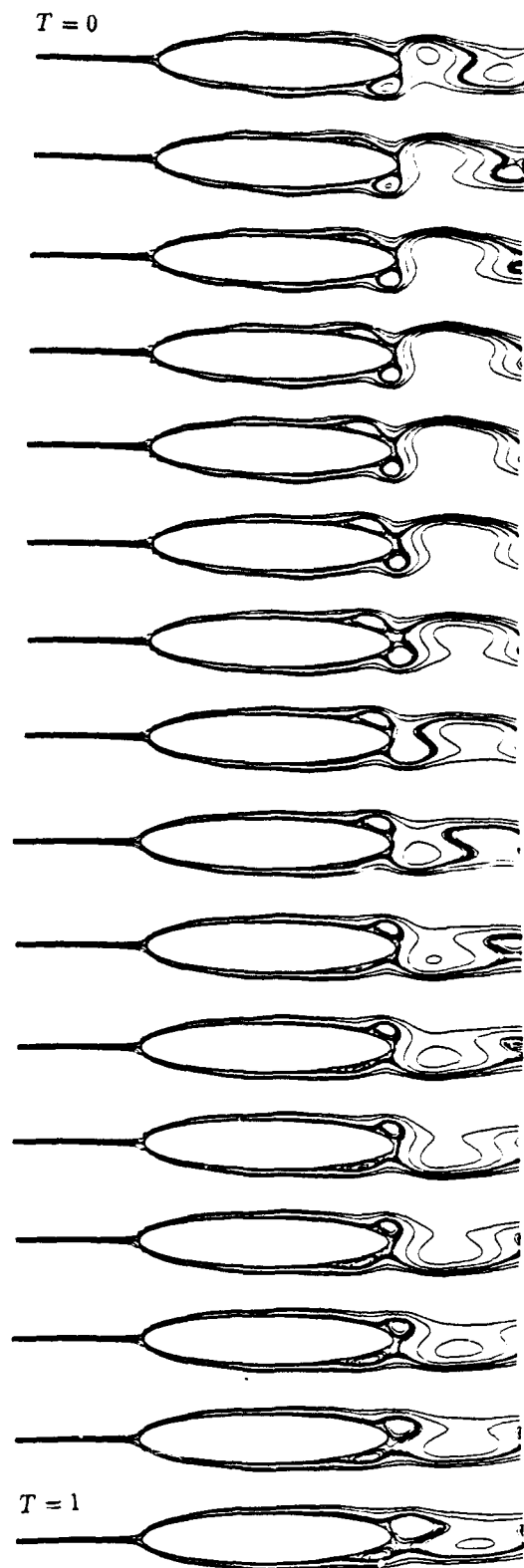


Figure 8: Tollmien-Schlichting waves - temporal evolution for the 1:5 ellipsoid flow,  $Re = 200$

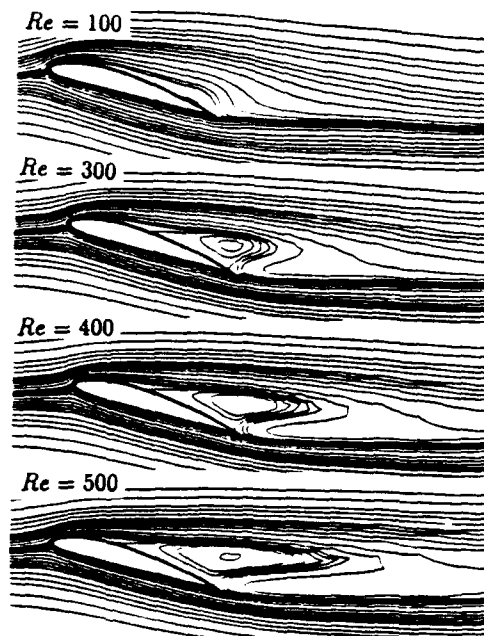


Figure 9: Steady flow solutions - NACA 4412,  $\alpha = 15^\circ$

it can emerge as the instability. Similar conclusions can be drawn on base of the Kim [11] results.

Different eigenvectors can be classified into at least two groups. One characteristic eigenvector pattern is connected with the onset of the Karman vortex street. Fig.3 shows this mode for the circular cylinder. Jackson [9] has shown the same patterns. Similar mode was detected by Karniadakis et al. [5] who investigated the flow around the circular cylinder placed in the channel bounded with two parallel plates. This mode is called there the central mode and dominates for the cylinder placed near the symmetry axis. Moving the cylinder toward the wall causes switching to the "wall mode" which is related to the Tollmien-Schlichting waves. For the external flow around the cylinder the "wall" mode forms similar cells located however on the body and in the shear layer.

#### The airfoil flow

The another cylinder flow which was considered is the airfoil flow. As the example geometry the NACA4412 airfoil is taken. Two different angles of attack were considered. For  $\alpha = 15^\circ$  the stall is evident and the regular Karman vortex street appears for high enough Reynolds number. The numerical simulation of such a flow was performed by Shütz [6]. For  $\alpha = 0^\circ$  dominating phenomena take place in the boundary and shear layer.

First the steady flow solution has been found (Fig.9). The character of the steady flow solution for  $\alpha = 15^\circ$  is different from the circular cylinder one. (Fig.1, Fig.9). While for the circular cylinder the wake consist of two bubbles, there is only one for the airfoil flow.

The eigenvalue analysis gave the fastest growing mode (Fig.10).

For  $\alpha = 15^\circ$  the flow becomes unstable at  $Re = 335$ . The eigenvector patterns are in this case also very similar to ones for the circular cylinder (Fig.11). In Fig.13 the comparison

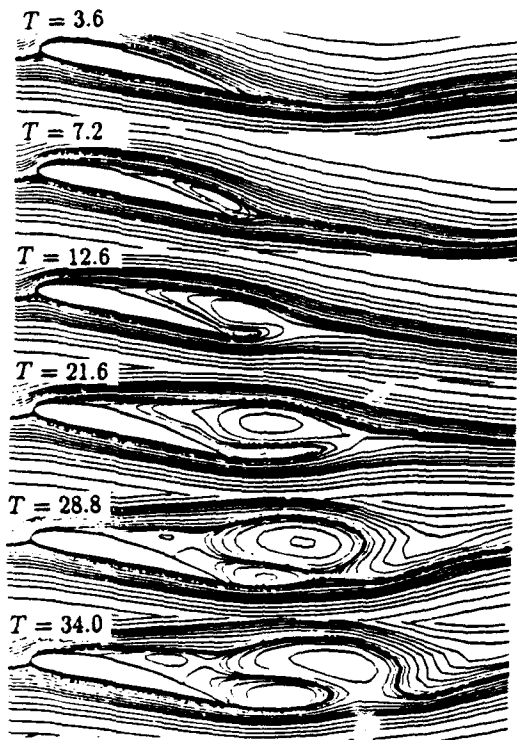


Figure 12: Early time steps, NACA 4412 flow,  $Re = 1000$ , unsteady simulation

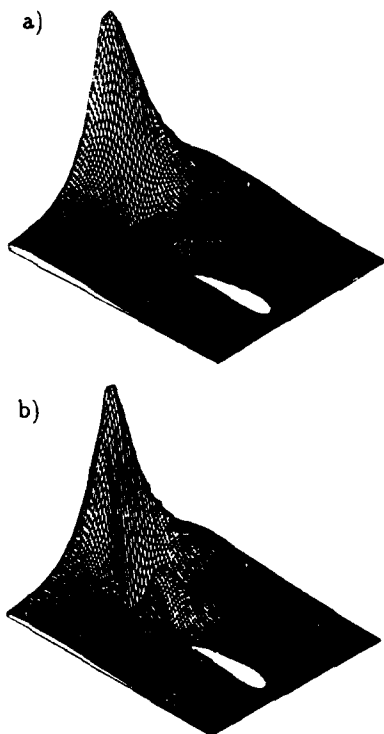


Figure 13: Real part of the eigenvector - airfoil flow,  $\alpha = 15^\circ$   
a)  $Re = 100$ , b)  $Re = 600$

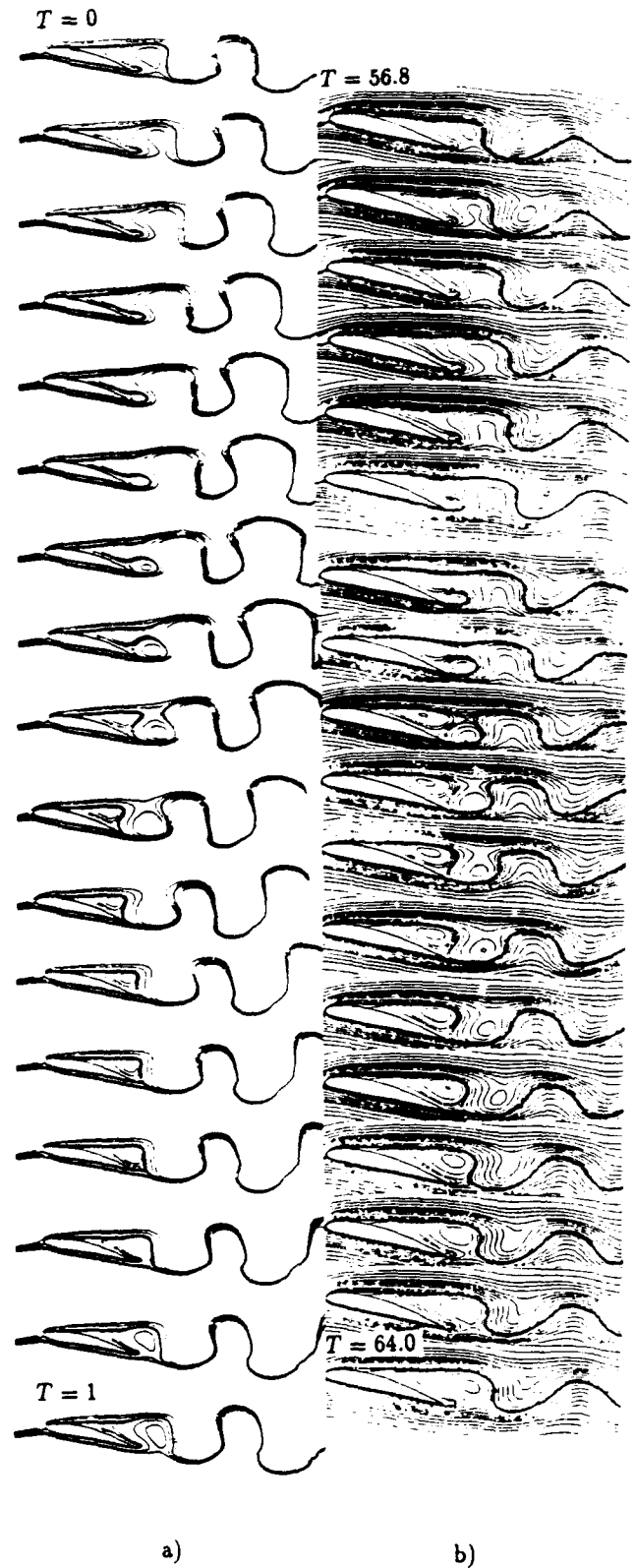


Figure 14: NACA 4412 airfoil flow: (a) superposition of the steady solution and disturbance fields,  $Re = 600$ , (b) unsteady simulation,  $Re = 1000$

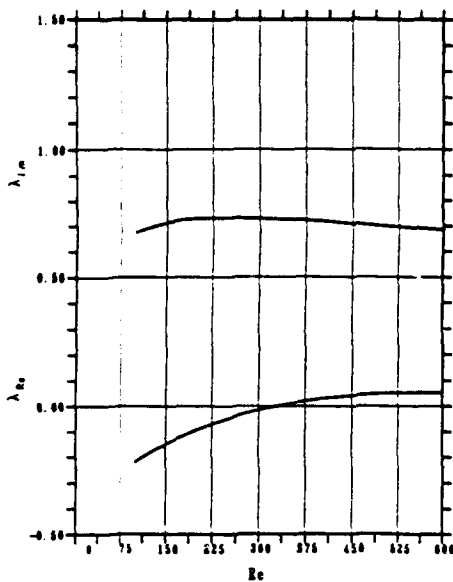


Figure 10: The growth-rate and the Strouhal number for the airfoil flow

between the real part of the eigenvector for  $Re = 100$  and  $Re = 500$  is shown. The value of the disturbance is growing with the flow direction for both cases. It is normalized, so the disturbance reaches the same maximum, located in the vicinity of the outflow boundary. Because for  $Re = 100$  (Fig.13) the growth-rate is negative the disturbance will be damped after a long enough time. The flow for  $Re = 500$  is unstable. The disturbance is growing both in time and in the flow direction. The characteristic feature for the higher Reynolds numbers flows is the much larger amplitudes of the disturbance in the wake close to the airfoil.

To compare the obtained eigenvalue analysis results with the real flow patterns the unsteady simulation was used. The simulation was performed for  $Re = 1000$ . The early stages of unsteady simulation exhibit patterns significantly different from the "fully developed" ones (Fig.12). This discrepancy is even greater in the neighborhood of the critical value. For this reason to compare with the eigenvalue analysis one period was taken after long enough time ( $t = 56.8$  to  $t = 64.0$ ). Earlier periods are "spoiled" by the initial flow development. The comparison of the flow patterns for  $Re = 600$  (eigenvalue analysis) and  $Re = 1000$  (unsteady simulation) show very good qualitative agreement. All the mechanisms of the vortex shedding are properly reproduced. This fact is one more proof that the Karman vortex street, especially near the body has the linear character.

For the angle of attack equal  $0^\circ$  till  $Re = 800$  exists no separation on the airfoil. The higher mode solution forms two row of cells (Fig.15) which are close to the airfoil only near the leading edge. When added to the steady flow solution only the shear layer behind the airfoil is effected (Fig.16). The flow is stable because the growth-rate is negative, but if it becomes unstable it is the Kelvin-Helmholtz type of instability of the shear layer. For increasing Reynolds numbers the cells

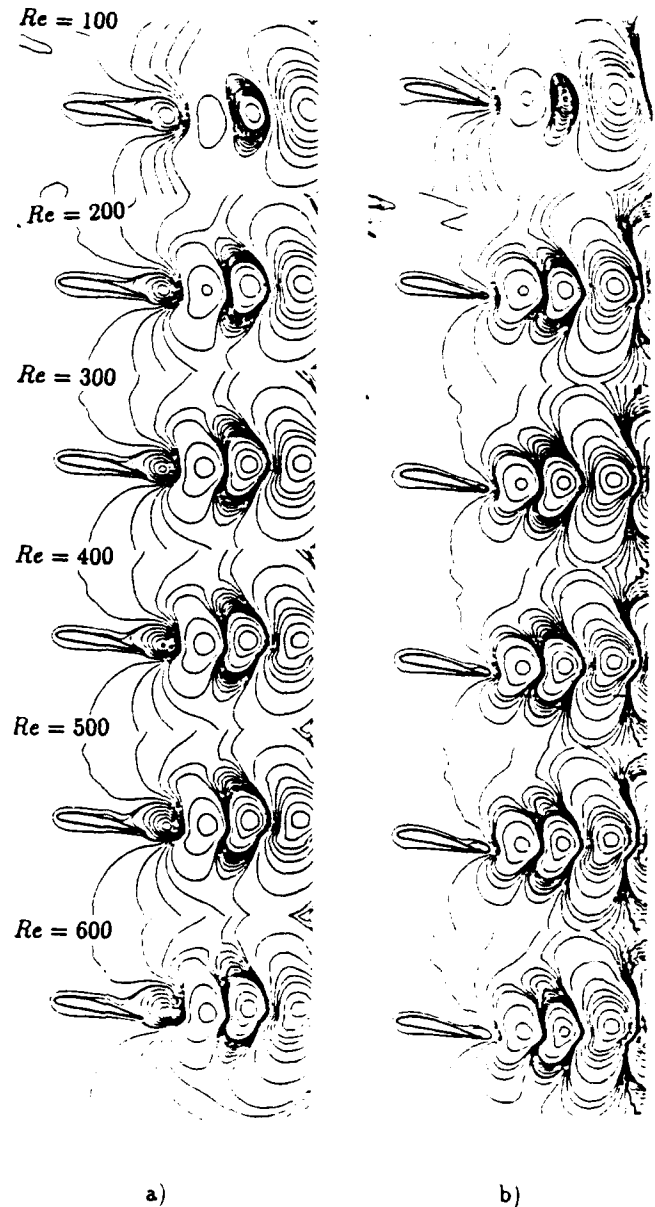


Figure 11: Real (a) and imaginary (b) part of the eigenvector - airfoil flow,  $\alpha = 15^\circ$

are moving closer to the airfoil. The disturbances form now cells attaching the airfoil and forming the "wall" mode. The boundary layer is now "modulated" in the way similar to the ellipsis flow. For  $\alpha = 0^\circ$  the Karman vortex street mode also exists, although it is strongly damped for the small Reynolds numbers.

### Conclusions

It was shown that non-parallel flow stability analysis is a method most suitable for determination of the wake flow instability. Several examples, calculated for different Reynolds numbers and geometries ranging from circular cylinder to the airfoil with the angle of attack, show that the method is a general tool for prediction of the wake instability. It is of advantage of this method, comparing to other numerical ap-



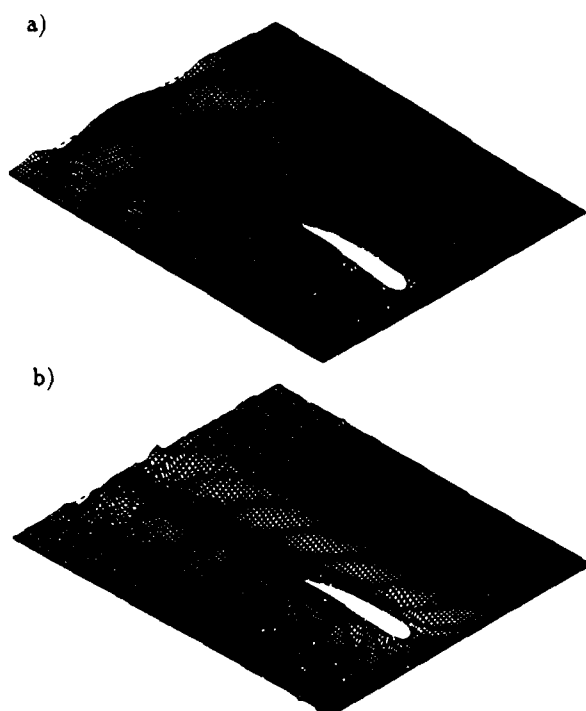


Figure 15: Higher mode solution for the NACA 4412 airfoil  $\alpha = 0^\circ$ , a)  $Re = 300$ , b)  $Re = 900$



Figure 16: Superposition of the steady solution and higher mode disturbance for the NACA 4412 airfoil.  $Re = 300$

proaches, that the critical Reynolds numbers and respective frequencies are determined more precisely. The method is able to handle the unsymmetrical wake flow. In this calculations the superiority of the stream function formulation and iterative determination of the eigenvalue has been proved.

Using the same method higher modes were investigated for the ellipsis and airfoil flow. Although the investigations had a preliminary character it can be concluded, that the results obtained differ significantly from the first mode solution. The higher mode disturbance patterns, obtained for the ellipsis flow, added to the steady solution appear to be the Tollmien-Schlichting wave originating in the boundary layer. The wave propagates further along the mixing layer. For the airfoil flow these types of modes were found but also another instability phenomena are present in the eigenvalue solutions. The investigation of large spectrum of eigenmodes is even more difficult because some instability phenomena are smoothly "switching" to another ones. The result of the higher-mode analysis gives the qualitative insight into the stability problem. The limitation of the method on present state of its development is not the formulation but the numerical approach. These difficulties we hope to overcome in our future investigations.

We believe that the method presented here will enable the stability analysis of any flow as a whole, without breaking it into pieces or restricting considerations to single type and that all instability phenomena are reflected in the non-parallel flow eigenvalue solutions.

### References

- [1] M.E.Goldstein, The evolution of Tollmien-Schlichting waves near a leading edge, *J. Fluid Mech.* 127, (1983), 59-81.
- [2] M.E.Goldstein, Scattering of acoustic waves into Tollmien-Schlichting waves by small streamwise variations in surface geometry, *J. Fluid Mech.* 154, (1985), 509-529.
- [3] A.I.Ruban, On the generation of Tollmien-Schlichting waves by sound, *Fluid Dyn.* 19, (1985), 709-716.
- [4] M.V.Morkovin, Critical evaluation of transition from laminar to turbulent shear layers with emphasis on hypersonically traveling bodies, *AFFDL-TR-68-149*, (1969).
- [5] G.E.Karniadakis, B.B.Mikic, A.T.Patera, Minimum-dissipation transport enhancement by flow destabilization: Reynolds' analogy revisited, *J. Fluid Mech.* 192, (1988), 365-391.
- [6] H.Schütz, Ein direktes Lösungsverfahren der Navier-Stokes Gleichungen in reiner Stromfunktionsformulierung zur Simulation instationärer inkompressibler Strömungen in zweidimensionalen Geometrien, *Doktor Dissertation*, Berlin 1990.
- [7] D.Wolter, M.Morzynski, H.Schütz, F.Thiele, Numerische Untersuchungen zur Stabilität der Kreiszyklinderströmung, *Z. angew. Math. Mech.*, 69, (1989), 6, 601-604.
- [8] M. Morzyński, F.Thiele, Numerical stability analysis of a flow about a cylinder, *Z. angew. Math. Mech.*, 71, (1991), 5, T424-T428.
- [9] C.P.Jackson, A Finite-Element study of the onset of vortex shedding in flow past variously shaped bodies, *J. Fluid Mech.* 182, (1987), 23-45.
- [10] A.Zebib, Stability of viscous flow past a circular cylinder, *J. of Eng. Math.*, 21, (1987), 155-165.
- [11] I.Kim, A.J.Pearlstein, Stability of the flow past a sphere, *J. Fluid Mech.* 211, (1990), 73-93.
- [12] M. Morzyński, F.Thiele, Non-parallel stability analysis of wake and boundary layer flow, *Boundary Layer Control Conference*, Cambridge, 9-12 April 1991, 15.1-15.11.
- [13] A.Kourta, H.C.Boisson, P.Chassaing, H.Ha Minh, Non-linear interaction and transition to turbulence in the wake of a circular cylinder, *J. Fluid Mech.* 181, (1987), 141-161.
- [14] M.F.Unal, D.Rockwell, On vortex formation from a cylinder. Part 1. The initial instability. Part 2. Control by splitter-plate interference, *J. Fluid Mech.*, 190, (1988), 491-529.

**AIRCRAFT ICING, 1**  
**SESSION 3**

# AERODYNAMICS OF A FINITE WING WITH SIMULATED ICE

M. B. Bragg\*, A. Khodadoust\*, and M. Kerho\*

University of Illinois at Urbana-Champaign  
Urbana, Illinois

## ABSTRACT

The effect of a simulated glaze ice accretion on the aerodynamic performance of a three-dimensional wing is studied experimentally. Results are reviewed from earlier two-dimensional tests which show the character of the large leading-edge separation bubbles caused by the simulated ice accretion. The 2-D bubbles are found to closely resemble well known airfoil laminar separation bubbles. For the 3-D experiments a semispan wing of effective aspect ratio five was mounted from the sidewall of the UIUC subsonic wind tunnel. The model uses a NACA 0012 airfoil section on a rectangular planform with interchangeable tip and root sections to allow for 0- and 30-degree sweep. A three-component sidewall balance was used to measure lift, drag and pitching moment on the clean and iced model. Fluorescent oil flow visualization has been performed on the iced model and reveals extensive spanwise and vortical flow in the separation bubble aft of the upper surface horn. Sidewall interaction and spanwise nonuniformity are also seen on the unswept model. Comparisons to the computed flow fields are shown. Results are also shown for roughness effects on the straight wing. Sand grain roughness on the ice shape is seen to have a different effect than isolated 3-D roughness elements.

## I. INTRODUCTION

The operation of aircraft in icing conditions are affected by large performance penalties due to ice accretion on unprotected surfaces. Understanding the aerodynamic penalties due to ice accretion on both lifting and non-lifting surfaces is important since many components are not ice protected. The initial cost, cost of maintenance and weight penalty associated with ice protection systems makes their use practical on only the most critical components.

Most icing experiments, where aerodynamic measurements have been made, have only dealt with two-dimensional aircraft components. The experimental work of Bragg et. al.<sup>1-3</sup>, and the corresponding computational research of Potapczuk<sup>4</sup>, Cebeci<sup>5</sup>, and Sankar<sup>6</sup>, have focused on a 2-D NACA 0012 airfoil with a simulated glaze ice accretion. Only the most recent work, Bragg et. al.<sup>7-9</sup> and Kwon<sup>10</sup> have begun to investigate the flow field about a wing with simulated glaze-ice accretion. Bragg<sup>7</sup> measured the surface

pressures on a straight aspect ratio 5 wing with a NACA 0012 section and the simulated ice shape of ref. 1 - 3. Kwon<sup>10</sup> compared Navier-Stokes calculations to these data and showed good results except near the root where the sidewall boundary conditions differed. Sankar<sup>11</sup> modeled the tunnel sidewall and improved the prediction near the root. Khodadoust<sup>2</sup> and Bragg<sup>2</sup> extended the 3-D wing pressure measurements to include the effect of wing sweep.

In this paper, the 3-D results on both the straight and swept wing will be reviewed. Emphasis will be on the experimental results with some comparison to the computational data. Flow visualization results will be presented which clearly show the very 3-D features of the flow field about the iced, swept wing. The effect of sandgrain and isolated 3-D roughness on the unswept wing are discussed. The two roughness models are shown to have a very different effect on the wing maximum lift coefficient. However, first a brief review of earlier 2-D data taken using

---

\* Associate Professor, Department of Aeronautical and Astronautical Engineering, Associate Fellow AIAA.

\* Graduate Research Assistant, Department of Aeronautical and Astronautical Engineering, Member AIAA.

this ice shape should help put the current 3-D results in perspective.

## II. EXPERIMENTAL PROCEDURE

The most recent tests were conducted in the subsonic wind tunnel at the University of Illinois at Urbana-Champaign. The tunnel is of conventional design with approximately a three-by-four foot test section, eight feet in length. The tunnel operates at speeds from zero to 165 mile per hour at Reynolds numbers of up to  $1.5 \times 10^6$  per foot. The tunnel is of open return type and uses four turbulence screens and honeycomb in the settling chamber to reduce tunnel turbulence to approximately .07 percent. Earlier experimental data were acquired in a similar, three-by-five foot tunnel, at The Ohio State University.

The 2-D model used for these tests was a 21-inch chord NACA 0012 airfoil. The first 15 percent of the leading edge was removable so a simulated ice accretion could be installed. The ice accretion used was a simulation of that measured on a NACA 0012 airfoil in the NASA Icing Research Tunnel, Fig. 1. The icing conditions were a free-stream velocity of 130 mph, angle of attack of 4 degrees, icing time of 5 minutes, volume median diameter droplet of 20 microns,  $LWC=2.1 \text{ g/m}^3$  and a temperature of  $18^\circ \text{ F}$ . Under these conditions the ice which accretes is considered glaze. Data on the 2-D model was taken from its approximately 95 surface pressure taps and a wake-survey probe. Detailed measurements were taken in the separation bubble with a split hot-film probe<sup>3</sup> which could detect and measure reverse flow.

The 3-D model used for this test is a semispan wing with a chord of 15.0 inches and a span of 37.5 inches when in the unswept position, Fig. 2. The swept wing has a sweep of 30 degrees and a span of 35.18 inches. A NACA 0012 airfoil section was chosen to compare to earlier 2-D tests. The model consists of several components to allow wing sweep and to allow different simulated ice shapes to be tested through interchangeable leading edges. Two leading edges have been constructed for the model ahead of the 15 percent station, a NACA 0012 leading edge and the simulated glaze ice accretion.

The model is equipped with surface static pressure taps. The taps are located in 5 major rows plus a row on the tip section. The centerline

row of taps has 80 taps in the no-ice configuration and 83 in the iced configuration. The other 4 rows on the main element have 40 and 41 taps in the no-ice and iced configurations, respectively. Including the 21 taps on the wing tip section, the model has a total of 261 taps in the no-ice configuration and 268 taps in the iced configuration. Pressure measurements were made using 6 Scanivalves.

A three-component sidewall balance was designed and constructed for the 3-D experiment. The balance is used to determine model lift, drag and pitching moment by measuring the normal, axial and moment. The balance is mounted outside the tunnel with the model spar passing through the tunnel wall and down the center of the balance. A 0.1 inch gap was left between the model and the sidewall to avoid any balance interference. Doubling the gap had no measurable effect on the model measured loads. Balance calibration resulted in linear primary coefficients and balance interactions.

Flow visualization was performed on the models using fluorescent oil. The oil is placed on the models and the tunnel is run until the flow pattern is established. The oil is illuminated with ultraviolet light and photographed with a 35mm camera. The flow visualization was performed at a chord Reynolds number of 1.2 million.

Data acquisition and reduction was performed at UIUC using an AT&T 6386WGS PC and the ASYST version 3.1 software written by ASYST Technologies Software Inc. A Data Translation model DT2821-F16SE A to D board (12 bit, 16 channel and 140kHz) was used to acquire the data. The sensors were excited, and the outputs filtered and gained as needed by eight Measurement Group model 2200 signal conditioners.

The pressure data, both model surface pressures and facility transducers, were acquired and reduced in the usual fashion and a detailed discussion will not be presented here. Pressure data were taken at a nominal Reynolds number of 1.5 million. Model pressures were converted to pressure coefficients using the tunnel dynamic pressure measured on each of the Scanivalves. Note that when span loads are shown,  $Y$  is taken parallel to the leading edge and  $C_q$  is taken along the tap lines perpendicular to the leading edge. Balance data were acquired using 300 samples per channel at 200 Hz and averaged to get one data point. The balance and model gravity tares are taken and subtracted from the data. Wall

corrections are made to the data based on the method of Rae and Pope<sup>12</sup>. These data were taken at a chord Reynolds number of 1.2 million.

### III. RESULTS AND DISCUSSION

#### 2-D Results

Two-dimensional experimental results on an airfoil with a simulated ice accretion have been taken by Bragg et. al.<sup>1-3</sup>. The results shown are with and without the simulated glaze ice accretion shown in Fig. 1. Glaze ice accretions are characterized by the "horns" which are the spoiler like protrusions that are formed. These horns cause significant alteration of the airfoil flow field through the formation of separation bubbles. Here some information on these bubbles is presented as an introduction for the 3-D data. A more detailed discussion of the 2-D ice-induced separation bubbles can be found in ref. 13.

Figure 3 shows the split hot-film measured velocity profiles in the upper and lower surface separation bubbles at an angle of attack of 4 degrees. First, consider the upper surface measurements. The first profile is taken at  $x/c = -0.02$ , just behind the ice horn. The flow is separated here with a very thin region of reverse and shear flow. The reverse flow region grows rapidly as we move downstream to  $x/c = 0.02$ . Note that the reverse flow is very slow, rarely exceeding 20 ft/sec or about 15 percent of the free-stream velocity. As the flow moves downstream the shear layer thickens and the amount of reverse flow decreases until the boundary layer reattaches around  $x/c = 0.16$ . Immediately downstream a distorted turbulent boundary layer is seen. Flow in the lower surface bubble is similar with reattachment of the bubble occurring between  $x/c = 0.12$  and 0.14. Similar trends are also seen at 0 and 2 degrees angle of attack.

In Fig. 4 the measured pressure distribution about a NACA 0012 airfoil, with and without the simulated ice accretion of Fig. 1, is shown. The clean airfoil shows the well known pressure distribution about a NACA 0012 airfoil. Looking on the upper surface of the iced airfoil, a region of almost constant pressure is seen extending from the leading edge to  $x/c = 0.08$ . This indicates that a leading-edge separation bubble is present. These bubbles, although quite large, act like classical airfoil laminar separation bubbles<sup>13</sup>.<sup>14</sup> The bubble and shear layer are initially laminar with shear layer transition occurring in the region

where the constant pressure ends. The turbulent mixing in the shear layer leads to reattachment downstream after some degree of pressure recovery. In this case reattachment occurs at  $x/c = 0.16$ <sup>13</sup>. A separation bubble is also seen in the pressure distribution on the lower surface. Its behavior is similar to the upper surface bubble. Note that comparing the pressure distribution to the profiles of Fig. 3, the largest reverse flow velocity occurs at  $x/c = 0.08$ , the end of the constant pressure plateau. This compares qualitatively to the classic model of a reattachment vortex in a laminar separation bubble.

Figure 5 shows the bubble size and shape as indicated by the separation streamlines for the upper and lower surface bubbles calculated from the mean velocity measurements. At  $\alpha = 0$  degrees both upper and lower surface bubbles are quite large. As the angle of attack increases, the upper surface bubble grows slowly from 0 to 2 degrees and more rapidly from 2 to 4 degrees. Between 4 and 6 degrees the bubble grows rapidly and the bubble becomes unsteady. The bubble fails to reattach at angles much above 6 degrees. The lower surface bubble decreases rapidly in size at first as  $\alpha$  is increased, but changes little in length between 2 and 4 degrees angle of attack. The location of maximum bubble thickness measured normal to the surface occurs at the transition location for bubbles on smooth airfoils<sup>14</sup>. However, here due to the surface geometry, this does not correlate to the transition locations indicated by the surface pressures.

Measured boundary-layer momentum thickness for the upper surface taken from the split hot-film data<sup>13</sup> are shown in Fig. 6. The momentum thickness grows rapidly from the separation point at a rate relatively independent of angle of attack. For angles of attack of 0, 2 and 4 degrees a maximum value is reached in the bubble. This maximum value moves downstream with angle of attack,  $x/c = .02$ ,  $.04$  and  $.08$  respectively, and the maximum value increases with angle of attack. A local minima is reached further downstream in the vicinity of, but slightly ahead of the reattachment point. The values are  $x/c = .06$ ,  $.08$  and  $.14$ , for the angles of attack of 0, 2 and 4 degrees, respectively. Downstream of the bubble reattachment, the momentum thickness rises slightly, falls again, then grows steadily over the region  $x/c = 0.3$  to the trailing edge. At 6 degrees angle of attack the character of the curve has changed. Here reattachment is shown by a leveling off of the momentum thickness and a slight decrease around  $x/c = .35$ . The momentum thickness rises rapidly thereafter.

This simulated iced airfoil reaches maximum lift at 7 degrees angle of attack and the bubble is completely burst at 8 degrees angle of attack. At 6 degrees the separated flow is observed to be very unsteady and the bubble large and approaching a bursting condition.

Briley and McDonald<sup>15</sup> show calculated momentum thickness values in a laminar separation bubble on a NACA 66<sub>3</sub>-018 airfoil. Their results show a slight reduction in momentum thickness after shear layer transition, and a rapid rise occurring just before reattachment. These trends compare well to the data presented here. In fact, as shown in reference 13, the measurements made in the separation bubble aft of the ice horn compare qualitatively to a classic laminar separation bubble of the long bubble type.

### 3-D Results

A sketch of the 3D model in the swept and straight configurations is shown in Fig. 2. Initial tests with the 3-D model were carried out in the straight-wing configuration. These tests were conducted primarily to generate data to compare to the 2-D data already available<sup>1-3</sup>. More recent measurements, which have been used for comparison to the Navier-Stokes computations of Kwon and Sankar, have utilized the 3-D model in both the swept and straight configurations.

Figure 7 shows flow visualization results on the straight wing at  $\alpha = 4$  and  $8^\circ$ . At 4 degrees the oil flow reveals a very 2-D flow. The only 3-D character is a small interaction seen with the wing tip vortex. Although difficult to see in these reproductions, an ice-induced separation bubble exists at the leading edge. It reattaches around 15 percent chord. In the 8 degree case the bubble reattachment can be seen to vary greatly in the spanwise direction. The maximum extent of the bubble is over fifty percent chord, about 1/3 of the semispan inboard. Due to the 3-D induced flow, the effective angle of attack reduces as the wing tip is approached, and the bubble reattachment moves forward. Near the root, the bubble also reduces in length. This is due to a sidewall separation which forces early reattachment of the bubble<sup>11,16</sup>.

The presence of spanwise flow on the wing is greatly affected by the wing sweep. This result can be seen in CFD flow visualization<sup>17</sup> shown in Fig. 8. For the CFD flow visualization, the location of several massless air-stream particles is

tracked over the wing. The  $\alpha = 4^\circ$  flow visualization clearly shows the formation of a leading edge vortex. This vortex forms in the separation bubble aft of the upper surface ice horn. The vortex grows in diameter as it moves out from the root to the tip. Spanwise velocities in the vortex are seen to be quite large<sup>3</sup>. Also note that significant spanwise flow is seen aft of the leading-edge vortex, particularly near the tip.

The CFD particle-trace flow visualization shows a complex flow field for the iced swept wing at  $\alpha = 8^\circ$ . The leading edge separation bubble seen at 4 degrees has now enlarged significantly. The particles tracked in the separation bubble are shown to heavily interact with the particles tracked on the wing further downstream. This is partly due to the stall characteristics of a swept wing. A swept wing tends to stall at the wing tip first. The CFD flow visualization shows a massively separated flow region on the swept wing starting near the wing tip and extending into the midspan region of the wing, engulfing the separation bubble region.

In Fig. 9, experimental and computational surface flow visualization results are shown. The computational results are from simulated oil flow generated by tracing the trajectories of massless particles introduced into the Navier-Stokes flow field. The experiment was conducted at a chord Reynolds number of 1.2 million while the computation was carried out at 1.5 million. Here, the leading edge vortex grows in size as it moves from the root to the tip. In the computational result, the reattachment line moves back to about 80 percent chord near the tip. Ahead of this line the vortex-induced surface flow is forward into the free stream and towards the tip as before. A similar result is seen in the experimental data. Near the tip the flow is essentially parallel to the trailing edge behind the reattachment line. The interaction of the large leading-edge vortex and the tip vortex causes an interesting flow at the tip. The flow moves forward toward the leading edge then turns back towards the trailing edge, all the time flowing outboard. Near the trailing edge this motion is more pronounced in the experimental data. The experimental data shows a somewhat different flow at the tip in the midchord to leading-edge region. This is probably due to the simpler leading-edge geometry used in the CFD model.

Span loads for both the iced and no-iced configurations of the 3-D straight wing are shown in Fig. 10. These data were obtained by integrating the pressure data to obtain sectional lift coefficients. At 0 and 2 degrees angle of

attack the two span loads are amazingly similar. This indicates, as can also be seen in the 3-D lift, that the zero-lift angle and lift-curve slopes are not affected by the simulated ice. It is well known that a straight rectangular wing stalls first at the root. This is clearly seen in the iced span load data as the sectional lift values on the inboard wing fall below those of the clean model as the angle of attack is increased. This occurs due to the bursting of the ice-induced separation bubble near the root where the effective angle of attack is high.

The spanwise wing loading for the swept wing is shown in Fig. 11 for positive angles of attack from 0 to 8 degrees. As expected, the presence of the ice shape has caused a reduction in wing loading, especially on the outboard sections where stall occurs first on a swept wing. Contrast this to the straight wing in Fig. 10 where the root stalls first.

As a part of the experimental icing research, the effect of roughness was studied on the aerodynamic performance of the straight wing in the iced and un-iced configurations. Two types of roughness were examined on the straight wing: isotropic and three-dimensional roughness. The isotropic roughness was a 50-grit sandpaper roughness with  $k/c = 0.0010$ . The 3-D roughness were  $0.25 \times 0.25$  inch squares, 0.054 inch high, placed offset 0.5 inches apart in rows. In Fig. 12, the section lift performance of the smooth ice shape is compared with the section lift performance of the iced wing when isotropic and 3-D roughness is added. The results indicate that in the linear region,  $\alpha = -6$  to  $6$  deg., neither the isotropic nor the 3-D roughness significantly affect the lift performance of the wing. In the non-linear region, the isotropic roughness has little effect on the positive stall angle, with a small reduction in maximum lift. At negative angles of attack, an earlier stall onset is seen with a reduction in lift due to the roughness.

The effect of the 3-D roughness on the section performance of the model seems to be somewhat different in the stall regime. Here, a distinct stall angle can not be detected in either the positive or the negative range of angles of attack. Rather, at the angle where the wing section stalls in the smooth-ice case, the lift-curve slope changes but the lift continues to increase.

This phenomena could be attributed to the size of the three-dimensional roughness used. The 3-D roughness is three times larger than the particles which form the isotropic roughness. The

result of the particles' action is similar to the results of vortex generators. The effect of the roughness becomes particularly evident near the stall regime. In this regime, the flow seems to remain attached somewhat longer, therefore producing a potentially softer stall at both positive and negative angles of attack. Neither of these two types of roughness may correctly model the actual 3-D, and highly irregular roughness found on actual ice accretions. More research on surface roughness effects is needed.

The lift performance of the straight wing, measured with a three component balance, is shown in Fig. 13. Comparison between the clean wing, the clean wing with roughness, and the iced wing with rough leading edge reveal no appreciable change in the lift curve slope of the wing. The angle of stall, however, is shown to be directly affected by the presence of roughness. The straight wing stalls at  $\alpha = 17^\circ$  in the clean configuration. With the addition of roughness, the stall angle is reduced to  $13^\circ$ . The presence of leading edge ice in addition to roughness further reduces the stall angle to  $10^\circ$ . In addition to the stall angle, roughness is shown to affect the post stall performance of the straight wing.

#### IV. SUMMARY

The glaze ice accretion studied in this paper had a severe effect on the aerodynamics of the NACA 0012 airfoil. The 2-D data clearly showed the laminar separation bubble which is a dominant feature of the iced airfoil flow field. The bubble causes a large drag increase and early airfoil stall when the bubble bursts and fails to reattach. The bubble has the characteristics of a classic long bubble type airfoil laminar separation bubble. A straight aspect ratio five wing was tested with the same simulated ice accretion. Flow visualization results showed a fairly 2-D flow on this unswept wing. Significant sidewall boundary-layer interaction was seen in the flow visualization as well. The wall boundary layer in the tunnel affected the results by delaying the root stall. When this was modelled properly in the CFD code the results for span load compared favorably.

The swept wing was seen to have a very three-dimensional flow field. At low angle of attack, flow visualization shows a strong leading edge vortex formed in the separated flow aft of the upper surface ice horn. Spanwise flow in the vortex is significant. As the angle of attack is

increased, the vortex grows, especially near the tip, and a very three-dimensional flow develops. Since the swept wing stalls first at the tip, the wall boundary layer has little effect on these results. Comparison of the experimental results to the computations are good.

Surface roughness effects were presented on the unswept wing. Both sandgrain roughness and isolated 3-D roughness elements were placed on the simulated ice accretion. The effects were exactly the opposite with the 3-D roughness actually increasing the maximum lift of the iced, unswept wing. Much more research is needed on roughness effects on iced airfoils and its effect on the leading-edge separation which is so critical to the iced airfoil performance. Roughness models more complex than simple sandgrain roughness will have to be developed to properly reproduce actual ice roughness effects.

Future research will include laser Doppler velocimeter data for a more detailed look at these 3-D flow fields. This will provide a more complete picture of the 3-D separation bubbles. Research on roughness effects and its proper modelling are also underway to improve our understanding of this complex flow.

#### ACKNOWLEDGEMENT

This work was supported in part by a grant from NASA Lewis Research Center. The authors wish to thank Dr. M. G. Potapczuk of NASA Lewis for his support of this research.

#### REFERENCES

1. Bragg, M. B. and Coirier, W. J., "Aerodynamic Measurements of an Airfoil with Simulated Glaze Ice", AIAA-86-0484, paper presented at the 24th Aerospace Sciences Meeting, Reno, Nevada, Jan. 6-9, 1986.
2. Bragg, M. B. and Spring, S. A., "An Experimental Study of the Flow Field about an Airfoil with Glaze Ice", AIAA-87-0100, paper presented at the 25th Aerospace Sciences Meeting, Reno, Nevada, January 12-15, 1987.
3. Bragg, M. B. and Khodadoust, A., "Experimental Measurements in a Large Separation Bubble Due to a Simulated Glaze Ice Accretion", AIAA-88-0116, paper presented at the 26th Aerospace Sciences Meeting, Reno, Nevada, January 11-14, 1988.

4. Potapczuk, M. G., "Navier-Stokes Computations for a NACA 0012 Airfoil with Leading Edge Ice", AIAA Paper No. 87-0101, presented at the 25th Aerospace Sciences Meeting, Reno, Nevada, Jan. 12-15, 1987.
5. Cebeci, T., "Effects of Environmentally Imposed Roughness on Airfoil Performance", NASA CR 179639, June 1987.
6. Sankar, L. N., Wu, J. C. and Kwon, O. J., "Development of Two- and Three-Dimensional Navier-Stokes Solvers for Aircraft Icing Studies", presented at the Annual Airfoil Performance-icing Workshop, NASA Lewis Research Center, Cleveland, Ohio, July 25, 1988.
7. Bragg, M. B. and Khodadoust, A., "Effect of Simulated Glaze Ice On a Rectangular Wing", AIAA-89-0750, paper presented at the 27th Aerospace Sciences Meeting, Reno, Nevada, January 9-12, 1989.
8. Khodadoust, A. and Bragg, M. B., "Measured Aerodynamic Performance of a Swept Wing With a Simulated Glaze Ice Accretion", AIAA Paper 90-0490, 1990.
9. Bragg, M., Khodadoust, A., Soltani, R., Wells, S. and Kerho, M., "Effect of Simulated Ice Accretion on the Aerodynamics of a Swept Wing", AIAA-91-0442, paper presented at the 29th Aerospace Sciences Meeting, Reno, Nevada, Jan. 7-10, 1991.
10. Kwon, O. and Sankar, L., "Numerical Study of the Effects of Icing on Finite Wing Aerodynamics", AIAA-90-0757, paper presented at the 28th Aerospace Sciences Meeting, Reno, Nevada, January 8-11, 1990.
11. Sankar, L. and Kwon, L., "Numerical Studies of the Effects of Icing on Fixed and Rotary Wing Aircraft Aerodynamics", presentation at the Airfoil-icing Workshop, Nasa Lewis Research Center, Sept. 1990.
12. Rae, W. H. and Pope A., **Low-Speed Wind Tunnel Testing**, Second Edition, John Wiley & Sons, New York, 1984.
13. Bragg, M. B., Khodadoust, A. and Spring, S. A., "Experimental Measurements in a Large Leading-Edge Separation Bubble Due to a Simulated Airfoil Ice Accretion", to be published, **AIAA Journal**.



14. Tani, I., "Low Speed Flows Involving Bubble Separations", **Progress in Aeronautical Sciences**, Pergamon Press, 1964, pp. 70-103.

15. Briley, W. R. and McDonald, H., "Numerical Prediction of Incompressible Separation Bubbles", **Journal of Fluid Mechanics**, Vol. 69, June 1975, pp. 631-656.

16. Potapczuk, M.G., and Bragg, M.B., Kwon, O.J. and Sankar, L.N., "Simulation of Iced Wing Aerodynamics", 68th AGARD Fluid Dynamics Panel Specialists Meeting, Toulouse, France, April 29 - May 1, 1991.

17. Potapczuk, M. G., private communication. Dec. 1990.

#### NACA 0012 ICING CONDITIONS

$\alpha = 4^\circ$        $V = 130$  mph  
 $\bar{d} = 20\mu\text{m}$        $LWC = 2.1 \text{ g/m}^3$   
 $T = 18^\circ\text{F}$

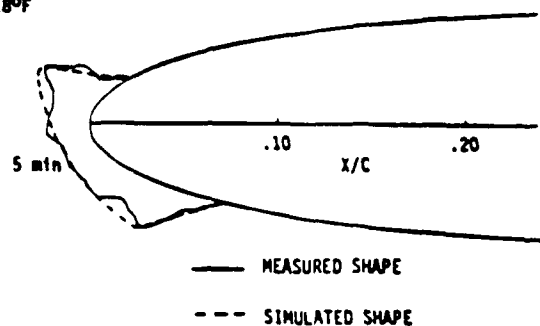


Fig. 1 Simulated Glaze Ice Accretion.

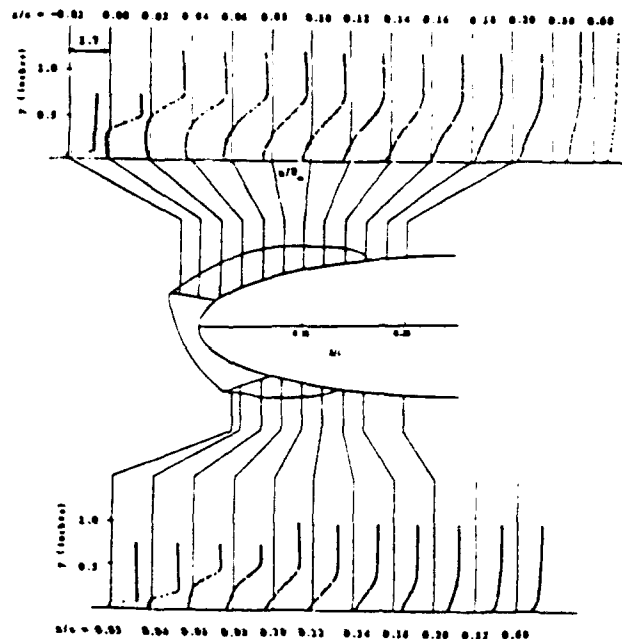


Fig. 3 Split Hot-Film Measurements on the NACA 0012 Airfoil with Simulated Ice at  $\alpha = 4$  deg.

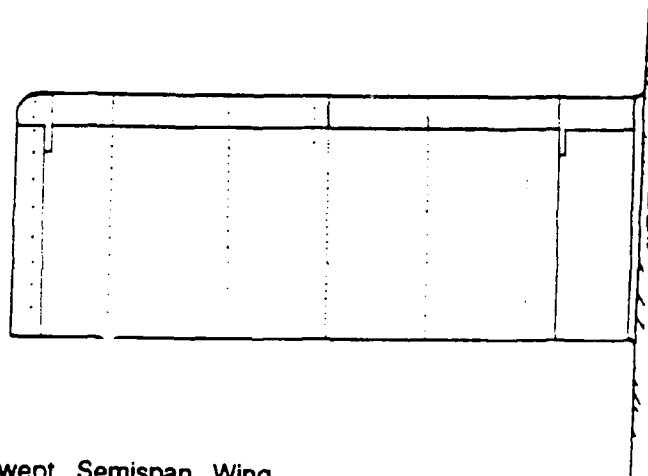
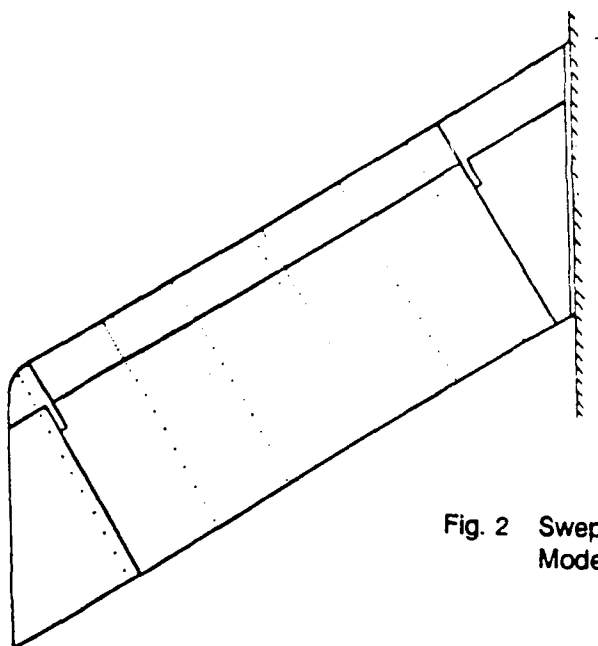


Fig. 2 Swept and Unswept Semispan Wing Models.

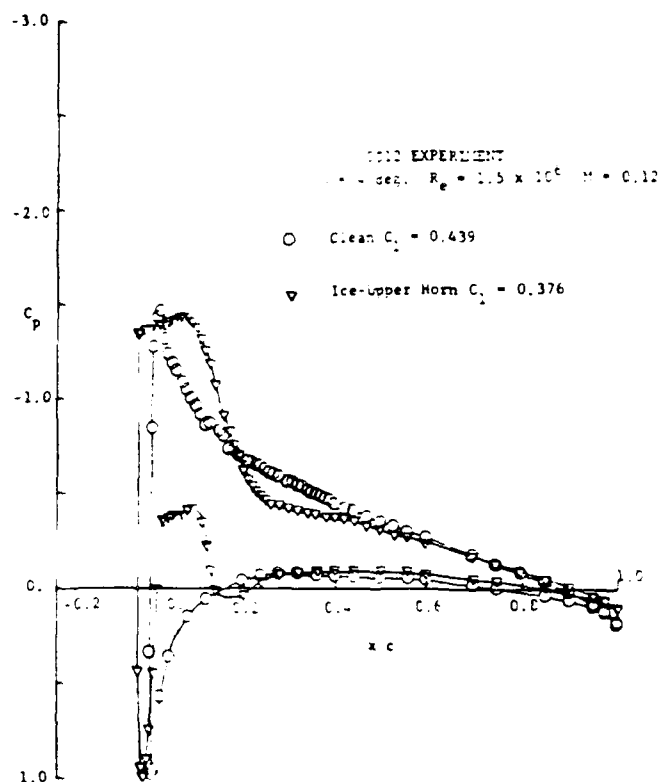


Fig. 4 Pressure Distribution on the NACA 0012 Airfoil With and Without Simulated Ice.

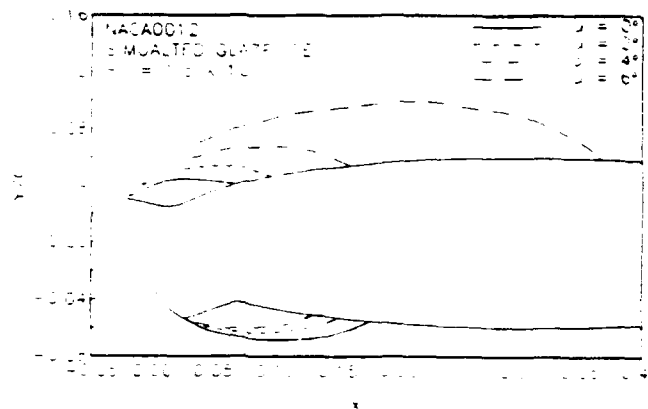


Fig. 5. Separation Streamlines on the NACA 0012 Airfoil With Simulated Glaze Ice.

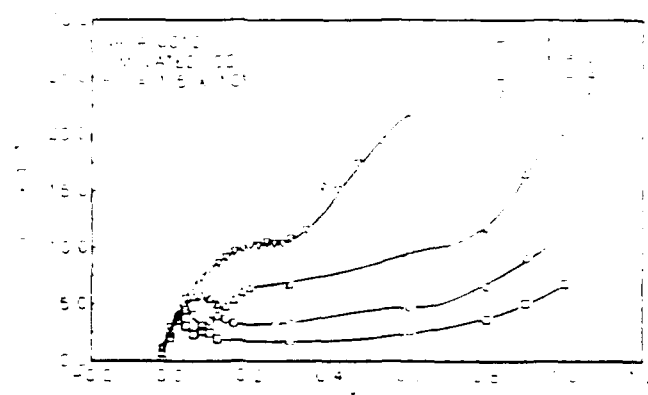
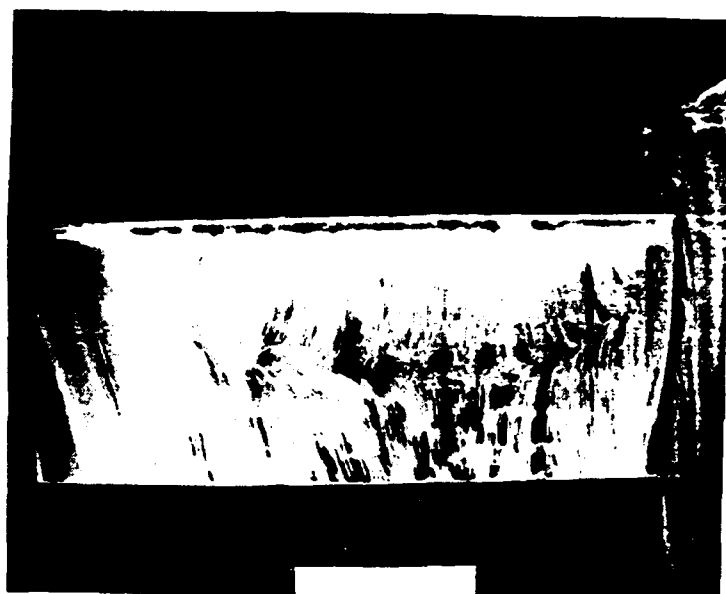


Fig. 6 Measured Momentum Thickness in the Upper Surface Separation Bubble.



$\alpha = 4^\circ$



$\alpha = 8^\circ$

Fig. 7 Experimental Surface Oil Flow on the Straight Wing With Simulated Ice.

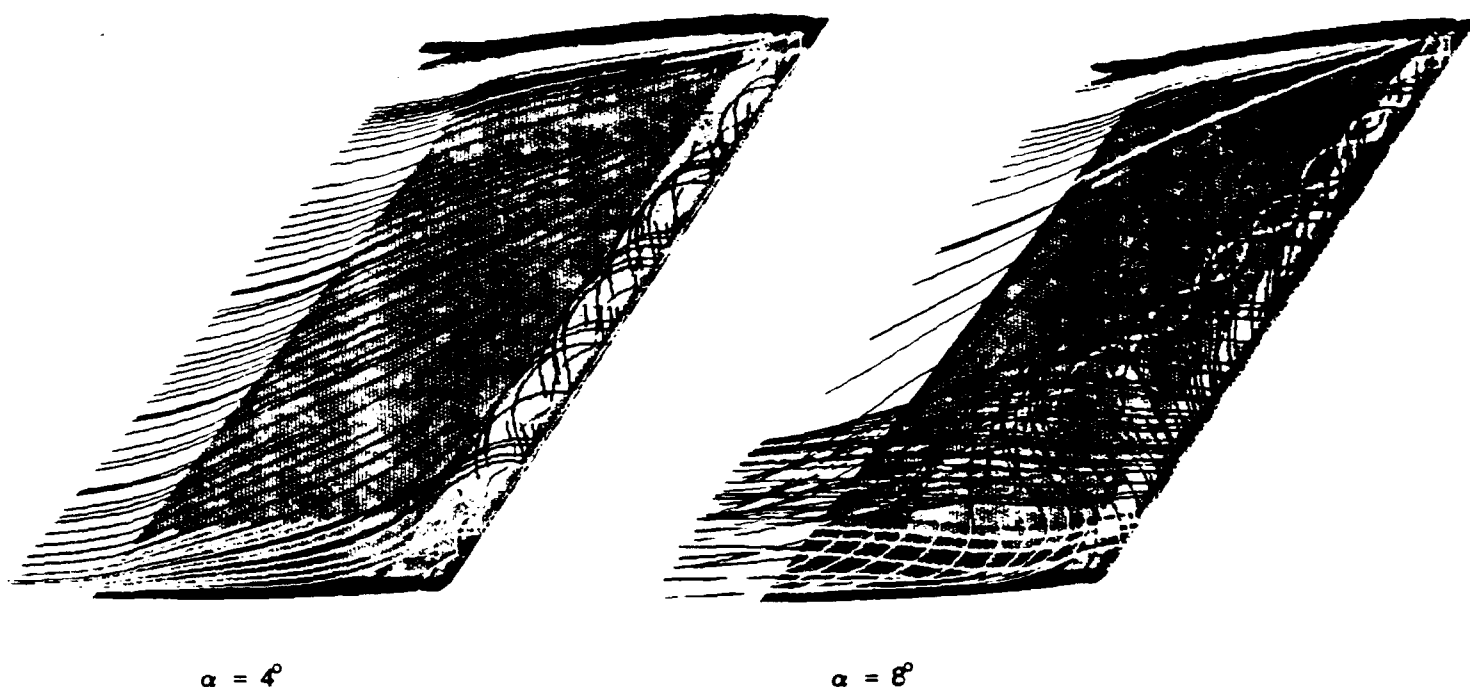


Fig. 8 Computational Flow Tracers on the Swept Wing With Simulated Ice<sup>17</sup>.

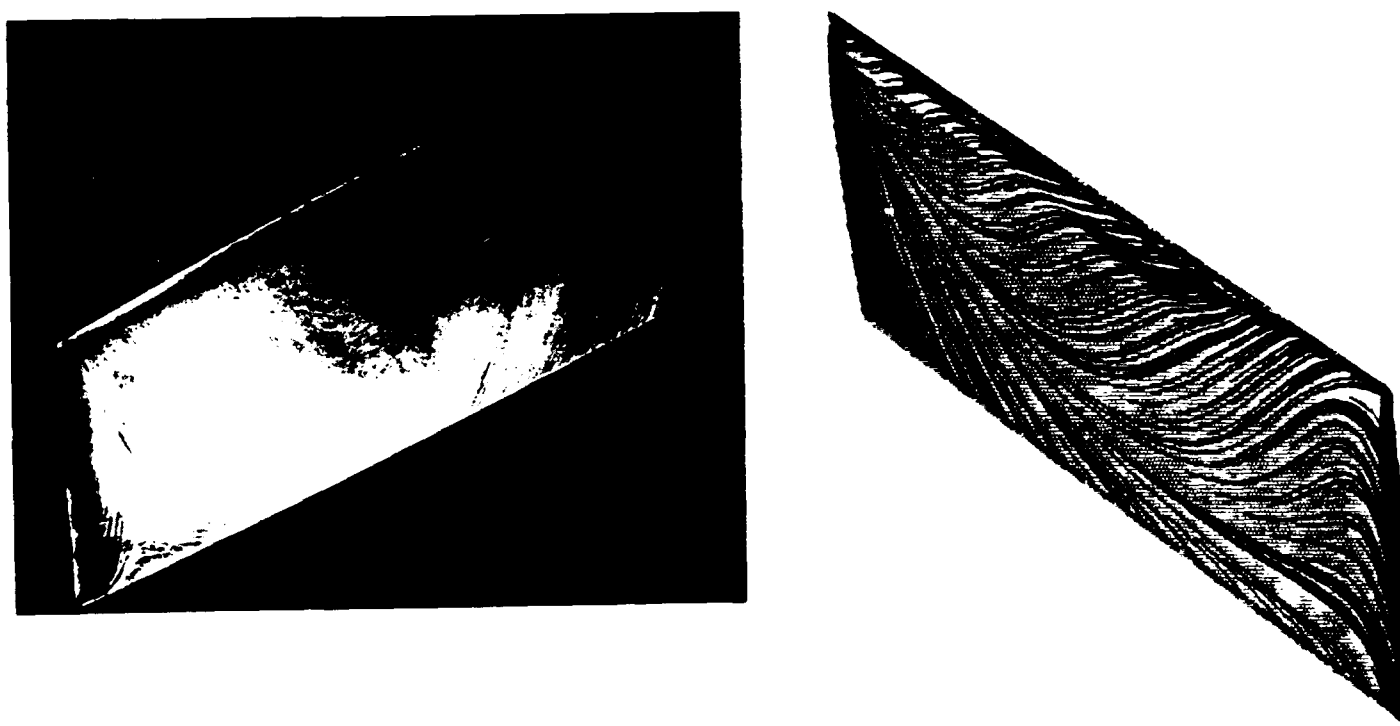


Fig. 9 Experimental and Computational<sup>17</sup> Surface Oil Flow on the Swept Wing With Ice at  $\alpha = 8$  deg.

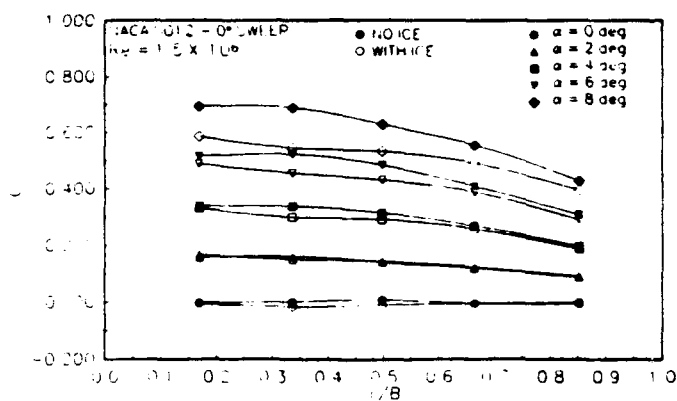


Fig. 10 Measured Span Loads for the Straight Wing With and Without Simulated Ice.

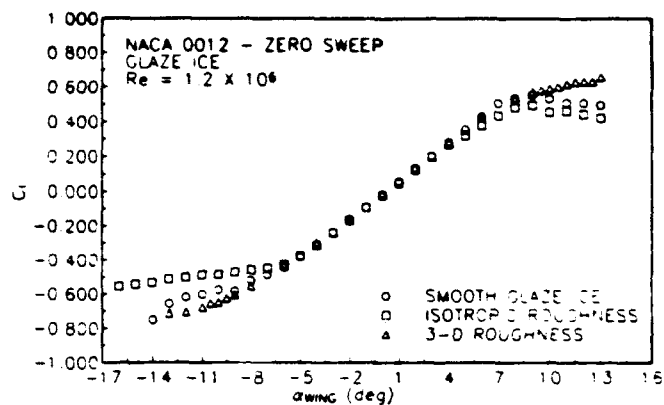


Fig. 12 Effect of Roughness Type on the Lift from the Centerline of the Unswept Wing With Ice.

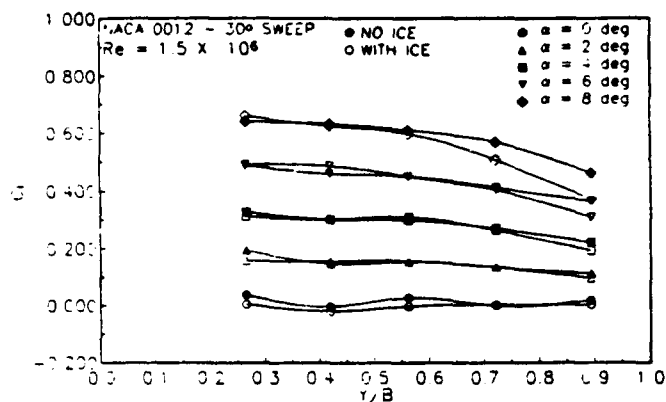


Fig. 11 Measured Span Loads for the Swept Wing With and Without Simulated Ice.

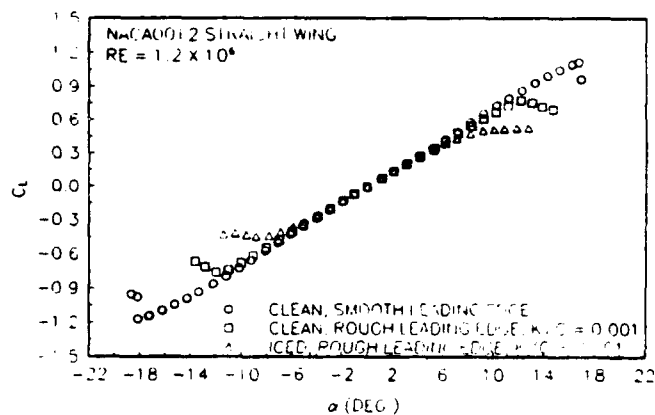


Fig. 13 Effect of Roughness on the Lift of the Unswept Wing With and Without Ice.

# Numerical Modeling of Runback Water on Ice Protected Aircraft Surfaces

Kamel M. Al-Khalil\*

National Research Council, Washington, D.C. 20418

and,

Theo G. Keith, Jr.<sup>†</sup>, Kenneth J. De Witt<sup>‡</sup>

The University of Toledo, Toledo, Ohio 43606

A numerical simulation for "running wet" aircraft anti-icing systems is developed. The model includes breakup of the water film, which exists in regions of direct impingement, into individual rivulets. The wetness factor distribution resulting from the film breakup and the rivulet configuration on the surface are predicted in the numerical solution procedure. The solid wall is modeled as a multi-layer structure and the anti-icing system used is of the thermal type utilizing hot air and/or electrical heating elements embedded within the layers. Details of the calculation procedure and the methods used are presented.

## Nomenclature

$C_p$	=	specific heat
$F$	=	wetness factor
$h_i$	=	heat transfer coefficient between the hot air and the inner surface of the wall
$h_w$	=	heat transfer coefficient between the outer surface of the wall and the runback water
$h_\infty$	=	heat transfer coefficient between the free stream and the outer surface of the wall
$k$	=	thermal conductivity
$L_v$	=	latent heat of vaporization of water
$LWC$	=	liquid Water Content
$M$	=	molecular mass, number of grids across film
$m$	=	runback water mass flow rate
$m''$	=	rate of mass transfer per unit area
$P$	=	static pressure
$Pr$	=	Prandtl number
$q$	=	rate of heat transfer
$q''$	=	rate of heat transfer per unit area
$\dot{q}$	=	rate of heat generation per unit volume
$R$	=	rivulet radius
$r$	=	recovery factor
$Sc$	=	Schmidt number
$V$	=	flowfield velocity

$w$	=	velocity in a rivulet in the flow direction
$T$	=	temperature
$\alpha$	=	thermal diffusivity
$\beta$	=	rivulet contact angle with the solid surface
$\delta_f$	=	equivalent rectangular film thickness of a rivulet
$\lambda$	=	ratio of rivulet width to wetness factor, or distance between two adjacent surface streamlines
$\eta$	=	droplet collection efficiency
$\mu$	=	dynamic viscosity of water
$\xi$	=	area correction factor for heat loss from a rectangular film to the ambient
$\rho$	=	density
$\tau$	=	surface shear force (friction)
$\phi_\infty$	=	free stream relative humidity

## Subscripts

$a$	=	anti-ice air
$\bar{a}$	=	anti-ice
$e$	=	property at edge of the boundary layer
$evap$	=	evaporation from outer cowl surface
$f$	=	liquid film
$imp$	=	impingement on outer cowl surface
$m$	=	solid wall composed of several layers
$r$	=	rivulet
$vap, v$	=	vapor, saturated vapor
$w$	=	wall or runback water
$\infty$	=	at free stream conditions

\* NRC Research Associate, NASA Lewis Research Center.

<sup>†</sup> Professor, Mechanical Engineering Dept.

<sup>‡</sup> Professor, Chemical Engineering Dept.

### Superscripts

- $l$  = layer number in the composite wall  
 $n$  =  $\Delta z$  step level (grid number in the z-direction)

## I. Introduction

The problem of aircraft icing has been the focus of study of many researchers for a number years. The detrimental effects of ice accretion on critical surfaces can jeopardize flight safety as well as the overall aircraft performance. Consequently, accurate modeling and extensive study of the icing process are necessary. Two general methods of ice protection have been developed: De-icing methods for the intermittent removal of ice buildup by destroying the bond between the ice and the surface, and anti-icing methods for the prevention of ice formation on critical surfaces such as engine nacelles.

The availability of high-speed digital computers has favored the use of numerical techniques and the development of computer codes to design and analyze ice protection systems. It is felt that the latter can minimize the cost associated with the required experimental testing by providing a tool that is at least capable of predicting preliminary results.

Most studies related to aircraft icing have been committed to the prediction of ice shapes and the determination of their detrimental effects on aerodynamic performance of the aircraft components. At this time, research in running wet anti-icing systems is quite basic, and runback is treated in a primitive manner. The NASA Lewis Research Center has been a major contributor in conducting and sponsoring studies related to computer modeling of aircraft icing processes as well as experimental testing in its Icing Research Tunnel (IRT). As a result, LEWICE [1], an ice accretion prediction code, was developed for unprotected airfoil surfaces. The approach used in the modeling consists of performing mass and energy balances on the surface water. The wetness factor issue is ignored and the runback water is assumed to wet the entire surface at a particular location. Consequently, the amount of required heat to anti-ice the surface is under-estimated.

Several investigators have produced different versions of the LEWICE code in order to improve it. To name a few, Cebeci et. al [2] modified the flowfield calculation module of the code to avoid the problem of multiple stagnation points. Yamaguchi et. al [3] proposed a multi-zone roughness model: a zone of uniform water film in the stagnation region, a rough zone of stationary water beads, and lastly, a zone where surface water run back as rivulets [4]. The runback water was recently modeled by Al-Khalil et. al [5,6,7] by incorporating a rivulet model. This paper is intended to present the numerical calculation procedures used including the most recent improvements of the latter model.

## II. Mathematical

The runback model introduced in this paper is based on a two-dimensional mathematical formulation. The surface water and the solid structure temperatures vary across their

thicknesses and in the flow direction along a streamline on the surface. Spanwise temperature dependence is assumed to be negligible. However, the latter is accounted for by performing energy balances on control volumes whose spanwise widths extend between two adjacent streamlines on the aircraft surface.

### II.1 Runback Water

#### II.1.1 Hydrodynamics:

The rate of water impingement on aircraft surfaces, due to the existence of undisturbed supercooled liquid water droplets in clouds, is relatively small. This and aerodynamic forces result in a very shallow water film flowing over the skin surface. Consequently, the surface water behavior is controlled not only by aerodynamic and body forces, but also by surface tension forces and surface roughness.

In the direct impingement regions, i.e., in the neighborhood of the stagnation point, the water tends to wet the entire surface due to incoming droplets and due to water running back from upstream locations. However, at or downstream of the impingement limit, the liquid film could become unstable due to surface tension forces that cause the surface water to coalesce into individual streams, referred to as rivulets, separated by dry areas.

A detailed study on the hydrodynamics and a stability analysis of surface water was presented in Ref. [5]. For completeness, some of the essential features are presented here without further discussion. The film/rivulet flow in the streamwise (z) direction is caused by a shear force acting at the liquid-air interface. The latter force is obtained from the results of the skin friction factor computed from viscous aerodynamic calculations of the flowfield.

A rectangular film model was chosen to mathematically represent the heat transfer process in a rivulet as shown in Fig 1. This model was found appropriate to the current problem for various reasons discussed in Ref. [6]. The criteria used for the new runback water configuration are as follows:

- The wetness factor is preserved, i.e., the widths of a rectangular film is equal to that of its corresponding rivulet.
- The law of mass conservation requires equal mass flow rates in a rivulet and its equivalent rectangular film. This criterion enables one to compute the film thickness  $\delta_f$ .
- Mass loss due to evaporation is associated with a decrease in the rivulet size, i.e., its radius and, consequently, its base width that is also equal to the rectangular film width. This criterion enables one to update the value of the wetness factor.

The velocity distributions within the film and the rivulet were derived and used to obtain the mass flow rates in each [5], as shown, respectively:

$$m_f = \frac{\rho \lambda F \tau}{2 \mu} \delta_f^2 \quad (1)$$

$$m_r = \frac{\rho \tau F_1(\beta)}{\mu} R^3 \quad (2)$$

The second criterion is used, equating the above equations, to give:

$$\delta_f = R \sqrt{\frac{F_1(\beta)}{\sin \beta}} \quad (3)$$

where  $F_1(\beta)$  is a function of  $\beta$  derived in [7]. The above equation shows the rectangular film thickness is directly proportional to its equivalent rivulet radius. This equation will later be used to update  $\delta_f$  when  $R$  is reduced due to evaporation. Procedures to determine the conditions and location for the breakup of the liquid layer flowing downstream of impingement regions were thoroughly discussed in Ref. [5]. The prediction of initial values of  $R$  and  $F$  at breakup was also described.

### II.1.2 Thermal Analysis:

The principal objective of this study has been to analyze and predict the performance of anti-icing systems. In such applications, the worse case occurs at equilibrium state conditions. Consequently, the mathematical formulation of the heat transfer process is based on the steady-state energy equations. The unsteady equations are more relevant to de-icing applications. The runback water energy equation then follows:

$$\frac{\partial T_w}{\partial z} = \gamma \frac{\partial^2 T_w}{\partial y^2} \quad (4)$$

$$\text{where, } \gamma = \frac{\alpha_w}{w(y)}$$

The above equation is based on the fact that conduction heat transfer within the liquid water in the  $z$ -direction (flow direction) is negligible compared to that in the  $y$ -direction (across film thickness). The solution of Eq. (4) requires two boundary conditions in the  $y$ -direction, one at the solid-liquid interface, and one at the liquid-air interface, and an initial condition ( $z=0$ ). The latter condition requires knowledge of the water temperature at the stagnation point. Analytically, this is impossible because that depends on the final temperature solution in the water film and in the solid structure layers. However, this may be obtained numerically in an iterative procedure described in a later section.

The boundary condition at the liquid-air interface is written as:

$$\begin{aligned} -k_w \frac{\partial T_w}{\partial y} = & h_\infty \xi \left[ T_w - T_e - \frac{r V_e^2}{2 C_{p_{air}}} \right] + m_{evap} \xi L_v \\ & - m_{imp} C_{p_{w,\infty}} (T_\infty - T_w) - \frac{m_{imp} V_\infty^2}{2} \end{aligned} \quad (5)$$

where the first and second term terms on the right-hand side represent heat loss to the ambient by convection and evaporation, respectively; and the third and fourth terms are the sensible and kinetic heat contributions of the

impinging droplets which are of value only in the direct impingement region.

The rate of impingement per unit area,  $m''_{imp}$ , is calculated from the local value of the collection efficiency as shown:

$$m''_{imp} = \eta LWC V_\infty \quad (6)$$

and the rate of evaporation per unit area is computed using the Chilton-Colburn heat-mass transfer analogy. This may be expressed as:

$$m''_{evap} = \frac{h_\infty}{C_{p_{air}}} \left( \frac{Pr}{Sc} \right)^{2/3} \frac{M_{H_2O}}{M_{air}} \left[ \frac{P_{v,w} - P_{vap}}{P_e - P_{v,w}} \right] \quad (7)$$

where,

$P_{v,w}$  = saturated vapor pressure at the local runback water temperature  $T_w$ .

$P_{vap}$  = local vapor pressure at the edge of the boundary layer at the local relative humidity.

Application of Dalton's Law of partial pressures and knowledge of ambient conditions yields:

$$P_{vap} = P_e \frac{P_{v,\infty}}{P_\infty} \phi_\infty \quad (8)$$

where the relative humidity  $\phi_\infty$  in a cloud is generally taken to be 100%. The saturation vapor pressure of water is written as function of temperature:

$$P_v(T) = 2337 \exp \left\{ 6789 \left[ \frac{1}{293.15} - \frac{1}{T} \right] - 5.031 \ln \left[ \frac{T}{293.15} \right] \right\} \quad (9)$$

where the units of  $P_v$  and  $T$  are (Pa) and (K), respectively.

The recovery factor  $r$  in Eq. (5) accounts for viscous dissipation in the boundary layer and is approximated by [8]:

$$r = 1 - \frac{V_e^2}{V_\infty^2} \left( 1 - Pr_{air}^n \right), \quad n = \begin{cases} \frac{1}{2} & \text{laminar flow} \\ \frac{2}{3} & \\ \frac{1}{3} & \text{turbulent flow} \end{cases} \quad (10)$$

The properties at the edge of the boundary layer, i.e.,  $P_e$ ,  $T_e$ , and  $V_e$  are computed using the perfect gas relations for isentropic flow and the local values of the pressure coefficient obtained from a flowfield solver.

Note that  $\xi$ , in Eq. (5), is an area correction factor to account for the area differences in the rivulet and the rectangular film models through which heat exchange with the ambient occurs. This factor is defined as the ratio of the rivulet free surface area to the upper surface area of the corresponding rectangular film. From geometric considerations, the following may be written:

$$\xi = \begin{cases} \frac{\beta}{\sin \beta} & (0 < F < 1) \\ 1 & (F = 1) \end{cases} \quad (11)$$

This factor is less than 10% for contact angles smaller than  $42^\circ$ , and is unity for uniform film flow.

The boundary conditions concerning the solid-liquid interface which represents the heat exchange between the solid wall and the runback water remains to be discussed. These two conditions will be presented with the energy equation of the wall structure since they are common between the two regions.

## II.2 Anti-Ice Bleed Air:

A widely used method of preventing ice formation is the hot air type due to its high reliability. In these systems, hot air is drawn from an intermediate or high stage compressor bleed port and ducted through passages to the leading edges of wings, empennages, engine nacelles or other critical areas. Due to the complexity of the flow of the anti-icing air inside the irregular duct shapes and the uniqueness of each design, a generalized model requires the following assumptions:

1. The heating requirement by such a system is generally specified by the amount of hot air supply,  $m_a$ , and its delivery temperature at the stagnation region.
2. The internal heat transfer coefficients  $h_i$ , between the air and the inside surface of the structure, is assumed to be known from previous experience or from experimental testing on the particular system in consideration.
3. The hot air temperature varies in the flow direction and is assumed to be lumped in the transverse direction.

With regards to the above assumptions, the energy equation of the anti-ice air may be written as:

$$m_a C_{pa} \frac{dT_a}{dz} = h_i(z) [T_a(z) - T_m(y=0, z)] \quad (12)$$

Obviously,  $T_a(z)$  depends on the solid wall temperature distribution which also depends on the runback water solutions. Therefore, the energy equations of those three regions must be solved simultaneously.

## II.3 Wall Structure:

Based on the assumption that the wall temperature is dependent on the  $y$  and  $z$ -direction [6], the following energy equation may be written for each layer in the composite structure:

$$\frac{1}{\lambda(z)} \frac{\partial}{\partial z} \left[ \lambda(z) \frac{\partial T_m}{\partial z} \right] + \frac{\partial^2 T_m}{\partial y^2} + \frac{q''}{k_m} = 0 \quad (13)$$

where  $\lambda(z)$  may be taken as the distance between two adjacent surface streamlines which make up the strip being analyzed. This distance is constant for a 2-dimensional flow over a surface. The above formulation allows one to model a heating element as one of the layers. If anti-icing is achieved by means of a hot air system alone, the value of  $q''$  may be conveniently set to zero for all the layers.

The boundary condition at the inner surface of the wall may be written for the innermost layer as:

$$-k_m \frac{\partial T_m}{\partial y} = q''_{ai} + h_i (T_a - T_m) \quad (14)$$

where  $q''_{ai}$  is an optional prescribed heat flux distribution. This value and  $h_i$  may be set to zero for a perfectly insulated inner surface. The above equations were formulated as such to give the flexibility of modeling different systems.

The two conditions that must be satisfied at each solid-solid interface between the wall layers are continuity of temperature and heat flux normal to the interface. As to the boundary conditions on the left side (stagnation point) and the right side of the wall, they may be extrapolated from the solutions using insulated conditions, or they may be specified if the temperature distribution is known at either end.

The last boundary conditions that remain are those pertaining to the outermost layer at the solid-liquid (partially or fully wetted surface) and solid-air (dry surface) interfaces. They may be written as follows:

$$T_m = T_w \quad (0 \leq F < 1) \quad (15)$$

and,

$$\dot{q}_m = -k_w F \frac{\partial T_w}{\partial y} + h_m (1-F) (T_m - T_\infty - \frac{r V_\infty^2}{2 C_{pwr}}) \quad (0 \leq F \leq 1) \quad (16)$$

The first condition is only necessary in the fully or partially wetted regions. The second condition simply states that heat,  $q''_m$ , is transferred from the wall proportionally through the wetted (to the water) and the dry (to the ambient) surface areas as defined by the wetness factor  $F$ . Note that  $T_m$ , in Eq. (16), may be replaced with  $T_w$  according to Eq. (15).

## III. Numerical Solution Techniques

### III.1 Runback Water:

A fully implicit method was used to numerically solve Eq. (5) because of the positive stability properties [9]. Backwards differencing in the  $z$ -direction, and central differencing in the  $y$ -direction were employed. Applying this scheme to Eq. (5) and rearranging terms yields:

$$-\left[ \frac{\gamma_j \Delta z}{2 \Delta y^2} \right] T_{j-1}^{n+1} + \left[ 1 + \frac{\gamma_j \Delta z}{\Delta y^2} \right] T_j^{n+1} - \left[ \frac{\gamma_j \Delta z}{2 \Delta y^2} \right] T_{j+1}^{n+1} = T_j^n \quad (17)$$

for  $j=2,3,\dots,M-1$ , where  $M$  is the total number of grid points across the film thickness (in the  $y$ -direction), and  $n$  is the grid number in the flow direction ( $z$ ). Equation (17) is written for each corresponding node which results in a set of linear equations. The latter may be rewritten in a matrix form and solved using the Thomas Algorithm for tridiagonal system of equations.

However, before carrying the solution, two equations, corresponding to  $j=1$  (solid-liquid boundary) and  $j=M$  (liquid-air boundary), are still required. A one-sided difference representation of Eqs. (16) and (5) is used for



this purpose, respectively. Equation (15) could have been used in the runback solution while Eq. (16) is used in the wall solution, instead. However, that procedure was found to be highly unstable. Thus:

$$\left[ 1 + \frac{h_m (1-F) \Delta y}{F k_w} \right] T_j^{n+1} - T_{j+1}^{n+1} = \frac{\Delta y}{F k_w} \left[ \dot{q}_m + h_m (1-F) (T_e - \frac{r V_e^2}{2 C_{p,w}}) \right] \quad (18)$$

where  $j=1$ , and  $\dot{q}_m$  is the rate of heat flux normal to the solid-liquid interface computed from the temperature distribution in the wall from the following:

$$\dot{q}_m = -k_m \frac{\partial T_m}{\partial y} \quad (\text{at solid-liquid interface}) \quad (19)$$

A second order finite differencing was used to compute the right-hand side of Eq. (19). At  $j=M$ , one may write, after rearranging terms:

$$-T_{j-1}^{n+1} + \left[ 1 + \frac{\Delta y}{k_w} (h_m \xi + \dot{m}_{imp} C_{p,w,m}) \right] T_j^{n+1} = \frac{\Delta y}{k_w} \left[ h_m \xi (T_e + \frac{r V_e^2}{2 C_{p,w}}) - \dot{m}_{evap} L_v \xi + \dot{m}_{imp} (C_{p,w,m} T_m + \frac{V_m^2}{2}) \right] \quad (20)$$

The above equations may now be solved for the temperatures at nodes  $j=1$  through  $M$  at location  $z+\Delta z$  (i.e.,  $n+1$ ), knowing the nodal temperatures at location  $z$  (i.e.,  $n$ ). The evaporation term  $\dot{m}_{evap}$  is computed using the temperature at  $z$  in order to preserve the linearity of the system of equations.

The procedure described above requires knowledge of the water temperature at the stagnation point ( $z=0$ , or  $n=1$ ). This is obtained by extrapolation from the temperature distributions at  $n=2$  and  $n=3$ . Since the solution procedure is iterative, as discussed later, an initial guess is required to start the computations. This is achieved by performing mass and energy balances on a differential control volume of the surface water at the stagnation point, which yields the following approximate expression:

$$T_w^{n+1} (\text{initial}) = \left[ \dot{m}_{imp} (C_{p,w,m} T_m + \frac{V_m^2}{2}) - \dot{m}_{evap} L_v + \dot{q}_m + h_m (T_e + \frac{r V_e^2}{2 C_{p,w}}) \right] / (\dot{m}_{imp} C_{p,w,m} + h_m) \quad (21)$$

where  $\dot{q}_m$  is estimated assuming that heat conduction within the solid structure occurs in the outward direction ( $y$ ). Equation (21) is only used at the first iteration. In subsequent iterations, the extrapolation technique mentioned previously may be used. However, this caused slight fluctuations in the temperature distribution at the first few nodes ( $n=1,2,3,4$ ). The problem was remedied by setting the initial water temperature equal to the average temperatures of nodes  $n=2$  and  $3$  without affecting the remaining results.

In addition to an initial temperature, an initial water film thickness is required. A mass balance may be

performed on a control volume of length  $\Delta z_1$  (distance between node  $n=1$  and  $n=2$ ), thickness  $\delta_f$ , and a unit depth. Using Eq. (1) with  $\lambda=1$  and  $F=1$ , this yields:

$$(\dot{m}_{imp} - \dot{m}_{evap}) \Delta z_1 = \frac{\rho \tau}{2 \mu} \delta_f^2$$

Solving for  $\delta_f$ , gives:

$$\delta_f^{n+1} (\text{initial}) = \sqrt{\frac{2 \mu \Delta z_1}{\rho \tau} (\dot{m}_{imp} - \dot{m}_{evap})} \quad (22)$$

where  $\tau$  is taken as the average wall shear force between nodes  $n=1$  and  $n=2$ .

The conservation of mass equation of the runback water may be readily obtained and shown to be:

$$\dot{m}^{n+1} = \dot{m}^n + \lambda^{n+1} \Delta z (\dot{m}_{imp} - \dot{m}_{evap} \xi) \quad (23)$$

Knowing the mass flow rate, the film thickness in the fully or partially wetted regions may be derived from Eqs. (1), (2) and (3):

$$\delta_f^{n+1} = \sqrt{\frac{2 \mu \dot{m}^{n+1}}{\rho \tau \lambda}} \quad (F=1) \quad (24)$$

$$\delta_f^{n+1} = \left[ \frac{\dot{m}^{n+1} \mu}{\rho \tau F_1(\beta)} \right]^{1/3} \sqrt{\frac{F_1(\beta)}{\sin(\beta)}} \quad (0 < F < 1) \quad (25)$$

where  $\dot{m}_r$  is the mass flow rate per rivulet. In the case where the runback water is flowing as rivulets ( $F < 1$ ), the wetness factor must be updated at each  $z$ -location. From geometric considerations, this is derived from  $F = (2R \sin \beta) / \lambda$  where  $R$  is obtained from Eq. (3). However, if surface streamlines are not parallel (3-D flow), great care must be taken when evaluating  $\lambda$  to account for variations in the distance between two surface streamlines which identify the strip being analyzed.

The numerical solution of Eqs. (17), (18) and (20) requires the discretization of the water domain into grid points. Across the liquid layer thickness, equal spacing between the grid points was used. Along the flow direction, two zones were selected: direct impingement region, and downstream region. The grid spacing is constant in each zone, but is much smaller in the direct impingement region to accommodate for the rapidly changing variables due to the impinging water droplets and the flowfield characteristics.

The current model was specifically developed for anti-icing applications where at least the minimum heat required to keep the surface water from freezing is supplied to the surface. This is because a two-dimensional phase-change model was found to be inappropriate since freezing will normally start at the liquid-air interface, which creates a problem in modeling the flow characteristics of the unfrozen water. However, since the temperature drop across the film thickness is small, the temperature may be assumed to be uniform across the layer. Therefore, when a freezing temperature, or lower, is obtained during the calculation process, an alternate method is used. This

consists of performing a macroscopic energy balance on the surface water to obtain the freezing fraction, such as done in the LEWICE code [1]. Nevertheless, the rivulet configuration and its prediction remain the same. This enables one to predict the amount and location of ice accumulation during a specified period of exposure time.

### III.2 Anti-Ice Bleed Air:

The governing energy equation of the anti-ice bleed air, Eq. (12), is a first order ordinary differential equation (ODE). Due to the arbitrary distribution of the heat transfer coefficient and the wall temperature at the inside surface of the solid structure, a numerical technique must be used to solve the latter equation.

A forward finite difference scheme is only first order accurate. A more accurate and widely used technique for solving ODE's, is the fourth order Runge-Kutta method [10]. Knowing the temperature distribution in the wall, from the most recent iteration, the latter method is used to predict or update the hot air temperature distribution in the cowl. The result is subsequently used in the wall temperature solution at the next iteration.

In cases where anti-icing is achieved by means other than the hot air type (i.e.,  $m_a=0$ ), the solution of Eq. (12) using the aforementioned technique should be avoided. Instead, the air in the cowl is considered to be stagnant and at a prescribed temperature. Also, when the internal heat transfer coefficient is zero (i.e., insulated inner surfaces), there is no need to solve Eq. (12) since the result is a constant air temperature which does not affect the wall temperature, and consequently the runback water temperature.

### III.3 Wall Structure:

A solution for the different layers in the wall structure may be obtained by direct approximation of the governing equation, Eq. (13), and the corresponding boundary conditions by finite differences. However, the control volume approach was chosen due to its accurate conservation properties [7]. Difference equations are derived by performing an energy balance on each control volume corresponding to a particular node. The control surfaces of each control volume are half way between the corresponding node and its adjacent surrounding nodes. There exist eleven types of nodes in the wall structure. These types are listed below and correspondingly numbered as shown in Fig 2, which illustrates a two-layer wall (note that the wall thickness dimension compared with its length is exaggerated for clarity):

1. Totally internal node.
2. Inner surface side node.
3. Inner surface left-corner node.
4. Inner surface right-corner node.
5. Left-side internal node.
6. Right-side internal node.
7. Solid-solid interface internal node.
8. Solid-solid interface left-side node.
9. Solid-solid interface right-side node.

10. Outer totally/partially wetted surface node.

11. Outer totally dry surface node.

Energy balance equations for all node types are derived and presented below. The following definitions were used:

$$\beta = \frac{\Delta z}{\Delta y}, \quad \kappa_l = \frac{k_{l+1}}{k_l}, \quad \varepsilon_l = \frac{\Delta z}{\Delta y_l}, \quad \text{and} \quad \Omega_l = \frac{\Delta y_{l+1}}{\Delta y_l} \quad (26)$$

where  $l$  and  $l+1$  indicate the layer numbers corresponding to a particular solid-solid interface. Note that in the following, node  $(i,j)$  denotes the grid point at row " $i$ " and column " $j$ ", and that  $\lambda_i$  represents the distance between the two surface streamlines, defining the width of the wall strip being analyzed, at column " $i$ ":

Node type 1:

$$\begin{aligned} & \beta^2 T_{i,j-1} + \left[ 1 - \frac{\lambda_i - \lambda_{i-1}}{2 \lambda_i} \right] T_{i-1,j} \\ & - \left[ 2(\beta^2 + 1) - \frac{\lambda_i - \lambda_{i-1}}{2 \lambda_i} + \frac{\lambda_{i+1} - \lambda_i}{2 \lambda_i} \right] T_{i,j} \\ & + \left[ 1 + \frac{\lambda_{i+1} - \lambda_i}{2 \lambda_i} \right] T_{i+1,j} + \beta^2 T_{i,j+1} = - \frac{\Delta z^2}{k} q^o \end{aligned} \quad (27)$$

Node type 2:

$$\begin{aligned} & \left[ 2(\beta^2 + 1) - \frac{\lambda_i - \lambda_{i-1}}{2 \lambda_i} + \frac{\lambda_{i+1} - \lambda_i}{2 \lambda_i} + \frac{2 \Delta z^2 h_i}{k \Delta y} \right] T_{i,j} \\ & - \left[ 1 - \frac{\lambda_i - \lambda_{i-1}}{2 \lambda_i} \right] T_{i-1,j} - \left[ 1 + \frac{\lambda_{i+1} - \lambda_i}{2 \lambda_i} \right] T_{i+1,j} - 2 \beta^2 T_{i,j+1} \\ & = \frac{\Delta z^2}{k} \left[ \frac{2}{\Delta y} (h_i T_a + q_{ai}) + q^o \right] \end{aligned} \quad (28)$$

Node type 3:

If the temperature distribution is not specified at  $z=0$ , an insulated boundary condition is used:

$$\begin{aligned} & \left[ 1 + \beta^2 + \frac{\lambda_{i+1} - \lambda_i}{2 \lambda_i} + \frac{\Delta z^2 h_i}{k \Delta y} \right] T_{i,j} - \left[ 1 + \frac{\lambda_{i+1} - \lambda_i}{2 \lambda_i} \right] T_{i+1,j} \\ & - \beta^2 T_{i,j+1} = \frac{\Delta z^2}{k} \left[ \frac{1}{\Delta y} (h_i T_a + q_{ai}) + \frac{q^o}{2} \right] \end{aligned} \quad (29)$$

Node type 4:

Similarly, for unspecified temperature:

$$\begin{aligned} & \left[ 1 + \beta^2 - \frac{\lambda_i - \lambda_{i-1}}{2 \lambda_i} + \frac{\Delta z^2 h_i}{k \Delta y} \right] T_{i,j} - \left[ 1 - \frac{\lambda_i - \lambda_{i-1}}{2 \lambda_i} \right] T_{i-1,j} \\ & - \beta^2 T_{i,j+1} = \frac{\Delta z^2}{k} \left[ \frac{1}{\Delta y} (h_i T_a + q_{ai}) + \frac{q^o}{2} \right] \end{aligned} \quad (30)$$

Node type 5:

For unspecified temperature:

$$\begin{aligned}
& -\beta^2 T_{i,j-1} + \left[ 2(\beta^2 + 1) + \frac{\lambda_{i+1} - \lambda_i}{\lambda_i} \right] T_{i,j} \\
& - \left[ 2 + \frac{\lambda_{i+1} - \lambda_i}{\lambda_i} \right] T_{i+1,j} - \beta^2 T_{i,j+1} = \frac{\Delta z^2}{k} q''_o \quad (31)
\end{aligned}$$

#### Node type 6:

For unspecified temperature:

$$\begin{aligned}
& -\beta^2 T_{i,j-1} - \left[ 2 - \frac{\lambda_i - \lambda_{i-1}}{\lambda_i} \right] T_{i-1,j} \\
& + \left[ 2(\beta^2 + 1) - \frac{\lambda_i - \lambda_{i-1}}{\lambda_i} \right] T_{i,j} - \beta^2 T_{i,j+1} = \frac{\Delta z^2}{k} q''_o \quad (32)
\end{aligned}$$

#### Node type 7:

$$\begin{aligned}
& - \left[ \frac{1 + \kappa_l \Omega_l}{2} \right] \left[ 2 - \frac{\lambda_i - \lambda_{i-1}}{2\lambda_i} + \frac{\lambda_{i+1} - \lambda_i}{2\lambda_i} \right] + \varepsilon^2 \left[ 1 + \frac{\kappa_l}{\Omega_l} \right] T_{i,j} \\
& + \left[ \frac{1 + \kappa_l \Omega_l}{2} \right] \left[ 1 + \frac{\lambda_{i+1} - \lambda_i}{2\lambda_i} \right] T_{i+1,j} + \varepsilon^2 \frac{\kappa_l}{\Omega_l} T_{i,j+1} = \\
& - \frac{\Delta z^2}{2k_i} [q''_o + \Omega_l q''_{o+1}] \quad (33)
\end{aligned}$$

#### Node type 8:

For unspecified temperature:

$$\begin{aligned}
& \varepsilon^2 T_{i,j-1} - \left\{ (1 + \kappa_l \Omega_l) \left[ 1 + \frac{\lambda_{i+1} - \lambda_i}{2\lambda_i} \right] + \varepsilon^2 \left[ 1 + \frac{\kappa_l}{\Omega_l} \right] \right\} T_{i,j} \\
& + (1 + \kappa_l \Omega_l) \left[ 1 + \frac{\lambda_{i+1} - \lambda_i}{2\lambda_i} \right] T_{i+1,j} + \varepsilon^2 \frac{\kappa_l}{\Omega_l} T_{i,j+1} = \\
& - \frac{\Delta z^2}{2k_i} [q''_o + \Omega_l q''_{o+1}] \quad (34)
\end{aligned}$$

#### Node type 9:

$$\begin{aligned}
& \varepsilon^2 T_{i,j-1} + (1 + \kappa_l \Omega_l) \left[ 1 - \frac{\lambda_i - \lambda_{i-1}}{2\lambda_i} \right] T_{i-1,j} \\
& - \left\{ (1 + \kappa_l \Omega_l) \left[ 1 - \frac{\lambda_i - \lambda_{i-1}}{2\lambda_i} \right] + \varepsilon^2 \left[ 1 + \frac{\kappa_l}{\Omega_l} \right] \right\} T_{i,j} \\
& + \varepsilon^2 \frac{\kappa_l}{\Omega_l} T_{i,j+1} = - \frac{\Delta z^2}{2k_i} [q''_o + \Omega_l q''_{o+1}] \quad (35)
\end{aligned}$$

#### Node type 10:

In this region, the node temperature is set equal to the local liquid temperature at the base of the film. This is achieved using a cubic spline interpolation technique because the interfacial grid points of the water and the solid do not coincide.

#### Node type 11:

For consistency with the lower boundary of the liquid layer, a direct differencing of the equation representing convective heat loss to the ambient is applied. This yields:

$$-T_{i,M-1} + \left( 1 + \frac{h_\infty \Delta y}{k} \right) T_{i,M} = \frac{h_\infty T_\infty \Delta y}{k} \quad (36)$$

### III.4 Solution Procedure:

The required solutions are the temperature distributions in the anti-ice hot air, the solid structure, and the runback water. In addition, the surface water mass flow rate and the film/rivulets configuration must be determined. A simultaneous solution must be carried in the three regions: (1) runback water; (2) solid structure; and (3) anti-ice bleed air. This may not be accomplished in a single step due to the dependency of some boundary conditions of a particular region on the final solution in the adjacent region. This suggests the use of an iterative type of numerical solution between the three regions.

The sequence of the steps utilized in the numerical solution iterative procedure may be listed as follows:

- (1) Estimate  $q''_m$ , in Eq. (18), at all nodes corresponding to the runback water at  $j=1$ . The procedure is to use a local one-dimensional heat transfer model from the wall to the free stream air (i.e., no conduction within the wall in the flow direction), assuming a fully dry surface. Any heat transfer generated due to electrical heating elements is assumed to flow outboard to the ambient. These assumptions were necessary to get the iterative solution started.
- (2) Compute the "initial" water temperature and the film thickness at the stagnation location from Eqs. (21) and (22), respectively.
- (3) Solve Eqs. (17), (18), and (20) for the runback water temperature distribution across the film thickness at the next  $z$ -location. Proceed with the solution of the latter equations by marching to the location of the impingement limit. This, of course, corresponds to the direct impingement region where the wetness factor is unity. Note that the runback water mass flow rate and the film thickness are updated using Eqs. (23) and (24), respectively, as the solution is brought to the next level.
- (4) From the impingement limit onward, check if the criteria for film breakup are met as the march proceeds downstream with the solution. If breakup occurs, the wetness factor and the rivulet configuration are predicted [5]. Then proceed with the calculations for each step up to the end of the structure or up to the location where total evaporation occurs. The film thickness is updated using Eq. (24) or (25), and the wetness factor is updated by geometric considerations after each  $\Delta z$  step.
- (5) Generally, a larger number of nodes is used in the runback water than in the wall at the solid-liquid interface. Thus, a cubic spline interpolation technique is used to predict the wall nodal temperatures, for node type 10, from the water nodal temperatures at the interface.
- (6) Setup the equations corresponding to convective boundary condition, Eq. (36), for nodes of type 11, if total evaporation occurs upstream of the end of the structure.

- (7) Assume a constant anti-ice bleed air temperature equal to the delivery temperature at the stagnation region.
- (8) Setup the equations corresponding to the rest of the solid structure nodes, types 1 through 9.
- (9) Solve the linear system of equations for the wall nodal temperatures. This terminates the first iteration.
- (10) Compute  $q''_m$  from Eq. (19) using the temperature distribution obtained in the previous step, and interpolate for the runback nodes using cubic splines. Under-relaxation of the latter values should be used to carry a stable solution as follows:

$$q''_m^{n+1} = q''_m^n + F (q''_m^{n+1} - q''_m^n)$$

where  $F$  is the under-relaxation factor and has a value between zero and unity. Its actual value depends on the particular problem under consideration.

- (11) Evidently, the solution would not converge in one iteration. Extrapolate for the initial water temperature as previously discussed, and compute the film thickness at stagnation from Eq. (22).
- (12) Repeat the runback water solution as described in steps (3) and (4).
- (13) Set the wall temperature at the solid-liquid interfacial nodes in the wet region by interpolation from the water solution of step (12). Also setup the convective boundary condition equations in the dry region as done in step (6).
- (14) Solve for the temperature of the anti-ice bleed air as described in section III.2, using the most recent wall temperature distribution at the inner surface.
- (15) Setup the equations corresponding to the remaining wall nodes as in step (8), then solve the system of linear equations for the wall nodal temperatures.
- (16) Compare the solutions obtained in the previous step with the corresponding solutions of step (5). If the difference is within an acceptable tolerance, the solution is considered converged. Otherwise, perform another iteration by repeating the last few steps starting with step (9).

#### IV. Sample Calculations and Discussion

The primary purpose of this paper was to present the details of the mathematical development and the numerical solution techniques of the current model. Therefore, only one example problem will be considered in order to demonstrate the calculation procedure. However, several other cases were considered and presented in Ref. [11]. The complete solution to the problem is resolved in three major steps: (1) flowfield calculations, including the viscous layer near the wall; (2) individual water droplet trajectory calculations using the velocities calculated in the previous step; and, finally, (3) the heat transfer calculations for the anti-ice hot air, the solid structure, and the surface water.

In the following example, the solid structure is assumed to be a NACA 0012 airfoil of chord length equal to 1.0 m, as illustrated in Fig. 3. The wall structure of

the airfoil is composed of five layers, typical of some aircraft surfaces. Properties and dimensions of these layers are illustrated in Table 1. The electrical heater, center layer, is assumed to be turned off and heating of the surface is accomplished by spraying hot air on the inside surface of the cowling near the stagnation region. The air is delivered at a temperature of 200 °C and a mass flow rate of 0.1 Kg/sec per unit spanwise distance.

The ambient operating conditions are the following:

- Flight Mach number = 0.25
- Ambient static temperature = -12 °C
- Ambient static pressure = 90.75 kPa
- Angle of attack = 0°
- Cloud Liquid Water Content = 1.0 g/m<sup>3</sup>
- Relative humidity = 100%
- Mean volume droplet diameter = 20 μm

The flowfield around the airfoil was computed using the ARC2D code which solves the two-dimensional thin layer Navier-Stokes equation. A hyperbolic grid generator was used to produce a C-type grid structure around the airfoil: 239 nodes along the surface and 55 nodes in the normal direction. Grids were packed near the wall for accurate prediction of the large gradients induced by viscous effects in these regions. The resulting pressure coefficient and friction coefficient distributions are illustrated in Figs. (4) and (5), respectively. These coefficients are defined as follows:

$$C_p = \frac{P - P_\infty}{\frac{1}{2} \rho_\infty V_\infty^2}$$

$$\text{and, } C_f = \frac{\tau}{\frac{1}{2} \rho_\infty V_\infty^2}$$

The first coefficient may be used to calculate properties at the edge of the boundary layer, and the second is used to compute the wall shear stress that cause the water to run back.

A particle trajectory code was then used to produce a collection efficiency distribution on the surface, as illustrated in Fig. 6. Note that all the results presented thus far are symmetric between the upper and the lower surfaces of the airfoil. This is due to the fact that the flow angle of attack is zero and the airfoil geometry is symmetric.

The final step involves the heat transfer calculations. The external convective heat transfer coefficients, between the wall surface and the ambient air, were computed using a sand roughness factor of  $k_s/c=0.0002$  [1]. The internal heat transfer coefficients, between the hot air and the inner surface of the airfoil cowl were arbitrarily assumed since they depend on the particular air jet nozzles design, the rate of air flow, and the air passages geometry. These coefficients are shown in Fig. 7.

The procedure described earlier is applied, using the results thus far obtained, to solve for the problem variable parameters. The contact angle between the rivulets and the surface, when breakup of the film occurs, is assumed to be

$\beta=40^\circ$ . The actual value of  $\beta$  depends on the properties of the solid surface and its roughness.

The resulting average temperature distribution of the anti-ice air inside the cowl is illustrated in Fig. 8. The air temperature drop across the entire length of the airfoil is approximately 85 °C. The drop occurs in a relatively smoother manner compared to that of the runback water average temperature, shown in Fig. 9. This is due to the distribution of the corresponding convective heat transfer coefficients. Since the solid wall conductivity is relatively larger than that of water, its average temperature distribution tends to be smoother as depicted in Fig. 9.

The distribution of the heat flux leaving the outer surface of the airfoil is plotted in Fig. 10. The curve peaks are due to the peaks in the distribution of the external heat transfer coefficients which correspond to a transition from laminar to turbulent flow. Figures 11 and 12 are plots of the runback water film thickness and the wetness factor, respectively. The sudden jumps in the curves correspond to the breakup of the uniform film in the direct impingement region ( $F=1$ ) into individual rivulets ( $F<1$ ).

The corresponding distribution of the runback surface mass flow rate per unit spanwise distance is shown in Fig. 13. This system is clearly a running wet anti-icing system. Total evaporation may be better accomplished with electrical heating elements such that a large amount of heat is supplied to the direct impingement regions.

## V. Concluding Remarks

A numerical simulation for "running wet" aircraft anti-icing systems was developed. The model includes breakup of the water film, which exists in regions of direct impingement, into individual rivulets. The wetness factor distribution resulting from the film breakup and the rivulet configuration on the surface were predicted in the numerical solution. The solid wall was modeled as a multi-layer structure and the anti-icing system used was of the thermal type utilizing hot air and/or electrical heating elements embedded within the layers. The mathematical formulation of the heat transfer process as well as details of the numerical solution procedure were presented.

Experimental tests were recently conducted in the NASA Lewis Icing Research Tunnel to validate the current model. A detailed comparison with the numerical results was not possible at the time this manuscript was written since the data acquired were not reduced. However, similar trends were observed between the computer code predictions and the experimental results. Further detailed comparisons will be carried in the near future.

## Acknowledgements

A portion of his work was done while the first author held a *National Research Council Research Associateship* at *NASA Lewis Research Center*. The sponsorship of these two organizations is gratefully acknowledged.

## References

1. Ruff, G.A., and Berkowitz, B.M., "Users Manual for the NASA Lewis Ice Accretion Prediction Code (LEWICE)," NASA CR-185129, May 1990.
2. Cebeci, T., Chen, H.H., and Alemdaroglu, N., "Fortified LEWICE with Viscous Effects," AIAA Paper 90-0754.
3. Yamaguchi, K., Hansman, R., and Karmierczak, M., "Deterministic Multi-Zone Ice Accretion Modeling," AIAA Paper 91-0265.
4. Hansman, R.J., Yamaguchi, K., Berkowitz, B., and M. Potapczuk, "Modeling of Surface Roughness Effects on Glaze Ice Accretion," AIAA Paper 89-0734, Jan 1989.
5. Al-Khalil, K.M., Keith, T.G., De Witt, K.J., "Development of an Anti-Icing Runback Model," AIAA Paper 90-0759, Jan 1990.
6. Al-Khalil, K.M., Keith, T.G., De Witt, K.J., "Further Development of an Anti-Icing Runback Model," AIAA Paper 91-0266, Jan 1991.
7. Al-Khalil, K.M., "Numerical Simulation of an Aircraft Anti-Icing System Incorporating a Rivulet Model for the Runback Water," PhD Dissertation, University of Toledo, Toledo, Ohio, June 1991.
8. Gelder, T. F., and Lewis, J. P., "Comparison of Heat Transfer from Airfoil in Natural and Simulated Icing Condition," NACA TN - 2480, September, 1951.
9. Anderson, D.A., Tannehill, J.C., and Pletcher, R.H., *Computational Fluid Mechanics and Heat Transfer*, Hemisphere Pub. Corp., 1984.
10. Carnahan, B., Luther, H. A., and Wilkes, J. O., *Applied Numerical Methods*, John Wiley & Sons, Inc., 1969, pp. 363-366.
11. Al-Khalil, K.M., Keith, T.G., De Witt, K.J., "Development of an Improved Model for the Runback Water on Aircraft Surfaces," AIAA Paper 92-0042, Jan 1992.

**Table 1: Composite Wall Physical and Thermal Properties.**

Layer number	Description	Material	Thickness (mm)	Thermal Conductivity (W/m.K)
1	Substrate	Aluminum Alloy	2.20	220
2	Inner Insulation	Epoxy/Glass	1.30	1.25
3	Heater*	Copper	0.20	340
4	Outer Insulation	Epoxy/Glass	0.25	1.25
5	Abrasion Shield	Stainless Steel	0.30	50

\*Heater turned off

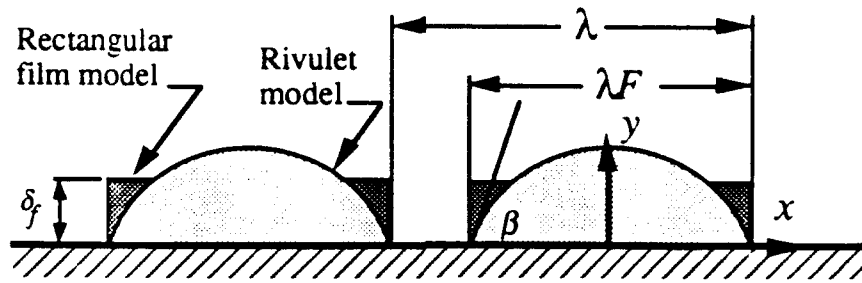


Fig. 1: Rivulet and equivalent rectangular film models.

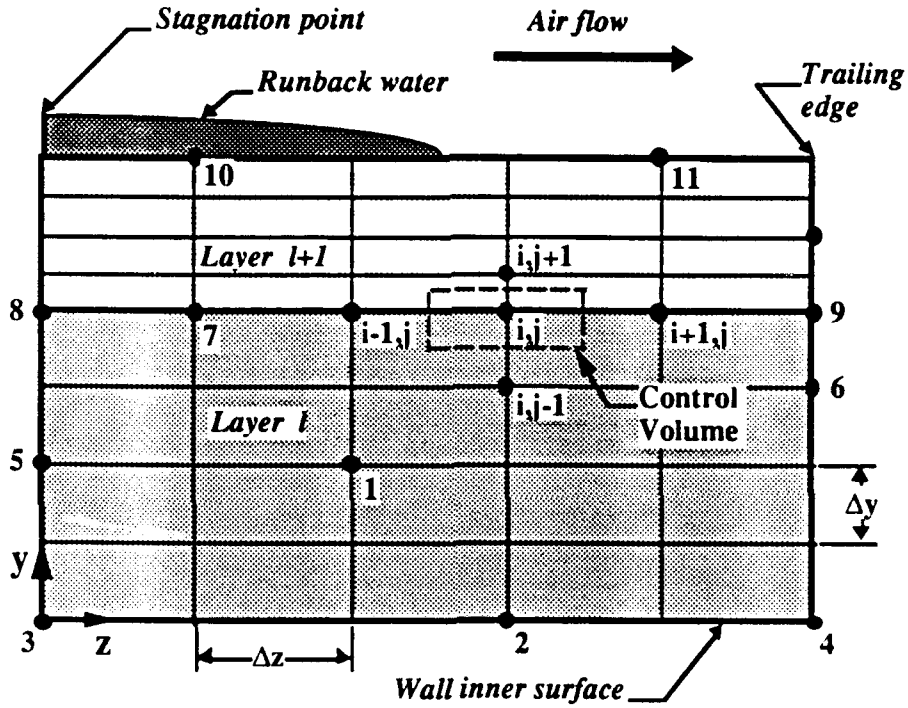


Fig. 2: Type of grid points in the wall.

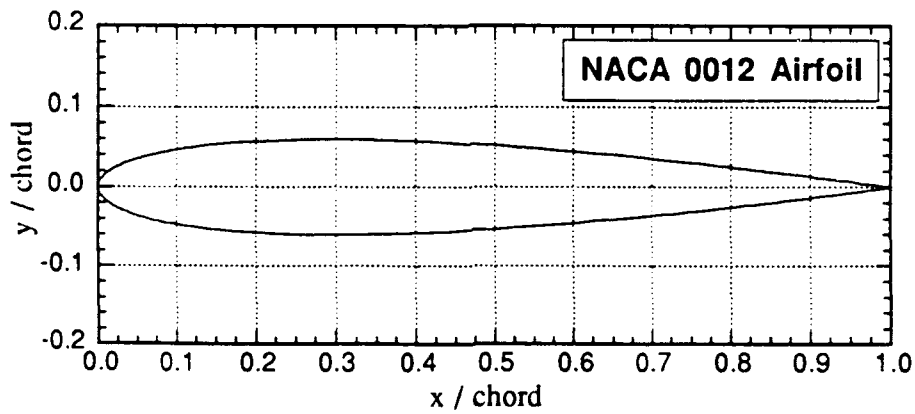


Fig. 3: NACA 0012 airfoil geometry.

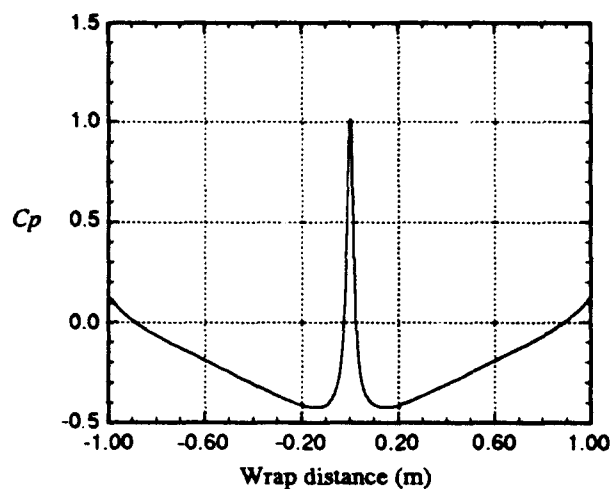


Fig. 4: Surface pressure coefficient.

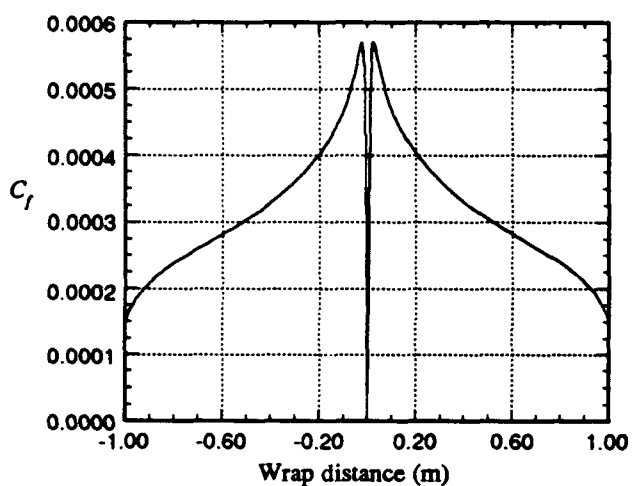


Fig. 5: Skin friction coefficient.

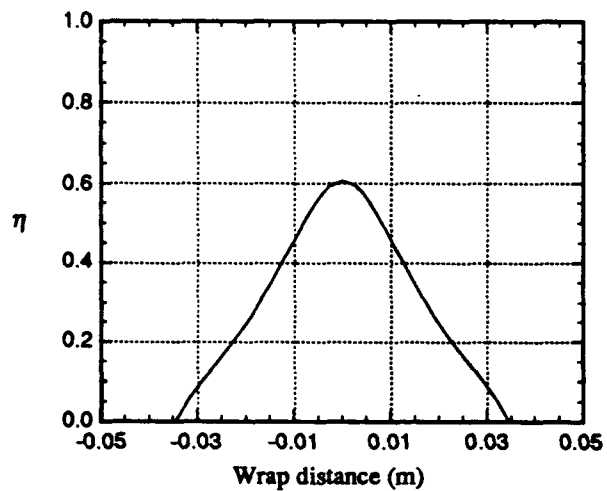


Fig. 6: Droplet collection efficiency.

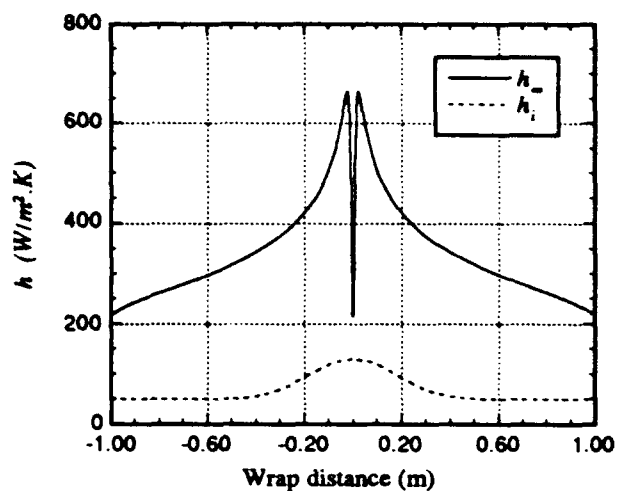


Fig. 7: Internal and external heat transfer coefficients.

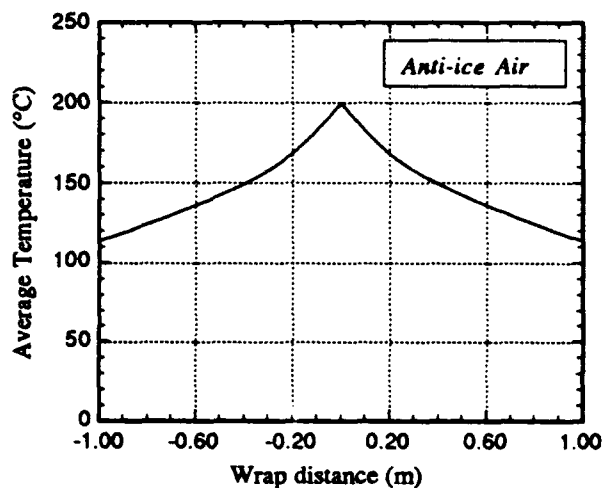


Fig. 8: Anti-ice air temperature.

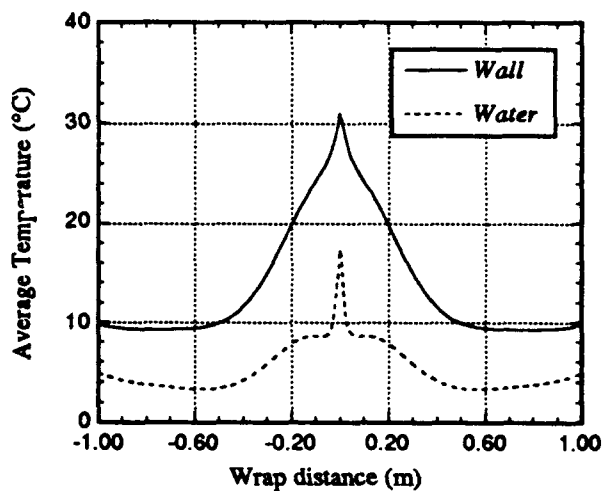
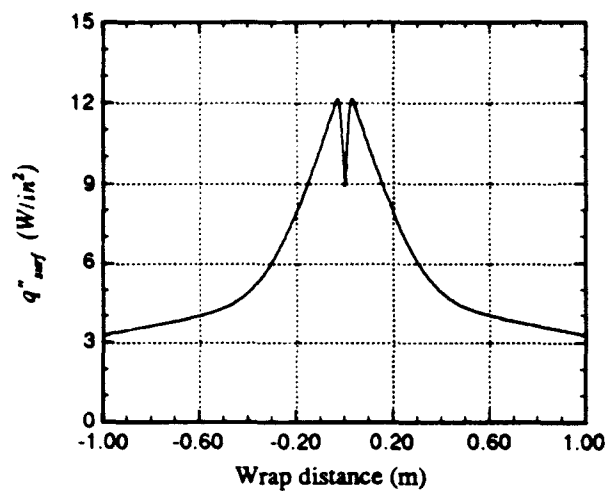
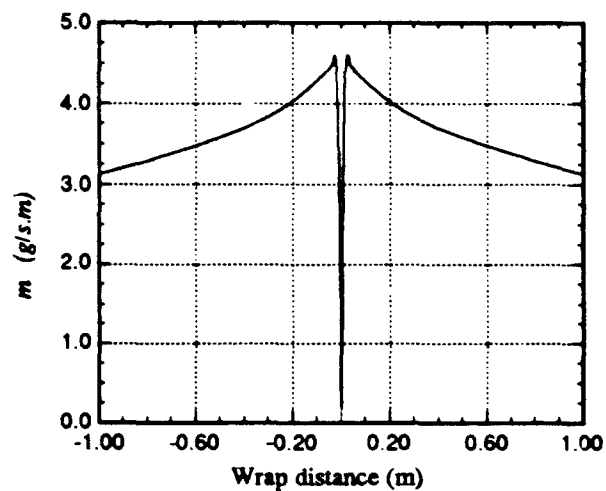


Fig. 9: Average water and wall temperatures.



**Fig. 10: Surface heat flux.**



**Fig. 13: Surface water mass flow rate.**

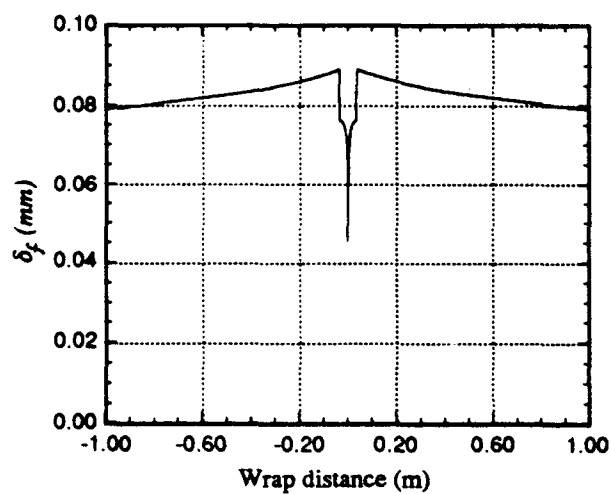


**Fig. 11: Runback water film thickness.**

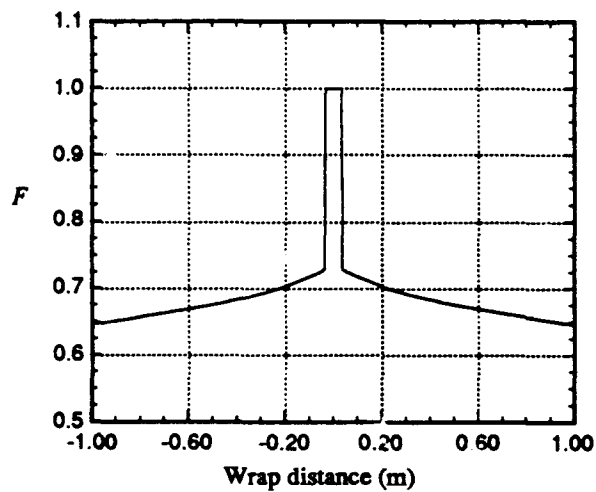


**Fig. 12: Wetness factor.**



**AIRCRAFT ICING, 2**  
**SESSION 4**

# A COMPOSITE STRUCTURED/UNSTRUCTURED-MESH EULER METHOD FOR COMPLEX AIRFOIL SHAPES

by

H. Hefazi\*  
Aerospace Engineering Department  
California State University, Long Beach

and

L. T. Chen\*\*  
Douglas Aircraft Company  
Long Beach, California

## Abstract

A general two-dimensional Euler zonal method has been developed for computing flows about complex airfoil geometries such as multielement and iced airfoils. The method utilizes a composite structured and unstructured grid generated using conformal mapping and Delaunay triangulation, respectively. The finite-volume Euler method is then modified to couple solutions in the zones with structured and unstructured grids. Solutions about an iced airfoil and a multielement airfoil are given as examples of applications of the scheme.

## 1.0 Introduction

The aerodynamic analysis of complex airfoil sections continues to receive much attention in experimental, theoretical and computational studies. Such analyses of airfoil flows include iced airfoils, multielement airfoils, and advanced airfoil concepts with divergent trailing edges. Conventional computational methods based on a single zone mesh, developed for simple airfoil configurations, are generally not suitable for these geometries since a single structured grid of sufficient quality cannot be generated. Zonal or unstructured-mesh methods that can provide adequate mesh resolution near high pressure gradient regions in each zone are needed to handle the complexity of the flowfields. An attractive zonal approach is to use structured meshes in most parts of the domain and unstructured meshes in enclosed regions next to the portions of airfoil that are difficult to model with structured grids. The objective of this paper is to develop a general two-dimensional Euler method based on this approach.

Although many methods have been developed for the generation of structured grids around simple geometries, few can be readily extended to complicated two- and three-dimensional shapes such as multielement or iced airfoils or multicomponent aircraft configurations. Also, in many applications of structured grids, the quality of the generated mesh is not uniform throughout the computational domain, resulting in poor resolution in specific regions of importance. For this reason, triangular (tetrahedral) meshes have proven very attractive, since relatively complex geometries can be meshed efficiently, and an almost arbitrary degree of mesh adaption and refinement can be achieved by the addition of control points. Furthermore, the development of flow algorithms that

do not depend on the inherent structure of the grid points have eliminated the restriction of grid structure and made triangles and tetrahedrons suitable shapes with which to resolve complicated geometric regions.

The debate over relative advantages of structured and unstructured grid methods is an ongoing matter. While unstructured grid methods have the clear advantage in that they can treat complicated problems such as a complete aircraft configuration under static or dynamic deformation,<sup>1</sup> they have been regarded as less efficient and less accurate than their structured counterparts.<sup>2,3</sup> Lack of robust acceleration techniques, such as multigrid schemes for three-dimensional problems, is also a clear disadvantage. Furthermore, direct and implicit solvers for unstructured grids are developed, but in general are not as efficient and effective as their structured counterparts.<sup>4,5</sup> Structured flow solvers have many other highly desirable features including efficient grid generation techniques and smaller computer time and memory requirements.

An efficient way of analyzing a complex geometry of several components is through a zonal approach, using composite structured and unstructured grids. This approach requires considerably less memory than using an entire unstructured mesh capable of handling the same geometry. In view of the different desirable features of structured and unstructured meshes, the present zonal approach takes advantage of structured meshes in appropriate regions while using the versatility of the unstructured grids in others.

In this paper, a general two-dimensional zonal boundary interactive scheme utilizing combinations of structured and unstructured mesh types is presented. Solutions for flow about multielement and iced airfoils are given as an example of the application of the scheme.

## 2.0 Grid Generation

A brief grid generation process will be described in this section. A base structured grid which encompasses the entire flowfield is first generated using existing methods. Regions of undesirable grid quality are then identified and categorized as subsequent unstructured-mesh zones. Triangular grids can be generated in these regions using existing mesh points and additional points as necessary. An unstructured grid generation method based on Delaunay triangulation, developed earlier,<sup>6</sup> is applied for this purpose. An essential requirement for obtaining satisfactory meshes when using the Delaunay triangulator is

\*Associate Professor.

\*\*Senior Principal Engineer/Scientist.

appropriate placement of interior points, since this scheme gives no guidance on where to place the mesh points. Inappropriate placement of mesh points results in poor quality meshes, even though they satisfy the Delaunay criteria. Therefore, certain criteria for introducing interior mesh points have to be established before applying the Delaunay triangulation.

The Delaunay triangulation method is applied in three steps to generate triangular meshes in the unstructured zone enclosed by the surrounding structured meshes and solid surface boundary. The first step is to triangulate the points along the body and zonal boundaries in order to obtain an initial triangulation based solely on existing boundary points.

The second step deals with the placement of interior points. It is important to place a sufficiently dense mesh of points in high gradient regions such as corner regions, leading- and trailing-edge regions, etc. A combination of C-mesh points around the leading edge and Cartesian mesh points in other parts of the domain can be chosen as the interior points. Based on Bowyer's algorithm,<sup>7</sup> a series of new points are added one by one to the existing triangulation, removing triangles close to the point being inserted, and reconnecting the new point to the existing nodes in such a way as to form new triangles which satisfy the Delaunay criteria. This procedure is repeated for all new points introduced in the domain.

The final phase is a grid-smoothing procedure. This is necessary because points that are introduced sometimes fall too close to each other, resulting in skewed triangles, such as triangles with large aspect ratios. An iterative Laplacian smoothing scheme is applied to improve the overall quality of the unstructured mesh.

### 3.0 Finite Volume Scheme and Time-Stepping

Finite volume Euler methods of Jameson<sup>8</sup> and Mavriplis and Jameson<sup>9</sup>, using fourth-order Runge-Kutta time-stepping, are adopted to interactively solve for the flows in different zones. These methods are briefly reviewed here to point out some modifications that are made in the present work.

The Euler equation for two-dimensional inviscid flow in integral form for a region  $\Omega$  with a boundary  $\partial\Omega$  is given as

$$\frac{\partial}{\partial t} \iint_{\Omega} w dx dy + \int_{\partial\Omega} (f dy - g dx) = 0 \quad (1)$$

where  $x$  and  $y$  are Cartesian coordinates and

$$w = \begin{bmatrix} \rho \\ \rho u \\ \rho v \\ \rho E \end{bmatrix}; \quad f = \begin{bmatrix} \rho u \\ \rho v^2 + p \\ \rho uv \\ \rho uH \end{bmatrix}; \quad g = \begin{bmatrix} \rho v \\ \rho uv \\ \rho v^2 + p \\ \rho vH \end{bmatrix} \quad (2)$$

Here  $\rho$ ,  $u$ ,  $v$ ,  $p$ ,  $E$  and  $H$  are density, velocity components, pressure, total energy, and total enthalpy, respectively. For a perfect gas we have

$$E = \frac{p}{(\gamma-1)\rho} + \frac{u^2 + v^2}{2}, \quad H = E + \frac{E}{\rho}$$

Thus, we only need to solve for four variables:  $\rho$ ,  $\rho u$ ,  $\rho v$  and  $\rho E$ . Equation (1) is discretized over individual control volumes (triangles) in a cell-centered approximation in which the flow variables are stored at the center of each cell. The above discretization procedure with the addition of artificial dissipation terms results in a set of ordinary differential equations.

$$S_1 \frac{dw_1}{dt} + [Q(w_1) - D(w_1)] = 0 \quad (3)$$

where  $S_1$  is the area of the cell,  $Q$  is the spatial approximation of fluxes given by the second part of Eq. (1), and  $D$  is an appropriately constructed dissipation operator.

The fourth-order Runge-Kutta scheme is used to advance the solution in time from time step  $n$  to time step  $n+1$ . With the nonlinear operator  $P$  defined as

$$P(w) = \frac{1}{S} [Q(w) - D(w)] \quad (4)$$

we have

$$\begin{aligned} w^{(0)} &= w^n \\ w^{(1)} &= w^{(0)} - \frac{\Delta t}{2} P[w^{(0)}] \\ w^{(2)} &= w^{(0)} - \frac{\Delta t}{2} P[w^{(1)}] \\ w^{(3)} &= w^{(0)} - \Delta t P[w^{(2)}] \\ w^{(4)} &= w^{(0)} - \frac{\Delta t}{6} \{P[w^{(1)}] + 2P[w^{(1)}] \\ &\quad + 2P[w^{(2)}] + P[w^{(3)}]\} \\ w^{n+1} &= w^{(4)} \end{aligned} \quad (5)$$

The artificial dissipation operator is calculated in the first and third step only to save computing costs.

In the region with structured grids implicit residual averaging is used to increase the base of the CFL number. It is shown<sup>10</sup> that implicit smoothing increases the stability to Courant numbers much greater than the Courant number limit of the explicit scheme. The calculations presented in this work are obtained with a CFL number of 7. In addition, a variable time step, based on the maximum stability limit set by the local Courant number, and enthalpy damping are used to accelerate the convergence of the solution. Dissipation terms are formed as a blend of second- and fourth-order terms, coefficients of which are adapted to the flow. The resulting scheme is second-order accurate in the regions of smooth flow and first-order accurate near the shocks. To ensure that these dissipative terms are significant only in the vicinity of a shock, the second-order dissipation terms are scaled by the local Laplacian in the pressure.

Similar to the structured flow solver, in the unstructured flow solver fourth-order Runge-Kutta time stepping is also used to advance the solution in time. The support of the time-stepping scheme

here is, however, increased by an explicitly residual averaging scheme. If the residuals at cell 1 are

$$R_1(w) = \frac{1}{S_1} [Q(w_1) - D(w_1)]$$

they are replaced by

$$\bar{R}_1 = \epsilon R_1 + \frac{1-\epsilon}{3} \sum_{k=1}^3 R_{1k}$$

where  $R_{1k}$  are residuals at three forming points of the triangular cell. The residuals at nodal points are obtained as the average of residuals at all cells having that point in common.  $\epsilon$  is a constant which is chosen as 0.6. With this smoothing scheme, the CFL number for the unstructured flow solver could also be increased to about 7.

It is found that the CFL number in the two zones must be similar to facilitate the convergence of the solution in the entire domain.

#### 4.0 Dissipative Terms

The structured flow solver uses a blend of second- and fourth-order dissipation terms to prevent odd and even decoupling of the solution. The artificial dissipation for the unstructured flow solver is similarly constructed as a blend of undivided Laplacian and biharmonic operators. Generally, in the absence of shocks in subsonic flows, only biharmonic dissipation is required. However, it is found that in regions of large pressure gradients such as at the leading edge of the flap, second-order dissipation terms are still needed even in the subsonic flow regime.

To obtain the fourth-order dissipation term in the triangular mesh zone, an undivided four-point Laplacian operator is first defined as

$$\nabla^2 w_1 = \sum_{k=1}^3 w_k - 3w_1$$

where  $w$  represents the flow variables  $\rho$ ,  $\rho u$ ,  $\rho v$ , and  $\rho h$ . The dissipation flux across a cell face,  $1k$ , delimiting cells, 1, and its neighbors,  $k$ , are then calculated as

$$d_{1k} = \epsilon_{1k}^{(4)} A_k (\nabla^2 w_1 - \nabla^2 w_k) \quad (6)$$

where

$$A_k = |u_k \Delta y_k - v_k \Delta x_k| + c_k \sqrt{\Delta x_k^2 + \Delta y_k^2}$$

Here  $\Delta x_k$  and  $\Delta y_k$  are coordinate increments of the edge and  $u_k$ ,  $v_k$ ,  $c_k$  are velocity components and the speed of sound along the edge, respectively, and are taken as the average of the values at cells 1 and  $k$ . The  $A_k$  term, which is proportional to the size of the cell face,  $k$ , and represents the maximum eigenvalue of the Euler equation in the direction normal to the face, scales appropriately with the time derivative in Eq. (3). In order to more accurately scale the cells which have higher aspect ratios,  $A_k$  is not integrated around the boundary of the control volume, as is commonly done. The  $\epsilon_{1k}^{(4)}$  is a constant defined later.

The second-order dissipation term is similarly constructed by replacing  $\nabla^2 w_1$  and  $\nabla^2 w_k$  in Eq. (6) with  $w_1$  and  $w_k$ , respectively, so that we have

$$d_{1k} = \epsilon_{1k}^{(2)} A_k (w_1 - w_k)$$

where  $\epsilon_{1k}^{(2)}$  should be of order one near a shock and of order  $(\Delta x)^2$  in regions of smooth flow to preserve the second-order accuracy of the scheme. To ensure this,  $\epsilon_{1k}^{(2)}$  is then scaled proportional to an undivided Laplacian in the pressure

$$\epsilon_{1k}^{(2)} = \epsilon_2 \frac{\left| \sum_{k=1}^3 p_k - p_1 \right|}{\sum_{k=1}^3 p_k - p_1}$$

It is found, however, that a better scaling factor for the edges that are on the solid boundary is the pressure gradient in the surface-wise direction. Thus, the pressure gradient term for cells on the solid boundary is defined here as

$$\mu_1 = \left( \frac{p_{1+1} - 2p_1 + p_{1-1}}{p_{1+1} + 2p_1 + p_{1-1}} \right)$$

where 1, 1-1, and 1+1 are the adjacent cells to cell 1, which are on the surface boundary. For these cells,  $\epsilon_{1k}^{(2)}$  is then taken as

$$\epsilon_{1k}^{(2)} = \epsilon_2 \max(\mu_{1-1}, \mu_1, \mu_{1+1})$$

It is known that the fourth-order dissipation term may produce overshoots in the vicinity of a shock; therefore, they are turned off by defining

$$\epsilon_{1k}^{(4)} = \max[0, \epsilon_{1k}^{(4)} - \epsilon_{1k}^{(2)}]$$

Here  $\epsilon_2$  and  $\epsilon_4$  are empirically determined constants.

The final form of the dissipative flux is then

$$d_{1k} = \epsilon_{1k}^{(2)} A_k (w_1 - w_k) + \epsilon_{1k}^{(4)} A_k (\nabla^2 w_1 - \nabla^2 w_k)$$

This dissipation flux,  $d_{1k}$ , is added or subtracted from its adjacent cells consistent with the direction of the normal to each edge. This ensures that dissipation is conserved throughout the region.

The treatment of the boundary conditions is known to affect the convergence and accuracy of the solution. The wall pressure can be extrapolated from the pressure at the center of the boundary cell using the method given in Ref. 8. However, in the present calculations it is found, in both the structured and unstructured solvers, that the normal pressure gradient,  $\partial p / \partial n$ , is negligible, and the pressure of the boundary could be assumed equal to the pressure at the center of the boundary cell.

It is important to note that when the solid boundary condition is imposed in the unstructured flow solver, however, is that setting the normal components of the fluxes to zero and only accounting for the pressure terms in the momentum equation does not necessarily satisfy the flow tangency condition on the boundary. A stronger

formulation is needed to ensure this requirement. In the present cell-centered scheme, a stronger form of the boundary condition is imposed in order to compute the artificial dissipation terms more exactly. Flow variables  $\rho$ ,  $\rho u$ ,  $\rho v$ ,  $H$  in imaginary cells inside the solid surface are extrapolated based on the assumptions of no normal flux and equal tangential fluxes between cells outside and inside the boundary. These values are then used in the calculation of dissipation terms associated with the edges that are on the boundary. This can be shown to be equivalent to explicitly setting velocities to be tangent to the wall, as suggested in Ref. 11.

## 5.0 Zonal Interference Scheme

Interaction between neighboring zones could be greatly simplified by ensuring that neighboring structured and triangular grids have complete, common, edges. This could easily be done along the zonal boundaries by choosing the structured grid points as forming points of the triangular grids. Mass, momentum and energy fluxes through the zonal boundaries are conserved by using the values from neighboring zones when calculating fluxes. This requires maintaining information on the grid interaction, including indexes of structured grids next to the boundary triangular meshes, and vice versa.

Careful attention must be given to calculation of dissipation terms for the boundary cells in order to ensure conservation of dissipation terms throughout the flow. Dissipation terms for the triangular, boundary cells are calculated by extracting information from both the structured and unstructured zones and vice versa. Inappropriate treatment of dissipation terms can result in solution inaccuracy along the zonal boundaries or can produce considerable decoupling of the solution in boundary regions of both zones and contaminate the solution in the entire region. It is also found that comparable CFL numbers and degrees of smoothing in different zones, are essential to improve the overall convergence of the solution in the entire region.

## 6.0 Results

The multielement airfoil of Fig. 1 with overhang of 5%, gap-to-chord ratio of 10%, and flap angle of rotation of  $15^\circ$  is considered as the first computational example. The isobar solution at a Mach number of 0.2 is shown in Fig. 2, which indicates a smooth solution across the zonal boundaries. This solution is obtained by using  $256 \times 32$  O-meshes, part of which are replaced by 976 triangular meshes. A CFL of 7, along with a variable time step based on a maximum limit set by local Courant number, is used in both zones.

Figure 3 shows the details of the solution in the unstructured zone and indicates that the strong form of the boundary condition discussed earlier in Section 4.0 adequately satisfies the flow tangency requirements on the solid boundary. The solution also accurately predicts the location of the stagnation point on the leading edge of the flap. Furthermore, even though the equations are inviscid, the addition of dissipation terms introduces viscous flow like vorticity in the flap well.

Calculated surface pressures for both the main airfoil and the flap are compared with experimental data of Ref. 12 in Fig. 4(a,b). The experimental results are obtained at a  $M = 0.195$  and Reynolds number of 500,000 based on unextended chord length. The comparison is obviously very poor in the flap well region due to the viscous effects which are dominant in this region. Our inviscid model also is unable to predict the separation that occurs on the upper surface of the flap as indicated by the experimental data.

Our second computational example deals with iced airfoils. The analysis of the aerodynamic performance of iced airfoils has been of great interest to aircraft designers. In order to find ways to prevent ice formation on wings, one needs to accurately predict the flowfield about iced airfoils with various forms of ice shapes.<sup>13</sup> Ice accretion on an airfoil produces very irregular and rough surfaces on the leading edge region. These shapes normally have concavities and convexities which cannot be modeled using a single zone structured grid.

An iced NACA 0012 airfoil with an eight-minute ice surface computed using the fortified Lewice program of Ref. 14 is shown in Fig. 5. A composite structured and unstructured grid is generated consisting of  $198 \times 32$  O-meshes, part of which are replaced by 932 triangular meshes. The unstructured mesh region is extended far enough to cover the irregular ice shape on the leading edge. A converged solution obtained using this mesh is presented in subsequent figures.

Figure 6 shows the isobar solution obtained at  $M = 0.2$  and  $\alpha = 4^\circ$ . The compressibility effects at this Mach number are less than 2%, according to the Prandtl Glauert rule. The contour lines vary smoothly across the zonal boundary indicating that the conservation of fluxes is well satisfied.

Figure 7 shows the velocity vectors in the leading-edge region. This figure clearly indicates that there are multiple stagnation regions where streamlines approach the surface from the farfield and are divided in two opposite directions on the surface. There is also a small region of reverse flow on the upper surface. Similar to the first example, although the equations are inviscid, the addition of dissipation terms produces viscous flow like vorticity behind the ice shape on the upper surface.

The computed pressure distribution on the surface is compared with the surface panel method results in Fig. 8; good agreement is indicated.

## 7.0 Conclusion

The objective of the present work is to develop an efficient and reliable two-dimensional zonal approach capable of coupling structured and unstructured grid zones for complex airfoil shapes. This approach requires considerably less memory compared to using an entirely unstructured mesh capable of handling complex geometries. It also takes advantage of the different desirable features of structured and unstructured meshes. Computational examples are presented that demonstrate the applicability of this method to the analysis of the flowfields such as those around

iced airfoils, multielement airfoils, and blunt and divergent-trailing-edge airfoils. The method could also be coupled with a boundary-layer method to include the viscous effects.

### 8.0 References

1. Batina, J.T., "Unsteady Euler Algorithm with Unstructured Dynamic Mesh for Complex-Aircraft Aerodynamic Analysis," AIAA Journal, Vol. 29, 1991, p. 37.
2. Roe, P.R., "Error Estimates for Cell-Vertex Solution for the Compressible Euler Equations," ICASE Report No. 87-6, NASA CR-178235, 1987.
3. Mavriplis, D.J., "Accurate Multigrid Solution of the Euler Equations on Unstructured and Adaptive Meshes," AIAA Journal, Vol. 28, 1990, p. 213.
4. Venkatakrishnan, V., Mavriplis, D.J., "Implicit Solvers for Unstructured Meshes," AIAA Paper 91-1537-CP, Honolulu, Hawaii, 1991.
5. Venkatakrishnan, V. and Batina, J.T., "Application of Direct Solvers to Unstructured Meshes for the Euler and Navier-Stokes Equations Using Upwind Schemes," AIAA Paper 89-0364, 1989.
6. Chin, V.D., "2-D Unstructured Grid Generation," M.S. Thesis, California State University, Long Beach, 1991.
7. Bowyer, A., "Computing Dirichlet Tessellation," The Computer Journal, Vol. 24, No. 2, 1981.
8. Jameson, A., Schmidt, W. and Turkel, E., "Numerical Solution of the Euler Equation by Finite-Volume Method Using a Runge-Kutta Time-Stepping Scheme," AIAA Paper 81-1259, 1981.
9. Mavriplis, D.J. and Jameson, A., "Multigrid Solution of the Two-Dimensional Euler Equation on Unstructured Triangular Mesh," AIAA Paper 87-0353, 1987.
10. Jameson, A. and Baker, J.J., "Solution of the Euler Equation for Complex Configurations," AIAA Paper 83-1929, 1983.
11. Mavriplis, D.J., "Accurate Multigrid Solutions of the Euler Equation on Unstructured and Adaptive Meshes," AIAA Journal, Vol. 28, 1990.
12. Chen, H.H., Private communication.
13. Shaw, R.J., Potapczuk, M.G. and Bidwell, C.S., "Prediction of Airfoil Aerodynamic Performance Degradation Due to Icing," Numerical and Physical Aspects of Aerodynamic Flows, IV (ed. T. Cebeci), Springer-Verlag, 1990.
14. Cebeci, T., Chen, H. and Alemdaroglu, N., "Fortified Lewice with Viscous Effects," Journal of Aircraft, Vol. 28, No. 9, pp. 564-571, Sept. 1991.

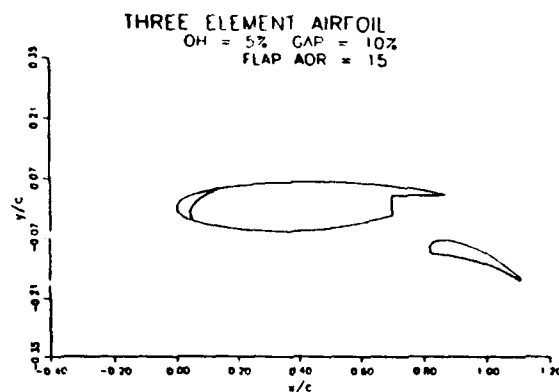


Fig. 1. Multielement airfoil with large flap deflection.

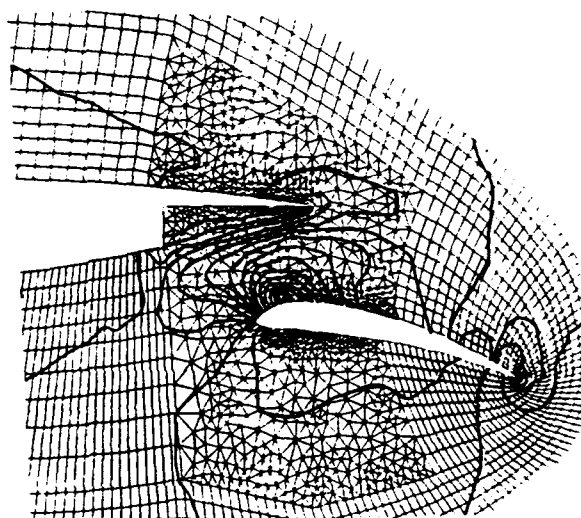


Fig. 2. Isobar solution for multielement airfoil of Fig. 1 using composite grid.  $M = 0.125$ ,  $\alpha = 0$ .

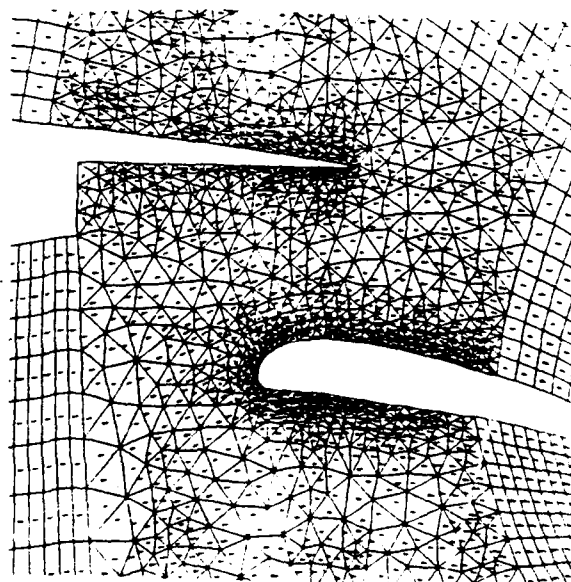


Fig. 3. Total velocity direction for multielement airfoil of Fig. 1 using composite grid  $M = 0.125$ ,  $\alpha = 0$ .

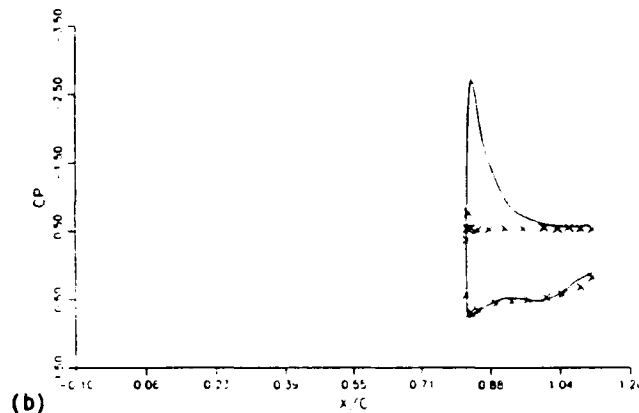
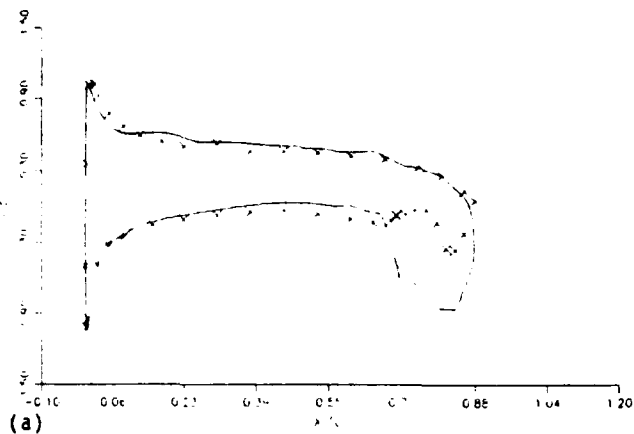


Fig. 4. Comparison of calculated  $C_p$  with experimental results; (a) main airfoil, (b) flap.

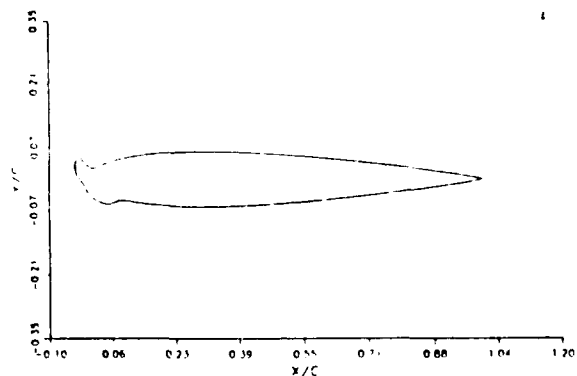


Fig. 5. Eight minute ice shape on a NACA 0012 airfoil at  $\alpha = 4^\circ$ .

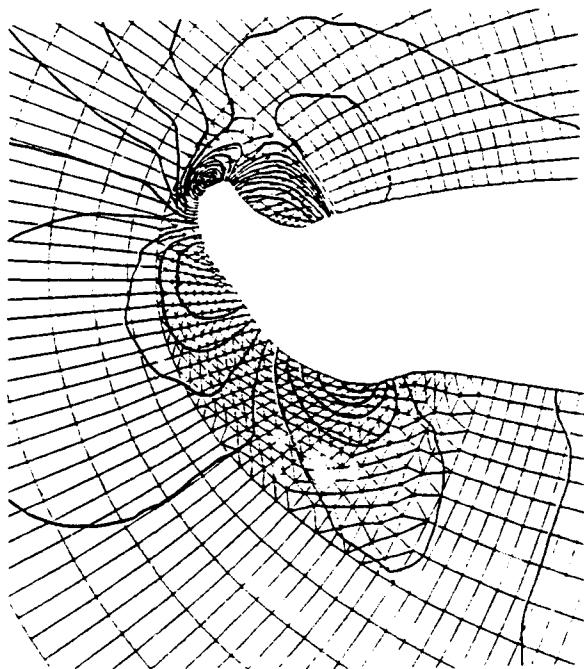


Fig. 6. Isobar solution obtained using composite grid,  $M = 0.2$ ,  $\alpha = 4^\circ$ .

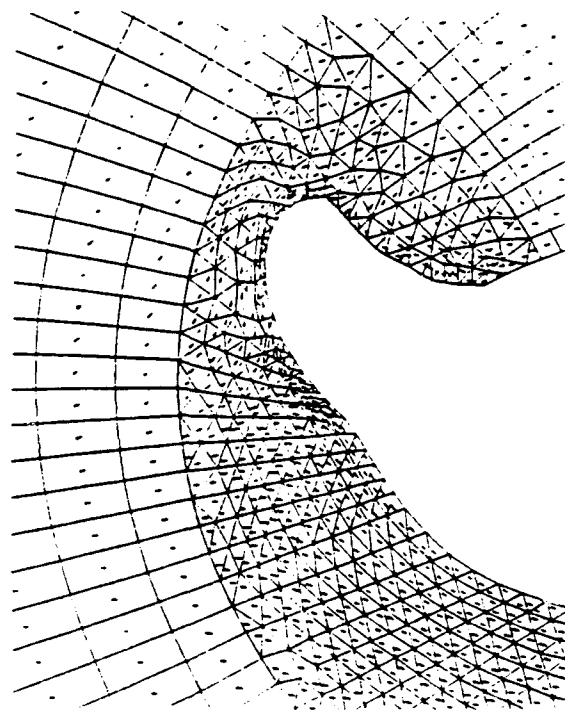


Fig. 7. Total velocity vectors for iced airfoil of Fig. 5 using composite grid.

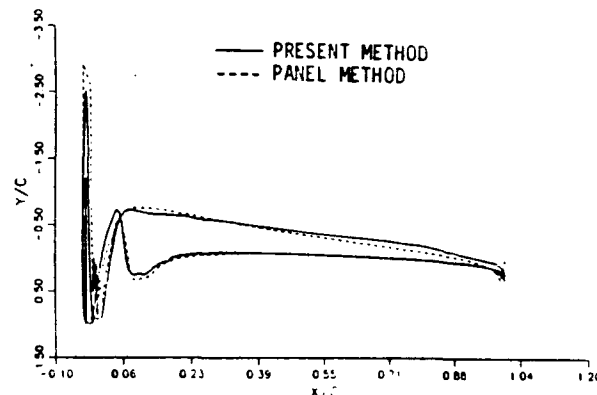


Fig. 8. Comparison of calculated pressure coefficient with panel method calculation.

# Experimental and Computational Ice Shapes and Resulting Drag Increase for a NACA 0012 Airfoil

Jaiwon Shin and Thomas H. Bond  
Aerospace Engineer  
NASA Lewis Research Center  
Cleveland, Ohio

## Abstract

Tests were conducted in the Icing Research Tunnel (IRT) at the NASA Lewis Research Center to document the repeatability of the ice shape over the range of temperatures varying from  $-15^{\circ}\text{F}$  to  $28^{\circ}\text{F}$ . Measurements of drag increase due to the ice accretion were also made. The ice shape and drag coefficient data, with varying total temperatures at two different airspeeds, were compared with the computational predictions. The calculations were made with the 2D LEWICE/IBL code which is a combined code of LEWICE and the interactive boundary layer method developed for iced airfoils. Comparisons show good agreement with the experimental data in ice shapes. The calculations show the ability of the code to predict drag increases as the ice shape changes from a rime shape to a glaze shape.

## Introduction

Over the past few years, the Icing Research Tunnel (IRT) at the NASA Lewis Research Center has gone through several rehabilitations which have improved its capabilities in simulating real icing conditions. Some of the improvements include a new and more powerful fan motor, a new spray bar system, a new digital control system, and various improvements to the IRT structure. As a result, the IRT can now provide more accurate control of the airspeed and temperature, more uniform clouds covering a larger cross-section of the test section, and lower liquid water content.

Although various test programs have been conducted in the IRT with the improved capabilities, there has not been a comprehensive test program to document the repeatability of the data obtained in the IRT. Tests were conducted to address the repeatability issue during the months of June and July of 1991. The test matrix was focused to document the repeatability of the ice shape over a range of air temperatures. During the tests, the drag increase due to the ice accretion was also measured. This test program also provided a new database for code validation work.

The LEWICE code, which is being used by industry and government to predict two-dimensional ice accretions, was combined with the interactive boundary layer method to also predict the resulting aerodynamic penalties<sup>1</sup> (This combined code is referred to as the 2D LEWICE/IBL code.). An initial validation study<sup>2</sup> was made last year, in which the code predictions were compared with the experimental results of Olsen, et al.<sup>3</sup> The results showed good agreement between the experiment and the calculation for both ice shapes and the resulting drag. More comparisons of calculations with experimental data were recommended and the recent repeatability test provided a needed data set.

In this paper, comparisons of measured ice shapes and predicted ice shapes are presented for a range of temperatures with two different airspeeds and liquid water contents. Resulting drag increase is also compared between the experiment and the calculation.

## Nomenclature

A	damping-length constant
c	airfoil chord
$C_d$	drag coefficient
$k_s$	equivalent sand-grain roughness
$k_s^+$	dimensionless sand-grain roughness
L	mixing length
$T_T$	total air temperature
$T_s$	static air temperature
$u_\tau$	friction velocity
$V_\infty$	airspeed
x	surface coordinate
y	coordinate perpendicular to x
$y^+$	a Reynolds number, $y u_\tau / \nu$
$\kappa$	universal constant, also used as a sweep parameter
$\nu$	kinematic viscosity

## Description of the Experiment

### Icing Research Tunnel

The NASA Lewis Icing Research Tunnel is a closed-loop refrigerated wind tunnel. Its test section is 6 ft. high, 9 ft. wide, and 20 ft. long. A 5000 hp fan provides airspeeds up to 300 mph in the test section. The 21,000 ton capacity refrigeration can control the total temperature from  $-40^{\circ}\text{F}$  to  $30^{\circ}\text{F}$ . The spray nozzles provide droplet sizes from approximately 10 to 40  $\mu\text{m}$  median volume droplet diameters (MVD) with liquid water contents (LWC) ranging from 0.2 to 3.0  $\text{g}/\text{m}^3$ . A schematic of the tunnel, shop, and control room is shown in Fig. 1. A detailed description of the IRT can be found in reference 4.

### Test Model

The test model was a 6 ft. span, 21 in. chord NACA 0012 airfoil with a fiberglass skin. The model was mounted vertically in the center of the test section. During all icing runs, the model was set at  $4^{\circ}$  of angle of attack. The model installed in the test section is shown in Fig. 2.

### Test Conditions

The test points used to make comparisons with the calculation in this paper were selected from the larger test matrix which is fully described in reference 5.



The test conditions given in Table 1 can be grouped into two: 1) low airspeed and high LWC, and 2) high airspeed and low LWC. Water droplet size was held constant for both groups. Airspeed, LWC, and spray time were selected so that both groups would have the same water intercept (i.e.  $\text{airspeed} \times \text{LWC} \times \text{spray time} = \text{constant}$ ). Temperatures were selected to cover glaze, rime, and transition regimes.

### Test Methods

A typical test procedure for icing runs is listed below.

1. The model angle of attack was set.
2. The target airspeed and total temperature were set.
3. The spray system was adjusted to the desired MVD and LWC.
4. The spray system was turned on for the desired spray time.
5. The tunnel was brought down to idle and the frost beyond the ice accretion was removed.
6. The wake survey was traversed across the airfoil wake with the tunnel at the target airspeed.
7. The tunnel was brought down to idle again for ice shape tracings and photographs.
8. The airfoil was then cleaned and the next data point was performed.

### Drag Wake Survey

The section drag at the mid-span of the airfoil was calculated from total pressure profiles measured by a pitot-static wake survey probe. The wake survey probe was positioned two chord lengths downstream of the airfoil as shown in Fig. 2. The wake surveys were made only when the spray cloud was turned off. During sprays, the probe was kept behind a shield to prevent any ice accretion on the tip of the probe. The wake probe was mounted on an automatic traverse system, and the traversing speed was adjustable.

### Description of 2D LEWICE/IBL

LEWICE is a two-dimensional ice accretion code which has a Hess-Smith two-dimensional panel code for a flow calculation, a droplet trajectory and impingement calculation code, and an icing thermodynamic code. Detailed description of the code can be found in reference 6.

Several modifications have been made to the original LEWICE code to add a capability of calculating aerodynamic characteristics by making use of the interactive boundary layer method developed by Cebeci, et al<sup>7</sup>. Along with this new capability, a modification was made to the original LEWICE so that the calculation can be made in a user interaction-free environment. This was achieved by using a smoothing routine<sup>1</sup> to avoid the occurrence of multiple stagnation points caused by the formation of irregular ice surfaces on the ice shape.

During the development of the 2D LEWICE/IBL code, a turbulence model has also been developed to deal with surface roughness such as that associated with ice. This was done by modifying the mixing length and wall-damping expression of the Cebeci-Smith model, that is

$$L = \kappa(y + \Delta y) \{1 - \exp[-(y + \Delta y)/A]\} \quad (1)$$

where  $\Delta y$  is a function of an equivalent sand grain roughness  $k_s$ . In terms of dimensionless quantities, with  $k_s^+ = k_s u_\tau / \nu$  and  $\Delta y^+ = \Delta y u_\tau / \nu$

$$\Delta y^+ = \begin{cases} 0.9[\sqrt{k_s^+} - k_s^+ \exp(-k_s^+/6)] & 5 < k_s^+ \leq 70 \\ 0.7(k_s^+)^{0.58} & 70 \leq k_s^+ \leq 2000 \end{cases} \quad (2)$$

The equivalent sand grain roughness for ice is determined from the expressions used in the original LEWICE code.

The heat transfer model used in the LEWICE code makes use of an equivalent sand grain roughness,  $k_s$ , expressed as a function of LWC, static air temperature ( $T_s$ ), and airspeed ( $V_\infty$ ).

The original expression for  $k_s$  is in the following form with  $c$  denoting the airfoil chord and  $(k_s/c)_{base} = 0.001177$

$$k_s = \left[ \frac{k_s/c}{(k_s/c)_{base}} \right]_{LWC} \cdot \left[ \frac{k_s/c}{(k_s/c)_{base}} \right]_{T_s} \cdot \left[ \frac{k_s/c}{(k_s/c)_{base}} \right]_{V_\infty} \cdot \left( \frac{k_s}{c} \right)_{base} \cdot c \quad (3)$$

where each sand grain roughness parameter is given by

$$\left[ \frac{k_s/c}{(k_s/c)_{base}} \right]_{LWC} = 0.5714 + 0.2457(LWC) + 1.2571(LWC)^2 \quad (4)$$

$$\left[ \frac{k_s/c}{(k_s/c)_{base}} \right]_{T_s} = 0.047 T_s - 11.27 \quad (5)$$

$$\left[ \frac{k_s/c}{(k_s/c)_{base}} \right]_{V_\infty} = 0.4286 + 0.0044139 V_\infty \quad (6)$$

Recent numerical studies conducted by Shin, et al.<sup>2</sup> showed that the equivalent sand grain roughness did not depend on airspeed, but did depend on the median volume diameter (MVD) of the water droplets. As a result, equation (3) is modified, as given by equation (7).

$$k_s = 0.6839 \left[ \frac{k_s/c}{(k_s/c)_{base}} \right]_{LWC} \cdot \left[ \frac{k_s/c}{(k_s/c)_{base}} \right]_{T_s} \cdot \left[ \frac{k_s/c}{(k_s/c)_{base}} \right]_{MVD} \cdot \left( \frac{k_s}{c} \right)_{base} \cdot c \quad (7)$$

where

$$\left[ \frac{k_s/c}{(k_s/c)_{base}} \right]_{MVD} = \begin{cases} 1 & MVD \leq 20 \\ 1.667 - 0.0333 MVD & MVD > 20 \end{cases} \quad (8)$$

The interactive boundary layer method then uses a roughness parameter as given in equation (9) over the predicted iced surface.

$$(k_s)_{IBL} = 2(k_s)_{equation (7)} \quad (9)$$

Present studies as well as those conducted in reference 2 showed that drag coefficients calculated with the roughness parameter by the above method were much lower than measured drag coefficients, especially for rime ice shapes. Numerical studies were conducted to investigate the effect of the extent of the iced airfoil surface on drag. In the original version of the 2D LEWICE/IBL code, roughness is only applied over the surface of the ice. The code was modified to allow for roughness on both the ice and the airfoil surface downstream of the ice. The results showed that agreement between calculated and measured drag coefficients for rime ice shapes became much better by extending the range of the roughness on the airfoil surface and placing a lower limit of  $k_s/c = 0.002$  on the equivalent sand grain roughness, which otherwise would become very small for rime ice. The extent of the iced airfoil surface which resulted in the best agreement with the experimental drag coefficients for rime ice shapes was found to be 50 percent of the airfoil chord, and this extent was used in all drag calculations presented in this paper.

### Results and Discussion

This section contains a discussion of the quality of the experimental data, and discussions of the ice shape comparison and the iced airfoil drag comparison.

#### Quality of Experimental Data

Dry airfoil drag results - Section drag was measured with the clean airfoil under the dry condition and the results are compared with the published data<sup>3,8,9</sup> as shown in Fig. 3. The data of Abbott and Doenhoff<sup>8</sup> was taken in the Low Turbulence Pressure Tunnel (LTPT) at the NASA Langley Research Center. The data of Olsen, et al.<sup>3</sup> and the data of Blaha and Evanich<sup>9</sup> were taken in the IRT.

The difference between the data from the LTPT and the IRT can occur for several reasons: differences in wake survey method, tunnel turbulence level, and model condition. The LTPT tests used a wake rake while the IRT tests used a traversing probe. The LTPT had the freestream turbulence intensity of the order of a few hundredths of 1 percent. The freestream turbulence intensity in the IRT is about 0.5 percent. The difference in the surface finish of a model can also have an effect on drag.

The current IRT drag data is higher than the previous IRT data. All three tests used the wake survey method and the airfoils had the same chord length. This kind of difference in drag data can come from differences in the wake survey location and model condition. The wake survey probe was located at one chord length behind the model for Blaha's test while it was located at two chord lengths behind the model for Olsen's test and the current test. The leading edge and the trailing edge part of the current model were joined at the maximum thickness location (30 percent of the chord) while the model used in both reference 3 and 9 was the same one-piece

airfoil.

According to the experimental results of Gregory and O'Reilly<sup>10</sup> shown in Fig. 4, transition occurs at around 40 percent chord at 0° of angle of attack for an NACA 0012 airfoil at a Reynolds number of 3 million. The transition location moves upstream very rapidly as the angle of attack increases. A small step at the joint in the current model may have acted as a trip at low angles of attack causing an early transition to turbulent boundary layer. At higher angles of attack, the step may have acted as an additional roughness source in the turbulent boundary layer, which increased drag.

Drag associated with an iced airfoil is normally dominated by the pressure drag due to a large separation caused by a pressure spike at the upper horn. At 4° of angle of attack, where all the icing runs were made, an increase of the friction drag by the step of the current model is believed to have a minimal effect on icing drag data.

#### Repeatability of dry airfoil drag measurements

- Dry runs were made prior to each icing run. Each icing run was repeated at least twice, which resulted in more than 28 dry airfoil drag measurements at a 4° angle of attack. The percent variation was calculated in the same way as Olsen<sup>3</sup> by taking the standard deviation and dividing it by the average. The average  $C_d$  value at a 4° angle of attack was 0.01068. The percent variation was 7.1 percent of the average value. The percent variation reported by Olsen was 7.7 percent.

#### Repeatability of the ice shapes and resulting drag

- Each data point was repeated at least twice to ensure repeatability of the ice shape and drag measurement. Ice shapes and measured drag coefficients of three repeat runs for typical glaze ice (22°F) and rime ice (-15°F) cases at two airspeeds are shown in Figs. 5 and 6.

At all four conditions, the ice shape repeats well and the variation of the drag coefficient is within the percent variation of the measurement. The larger percent variation is seen with glaze ice, however the variation is much smaller than that reported in Olsen<sup>3</sup>.

#### Comparison Between Calculated and Measured Ice Shapes

Ice shapes were computed with the 2D LEWICE/IBL code for the icing conditions shown in Table 1. Since the code runs without any user interactions, the only variable which can influence the ice shape for a given icing condition is the time step. Previous investigation<sup>2</sup> suggested that the use of 1 minute time interval resulted in the best agreement with the experimental ice shapes.

To ensure the above finding still holds true, the effect of time step was investigated with all icing conditions at the airspeed of 150 mph. Four different time intervals, 0.5, 1, 2, and 6 minutes, were used. Figure 7 shows the results for a glaze ice, a rime ice, and a transition case. The use of a longer time interval results in more ice accretion as seen in all cases. Based on the comparison with the experimental data, 1 min time step was chosen for all the calculations.

Figure 8 shows calculated and measured ice shapes at various temperatures. The experimental ice shape changes from white, opaque rime ice to slushy, clear glaze ice with increased temperature. Airspeed was set at 150 mph. Experimental ice shapes were taken at the mid-span of the model where the wake survey was made. The agreement between calculated and measured ice shapes is good, particularly for rime ice cases. Icing limits are predicted well for the temperatures below 18°F. At warmer temperatures, the calculation predicted more run back which resulted in more ice accretion beyond the experimental icing limits. The direction of horn growth is predicted reasonably well, but in general the size of the predicted ice shape is larger than the measured shape.

Figure 9 shows ice shape comparison as a function of temperature at the airspeed of 230 mph. Comparisons show similar results as the lower speed cases. Good agreement is shown at all temperatures except at 28°F where an overprediction of upper horn is seen.

#### Comparison between Calculated and Measured Drag

Calculated drag coefficients were compared with measured drag coefficients for the ice shapes shown in Figs. 8 and 9. With each icing run, the wake survey was made twice: one made while the probe traversed away from the shield, and the other made while the probe traversed back to the shield. Each measured drag coefficient in Table 2 is the averaged value of the two measurements at each icing run. Calculated drag coefficients are also included in Table 2 for comparisons.

Results in Table 2 are plotted in Figs. 10 and 11. For both airspeeds, the experimental data show almost constant measured drag coefficients up to around 12°F and a sharp increase toward near freezing temperatures as the ice shape changes to glaze ice. For  $V_\infty = 150$  mph, calculated drag coefficients agree very well with measured drag coefficients up to 12°F and begin to rise sharply at around 18°F. While calculated drag coefficients reach a peak at around 22°F and begin to decrease, measured drag coefficients continue to rise and reach a peak at around 28°F. For  $V_\infty = 230$  mph, however, the calculated results does a good job of following the trend in measured values.

#### Concluding Remarks

The ice shape and drag coefficient results of the experimental program conducted in the IRT were compared with the predictions using the 2D LEWICE/IBL code. Experimental data provided validation data to further calibrate the code with various icing parameters such as the temperature, airspeed, and LWC. Good agreement in the ice shape was shown for the rime ice. The agreement deteriorated for the glaze ice, although the direction of the horn growth was generally predicted well. Deterioration in ice shape prediction for glaze ice is a typical characteristic shown with the original LEWICE code. The ice shape comparison results indicate that the modifications made to the original LEWICE code in the process of combining it with the interactive boundary layer method work well.

The results of the drag comparison study show the ability of the code to predict the sharp drag increase displayed by the experimental data as the ice shape changes from rime to glaze. The adjustment made by extending the roughness beyond the icing limit on the airfoil allows the calculated drag values to agree well with experimental data. More studies are needed to better estimate the extent of icing on the airfoil surface.

The big strength of the 2D LEWICE/IBL code is the economy of the computing time. A typical computing time (CPU time only) to complete a calculation of 6 or 7 minutes ice accretion and its aerodynamic characteristics was less than 50 seconds on a CRAY X-MP.

More comparison work is needed to check the 2D LEWICE/IBL code for further improvements. The test points of the repeatability test in the IRT were reduced from the original test plan due to the loss of tunnel time. More tests are planned to document the effects of other icing parameters on the ice shape and resulting drag. It is also planned to obtain experimental lift data with iced airfoils for code validation work.

#### References

1. Cebeci, T., Chen, H.H., and Alemdaroglu, N., "Fortified LEWICE with Viscous Effects," *Journal of Aircraft*, Vol. 28, No. 9, pp. 564-571, Sept. 1991.
2. Shin, J., Berkowitz, B., Chen, H.H., and Cebeci, T., "Prediction of Ice Shapes and Their Effect on Airfoil Performance," AIAA-91-0264, 1991.
3. Olsen, W., Shaw, R., and Newton, J., "Ice Shapes and the Resulting Drag Increase for a NACA 0012 Airfoil," NASA TM 83556, 1984.
4. Soeder, R.H. and Andracchio, C.R., "NASA Lewis Icing Research Tunnel User Manual," NASA TM 102319, 1990.
5. Shin, J. and Bond, T., "Results of an Icing Test on a NACA 0012 Airfoil in the NASA Lewis Icing Research Tunnel," AIAA-92-0647, 1992.
6. Ruff, G.A. and Berkowitz, B.M., "Users Manual for the NASA Lewis Ice Accretion Prediction Code (LEWICE)," NASA CR 185129, 1990.
7. Cebeci, T., "Calculation of Flow Over Iced Airfoils," *AIAA Journal*, Vol. 27, No. 7, pp. 853-861, 1989.
8. Abbott, I.H. and Von Doenhoff, A.E., *Theory of Wing Sections*, pp. 462-463, Dover Publications, Inc., 1959.
9. Blaha, B.J. and Evanich, P.L., "Pneumatic Boot for Helicopter Rotor Deicing," NASA CP-2170, 1980.
10. Gregory, N. and O'Reilly, C.L., "Low-Speed Aerodynamic Characteristics of NACA 0012 Airfoil Section, Including the Effects of Upper-Surface Roughness Simulating Hoar Frost," NPL AERO Report 1308, 1970.

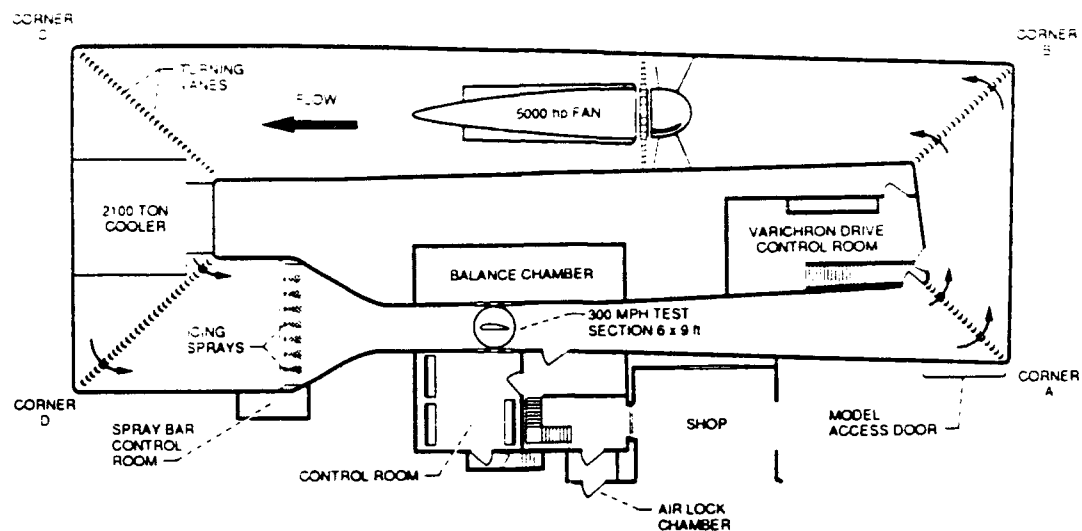


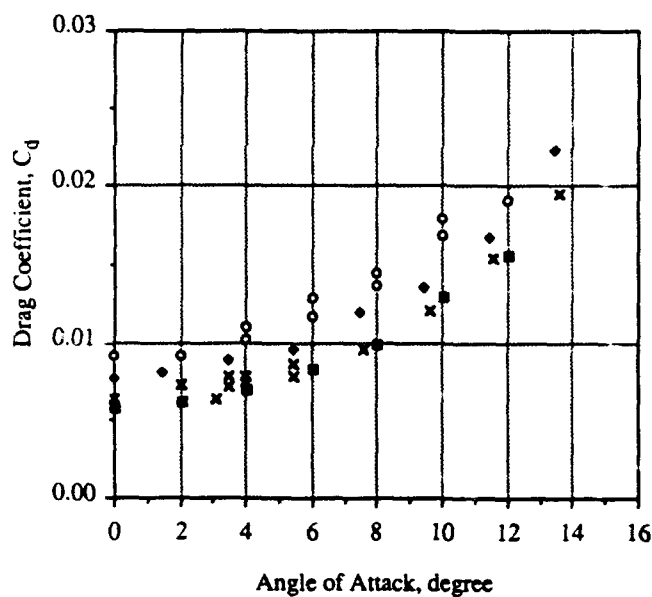
Fig.1. Plan View of IRT, Shop, and Control Room.

Table 1. Test Conditions

AOA (deg.)	Air Speed (mph)	LWC (g/m <sup>3</sup> )	MVD (μm)	Total Temperature (°F)	Ice Accretion Time (min.)
4	150	1.0	20	28	6
4	150	1.0	20	25	6
4	150	1.0	20	22	6
4	150	1.0	20	18	6
4	150	1.0	20	12	6
4	150	1.0	20	1	6
4	150	1.0	20	-15	6
4	230	0.55	20	28	7
4	230	0.55	20	25	7
4	230	0.55	20	22	7
4	230	0.55	20	18	7
4	230	0.55	20	12	7
4	230	0.55	20	1	7
4	230	0.55	20	-15	7



Fig.2. NACA 0012 Airfoil and Wake Survey Probe.



Legend: Facility, Reynolds Number

- IRT, 3 Million
- LTPT, 3 Million (Reference 8)
- × IRT, 3 Million (Reference 3)
- ◆ IRT, 3 Million (Reference 9)

Fig. 3. Comparison of Measured Clean Airfoil Drag with Published Data for the NACA 0012 Airfoil.

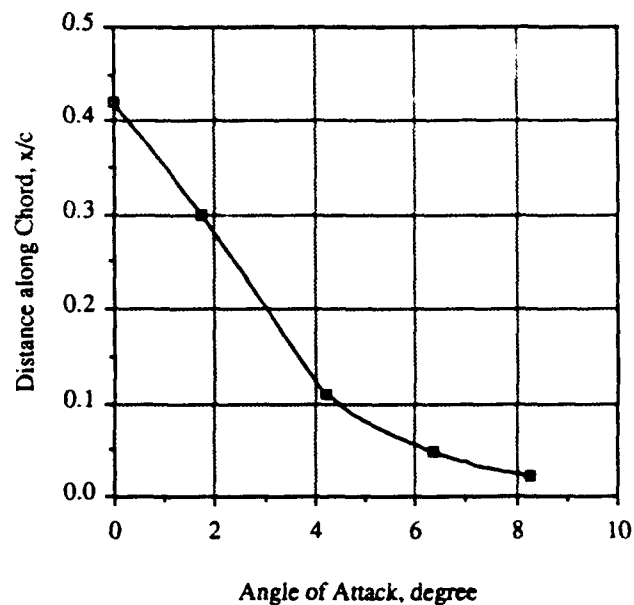
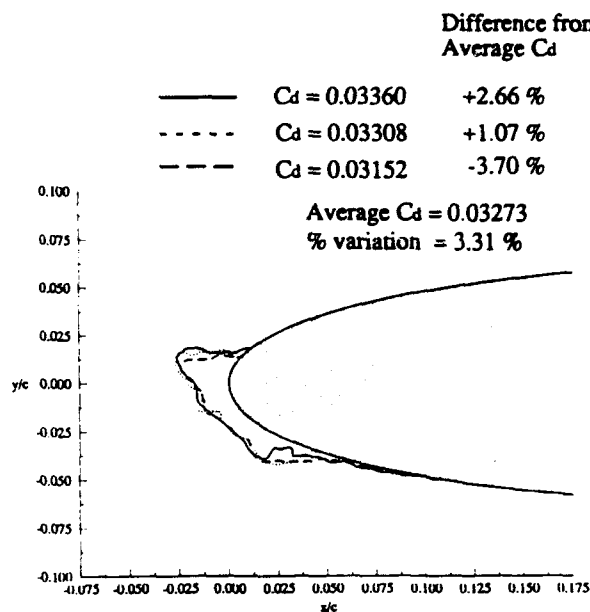
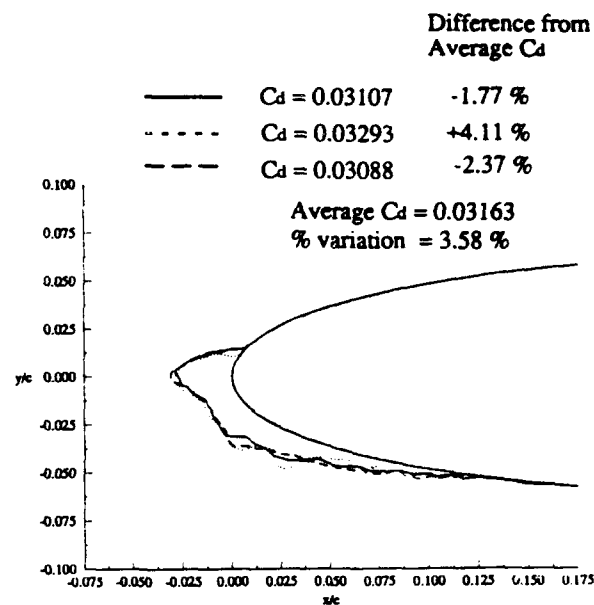


Fig. 4. Transition Locations on the NACA 0012 Airfoil for  $Re = 2.88 \times 10^6$ .

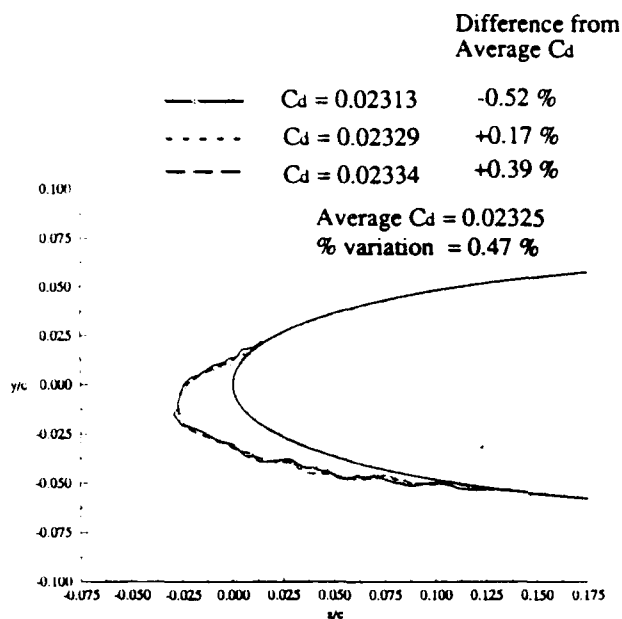


(a) AOA=4°,  $V_\infty=150$  mph,  $T_T=22^\circ\text{F}$ ,  $LWC=1.0\text{g/m}^3$ ,  $MVD=20\mu\text{m}$ , Accretion Time = 6 min.

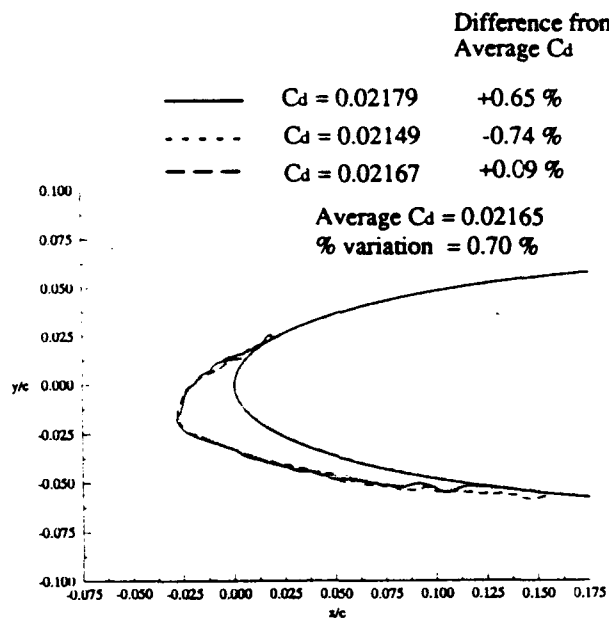


(b) AOA=4°,  $V_\infty=230$  mph,  $T_T=22^\circ\text{F}$ ,  $LWC=0.55\text{g/m}^3$ ,  $MVD=20\mu\text{m}$ , Accretion Time = 7 min.

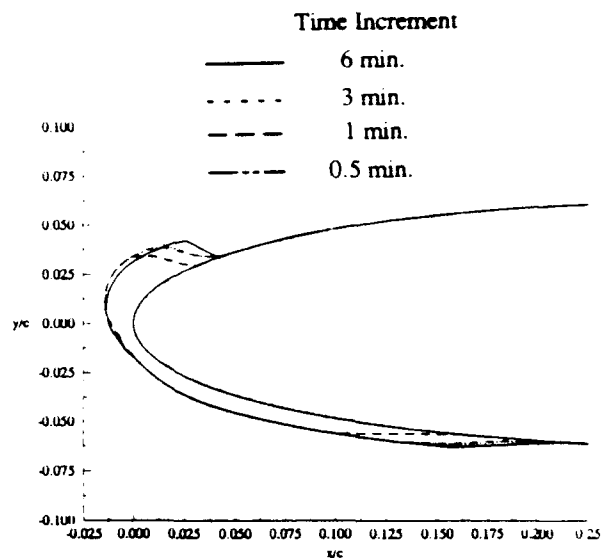
Fig. 5. Repeatability of Ice Shape and Drag for Glaze Ice Shapes.



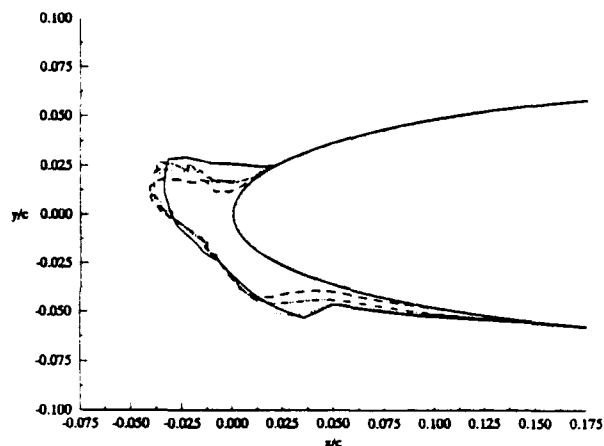
(a)  $AOA=4^\circ$ ,  $V_\infty=150$  mph,  $T_T=-15^\circ\text{F}$ ,  $LWC=1.0\text{g/m}^3$ ,  $MVD=20\mu\text{m}$ , Accretion Time = 6 min.



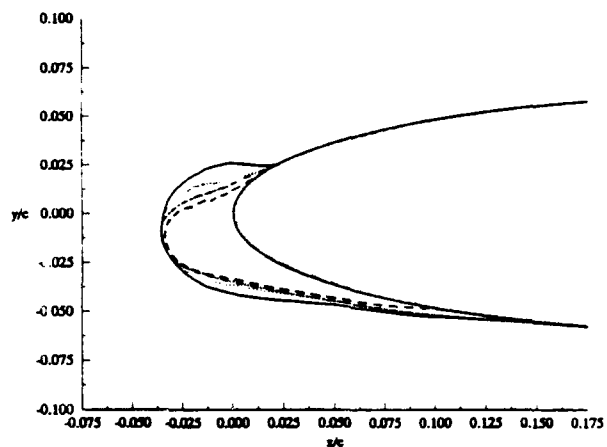
(b)  $AOA=4^\circ$ ,  $V_\infty=230$  mph,  $T_T=-15^\circ\text{F}$ ,  $LWC=0.55\text{g/m}^3$ ,  $MVD=20\mu\text{m}$ , Accretion Time = 7 min.



(a)  $AOA=4^\circ$ ,  $V_\infty=150$  mph,  $T_T=28^\circ\text{F}$ ,  $LWC=1.0\text{g/m}^3$ ,  $MVD=20\mu\text{m}$ , Accretion Time = 6 min.



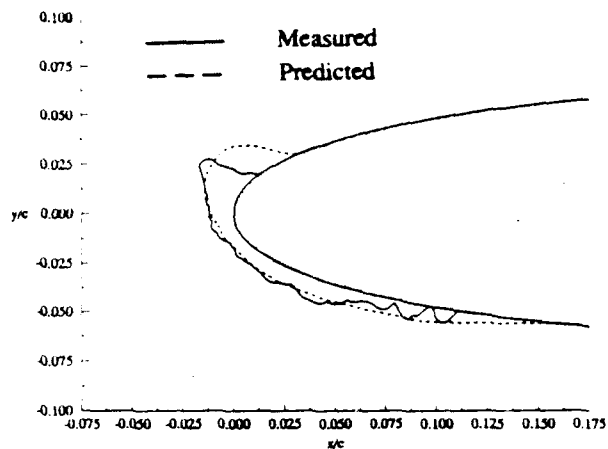
(b)  $AOA=4^\circ$ ,  $V_\infty=150$  mph,  $T_T=18^\circ\text{F}$ ,  $LWC=1.0\text{g/m}^3$ ,  $MVD=20\mu\text{m}$ , Accretion Time = 6 min.



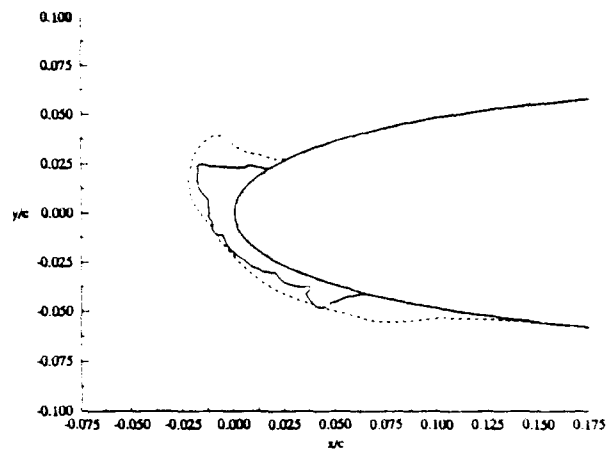
(c)  $AOA=4^\circ$ ,  $V_\infty=150$  mph,  $T_T=-15^\circ\text{F}$ ,  $LWC=1.0\text{g/m}^3$ ,  $MVD=20\mu\text{m}$ , Accretion Time = 6 min.

Fig. 6. Repeatability of Ice Shape and Drag for Rime Ice Shapes.

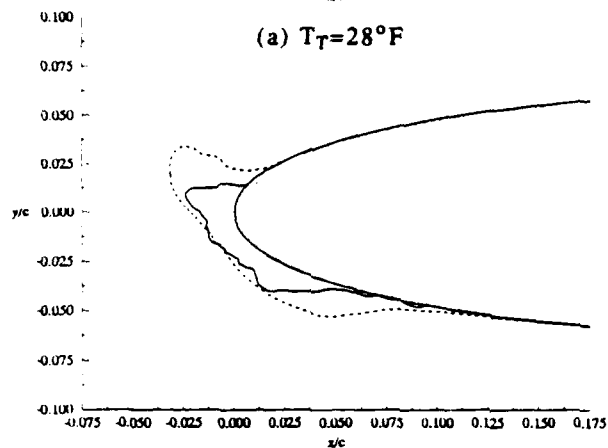
Fig. 7. Effect of Computational Time Step on Ice Shape.



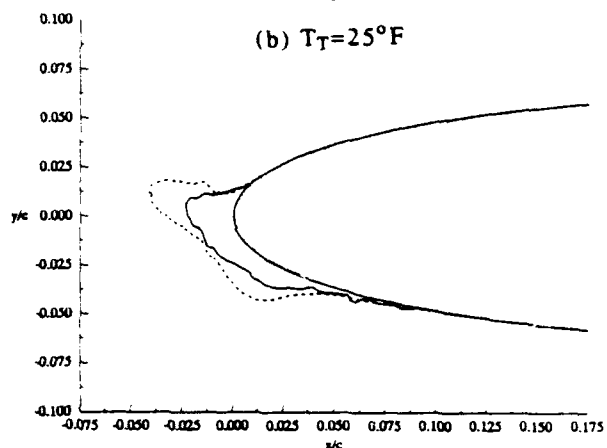
(a)  $T_T = 28^\circ\text{F}$



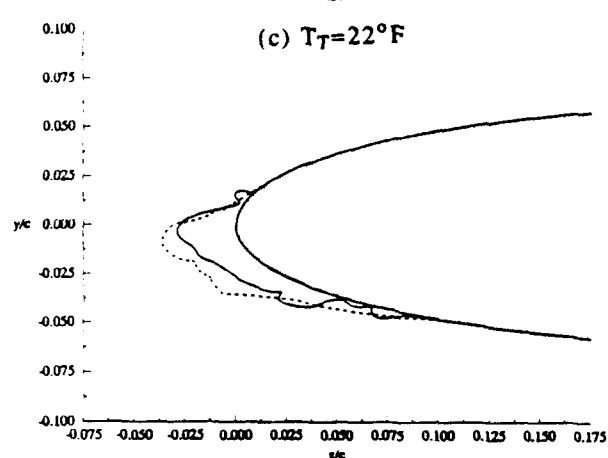
(b)  $T_T = 25^\circ\text{F}$



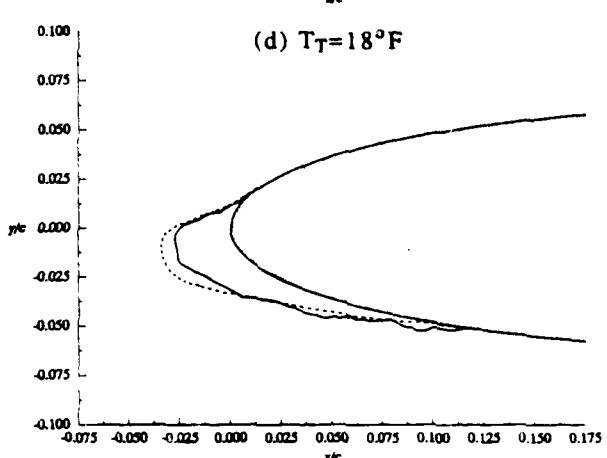
(c)  $T_T = 22^\circ\text{F}$



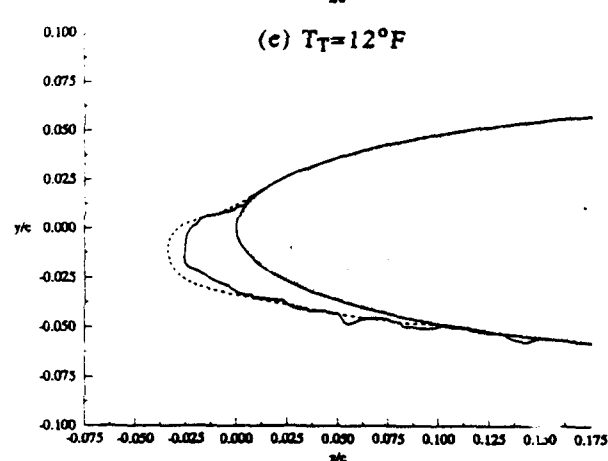
(d)  $T_T = 18^\circ\text{F}$



(e)  $T_T = 12^\circ\text{F}$



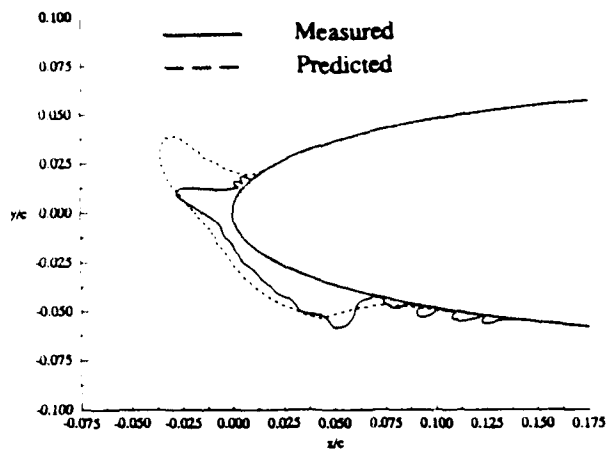
(f)  $T_T = 1^\circ\text{F}$



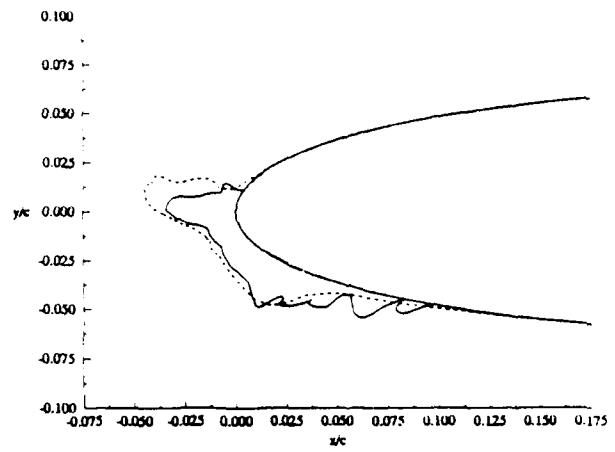
(g)  $T_T = -15^\circ\text{F}$

Fig. 8. Effect of Total Air Temperature on Ice Shape.

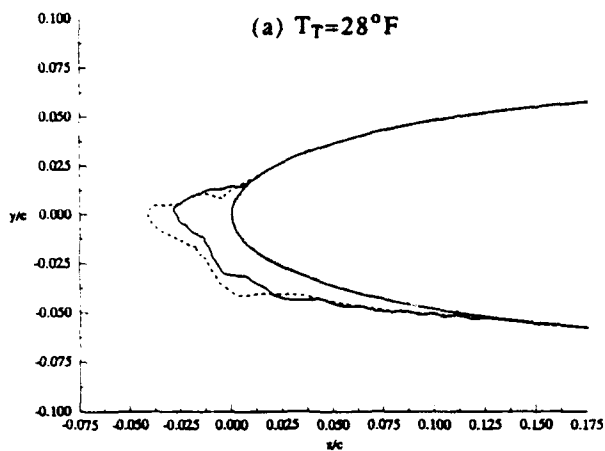
AOA=4°,  $V_\infty=150$  mph, LWC=1.0g/m<sup>3</sup>, MVD=20μm, Accretion Time = 6 min.



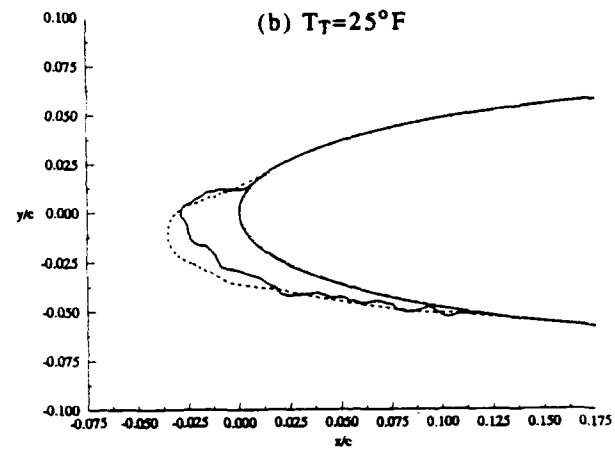
(a)  $T_T = 28^\circ\text{F}$



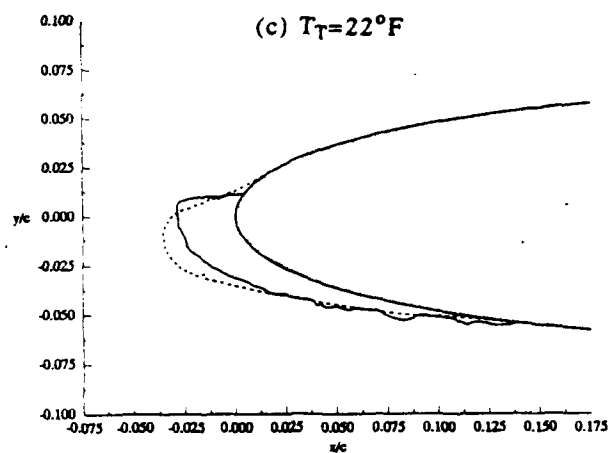
(b)  $T_T = 25^\circ\text{F}$



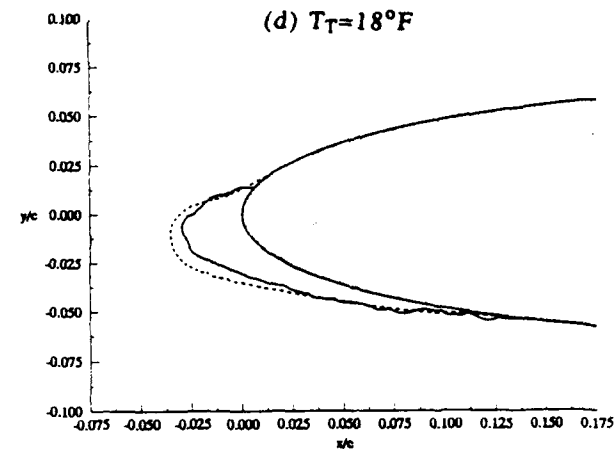
(c)  $T_T = 22^\circ\text{F}$



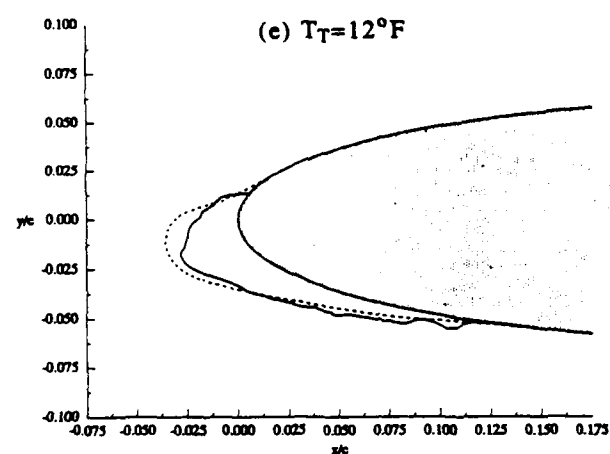
(d)  $T_T = 18^\circ\text{F}$



(e)  $T_T = 12^\circ\text{F}$



(f)  $T_T = 1^\circ\text{F}$



(g)  $T_T = -15^\circ\text{F}$

Fig. 9. Effect of Total Air Temperature on Ice Shape.

AOA=4°,  $V_\infty=230$  mph, LWC=0.55g/m<sup>3</sup>, MVD=20μm,  
Accretion Time = 7 min.



Table 2. Effect of Total Air Temperature on Drag Coefficient.

(a) Airspeed=150 mph, LWC=1.0g/m<sup>3</sup>, MVD=20μm

Total Temperature (°F)	Experimental Drag Coefficient	Calculated Drag Coefficient
28	0.0578	0.0346
25	0.0540	0.0372
22	0.0315	0.0392
18	0.0271	0.0351
12	0.0229	0.0217
1	0.0229	0.0209
-15	0.0233	0.0202

(b) Airspeed=230 mph, LWC=0.55g/m<sup>3</sup>, MVD=20μm

Total Temperature (°F)	Experimental Drag Coefficient	Calculated Drag Coefficient
28	0.0428	0.0470
25	0.0371	0.0294
22	0.0311	0.0202
18	0.0268	0.0195
12	0.0255	0.0195
1	0.0234	0.0195
-15	0.0218	0.0192

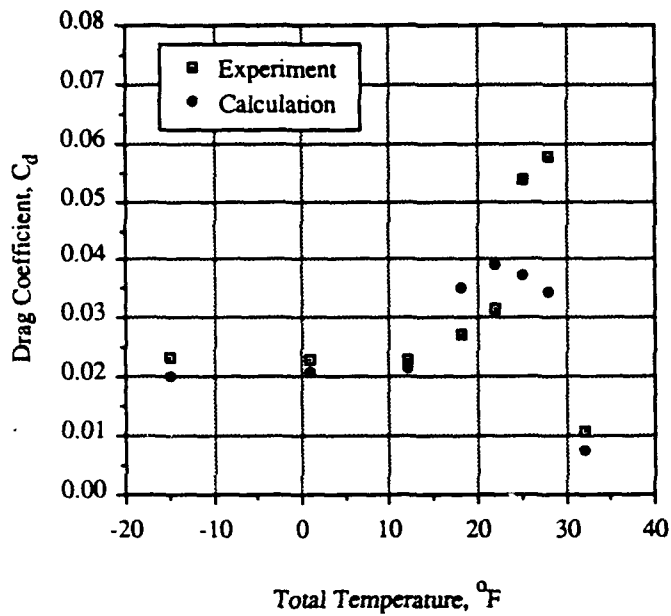


Fig.10. Effect of Total Temperature on Drag ( $V_{\infty}$ =150 mph).

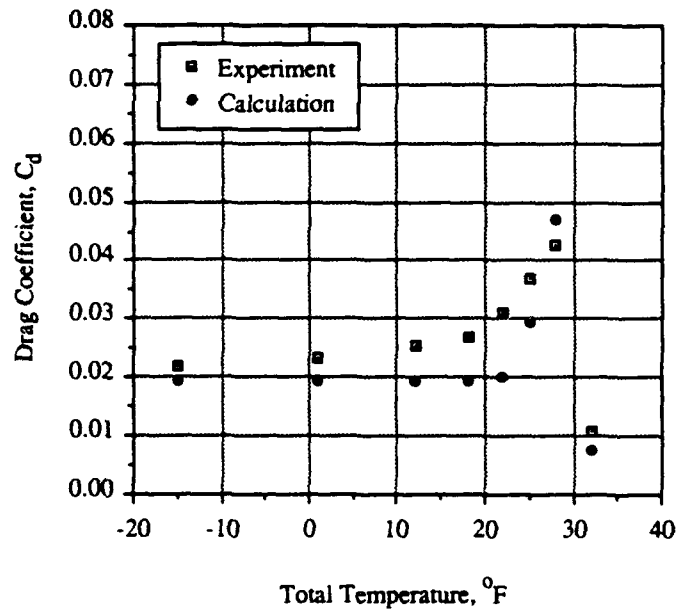


Fig.11. Effect of Total Temperature on Drag ( $V_{\infty}$ =230 mph).

# RECENT PROGRESS IN THE ANALYSIS OF ICED AIRFOILS AND WINGS

by

Tuncer Cebeci\*, Hsun H. Chen\*\*, Kalle Kaup† and Sue Schimke††  
Aerospace Engineering Department,  
California State University, Long Beach

## Abstract

Recent work on the analysis of iced airfoils and wings is described. Ice shapes for multi-element airfoils and wings are computed using an extension of the LEWICE code that was developed for single airfoils. The aerodynamic properties of the iced wing are determined with an interactive scheme in which the solutions of the inviscid flow equations are obtained from a panel method and the solutions of the viscous flow equations are obtained from an inverse three-dimensional finite-difference boundary-layer method. A new interaction law is used to couple the inviscid and viscous flow solutions.

The newly developed LEWICE multielement code is applied to a high-lift configuration to calculate the ice shapes on the slat and on the main airfoil and on a four-element airfoil.

The application of the LEWICE wing code to the calculation of ice shapes on a MS-317 swept wing shows good agreement with measurements. The interactive boundary-layer method is applied to a tapered iced wing in order to study the effect of icing on the aerodynamic properties of the wing at several angles of attack.

## 1.0 Introduction

In recent years there has been considerable research activity in the area of aircraft icing to combat the adverse effects of leading-edge ice formation on fixed and rotary wing aircraft and on engine intakes. Computational work and related experimental studies have been initiated and are being carried out under the NASA Aircraft Icing Research Program to develop and validate a series of mutually compatible computer codes to predict the details of an aircraft icing encounter.<sup>1</sup> The papers presented each year at the the AIAA Aerospace Sciences Meeting and the papers presented in this symposium show that indeed much progress has been made in this area.

In this paper we report a summary of our progress in predicting ice shapes on airfoils and wings and in determining the effect of ice formation on aerodynamic performance degradation. For airfoil flows, our research has led to improvements in the LEWICE code<sup>2</sup> for predicting leading-edge ice formation<sup>3</sup> and to the development of an interactive boundary-layer (IBL) method<sup>4</sup> for determining the increase in drag and loss of lift of airfoils<sup>5,6</sup> and helicopter blades<sup>7</sup> due to icing. This capability for predicting ice shapes on airfoils has also been extended by the authors to include airfoils with slats, and very recently

to multielement airfoils so that ice shapes on the main airfoil and on the flap can be computed as well as on the slat. This will permit the effects of icing on high-lift configurations to be computed using the interactive boundary-layer method recently developed by Cebeci et al.<sup>8</sup>

For wing flows, our research followed a similar path, concentrating on the development of (1) a three-dimensional version of the LEWICE code, (2) a three-dimensional interactive boundary-layer (IBL) method for iced wings, and (3) the coupling of the IBL method to the LEWICE code to determine the ice shapes and their effects on lift, drag and moment coefficients for wing flows.

The progress to date for airfoil flows is described in several papers. For this reason the present paper concentrates mainly on three-dimensional flows and describes the extension to wing flows of the combined LEWICE/IBL procedure developed for airfoils. Section 2 describes the method for calculating ice shapes on the leading edge of a wing and presents a comparison between calculated and experimental results. Section 3 describes the interactive boundary-layer method for computing three-dimensional flows on iced wings. In addition, this section presents the results obtained from the application of this method to a NASA MS 317 tapered wing with ice and to an unswept NACA 0012 wing without ice. In each case, the inviscid and viscous flow equations are solved interactively to determine the increase in drag due to ice and to compare the calculated pressure coefficients with measured values. Section 4 presents recent results obtained for multielement airfoils and is followed by concluding remarks.

## 2.0 Extension of LEWICE to Wings and Its Validation

The extension of the LEWICE airfoil code to wings is not so straightforward. There are several possible approaches that can be pursued. In each approach the flowfield calculations should be performed in principle using a three-dimensional inviscid method, and the impingement pattern of the water droplets on the surface should be determined by performing trajectory calculations for the three components of the velocity obtained from the inviscid method. The heart of the LEWICE code, however, is the third module that contains the quasi-steady-state surface heat transfer analysis in which mass and energy equations are solved for a two-dimensional flow in order to determine the ice shape and size. The extension of this module to three-dimensional flows would require the heat balance equation, developed for airfoil flows, to be modified to wing flows. And, as discussed in Ref. 9, this can only be done with the help of experimental data that presently do not exist. As a first step, it is best to leave the heat balance in its

\* Professor and Chairman.

\*\* Associate Professor.

† Research Professor.

†† Research Associate.

two-dimensional form and assume it to apply to a three-dimensional body expressed in an equivalent two-dimensional form. One approach, followed by Potapczuk and Bidwell,<sup>10</sup> is to perform the trajectory calculations for a three-dimensional flow-field and apply them along the streamlines on the wing. Another approach, followed in Ref. 9, is to approximate the 3-D wing by an equivalent yawed infinite wing at each spanwise station. In this case, the flowfield is calculated by a three-dimensional panel method and the particle trajectories calculated for flow normal to the leading edge subject to the infinite swept-wing assumption. Another approach is to apply the LEWICE airfoil code to the streamwise cross-section of the wing. This approach has at least two alternatives, one of which is described in this paper. The accuracy of these three approaches and others depend on the angle of attack and the spanwise location of the airfoil section, and they require a careful evaluation through comparisons with experimental data.

## 2.1 Comparison of Measured Ice Shapes and Predictions Obtained with Yawed Wing Approximation

The calculated results obtained with the extension of the LEWICE airfoil code to wing flows by the method of Ref. 9 are shown in Figs. 1 and 2 together with the experimental results<sup>11</sup> on an MS-317 swept wing. A summary of test conditions used in the calculations are given in Table 1. Additional studies for other test conditions are in progress and will be reported later. The calculated ice shapes in Figs. 1 and 2 were obtained for the untapered wing with a MS-317 airfoil section defined streamwise with a sweep angle of 30° and an aspect ratio of six. All trajectory and ice accretion calculations were carried out for inviscid flow computed on the mid-semispan section where the spanwise pressure gradient was negligible. All calculations were performed for one time step to save computer time, which is approximately 7 minutes per run on the Cray computer. The increase in time, in comparison with the two-dimensional case, is primarily due to the trajectory calculations where, despite the yawed infinite wing approximations, the computation of the off-body velocities involves repeated large matrix multiplications in which all wing panels are represented.

Figure 1a shows a comparison of measured and calculated ice shapes for Run 8, which corresponds to  $T_\infty = 0^\circ$ ,  $\alpha = 2^\circ$ ,  $t = 390$  sec. As can be seen, the agreement between measured and calculated results is remarkably good. The calculated results for a calculation time of 1164 sec and for  $T_\infty = 0^\circ\text{F}$  and  $\alpha = 2^\circ$  (Run 11) are shown in Fig. 1b and indicate reasonable agreement with measurements despite the one time step used in the calculations. It is expected that the ice growth will have some effect on the velocity field and on the calculated droplet impingement. A comparison of predicted and measured ice shapes obtained for  $T_\infty = 0^\circ\text{F}$  at  $\alpha = 8^\circ$  for  $t = 390$  and 1164 sec. (Runs 9 and 10) are shown in Figs. 1c and 1d, respectively. The agreement is again reasonable, keeping in mind that only one time step was used in the calculations.

The next set of studies was conducted for a slightly higher freestream temperature of  $T_\infty = 15^\circ\text{F}$ , representing an icing condition for which

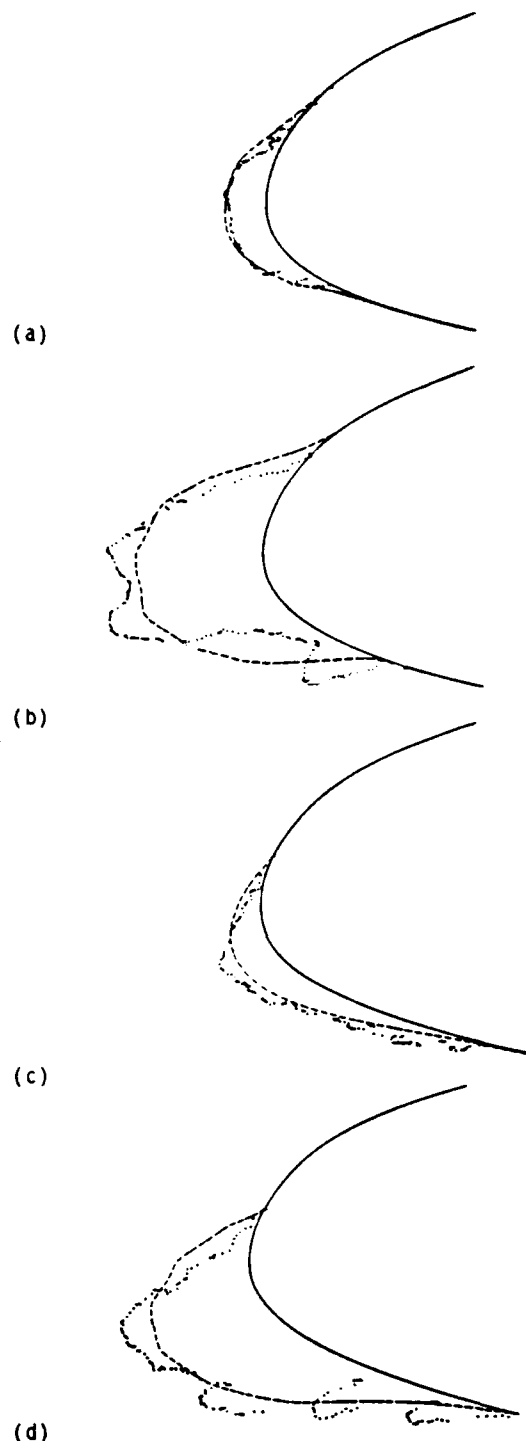


Fig. 1. Comparison of calculated (solid lines) and measured (dashed lines) ice shapes. Rime ice: (a) Run 8, (b) Run 11, (c) Run 9, (d) Run 10.

a mixed ice growth was observed. Run 7 in Fig. 2a for  $\alpha = 2^\circ$  and  $t = 390$  sec. indicates good agreement between experiment and theory, except for some deviation on the upper surface. The results in Fig. 2b at the large time step of  $t = 1164$  sec. (Run 1) are more or less in agreement in predicting the amount of ice accumulated, but they differ in predicting its shape. It is known from two-dimensional calculations that a large number of relatively short time steps are needed to predict horn-shaped ice for glaze ice. Since the mixed ice formation tends toward glaze ice shapes for

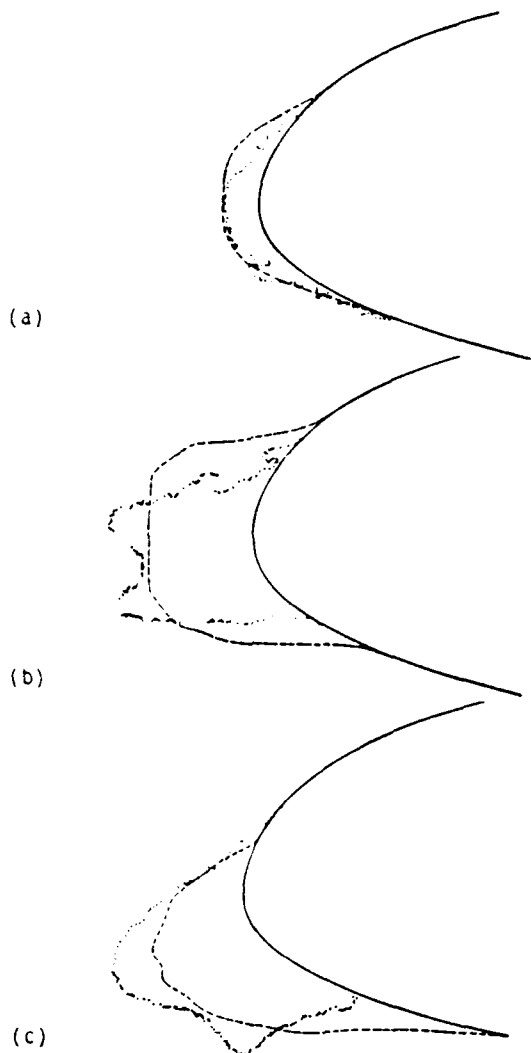


Fig. 2. Comparison of calculated (solid lines) and measured (dashed lines) ice shapes. Mixed ice: (a) Run 7, (b) Run 1, (c) Run 6.

Table 1. Test Conditions for MS-317 Ice Accretion  
Experiment of Ref. 8,  $V_\infty = 150$  mph,  $d = 20$   $\mu$ m,  
 $LWC = 1.03$  gm $^{-3}$ .

Run	$T$ ( $^{\circ}$ F)	$t$ (sec)	$\alpha$ (deg)	$(k_s/c)_1$
1	15	1164	2.0	0.00192
6	15	1164	8.0	0.00192
7	15	390	2.0	0.00192
8	0	390	2.0	0.00127
9	0	390	8.0	0.00127
10	0	1164	8.0	0.00127
11	0	1164	2.0	0.00127

large times, it is not surprising that one time step calculation is not sufficient to predict the actual growth of the ice shapes. Similar comments apply to Fig. 2c, where comparisons are for a large time step of  $t = 1164$  sec. (Run 6), but at  $\alpha = 8^{\circ}$ .

## 2.2 Comparison of Measured Ice Shapes and Predictions Obtained with Strip Theory Approximation

Additional calculations were also performed with the LEWICE code to determine the ice shapes on the leading edge of the MS-317 swept wing discussed in the previous subsection. This time we

used the strip theory approximation rather than the yawed wing approximation. We calculated the three-dimensional velocity field from the panel method and used the velocity distribution in the LEWICE code for the streamwise airfoil section. Figure 3 shows a comparison between the ice shapes computed with strip theory (2-D) and yawed wing (3-D) approximations together with the measured ice shape for run 11. As can be seen, both calculated ice shapes, at least for this run, agree reasonably well with experimental data. Additional studies are underway to further investigate the differences between the two procedures.

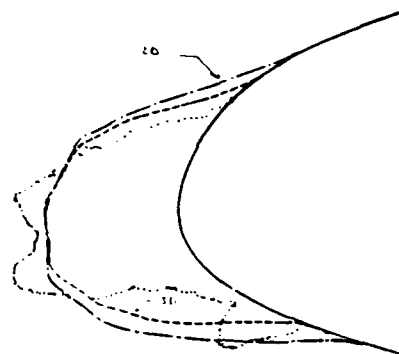


Fig. 3. Comparison of calculated ice shapes with experimental data. 2-D represents the ice shape with strip theory approximation and 3-D that with yawed wing approximation.

## 2.3 The Role of Wind Tunnel Effect on the Calculation of Ice Shapes

In general, infinite yawed wing conditions apply to the mid-semispan section of wings with an aspect ratio greater than about five. This approximation becomes progressively less accurate as the tip or the root of the wing is approached, but in most instances it can still provide reasonable answers. A point to remember about the use of this approximation with finite aspect ratio wings is that although the flow may have the desired characteristics, its lift is always less than the lift of a wing with infinite aspect ratio. This may lead to problems in comparing calculations with experimental data unless the aspect ratio or the pressure distribution is also given. If the pressure distribution is not available, the given angle of attack may not properly represent the experimental conditions. Similar problems may also arise in simulating wind-tunnel conditions by calculating the corrected incidence and lift coefficient in free air, because the trajectories in the two cases may be far from identical. One solution to the wind-tunnel problem, which may be the only acceptable solution for a swept wing spanning the tunnel, is to calculate the flowfield about the wing in the presence of the tunnel walls.

The comparisons between the calculated and experimental ice shapes presented in Subsections 2.1 and 2.2 were obtained for the icing conditions and angle of attack given in Table 1. Care, however, is required to perform the calculations as closely as possible to the stated experimental conditions. Even though the atmospheric icing conditions are properly defined in the LEWICE calculations, the angle observed in the wind tunnel together with the wing aspect ratio may

need to be different when the flowfield calculations are performed with the panel method for a free air model.

To investigate this possibility further, we have calculated the pressure distributions for a constant chord wing with MS-317 streamwise sections and with a  $30^\circ$  sweep, having a finite aspect ratio in free air and spanning the side walls of a wind tunnel, using the panel method of Ref. 12. The free air model was chosen to have an aspect ratio of 6 in order to reduce the root and tip effects at the mid-semispan location. It was found that the angle of attack of the free-air model had to be increased to  $4^\circ$  for the pressure distributions to match the experimental data of Bidwell<sup>2</sup> measured at  $2^\circ$  angle of attack in the wind tunnel. The  $8^\circ$  angle-of-attack case in Table 1 required an increase of  $3.5^\circ$  angle of attack in free air to obtain satisfactory agreement with the pressure distributions. Since there is some doubt about the flowfields being matched at the widely differing angles of attack in the wind tunnel and in free air, the flow was calculated about the wing in the wind tunnel. This requires additional paneling of the tunnel floor, ceiling and one sidewall, while taking advantage of one plane of symmetry. Figure 4 shows the calculated and measured pressure distributions at  $\alpha = 2^\circ$  in the wind tunnel compared with results from the calculations in free air at  $\alpha = 2^\circ$  and  $4^\circ$ . Agreement between the experimental data and the calculations for the wing in the wind tunnel is very good, considering that the calculated pressure distribution corresponds to inviscid pressure distribution and does not include any viscous effects. As can be seen, matching of free-air calculations with

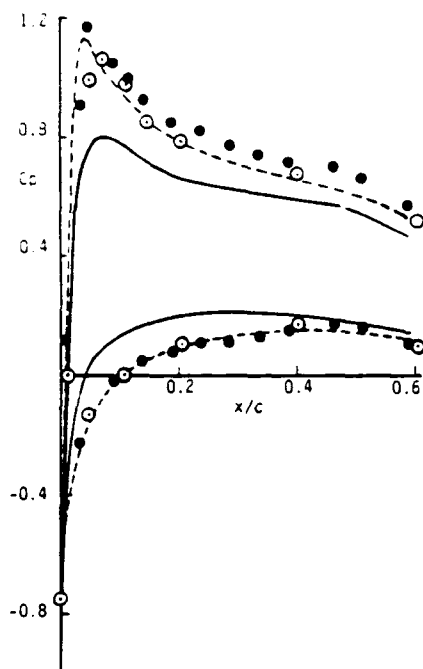


Fig. 4. Computed and experimental pressure distributions for the MS-317 airfoil. — denotes results for  $\alpha = 2^\circ$ , free air, ---  $\alpha = 4^\circ$ , free air. Symbol o denotes experimental results for  $\alpha = 2^\circ$ , wing tunnel and o denotes calculated results for  $\alpha = 2^\circ$ , wind tunnel.

wind-tunnel data is a trial and error process. Studies are underway to extend these calculations to include a wing with ice. This is relatively easy, except for the longer computing times for the particle trajectories resulting from the large number of panels used in the calculation of the inviscid flowfield.

### 3.0 Three-Dimensional Interactive Boundary-Layer Method

A complete description of the three-dimensional interactive boundary-layer method is described in Ref. 9 and is presented here for completeness.

As in two-dimensional flows, the interactive method for three-dimensional flows is based on the solutions of the inviscid and boundary-layer equations. An interface program, illustrated by Fig. 5, is placed between the inviscid and three-dimensional inverse boundary-layer methods to process the geometry and inviscid velocity data for input to the boundary-layer program. The basic input to this program is (1) the definition of the wing configuration that is used by a geometry subroutine to construct a nonorthogonal coordinate system and (2) the associated geometrical parameters, which consist of the geodesic curvatures and metric coefficients needed in the boundary-layer calculations. Some of the generated data is used later in a velocity subroutine to determine the inviscid velocity components at the boundary-layer grid points and to transform the inviscid velocity components on the surface, calculated in a Cartesian coordinate system, into the boundary-layer coordinate system. This operation consists of calculating dot products of velocity vectors as well as chordwise and spanwise interpolation. Further velocity and geometry data processing is carried out in a subroutine that separates the generated information into upper and lower surfaces of the wing for boundary-layer calculations.

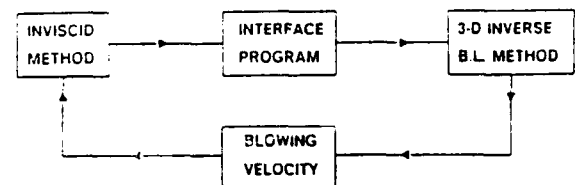


Fig. 5. The interactive boundary-layer method.

The above procedure is appropriate to wings without ice and has been used to compute transonic flows on wing/body configurations<sup>18</sup> where, since the wing leading edge was free of ice, there was no difficulty in generating solutions near the attachment line by constructing the nonorthogonal coordinate system and computing the geometrical properties of the wing. For a wing with ice, generation of the boundary-layer solutions near the leading edge can pose problems since the geodesic curvatures and metric coefficients must be determined for an irregular surface. In addition, the formulation of the interactive boundary-layer method developed for iced airfoils must take account of the three-dimensional nature of the flow. Thus, it is necessary to make changes in the strategy for solving the three-dimensional boundary-layer equations for an iced wing. These are considered below.

### 3.1 Boundary-Layer Equations

The three-dimensional boundary-layer equations for a nonorthogonal coordinate system are given in several references. With Reynolds stresses modeled by the eddy-viscosity concept, they can be written as,

$$\frac{\partial}{\partial x} (u h_2 \sin \theta) + \frac{\partial}{\partial z} (w h_1 \sin \theta) + \frac{\partial}{\partial y} (v h_1 h_2 \sin \theta) = 0 \quad (1)$$

$$\begin{aligned} \frac{u}{h_1} \frac{\partial u}{\partial x} + \frac{w}{h_2} \frac{\partial u}{\partial z} + v \frac{\partial u}{\partial y} - K_1 u^2 \cot \theta + K_2 w^2 \operatorname{cosec} \theta \\ + K_{12} u w = - \frac{\operatorname{cosec}^2 \theta}{\rho h_1} \frac{\partial p}{\partial x} + \frac{\cot \theta \operatorname{cosec} \theta}{\rho h_2} \frac{\partial p}{\partial z} \\ + v \frac{\partial}{\partial y} (b \frac{\partial u}{\partial y}) \end{aligned} \quad (2)$$

$$\begin{aligned} \frac{u}{h_1} \frac{\partial w}{\partial x} + \frac{w}{h_2} \frac{\partial w}{\partial z} + v \frac{\partial w}{\partial y} - K_2 w^2 \cot \theta + K_1 u^2 \operatorname{cosec} \theta \\ + K_{21} u w = \frac{\cot \theta \operatorname{cosec} \theta}{\rho h_1} \frac{\partial p}{\partial x} - \frac{\operatorname{cosec}^2 \theta}{\rho h_2} \frac{\partial p}{\partial z} \\ + v \frac{\partial}{\partial y} (b \frac{\partial w}{\partial y}) \end{aligned} \quad (3)$$

Here  $x$  denotes the coordinate along the lines formed by the intersection of the wing surface and planes representing constant percent semispan;  $z$  is the coordinate along the constant percent chordlines that generate the wing surface, with chord defined as the maximum length line between leading edge and trailing edge. The third coordinate  $y$  denotes the direction normal to the wing surface, and the parameter  $h$  denotes the metric coefficients, with  $\theta$  the angle between the coordinate lines  $x = \text{const}$  and  $z = \text{const}$ . For an orthogonal system,  $\theta = \pi/2$ . The parameters  $K_1$  and  $K_2$  are known as the geodesic curvatures of the curves  $z = \text{const}$  and  $x = \text{const}$ , respectively. Equations (1) to (3) are subject to the following boundary conditions

$$y = 0, \quad u = 0, \quad v = 0, \quad w = 0 \quad (4a)$$

$$y = \delta, \quad u = u_e(x, z), \quad w = w_e(x, z) \quad (4b)$$

The solution of the above equations also requires initial conditions on two intersecting planes; those in the  $(y, z)$  plane at a specified chordwise location are determined from the solutions of the equations discussed in Subsection 2.2. Those on the  $(x, y)$  plane, at a specified spanwise location  $z = z_0$ , with  $z_0$  corresponding to the root location, are determined from the solutions of the quasi-three-dimensional form of Eqs. (1) to (3) with all derivatives with respect to  $z$  neglected, that is,

$$\frac{\partial}{\partial x} (u h_2 \sin \theta) + \frac{\partial}{\partial y} (v h_1 h_2 \sin \theta) = 0 \quad (5)$$

$$\begin{aligned} \frac{u}{h_1} \frac{\partial u}{\partial x} + v \frac{\partial u}{\partial y} - K_1 u^2 \cot \theta + K_2 w^2 \operatorname{cosec} \theta + K_{12} u w \\ = - \frac{\operatorname{cosec}^2 \theta}{\rho h_1} \frac{\partial p}{\partial x} + v \frac{\partial}{\partial y} (b \frac{\partial u}{\partial y}) \end{aligned} \quad (6)$$

$$\begin{aligned} \frac{u}{h_1} \frac{\partial w}{\partial x} + v \frac{\partial w}{\partial y} - K_2 w^2 \cot \theta + K_1 u^2 \operatorname{cosec} \theta + K_{21} u w \\ = \frac{\cot \theta \operatorname{cosec} \theta}{\rho h_1} \frac{\partial p}{\partial x} + v \frac{\partial}{\partial y} (b \frac{\partial w}{\partial y}) \end{aligned} \quad (7)$$

subject to the same boundary conditions given in Eq. (4).

### 3.2 Interaction Law

To account for possible flow separation, as in two-dimensional flows, we use the interaction law of Veldman<sup>13</sup> where, for airfoil flows, the edge velocity is expressed as the sum of an inviscid velocity  $u_e^0(x)$  and perturbation velocity  $\delta u_e(x)$  due to viscous effects, that is,

$$u_e(x) = u_e^0(x) + \delta u_e(x) \quad (8)$$

The perturbation velocity is given by the Hilbert integral

$$\delta u_e(x) = \frac{1}{\pi} \int_{x_a}^{x_b} \frac{d}{d\sigma} (u_e^0 \delta^*) \frac{d\sigma}{x - \sigma} \quad (9)$$

in the interaction region  $(x_a, x_b)$ .

To extend this inverse formulation to three-dimensional flows, it is necessary that the two-dimensional interaction formula given by Eq. (9) be either modified to account for the interaction in the  $x$ - and  $z$ -directions or be replaced by another formulation which provides a relationship between displacement surface and external velocity. Here we use the former approach, as described in Ref. 14, and first generate an initial displacement surface by solving the quasi-three-dimensional boundary-layer equations subject to the boundary conditions given by Eqs. (4) and (8) with the external velocity distribution  $u_e^0(x)$  obtained from the panel method. The second step involves interaction between the inviscid flow equations and the quasi-three-dimensional flow equations. As in two-dimensional flows, the solutions of the boundary-layer equations are used to compute distributions of blowing velocity on the surface, and these allow the inviscid flow solutions to be updated. In step three, after the calculation of the initial conditions in the  $(y, z)$  and  $(x, y)$  planes, the fully three-dimensional boundary-layer equations are solved with the external velocity components resulting from step two. As before, the spanwise velocity component is assumed to correspond to its inviscid value. The viscous flow solutions are obtained by marching in the spanwise direction at each advancing chordwise location. This represents the first phase in an interactive loop that involves the fully three-dimensional boundary-layer equations. In the subsequent phases, as before, the blowing velocity distribution is used to obtain improved inviscid flow solutions, so the fully three-dimensional boundary-layer equations are solved for iced wings as for clean wings in transonic flow.<sup>14</sup>

The viscous effects in the spanwise component  $w_e$  are assumed to be second order, although their neglect is contrary to the irrotationality condition. However, trial calculations involving variations of both velocity conditions showed that errors were smaller than those associated with the convergence of the solutions.

### 3.3 Transformed Equations

As in two-dimensional flows, we express the boundary-layer equations in transformed variables for computational purposes. At first, when the equations are solved for a prescribed external velocity distribution (standard problem), we use the Falkner-Skan transformation and a modified version of this transformation for the inverse mode. In the former case, the independent variables are defined by

$$x = x, \quad z = z, \quad n = \left(\frac{u_e}{v_s}\right)^{1/2} y, \quad s = \int_0^x h_1 dx \quad (10)$$

For the dependent variables  $u$ ,  $v$  and  $w$ , we introduce a two-component vector potential such that

$$\begin{aligned} u h_2 \sin \theta &= \frac{\partial \psi}{\partial y}, \quad w h_1 \sin \theta = \frac{\partial \phi}{\partial y}, \\ v h_1 h_2 \sin \theta &= - \left( \frac{\partial \psi}{\partial x} + \frac{\partial \phi}{\partial z} \right) \end{aligned} \quad (11)$$

In addition, dimensionless parameters  $f$  and  $g$  are defined by

$$\psi = (u_e v_s)^{1/2} h_2 \sin \theta f(x, z, n) \quad (12)$$

$$\phi = (u_e v_s)^{1/2} \frac{u_0}{u_e} h_1 \sin \theta g(x, z, n)$$

$$\begin{aligned} (bf'')' + ef'' + m_2(f')^2 + m_5 f' g' + m_8 (g')^2 + m_{11} \\ = m_{10} f' \frac{\partial f'}{\partial x} + m_7 g' \frac{\partial f'}{\partial z} \end{aligned} \quad (13)$$

$$\begin{aligned} (bg'')' + eg'' + m_4 f' g' + m_3 (g')^2 + m_9 (f')^2 + m_{12} \\ = m_{10} f' \frac{\partial g'}{\partial x} + m_7 g' \frac{\partial g'}{\partial z} \end{aligned} \quad (14)$$

$$e' = m_1 f' + m_6 g' + m_{10} \frac{\partial f'}{\partial x} + m_7 \frac{\partial g'}{\partial z} \quad (15)$$

The coefficients  $m_1$  to  $m_{12}$  are defined in Ref. 9.

In terms of transformed variables, boundary conditions given by Eq. (4) become

$$\begin{aligned} n = 0: \quad f = g = f' = g' = 0 \\ n = n_e: \quad f' = 1, \quad g' = \frac{w_e}{u_0} \end{aligned} \quad (16)$$

The form of the transformed quasi-three-dimensional equations is identical to the form of Eqs. (13) to (15), except for small differences discussed in Ref. 9.

To solve the equations in the inverse mode, we define independent variables by

$$x = x, \quad z = z, \quad Y = \left(\frac{u_0}{v_s}\right)^{1/2} y, \quad s = \int_0^x h_1 dx \quad (17)$$

and relate the vector potentials  $\psi$  and  $\phi$  to  $f$  and  $g$  by

$$\psi = (u_0 v_s)^{1/2} h_2 \sin \theta f(x, z, n) \quad (18)$$

$$\phi = (u_0 v_s)^{1/2} h_1 \sin \theta g(x, z, n)$$

and with a prime now denoting differentiation with respect to  $Y$  and  $u_e$  and  $w_e$  denoting edge velocity components normalized by reference velocity  $u_0$ , Eqs. (1) to (3), with  $e'$  defined by Eq. (15) and  $m$ 's given in Ref. 9, are written as

$$\begin{aligned} (bf'')' + ef'' + m_2[(f')^2 - (\bar{u}_e)^2] + m_5[f'g' - \bar{u}_e \bar{w}_e] \\ + m_8[(g')^2 - (\bar{w}_e)^2] = m_{10}(f' \frac{\partial f'}{\partial x} - \bar{u}_e \frac{\partial \bar{u}_e}{\partial x}) \\ + m_7(g' \frac{\partial f'}{\partial z} - \bar{w}_e \frac{\partial \bar{u}_e}{\partial z}) \end{aligned} \quad (19)$$

$$\begin{aligned} (bg'')' + eg'' + m_3[(g')^2 - (\bar{w}_e)^2] + m_4[f'g' - \bar{u}_e \bar{w}_e] \\ + m_9[(f')^2 - (\bar{u}_e)^2] = m_{10}(f' \frac{\partial g'}{\partial x} - \bar{u}_e \frac{\partial \bar{w}_e}{\partial x}) \\ + m_7(g' \frac{\partial g'}{\partial z} - \bar{w}_e \frac{\partial \bar{w}_e}{\partial z}) \end{aligned} \quad (20)$$

The transformed boundary conditions for the system of Eqs. (19) and (20), with  $u_e$  given by Eq. (8) and with  $w_e$  corresponding to its inviscid value, are

$$n = 0: \quad f = g = f' = g' = 0 \quad (21a)$$

$$n = n_e: \quad f' = \bar{u}_e, \quad g' = \bar{w}_e \quad (21b)$$

The quasi-three-dimensional form of the equations, which are subject to the boundary conditions given by Eq. (21), are obtained from the above equations by setting

$$\frac{\partial f'}{\partial z} = \frac{\partial g'}{\partial z} = \frac{\partial \bar{u}_e}{\partial z} = \frac{\partial \bar{w}_e}{\partial z} = 0 \quad \text{and} \quad m_6 = 0 \quad (22)$$

To generate the initial conditions near the leading edge of the iced wing, we use quasi-three-dimensional boundary-layer equations expressed in the inverse mode given by

$$\begin{aligned} (bf'')' + ef'' + m_2[(f')^2 - (\bar{u}_e)^2] + m_5(f'g' - \bar{u}_e \bar{w}_e) \\ + m_8[(g')^2 - (\bar{w}_e)^2] = m_{10}(f' \frac{\partial f'}{\partial x} - \bar{u}_e \frac{\partial \bar{u}_e}{\partial x}) \end{aligned} \quad (23)$$

$$\begin{aligned} (bg'')' + eg'' + m_3[(g')^2 - (\bar{w}_e)^2] + m_4(f'g' - \bar{u}_e \bar{w}_e) \\ + m_9[(f')^2 - (\bar{u}_e)^2] = m_{10}(f' \frac{\partial g'}{\partial x} - \bar{u}_e \frac{\partial \bar{w}_e}{\partial x}) \end{aligned} \quad (24)$$

$$e' = m_1 f' + m_{10} \frac{\partial f'}{\partial x} \quad (25)$$

The above equations can be further simplified if we assume that two adjacent defining sections of a wing are connected by straight line development, as commonly used in the wing design. This

feature simplifies the problem of shaping the metal for a wing surface. As a consequence, we can neglect the geodesic curvature of  $x = \text{constant}$  lines, namely  $k_2$ , and thus set  $m_3 = m_6 = 0$ . From the definitions of  $m_4$  and  $m_5$ , it can be seen that as a result of the above assumption, these two terms are also small and can be neglected. We further assume that the local variations in cross sections in the spanwise direction are small. Examination of the terms  $m_1$ ,  $m_2$  and  $m_6$  for a typical wing shows that  $m_2$  reaches a value less than 0.1 very close to the leading edge ( $x/c < 0.01$ ) and  $m_6$  reaches a maximum value of 0.2. However, their magnitudes rapidly decrease with increasing  $x$  and reach a very small value at  $x/c < 0.1$ . This behavior allows us to neglect  $m_2$  and  $m_6$  in the equations and set  $m_1 = 1/2$ .

### 3.4 Solution Procedure

A detailed description of the solution procedure will be reported separately. Briefly, the boundary-layer equations expressed in terms of transformed variables are solved with Keller's two-point finite-difference method<sup>15</sup> (box scheme) with boundary conditions expressed in inverse form with the interaction law described in Subsection 3.2. Depending on the complexity of the flow field, two forms of the box scheme are employed. In regions where all velocity components are positive, the regular box scheme is used. In regions of either a negative spanwise velocity component or negative streamwise velocity component, the zig-zag box scheme described in Ref. 15 is used.

### 3.5 Performance Degradation of an Iced Tapered Wing

The interactive boundary-layer method of Section 3 was used to study the performance degradation of an iced wing having MS-317 airfoil streamwise sections, an aspect ratio of 3.43, and a taper ratio of 0.4. Icing conditions were chosen to correspond to those in Runs 8 and 11, shown in Table 1. The pressure distribution on the wing was computed at four locations defined by the midsection of each wing-section with a hundred panels on each defining airfoil section. The ice shapes corresponding to this pressure distribution were computed with the method of Section 2 in the middle of each wing section and were used to distribute ice along the leading edge of the tapered wing. The computed ice shapes for  $\alpha = 2^\circ$  were then assumed to be the same for all angles of attack on the wing in the investigation of the performance degradation of the wing due to ice shapes corresponding to the atmospheric conditions given in Runs 8 and 11. At a specified angle of attack, with the defined ice shapes along the leading-edge of the wing, calculations were performed with the method of Section 3; that is, inviscid flow calculations performed for an iced wing were followed by the inverse three-dimensional boundary-layer calculations to determine the blowing velocity distribution to be used in the incorporation of viscous effects into the inviscid method. The inviscid flow solutions made use of four lifting strips, and the viscous flow calculations included boundary-layer calculations on the wing and in the wake, the latter requiring velocities at off-body points in the potential field. This interactive and iterative procedure was repeated until the solutions converged. The lift coefficients were then calculated from the

inviscid method for each individual strip and included the contribution of ice protruding beyond the wing contour and the drag coefficients from the boundary-layer calculations.

Figure 6 shows the variation of the calculated lift coefficients as a function of angle of attack. Since the primary purpose of the calculations was to demonstrate the increase in drag due to ice on a tapered wing, the angle of attack range was not extended to stall, which would occur at relatively high angles of attack for low aspect ratio wings. The higher lift coefficient than for the clean wing shown for the two iced wings is due to the normalization with the wing area of the clean wing in both cases. The conclusion from this figure is that lift is not affected by the rime ice accretion for the angle of attack range considered here because the ice shapes along the leading edge of the wing for runs 8 and 11 do not cause premature flow separation on the wing.

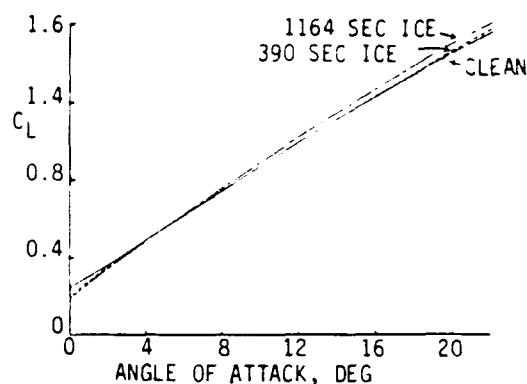


Fig. 6. Effect of leading-edge 390 and 1164 second rime ice on the lift coefficient of a tapered wing for  $R = 4.6 \times 10^6$  based on root chord.

The calculated drag coefficients shown in Fig. 7 represent the profile drag of the wing only and do not represent the total drag, since that requires the contribution of the induced drag. The profile drag was calculated sectionwise from the Squire-Young formula based on the resultant velocity at the trailing edge. Comparable results were also obtained from the momentum deficiency in the far wake. Here we see considerable differences between the clean wing and the two iced wings because the Reynolds number is relatively low ( $Re = 4.6 \times 10^6$  for the root chord) and

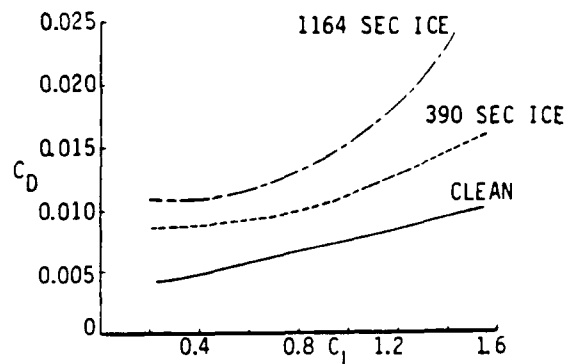


Fig. 7. Effect of leading edge 390 and 1164-second rime ice on the profile drag coefficient of a tapered wing for  $R_c = 4.6 \times 10^6$  based on root chord.



there are large regions of laminar flow on the clean wing. The principal contributor to the drag increase for the iced wing is the shift in transition to near the leading edge due to roughness of the iced surface. The contribution of the surface roughness itself to the drag is very small for Run 8 because the extent of ice is small and its shape emulates an airfoil leading edge. The additional drag increase for Run 11 results from the surface roughness spread over a large wetted area increment. The main conclusion that can be drawn from these comparisons is that drag increments obtained between clean and iced airfoils in wind tunnels depend on transition locations on the clean wing. If the Run 8 case represents a wing with transition fixed at the leading edge and the clean wing case is transition free, the observed drag increments from the Run 11 case are quite different from each other. As a corollary, drag increments obtained from wind-tunnel tests may be meaningless without fixing transition or knowing where transition occurs during the tests.

### 3.6 Results for an Unswept NACA 0012 Wing

Bragg et al.<sup>16</sup> have tested two wings with a simulated ice shape to determine its effect on wing aerodynamic characteristics. They also tested the same wings in clean conditions to establish the base case. Their measurements include selected chordwise pressure distributions, balance data on lift and drag coefficients, and section drag data by wake measurements. Since these measurements were conducted in a wind tunnel and our calculations were to be done for freestream conditions, at first we decided to perform the calculations for the clean unswept wing with the interactive method of Section 3. The inviscid code used seven lifting strips, each with 180 chordwise panels along the semispan.

Figure 8 shows the calculated pressure distributions for  $\alpha = 4$  degrees together with the experimental results. The overall agreement is very good. Also shown are the integrated sectional lift coefficients which differ somewhat from case to case, but this is expected from integration of nonsmooth data. Studies are in progress to evaluate the interactive method for the swept clean wing and then apply the method to both unswept and swept wings with ice.

### 4.0 Calculation of Ice Shapes on Multielement Airfoils

To extend the method developed for analyzing iced airfoils and wings to high-lift configurations, our studies first concentrated on the calculation of ice shapes on the slat of a four-element airfoil shown in Fig. 9. Figure 10 shows the inviscid pressure distribution of the clean four-element airfoil at  $\alpha = 0^\circ$ . The ice shapes of the first element corresponding to times up to two minutes are shown in Fig. 11 for a time step  $\Delta t$  of one minute. With ice build-up on the first element, the computed pressure distribution build-up remains essentially the same except along the first element. Figure 12 shows the progression of the pressure distributions of the first element with time. As can be seen, the ice accretions cause rapid changes in the pressure distribution with large leading-edge peaks.

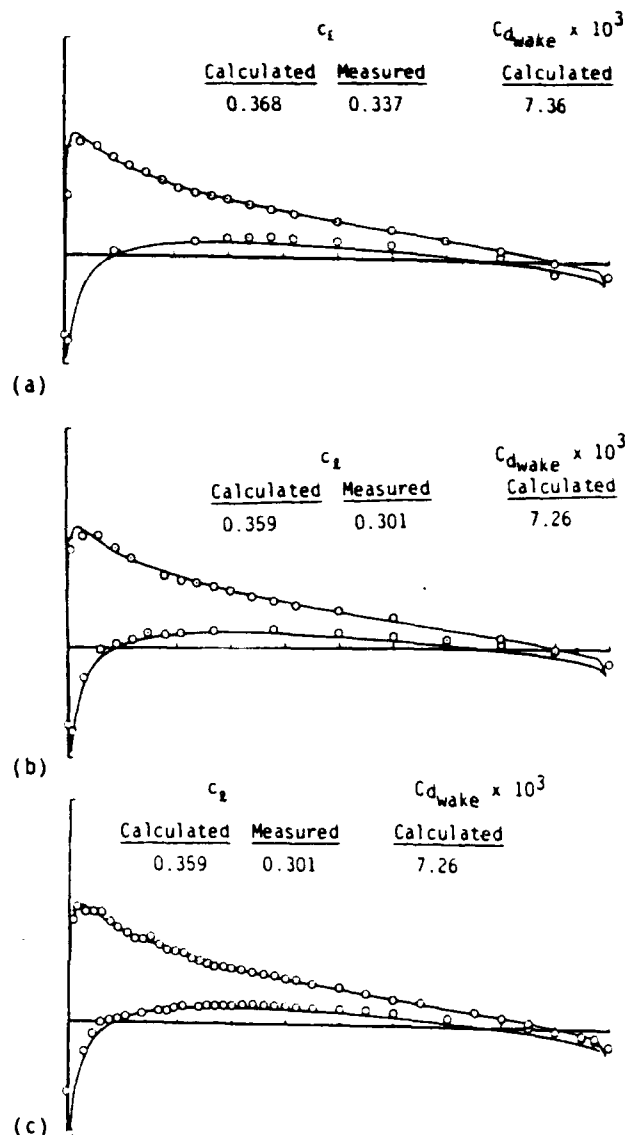


Fig. 8. Comparison of calculated (solid lines) and measured (symbols) results for the unswept clean wing of Ref. 16 at  $\alpha = 4^\circ$ : (a)  $y/b = 0.168$ , (b)  $y/b = 0.336$ , (c)  $y/b = 0.497$ .

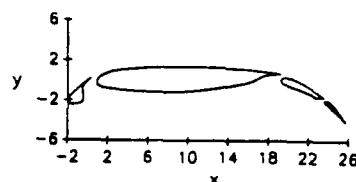


Fig. 9. Geometry of the four-element airfoil.

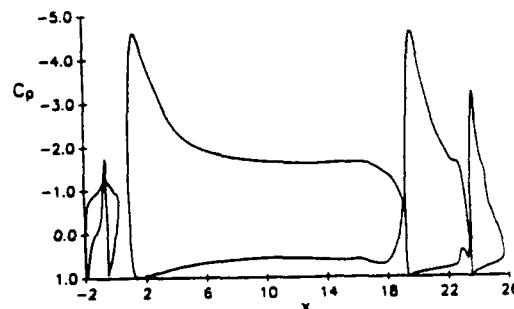


Fig. 10. Pressure distribution for the clean four-element airfoil at  $\alpha = 0^\circ$ .

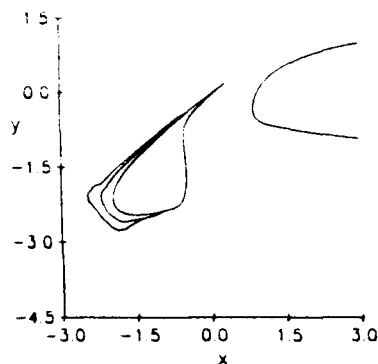


Fig. 11. Glaze ice shapes on the first element of the four-element airfoil at  $\alpha = 0^\circ$ .

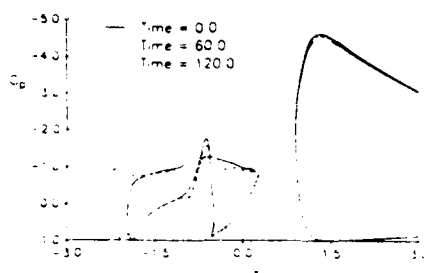


Fig. 12. Pressure distribution along the first element of the four-element airfoil with glaze ice accretion at  $\alpha = 0^\circ$ .

Very recently, the above method has also been extended to multielement airfoils. Figures 13 to 16 show the pressure distributions and the ice shapes on the first two elements of the four-element airfoil at  $\alpha = 4^\circ$  and  $6^\circ$ . The ice shapes correspond to 2 and 5 minutes.

Figures 17 and 18 show the results for the four-element airfoil at  $\alpha = 0^\circ$  for a two-minute glaze ice computed by the multielement LEWICE code. Additional studies are in progress and will be reported later.

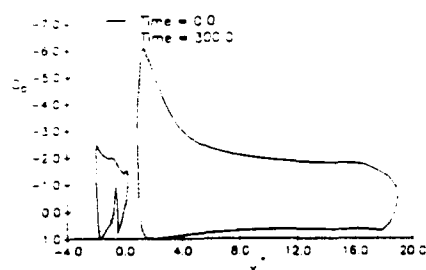


Fig. 13. Pressure distribution for the clean four-element airfoil at  $\alpha = 4^\circ$ .

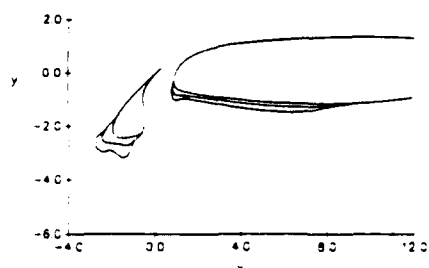


Fig. 14. Glaze ice shapes on the first two elements of the four-element airfoil at  $\alpha = 4^\circ$ . The ice shapes correspond to 2 and 5 minutes.

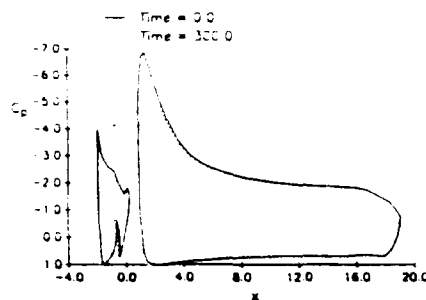


Fig. 15. Pressure distribution for the clean four-element airfoil at  $\alpha = 6^\circ$ .

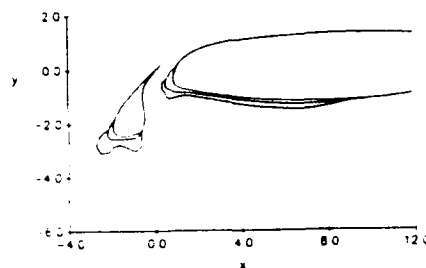


Fig. 16. Glaze ice shapes on the first two elements of the four-element airfoil at  $\alpha = 6^\circ$ . The ice shapes correspond to 2 and 5 minutes.

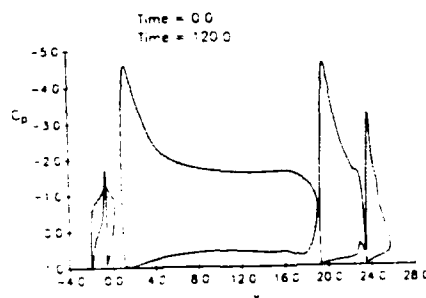


Fig. 17. Pressure distribution for clean and iced four-element airfoil at  $\alpha = 0^\circ$ .

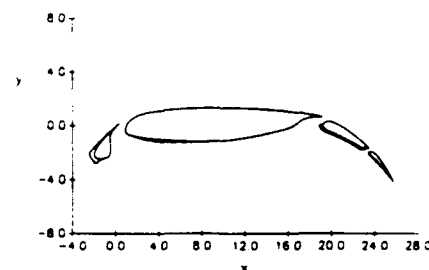


Fig. 18. Computed two-minute glaze ice shapes on a four-element airfoil at  $\alpha = 0^\circ$ .

## 5.0 Concluding Remarks

Until recently, the only capability for predicting ice shapes on aerodynamic configurations was limited to single airfoils. With the methods described here and with the method described in Ref. 17 for wings, this capability now includes wings and multielement airfoils. These methods, however, are in their infancy and require improvements and validation with experimental data.

The interactive method for three-dimensional flows also provides a new capability that, except for the recent work of Ref. 18, did not exist for iced wings. Both methods are, also in the early development stages and require additional work and validation with experimental data.

#### 6.0 References

1. Shaw, R.J., Potapczuk, M.G. and Bidwell, C.S., "Predictions of Airfoil Aerodynamic Performance Degradation Due to Icing," in Numerical and Physical Aspects of Aerodynamic Flows IV (ed. T. Cebeci), p. 19, Springer-Verlag, Berlin-Heidelberg, 1990.
2. Ruff, G.A. and Berkowitz, B.M., "User's Manual for the NASA Lewis Ice Accretion Code (LEWICE)," NASA CR-185129, May 1990.
3. Cebeci, T., Chen, H.H. and Alemdaroglu, N., "Fortified LEWICE with Viscous Effects," *Journal of Aircraft*, Vol. 28, No. 9, pp. 564-571, Sept. 1991.
4. Cebeci, T., "Calculation of Flow Over Iced Airfoils," *AIAA J.*, Vol. 27, p. 853, 1989.
5. Shin, J., Berkowitz, B., Chen, H.H. and Cebeci, T., "Prediction of Ice Shapes and Their Effect on Airfoil Performance," *AIAA Paper 91-0264*, Jan. 1991.
6. Shin, J., Chen, H. H. and Cebeci T., "A Turbulence Model for Iced Airfoils and Its Validation," *AIAA Paper No. 92-0417*, Jan. 1992.
7. Britton, R., "Development of an Analytical Method to Predict Helicopter Main Rotor Performance in Icing Conditions," *AIAA Paper No. 92-0418*, Jan. 1992.
8. Cebeci, T., Jau, J. and Vitiello, D., "An Interactive Boundary-Layer Approach to Multi-element Airfoils at High Lift," *AIAA Paper No. 92-0404*, Jan. 1992.
9. Cebeci, T., Chen, H. H., Kaups, K. and Schimke, S., "Analysis of Iced Wings," *AIAA Paper No. 92-0416*, Jan. 1992.
10. Potapczuk, M.G. and Bidwell, C.S., "Numerical Simulation of Ice Growth on a MS-317 Swept Wing Geometry," *AIAA Paper No. 91-0263*, 1991.
11. Bidwell, C.S., "Icing Characteristics of a Natural Laminar Flows, a Medium-Speed, and a Swept Medium-Speed Airfoil," *AIAA Paper 91-0447*, Jan. 1991.
12. Hess, J.L., "The Problem of Three-Dimensional Lifting Flow and Its Solution by Means of Surface Singularity Distribution," *Computer Methods in Applied Mechanics and Engineering*, Vol. 4, pp. 283-319, 1974.
13. Veldman, A.E.P., "New Quasi-Simultaneous Method to Calculate Interacting Boundary Layers," *AIAA Journal*, Vol. 19, p. 679, 1981.
14. Cebeci, T., Khattab, A.A., Chen, H.H. and Chen, L.T., "An Approach to the Design of Wings: The Role of Mathematics, Physics and Economics," *AIAA Paper No. 92-0286*, Jan. 1992.
15. Bradshaw, P., Cebeci, T. and Whitelaw, J.H., Engineering Calculation Methods for Turbulent Flows, Academic Press, London, 1981.
16. Bragg, M., Khodadoust, A., Soltani, R., Wells, S. and Kenko, M., "Effect of a Simulated Ice Accretion on the Aerodynamics of a Swept Wing," *AIAA Paper No. 91-0442*, 1992.
17. Potapczuk, M.G., "Navier-Stokes Analysis of Airfoils with Leading-Edge Ice Accretions," Ph.D. Dissertation, The University of Akron, May 1989.
18. Kwon, O.J. and Sankar, L.N., "Numerical Study of the Effect of Icing on Fixed and Rotary Wing Performance," *AIAA Paper 91-0662*, 1991.

**HIGH LIFT, 1**  
**SESSION 5**

## HIGH-LIFT AERODYNAMICS: PROSPECTS AND PLANS

by

Lawrence E. Olson

Fixed Wing Aerodynamic Branch  
NASA Ames Research Center, Moffett Field, CA

### Abstract

The emergence of high-lift aerodynamics is reviewed as one of the key technologies to the development of future subsonic transport aircraft. Airport congestion, community noise, economic competitiveness, and safety - the drivers that make high-lift an important technology - are discussed. Attention is given to the potentially synergistic integration of high-lift aerodynamics with two other advanced technologies: ultra-high bypass ratio turbofan engines and hybrid laminar flow control. A brief review of the ongoing high-lift research program at Ames Research Center is presented. Suggestions for future research directions are made with particular emphasis on the development and validation of computational codes and design methods. It is concluded that the technology of high-lift aerodynamics analysis and design should move boldly into the realm of high Reynolds number, three-dimensional flows.

# EFFICIENT SIMULATION OF INCOMPRESSIBLE VISCOUS FLOW OVER MULTI-ELEMENT AIRFOILS

Stuart E. Rogers  
N. Lyn Wiltberger  
Dochan Kwak

MS 258-1, NASA Ames Research Center, Moffett Field, CA 94035

## Abstract

The incompressible, viscous, turbulent flow over single and multi-element airfoils is numerically simulated in an efficient manner by solving the incompressible Navier-Stokes equations. The computer code uses the method of pseudo-compressibility with an upwind-differencing scheme for the convective fluxes, and an implicit line-relaxation solution algorithm. The motivation for this work includes interest in studying high-lift take-off and landing configurations of various aircraft. In particular, accurate computation of lift and drag at various angles of attack up to stall is desired. Two different turbulence models are tested in computing the flow over an NACA 4412 airfoil; an accurate prediction of stall is obtained. The approach used for multi-element airfoils involves the use of multiple zones of structured grids fitted to each element. Two different approaches are compared; a patched system of grids, and an overlaid Chimera system of grids. Computational results are presented for two-element, three-element, and four-element airfoil configurations. Excellent agreement with experimental surface pressure coefficients is seen. The code converges in less than 200 iterations, requiring on the order of one minute of CPU time on a CRAY YMP per element in the airfoil configuration.

## Introduction

An increased understanding of high-lift systems will play an important role in designing the next generation of transport aircraft. Current designs for such aircraft typically involve multiple elements, such as leading edge slats and multiple-slotted flaps. The current trend is toward a more efficient, yet simpler design which will lead to reduced manufacturing and maintenance costs. At the same time, increases in lift coefficients for a given angle of attack and increases in maximum lift coefficient will lead to a larger payload capability. Improved designs will also allow for reduced noise in areas surrounding airports. Understanding of high-lift flow physics harbors the potential to improve airport capacity through a reduction of an airplane's wake vortices, allowing closer spacing between subsequent airplanes taking off and landing.

Increased knowledge of the flow physics involved with high-lift systems is therefore of greater interest than ever before as the need to improve over current designs becomes acute. Study of these configurations will require both computational and experimental efforts. Computational fluid dynamics (CFD) is playing a large role in this work. Multi-element configurations present a number of

challenging problems to the numerical investigators. These include problems involving turbulent boundary layer separation, confluent boundary layers and wakes, Reynolds number effects, three-dimensional effects, compressibility effects, transition, and complex geometries. Although the problems are inherently three-dimensional, there is still much to be learned about the flow physics by studying two-dimensional models.

The computational tools available range from the more efficient inviscid/viscous coupled methods, to a Reynolds-averaged Navier-Stokes (RANS) analysis. An example of the former method is given by Kusunose et al.<sup>1</sup> They use a full potential method coupled with an integral boundary-layer method. These methods have been found to be successful in accurately computing the pressure distribution for multi-element airfoils, including cases up to maximum lift, some of which involve separation. The coupled method has been proven to be useful as an effective engineering design tool. This method is limited by its inability to compute beyond maximum lift conditions, and may have problems with certain features of some airfoil systems such as flap wells, thick trailing edges, or unsteady effects.

Navier-Stokes calculations for high-lift systems have been investigated by a number of authors.<sup>2-4</sup> Schuster and Birkelbaw<sup>2</sup> computed the flow over a two-element airfoil using a structured, compressible, RANS solver. The grid system used was a pointwise patched system with three zones, with C-grids around both the main element and flap, and another outer C-grid surrounding those. Good results were obtained for low Reynolds number turbulent flow. The next two authors, Barth,<sup>3</sup> and Mavriplis<sup>4</sup> both used an unstructured grid approach to handle the difficulty of discretizing multi-element geometries. They were each able to produce accurate pressure coefficient information on the airfoil surfaces. The accuracy of the unstructured grid approach, however, is limited because of the very large aspect ratio of the triangular cells required to resolve high Reynolds number boundary layer flows. Also, this approach is not well developed for three-dimensional problems. Large computational resources are required, especially CPU memory, to make these methods work for viscous flows. Unstructured methods are currently generating a lot of interest in the research community; improvements to these limitations are to be expected in the near future. Until such a time, the current authors believe that a structured grid approach is the most suitable for solving viscous multi-element problems in two and three dimensions.

The current work uses an incompressible RANS flow solver to compute the flow over multi-element airfoils. Two different grid approaches are used; the first approach em-

employs the patched grids utilized in Ref. 2, and the second uses an overlaid grid approach known as the Chimera scheme.<sup>5</sup> The current work examines several airfoil flow problems in two dimensions in an effort to characterize current capability to numerically study such problems. Grid topology, computational efficiency, and resulting accuracy are issues to be examined in the current work. An incompressible flow solver is being utilized because the flow conditions for take-off and landing will generally be less than a Mach number of 0.2. In the actual flow, compressibility effects will generally be confined to a small localized region, such as near the area of a leading-edge slat. Since the incompressible Navier-Stokes system has one less equation than its compressible counterpart, less computing resources are required.

### Algorithm

The current computations are performed using the INS2D computer code which solving the incompressible Navier-Stokes equations for steady-state flows<sup>6</sup> and for unsteady computations.<sup>7</sup> This algorithm has also been applied to problems in three dimensions using the INS3D-UP code.<sup>8</sup> The code is based on the method of artificial compressibility as developed by Chorin<sup>9</sup> in which a pseudo-time derivative of pressure is added to the continuity equation. Thus the convective part of the equations form a hyperbolic system, which can be iterated in pseudo-time until a steady-state solution is found. For unsteady problems, subiterations in pseudo-time are performed for each physical time step. Since the convective terms of the resulting equations are hyperbolic, upwind differencing can be applied to these terms. The current code uses flux-differencing splitting modeled after the scheme of Roe.<sup>10</sup> The upwind differencing leads to a more diagonally dominant system than does central differencing and does not require the additional use of artificial dissipation. The system of equations is solved using a Gauss-Seidel type line-relaxation scheme. The line-relaxation scheme is very useful for computing multi-zonal grids because it makes it possible to iteratively pass  $\Delta Q$  (which is the change in the dependent variables for one time step) information between the zonal boundaries as the line-relaxation sweeping takes place. The result is a semi-implicit passing of boundary conditions between zones, which further enhances the code stability.<sup>11</sup> The resulting code is very robust and stable. It is capable of producing steady-state solutions to fine-mesh problems in 100 to 200 iterations. More detail about the computer code can be found in Refs. 6-8.

Most of the present calculations used the turbulence model developed by Baldwin and Barth,<sup>12,13</sup> where the specific formulation found in Ref. 12 was used. This is a one-equation turbulence model that avoids the need for an algebraic length scale and is derived from a simplified form of the standard  $k - \epsilon$  model equations. In the current application, the equation is solved using a line-relaxation procedure similar to that used for the mean-flow equations. This model has been found to be very robust and easy to implement for multiple-body configurations. The next section includes computations of flow over a single airfoil.

One of the studies for this problem includes a comparison of the Baldwin-Barth turbulence model with the Baldwin-Lomax<sup>14</sup> algebraic turbulence model.

### Computed Results

#### NACA 4412 Airfoil

Calculations were performed for the flow over an NACA 4412 airfoil at a Reynolds number of 1.52 million. A C-grid with dimensions of 241x63 was used, with wall spacings on the order of  $10^{-5}$  which corresponds to  $y^+$  values on the order of one. The grid was computed using a hyperbolic grid generator.<sup>15</sup> A close view of this grid is shown in fig. 1.1. In order to compute flow quantities for the points on the computational boundary in the "wake cut" line of the c-mesh, two lines of dummy points are added such that these dummy points coincide with points on the other side of the wake line. The first line of these dummy points is updated by injecting values from the coincident interior points on which they lie. Using this overlap produces smooth solutions to the equations across this computational boundary. This procedure also adds dummy points inside the airfoil. These points are merely blanked out and never used in the solution procedure. All of the C-grids in this work use this overlap.

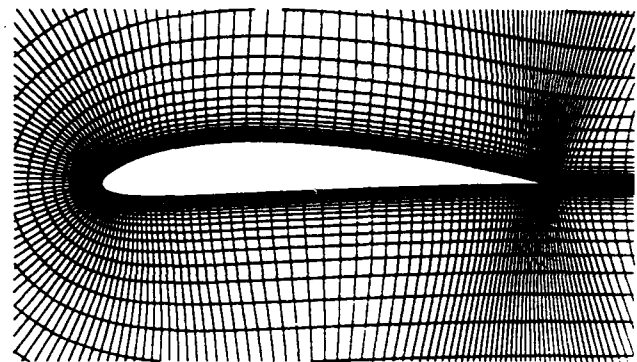


Fig. 1.1. 241x63 grid used for flow over an NACA 4412 airfoil.

This flow was computed using two different turbulence models, the Baldwin-Barth model<sup>12</sup> and the Baldwin-Lomax model.<sup>14</sup> Figure 1.2 shows a comparison between these computations and the experimental results of Coles and Wadcock<sup>16</sup> at an angle of attack of 13.87 degrees, which is very nearly maximum lift conditions. In the experiment the flow separated at approximately 85 percent of chord. Trip-strips were employed in the experiment on the suction and pressure surfaces at chord locations of  $x/c$  of 0.023 and 0.1, respectively. The computations thus specify these as the transition points. For the Baldwin-Barth model this is implemented by setting the the production terms to zero upstream of these locations; for the Baldwin-Lomax model the eddy viscosity is set to zero upstream of the transition location. The agreement is fairly good, with the biggest

discrepancy occurring at the trailing edge where the predicted pressure is too high. However, the Baldwin-Barth model does give a flattening of the pressure over the aft 15 percent of chord, indicating flow separation, where the Baldwin-Lomax solution does not show this tendency. This figure also shows that the computations with the transition predict a leading-edge laminar separation bubble. The experiment reports that there was no laminar separation bubble at this angle of attack, so an additional computation was run using the Baldwin-Barth model with the production terms turned on everywhere, thus the boundary layer was fully turbulent. The pressure coefficient for this is also shown in fig. 1.2. There is a slight improvement in the trailing edge area for this solution. The Baldwin-Lomax model showed no difference in the pressure or velocity solution when it was run without specifying transition, except that it removed the laminar separation bubble.

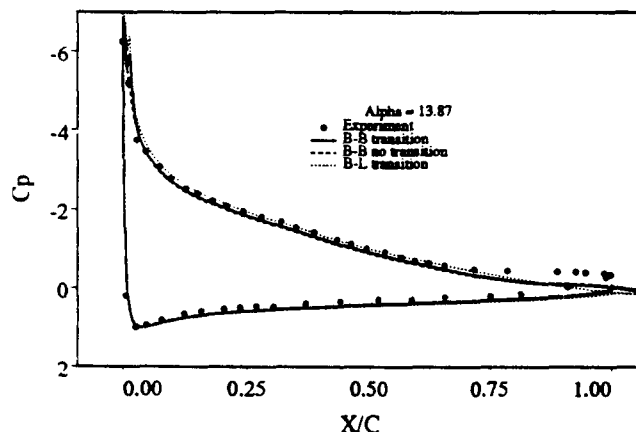


Fig. 1.2. Pressure coefficient on surface of an NACA 4412 airfoil at Reynolds number of 1.52 million comparing calculations with Baldwin-Barth and Baldwin-Lomax turbulence models and experimental data.

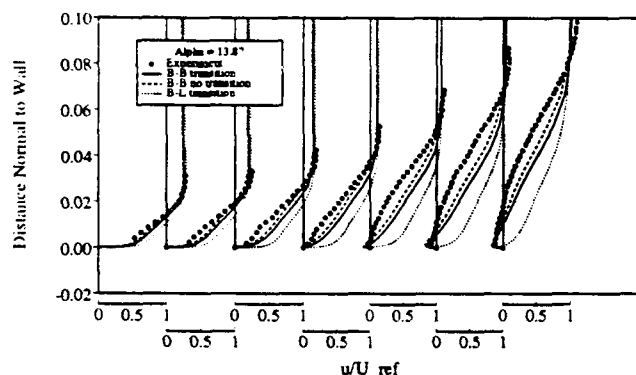


Fig. 1.3. Velocity profiles on upper surface of an NACA 4412 airfoil at streamwise stations of  $x/c = 0.62, 0.675, 0.731, 0.786, 0.842, 0.897, \text{ and } 0.953$ .

Velocity profiles from the suction surface boundary layer are plotted in fig. 1.3 at streamwise stations of  $x/c = 0.62, 0.675, 0.731, 0.786, 0.842, 0.897, \text{ and } 0.953$ . The profiles are shown using the streamwise component of velocity

in boundary-layer coordinates, that is, the velocity component tangential to the local airfoil surface. This figure shows in greater detail the problems of the Baldwin-Lomax solutions in this region: the boundary layer profile is too full and the solution shows only a tiny region of separation. The Baldwin-Barth solution is in closer agreement with the experimental results, but also suffers from too small of a separation region. The case without transition shows the best agreement with the experimental profiles.

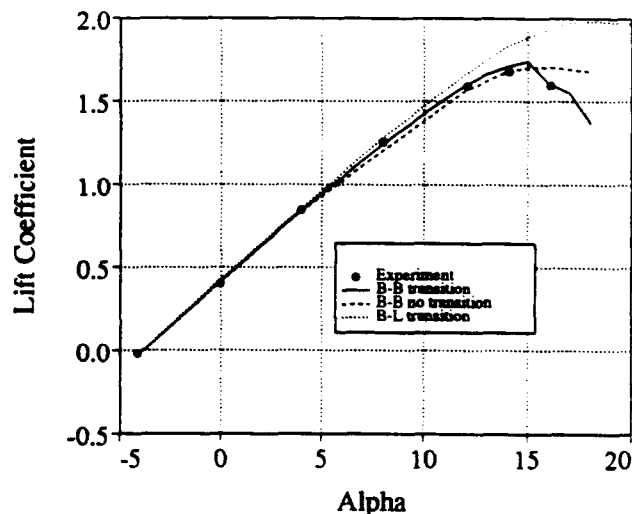


Fig. 1.4. Lift coefficient versus angle of attack for flow over an NACA 4412 airfoil.

Computations were run for a range of angles of attack from zero lift to maximum lift. The lift coefficient versus angle of attack is plotted in Fig. 1.4. This shows that the Baldwin-Barth solution with transition gives very good agreement in the lift, including the prediction of stall. For all cases, as the angle of maximum lift was approached the flow tended toward unsteadiness. That is, the steady-state computations did not converge completely, which, for the artificial compressibility formulation means that the results do not satisfy the continuity equation. In these cases the code was then run in a time-accurate, unsteady mode. For the Baldwin-Barth model with transition, at an angle of attack of 14 degrees, the unsteadiness dies out when the computations are run in a time-accurate mode. At 16 degrees, an unsteady periodic behavior ensues; as shown in the figure, the mean lift drops sharply below the values from smaller angles of attack. Examination of the flow shows that the leading-edge laminar separation bubble is periodically shedding and traveling through the boundary layer on the top surface of the airfoil, and past the trailing edge. Figure 1.5 shows the pressure coefficient on the surface of the airfoil at seven different times through the period of this flow. The forming of the leading-edge vortex is evident, and it can be seen that it travels downstream and past the trailing edge.

For the Baldwin-Barth model without transition at an angle of attack of 16 degrees, all oscillations damp out and it converges to a steady-state solution. At 18 degrees, the lift continues to oscillate periodically, yet there is only a slight



drop in the lift, and there is a complete absence of a leading-edge separation bubble. The Baldwin-Lomax computations do not have any type of periodic unsteady behavior with or without transition. The results from this model show that a drop in lift does not occur until an angle of attack of 20 degrees.

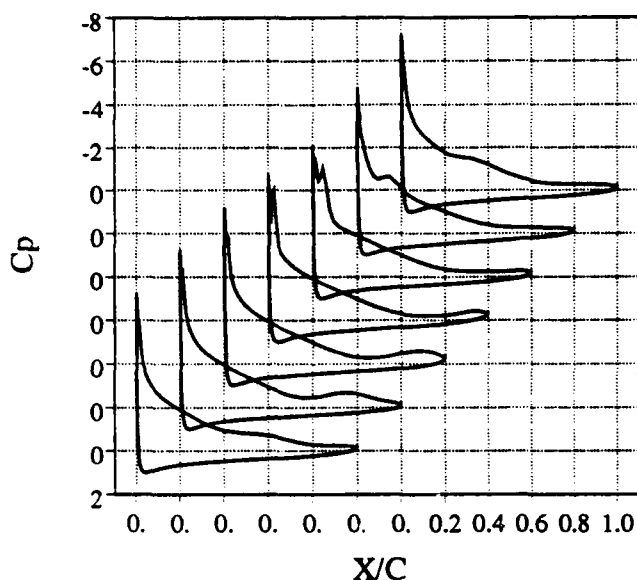


Fig. 1.5. Pressure coefficient on the surface of the NACA airfoil at 16 degrees angle of attack for seven different times during the unsteady periodic motion.

In short, the Baldwin-Barth model shows promise for use in predicting high-lift flows, and although some deficiencies are shown here, it is significantly better than the Baldwin-Lomax model. In addition, the Baldwin-Barth model is much easier to use than the Baldwin-Lomax model, in that it does not require a length scale; it is straightforward to implement for a multi-element airfoil computation. All of the results in the later sections of this paper use the Baldwin-Barth model.

The convergence history is shown in Fig. 1.6 for the angle of attack of 13.87 degrees for both turbulence models with and without transition. In general, fast convergence is seen, with converged solutions obtained in 100 to 200 iterations. Specifying the transition tends to produce an unsteady component into the flow field which somewhat delays the convergence. It can also be seen that the Baldwin-Lomax computations converge much faster than the Baldwin-Barth model. The computing time on a Cray YMP required for this 241 x 63 mesh is 100 seconds for 200 iterations when using the Baldwin-Barth model, 90 seconds for 200 iterations with the Baldwin-Lomax model. When running the unsteady cases, the algorithm requires subiterations at each physical time step to converge the divergence of velocity toward zero. When running the steady 16 degree angle of attack case with a non-dimensional time step of 0.05, 40 physical time steps resulted in one period of the flow. This took about 10 minutes of computing time. Due

to the difficult nature of solving the unsteady incompressible Navier-Stokes equations, it probably would not be computationally cheaper to use an incompressible formulation over a compressible Navier-Stokes code to study post-stall, unsteady airfoil flows.

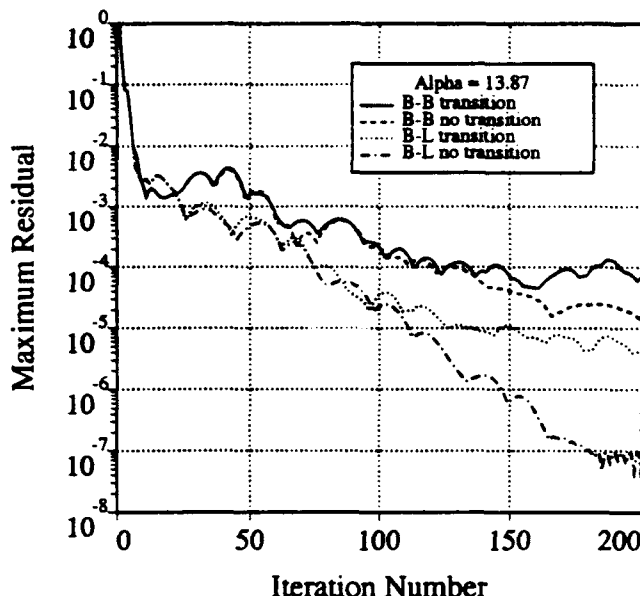


Fig. 1.6. Convergence history showing Maximum residual versus iteration number for flow over an NACA 4412 airfoil at 13.87 degrees angle of attack.

#### Two-Element Airfoil

The geometry is made up of an NACA 4412 airfoil with an NACA 4415 flap deployed at 21.8 degrees, with the entire configuration at 8.2 degrees angle of attack. This geometry was studied experimentally by Adair and Horne.<sup>17</sup> The chord Reynolds number was 1.8 million, and the Mach number in the experiment was 0.09. The blockage in the wind-tunnel was severe enough that the wind-tunnel walls needed to be included in the calculations in order to get good agreement with the experimental pressure coefficients.

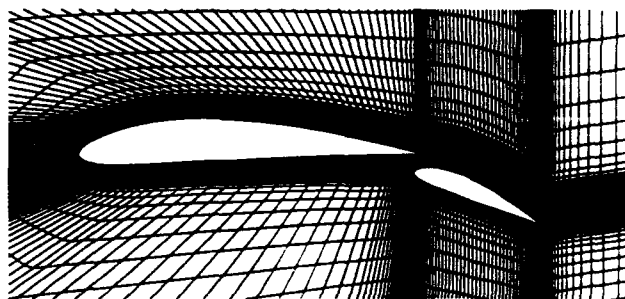


Fig. 2.1. Three-zone patched grid used to compute flow over an NACA 4412 airfoil with an NACA 4415 flap.

The airfoils were discretized using two different grid approaches. The first follows the work of Schuster and

Birckelbaw<sup>2</sup> and uses 3 zones which are patched together using coincident points. This grid is shown in Fig. 2.1. Each of the elements is surrounded by a C-grid, and these two grids are surrounded by another C-grid which extends out to the wind-tunnel walls. The dimension of these grids are 374x44, 241x33, and 352x32, respectively, for a total of 35,000 points.

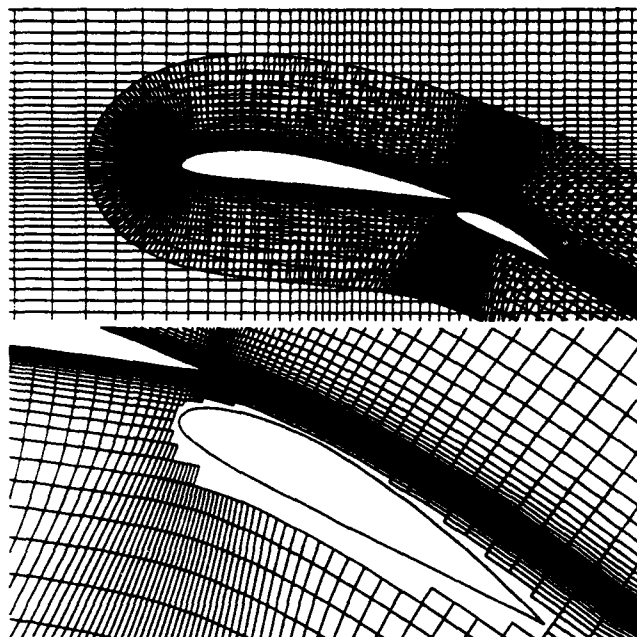


Fig. 2.2. Overlaid Chimera grid used to compute flow over an NACA 4412 airfoil with an NACA 4415 flap.

The second type of grid uses a Chimera<sup>5</sup> approach, in which C-grids were generated about each of the elements. To include the effects of the wind-tunnel walls these grids were inset into a third zone composed of an h-grid. A partial view of these three grids is shown at the top of Fig. 2.2, with a close-up of the main-element grid in the vicinity of the flap shown in the bottom half of this figure. These grids had dimensions of 261x49, 203x35, and 121x61, for a total of 27,500 points. To implement the Chimera approach, these grids are given to the PEGSUS<sup>5</sup> code. This code first punches holes into grids where they overlap a body (as shown in the bottom of Fig. 2.2). It then computes the interpolation stencils used to update the flow quantities at the fringe points of these holes, and to update the flow quantities at the outer boundaries of grids which lie inside another grid (like the outer boundaries of the c-grids seen in the top of Fig. 2.2). For both the Chimera and the patched grid approaches, the spacing next to the surfaces was set to  $2 \times 10^{-5}$ , which correspond to  $y^+$  values at the wall on the order of one.

The computational results compare well with the experimental results of Adair and Horne.<sup>17</sup> A plot of the pressure coefficient on the surface of the elements is shown in Fig. 2.3. Results from both of the grid approaches is shown. The biggest difference between the computation and exper-

iment is seen in the suction peak at the leading edge of the flap. The difference might be explained by a difference in the geometry between the computations and the experiment. There was an ambiguity in the way in which the flap position is defined.

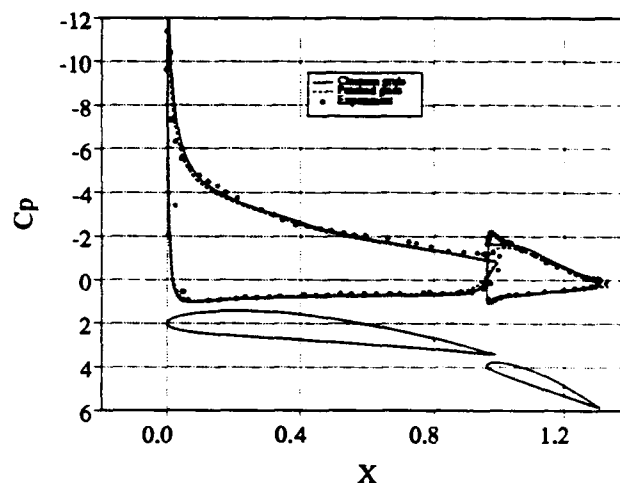


Fig. 2.3 Pressure coefficient on surface of two-element airfoil comparing both patched grid and overlaid grid schemes to experimental results.

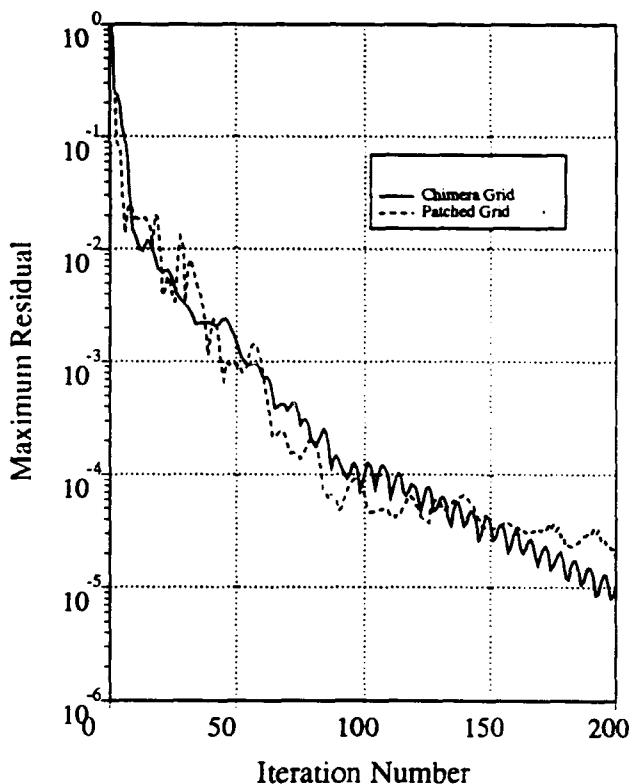


Fig. 2.4 Convergence history for flow over two-element airfoil for patched grid and overlaid grid schemes.

Figure 2.4 shows the convergence history for these computations. They both converge very well, giving a steady-

state solution in about 100 iterations. Each of these grid cases takes about 100 seconds of CPU time on a Cray YMP for 100 iterations. The code runs at about a rate of 80 MFLOPS, and requires  $36 \times 10^{-6}$  CPU seconds per grid point per iteration. Since the Chimera approach uses about 20% fewer grid points, it takes a little less computing time. The major difference between these approaches is the amount of time and effort it takes to generate the grids. The patched grid case takes on the order of several hours of work: it involves generating inner boundaries which define the surface with the proper point distribution to ensure that the grids can be patched together. Then hyperbolic grids are marched halfway across the gap from each of the elements. The resulting outer boundaries of these are merged into a common interface where they match. The inner grids are recalculated to match this interface. Finally, the outer C-grid is marched outward using a hyperbolic grid generator. The process is tedious and is not easily repeatable for a different case (new flap placement, or flap angle), or for a different geometry. On the other hand, the overlaid grids can be generated in only a matter of minutes; one need only generate two independent hyperbolic grids about each of the elements, and then feed these into the PEGSUS code<sup>5</sup> as described above. Once this has been set up for one case it is very easy to reproduce it for another case or another geometry. It is for these reasons that the overlaid grid approach was adopted for the rest of the cases and geometries in this work.

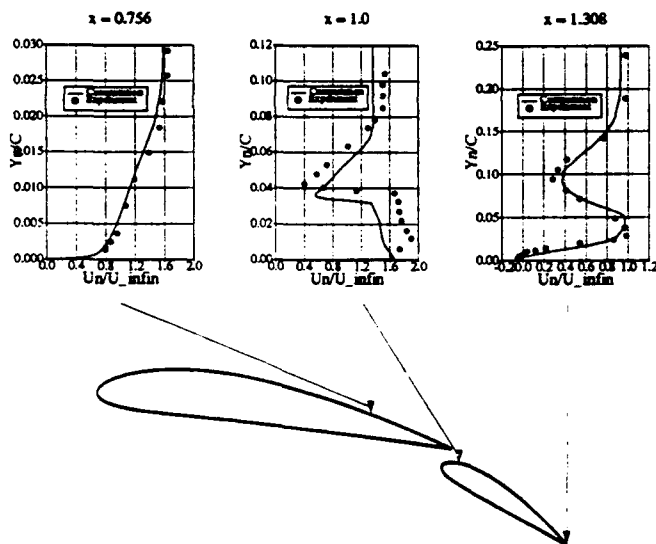


Fig. 2.5 Velocity profiles from overlaid grid calculations compared to experimental data.

Figure 2.5 shows velocity profiles from the Chimera calculations at three locations on the top surface of the main element and flap. These are plotted with experimental measurements of the profiles by Adair and Horne.<sup>17</sup> These plots show fairly good agreement with the experimental results. The biggest discrepancy is the difference in the gap velocity off the surface of the flap's leading edge. This is related to the difference seen in the pressure coefficient plot in Fig. 2.3. The velocity profile from the trailing

edge of the flap shows that there is a separation occurring over the top surface of the flap. This profile shows that the computational separation bubble is not as thick as that seen in the experiment, but that the computations do an excellent job of capturing the wake from the main element in this region.

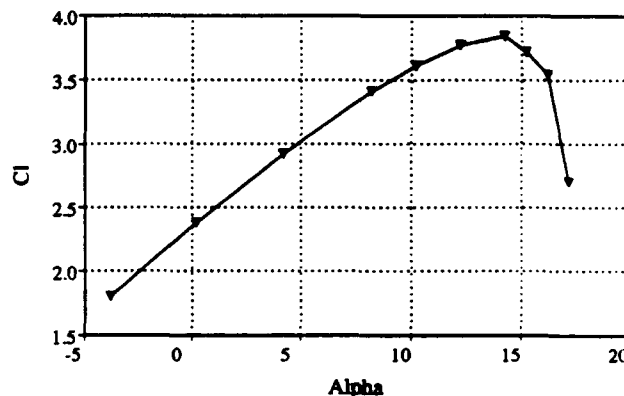


Fig. 2.6 Coefficient of lift versus angle of attack as computed by the overlaid grid approach for the two-element airfoil.

Further calculations were carried out using free-stream outer boundaries (neglecting wind-tunnel walls). These calculations use the overlaid grids with two zones, where the main element grid extends beyond ten chord lengths from the airfoil. These were run at various angles of attack to show the capability to compute maximum lift conditions as well as post-stall conditions. The curve of lift coefficient versus angle of attack is shown in Fig. 2.6. The lift drops off sharply at  $\alpha = 15$  degrees, and the calculations indicate that the flow becomes unsteady beyond that angle of attack. The skin friction along the surfaces of the airfoil elements is shown in Fig. 2.7. It can be seen that the flow separates at the trailing edge of the flap even at zero angle of attack, and that this separation reduces in size with increasing angle of attack. The main element has trailing edge separation occurring at angles of attack of 12 degrees and greater. It becomes massively separated at an angle of attack of 16 degrees. At this angle of attack the flap shows evidence of a vortex passing over the top because of the large dip in the skin friction on the surface of the flap.

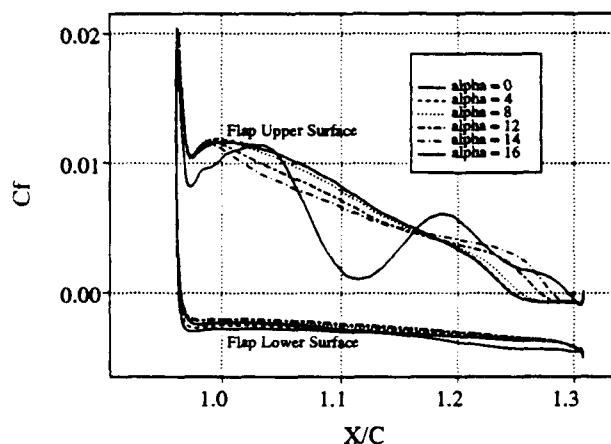
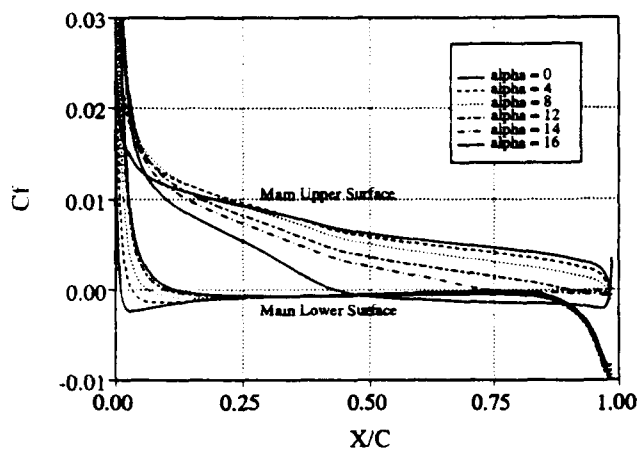


Fig. 2.7 Skin friction on the surface of the main element and flap for various angles of attack.

### Three-Element Airfoil

The three element computational configuration was taken from an experimental geometry of a supercritical airfoil which has been tested by Valarezo et al.<sup>18</sup> This airfoil consisted of a leading edge slat deployed at -30 degrees, a main element, and a trailing edge flap deployed at 30 degrees. The experimental Mach number was 0.2 and the chord Reynolds number was 9 million. The Chimera approach was used to discretize the geometry and produce a computational grid. A C-grid was placed around each element, with the main-element grid extending out to the far field. The grids for the slat-, main-, and flap-element had dimensions of 221x41, 401x75, and 221x47, respectively, for a total just under 51,000 points. The top of Fig. 3.1 shows every other grid point in the first and third element grids, with the resulting holes caused by the main element. The second half of this figure shows the main element grid. The wake cut boundary of this grid has been aligned just above the top surface of the flap element in an attempt to put as many points as possible in the wake and boundary-layer region found there.

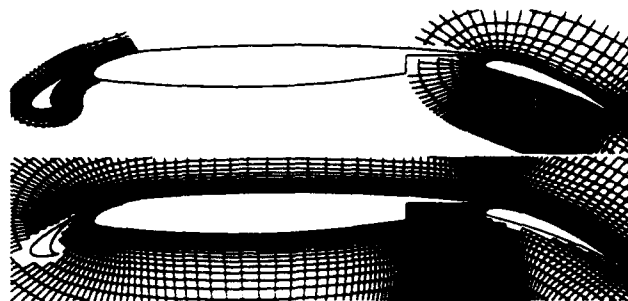


Fig. 3.1 Grid and geometry for the three-element airfoil, showing every other grid point around the slat and flap.



Fig. 3.2 Velocity magnitude contours at 20.4 degrees angle of attack.

Figure 3.2 shows velocity magnitude contours of the three element configuration run at 20.4 degrees angle of attack. The wake of the slat is clearly seen across the top of the succeeding elements. The experimental results of Valarezo et al.<sup>18</sup> and the computational results of this study are compared in Fig. 3.3. These figures show pressure coefficients on the surfaces of each element at three different angles of attack, 8.1, 20.4, and 23.4 degrees. Very good agreement is seen except on the suction side of the slat. Also, there is a discrepancy on the upper surface of the flap trailing edge. The experimental results show a strong adverse pressure gradient followed by a flattening in the pressure coefficient curve, which is generally evidence of flow separation. The computational results do not show this. This is probably due to the general trend of the turbulence model to underpredict the amount of separation. The experiment allowed free transition on the elements, and the computations assumed a turbulent boundary layer everywhere. Further work in this area could include use of a transition model for this calculation.

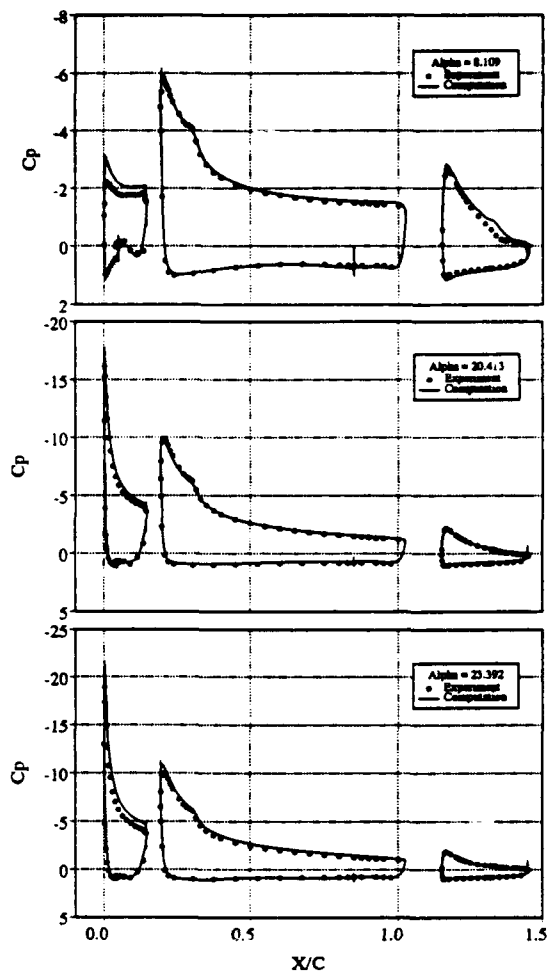


Fig. 3.3 Pressure coefficient comparing computation and experiment for angles of attack of 8.1, 20.4, and 23.4 degrees.

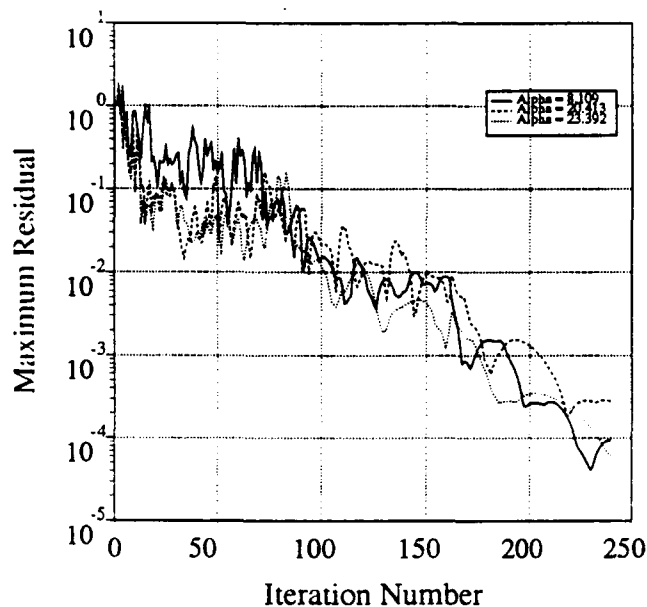


Fig. 3.4 Convergence for the three-element airfoil.

Convergence histories of these computations are shown in Figure 3.4. These computations converge well, with steady state solutions being obtained after 200 iterations, which corresponds to about 4 minutes of CPU time on a Cray YMP.

#### Four-Element Airfoil

The geometry is made up of a NASA 9.3 percent blunt-based, supercritical airfoil with a leading edge slat deployed at -47.2 degrees and two trailing edge flaps at 30 degree and 49.7 degrees respectively. This configuration matches the geometry used in the experimental work done by Omar et al.<sup>19</sup> The Mach number in the experiment was 0.201 and the chord Reynolds number was 2.83 million. The geometry was discretized using the Chimera approach. C-grids were generated around each of the elements, with the main element grid being marched out to the outer boundary. These grids were overlaid and the PEGSUS<sup>5</sup> code was used to create an overlaid grid. Approximately 55,000 points were used in the resulting composite grid in order to resolve the flow physics adequately in the boundary layers and wakes. The grid spacing next to the surfaces of the airfoils was  $10^{-5}$  which ensures  $y^+$  values of one near the wall.



Fig. 4.1 Velocity magnitude contours at 14.25 degrees angle of attack.

The computational results of this study were compared with the experimental results of Omar et al.<sup>19</sup>. Figure 4.1 shows velocity magnitude contours around the four element configuration at 14.25 degrees angle of attack. In this figure the wake from the leading edge slat is apparent over the main element. Subsequent wakes from the main element and flaps can also be observed. Plots of the pressure coefficient on the surfaces of the elements at angles of attack of 0.0, 8.13, and 14.25 degrees are shown in Fig. 4.2. Again, excellent agreement is seen except there is once more evidence that the computation of the flow over the flap underpredicts the amount of separation at the lower angles of attack.

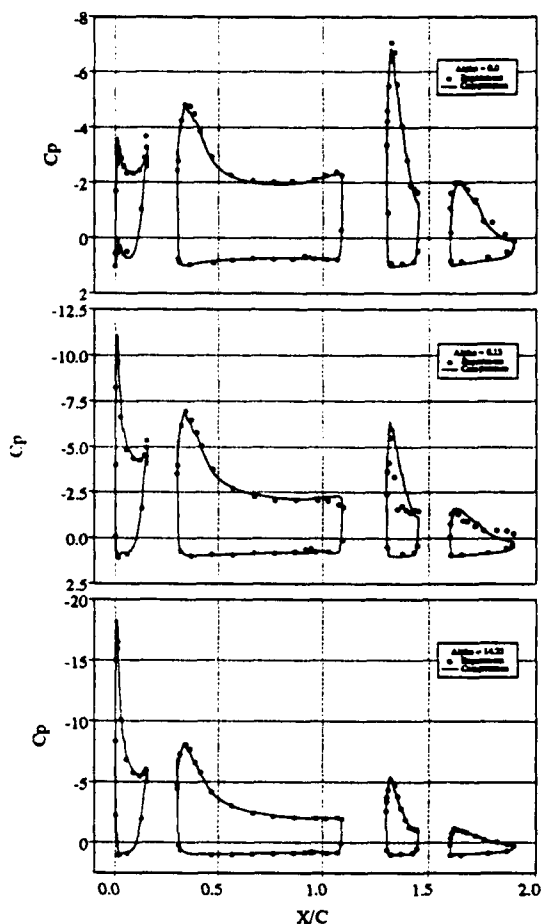


Fig. 4.2 Pressure coefficient comparing computation and experiment for angles of attack of 0.0, 8.13, and 14.25 degrees.

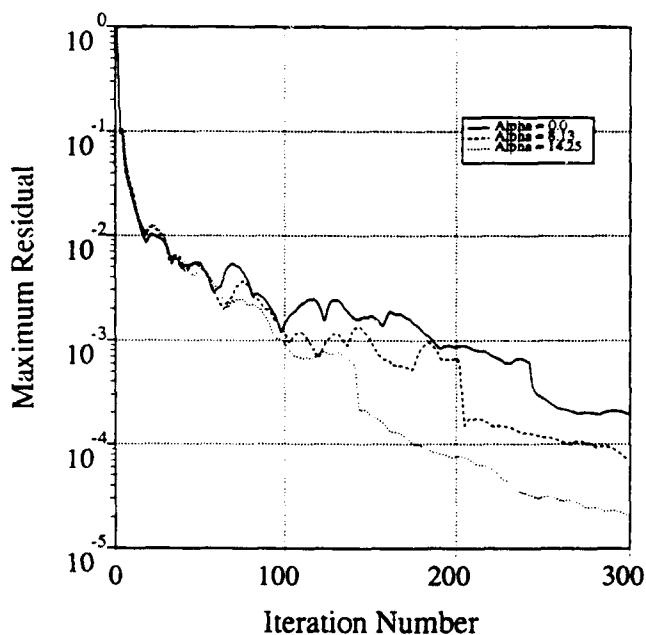


Fig. 4.3 Convergence for the four-element airfoil.

The convergence histories for the four element configuration at three different angles of attack are shown in Fig. 4.3. The computations converge well and a steady state solution is produced after about 200 iterations, which corresponds to approximately four minutes of CPU time on the Cray YMP.

### Conclusions

An incompressible flow solver has been used to compute flow over several airfoil geometries for the purpose of developing a tool to study takeoff and landing configurations. The code is robust and produces numerical simulations in a matter of minutes. The flow over an NACA 4412 airfoil was investigated, and the Baldwin-Barth and Baldwin-Lomax turbulence models were compared. The Baldwin-Barth model gave significantly better results, and was much easier to use, particularly for multi-element flows. The use of the Chimera overlaid grid approach was found to be much easier than using a patched grid scheme for solving multiple element airfoil flows. Both approaches are capable of producing accurate solutions. Accurate pressure prediction was shown for geometries with two, three, and four airfoil elements. The common discrepancy between these calculations and experimental results involves separated flow. The results for the NACA 4412 airfoil indicate that deficiencies with the turbulence model are the most likely cause of these inaccuracies. Work in progress with different turbulence models shows promise in remedying this. Investigation of other turbulence models and their implementation for a multi-element airfoil calculation will be the focus of future work. In addition, future work will include the extension of the current work to three dimensions.

### References

- <sup>1</sup> Kusunose, K., Wigton, L. and Meredith, P., "A Rapidly Converging Viscous/Inviscid Coupling Code for Multi-Element Airfoil Configurations," AIAA Paper 91-0177, January, 1991.
- <sup>2</sup> Schuster, D. M. and Birckelbaw, L. D., "Numerical Computations of Viscous Flowfields about Multiple Component Airfoils," AIAA Paper 85-0167, January, 1991.
- <sup>3</sup> Barth, T. J., "Numerical Aspects of Computing Viscous High Reynolds Number Flows on Unstructured Meshes," AIAA Paper 91-0721, January, 1991.
- <sup>4</sup> Mavriplis, D., "Turbulent Flow Calculations Using Unstructured and Adaptive Meshes," ICASE Report 90-61, September, 1990.
- <sup>5</sup> Benek, J. A., Buning, P. G., and Steger, J. L., "A 3-D Chimera Grid Embedding Technique," AIAA Paper 85-1523-CP, July 1985.
- <sup>6</sup> Rogers, S. E. and Kwak, D., "An Upwind Differencing Scheme for the Steady-state Incompressible Navier-Stokes

Equations," NASA TM 101051, November 1988. Accepted for publication in *Journal of Applied Numerical Mathematics*, to appear in 1991.

<sup>7</sup> Rogers, S. E. and Kwak, D., "An Upwind Differencing Scheme for the Time Accurate Incompressible Navier-Stokes Equations," AIAA Paper 88-258, June 1988. See also *AIAA J.*, Vol. 28, No. 2, February, 1990, pp. 253-262.

<sup>8</sup> Rogers, S. E., Kwak, D., and Kiris, C., "Numerical Solution of the Incompressible Navier-Stokes Equations for Steady-State and Time-Dependent Problems," AIAA Paper 89-0463, January, 1989. See also *AIAA J.*, Vol. 29, No. 4, 1991, pp. 603-610.

<sup>9</sup> Chorin, A. J., "A Numerical Method for Solving Incompressible Viscous Flow Problems," *J. Comput. Phys.*, Vol. 2, 1967, pp. 12-26.

<sup>10</sup> Roe, P. L., "Approximate Riemann Solvers, Parameter Vectors, and Difference Schemes," *J. Comput. Phys.*, Vol. 43, pp. 357-372, 1981.

<sup>11</sup> Rogers, S. E., "On The Use of Implicit Line-Relaxation and Multi-Zonal Computations," AIAA Technical Note 91-1611-CP, AIAA CFD Conference, Honolulu, HI, June 24-27, 1991.

<sup>12</sup> Baldwin, B. and Barth, T., "A One-Equation Turbulence Transport Model for High Reynolds Number Wall-Bounded Flows," NASA TM 102847, Aug. 1990.

<sup>13</sup> Baldwin, B. and Barth, T., "A One-Equation Turbulence Transport Model for High Reynolds Number Wall-Bounded Flows," AIAA Paper 91-0610, January, 1991.

<sup>14</sup> Baldwin, B. and Lomax, H., "Thin Layer Approximation and Algebraic Model for Separated Turbulent Flows," AIAA Paper 78-257, January, 1978.

<sup>15</sup> Cordova, J. Q. and Barth, T. J., "Grid Generation for General 2-D Regions Using Hyperbolic Equations," AIAA Paper 88-0520, January, 1988.

<sup>16</sup> Coles, D. and Wadcock, A. J., "Flying-Hot-Wire Study of Flow Past an NACA 4412 Airfoil at Maximum Lift," *AIAA J.*, Vol. 17, No. 4, 1979, pp. 321-329.

<sup>17</sup> Adair, D. and Horne, W. C., "Turbulent Separated Flow Over and Downstream of a Two-Element Airfoil," *Experiments in Fluids*, Vol. 7, pp. 531-541, 1989.

<sup>18</sup> Valarezo, W. O., Dominik, C. J., McGhee, R. J., Goodman, W. L., and Paschal, K. B., "Multi-Element Airfoil Optimization for Maximum Lift at High Reynolds Numbers," AIAA Paper 91-3332, September, 1991.

<sup>19</sup> Omar E., Zierten, T., Hahn, M., Szpiro, E., and Mahal, A., "Two-Dimensional Wind-Tunnel Tests of a NASA Supercritical Airfoil with Various High-Lift Systems," NACA CR-2215, September, 1973.

# UNSTRUCTURED MESH ALGORITHMS FOR AERODYNAMIC CALCULATIONS

D. J. Mavriplis

Institute for Computer Applications in Science and Engineering  
NASA Langley Research Center  
Hampton, VA

## 1. ABSTRACT

The use of unstructured mesh techniques for solving complex aerodynamic flows is discussed. The principle advantages of unstructured mesh strategies, as they relate to complex geometries, adaptive meshing capabilities, and parallel processing are emphasized. The various aspects required for the efficient and accurate solution of aerodynamic flows are addressed. These include mesh generation, mesh adaptivity, solution algorithms, convergence acceleration and turbulence modeling. Computations of viscous turbulent two-dimensional flows and inviscid three-dimensional flows about complex configurations are demonstrated. Remaining obstacles and directions for future research are also outlined.

## 2. INTRODUCTION

Over the last decade, much attention has been devoted to the development and use of unstructured mesh methodologies within the research community. This enthusiasm however, has not always been shared by the applications and industrial community. The promise of easily enabling the discretization of complex geometries has been counterbalanced by questions of accuracy and efficiency. Furthermore, the dearth of results concerning viscous flow calculations using unstructured meshes has produced skepticism concerning the value of unstructured mesh techniques for practical aerodynamic calculations.

There is no doubt that block-structured techniques have proved extremely effective in discretizing very complex geometries. However, unstructured grid techniques offer additional inherent advantages which may not at first appear evident. The possibility of easily performing adaptive meshing is perhaps the largest advantage of unstructured grid methods. In fact, the implementation of adaptive meshing techniques for structured meshes has generally been found to incur unstructured-mesh type overheads [1]. Furthermore, although unstructured grid data-sets are irregular, they are homogeneous (as opposed to block structured grids where differentiation between block boundaries and interiors must be made). One of the consequences of this property is that unstructured-mesh type solvers are relatively easily parallelizable. While unstructured mesh solvers always incur additional memory and CPU-time overheads due to the random nature of their data-sets, large gains in efficiency can be obtained by careful choices of data-structures, and by resorting to more efficient implicit or multi-level solution procedures. When combined with adaptive meshing and parallelization, these can result in truly competitive solution procedures.

In the following sections, the application of unstructured mesh techniques to various aerodynamic flow problems are discussed. The particular approach chosen (i.e. a vertex based Galerkin finite-element discretization with additional artificial dissipation terms and an unstructured multigrid algorithm for convergence acceleration), represents the methodology adopted over several years of research by the author, and constitutes just one of several competing approaches. Both inviscid and viscous flows are considered, although exclusively steady-state solution procedures are discussed. Both two and three-dimensional problems are addressed.

## 3. SOLUTION PROCEDURE

In non-dimensional conservative vector form, the Navier-Stokes equations read

$$\frac{\partial w}{\partial t} + \nabla \cdot F_c = \frac{1}{Re_\infty} \nabla \cdot F_v \quad (1)$$

where  $Re_\infty$  denotes the overall flow Reynolds number, and  $w$  represents the conserved variables

$$w = \begin{pmatrix} \rho \\ \rho u \\ \rho v \\ \rho w \\ \rho E \end{pmatrix} \quad (2)$$

$\rho$  being the fluid density,  $u$ ,  $v$ , and  $w$  the cartesian velocity components, and  $E$  the internal energy.  $F_c$  represents the convective flux vector, the components of which are algebraic functions of the conserved variables and the pressure, which itself can be related to the conserved variables through the perfect gas relation.  $F_v$  denotes the viscous flux vector, the components of which are functions of the first derivatives of the conserved variables. Equation (1) represents a set of partial differential equations which must be discretized in space in order to obtain a set of coupled ordinary differential equations, which can then be integrated in time to obtain the steady-state solution. Spatial discretization is performed using a Galerkin finite-element type formulation. The following derivation is restricted to the two-dimensional case for the sake of clarity, since the extension from two-dimensions to three-dimensions is entirely straight-forward. Multiplying equation (1) by a test function  $\phi$ , and integrating over physical space yields

$$\frac{\partial}{\partial t} \int_{\Omega} \phi w \, dxdy + \int_{\Omega} \phi \nabla \cdot F_c \, dxdy = \frac{1}{Re_\infty} \int_{\Omega} \phi \nabla \cdot F_v \, dxdy \quad (3)$$

Integrating the flux integrals by parts, and neglecting boundary terms gives

$$\frac{\partial}{\partial t} \int_{\Omega} \phi w \, dxdy = \int_{\Omega} F_c \cdot \nabla \phi \, dxdy - \frac{1}{Re_\infty} \int_{\Omega} F_v \cdot \nabla \phi \, dxdy \quad (4)$$

In order to evaluate the flux balance equations at a vertex  $P$ ,  $\phi$  is taken as a piecewise linear function which has the value 1 at node  $P$ , and vanishes at all other vertices. Therefore, the integrals in the above equation are non-zero only over triangles (tetrahedra in three dimensions) which contain the vertex  $P$ , thus defining the domain of influence of node  $P$ , as shown in Figure 1, for the two-dimensional case. To evaluate the above integrals, we make use of the fact that  $\phi_x$  and  $\phi_y$  are constant over a triangle, and evaluate spatial derivatives of  $\phi$  and  $w$  over a triangle using vertex values, by Green's contour integral theorem. The convective fluxes  $F_c$  are taken as piecewise linear functions in space, and the viscous fluxes  $F_v$  are piecewise constant over each triangle, since they are formed from first derivatives in the flow variables. Evaluating the flux integrals with these assumptions, one obtains

$$\frac{\partial}{\partial t} \int_{\Omega} \phi w \, dxdy = \sum_{a=1}^n \frac{F_c^a + F_c^b}{6} \Delta L_{AB} - \frac{1}{Re_\infty} \sum_{a=1}^n \frac{F_v^a}{2} \Delta L_{AB} \quad (5)$$



where the summations are over all triangles in the domain of influence, as shown in Figure 1.  $\Delta_{AB}$  represents the directed (normal) edge length of the face of each triangle on the outer boundary of the domain,  $F_c^A F_c^B$  are the convective fluxes at the two vertices at either end of this edge, and  $F_v^e$  is the viscous flux in triangle  $e$ ,  $e$  being a triangle in the domain of influence of  $\phi$ . If the integral on the left hand side of equation (5) is evaluated in the same manner, the time derivatives become coupled in space. Since we are not interested in the time-accuracy of the scheme, but only in the final steady-state solution, we employ the concept of a lumped mass matrix. This is equivalent to assuming  $w$  to be constant over the domain of influence while integrating the left hand side. Hence, we obtain

$$\Omega_p \frac{\partial w_p}{\partial t} = \sum_{e=1}^n \frac{F_c^A + F_c^B}{2} \Delta_{AB} - \frac{1}{Re_\infty} \sum_{e=1}^n \frac{3}{2} (F_v^e \Delta_{AB}) \quad (6)$$

where the factor of  $1/3$  is introduced by the integration of  $\phi$  over the domain, and  $\Omega_p$  represents the surface area of the domain of influence of  $P$ . For the convective fluxes, this procedure is equivalent to the vertex finite-volume formulation described in [2,3]. For a smoothly varying regular triangulation, the above formulation is second-order accurate.

Additional artificial dissipation terms are required to ensure stability and to capture shocks without producing numerical oscillations. This is necessary for both inviscid and viscous flow computations, since in the later case, large regions of the flow-field behave essentially inviscidly and the physical viscosity is not sufficient to guarantee numerical stability for the type of mesh spacings typically employed. Artificial dissipation terms are thus constructed as a blend of a Laplacian and a biharmonic operator in the conserved flow variables. The Laplacian term represents a strong formally first-order accurate dissipation which is turned on only in the vicinity of a shock, and the biharmonic term represents a weaker second-order accurate dissipation which is employed in regions of smooth flow [4,5,6].

The spatially discretized equations are integrated in time to obtain the steady-state solution. For inviscid flow calculations, a five-stage Runge-Kutta scheme is employed for the time integration, where the convective terms are evaluated at each stage in the time-stepping scheme, and the dissipative terms are only evaluated at the first two stages and then frozen for the remaining stages. A complete multistage time-step, in which the solution is advanced from time level  $n$  to level  $n+1$ , can be written as

$$\begin{aligned} w^{(0)} &= w^n \\ w^{(1)} &= w^{(0)} - \alpha_1 \Delta t [Q(w^{(0)}) - D(w^{(0)})] \\ w^{(2)} &= w^{(0)} - \alpha_2 \Delta t [Q(w^{(1)}) - D(w^{(1)})] \\ w^{(3)} &= w^{(0)} - \alpha_3 \Delta t [Q(w^{(2)}) - D(w^{(1)})] \\ w^{(4)} &= w^{(0)} - \alpha_4 \Delta t [Q(w^{(3)}) - D(w^{(1)})] \\ w^{(5)} &= w^{(0)} - \alpha_5 \Delta t [Q(w^{(4)}) - D(w^{(1)})] \\ w^{(n+1)} &= w^{(5)} \end{aligned} \quad (7)$$

with

$$\alpha_1 = 1/4 \quad \alpha_2 = 1/6 \quad \alpha_3 = 3/8 \quad \alpha_4 = 1/2 \quad \alpha_5 = 1$$

where  $w$  represents the conserved flow variables,  $Q$  is the convective residual,  $D$  denotes the dissipative operator, and  $\Delta t$  represents the discrete time-step. For viscous flow computations, a variant of this scheme is employed, where the dissipative terms are evaluated at the first, third and fifth stages, and frozen at alternate stages. These particular schemes have been designed to rapidly damp out high frequency error components [4,5], which is a necessary characteristic for a multigrid driving scheme. Convergence to

steady-state is accelerated by employing local time-stepping and implicit residual averaging [2,3,4], which have previously been described in the context of unstructured meshes.

#### 4. MULTIGRID STRATEGY

The idea of a multigrid strategy is to perform time steps on coarser meshes to calculate corrections to a solution on a fine mesh. The advantages of time stepping on coarse meshes are two-fold: first, the permissible time-step is much larger, since it is proportional to the cell size, and secondly, the work is much less because of the smaller number of grid points. On the finest grid of the sequence, the flow variables are updated by the 5-stage scheme as shown in equations (7). The residuals and flow variables are then transferred to the next coarser grid. If  $R'$  represents the transferred residuals and  $w'$  the transferred flow variables, a forcing function on the coarse grid can be defined as

$$P = R' - R(w') \quad (8)$$

Now on the coarse grid, time stepping proceeds as shown below:

$$w^{(q)} = w^{(q-1)} - \alpha_q \Delta t (R(w^{(q-1)}) + P) \quad (9)$$

for the  $q$ -th stage. In the first stage,  $w^{(q-1)}$  reduces to the transferred flow variable  $w'$ . Thus, the calculated residuals on the coarse grid are canceled by the second term in the forcing function  $P$ , leaving only the  $R'$  term. This indicates that the driving force for the solution on the coarse grid is provided by the fine grid residuals. Thus we are ensured that, when the fine grid solution is fully converged, no further corrections will be generated by the coarser grids. This procedure is repeated on successively coarser grids. When the coarsest grid is reached, the corrections are transferred back to the finer grids. The use of a multigrid method with unstructured meshes presents an additional challenge. Consistent coarse tetrahedral grids can no longer be formed by simply considering subsets of the fine grid vertices. An alternative would be to generate the fine mesh by repeatedly subdividing an initial coarse mesh in some manner. However, generally poor topological control of the fine mesh results from such a procedure. Another approach, known as the agglomeration technique, reconstructs coarse grids from a given fine unstructured grid by grouping neighboring elements together to form large polyhedral coarse-grid cells [7,8]. In the present work, it has been decided to pursue an unstructured multigrid approach in which a sequence of completely unrelated coarse and fine meshes are employed. This approach provides great flexibility in determining the configuration of the coarsest and finest meshes. Coarse meshes may be designed to optimize the speed of convergence, whereas fine meshes may be constructed based on solution accuracy considerations. In general, beginning from a fine grid, a coarser level is constructed which contains roughly half the resolution in each coordinate direction throughout the domain (about  $1/8$  the number of vertices in three dimensions, or  $1/4$  in two dimensions). This process is repeated until the coarsest grid capable of representing the geometry topology is obtained. In the context of adaptive meshing, new finer meshes may be added to the multigrid sequence, using any given adaptive refinement technique, since no relation is assumed between the various meshes of the sequence.

The key to the success of such a strategy lies in the ability to efficiently transfer variables, residuals and corrections back and forth between unrelated unstructured meshes. In the present context, this is performed using linear interpolation. For each vertex of a given grid, the tetrahedron which contains this vertex on the grid to which variables are to be interpolated is determined. The variable at this node is then linearly distributed to the four vertices of the enclosing tetrahedron (three vertices of the enclosing triangle in two dimensions). The main difficulty lies in efficiently determining the enclosing cell for each grid point. A naive search over all cells would lead to an  $O(N^2)$  complexity algorithm, where  $N$  is the total number of grid points, and would be more expensive than

the flow solution itself. In this work, a graph traversal search routine with best case complexity of  $O(N)$  is employed. The search begins by choosing a node on one grid, and locating the enclosing tetrahedron on the other grid. This can usually be determined a priori, for example, by choosing the minimum  $x$ - $y$ - $z$  node and the minimum  $x$ - $y$ - $z$  tetrahedron for the respective grids. We next chose a new node for which the enclosing cell is to be searched, and this node is taken as a neighbor of the previous node. As a starting guess we choose the tetrahedron which was previously found to enclose the first node, which is in the same vicinity as the new node. If this cell is not found to enclose the new node, we search the four neighbors of this cell, and then the neighbors of these neighbors, thus traversing through the mesh until the enclosing cell is located, at which point the process is repeated for a new node.

The interpolation patterns between the various meshes are completely determined by assigning to each mesh vertex four interpolation addresses and four interpolation weights, which are all computed in a preprocessing phase. In practice, this preprocessing has been found to require an amount of CPU time roughly equivalent to one or two flow solution cycles on the finest grid.

## 5. ADAPTIVITY

One of the most efficient adaptive mesh enrichment techniques consists of sequential point insertion and local grid restructuring. This can be achieved using Bowyer's algorithm for Delaunay triangulation. A Delaunay triangulation is a unique triangulation (tetrahedrization in 3-D) of a given set of points which exhibits certain desirable properties (maximizes small angles, provides a discrete maximum principle for Laplace's equation [9] etc ...). One of these properties, the empty circumcircle property, states that no vertex from any other triangle/tetrahedron can be contained in the circumcircle/sphere of a given triangle/tetrahedron. This property has often been employed as the basis for an algorithm known as Bowyer's method for the generation of unstructured meshes [10,11]. Bowyer's algorithm is also useful for adaptive mesh refinement. Assuming we have discretized the geometry with a Delaunay triangulation/tetrahedrization, and have solved the flow on this grid, we seek to refine the mesh in regions of high local truncation error. The first undivided differences of some key flow variable (density for example) are examined along every edge of

the mesh. When this difference is larger than some fraction of the average differences across all edges of the mesh, a new point is added midway along that edge. Each new point must be inserted into the mesh, which must then be locally restructured accordingly. Following Bowyer's algorithm, we first locate all triangles/tetrahedra whose circumcircles/spheres are intersected by this new point. The union of these cells are removed, as this determines the region of the mesh which must be restructured. A new structure is then formed by joining the new point to all vertices of the polygonal/hedral cavity formed by the cell removal operation, as shown for the two-dimensional case in Figure 2. This has been proven to result in a consistent Delaunay triangulation provided the original mesh is a Delaunay construction [11]. In cases where a non-Delaunay triangulation is employed for the original mesh, a consistency check must be executed after each new point is inserted. If negative volume cells are created, the new point must either be rejected or displaced and reinserted [12]. When new boundary points are introduced, they are repositioned onto the analytic surface-patch definition (or spline curve definition in two dimensions) of the geometry by recomputing the physical coordinates of the new point based on the assigned parametric patch coordinates,  $s$  and  $t$ , which are taken as the average of the parametric coordinates of the two vertices at either end of the generating boundary edge.

## 6. TWO-DIMENSIONAL RESULTS

### 6.1. An Inviscid Case

In order to illustrate the effectiveness of the simultaneous use of adaptive meshing and the multigrid strategy, the inviscid flow through a two-dimensional turbine blade cascade geometry has been computed. The particular blade geometry has been the subject of an experimental and computational investigation at the occasion of a VKI lecture series [13]. A total of seven meshes were used in the multigrid algorithm, with the last three meshes generated adaptively, using the undivided density difference criterion. The coarsest mesh of the sequence contains only 51 points, while the finest mesh, depicted in Figure 3, contains 9362 points. Extensive mesh refinement can be seen to occur in the neighborhood of shocks, and in other regions of high gradients. The inlet flow incidence is 30 degrees, and the average inlet Mach number is 0.27. The flow is turned 96 degrees by the blades, and the average exit isentropic Mach number is 1.3. At these conditions, the flow becomes supersonic as it passes through the cascade, and a complex oblique shock wave pattern is formed. These are evident from the computed Mach contours depicted in Figure 4. All shocks are well resolved, including some of the weaker reflected shocks, which non-adapted mesh computations often have difficulty resolving. Details of the flow in the rounded trailing edge region of the blade, where the flow separates inviscidly and forms a small recirculation region, are also well reproduced. Once the first four globally generated meshes were constructed, the entire flow solution - adaptive mesh enrichment cycle was performed three times, executing 25 multigrid cycles at each stage. This entire operation required 40 CPU seconds on a single processor of a Cray-YMP supercomputer. The residuals on the finest mesh were reduced by two and a half orders of magnitude, which should be adequate for engineering calculations.

### 6.2. Viscous Flows

While the discretization of the viscous terms for the Navier-Stokes equations as outlined in Section 2 is relatively straightforward, the main difficulties involved in computing high-Reynolds-number viscous flows relate to the grid generation and turbulence modeling requirements. In order to efficiently resolve the thin viscous layers encountered in such flows, highly stretched grids with very high resolution in the direction normal to the flow must be employed. Standard unstructured grid generation techniques (i.e. advancing front methods [14,15], or Delaunay triangulations [11,16]) generally break down when attempting to generate such highly stretched grids (normal to streamwise resolution ratios of 100 to 1000 are typically required). The procedure adopted in this work is to employ one of these standard techniques (in this case, the Delaunay construction) in a locally mapped space, as opposed to physical space [17]. A suitable mesh-point distribution with the required normal and streamwise resolution must first be obtained. This is achieved by generating a structured hyperbolic mesh about each geometry component, and employing the union of the points of these overlapping local structure meshes as the basis of a Delaunay triangulation. However, a Delaunay triangulation of a given set of points tends to produce the most equiangular triangles possible, and therefore in general, is not well suited for the generation of highly stretched mesh elements. Thus, an alternate triangulation procedure must be employed. The approach taken consists of defining a stretching vector (stretching magnitude and direction) at each node of the initial point distribution throughout the flow field. Assuming an initial triangulation has been obtained, when a new mesh point is to be inserted, the associated stretching vector is employed to construct a locally mapped space such that,

within this mapped space, the local point distribution appears isotropic. A Delaunay triangulation is then performed to triangulate the new point into the mesh in this mapped space, and the resulting triangulation is mapped back into physical space, thus resulting in the desired stretched triangulation. Hence, a fully unstructured mesh with highly stretched elements in the boundary layer and wake regions, nearly equilateral triangles in the inviscid regions of flow, and a smooth variation of elements throughout the transition regions is obtained. The use of fully unstructured meshes for viscous flow calculations has been pursued, as opposed to the hybrid structured-unstructured meshes often advocated in the literature [18,19], due to the increased generality they afford in dealing with geometries with close tolerances between neighboring bodies, where confluent boundary layers may occur, and due to the ease with which adaptive meshing may be incorporated throughout the viscous and inviscid regions of flow.

The use of a turbulence model is required for the practical solution of high-Reynolds number viscous flows. The most common turbulence models employed for aerodynamic flows are of the algebraic type. Such models typically require information concerning the distance of each point from the wall. Turbulence length scales are determined by scanning appropriate flow variables along specified streamwise stations. In the context of unstructured meshes, such information is not readily available and hence, the implementation of algebraic turbulence models on such meshes introduces additional complexities. The approach adopted in this work [20] consists of generating a set of background turbulence mesh stations. These are constructed by generating a hyperbolic structured mesh about each geometry component, based on the boundary-point distribution of the original unstructured mesh, and extracting the normal lines of the mesh. When performing adaptive meshing, new turbulence mesh stations must be constructed for each new adaptively generated boundary point, as illustrated in Figure 5. Each time the turbulence model is executed, the flow variables are interpolated onto the normal turbulence stations, the turbulence model is executed on each station, and the resulting eddy viscosity is interpolated back to the unstructured mesh. The method employed for interpolating variables back and forth between the unstructured mesh and the turbulence mesh stations is similar to that previously described for the unstructured multigrid algorithm.

Figures 6 through 9 illustrate a calculation which makes use of these various techniques to compute a complicated two-dimensional viscous flow over a high-lift multi-element airfoil. The final mesh employed is depicted in Figure 6, and contains a total of 48,691 points. This mesh was obtained using the stretched Delaunay triangulation technique previously described, followed by two levels of adaptive refinement. The height of the smallest cells at the wall is of the order of  $2 \times 10^{-5}$  chords and cell aspect ratios up to 500:1 are observed. The computed Mach number contours for this case are depicted in Figure 7. The freestream Mach number is 0.1995, the chord Reynolds number is 1.187 million, and the corrected incidence is 16.02 degrees. At these conditions, the flow remains entirely subcritical. Compressibility effects are nevertheless important due to the large suction peaks generated about each airfoil. For example, in the suction peak on the upper surface of the leading-edge slat, the local Mach number achieves a value of 0.77. The computed surface pressure coefficients are compared with experimental wind tunnel data [21] in Figure 8, and good overall agreement is observed, including the prediction of the height of the suction peaks. This case provides a good illustration of the importance of adaptive meshing in practical aerodynamic calculations. Adequate resolution of the strong suction peak on the upper surface of the slat can only be achieved with a very fine mesh resolution in this region. Failure to adequately capture this large suction peak results in the generation of numerical entropy which is then convected downstream, thus contaminating the solu-

tion in the downstream regions, and degenerating the global accuracy of the solution. Because these suction peaks are very localized, they are efficiently resolved with adaptive techniques. In order to obtain a similar resolution using global mesh refinement, of the order of 200,000 mesh points would be required, greatly increasing the cost of the computation. The convergence history for this case, as measured by the density residuals and the total lift coefficient versus the number of multigrid cycles, is depicted in Figure 9. A total of 400 multigrid cycles were executed, which required roughly 35 minutes of single processor CRAY-YMP time, and 14 Mwords of memory.

The discrepancy between the computed and experimental pressure coefficients on the trailing edge flap is due to a separated flow condition which is not reproduced by the algebraic turbulence model. Figure 10 compares computed and experimental lift coefficients at various angles of attack for a three-element high-lift airfoil [22]. The failure of the computations to predict the maximum lift point are directly attributable to the inability of the turbulence model to predict the onset of separation. These results strongly indicate the need for more sophisticated turbulence modeling. The use of single or multiple field-equation models appears to be the most appropriate choice for turbulent unstructured mesh computations. Such models can be discretized in a straight-forward manner on unstructured meshes. However, the task is now to ensure that such models adequately represent the flow physics, and that they can be solved in an efficient and robust manner. In this work, the implementation of a standard high-Reynolds-number  $k - \epsilon$  turbulence model with low-Reynolds-number modifications proposed by Speziale, Abid and Anderson [23], has been pursued. The main effort was focused on devising a technique for efficiently solving the two turbulence equations in the context of the unstructured multigrid strategy [24]. The four flow equations and the two turbulence equations are solved as a loosely coupled system. The flow equations are solved explicitly, and the turbulence equations point-implicitly, using a time-step limit which ensures stability and positivity of  $k$  and  $\epsilon$ . In the context of the unstructured multigrid algorithm, the turbulence eddy viscosity is assumed constant on all but the finest grid level where it is recomputed at each time-step. The transonic flow over a two-element airfoil configuration has been computed using this implementation of the model. For this case, the freestream Mach number is 0.5, the incidence is 7.5 degrees, and the Reynolds number is 4.5 million. Figures 11 and 12 depict the mesh and the solution obtained with the current implementation of the  $k - \epsilon$  turbulence model. Four meshes were employed in the multigrid sequence, with the finest mesh containing a total of 28,871 points. The convergence rates of the various equations for this case are plotted in Figure 13. As can be seen, the turbulence equations and flow equations converge at approximately the same rates. The computed flow field exhibits regions of transonic flow with a small region of separated flow at the foot of the shock. These features appear to be well reproduced by the turbulence model. Future efforts will concentrate on computationally predicting flows with large regions of separation, such as that inferred by Figure 8, and on modifying the model to better represent the flow physics.

### 7. THREE DIMENSIONAL RESULTS

Due to the limitations of present day supercomputers, and the difficulties associated with generating highly stretched tetrahedral meshes, three-dimensional computations have presently been confined to inviscid flows. The techniques described in the context of two-dimensional inviscid flows extend readily to three dimensions. In particular, the unstructured multigrid algorithm and the adaptive meshing strategy have been found to be particularly effective for three-dimensional computations [12]. As an example, an adaptive multigrid calculation of transonic flow about an ONERA M6 wing is illustrated in Figures 14 through 16. The

final mesh, depicted in Figure 14, contains a total of 174,412 points and just over 1 million tetrahedral volumes. This represents the fourth mesh in the multigrid sequence and the second adaptive refinement level. Mesh refinement was based on the undivided gradient of density. The freestream Mach number and incidence for this case are 0.84 and 3.06 degrees respectively. The well known double shock pattern for this case is reproduced in the computed Mach contours of the solution in Figure 15. The leading edge expansion and shocks are well resolved due to the extensive mesh refinement in these regions. A globally refined mesh of this resolution would result in roughly 600,000 points and would thus require 3 to 4 times more computational resources. The multigrid convergence rate for this case is depicted in Figure 16, where 50 cycles were performed on the original grid, prior to adaptation, 50 cycles on the first adapted mesh, and 100 cycles on the finest adapted mesh. On this final mesh, the residuals were reduced by 5 orders of magnitude over 100 cycles, requiring a total of 35 CRAY-YMP single CPU minutes and 22 MW of memory.

### 7.1. Parallel Computing Results

As mentioned previously, due to their homogeneous (although random) nature, unstructured mesh data-sets are particularly well suited for parallel processing. An unstructured mesh solver typically consists of a single (indirect addressed) loop over all interior mesh elements, and another similar loop over all boundary elements. On a vector machine, each loop may be split into groups (colors) such that within each group, no recurrences occur. Each group can then be vectorized. A simple parallelization strategy for a shared memory machine is to further split each group into  $n$  subgroups, where  $n$  is the number of available processors. Each subgroup can then be vectorized and run in parallel on its associated processor. Because the original number of groups is not large (usually 20 to 30), the vector lengths within each subgroup are still long enough to obtain the full vector speedup of the machine, for a moderate number of processors. For more massively parallel distributed-memory scalar machines, the entire mesh must be subdivided and each resulting partition associated with a single processor. On each processor, the single scalar interior and boundary loops are then executed, with inter-processor communication occurring at the beginning and end of each loop. The mesh partitioning strategy must ensure good load balancing on all processors while minimizing the amount of inter-processor communication required.

### 7.2. CRAY-YMP-8 Results

Figure 17 illustrates an unstructured mesh generated over a three-dimensional aircraft configuration. This mesh contains a total of 106,064 points and 575,986 tetrahedra. This represents the second finest mesh employed in the multigrid sequence. The finest mesh, which is not shown due to printing resolution limitations, contains a total of 804,056 points and approximately 4.5 million tetrahedra. This is believed to be the largest unstructured grid problem attempted to date. The inviscid flow was solved on this mesh using all eight processors running in parallel on the CRAY-YMP supercomputer. A total of 4 meshes were used in the multigrid sequence. The convergence rate for this case is depicted in Figure 19. In 100 multigrid cycles, the residuals were reduced by almost 6 orders of magnitude. This run required a total of 16 minutes wall clock time running in dedicated mode on the 8 processor CRAY-YMP, including the time to read in all the grid files, write out the solution, and monitor the convergence by summing and printing out the average residual throughout the flow field at each multigrid cycle. The total memory requirements for this job were 94 million words. The ratio of CPU time to wall clock time was 7.7 on 8 processors, and the average speed of calculation was 750 Mflops, as measured by the CRAY hardware performance monitor [25]. For this case, the freestream Mach number is 0.768 and the incidence is 1.116 degrees. The computed Mach contours are shown in Figure 18, where good resolution of the shock on the wing is observed, due to the large number of mesh points employed.

### 7.3. Intel iPSC 860 Results

The implementation of the unstructured multigrid Euler solver on the Intel iPSC 860 distributed memory scalar multiprocessor machine, has been pursued using a set of software primitives designed to ease the porting of scientific codes to parallel machines [26]. The present implementation was undertaken as part of a more general project aimed at designing and constructing such primitives with experience gained from various implementations. The net effect of the use of such primitives is to relieve the programmer of most of the low level machine dependent software programming tasks. The mesh was partitioned using a spectral partitioning algorithm which had previously been shown to produce good load balancing and minimize inter-processor communication [27]. At present, the partitioning of the mesh is done in a preprocessing stage on a sequential machine. At the time of writing, the fine aircraft mesh (804,056 vertices) has not been run on the Intel machine. Thus, results with coarser meshes are quoted. Table 1 gives an overview of the results obtained to date. A small 3600 point mesh was found to run at about 4.1 Mflops on a single Intel iPSC 860 processor. The largest case tried to date, a 210,000 point mesh, resulted in a 144 Mflop rate on 64 processors, which represents an efficiency of about 55% percent, based on the single processor results. It is anticipated that the fine 804,056 point grid, when implemented on 512 processors, will achieve an equivalent or greater computational speed than that observed with the full CRAY-YMP 8-processor machine.

## 8. CONCLUSION

This paper has illustrated the application of unstructured mesh techniques to various types of aerodynamic flows, and emphasized the advantages which can be obtained for complex geometries using adaptive meshing and parallelization. In two dimensions, a viscous flow solution capability has been demonstrated, while in three dimensions, efficient Euler solutions are possible. The main problems associated with three-dimensional viscous solutions are related to the development of reliable grid generation strategies, particularly with regards to the generation of highly stretched tetrahedral elements for capturing thin viscous layers. Turbulence modeling is also a limiting factor, although this difficulty is not particular to the field of unstructured meshes. Future work should also concentrate on more complete parallelization of the entire solution process, including items such as grid generation, partitioning, and adaptive meshing.

## ACKNOWLEDGEMENTS

Much of this work has been possible due to the generous assistance of a large number of people. Among those, Daryl Bonhaus is acknowledged for his work in helping validate the 2-D viscous flow solver. The help of Shahyar Pirzadeh and Clyde Gumbert in providing assistance with the generation of three-dimensional unstructured grids using the VGRID program is acknowledged. Rob Vermeland and CRAY Research Inc. are thanked for providing dedicated time on the CRAY-YMP-8 machine, and the National Aerodynamic Simulation Facility (NAS), for providing the computational facilities which have made most of this work possible. Finally, Raja Das, Joel Saltz and Ravi Ponnusamy are acknowledged for actually having done most of the work on the distributed memory parallel implementation.

## REFERENCES

1. Dannenhoffer, J. F., "Grid Adaptation for Complex Two-Dimensional Transonic Flows", *Sc.D Thesis. Department of Aeronautics and Astronautics, Massachusetts Institute of Technology*, August 1987.
2. Jameson, A., Baker, T. J., and Weatherill, N. P., "Calculation of Inviscid Transonic Flow over a Complete Aircraft", *AIAA paper 86-0103*, January, 1986.

3. Mavriplis, D. J., "Solution of the Two-Dimensional Euler Equations on Unstructured Triangular Meshes", *Ph.D. Thesis, Department of Mechanical and Aerospace Engineering, Princeton University*, June 1987.
4. Jameson, A., "Transonic Flow Calculations" *Princeton University Report MAE 1751*, 1984
5. Martinelli, L., "Calculations of Viscous Flows with a Multigrid Method" *Ph.D. Thesis, Department of Mechanical and Aerospace Engineering, Princeton University*, October, 1987.
6. Mavriplis, D. J., and Jameson, A., "Multigrid Solution of the Navier-Stokes Equations on Triangular Meshes", *AIAA Journal*, Vol 28, No. 8, pp. 1415-1425, August 1990.
7. Lallemand, M. H., Dervieux, A., "A Multigrid Finite-Element Method for Solving the Two-Dimensional Euler Equations", *Proceedings of the Third Copper Mountain Conference on Multigrid Methods, Lecture Notes in Pure and Applied Mathematics*, Ed S. F. McCormick, Marcel Dekker Inc., April 1987, pp. 337-363.
8. Smith, W. A., "Multigrid Solution of Transonic Flow on Unstructured Grids", *Recent Advances and Applications in Computational Fluid Dynamics, Proceedings of the ASME Winter Annual Meeting*, Ed. O. Baysal, November 1990.
9. Barth, T. J., "Numerical Aspects of Computing Viscous High-Reynolds Number Flows on Unstructured Meshes", *AIAA Paper 91-0721* January, 1991
10. Bowyer, A., "Computing Dirichlet Tessalations", *The Computer Journal*, Vol. 24, No. 2, 1981, pp. 162-166
11. Baker, T. J., "Three Dimensional Mesh Generation by Triangulation of Arbitrary Point Sets", *Proc. of the AIAA 8th Comp. Fluid Dyn. Conf.*, AIAA paper 87-1124, June, 1987.
12. Mavriplis, D. J., "Three Dimensional Unstructured Multigrid for the Euler Equations", *Proc. of the AIAA 10th Comp. Fluid Dyn. Conf.*, AIAA paper 91-1549, June, 1991.
13. Sieverding, C. H., "Experimental Data on Two Transonic Turbine Blade Sections and Comparisons with Various Theoretical Methods", *Transonic Flows in Turbomachinery*, VKI Lecture Series 59, 1973.
14. Peraire, J., Vahdati, M., Morgan, K., and Zienkiewicz, O. C., "Adaptive Remeshing for Compressible Flow Computations", *J. Comp. Phys.*, Vol 72, October, 1987, pp. 449-466
15. Gumbert, C., Lohner, R., Parikh, P., and Pirzadeh, S., "A Package for Unstructured Grid Generation and Finite Element Flow Solvers", *AIAA paper 89-2175* June, 1989.
16. George, P. L., Hecht, F., Saltel, E., "Maillage Automatique de Domaines Tridimensionnels Quelconques", *INRIA Report No. 1021, Institut National de Recherche en Informatique et en Automatique, Rocquencourt, France*, April 1989.
17. Mavriplis, D. J., "Unstructured and Adaptive Mesh Generation for High Reynolds Number Viscous Flows", *Proc. of the 3rd Int. Conf. on Numerical Grid Generation in Comp. Fluid Dyn.*, Eds. A. S. Arcilla, J. Hauser, P. R. Eisman, and J. F. Thompson, Pineridge Press Ltd., 1988, pp. 79-91.
18. Nakahashi, N., "FDM-FEM Zonal Approach for Viscous Flow Computations Over Multiple Bodies", *AIAA paper 87-0604*, January, 1987.
19. Holmes D. G., and Connell, S., "Solution of the 2-D Navier-Stokes Equations on Unstructured Adaptive Grids", *AIAA paper 89-1932, Proc. of the AIAA 9th Computational Fluid Dynamics Conference, Buffalo, NY*, June, 1989.
20. Mavriplis, D. J., "Algebraic Turbulence Modeling for Unstructured and Adaptive Meshes", *AIAA Paper 90-1653*, June, 1990.
21. Wigton, L. B., *Private Communication*, The Boeing Company
22. Bonhaus, D., "Computed Flows of Sulfur Hexafluoride Over Multi-Element Airfoils" *NASA TP (Technical Paper)*, To Appear.
23. Speziale, C. G., Abid, R., and Anderson, E. C., "A Critical Evaluation of Two-Equation Models for Near Wall Turbulence", *ICASE Report 90-46, NASA CR 182068, AIAA paper 90-1481*, June, 1990
24. Mavriplis, D. J., "Multigrid Solution of Compressible Turbulent Flow on Unstructured Meshes Using a Two-Equation Model", *AIAA Paper 91-0237*, January 1991
25. UNICOS Performance Utilities Reference Manual, SR-2040 6.0 Cray Research Inc.
26. Das, R., Mavriplis, D. J., Saltz, J., Ponnusamy, R., "The Design and Implementation of a Parallel Unstructured Euler Solver Using Software Primitives", *AIAA paper 92-0562*, January 1992.
27. Simon, H., "Partitioning of Unstructured Mesh Problems for Parallel Processing", *Proceedings of the Conference on Parallel Methods on Large Scale Structural Analysis and Physics Applications*, Pergamon Press, 1991.

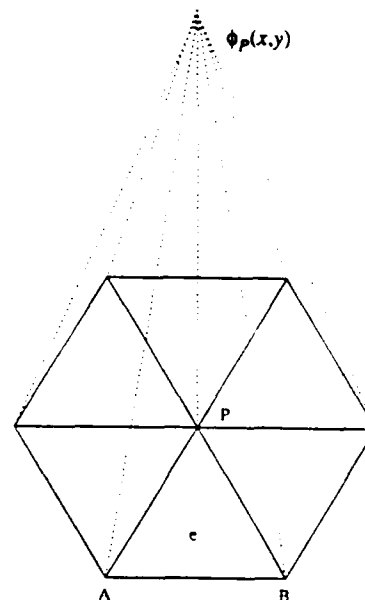
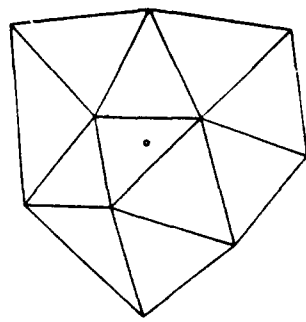
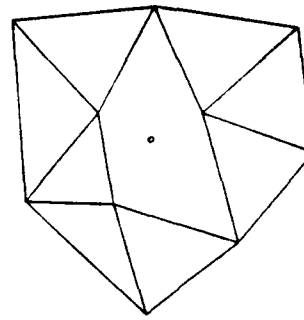


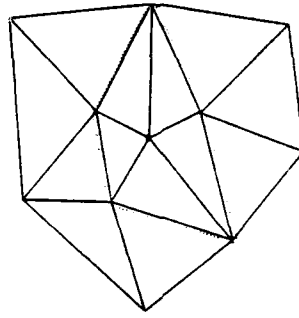
Figure 1: Domain of Influence of Finite-Element Basis Function and Equivalent Finite-Volume Control Volume



a)  
Insertion of New Point



b)  
Determination of Intersected Triangles  
and Removal of Mesh Structure in this Region



c)  
Local Restructuring of Mesh in Affected Region

Figure 2: Illustration of Bowyer's Algorithm for Delaunay Triangulation

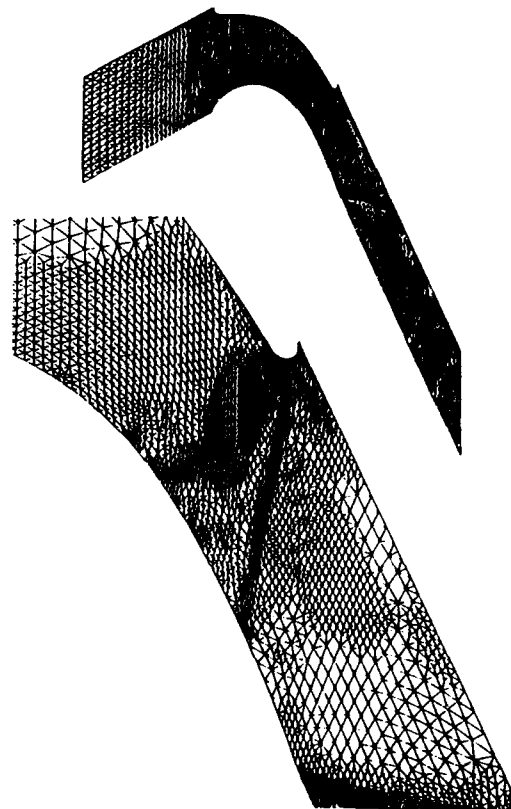


Figure 3: Adaptive Mesh Employed for Computing Transonic Inviscid Flow Through a Periodic Turbine Blade Cascade Geometry; Number of Nodes = 9362

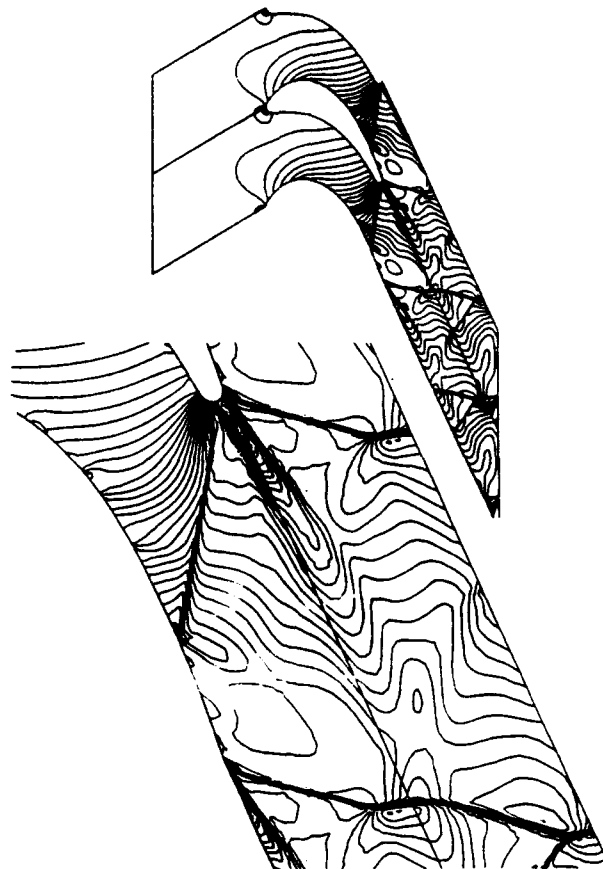


Figure 4: Computed Mach Contours for Flow Through a Periodic Turbine Blade Cascade Geometry

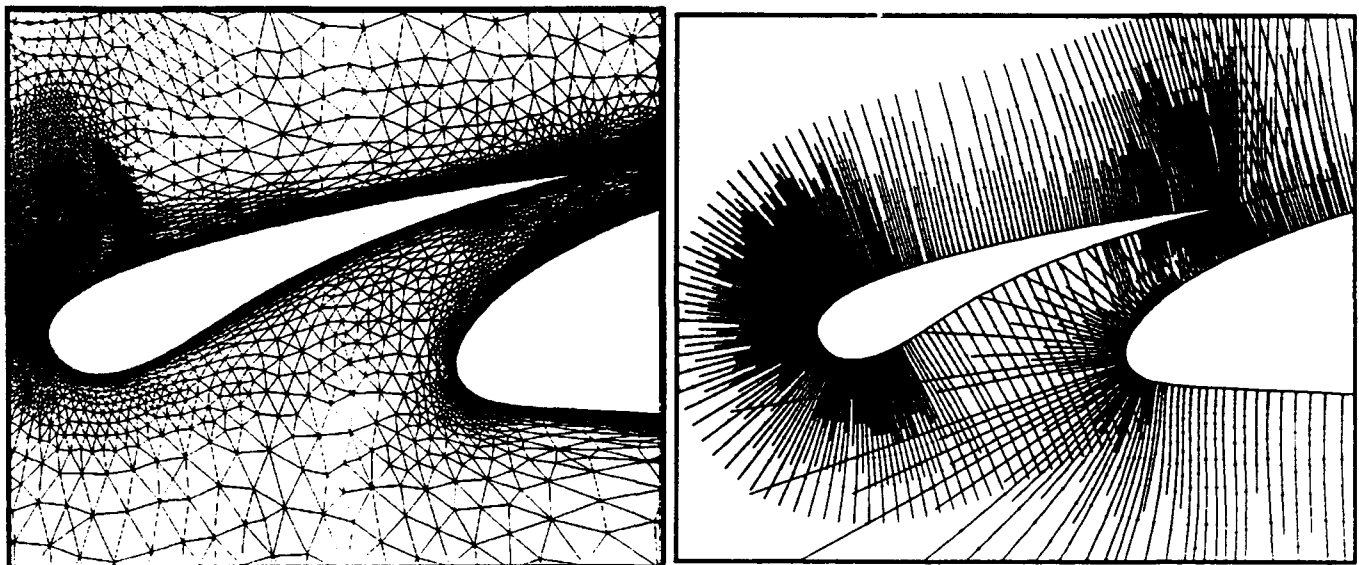


Figure 5: Illustration of Turbulence Mesh Stations Employed in Algebraic Model for an Adaptively Generated Mesh

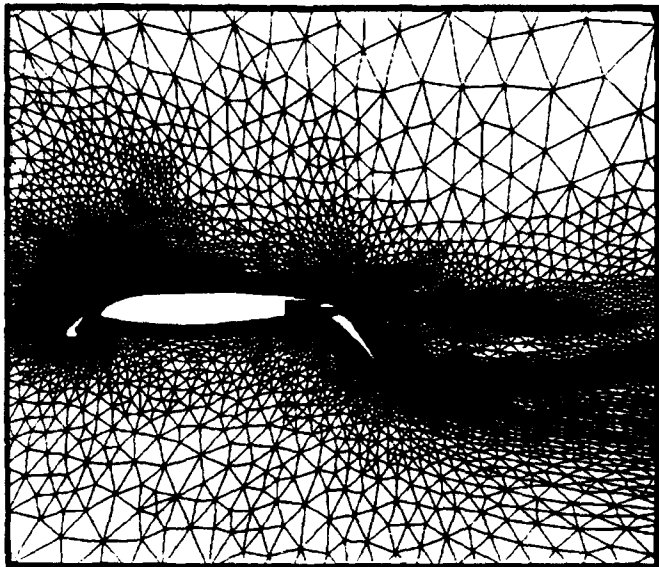


Figure 6: Adaptively Generated Unstructured Mesh about Four-Element Airfoil; Number of Nodes = 48,691

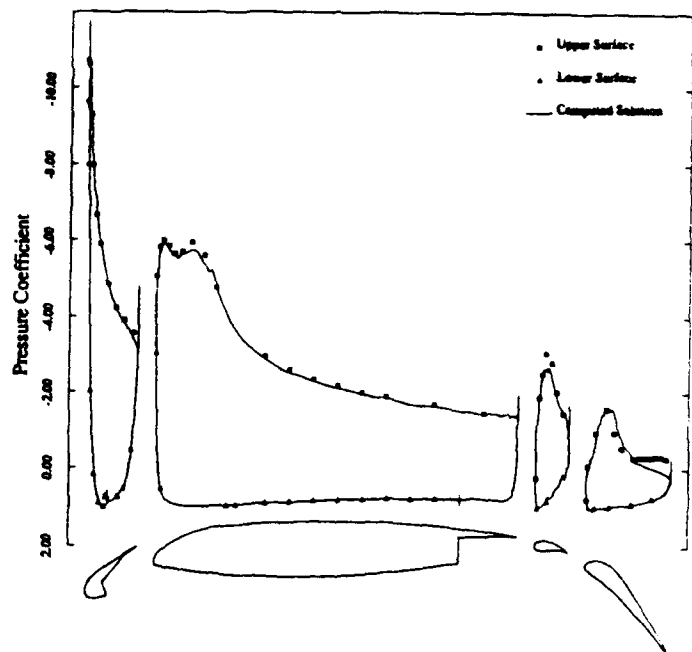


Figure 8: Comparison of Computed Surface Pressure Distribution with Experimental Wind-Tunnel Data for Flow Over Four-Element Airfoil Configuration; Mach = 0.1995, Reynolds Number = 1.187 million, Incidence = 16.02 degrees

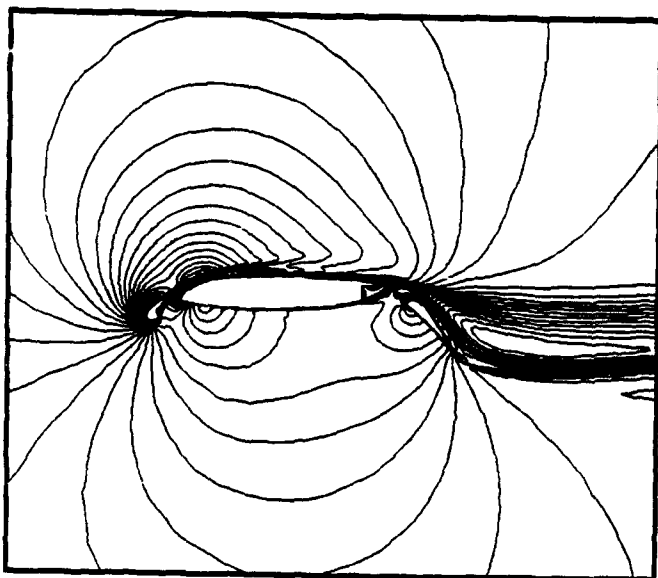


Figure 7: Computed Mach Contours for Flow over Four-Element Airfoil; Mach = 0.1995, Reynolds Number = 1.187 million, Incidence = 16.02 degrees

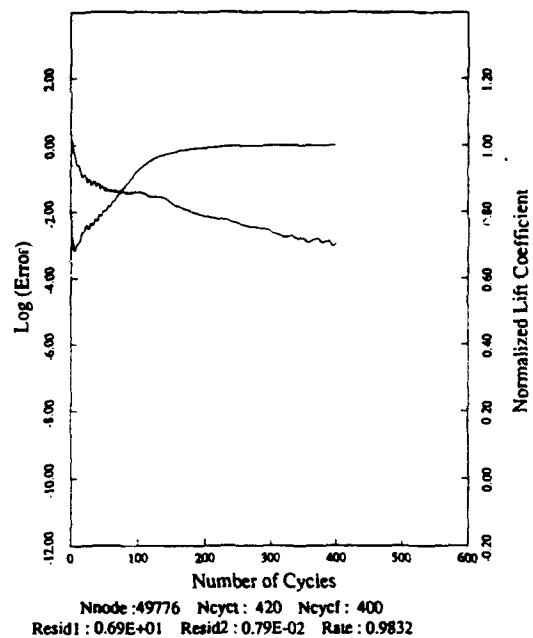


Figure 9: Convergence as Measured by the Computed Lift Coefficient and the Density Residuals Versus the Number of Multigrid Cycles for Flow Past a Four-Element Airfoil



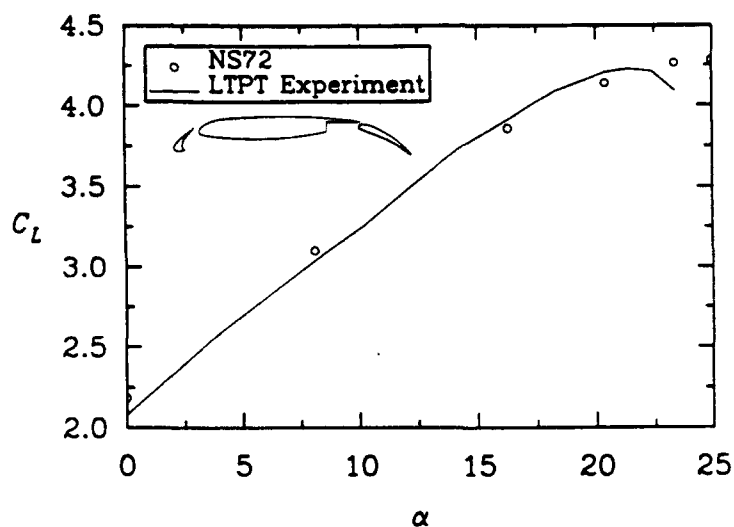


Figure 10: Comparison of Computed and Experimental Lift Coefficients as a Function of Incidence for a Three-Element Airfoil Configuration

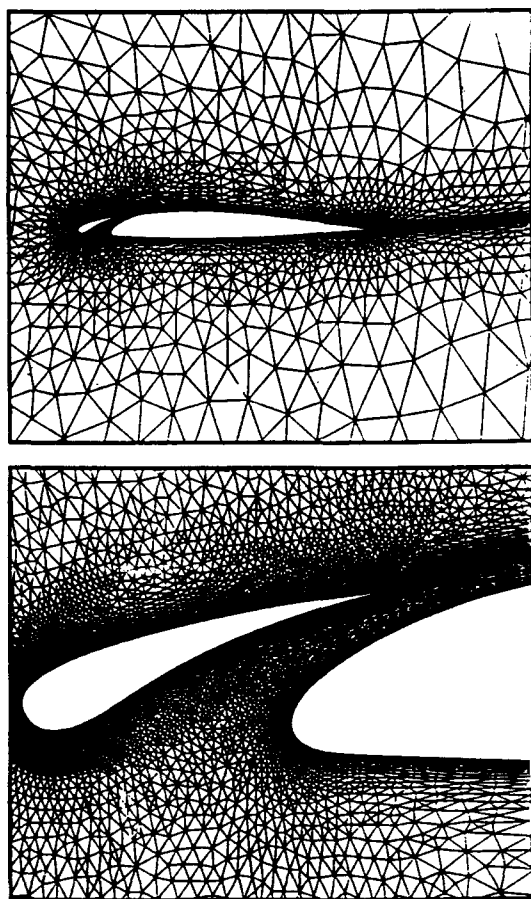


Figure 11: Global View of Coarse Unstructured Mesh and Close-Up View of Fine Unstructured Mesh Employed for Computing Flow Past a Two-Element Airfoil (Coarse Mesh Points = 7272, Fine Mesh Points = 28871)

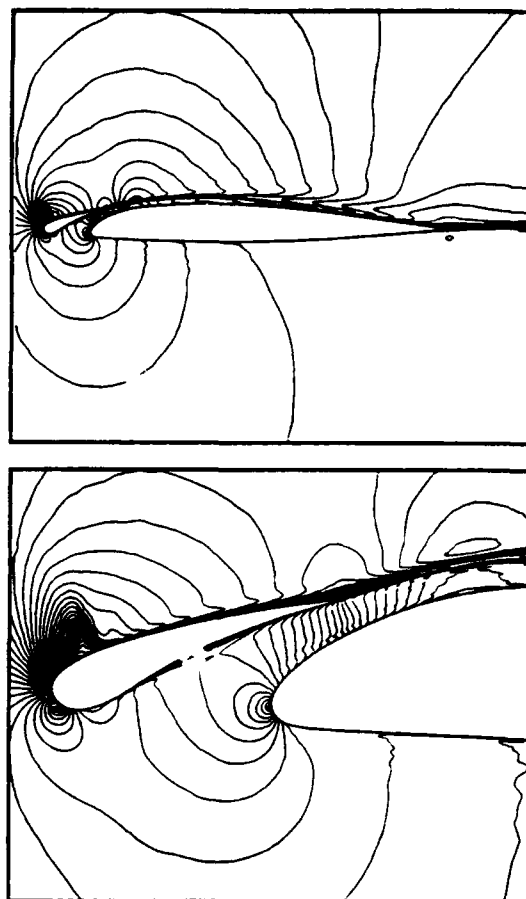


Figure 12: Computed Mach Contours Using Low-Reynolds Number Modification for Turbulence Equations for Supercritical Flow over a Two-Element Airfoil (Mach = 0.5, Re = 4.5 million, Incidence = 7.5 degrees)

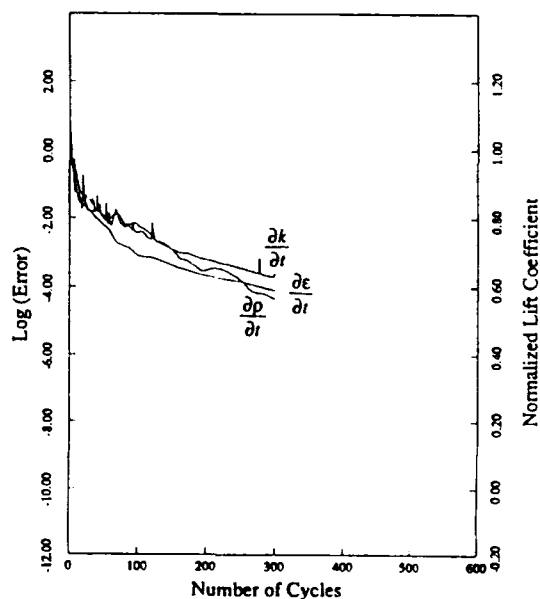


Figure 13: Multigrid Convergence Rate of the Density Equation and the Two Turbulence Equations Using Low-Reynolds Number Modifications for Flow Over Two-Element Airfoil (Mach = 0.5, Re = 4.5 million, Incidence = 7.5 degrees)

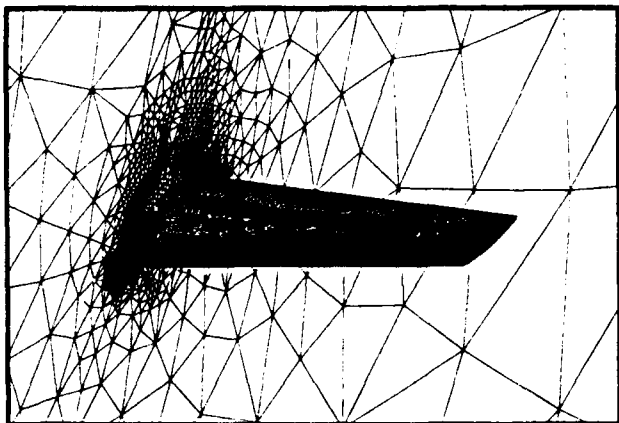


Figure 14: Finest Adapted Mesh Generated About ONERA M6 Wing (Number of Nodes = 173,412 Number of Tetrahedra = 1,013,718)

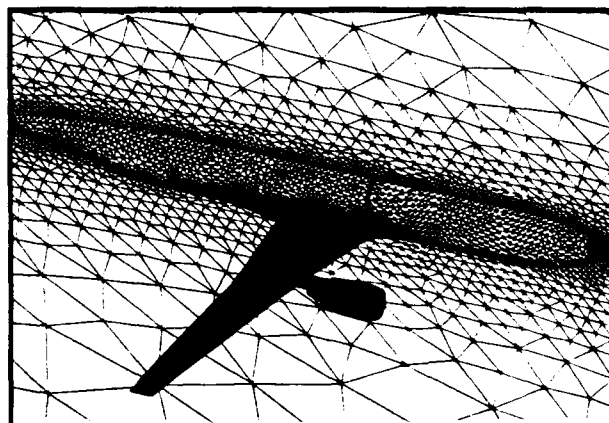


Figure 17: Coarse Unstructured Mesh about an Aircraft Configuration with Single Nacelle; Number of Points = 106,064, Number of Tetrahedra = 575,986 (Finest Mesh Not Shown)

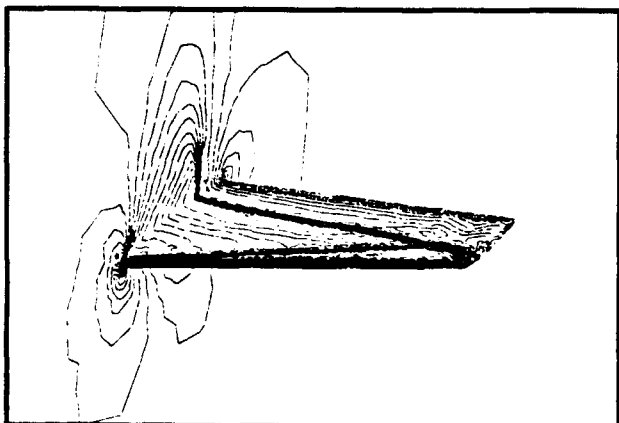


Figure 15: Computed Mach Contours on the Adaptively Generated Mesh About the ONERA M6 Wing (Mach = 0.84, Incidence = 3.06 degrees)

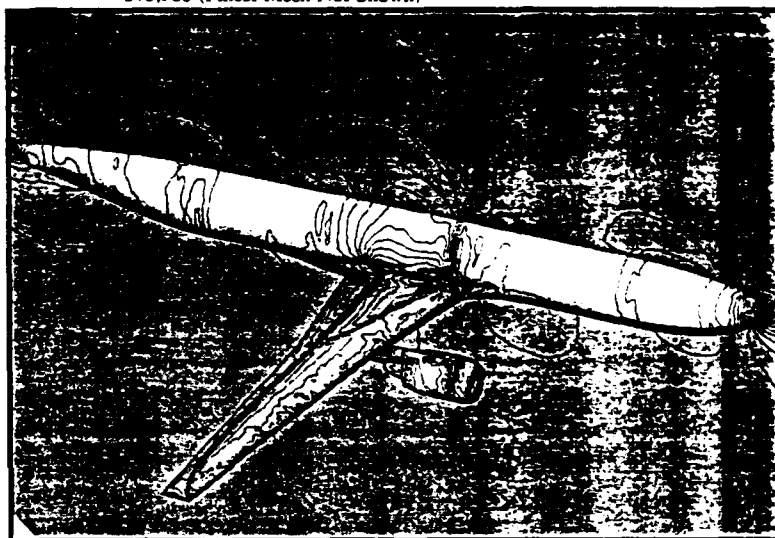


Figure 18: Mach Contours for Flow over Aircraft Configuration Computed on Fine Mesh of 804,056 Vertices and 4.5 million Tetrahedra (Mach = 0.768, Incidence = 1.116 degrees)

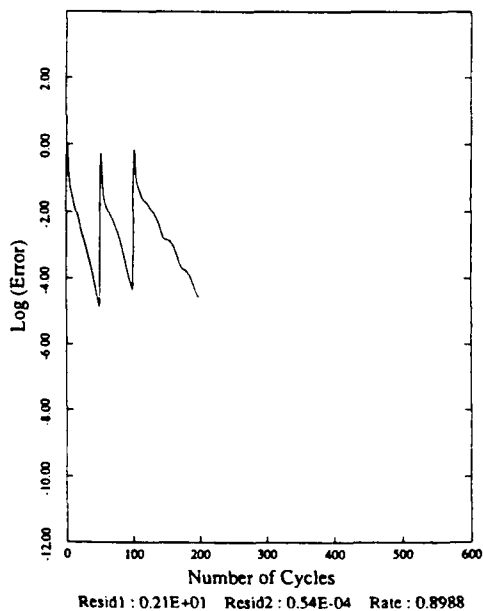


Figure 16: Convergence Rate of the Unstructured Multigrid Algorithm on the Adaptively Generated Sequence of Meshes about the ONERA M6 Wing as Measured by the Average Density Residuals Versus the Number of Multigrid Cycles

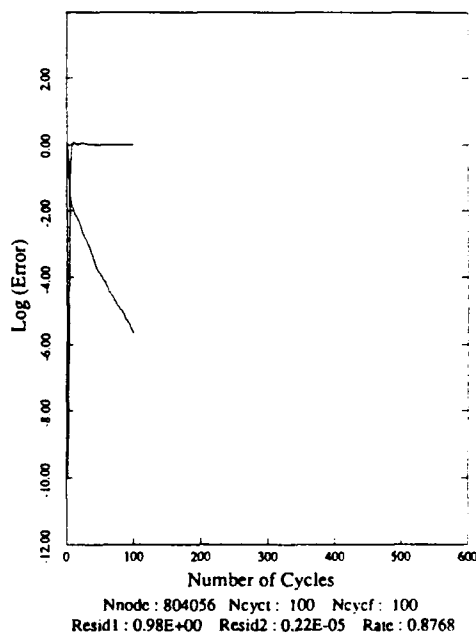


Figure 19: Multigrid Convergence Rate on Finest Mesh of the Multigrid Sequence for Transonic Flow over Aircraft-with-Nacelle Configuration

Size Mesh	Number of Processors					
		1	2	8	16	64
3600	Mflops	4.1	7.1	16.9	17.4	-
	comp/iter(s)	4.6	2.4	0.6	0.34	-
	comm/iter(s)	-	0.25	0.48	0.73	-
26K	Mflops	-	-	23.8	38.8	
	comp/iter(s)	-	-	4.5	2.3	
	comm/iter(s)	-	-	1.1	1.1	
210K	Mflops	-	-	-	-	144.3
	comp/iter(s)	-	-	-	-	4.75
	comm/iter(s)	-	-	-	-	2.3

Table 1: Observed Computational Rates and Timings per Iteration of Computational Work and Communication Overhead for Various Sizes of Unstructured Meshes on Intel iPSC/860

# AN INTERACTIVE BOUNDARY-LAYER APPROACH TO MULTIELEMENT AIRFOILS AT HIGH LIFT

Tuncer Cebeci\*  
Aerospace Engineering Department  
California State University, Long Beach

## Abstract

A calculation method based on an interactive boundary-layer approach to multielement airfoils is described and is applied to three types of airfoil configurations with and without flap-wells in order to demonstrate the applicability of the method to general high-lift configurations. This method, well tested for single airfoils as a function of shape, angle of attack and Reynolds number, is here shown to apply equally well to two-element airfoils and their wakes, to a flap-well region, and to a three-element arrangement which includes the effects of co-flowing regions, a flap well, and the wake of the elements. In addition to providing accurate representation of these flows, the method is general so that its extension to three-dimensional arrangements is likely to provide a practical, accurate and efficient tool to assist the design process.

## 1.0 Introduction

The design of multielement airfoils for high lift requires consideration of a range of configurations so that care must be taken to ensure that the essential experiments and calculations can be undertaken with acceptable cost as well as accuracy.<sup>1,2</sup> We are concerned here with the development of a calculation method which meets this requirement and is able to represent the flow over and between the individual airfoils with consideration of flap wells and wakes. These requirements imply the need for a method which has an economical and accurate numerical solution procedure; a flexible turbulence model to represent wall boundary layers, wall jets and wakes, and the wake of the last element; and the ability to represent the separated flows associated with the upper surface and the flap well. In addition, the preferred procedure should be readily extendible to deal with three-dimensional components such as wings and empennage.

In recent years there has been a renewed interest in experimental work on high-lift systems. Extensive measurements have been reported by Nakayama<sup>3</sup>, Alemdaroglu summarized by Nakayama<sup>4</sup>, and Valarezo et al.<sup>5</sup> The data of Nakayama are for a three-element airfoil with a leading-edge slat and for a single-segment flap; they were obtained at NASA Langley's Low Turbulence Pressure Tunnel (LTPT). Those of Alemdaroglu are essentially for the same but smaller model and were obtained at the low-speed wind tunnel of California State University, Long Beach. The data of Valarezo et al. were also obtained at NASA Langley's LTPT and correspond to measurements at high Reynolds numbers. These data add to the previously obtained data on multielement airfoils by van den Berg,<sup>6</sup> van den Berg and Oskam,<sup>7</sup> Oskam et al.<sup>8</sup>, Omar et al.<sup>9,10</sup>

and Olson and Orloff<sup>11</sup> which allow the validation of computer programs to analyze high-lift systems.

Several airfoil-analysis and design algorithms have been developed in the last decade and have been based on one of two approaches: numerical solutions of the Reynolds-averaged Navier-Stokes equations or solutions of the interaction between inviscid and boundary-layer equations. The former approach involves the numerical solution of elliptic equations so that information travels in all directions through pressure, velocity and viscous and turbulent stress gradients. As a result, the solution method requires simultaneous processing of the pressure and velocity components and stress tensor throughout the flowfield and this, in turn, implies a trade-off between accuracy and cost which tends to limit the validity of this approach. This limitation is a function of computers and programming methods, and these are likely to improve with time so that solutions of the Navier-Stokes equations, with proper consideration of momentum conservation in two directions together with longitudinal diffusion, are likely to be a major component of design methods of the future. The combination of the largest mainframe computers and unstructured and multigrid techniques has already been shown to be very powerful as, for example, by Mavriplis<sup>12</sup>, Rogers et al.<sup>13</sup>, and Barth.<sup>14</sup>

The present approach is based on the interactive boundary-layer approach which has been tested extensively for single-element airfoils, as described for example in References 15 to 17. These papers have shown that this approach can represent accurately, and with low cost, the flows around a number of airfoil geometries, with angles of attack up to and beyond that of stall, and including regions of separated flow which may cause transition from laminar flow. It is based on solutions of inviscid and boundary-layer equations with a surface and wake blowing velocity obtained from the Hilbert integral and ensuring interaction between the calculated inviscid and viscous flows. It has also been shown that, in extended form, it is able to represent the three-dimensional flows over wings<sup>18</sup> and, therefore, meets many of the requirements for a design method as discussed above.

It should be emphasized that alternative interactive methods have been reported, for example by Veldman<sup>19</sup>, LeBalleur<sup>20,21</sup>, Williams and Smith<sup>22</sup>, Drela and Giles<sup>23</sup>, and Kusunose, Wigton and Meredith.<sup>24</sup> The last of these deserves further research in the context of this paper since it has been reported recently and has been applied to multielement airfoils. It uses a finite-element full-potential code to compute the outer flow with a modified streamline H-grid, and solves the boundary-layer equations in integral form with modeling similar to that of Bradshaw and Ferris.<sup>25</sup>

\*Professor and Chairman.

The results encompass single, two- and three-element airfoils at angles of attack up to around 13 degrees and are in close agreement with measurements. It is also evident that the method is cost efficient and is already part of a design method. It can be expected, however, that the turbulence model will be less successful where pressure gradients are severe and will not cope well with inter-element flows where there is a distinct velocity maximum. In addition, and perhaps of greatest importance, attempts to extend integral boundary-layer methods to three-dimensional flows have not been successful.

This paper is concerned with the extension of the interactive boundary-layer method of Refs. 15 to 17 to represent multielement airfoils where the flows between airfoils, flap wells and the possible influence of the overall wake in all elements are new features. The computational investigation was carried out in three parts which are reflected in the presentation of results and correspond to two-element airfoils with emphasis on the flow between elements and the wake, a single-element airfoil with a flap well where the calculation of the flow in the flap well is the major novelty, and the combination of these features in three-element airfoils which involve a flap well. This results section is preceded by descriptions of the interactive and solution procedures and followed by concluding remarks.

## 2.0 Interactive Boundary-Layer Method

The interactive boundary-layer method makes use of the panel method of Hess and Smith<sup>26</sup> and a solution of the boundary-layer equations in which the turbulence model is given by the algebraic eddy viscosity ( $\epsilon_m$ ) formulation of Cebeci and Smith.<sup>27</sup> With  $b$  denoting  $1 + \epsilon_m/\nu$ , the continuity and momentum equations can be written as

$$\frac{\partial u}{\partial x} + \frac{\partial v}{\partial y} = 0 \quad (1)$$

$$u \frac{\partial u}{\partial x} + v \frac{\partial u}{\partial y} = u_e \frac{du_e}{dx} + \nu \frac{\partial}{\partial y} \left( b \frac{\partial u}{\partial y} \right) \quad (2)$$

In the absence of mass transfer, the boundary conditions for the above equations on the airfoil are:

$$u = v = 0, \quad y = 0 \quad (3a)$$

$$u \rightarrow u_e(x), \quad y \rightarrow \infty \quad (3b)$$

and in the wake, where a dividing line at  $y = 0$  is required to separate the upper and lower parts of the inviscid flow and in the absence of the normal pressure gradient, they are:

$$y \rightarrow \pm\infty, \quad u \rightarrow u_e(x); \quad y = 0, \quad v = 0 \quad (4)$$

## 2.1 Interaction Law

To perform the calculations for flows with separation, it is necessary to use an inverse procedure and compute the external velocity as part of the solution. Here we use the formulation discussed in Ref. 15 and write the edge boundary condition as

$$u_e(x) = u_e^0(x) + \delta u_e(x) \quad (5a)$$

with  $\delta u_e(x)$  computed from the Hilbert integral

$$\delta u_e(x) = \frac{1}{\pi} \int_{x_a}^{x_b} \frac{d}{d\sigma} (u_e^{\delta*}) \frac{d\sigma}{x - \sigma} \quad (5b)$$

This inverse boundary-layer formulation is appropriate to airfoils and to those parts of airfoils without surface discontinuities such as flap wells. Where flap wells occur, a different formulation of the inverse procedure is required, and the formulation used here is described below.

The calculation of the flow in the flap-well region is similar to that over a backward-facing step. A large portion of the flow separates immediately after the sudden change of the geometry, and the size of the reversed-flow region depends mainly on the step height, on the gap, and the overhang. The flow reattaches and gradually recovers downstream in the flap-well region or in the wake. The calculation of flows of this kind is difficult, and potential theory is not adequate because of the singularity that occurs at the geometry discontinuity and the strong viscous effects in the separated flowfield. Thus, an initial distribution of displacement thickness is assumed and the relaxation formula

$$(\delta^*)^{v+1} = (\delta^*)^v [1 + \omega \left( \frac{u_{ev}}{u_{e1}} - 1 \right)] \quad (6)$$

is used in the inverse method to replace the Hilbert integral formulation of the external boundary condition. The new edge boundary conditions are given by Eq. (3b) and Eq. (6), where  $u_{ev}$  and  $u_{e1}$  correspond to the external velocities computed by the boundary layer and inviscid methods, respectively, and  $\omega$  is a relaxation parameter. At the end of the flap-well region, the solution procedure reverts to the Hilbert-integral approach.

## 2.2 Turbulence Model

The turbulence model used to represent the flow on the airfoil may be expressed in terms of the Cebeci and Smith eddy-viscosity formulation,

$$\epsilon_m = \begin{cases} (\epsilon_m)_1 = \{0.4y[1 - \exp(-\frac{y}{A})]\}^2 \left| \frac{\partial u}{\partial y} \right| \gamma_{tr} & 0 \leq y \leq y_c \quad (7a) \\ (\epsilon_m)_0 = 0.0168 \left| \int_0^\infty (u_e - u) dy \right| \gamma_{tr} \gamma & y_c \leq y \leq \delta \quad (7b) \end{cases}$$

where

$$A = 26\nu u_\tau^{-1}, \quad u_\tau = \left( \frac{\tau}{\rho} \right)^{1/2}_{\max}, \quad \gamma = \frac{1}{1 + 5.5(y/\delta)^6} \quad (8a)$$

The condition used to define  $y_c$  is the continuity of the eddy viscosity so that Eq. (7a) is applied from the wall outward (inner region) until its value is equal to that given for the outer region by Eq. (7b). The expression  $\gamma_{tr}$  represents the transition region and is given by

$$\gamma_{tr} = 1 - \exp[G(x - x_{tr}) \int_{x_{tr}}^x \frac{dx}{u_e}] \quad (8b)$$

Here  $x_{tr}$  is the location of the beginning of transition and  $G$  is defined by

$$G = \frac{1}{1200} \frac{u_e^3}{v^2} R_{x_{tr}}^{-1.34}$$

where the transition Reynolds number  $R_{x_{tr}} = (u_e x / \nu)_{tr}$ .

The location of the onset transition is obtained from Michel's formula, given by Ref. 28,

$$R_\theta = 1.174 \left(1 + \frac{22,400}{R_x}\right) R_x^{0.46} \quad (9)$$

When flow separation takes place upstream of the transition location predicted by this formula, transition is assumed to coincide with the location of separation.

In the flap-well region, the above formulas are modified so that

$$c_m = c_m^{(I)} + (c_m^{(F)} - c_m^{(I)}) (1 - e^{-(x-x_0)/\lambda L}) \quad (10)$$

Here  $c_m^{(I)}$  denotes the eddy viscosity corresponding to the velocity profile above the separated region and  $c_m^{(F)}$  includes the total region from the wall. The expressions for  $c_m^{(I)}$  and  $c_m^{(F)}$  are given by:

$$c_m^{(I)} = \begin{cases} \{0.4(y - y_0)[1 - e^{-(y-y_0)/A}]^2 \left| \frac{\partial u}{\partial y} \right| \gamma_{tr} & \text{for } y > y_0 \\ 0.0168 u_e \left| \int_{y_0}^{\infty} (1 - \frac{u}{u_e}) dy \right| \gamma_{tr} & \text{for } y > y_0 \\ 0 & \text{for } y < y_0 \end{cases} \quad (11a)$$

$$c_m^{(F)} = \begin{cases} \{0.4y [1 - e^{-y/A}]^2 \left| \frac{\partial u}{\partial y} \right| \gamma_{tr} & \text{for } y > 0 \\ 0.0168 u_e \left| \int_0^{\infty} (1 - \frac{u}{u_e}) dy \right| \gamma_{tr} & \end{cases} \quad (11b)$$

where  $y_0$  is the location of  $u = 0$ ,  $\lambda$  is a relaxation parameter (usually around 10),  $L$  is a characteristic length, and  $x_0$  is the beginning of the flap-well.

In the wake the corresponding expressions are:

$$c_m = (c_m)_w + [(c_m)_{t.e.} - (c_m)_w] \exp \left[ -\frac{(x - x_0)}{20\delta} \right] \quad (12)$$

where  $(c_m)_{t.e.}$  is the eddy viscosity at the trailing edge computed from Eqs. (7) and (10) and  $(c_m)_w$  is the eddy viscosity in the far wake given by the larger of

$$(c_m)_w^L = 0.064 \int_{-\infty}^{y_{min}} (u_e - u) dy \quad (13a)$$

and

$$(c_m)_w^U = 0.064 \int_{y_{min}}^{\infty} (u_e - u) dy \quad (14b)$$

with  $y_{min}$  denoting the location where the velocity is a minimum.

The eddy-viscosity model for the flap-well, like all expressions for turbulent flows, is empirical and was first tested for flow over a backward facing step before its application to the present problem. While the agreement with backward facing data was satisfactory, it should be tested further and possibly replaced by "better" expressions or models.

### 2.3 Solution Procedure

In general, it is convenient to solve the equations of the previous section in transformed variables. The Falkner-Skan transformation defined by

$$\eta = \left( \frac{u_e}{\nu x} \right)^{1/2} y, \quad \psi = (u_e \nu x)^{1/2} f(x, \eta) \quad (15)$$

is used here and, with the usual definition of stream function, Eqs. (1) - (3) lead to

$$(bf'')' + \frac{1}{2}(m+1)ff'' + m(1-f'^2) = x(f' \frac{\partial f'}{\partial x} - f'' \frac{\partial f}{\partial x}) \quad (16)$$

$$\eta = 0, \quad f = f' = 0, \quad \eta = \eta_e, \quad f' = 1, \quad (17)$$

where primes denote differentiation with respect to  $\eta$  and

$$f' = \frac{u}{u_e}, \quad m = \frac{x}{u_e} \frac{du_e}{dx}$$

A slightly modified form of this transformation is used when the calculations are performed in the inverse mode by replacing  $u_e$  with a reference velocity  $u_0$ , that is,

$$Y = \sqrt{u_0/\nu x} y, \quad \psi = \sqrt{u_0 \nu x} F(x, Y) \quad (18)$$

so that the continuity and momentum equations and their boundary conditions, given by Eqs. (16) and (17) become,

$$(bF'')' + \frac{1}{2}FF'' + xw \frac{dF}{dx} = x[F' \frac{\partial F'}{\partial x} - F'' \frac{\partial F}{\partial x}] \quad (19)$$

$$Y = 0, \quad F = F' = 0 \quad (20a)$$

$$Y = Y_e, \quad F' = w \quad (20b)$$

The boundary conditions corresponding to Eq. (5b) are obtained by applying a discretization approximation to the Hilbert integral, Eq. (5b),

$$u_e(x_1) = u_e^0(x_1) + c_{11}D_1 + \sum_{j=1}^{1-1} c_{1j}D_j + \sum_{j=1+1}^N c_{1j}D_j \quad (21)$$

where the subscript 1 denotes the x-station where the inverse calculations are to be performed,  $c_{ij}$  is a matrix of interaction coefficients, and  $D$  is given by  $D = u_e \delta^*$ . Further details are available in Ref. 15. In terms of transformed variables, the parameter  $D$  can be written as

$$D = \left( \frac{\nu x}{u_0} \right)^{1/2} (Y_e w - F_e) \quad (22)$$

and the relation between the external velocity  $w$  and displacement thickness  $\delta^*$  provided by the Hilbert integral can then be written as

$$Y = Y_e, \quad w = c_{11} \left( \frac{yx}{u_0} \right)^{1/2} (Y_e - F) + g_1 \quad (23)$$

where

$$g_1 = u_e^0(x_1) + \sum_{j=1}^{1-1} c_{1j} D_j + \sum_{j=1+1}^N c_{1j} D_j \quad (24)$$

In the flap-well region, Eq. (23) is replaced by

$$Y = Y_e, \quad F_e = w[Y_e - \left( \frac{u_0}{yx} \right)^{1/2} \delta^*] \quad (25)$$

The corresponding boundary conditions in the wake are

$$Y = Y_{-e}, \quad F' = w; \quad Y = 0, \quad F = 0;$$

$$Y = Y_e, \quad F' = w,$$

with  $w$  now given by

$$w = c_{11} [w(Y_e - Y_{-e}) - (F_e - F_{-e})] \left( \frac{yx}{u_0} \right)^{1/2} + g_1, \quad (26)$$

The solution of the above transformed equations is obtained by Keller's box method, as described in Ref. 15. Where separation occurred, the convective term  $u(\partial u / \partial x)$  was set to zero and this assumption proved to be satisfactory for the flow on the airfoil. The larger regions of separation associated with the flap well and the near wake required an additional iteration scheme based on a continuation method. Since a linearized form of the boundary-layer equations is being solved, it is necessary that the calculations at station  $x_1$  have initial profiles which are usually assumed to correspond to those at a previous  $x$ -station,  $x_{1-1}$ . With increasing flow separation, the effect of the initial profiles on the solutions at  $x_1$  increases and can lead to breakdown. A remedy to this problem is to define the velocity profile at  $x_1$  to be of the form

$$u = u_{ref} + n(u_a - u_{ref}) \quad (27)$$

where  $u_a$  denotes the velocity profile at  $x_{1-1}$  and  $u_{ref}$  to a profile which allows solutions to be obtained at  $x_1$ . The iteration process at  $x_1$  proceeds with values of  $n$  ranging from 0 to unity.

The sequence of the calculations is as follows. The panel method provides an external velocity distribution based on a body shape in which the flap-well region is assumed to be absent. The interactive boundary-layer approach leads to solutions on the upper surface from the stagnation point through the regions of laminar, transitional and turbulent flow to the trailing edge. Similarly, it provides results for the lower surface up to the beginning of the flap-well. A displacement thickness distribution,  $\delta^*(x)$ , is assumed in the flap well and, with the continuation method described above and with the initial velocity profile similar to that of a backward-facing step, calculations proceed to the trailing edge. With the upper and lower surface velocity profiles at the trailing edge, the calculations are extended

into the wake. As a consequence of the above, a blowing velocity is available on the airfoil and in the wake. In the flap-well region, the blowing velocity  $v_n$  is defined by

$$v_n = \frac{d}{dx} (u_e \delta_m^*) \quad (28)$$

where  $\delta_m^* = \delta^* - \delta_t$ . Here  $\delta_t$  corresponds to the body shape assumed to exist over the flap-well. Elsewhere, the blowing velocity is given by

$$v_n = \frac{d}{dx} (u_e \delta^*) \quad (29)$$

With the blowing velocity distribution known everywhere in the flowfield, a new distribution of external velocity  $u_{e1}(x)$  is obtained from the panel method. As before, the boundary-layer solutions on the upper and lower surfaces of the airfoil are obtained with the Hilbert integral in which the edge boundary condition, Eq. (21), is now written as

$$u_e(x) = u_e^k(x_1) + c_{11} D_1 + \sum_{j=1}^{1-1} c_{1j} (D_j - D_j^k) + \sum_{j=1+1}^N c_{1j} (D_j - D_j^k) - c_{11} D_1^k \quad (30)$$

with  $k$  indicating the iteration cycle. Equation (23) also changes to

$$g_1 = u_e^k(x_1) + \sum_{j=1}^{1-1} c_{1j} (D_j - D_j^k) + \sum_{j=1+1}^N c_{1j} (D_j - D_j^k) - c_{11} D_1^k \quad (31)$$

In the flap-well, with  $u_{ev}$  known from the previous flap-well calculation, a new  $\delta^*$ -distribution is available from Eq. (6) and is used to obtain solutions up to the trailing edge. This sequence of calculations is repeated for the whole flowfield until convergence is achieved. The continuation method discussed before is involved within this sequence of calculations where necessary.

### 3.0 Results and Discussion

#### 3.1 Two-Element Airfoil

In a previous study, a similar interactive approach was used to compute the performance characteristics of three two-element airfoils.<sup>29</sup> The inviscid flow solutions were obtained by the conformal-mapping method of Halsey<sup>30</sup>, rather than the panel method used here, and the viscous-flow calculations were performed without accounting for the wake effects, either behind the main airfoil or the flap. The calculation method provided results which agreed well with experimental information within the accuracy of the measurements up to an angle of attack which was sufficiently small so that there was either no or very small separation on the airfoil and the gaps between the elements were comparatively large. In this way, the difficulties in computing the wake of each airfoil and accounting for the merging of the shear layers between the airfoil and the flap, and extending the range of the computational method to higher angles of attack were postponed to a later time.

In the studies reported here, we first performed calculations with the present method which did not include the wake effect and compared the results with those obtained with the earlier code<sup>29</sup> with its different inviscid flow method. After ensuring that the results of both codes were essentially the same, the wake effects were introduced into the present method and calculations were repeated for the three two-element airfoils to investigate the role of the wake effect on the solutions.

The first results of this paper are for two-element airfoils for which corresponding experimental investigations have been reported by Van den Berg<sup>6</sup>, by Omar et al.<sup>9,10</sup> and Olson and Orloff.<sup>11</sup> There are no flap wells in these arrangements and the novel features of the calculations are the flow between elements and the inclusion of the wakes.

Figures 1-3 present the results of the data of Van den Berg<sup>6</sup>, also discussed by Van den Berg and Oskam<sup>7</sup> and Oskam et al.<sup>8</sup>, which correspond to a supercritical main airfoil (NLR 730) with a flap of 32% of the main chord at a deflection angle of 20 degrees. Measurements of surface pressure and velocity profiles were obtained at a chord Reynolds number of  $2.51 \times 10^5$  and for angles of attack of 6 and 13.1 degrees, the latter recognized as the highest angle which corresponded to fully attached flow. Lift coefficients were deduced for

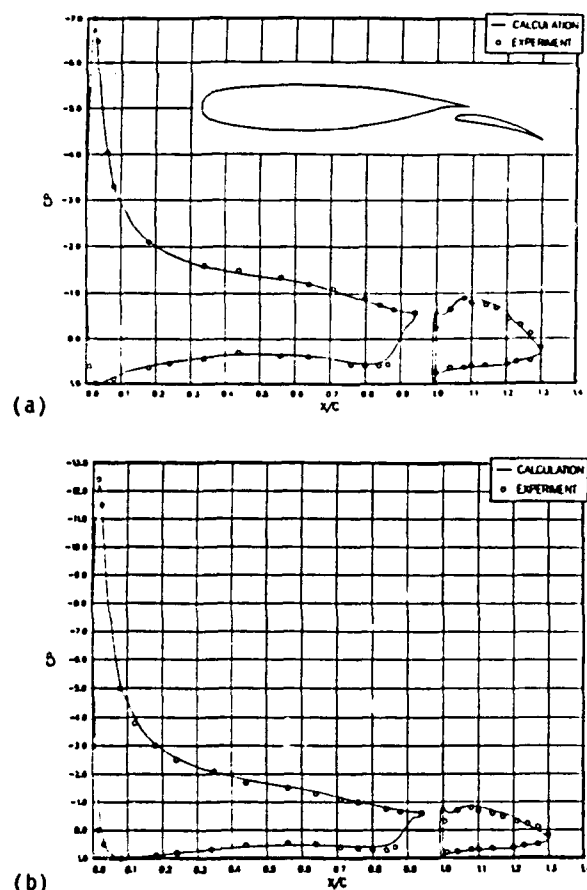


Fig. 1. NLR 730 wing with flap. Calculated and measured: pressure distribution at (a)  $\alpha = 6^\circ$ , (b)  $\alpha = 13.1^\circ$ .

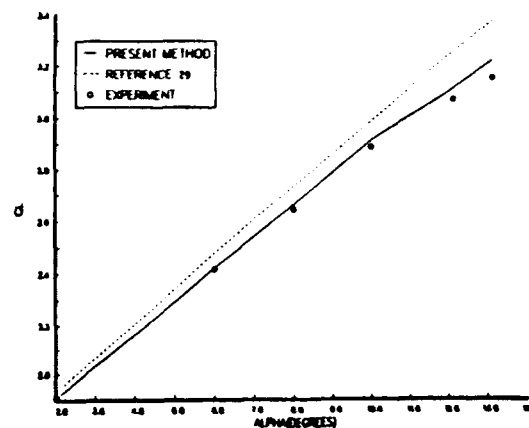


Fig. 2. NLR 730 wing with flap. Calculated and measured lift coefficients.

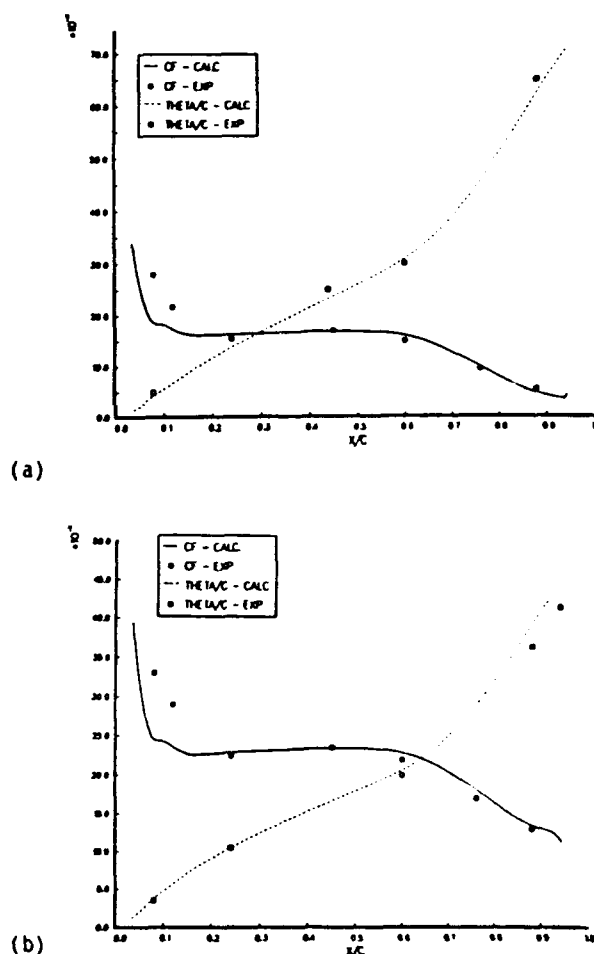


Fig. 3. NLR 730 wing with flap. Calculated and measured: local skin-friction coefficients,  $c_f$ , and momentum thicknesses,  $\theta/c$ , on the upper wing surfaces at (a)  $\alpha = 6^\circ$ , (b)  $\alpha = 13.1^\circ$ .

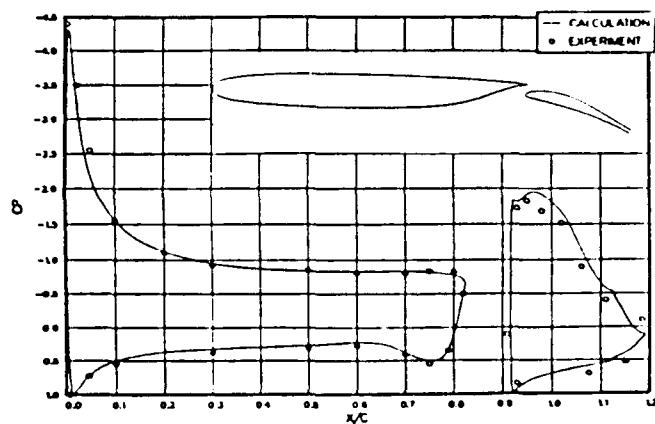
five angles of attack. The airfoil arrangement is shown on Fig. 1a and it is evident that the distributions of pressure coefficients are in close agreement with the measured values over the surfaces of both elements. The results at the angle of attack of 13.1 degrees confirm the absence of separation and the lift coefficients of Fig. 2 that stall occur at an angle larger than this



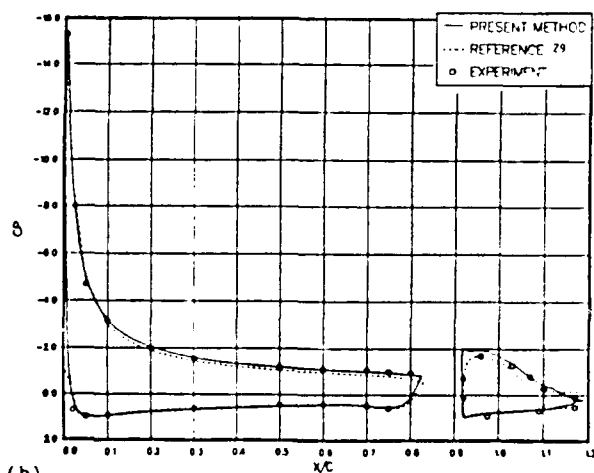
value. The calculated variation of lift coefficient with angle of attack is close to the measurement and some 3% lower than that calculated without consideration of the wake. It is to be expected that this difference will increase with angle of attack and particularly as separation occurs and expands over the upper trailing-edge region, and this trend is evident in the figure.

Figures 3a and 3b show the variations of momentum thickness and skin-friction coefficient with chord distance over the main airfoil. The agreement between calculated and measured results is remarkable for both angles of attack, the only significant discrepancies being in the skin-friction coefficient in the upstream region of maximum rate of change. Again, the results at 13.1 degrees confirm the absence of separation, although this result conveys little about the flow on the second element.

Figure 4 presents the results for a NASA supercritical airfoil, 24" in length, with a 7" flap at a deflection angle of 20 degrees. The experiments were carried out in the 36 x 96 in. wind tunnel of the Boeing Research Laboratories at a Mach number of 0.2 and have been documented by Omar et al.<sup>9,10</sup> The pressure-coefficient distributions of Figs. 4a and 4b correspond to angles of attack of zero and



(a)



(b)

Fig. 4. NASA supercritical two-element airfoil. Calculated and measured: (a) pressure distribution at  $\alpha = 0^\circ$ , (b) pressure distribution at  $\alpha = 8.93^\circ$ . The results of Ref. 29 are without wake effect.

8.93 degrees with the measured and calculated values again within experimental uncertainty. The wake had no effect at zero angle of attack, as expected, and had a slight effect on the pressure coefficients at the 8.93 degree angle, although the improvement on the main airfoil is coupled with an apparent lack of improvement on the flap. These results are reflected in the lift coefficients of Fig. 5 where the calculated results with the wake effect are in better agreement with data than those without the wake effect.

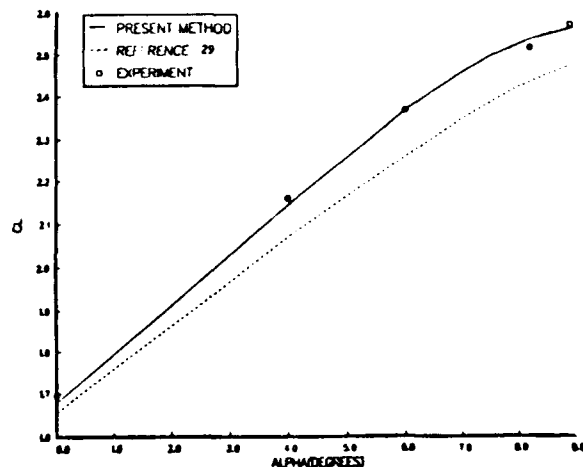


Fig. 5. NASA supercritical two-element airfoil. Calculated and measured lift coefficients. The results of Ref. 29 are without wake effect.

The third two-element airfoil corresponds to that investigated by Olson and Orloff<sup>11</sup> which involves a NACA 4412 airfoil with a chord length of 0.9m upstream of a flap which has the section of a NACA 4415 airfoil and a chord of 0.36m with a deflection angle of  $10^\circ$ . Figure 6 shows the measured and calculated surface pressure distributions for a Reynolds number of  $1.3 \times 10^6$  at an angle of attack of  $2.2^\circ$ . As in the first case, there is a slight improvement over the results obtained without the wake which, again, may be due to the absence of flow separation.

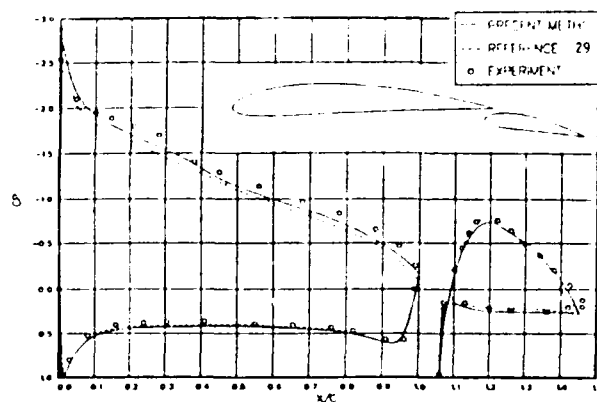


Fig. 6. NACA 4412/4415 airfoil. Calculated and measured pressure distributions for  $\alpha = 2.2^\circ$ .

It is evident from the comparisons of Figs. 1-6 that the flow between the airfoil elements and the wake have been satisfactorily incorporated in the interactive procedure with results which are virtually identical to the measurements. It should, however, be noted that the effect of merging of the

boundary layers in these three configurations is negligible.

### 3.2 Single Airfoil with a Flap-Well

An appraisal of the interactive boundary-layer procedure, as applied to the flow in and around a flap well, required corresponding measurements and a parallel experimental program which was carried out at the California State University, Long Beach, with the single airfoil arrangement of Fig. 7. The experiment described in Ref. 4 used this 12-inch chord airfoil, which corresponds to the main element of the three-element configuration tested in the low-turbulence tunnel of the NASA Langley Research Center, and described by Nakayama.<sup>3</sup> The chord Reynolds number was  $0.5 \times 10^6$ , and surface pressures were measured for angles of attack up to 14 degrees with local velocity information in the flap well at an angle of attack of 5 degrees. Figure 8 presents the measured and calculated surface-pressure distributions for angles of attack of 5, 8 and 12 degrees with transition tripped at  $0.25c$ , and the agreement is generally good. The calculated upper-surface pressure peak close to the leading edge reflects the better spatial resolution of the interactive method, and close to the trailing edge there are some small disagreements which may stem from the flap-well results. Nevertheless, the pressure-coefficient distributions represent closely the measurements in the flap-well with the near constant values indicating the region of recirculation followed, as can be seen, by a rapid increase in pressure coefficient after reattachment.

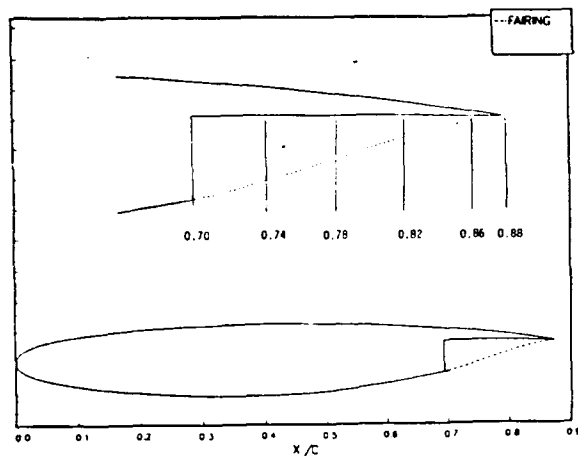


Fig. 7. Single airfoil with flap-well cut.

Figure 9 shows calculated profiles of stream-wise velocity, streamlines and the distribution of skin-friction coefficients within the flap well. The profiles differ increasingly from the measurements in the near-wall region, although reattachment occurs at about the same location. The reasons for the discrepancy are likely to be associated with the turbulence model that is used here to represent a near-wall flow, which undoubtedly involves low-Reynolds-number characteristics together with a switch from a wall jet in the negative to a boundary layer in the positive direction. It is unlikely that these local differences will affect greatly the outer region, particularly since the negative velocities and momentum are small, so that the calculated distribution of displacement thickness of Fig. 9b is likely to be correct. The

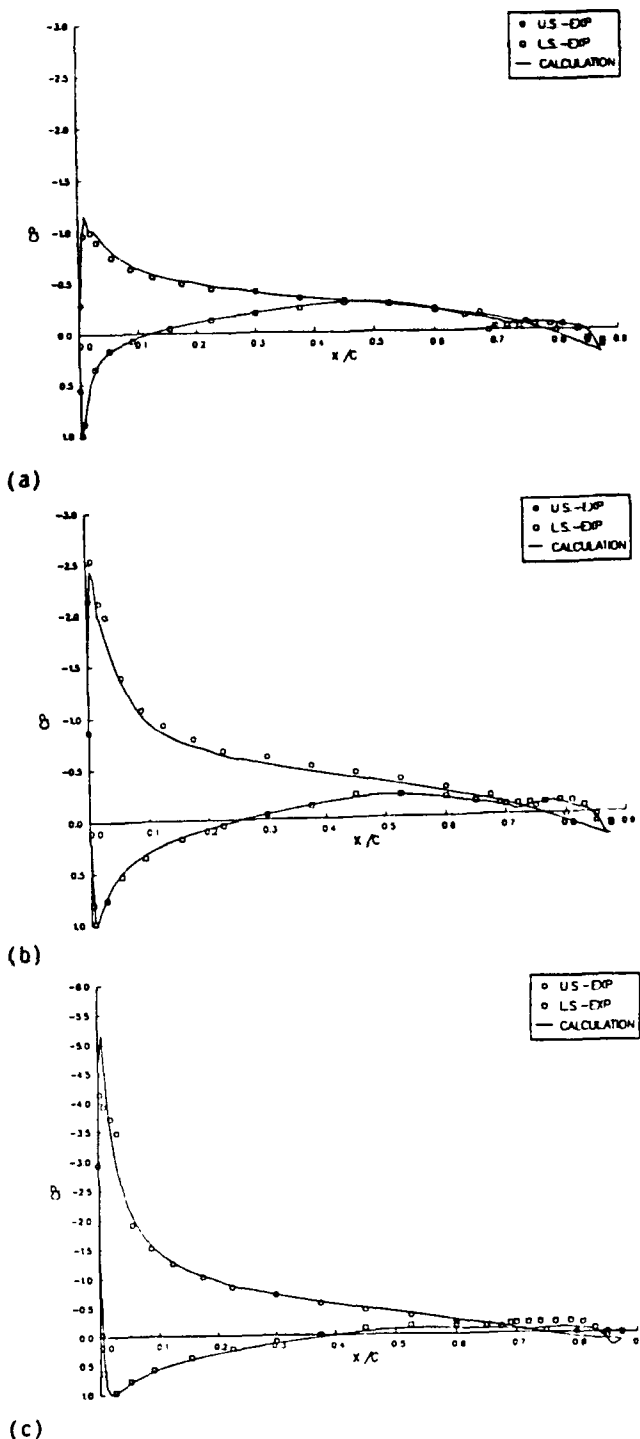
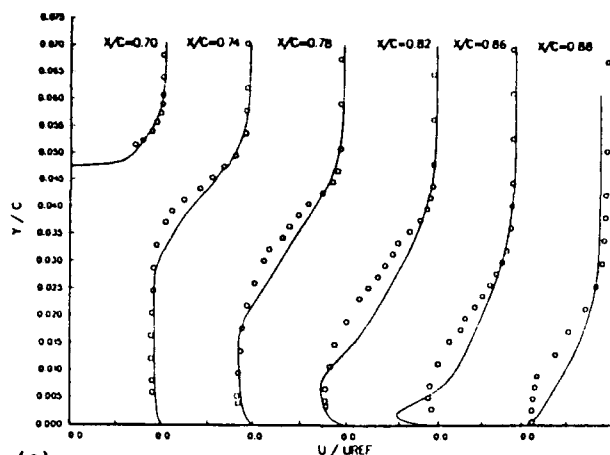


Fig. 8. Comparison of calculated pressure distributions with data for  $R_c = 0.5 \times 10^6$  at (a)  $\alpha = 5.0$ , (b)  $\alpha = 8.0$ , (c)  $\alpha = 12.0$ .

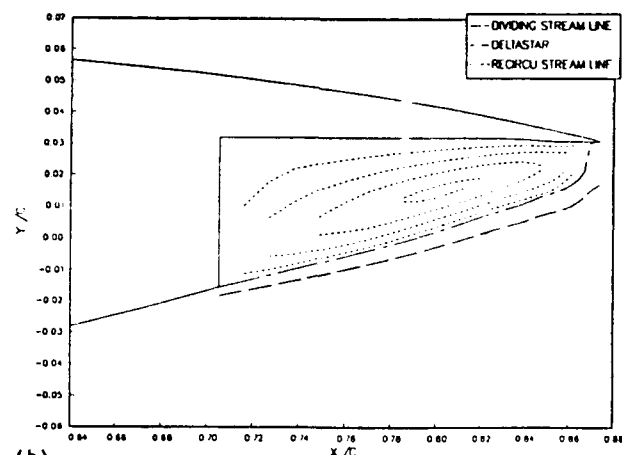
distribution of skin-friction coefficient, Fig. 9c, indicates negative values up to reattachment at  $0.87c$  which is in agreement with the velocity profiles.

### 3.3 Three-Element Airfoils

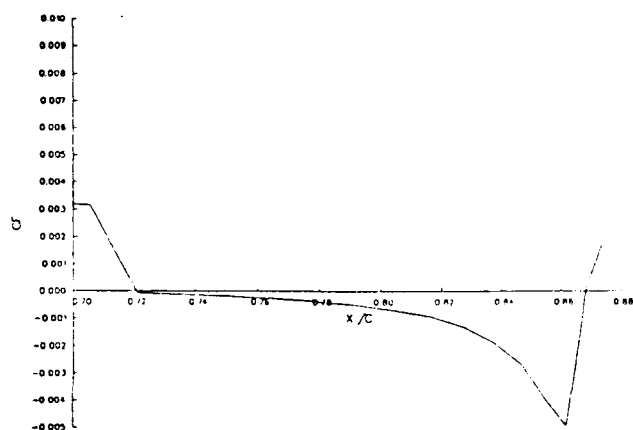
With the positive results of Figs. 1 to 9 for three two-element airfoils and for an airfoil with a flap-well, it is appropriate to consider the application of the interactive boundary-layer method to a three-element airfoil with a flap well.



(a)



(b)



(c)

Fig. 9. Results for  $R_c = 0.5 \times 10^6$  at  $\alpha = 5.0$ . (a) Velocity profiles in the flap-well region. (b) Recirculation streamline and the location of the displacement thickness. (c) Calculated local skin-friction coefficient in the flap-well region.

The chosen configuration is shown on Fig. 10 and corresponds to the high-lift model, tested in the NASA, Langley and California State wind tunnels at Reynolds numbers of  $5 \times 10^6$  and  $0.5 \times 10^6$ , respectively.<sup>3,4</sup> The slat deflection angle was  $-30$  degrees and the flap deflection angles  $15$  and  $30$  degrees with angles of attack of  $4$  to  $20$  degrees. The measurements were made by a combination of hot-wire and laser-velocimetry techniques, the latter was primarily used in regions of separated flow.



Fig. 10. The three-element airfoil with analytical and experimental fairing,  $\delta_s = -30^\circ$ ,  $\delta_f = 15^\circ$ .

Calculations were initially made on smooth bodies without explicitly considering the flow in the flap-well region. Also, because the potential flow theory predicts flow singularities at the discontinuity of the airfoil geometry, the sharp corner of the slat and the flap-well cut out of the main airfoil were smoothed to prevent solutions from breaking. Figure 10 shows the modified geometry of this airfoil with the flap-well fairing and the rounded slat used in calculations. The so-called "experimental fairing" refers to the dividing streamline which was determined from measurements, while the "analytical fairing" was drawn arbitrarily. Figure 11 shows the velocity vectors for a particular combination of gap and overhang and the position of the streamline dividing the recirculating flow behind the flap-well step from the outside flow, as determined from the mean-velocity vector data. The position of this dividing streamline is important since it corresponds roughly to the equivalent smooth body with pressure distribution close to the real one. Hence, this dividing streamline was used as the "experimental fairing" in the calculations. Figure 12 shows the surface-pressure distributions on the slat, main airfoil, and flap at three angles of attack ( $4^\circ$ ,  $12^\circ$  and  $16^\circ$ ) for the configuration with the experimental fairing, and Fig. 13 shows the corresponding distributions at the same angles of attack for the configuration with analytical fairing. Overall, the calculated results agree well with experimental data except for the slat at low angles of attack and the pressure peak on the main airfoil. This discrepancy may be caused by the differences between the assumed slat shape and the real one. In the flap-well region, the results are in better agreement with measurements when the fairing is close to a real streamline.

Finally, the method of Section 4.2 was applied to include the calculation inside the flap-well. The results, shown in Fig. 14, agree well with measurements for all the cases indicated above and including angles of attack up to  $20^\circ$ . This confirms that it is unnecessary to make a priori

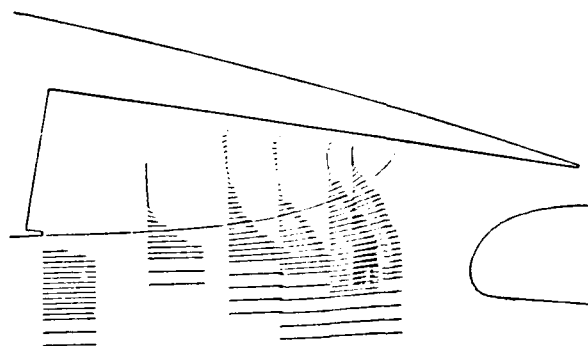
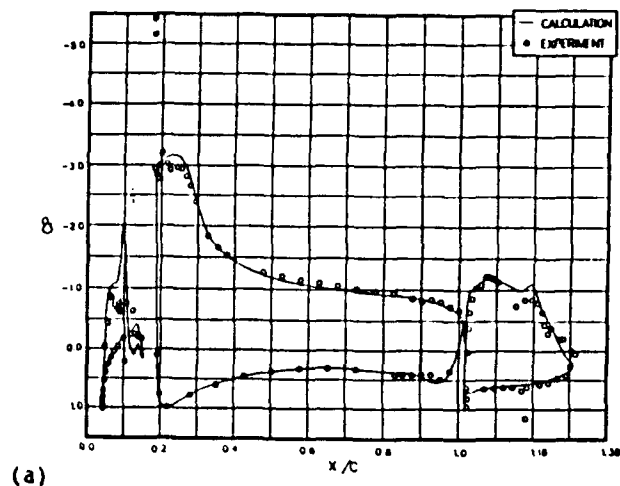
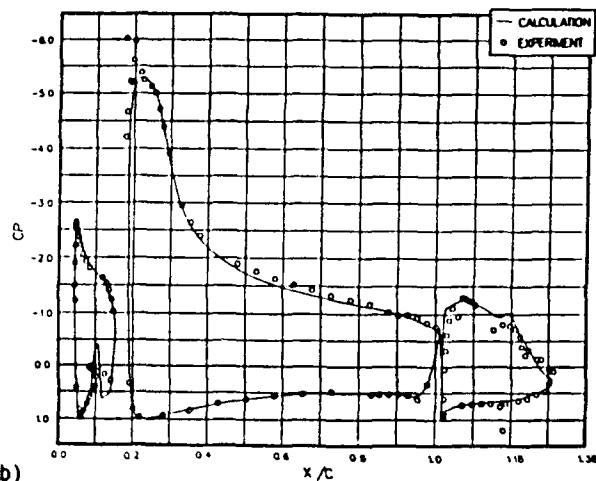


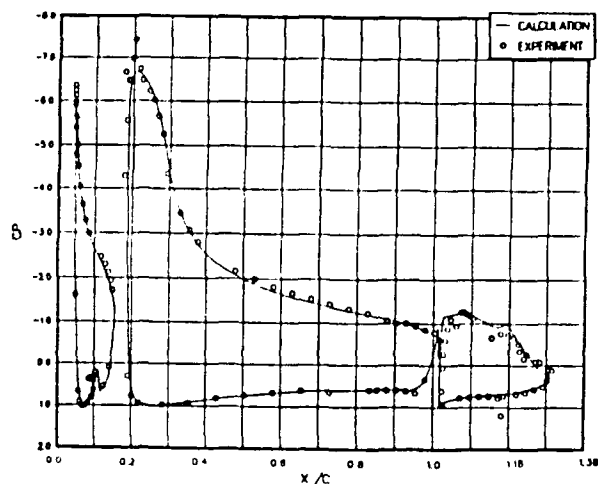
Fig. 11. Velocity vectors in the flap-well region by laser velocimeter.



(a)



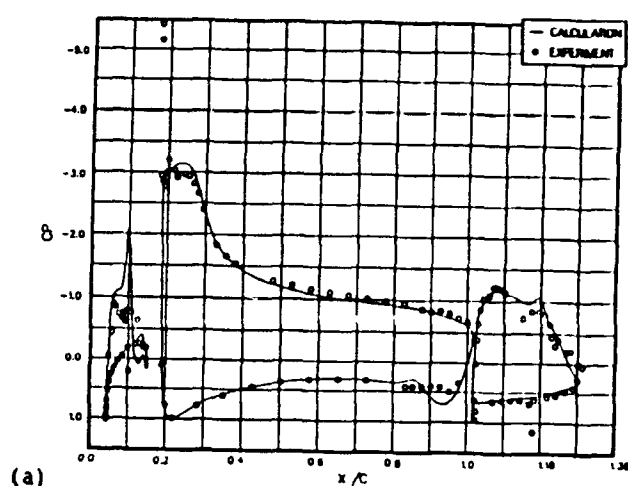
(b)



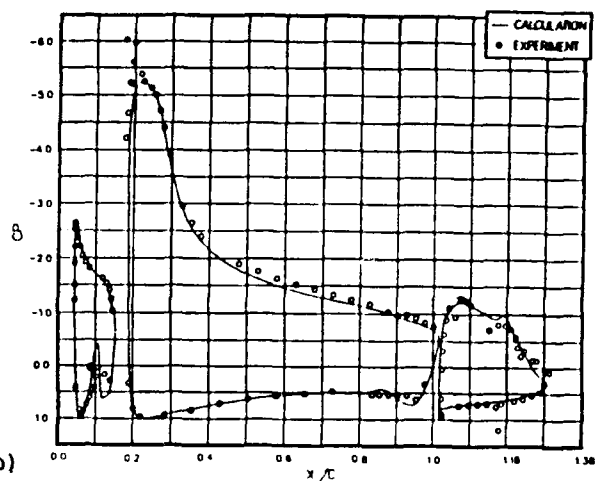
(c)

Fig. 12. Pressure distribution on the three-element airfoil with experimental fairing for  $\delta_f = 15^\circ$  and  $R_c = 5 \times 10^6$ , (a)  $\alpha = 4^\circ$ , (b)  $\alpha = 12^\circ$ , (c)  $\alpha = 16^\circ$ .

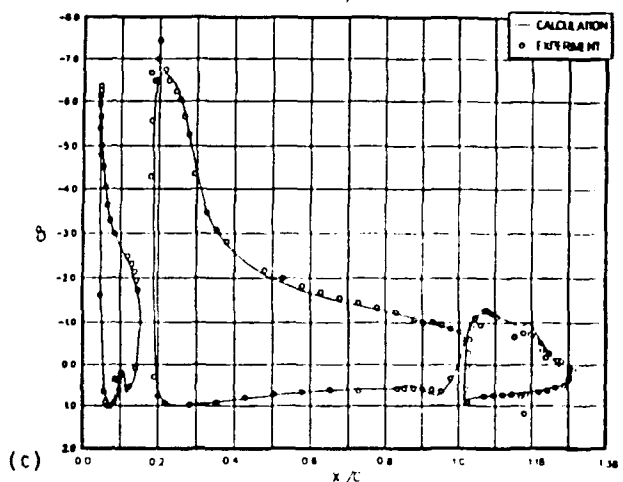
assumptions about the fairing shape, and allows for further detailed investigations of the recirculation flow in the flap-well, such as the gap and overhang effects. Figure 15 shows the variation of lift coefficient with angle of attack, confirming that the present calculation method leads to values which are in close agreement with experiment.



(a)



(b)



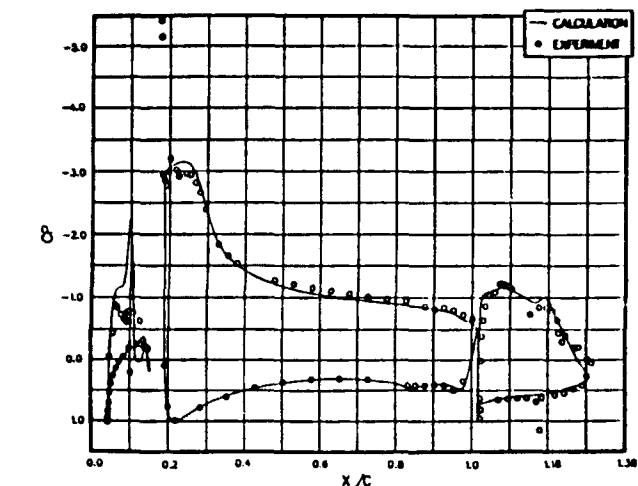
(c)

Fig. 13. Pressure distribution on the three-element airfoil with analytical fairing for  $\delta_f = 15^\circ$  and  $R_c = 5 \times 10^6$ , (a)  $\alpha = 4^\circ$ , (b)  $\alpha = 12^\circ$ , (c)  $\alpha = 16^\circ$ .

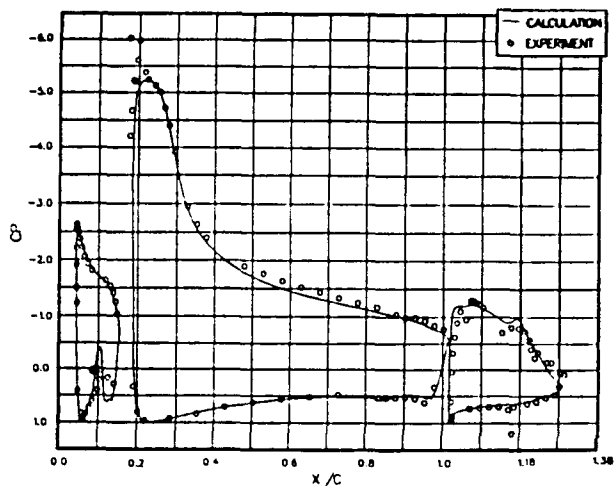
Comparison of pressure coefficients for a flap deflection angle of  $30^\circ$ , Fig. 16, allows similar conclusions to be drawn to those of the previous paragraph. Also, the calculated lift coefficients shown in Fig. 17 are very close to measurements.

#### 4.0 Concluding Remarks

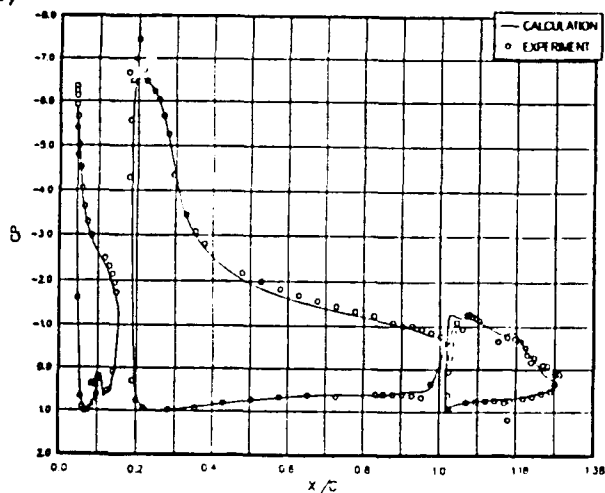
The results and discussion of the previous section show that the present interactive method, with its consideration of the flap-well region and



(a)

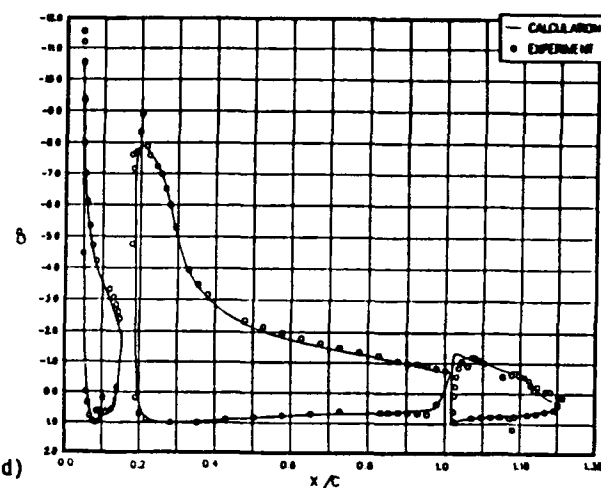


(b)



(c)

Fig. 14. Calculated and measured pressure distributions on the three-element airfoil for  $\delta_f = 15^\circ$  and  $R_c = 5 \times 10^6$  at (a)  $\alpha = 4^\circ$ , (b)  $\alpha = 12^\circ$ , (c)  $\alpha = 16^\circ$ , (d)  $\alpha = 20^\circ$ .



(d)

Fig. 14. Continued.

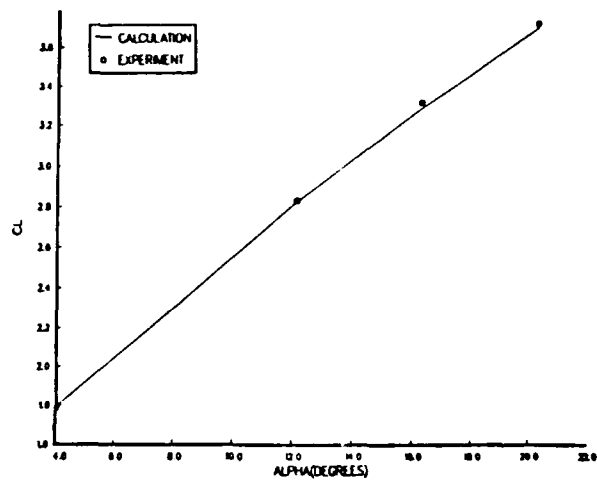
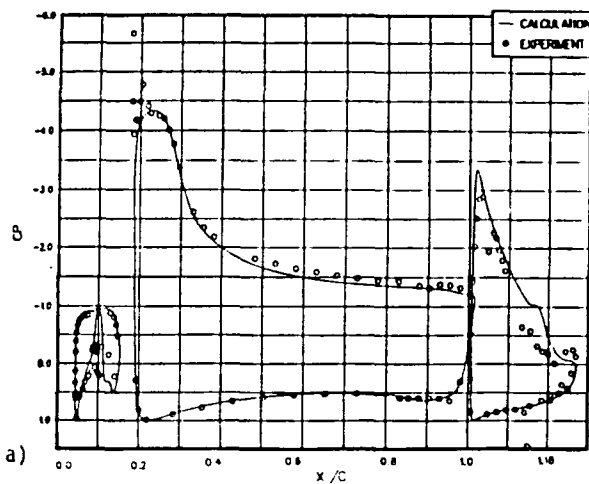


Fig. 15. Variation of the lift coefficient with angle of attack for the three-element airfoil with  $\delta_f = 15^\circ$  and  $R_c = 5 \times 10^6$ .



(a)

Fig. 16. Calculated and measured pressure distributions on the three-element airfoil with  $\delta_f = 30^\circ$  and  $R_c = 5 \times 10^6$ , (a)  $\alpha = 5^\circ$ , (b)  $\alpha = 15^\circ$ , (c)  $\alpha = 18^\circ$ , (d)  $\alpha = 20^\circ$ .

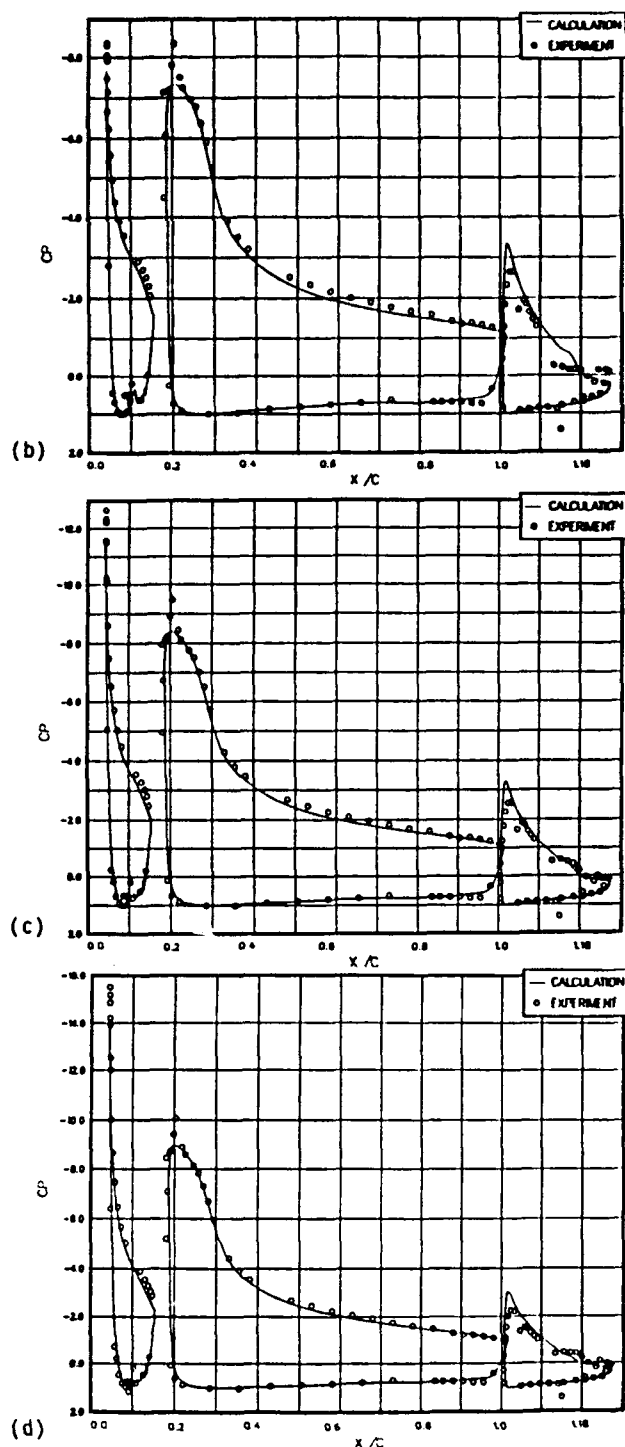


Fig. 16. Continued.

the wakes, leads to pressure coefficient distributions and values of lift which are in good agreement with experiment for single and multielement configurations with angles of attack up to  $20^\circ$ .

The present method neglects the confluent boundary layers, which become important as the distance between the main airfoil and the flap becomes smaller or where the shear layer thickens with angle of attack. Also, close examination of the turbulence model in the vicinity of this merging region is desirable. The incorporation of improvements to consider these aspects is likely to lead to a more generally applicable method.

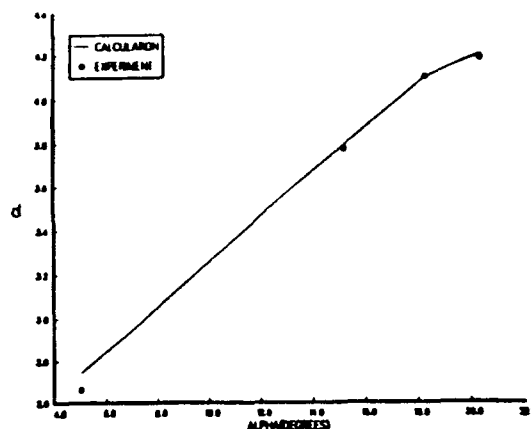


Fig. 17. Variation of the lift coefficient with angle of attack for the three-element airfoil with  $\delta_f = 30^\circ$  and  $R_c = 5 \times 10^6$ .

### 5.0 References

1. Smith, A.M.O., "High-Lift Aerodynamics," AIAA Paper No. 74-939, Aug. 1974
2. Garner, P.L., Meredith, P.T. and Stoner, R.C., "Areas for Future CFD Development as Illustrated by Transport Aircraft Applications," AIAA Paper No. 91-1527, 1991.
3. Nakayama, A., "Flowfield Survey Around High-Lift Airfoil Model LB 546," McDonnell Douglas Co. Report MDC J4827, 1987.
4. Nakayama, A., "An Experimental Investigation of a Flow Around the Flap Well of a Multielement Airfoil," Douglas Aircraft Co. Report MDC K4310, 1990.
5. Valarezo, W.O., Dominik, C.J. and Wilcox, P.A., "High Reynolds Number Test Results for a Supercritical Multielement Airfoil," McDonnell Douglas Report No. MDC K5545, Dec. 1990.
6. Van den Berg, B., "Boundary-Layer Measurements on a Two-Dimensional Wing with Flap," NLR TR 79009U, 1979.
7. Van den Berg, B. and Oskam, B., "Boundary-Layer Measurements on a Two-Dimensional Wing with Flap and a Comparison with Calculations," Paper 18 of AGARD CP-271, 1979.
8. Oskam, B., Hahn, D.J. and Volkers, D.F., "Recent Advances in Computational Methods to Solve the High-Lift Multicomponent Airfoil Problem," NLR Report MP84042U, 1984.
9. Omar, E., Zierden, T. and Mahal, A., "Two-Dimensional Wind-Tunnel Tests of a NASA Supercritical Airfoil with Various High-Lift Systems. 1 - Data Analysis," NASA CR-2214, 1973.
10. Omar, E., Zierden, T., Hahn, M., Szpiro, E. and Mahal, A., "Two-Dimensional Wind-Tunnel Tests of a NASA Supercritical Airfoil with Various High-Lift Systems. 2 - Test Data," NASA CR-2215, 1977.
11. Olson, L. and Orloff, K.L., "On the Structure of Turbulent Wakes and Merging Shear Layers of Multielement Airfoils," AIAA paper 81-1238, June 1981.

12. Mavriplis, D.J., "Research on Unstructured Grid Techniques for CFD at ICASE," Paper presented at the CFD Conference, NASA Ames, 12-14 March 1991.
13. Rogers, E.S., Wiltberger, N.L. and Kwak, D., "Efficient Simulation of Incompressible Viscous Flow Over Single and Multielement Airfoils," AIAA Paper No. 92-0405.
14. Barth, J.J., "CFD Algorithms on Unstructured Meshes," Paper presented at the CFD Conference, NASA Ames, 12-14 March 1991.
15. Cebeci, T., Clark, R.W., Chang, K.C., Halsey, N.D. and Lee, K., "Airfoils with Separation and the Resulting Wakes," *Journal Fluid Mechanics*, Vol. 153, pp. 323-347, 1986.
16. Cebeci, T., Jau, J., Vitiello, D. and Chang, K.C., "Prediction of Post-Stall Flows on Airfoils," in Numerical and Physical Aspects of Aerodynamic Flows, IV, (ed. T. Cebeci) Springer-Verlag, Heidelberg, 1990.
17. Cebeci, T., "Essential Ingredients of a Method for Low Reynolds-Number Airfoils," *AIAA Journal*, Vol. 27, pp. 1680-1688, 1983.
18. Cebeci, T., Khattab, A.A., Chen, H.H. and Chen, L.T., "An Approach to the Design of Wings: The Role of Mathematics, Physics and Economics," AIAA Paper 92-0286, 1992.
19. Veldman, A.E.P., Lindhout, J.P.F., deBoer, E., Somers, M.A.M., "VISTRAFS: A Simulation Method for Strongly Interacting Viscous Transonic Flow," in Numerical and Physical Aspects of Aerodynamic Flows, IV, (ed. T. Cebeci) Springer-Verlag, Heidelberg, 1990.
20. LeBalleur, J.C., "Couplage Visqueux-Non Visqueux: Methods Numerique et Applications Aux Ecoulements Bidimensionnels Transsoniques et Supersoniques," *La Recherche Aerospatiale*, Mar-Apr 1978.
21. LeBalleur, J.C., "New Possibilities of Viscous-Inviscid Numerical Techniques for Solving Viscous Flow Equations with Massive Separation," in Numerical and Physical Aspects of Aerodynamic Flows, IV, (ed. T. Cebeci) Springer-Verlag, Heidelberg, 1990.
22. Williams, B.R. and Smith, P.D., "Coupling Procedures for Viscous-Inviscid Interaction for Attached and Separated Flows on Swept and Tapered Wings," in Numerical and Physical Aspects of Aerodynamic Flows, IV, (ed. T. Cebeci), pp. 53-70, Springer-Verlag, Heidelberg, 1990.
23. Orel, M. and Giles, M.B., "Viscous-Inviscid Analysis of Transonic and Low Reynolds Number Airfoils," *AIAA Journal*, Vol. 25, 1987.
24. Kusunose, K., Wigton, L. and Meredith, P., "A Rapidly Converging Viscous/Inviscid Coupling Code for Multielement Airfoil Configurations" AIAA Paper 91-0177, 1991.
25. Bradshaw, P. and Ferris, D.H., "Calculations of Boundary-Layer Development Using Turbulent Energy Equation: Compressible Flow on Adiabatic Walls," *Journal Fluid Mechanics*, Vol. 46, 1970.
26. Hess, J.L. and Smith, A.M.O., "Calculation of Potential Flow About Arbitrary Bodies," *Progress in Aerospace Sciences*, Vol. 8, Pergamon Press, New York, 1966.
27. Cebeci, T. and Smith, A.M.O., Analysis of Turbulent Boundary Layers, Academic Press, New York, 1974.
28. Cebeci, T. and Bradshaw, P., Physical and Computational Aspects of Convective Heat Transfer, Springer-Verlag, N.Y., 1988.
29. Cebeci, T., Chang, K.C., Clark, R.W. and Halsey, N.D., "Calculation of Flow Over Multielement Airfoils at High Lift," *Journal of Aircraft*, Vol. 14, pp. 546-551, 1987.
30. Halsey, N.D., "Potential Flow Analysis of Multielement Airfoils Using Conformal Mapping," *AIAA Journal*, Vol. 17, p. 1281, 1979.

0750c

**HIGH LIFT, 2**  
**SESSION 6**



# REYNOLDS AND MACH NUMBER EFFECTS ON MULTIELEMENT AIRFOILS

Walter O. Valarezo\*, Chet J. Dominik\*\*  
Aerodynamics Technology  
Douglas Aircraft Company

and

Robert J. McGhee\*  
Experimental Flow Physics Branch  
NASA Langley Research Center

## Abstract

Experimental studies have been conducted to assess Reynolds and Mach number effects on a supercritical multielement airfoil. The airfoil is representative of the stall-critical station of an advanced transport wing design. The experimental work was conducted as part of a cooperative program between the Douglas Aircraft Company and the NASA Langley Research Center to improve current knowledge of high-lift flows and to develop a validation database with practical geometries/conditions for emerging computational methods. This paper describes results obtained for both landing and takeoff multielement airfoils (four and three-element configurations) for a variety of Mach/Reynolds number combinations up to flight conditions. Effects on maximum lift are considered for the landing configurations and effects on both lift and drag are reported for the takeoff geometry. The present test results revealed considerable maximum lift effects on the three-element landing configuration for Reynolds number variations and significant Mach number effects on the four-element airfoil.

## Nomenclature

$C_d$	Drag Coefficient
$C_l$	Lift Coefficient
$C_{l_{max}}$	Maximum Lift Coefficient
$C_p$	Pressure Coefficient
L/D	Lift-to-Drag Ratio
M	Mach Number
RN	Chord Reynolds Number
$\alpha$	Angle of Attack
$\delta_f$	Flap Deflection
$\delta_s$	Slat Deflection

## Introduction

Commercial transport aircraft wings are configured with leading-edge slats and trailing-edge flaps to meet takeoff and landing operational requirements. High-Lift systems have traditionally been complex in order to attain the aerodynamic capability of generating high L/D in climb and high maximum lift on approach. However, increased financial pressures in the airline business demand high-lift wing designs that are simpler and easier to maintain while achieving improved aerodynamic performance over previous-generation designs. A major obstacle in the design process towards more efficient multielement airfoils has been the lack of published data on the effects of Reynolds and Mach number over a realistic range for representative multielement airfoils. This lack of data is also likely to have delayed the development of computational methods

---

\* Principal Technical Specialist  
Team Leader-Subsonics & High Lift  
\*\* Engineer/Scientist.  
\* Section Head, Low-Turbulence Pressure Tunnel

suitable for the analysis of practical multi-element airfoils at conditions of interest (maximum lift). Several purely computational methods have been recently reported in the literature<sup>1-10</sup> that can handle, to various degrees of success, the viscous flow over multielement airfoils. However, these methods have largely been applied to either geometries that are not really representative of transport high lift airfoils or to flow conditions that do not include maximum lift. It is expected that some of these methods (either Navier-Stokes or boundary-layer based) hold significant promise but may not be substantially improved by their developers in the absence of a quality database at realistic conditions for a practical airfoil. The work reported in this paper is the result of a cooperative experimental program conducted by the Douglas Aircraft Company and the NASA Langley Research Center to establish a database for Reynolds and Mach number (including flight condition) effects on the flow over transport multielement airfoils.

### Test Facility and Model Description

The Langley Low Turbulence Pressure Tunnel (LTPT) is a single return, closed-throat wind tunnel that can be operated up to 10 atmospheres thus allowing very high Reynolds number capability<sup>11</sup> (Fig. 1). The test section is 3 feet wide by 7.5 feet high by 7.5 feet long. To promote two-dimensional flow over the model in view of its low aspect ratio and strong wall-model aerodynamic interference, a new side-wall boundary layer control (BLC) system was installed at the LTPT for the present test<sup>12</sup>. The BLC system employed the differential pressure between the test section and the atmosphere to provide suction of the boundary layer through porous endplates. The system yielded good quality two-dimensional flow over the model for the Reynolds numbers tested<sup>12</sup>. The model spanned the width of the test section and had a clean (stowed) airfoil chord of 22 inches. The clean airfoil and the takeoff and landing multielement configura-

tions tested are shown in Fig. 2. The slat chord

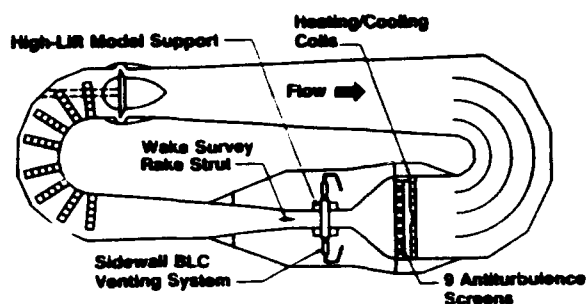


Figure 1. Schematic of Low Turbulence Pressure Tunnel

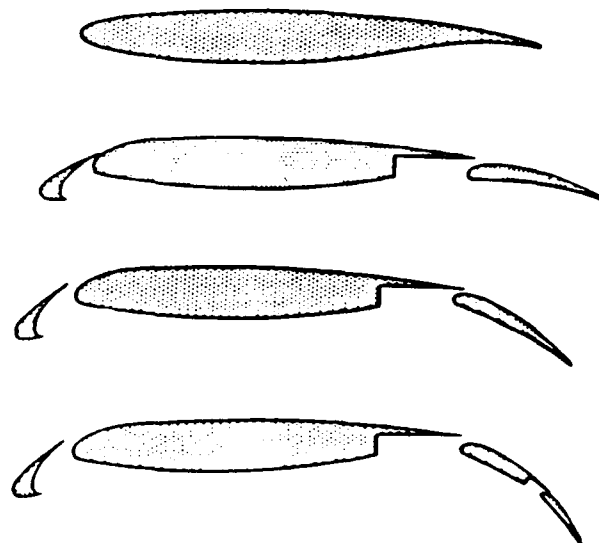


Figure 2. Airfoil Configurations Tested in the LTPT

ratio was 14.48%, the single-segment flap chord ratio was 30%, and the two-segment flap had a chord ratio of 21% for the main segment and 13% for the auxiliary flap. Pressure orifices were located along the centerline of the model (142 taps for the four-element configuration). Additionally, pressure taps were located along (or near) the trailing edge of each airfoil element to monitor two-dimensionality of the flow at run time. Integration of the pressure measurements yielded the forces presented here. The data is corrected for the effects of the sidewall suction system on the tunnel parameters and no blockage corrections were applied. Four rows of streamlined support brackets for the high-lift devices (Fig. 3)

were required due to the very high loads (up to 15,000 pounds) associated with the high freestream dynamic pressure and lift coefficients attained. Drag data were computed by integration of the static and total pressures obtained from the LTPT wake survey rake system.

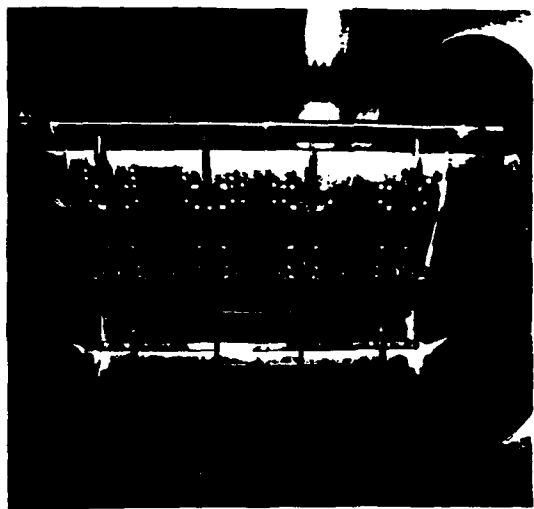


Figure 3. LTPT High-Lift Model Support Brackets

### Results

A significant fraction of the wind tunnel testing associated with multielement airfoils is aimed at optimizing the rigging of a particular airfoil with fixed slat and flap chord ratios. Parameters defining rigging nomenclature for multielement airfoils are shown in Fig 4. The optimization work is traditionally performed at a given Mach/Reynolds number that should be representative of nominal flight conditions. However, it is also very important to determine the effects on the performance of the optimized airfoil for departures in Reynolds or Mach number from the nominal conditions. It was possible to perform these measurements (Reynolds and Mach number sweeps) at the Langley Low Turbulence Pressure Tunnel because of its considerable operational capability (Fig. 5).

The application of so-called transition strips in wind tunnel testing is an attempt to simulate

the extent of turbulent flow that would naturally occur at flight Reynolds numbers on an airfoil (or wing) but not at the low

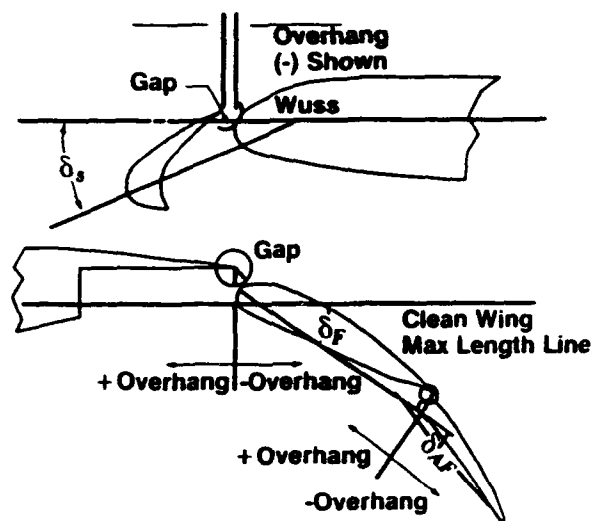


Figure 4. Nomenclature for Multielements

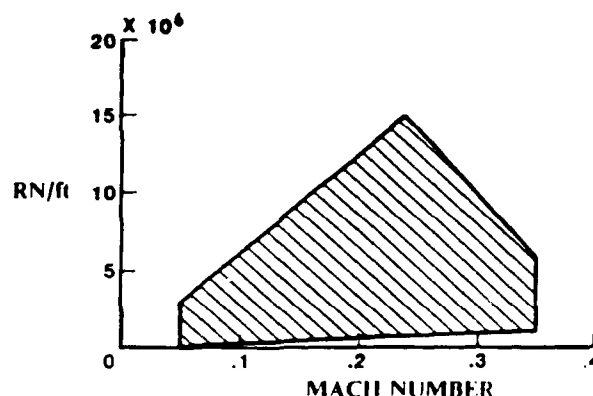


Figure 5. Operational Capability of the LTPT

wind tunnel Reynolds numbers typically attainable. Hence, in a facility such as the LTPT where flight Reynolds can actually be achieved it is not necessary to attempt to simulate transition on the airfoil. Additionally, the low turbulence level achieved in the test section increases the applicability of results obtained at a given Reynolds number since this is more representative of flight conditions. The accurate modeling of transition over a wide range of angles-of-attack, Reynolds/Mach number combinations, and multiple airfoil elements is not practical. All results shown here were obtained transition-free.

The effects of Reynolds number on the clean airfoil maximum lift capability at various Mach numbers is shown in Fig. 6. It can be seen that there is a considerable increase in maximum lift between Reynolds numbers of  $2.5 \times 10^6$  and  $9 \times 10^6$ . Corresponding surface pressures on the clean airfoil at maximum lift are shown in Figs 7-10. The effects of Mach number on maximum lift are shown in Fig. 11 for Reynolds numbers from 5 to  $18 \times 10^6$ . It can be seen that the effect of Mach number is substantially more pronounced at the lower Reynolds numbers. Lifts curves at  $5 \times 10^6$  and  $9 \times 10^6$  are shown in Figs. 12 and 13 where Mach number can be seen to affect the stall angle as well.

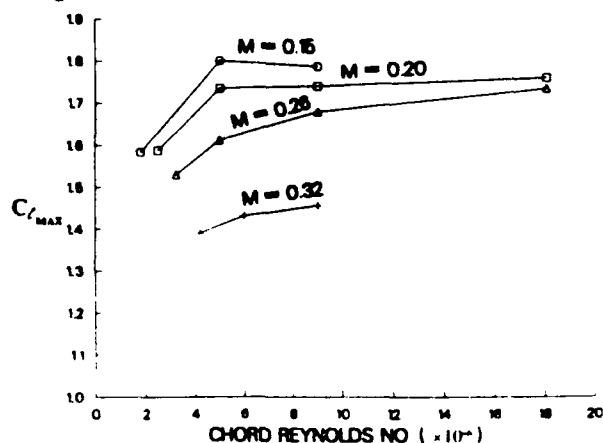


Figure 6. Reynolds Number Effect on Maximum Lift.

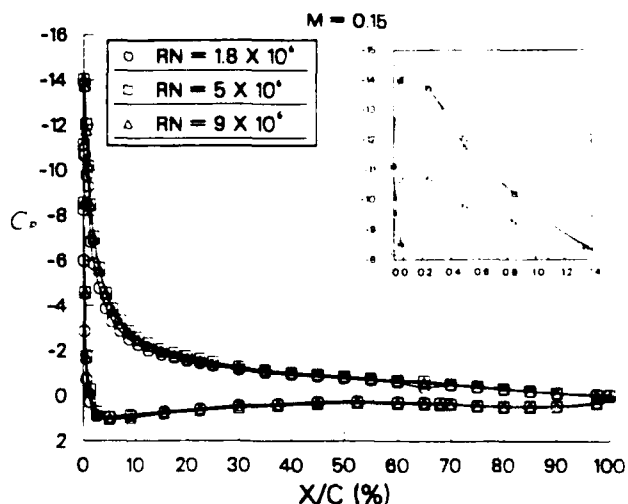


Figure 7. Reynolds Number Effect at Maximum Lift.

These results shown for the basic clean airfoil (Figs. 6-13) served to establish a baseline for both Reynolds and Mach number effects for the subsequent multielement airfoil measurements and they may also represent a logical starting point for the validation of any viscous flow method since surface grid complications are at a practical minimum and flow features through the maximum lift condition are still complex enough to be of interest.

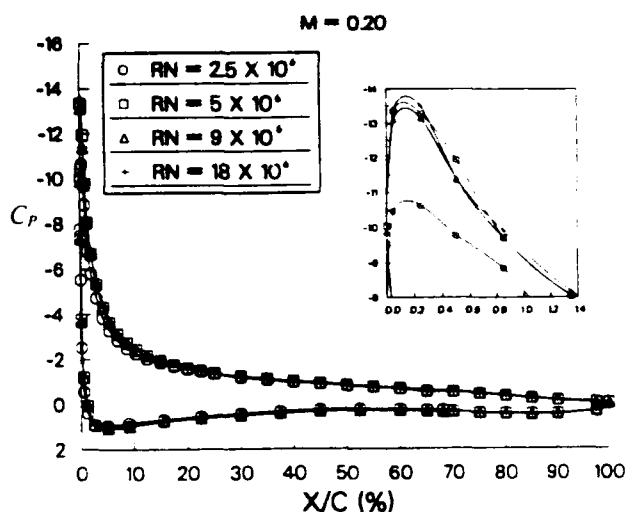


Figure 8. Reynolds Number Effect at Maximum Lift.

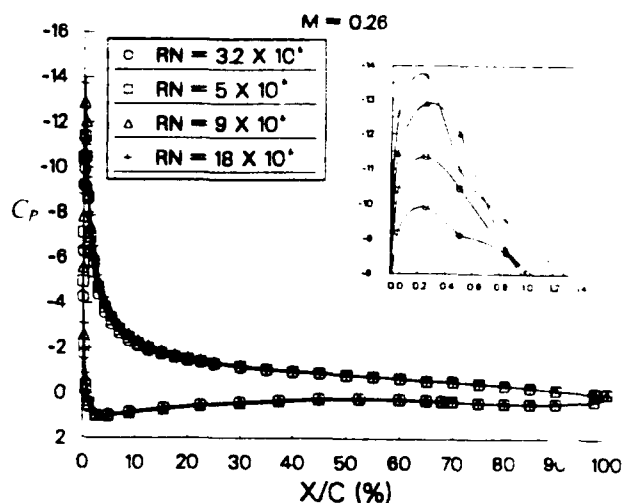


Figure 9. Reynolds Number Effect at Maximum Lift.

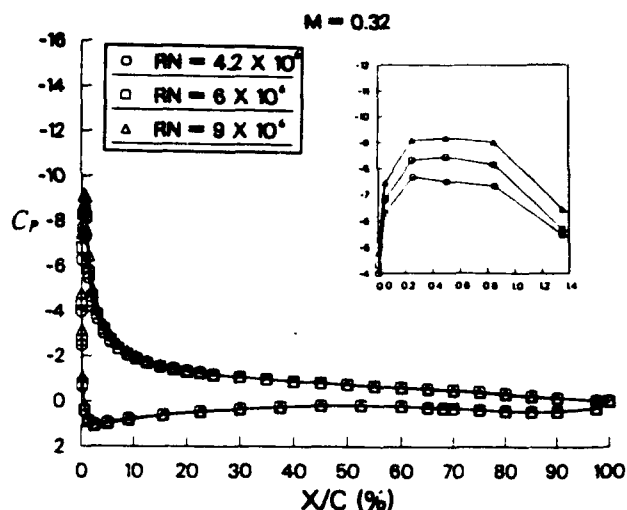


Figure 10. Reynolds Number Effect at Maximum Lift.

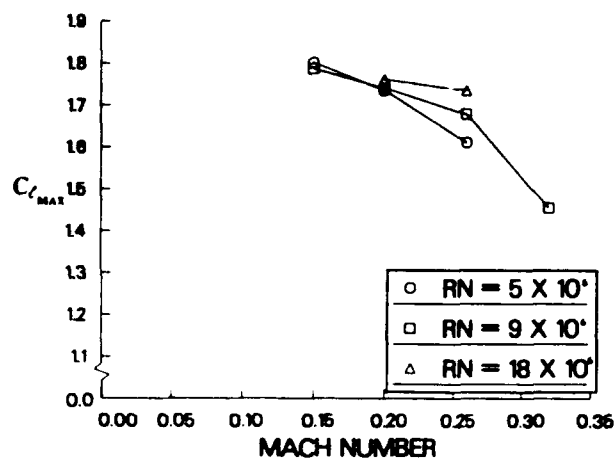


Figure 11. Mach Number Effect on Maximum Lift.

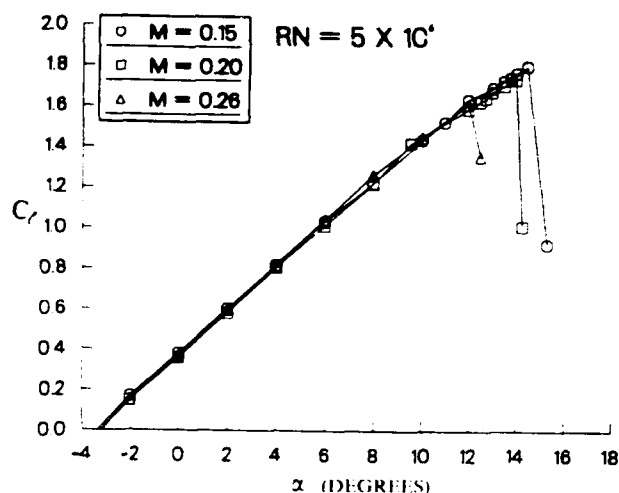


Figure 12. Mach Number Effect on Lift.

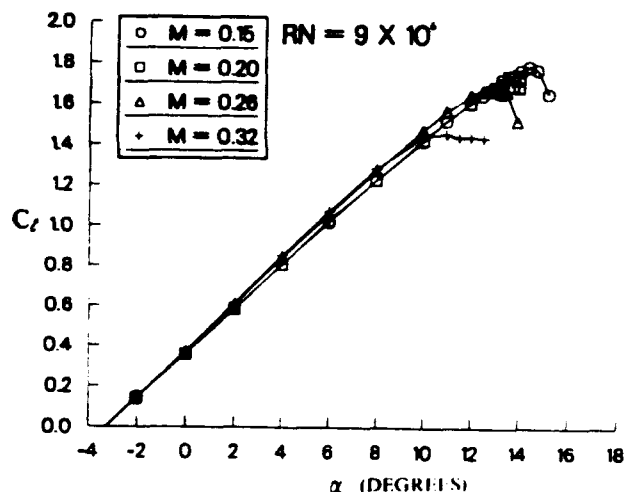


Figure 13. Mach Number Effect on Lift.

### Takeoff Configuration

A three-element airfoil configured for takeoff was tested at various combinations of Reynolds and Mach number as shown below:

		Freestream Mach Number				
		0.15	0.20	0.26	0.30	0.32
RN x 10 <sup>-6</sup>	5	x	x	x	x	
	9	x	x	x	x	x
	16	x	x			
	20		x			

The slat deflection was 20° (gap = 0.55%, overhang = + 1.0%), and the flap was rigged at a gap of 1.82%, overhang of 1.5%, and 10° of deflection. For a takeoff configuration the slat is normally sealed (gap = 0%) to minimize profile drag, however, an open slat was chosen for this study since it should be less difficult to grid from a computational analysis perspective. Additionally, this particular open slat configuration yielded takeoff performance close to that of a sealed slat at a representative lift coefficient.

Lift curves and drag polars for Reynolds numbers from  $5$  to  $16 \times 10^6$  at Mach 0.15 are shown in Fig. 14. There is a loss in maximum lift and improved drag performance with increasing Reynolds number. It is also interesting to note that while the main element enters the stall first, it is soon followed by the slat and not the flap. In fact, the flap lift coefficient increases after the stall. This effect appears to be due to the drastically reduced downwash from both the slat and the main element and the fact that the geometric deflection of the flap ( $10^\circ$ ) is not enough by itself to cause the flow on the flap to separate. Reynolds number effects on lift and drag obtained at Mach 0.20 are shown in Fig. 15. Here, it is evident that the Reynolds number effect is largely on drag and not on lift. Differences in measured drag are approximately 10% between  $5 \times 10^6$  and  $20 \times 10^6$  Reynolds number. Again, the flap loads up after the main element and the slat enter the stall. In fact, it is now clear that the flap loads up after the slat stalls. Results at Mach 0.26 and 0.30 are shown in Figs. 16 and 17, respectively. At these two Mach numbers the Reynolds number effect is to increase maximum lift (opposite trend from Mach 0.15) but, in general, the Reynolds number effect on either lift or drag is minimal. It is worth noting that at these conditions even though the main element exhibits a pronounced stall, the slat does not, and the flap displays only a slight tendency to load up beyond the stall. That the slat does not really stall, as it did at lower Mach numbers, is a result of the slat being exposed to a lower geometric angle-of-attack (lower airfoil stall angles at higher Mach numbers). Mach number effects on the takeoff configuration at Reynolds numbers of  $5 \times 10^6$ ,  $9 \times 10^6$ , and  $16 \times 10^6$  are shown in Figs. 18, 19, and 20, respectively. Overall, the measured effect of Mach number on  $C_d$  at a given Reynolds number can be seen to be in the scatter band of the data (within 10 counts). However, the Mach effect on lift is substantial.

## Landing Configurations

Two landing configurations were selected for Reynolds and Mach number effects studies. The leading-edge slat was optimized for both configurations and was positioned at a gap of 2.95% with an overhang of -2.5% and  $30^\circ$  of deflection.

The single-segment flap airfoil was configured with the flap optimized at a Reynolds number of  $9 \times 10^6$  at  $30^\circ$  of deflection with a gap of 1.32% and an overhang of +1.0%. A Reynolds number sweep was conducted at Mach 0.20 and effects on maximum lift are shown in Fig. 21. There is a considerable loss in  $C_{l_{max}}$  ( $\sim 0.1$ ) at Reynolds numbers other than  $9 \times 10^6$ . Total and component loadings are shown in Fig. 22 where it can be seen again that the airfoil stall is caused by the main element. Unlike the takeoff cases reviewed above, the slat continues to load up beyond the airfoil stall. This is possibly due to the slat position being aerodynamically underdeflected ( $-10^\circ$ ) with respect to the takeoff slat discussed. Surface pressure measurements obtained at the three Reynolds numbers at maximum lift are shown in Fig. 23. Although the data are closely matched, being able to discern a difference of 0.10 in  $C_{l_{max}}$  performance is of considerable importance in transport high-lift aerodynamics.

The second landing arrangement tested was a four-element airfoil with a two-segment flap. The optimum slat position was the same as for the three-element landing airfoil. The main flap was optimized at  $35^\circ$  with a gap of 2.9% and an overhang of -1%. The auxiliary flap was deflected an additional  $15^\circ$  and had a non-optimized gap of 0.68% and an overhang of 0.75%. Reynolds number effects at 0.20 Mach number are shown in Fig. 24. It is evident that the effects of Reynolds number on maximum lift are minimal for the Reynolds number range tested. This can be contrasted with the substantial Reynolds number effects shown for the

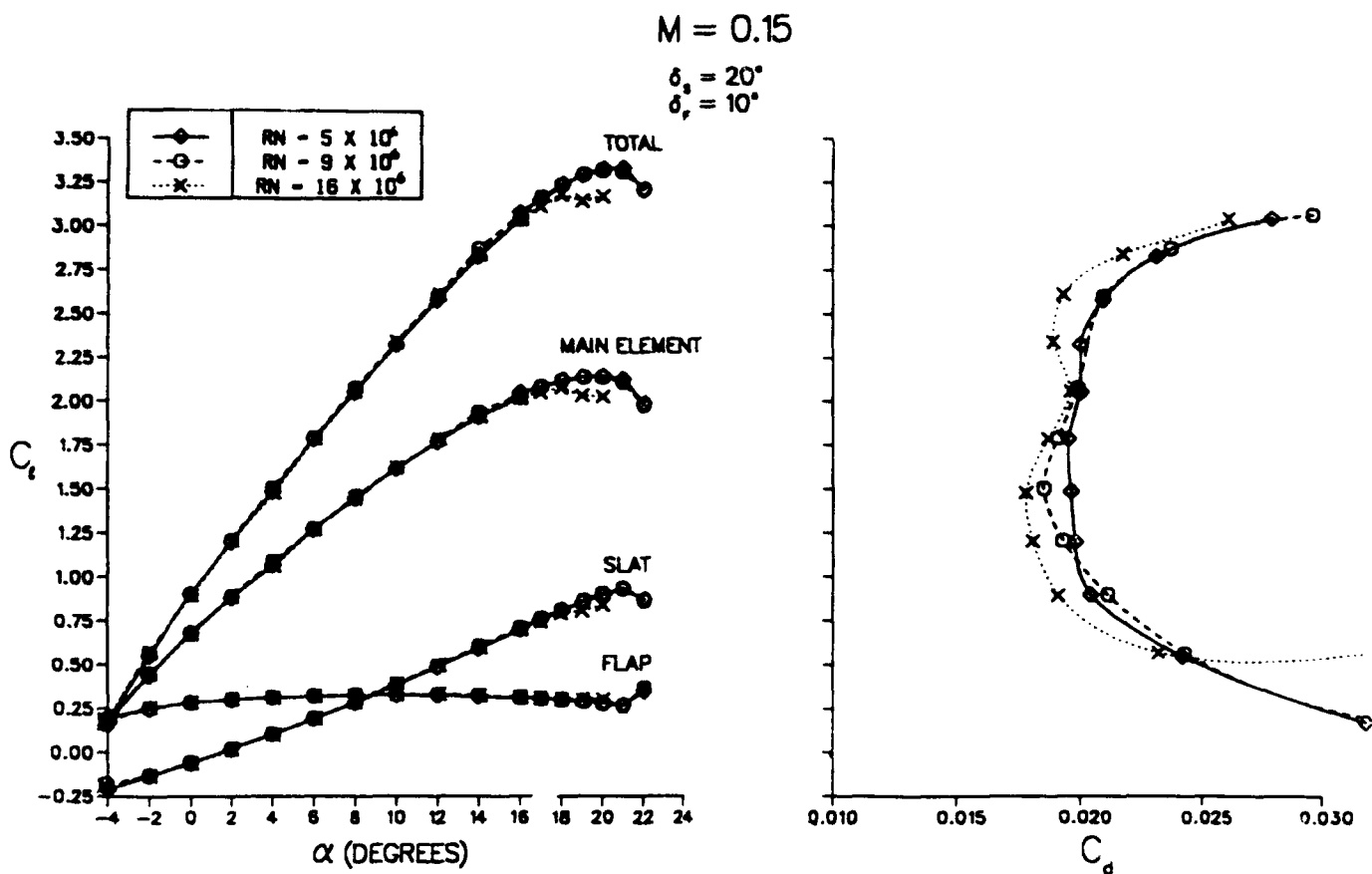


Figure 14. Reynolds Number Effect

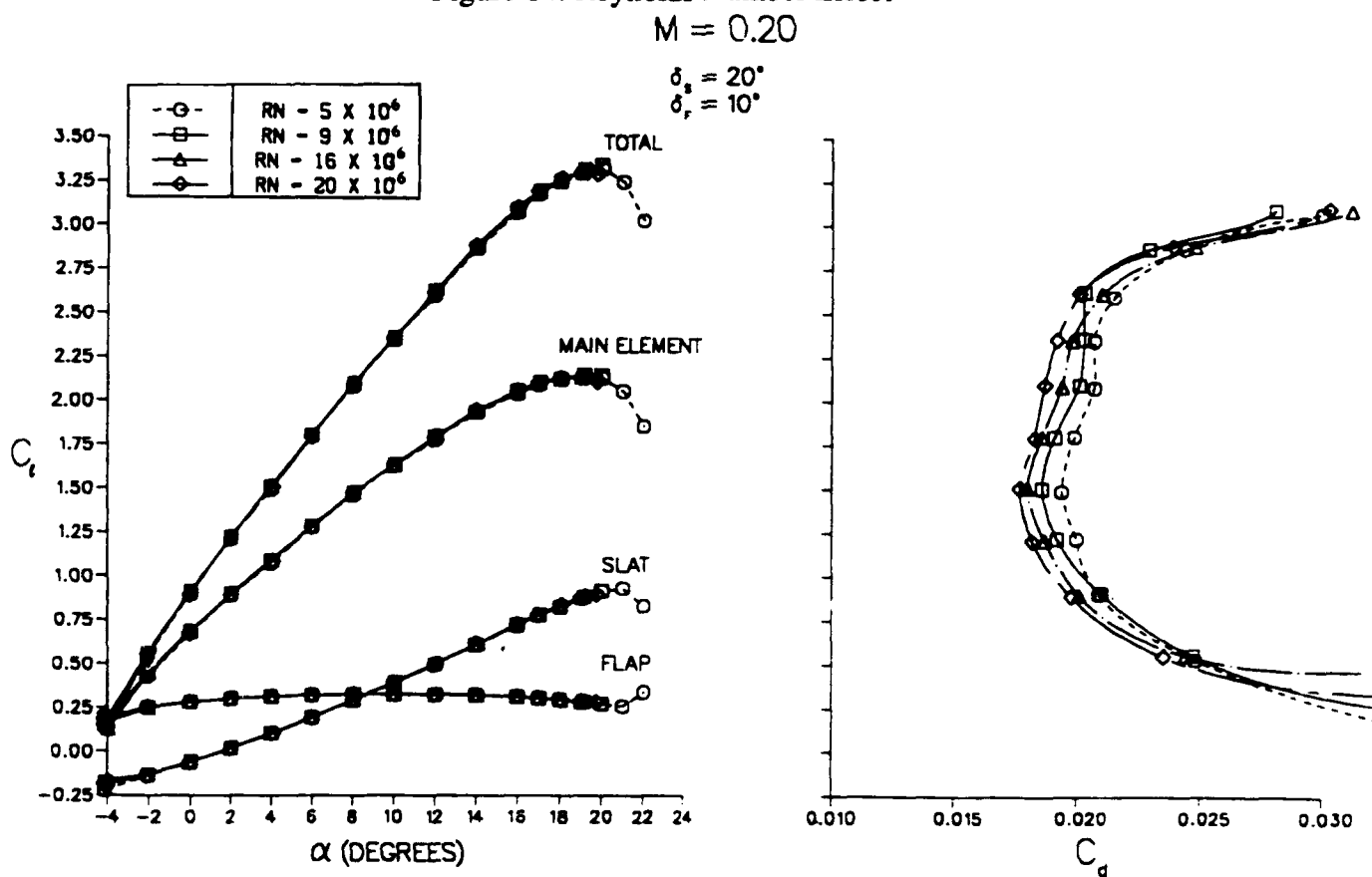


Figure 15. Reynolds Number Effect

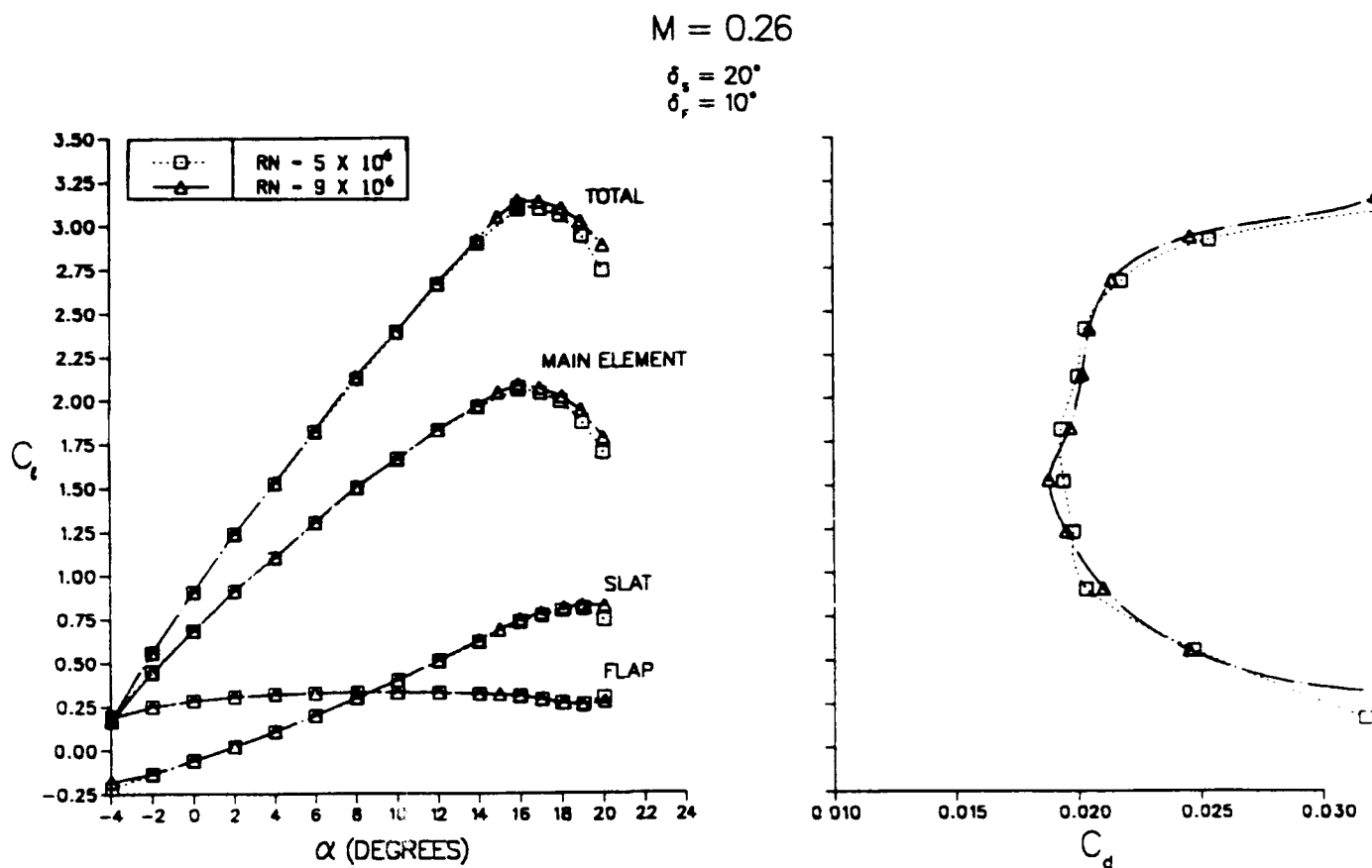


Figure 16. Reynolds Number Effect

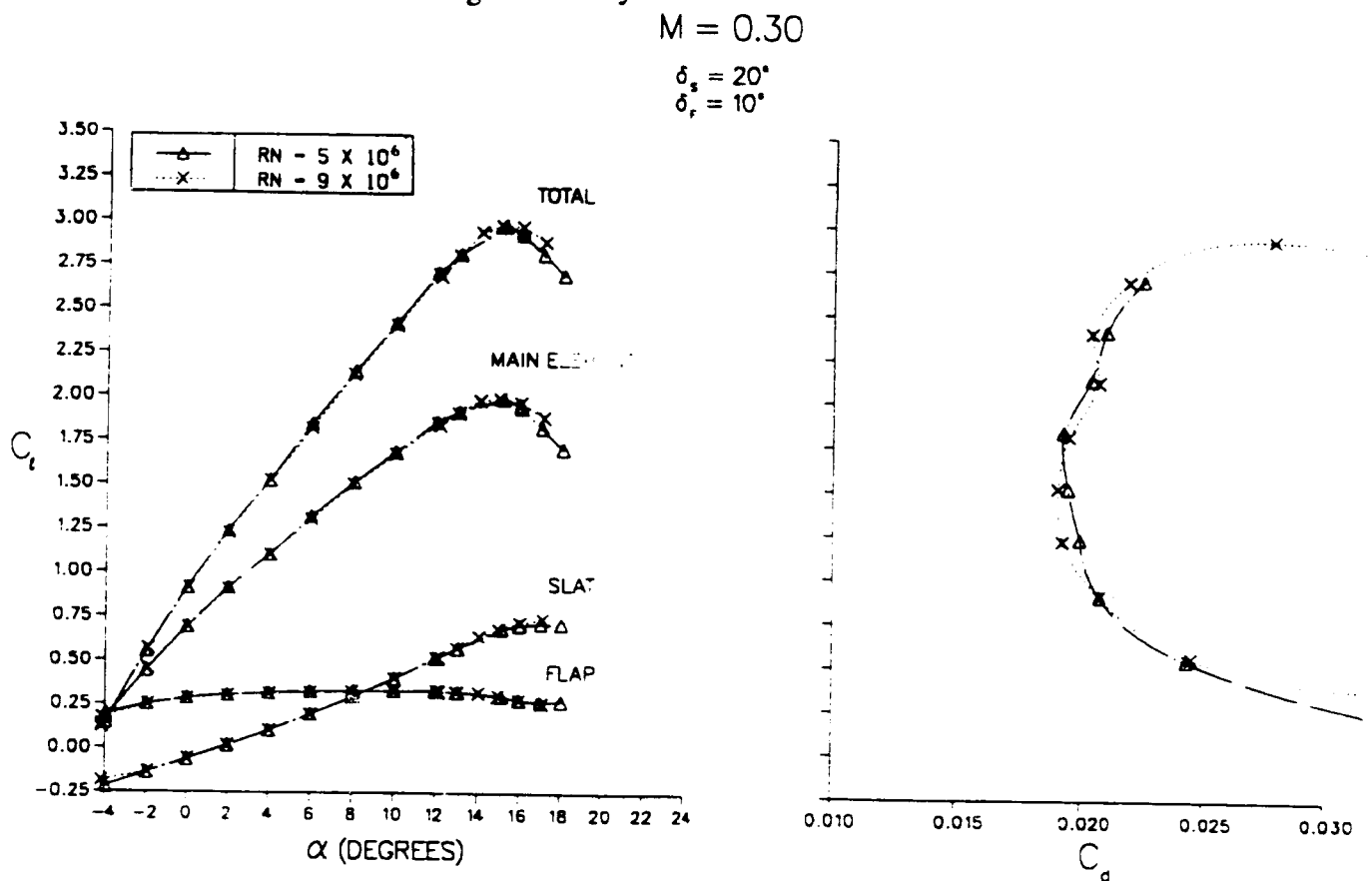


Figure 17. Reynolds Number Effect



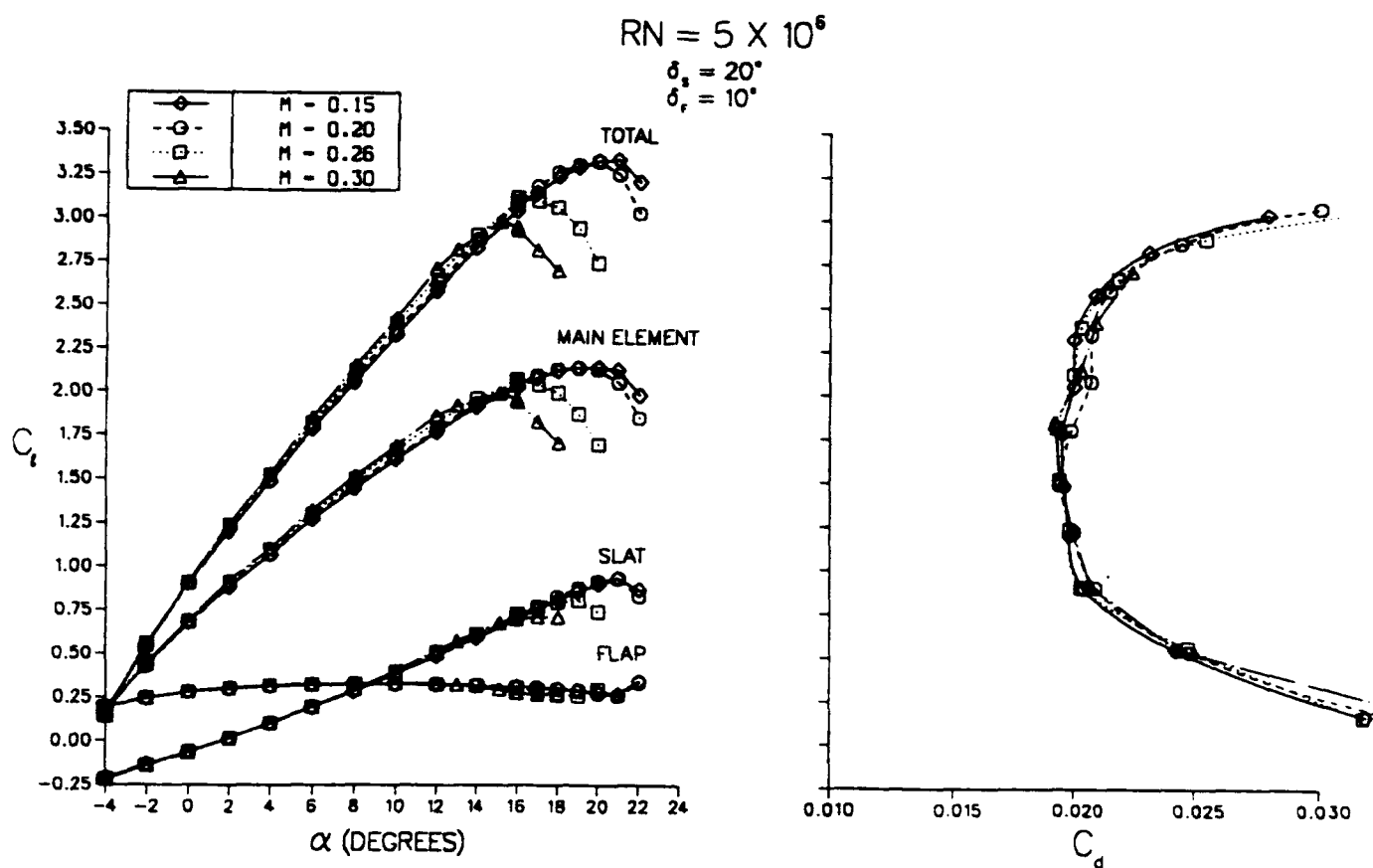


Figure 18. Mach Number Effect

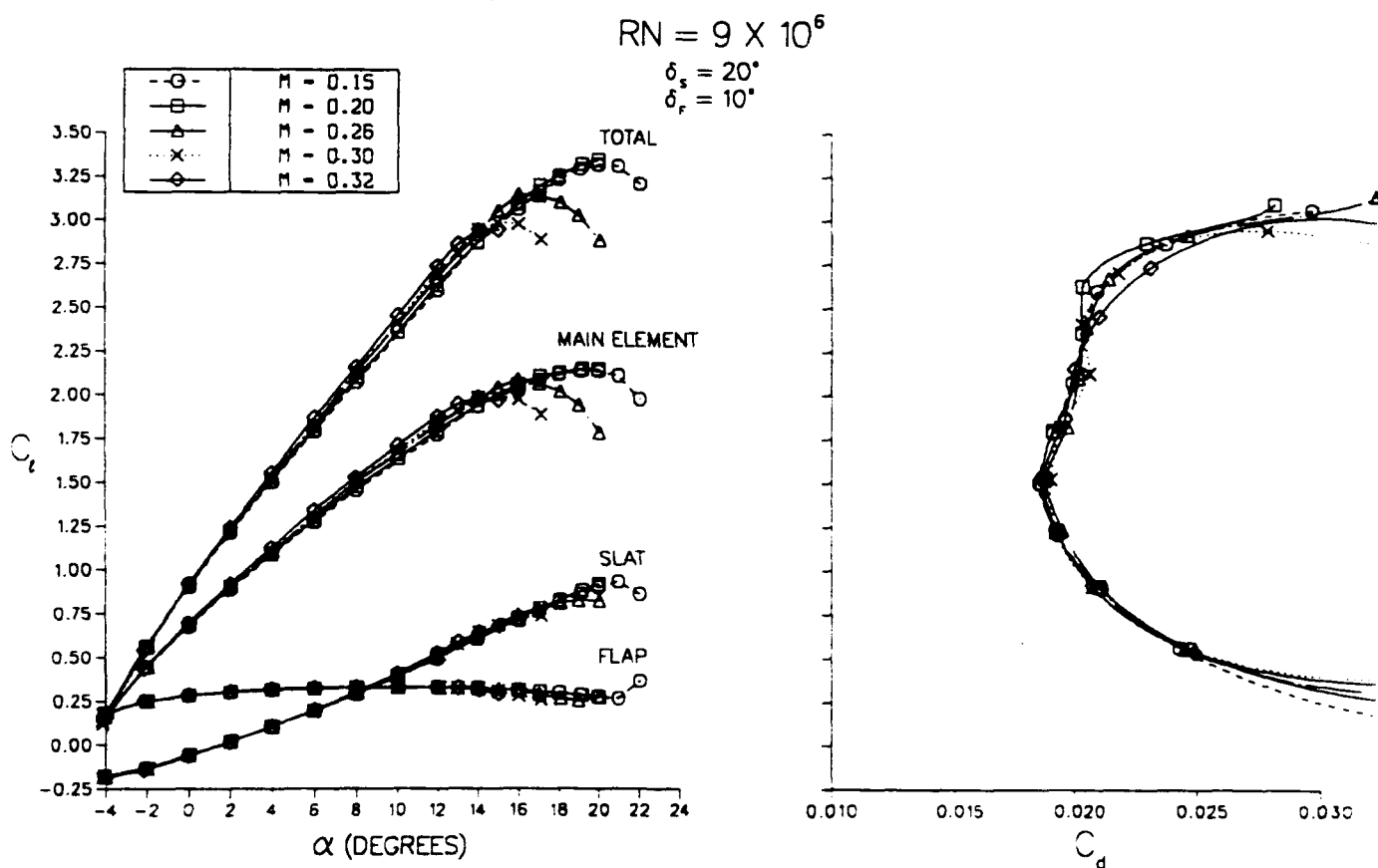


Figure 19. Mach Number Effect

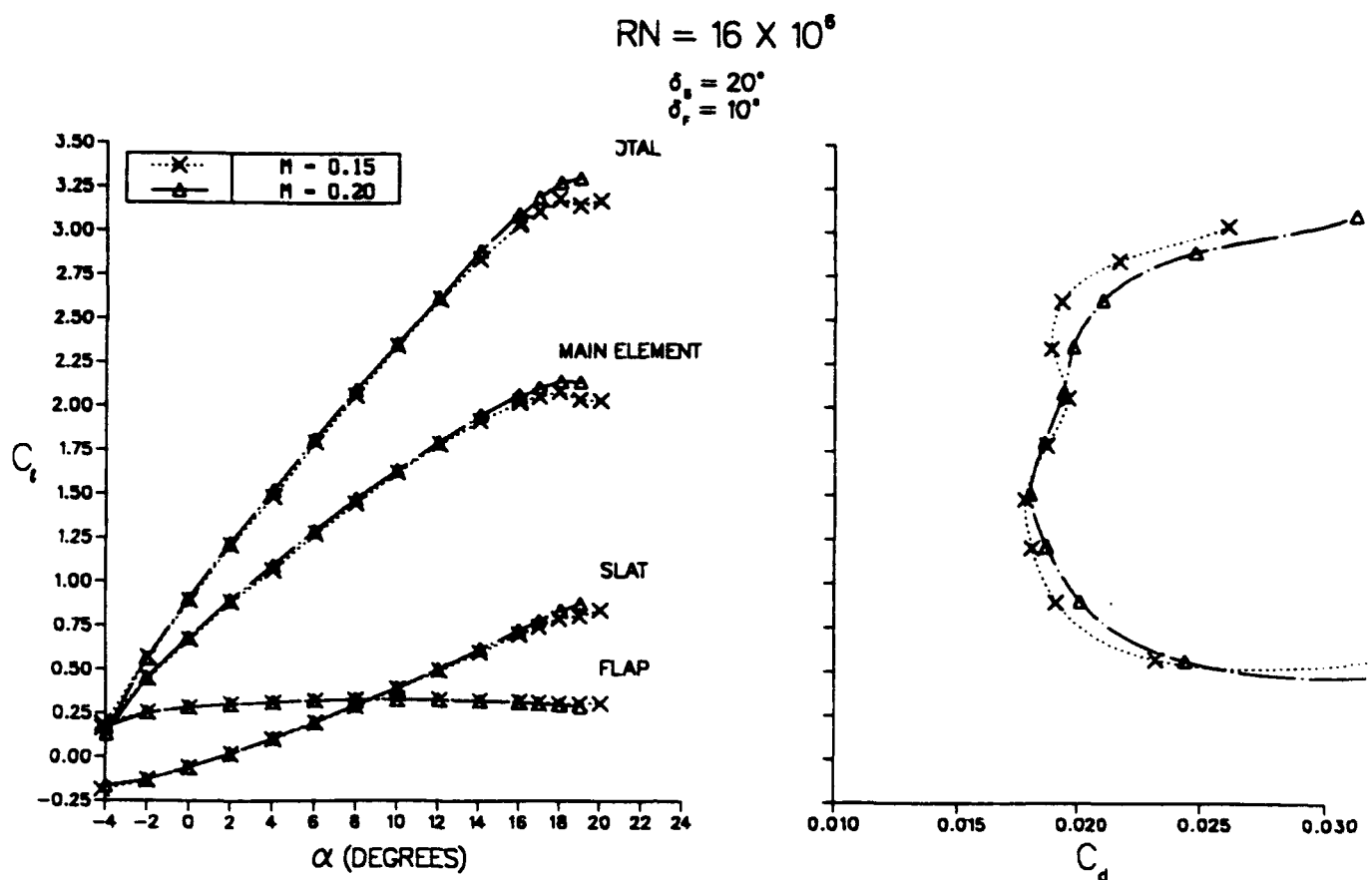


Figure 20. Mach Number Effect

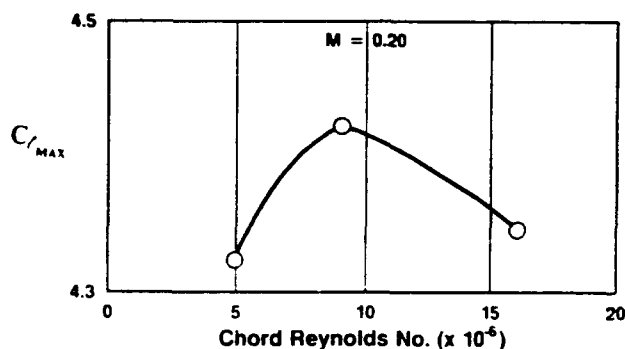


Figure 21. Reynolds Number Effect on Configuration Optimized at  $RN = 9 \times 10^6$  ( $\delta_s = 30^\circ$ ,  $\delta_f = 30^\circ$ )

single-segment flap configuration. It is possible that this difference in dependence on Reynolds number could be due to the large optimum gap for the two-segment flap and the much smaller (approximately half) optimum gap for a single-segment flap. These different gaps represent different enough slot geometries between the main element and the flap which could lead one configuration (single-segment flap) to be more Reynolds number sensitive

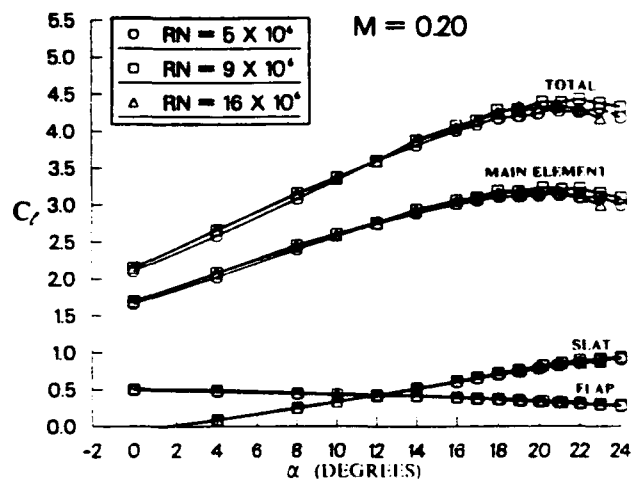


Figure 22. Reynolds Number Effect on Lift ( $\delta_s = 30^\circ$ ,  $\delta_f = 30^\circ$ )

than the other. Total and component loadings are shown in Fig. 25 and the corresponding surface pressures at maximum lift are shown in Fig. 26. It is interesting to note from Fig. 25 that there is a reduction in stall angle with increased Reynolds number for this four-element configuration. This stall angle reduction trend was not as apparent for the three-

element airfoil. The effect of Mach number on maximum lift at a Reynolds number of  $9 \times 10^6$  is shown in Fig. 27. Total and component loadings are shown in Fig. 28. It can be seen that increasing Mach number causes reductions in both maximum lift and stall angle.

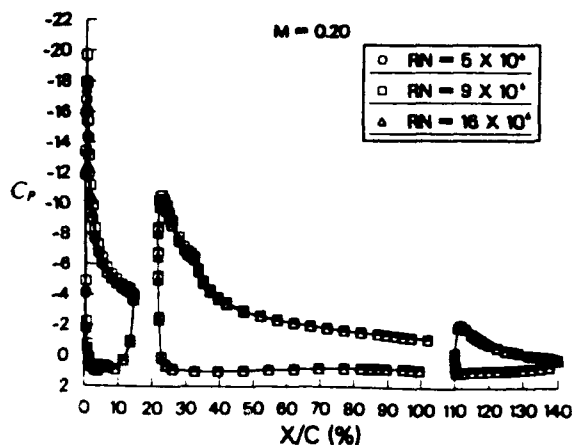


Figure 23. Reynolds Number Effect on Maximum Lift ( $\delta_s=30^\circ$ ,  $\delta_f=30^\circ$ )

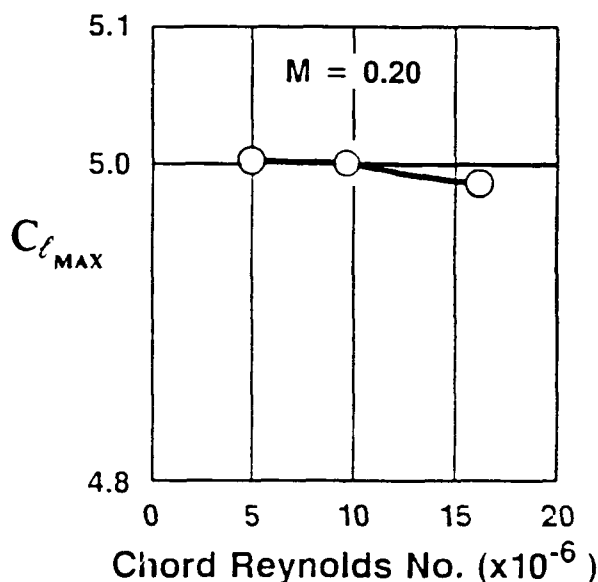


Figure 24. Reynolds Number Effect on Maximum Lift ( $\delta_s=30^\circ$ ,  $\delta_f=35^\circ/15^\circ$ )

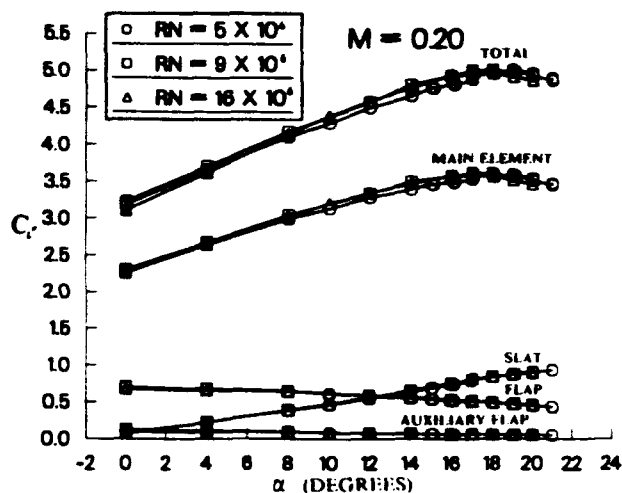


Figure 25. Reynolds Number Effect on Lift ( $\delta_s=30^\circ$ ,  $\delta_f=35^\circ/15^\circ$ )

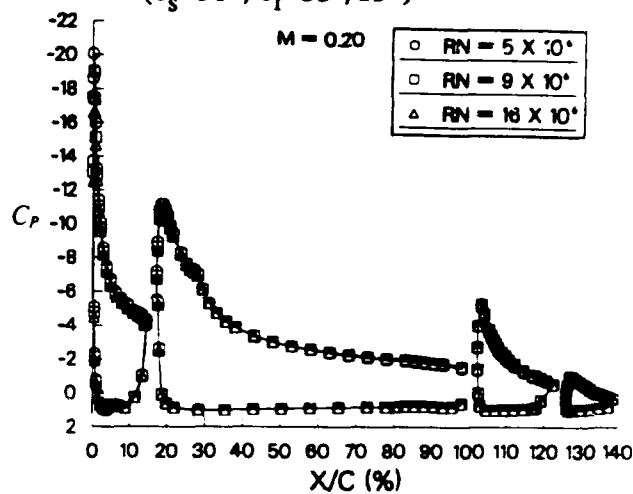


Figure 26. Reynolds Number Effect at Maximum Lift ( $\delta_s=30^\circ$ ,  $\delta_f=35^\circ/15^\circ$ )

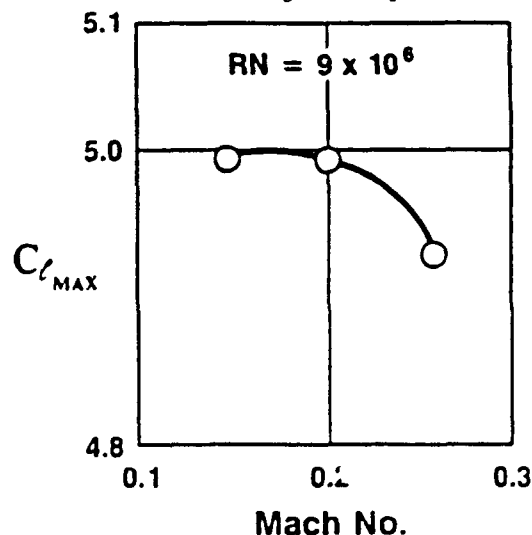


Figure 27. Mach Number Effect on Maximum Lift. ( $\delta_s=30^\circ$ ,  $\delta_f=35^\circ/15^\circ$ )

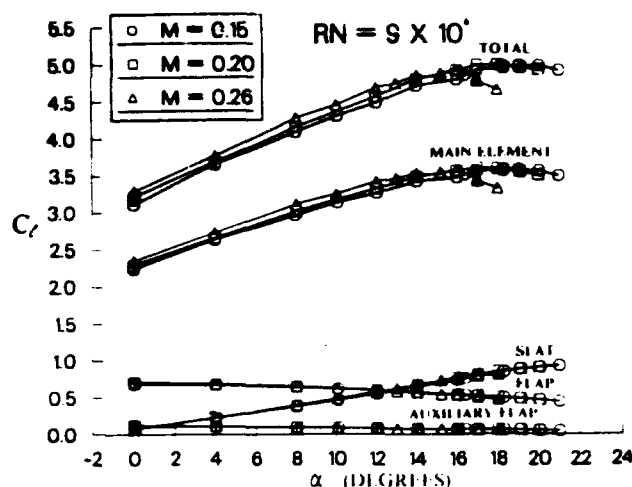


Figure 28. Mach Number Effect on Lift.  
( $\delta_i=30^\circ$ ,  $\delta_f=35^\circ/15^\circ$ )

### Conclusions

Experimental studies of the effects of Reynolds and Mach number variations on the performance of a practical transport-type multielement high-lift airfoil have been presented. The studies were conducted at the NASA Langley Low Turbulence Pressure Tunnel under a cooperative program between the Douglas Aircraft Company and the NASA Langley Research Center to establish a high-quality database for these effects that can be used in the calibration/validation of computational methods in development for practical multielement airfoil configurations. Salient findings of the present work are:

1. Reynolds number effects are significant even on the single-element airfoil below  $5 \times 10^6$  Reynolds number.
2. Mach number effects were more pronounced at the lower Reynolds numbers.
3. Extensive Reynolds and Mach number surveys were conducted on a three-element takeoff configuration ( $\delta_i = 20^\circ$ ,  $\delta_f = 10^\circ$ ). In general, Reynolds number effects on both lift and drag were minimal but different trends were exhibited depending on the Mach number. Mach number

effects on maximum lift were substantial.

4. For the three-element takeoff configuration the main element of the airfoil enters the stall first and is followed by the slat stalling. The flap does not stall.
5. Significant Reynolds number effects were apparent for the three-element landing configurations. As observed in the takeoff work, the main element of the airfoil stalls first. However, both the slat and flap continue to load up after the main element stalls.
6. Mach number effects on the four-element landing configuration were substantial. Reynolds number effects were not as large as those measured on the three-element airfoil. Additionally, the four-element results show a definite reduction in stall angle with increased Reynolds Number which was not apparent in either the takeoff configuration or the three-element landing configuration.

### References

1. Cebeci, T., Chang, K.C., Clark, R.W., and Halsey, N. D.: Calculation of Flow Over Multielement Airfoils at High Lift. ICAS Paper No. 86-2.3.1..
2. Shima, Eiji: Numerical Analysis of Multiple Element High Lift Devices by Navier Stokes Equation Using Implicit TVD Finite Volume Method. AIAA Paper No. 88-2574-CP.
3. Wang, G., and Wu, J.: A Numerical Study of General Viscous Flows Around Multi-Element Airfoils. AIAA Paper No. 90-0572.
4. Drela, M.: Newton Solution of Coupled Viscous/Inviscid Multielement Air:

Flows. AIAA Paper No. 90-1470.

5. Mavriplis, D.J.: Algebraic Turbulence Modeling for Unstructured and Adaptive Meshes. NASA Contractor Report No. 182035.
6. Mavriplis, D. J.: Turbulent Flow Calculations Using Unstructured and Adaptive Meshes. NASA Contractor Report 182102.
7. Mavriplis D. J.: Multigrid Solution of Compressible Turbulent Flow on Unstructured Meshes Using a Two-Equation Model. AIAA Paper No. 91-0237.
8. Kusunose, K., Wigton, L., and Meredith, P.: A Rapidly Converging Viscous/Inviscid Coupling Code for Multi-Element Airfoil Configurations. AIAA Paper No. 91-0177.
9. Chow, R., and Chu, K.: Navier-Stokes Solution for High-Lift Multielement Airfoil System with Flap Separation. AIAA Paper No. 91 -1 623.
10. Cebeci, T., Jau, J., and Vitiello, D.: An Interactive Boundary-Layer Approach to Multielement Airfoils at High Lift. AIAA Paper No. 92-0404.
11. Valarezo, W.O., Dominik, C.J., McGhee, R.J., Goodman, W.L., and Paschal, K.B.: Multi-Element Airfoil Optimization for Maximum Lift at High Reynolds Numbers. AIAA Paper No. 91-3332.
12. Paschal, K.B., Goodman, W.L., McGhee, R.J., Walker, B., and Wilcox, P.A.: Evaluation of Tunnel Sidewall Boundary-Layer Control Systems for High-Lift Airfoil Testing. AIAA Paper No. 91 - 3243.

# Quantitative Three-Dimensional Low-Speed Wake Surveys

by  
G. W. Brune\*

Boeing Commercial Airplane Group  
Seattle, Washington 98124

## Summary

Theoretical and practical aspects of conducting three-dimensional wake measurements in large wind tunnels are reviewed with emphasis on applications in low-speed aerodynamics. Such quantitative wake surveys furnish separate values for the components of drag such as profile drag and induced drag but also measure lift without the use of a balance. In addition to global data, details of the wake flowfield as well as spanwise distributions of lift and drag are obtained. The paper demonstrates the value of this measurement technique using data from wake measurements conducted by Boeing on a variety of low-speed configurations including the complex high-lift system of a transport aircraft.

## Nomenclature

b	model span
c	local wing chord
$C_D$	total drag coefficient
$C_{Di}$	induced drag coefficient
$c_{di}$	wing section induced drag coefficient
$C_{Dp}$	profile drag coefficient
$c_{dp}$	wing section profile drag coefficient
$C_L$	total lift coefficient
$c_l$	wing section lift coefficient
M	Mach number
p	static pressure
$p_t$	total pressure
q	dynamic pressure
Re	Reynolds number
S	tunnel cross-section area
U	axial velocity component
V, W	crossflow velocity components
y, z	Cartesian coordinates in measuring plane
$\alpha$	angle of attack
$\Delta C_D$	upsweep drag
$\Phi$	velocity potential, equation 11
$\rho$	density
$\sigma$	source, equation 9

$\xi$	axial component of vorticity, equation 8
$\Psi$	stream function, equation 10

## Subscripts

ft	value per foot
MAC	mean aerodynamic chord
ref	reference condition
$\infty$	freestream values

## Introduction

Qualitative wake surveys employing wake imaging (ref. 1) have verified that most aerodynamic flows of interest are stable. Moreover, they can be surveyed economically in large wind tunnels using mechanical traversers and pneumatic probes. Qualitative wake surveys are conducted to visualize the flowfield, which is a prerequisite to a better understanding of aerodynamic performance.

Quantitative three-dimensional wake surveys are a natural extension of wake imaging. They allow separate measurements of profile drag, induced drag, and lift including spanwise distributions. However, there are significant differences in data acquisition and processing between wake imaging and quantitative wake surveys. The latter requires the use of a pneumatic probe with multiple holes instead of a single total pressure probe to record pressures and velocities which can then be converted into aerodynamic forces. Furthermore, quantitative wake surveys require very accurate probe position measurements since spatial derivatives of flow velocities must be computed during data reduction.

Quantitative wake surveys are of much value to the aerodynamic design of airplanes for the following reasons:

- a. They can be used as a diagnostic tool during airplane

\* Principal Engineer, Aerodynamics Engineering  
Copyright retained by The Boeing Company, 1991.

development to study the effect of configuration changes on the components of drag.

- b. Separate measurements of induced drag and profile drag facilitate the prediction of flight drag based on measurements at low Reynolds number wind tunnel test conditions. This is because induced drag and profile drag are associated with different flow phenomena which must be scaled differently to account for changing Reynolds number.
- c. Separate measurements of the components of drag are also of value to the developer of CFD codes since profile drag and induced drag are usually predicted with different aerodynamic flow models that must be validated separately.

This paper describes the wake survey technique in use at the Boeing Aerodynamics Laboratory which is based on the work of Maskell and Betz. The underlying theory for the measurement of induced drag and lift had been published by Maskell (ref. 2), who also conducted an exploratory wind tunnel test confirming the validity of his method. The theory for the measurement of profile drag is that of Betz (refs. 3, 4). Briefly, model drag and lift can be written as integrals of flow velocities and total pressure, as is well known from basic aerodynamic principles. However, a straightforward application of these equations would not be practical since all three components of velocity would have to be measured throughout the wind tunnel test section. The basic approach employed by Maskell and Betz was to rewrite the drag integrals in terms of flow variables that vanish outside the viscous wake, thereby limiting the wake measurements to a small part of the flowfield. Maskell expressed the main contribution to the induced drag integral in terms of the streamwise component of vorticity, whereas Betz limited the profile drag integration to the viscous wake by introducing an artificial streamwise velocity. This opened the door for practical applications of quantitative three-dimensional wake surveys.

The wake survey methodology in use at Boeing also includes certain features of the work of others. Among them are Hackett and Wu (refs. 5, 6, and 7), who contributed to the theoretical foundation and developed a practical wake survey method with emphasis on applications in automotive engineering.

Several other experimentalists reported quantitative wake surveys. Onorato et al. (ref. 8) conducted wake measurements behind models of automobiles, but their drag analysis does not utilize the simplifications introduced by Maskell and Betz. Chometon and Laurent (ref. 9) performed wake measurements

on a simple wing to investigate the relation between induced drag and vortex drag. Weston of NASA Langley (ref. 10) conducted quantitative wake surveys behind wing half models based on the theory of Maskell and Betz. In his data analysis, Weston focused on the role of vortex cores and modified the definitions of profile drag and induced drag implementing an earlier proposal of Batchelor (ref. 11). El-Ramly and Rainbird published a number of papers (refs. 12 to 15) describing complete flowfield measurements behind wings from which aerodynamic forces were calculated, but they do not provide details of their theoretical analysis.

Wakes of two-dimensional airfoils have been routinely measured for many years with the primary objective of getting accurate profile drag data that cannot be obtained from balances. Wake surveys of three-dimensional configurations have occasionally been conducted but are not widely accepted by design aerodynamicists. The main reason for this is a legitimate concern about the cost of such wake measurements that require the measurement of a large number of data points. This can indeed be a time-consuming and, hence, expensive process if methods that work so well in two-dimensional wake surveys are applied without further refinements. In addition, three-dimensional wake surveys were suspected to be inaccurate since the desired drag and lift values are the composites of a large number of individual measurements. This paper addresses these and other issues and reports on the progress made since Maskell conducted the first wind tunnel test of this kind at the Royal Aircraft Establishment in the U.K. some 20 years ago.

## Theory

### Assumptions

Aerodynamic forces are calculated from the measured wake flow data assuming:

- a. Wake flow data are measured in a single plane downstream of the model. This plane, located at the so-called wake survey station (fig. 1), is assumed to be perpendicular to the wind tunnel axis. In most wind tunnels, the wake survey station must be moved very close to the model because of test section and hardware limitations.
- b. The flow at the wake survey station is steady and incompressible which limits the freestream Mach number in the wind tunnel to about 0.5. This does not turn out to be a serious limitation, as will be discussed later.

- c. The flow in the empty wind tunnel is a uniform freestream parallel to the tunnel axis. Any deviations from this ideal wind tunnel, as well as instrumentation misalignments, are assumed to be accounted for by measurements at the wake survey station with the model and its support apparatus removed.
- d. The effective ceiling, floor, and side walls of the empty wind tunnel, defined as the geometric walls modified by the displacement thickness of the wall boundary layers developing in the empty tunnel, are such that the tunnel freestream velocity is everywhere tangent to these surfaces. Note that the presence of a model, particularly a model that is large compared to the test section size, will disturb this displacement surface. Also notice that this choice neglects the possible effect of an axial pressure gradient in the empty tunnel (buoyancy).
- e. Viscous shear stresses at the wake survey station are neglected.
- f. As written, the equations do not account for blowing or suction through the model surface but could easily be modified.

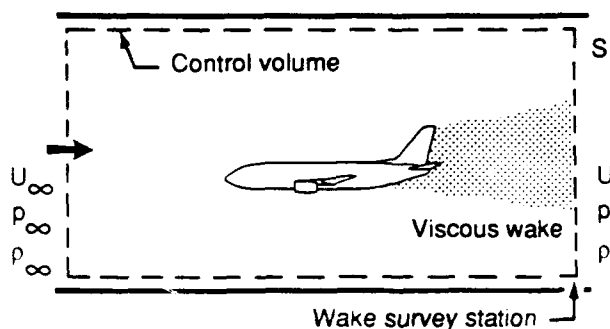


Figure 1. Control Volume for Derivation of Wake Equations

### Components of Drag

With these assumptions, an application of the momentum integral theorem, employing the control volume shown in figure 1, provides the following equation for model drag

$$D = \iint_{\text{wake}} (p_{t\infty} - p_t) ds + \frac{\rho}{2} \iint_S (V^2 + W^2) ds + \frac{\rho}{2} \iint_S (U_\infty^2 - U^2) ds \quad (1)$$

in which the symbol  $p_t$  denotes total pressure and  $V, W$  are the components of the crossflow velocity in the

measuring plane perpendicular to the tunnel axis (fig. 2).  $U$  and  $\rho$  denote the velocity in the direction of the tunnel axis and density, respectively. Undisturbed freestream values are indicated by the subscript  $\infty$ .

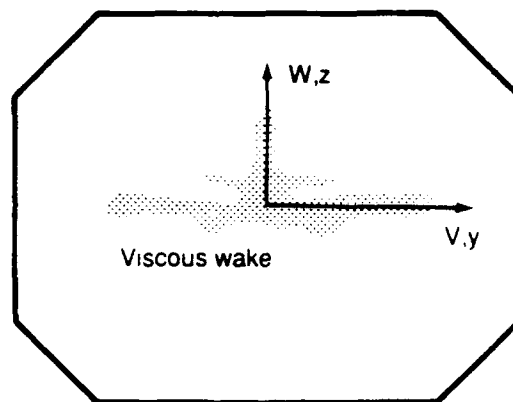


Figure 2. Crossflow Notation

Here, the first term is an integral of the total pressure deficit that is sometimes used as a measure for profile drag even though it is not the only contribution to this type of drag. As indicated, this integral is limited to the viscous wake since the total pressure deficit is zero outside this region of the flow. The second term, representing the kinetic energy of the crossflow, is called vortex drag whereas the third term containing axial velocities does not have any particular name in traditional nomenclature. We will see below that this third term contains contributions to both profile drag and induced drag.

It should be emphasized that equation 1 is valid for configurations in locally compressible flow since the assumption of incompressible flow has only been applied to simplify the velocity and pressure terms at the wake survey station and far ahead of the model.

Equation 1 is not well suited for use in a practical wake measurement technique since only the first integral is limited to the viscous part of the wake. An evaluation of the other two terms would require the measurement of all three velocity components throughout the tunnel cross-section area  $S$ .

In order to obtain an equation for profile drag that is suitable for practical wake measurements, Betz (ref. 4) introduced an artificial axial velocity,  $U^*$ , defined by the equation

$$U^{*2} = U^2 + \frac{2}{\rho} (p_{t\infty} - p_t) \quad (2)$$



Notice that  $U^*$  is the same as the true axial velocity  $U$  outside the viscous wake, where the total pressure is  $p_{t\infty}$ . If one also introduces a perturbation velocity, defined by  $u = U^* - U_\infty$ , drag can be written as the sum of profile drag  $D_p$  and induced drag  $D_i$

$$D = D_p + D_i \quad (3)$$

with

$$D_p = \iint_{wake} [p_{t\infty} - p_t + \frac{\rho}{2}(U^* - U)(U^* + U - 2U_\infty)] ds \quad (4)$$

$$D_i = \frac{\rho}{2} \iint_{wake} (V^2 + W^2 - u^2) ds \quad (5)$$

The measurement of profile drag can now be conducted economically by measuring total pressure deficit and axial velocity in the viscous wake only.

Motivated by the need to also limit the measurement of induced drag to the viscous part of the wake, Maskell (ref. 2) interpreted the axial velocity perturbation term in equation 5 as a blockage correction in which blockage velocity is calculated from

$$u_b = \frac{1}{2S} \iint_{wake} (U^* - U) ds \quad (6)$$

This blockage correction can easily be implemented by replacing the tunnel freestream velocity in the profile drag equation by an effective freestream velocity,  $U_e = U_\infty + u_b$ .

The elimination of the  $u$ -term from the induced drag equation is the most questionable aspect of Maskell's theory since the distinction between vortex drag and induced drag disappears. In principle, the  $u$ -term should remain part of induced drag even though it is probably small compared to vortex drag in many applications (ref. 16).

### Induced Drag

According to Maskell, the remainder of the induced drag equation can be approximated by

$$D_i = \frac{\rho}{2} \iint_{wake} \Psi \xi ds - \frac{\rho}{2} \iint_S \Phi \sigma ds \quad (7)$$

where the symbol  $\xi$  represents the component of wake vorticity in the direction of the tunnel axis, referred to below as axial component of vorticity,  $\sigma$  is the crossflow divergence or source. They are calculated from the measured crossflow velocities  $V$ ,  $W$  using the definitions

$$\xi = \frac{\partial W}{\partial y} - \frac{\partial V}{\partial z} \quad (8)$$

$$\sigma = \frac{\partial V}{\partial y} + \frac{\partial W}{\partial z} = -\frac{\partial U}{\partial x} \quad (9)$$

The symbol  $\Psi$  is the stream function obtained from a solution of

$$\frac{\partial^2 \Psi}{\partial y^2} + \frac{\partial^2 \Psi}{\partial z^2} = -\xi \quad (10)$$

It describes a flowfield that is induced by the axial component of vorticity. Equation 10 must satisfy the boundary condition  $\Psi = 0$  at the tunnel walls so that they become a streamline of this two-dimensional flowfield.

The symbol  $\Phi$  denotes a velocity potential calculated from

$$\frac{\partial^2 \Phi}{\partial y^2} + \frac{\partial^2 \Phi}{\partial z^2} = \sigma \quad (11)$$

and the following boundary condition of no flow through the tunnel walls

$$\frac{\partial \Phi}{\partial n} = 0$$

Notice that the first integral in equation 7 is limited to the viscous wake since vorticity vanishes outside. The second term would still require measurements throughout the test section area but wake measurements behind models of airplane configurations have shown that the source  $\sigma$  is negligibly small outside the viscous wake. Hence, induced drag can be approximated by

$$D_i = \frac{\rho}{2} \iint_{wake} (\Psi \xi - \Phi \sigma) ds \quad (12)$$

### Lift

The momentum integral theorem together with the control volume of figure 1 yields the following equation for lift

$$L = \iint_{S_4} p ds - \iint_{S_3} p ds - \rho \iint_S W U ds \quad (13)$$

where the first two terms represent the difference in static pressure between tunnel floor and ceiling. This integration is performed along upper and lower surfaces of the control volume, denoted respectively by  $S_3$  and  $S_4$ . The third term arises from the downwash behind the model. The equation for lift can be cast into the following form (refs. 2, 16)

$$L = \rho U_\infty \iint_{wake} y \xi ds + \rho \iint_S (U_\infty - U) W ds \quad (14)$$

in which the first integral is expressed in terms of axial vorticity that vanishes outside the viscous wake and, hence, only requires measurements in the wake. In most cases the second integral is expected to be small so that lift can be approximated by

$$L = \rho U_{\infty} \iint_{\text{wake}} \gamma \xi ds \quad (15)$$

### Instrumentation

#### Five-Hole Probe

Most three-dimensional wake surveys conducted by Boeing employ pneumatic probes with multiple orifices mounted on mechanical traversers. All wake survey tests described in this paper used a single five-hole conical probe 0.25 inches in diameter (fig. 3) in a fixed position or nonnulling mode for fast data acquisition. Rakes of pneumatic probes have been considered in order to shorten data acquisition time but were discarded to avoid the increased data handling complexity associated with their use and possible mutual probe interference. Pneumatic probes have the following advantages for testing in large low-speed wind tunnels:

- They can accurately and simultaneously measure all three components of wake velocity and total pressure.
- They provide time averages of data, thereby limiting the data volume and data processing time.
- They are rugged and not easily contaminated by dirt in the tunnel circuit.

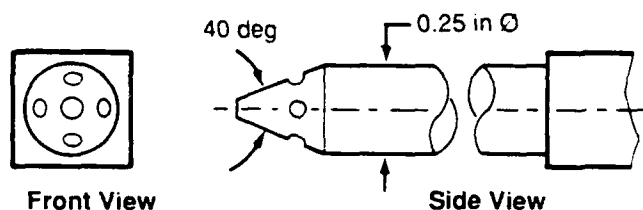


Figure 3. Five-Hole Probe Geometry

These features are not shared by most data acquisition systems developed for experiments in small research facilities. However, the probes and the mechanical traversers on which they are mounted are intrusive and will disturb the flow to some degree. Under certain conditions, intrusive probes are known to cause meandering of the vortex in which they are inserted and make the vortex core appear larger than its true size (ref.17). Perhaps an

even greater concern in using such measuring systems is the flow disturbance due to the traverser, which can cause significant perturbations of model lift and drag. These potential problems represent a great challenge to the experimentalist who must achieve a workable compromise between the rigidity of the measuring system and its intrusiveness.

#### Probe Calibration

Probes are calibrated by placing them at selected pitch and yaw angles in a flow of known total and static pressures (ref. 18). This provides calibration curves for the deviation between true and indicated values of total pressure measured by the center hole of the five-hole probe as a function of flow angle, probe design, and Reynolds number based on probe size. Furthermore, this procedure relates flow angles and velocity components to pressures measured by the orifices on the side faces of a multiple hole probe, and also furnishes static pressure.

#### Mechanical Traverser

Most wake survey tests conducted by Boeing utilize vertical traversing struts that are a permanent part of the wind tunnel test section equipment. Sometimes an additional mechanical traverser is mounted on this strut to move the probe in a lateral direction while the strut traverses the vertical direction. Employing the wind tunnel strut usually simplifies the test setup, but requires compensation for the mechanical backlash of the strut.

All wake measurements discussed in this paper used traversers that move the probe parallel to the tunnel side walls, providing data points arranged in a Cartesian grid. Work is in progress on improved traversers that move the probe along circular arcs while the wind tunnel strut, on which the traverser is mounted, is temporarily at rest (fig. 4). These second generation traversers are less intrusive and are computer controlled, which simplifies data acquisition. However, the task of aligning the probe with the wind tunnel axis during the entire wake survey becomes very difficult. A probe that is not aligned well with the tunnel axis will measure crossflow velocities and a corresponding apparent wake vorticity that are partially due to probe misalignment. One can account for this probe misalignment by mapping the flow in the empty tunnel at the same location where wake surveys are normally conducted. The measured empty tunnel crossflow velocities are then used to compute a correction to the final drag and lift data. Notice, however, that empty tunnel surveys need not be conducted to determine the flow qualities of a tunnel

that are known from earlier calibration tests.

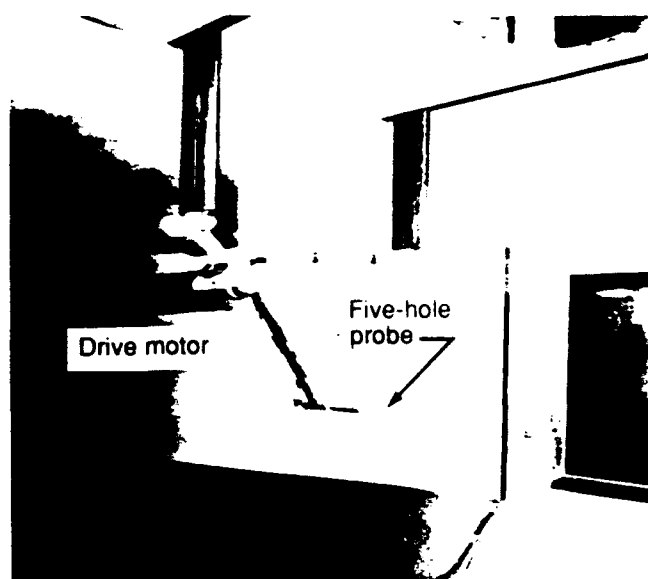


Figure 4. Mechanical Traverser in Empty University of Washington Wind Tunnel

### Data Reduction

In the usual procedure, the five-hole probe measures total pressure deficit and all three components of wake velocity at a large number of points, normally in excess of 10,000. Handling this data volume in a timely fashion is the most difficult aspect of the data reduction procedure. Basically, the procedure consists of two steps: A review of the data for erroneous and duplicate data sets, and the calculation of lift and drag from the final data set.

The calculation of profile drag using equation 4 is straightforward and only requires integration. The calculation of induced drag and lift using equations 12 and 15 is more difficult since vorticity and source strength must be computed as intermediate results. These calculations require numerical differentiation of measured crossflow velocity components,  $V$  and  $W$ , which can easily lead to erroneous values of induced drag and lift if not done properly. Numerical experimentation with various schemes showed that accurate vorticity and source data could be calculated by fitting cubic splines to the measured crossflow velocities.

In order to obtain the stream function  $\Psi$  and the velocity potential  $\Phi$  from equations 10 and 11, the computational domain is extended with uniform grid spacing from the wake survey region to the walls of the wind tunnel. Where necessary, fillets in the corners of the test section are neglected. Values of axial vorticity and source strength are prescribed throughout the computational domain,

which are in general nonzero in the wake survey region and zero outside. A fast Poisson solver of the FISHPAK library (ref. 19) provides solutions for  $\Psi$  and  $\Phi$ . Since the total number of grid points necessary for the calculation frequently exceeds 200,000, the use of a supercomputer is required for this phase of the data reduction. Software for this purpose has been developed at Boeing.

Standard correction methods (ref. 20) are applied to lift and drag obtained from wake surveys to account for the effects of wind tunnel walls. The effect of model support struts is accounted for by including part of the model support wake during wake surveys. Most support struts shed very little axial vorticity since they are designed to minimize the disturbance of the circulation around the model. Hence, their presence is primarily visible in the spanwise distribution of profile drag and not in the spanwise data of induced drag or lift. Assuming a spanwise variation of profile drag that might exist in the absence of the strut, profile drag can then be corrected.

Since wake surveys are time-consuming and some low-speed wind tunnels are not equipped with a heat exchanger to control temperature, profile drag must sometimes be corrected for the effect of temperature increases with time.

### Wake Survey Test Results

Three tests are described, ranging in complexity from measurements behind a simple wing to a wing-body-nacelle combination in high-lift configuration. They illustrate the practical aspects of quantitative wake measurements such as model installation, data acquisition, test procedure, and provide examples of the type and quality of data obtained from wake surveys. Each of these tests has unique features dictated by different test objectives, type and availability of model and wind tunnel, and testing budget. All tests used basically the same data acquisition system and data reduction procedure but different hardware.

#### High-Lift Test of Transport Aircraft

A large half model of a twin engine transport was tested at Mach 0.22 and 1.4 million chord Reynolds number in the Boeing Transonic Wind Tunnel (fig. 5). The tunnel features an 8- by 12-ft test section with slotted walls. The wing was in high-lift configuration with take-off flaps deployed. The model had a half-span of 52 inches and was installed vertically above a horizontal splitter plate. Two different engine simulations were employed including a flowthrough nacelle and a turbo-powered simulator

(TPS). The purpose of this experiment was to determine the feasibility of making quantitative wake surveys using models of realistic high-lift configurations.

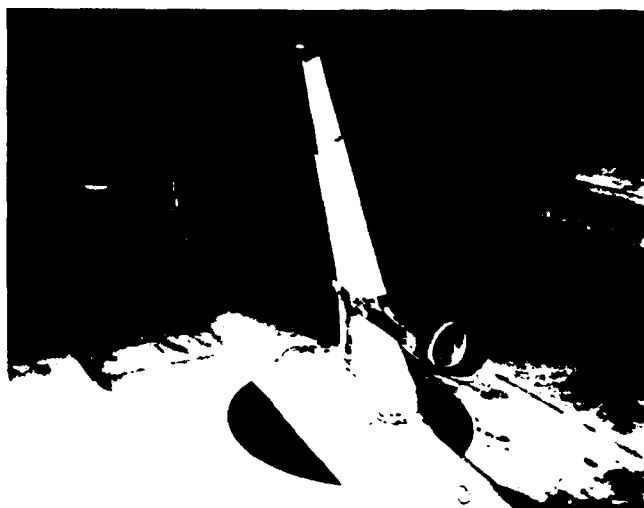


Figure 5. High-Lift Half-Model in Boeing Transonic Wind Tunnel

Wake surveys were conducted in a plane two mean aerodynamic chord lengths (24 inches) downstream of the inboard wing trailing edge, which was as far downstream as test section and data acquisition hardware permitted. The boundaries of the wake survey region (fig. 6) were chosen to capture wing and nacelle wakes but did not include the wake behind the fuselage.

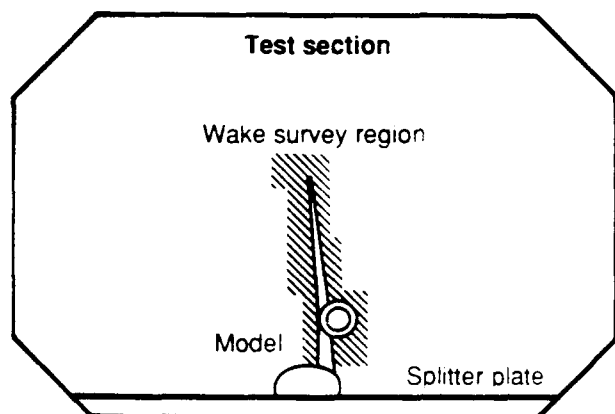


Figure 6. Example of Wake Survey Region

Wake surveys are time-consuming since a large number of data points must be taken to adequately describe the wake. In this case measurements had to be performed at about 15,000 wake points. In order to complete a wake survey within a reasonable time of about 2 hours, data were recorded while the probe traversed at a fixed speed. Preliminary investigations in which the traversing speed was varied showed that this mode of testing produced accurate data up to a probe speed of 1 inch per second.

Measured velocities of the crossflow perpendicular to the tunnel axis were converted into axial vorticity as described above. Such vorticity data together with the measured total pressure deficit provides much insight into the structure of wing wakes. Figures 7 and 8 show contour plots of these data for the model with two different engine representations. Wind tunnel test conditions and model geometry are the same for both sets of data. The wake flows are shown in airplane view with the wing tip vortex of the right wing on the right side of the plots. The nacelle region is visible on the left side of each plot. Inboard total pressure and vorticity contours are quite different for the two nacelle configurations with the TPS data indicating the extent of the powered jet. However, the outboard contours, including the tip vortex and the powerful vortex to the left of the tip vortex, shed from the outer edge of the trailing edge flap, are almost identical for the two wakes.

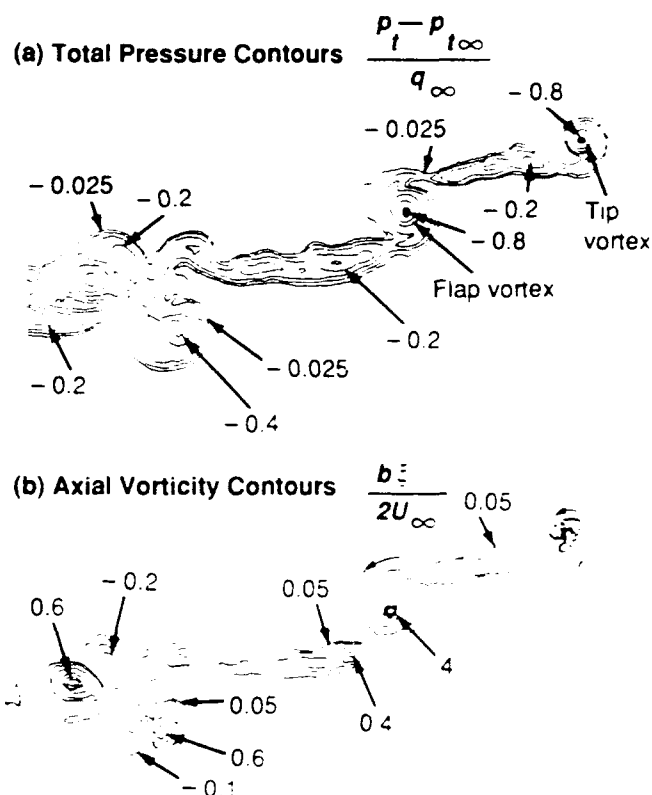


Figure 7. Wake Flow Data of Transport High-Lift Model With Flowthrough Nacelles

Wake flow data provide important qualitative information during airplane design but are also useful for the validation of CFD codes. An example of the latter is given in figure 9 where the total pressure contours of figure 7 are compared with wake rollup predictions obtained from A502/PANAIR (ref. 21) for this high-lift airplane configuration with flowthrough nacelle.

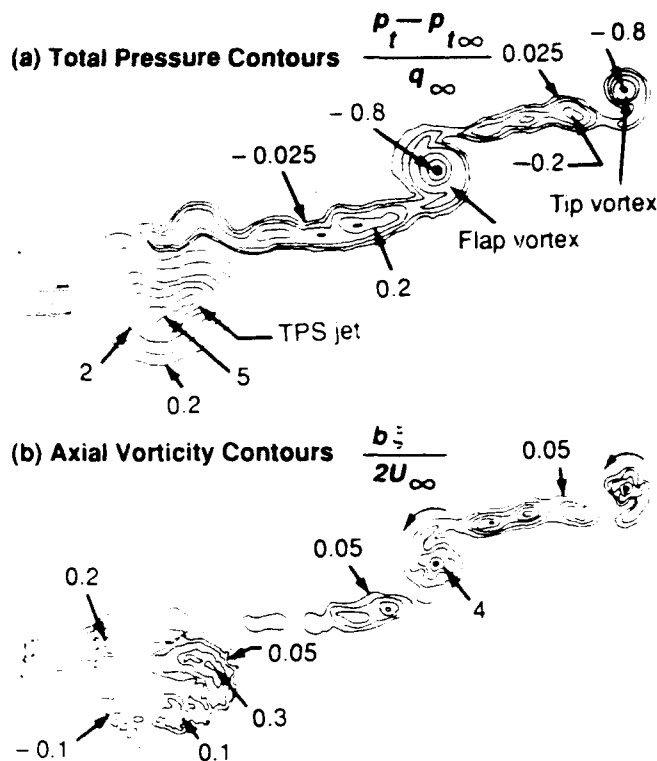
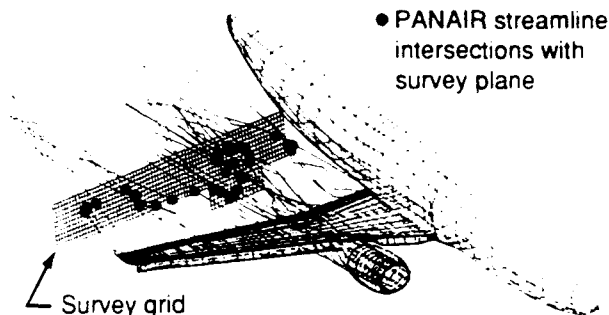
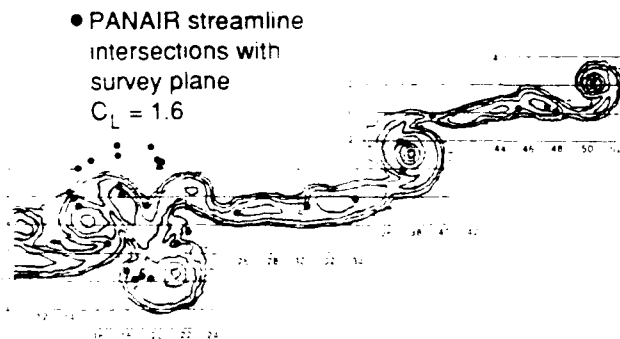


Figure 8. Wake Flow Data of Transport High-Lift Model With Turbo-Powered Simulator (TPS) Powered Nacelles

#### (a) Panel Model and Streamline Calculations



#### (b) Streamline Intersections With Survey Plane



Total pressure wake contours from flowthrough nacelle test

Figure 9. A502/PANAIR Prediction of Wake Shape of Transport High-Lift Configuration.

Spanwise distributions of profile drag and induced drag derived from the wake data of figures 7 and 8 and the corresponding axial velocity data are plotted in figure 10. Spanwise induced drag is defined here as the integral of the integrand of equation 12 in the direction normal to the wing surface, which is different from the usual definition of spanwise induced drag defined as the product of wing section lift and induced angle of attack. As seen in the figure, the major contribution to induced drag arises from the strong tip and flap edge vortices. Profile drag of the model with TPS nacelle includes a large region of negative values representing the thrust of the TPS jet. The two configurations have almost identical distributions of induced drag and profile drag for the outer half of the wing, except that wing and flap vortices from the TPS configuration are shifted slightly outboard, possibly being displaced by the TPS jet. Such good agreement of the outboard data taken at the same angle of attack and behind the same wing geometry demonstrates the excellent repeatability of these measurements. It should be emphasized that the spanwise distributions of drag shown in figure 10 are somewhat distorted because of wake deformations between wing trailing edge and wake survey station. Thus, any comparison of spanwise drag or lift data with data from other sources should be interpreted with caution. However, spanwise wake data frequently reveal the origin of major contributions to drag and lift and are therefore of much value in aerodynamic design.

The vorticity data in the wake of the TPS-powered model were used to calculate wing spanload as described in reference 22. The result is shown in figure 11 together with inviscid theoretical predictions of the A502/PANAIR code. These theoretical data represent a spanwise lift distribution, scaled by the local wing chord and nondimensionalized by the sum of all lift and side forces in the outboard wing and nacelle region. Good agreement is demonstrated outboard of the nacelle. The large differences in the nacelle region are mainly due to sideforces, which, in the wake survey data, could not be distinguished from lift.

#### Simple Wing Study

The main objective of this test was to learn more about the accuracy and measurement repeatability of quantitative wake surveys (ref. 23). In this test, the wake was mapped behind a simple rectangular wing model that had a span of 6 feet and an untwisted NACA0016 airfoil section. The test was conducted at the University of Washington Aeronautical Laboratory in an 8- by 12-ft low-speed

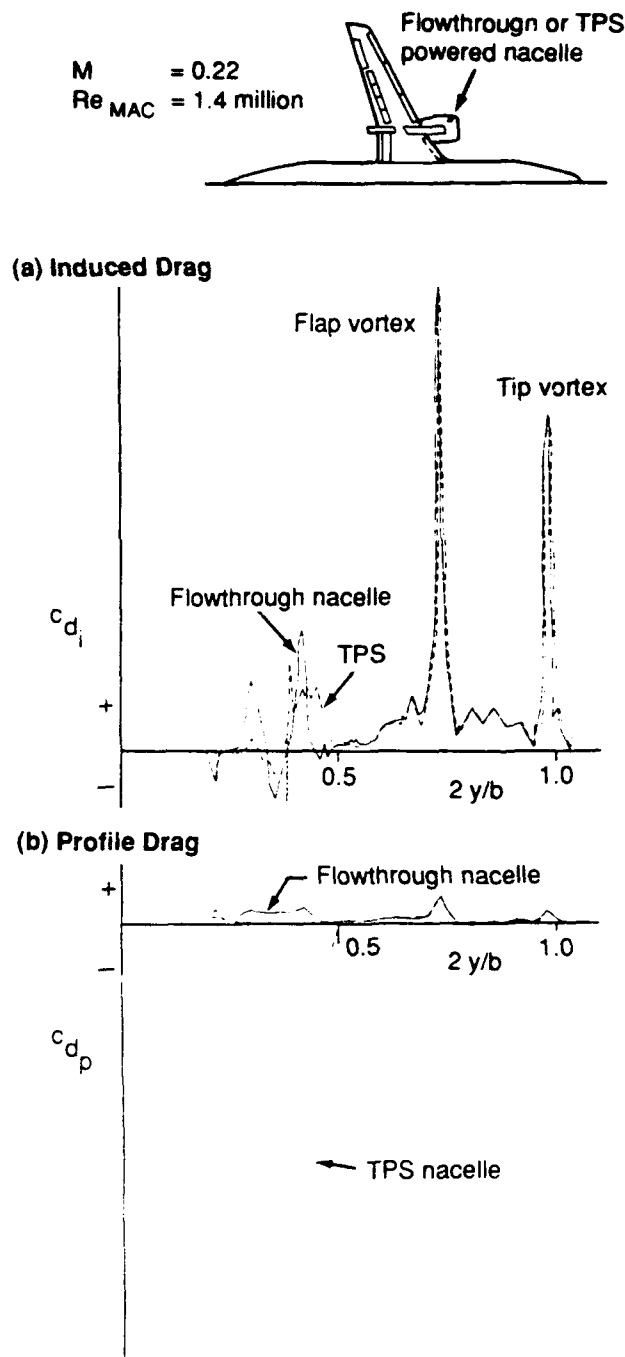


Figure 10. Spanwise Drag Data From Wake Surveys Behind Transport High-Lift Configuration

wind tunnel. All measurements were taken at 0.18 Mach number and 1.27 million chord Reynolds number. The model was installed horizontally at the center of the test section. It was supported by a floor-mounted strut that in turn was mounted on an external balance located below the wind tunnel (fig.12).

Wake surveys were conducted one chord length behind the wing trailing edge and at several angles of attack below stall. A very important purpose of this and other wake tests had been to verify that the

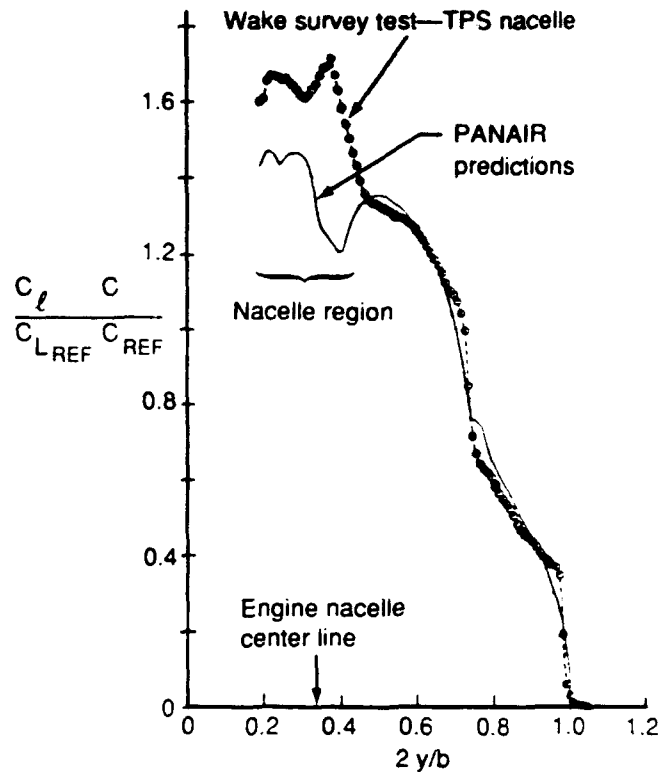
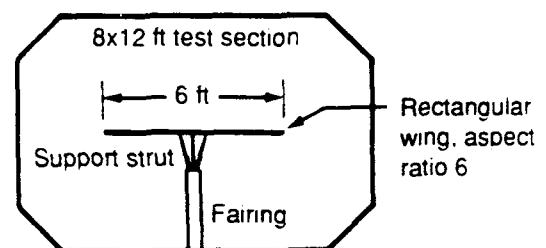


Figure 11. Spanwise Wing Loads of Transport High-Lift Model From Wake Survey and A502 PANAIR Code Prediction

planned quantitative wake survey would indeed capture the wake. This was done by applying the wake imaging technique (ref. 1), which displays total pressure contours measured by the center hole of the five-hole probe. Since viscous wakes can be seen as regions of total pressure loss, the regions in which wakes have to be surveyed can easily be identified.

#### (a) Front View of Model in Test Section



#### (b) Side View of Model and Probe Traverser

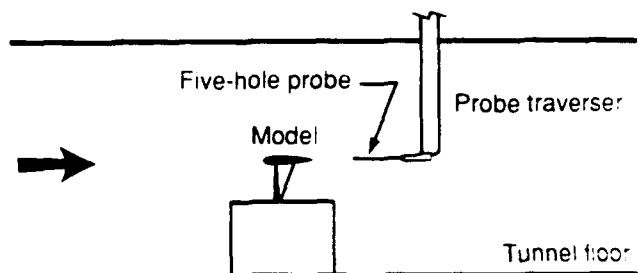


Figure 12. Simple Wing Model in the University of Washington Low-Speed Wind Tunnel

Lift curve and drag polar obtained from wake surveys are compared in figure 13 with corresponding balance data measured during this test. Wake and balance data were recorded at the same test conditions defined by the quoted angles of attack, Mach number and Reynolds number. After the test, both types of data were corrected for wind tunnel wall effects in exactly the same way. The figure also shows the variation of profile drag with lift measured during wake surveys. Excellent agreement of wake and balance data is shown in these figures, providing proof of the high measurement accuracy that can be achieved in quantitative wake surveys.

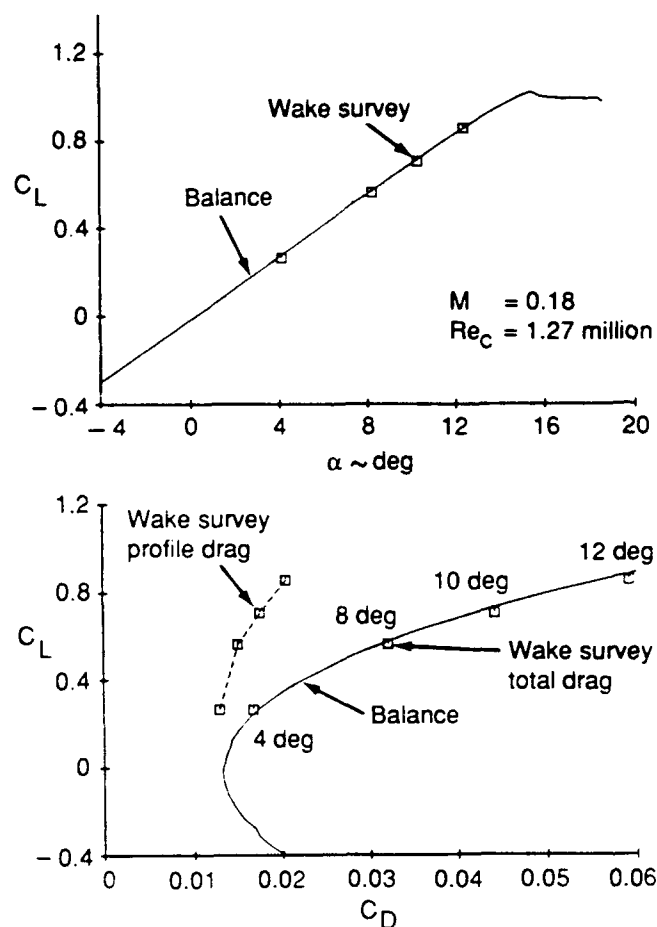


Figure 13. Lift and Drag of Simple Wing From Wake Surveys and Balance

For practical applications, the ability of a wake survey technique to repeat the measurements with very little data scatter is as important as a good absolute measurement accuracy. Figure 14 contains tabulated data for lift and drag components measured in three different wake surveys at the same angle of attack and at the same wake location. These are true repeat runs conducted several days apart. All wake data repeated very well, particularly lift, total drag, and induced drag. Profile drag

scatter is slightly higher than the scatter in the other data. For comparison, figure 14 also contains a table with repeat balance data at the same wind tunnel test conditions.

(a) Wake survey data for  $\alpha = 8.22$  deg

Wake survey	$C_L$	$C_D$	$C_{Dp}$	$C_{Di}$
1	0.5668	0.0323	0.0155	0.0168
2	0.5653	0.0319	0.0148	0.0171
3	0.5651	0.0321	0.0150	0.0171

(b) Balance data for  $\alpha = 8.22$  deg

Balance run	$C_L$	$C_D$
1	0.5738	0.0319
2	0.5722	0.0318
3	0.5722	0.0319
4	0.5709	0.0319

Figure 14. Wake and Balance Measurement Repeatability

During this wind tunnel experiment, vortex generators were mounted on the model in order to determine the accuracy of wake surveys in measuring drag increments due to configuration changes. Measured total wake drag increments were found to be within one drag count of balance drag increments. Note that this difference is the same as the scatter in the balance drag data (fig. 14). These results not only demonstrated excellent accuracy in measuring wake drag increments, but also provided the increments of profile drag and induced drag associated with the addition of vortex generators.

#### Aftbody Drag Tests

Wake surveys were conducted with various fuselage models of transport airplanes in order to improve our understanding of aftbody flowfields and the drag associated with them. Contrary to most military transports, civil transports feature moderate aftbody upsweep with a correspondingly smaller contribution to drag. The vortices shed from such aftbodies are relatively weak, but their associated drag must nevertheless be understood when seeking opportunities for airplane drag reduction.

Aftbody drag experiments were carried out in the Boeing Research Wind Tunnel in Seattle at 0.18 Mach number and 1.18 million Reynolds number per foot. In all tests, the fuselage was supported by wing stubs extending through the tunnel side walls that are 5 feet apart (fig. 15). Notice that in this test setup wing lift distribution and, hence, wing induced downwash at the location of the tail were not realistically simulated. The wing tips, in turn, were

mounted on an external balance, situated below the test section. This allowed a comparison of wake survey drag measurements with balance drag.

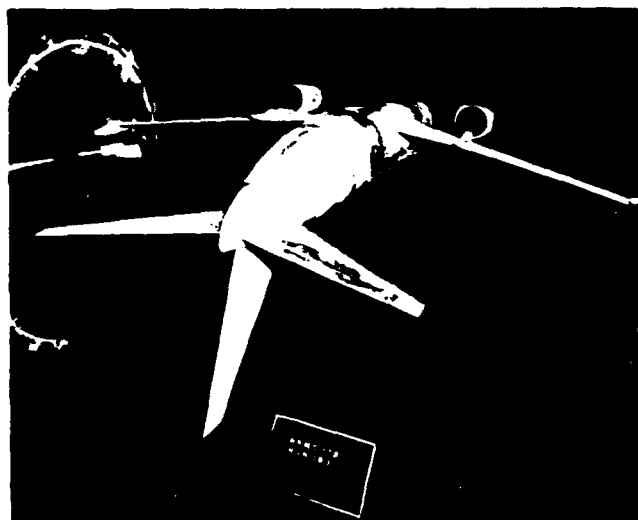


Figure 15. Aftbody Drag Test in Boeing Research Wind Tunnel

Parametric studies investigating the effect of aftbody length and upsweep angle on 7-7 fuselage drag provided quantitative data for vortex drag and profile drag as functions of angle of attack (ref. 24). As shown in the example of figure 16, vortex drag of upswept and symmetric aftbodies of civil transports can be measured in wake surveys with very little data scatter even though aftbody vortex drag is indeed very small.

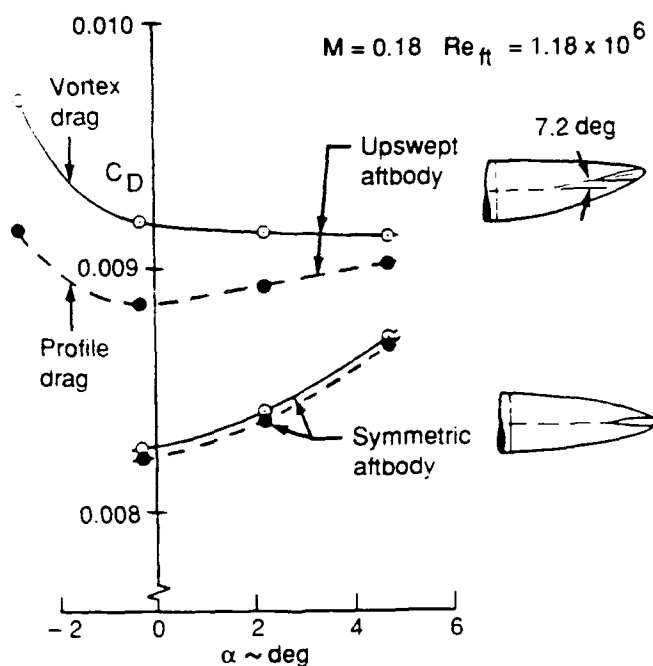


Figure 16. Drag Components of Symmetric and Upswept Aftbody Configurations

Wake measurements of upsweep drag of the 737 are compared in figure 17 with balance data. This kind of drag is defined as the difference in drag between symmetric and upswept aftbodies at the same test condition. As seen, wake drag is well within the uncertainty band of the force measurements providing further demonstration for the accuracy of three-dimensional wake measurements.

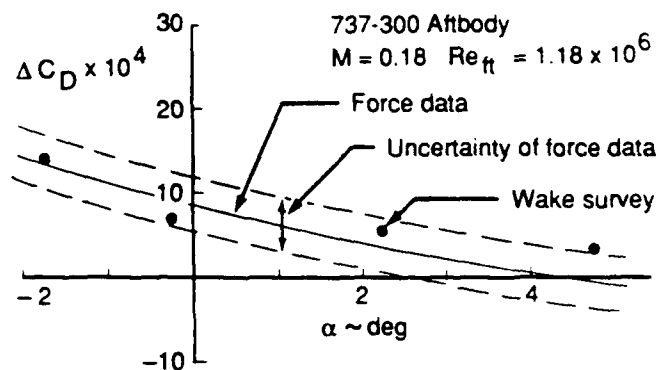


Figure 17. Upsweep Drag From Balance and Wake Surveys

### Conclusions

The paper describes the wake survey methodology developed at Boeing for the purpose of measuring the components of drag of low-speed, high-lift configurations. Important elements of this technique including mechanical probe traverser and pneumatic probe design, refinement of the underlying theory, and data reduction procedures are still under development at the present time. However, the technique has already been successfully applied in several wind tunnel tests as shown in this paper. The following valuable features of this measuring technique should be noted:

- They provide separate measurements of induced drag, profile drag, and lift.
- Measurement accuracy and data repeatability are comparable to balance measurements even though lift and drag data are the composites of a large number of individual measurements.
- Small increments in individual components of drag due to minor configuration changes can be measured accurately.
- Spanwise distributions of lift can be obtained. This is of value in high-lift aerodynamics since the small flap sizes of most high-lift models make it extremely difficult to measure spanlift data using surface pressure taps. However, all



spanwise wing data measured in wake surveys should be interpreted with caution since they are usually distorted to some degree by wake rollup and, hence, are influenced by practical limitations on the location of the plane in which the survey is conducted.

- e. Wake surveys provide spanwise distributions of profile drag and induced drag, which are of value in diagnosing the effects of local changes to the configuration geometry.
- f. During each wake survey a large number of velocity and pressure data are recorded which can serve as validation data for CFD codes in addition to providing lift and drag data.

### Acknowledgements

I would like to acknowledge the technical contributions of my present and former colleagues at Boeing, in particular, Messrs. P. Bogataj, J. Crowder, T. Hallstaff, M. Hudgins, D. Kotker, R. Stoner, and E. Tinoco. I would also like to thank Dr. J. McMasters, and Messrs. M. Mack and K. Moschetti for their review and comments on the draft of this paper.

### References

1. Crowder, J. P., "Quick and Easy Flow Field Surveys," *Astronautics and Aeronautics*, November 1980
2. Maskell, E. C., "Progress Towards a Method for the Measurement of the Components of the Drag of a Wing of Finite Span," *RAE Technical Report 72232*, 1972
3. Schlichting, H., *Boundary-Layer Theory*, 6th ed., McGraw-Hill, 1968
4. Betz, A., "A Method for the Direct Determination of Profile Drag," *ZFM*, vol. 16, 42, 1925 (in German)
5. Wu, J. C., J. E. Hackett, and D. E. Lilley, "A Generalized Wake-Integral Approach for Drag Determination in Three-Dimensional Flows," *AIAA Paper 79-0279*, January 1979
6. Hackett, J. E. and J. C. Wu, "Drag Determination and Analysis from Three-Dimensional Wake Measurements," *ICAS Paper No. S2-644*, August 1982 (text not available)
7. Hackett, J. E. and A. Sugavanam, "Evaluation of a Complete Wake Integral for the Drag of a Car-Like Shape," *SAE Paper 840577*, February 1984
8. Onorato, M., A. F. Costelli, and A. Garrone, "Drag Measurement Through Wake Analysis," *SAE Paper 840302*, 1984
9. Chometon, F. and J. Laurent, "Study of Three-Dimensional Separated Flows, Relation between Induced Drag and Vortex Drag," *European Journal of Mechanics, B/Fluids*, vol. 9, No. 5, 1990, pp. 437-455
10. Weston, R. P., "Refinement of a Method for Determining the Induced and Profile Drag of a Finite Wing from Detailed Wake Measurements," PhD thesis, University of Florida, 1981
11. Batchelor, G. K., "Axial Flow in Trailing Line Vortices," *Journal of Fluid Mechanics*, vol. 20, part 4, 1964, pp. 645-653
12. El-Ramly, Z., W. J. Rainbird, and D. G. Earl, "Wind Tunnel Measurements of Rolling Moment in a Swept-Wing Vortex Wake," *Journal of Aircraft*, vol. 13, No. 12, December 1976, pp. 962-967
13. El-Ramly, Z. M. and W. J. Rainbird, "Effect of Simulated Jet Engines on the Flowfield behind a Swept-Back Wing," *Journal of Aircraft*, vol. 14, No. 4, April 1977, pp. 1343-1349
14. El-Ramly, Z. M. and W. J. Rainbird, "Computer-Controlled System for the Investigation of the Flow behind Wings," *Journal of Aircraft*, vol. 14, No. 7, July 1977, pp. 668-674
15. El-Ramly, Z. M. and W. J. Rainbird, "Flow Survey of the Vortex Wake behind Wings," *Journal of Aircraft*, vol. 14, No. 11, November 1977, pp. 1102-1108
16. van Dam, C. P., K. Nikfetrat, I. C. Chang, and P.M.H.W. Vijgen, "Drag Calculations of Wings Using Euler Methods," *AIAA Paper 91-0338*, January 1991
17. Green, S. I. and A. J. Acosta, "Unsteady Flow in Trailing Vortices," *Journal of Fluid Mechanics*, vol. 227, 1991, pp. 107-134
18. Treaster, A. L. and A. M. Yocum, "The Calibration and Application of Five-hole Probes," *ISA Transactions*, vol. 18, No. 3, 1979, pp. 23-34

19. Schwarztrauber, P. N. and R. A. Sweet, "Efficient Fortran Subprograms for the Solution of Separable Elliptic Partial Differential Equations," *ACM Trans. Math. Software*, vol. 5, No. 3, 1979, pp. 352-364
  20. Rae Jr., W. H. and A. Pope, *Low Speed Wind Tunnel Testing*, 2nd ed., John Wiley & Sons, New York, 1984
  21. Tinoco, E. N., "CFD Applications to Complex Configurations: A Survey," in *Applied Computational Aerodynamics*, vol. 125 of *Progress in Aeronautics and Astronautics*, AIAA, 1990, pp. 559-584
  22. Brune, G. W. and T. H. Hallstaff, "Wing Span Loads of Complex High-Lift Systems from Wake Measurements," *Journal of Aircraft*, vol. 22, No. 9, September 1985, pp. 831-832
  23. Brune, G. W. and P. W. Bogataj, "Induced Drag of a Simple Wing from Wake Measurements," SAE Paper 901934, October 1990
  24. Hallstaff, T. H. and G. W. Brune, "An Investigation of Civil Transport Aft-Body Drag Using a Three-Dimensional Wake Survey Method," AIAA Paper 84-0614, March 1984
-

# FLOW PREDICTION OVER A TRANSPORT MULTI-ELEMENT HIGH-LIFT SYSTEM AND COMPARISON WITH FLIGHT MEASUREMENTS

By

P. M. H. W. Vijgen<sup>1</sup>, J. D. Hardin<sup>2</sup>, L. P. Yip<sup>3</sup>

## Abstract

Accurate prediction of surface-pressure distributions, merging boundary-layers and separated-flow regions over multi-element high-lift airfoils is required to design advanced high-lift systems for efficient subsonic transport aircraft (Ref. 1). The availability of detailed measurements of pressure distributions and both averaged and time-dependent boundary-layer flow parameters at flight Reynolds numbers is critical to evaluate computational methods and to model the turbulence structure for closure of the flow equations. Several detailed wind-tunnel measurement at sub-scale Reynolds numbers have been conducted to obtain detailed flow information including the Reynolds-stress components (e.g. Refs. 2&3).

As part of a subsonic-transport high-lift research program flight experiments are conducted using the NASA-Langley B737-100 research aircraft (see Figure 1) to obtain detailed flow characteristics for support of computational and wind-tunnel efforts. Planned flight measurements include pressure distributions at several spanwise locations, boundary-layer transition and separation locations, surface skin friction, as well as boundary-layer profiles and Reynolds stresses in adverse pressure-gradient flow.

In the initial phase of the flight program, surface-pressure distributions, skin-friction and flow-visualization measurements were obtained on the triple-slotted flap system of the research aircraft. A range of flap settings for angles of attack up to stick-shaker speed were investigated at several flight altitudes, resulting in Reynolds numbers (based on mean-average chord and freestream speed) between 10 and 20 million, and Mach numbers between 0.18 and 0.36. For the highest flap setting, separated flow was measured over the vane element as the aircraft attitude was increased, evidenced by the vanishing skin-friction coefficient obtained from a Preston tube near the vane trailing edge (Figure 2).

To analyze the flight measurements and to predict the flow field with sufficient detail for the purpose of instrumentation sizing, several widely-used two-dimensional multi-element methods are employed for the present geometry, progressing from potential flow/integral boundary layer to N.S. methods (Refs. 4, 5, and 6, respectively). Figure 3 presents the predicted inviscid pressure

distribution obtained from a 2-D panel method for the five-element airfoil with a 40° flap setting. The paper will compare viscous computational results from several methods with the measured pressure distributions and skin-friction values at selected flight conditions.

Large favorable pressure gradients exist in the leading-edge region of the slat and the fixed leading edge of the airfoil (see Figure 3). Relaminarization (Ref. 7) of the flow from a turbulent attachment line due to the large flow acceleration and the possibility for subsequent crossflow instability and transition ahead of the laminar separation bubble can lead to significant Reynolds-number effects (Refs. 8 and 9). The paper will present an analysis of the flow field near the swept edges of the aircraft using a swept-wing boundary-layer method (Ref. 10) and boundary-layer stability theory.

## References

1. Brune, G. W. and McMasters, J. H., "Computational Aerodynamics Applied to High-Lift Systems," Progress in Aeronautics and Astronautics: Applied Computational Aerodynamics, Vol. 125, AIAA, New York, 1990, pp. 389-433.
2. Olson, L. E., and Orloff, K. L., "On the Structure of Turbulent Wakes and Merging Shear Layers of Multi-Element Airfoils," AIAA Paper 81-1238, June 1981.
3. Brune, G. W., and Sikavi, D. A., "Experimental Investigation of the Confluent Boundary Layer of a Multi-Element Low-Speed Airfoil," AIAA Paper 83-0566, Jan. 1982.
4. Stevens, W. A., Goradia, S. H. and Braden, J. A., "Mathematical Model for Two-Dimensional Multi-Component Airfoils in Viscous Flows," NASA CR-1843, 1971.
5. Drela, M., "Newton Solution of Coupled Viscous/Inviscid Multi-Element Airfoil Flows," AIAA Paper 90-1470, June 1990.
6. Mavriplis, D., "Turbulent Flow Calculations using Unstructured and Adaptive Meshes," ICASE Report 90-61, NASA CR 182102, Sept. 1990.
7. Launder, B. E. and Jones, W. P., "On the Prediction of Relaminarization," ARC CP 1036, 1969.

-----  
<sup>1</sup>High Technology Corp., Hampton, VA  
<sup>2</sup>North-Carolina State University, Raleigh, NC  
<sup>3</sup>NASA Langley Research Center, Hampton, VA

8. Hardy, B. C., "Experimental Investigation of Attachment-Line Transition in Low-Speed High-Lift Wind Tunnel Testing," AGARD CP 438, Proceedings of the Symposium on Fluid Dynamics of Three-Dimensional Turbulent Shear Flows and Transition, Turkey, 1988, pp. 2-1 to 2-17.
9. Meredith, P. "Private Communication". Feb. 1991.
10. Kaups, K. and Cebeci, T., "Compressible Laminar Boundary Layers with Suction on Swept and Tapered Wings," Journal of Aircraft, Vol. 14, No. 7, July 1977, pp. 661-667.

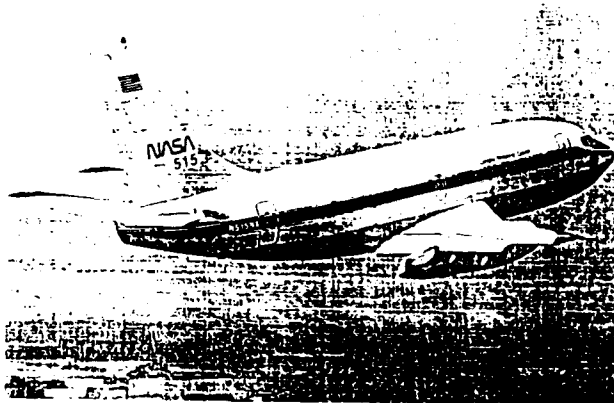


Figure 1. NASA515 ATOPS Research Aircraft (B737-100) in Flight

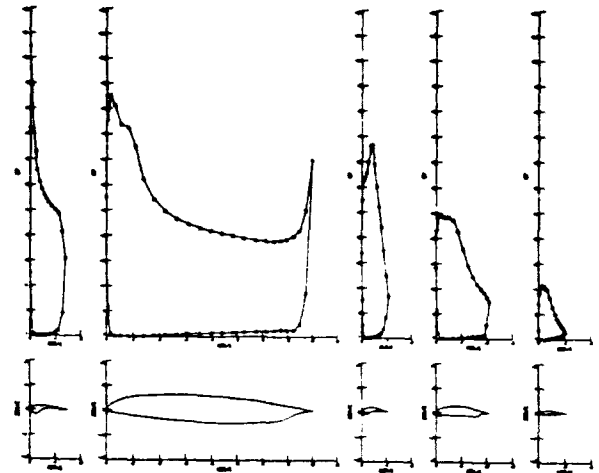


Figure 3. Inviscid 2-D Surface-Pressure Distribution over Research Aircraft Geometry,  $M = 0.25$ ,  $\alpha = 4^\circ$ , 40 degree Flap Setting.

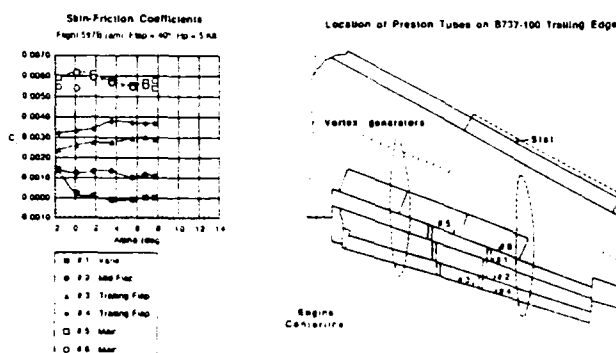


Figure 2. Measured Skin-Friction Coefficients at Trailing-Edge of Main Airfoil and Flaps

ASSESSMENT OF COMPUTATIONAL ISSUES  
ASSOCIATED WITH ANALYSIS OF HIGH-LIFT SYSTEMS

R. Balasubramanian<sup>\*</sup>  
Spectrex Inc., Gloucester, Virginia

and

Kenneth M. Jones<sup>++</sup> and Edgar G. Waggoner<sup>+++</sup>  
NASA Langley Research Center

Abstract

Thin-layer Navier-Stokes calculations for wing-fuselage configurations from subsonic to hypersonic flow regimes are now possible. However, efficient, accurate solutions for using these codes for two- and three dimensional high-lift systems have yet to be realized. A brief overview of salient experimental and computational research is presented. An assessment of the state-of-the-art relative to high-lift system analysis and identification of issues related to grid generation and flow physics which are crucial for computational success in this area are also provided. Research in support of the high-lift elements of NASA's High Speed Research and Advanced Subsonic Transport Programs which addresses some of the computational issues is presented. Finally, fruitful areas of concentrated research are identified to accelerate overall progress for high lift system analysis and design.

1. Introduction

An area of special interest to aerospace designers is high-lift systems. Future transport aircraft will have multiple requirements playing important roles in their design. These requirements include improved energy efficiency, reduced noise, and lower maintenance costs. Improved high-lift concepts for subsonic transports may result in designs which have increased section thicknesses, larger aspect ratios, lower sweeps, optimized multi-component designs, highly integrated propulsion systems, and integrated pneumatic concepts such as circulation control. Conversely, transports designed for supersonic cruise typically have geometric characteristics (highly swept, slender wings) which do not lend themselves to efficient aerodynamics at low subsonic speeds and moderate-to-high angles of attack (flight conditions associated with takeoff and climb-out). The need for high-lift augmentation concepts is further accentuated by contemporary community noise standards and traffic congestion at Air Traffic Control stations. While there is ongoing research

---

<sup>\*</sup> Senior Scientist

<sup>++</sup> Aerospace Engineer, Subsonic Aerodynamics Branch

<sup>+++</sup> Head, Subsonic Aerodynamics Branch

in this area at national research laboratories and private industry, (Brune and McMasters<sup>1</sup> provide an extensive review of computational high-lift design in practice at industry), a critical need exists for further innovations. For this to be realized, major breakthroughs in several areas must occur. From a computational perspective improved methods are needed to analyze geometrically complex systems and include key physics, such as flow separation, transition and turbulence, which dominate the flow fields. This paper attempts to review some of the issues which are crucial for computational fluid dynamics (CFD) to truly complement ground and flight based research and development for advanced high-lift systems.

Advanced transport designs currently receiving considerable attention include configurations designed for supersonic cruise, such as the High Speed Civil Transport (HSCT), as well as more conventional subsonic transports. High-lift systems for subsonic transports, typically use deflected leading edge slat surfaces and trailing edge slotted flaps for lift augmentation, see Figure 1. Figure 1a shows a relatively simple 3-component system consisting of a main element, slat and single slotted flap configuration which was tested by Lockheed-Georgia<sup>2</sup>. A more complex system shown in Figure 1b depicts a double slotted trailing-edge flap in addition to the slat and main element. This configuration was tested in the NASA Langley Low Turbulence Pressure Tunnel (LTPT)<sup>3</sup>. Subsonic high-lift systems, when fully deployed, can have regions of separation on the slat or flap, or in the cove regions. The subsonic systems may also have confluent boundary layers as a result of the strong interaction of shear layers. The subsonic high-lift systems are thus viscous dominated flow fields and have considerable geometrical complexity. Computational methods for high-lift systems must be carefully chosen to incorporate these varying requirements in flow

physics and geometry.

High-lift systems for supersonic configurations differ from those for subsonic transport systems both in system geometry and physics which dominate the flow. In order to achieve the desired high levels of supersonic cruise efficiency, many advanced supersonic configurations employ a low aspect ratio, highly swept wing. Unfortunately, these configurations typically have poor low-speed performance characteristics. Often, the low speed performance characteristics of these systems are enhanced either by attached flow or vortex flaps along the wing leading edge. Attached flow flaps are designed to suppress the formation of leading-edge vortices. Conversely, vortex flaps are designed to position the leading edge vortex within the bounds of the flap chord to provide a component of thrust which results from a vortex induced suction force. The trailing edge flap system for these configurations may consist of a segmented system of hinged flaps. Figure 2 shows the schematic of a low aspect ratio highly swept wing configuration tested at NASA<sup>4</sup>; the leading edge flap segments can be deflected independently about the hinge line. The trailing edge flap segments can also be deflected independently about the flap hinge lines. Also shown in Figure 2 are schematics of attached flow and vortex flap concepts. Grid systems to model these complex, segmented geometries must be highly versatile. In addition, the computational methods employed in the study of high-lift systems for supersonic configurations must be capable of capturing vortex structures with minimum smearing and phase distortion since the nature of the flow is highly vortical in these systems.

The problems of high-lift system analysis often include such issues as engine airframe integration and three-dimensional effects resulting from wing sweep, pylons, partial-span-flap deflections and tip ef-

fects. These attributes yield extremely complex geometries and attendant complex, interactional physical phenomena. While incremental progress by way of interactional methods or in development of quasi-three-dimensional analyses is being accomplished, we are not confident that such progress will computationally support innovative breakthroughs for future high-lift system design and development. Low cost, computationally efficient solutions (multi-grid, local time stepping) for three-dimensional steady flows for relatively simple geometries are available using thin-layer Navier-Stokes codes. We feel emphasis on these methods will yield substantial progress toward alleviation of the two major obstacles to accurate, efficient high-lift system analysis, viz., complex geometry and physics. Hence, our principal perspective will focus on Navier-Stokes solutions. In this paper, we explore some of the crucial issues which must be successfully addressed in order to develop computational methodology to analyze three-dimensional high-lift systems.

The following sections present a brief overview of experimental efforts useful for code calibration or validation along with a brief assessment of the computational state-of-the art. Geometric considerations are addressed within the context of the implications for grid generation. Issues related to code algorithms and dominant physics are briefly discussed for high-lift system applicability. Some of the salient efforts currently being pursued at NASA Langley are also presented. Concluding remarks consist of suggestions of major research areas where coordinated work is required to sustain progress for computational high-lift system analysis and design.

## II. Literature Overview

### Experimental database

While it is not the intent of this paper to review the available high-lift research literature, a brief overview of some salient reports is appropriate. Among the published data on multi-element airfoils, Braden, Whipkey, Jones and Lilley<sup>2</sup> report on a study of the confluent boundary layer development and separation characteristics on a NASA GAW-1. The section was equipped with a 29% chord single-slotted trailing edge flap and a 15% chord leading edge slat. Various combinations of slat and/or flap deflections and angle of attack were investigated in the study. The report contains surface pressure measurements on the airfoil as well as lift versus angle of attack curves for various flap/slat arrangements. Surface oil flows were used to provide flow visualization of boundary layer transition patterns. Boundary layer velocity profiles, turbulence intensities and Reynolds shear stresses for the configurations are reported under a separate cover<sup>5</sup>. A supplement to this report contains over 30000 sets of laser velocimetry (LV) derived boundary layer and wake data for the various combinations of geometric arrangements and angles of attack. In addition, off body flow field data were obtained using hot wire and LV.

Valerazo, Dominik, McGhee, Goodman and Paschal<sup>3</sup> have conducted multi-element airfoil optimization studies for maximum lift. This is a cooperative study between NASA and Douglas Aircraft Company. The primary focus of the study was to discern the high Reynolds number sensitivities of the multi-element airfoils at chord Reynolds numbers up to 16 million. The high-lift system consists of a double slotted flap and a single slotted slat as shown in Figure 2b. Among the data that are presented is the variation of  $C_{lmax}$  with Reynolds number, the variation of  $C_{lmax}$  with slat gap and the effect of flap

gap on  $C_{l,max}$ . No flow field surveys are reported from the study. In addition, there were no mechanisms used in the study for transition detection.

Olson and Orloff<sup>6</sup> report on the study of an airfoil with flap arrangement conducted in the NASA Ames Research Center 7 by 10 foot tunnel for Mach Number of 0.06 and a Reynolds number of 1.3 million. Surface pressure measurements, Reynolds stresses and detailed measurements of mean velocity in the boundary layers, wakes and merging layers are reported. The data should be considered purely incompressible and codes with compressible formulations will have difficulty in simulating this extremely low Mach number.

Wentz, Seetharam and Fisco<sup>7</sup> tested an aileron and a fowler flap applied to a GAW-1 airfoil. The experiment was conducted at  $M = 0.13$  and Reynolds number of 2.2 million. Aileron control effectiveness and hinge moments are presented for various gaps from 0 to 2% chord. For the fowler flap study, pressure distributions for various flap settings were obtained for a limited angle of attack range.

Adair and Horne<sup>8</sup> present pressure and velocity characteristics in the vicinity of the flap of a single slotted airfoil at a Mach number of 0.09 and a chord Reynolds Number of 1.8 million at the NASA Ames 7x10 foot tunnel. They report strong confluence effects on the boundary layer development on the flap suction surface due to the presence of a strong jet emanating from the slot flow. The flap is separation free except at the trailing edge where intermittent separation is observed. As a result of this the data may only be of limited use for steady state calculations. The flap wake development is reported to be asymmetric due to strong destabilizing curvature effects on the suction side. These data should therefore provide some guidance for studies of non-equilibrium effects on turbulence.

Morgan<sup>9</sup> and Morgan and Paulson<sup>10</sup> report on the study of static longitudinal and lateral directional aerodynamic characteristics of an advanced aspect ratio 10 and aspect ratio 12 supercritical wing transport model. The model was equipped with a high-lift system consisting of a full-span leading edge slat and partial-span and full-span trailing edge flaps. The Reynolds number of the tests varied from 0.97 to 1.63 million over a Mach number range of 0.12 to 0.20. The model was tested at angles of attack from -4 to 24 degrees and sideslip from -10 to 5 degrees. The model has engine nacelles, landing gear and movable horizontal tails. Six basic wing configurations were tested. These consisted of cruise (nested case), partial-span flap, full-span flap, full-span flap with low-speed ailerons and full-span flap with high-speed ailerons with slat and flap deflected to represent takeoff and landing conditions. Lift, drag and pitching moment data are presented for various cases.

Nakayama, Kreplin and Morgan<sup>11</sup> report detailed flow field measurements for a three-element airfoil with a conventional slat and single slotted flap. Reynolds stress distributions and mean flow measurements are presented on the main element and in the flap and wake regions. These suggest strong confluence effects in the flap region involving a jet-like stream from the flap-airfoil gap, the wake region of the main element with slat and the boundary layer on the flap itself.

The above cited works provides some data for code calibration or validation. However, there are large voids in the data base and measurements are not in sufficient detail to understand the complex flow physics that a computational study seeks to model. The flow in the gap region and pressure sides of many of these configurations needs to be documented



fully. There is also a need to obtain turbulent fluctuations data ( $u'$ ,  $v'$ ,  $u'v'$ ), transition location and mapping of flow confluence. Further studies in this area must be designed to closely follow the CFD needs to construct proper turbulence models and flow modules for Reynolds averaged Navier-Stokes calculations.

#### Computational database

Brune and McMasters<sup>7</sup> provide an excellent review of existing computational methods for analysis of high-lift systems. The status of these methods can be summarized as follows: there are presently no truly three-dimensional CFD methods for high-lift studies. Most three-dimensional studies use quasi-three-dimensional viscous approaches such as three-dimensional inviscid codes coupled with two-dimensional boundary layer codes. Existing viscous, two-dimensional airfoil codes can be classified, according to Ref.1, as, (I) Coupled Attached-Flow Methods, (II) Coupled Separated-Flow Methods, (III) Navier-Stokes Methods and (IV) Design and Optimization Methods. Categories (I), (II) and (IV) are widely used in industry today, while Category (III) is considered to be at the developmental stage. Both the attached and separated flow methods (Category (I) and (II)) are based on interactional boundary layer approaches while the Design and Optimization methods are clearly a patchwork of methods (I), (II) and simple inviscid analyses. In category (I), a boundary layer method is coupled to an inviscid flow calculation<sup>12,13,14</sup> and in (II), some form of modelling of the separated region is attempted<sup>15,16,17</sup>. The attached flow methods provide good agreement for lift at low angles of attack, where there is no flow separation. The separated flow models have been successful for some cases to compute maximum lift up to stall. These methods are at best useful in a limited fashion and do not promise to provide a successful methodology for high-lift system design. There

are also a few applications of two-dimensional Navier-Stokes solvers for high-lift configuration analysis in the literature. Schuster and Birckelbaw<sup>18</sup> and Shima<sup>19</sup> have obtained two-dimensional Navier-stokes solutions for multi-element airfoil systems using patched structured-grids. Using an unstructured-grid solver, Mavriplis and Martinelli<sup>20</sup> have also obtained solutions of two-dimensional multi-element airfoils. This work may well be a bellwether for high-lift system computations.

### III. Geometrical Considerations

Complex geometry issues associated with high-lift system analysis are non-trivial to say the least. Even when the problem is simplified to a wing with deflected surfaces (disregarding pylons, engines, flap track fairings, etc.), the task of surface modelling and field discretization is formidable. Geometries which are discontinuous in the streamwise and spanwise directions offer a significant challenge to the CFD community. Within these discontinuous regions flow interactions are occurring which can have significant and dominant effects on the resulting flow field. An example of this is the vortical flow occurring at the edge of a partial span leading-edge flap as it is deflected on a highly swept wing. The following sections address in some detail the manner in which CFD code developers are addressing these issues. From the structured grid perspective, single block, multi-block and Chimera schemes are each addressed. The promising work going on in the development of efficient unstructured grid generation techniques is also discussed. Finally, zonal methods are addressed including an example of their applications.

#### Structured-grid solvers

##### (a) Single and Multi-block methods

The rapid progress in CFD of the last

decade has made it possible to analyze simple wing-body geometries with relatively little effort. This is due, in part, to efficient grid generation techniques and acceleration techniques such as mesh sequencing, local time stepping and multi-grid techniques. Structured-grid algorithms, such as TLNS3D<sup>21,22,23</sup> and CFL3D<sup>24</sup>, have shown that for many steady flow problems, efficient solutions are possible using multigrid acceleration schemes. However, for the multi-element problems, the single block structured solvers are difficult to use. Fortunately, multi-block versions of these codes are currently being developed. These multi-block solvers may have the power to analyze complex domain problems by breaking the flow domain into smaller sub-domains or blocks of individual grid topology (such as grid system for each component of a multi-component system). The appropriate set of flow equations in each of these blocks can then be solved. Another significant development is the availability of powerful new grid generation packages which in the hands of experienced users can be used to do virtually any type of gridding (C-O; C-H; C-C) with relative ease. Among the most promising grid-generation packages are GRIDGEN<sup>25</sup> and EAGLE<sup>26</sup>. These are both user-friendly packages for generating two-dimensional and three-dimensional structured volume grids for finite volume analyses. Single or multi-blocked grids may be generated using these packages. The grid systems that may be constructed in the multi-blocks may or may not have  $C^0$  (common grid points) or  $C^1$  continuity (slope continuity as well as common grid locations) at the interface of these blocks. Depending on the nature of these interface conditions many variations of boundary coupling between various blocks are possible.

Previously, the utility of using structured-grid solvers for multi-element airfoil cases has been explored in the

context of two-dimensional flows. Using a structured-grid solver as the base code, Schuster and Birckelbaw<sup>18</sup> developed solutions for the multiple element airfoil problem by a multi-block approach using two-dimensional Navier-Stokes solutions. Figure 3 shows the schematic of the multiple-block grid topology used by them for a two-element airfoil. Figure 3a shows the arrangement of the various blocks in physical space and Figure 3b shows the arrangement in computational space. The line marked S is a line of singularity where all three blocks intersect and it requires special connectivity relations. The composite grid in Figure 3c is obtained by an iterative approach such that the grid systems in the regions retain  $C^0$  continuity at the block interfaces. The flow solver used in Ref.18 is a modified ADI scheme closely related to the Beam-Warming algorithm and the turbulence model used in the calculations is the Baldwin-Lomax model. Schuster and Brickelbaw obtain a reasonable comparison of  $C_L$  with experimental data at angles of attack up to stall as can be seen from the lift versus angle of attack curve shown in Figure 3d. They also state that their solution at the stall angle and beyond did not converge to a steady state solution. The curve shown by the dotted line in the figure is an average of the oscillatory solution. The  $C_p$  predictions on the main element obtained by them (not shown here) indicate some systematic variations from experimental measurements, the cause of which was unknown.

Shima<sup>19</sup> also obtained Navier-stokes solutions for a multi-element airfoil system using a patched grid system. The grid generation for the multiply connected domain in this work is again a non-trivial problem. Here, the composite grid is obtained in a two-step process. Initially, a potential flow solution around the multi-element airfoil is generated using a panel method. Next, conventional grid generation techniques<sup>27</sup>, using finite-dif-

ference methods, are employed where the computational co-ordinates are now the known potential and streamfunctions around the multi-element airfoil. This allows control of grid spacing required for the Navier-Stokes solutions near the body. The flow solver in Ref.19 uses an upwind (Total Variation Diminishing or TVD) scheme modified for low Mach number applications. Computed solutions are compared to experimental measurements of Foster, Irwin and Williams<sup>28</sup>. The results obtained for a two-element configuration (consisting of main element and flap) are shown in Figure 4 reproduced from Reference 19. The agreement between experimental data and computations for  $C_l$  is reasonable; the stall angle of attack predicted from the solution by the averaging method similar to that used in Reference 18 is under-predicted in the calculations. The authors postulate that this could be a result of numerical problems. The results for stall and post-stall cases are once again suspect since they are obtained by averaging an oscillatory solution obtained by the computer simulation.

While these results for two-dimensional cases suggest the utility of multi-block systems for high-lift analysis, further research is required to establish the usability of such methods for a highly complex three-dimensional configuration. For three-dimensional applications, the multi-block methods with rule based expert systems may provide a natural way for generating structured grids for analysis. Dannenhoffer<sup>29</sup> discusses the development of such a system for two-dimensional multi-body configurations. With elements in close proximity, the nature and quality of such grids and their resultant sensitivity to overall flow solution need to be examined closely. Many of the finite volume structured solvers are highly sensitive to grid quality. The inability of these methods to provide reasonable simulations in regions where the grid may be highly distorted and stretched, such as,

in the narrow regions of flow passage around the multi-element airfoil case, may limit the use of these methods for 3D-high-lift analysis. The complexity of the grid-generation and flow solver may also have some bearing on their eventual acceptance.

#### (b) Overlapping Grids/Chimera Schemes

In addition to the multi-block method, grid overlapping methods are another commonly used technique for domain decomposition. In overlapping schemes the sub-domains and the grid systems associated with them may overlap, or it may be possible to embed one sub-domain completely in another. In the "chimera scheme"<sup>30</sup>, the regions of a grid common to others is removed thereby creating voids or holes inside the grid. Baysal et. al.<sup>31</sup>, have looked at the quality of chimera solutions by studying the solutions with and without embedding for a test problem and conclude that there are only "minor" differences between the solutions. If this is true, chimera schemes may offer the flexibility to study multi-element airfoil flows. An example of a chimera grid developed at NASA Langley Subsonic Aerodynamics Branch for the GAW-1 airfoil with a deployed slat is shown in Figure 5. Figure 5a is an example of a sub-domain which consists of the slat geometry. Each sub-domain (see, Figure 5a,b) contains a "hole" or void in it which is a region of overlap of another sub-domain. The void is identified for each sub-domain in a preprocessing step. The solution strategy for the composite flow field involves computation of flow fields in each sub-domain with the associated boundary values including those for the boundaries of the void region. Since the boundary values for the voids are generated iteratively (by solutions from the sub-domains that create the voids), convergence of these methods depends strongly on how well the boundary values are approximated.

Figure 6 shows Euler solutions obtained by Biedron<sup>32</sup> using CFL3D employing an overlapped grid option for an airfoil with a slat. The calculated conditions are at  $M=0.5$  and  $\alpha = 7.5^\circ$ . These excellent results suggest that the overlapped grid option may be exploited to generate grid structures over multi-component airfoils.

An important advantage of the chimera scheme or the overlapped grid methods is the relative ease with which structured-grids can be generated around "simple" sub-domains of a complex three-dimensional domain. Buning, Parks, Chan and Renze<sup>33</sup> describe the application of a chimera scheme for the space shuttle ascent geometry. The component grids were generated using a hyperbolic grid generation technique which is faster than elliptical grid generators. Due to the complexity of the geometry, the grid joining process does become somewhat involved at the intersection of geometrical components. Further innovation in the form of "collar grids"<sup>34</sup> were required to develop solutions for the shuttle ascent geometry. An example of a "collar grid" for a cylinder intersecting a curved surface is shown in Figure 7 (reproduced from Ref.34). Figure 7a shows the combined collar surface grid. The white region in the figure is the void in the cylinder and the plane surfaces. The collar grid separates the intersecting surfaces and acts as a transitional zone between them. Figure 7b shows a slice of the collar grid and the chimera grids around it.

The overlapping schemes and in particular, the chimera scheme provide a simple way to generate computational grids. However, further study is required to sort out any sources of error in such an approach before recommending these methods as a panacea for high-lift system analyses. Buning et.al.<sup>33</sup> point out that while the accuracy of their solutions improved with improved modelling of the geo-

metry, the accuracy required for wing loading analyses is significantly higher than obtainable with chimera schemes. Effective use of chimera is also limited, according to them, by difficulties for the scheme in implementing turbulence models based on length scales for multi-body configurations.

### Unstructured-grid methods

Navier-Stokes solvers using unstructured-grids (triangular, tetrahedral meshes) are relative newcomers to the field. While finite element methods using triangular and quadrilateral and tetrahedral elements have been used in the past, their applications have been limited to low Reynolds number flows. Mavriplis<sup>35</sup>, Mavriplis and Martinelli<sup>20</sup> and Mavriplis and Jameson<sup>36</sup> have led the way in developing viable solutions to flow over airfoils. The implementation of multigrid strategy and turbulence modelling for the two-dimensional cases are major assets to the flow solver used in Reference 20. At present several multi-component flows have been calculated using this version of the code and good agreement with experimental data has been obtained for many of these cases. For example, Reference 20 documents solutions of multi-element airfoils which show excellent agreement with experimental data using a two-equation ( $k-\epsilon$ ) model.

The advantage of using unstructured-grids for analyzing high-lift systems is obvious. They are capable of properly modelling all the geometric complexity associated with high-lift systems in a straightforward manner. Figure 8 shows an unstructured-grid system developed at Subsonic Aerodynamics Branch (SAB), NASA Langley Research Center, for the study of a fully deployed low speed multi-element airfoil. An important merit of these methods is the ease and ability to adapt to an evolving solution. By using Delaunay triangulation techniques, the re-gridding in the region of interest can be

carried out in  $O(N^{3/2})$  operations for 2-D applications and in  $O(N^{5/2})$  operations for 3-D applications.

While the unstructured-grid techniques offer ease of grid generation and grid adaptation, the solvers used in these methods do not appear as computationally efficient as the structured-grid solvers. Indeed, comparisons have found them slower by a factor of 3 to 4 for many test cases<sup>37</sup> (the estimate given is for a 2-D code here; the estimate for 3-D viscous flows is much worse for the same accuracy; see for example the timings given in Ref. 21 for viscous calculations). The relative merit of such comparisons is somewhat suspect, since these test problems have no geometrical complexity and thus belong naturally in the domain of structured-grid solvers. The unstructured-grid methods do provide the power to analyze complex flow problems that are difficult to analyze using structured-grid solvers. Thus the development of unstructured-grid technology is receiving considerable attention and is progressing rapidly at various laboratories.

However, many major hurdles remain to be overcome before we have available a good three-dimensional unstructured-grid solver for viscous flows. The most significant of these hurdles is related to the directional sensitivity of the viscous flows. While the triangulation or tetrahedral domain discretization does not have a preferred orientation, flows with boundary layers do have directional sensitivity (i.e., boundary layers grow normal to the surface). Hence, some directivity needs to be introduced into the grid generation (non-Delaunay and hence more time consuming) and solution algorithms (background grids for turbulence, generation of many levels of grid for multi-grid implementations, etc.). Thus, while the Euler solver implementation is rather straightforward for the unstructured meshes, the implementation for high

Reynold number viscous flows offers a significant challenge. At present, this complexity seems to be the stumbling block in extending these methods to three-dimensional viscous flow problems. Obviously, new development in this area needs to occur.

### Zonal Methods

In zonal methods, the computational domain is divided into sub-domains where grids are patched together. A discriminating feature of these techniques relative to multi-block or chimera schemes is that the sub-domains may have varying degrees of latitude in the modelled physics. Normally, the zonal boundaries will be two-dimensional surfaces and they will have to be regular. The zonal approach offers the ability to properly model the physics through solution approximation valid to particular zones. For example, a fully elliptic flow problem may be solved using a zonal method where the flow regime may be approximated by a parabolic system of equations in a large zone and by the full elliptic system in a smaller zone. Depending on the size of these domains a large savings in computational resources may occur. Sankar, Bharadvaj and Tsung<sup>38</sup> use a zonal approach employing a full Navier-Stokes solution zone embedded in an outer potential flow field to study an F5 wing and an isolated helicopter rotor in hover. They show a savings of roughly 50% in computational time over full Navier-Stokes solutions for similar accuracy.

From the perspective of high-lift system studies, zonal approaches offer possibilities that are yet to be fully explored. Using zonal approaches, it may be possible to couple structured-grids with unstructured meshes to develop a flexible approach to three-dimensional problems. Another application of this technique may be in the analysis of separated flows, where the thin-layer approximations may break down and a full Navier-Stokes solu-

tion may be required in some zones of the flow field. Such an approach has the potential for generating a computationally efficient and accurate prediction method.

#### IV. Algorithmic Issues

##### Differencing schemes

There are several issues related to algorithms for high-lift studies that need to be examined. Upwind schemes which perform very well for supersonic flows have been known to perform rather poorly for low subsonic flows<sup>39</sup>. Central difference schemes, which work well for subsonic flows do depend to a degree on carefully tuned artificial dissipation to stabilize calculations (blended second and fourth order dissipations, residual smoothing, etc.). However, for subsonic flow calculations the central differencing algorithm is probably the most well behaved. The accuracy of these two schemes should be studied on prototype problems by systematic application. Based on the outcome it may turn out that one particular solution algorithm is more suitable than the other for a given configurational analysis. An unstructured-grid algorithm, for example Mavriplis<sup>36</sup>, which uses central differencing schemes may be more suitable for subsonic configuration studies, while other unstructured-grid solvers such as that by Batina<sup>40</sup> and Frink<sup>41</sup> which use upwind-based schemes may be more suited for vortical flows. It is possible that no single scheme (central difference / upwind scheme) will be appropriate for all cases. For example, consider the low aspect ratio, highly swept wing case. Here an upwind based scheme with controlled dissipation (e.g., TVD schemes) should predict the formation of vortices and their evolution in space more accurately than the central difference method where some smearing of the vorticity may occur due to added dissipation in most models.

For unstructured-grid solvers, there are other issues related to their speed and accuracy that need to be fully explored, such as, whether vertex based or cell centered schemes are the most appropriate for the solver. The formal accuracy of these methods depends to a large degree on the particular reconstruction method chosen. Cell vertex schemes are more economical for three-dimensional (tetrahedral elements) unstructured grids<sup>42</sup>, while cell centered schemes are more robust compared to cell vertex schemes<sup>43</sup>. Efficient cell-centered schemes for three-dimensional problems are possible with tetrahedral elements as demonstrated by Frink<sup>41</sup>. There are also approaches which combine vertex based schemes with cell-centered approach for integration of fluxes (see Reference 43). The computational efficiency and accuracy of these approaches must also be examined in detail. Lomax<sup>44</sup> suggests that there needs to be a further examination of special forms of structured grids in 2D and 3D to serve as a means for understanding and evaluating unstructured grid solvers and their formal accuracies.

While many of these issues will be considered by code developers, the applied scientist working on high-lift system studies will probably be involved in developing methods and grids that will support solving flow fields around configurations with considerable geometrical complexities. It is quite conceivable that the most useful approach might be one that incorporates hybrid techniques. An example of this approach is a multi-zonal scheme employing hybrid computational algorithms, grid structures and/or flow equation models for the high-lift system configurations.

##### Flow physics

Progress in computational methods for high-lift systems strongly depends on the ability to model turbulence, and predict transition, flow separation and reattach-

ment. For subsonic transport systems, in deployed high-lift situations, there may be cove, leading-edge slat, trailing-edge flap or main element flow separation. In some of these cases, the separated flow may be a massive shear layer which interacts with a boundary layer developing on an element downstream. The current state of the art in CFD does not address massively separated flows adequately. This deficiency leaves CFD yielding rather impotent analyses for high-lift systems as a result of the inability to predict where the flow begins to break down.

There are also other important flow physics which CFD is at present unable to address. For example scale effects for high-lift systems do not show a consistent pattern<sup>45</sup>. These anomalies are difficult to simulate computationally as a result of the significant computational resources required to compute flow conditions at flight Reynolds numbers. Relaminarization is a phenomenon which often occurs on the main element of a high-lift system in the influence of a deployed slat. This results as the flow on the main element accelerates around the leading edge due to extremely favorable pressure gradients at high Reynolds numbers<sup>46</sup>. Viscous wake interactions is another area requiring further insightful studies.

There are also areas that require immediate attention from a computational viewpoint. For example, the status of turbulence modelling for aerodynamic flows is rather primitive. There are two types of problems to be addressed here. One involves a limited understanding of transitional flows and boundary layers and the other is the inability to properly model turbulence. As a result of the inability to predict transition, calculations are often run in full "laminar" or "turbulent" options for many code comparisons. However, most experimental data are obtained for mixed laminar/turbulent flow fields. Some codes such as TLNS3D can be

run in the tripped mode. That is, if the location of transition from the laminar to turbulent state is known, the code will be able to compute non-zero eddy viscosity in the turbulent region. Even this approach is inherently deficient since the initial evolution of turbulence (low turbulent Reynolds numbers,  $R_T < 500$ ) is not properly modeled by existing turbulence models. An improved understanding of transitional boundary layers and transitional zonal modelling is clearly needed. Narasimha<sup>47</sup> advocates using a semi-empirical approach to the problem.

The other problem relates to the actual turbulence modelling itself. Menter<sup>48</sup> evaluated the performance of four popular turbulence closure models for flows under adverse pressure gradients. The Baldwin-Lomax, Johnson-King, Baldwin-Barth and Wilcox's  $k-\omega$  models were implemented in an incompressible Reynolds-averaged Navier-Stokes solver (INS code). Menter concluded that "the three non-equilibrium models gave significantly better results than the algebraic Baldwin-Lomax model" under strong adverse pressure gradients. Conclusions, which are not discussed here, were also presented relative to the performance of the three models. The authors feel that similar rigorous studies are crucial to understand the performance of these and other proposed turbulence models for multi-component airfoils and wings.

In addition, we feel for multi-element airfoil and wing problems, turbulence models based on length scales are more likely to fail since the choice of the appropriate length scale is difficult to identify. Complex turbulence models which do not depend on length scales may be the only answer. Even after solving the length scale problem, experience with many higher moment methods has been that their performance may not be that attractive considering the additional complexities they introduce, see the discussion by Lumley<sup>49</sup> as well as the comparison of various

turbulence models conducted in the AFOSR-Stanford Turbulence Meeting<sup>50</sup>.

However, there are some promising new developments in turbulence modelling, such as, second-order closure<sup>51</sup> and the Re-Normalized Group (RNG) based models<sup>52</sup>, that have appeared over the horizon. Results obtained using RNG methods are compared in Figure 9 (reproduced here from Reference 52) with those using Baldwin-Lomax model for the RAE2822 airfoil case. Figure 9a presents the results obtained using RNG model and Figure 9b presents results obtained using Baldwin-Lomax model. Note that the RNG solutions improve the prediction of the shock structure relative to the Baldwin-Lomax model both in shock location and strength. This model has undergone further developments since that time and appears to be ready for application to two and three-dimensional solvers of multi-component configurations. For example, a modified RNG  $k-\epsilon$  formulation<sup>53</sup> has been shown to produce excellent agreement for the classical backward-facing step problem which all of the other turbulence models in use have difficulty in predicting (see Reference 50 and the discussions pertaining to the backward facing step pp 275-283; pp 886-911). A notable feature of the RNG formulation is that the model constants are not ad hoc and are derived by a consistent perturbation analysis of the Renormalised Navier-Stokes equations. These models may provide an avenue to improve the prediction for high angle of attack problems where the effects of turbulence are much more pronounced. As more and more reliance is placed in optimizing configurations for maximum lift to drag ratios or minimum drag, we will be forced to examine in detail the agreement that these Navier-Stokes codes provide for integral quantities.

#### V. Ongoing work

The high-lift elements of NASA's High

Speed Research (HSR) and Advanced Subsonic Transport Program have provided the impetus for several significant high-lift efforts at Langley Research Center. The elements consist of a balanced experimental and computational research program. Experimental work supporting the HSR Program involves testing a series of configurations with different types of leading-edge high-lift devices (attached flow and vortex flaps) and planform variations (different leading edge sweeps and aspect ratios). Data obtained in these tests include force and moment, surface pressure and flow visualization. A complementary computational program is being pursued to study the grid generation tools and computational methods required to analyze this class of vehicle. Due to the complexity of modelling the three dimensional high-lift system, the initial CFD effort concentrated on gridding and analyzing geometries with undeflected leading-edge devices. Once the cruise geometry is successfully analyzed the next step will be to analyze the high-lift configuration. Figure 10a is an example of an HSTC concept that was designed for a cruise Mach number of 3.0. This design consists of a blended wing body with a flattened or "platypus" forebody. The configuration was analyzed by Victor Lessard of Vigyan with the multi-block version of CFL3D<sup>24</sup> (a thin layer, upwind N-S code). Figure 10b shows a comparison of the surface pressure distributions obtained computationally with results obtained in the 8-foot Transonic Pressure Tunnel at NASA Langley. The comparisons shown are for two cross sections on the configuration. The first is near the nose and the second is just upstream of the wing crank. Both comparisons show excellent agreement between the computations and experiment. The pressure peaks indicative of vortex flow are well captured by the analysis. Due to the agreement between theory and experiment obtained on this and other cruise geometries, we feel the method will prove useful for analyzing simple three-



dimensional high-lift systems such as full-span attached flow flaps.

Another CFD effort that is being pursued by Kevin Kjerstad of NASA Langley in support of the HSR Program includes evaluation of the three-dimensional unstructured grid generator and Euler code developed by Frink, et al.<sup>4</sup>. The grid generation method is based on the "advancing front technique" and uses a structured background grid to ease implementation of the grid generation process. An example of an unstructured grid generated for a generic high speed research configuration is shown in Figure 11a. The Euler solver, known as USM3D, is an upwind scheme developed for solving the three-dimensional Euler equations on unstructured tetrahedral meshes. The code uses a cell-centered, finite-volume formulation with flux-difference splitting for spatial discretization. Experimental and USM3D results on the generic configuration at subsonic speeds for lift, drag and pitching moment are compared in Figure 11b. Since the model has a sharp leading edge, the point of separation for the primary vortex is well defined and the Euler results should be reasonable. The comparisons in Figure 11b show excellent agreement between theory and experiment for all three quantities at the three angles of attack analyzed. The next step is to use the codes to analyze a three-dimensional high-lift system. The vortex flap concept is a good candidate for analysis since it has a sharp leading edge, hence, the separation point is known a priori. This configuration will be analyzed in the near future.

One of the efforts supporting the Advanced Subsonic Transport Program at NASA Langley involves assessing the capability of various computational techniques for high-lift system application. We are currently involved in assessing the capability of a structured-grid solver (TLNS3D) to predict the subsonic characteristics of a standard low-speed airfoil (GAW-1) at

angles of attack up to  $C_{l,max}$ . This solver is a transonic code with a central differencing scheme, that can be run with either the Baldwin-Lomax or the Johnson-King turbulence model. Experimental data for a GAW-1 airfoil obtained by McGhee and Beasley<sup>54</sup> has been chosen for computational studies. This particular airfoil has geometrical characteristics (thick airfoil section with blunt trailing edge) which can pose problems for a grid sensitive algorithm. Tests were conducted between Mach numbers of 0.10 to 0.28 and angles of attack from  $-10^\circ$  to  $24^\circ$ . The low Mach number data at  $M=0.15$  has been chosen by us to study the robustness of the transonic structured-grid code. For the experiments, transition was fixed at 8% chord and the solver has the capability to compute laminar calculations up to this location and thereafter, switch to a turbulent calculation. The results presented below are only for the Baldwin-Lomax model since the performance of the Johnson-King model was affected by grid quality for this particular geometry. Figure 12 shows the  $C_p$  comparison between experimental measurements and computation using the Baldwin-Lomax turbulence model in TLNS3D. Computations employing the Johnson-King model were adversely affected by grid quality for this particular geometry and are not presented here. The agreement between the computed solution and experimental data is extremely favorable up to  $8^\circ$  angle of attack. Beginning at  $12^\circ$ , the computed pressure distributions show differences with experimental data at the trailing edge region. These differences become progressively worse at higher angles of attack. At  $12^\circ$  and beyond, it was noted by the experimenters that there was trailing edge flow separation which became progressively larger with angle of attack. The computed wall shear stress data as well as Mach contour plots (not shown here) do indicate trailing edge flow separation at  $12^\circ$  which becomes progressively worse at higher angles of attack. The degree and extent of agreement between

experiment and theory in this separated zone is suspect since the included physics is deficient e.g, thin-layer approximation which breaks down in the vicinity of separation point (no streamwise viscous stress variation) and the turbulence model (Baldwin-Lomax model) used. The comparison of sectional lift versus angle of attack (Figure 13) shows that the lift is predicted rather well by the code up to an angle of attack of  $18^\circ$ , indicating that sectional lift is insensitive to the minor differences in pressure distribution observed. The drag comparison (Figure 14) shows the predictions are only accurate up to an angle of attack of  $8^\circ$ . Obviously, minor differences that are observed in pressure distributions have a larger influence on  $C_d$  than  $C_l$ . Since, lift to drag ratio issues may dominate future system designs, the challenge to code validators is obvious.

Bonhaus, Anderson and Mavriplis<sup>55</sup> are using the unstructured-grid solver of Mavriplis to analyze multi-component airfoils for subsonic transport applications. The experimental data used in this comparison is from a Douglas four element configuration tested at the Langley LTPT tunnel. The computed pressure distribution over the elements have been compared against experimental data for angles of attack of 0, 12, 18 and 20 degrees. These results were obtained using the Baldwin-Lomax turbulence model. The agreement between experimental data and computations are extremely good up to  $C_{lmax}$ . At 0 degree angle of attack, (not shown here), the biggest difficulty is in predicting the slat pressure distribution in the cove region. At higher angles of attack, the computed results agree very well with measurements on the slat surface, while the prediction is off from experiment in the auxiliary flap as can be seen from Figure 15a. At 20 degree angle of attack, Figure 15b, the disagreement is quite pronounced for both the main and aft flap indicating the wake viscous interactions are not fully cap-

tured by the code. Figure 16 shows the lift vs angle of attack curve. Again, the predictions are in good agreement with experiment up to  $C_{lmax}$ . Beyond  $C_{lmax}$ , the computed lift curve shows an increase in lift with angle of attack, demonstrating the inability of the method to predict stall behavior.

Previously in this paper discussions and examples of grids for multi-element airfoils have been presented. As has been stated, the gridding and analysis of a three-dimensional high-lift system is quite difficult. The grid generator and Euler code described above (Reference 41) were used by Dr. Mohammad Takallu of Lockheed and Dr. Simha Dodbele of Vigyan to study a multi-element wing. The wing chosen was a unswept, semi-span wing consisting of a main element and full-span, double slotted flap. The surface grid on the configuration and part of the symmetry plane mesh is shown in Figure 17. Even though this geometry is complex, the grid generation process was relatively straight forward. As data become available, the results of the Euler analysis will be evaluated to determine the utility of the code for high-lift configuration analysis for attached flow conditions.

Another difficulty with high-lift system design and analysis is the proximity of the ground and the effect this has on the flow field surrounding the configuration. Often there is a significant effect on lift due to the interference of the wing flow field and the ground. Figure 18 is an example of an unstructured grid developed by Kyle Anderson of NASA Langley for a multi-component airfoil in ground effect. The airfoil is placed in the proper orientation above the ground and then the grid is generated using Delaunay triangulation techniques. The ground is simulated by adding a zero transpiration boundary condition to the boundary below the airfoil. To analyze other ground heights for this same airfoils, the grid

must then be regenerated with the airfoil placed in its new position. Due to the adaptability of unstructured grid generation techniques, this requires relatively little input by the researcher.

Ground effect analysis can also be done using a structured grid approach. Fig. 19 is an example of a structured grid generated by Dr. Steve Yaros of Langley for a National Aerospace Plane (NASP) type configuration in close proximity to the ground. In this case the analysis was done using a Navier-Stokes code; so a no slip boundary condition was imposed at the wall. Again, to analyze the configuration at different ground heights requires regeneration of the grid. For this simple geometry in Figure 19 the process is straightforward. However, for more complex configurations, generating new multi-block grids could be time consuming.

#### VI. Future Plans

Based on the discussions above it is possible to identify several areas where further coordinated work is needed.

(i) Generation of a data base that can be used for developing models of flow physics for computer simulation. This requires the generation of detailed L-V data, shear stress, energy and fluctuation measurements. These measurements pose a significant challenge for multi-component airfoils where there are narrow regions of flow. A systematic effort should also be made to compare computed solutions using heuristic models with existing data bases.

(ii) Further research is necessary to develop three-dimensional structured and unstructured-grid generation techniques and development of hybrid (zonal) methods for viscous flows. Intelligent use of an expert system may allow development of efficient three-dimensional blocked grids for geometrically complex configurations.

(iii) A concerted effort should be made to develop new turbulence models for separated flows and to test these models in flow codes. There are few and relatively poor performing turbulence models for separated flows currently available. Progress made in this field is bound to provide rich rewards. There are currently several good candidates such as the model of Wilcox<sup>56</sup>, RNG models, and second order closure models, that need to be validated.

(iv) The need for co-ordinated efforts between industry and government laboratories needs to be addressed. With such vast areas of research to be done, a collaborative industrial-government consortium would serve to reduce duplication of data and effort at this critical juncture.

#### References

1. Brune, W. and McMasters, J. H., "Computational Aerodynamics Applied to High-lift systems," In Applied Computational Aerodynamics, pp. 389-433, AIAA, 1990.
2. Braden, J. A., Whipkey, R. R., Jones, G. S. and Lilley, D. E., "Experimental Study of the Separating Confluent Boundary-Layer Volume I- Summary," NASA CR-3655, 1983.
3. Valarezo, W. O., Dominik, C. J., McGhee, R. J., Goodman, W. L. and Paschal, K. B., "Multi-Element Airfoil Optimization for Maximum Lift at High Reynolds Numbers," AIAA Paper 91-3332, September 1991.
4. Coe, P. L. and Weston, R. P., "Effects of Wing Leading-Edge Deflection on Low-Speed Aerodynamic Characteristics of a Low-Aspect-Ratio Highly Swept Arrow-Wing Configuration," NASA TP 1434, 1979.
5. Braden, J. A., Whipkey, R. R., Jones, G. S. and Lilley, D. E., "Experimental Study of the Separating Confluent Boundary-Layer Volume II - Experimental Data," NASA CR 166018, March 1983.
6. Olson, L. E. and Orlof, K. L., "On the Structure of Turbulent Wakes and Merging Layers of Multi-Element Airfoils," AIAA Paper 81-1248, June 1981.

7. Wentz, W. H. Jr., Seetharam, H. C. and Fisco, K.A., "Force and Pressure Tests of the GA(W)-1 Airfoil with a 20% Aileron and Pressure Tests with a 30% Fowler Flap," NASA CR-2833, June 1977.
8. Adair, D. and Horne, W. C., "Turbulent Separated Flow in the Vicinity of a Single Slotted Airfoil Flap," AIAA Paper 88-0613, January 1988.
9. Morgan, H. L., Jr., "Low-Speed Aerodynamic Performance of an Aspect-Ratio-10 Supercritical Wing Transport Model Equipped with a Full-Span Slat and Part-Span and Full-Span Double-Slotted Flaps," NASA TP 1805, April 1981.
10. Morgan, H. L. Jr. and Paulson, J.W., "Low-Speed Aerodynamic Performance of a High-Aspect Ratio Supercritical-Wing Transport Model Equipped with Full-Span Slat and Part-Span Double Slotted Flaps," NASA TP 1580, 1979.
11. Nakayama, A., Kreplin, H.P. and Morgan, H.L., "Experimental Investigation of Flow-field About a Multi-Element Airfoil," AIAA Journal, January 1990.
12. Stevens, W. A., Goradia, S.H. and Braden, J.A., "Mathematical Model for Two-Dimensional Multi-Component Airfoils in Viscous Flows," NASA CR1843, July 1971.
13. Morgan, H. L., Jr., "A Computer Program for the Analysis of Multi-Element Airfoils in Two-Dimensional Subsonic, Viscous Flows," NASA SP-347, March 1975.
14. Dvorak, F.A., and Woodward, F.A., "A Viscous/Potential Flow Interaction Analysis Method for Multi-Element Swept Wings," NASA CR-2476, November 1974.
15. Mani, K. K., "A Multiple Separation Model for Multi-Element Airfoils," AIAA Paper 83-1844, July 1983.
16. King, D.A., and Williams, B.R., "Developments in Computational Methods for High-Lift Aerodynamics," Aeronautical Journal, Vol. 92, No. 917, 1988, pp 265-288.
17. Cebeci, T., Chang, K.C., Clark, R.W. and Halsey, N.D., "Calculation of Flow over Multi-Element Airfoils at High Lift," Journal Of Aircraft, Vol. 24, No.8, 1988.
18. Schuster, D.M. and Brickelbaw, L.D., "Numerical Computation of Viscous Flow-fields about Multiple Component Airfoils," AIAA Paper 85-0167, January 1985.
19. Shima, E., "Numerical Analysis of Multiple Element High Lift Devices by Navier Stokes Equation using Implicit TVD Finite Volume Method," AIAA Paper 88-2574-CP, June 1988.
20. Mavriplis, D.J., and Martinelli, L., "Multigrid Solution of Compressible Turbulent Flows on Unstructured Meshes Using a Two-Equation Model," AIAA Paper 91-0237, January 1991.
21. Vatsa, V.N. and Wedan, B.W., "Development of a Multigrid Code for 3-D Navier-Stokes Equations and its Application to a Grid Refinement Study," Computers and Fluids, Vol. 18, No.4, 1990.
22. Vatsa, V. N., "Accurate Numerical Solutions for Transonic Viscous Flows over Finite Wings," Journal Of Aircraft, Vol. 24, No. 6, 1987.
23. Vatsa, V.N., Turkel, E., and Abolhasani, J.S., "Extension of Multigrid Methodology to Supersonic/Hypersonic 3-D Viscous Flows," Fifth Copper Mountain Conference on Multigrid Methods, 1991.
24. Thomas, J.L., Krist, S.T., and Anderson, W. K., "Navier-Stokes Computations of Vortical Flows Over Low Aspect Ratio Wings," AIAA Journal , Vol.28, No.2, 1990.
25. Steinbrenner, J.P., Chawner, J.R., and Fouts, C.L., "The GRIDGEN 3D Multiple Block Grid Generation System , Volume I: Final Report," WRDC-TR-90-3022.
26. Thompson, J.F., "Project EAGLE -Numerical Grid Generation System User's Manual, Vol.3: Grid Generation Code," USAF Armament Laboratory Technical Report, AFATL-TR-87-15, 1987.
27. Thompson, J.F., Thames, F.C. and Mastin, C.W. "TOMCAT- A Code for Numerical Generation of Boundary Fitted Curvilinear Coordinates on Field Containing Any Number of Two-Dimensional Bodies," J. Comp.Phys., Vol.24, 1977.
28. Foster, D. N., Irwin, H.P.A., and Williams, B.R., "The Two-Dimensional Flow Around a Slotted Flap," ARC Report and Memoranda No. 3681, 1970.
29. Dannenhoffer, J. F., III, "Computer-Aid-

- ed Block Structuring Through the Use of Optimization and Expert System Techniques," AIAA Paper 91-1589-CP, Honolulu, June 1991.
30. Steger, J.L., Dougherty, F.C. and Benek, J.A., "A Chimera Grid Scheme," Advances in Grid Generation, ASME, New York, FED-Vol.5, June 1983.
  31. Baysal, O., Fouladi, K., and Lessard, V. R., "Multigrid and Upwind Viscous Flow Solver on Three-Dimensional Overlapped and Embedded Grids," AIAA Journal, Vol.29, No. 6, 1991.
  32. B.Biedron, A. S & M Inc., Private Communications.
  33. Buning, P. G., Parks, S. J., Chan, W. M. and Renze, K.J., "Application of the Chimera Overlapped Grid Scheme to Simulation of Space Shuttle Ascent Flows," Proceedings of the Fourth International Symposium on Computational Fluid Dynamics, Vol I, pp.132-137, Sept. 1991.
  34. Parks, S. J., Buning, P. G., Steger, J.L. and Chan, W.M., "Collar Grids for Intersecting Geometrical Components Within the Chimera Overlapped Grid Scheme," AIAA Paper No. 91-1567-CP, Honolulu, June 1991.
  35. Mavriplis, D.J., "Multigrid Solution of the 2-D Euler Equations on Unstructured Triangular Meshes," AIAA Journal, Vol.26, July 1988.
  36. Mavriplis, D. J. and Jameson, A., "Solution Of the Navier-Stokes Equations on Triangular Meshes," AIAA Journal, vol. 28, No. 8, 1990.
  37. Mavriplis, D.J., "Accurate Multigrid Solution of the Euler Equations On Unstructured and Adaptive Meshes," NASA CR-181786, February 1989.
  38. Sankar, L.N., Bharadwaj, B.K. and Tsung, Fu-Lin, "A Three-Dimensional Navier-Stokes/Full Potential Coupled Analysis for Viscous Transonic Flow," AIAA Paper No. 91-1595-CP, Honolulu, June 1991.
  39. Hanel, D., Schwane, R. and Seider, G., "On the Accuracy of Upwind Schemes for the Solution of the Navier-Stokes Equations," AIAA Paper 87-1105, January 1987.
  40. Batina, J.T., "Accuracy of an Unstructured-Grid Upwind-Euler Algorithm for the Onera Wing," Presented at Accuracy Of Unstructured Grid Techniques Workshop, NASA LaRC, January 1990.
  41. Frink, N.T., Parikh, P. and Pirzadeh, S., "A Fast Upwind Solver for the Euler Equations on Three-Dimensional Unstructured Meshes," AIAA Paper No. 91-0102, January 1991.
  42. Barth, T. J., "A 3-D Upwind Euler Solver for Unstructured Meshes," AIAA Paper No. 91-1548-CP, Honolulu, June 1991.
  43. Hall, M. G., "A Vertex -Centroid Scheme for Improved Finite- Volume Solution of the Navier-Stokes Equations," AIAA Paper No. 91-1540-CP, Honolulu, June 1991.
  44. Lomax, H., "CFD in the 1980'S from One Point of View," AIAA Paper No. 91-1526-CP, Honolulu, June 1991.
  45. Woodward, D.S. , Hardy B.C. and Ashill, P. R., "Some Type of Scale Effects in Low-Speed High-Lift Flows," ICAS Paper 4.9.3, Jerusalem, 1988.
  46. Garner, P. L., Meridith, P.T. and Stoner, R.C., "Areas for Future CFD Development as Illustrated by Transport Aircraft Applications," AIAA Paper No. 91-1527-CP, Honolulu, June 1991.
  47. Narasimha, R., "Modelling the Transitional Boundary Layer", NASA CR-187487, 1990.
  48. Menter, F.R., "Performance of Popular Turbulence Models for Attached and Separated Adverse Pressure Gradient Flows," AIAA Paper No. 91-1784-CP, Honolulu, June 1991.
  49. Lumley, J.L., "Turbulence Modeling," J. App. Mechanics, Vol.50, No.12, 1983, pp.1-097-1103.
  50. Kline, S.J., Cantwell, B.J. and Lilley, G.M., "The 1980-81 AFOSR-HTTM-Stanford Conference on Complex Turbulent flows: Comparison of Computations and Experiment I, II, and III," Thermosciences Division, Mechanical Engineering Department, Stanford University, Stanford, Calif., 1981.
  51. Sarkar, S and Speziale, C. G., "A Simple Nonlinear Model for the Return to Isotropy in Turbulence," Phys. Fluids A, Vol. 2, No.1, January 1990.
  52. Martinelli, L. and Yakhot, V., "RNG-Based Turbulence Transport Approximations

with Applications to Transonic Flows," AIAA Paper 89-1950, June 1989.

53. Yakhot, V., Thangam, S., Gatski, T. B., Orszag, S.A. and Speziale, C.G., "Development of Turbulence Models for Shear Flows by a Double Expansion Technique," NASA CR-187611, July, 1991.

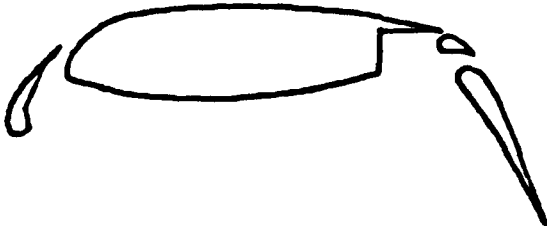
54. McGhee, R. J., and Beasley, W. D., "Low-Speed Aerodynamic Characteristics of a 17-Percent-Thick Airfoil Section Designed for General Aviation Applications," NASA TN D-7428, 1973.

55. Bonhaus, D., Anderson, K. and Mavriplis D., "Computed Flows of Sulfur Hexa-fluoride over Multi-element Airfoils," NASA TP to be published (1992).

56. Wilcox, D. C., "A Half-Century Historical Review of the  $k-\omega$  Model," AIAA Paper No. 91-0615, January 1991.

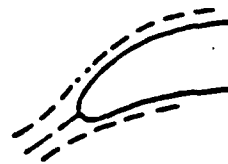


(a) Slat and single slotted flap (Ref.2)



(b) Slat and double slotted flap (Ref.4)

Figure 1: Examples of Multi-component Airfoil Configurations for Subsonic Transport High-lift Studies.



(a) Attached Flow Flap



(b) Vortex Flow Flap

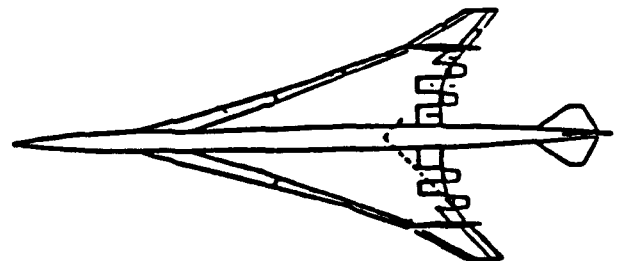
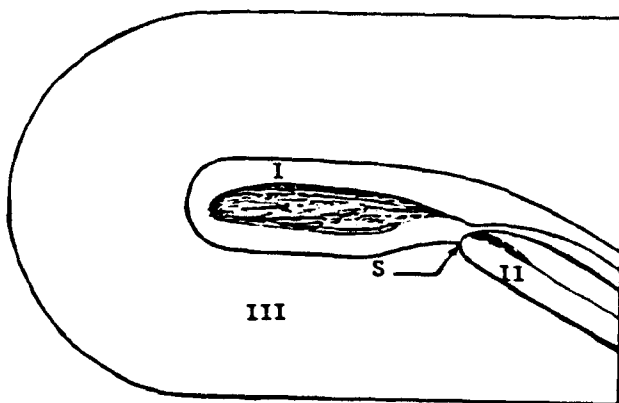
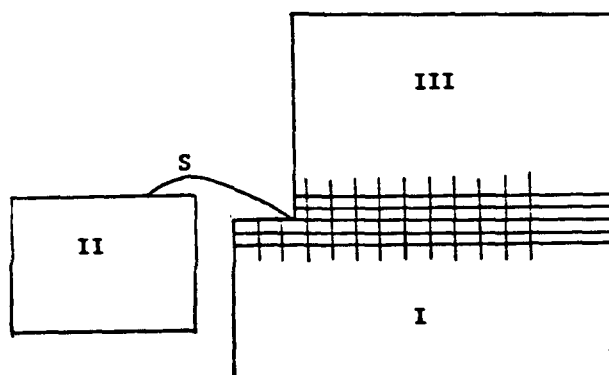


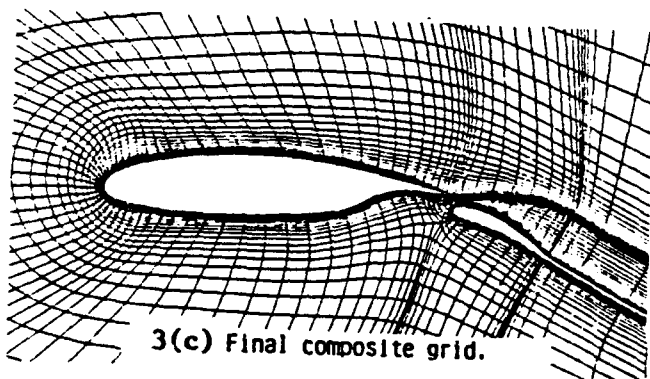
Figure 2: Schematic of a low aspect ratio highly swept arrow wing configuration with leading and trailing edge segmented flaps.



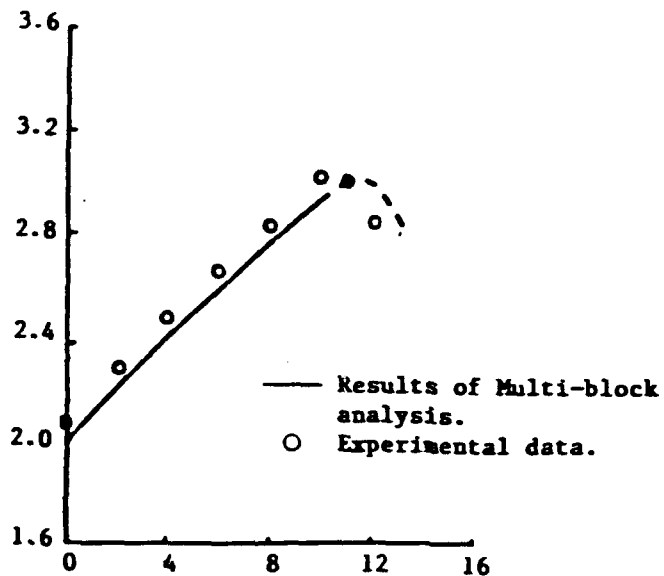
3(a) Patched grid system.



3(b) Patched computational space.

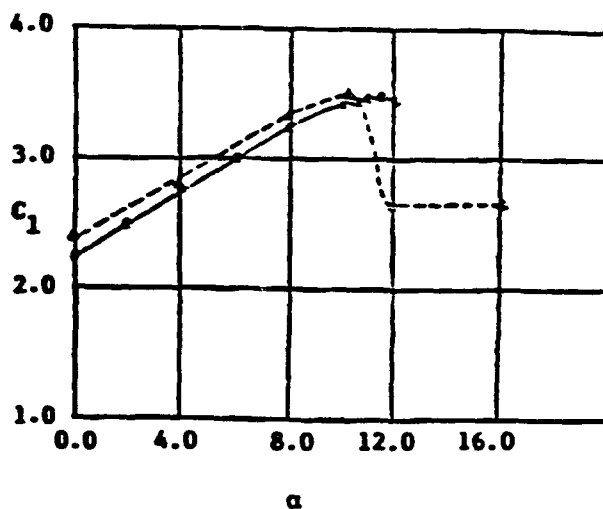


3(c) Final composite grid.



3(d)  $C_l$  vs  $\alpha$

Figure 3: Multi-block grid system and comparison of theoretical and experimental lift curves for a GAW-1 multi-element airfoil arrangement.



—○— Experimental results.  
--△-- Computational predictions.

Figure 4:  $C_l$  vs  $\alpha$  for a multi-airfoil arrangement from Ref. 19.

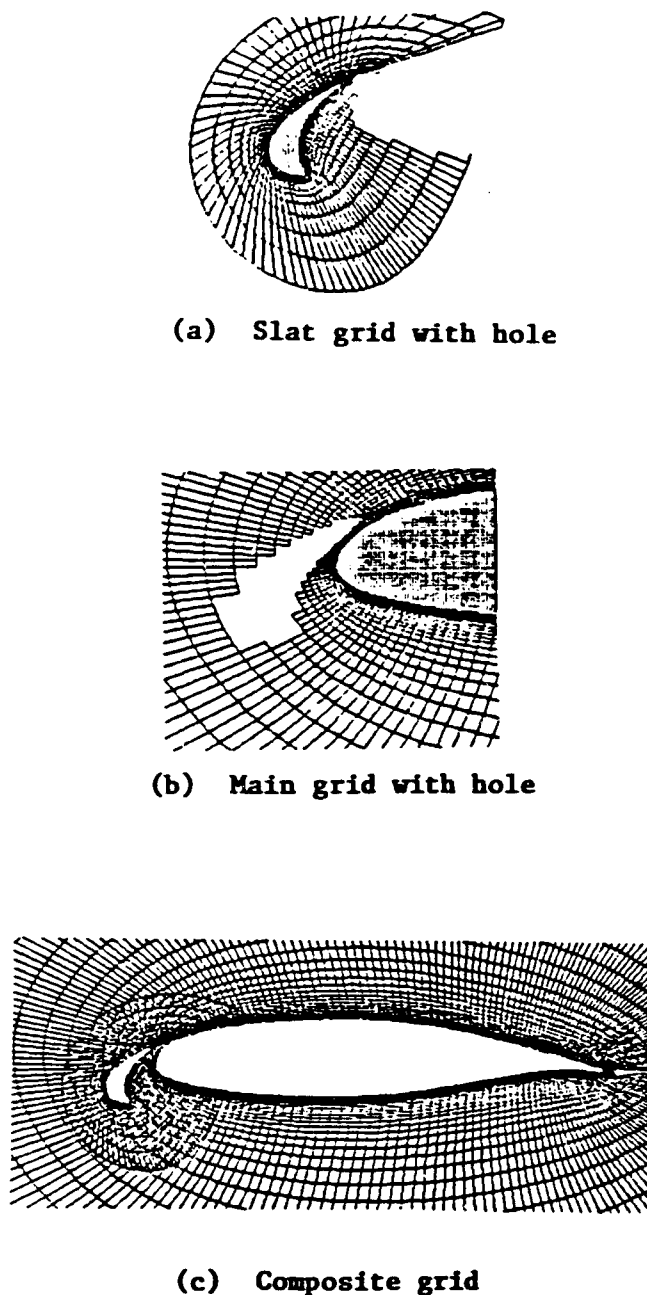
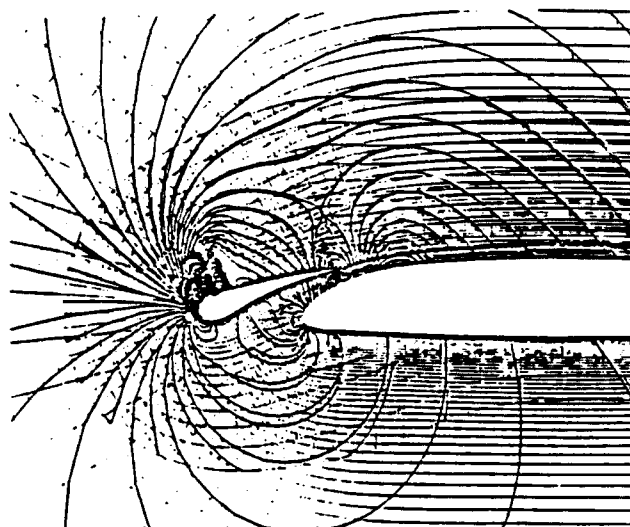


Figure 5: Chimera grid for a GAW-1 airfoil with deployed slat.

(a) Grid with Pressure Contours



(b) Surface Pressure Coefficient

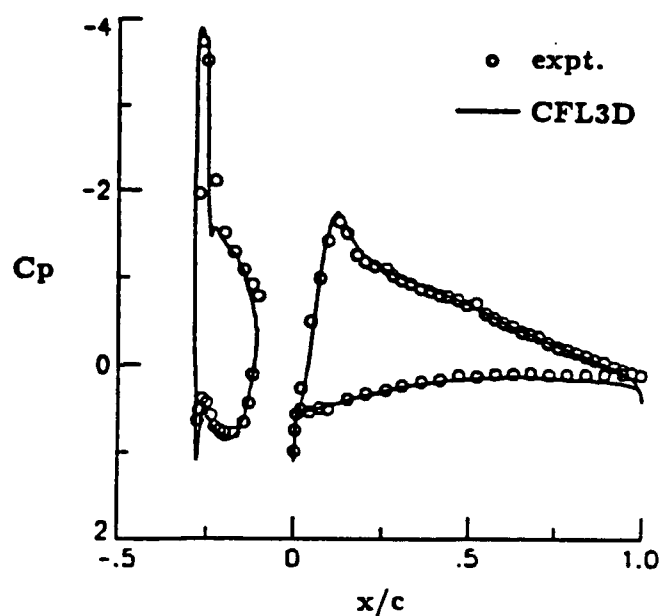
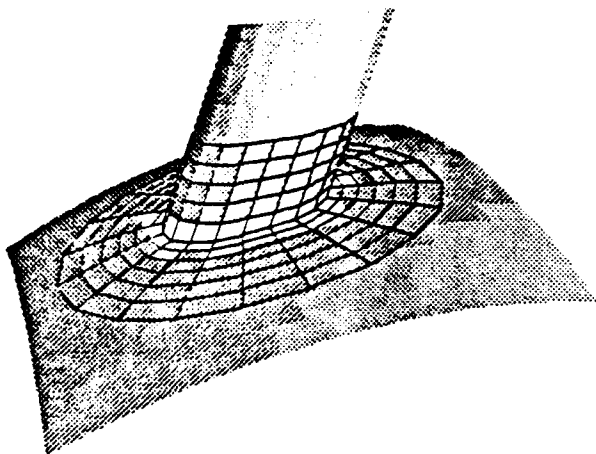
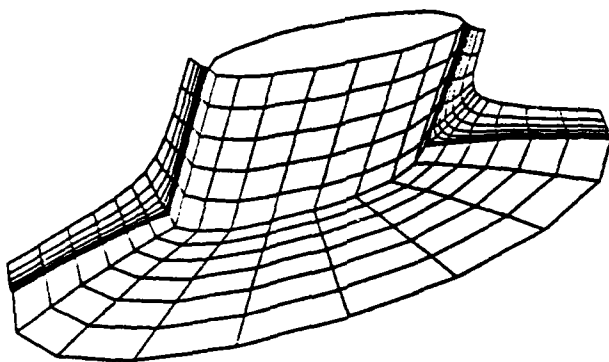


Figure 6: Euler solutions for an airfoil with slat at angle of attack,  $\alpha = 7.5^\circ$  and  $M_\infty = .5$  from Biedron.<sup>32</sup> The calculations were obtained using CFL3D overlapped grid option.





(a)



(b)

Figure 7: An example of a "collar grid" for a cylinder intersecting a curved surface; (A simplified model of the Shuttle External Tank and liquid hydrogen feed line) from Ref. 34. (a) Combined collar surface grid; (b) Slices of the completed collar grid.

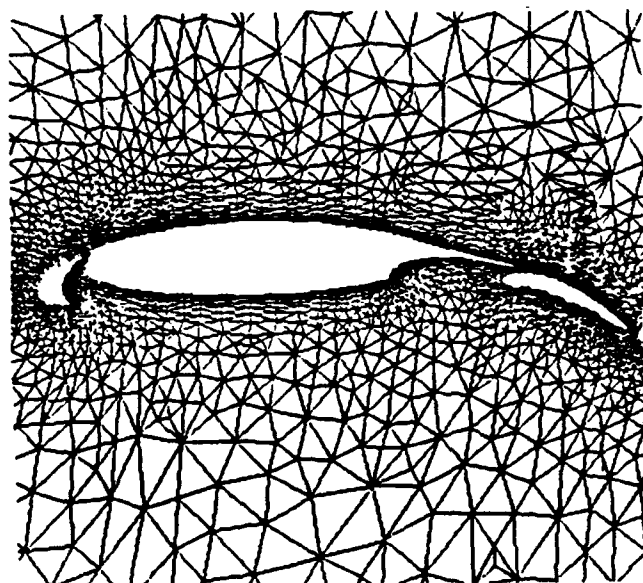
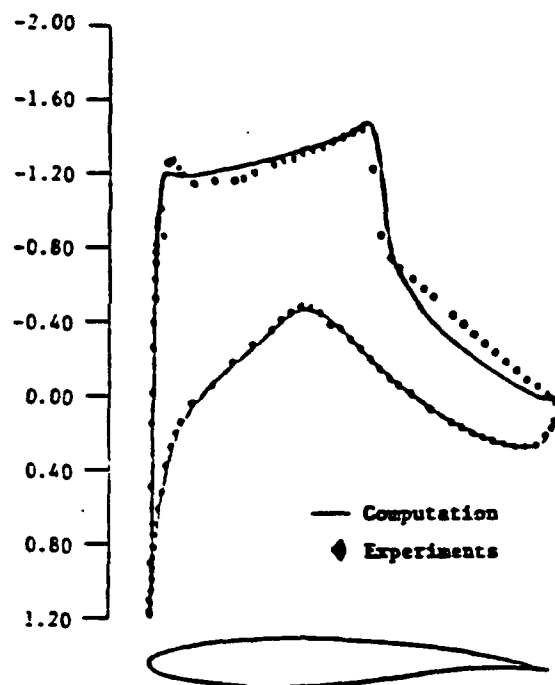


Figure 8: An unstructured mesh for computation of a GAW-1 multi-element airfoil configuration in a deployed state.

(a) RNG Turbulence Model



(b) Baldwin Lomax Model

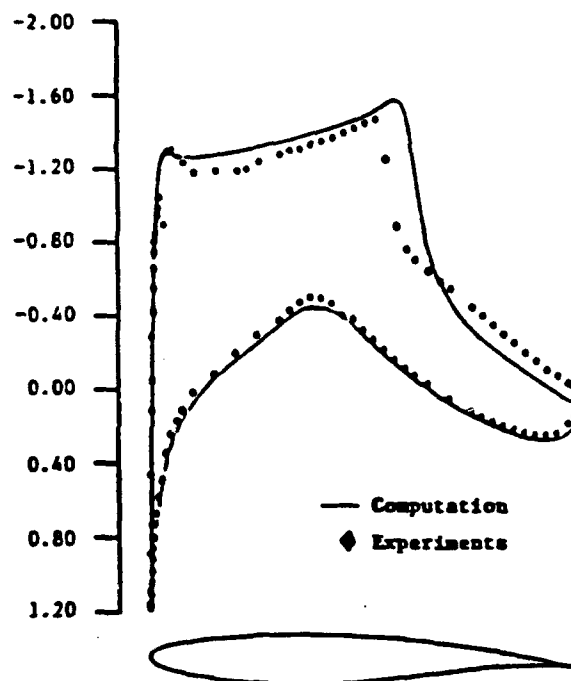


Figure 9: Comparison of RNG Turbulence Model and Baldwin Lomax Model for an RAE2822 airfoil at  $M_\infty = 0.75$ ;  $Re_\infty = 6.26 \times 10^6$  and  $\alpha = 2.8^\circ$  from Reference 49.

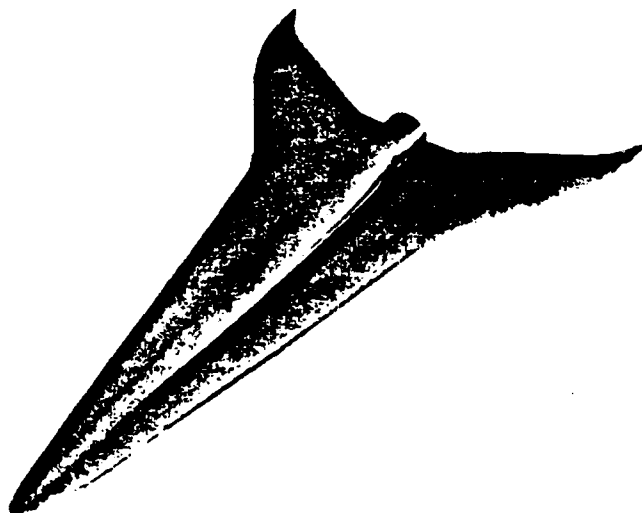


Figure 10a: Blended body HSCT configuration designed for  $M_\infty = 3.0$  cruise.

HSCT Configuration  
Surface Pressure Distributions  
 $M_\infty = 0.3$ ,  $\alpha = 18^\circ$ ,  $Re_\infty = 4.4 \times 10^6$

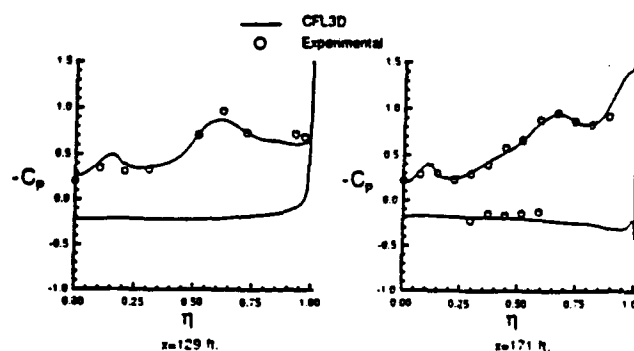


Figure 10b: Comparisons of surface pressure distribution for the HSCT configuration.

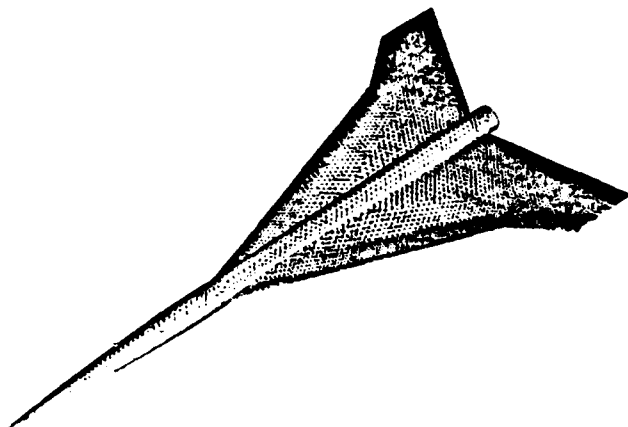


Figure 11a: An unstructured grid for a generic high speed research configuration.

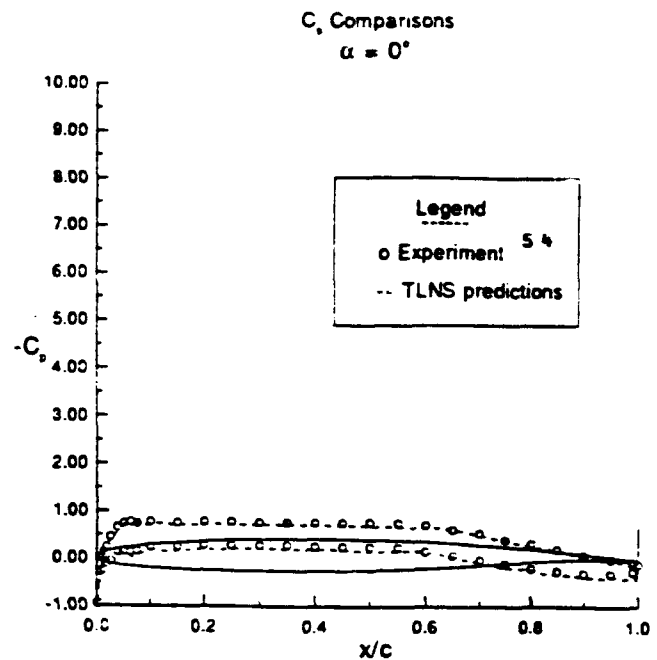


Figure 12a: Comparison of  $C_p$  for GAW-1 airfoil.

Generic HSR Configuration  
Mach = 0.2

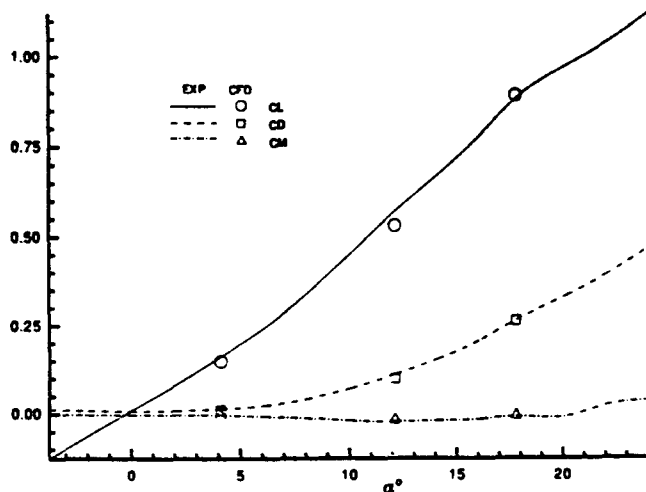


Figure 11b: Euler comparison of Lift, Drag, and Pitching moment for a generic HSR configuration.

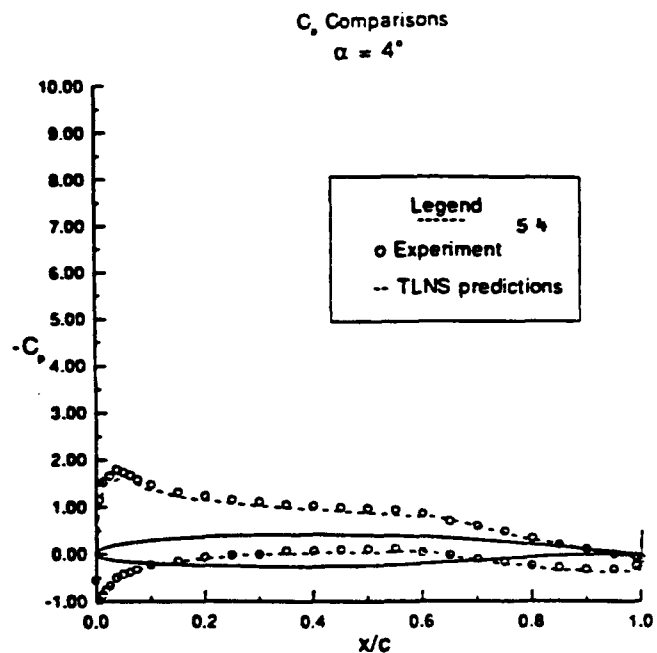


Figure 12b: Comparison of  $C_p$  for GAW-1 airfoil.

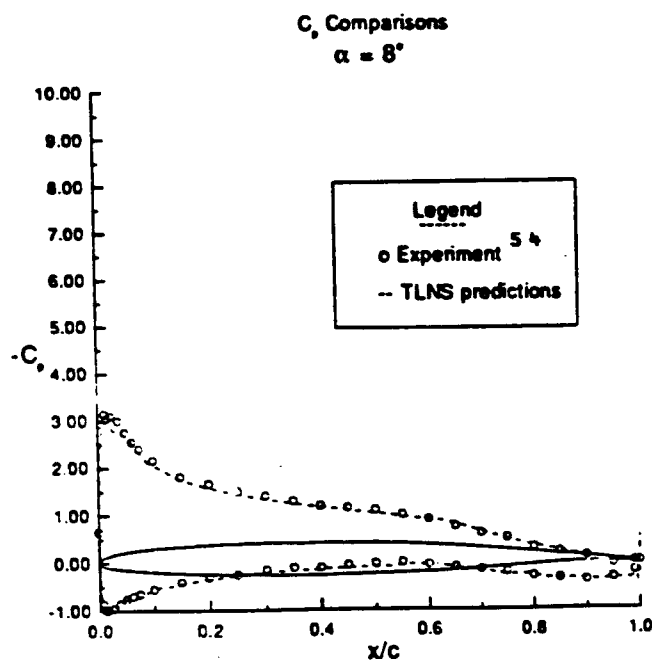


Figure 12c: Comparison of  $C_p$  for GAW-1 airfoil.

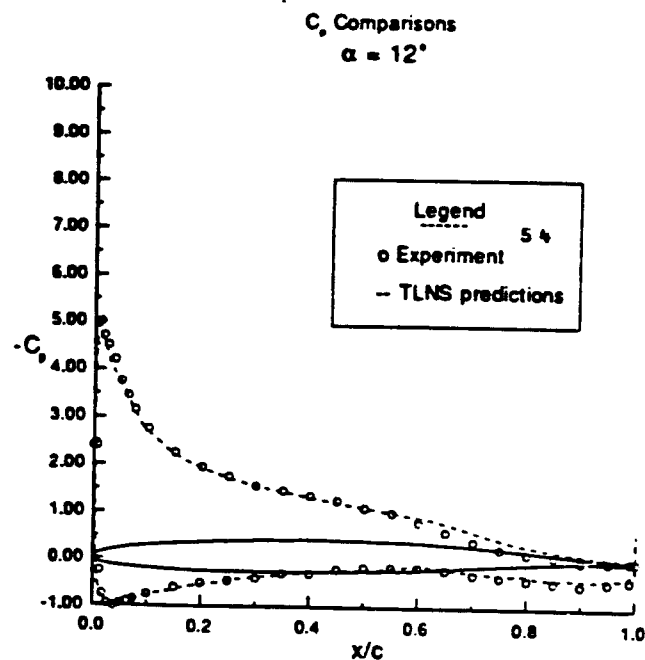


Figure 12d: Comparison of  $C_p$  for GAW-1 airfoil.

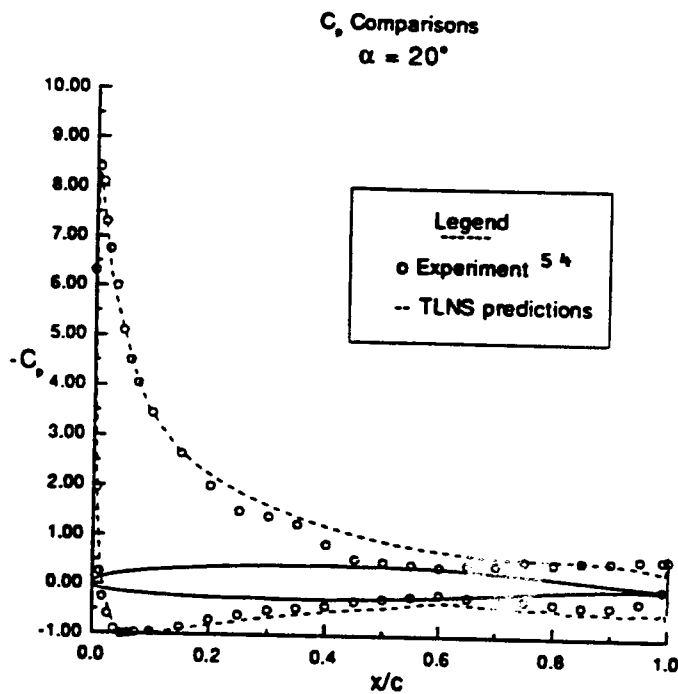


Figure 12f: Comparison of  $C_p$  for GAW-1 airfoil.

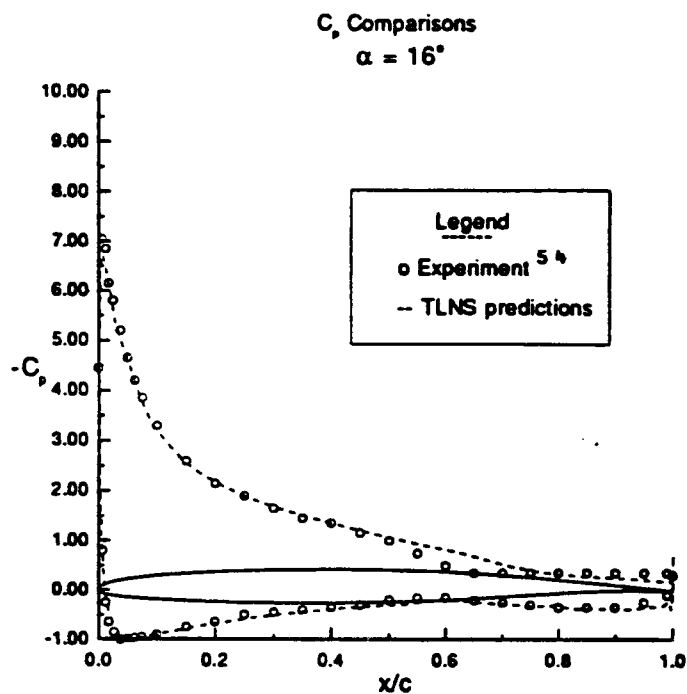


Figure 12e: Comparison of  $C_p$  for GAW-1 airfoil.

Variation of  $C_l$  vs  $\alpha$

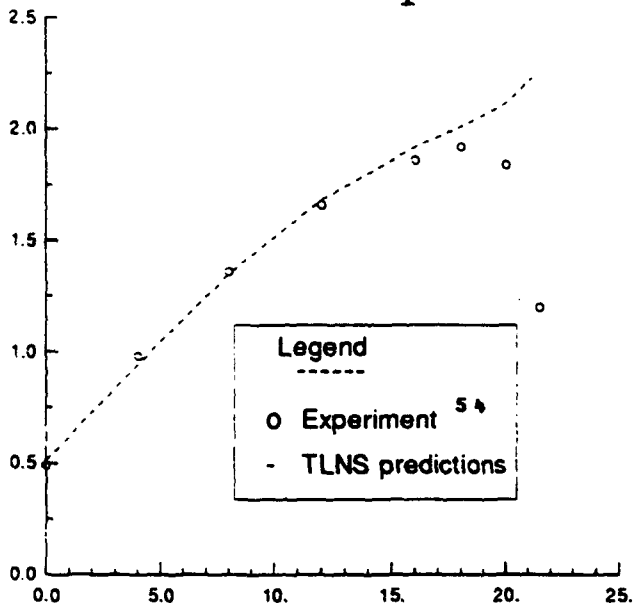


Figure 13: Comparison of  $C_l$  for GAW-1 airfoil.

Variation of  $C_d$  vs  $\alpha$

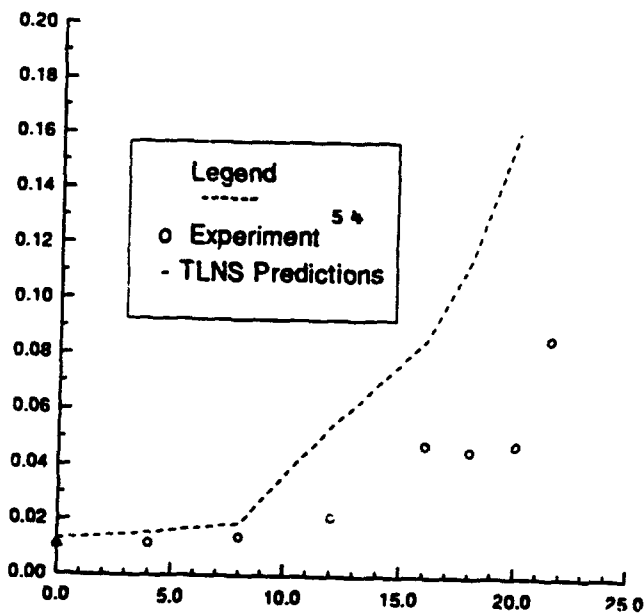


Figure 14: Comparison of  $C_d$  for GAW-1 airfoil.

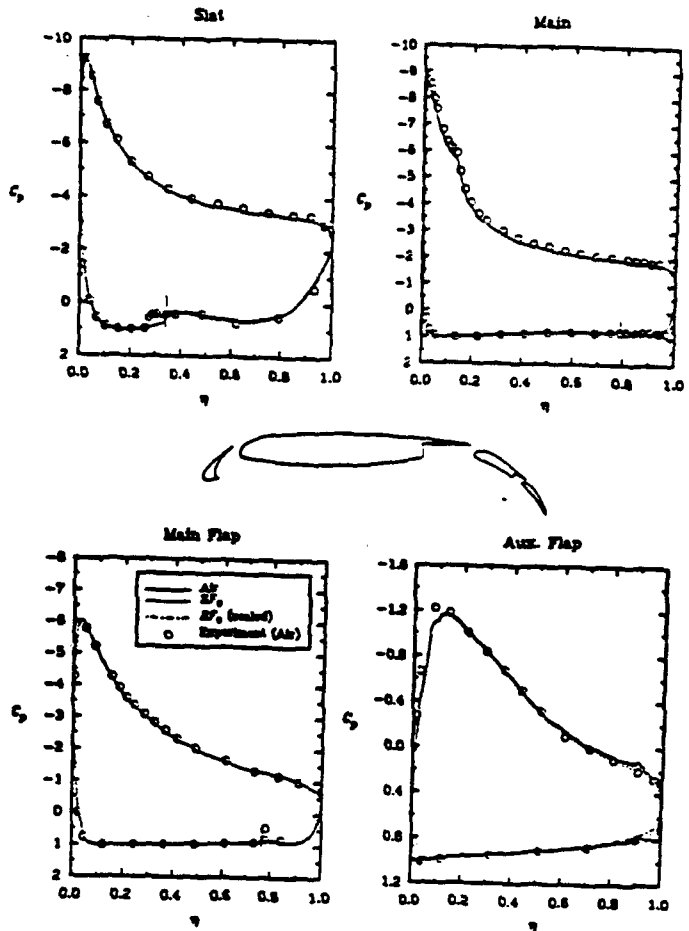


Figure 15a:  $C_p$  comparisons for a multi-element airfoil arrangement at  $M = 0.2$ , and with  $\alpha = 12^\circ$ .

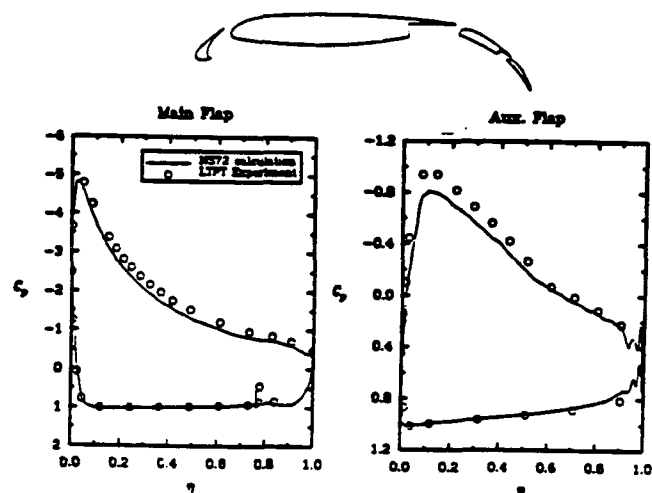
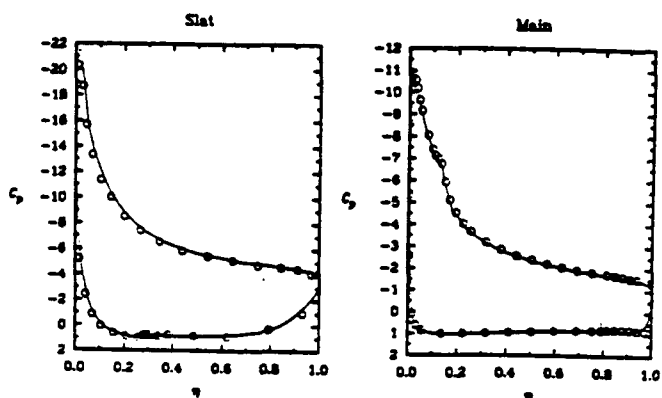


Figure 15b:  $C_p$  comparisons for a multi-element airfoil arrangement with  $\alpha = 20^\circ$ ,  $M_\infty = .2$

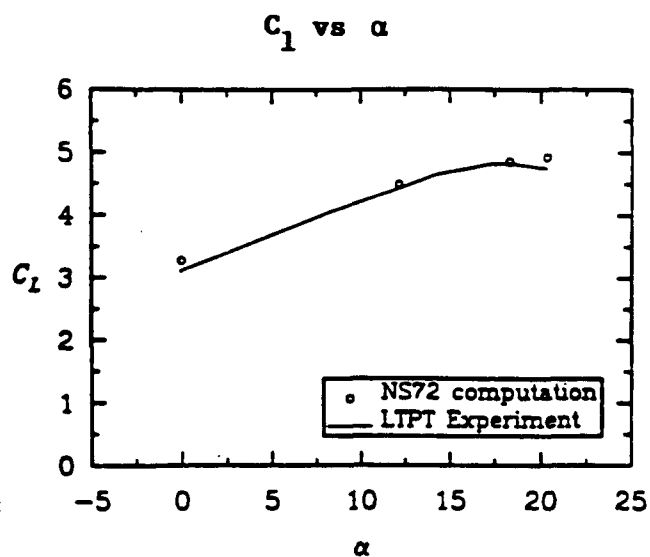


Figure 16:  $C_l$  vs  $\alpha$  comparisons for a multi-element configuration.

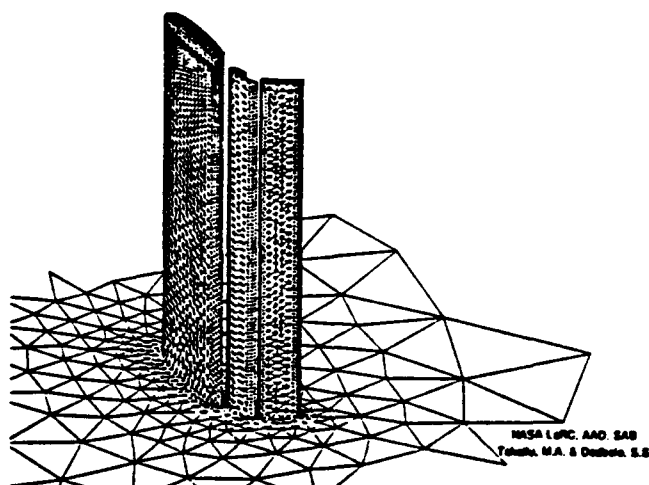
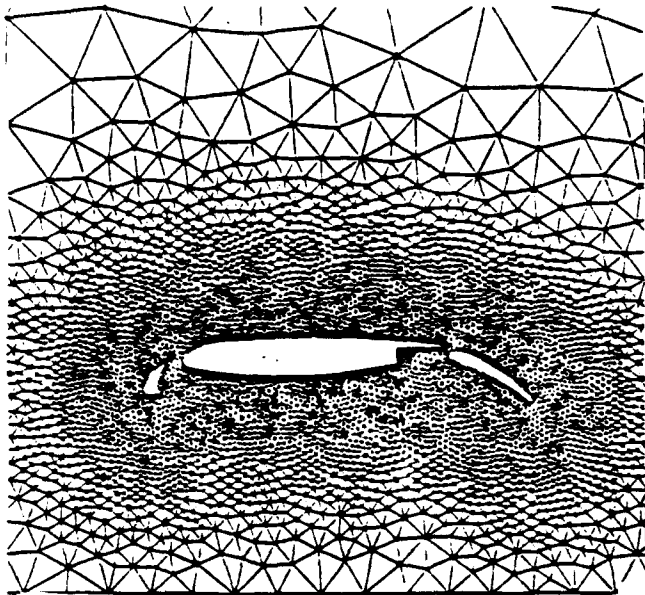
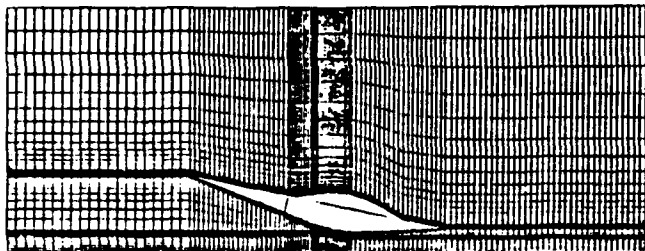


Figure 17: An example of a three-dimensional unstructured grid system for a semi-span high lift wing.



**Figure 18: Unstructured grid for a multi-component airfoil in ground effect study.**



**Figure 19: Cross section of a structured multi-block grid system for a high speed configuration in ground effects studies.**

**UNSTEADY FLOWS, 1**  
**SESSION 7**



# UNSTEADY TRANSITION MEASUREMENTS ON A PITCHING THREE-DIMENSIONAL WING

Peter F. Lorber and Franklin O. Carta

United Technologies Research Center  
East Hartford, CT 06108

## ABSTRACT

Boundary layer transition measurements have been made during an experimental study of the aerodynamics of a rectangular wing undergoing unsteady pitching motions. The wing was tested at chordwise Mach numbers between 0.2 and 0.6, at sweep angles of 0, 15, and 30°, and for steady state, sinusoidal, and constant pitch rate motions. The model was scaled to represent a full size helicopter rotor blade, with chord Reynolds numbers between 2 and  $6 \times 10^6$ . Sixteen surface hot film gages were located along three spanwise stations: 0.08, 0.27, and 0.70 chords from the wing tip. Qualitative heat transfer information was obtained to identify the unsteady motion of the point of transition to turbulence. In combination with simultaneous measurements of the unsteady surface pressure distributions, the results illustrate the effects of compressibility, sweep, pitch rate, and proximity to the wing tip on the transition and relaminarization locations.

## NOMENCLATURE

$A$	pitch rate, $\dot{\alpha}c/2U_c$
$c$	airfoil chord (17.3 in.)
$C_P$	pressure coefficient, $(P - P_\infty)/q$
$C_P^*$	pressure coefficient for locally sonic chordwise velocity
$k$	reduced frequency, $\omega c/2U_c$
$M_c$	chordwise Mach number, $M_\infty \cos \Lambda$
$M_\infty$	freestream Mach number
$P_\infty$	freestream static pressure
$q$	dynamic pressure, $\frac{1}{2}\rho_\infty U_c^2$
$t$	time
$T$	oscillation period
$Re$	Reynolds number, $cU_c/\nu$
$U_c$	chordwise component of freestream velocity, $U_\infty \cos \Lambda$
$U_\infty$	freestream velocity
$x$	distance along chord from leading edge
$z$	distance along span from tip leading edge
$\dot{\alpha}$	pitch rate, rad/sec
$\alpha$	geometric angle of attack
ramp: $\alpha = \alpha_{min}, \tau \leq 0.125$	
$\alpha = \alpha_{min} + 2(\tau - 0.125)(\alpha_{max} - \alpha_{min}),$	
$0.125 \leq \tau < 0.625$	
$\alpha = \alpha_{max}, \tau \geq 0.625$	
sine: $\alpha = \alpha_0 - \alpha_1 \cos 2\pi\tau$	

$\alpha_{ss}$	steady state stall angle
$\Lambda$	sweep-back angle
$\nu$	kinematic viscosity
$\rho_\infty$	freestream density
$\tau$	nondimensional time, $t/T$
$\omega$	circular frequency, $2\pi/T$

## INTRODUCTION

Knowledge of the state of the boundary layer is a prerequisite to understanding the aerodynamics of airfoils and wings in unsteady motion. In particular, the response during dynamic stall (pitching motions penetrating beyond the steady-state stall angle) may differ substantially, depending upon whether the boundary layer prior to separation is laminar or turbulent, completely subsonic or locally supersonic, fully attached or containing regions of reversed flow. The boundary layer state is in turn influenced by the Reynolds and Mach numbers of the external flow, airfoil contours and surface roughness, freestream turbulence level, and the presence of sweep and three-dimensionality.

Numerous investigations of dynamic stall have been conducted, at Reynolds numbers from  $10^3$  to  $10^7$ , at Mach numbers from essentially incompressible to nearly transonic, and for a wide variety of two- and three-dimensional geometries. Most have concentrated on measurements of either the aerodynamic forces (surface pressures or overall model loads) or the flow field characteristics (using various visualization techniques). Only a few studies have included measurements of the boundary layer state. The most informative approach is to obtain complete boundary layer profiles at numerous stations by means of hot wire anemometry<sup>1</sup> or laser velocimetry.<sup>2</sup> This is usually a difficult and time-consuming process. A simpler approach is to use surface-mounted instrumentation to obtain qualitative characteristics. Sublimation, surface visualization, and shear-sensitive liquid crystal techniques have proven useful in steady or slowly varying flow. For higher frequency ( $f \approx 10\text{Hz}$ ) conditions, and when data can only be efficiently acquired electronically, the surface hot film gage is preferred.<sup>3-6</sup>

This paper presents the results of such surface hot film gage measurements of the state of the boundary layer on a three-dimensional wing model. The model was scaled to be representative of a full scale helicopter main rotor, with Reynolds numbers of  $2-6 \times 10^6$ . It was tested at freestream Mach numbers between 0.2 and 0.6, and in both swept and unswept configurations. Previous publications<sup>6-10</sup> have described the surface pressure and integrated aerodynamic

load results from the current experiment and from an earlier experiment using a two-dimensional (tunnel-spanning) version of this model. The boundary layer state measurements described in the current paper should contribute to the understanding of the previous results. The measured transition locations should also be useful for computational simulation of the experiment.

## DESCRIPTION OF EXPERIMENT

The model was a straight, rectangular, untwisted, semi-span wing of 17.3 in. (44 cm) chord and 48 in. (122 cm) span (Fig. 1). The aspect ratio of a full wing would be 5.6. The wing consisted of a steel spar and fiberglass airfoil panels, and had a Sikorsky SSC-A09 9% thickness cambered section (Fig. 2). Airfoil coordinates have been provided in Ref. 6. The surface was kept smooth, with no artificial roughness added to alter the transition characteristics. The wing was mounted at sweep angles of 0, 15, and 30° from the side wall of the 8 ft (2.4 m) octagonal test section of the UTRC Large Subsonic Wind Tunnel. Additional airfoil panels were added to the spar at non-zero sweep angles in order to keep the wing tip  $\frac{1}{4}$  chord at the tunnel centerline. The experiment was conducted at five chordwise Mach numbers,  $M_c = 0.2, 0.3, 0.4, 0.5$ , and  $0.6$ . Based upon the model chord and the fact that this wind tunnel is vented to atmosphere in the stilling section, the chord Reynolds numbers for these experiments were approximately equal to  $10^7 \times M_c$ . Longitudinal turbulence levels have been measured in this facility using an LDV system to be between 0.7 and 1.2% of the freestream velocity<sup>11</sup>. Measurements with an unsteady pitot-static probe during the current experiment indicated root-mean-square unsteadiness equivalent to 0.35–0.5% of the freestream velocity for  $0.3 \leq M_c \leq 0.6$ , and 0.9% at  $M_c = 0.2$ .

A hydraulic rotary drive oscillated the model in pitch about the line connecting the root and tip  $\frac{1}{4}$  chord. Two

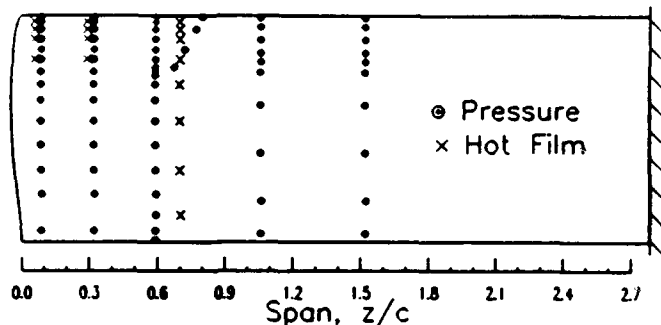


Fig. 1. Wing planform and instrumentation locations.



Fig. 2. SSC-A09 airfoil section.

pitching waveforms were used, sinusoids and ramps. The sinusoids were performed at frequencies from 1.25 to 12 Hz ( $0.025 \leq k \leq 0.15$ ), at amplitudes primarily of 6 and 10°, and at numerous mean angles. The ramps began at a steady-state condition (usually  $\alpha = 0$ ), increased at constant rate to a maximum angle, maintained that maximum for a short time, and then returned to the initial condition. The maximum pitch angles were 30° at  $M_c = 0.2$  and 0.3, 25° at  $M_c = 0.4$ , 18° at  $M_c = 0.5$ , and 13.5° at  $M_c = 0.6$ . The nondimensional pitch rates were selected between  $A = \dot{\alpha}c/2U_\infty$  of 0.001 and 0.025, bounded by a limiting dimensional rate of 560°/sec. Data were obtained for a total of 259 large amplitude sinusoids, 120 ramps, 260 small amplitude sinusoids, and 295 steady-state conditions. The complete data set will be made available in a technical report and a set of digital data tapes.

Unsteady surface pressure measurements were made on the wing model by 112 miniature transducers distributed among five spanwise stations. The suction surface transducer locations are shown by the dots in Fig. 1. The chordwise arrays on the upper surface had 10, 14, or 18 transducers each. The lower surface arrays were less dense, containing 6 or 18 transducers each. The transducers were installed so as to retain a smooth surface contour and achieve a flat frequency response to at least 4 kHz. The pressures were integrated along the chord at each spanwise station to determine the unsteady lift, pressure drag, and pitching moment coefficients.

Sixteen flush-mounted surface hot film gages were used to determine transition and separation locations. As shown by the x-marks in Fig. 1, the gages were located in chordwise arrays at three spanwise stations,  $z/c = 0.08, 0.27$ , and  $0.70$ . (Note that  $z = 0$  is at the wing tip.) The chordwise stations were  $x/c = 0.026, 0.060, 0.103, 0.192, 0.302, 0.464, 0.682$ , and  $0.880$ . All eight chordwise stations were used at  $z/c = 0.70$ , while only the forward four stations were used at  $z/c = 0.08$  and  $0.27$ . The  $x/c = 0.026$  and  $0.103$  gages at  $z/c = 0.70$  were offset by 1 in. (to  $z/c = 0.65$ ) to reduce the chance for thermal interference. TSI model 1268 gages were installed in holes drilled through the fiberglass airfoil skins. Each gage consists of a heated element deposited on the end of a 0.15 in. (0.38 cm) diameter quartz rod. The hot films were operated in the constant-temperature mode, at a nominal operating temperature of 225°C, corresponding to an overheat ratio (hot to cold gage resistance) of 1.35. The output voltage will increase with the heat transfer from the gage, and therefore, by the Reynolds analogy, with the shear stress at the wall. The anemometer circuits were mounted immediately outside of the wind tunnel wall to minimize lead resistance and noise.

The output voltages from both the pressure transducers and hot film gages were passed through a 10 kHz low pass filter, and digitized (to 15 bit accuracy) at a rate of 1024 samples per oscillation period (T). Ensemble-averaged time histories were computed using data from 20 pitching oscillations. Both the individual oscillations and the ensemble averages were recorded on digital magnetic tape.

The hot film results were intended to provide only qualitative information on transition and separation locations. When the flow over the hot film gage is laminar, the heat transfer is generally low, with little random unsteadiness. Movement of transition past the gage is indicated by a rapid rise in heat transfer, accompanied by an increase in the higher frequency, random portion of the signal. Separation is indicated by a low level of average heat transfer, but a high level of unsteadiness. Interpretation of hot film signals is simplified in a periodic unsteady flow because the changes from one flow state to another can be more readily identified than the characteristics of a steady-state flow. It is particularly difficult to determine if an individual signal with moderate unsteadiness is turbulent, separated, or transitional.

No attempt was made to obtain quantitative values of skin friction. Calibration of multiple surface mounted gages for unsteady flow is quite difficult, because of the need to either a) calibrate all probes in a reference unsteady flow prior to installation, b) provide a reference flow at each probe, or c) calibrate the probes by comparison to a traceable and portable reference probe. Surface-mounted quartz substrate gages (such as used here) have been shown to have limitations in unsteady flow, including different steady and unsteady calibrations<sup>12,13</sup>. The difficulties are created because heat is transferred not only from the active element to the fluid, but also from the element to the substrate, from the substrate to the model, and from the substrate to the fluid. The characteristic lengths and times for these various processes differ, resulting in different steady and unsteady responses.<sup>12</sup> Surface gages with a cavity below the heated element have been more successful in obtaining quantitative unsteady data.<sup>14,15</sup> The qualitative information at the relatively low frequencies (1-10Hz) of interest here should, however, be valid.

Transition information may also be obtained from the surface pressure data. As described in Refs. 1, 5, 6, and 16, transition is frequently accompanied by an increase in the higher frequency random component of the pressure, and by a small shift in the ensemble-average. The problem with this technique is that transition is not the only source of such pressure changes. The pressure information is most useful in confirming or extending transition information obtained from other means. For example, several hot film gages were not operating properly during the unswept portion of this experiment. The data from adjacent pressure transducers was used to cover the resulting gaps between functional hot films. Comparison between hot film and pressure information at other stations confirmed that the pressure changes were actually caused by transition.

## STEADY CHARACTERISTICS

For each steady (fixed  $\alpha$ ) condition, hot film gage voltages were recorded over a 5 second period and averaged. Results for each value of  $\alpha$  during a particular test series (at fixed  $M_c$  and  $\Lambda$ ), were used to form a 'quasi-steady' data

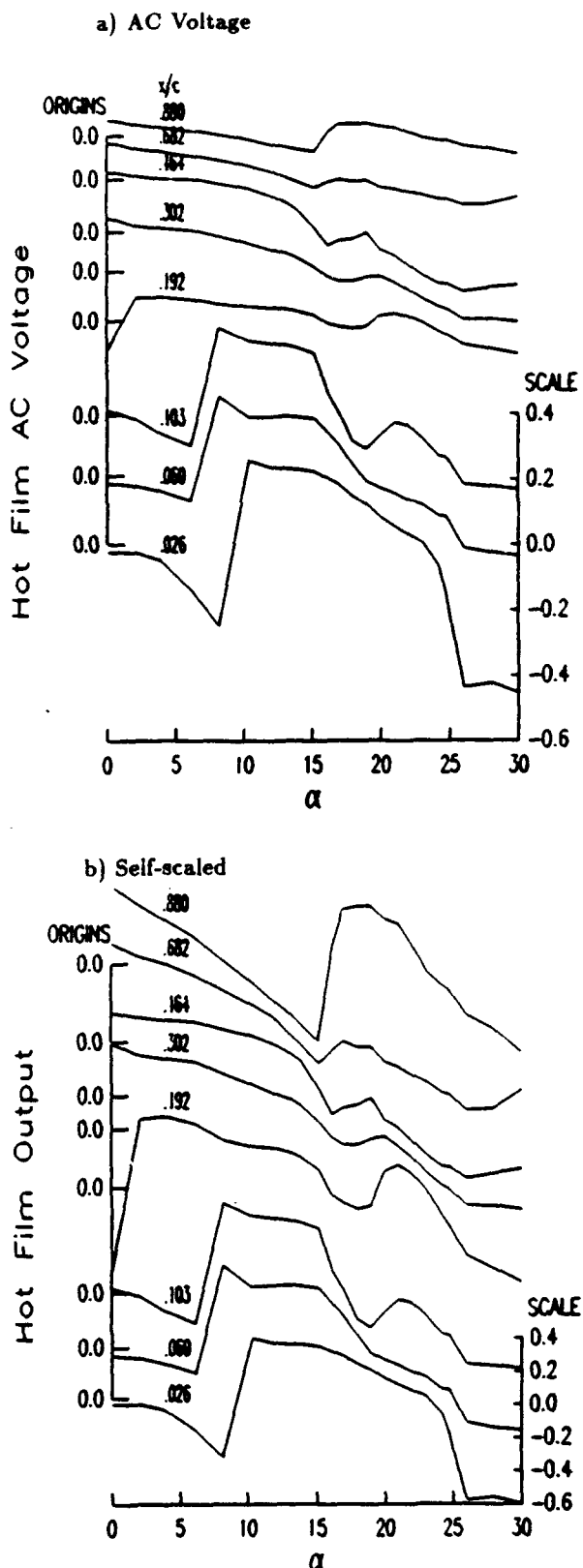


Fig. 3. Steady hot film results at  $M_c = 0.3$ ,  $\Lambda = 30$ , and  $z/c = 0.7$ .

file containing hot film outputs as a function of  $\alpha$ . Figure 3 shows an example for  $M_c = 0.3$  and  $\Lambda = 30$ . The results for the 8 gages at  $z/c = 0.7$  (the station furthest from the wing tip) are shown in two formats: as AC voltages (Fig. 3a)

and self-scaled to a peak-to-peak value of 1 (Fig. 3b). The AC voltage illustrates the magnitude of the output variations, while the self-scaled output allows regions of change to be easily identified and provides a clear qualitative picture. (Since the gages are not calibrated, quantitative comparisons between gages are not possible.) The origins for the output at each chordwise position ( $x/c$ ) are along the left of the figure, and the scale is at the lower right. Because data points were only acquired every 1 or 2°, the quasi-steady series appear somewhat rough.

At  $x/c = 0.026$  the sharp increase in heat transfer corresponding to the passage of the transition point over the gage occurs between  $\alpha = 8$  and  $10^\circ$ . Similar sharp increases are also present for the  $x/c = 0.06, 0.10$ , and  $0.19$  gages, but at successively lower values of  $\alpha$ . This indicates that at  $\alpha = 0$ , transition occurs between the  $x/c = 0.19$  and  $0.30$  gages, and as  $\alpha$  increases the transition point moves forward, occurring upstream of the  $x/c = 0.026$  gage for  $\alpha \geq 10^\circ$ . Away from transition, the heat transfer decreases with increasing  $\alpha$  in both laminar and turbulent regions prior to separation. This decrease is a consequence of the thickening of the boundary layer. It is present for  $0 \leq \alpha \leq 8^\circ$  and  $10^\circ \leq \alpha \leq 20^\circ$  at  $x/c = 0.026$ , and at  $\alpha \leq 15^\circ$  for  $x/c = 0.682$ .

Separation is manifested by the sharp drop in heat transfer that occurs after  $\alpha = 15^\circ$ , most noticeably at  $x/c = 0.06, 0.10$ , and  $0.19$ . This sharp drop does not occur at the  $x/c = 0.026$  station until  $\alpha = 25^\circ$ . On the aft portion of the wing, where the boundary layer is never laminar, the self-scaling emphasizes a 'bump' of increased heat transfer that occurs while the separation process is underway (between its initiation at  $\alpha \approx 15^\circ$  and completion at  $\alpha \approx 26^\circ$ ). A possible explanation is that the turbulent boundary layer near the trailing edge is already quite thick at  $\alpha = 15^\circ$ , and in fact may have thin regions of reversed flow. The resulting heat transfer from the hot film gages would be quite low. The vorticity shed during separation energizes the trailing edge flow, increasing the heat transfer. Once the process is completed and the flow has separated over the entire section, the average output returns to a low level. (The random variations, not shown here, remain high.)

A more quantitative picture of the effect of changes in Mach number, sweep angle, and spanwise position on steady flow transition is provided in Fig. 4. The symbols represent the angle of attack,  $\alpha$ , at which the transition point moves past the hot film gage at each chordwise position,  $x/c$ . The selected value of  $\alpha$  was that corresponding to the most rapid increase of hot film output, which generally occurred 20–40% of the way from the start to the finish of the transition process. Figure 4a illustrates the effect of Mach number at fixed spanwise position ( $z/c = 0.70$ ) and sweep angle ( $\Lambda = 30^\circ$ ). At  $M_c = 0.2$  transition occurs near  $x/c = 0.3$  at  $\alpha \approx 0$ , and moves forward of  $x/c = 0.026$  by  $\alpha = 10^\circ$ . At  $M_c = 0.3$  transition is always forward of  $x/c = 0.3$ , and moves past the  $x/c = 0.19, 0.10, 0.06$ , and  $0.026$  gages at somewhat lower angles of attack than at  $M_c = 0.2$ . This trend continues at  $M_c = 0.4$ , as transition always occurs before  $x/c = 0.19$ ,

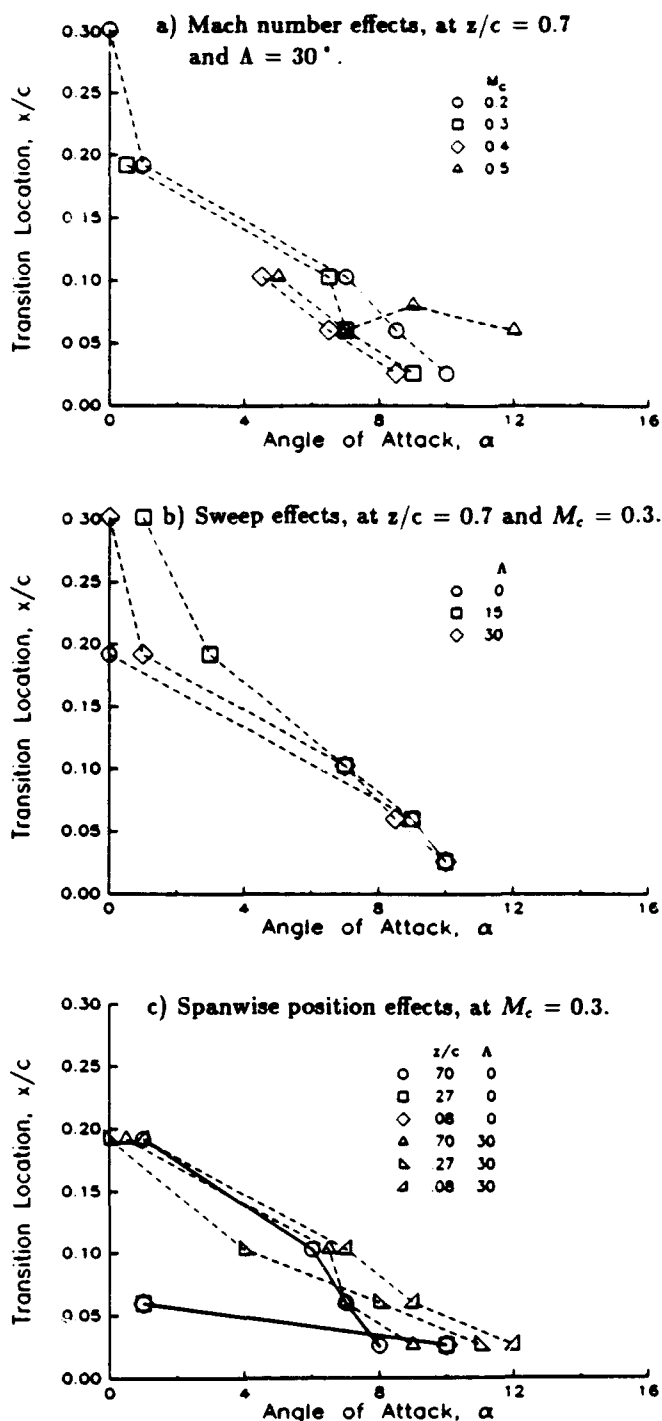
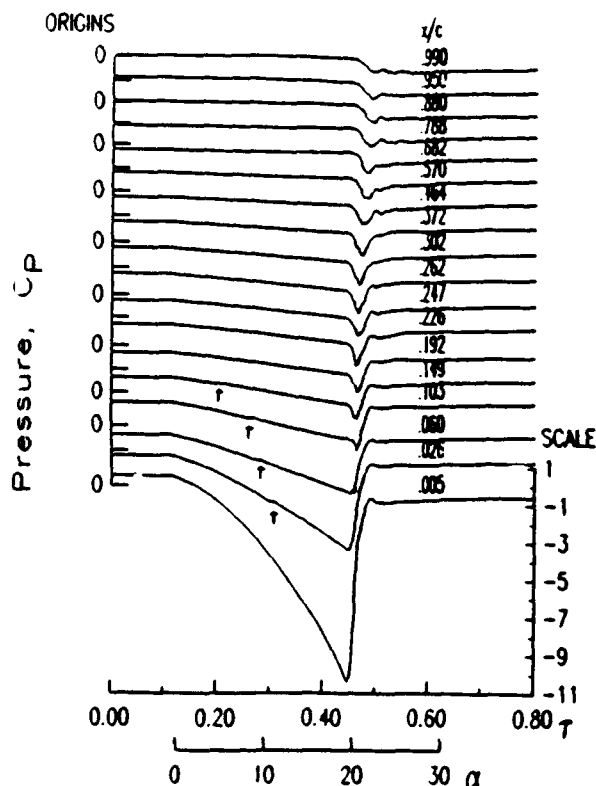


Fig. 4. Mach number, sweep angle, and spanwise position effects on transition locations in steady flow.

and moves forward of  $x/c = 0.026$  at  $\alpha \approx 8.5^\circ$ , a value approximately  $1.5^\circ$  less than at  $M_c = 0.2$ . These results are consistent with previous data from the unswept 2-D version of this model at  $M_c = 0.2$  and  $0.4$ .<sup>6</sup> The primary difference is that the lower effective angle of attack of the 3-D model (a result of the wing tip vortex<sup>9</sup>) delays the forward motion of transition to slightly higher geometric angles. The final data shown on Fig. 4a are at  $M_c = 0.5$ . The transition point ceases forward motion near  $x/c = 0.06$  at  $\alpha \approx 7^\circ$ . The shock effects responsible for this will be discussed in the section on Mach number effects on unsteady transition.

Figure 4b illustrates the effect of sweep angle for fixed spanwise location ( $z/c = 0.7$ ) and Mach number ( $M_c = 0.3$ ). At lower angles of attack ( $\alpha \leq 6^\circ$ ), transition is delayed by non-zero sweep. At  $\alpha = 0$  transition on the swept wing occurs near  $x/c = 0.3$ , approximately 10% of chord further downstream than at  $\Lambda = 0$ . The forward motion of transition is delayed by up to  $3^\circ$  in  $\alpha$  at  $\Lambda = 15^\circ$ , and by up to  $1^\circ$  at  $\Lambda = 30^\circ$ , in comparison to the  $\Lambda = 0$  results. As  $\alpha$  increases this difference is reduced. The motion of the transition point past the  $x/c = 0.026$  gage occurs at  $\alpha \approx 10^\circ$  for all three sweep angles.

The effect of spanwise position is illustrated in Fig. 4c at fixed Mach number ( $M_c = 0.3$ ) and at two sweep angles ( $\Lambda = 0$  and  $30^\circ$ ). At  $\Lambda = 0$  (the solid lines) there is a substantial difference between the inboard ( $z/c = 0.7$ ) and tip ( $z/c = 0.27$  and  $0.08$ ) stations. Compared to the inboard results, transition near the tip occurs further forward (at  $x/c \approx 0.06$ ) at low  $\alpha$  but moves forward more slowly (passing  $x/c = 0.026$  at  $2^\circ$  higher  $\alpha$ ). Several mechanisms appear to be involved. Proximity to the wing tip implies proximity to the tip vortex, which reduces the effective angle of attack. This would tend to delay forward motion of transition. In contrast, transition may be promoted by the three-dimensionality and unsteadiness introduced by the tip vortex. It is possible that at low  $\alpha$  this second mechanism causes early transition, while the forward motion of transition is delayed by the reduced effective angle of attack. These differences do not appear at  $\Lambda = 30^\circ$ , or at  $\Lambda = 15^\circ$  (not shown). This is plausible since the tip vortex has less influence on the aerodynamic loading when the wing is swept.<sup>9</sup>



## UNSTEADY TRANSITION

The simplest example of transition in unsteady flow is provided by data obtained during constant pitch rate ramps. Figure 5 shows ensemble averaged hot film and pressure time histories for an  $\alpha = 0$  to  $30^\circ$  ramp at  $M_c = 0.2$ ,  $\Lambda = 15^\circ$ , and  $A = 0.005$ . The series of pressure coefficient time histories at  $z/c = 0.59$  shown at the left of the figure show a smooth increase in pressure until an abrupt separation occurs at a nondimensional time of  $\tau = 0.45$  (corresponding to  $\alpha = 20^\circ$ ). After separation a negative pressure peak associated with the dynamic stall vortex travels aft along the chord. This is followed by a region of constant pressure indicating massive separation. Further details on the pressure measurements during dynamic stall are provided in Refs. 6, 9, and 10.

The corresponding hot film time gage time histories at  $z/c = 0.7$  are shown at the lower right of Fig. 5. Note that because data are acquired 1024 times over the period,  $T$ , the temporal resolution of the unsteady measurements is much greater than that of the quasisteady measurements (Fig. 3). Thus the movement of transition past the gages

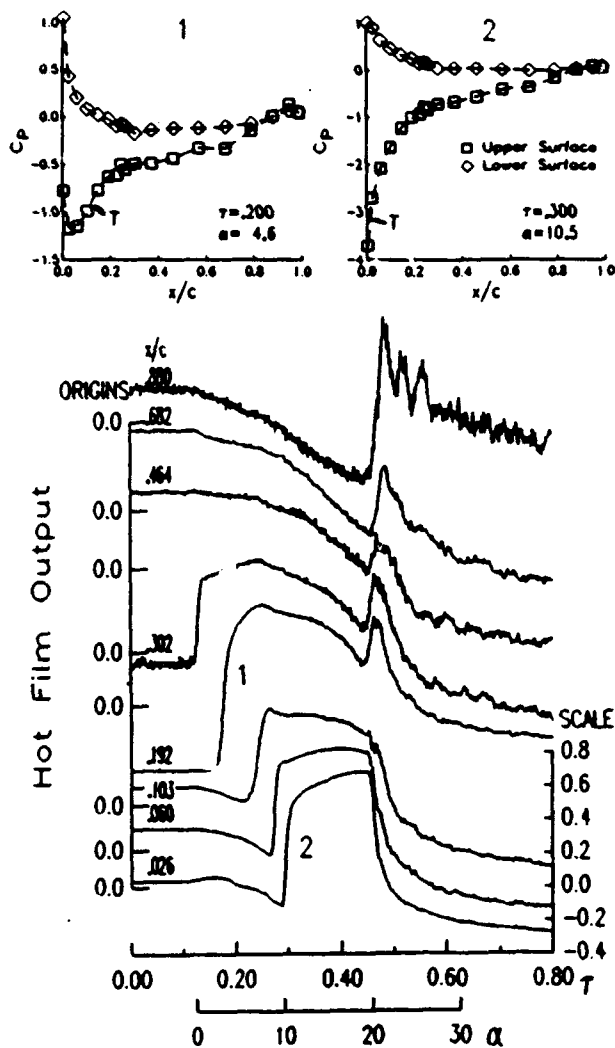


Fig. 5. Pressure and hot film time histories and chordwise pressure distributions at  $M_c = 0.2$ , for a ramp at  $\Lambda = 0.005$ ,  $\Lambda = 15^\circ$ , and  $z/c = 0.7$ .

is very sharply defined. Over the initial (steady state,  $\alpha = 0$ ) portion of the cycle, transition occurs just aft of the  $x/c = 0.30$  gage, but once the pitching motion begins at  $\tau = 0.125$ , transition immediately moves forward. The motion continues until  $\tau = 0.3$  ( $\alpha \approx 10^\circ$ ), when transition occurs ahead of the  $x/c = 0.026$  gage. As shown by the chord-wise pressure distributions at  $\tau = 0.2$  (number 1 in Fig. 5) and at  $\tau = 0.3$  (number 2), transition (indicated by the 'T') typically occurs shortly after the suction peak. This is in agreement with the experimental and theoretical work reported in Ref. 17 for incompressible flow over airfoils at a Reynolds number range of  $10^5 \leq Re \leq 10^6$ . The strong adverse pressure gradient downstream of the suction pressure peak was found to induce transition within 1-2% of chord aft of the peak.

The series of arrows on the pressure time histories (the left portion of Fig. 5) indicate local pressure increases that approximately correspond to the transition measurements obtained with the hot film gages (the right portion of the figure). The pressure increases are quite small, and are only apparent between  $x/c = 0.026$  and  $0.149$ . They generally occur slightly after the hot film gage output rises, i.e. when transition is complete.

The results in Fig. 5 indicate that transition has moved very close to the leading edge by  $\tau = 0.3$ , well before the onset of separation at  $\tau = 0.45$  ( $\alpha = 20^\circ$ ). There is no indication of a significant transitional separation bubble. This implies that dynamic stall for the SSC-A09 section at Reynolds numbers greater than  $2 \times 10^6$  is a result of turbulent boundary layer separation. This differs from the observations reported in Refs. 1 and 2, for the NACA 0012 airfoil at lower Reynolds numbers (approximately  $3-5 \times 10^5$ ). For those conditions, the transitional separation bubble appears to be a key participant in the dynamic stall process. The sequence observed in the current experiment, laminar boundary layer - turbulent boundary layer - separation, has also been observed during other high Reynolds number experiments, such as Refs. 3 and 4. The separation process for the current model is discussed at greater length in Ref. 10.

The preceding paragraphs have described the general behavior of transition during an unsteady pitching motion. This behavior is similar to that observed at other pitch rates, sweep angles, spanwise positions, and Mach numbers (at least when local supersonic flow effects are minimal). The actual location of the transition point, and its motion as  $\alpha$  is increased is, however, dependent on all of these parameters. These dependencies will be discussed next.

### Pitch Rate Effects

The effect of pitch rate on the location of transition is illustrated in Fig. 6. Figure 6a shows results at the inboard station,  $z/c = 0.7$ , for ramps at a series of five pitch rates between  $A = 0.001$  and  $0.02$ , at fixed Mach number ( $M_c = 0.3$ ) and sweep angle ( $\Lambda = 0$ ). Steady results are also included. Note that the results at  $x/c = 0.10$  and  $0.149$  were obtained using RMS pressure data, because of the problems with the  $0.10$  hot film gage described above. (There is no

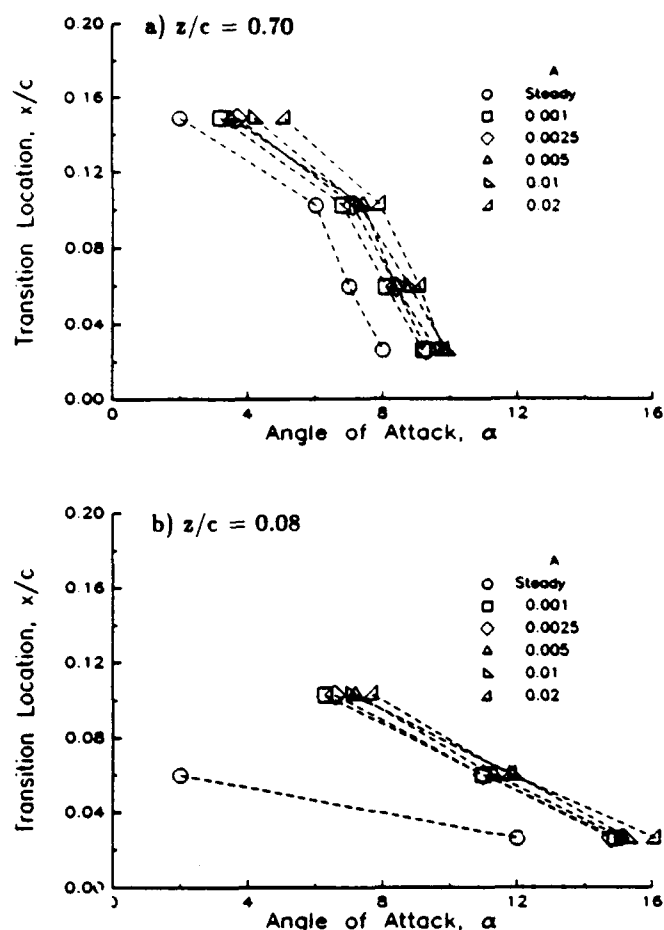


Fig. 6. Effect of pitch rate on transition locations for ramp motions at  $M_c = 0.3$ , and  $A = 0$ .

hot film at  $x/c = 0.149$ ). The primary effect of increasing the pitch rate is to delay forward motion of the transition point. There is a delay of approximately  $0.8^\circ$  between the steady and  $A = 0.001$  conditions, and an additional delay of approximately  $1.2^\circ$  from  $A = 0.001$  to  $A = 0.02$ . The unsteady delays are consistent with the results for the 2-D model<sup>6</sup>. Data at  $z/c = 0.027$  and at other pitch rates and sweep angles (not shown) exhibit similar lags with increased pitch rate.

Close to the wing tip, at  $z/c = 0.08$  (Fig. 6b), there is still a transition delay associated with increased pitch rate, but there is also a substantial difference between the steady and unsteady response. In steady flow the transition point moves from  $x/c = 0.06$  at  $\alpha \approx 2^\circ$  to  $x/c = 0.026$  at  $\alpha = 10^\circ$ . This behavior has been discussed above in connection with Fig. 4c. In unsteady flow transition occurs considerably further aft, between  $x/c = 0.10$  and  $0.19$  at low  $\alpha$ , and moves forward of  $x/c = 0.026$  only at  $\alpha = 15-16^\circ$ , a delay of at least  $5^\circ$  compared to the steady results. Since the relatively early transition in the steady flow was attributed to unsteadiness and three-dimensionality associated with the tip vortex, it is possible that these disturbances do not develop rapidly enough during the unsteady ramp to cause early transition.

### Sweep Effects.

Figure 7 illustrates the effect of sweep angle on the transition location during ramps at  $A = 0.01$  and  $M_c = 0.3$ . At the inboard location of  $z/c = 0.70$  (Fig. 7a), the effect of sweep appears limited to a somewhat earlier transition at low  $\alpha$  for the unswept wing. For  $\alpha \geq 8^\circ$ , the transition location exhibits no dependence on sweep. This is consistent with the steady-state,  $M_c = 0.2$  data shown in Fig. 4b, and with pressure data<sup>9</sup> showing little effect of sweep on the inboard portion of the wing prior to stall. At  $z/c = 0.08$  (Fig. 7b) sweep effects are more significant. Transition on the unswept wing occurs further forward for  $\alpha \leq 8^\circ$ , and further aft for  $\alpha \geq 10^\circ$ . This is also consistent with the steady-state results (Fig. 4c).

### Mach Number Effects.

The effect of Mach number will be illustrated using ramp data for the  $\Lambda = 15^\circ$  wing, at a nondimensional pitch rate of  $A = 0.005$ , and at the  $z/c = 0.70$  station. Ensemble averaged hot film time histories and instantaneous chordwise pressure distributions will be discussed at  $M_c = 0.2$ , 0.3, 0.4, 0.5, and 0.6. This sweep angle and spanwise position was selected for in-depth discussion because the spanwise variations appear relatively low. The pitch rate of 0.005 was selected because it was the highest value that was within

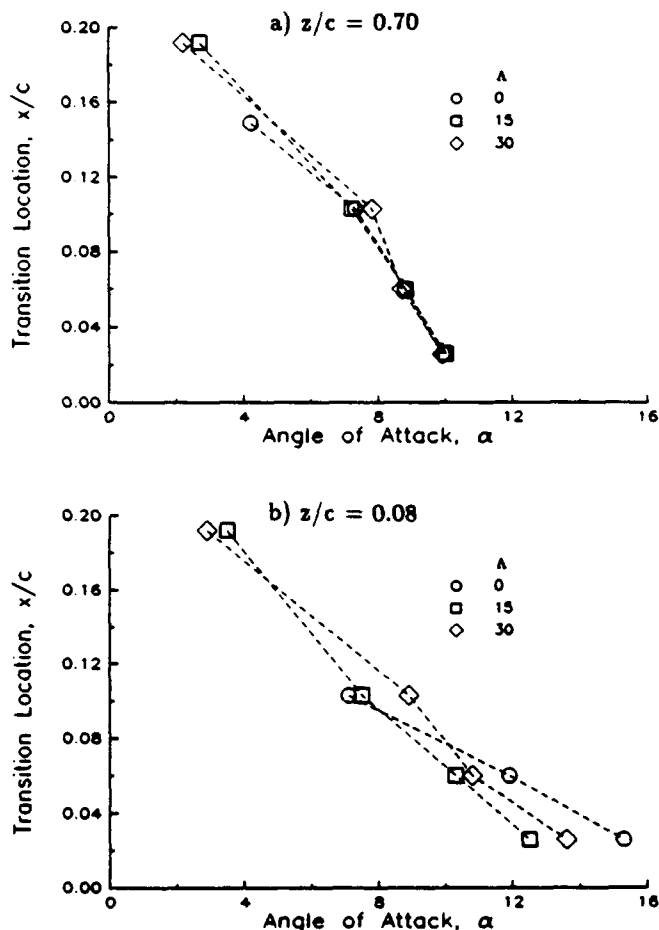
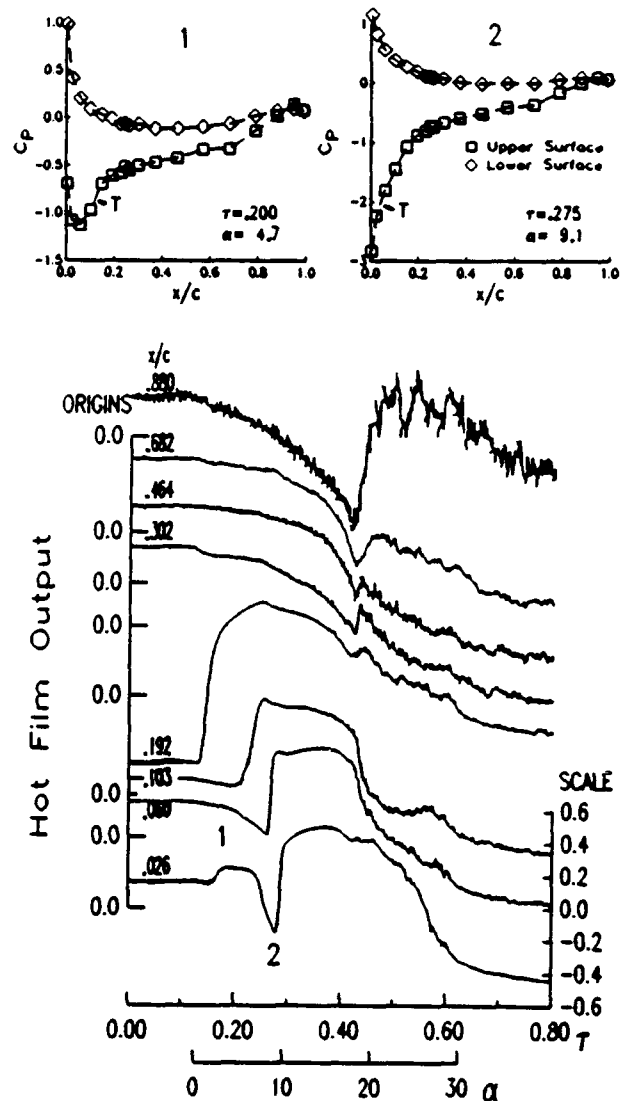


Fig. 7. Effect of sweep on transition locations for ramp motions at  $M_c = 0.3$ , and  $A = 0.01$ .

the drive system limits at all Mach numbers. Qualitatively similar variations with  $M_c$  were measured at other test conditions.

At  $M_c = 0.3$  (Fig. 8) the results are generally similar to those already described at  $M_c = 0.2$  (Fig. 5), with two differences. The first is that the initial transition location is somewhat further forward, near the  $x/c = 0.19$  gage rather than at the  $x/c = 0.30$  gage. As shown by the chordwise pressure distribution at  $\tau = 0.2$  ( $\alpha = 4.7^\circ$ , number 1 in Fig. 8), the transition location (indicated by the 'T') is still slightly downstream of the suction peak. A more interesting difference from the  $M_c = 0.2$  results is the rapid drop in hot film output prior to transition present at  $x/c = 0.026$ . This drop is sharper than the gradual reduction that typically occurs as increases in  $\alpha$  cause the boundary layer to thicken and thereby reduce the heat transfer. More rapid reductions tend to occur at  $M_c \geq 0.3$ , both in the current experiment and also in the earlier two-dimensional unswept experiment<sup>6</sup>. The cause appears to be compressibility. The minimum hot film output is at  $\tau = 0.275$  and  $\alpha = 9.1^\circ$ .



Based upon the measured pressure distribution (number 2 in Fig. 8) and the steady isentropic relations, the maximum local Mach number at this time is approximately 0.6, double the freestream value. Increasing the local Mach number generally increases the temperature, increases boundary layer thickness, reduces the density, and increases the molecular viscosity and thermal conductivity.<sup>18</sup> The first three effects will tend to reduce the heat transfer from the heated element to the air (and therefore to decrease hot film output), while the increase in conductivity will tend to increase heat transfer. The actual balance between the effects in this unsteady, variable pressure gradient flow is not known, but it appears that the effects tending to decrease heat transfer are stronger. There is in general a good correlation between rapid drops in hot film output and regions of high subsonic local Mach numbers. No evidence has been found for the other possible cause of the decreased heat transfer, a laminar separation bubble. Neither the surface pressure distributions, the magnitude of random unsteadiness in the hot film and pressure signals, nor limited surface oil flow visualization indicate separation at these low angles of attack ( $\alpha \leq 10^\circ$ ).

At  $M_c = 0.4$  (Fig. 9) the drop in the heat transfer near the leading edge prior to transition is more pronounced. The maximum local Mach number at  $\tau = 0.35$ , the time of minimum hot film output, is 0.83. The sequence of events is quite compressed for this condition. First, the transition point moves forward of  $x/c = 0.026$  at  $\tau = .37$  ( $\alpha = 9.7^\circ$ ), as shown by pressure distribution number 1 in Fig. 9). Next, the flow becomes locally supersonic at  $\tau \approx 0.4$  ( $\alpha = 10.9^\circ$ ).

This is indicated in pressure distribution number 2 by the  $C_p^*$  arrow. The supersonic bubble expands past  $x/c = 0.060$  at  $\tau = 0.475$  ( $\alpha = 13.9^\circ$ , pressure distribution number 3), with a maximum local Mach number of 1.27. This is almost immediately followed by separation, as indicated by the loss of leading edge suction starting at  $\tau = 0.5$  ( $\alpha = 14.9^\circ$ , pressure distribution number 4). The separation appears to initiate near  $x/c = 0.02-0.10$  (as indicated by the earliest drop in heat transfer). The rapid sequence of transition, supersonic flow, and separation in a very compact region near the leading edge illustrates the complexity of the flow and demonstrates the need for high spatial and temporal resolution in both experimental or computational experiments.

At  $M_c = 0.5$  the region of supersonic flow is more extensive, leading to the more complex hot film response shown in Fig. 10. At lower  $\alpha$  the flow remains subsonic, and the behavior is similar to that at lower  $M_c$ . The transition point moves forward from its initial position near  $x/c = 0.19$ , and passes  $x/c = 0.10$  at  $\tau = 0.3$ . Pressure distribution number 1 (at  $\alpha = 7.1^\circ$ ) in Fig. 10 illustrates this portion of the cycle. By  $\tau = 0.4$  ( $\alpha = 8.8^\circ$ , pressure distribution number 2), the flow ahead of  $x/c = 0.06$  has become supersonic. Although the maximum local Mach number is quite low (1.05) at  $\tau = 0.4$ , it increases rapidly, reaching a maximum of 1.4 at  $\tau = 0.5$  ( $\alpha = 12^\circ$ , pressure distribution number 3). The hot film time histories reflect the formation of the shock at  $\tau \approx 0.4$  by the rapid drop in heat transfer at the  $x/c = 0.026$  gage and the rapid increase in heat transfer at the  $x/c = 0.06$  gage. The decrease at the  $x/c = 0.026$  gage is similar to the decreases caused by compressibility that were previ-

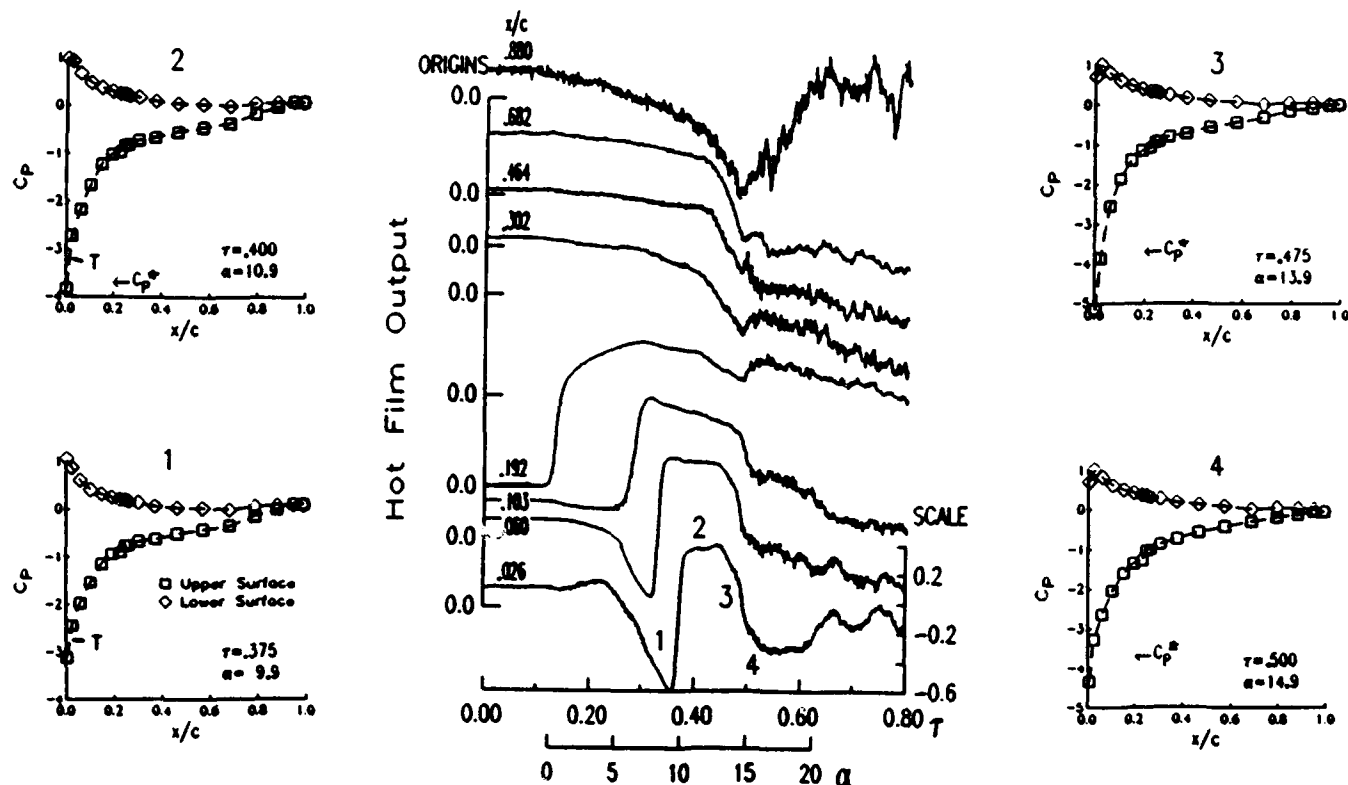


Fig. 9. Hot film time histories and chordwise pressure distributions at  $M_c = 0.4$ , for a ramp at  $\Lambda = 0.005$ ,  $\Lambda = 15^\circ$ , and  $z/c = 0.7$ .



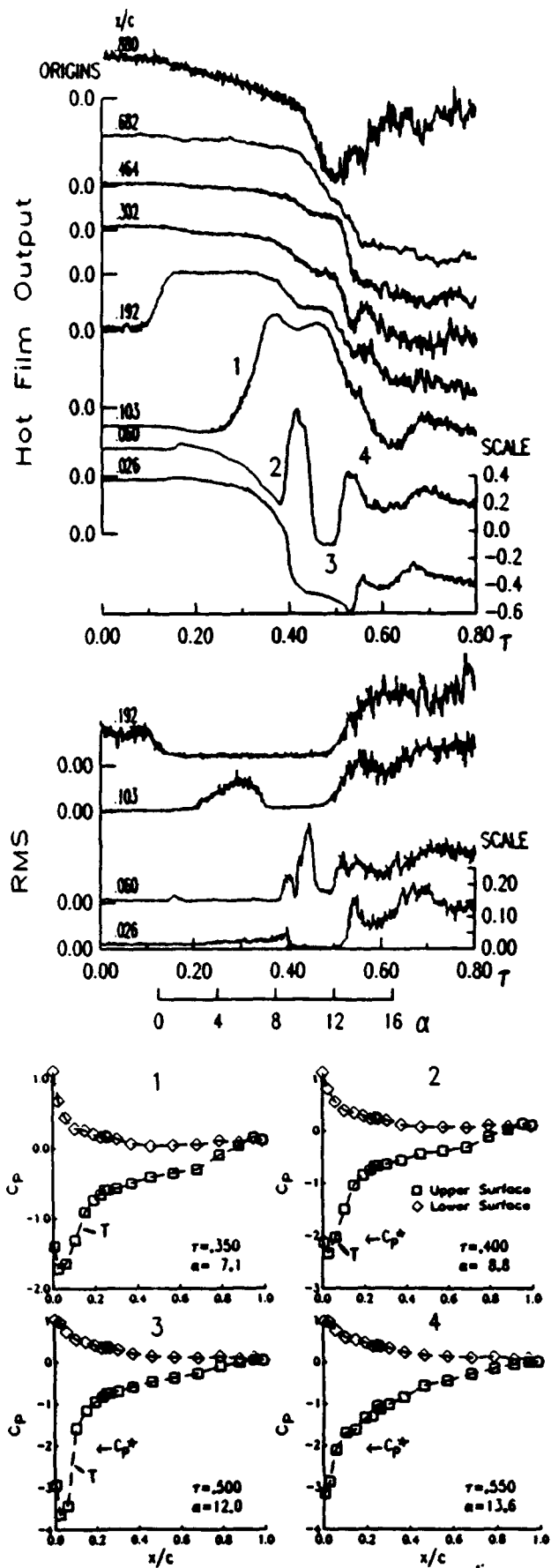


Fig. 10. Hot film time histories and chordwise pressure distributions at  $M_c = 0.5$ , for a ramp at  $A = 0.005$ ,  $\Lambda = 15^\circ$ , and  $z/c = 0.7$ .

ously described at lower  $M_c$ . The increase at  $x/c = 0.06$ , which is now downstream of a shock, appears to be a combination of two factors. The first is transition, induced at the shock, and the second is the increase in density behind the shock (a 50% increase is predicted by the normal shock relations). An increase in temperature will also occur behind the shock, tending to reduce heat transfer from the hot film, but the effects of the density increase and of transition are apparently dominant.

As  $\alpha$  increases further, the supersonic region expands aft past the  $x/c = 0.06$  gage at  $\tau \approx 0.45$ . The heat transfer from this gage drops since it is now in the supersonic flow ahead of the shock. Pressure distribution number 3 in Fig. 10, at  $\tau = 0.5$  and  $\alpha = 12.0^\circ$ , illustrates this situation. It is likely that the transition point has returned aft with the shock, to between the  $x/c = 0.06$  and  $0.10$  gages. RMS hot film time histories (shown at the center of Fig. 10) support this hypotheses. The RMS is the variation at each value of  $\tau$  of the data for 20 individual cycles about the ensemble average. The RMS at the  $x/c = 0.06$  gage is considerably lower at  $\tau \approx 0.4$  and  $0.5$ , when the ensemble averaged output is low (and the flow is presumed to be laminar at this gage), than at  $\tau \approx 0.425$ , when the ensemble averaged output is high (and transition is presumed to be forward of the gage). At  $\tau = 0.55$  ( $\alpha = 13.6^\circ$ , pressure distribution number 4) the boundary layer has begun to separate near the shock. The time and location of the separation are indicated by the initial reductions in heat transfer and suction pressure. Pressure distribution number 4 clearly shows the loss of suction and the disappearance of a sharply defined shock. The flow very quickly becomes massively separated over the entire upper surface. This process is more completely described in Refs. 9 and 10.

At the highest Mach number,  $M_c = 0.6$ , compressibility effects are even more dominant. As shown by pressure distribution 1 in Fig. 11, locally supersonic flow begins at  $\tau \approx 0.3$  and  $\alpha = 4.5^\circ$ . Transition occurs between the  $x/c = 0.10$  and  $0.19$  gages, just aft of the suction pressure peak. Transition moves forward past the  $x/c = 0.10$  gage at  $\tau = 0.35$  ( $\alpha = 5.5^\circ$ , pressure distribution number 2). While the maximum local Mach number at  $M_c = 0.6$  is 1.45, almost the same as the value measured at  $M_c = 0.5$ , the supersonic region extends further aft, to  $x/c = 0.19$  at  $\tau = 0.45$  ( $\alpha = 7.6^\circ$ , pressure distribution number 3). As at  $M_c = 0.5$ , there is reduced heat transfer from the hot film gage ahead of the shock and increased transfer from the gage behind the shock. Transition is again linked with the shock, and appears to move aft as the supersonic zone strengthens between  $\tau = 0.35$  and  $0.45$ . Separation occurs starting at  $\tau \approx 0.55$ , as indicated by drops in the ensemble averaged hot film output, increased randomness, and the disappearance of a sharply defined shock. This last effect is shown in pressure distribution number 4, at  $\tau = 0.6$  and  $\alpha = 11.1^\circ$ . At  $M_c = 0.6$  the loss of leading edge suction is not as sudden as at  $M_c = 0.5$ , and massive separation of the entire upper surface is somewhat delayed. Further details on the separation process are provided in Ref. 10.

The transition results described in this section are summarized in the form of a transition location versus angle of attack plot in Fig. 12. The low angle of attack ( $\alpha \leq 4^\circ$ ) data indicate that as  $M_c$  increases, the transition point moves forward earlier. Motion past the  $x/c = 0.19$  gage occurs at approximately  $4^\circ$  earlier at  $M_c = 0.6$  than at  $M_c = 0.2$ . The earlier transition at higher  $M_c$  may be at least in part a result of increased Reynolds number. At low angle

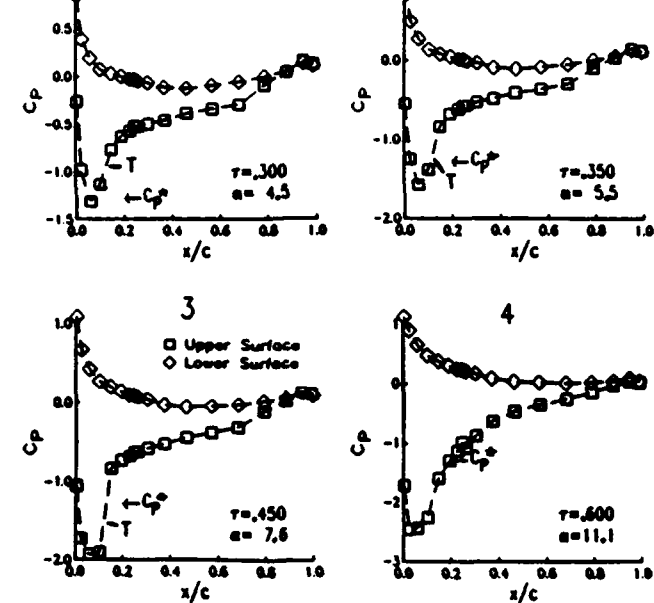
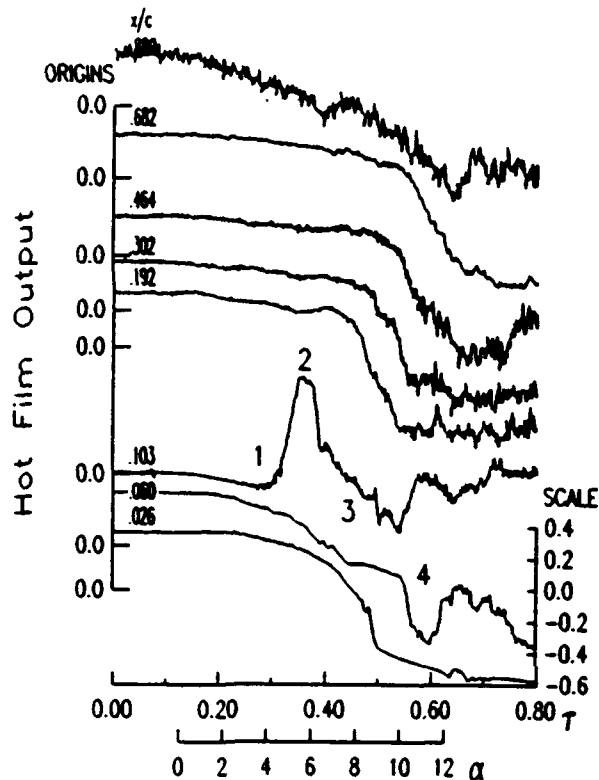


Fig. 11. Hot film time histories and chordwise pressure distributions at  $M_c = 0.6$ , for a ramp at  $A = 0.005$ ,  $A = 15^\circ$ , and  $z/c = 0.7$ .

of attack the adverse pressure gradient aft of the suction peak is relatively weak, so transition may be induced by the amplification of natural disturbances, similar to the process on a flat plate. The concept of a critical Reynolds number based on  $x$ ,  $\frac{U_\infty x}{\nu}$ , is applicable. For the 0.4-1% freestream turbulence levels present in this experiment, a critical Reynolds number of approximately  $5 \times 10^5$  is likely.<sup>19</sup> The value of  $x/c$  yielding this Reynolds number varies from  $x/c = 0.25$  at  $M_c = 0.2$  to  $x/c = 0.08$  at  $M_c = 0.6$ . The  $M_c \leq 0.4$  data in Fig. 12 are in rough agreement with this trend, but at  $M_c = 0.5$  and  $0.6$ , the experimental transition locations are considerably further aft.

At higher angles of attack ( $6 \leq \alpha \leq 10^\circ$ ), the dependence of the transition location on  $M_c$  is reduced (Fig. 12), as long as the regions of supersonic flow are very small and weak. Under these conditions ( $M_c \leq 0.4$ ), transition appears to be initiated by the adverse pressure gradient immediately aft of the suction peak. As shown by the pressure distributions in Figs. 5, 8, and 9, the position of the suction peak does not vary strongly with  $M_c$ .

For  $M_c = 0.5$  and  $0.6$ , sizable regions of supersonic flow develop at moderate angles of attack. The shock terminating these regions becomes the initiator of transition. As shown in Fig. 12, at  $M_c = 0.5$  this link between the transition point and the shock causes the forward motion of the transition point to be halted near  $x/c = 0.06-0.10$  at  $\alpha \approx 10^\circ$ . At  $M_c = 0.6$ , the transition point also remains near the shock ( $x/c \geq 0.1$ ) for  $\alpha \geq 5^\circ$ . The chordwise resolution of the hot film measurements is too coarse to determine whether transition occurs immediately following or preceding the shock. The results only indicate laminar conditions forward of the shock and turbulence aft. There is no clear indication of the separation that is the classic response of a laminar boundary layer to the presence of a shock. There is also no evidence of the multiple 'lambda' shocks that are commonly observed with laminar boundary layers.<sup>20,21</sup> It must be emphasized that there are potentially significant differences between the current experiment and the traditional results. This experiment is at a low freestream Mach

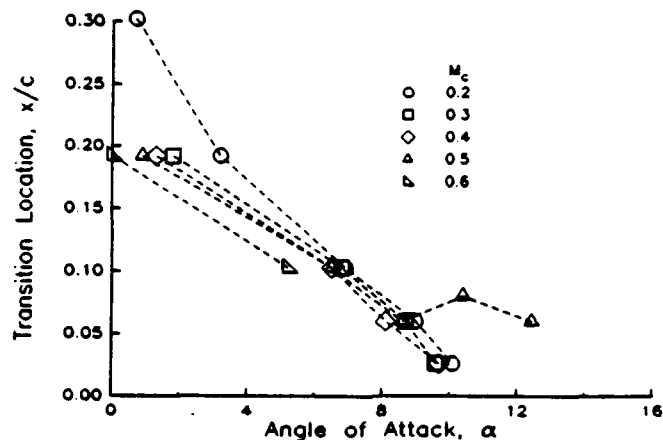


Fig. 12. Effect of Mach number on transition locations for ramp motions at  $A = 0.005$  and  $A = 15^\circ$ .

number and moderate angle of attack, generating a thin supersonic region near the highly curved leading edge, while the traditional experiments were typically performed at low angle of attack and higher freestream Mach number, generating a thick region of supersonic flow over the aft (low curvature) region of an airfoil or plate. The combination of a relatively weak shock ( $M \approx 1.3-1.4$ ), a thin supersonic region, and a curved surface may result in a shock that induces transition, but, at least temporarily, no significant separation. At higher angle of attack ( $\alpha \geq 12^\circ$  at  $M_c = 0.5$ ) the dynamic separation process does begin in the vicinity of the shock.<sup>9,10</sup>

## TRANSITION AND RELAMINARIZATION DURING SINUSOIDAL MOTIONS

The previous sections have described the transition process at steady state and during constant pitch rate ramps. This section will discuss results obtained for periodic sinusoidal pitching motions. The primary differences are the introduction of a time-varying pitch rate, and a periodic wake. The pitch-down portion of the sinusoidal motion also allows reattachment and relaminarization to be studied.

Figure 13 provides an example of the hot film and pressure results during sinusoidal motion. The conditions are  $\alpha = 10^\circ - 10^\circ \cos \omega t$ ,  $M_c = 0.2$ ,  $k = 0.05$ ,  $\Lambda = 15^\circ$ , and  $z/c = 0.7$ . The pressure results (Fig. 13a) show a generally smooth response, punctuated by a sharp separation at  $\tau \approx 0.46$ . The separation occurs at  $\alpha \approx 19.8^\circ$ , after the pitch rate has dropped substantially from its maximum value of  $A = 0.009$ . The negative pressure peak associated with the dynamic stall vortex propagates aft, followed by a constant pressure region indicating massive separation. Reattachment begins near the leading edge at  $\tau \approx 0.67$  ( $\alpha \approx 15^\circ$ ).

The hot film time histories (Fig. 13b) are qualitatively quite similar during pitch-up to the ramp results at  $M_c = 0.2$  shown in Fig. 5. As with the ramp, the transition point moves forward from  $x/c \geq 0.30$  at  $\alpha = 0$  past  $x/c = 0.026$  at  $\alpha \approx 10.7^\circ$ . The region of low heat transfer caused by separation corresponds to the constant pressure region shown in Fig. 13a. Starting at  $\tau \approx 0.66$ , the boundary layer reattaches from the leading edge aft, as shown by the rapid increase in heat transfer at the  $x/c = 0.026, 0.06$ , and  $0.10$  gages (Fig. 13b). The high level indicates that the flow reattaches as a turbulent boundary layer. The subsequent drop in heat transfer, starting at the  $x/c = 0.026$  gage at  $\tau \approx 0.74$  ( $\alpha = 10.9^\circ$ ), corresponds to a relaminarization of the boundary layer, again moving from the leading edge aft. The relaminarization at  $x/c = 0.026$  occurs at approximately the same value of  $\alpha$  as transition. This symmetry is not present for separation and reattachment, since at  $x/c = 0.026$  separation occurs at  $\alpha = 19.8^\circ$  and reattachment at  $\alpha = 15^\circ$ . The symmetry of transition and relaminarization does not persist through the conclusion of relaminarization. The transition point moves aft past  $x/c = 0.30$  at  $\tau = 0.97$  ( $\alpha = 0.2^\circ$ ), but does not return forward until  $\tau = 0.07$  ( $\alpha = 0.9^\circ$ ).

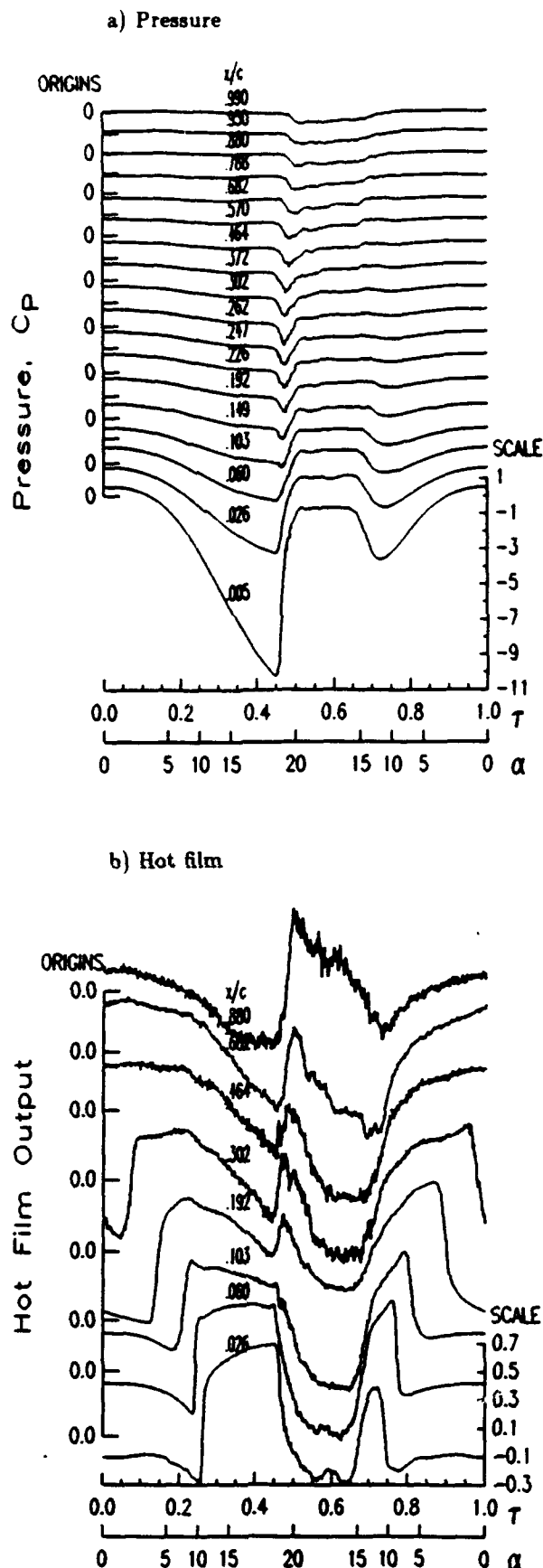


Fig. 13. Hot film and pressure time histories for sinusoidal oscillation at  $\alpha = 10^\circ - 10^\circ \cos \omega t$ ,  $M_c = 0.2$ ,  $k = 0.05$ ,  $\Lambda = 15^\circ$ , and  $z/c = 0.7$ .

Transition and relaminarization locations for a series of sinusoidal oscillations at reduced frequencies of  $k = 0.025, 0.05, 0.1$ , and  $0.15$  are shown in Fig. 14. The Mach number, sweep angle, and spanwise position are the same as in Fig. 13. These results show significant hysteresis in the transition-relaminarization cycle at higher frequency. At a given chordwise position, relaminarization generally occurs at a lower  $\alpha$  than transition. The largest measured difference is at  $x/c = 0.19$ , where data at  $k = 0.15$  show a  $3.6^\circ$  lower relaminarization angle. The hysteresis decreases at higher  $\alpha$ , as the transition point approaches the leading edge, to a maximum of  $1.8^\circ$  at  $x/c = 0.103$  and  $0.9^\circ$  at  $x/c = 0.026$ . At higher  $\alpha$ , transition is primarily influenced by the strong adverse pressure gradient immediately aft of the suction peak. Thus there is less variation in transition location than at lower  $\alpha$ , where transition occurs further aft, in a region with a more moderate pressure gradient. The hysteresis observed in Fig. 14 for  $\alpha = 10^\circ - 10^\circ \cos \omega t$  motions, in which there are large regions of flow separation, is also present in Fig. 15 for  $\alpha = 6^\circ - 6^\circ \cos \omega t$  motions, in which the boundary layers always remain attached. Separation is therefore not an essential requirement for hysteresis.

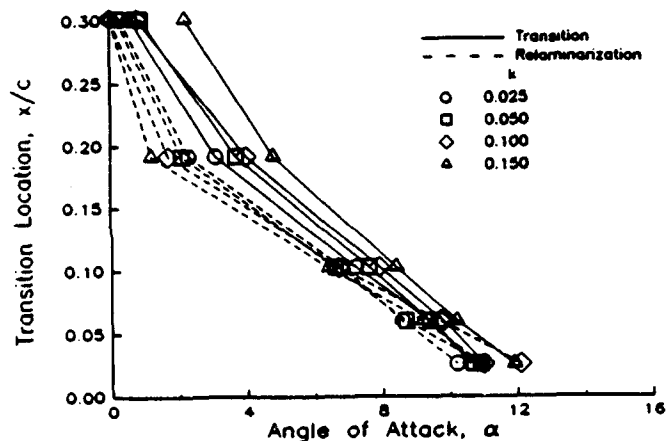


Fig. 14. Transition and relaminarization locations for sinusoidal motions at  $\alpha = 10^\circ - 10^\circ \cos \omega t$ ,  $M_c = 0.2$ ,  $\Lambda = 15^\circ$ , and  $z/c = 0.7$ .

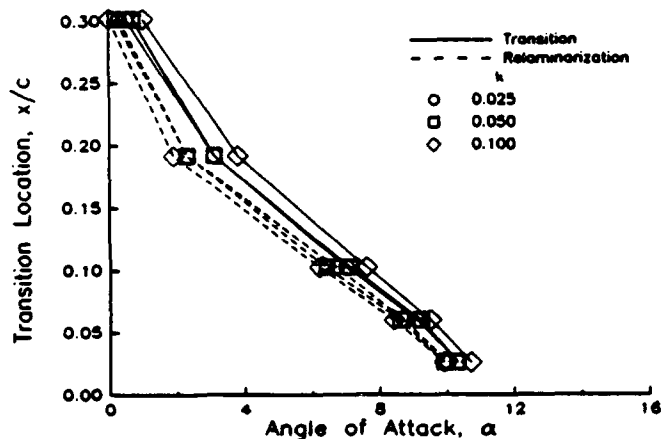


Fig. 15. Transition and relaminarization locations for sinusoidal motions at  $\alpha = 6^\circ - 6^\circ \cos \omega t$ ,  $M_c = 0.2$ ,  $\Lambda = 15^\circ$ , and  $z/c = 0.7$ .

Time histories at higher Mach number,  $M_c = 0.5$ , are shown in Fig. 16, for an  $\alpha = 6^\circ - 6^\circ \cos \omega t$  oscillation at  $k = 0.05$ . The pressure time histories (Fig. 16a) show a flow

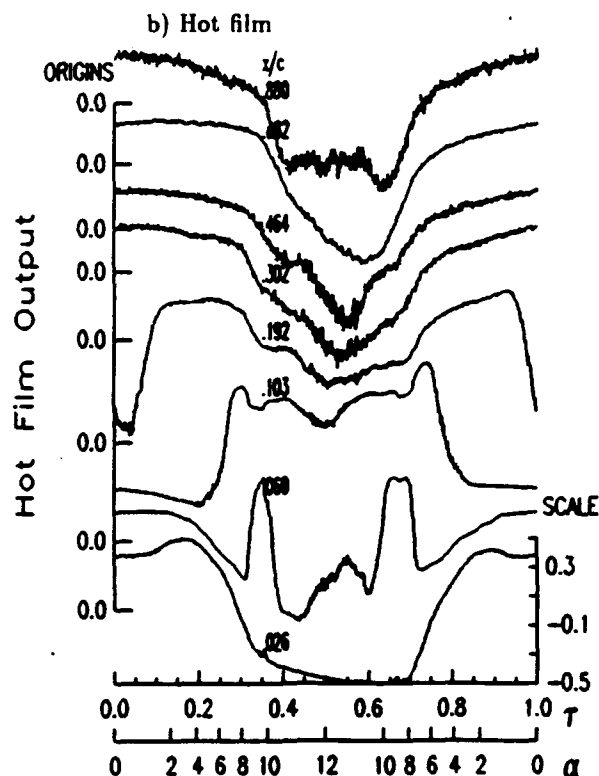
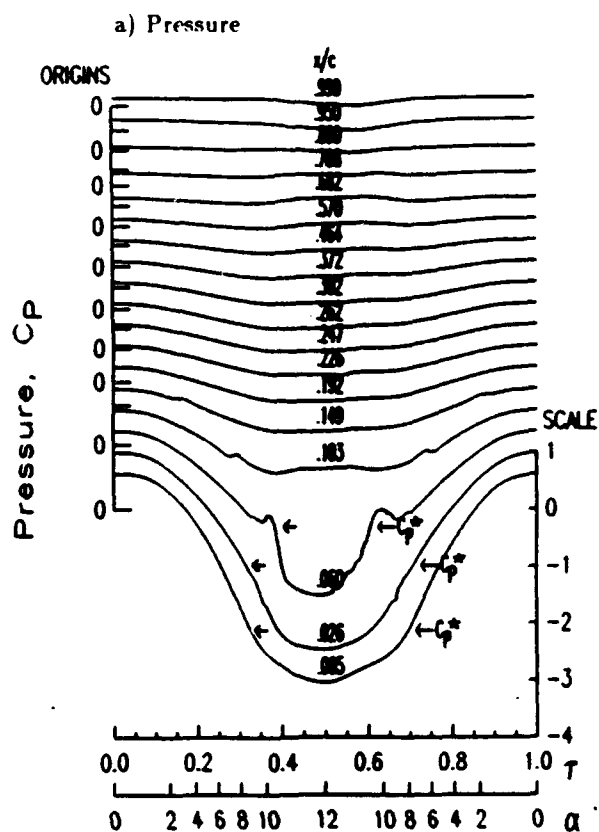


Fig. 16. Hot film and pressure time histories for sinusoidal oscillation at  $\alpha = 6^\circ - 6^\circ \cos \omega t$ ,  $M_c = 0.5$ ,  $k = 0.05$ ,  $\Lambda = 15^\circ$ , and  $z/c = 0.7$ .

that remains attached, but becomes supersonic for  $x/c = 0.026$  and  $0.06$  at  $r = 0.3$  and  $\alpha \approx 8^\circ$ . The expansion of the supersonic region and rearward movement of the shock past  $x/c = 0.06$  at  $r = 0.38$  distorts the pressure time history by creating a rapid pressure drop. The hot film time histories (Fig. 16b) during the pitch-up portion of the cycle appear quite similar to the ramp results at this Mach number (Fig. 10). The increase in heat transfer at the  $x/c = 0.06$  gage between  $r = 0.32$  and  $0.38$  correlates closely with the pressure time histories (Fig. 16a), which indicate that the shock forms upstream of  $x/c = 0.06$ , and then moves aft past this position. A similar, but reversed, sequence occurs during the pitch-down.

Transition and relaminarization locations are shown in Fig. 17 for  $M_c = 0.5$  sinusoids at  $k = 0.025, 0.05$ , and  $0.1$ . As at  $M_c = 0.2$ , there is significant hysteresis (up to  $1.6^\circ$ ) involved in the movement of the transition between  $x/c = 0.19$  and  $0.06$ . The differences between the transition and relaminarization angles for  $\alpha \geq 9^\circ$  are reduced to less than  $0.5^\circ$ . Under these conditions, the shock is believed to be the primary determinant of the transition location.

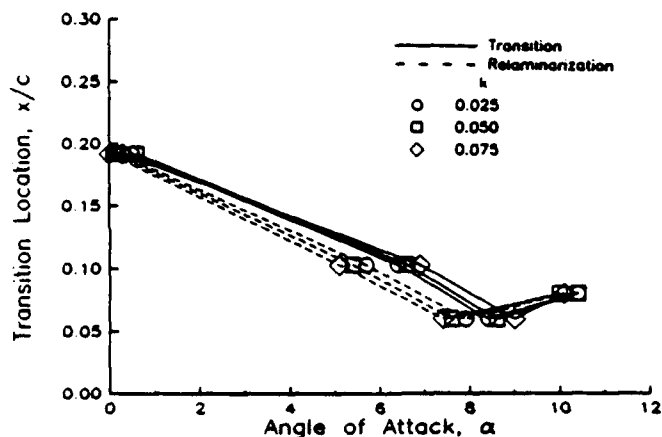


Fig. 17. Transition and relaminarization locations for sinusoidal motions at  $\alpha = 6^\circ - 6^\circ \cos \omega t$ ,  $M_c = 0.5$ ,  $\Delta = 15^\circ$ , and  $z/c = 0.7$ .

## CONCLUSIONS

Experimental measurements of transition locations on a rectangular wing model during steady-state and unsteady pitching motions at Mach numbers between  $0.2$  and  $0.6$  and Reynolds numbers of  $2-6 \times 10^6$  have resulted in the following observations.

1. At low angle of attack ( $\alpha \leq 4^\circ$ ) transition generally occurs between  $x/c = 0.14$  and  $0.3$ . Transition occurs furthest aft at  $M_c = 0.2$ , and closest to the leading edge at  $M_c = 0.6$ . Under these conditions, where the adverse pressure gradient is relatively mild, the occurrence of transition may be associated with reaching a critical Reynolds number, based on  $x$ , of approximately  $5 \times 10^5$ .

2. As  $\alpha$  is increased, the adverse pressure gradient increases and the transition point moves forward. For  $\alpha \geq 6-8^\circ$ , transition occurs a very short distance aft of the suction pressure peak. Under these conditions, the dependence on  $M_c$  (and therefore also Reynolds number) is reduced, for  $M_c \leq 0.4$ . Transition moves forward of the first hot film gage ( $x/c = 0.026$ ) at  $\alpha \approx 10-12^\circ$ .
3. For the relatively high Reynolds number range of this experiment, the boundary layer becomes essentially turbulent prior to separation. There is no indication of the transitional separation bubble frequently observed at lower Reynolds number.
4. At  $M_c = 0.5-0.6$ , significant regions of supersonic flow develop near the leading edge at  $\alpha \geq 7-10^\circ$ , with maximum local Mach numbers of  $1.3-1.4$ . Transition is initiated at the shock that terminates the supersonic region at  $x/c \approx 0.1-0.15$ . There does not appear to be any substantial shock-induced separation at these moderate angles of attack.
5. Increasing pitch rate from  $A = 0.001$  to  $0.02$  introduces a lag in the forward motion of the transition point, by up to  $\Delta \alpha = 2^\circ$ .
6. Wing sweep angles of  $\Lambda = 0, 15$ , and  $30^\circ$  do not substantially alter the transition locations at the inboard station ( $z/c = 0.7$  chords from the tip). However, very close to the wing tip, transition occurs earlier for the unswept wing at low  $\alpha$  than for the swept wing, possibly because of disturbances induced by the tip vortex.
7. During sinusoidal pitching motions, the transition point moves forward as  $\alpha$  increases, and aft as  $\alpha$  decreases. At higher reduced frequency, a significant hysteresis of up to  $3.6^\circ$  develops between the values of  $\alpha$  for transition and relaminarization. The hysteresis is much stronger near  $x/c = 0.15-0.30$  than it is closer to the leading edge.

## ACKNOWLEDGMENTS

The instrumented model, the wind tunnel test, and the analysis of the results were funded by the U.S. Army Research Office and the U.S. Air Force Office of Scientific Research, under Contract DAAL03-89-C-0013. Dr. Thomas Doligalski of ARO was the technical monitor. Capt. Hank Helin and Maj. Daniel Fant were the AFOSR representatives. The model support and drive system was supplied by the Sikorsky Aircraft Division of United Technologies. The authors thank Alfred Covino, John Ayer, and the staff of the UTRC LSWT for their assistance during the test.

## REFERENCES

1. De Ruyck, J., Hazarika, B., and Hirsch, C., "Transition and Turbulence Structure in the Boundary Layers of an Oscillating Airfoil," Vrije Univ. Brussels Report STR-16, Dec. 1989.
2. Chandrasekhara, M.S., and Ahmed, S., "Laser Velocimetry Measurements of Oscillating Airfoil Dynamic Stall Flow Field," AIAA Paper 91-1799, 22nd Fluid Dynamics, Plasma Dynamics, and Lasers Conference, Honolulu HI, June 1991.
3. Carr, L.W., McCroskey, W.J., McAlister, K.W., Pucci, S.L., and Lambert, O., "An Experimental Study of Dynamic Stall on Advanced Airfoil Sections, Volume 3: Hot-Wire and Hot-Film Measurements," NASA TM 84245, Dec. 1982.
4. Carta, F.O., "Dynamic Stall of Swept and Unswept Oscillating Airfoils, AGARD FDP Symposium on Unsteady Aerodynamics," May 1985.
5. Lorber, P.F., and Carta, F.O., "Airfoil Dynamic Stall at Constant Pitch Rate and High Reynolds Number," *Journal of Aircraft*, Vol. 25, June 1988, pp. 548-556.
6. Lorber, P.F., and Carta, F.O., "Unsteady Stall Penetration Experiments at High Reynolds Number", AFOSR TR-87-1202, April 1987.
7. Patterson, M.T., and Lorber, P.F., "Computational and Experimental Studies of Compressible Dynamic Stall," *Journal of Fluids and Structures*, Vol. 4, 1990, pp. 259-285.
8. Lorber, P.F., and Carta, F.O., "Incipient Torsional Stall Flutter Experiments on a Swept Three-Dimensional Wing," AIAA Paper 91-0935, 32nd Structures, Structural Dynamics, and Materials Conference, Baltimore MD, April 1991.
9. Lorber, P.F., Carta, F.O., and Covino, A.F. Jr., "Dynamic Stall Experiments on a Swept Three-Dimensional Wing In Compressible Flow," AIAA Paper 91-1795, 22nd Fluid Dynamics, Plasma Dynamics, and Lasers Conference, Honolulu HI, June 1991.
10. Lorber, P.F., "Sweep and Compressibility effects on the Dynamic Stall of a Three-Dimensional Wing," AIAA Paper 92-0191, 30th Aerospace Sciences Meeting, Reno NV, Jan. 1992.
11. Williams, M.C., Pratt & Whitney Aircraft Internal Correspondence, September 1988.
12. Haritonidis, J.H., "The Measurement of Wall Shear Stress," *Advances in Fluid Mechanics Measurements, Lecture Notes in Engineering* (ed. M. Gad-el-Hak), Springer-Verlag, pp. 229-261, 1989.
13. Cook, W., "Response of Hot Element Wall Shear Stress Gages in Unsteady Turbulent Flows," AIAA Paper 91-0167, 29th Aerospace Sciences Meeting, Reno NV, Jan. 1991.
14. Houdeville, R., Juillen, J.C., and Cousteix, J., "Skin Friction Measurements with Hot-Element Gages," *Recherche Aerospatiale*, Vol. 1, 1984, pp. 67-79.
15. Flutie, K.J., and Covert, E.E., "Unsteady Measurement of Skin Friction in Adverse Pressure Gradients; A New Approach to a Well-Known Gauge," AIAA Paper 91-0168, 29th Aerospace Sciences Meeting, Reno NV, Jan. 1991.
16. Greff, E., "In-Flight Measurement of Static Pressures and Boundary-Layer State with Integrated Sensors," *Journal of Aircraft*, Vol. 28, pp. 289-299, May 1991.
17. Schlichting, H., *Boundary Layer Theory*, Seventh Edition, McGraw Hill Book Co., New York NY, 1979, pp. 496-502.
18. Ibid., pp. 719-723.
19. Ibid., pg. 476.
20. Ibid., pp. 358-372.
21. Van Dyke, M., *An Album of Fluid Motion*, Parabolic Press, Stanford CA, 1982, pp. 150-152.

# INVESTIGATION OF FORCED UNSTEADY SEPARATED FLOWS USING VELOCITY-VORTICITY FORM OF NAVIER-STOKES EQUATIONS

by

K. N. Ghia, U. Ghia\* and G. A. Osswald

Department of Aerospace Engineering and Engineering Mechanics

\*Department of Mechanical, Industrial and Nuclear Engineering

Computational Fluid Dynamics Research Laboratory

University of Cincinnati

Cincinnati, Ohio 45221

## Abstract

The phenomenon of forced unsteady separation and eruption of boundary-layer vorticity is a highly-complex, high-Reynolds number flow phenomenon, which abruptly leads to the formation of a dynamic stall vortex as demonstrated earlier by the authors for a NACA 0015 airfoil undergoing constant rate pitch-up motion. This, as well as the results of other researchers, have convincingly demonstrated a complex vortical structure within the state of unsteady separation prior to the evolution of dynamic stall. This phenomenon of vortex eruption, although observed in studying dynamic stall phenomena, is also associated with transition from laminar to turbulence flow and its generic nature has been stressed by many researchers including the present investigators.

An unsteady Navier-Stokes (NS) analysis is developed for arbitrarily maneuvering bodies using velocity-vorticity variables; this formulation is nearly form-invariant under a generalized non-inertial coordinate transformation. A fully-implicit uniformly second-order (except convective terms) accurate method is used, with the nonlinear convective terms approximated using a biased third-order upwind differencing scheme to be able to simulate higher-Re flows. No explicit artificial dissipation is added. The numerical method is fully vectorized and currently achieves a computational index of 7 micro-seconds per time step per mesh point, using a single processor on the CRAY Y-MP 8/864 at the Ohio Supercomputer Center. The simulation results show that the energetic free shear from the leading edge is responsible for the wall viscous layer to abruptly erupt near the center of the counterclockwise rotating eddy in the unsteady boundary layer. Primary, secondary, tertiary and quaternary vortices have been observed before the dynamic stall vortex evolves and gathers its maximum strength. This study will discuss the simulation results of Reynolds number up to  $Re = 45,000$  and will also discuss the effort of initial acceleration in a specific maneuver, on the evolution of the stall vortex.

# NUMERICAL SIMULATIONS OF DYNAMIC STALL PHENOMENA BY DISCRETE VORTEX METHOD AND VISCOUS FLOW CALCULATION

Shigeru ASO\* and Masanori HAYASHI\*\*

\* Department of Aeronautical Engineering, Kyushu University, Fukuoka, JAPAN

\*\* Nishinippon Institute of Technology, Fukuoka, JAPAN

## ABSTRACT

Dynamic stall phenomena have been simulated numerically by a discrete vortex method and viscous flow calculations. Both simulations could capture the characteristics of dynamic stall phenomena qualitatively. Also some numerical results show good agreements with experiments.

In the calculations by a discrete vortex method combined with a panel method the potential flows around wing sections is expressed by vortex sheets and separated shear layers are expressed by discrete vortices. Separated flows around pitching airfoils(NACA0012) are simulated for various conditions. A hysteresis of lift of airfoil at dynamic stall is obtained. The results suggest that the method has a excellent capability of simulating vortical flows with excellent small computation cost. In the calculations by viscous flow calculations incompressible Navier-Stokes equations have been solved by a third-order upwind scheme in order to understand the flow structure and mechanism of dynamic stall. Especially the flow mechanics of movement of separation point on the wing surface, vortex formation from the surface of the wing and unsteady Kutta conditions at the trailing edge of the wing are investigated carefully. The unsteady flow fields around a pitching airfoil are calculated by moving a grid system relative to the freestream. Remarkable characteristics of dynamic stall are obtained. Also the hysteresis curve of aerodynamic characteristics of  $C_L$  and  $C_M$  are obtained.

## 1. INTRODUCTION

Studies on dynamic stall have been conducted experimentally and theoretically by the many researchers<sup>1-5)</sup>. However as the phenomena are essentially non-linear and the flow field becomes complicated as the separated region is increased, those phenomena are not understood sufficiently.

In this paper two efforts for simulating dynamic stall phenomena are discussed. One is based on a discrete vortex method combined with a panel method and the other is based on viscous flow calculations. Both simulations could capture the qualitative properties on dynamic stall phenomena. Also some numerical results show good agreements with experiments.

In the calculations by a discrete vortex method combined with a panel method<sup>6,7)</sup> the potential flows around wing sections is expressed by vortex sheets and separated shear layers are expressed by discrete vortices. For the calculations a new numerical scheme developed by the present authors<sup>7)</sup> have been used. In the calculation a wing section is expressed by a set of linearly distributed vortex sheets and

the separation points are determined by boundary layer calculations. Separated flows around pitching airfoils are simulated for various conditions. A hysteresis of lift of airfoil at dynamic stall is obtained. The results suggest that the method has a excellent capability of simulating vortical flows with excellent small computation cost.

In the calculations by viscous flow calculations incompressible Navier-Stokes equations have been solved by a third-order upwind scheme in order to understand the flow structure and mechanism of dynamic stall. Especially the flow mechanics of movement of separation point on the wing surface, vortex formation from the surface of the wing and unsteady Kutta condition at the trailing edge of the wing are investigated carefully. The unsteady flow fields around a pitching airfoil are calculated by moving a grid system relative to the freestream. Remarkable characteristics of dynamic stall are obtained. Also the hysteresis curve of aerodynamic characteristics of  $C_L$  and  $C_M$  are obtained.

## 2. Numerical Simulation of Dynamic Stall by Discrete Vortex Method

### 2.1 Analytical Method

The complex potential  $f$  of the flow field is expressed by the following form:

$$f = Ue^{-i\alpha}z + i \int_B \frac{\gamma(\zeta)}{2\pi} \log(z - \zeta) d\zeta$$

$$+ i \sum_{k=1}^M \left( \frac{\Gamma_{Ak}}{2\pi} \log(z - z_{Ak}) + \frac{\Gamma_{Bk}}{2\pi} \log(z - z_{Bk}) \right) \quad (1)$$

, where  $U$  is the uniform flow velocity and  $\alpha$  is the angle of attack. The discrete vortices expressing separated shear layers are shed from the separation points on the wing surface. The circulation of each vortex is estimated using the velocity at the point assumed as the edge of the boundary layer near the separation point. Hence, unknown quantities in the flow field are the amount of strength of the singular points on the wing surface and solved at each time step by using boundary condition for normal velocity through the control point on the surface. The detailed description of the method are discussed in Ref. 7.

For the calculation of the flow around the pitching wing section, incident angle of the freestream is sinusoidally changed. Then the angle of attack of the wing section is given by following form:



$$\alpha = \alpha_0 + \alpha_1 \sin \omega t \quad (2)$$

, where the angular frequency  $\omega$  is related to the reduced frequency  $k$  by the following form:

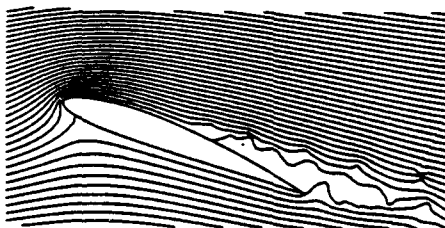
$$k = \frac{\omega c}{2U_\infty} \quad (3)$$

where  $c$  is the chord length. As the separation point on the wing section is not obvious a priori, the separation point is determined by the boundary layer calculations. The Thwaites' method<sup>(4,5)</sup> is used for the laminar boundary layer calculation and the Truckenbrodt's method<sup>(4,5)</sup> is used for the turbulent boundary layer calculation.

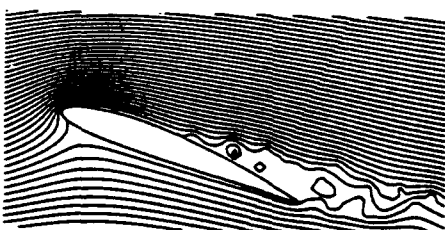
## 2.2 Separated Flows around a Wing Section at a Fixed Angle of Attack

Fig. 1 shows several calculated instantaneous stream lines around a wing section of NACA4412 at angle of attack of 20 degrees. As shown in the Figure the flow is quite unsteady and the changes of separation point and separated region can be observed. The calculated pressure distribution is compared with the experiments in Fig. 2. As shown in the Figure the calculated pressure distribution shows good agreement with that by experiment<sup>(9)</sup> including the separated region. Fig. 3 shows  $C_L$  and  $C_D$  with  $\alpha$ . A good agreement of  $C_L$  between the calculations and the experiments is obtained. Also the results of  $C_D$  show good agreement with the experiments. Those results suggest that a discrete vortex method is quite powerful for prediction of aerodynamic characteristics of a wing section at static angle of attack.

$$\frac{UT}{b} = 40.2$$



$$\frac{UT}{b} = 40.6$$



$$\frac{UT}{b} = 41.0$$

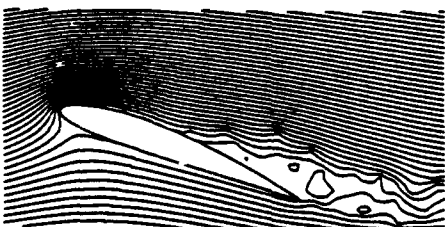


Fig. 1 Instantaneous stream lines(NACA4412,  $\alpha = 20$ degrees,  $Re = 1.0 \times 10^6$ )

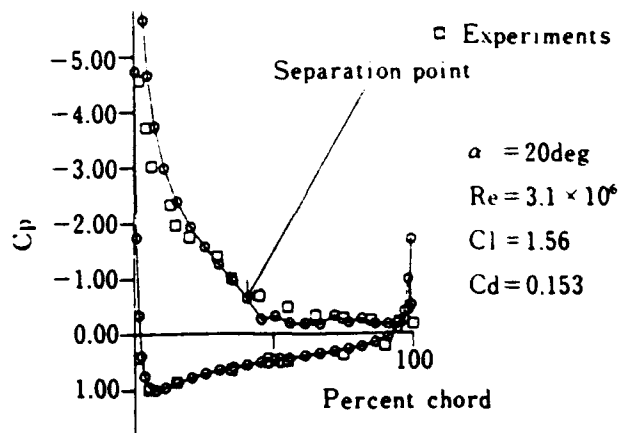


Fig. 2 Comparison of pressure distribution with experiments(NACA4412,  $\alpha = 20$ degrees,  $Re = 1.0 \times 10^6$ )

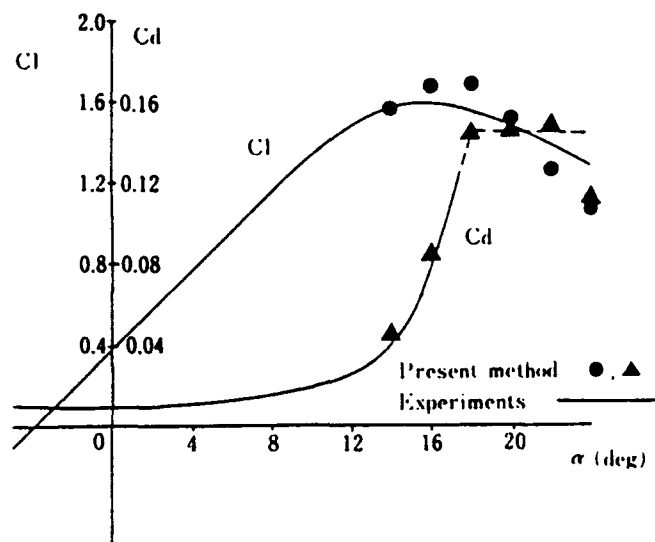


Fig. 3 Comparison of  $C_L$  and  $C_D$  with experiments

## 2.3 Separated Flows around an Oscillating Wing Section in Pitch

The calculated results of separated flows around pitching airfoil(NACA0012) under the condition of  $\alpha = 15^\circ + 10^\circ \sin \omega t$  ( $k = 0.15$ ) and Reynolds number  $= 1.0 \times 10^6$  is shown in Fig. 4. As shown in the figure separated region is small in pitching-up process and it becomes much larger in pitching-down process. Quite different characteristics of flow patterns between in pitching-up and pitching-down processes are obtained. The results show some features of dynamic stall. The calculated aerodynamic characteristics are compared with experiments<sup>(1)</sup> as shown in Fig. 5. The calculated Hysteresis curve of  $C_L$  show almost same tendency as the experiments. The results show fairly good agreements with experiments.

Another calculation have been conducted under the condition of  $\alpha = 15^\circ + 14^\circ \sin \omega t$  ( $k = 0.1$ ) and Reynolds number  $= 1.0 \times 10^6$  as shown in Fig. 6. In the Figure separated region is small in pitching-up process and it becomes much

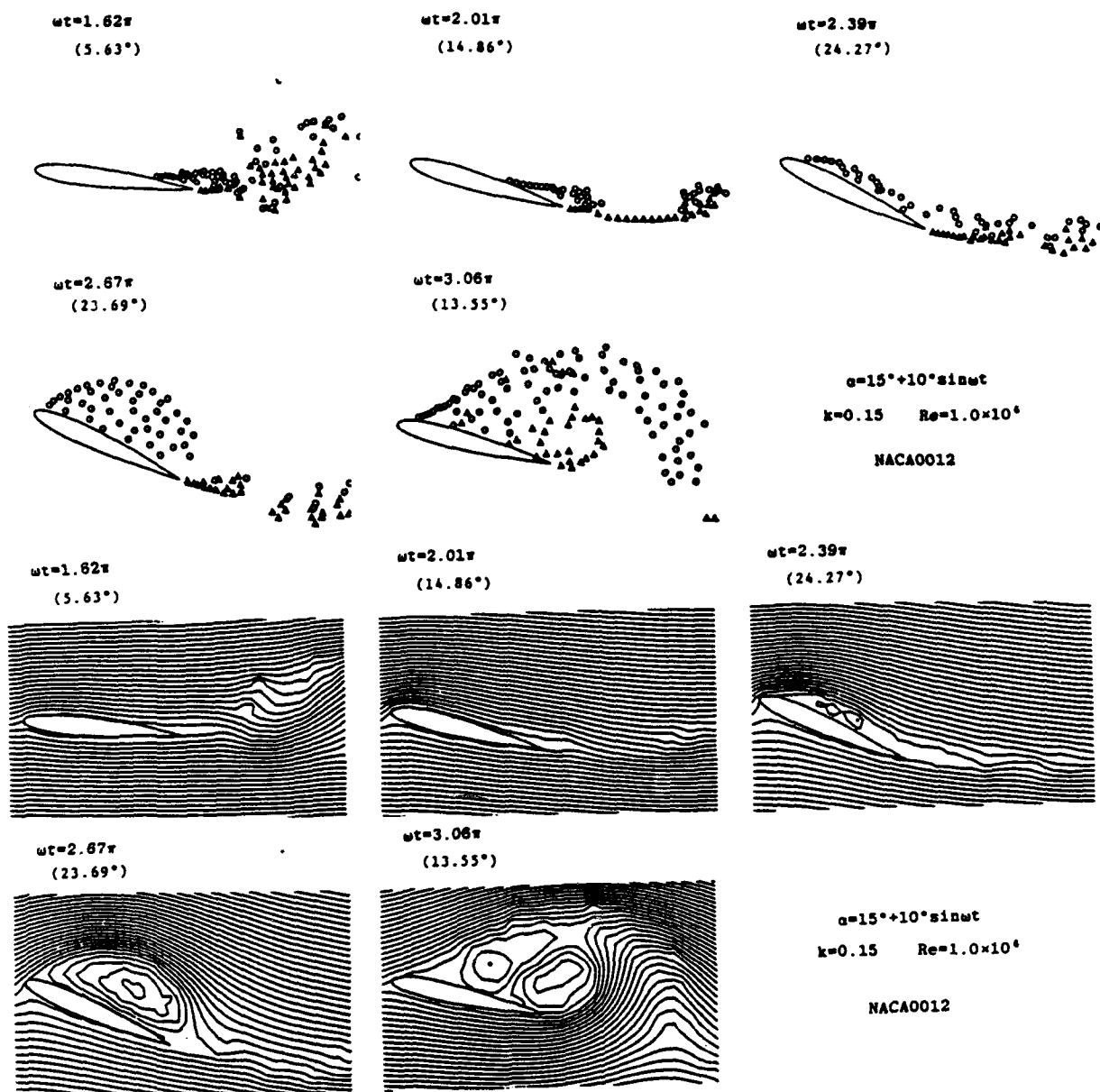


Fig. 4 Flow patterns at  $\alpha = 15^\circ + 10^\circ \sin \omega t$  ( $k = 0.15$ ; NACA0012,  $Re = 1.0 \times 10^6$ )

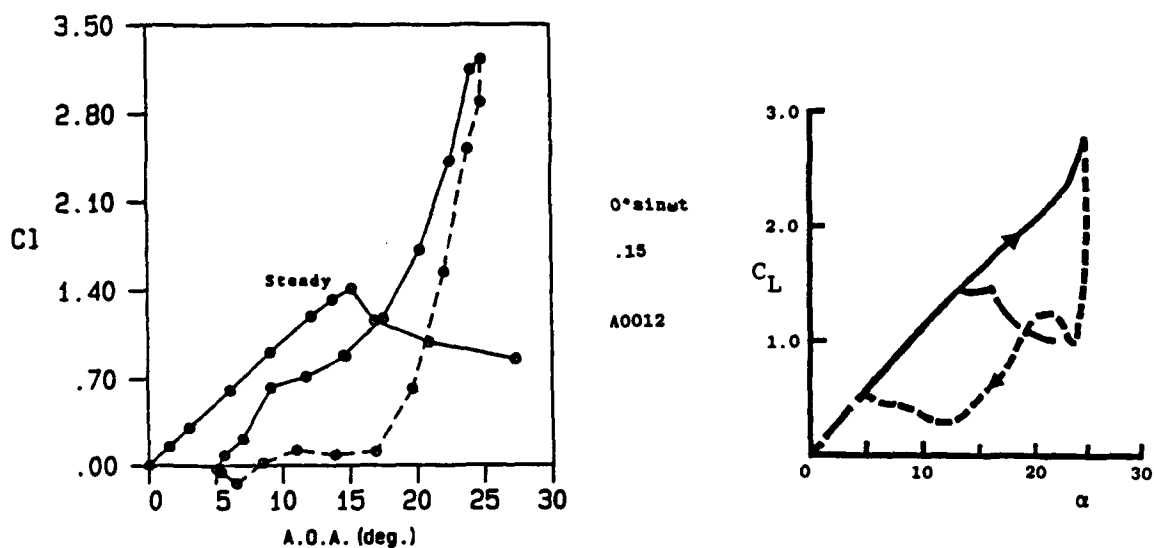


Fig. 5 Comparisons of calculated hysteresis curves of  $C_L$  with experiments<sup>1)</sup> ( $\alpha = 15^\circ + 10^\circ \sin \omega t$  ( $k = 0.15$ ; NACA0012,  $Re = 1.0 \times 10^6$ ))

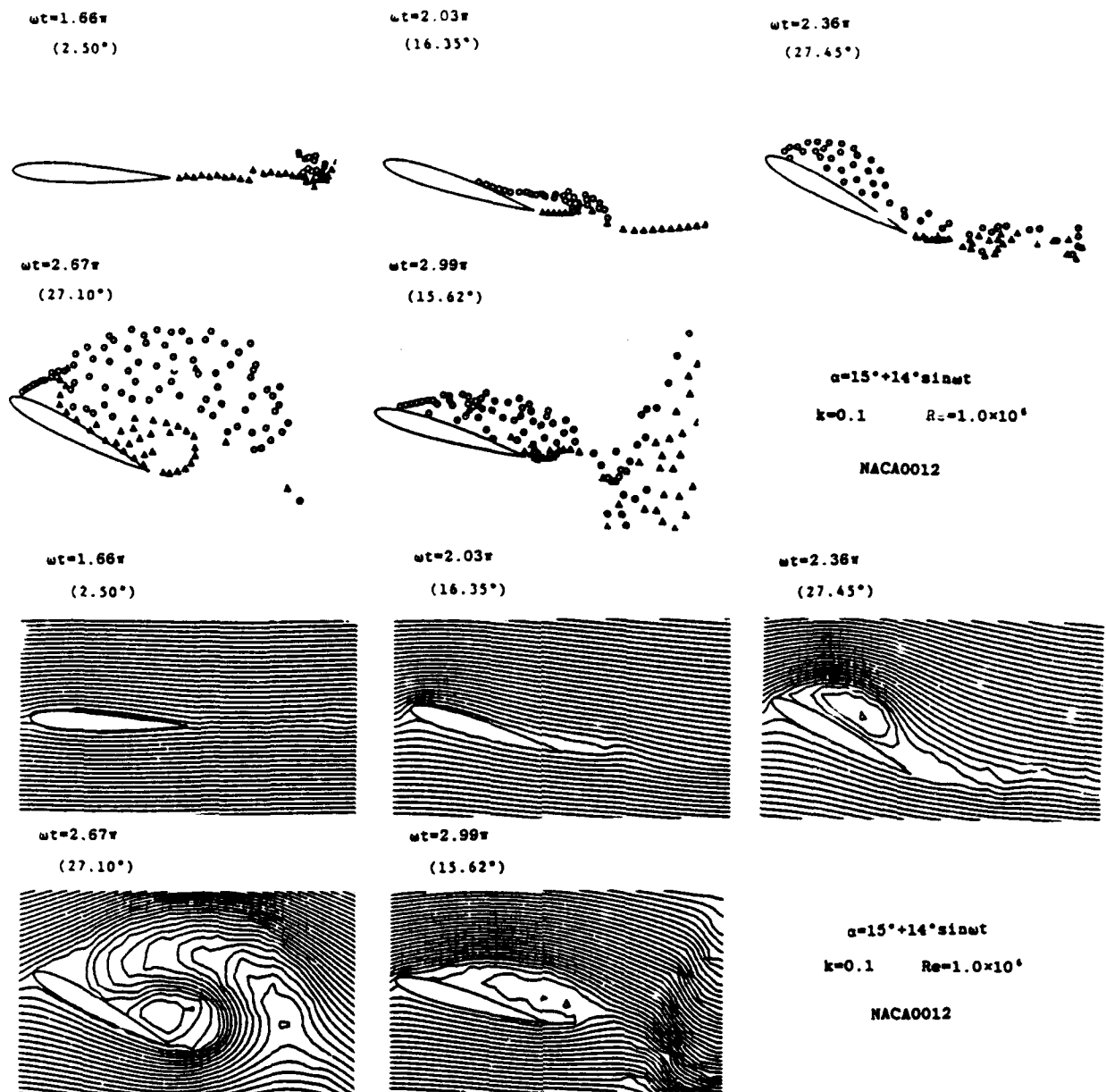


Fig. 6 Flow patterns at  $\alpha = 15^\circ + 14^\circ \sin \omega t$  ( $k = 0.1$ ; NACA0012,  $Re = 1.0 \times 10^6$ )

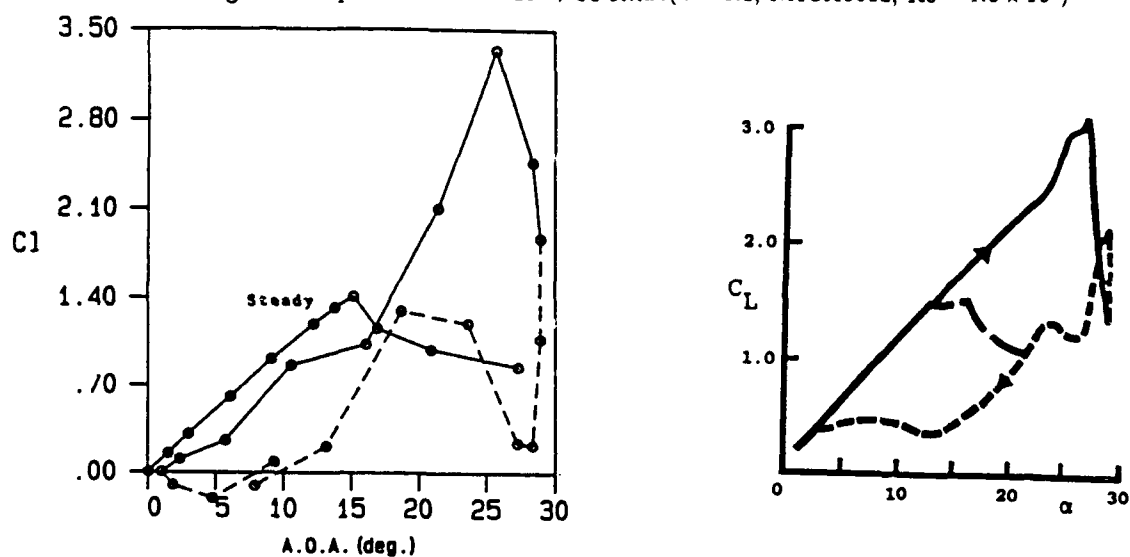


Fig. 7 Comparisons of calculated hysteresis curves of  $C_L$  with experiments<sup>1)</sup> ( $\alpha = 15^\circ + 14^\circ \sin \omega t$  ( $k = 0.1$ ; NACA0012,  $Re = 1.0 \times 10^6$ ))

larger in pitching-down process. Quite different characteristics of flow patterns between in pitching-up and pitching-down processes are also obtained. The calculated aerodynamic characteristics are compared with experiments<sup>11</sup> as shown in Fig. 7. The calculated Hysteresis curve of  $C_L$  show almost same tendency as the experiments. The results show fairly good agreements with experiments qualitatively. The results show  $C_L$  of oscillating airfoil shows higher maximum value compared with that of a stationary airfoil.

Those calculated results show qualitatively good agreement with experiments and excellent capability of the method is proved. Also as the computation time for each calculation is quite small compared with those of other finite-difference methods, the method is quite useful for the first estimation of the aerodynamic characteristics of a new wing section.

### 3. Numerical Simulation of Dynamic Stall by Viscous Flow Calculation

#### 3.1 Numerical Procedures

Unsteady flows of viscous incompressible fluid flow around a airfoil is considered. The governing equations are equations of continuity and incompressible Navier-Stokes equations:

$$\text{div } \mathbf{V} = 0 \quad (4)$$

$$\frac{\partial \mathbf{V}}{\partial t} + (\mathbf{V} \cdot \nabla) \mathbf{V} = -\text{grad } p + \frac{1}{Re} \Delta \mathbf{V} \quad (5)$$

where  $Re$  is Reynolds number. Following MAC method (Marker and Cell method)<sup>10</sup>, the Poisson equation for the pressure  $p$  is derived by taking divergence of Eq(5):

$$\Delta p = -\text{div}(\mathbf{V} \cdot \nabla) \mathbf{V} + R \quad (6)$$

where

$$R = -\frac{\partial D}{\partial t} + \frac{1}{Re} \Delta D, \quad D = \text{div } \mathbf{V} \quad (7)$$

Although  $R$  in Eq.(7) is identically zero due to Eq.(1), it is retained here as a corrective term in order to prevent the accumulation of numerical errors. If  $\mathbf{V}$  is given at certain time, then the Poisson equation (6) can be solved to get  $p$ , and then by substituting these value into Eq.(5),  $\mathbf{V}$  at next time is calculated from Eq.(5). The detailed numerical procedures will be given in Reference 11.

For mesh grid generation Steger and Sorenson's method<sup>12</sup> is used. The method is useful to generate a body-fitted mesh system for an arbitrary body with keeping almost orthogonal coordinates system at the wall. The mesh system is generated as O-grid type and quite fine mesh is prepared in the vicinity of the body surface. For the calculation of separated flow around oscillating airfoil a general coordinate system with time-dependent variables is introduced. However in the computation using those coordinate systems the displacement of the grid point and distortion of the mesh system for each time interval should be considered carefully. In the present computation the method proposed by Nakamichi<sup>13</sup> is used.

In the velocity fields non-slip conditions are used for the wing surface and uniform flow conditions are used for outer boundary. In the pressure fields zero derivative normal to the wing surface is used and zero derivative parallel to the freestream is used at exit boundary.

#### 3.2 Separated Flows around an Airfoil at Fixed Attack Angle

Before the calculations the preliminary calculation has been conducted for separated flows around circular cylinder at low Reynolds number in order to check the validity of the numerical scheme by the present authors<sup>14</sup>. The results show excellent agreements with experiments. The width of the separated region and flow patterns are predicted quite precisely. The results show the present numerical scheme is quite useful and reliable for incompressible viscous flow.

The mesh system(85 × 61) generated for a wing section of NACA0012 is shown in Fig. 8. Quite fine mesh is prepared in the vicinity of the wing surface and quite wide range of outer boundary are considered. The separated flows around airfoil at various attack angle is calculated at Reynolds number of 300. The representative results of in-

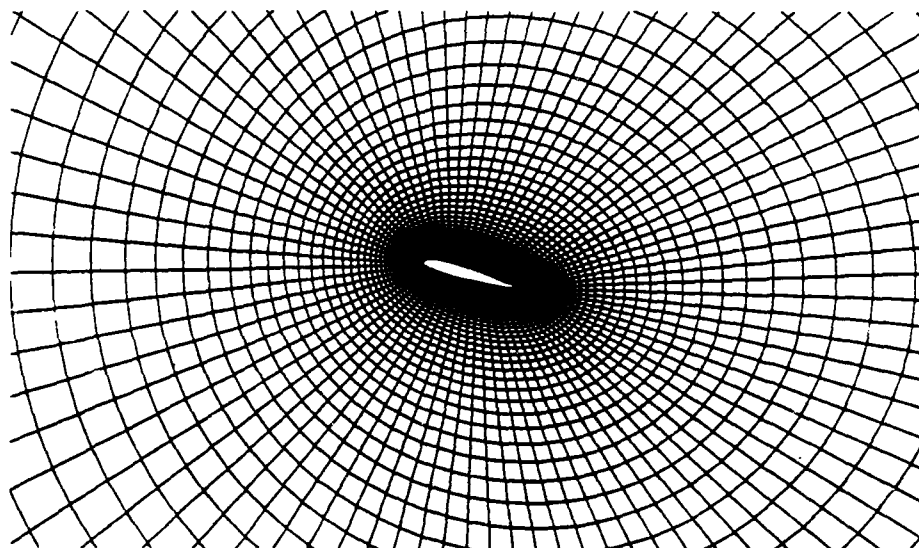
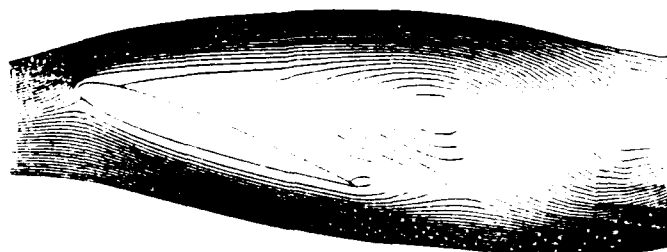
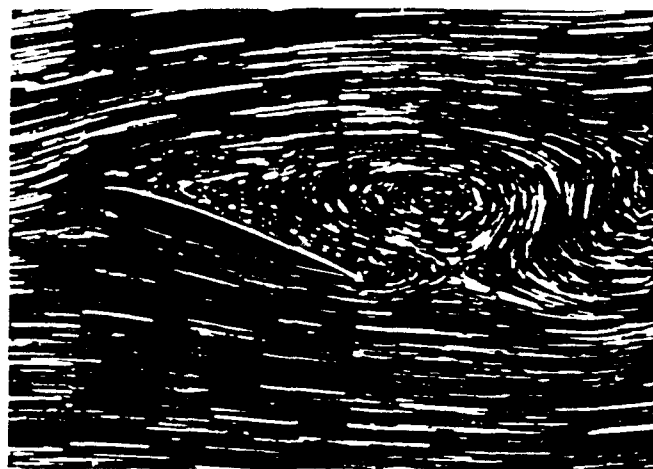
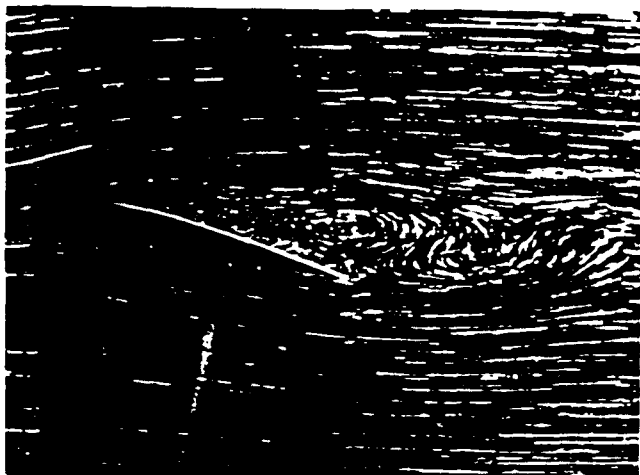


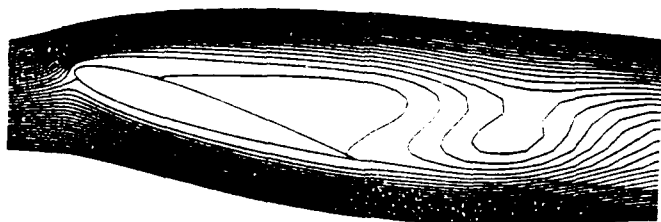
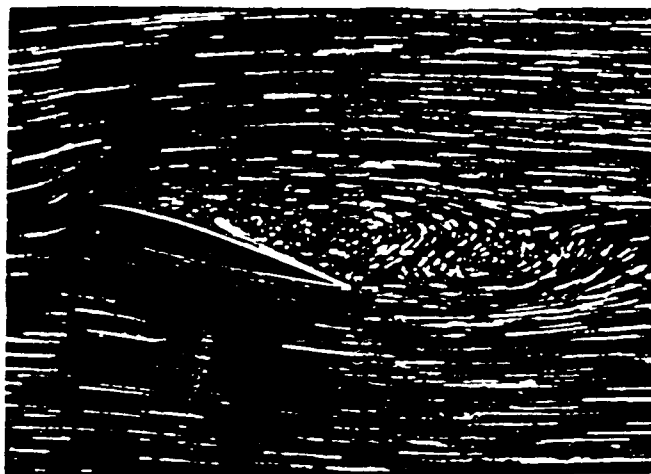
Fig. 8 Mesh system (NACA0012;IMAX=85, JMAX=61)



a)  $\alpha = 14^\circ$

b)  $\alpha = 20^\circ$

Fig. 9 Comparison of Flow patterns (instantaneous streamlines) between calculations and experiments (Aluminum powder) (NACA0012,  $Re=100$ )



time = 18.0

b)  $\alpha = 16^\circ$

Fig. 10 Comparison of flow patterns (electrolytic precipitation pictures) between calculations and experiments (NACA0012,  $Re=300$ ,  $\alpha = 20^\circ$ )

stantaneous stream lines are compared with experimental results obtained by the present authors as shown in Fig. 9. The results show excellent agreements with experiments at various attack angle. As shown in the Figures separated region become large as attack angle is increased. In the present conditions separated shear layer forms a vortex and convects in the freestream. Karman vortex shedding pattern is observed behind an airfoil section. A separated shear layer shed from the trailing edge forms another vortex and rolls up behind a airfoil and convects downstream. The flow is quite periodic and those flow patterns repeat at every interval.

The separated flow patterns can be also visualized by the electrolytic precipitation method. Fig. 10 shows comparison of calculated electrolytic precipitation picture and that obtained by the experiments. In the calculation numerous marker particles are introduced in the vicinity of the airfoil surface at some time interval and their temporal traces, which are induced by the velocity fields, are calculated. Those traces form streak lines of the flow fields. A Crank-Nicolson's implicit time integration is used in order to get accurate temporal resolution. The results show the numerical streak lines, i.e. numerical electrolytic precipitation pictures, is quite useful in order to understand the structure of the flow fields and compare the calculated results with experiments.

### 3.3 Separated Flows around an Oscillating Airfoil in Pitch

In the previous section the numerical scheme used in the present calculation is proved to be quite useful and reliable, the unsteady flow fields around a oscillating airfoil in pitch are calculated by moving a grid system relative to the freestream. The flow conditions are selected from the experiments conducted by the present authors. The center of rotation is located at 25 percent of the chord and an airfoil section of NACA0012 is oscillated sinusoidally in pitch at reduced frequency of  $k = \omega c/2U = 0.2$  and Reynolds number of  $7.0 \times 10^4$ .  $c$  is a chord length and  $U$  is freestream velocity.

The representative calculated results under the condition of  $\alpha = 12^\circ + 4^\circ \sin \omega t$ ,  $k = 0.2$  and Reynolds number  $= 7.0 \times 10^4$  is shown in Fig. 12. Instantaneous stream lines and numerical smoke wire diagrams are shown in the Figures. For the calculations of numerical smoke-wire picture numerous fluid particles are introduced at equi-spacing points along a perpendicular axis, which is set in front of an airfoil for several time interval and their temporal traces, which are induced by the velocity fields, are calculated. Those traces form streak lines and a numerical smoke-wire picture is obtained. A Crank-Nicolson's implicit time integration is used

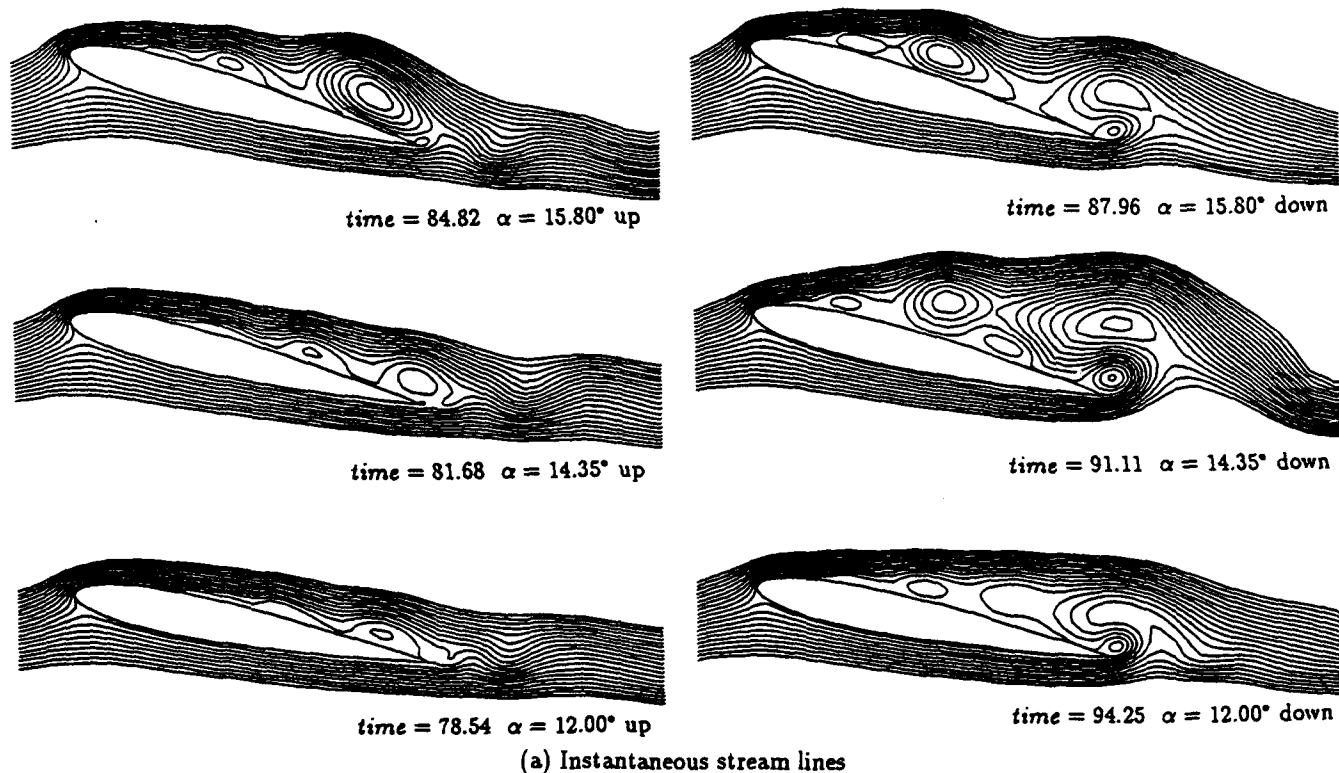


Fig. 11 Calculated flow patterns(NACA012,  $\alpha = 12^\circ + 4^\circ \sin \omega t$  ( $k = 0.2$ ),  $Re = 7.0 \times 10^4$ )

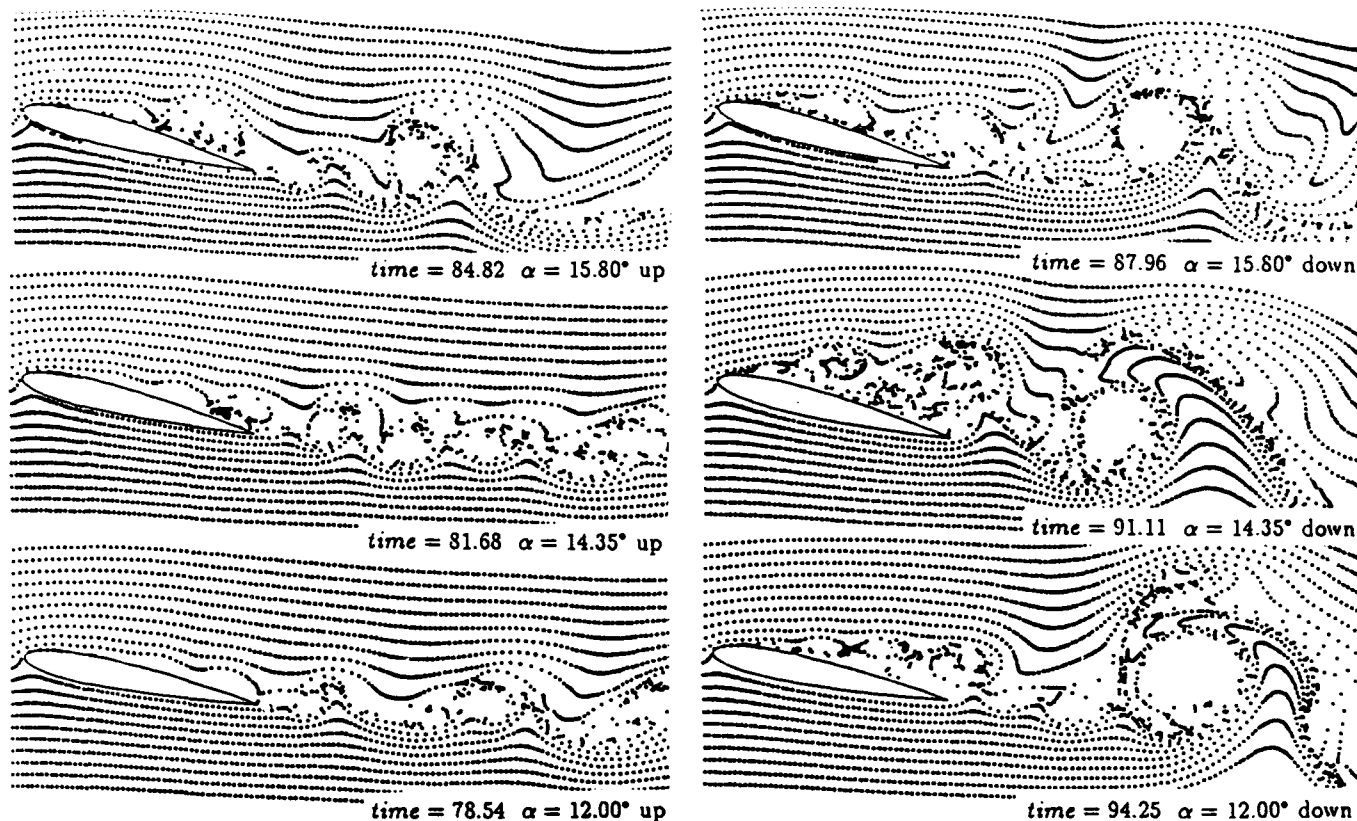


Fig. 11 (b) Numerical smoke-wire picture

in order to get accurate temporal resolution. The results show the numerical smoke-wire pictures are quite useful in order to understand the structure of the flow fields and compare the calculated results with experiments.

As shown in the figure separated region is small in pitching-up process and it becomes large in pitching-down process. Quite different characteristics of flow patterns between in pitching-up and pitching-down processes are obtained. The significant change of the flow patterns in pitching-up and pitching-down process show the existence of the Hysteresis of the aerodynamic characteristics. The hysteresis curve of aerodynamic characteristics of  $C_L$  and  $C_M$  at the same condition are shown in Fig. 13. In particular  $C_L$  at higher attack angle than the stalling angle of this airfoil section keeps higher value, then decreases rapidly. The results shows remarkable characteristics of dynamic stall.

#### 4. CONCLUSIONS

Dynamic stall phenomena have been simulated numerically by a discrete vortex method and viscous flow calculations and major results of using both numerical efforts are discussed. The major conclusions of the present study are summarized as follows:

In the calculations by a discrete vortex method combined with a panel method the potential flows around wing sections aerodynamic characteristics of dynamic stall is calculated properly and a hysteresis of lift of airfoil at dynamic stall is obtained. The results suggest that the method has a excellent capability of simulating vortical flows with excellent small computation cost.

In the calculations by viscous flow calculations separated flows around oscillating airfoil in pitch are simulated by using the third-order upwind scheme and a moving mesh system. The calculated separated region is small in pitching-up process and it becomes large in a pitching-down process. Quite different characteristics of flow patterns between in a pitching-up and pitching-down processes and hysteresis curve of aerodynamic characteristics are obtained.

#### ACKNOWLEDGEMENT

The present authors would like to express thier cordial gratitude to Mr. Naoki FUTATSUDERA, Mr. Atsushi FUJIMOTO and Mr. Atsuhiko SAKAMOTO for thier valuable support in the present study during thier stay in our laboratory.

#### REFERENCES

- 1) McCrosky, W. J. and Pucci, S.L.: Viscous-Inviscid Interaction on Oscillating Airfoils, AIAA paper 81-0051 (1981).
- 2) McCrosky, W. J.: Unsteady Airfoils, Ann. Rev. Fluid Mech., 14 (1982), pp.285-311.
- 3) Aihara, Y., Koyama, H. and Murashige, A.: Transient Aerodynamic Characteristics of a Two-Dimensional Airfoil During Stepwise Incidence Variation, J. Aircraft, 2 (1985), pp.661-668.
- 4) Carr, L. W.: Progress in Analysis and Prediction of Dynamic Stall, J. Aircraft, 25 (1988), pp.6-17.
- 5) Oshima, K and Oshima, Y.: Flow Simulation by Discrete Vortex Method, Proc. 8th ICNMF (1982), pp.94-106.

- 6) Sakata, H., Adachi, K. and Inamuro, R.: A numerical method of unsteady flows with separation by vortex shedding models(Part 1), J. Japan Society of Mechanical Engineering, 49B (1983), pp.801- 808.(in Japanese).
- 7) Aso, S., Hayashi, M. and Futatsudera, N.: Numerical Simulation of Separated Flows around Two-Dimensional Wing Section by a Discrete Vortex Method, Proc. Symp. on Mechanics for Space Flight 1988 of ISAS (1988), pp.11-20.
- 8) Hayashi, M. and Endo, E.: Measurement of Flow Fields around an Airfoil Section with Separation, Transaction of the Japan Society for Aeronautics and Space Sciences, 21 (1978), pp.69-75.
- 9) Schlichting, H.: Boundary Layer Theory(7th ed.), McGraw-Hill (1979).
- 10) Harlow, F. H. and Welch, J. E.: Numerical Calculation of Time- Dependent Viscous incompressible Flow of Fluid with Free Surface, Phys. Fluid, 8 (1965).Phys. Fluid, 8 (1965).

- 11) Kawamura, T. and Kuwahara, K.: Computation of High Reynolds Number Flow around a Circular Cylinder with Surface Roughness, AIAA paper 84-0340 (1984).
- 12) Steger, J. L. and Sorenson, R. L.: Automatic Mesh-Point Clustering near a Boundary in Grid Generation with Elliptic Partial Differential Equation, J. Computational Physics, 33 (1979), pp.405-410.
- 13) Nakamichi, J.: Calculations of Unsteady Navier-Stokes Equations around an Oscillating 3-D Wing Using Moving Grid System, AIAA paper 87-1158 (1987).
- 14) ASO, S. and SAKAMOTO, A.: A Numerical Simulation of Separated Flows around Bodies, Technology Reports of Kyushu University, Vol.64, No. 4 (1991), pp.249-255 (in Japanese).

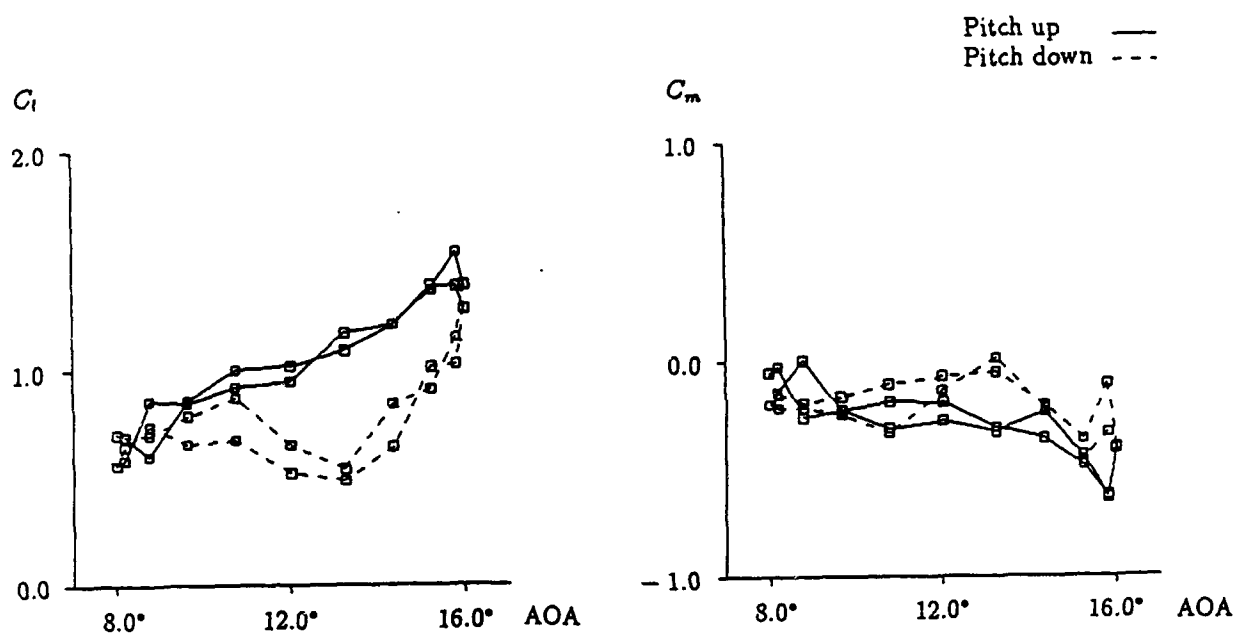


Fig. 12 The hysteresis curves of aerodynamic characteristics of  $C_L$  and  $C_M$  (NACA012,  $\alpha = 12^\circ + 4^\circ \sin \omega t$  ( $k = 0.2$ ),  $Re = 7.0 \times 10^4$ )



# SOME RECENT APPLICATIONS OF NAVIER-STOKES CODES TO ROTORCRAFT

W.J. McCroskey

Senior Research Scientist  
U.S. Army Aeroflightdynamics Directorate (AVSCOM)  
and NASA Ames Research Center  
Moffett Field, California

## ABSTRACT

Many operational limitations of helicopters and other rotary-wing aircraft are due to nonlinear aerodynamic phenomena, including unsteady, three-dimensional transonic and separated flow near the surfaces and highly vortical flow in the wakes of rotating blades. Modern computational fluid dynamics (CFD) technology offers new tools to study and simulate these complex flows. However, existing Euler and Navier-Stokes codes have to be modified significantly for rotorcraft applications, and the enormous computational requirements presently limit their use in routine design applications. Nevertheless, the Euler/Navier-Stokes technology is progressing in anticipation of future supercomputers that will enable meaningful calculations to be made for complete rotorcraft configurations.

## 1 INTRODUCTION

The flow fields of helicopters and other rotorcraft provide a rich variety of challenging problems in applied aerodynamics. Much of the flow near the rotating blades is nonlinear, three-dimensional, and often unsteady, with periodic regions of transonic flow near the blade tips, and with dynamic stall pockets inboard. The blades also shed complex vortical wakes, and detrimental aerodynamic interactions often arise between the major rotating and nonrotating components.

In recent years, CFD methods for isolated, nonlinear pieces of the overall problem have been developed to complement the mixture of analytical and empirical aerodynamic theories, wind tunnel data, and design charts traditionally used by helicopter engineers. References 1-4, for example, describe some of these modern developments, and the present author highlighted the activities of some of his colleagues in Ref. 5, as they existed in 1988. This paper represents a brief review and update of those efforts described in Ref. 5, with some additional discussion of the challenges that remain to our long-term goal of obtaining complete numerical simulations of realistic rotorcraft flow fields with as few physical approximations as possible. It must be emphasized that no attempt is made in this paper to review the bulk of research underway in this field; only the work of the author's immediate colleagues is described herein. Thus, more activities are neglected than included.

As can be gleaned from Refs. 1-5, many different levels of sophistication of CFD technology can be and are being gainfully applied to practical rotorcraft problems. The approach followed here, which is by no means unique (cf. Refs. 4, 6-10), is to develop, adapt, and apply advanced Euler/Reynolds-Averaged Navier-Stokes methodology to the special needs of future rotorcraft. While the near-term utility and practicality of this approach may be open to debate, the history of supercomputer growth and the contributions of

advanced CFD techniques to fixed-wing aircraft suggest that improved predictive tools are highly desirable for all flight vehicles. Such methodology should help to reduce the risks and testing requirements for new designs, and it should enable engineers to increase rotorcraft performance, efficiency, and maneuverability while reducing noise, vibrations, and detectability.

In the following section, a very brief description is given of the methods that are currently being developed and used by the author and his coworkers. In subsequent sections, some representative examples of recent results are given, along with descriptions of some of the major issues that remain unresolved.

## II NUMERICAL METHODS

Two different approaches are currently being pursued to solve the compressible Euler or Reynolds-Averaged Thin-Layer Navier-Stokes equations for aerodynamic configurations that consist of rotating lifting surfaces and nonrotating airframe components. The first approach employs several finite-difference, implicit approximate-factorization algorithms, with algebraic turbulence modeling, to solve the governing equations in strong conservation-law form [11] on either single- or multiple-block, body-conforming structured grids. The single-block code is called TURNS (Transonic Unsteady Rotor Navier Stokes), which is described in Ref. 12 and which borrows heavily from Obayashi's work [13]. This numerical scheme uses upwind-biased flux-difference splitting, an LU-SGS implicit operator, higher-order MUSCL-type limiting, and, in the case of unsteady calculations, Newton sub-iterations at each time step.

The current multi-block implicit code is called OVERFLOW, a new code being developed by Dr. Pieter Buning at the Ames Research Center, using elements of F3D [14] and ARC3D [15]. OVERFLOW currently has a two-factor, block tridiagonal option with upwind differencing in the streamwise direction, as in F3D, and a three-factor, scalar pentadiagonal option with central differencing, as in ARC3D. OVERFLOW uses the Chimera overset-grid scheme [16] to subdivide the

computational domain into subdomains, some of which may move relative to others.

Solution-adaptive grids are not currently used in the three-dimensional versions of either TURNS or OVERFLOW, although this technology will be pursued in the future. TURNS has been used to compute the aerodynamics and acoustics of isolated rotor blades, and OVERFLOW has been applied to fuselages and wing-body combinations. The Chimera overset-grid method is currently being combined with TURNS to improve the resolution of vortical structures in the wakes of rotor blades, and OVERFLOW with Chimera is beginning to be applied to rotor-body interactions.

Body-conforming C-O or C-H structured grid topologies are normally used in TURNS and OVERFLOW, with from approximately 100,000 to 1,000,000 grid points. Figure 1 shows a typical C-H grid for aerodynamic calculations. The grid lines are nearly orthogonal at the surface, and the grid spacing normally starts at about 0.00002 - 0.00005 chord in the normal direction. Figure 2 illustrates the distortion of the grid in the H, or spanwise, direction that is typically used for acoustic calculations. For these applications, it is important to align the grid lines with linear characteristics beyond the tip of the rotor, in order to capture the low-level radiating sound waves.

The second approach uses a solution-adaptive unstructured-grid subdivision scheme developed by Strawn [17], incorporating the explicit upwind finite-volume flow solver of Barth [18]. The code contains an efficient edge data structure for computational domains comprised of arbitrary polyhedra, which are subdivided in regions of high flowfield gradients to improve the solution. Barth's method uses a reconstruction scheme in each control volume that is exact for linear variations, and the reconstructed polynomials are flux-limited in regions of flow discontinuities. The explicit time operator is a four-stage Runge-Kutta method with local time stepping for steady problems. The motivation for this adaptive-grid approach is to convect vortical flow regions with minimal numerical dissipation, but it shows promise in convecting low-level acoustic waves, as well. Thus far, only the Euler equations have been solved by this method.

The adaptive-grid calculations normally start on a coarse structured grid. Error indicators, based, for example, on density gradients near the edges of the blade or on vorticity in the wake, determine which tetrahedra volume elements are to be subdivided into eight smaller tetrahedra and which ones are to be left alone. "Buffer" elements consisting of partially subdivided tetrahedra are introduced around the fully-subdivided ones. The process can be repeated until the desired solution accuracy is obtained. References 17-19 may be consulted for details.

### III. BLADE AERODYNAMICS AND WAKES

#### Tip Vortex Formation and Convection

The concentrated tip vortex of a rotor blade plays an important role in the aerodynamics and acoustics of rotary-wing aircraft; even more so than for fixed-wing aircraft, since the tip vortex may stay closer to and directly interact with the rotor or airframe. Calculations of the tip vortex formation and spanwise loading distribution on a rectangular wing tip, performed by Srinivasan, et al [20], were found to be in good overall

agreement with experiments, but the computed peak suction levels on the upper surface of the wing very near the tip were not as high as the measured ones, Fig. 3. More recently, Strawn [17] found similar discrepancies in his unstructured-grid calculations. In addition, Strawn found the calculated peak velocities in the vortex itself to be substantially less than recently reported by McAlister and Takahashi [21], although Strawn's computed vortex dissipated very little as it convected downstream. In unpublished work, Srinivasan has re-computed this problem on finer grids with his structured-grid code, with similar results. Thus the cause of the discrepancy remains undetermined, but it appears that even finer grids and/or better turbulence models may be required to resolve this issue. This, in turn, has important implications for the problem of computing rotor blade-vortex interaction accurately, as described below. The tip-vortex formation problem is currently being studied computationally by Dr. Jennifer Dacles-Mariani at the Ames Research Center, in conjunction with a new experimental program [22] designed to shed further light on the physics of this phenomenon.

Despite these limitations, the existing Navier-Stokes technology can provide useful information about the performance of modern blade tips. For example, Duque [23,24] has studied the unusual British Experimental Rotor Program (BERP) helicopter blade under nonrotating conditions, and he has computed the complex separation patterns that develop at high incidence. Figure 4 shows some of these results at low Mach number, in comparison with experimental oil-flow patterns. He also obtained excellent agreement with measured pressure distributions everywhere except in the immediate vicinity of the tip.

#### Hover

The axial symmetry and nominally steady-state conditions in blade-fixed coordinates make hovering flight of isolated rotor blades an attractive starting point for developing rotorcraft codes. Forerunners of the TURNS code were developed and applied to this problem by Srinivasan, et al [25] and Chen, et al [26]; these efforts were summarized in Ref. 5. Reference 25 showed some of the basic differences between rotating and nonrotating blades, but the induced flow due to the vortical wake was approximated by a simplistic model. However, this restriction was subsequently relaxed by both investigators [12,27], wherein the solution for the wake structure was included, or "captured," as part of the overall computation. Here, as in the fixed-wing tip-vortex problem described above, the vortical wake structure was smeared considerably by the coarseness of the grid and the attendant numerical dissipation. Nevertheless, the circulation and nearfield trajectory of the trailing tip vortex of the blade appeared to be well enough preserved that the induced inflow was computed satisfactorily, thus producing reasonable airloads on the blade. For example, the surface pressure distributions reported in Ref. 12 showed acceptable agreement with experiments. These encouraging results led to recent studies of more complex rotors, as reported in Ref. 28. For example, Fig. 5 shows calculations for the Sikorsky UH-60A main rotor, and Fig. 6 for a blade based on the Westland BERP rotor. The pressure distributions shown in Fig. 5 look very good, although the computed tip vortex structure is smeared and the uncertainty of the calculated induced and profile power of the rotor is greater than today's stringent engineering requirements

for determining hover performance. Therefore, these results should probably only be considered "semi-quantitative." Of course, the issue of the accuracy of drag calculations in three-dimensional applications is not unique to rotorcraft CFD, but it warrants further serious attention for applications such as these.

The ongoing application of the TURNS code to hovering rotors uncovered difficulties with the outer boundary conditions that were not evident at the beginning of the study, and which are still not fully resolved. Unlike a fixed wing, a hovering rotor induces significant velocities at large distances from the rotor. However, for economy, one would like to keep the computational domain as small as possible. In Refs. 12, 25-27, for example, the outer boundaries were placed relatively close to the rotor, and the characteristic far-field boundary conditions that were used effectively blocked flow across the outer surfaces of the computational domain. Thus the problem simulated in those studies was a rotor in a solid-wall enclosure, rather than in free air, and the wake of the rotor tended to recirculate within the computational "box."

This problem, and large time required for the initial transients to decay, were recognized by Kramer, Hertel, and Wagner [29], who used an approximate vortex-element solution to define an initial solution that produced flow through the far-field boundaries. However, a simpler and more economical alternative was introduced in Ref. 28, using simple momentum theory as a guide. Namely, the wake of the rotor was assumed to pass out of the computational box through a circular hole whose area is half that of the rotor disk, with an outflow velocity twice the momentum-theory average value through the plane of the rotor. A characteristic-type numerical outflow boundary condition was applied across this exit plane by prescribing this outflow mass flux, and the other four computational variables were extrapolated from within. The inflow through the rest of the outer boundary was approximated by a point sink at the axis of rotation, whose strength is proportional, again via momentum theory, to the thrust of the rotor. Here the pressure was extrapolated from within and the other four variables were specified. This combination of inflow and outflow boundary conditions is sketched in Fig. 7.

Figure 8 shows a comparison of the pressure distributions on a hovering rotor computed with the old and new outer boundary conditions, from Refs. 12 and 28, respectively. The trace of particles released near the tip, Fig. 9, is assumed to define approximately the trajectory of the tip vortex. The particle trace computed with the new boundary conditions exits the lower computational boundary after about 3-1/2 revolutions of the blade, and this trajectory agrees well with measurements. With the old boundary conditions of no inflow or outflow, the trace is approximately the same for the first 1-1/2 blade revolutions, but then it develops an irregular path that suggests a developing recirculation within the computational domain.

Unfortunately, the pressure distributions in Fig. 8 do not give a clear indication that the new boundary conditions have improved the solution. This is somewhat surprising, and also at variance with the usual results of vortex-element methods, that the airloads seem to be relatively insensitive to the details of the far-wake solutions. As noted earlier, the vortical wake structure of the Navier-Stokes calculations was smeared considerably by the coarseness of the grid away from the blade and the

attendant numerical dissipation. However, the circulation and trajectory of the trailing tip vortex through the first revolution of the blade appeared to be well enough preserved that the induced inflow, and hence the airloads, were computed satisfactorily. But this may turn out to be fortuitous. It is possible that as the grid in the wake is refined and the fidelity of the tip vortex solution improves, the computed blade airloads will become more sensitive to the details of the wake trajectory and structure. This aspect of the hover wake problem clearly warrants further investigation.

### Improved Vortex Wake Calculations

The issue of the fidelity of the wake solutions indicates the need for significant improvements in grid resolution and higher-order accuracy in the flow solver. As mentioned above, Dr. Roger Strawn and coworkers are developing solution-adaptive, unstructured-grid subdivision techniques to add grid points selectively in the wake [17,19]. Again, the current model problem is a hovering rotor blade. Initial calculations on a coarse, structured grid are used to determine where to subdivide the computational elements near the edges of the blade and in the wake. Preliminary results for an initial coarse grid are shown in Fig. 10 for the same rotor shown earlier in Figs. 8 and 9. Results with adaptive-grid refinement in the wake will be presented in Ref. 19.

As the wake structure is essentially inviscid, Strawn and Barth [19] have only solved the Euler equations for this problem up to now. The computational cost per time step per grid point is greater with this approach than with the structured-grid TURNS code. However, the efficiency gained by adding and deleting grid points only where they are needed, based on the errors in the local solution, promises to provide an improved resolution of the wake structure at a net savings in computer costs.

An alternative solution-adaptive scheme using structured grids is being developed and applied to the rotor wake problem by Earl P.N. Duque [30]. He is using the Chimera overlapped multiple-grid method [16] at the interface between various structured-grid blocks, each of which is designed to capture a particular region or feature of the flow. Figure 11 shows preliminary results for the same two-bladed rotor in hover, using three coarse-grid blocks. One grid block is fitted to each blade, to capture the flow features near the blades, and these rotate with a third global block, which has grid clustering designed to convect the wake with minimum dissipation. Essentially, the embedded rotor grids act like internal boundary conditions to the cylindrical wake grid, and the wake grid acts like a far-field boundary condition to the blade-fixed grids. Additional calculations will be presented in Ref. 30.

### Blade-Vortex Interaction (BVI)

The interaction of a rotor blade with the trailing tip vortex of another is a common event for helicopters, and this interaction is an important source of noise and vibrations. The contributions of two-dimensional Navier-Stokes computations to this problem were reviewed in Refs. 5 and 31. At that time, the near-field properties of airfoil-vortex interaction appeared to be well understood and properly accounted for in numerical simulations. Since then, Baeder [32] has completed a detailed study of the acoustic field generated by 2-D interactions of a prescribed vortex with an airfoil, concluding that the Mach number, vortex strength, and miss distance are the

most important parameters affecting the radiated noise. His results indicate that the noise is relatively independent of the airfoil geometry, thus contrasting with the hopes of many in the helicopter community, who continue to search for a low-BVI-noise blade section. Definitive experiments to settle this issue are planned for the near future at the Ames Research Center.

Three-dimensional interactions of a prescribed vortex with a rotor blade were computed by Srinivasan and McCroskey [33] using an early version of the TURNS code. Representative results are shown in Fig. 12. The test case here is a two-bladed rotor downstream of the tip of a wing in a wind tunnel [34]. The rotor is nominally nonlifting, except for the interaction with the concentrated vortex generated by the wing tip upstream. In this configuration, the approaching vortex is well defined experimentally, and this structure is prescribed in the computations; thus the modeling or computing of the conventional helicopter rotor wake is not an issue here.

For the conditions of Fig. 12, the flow field near the blade tip develops a shock wave on the advancing blade before the blade-vortex encounter in the second quadrant of the rotor, and the decay of this shock is intertwined with the interaction shown in the figure. The calculations agree fairly well with the measurements. This oblique BVI is qualitatively similar to 2-D or "parallel" interactions in many ways, but important quantitative differences exist. Namely, the interaction is spread out over a larger azimuthal travel of the blade, and the fluctuating loads at a given radial station appear to be weaker.

Although further refinements in these Navier-Stokes computations are desirable, the main unresolved issue in computing 3-D BVI is now the accurate simulation of the vortical structures approaching the blade. That is, improvements in the vortex wake calculations, as discussed in the previous section, have become the pacing item in this important aspect of rotor aerodynamics.

#### IV. ROTOR ACOUSTICS USING CFD

Impulsive-like pressure fluctuations that radiate from rotor blades represent an annoying source of noise that is difficult to calculate. One major source of impulsive noise is the blade-vortex interaction (BVI) phenomena described above; its accurate prediction depends on both the correct description of the vortical wake approaching a blade element and on the local details of the interaction itself. Another source is called High-Speed Impulsive (HSI) noise, which is caused primarily by compressibility effects. It can be accentuated by the phenomenon on transonic rotor tips known as delocalization, wherein the supersonic pocket on the rotor blade extends to the far field beyond the blade tip.

The influence of rotor lift and wakes on HSI noise is considered secondary [35], and Srinivasan and Baeder [36] have indicated that viscous effects are also secondary. Therefore, this source of noise can be investigated for nonlifting transonic configurations using an Euler formulation. On the other hand, the level of the radiated pressure fluctuations drops off inversely with the distance from the effective source, so that the real noise gets quickly lost in the "computational noise" away from the body unless special precautions are taken in the numerics.

Baeder [36-38] has combined high-order-accurate versions of the Euler TURNS code with the special grid-cluster techniques illustrated in Fig. 2 to produce new, high-precision, unified aerodynamic and acoustic results for HSI cases, out to several rotor radii. Some of his hover results are shown in Figs. 13 and 14. These results are the most successful to date for both waveform and peak pressure levels over a range of tip Mach numbers. They are now available as computational data bases, with greater detail and precision than available experimental results, for use by acousticians developing simpler, more approximate theories and models.

Forward flight is more challenging, as the solutions must be time accurate, and the characteristics along which the outgoing waves propagate are no longer fixed with respect to the blade. Nevertheless, Baeder [37] has used the TURNS code and grid clustering along selected linear characteristics to begin to investigate rotors in forward flight at tip-Mach-number conditions below and above that required for delocalization. The overall picture of the wave propagation for a nonlifting, untwisted rotor blade agrees well with what can be qualitatively inferred from wind tunnel measurements. Detailed comparisons have been made with experiments at specific microphone locations away from the rotor, as shown in Fig. 15, with good results for the case without delocalization.

The quantitative agreement is less satisfactory at advancing-tip Mach numbers above delocalization, as shown in Fig. 16, where the acoustic waves seem to be more sensitive to the basic parameters of the rotor. It should be noted that the measurements shown in the figure were obtained for lifting rotors with twisted blades. Also, there is some disagreement between measurements in a wind tunnel and those obtained in flight tests; these differences are discussed in Ref. 39. In any case, Baeder's calculations represent a significant advance, and they demonstrate the feasibility of using a unified CFD approach to examine nonlinear acoustics of rotors. However, they also suggest that further validation should be done for additional cases, that the actual blade conditions should be modeled more exactly, and that improvements in time-varying grids, including solution-adaptive techniques, will probably be required to obtain the quality of the hover results in Figs. 13-14.

#### V. TOWARD ROTOR-BODY INTERACTIONS

The aerodynamic interaction between rotating and nonrotating components of rotary-wing aircraft is widely recognized as an important feature that produces considerable additional complications for CFD analyses. Unfortunately, measurable progress on this important topic has been slow, consisting mostly of conceptualizing and developing viable grid-interface strategies.

However, as an intermediate step, Dr. Sharon Stanaway has developed an efficient method for embedding an actuator-disk representation of a rotor in a computational domain surrounding an arbitrary body. The method uses the Fortified Navier Stokes technique of Van Dalsem and Steger [40] to introduce a prescribed pressure jump, which may vary with time and space, across an internal boundary (the actuator disk). This is similar to the work of Rajagopalan [10], in which a momentum source term is added to the governing equations, causing a pressure jump at internal boundary points. The technique is intended to allow simplified

studies of the effect of the wake of a rotor on a nearby fuselage or wing, for example. The actuator disk will eventually be replaced by a finite-difference simulation of the rotor, as indicated in Fig. 17. A number of fuselage calculations have been performed in support of the rotor-body experiment of Norman and Yamauchi [41], but these have not been completed.

Another unpublished early application of this technology by Dr. Stanaway is illustrated in Fig. 18. This ducted-rotor model problem is an approximation of the novel Sikorsky Cypher unmanned aerial vehicle [42], which resembles a flying doughnut with two counterrotating rotors. The figure shows Mach contours on planes taken through the center of a toroidal body of circular cross section, with and without a thrusting rotor system spanning the inside of the toroid. The direction of the oncoming flow is indicated in the figure; the flow fields are axisymmetric in this example of vertical climb. The solution without the actuator disk, in the left half of the figure, exhibits the expected behavior of a pair of circular cylinders in a two-dimensional crossflow. The effect of the thrusting rotor is to accelerate the flow through the middle of the toroid, to move the stagnation point inward, and to alter the pressure distribution and separation point location significantly.

In a third preliminary and unpublished study, Dr. Venkat Raghavan is adapting the OVERFLOW code to the V-22 Osprey tiltrotor aircraft, with initial emphasis on the high-speed cruise configuration, or turboprop mode, of this vehicle. Figure 19 illustrates the surface and volume grids being developed for this problem, using OVERFLOW with Chimera. Progress to date includes full-potential and Navier-Stokes solutions for the wing-fuselage combination. The viscous results (not shown) demonstrate separated flow on the rear portion of the lower fuselage, whereas the inviscid results do not, of course. The addition of the aforementioned actuator-disk representation of the rotor is the next logical step in this progression toward a simulation of the complete aircraft.

## VI. CONCLUDING REMARKS

This paper has attempted to describe the progress made in the last four years by the author and his coworkers, and some of the current limitations and problems. As one of several teams actively working in the field of rotorcraft CFD, we are pursuing the Euler/Reynolds-Averaged Navier-Stokes approach, with growing emphasis on rotor wakes and rotor-body interactions. The examples shown are mostly for the aerodynamics and acoustics of rotors in hover, but the primary long-term goal is to develop improved predictive capability for forward flight. Solution-adaptive structured- and unstructured-grid methods are under development for improved wake capturing and acoustics, and variations on the Chimera overset grid scheme appear to be the most promising ways of treating rotor-body interactions.

In concluding his 1988 review [5], the author wrote, "The rotorcraft industry appears to be entering a new era in which computational fluid dynamics will play an increasingly important role in the design and analysis of advanced aircraft." Although the extent of CFD contributions to the new rotary-wing aircraft that have appeared since then may not have been overwhelming, the number of rotorcraft CFD papers in the technical literature by industry authors has risen dramatically. Since

1988, airfoil codes have improved significantly and are being used more. Also, the transonic aerodynamics of advancing-blade tips is being computed by a variety of methods with adequate precision for engineering applications, and these capabilities are beginning to be used in industry. Furthermore, accurate simulation of high-speed impulsive noise within a few radii from the tip of the blade now appears to be possible in those cases where wake effects are negligible. A logical next step is to try to extend this capability to the more difficult problem of blade-vortex interaction noise.

There has also been significant progress in CFD algorithms, grid techniques, and supercomputer technology during the past four years. However, much remains to be done in each of these areas to bring CFD to the state where it can be used as successfully for rotorcraft as for fixed wing aircraft. An accurate finite-difference simulation of the complete flow field about a helicopter is still not feasible. Wakes and blade-vortex interactions are not well predicted, and retreating-blade stall remains virtually untouched by the CFD community. The principal limitations remain the computer hardware costs, speeds, and memory capacities; algorithms and solution methods; grid generation; turbulence models; and accurate vortex-wake simulations. In general, today's rotorcraft CFD codes are not robust, they have not been exercised enough nor validated adequately, and they remain awkward to use. All of these factors undoubtedly discourage the user community from working with what is available. Nevertheless, the technical challenges are exciting and the potential payoff of future CFD developments remains well worth pursuing.

## VII. ACKNOWLEDGEMENTS

This paper draws heavily from the research activities of my coworkers, J.D. Baeder, E.P.N. Duque, V. Raghavan, G.R. Srinivasan, S. Stanaway, and R.C. Strawn. Their ideas and contributions are gratefully acknowledged. Also, hover-wake information provided by Dr. Chee Tung was instrumental in developing the new outer boundary conditions described in Section III, and his cooperation is deeply appreciated.

## VIII. REFERENCES

1. Caradonna, F.X. "The Application of CFD to Rotary Wing Flow Problems," Paper No. 5. AGARD Report 781, Nov. 1990.
2. Caradonna, F.X., and Tung, C. "A Review of Current Finite-Difference Rotor Flow Methods," American Helicopter Society 42nd Annual Forum, June 1986.
3. Strawn, R.C., Desopper, A., Miller, J., and Jones, A. "Correlation of Puma Airloads - Evaluations of CFD Prediction Methods," 15th European Rotorcraft Forum, Amsterdam, Sept. 1989.
4. Polz, G. "Current European Rotorcraft Research Activities on Development of Advanced CFD Methods for the Design of Rotor Blades," 17th European Rotorcraft Forum, Berlin, Sept. 1991.
5. McCroskey, W.J. "Some Rotorcraft Applications of Computational Fluid Dynamics," Second International Conference on Basic Rotorcraft Research, Univ. Maryland, Feb. 1988; also NASA TM 100067, 1988.

6. Wake, B.E., and Egolf, T.A. "Application of a Rotary-Wing Viscous Flow Solver on a Massively-Parallel Computer," AIAA Paper 90-0334, Reno, Jan. 1990.
7. Agarwal, R.K., and Deese, J.E., "Euler/Navier-Stokes Calculations for the Flowfield of a Helicopter Rotor in Hover and Forward Flight," Proc. Second International Conference on Rotorcraft Basic Research, Univ. Maryland, Feb. 1988.
8. Scott, M.T., and Narramore, J.C. "Navier-Stokes Correlation of a Swept Helicopter Rotor Tip at High Alpha," AIAA Paper 91-1752, Honolulu, June 1991.
9. Aoyama, T., Saito, S. and Kawachi, K. "Navier-Stokes Analysis of Blade Tip Shape in Hover," 16th European Rotorcraft Forum, Glasgow, Sept. 1990.
10. Rajagopalan, R.G., and Mathur, S.R. "Three-Dimensional Analysis of a Rotor in Forward Flight," American Helicopter Society 47th Annual Forum, Phoenix, May 1991.
11. Anderson, D.A., Tannehill, J.C., and Pletcher, R.H. Computational Fluid Mechanics and Heat Transfer, McGraw-Hill, 1984, pp. 421-424.
12. Srinivasan, G.R., Baeder, J.D., Obayashi, S., and McCroskey, W.J. "Flowfield of a Lifting Hovering Rotor - A Navier-Stokes Simulation," 16th European Rotorcraft Forum, Glasgow, Sept. 1990.
13. Obayashi, S. "Numerical Simulation of Underexpanded Plumes Using Upwind Methods," AIAA Paper 88-4360-CP, Minneapolis, Aug. 1988.
14. Ying, S.X., Steger, J.L., Schiff, L.B., and Baganoff, D. "Numerical Simulation of Unsteady, Viscous, High Angle of Attack Flows Using a Partially Flux-Split Algorithm," AIAA Paper 86-2179, Williamsburg, Aug. 1986.
15. Pulliam, T.H., and Chaussee, D.S. "A Diagonal Form of a Implicit Approximate-Factorization Algorithm," J. Computational Physics, Vol. 39, No. 2, Feb. 1981, pp. 347-363.
16. Steger, J.L., Dougherty, F.C., and Benek, J.A. "A Chimera Grid Scheme," Advances in Grid Generation, K.N. Ghia and U. Ghia, eds., ASME FED Vol. 5, 1983, pp. 59-69.
17. Strawn, R.C. "Wing-Tip Vortex Calculations with an Unstructured Adaptive-Grid Euler Solver," American Helicopter Society 47th Annual Forum, Phoenix, May 1991.
18. Barth, T.J. "A 3-D Upwind Euler Solver for Unstructured Meshes," AIAA Paper 91-1548, Honolulu, June 1991.
19. Strawn, R.C., and Barth, T.J. "A Finite-Volume Euler Solver for Computing Rotary-Wing Aerodynamics on Unstructured Meshes," American Helicopter Society 48th Annual Forum, Washington, June 1992.
20. G.R. Srinivasan, W.J. McCroskey, J.D. Baeder, and T.A. Edwards, "Numerical Simulation of Tip Vortices of Wings in Subsonic and Transonic Flow," AIAA Journal, Vol. 26, No. 10, Oct. 1988, pp 1153-1162.
21. McAlister, K.W., and Takahashi, R.K. "NACA 0015 Wing Pressure and Trailing Vortex Measurements," NASA TP 3151, Aug. 1991.
22. Chow, J.S., Zilliac, G.G., and Bradshaw, P. "Initial Roll-Up of a Wingtip Vortex," FAA International Wake-Vortex Symposium, Washington, Oct. 1991.
23. E.P.N. Duque, "A Numerical Analysis of the BERP Blade," American Helicopter Society 45th Annual Forum, May 1989; also NASA TM 102247, 1989.
24. Brocklehurst, A., and Duque, E.P.N., "Experimental and Numerical Study of the British Experimental Rotor Program Blade," AIAA Paper 90-3008, Portland, Aug. 1990.
25. G.R. Srinivasan and W.J. McCroskey, "Navier-Stokes Calculations of Hovering Rotor Flowfields," Journal of Aircraft, Vol. 25, No. 10, Oct. 1988, pp. 865-875.
26. C.L. Chen and W.J. McCroskey, "Euler Solution of Multiblade Rotor Flow," Vertica, Vol. 12, No. 3, Mar. 1988, pp. 303-313.
27. C.L. Chen and W. J. McCroskey, "Numerical Simulation of Helicopter Multi-Bladed Rotor Flow," AIAA Paper 88-0046, Reno, Jan. 1988.
28. Srinivasan, G.R., Raghavan, V., and Duque, E.P.N., "Flowfield Analysis of Modern Helicopter Rotors in Hover by Navier-Stokes Method," American Helicopter Society International Technical Specialists' Meeting, Philadelphia, Oct. 1991.
29. Hertel, J., Kramer, E., and Wagner, S. "Complete Euler Solution for a Rotor in Hover and a Propeller in Forward Flight," 16th European Rotorcraft Forum, Glasgow, Sept. 1990.
30. Duque, E.P.N. "Numerical Simulation of a Hovering Rotor Blade using Embedded Grids," American Helicopter Society 48th Annual Forum, Washington, June 1992.
31. Srinivasan, G.R., and McCroskey, W.J. "Numerical Simulations of Unsteady Airfoil-Vortex Interactions," Vertica, Vol. 11, No. 1/2, Jan. 1987, pp. 3-28.
32. Baeder, J.D. "The Computation and Analysis of Acoustic Waves in Transonic Airfoil-Vortex Interactions," PhD Thesis, Stanford University, Sept. 1989.
33. G.R. Srinivasan and W.J. McCroskey, "Viscous, Unsteady Interaction of a Rotor with a Vortex," AIAA Paper 89-1848, Buffalo, N.Y., June 1989.
34. Caradonna, F.X., Lautenschlager, J., and Silva, M. "An Experimental Study of Rotor Blade-Vortex Interactions," AIAA Paper 88-045, Reno, Jan. 1988.
35. Schmitz, F.H., and Yu, Y.H. "Helicopter Impulsive Noise: Theoretical and Experimental Status," Recent Advances in Aeroacoustics, ed. A. Krothapalli and C.A. Smith, Springer-Verlag, 1986, pp. 149-243; also NASA TM 84390, Nov. 1983.
36. Srinivasan, G.R., and Baeder, J.D. "Recent Advances in Euler and Navier-Stokes Methods for Calculating Helicopter Rotor Aerodynamics and Acoustics," 4th



International Symposium on Computational Fluid Dynamics, Davis, Sept. 1991.

37. Baeder, J.D. "Euler Solutions to Nonlinear Acoustics of Non-Lifting Hovering Rotor Blades," 16th European Rotorcraft Forum, Glasgow, Sept. 1990.
38. J.D. Baeder, "Euler Solutions to Nonlinear Acoustics of Non-Lifting Rotor Blades in Forward Flight," American Helicopter Society International Technical Specialists' Meeting, Philadelphia, Oct. 1991.
39. Splettstoesser, W.R., Schultz, K.J., Schmitz, F.H., and Boxwell, D.A. "Model Rotor High-Speed Impulsive Noise - Parametric Variations and Full-Scale Comparisons," American Helicopter Society 39th Annual Forum, St. Louis, May 1983.
40. Van Dalsem, W. R., "Study of Jet in Ground Effect with a Crossflow Using the Fortified Navier-Stokes Scheme," AIAA Paper 87-2279-CP, Monterey, Aug. 1987.
41. Norman, T.R., and Yamauchi, G.K. "Full-Scale Investigation of Aerodynamic Interactions between a Rotor and a Fuselage," American Helicopter Society 47th Annual Forum, Phoenix, May 1991.
42. DeMeis, R. "A Cypher That Adds Up," Aerospace America, Vol. 29, No. 1, Jan. 1991, p. 39.

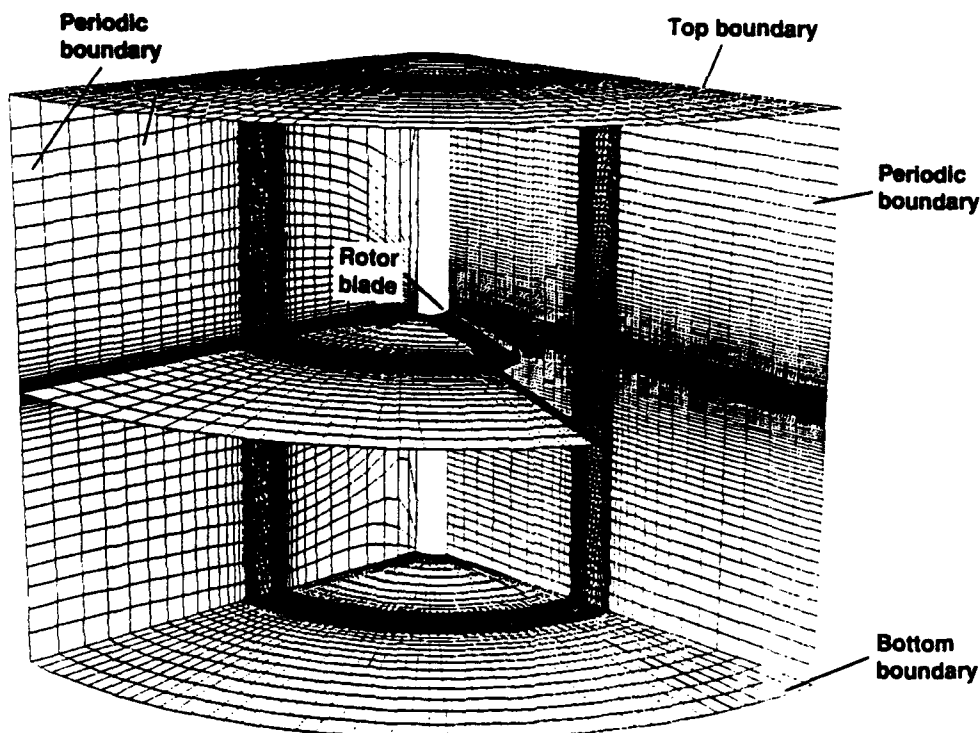


Fig. 1 Representative C-H grid topology for a rotor blade, showing the grid in the plane of the blade.

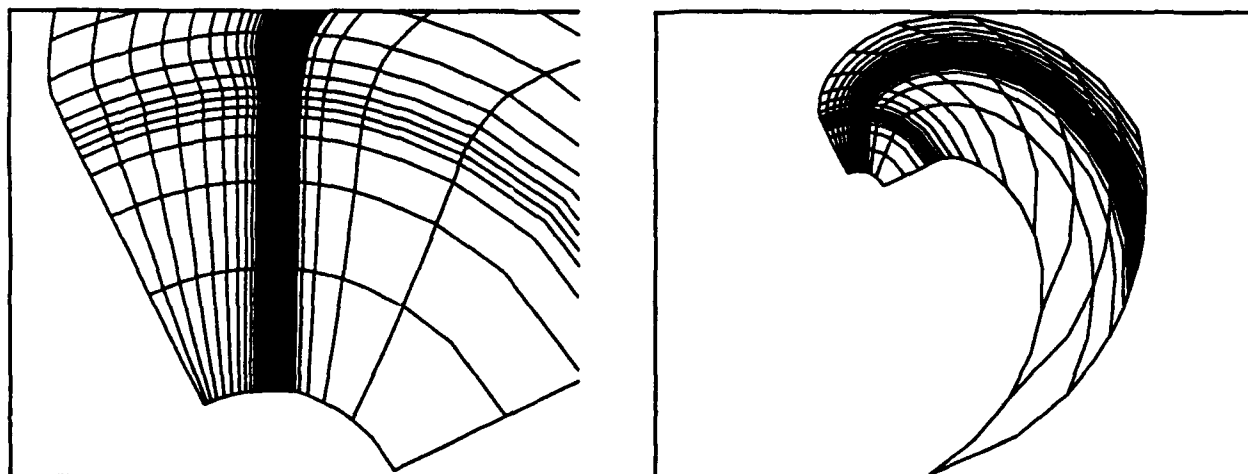


Fig. 2 Representative grid in the plane of the rotor blade for computing acoustic waves.

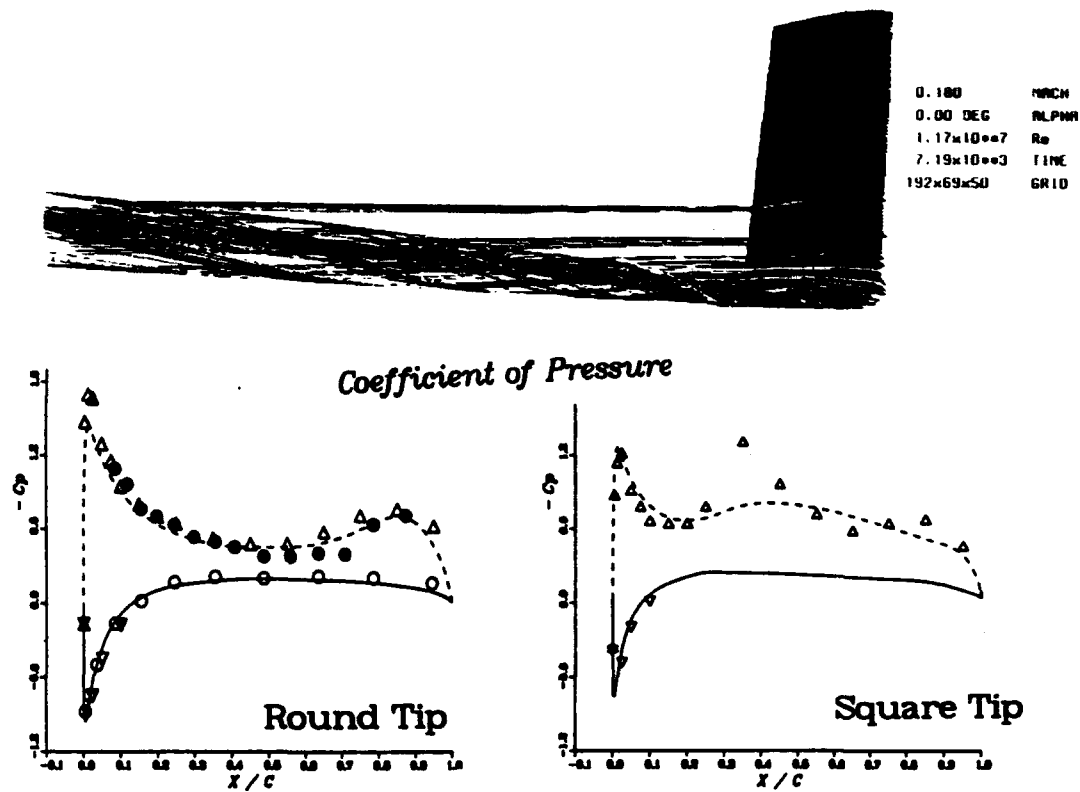


Fig. 3 Pressure distributions and streamlines near the tip of a rectangular wing in subsonic flow

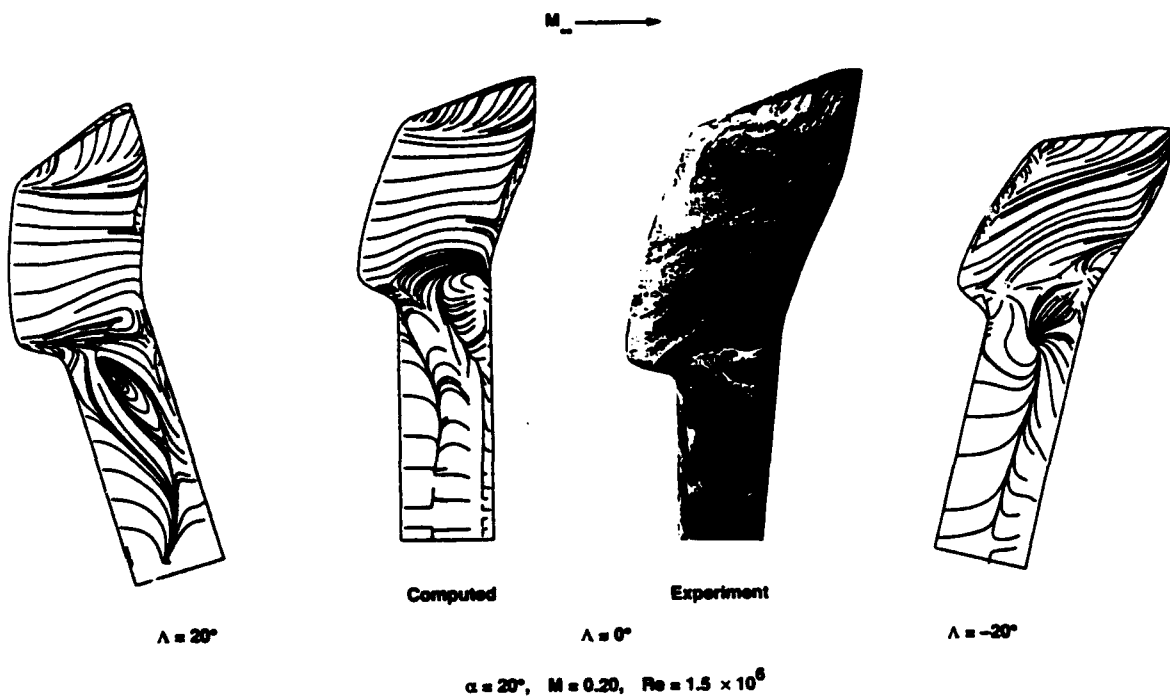


Fig. 4 Surface streamline patterns for a British Experimental Rotor Program blade tip, nonrotating at high incidence and sweep in subsonic flow



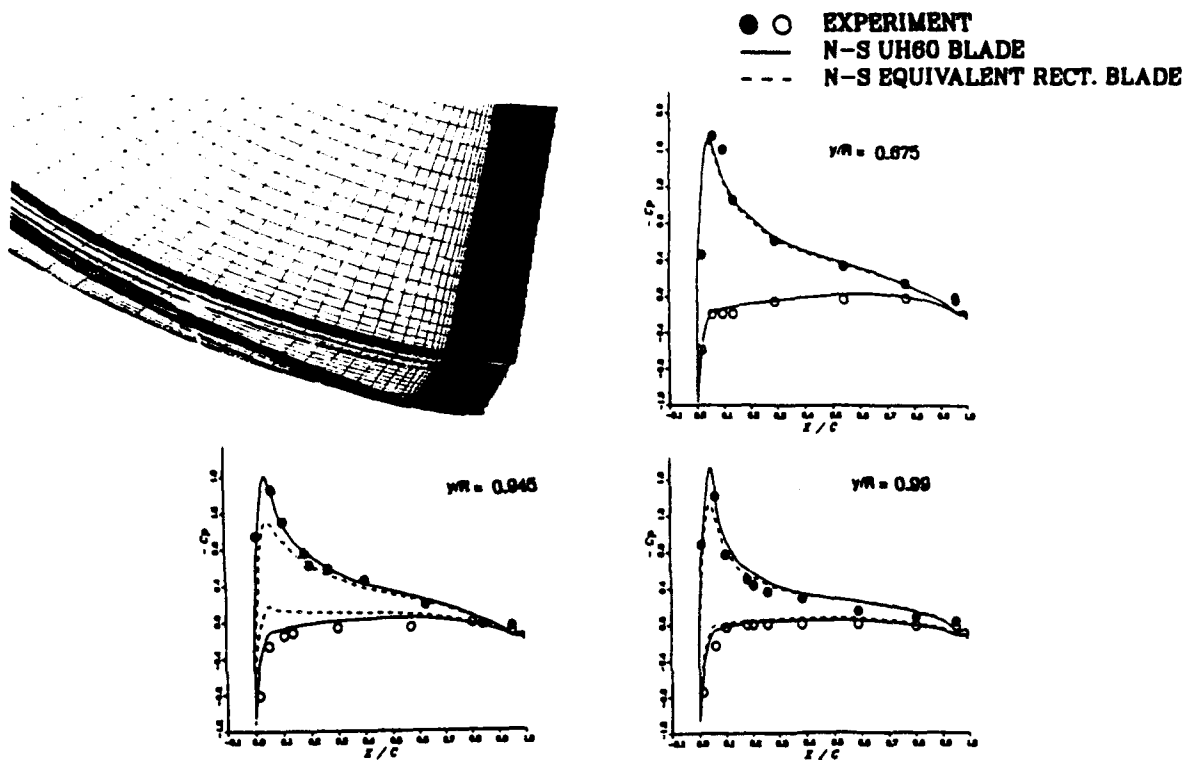


Fig. 5 Pressure distributions and streamlines on a model UH-60A rotor blade in hover

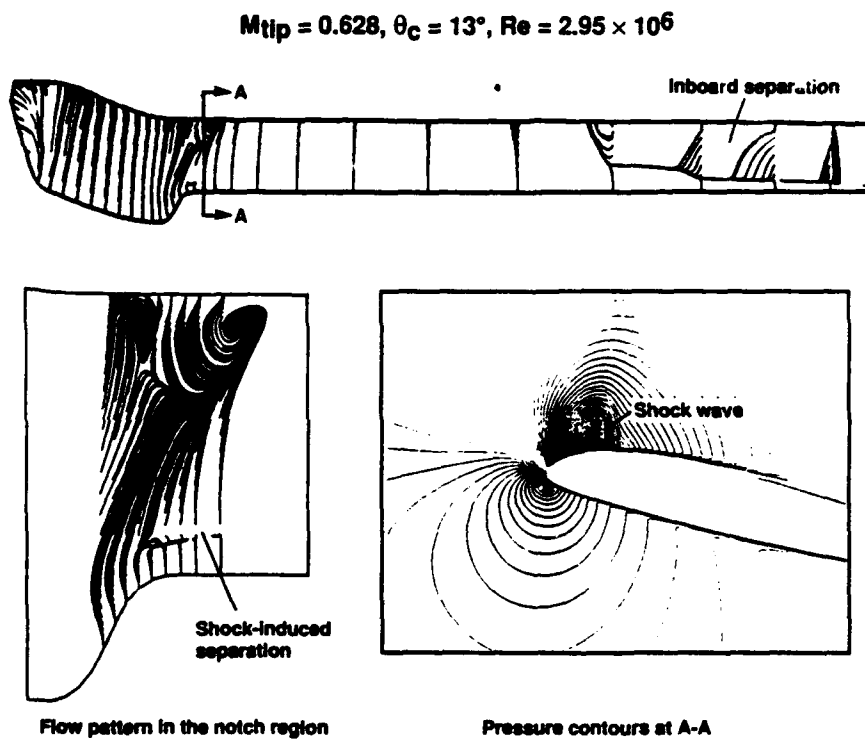


Fig. 6 Surface pressure contours and streamline patterns for a BERP blade in hover

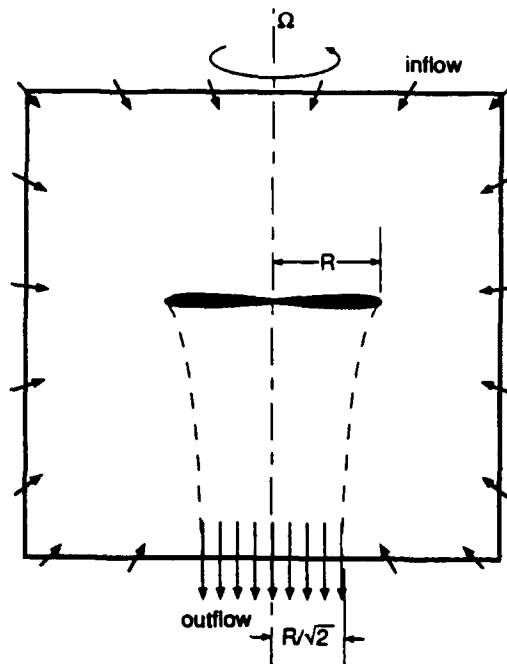


Fig. 7 Sketch of outer boundary conditions used in hover calculations

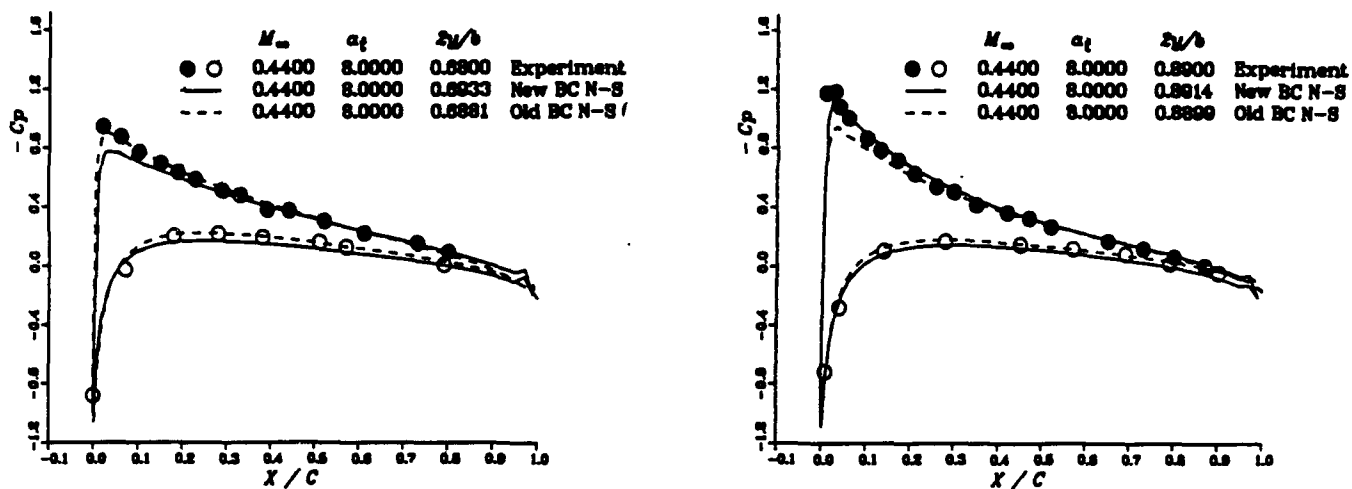


Fig. 8 Pressure distributions on a hovering rotor with original and modified outer boundary conditions.

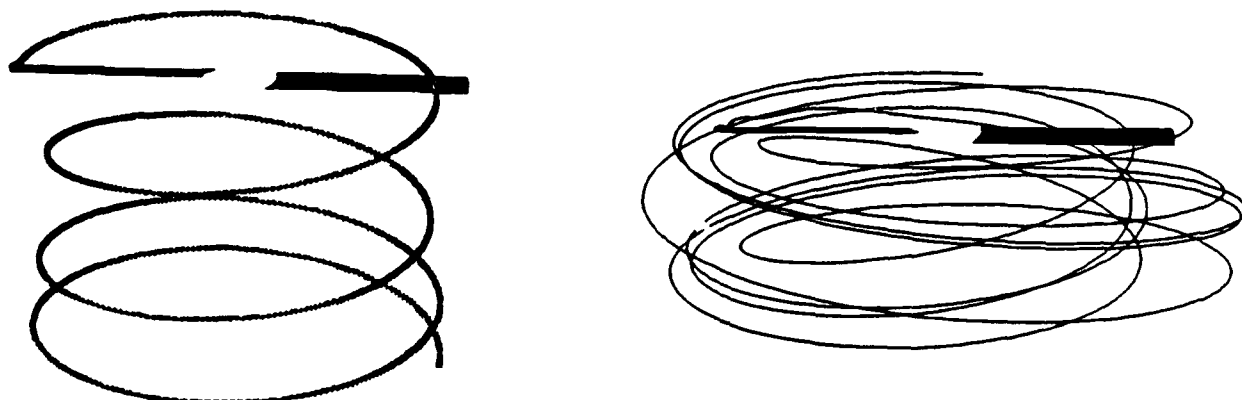
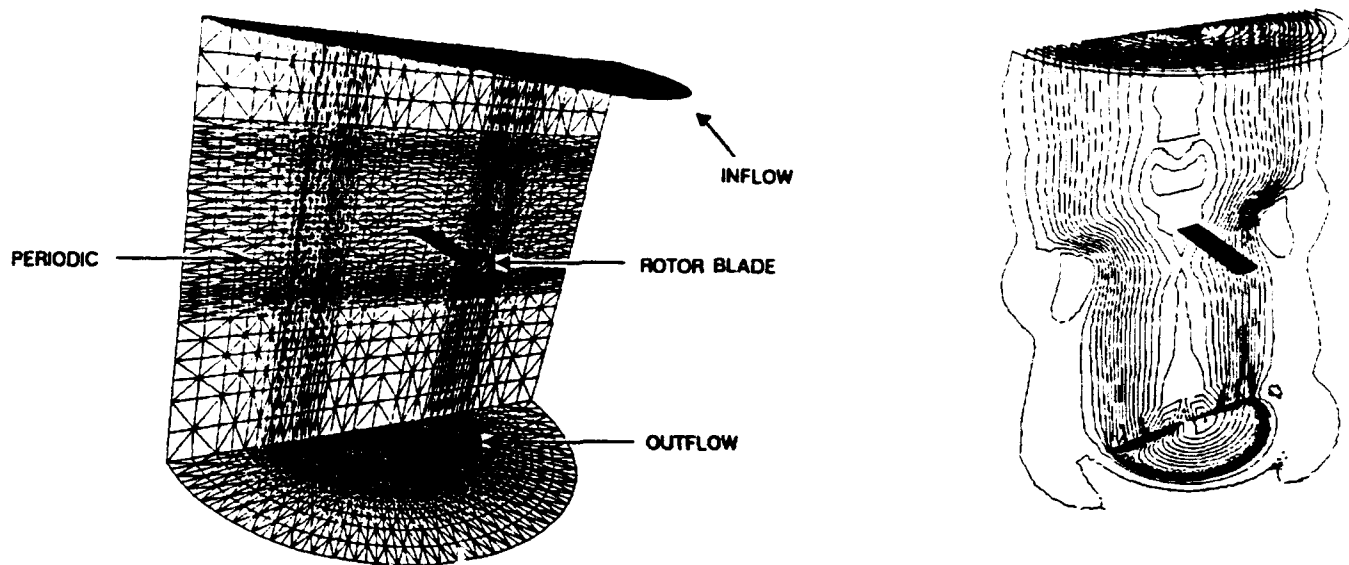
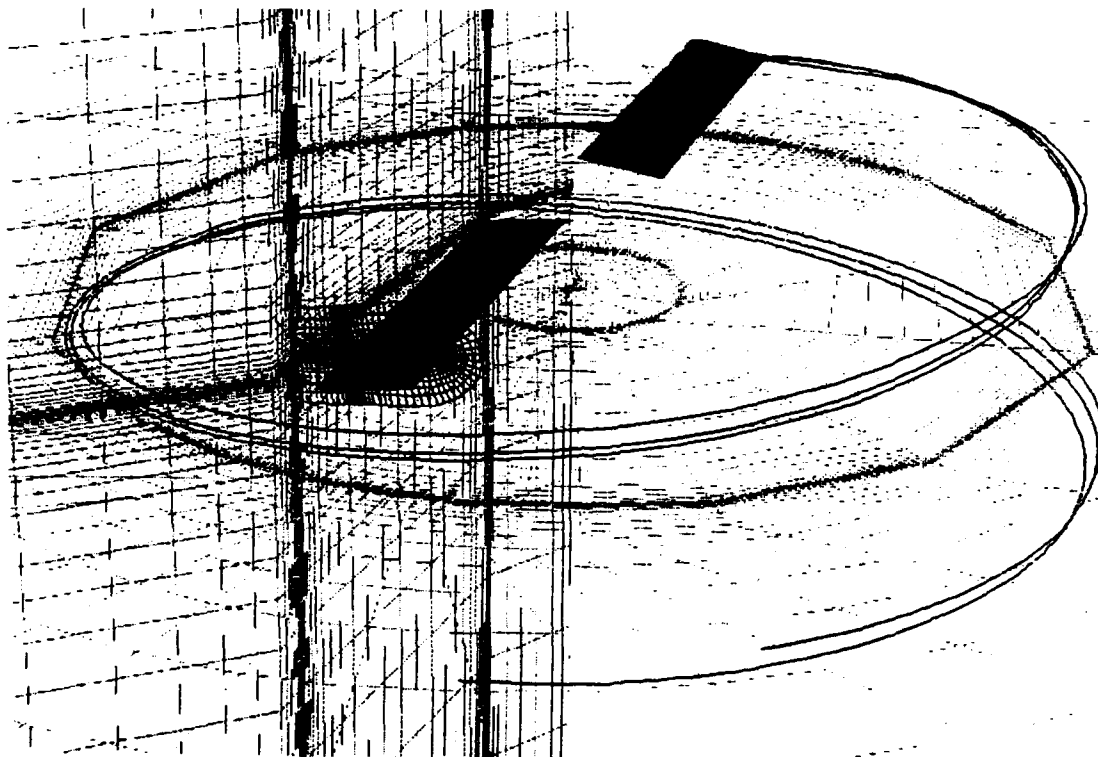


Fig. 9 Tip-vortex particle trajectories for a hovering rotor with original and modified outer boundary conditions.



**Fig. 10 Initial grid and density contours for an unstructured-grid calculation of a hovering rotor**



**Fig. 11 Grid and vortex trajectory for a three-zone calculation of a rotor in hover**

$$M_T = 0.763, \mu = 0.197, Re \times 10^6 = 2.75, r_B = 0.946$$

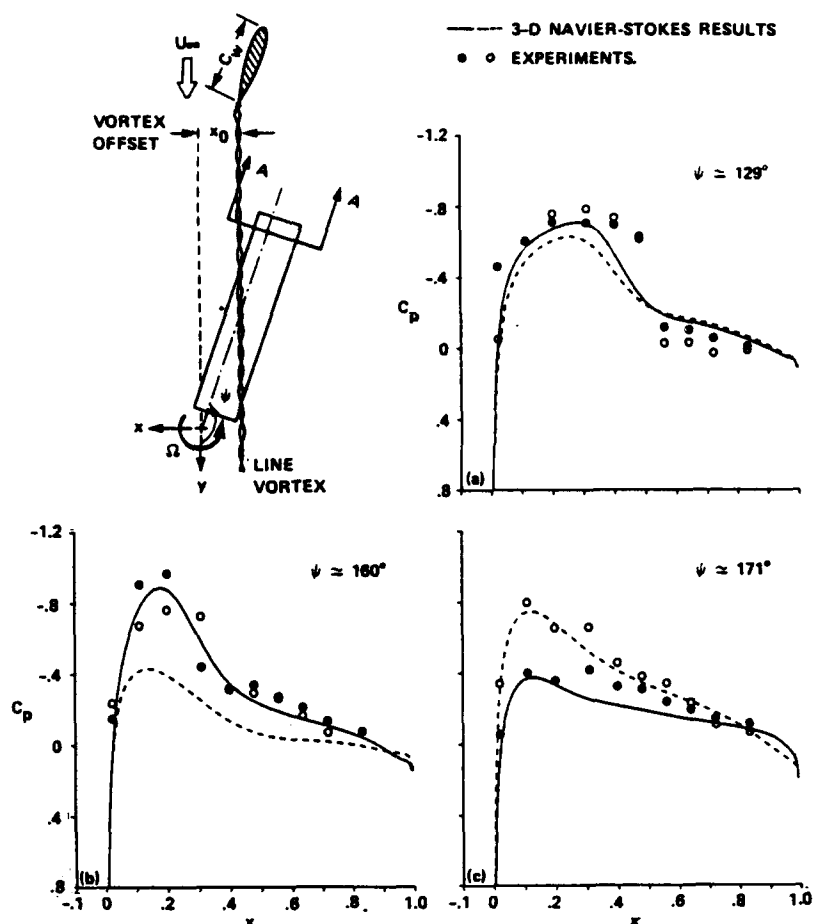


Fig. 12 Unsteady pressure distributions near the tip during an oblique blade-vortex interaction

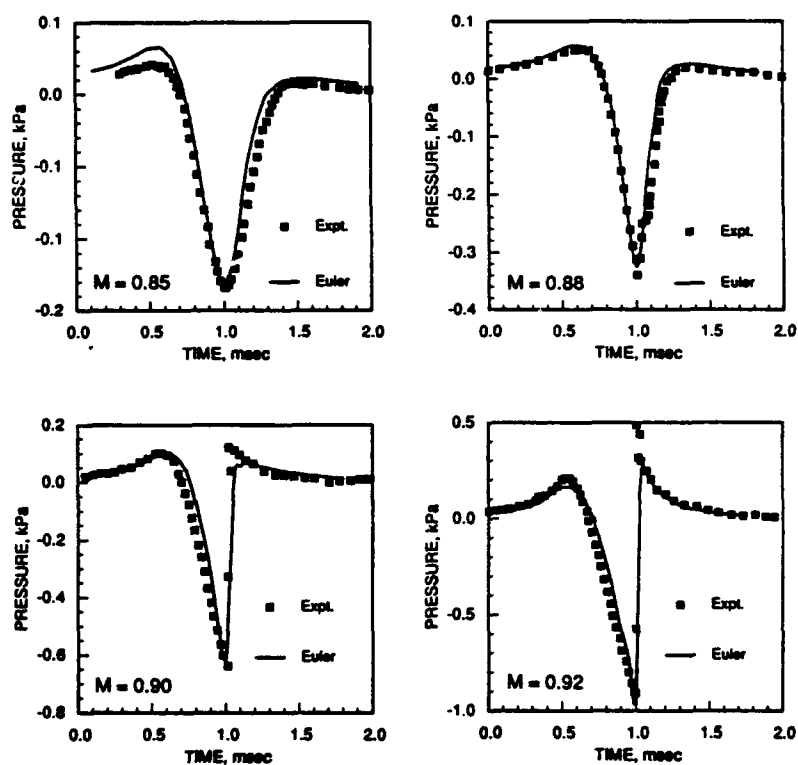


Fig. 13 Pressure time histories in the plane of a hovering rotor at  $r/R = 3.09$  for various tip Mach Numbers

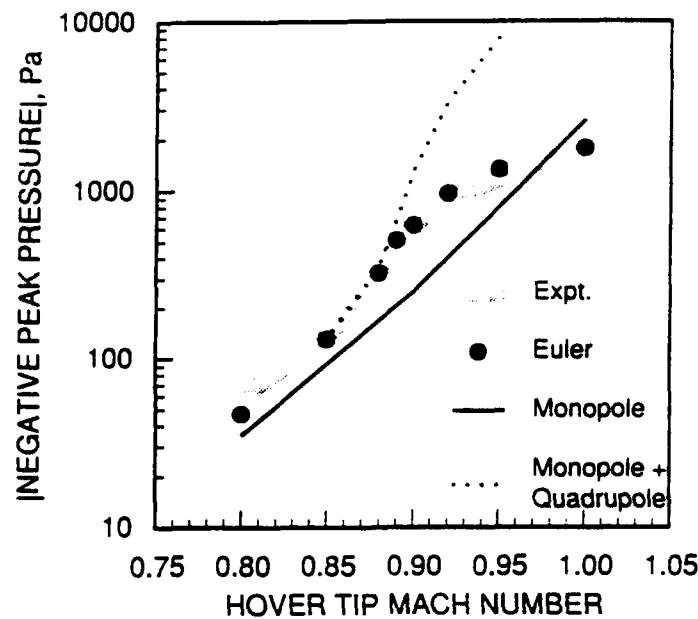


Fig. 14 Magnitude of the acoustic wave of a hovering rotor at  $r/R = 3.09$  for various tip Mach Numbers

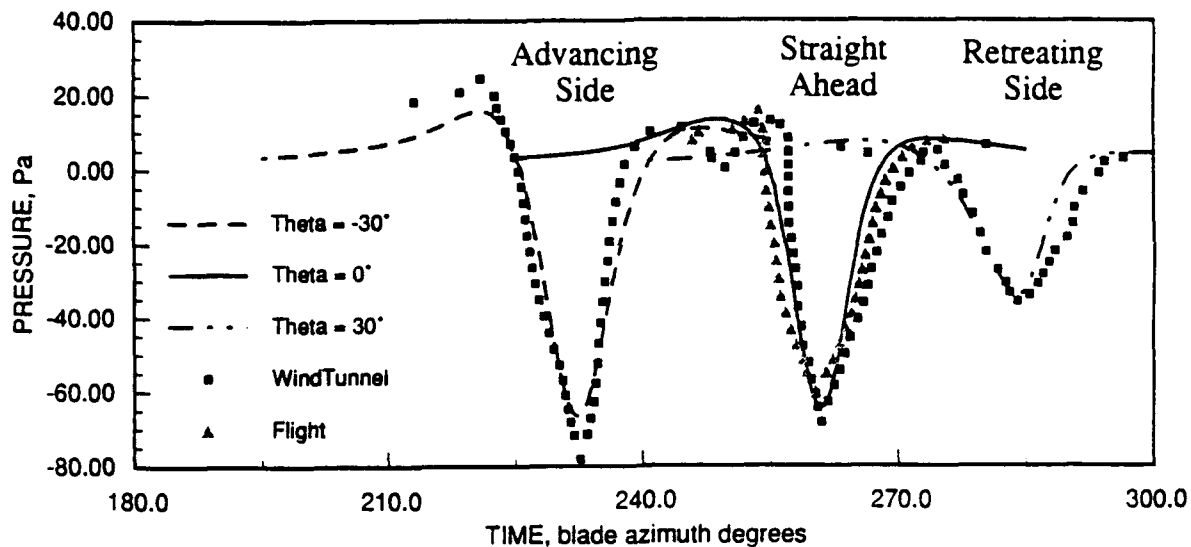


Fig. 15 Pressure time histories in the plane of a rotor in forward flight for maximum tip Mach number = 0.837

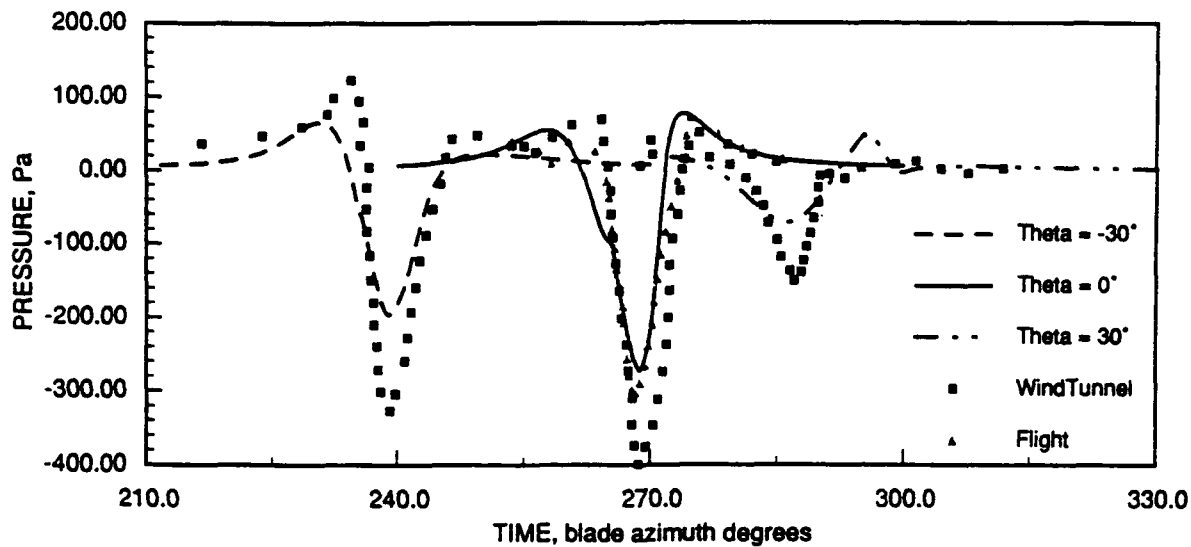
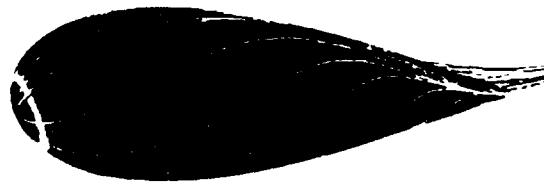
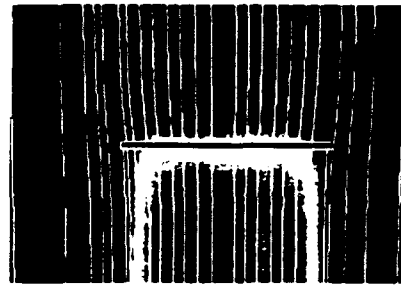


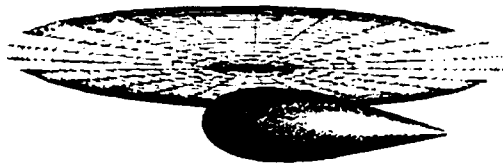
Fig. 16 Pressure time histories in the plane of a rotor in forward flight for maximum tip Mach number = 0.896



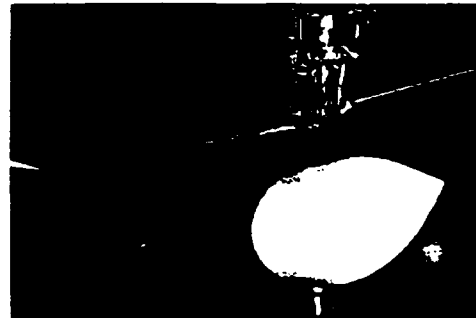
(a) Navier Stokes calculation on an isolated body  
(turbulent flow,  $Re=27,000,000$ ,  $\alpha=17^\circ$ ,  $M=0.18$ )



(b) Horizontal slice through an actuator disk rotor  
simulation of the Navier Stokes equations



(c) Body and rotor are combined using overset  
grids (Chimera/ F3D)



(d) 7 by 10 foot rotor-body interference wind  
tunnel test.

Fig. 17 Combination of components for studying rotor-body interactions

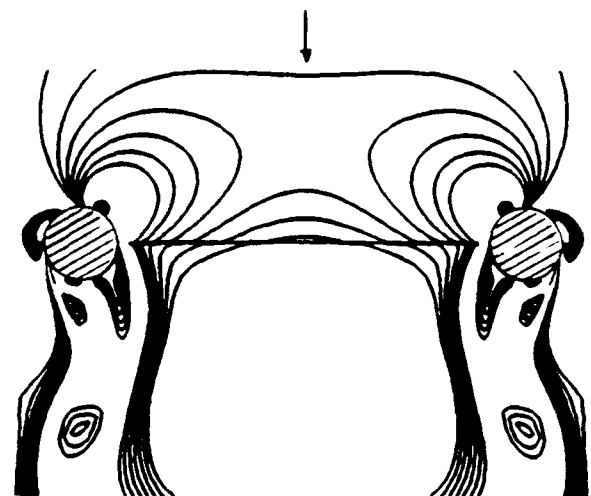
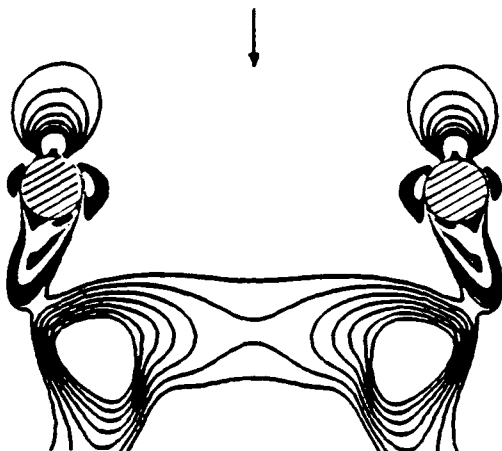
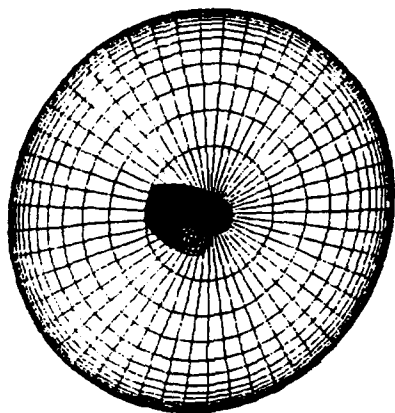
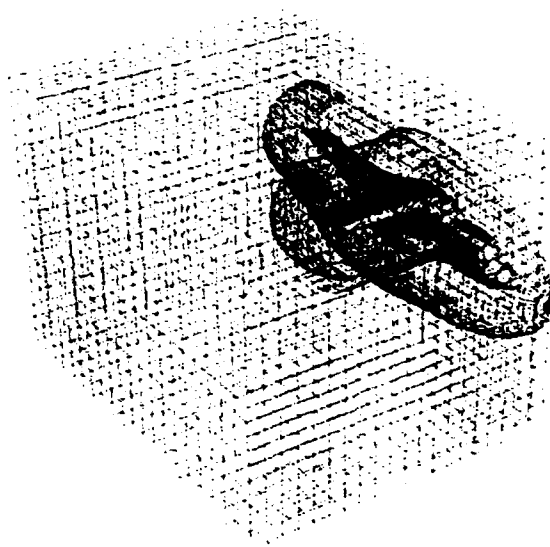


Fig. 18 Actuator-disk model of a toroidal ducted rotor.

### Surface Grids



### Volume Grids



**Fig. 19 Chimera multi-block grid topology for tiltrotor aircraft.**

**UNSTEADY FLOWS, 2**  
**SESSION 8**



## DYNAMIC AIRFOIL STALL INVESTIGATIONS

M.F. Platzter\*, M.S. Chandrasekhara\*, J.A. Ekaterinaris\*, L.W. Carr#

### 1. INTRODUCTION

Experimental and computational investigations of the dynamic stall phenomenon continue to attract the attention of various research groups in the major aeronautical research laboratories. There are two reasons for this continued research interest. First, the occurrence of dynamic stall on the retreating blade of helicopters imposes a severe performance limitation and thus suggests to search for ways to delay the onset of dynamic stall. Second, the lift enhancement prior to dynamic stall presents an opportunity to achieve enhanced maneuverability of fighter aircraft. A description of the major parameters affecting dynamic stall and lift and an evaluation of research efforts prior to 1988 has been given by Carr [1].

Unfortunately, the basic fluid physics underlying the dynamic stall phenomenon is still far from being fully understood. This is due to the difficulty of making sufficiently detailed measurements on fast moving airfoils so that the processes leading to unsteady flow separation, vortex formation/propagation, and unsteady flow reattachment can be identified. These processes are further complicated by the possibility of shock formation and unsteady shock/boundary layer interaction as the free-stream Mach number is increased. The development of reliable computational prediction methods, in turn, is dependent on the availability of sufficiently detailed flow information about the dynamic stall processes.

In this paper the authors' recent progress in the development of experimental and computational methods to analyze the dynamic stall phenomena occurring on NACA 0012 airfoils is reviewed. First, the major experimental and computational approaches and results are summarized. This is followed by an assessment of our results and an outlook toward the future.

### 2. EXPERIMENTAL PROGRESS

In this section we summarize the experimental results obtained in the Compressible Dynamic Stall Facility of the NASA Ames Fluid Mechanics Laboratory since our last review [2]. Additional details

about this facility and the experimental techniques used in these experiments can be found in references [3-9]. All the measurements described in this section were obtained on a NACA 0012 airfoil of 7.62 cm (3 inch) chord subjected to sinusoidal pitch oscillations about the quarter-chord point or to a ramp-change in angle of attack. The maximum frequency achieved was 100 Hz, the maximum pitch rate 3600 degrees per second. The Reynolds number ranged between 200,000 to 900,000. Further details can be found in the cited references.

#### 2.1 Effect of Mach Number and Pitch Rate on Dynamic Stall

A series of experiments was performed to determine the effect of Mach number and pitch rate on the dynamic stall initiation and evolution. To this end stroboscopic schlieren pictures were taken over a Mach number range from 0.2 to 0.45, a non-dimensional pitch rate range from 0.02 to 0.05 for airfoils undergoing a ramp change in angle of attack, and a reduced frequency range of 0.025 to 0.1 for airfoils in sinusoidal pitch motion. The non-dimensional pitch rate is defined as the pitch rate (radians/sec)  $\times$  chord / free-stream speed. The reduced frequency is defined as frequency of oscillation (Hz)  $\times$   $\pi$   $\times$  chord / free-stream speed.

Figure 1 shows the observed vortex release angles for ramp and sinusoidal motions as a function of Mach number and pitch rate or reduced frequency. The following trends are clearly discernible:

- a) an increase in reduced frequency delays the onset of dynamic stall to higher angles of attack
- b) at free-stream Mach numbers greater than 0.3 compressibility effects are significant, producing drastically reduced stall onset angles of attack.

#### 2.2 Visualization of Leading-Edge Details

Using the stroboscopic schlieren technique [3] locally supersonic flow near the leading edge could be successfully identified in a number of cases. For example, Figure 2 shows the leading edge flow details for a free-stream Mach number of 0.45 as the airfoil is pitching upwards at a non-dimensional pitch rate of 0.0313 through an angle of attack of 12.6 degrees. Several discontinuities are clearly visible within the first 5 - 8% chord distance. At this Mach number locally supersonic flow is reached (verified by interferometry). Therefore these discontinuities most likely are caused by the formation of weak multiple shocks due to the recompression and the interaction with the boundary layer.

\* Navy-NASA Joint Institute of Aeronautics  
Naval Postgraduate School, Monterey, CA

# U.S. Army Aeroflightdynamics Directorate  
and Fluid Dynamics Research Branch  
NASA Ames Research Center  
Moffett Field, California

Eventually, these weak interactions are followed by a stronger shock which recompresses the flow to subsonic values. Similar stroboscopic schlieren pictures were obtained over a range of angles of attack from 12.2 to 12.9 degrees for the same free-stream Mach number and pitch rate.

Another interesting observation is the formation of multiple vortices under certain circumstances rather than the roll-up into a single dynamic stall vortex. Figure 3 presents an enlarged schlieren picture for a free-stream Mach number of 0.25, as the airfoil pitches at a pitch rate of 0.025 through an angle of attack of 16.5 degrees. Two clockwise vortical structures can be identified. Multiple vortices were observed only at low pitch rates and low Mach numbers, whereas at higher Mach numbers a single dynamic stall vortex was seen to form.

### 2.3 Quantitative Measurements of Dynamic Stall Onset

A more quantitative determination of the leading edge flow details and therefore of the dynamic stall onset mechanism is made possible by means of point diffraction interferometry [6]. Typical interferograms obtained with this technique are shown in Figures 4 for the NACA 0012 airfoil oscillating at a reduced frequency of 0.05 in a  $M=0.33$  flow. In these interferograms the fringes (the alternating dark and light lines in the photographs) denote lines of constant Mach number [7]. In Figure 4a, the flow over the airfoil at an angle below stall is presented for an angle of 10 degrees. Note the fringes which leave the leading edge turn parallel to the surface, and then abruptly turn toward the surface of the airfoil once more. As explained in [6], this pattern is indicative of a laminar separation bubble. In contrast, Figure 4b shows the onset of dynamic stall as the airfoil oscillates through an angle of attack of 13.6 degrees. The fringes no longer rapidly curve back to the surface near the leading edge. Instead, they are displaced aft until, further downstream, they again turn normal to the surface, denoting the development of a dynamic stall vortex. Furthermore, the fringe patterns indicate that the dynamic stall develops from a region of strong gradients which encloses a low energy region, in contrast to the symmetric density field one would expect from a classical vortex.

Further quantification of the flow field around the leading edge is made possible by digital processing of the interferograms [7]. Using a specially designed, screen-oriented digitizing program fringe contour maps, as shown in Figure 5, could be obtained. As noted above each fringe is a line of constant density, and thus also of constant Mach number. Therefore, the fringe maps can be used to quantify the effect of unsteadiness on the local pressure distributions. Figure 5 shows

the fringe pattern differences near the leading edge of the NACA 0012 airfoil in a  $M=0.33$  flow at a steady 10 degrees angle of attack versus the case of oscillation at  $k=0.1$  when the airfoil passes through the same angle of attack. It can be seen that a separation bubble starts to develop in the steady case while no such development occurs as yet in the oscillating case. Figure 6 shows a plot of the suction peaks determined from the fringe maps [7] for several Mach numbers and reduced frequencies. It is seen that a maximum suction pressure coefficient of -4.96 is reached at  $M=0.3$  (corresponding to a Reynolds number of 540,000) for three different values of reduced frequency  $k=0.05$ , 0.075 and 0.10, thus suggesting that stall develops once the suction pressure reaches a maximum value, independent of reduced frequency. This value is reached at progressively higher angles of attack with increasing frequency. Figure 7 shows the leading edge pressure distributions inferred from the fringe patterns as a function of reduced frequency. Again, it can be seen that the development of leading edge pressure gradients is delayed due to the airfoil oscillation. This supports the suggestion that stall delay is brought about by the lag in pressure build-up due to inviscid unsteady flow effects. It remains to be seen whether this is the dominant effect. This point will be addressed further in section 3.2. Furthermore, it is noteworthy to observe from Figure 6 that the maximum suction pressure coefficient decreases as the Mach number is increased.

Additional flow field information about the dynamic stall onset mechanism was obtained by means of laser-doppler velocimetry [8]. Figure 8 shows the distribution of the axial and normal components of the velocity vectors in the separation bubble which has formed on the NACA 0012 airfoil as it oscillates in a  $M=0.3$  flow at a reduced frequency of  $k=0.05$  with an amplitude of 10 degrees about a mean angle of 10 degrees. The measuring station is at  $x/c=0.083$ , that is very close to the leading edge. The measured velocity profiles are plotted as a function of phase angle, such that a phase angle of 90 degrees corresponds to zero angle of attack, 180 degrees to 10 degrees angle of attack during the upstroke and so on. It is seen that at a phase angle of 160 degrees, corresponding to 6 degrees incidence on the upstroke, there is a rapid drop in the u-velocity component close to the airfoil surface at  $y/c=0.067$  from values significantly greater than the free-stream speed to values somewhat below the free-stream speed. Hence no flow reversal is observed yet at this measuring station although reverse flow can be expected very close to the wall. Unfortunately, no measurements could be taken closer to the wall due to the laser beam configuration used. The v-component of the velocity vector remains constant until a phase angle of 186 degrees is reached corresponding to an angle of attack slightly less than 11 degrees. At a phase angle of

about 200 degrees, (13.4 degrees incidence), an abrupt increase in the v-component develops near the leading edge which appears to be caused by the break-up of the separation bubble. Very closely spaced additional measurements [8] showed that the bubble extends from  $0.017 < x/c < 0.167$  along the surface and reaches out to about 15% chord.

Further LDV mapping of the flow field at additional measuring stations revealed that during the initial part of the upstroke the flow experiences rapid accelerations over a large region of the airfoil reaching instantaneous values 80% higher than the free-stream value. The corresponding PDI images confirmed the presence of these large velocities outside of the separation bubble, extending over a significant distance normal to the wall as well as downstream from the leading-edge. As the airfoil angle of attack starts to exceed the static stall angle a wake-like profile develops near the wall as a result of bubble breakdown.

## 2.4 Quantitative Measurements of the Reattachment Mechanism

The previously described three experimental techniques, schlieren visualization, point diffraction interferometry, and laser-doppler velocimetry, were also used to identify the detailed flow reattachment process during the downstroke [9]. The flow condition was again  $M=0.3$ , corresponding to a Reynolds number of 540,000. The airfoil again oscillated about a mean angle of 10 degrees with an amplitude of 10 degrees.

First, schlieren visualization identified the steady stall angle to be 12.33 degrees, with no measurable hysteresis effect. In contrast, schlieren visualization of the flow over the oscillating airfoil revealed that flow reattachment after dynamic stall is a continuous process which extends over a significant range of angles of attack (from about 14 degrees down to about 6 degrees in this particular case). At 13.82 degrees on the downstroke, the flow begins to reattach around the leading-edge while the remainder of the upper surface flow is still separated. At 10 degrees, reattachment has progressed to about 10% chord from the leading-edge. A further decrease in angle of attack leads to a further downstream progression of the reattachment while a separation bubble starts to form near the leading-edge. A further decrease in angle of attack tends to shrink the separation bubble which finally vanishes at about 6 degrees. This sequence of events is shown schematically in Figure 9. Additional point diffraction and LDV measurements lend further support to this scenario of evolution of the reattachment process. Figure 10 shows the maximum suction pressure history during the downstroke. As reattachment progresses, the leading-edge

suction increases with decreasing angle of attack, down to about 8 degrees incidence. Near the steady stall angle the suction reaches a plateau which is indicative of the bubble formation. This evolution of the pressure distributions during the downstroke is shown more clearly in Figure 11. The measured velocity profiles near the leading-edge at station  $x/c=0.083$  at 10 degrees and 5.46 degrees during the up and downstroke are shown in Figure 12. The large hysteresis effect can clearly be seen at 10 degrees while at 5.46 degrees the flow is fully attached and hence no hysteresis is present any longer.

## 3. COMPUTATIONAL PROGRESS

In this section we summarize the computational results obtained since our last review. Additional details can be found in references 10 and 11.

### 3.1 Numerical Solution of the Navier-Stokes Equations

The thin-layer approximation of the Navier-Stokes equations in conservation law form, written for an inertial reference frame, was used. All quantities were discretized at every node using finite differences. The physical space points were mapped to the computational domain points by means of a generalized coordinate transformation. For the time integration the implicit trapezoidal rule was used. After linearization and space discretization the space integration was performed with the Beam-Warming, factorized, iterative algorithm. A Jameson-type blended second and fourth-order dissipation term based on the computed pressure field was incorporated to suppress high-frequency numerical oscillations and to enable capturing of shocks. For subsonic shock-free solutions only the fourth-order dissipation was used. In addition, an implicit fourth-order smoothing was used on the left side of the equations for numerical stability. Both the implicit and explicit dissipation were scaled by the spectral radius and with the time step. The latter scaling makes the steady-state solution independent of time step. Since the added dissipation terms modify the original partial differential equation the dissipation coefficients were kept as small as possible for unsteady computation. Elimination of the error introduced by the linearization and approximate factorization may be accomplished by performing Newton subiterations to convergence within each time step.

The boundary conditions were specified as follows. At the outer boundaries zero-order Riemann invariant extrapolation was used. On the airfoil surface the non-slip condition was applied for the velocities, and the density and pressure were obtained from the interior by simple extrapolation. For

the C-type grids used in this investigation averaging of the flow variables across the wake-cut was incorporated.

Fully turbulent flow calculations only were performed by implementing three different turbulence models into the above-described numerical code. These were the Baldwin-Lomax and the RNG algebraic eddy viscosity models and the one-equation Johnson-King model. For a more detailed description of these models we refer to [11] and to the original references contained therein.

### 3.2 Computation of Dynamic Stall Onset

A series of calculations was performed with the above described Navier-Stokes code in combination with the Baldwin-Lomax turbulence model to investigate the evolution of dynamic stall in response to a ramp-change in angle of attack of a NACA 0012 airfoil. The Reynolds number was chosen to be sufficiently high so that fully turbulent flow could be assumed. Figure 13 shows the computed flow field as the airfoil pitches through an angle of attack of 17 degrees in a  $M=0.4$  and  $Re=4,000,000$  flow. It can be seen that the flow separates near the leading-edge but reattaches again further downstream thus forming a recirculatory flow region. Another recirculatory flow region then forms near the trailing-edge. A further increase in angle of attack produces a rapid growth and a merging of the two recirculatory flow regions and the formation of the dynamic stall vortex. A more detailed study of the effect of pitch rate and of Mach number on the onset of flow reversal near the leading edge of the NACA 0012 airfoil and of two modified NACA 0012 airfoils [10] showed that the onset of flow reversal follows the same trends as observed in the experiments. An increase in Mach number shifts the flow reversal to lower angles of attack, whereas an increase in pitch rate delays the flow reversal to higher angles of attack. More specifically, as shown in Figure 14, the onset of flow reversal appears to occur in response to substantially the same critical pressure gradient distribution. The delay to higher pitch rate therefore appears to be due primarily to the lag in inviscid pressure build-up.

### 3.3 Computation of the Reattachment Mechanism during Light Stall

Further details of the flow behavior were also computed for small amplitude sinusoidal pitch oscillations near static stall [11]. Figures 15 and 16 show a flow field comparison as the airfoil oscillates through 14.7 degrees during the up and downstroke for a pitch oscillation about the quarter chord point in a free-stream flow of  $M=0.3$  at a Reynolds number of 2 million. The airfoil oscillates with an amplitude of 2.5 degrees about a mean angle of 13 degrees.

This corresponds to the case of light stall because the static stall angle of approximately 13.5 degrees is slightly exceeded during part of the oscillation. As shown experimentally by Carta and Lorber [12], the light stall regime is prone to lead to stall flutter. Hence, there is considerable interest to develop computational procedures to predict this phenomenon. It is seen from Figures 15 and 16 that there is a substantial thickening of the boundary layer during the downstroke and that the computed flow field (in terms of instantaneous particle traces) is quite different during the up and downstroke at 14.7 degrees. As soon as the static stall angle is exceeded a reversed flow region forms near the trailing-edge during the upstroke. It continues to grow to its maximum value at an angle of attack of 15.3 degrees during the downstroke and then diminishes again until the flow is fully reattached at around 12 degrees. The flow field differences during the up and downstroke produce the well known lift and moment hysteresis effects. In Figure 17 the computed moment hysteresis loops are compared with the measured moment loops [11]. In this case the oscillation amplitude was 5.5 degrees about a mean angle of 10 degrees at a Mach number of 0.3, a Reynolds number of 4 million, and a reduced frequency of 0.1. The experimental curves resemble a figure eight. Instability occurs as soon as the area enclosed by the clockwise part of the loop exceeds the counterclockwise area. The computed loops are purely counterclockwise loops and hence fail to predict the onset of stall flutter. This failure can be traced to the Navier-Stokes code's inability to predict the measured collapse of the suction peak shown in Figure 18. The computed pressure distributions only indicate the formation of a recirculatory flow region near the trailing-edge. Additional calculations using the Johnson-King and the RNG turbulence model rather than the Baldwin-Lomax model produced significantly different recirculatory flow regions and hence hysteresis loops, but none were able to predict the experimental distributions [11].

## 4. DISCUSSION

For the analysis of the above experimental and computational results it appears to be useful to consider the characteristic response times which are likely to affect the flow phenomena. Introducing the aerodynamic time as the proper reference unit, i.e., the time it takes a free-stream particle to travel one chord length, the aerodynamic times used in the above described experiments varied from 0.00115 sec at  $M=0.2$  to 0.0005 sec at  $M=0.45$  (for the NACA 0012 airfoil of 7.62 cm chord). The ramp rise times to the maximum lift (at about 17 degrees incidence) used in these experiments varied from about 0.0125 sec at  $M=0.2$  to 0.005 sec at  $M=0.45$ , corresponding to about 10 aerodynamic time

units. Wagner's lift response to a step change in angle of attack indicates that it takes about 50 aerodynamic times to reach the steady-state lift value. Since the ramp rise time to maximum lift is significantly shorter than the time to reach steady-state lift significant inviscid unsteady aerodynamic effects (delays) can be expected to occur. On the other hand, the step response of the boundary layer typically is of the order of the aerodynamic time, as discussed for example by Hancock and Mabey [13]. Therefore it can be expected that the observed and computed stall onset delays are caused primarily by the lag in the inviscid pressure build-up. Since the boundary layer responds almost instantaneously to the imposed pressure the flow reversal and stall onset will occur as soon as a certain critical pressure level or pressure gradient distribution has been reached (see sections 2.3 and 3.2).

Although the Navier-Stokes computations appear to be capable of predicting the stall onset delay due to increasing pitch rate several serious deficiencies are apparent. One concerns the need for a greatly improved resolution and computation of the boundary layer region. A second deficiency concerns the inability to include the boundary layer transition phenomenon. Although recirculation regions can be obtained with a fully turbulent Navier-Stokes code (as shown in Figure 11) the realism of such computations is questionable. The importance of proper transition modelling has been shown in viscous-inviscid interaction calculations [14,15], especially for airfoil flows at Reynolds numbers less than one million. Therefore transition modelling will have to be incorporated into the present Navier-Stokes code if the separation bubbles described in section 2.2 for Reynolds numbers ranging from 200,000 to 900,000 are to be modelled successfully. A further uncertainty concerns the effect of flow unsteadiness on the transition process. Since no experimental data are available such modelling will have to be based on steady-state information only. Finally, the inability of the commonly used turbulence models (Baldwin-Lomax, Johnson-King, RNG) to predict the reattachment process (see section 3.3) is a further obstacle to the successful computation of dynamic stall phenomena.

It is likely that certain aspects of the dynamic stall phenomenon, such as the dynamic stall onset, can be modelled more efficiently and successfully with viscous-inviscid interaction approaches rather than with numerical solutions of the Navier-Stokes equations. Viscous-inviscid interaction procedures permit the efficient computation of detailed boundary layer information and the incorporation of transition modelling by either using empirical transition onset models or stability calculations and empirical transition length models. Cebeci et al [16,17] recently extended steady viscous-

inviscid airfoil computations to airfoils undergoing ramp-type and sinusoidal oscillations. Results obtained for a Sikorsky airfoil appear sufficiently encouraging to further develop this method and to apply it to the NACA 0012 measurements described in section 2.

## SUMMARY and OUTLOOK

Experimental and computational investigations of the dynamic airfoil stall phenomena occurring on NACA 0012 airfoils subjected to harmonic time oscillations or to ramp-type changes in angle of attack have been described. Using optical interference-free flow visualization and flow-measuring techniques, such as stroboscopic schlieren, point-diffraction interferometry, and laser-doppler velocimetry, flow information could be acquired which revealed hitherto unknown features about the flow reversal/separation onset processes, the influence of compressibility, and the mechanism of flow reattachment. The application of state-of-the-art Navier-Stokes computations showed their ability to correctly predict certain global trends, such as the dependence of lift and pitching moment on pitch rate, Mach number, and leading-edge geometry during the upstroke, but that they are deficient to model the detailed dynamic stall onset and the dynamic flow reattachment features.

It is felt that the experimental techniques are sufficiently well in hand to proceed from the study of the basic dynamic stall flow physics to the investigation of promising dynamic stall delay and control concepts because the successful implementation of such concepts will critically depend on the detailed visualization and measurement of the flow sensitivity to small changes in airfoil geometry, especially near the leading-edge. Efforts along these lines are planned for the near future.

## Acknowledgements

The authors gratefully acknowledge the support of the following organizations and individuals:

NASA Ames Research Center, Dr. S. Davis;  
U.S. Army Research Office, Fluid Mechanics Division, Dr. T. Doligalski;  
U.S. Air Force Office of Scientific Research, Aerospace Sciences Division, Capt. H. Helin, Maj. D. Fant;  
U.S. Naval Air Systems Command, Research and Technology Directorate, Mr. T. Momiyama.

## References

1. Carr, L.W., J.Aircraft Vol.25, No.1, Jan 1988, pp. 6-17
2. Carr, L.W., Platzer, M.F., Chandrasekhara, M.S., Ekaterinaris, J.A., Numerical and Physical Aspects of Aerodynamic Flows, IV (T.Cebeci Ed.), 239-256 (Springer Verlag 1990)
3. Chandrasekhara, M.S. and Carr, L.W., J.Aircraft, Vo.27, No.6, June 1990, pp. 516-522
4. Chandrasekhara, M.S. and Brydges, B.E., AIAA-90-0575 (1990)
5. Chandrasekhara, M.S. and Carr, L.W., AIAA-90-3038 (1990)
6. Carr, L.W., Chandrasekhara, M.S., Ahmed, S., Brock, N.J., AIAA-91-0007 (1991)
7. Carr, L.W., Chandrasekhara, M.S., Brock, N.J., AIAA-91-1683 (1991)
8. Chandrasekhara, M.S. and Ahmed, S., AIAA-91-1799 (1991)
9. Ahmed, S. and Chandrasekhara, M.S., AIAA-91-3225 (1991)
10. Grohsmeier, S.P., Ekaterinaris, J.A., Platzer, M.F., AIAA-91-1798 (1991)
11. Clarkson, J.D., Ekaterinaris, J.A., Platzer, M.F., 6th Int. Symp. Unsteady Aerodynamics, Aeroacoustics and Aeroelasticity University of Notre Dame, Indiana, 15-19 Sept. 1991
12. Carta, F.O. and Lorber, P.F., J. Propulsion, Vol.3, No.2, pp. 164-170, 1987
13. Hancock, G.J. and Mabey, D.G., AGARD-CP-465, Paper No. 14, 1989
14. Cebeci, T., Carr, L.W., Jang, H.M., AIAA-89-0020 (1990)
15. Walker, G.J., Subroto, P.H., Platzer, M.F., ASME-88-GT-32, 1988
16. Cebeci, T., Carr, L.W., Jang, H.M., AIAA-89-0020
17. Cebeci, T., Platzer, M.F., Chen, H.H., Jang, H.M., to be published

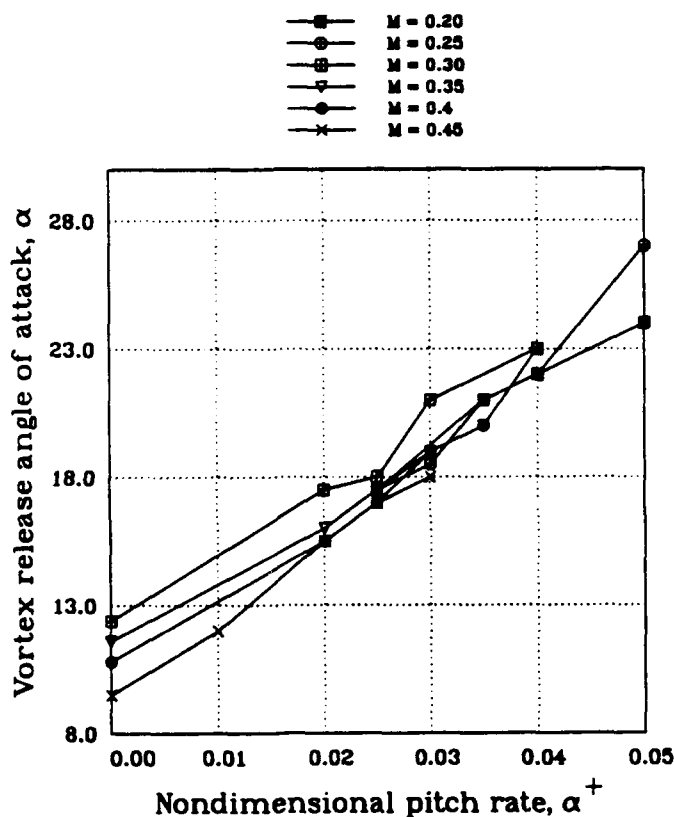


Fig. 1a Effects of Compressibility and Unsteadiness on Dynamic Stall Angle for a Transiently Pitching Airfoil

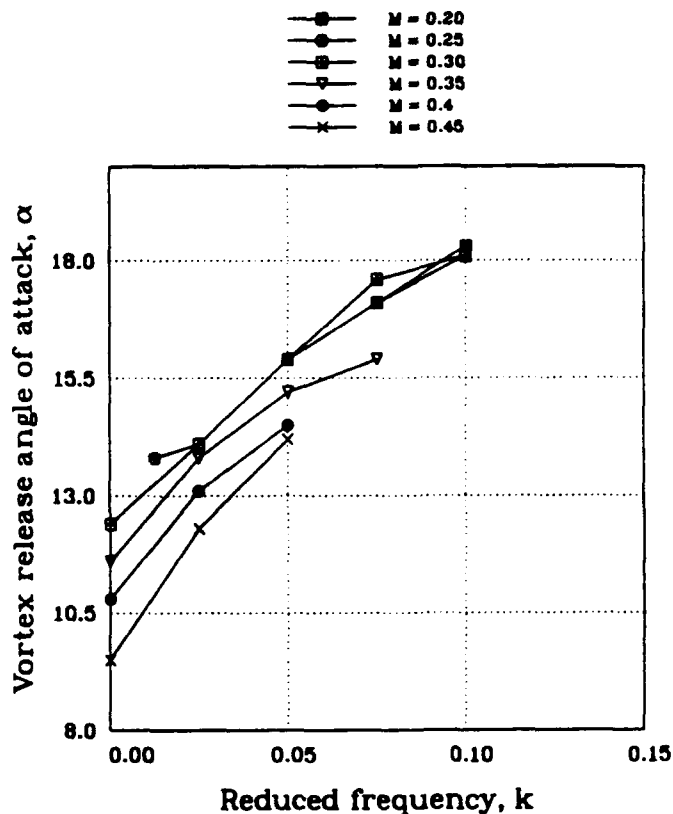


Fig. 1b Effects of Compressibility and Unsteadiness on Dynamic Stall Angle for an Oscillating Airfoil



Fig. 2 Schlieren Picture of Multiple Shocks on Rapidly Pitching NACA 0012 Airfoil



Fig. 3 Multiple Vortices on Rapidly Pitching NACA 0012 Airfoil



Fig. 4a Point Diffraction Interferogram of Oscillating NACA 0012 Airfoil  
AOA=10 degrees,  $M=0.33$ ,  $k=0.075$

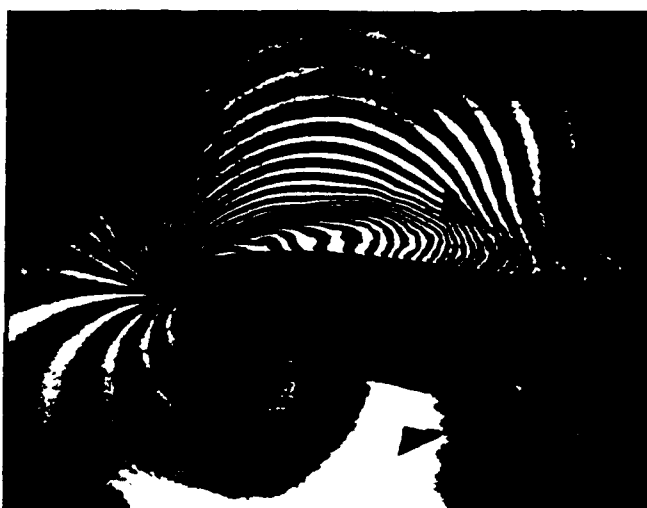


Fig. 4b Point Diffraction Interferogram of Oscillating NACA 0012 Airfoil  
AOA=13.6 degrees,  $M=0.33$ ,  $k=0.075$

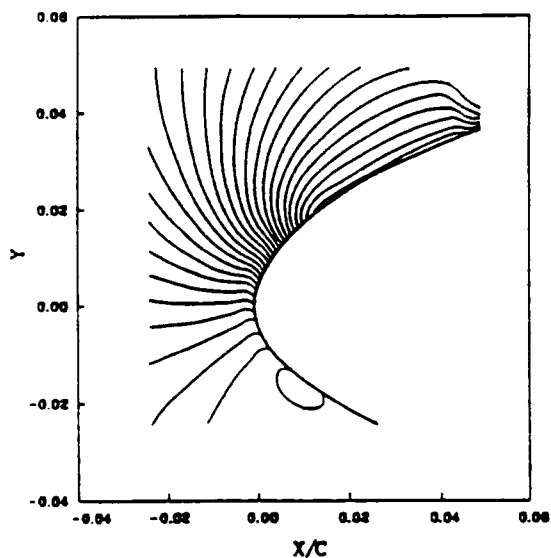


Fig. 5a Fringe Contours Near Leading Edge of Steady NACA 0012 Airfoil  
AOA=10 degrees,  $M=0.3$ ,  $k=0$

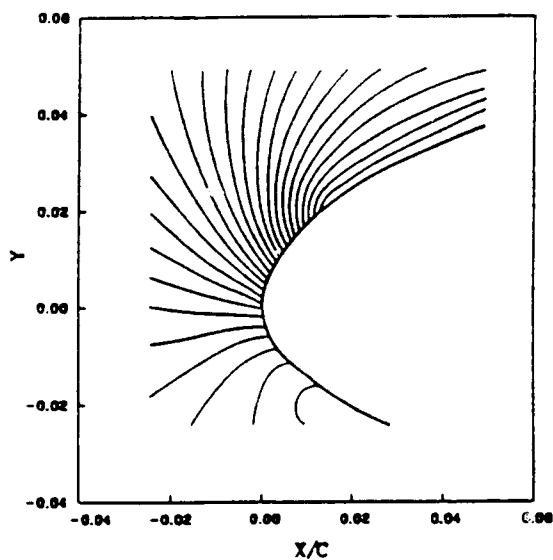


Fig. 5b Fringe Contours Near Leading Edge of Oscillating NACA 0012 Airfoil  
AOA=10 degrees,  $M=0.3$ ,  $k=0.1$

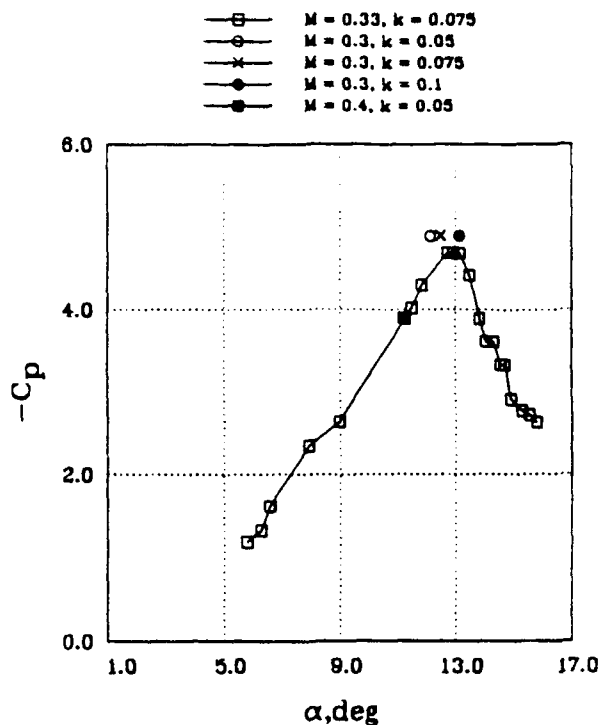


Fig. 6 Minimum Pressure Coefficient as Function of Angle of Attack at Various Mach Numbers, as Determined from PDI Interferograms

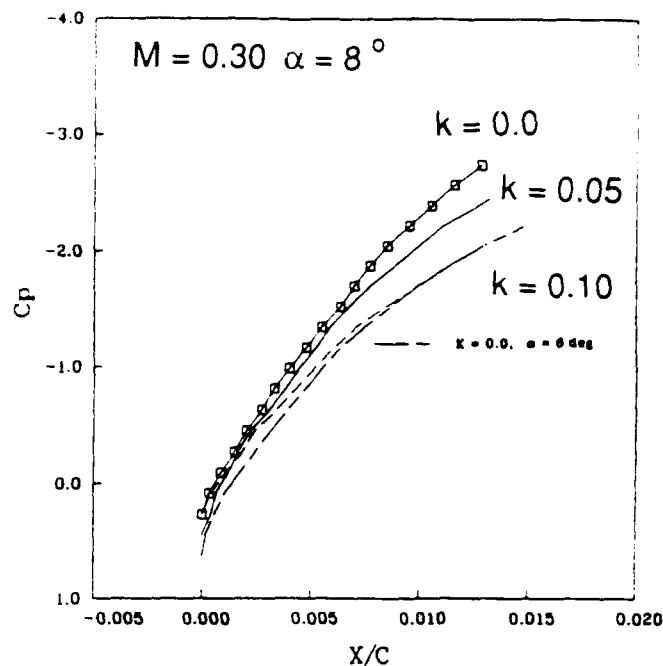


Fig. 7 Pressure Distributions for Several Reduced Frequencies for NACA 0012 Airfoil as Determined from PDI Interferograms  
M = 0.3, AOA = 8 degrees

PHASE DISTRIBUTION OF U at X/C = 0.083  
(ORIGIN SHIFTED BY 0.20 AT EACH Y/C)

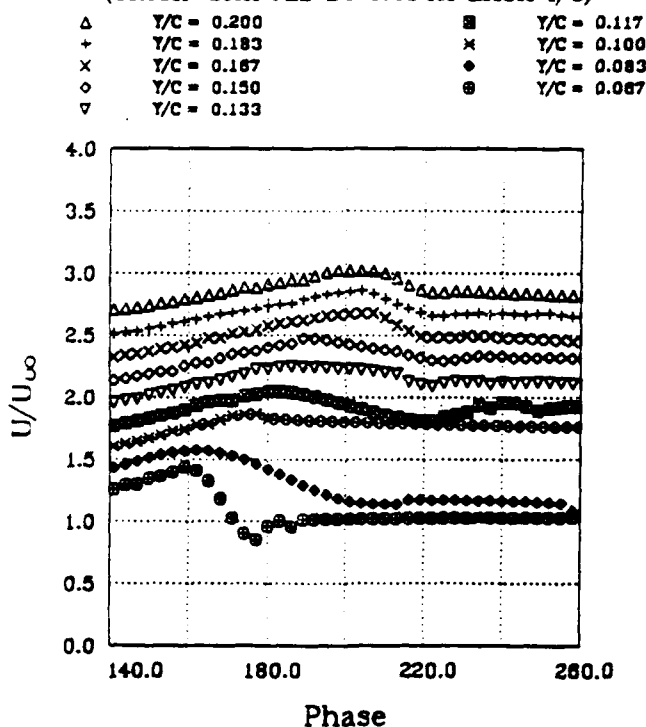


Fig. 8a U-Component Measurements in the Separation Bubble, x/c = 0.083

PHASE DISTRIBUTION OF V at X/C = 0.083  
(ORIGIN SHIFTED BY 0.20 AT EACH Y/C)

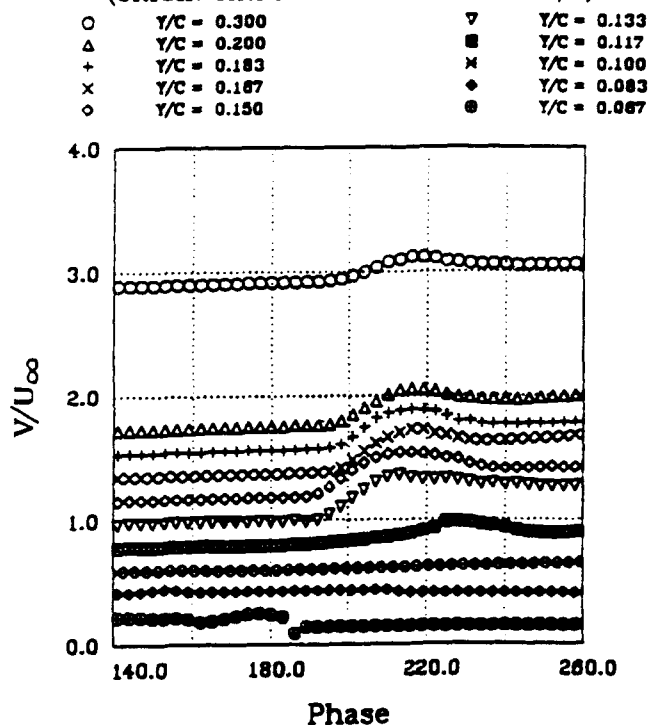


Fig. 8b V-Component Measurements in the Separation Bubble, x/c = 0.083



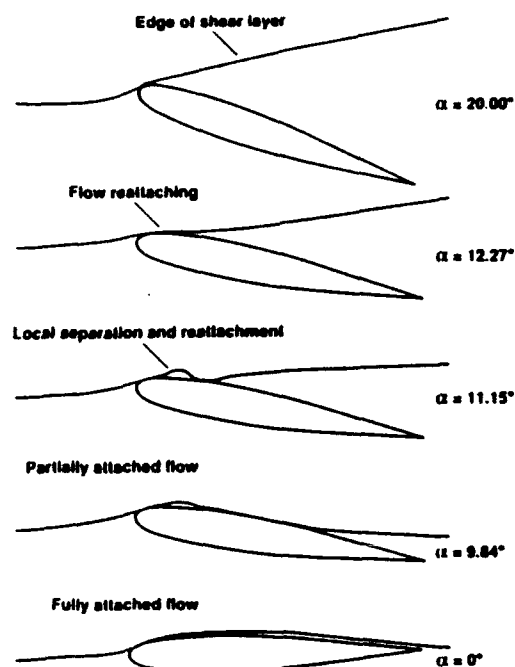


Fig. 9 Schematic of the Reattachment Process

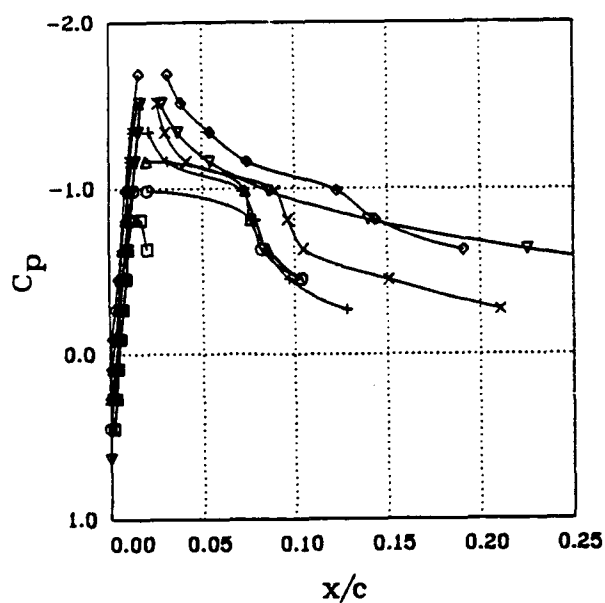


Fig. 11 Pressure Distribution during Reattachment

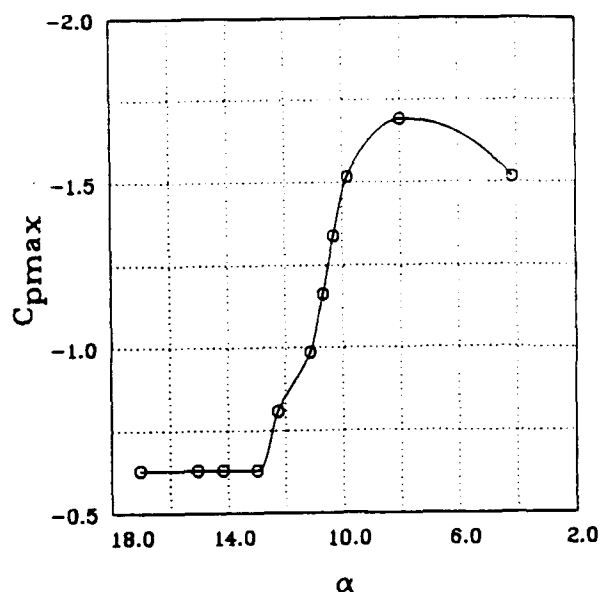
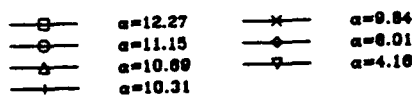


Fig. 10 Variation of Maximum Suction Pressure

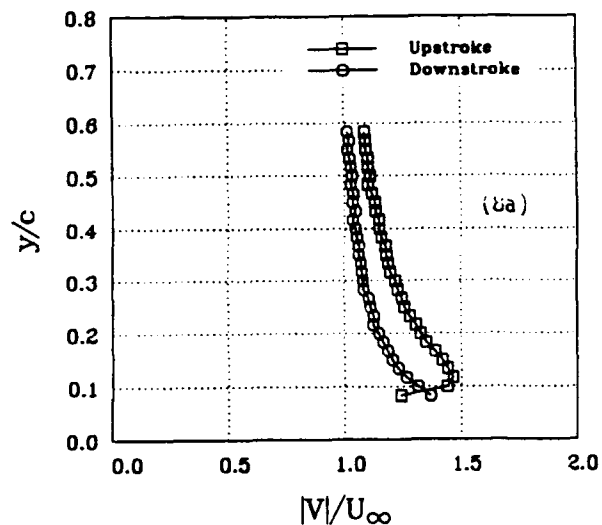


Fig. 12a Comparison of Velocity Magnitudes at AOA = 10 degrees

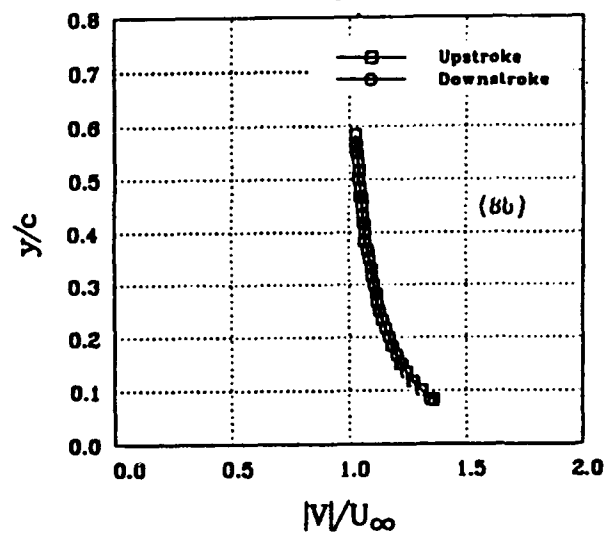


Fig. 12b Comparison of Velocity Magnitudes at AOA = 5.46 degrees

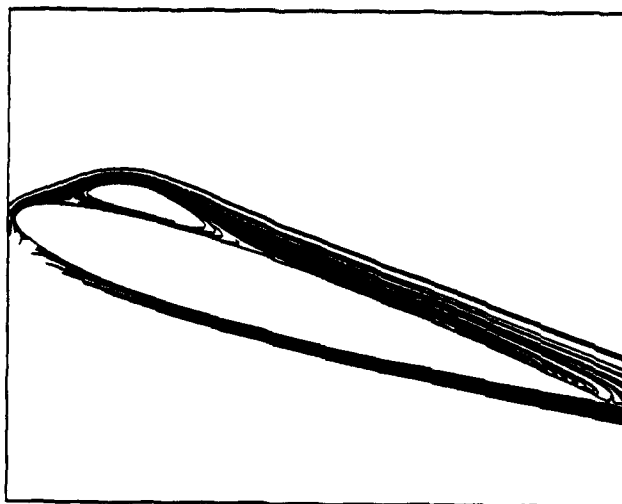


Fig. 13 Computed Flow Field on NACA 0012 Airfoil Pitching Upward at a Rate of 0.02 through AOA = 17 degrees,  $M = 0.4$ ,  $Re = 4$  million

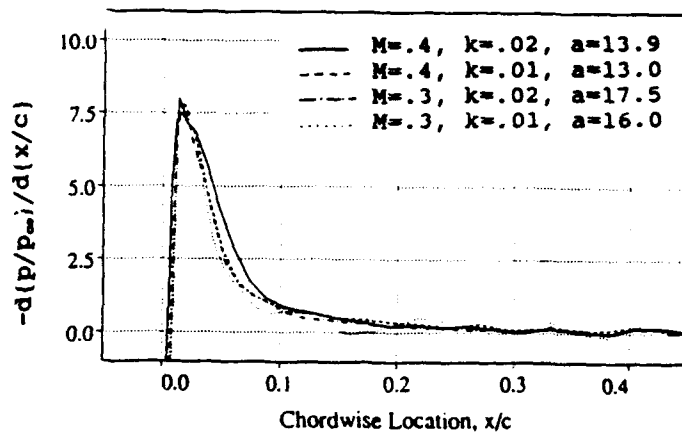


Fig. 14 Computed Pressure Gradient Distributions at the Onset of Flow Reversal on NACA 0012 Airfoil

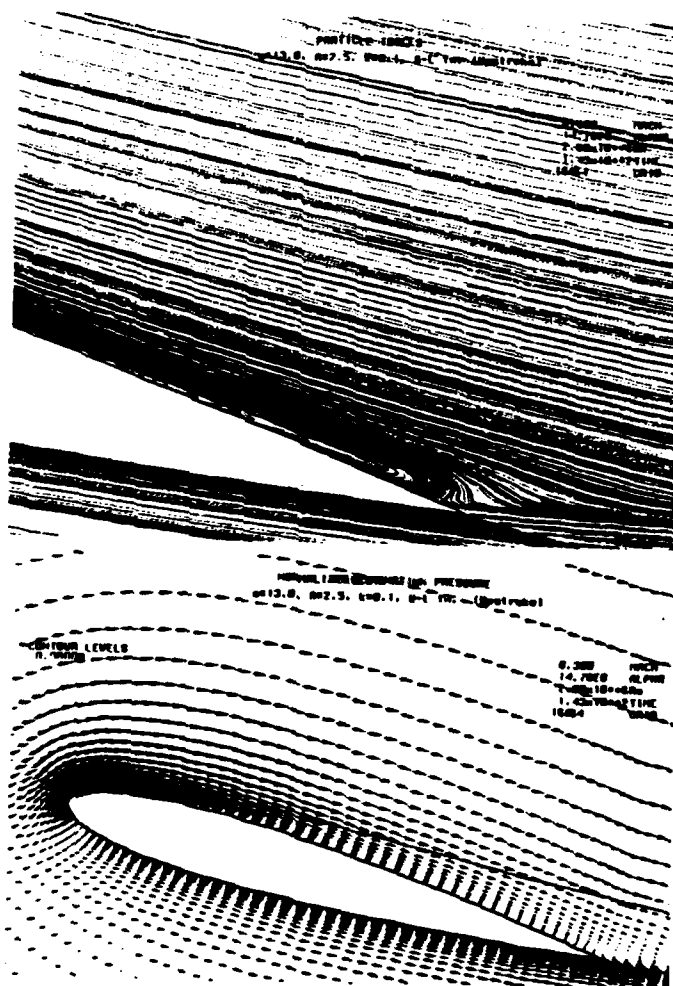


Fig. 15 Computed NACA 0012 Flowfield during Upstroke, AOA=14.7 degrees  $M=0.3$ ,  $k=0.1$ ,  $Re = 2$  million

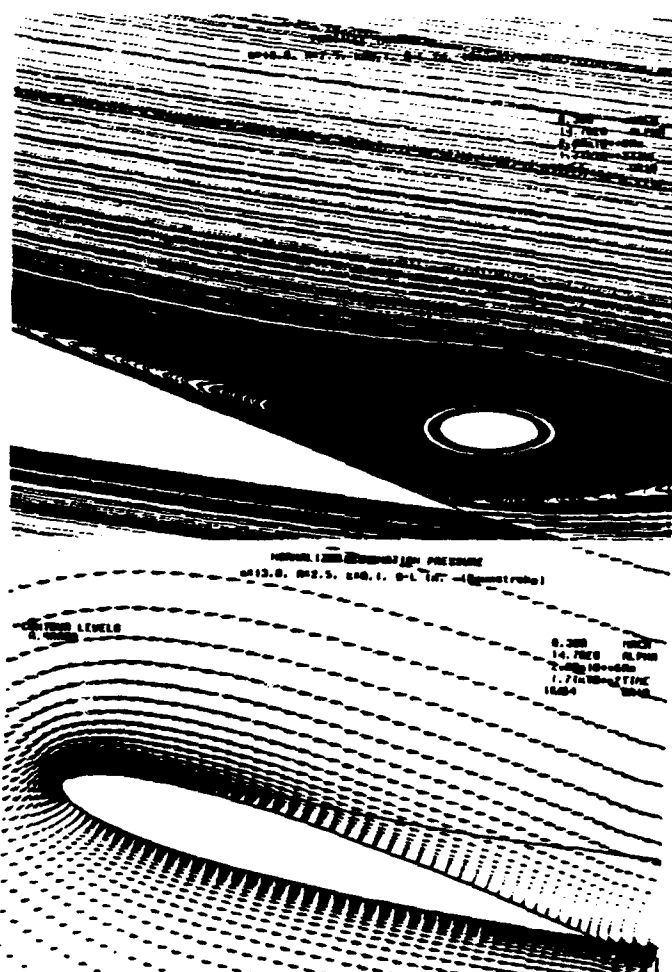


Fig. 16 Computed NACA 0012 Flowfield during Downstroke, AOA=14.7 degrees  $M=0.3$ ,  $k=0.1$ ,  $Re = 2$  million

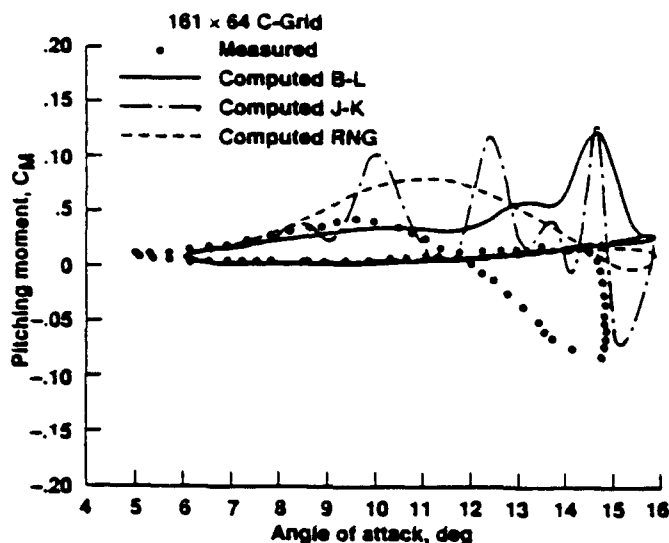


Fig. 17 Computed and Measured Pitching Moment Hysteresis on NACA 0012 Airfoil

$$M_\infty = 0.3, \alpha(t) = 11^\circ + 5^\circ \sin(\omega t), k = 0.1, Re = 4 \times 10^6$$

Experiment: McCroskey

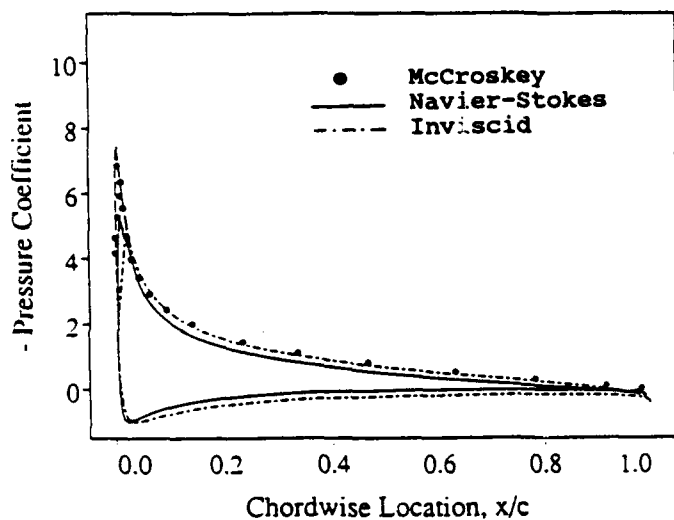


Fig. 18a Computed and Measured Pressures on NACA 0012 Airfoil during Upstroke at AOA = 11.9 degrees  
 $M = 0.3, k = 0.2, Re = 4$  million

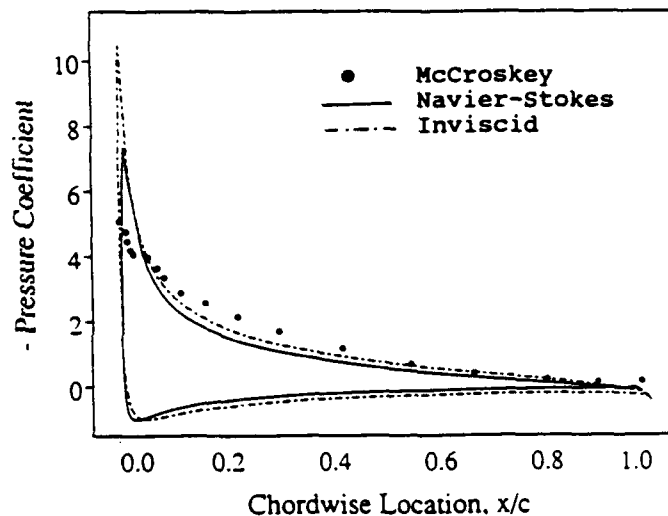


Fig. 18b Computed and Measured Pressures on NACA 0012 Airfoil during Downstroke at AOA = 13.7 degrees  
 $M = 0.3, k = 0.2, Re = 4$  million

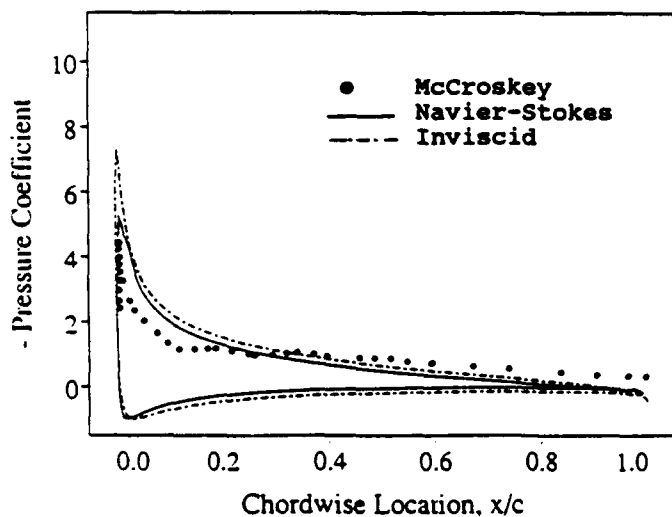


Fig. 18c Computed and Measured Pressures on NACA 0012 Airfoil during Downstroke at AOA = 10.5 degrees  
 $M = 0.3, k = 0.2, Re = 4$  million

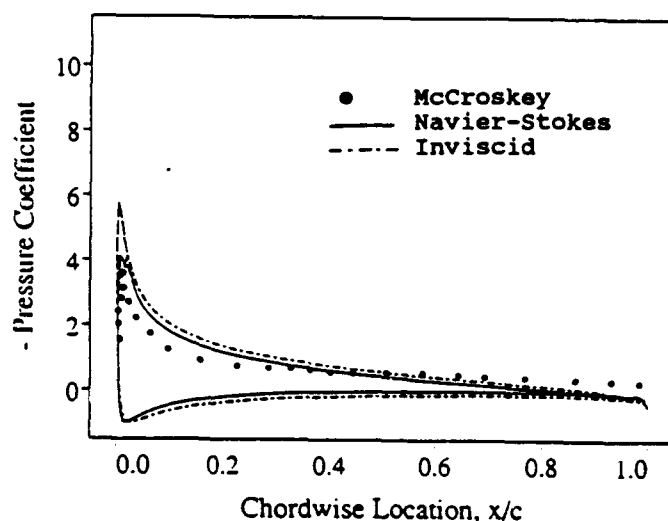


Fig. 18d Computed and Measured Pressures on NACA 0012 Airfoil during Downstroke at AOA = 8.9 degrees  
 $M = 0.3, k = 0.2, Re = 4$  million

SIMULTANEOUS MAPPING OF THE UNSTEADY FLOW FIELDS BY  
PARTICLE DISPLACEMENT VELOCIMETRY (PDV)

by

Thomas T. Huang, David J. Fry, Han-Lieh Liu  
David Taylor Research Center  
Bethesda, MD

and

Joseph Katz and Thomas C. Fu  
The Johns Hopkins University

Abstract

The current experimental and computational techniques must be improved in order to advance the prediction capability of the longitudinal vortical flows shed by underwater vehicles. The generation, development, and breakdown (bursting) mechanisms of the shed vortices at high Reynolds numbers have not been fully understood. The ability to measure hull separated vortices associated with vehicle maneuvering does not exist at present. The existing point-by-point measurement techniques can only capture approximately the large "mean" eddies but fail to meet the dynamics of small vortices during the initial stage of generation. A new technique, which offers a previously unavailable capability to measure the unsteady cross-flow distribution in the plane of the laser light sheet, is called Particle Displacement Velocimetry (PDV).

PDV consists of illuminating a thin section of the flowfield with a pulsed laser. The water is seeded with microscopic, neutrally buoyant particles containing imbedded fluorescing dye which responds with intense spontaneous fluorescence within the illuminated section. The seeded particles in the vortical flow structure shed by the underwater vehicle are illuminated by the pulse laser and the corresponding particle traces are recorded in a single photographic frame, each particle leaves multiple traces on the same film. Two distinct approaches have been utilized for determining the velocity distribution from the particle traces. The first method is based on matching the traces of the same particle and measuring the distance between them. The direction the flow can be identified by keeping one of the pulses longer than the other. The second method is based on selecting a small window within the image and finding the mean shift of all the particles within that region. The computation of the auto-correlation of the intensity distribution within the selected sample window is used to determine the mean displacement of particles. The direction of the flow is identified by varying the intensity of the laser light between pulses. Considerable computation resource is required to compute the auto-correction of the intensity distribution. Parallel processing will be employed to speed up the data reduction. A few examples of measured unsteady vortical flow structures shed by the underwater vehicles will be presented.

CALCULATION OF FULLY THREE-DIMENSIONAL SEPARATED FLOWS  
WITH AN UNSTEADY VISCOUS-INVISCID INTERACTION METHOD

By

J. C. Le Balleur, P. Girodroux-Lavigne

Abstract

The three previous papers given at the conference have shown that the viscous inviscid numerical methods were capable to calculate separated turbulent flows. The "Semi-inverse method" and models of the first author was giving access to computation of massive separations, stalled flows, and shock waves - boundary layer interactions, in two-dimensional or quasi-three-dimensional conditions, from low speeds to supersonic speeds. The "Semi-implicit" method of the authors for time-consistent coupling was given access to the time-accurate transonic separated flow and buffer computations, in two-dimensions.

The present paper shows that the viscous-inviscid interaction approach is also capable to compute the fully three-dimensional flow separation phenomena. The method is based again on a thin-layer approximation of the theory of "Defect-Formulation" that provides the viscous-inviscid splitting of the Navier-Stokes equations. A parametric analytical modeling of the 3D-turbulent velocity profiles (including separation) is involved.

Numerically, the 3D-velocity profiles are discretized in normal  $z$ -direction, and driven by parametric integral 3D-equations, in direct or inverse modes, marching in  $x$ -direction. The viscous-inviscid coupling is fully 3D, and solved time-consistently with an extension of the "Semi-implicit" method previously suggested in two-dimensions. A 3D inviscid subroutine with TSP approximation is used.

Results are obtained on one hand for transonic steady flows over wings, with shock-induced transonic separation. On the other hand, the method provides results for highly three-dimensional flow separations, such as induced by a three-dimensional through at the wall of a flat plate. The 3D viscous-inviscid coupling, and the 3D model of the velocity field, provide three-dimensional instantaneous skin-friction lines whose patterns exhibit the same complex topology as Navier-Stokes solvers, with foci, nodes and saddle-points.

**TWO- AND THREE-DIMENSIONAL FLOWS, 1**  
**SESSION 9**

# PREDICTION OF AIRFOIL STALL USING NAVIER-STOKES EQUATIONS IN STREAMLINE COORDINATES

D.H. Choi, C.H. Sohn\*, and C.S. Oh

*Korea Advanced Institute of Science & Technology  
Seoul, Korea*

## Abstract

A Navier-Stokes procedure to calculate the flow about an airfoil at incidence has been developed: The parabolized equations are solved in the streamline coordinates generated for an arbitrary airfoil shape using conformal mapping; A modified  $k-\epsilon$  turbulence model is applied in the entire domain, but the eddy viscosity in the laminar region is suppressed artificially to simulate the region correctly. The procedure has been applied to airfoils at various angles of attack and the results are quite satisfactory for both laminar and turbulent flows. It is shown that the present choice of the coordinate system reduces the error due to numerical diffusion and that the lift is accurately predicted for a wide range of incidence.

## Introduction

Aerodynamic characteristics of an airfoil at incidence, especially near and beyond the stall angle, is of paramount practical interest as these are closely related to the performance of engineering devices such as aircraft and turbomachinery. Because of the importance associated with the flow, much efforts have been devoted to develop prediction techniques for these flows.

One may approach the problem by using the interactive methods that explicitly couple the viscous and inviscid effects in an iterative manner. The methods by Maskew & Dvorak,<sup>1</sup> Gilmer & Bristow,<sup>2</sup> and Cebeci et al.<sup>3</sup> may belong to this category. By and large, the methods have been successful in predicting  $C_{l,max}$  and the subsequent stall. However, since these all adopt the boundary-layer procedure, special treatments are necessary to handle the reversed flow region; the details of the flow or the accuracy in this region may suffer.

On the other hand, the method based on the Navier-Stokes equations, which is gaining popularity with the advent of modern computer technology, is more rigorous and appropriate, in principle, than the former for the highly interacting flows as the equations are valid both in potential- and viscous-flow regions. Handling of the separated region is more straightforward, too. Among many earlier attempts, Shamroth & Gibelg<sup>4</sup> made compressible-flow calculations using a transitional  $k-\epsilon$  turbulence model and Rhie & Chow<sup>5</sup>

used a SIMPLE-type method with a  $k-\epsilon$  model to predict the pressure distribution and the near wake. Both adopted nonorthogonal computational grids due to their simplicity and generality. Although these calculations exhibit certain degree of success, the results are not entirely satisfactory: the flow at near- or post-stall angle has not been successfully predicted. Chang et al.<sup>6</sup> observed the similar shortfalls in an existing Navier-Stokes procedure in their comparative study of interactive boundary-layer and thin-layer Navier-Stokes procedures.

The intention of this paper is to present a new Navier-Stokes procedure, in which the various aspects of the calculation have been improved, and to show that the flow over a wide range of incidence has been predicted with reasonable accuracy and robustness.

## Grid Generation

Among various grid generation techniques, a method based on conformal mapping has been adopted as it has distinct advantages in treating the flow of present interest. Specifically, the grid lines so generated are orthogonal to each other and, moreover, the coordinates can readily be made to be intrinsic. These two points are not imperative. However, the equations do become simpler when the coordinates are orthogonal and the false diffusion in the numerical scheme is greatly reduced if the coordinate line is aligned with the local streamline. The results are, therefore, expected to be more accurate.

The conformal mapping used here transforms an arbitrary airfoil shape onto a unit circle by two successive transformations. The profile in the physical plane  $z$  is first transformed into a smooth near circular section in the plane  $\zeta$  by the Karman-Trefftz transformation, which removes the sharp corner at the trailing edge, and, subsequently, into a unit circle by solving the Gersgorin integral equation. The latter part is done numerically after the integrand is suitably modified to make the procedure more tractable and accurate. The details are referred to Choi & Landweber<sup>7</sup> and will not be repeated here.

The resulting mapping relations may be written as

$$z = f(\zeta) \quad (1)$$

and the Laurent series,

$$\zeta = A\tau + \frac{a_1}{\tau} + \frac{a_2}{\tau^2} + \frac{a_3}{\tau^3} + \dots \quad (2)$$

\* Presently Senior Researcher, Agency for Defense Development, Daejeon

where  $f$  denotes the Karman-Trefftz transformation and  $A$  &  $a$ 's are coefficients that are determined from the second transformation. It is important to point out that, since the profile in the intermediate plane  $\zeta$  is nearly circular, the number of terms required in the series, Eq. (2), to accurately compute  $\zeta$  is not large: 10 terms have been found sufficient and used in the present work.

From these relations, various types of grid, i.e., C-, H- and C-grid, can now be constructed. The radial lines and the concentric circles in the  $\tau$  plane give an O-type grid while the horizontal and vertical lines in the plane of complex potential ( $W$ ) and those in the  $W^{1/2}$  plane give, respectively, H- and C-type grids. The grid of H-type is used in the present calculation and the details of how it is obtained is described below.

The complex potential  $W$  for a stream velocity  $U$  at an angle of attack  $\alpha$  about a unit circle at the origin is

$$W = U \left( \tau e^{-i\alpha} + \frac{e^{i\alpha}}{\tau} \right) + i \frac{\Gamma}{2\pi} \ln \tau \quad (3)$$

where  $\Gamma$  is the circulation about the circle and is equal to  $4\pi U \sin(\alpha - \theta^\circ)$  so that Eq. (3) satisfies the Kutta condition that the velocity be zero at the trailing edge,  $\theta = \theta_0$ . The velocity  $U$  in the  $\tau$  plane is related to the undisturbed velocity  $U_\infty$  in the  $z$  plane by

$$U = U_\infty \left( \frac{d\zeta}{d\tau} \right) \left( \frac{dz}{d\zeta} \right) \quad (4)$$

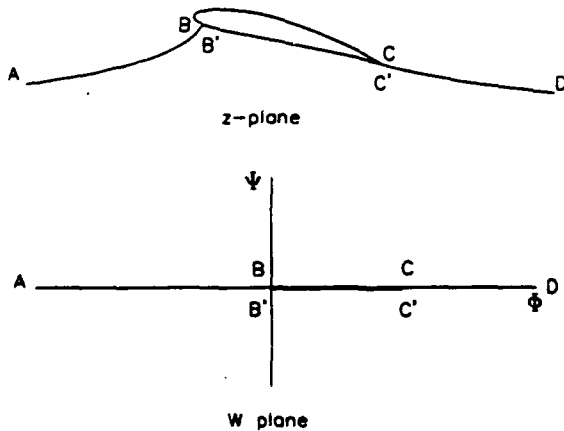


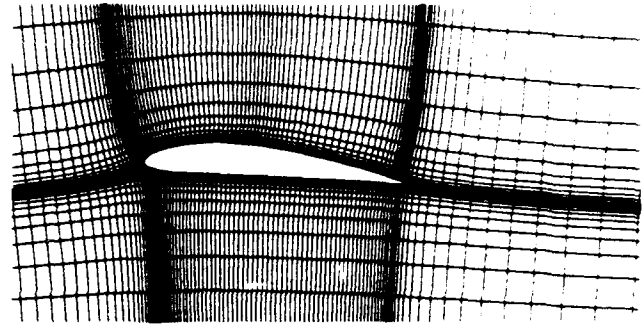
Fig. 1 Physical and computational domains for the flow about an airfoil at incidence.

The coordinate lines in the  $W$  plane are lines of constant potential ( $\phi$ ) and stream function ( $\psi$ ); corresponding lines in the physical plane are also equipotential lines and streamlines of the flow under consideration, and constitute an orthogonal grid of H-type. One point to observe is that,

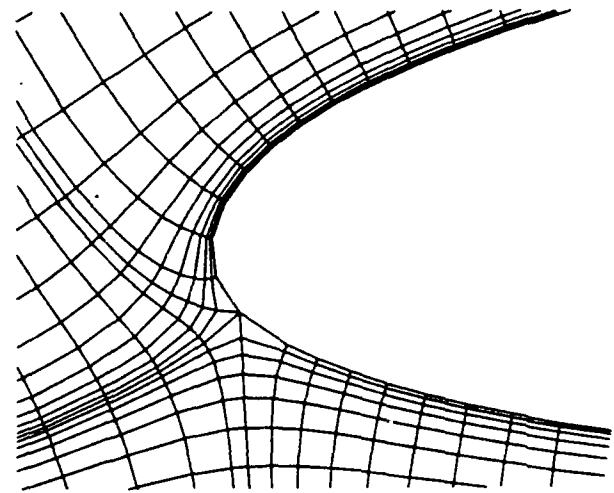
because of nonzero circulation,  $\Gamma$ , the potential at the trailing edge is double valued,

$$\phi_{TL} = \phi_{TR} + \Gamma \quad (5)$$

and a jump in  $\phi$  is present across the trailing streamline.



(a)



(b)

Fig. 2 Sample grid and the close-up view of the nose region about an airfoil at  $\alpha = 5$  deg.

The remaining task to complete the grid construction is to distribute the grids efficiently. This is accomplished by using  $\tanh$  as a distribution function to place more grids where needed, e.g., near the surface, around the leading and trailing edges. For the proper clustering in the streamwise direction, the grids are first distributed along the stagnation streamline  $ABCD$  and  $AB'C'D$  shown in Fig. 1 using the arc length as parameter. The number of grids for the segment  $BC$  may be different from that for  $B'C'$ . The transformed grids in the  $W$  plane can then be obtained by using the relations (1), (2), and (3). However, a direct attempt to do so involves rather time-consuming algebra; the following spline interpolation is used instead. For a given set of points along the  $\phi$  axis, the corresponding



points, which lie on the stagnation streamline, in the  $z$  plane are readily determined:  $\tau$  from Eq. (3) by Newton's rootfinding algorithm,  $\zeta$  by Eq. (2) and  $z$  by Eq. (1). The arc length,  $s$ , for each of these points is then calculated and the relation between  $s$  and  $\phi$  is established. A cubic spline function is used to relate the two and, for a point in the  $z$  plane, this interpolation function gives the matching point on the  $\phi$  axis in the  $W$  plane. The grid clustering in the vertical direction, on the other hand, is done in the  $W$  plane using  $\psi$  as parameter. A typical grid in the physical plane for  $\alpha = 5^\circ$  is shown in Fig. 2.

### Governing Equations

Following Nash & Patel,<sup>8</sup> the continuity and Reynolds-averaged Navier-Stokes equations in general orthogonal curvilinear coordinates  $(\xi, \eta)$  are written as:

Continuity:

$$\frac{1}{h_1 h_2} \left\{ \frac{\partial}{\partial \xi} (h_2 U) + \frac{\partial}{\partial \eta} (h_1 V) \right\} = 0 \quad (6)$$

$\xi$  momentum:

$$\begin{aligned} & \frac{1}{h_1 h_2} \frac{\partial}{\partial \xi} (h_2 U^2) + \frac{1}{h_1 h_2} \frac{\partial}{\partial \eta} (h_1 UV) + (K_{12} U \\ & - K_{21} V) V + \frac{1}{h_1} \frac{\partial p}{\partial \xi} + \frac{1}{h_1} \frac{\partial \bar{u}^2}{\partial \xi} + \frac{1}{h_2} \frac{\partial \bar{u} v}{\partial \eta} \\ & + 2K_{12} \bar{u} v + K_{21} (\bar{u}^2 - \bar{v}^2) - \frac{1}{Re} (\nabla^2 U \\ & - 2K_{21} \frac{1}{h_2} \frac{\partial V}{\partial \eta} + 2K_{12} \frac{1}{h_1} \frac{\partial U}{\partial \xi} + \alpha_{11} U + \alpha_{12} V) = 0 \end{aligned} \quad (7)$$

$\eta$  momentum:

$$\begin{aligned} & \frac{1}{h_1 h_2} \frac{\partial}{\partial \xi} (h_2 UV) + \frac{1}{h_1 h_2} \frac{\partial}{\partial \eta} (h_1 V^2) + (K_{21} V \\ & - K_{12} U) U + \frac{1}{h_2} \frac{\partial p}{\partial \eta} + \frac{1}{h_1} \frac{\partial \bar{u} v}{\partial \xi} + \frac{1}{h_2} \frac{\partial \bar{v}^2}{\partial \eta} \\ & + 2K_{21} \bar{u} v - K_{12} (\bar{u}^2 - \bar{v}^2) - \frac{1}{Re} (\nabla^2 V \\ & - 2K_{12} \frac{1}{h_1} \frac{\partial U}{\partial \xi} + 2K_{21} \frac{1}{h_2} \frac{\partial V}{\partial \eta} + \alpha_{21} U + \alpha_{22} V) = 0 \end{aligned} \quad (8)$$

and

$$\begin{aligned} \nabla^2 &= \frac{1}{h_2^2} \frac{\partial^2}{\partial \eta^2} + (-K_{11} + K_{21}) \frac{1}{h_1} \frac{\partial}{\partial \xi} \\ &+ (K_{12} - K_{22}) \frac{1}{h_2} \frac{\partial}{\partial \eta} \\ \alpha_{11} &= \alpha_{22} = -(K_{12}^2 + K_{21}^2) \end{aligned}$$

$$\alpha_{12} = \frac{1}{h_1} \frac{\partial K_{12}}{\partial \xi} - \frac{1}{h_2} \frac{\partial K_{21}}{\partial \eta}$$

$$\alpha_{21} = \frac{1}{h_2} \frac{\partial K_{21}}{\partial \eta} - \frac{1}{h_1} \frac{\partial K_{12}}{\partial \xi}$$

$$K_{12} = \frac{1}{h_1 h_2} \frac{\partial h_1}{\partial \eta}, \text{ etc.}$$

where  $(U, V)$  and  $(u, v)$  are the mean and fluctuating velocity components, respectively, in the  $(\xi, \eta)$  direction,  $p$  the pressure,  $Re$  ( $= \frac{U_\infty c}{\nu}$ ) the Reynolds number,  $\nu$  the kinematic viscosity, and  $h$  and  $K$  the metric coefficients and curvature parameters. The equations have been made dimensionless by using the freestream velocity  $U_\infty$  and the airfoil chord  $c$ . These equations are of conservative form and are exact except for the neglected streamwise diffusion terms. The conservative form appears to give more stable behavior of the numerical method in the neighborhood of the stagnation point where the H-grid becomes singular.

The Reynolds stresses in Eqs. (7) and (8) are related to the mean rates of strain through the eddy-viscosity hypothesis and are given in the next section.

### Turbulence Model

A modified  $k-\epsilon$  model is adopted as a closure relationship in the present study. The transport equations for the turbulent kinetic energy and the rate of dissipation compatible with Eqs. (6)-(8) are

$$\begin{aligned} & \frac{1}{h_1 h_2} \frac{\partial}{\partial \xi} (h_2 U k) + \frac{1}{h_1 h_2} \frac{\partial}{\partial \eta} (h_1 V k) \\ & - \frac{1}{h_1 h_2} \left\{ \frac{\partial}{\partial \xi} \left( \frac{1}{\sigma_k R_{eff}} \frac{h_2}{h_1} \frac{\partial k}{\partial \xi} \right) + \frac{\partial}{\partial \eta} \left( \frac{1}{\sigma_k R_{eff}} \frac{h_1}{h_2} \frac{\partial k}{\partial \eta} \right) \right\} \\ & - P_k + \epsilon = 0 \end{aligned} \quad (9)$$

$$\begin{aligned} & \frac{1}{h_1 h_2} \frac{\partial}{\partial \xi} (h_2 U \epsilon) + \frac{1}{h_1 h_2} \frac{\partial}{\partial \eta} (h_1 V \epsilon) \\ & - \frac{1}{h_1 h_2} \left\{ \frac{\partial}{\partial \xi} \left( \frac{1}{\sigma_\epsilon R_{eff}} \frac{h_2}{h_1} \frac{\partial \epsilon}{\partial \xi} \right) + \frac{\partial}{\partial \eta} \left( \frac{1}{\sigma_\epsilon R_{eff}} \frac{h_1}{h_2} \frac{\partial \epsilon}{\partial \eta} \right) \right\} \\ & - C_{\epsilon 1} \frac{\epsilon}{k} P_k + C_{\epsilon 2} \frac{\epsilon^2}{k} = 0 \end{aligned} \quad (10)$$

where

$$\begin{aligned} P_k &= P_{k,s} + P_{k,n} = -\bar{u} v \left( \frac{1}{h_1} \frac{\partial V}{\partial \xi} + \frac{1}{h_2} \frac{\partial U}{\partial \eta} - K_{12} U \right. \\ &\quad \left. - K_{21} V \right) - (\bar{u}^2 - \bar{v}^2) \left( \frac{1}{h_1} \frac{\partial U}{\partial \xi} + K_{12} V \right) \end{aligned} \quad (11)$$

$$P_\epsilon = P_{\epsilon,s} + \frac{C_{\epsilon 3}}{C_{\epsilon 1}} P_{k,n} \quad (12)$$

$$\frac{1}{R_{eff}} = \frac{1}{Re} + \nu_t, \quad \nu_t = C_\mu \frac{k^2}{\epsilon}$$

and the model constants  $C_\mu$ ,  $\sigma_k$ ,  $\sigma_\epsilon$ ,  $C_{\epsilon 1}$ ,  $C_{\epsilon 2}$  and  $C_{\epsilon 3}$  are given the values of 0.09, 1.0, 1.3, 1.44, 1.92 and 4.44, respectively.

The dissipation equation was first proposed by Hanjalic & Launder,<sup>9</sup> where they reasoned that the energy transfer rates across the spectrum are preferentially promoted by irrotational deformations and showed the improved prediction over the standard  $k$ - $\epsilon$  model, especially in the adverse pressure-gradient region. It should be noted that the dissipation equation assumes the  $\xi$  direction to be the predominant flow direction and the present intrinsic coordinate system is consistent with this assumption.

Two key modifications to this model have been made for the present study. Rather than using the wall function in the near-wall region, the two-layer approach of Chen & Patel<sup>10</sup> is adopted to make the model applicable in the separated-flow region and to provide a finer resolution in the near-wake region. The other change made is the use of the anisotropic  $k$ - $\epsilon$  model of Nisizima & Yoshizawa<sup>11</sup> to represent the Reynolds normal stresses. The Reynolds stresses are then expressed as

$$-\bar{u}v = v_t \left( \frac{1}{h_1} \frac{\partial V}{\partial \xi} + \frac{1}{h_2} \frac{\partial U}{\partial \eta} - K_{12}U - K_{21}V \right) \quad (13)$$

$$-\bar{u}^2 = -\frac{2}{3}k + 2v_t \left( \frac{1}{h_1} \frac{\partial U}{\partial \xi} + K_{12}V \right) + S_u^2 \quad (14)$$

$$-\bar{v}^2 = -\frac{2}{3}k + 2v_t \left( \frac{1}{h_2} \frac{\partial V}{\partial \eta} + K_{21}U \right) + S_v^2 \quad (15)$$

where

$$S_u^2 = \frac{1}{3}(-2C_{\tau 1} + C_{\tau 2}) \frac{k^3}{\epsilon^2} \left( \frac{1}{h_2} \frac{\partial U}{\partial \eta} - K_{21}V \right)^2 \quad (16)$$

$$S_v^2 = \frac{1}{3}(C_{\tau 1} - 2C_{\tau 2}) \frac{k^3}{\epsilon^2} \left( \frac{1}{h_2} \frac{\partial U}{\partial \eta} - K_{21}V \right)^2 \quad (17)$$

and  $C_{\tau 1} = 0.07$ ,  $C_{\tau 2} = -0.015$  from Ref. 11. The nonlinear terms in Eqs. (14) and (15) lead to the anisotropy of the turbulence intensities.

When using the  $k$ - $\epsilon$  model, it is customary to assume, for computational convenience, that the flow is turbulent everywhere as was done in Rhie & Chow.<sup>5</sup> Although this may be justifiable as the laminar portion of the flow is limited to the small region near the nose, the artificially produced turbulent flow, which may be healthier than the real flow, could greatly affect the leading-edge-separation pattern.

In order to get around this difficulty inherent to the  $k$ - $\epsilon$  model, the concept of intermittency is employed: the transport equations for  $k$  and  $\epsilon$  are solved in the entire domain, but the eddy viscosity is set to be zero in the laminar region. The procedure has been found more successful than solving the equations only in the turbulent region. The latter performed relatively poorly as the initial profiles for  $k$  and  $\epsilon$  at the transition location could not be provided accurately.

## Solution Procedure

The governing equations, Eqs. (6)-(10), are solved in the calculation domain bounded by constant  $\xi$  and  $\eta$  lines. Using the staggered grid, shown in Fig. 3, the diffusive derivatives of the equations are discretized by central differencing while the convective derivatives in the streamwise and cross-streamwise directions by upwind and hybrid differencings, respectively. The numerical scheme adopted in the study is the modified version of the CELS (Coupled Equation Line Solver) algorithm used in Ref. 12:

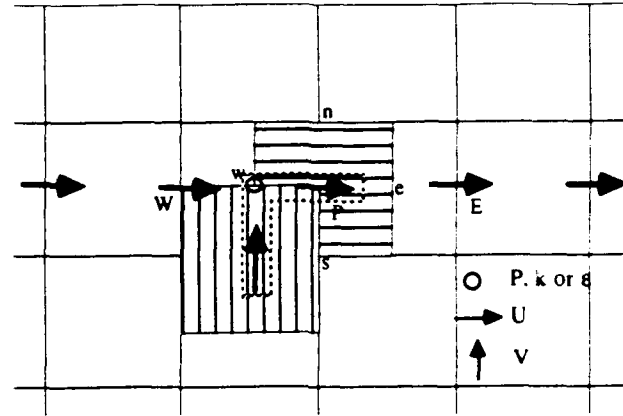


Fig. 3 Grid layout and storage location for each variable.

The calculation proceeds in the streamwise direction and the solution at a given streamwise station is obtained simultaneously. The penta-diagonal system of equations for  $V$ , which is derived from the continuity and momentum equations by eliminating the pressure and the streamwise velocity component, is solved first. The pressure and  $U$  then follow successively by the backward substitution. Using these values, the turbulence transport equations are solved for  $k$  and  $\epsilon$  by the Thomas tridiagonal matrix algorithm. To enhance the convergence, a backward pressure correction is applied at the end of each complete sweep. This is accomplished by forcing the  $\xi$ -momentum equation be satisfied, on the average, along each constant  $\xi$  line. The process is repeated until the specified convergence criterion is met. Maximum pressure variation of  $10^{-4}$  is used for the present calculation.

The calculation is performed for a sufficiently large domain that encompasses the entire profile and the following conditions are specified at the boundary:

$$\text{upstream:} \quad U = U_{\text{pot}}, \quad \frac{\partial V}{\partial \xi} = 0$$

$$\text{downstream:} \quad \frac{\partial p}{\partial \xi} = 0$$

$$\text{outer:} \quad U = U_{\text{pot}}, \quad \frac{\partial V}{\partial \eta} = 0$$

$$\text{wall:} \quad \text{no-slip condition}$$

where the subscript *pot* indicates the potential-flow value. The turbulence quantities at far boundaries except along the downstream end, where the conditions on turbulence are not needed, are assigned a very small value to simulate the non-turbulent flow.

## Results and Discussion

### Laminar flow

The calculation is first performed for the laminar flow about a 12%-thick symmetric Joukowski airfoil section at  $Re=1000$ . For the incidence angle of  $5^\circ$ , the grid of (140x40) and the calculation domain which covers the region  $-1 < x/c < 5$ ,  $-3 < y/c < 3$  were found adequate. A coarser grid (70x40) appears to give comparable results and an optimum grid may lie somewhere in between. However, no further attempt has been made to find this grid distribution.

The velocity vectors and the surface pressure distribution are presented in Figs. 4 and 5. The flow separates at about midsection and, consequently, the pressure distribution is altered substantially from that of the inviscid flow. The results are seen to be in excellent agreement with those by Ghia et al.<sup>13</sup>, who solved the streamfunction-vorticity equations on a (229x45) C-type grid.

Figure 6 illustrates the importance of the grid alignment with the flow. Here, the calculations have been made for  $\alpha = 8^\circ$  with two different grids: one grid is generated for  $\alpha = 0^\circ$  and the other for  $\alpha = 8^\circ$  and, as a result, the former is skewed by  $8^\circ$  in relation to the flow direction. It is observed from the figure that a finer grid is required when the grid is skewed to obtain the results of comparable accuracy. It is primarily due to the numerical diffusion caused by the first order upwind differencing and the discrepancy could be reduced by incorporating a higher order upwind scheme. This will, however, introduce additional complexities into the coding and it is desirable to construct a grid which follows the general flow direction whenever possible.

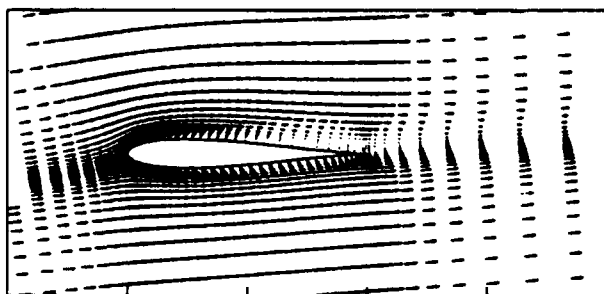


Fig. 4 Velocity vectors for the 12%-thick Joukowski airfoil section at  $\alpha=5$  deg and  $Re=1000$ .

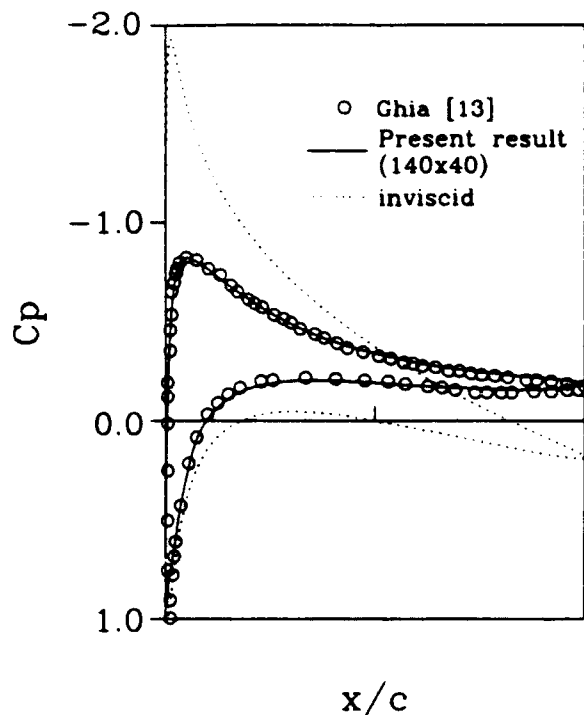


Fig. 5 Surface pressure distribution on the 12%-thick Joukowski airfoil section for  $\alpha=5$  deg and  $Re=1000$ .

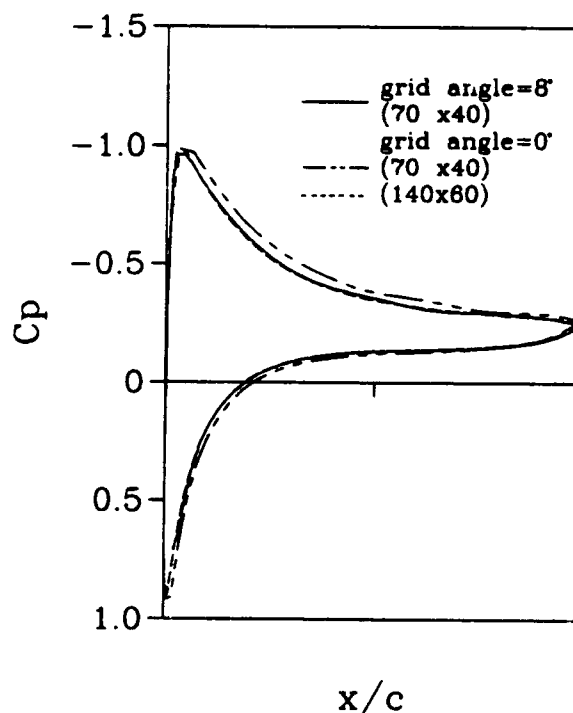


Fig. 6 Comparison of two different grids for  $\alpha=8$  deg.

## Turbulent flow

For turbulent flows, the calculations have been performed for NACA airfoil sections, namely 4412 and 0012, at various angles of attack. A  $140 \times 40$  grid is fitted over  $-1.5 < x/c < 10$ , with the first point normal to the surface being placed approximately at  $y^+ = 5$ . It is reminded that the grid needs to be reconstructed when the angle of attack or the Reynolds number varies. The vertical boundary is located at about where the tunnel wall is to closely mimic the experimental condition and the slip condition is imposed there. Since the wall and the constant  $\eta$  line do not coincide, we introduced a vertical velocity component of right amount during the computation to make the velocity vector parallel to the tunnel wall. The wall location is indicated by the dotted line on the present grid for the NACA 4412 airfoil at  $\alpha = 13.9^\circ$  in Fig. 7.

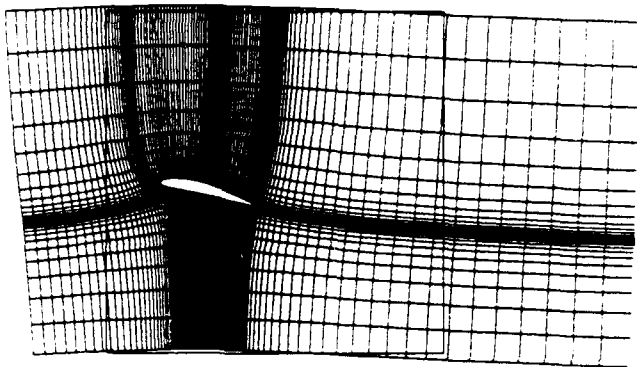


Fig. 7 Computational grid with tunnel wall location for the NACA 4412 airfoil at  $\alpha = 13.9$  deg.

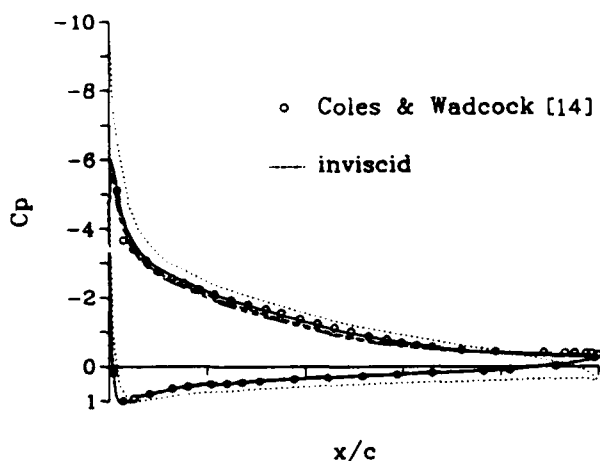


Fig. 8 Pressure distribution on the NACA 4412 airfoil section for  $\alpha = 13.9$  deg and  $Re = 1.5 \times 10^6$ :  $\circ$ , experiment [14]; —, present; ---, standard  $k-\epsilon$  model; - · -, standard  $k-\epsilon$  model with freestream condition; · · · ·, inviscid flow.

The pressure distribution for the NACA4412 airfoil at  $\alpha = 13.9^\circ$  and  $Re = 1.5 \times 10^6$  is presented in Fig. 8. In the calculation, the transition points for upper and lower surfaces are prescribed to be at  $0.025c$  and  $0.103c$ , respectively, as done in the experiment. The present result (solid line) is in near exact agreement with the experiment of Coles & Wadcock.<sup>14</sup> As in the laminar case, the pressure distribution is altered greatly from the inviscid one by the flow separation. Also shown in the figure are the results by the standard  $k-\epsilon$  model with and without the tunnel wall effects. Here, the result without the tunnel wall means that the calculation is performed in a larger domain ( $-5 < y/c < 5$ ) with the freestream boundary condition. Although these all are in relatively good agreement, it is evident that each of the changes results in noticeable discrepancies.

Figures 9 and 10 show the velocity vectors and the wall shear-stress distribution. The velocity vectors and the grid lines, which are the streamlines of the inviscid flow, coincide in most of the region. This is expected and validates the present choice of turbulence model and the approach of parabolization. The wall-shear stress shows that the boundary layer separates at  $x/c = 0.8$  and the laminar boundary layer is very close to separation before it becomes turbulent at  $x/c = 0.025$ . It is cautioned here, however, that the absolute values of wall-shear stress in the upstream section of the airfoil may not be accurate as the boundary layer is too thin to be adequately resolved by the present grid distribution. To check how well the turbulence model mimics the transition process, the turbulence quantities,  $k$  and  $\nu_t$ , and the wall-shear stress in the neighborhood of the transition point are examined in Fig. 11. The turbulent kinetic energy and the eddy viscosity plotted are the maximum values at the given station. The smooth but rather sharp increase in these quantities indicates that the present treatment for transition is qualitatively correct. The turbulent kinetic energy does not grow in the laminar region because the production terms in the transport equation are turned off by suppressing the eddy viscosity.

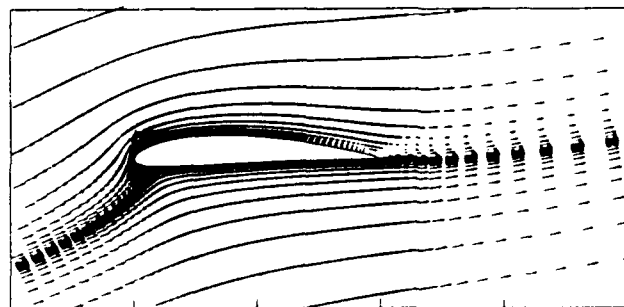


Fig. 9 Velocity vector for the NACA 4412 airfoil section for  $\alpha = 13.9$  deg and  $Re = 1.5 \times 10^6$ .

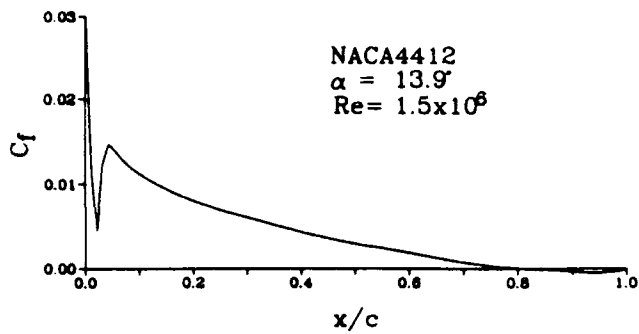
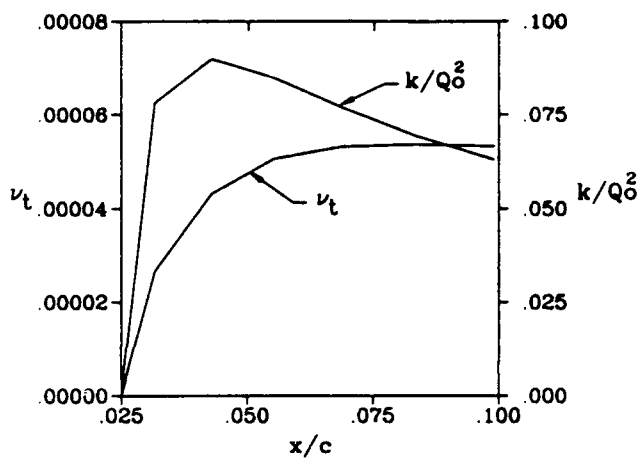
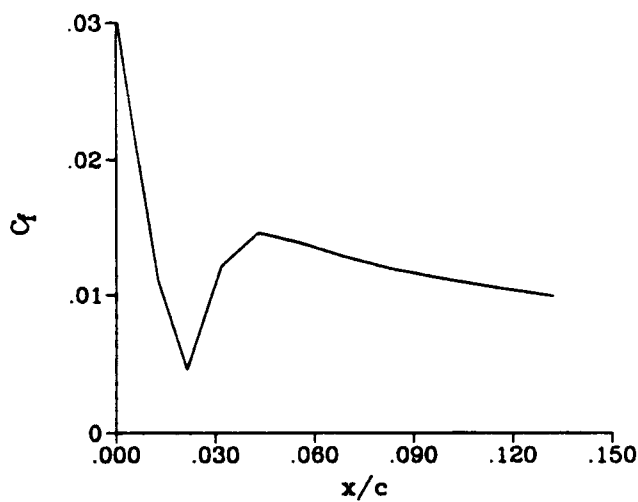


Fig.10 Wall-shear stress distribution on the NACA 4412 airfoil section for  $\alpha=13.9$  deg and  $Re=1.5 \times 10^6$ .



a) Turbulent kinetic energy and eddy viscosity



b) Skin-friction coefficient

Fig.11 Turbulence quantities in the neighborhood of transition location.

The lift distribution for various angles of attack is given in Fig. 12: the computed result agrees well with the experiment including  $C_{l,max}$ . The lift coefficient obtained without taking the wall effects into consideration follows the data closely when  $\alpha$  is small but begins to deviate as  $\alpha$  becomes large: this behavior is consistent with the actual tunnel blockage effect, which increases with the angle of attack.

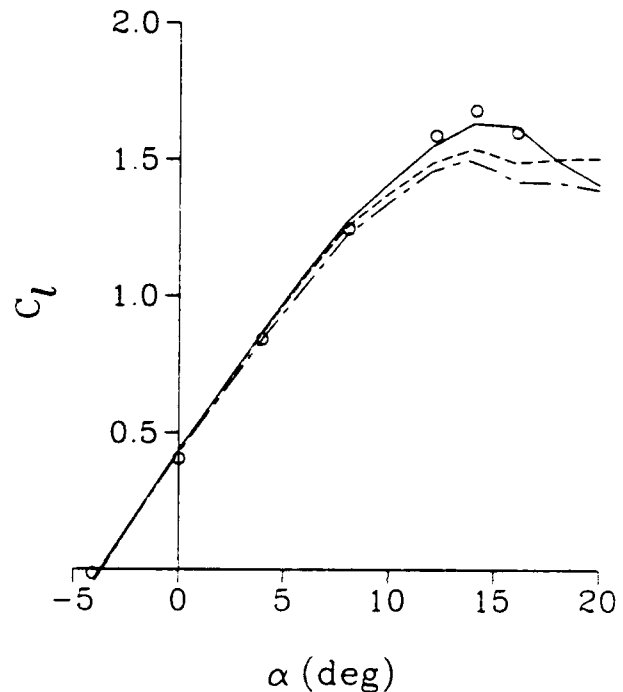


Fig.12  $C_l - \alpha$  curve for the NACA 4412 airfoil section at  $Re=1.5 \times 10^6$ :  $\circ$ , experiment[14]; —, present; ---, standard  $k-\epsilon$  model; - · -, standard  $k-\epsilon$  model with freestream condition.

The results for the NACA 0012 airfoil are shown in Figs.(13)-(15). The calculations have been performed for  $\alpha = 6^\circ$  at  $Re = 1.5 \times 10^6$  and  $2.8 \times 10^6$ . Figures (13) and (14) compare the pressure distributions for these cases with experiments[15]; a good agreement is observed. The computational results by Shamroth & Gibeling and Rhie & Chow are also plotted in Fig. 14. It is clear that these are much less successful especially in capturing the pressure peak near the leading edge. It needs to be noted that the results of Shamroth & Gibeling was obtained at a lower Reynolds number ( $1.0 \times 10^6$ ) and some of the discrepancy might have been caused by this.

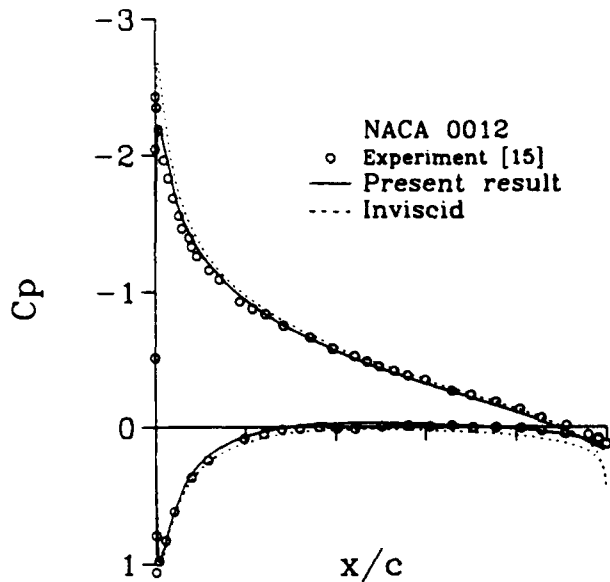


Fig.13 Pressure distribution on the NACA 0012 airfoil section for  $\alpha=6$  deg and  $Re = 1.5 \times 10^6$ :  $\circ$ , experiment[15]; —, present.

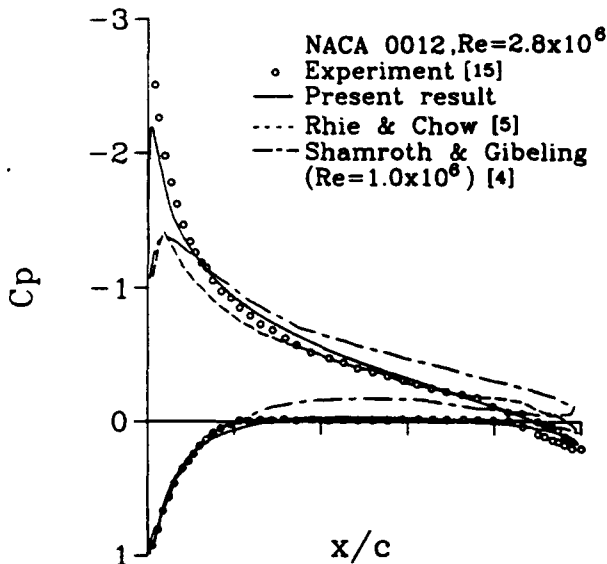


Fig.14 Pressure distribution on the NACA 0012 airfoil section for  $\alpha=6$  deg and  $Re = 2.8 \times 10^6$ :  $\circ$ , experiment[15]; —, present; - - -, Shamroth & Gibelg[4]; . . . , Rhie & Chow[5].

The  $C_l - \alpha$  curve for  $Re = 1.5 \times 10^6$  is depicted in Fig. 15, along with the curves obtained by the standard  $k-\epsilon$  model with and without the wall effect. The results are in good agreement with the data and show the similar characteristics as in the case for the NACA 4412 airfoil. For the incidence angle greater than that shown in the figure, the anisotropic turbulence model becomes less stable due to its nonlinear terms; the convergence is slowed as more under-relaxation is required. The calculation was thus not carried out for the case much beyond the stall angle.

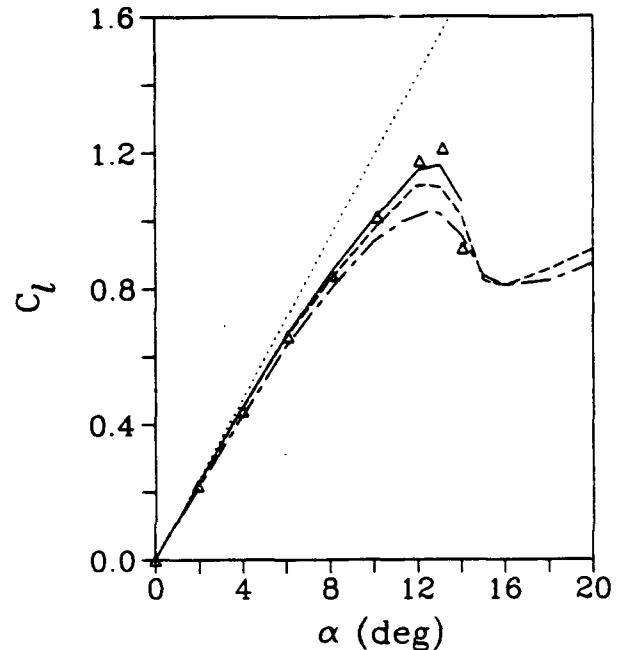


Fig.15  $C_l - \alpha$  curve for the NACA 0012 airfoil section at  $Re=1.5 \times 10^6$ :  $\Delta$ , experiment[15]; —, present; - - -, standard  $k-\epsilon$  model; - . - , standard  $k-\epsilon$  model with freestream condition.

### Concluding Remarks

A new and improved Navier-Stokes procedure has been developed and applied successfully to the flow about the airfoil at incidence: the lift of the airfoil is accurately predicted for a wide range of angles of attack. It has been shown that the present choice of the coordinates, i.e., the streamlines and the equi-potential lines of the inviscid flow, helps make the method more accurate and efficient. The modified  $k-\epsilon$  turbulence model, which is used in the whole domain with zero intermittency in the laminar region, gives a qualitatively correct transition behavior.

## References

- [1] Maskew, B. and Dvorak, F.A., "The Prediction of  $C_{lmax}$  Using a Separated Flow Model," *Journal of American Helicopter Society*, 1978.
- [2] Gilmer, B.R. and Bristow, D.R., "Analysis of Airfoils by Simultaneous Perturbations to Viscous and Inviscid Equations," *AIAA Journal*, Vol. 20, No. 9, 1982, pp. 1160-1166.
- [3] Cebeci, T., Jau, J., Vitiello, D., and Chang, K.C., "Prediction of Post-Stall Flows on Airfoils," *Fourth Symposium on Numerical and Physical Aspects of Aerodynamic Flows*, Jan., 1989, Calif. State Univ., Long Beach, CA.
- [4] Shamroth, S.J. and Gibeling, H.J., "A Compressible Solution of the Navier-Stokes Equations for Turbulent Flow About an Airfoil," NASA CR-3183, 1979.
- [5] Rhie, C.M. and Chow, W.L., "Numerical Study of the Turbulent Flow Past an Airfoil with Trailing Edge Separation," *AIAA Journal*, Vol. 21, No. 11, 1983, pp. 1525-1532.
- [6] Chang, K.C., Alemdaroglu, N., Mehta, U., and Cebeci, T., "Further Comparisons of Interactive Boundary-Layer and Thin-Layer Navier-Stokes Procedures," *Journal of Aircraft*, Vol. 25, No. 10, 1988, pp. 897-903.
- [7] Choi, D.H. and Landweber, L., "Inviscid Analysis of Two-Dimensional Airfoils in Unsteady Motion Using Conformal Mapping", *AIAA Journal*, Vol. 28, No. 12, 1990, pp. 2025-2033.
- [8] Nash, J.F., and Patel, V.C., *Three Dimensional Turbulent Boundary Layers*, SBC Tech Books, Atlanta, Ga, 1972.
- [9] Hanjalic, K. and Launder, B.E., "Sensitizing the Dissipation Equation to Irrotational Strains," *ASME Transaction, Journal of Fluids Engineering*, Vol. 102, March 1980, pp. 34-40.
- [10] Chen, H.C. and Patel, V.C., "Near-wall Turbulence Models for Complex Flows Including Separation," *AIAA Journal*, Vol. 26, No. 6, 1988, pp. 641-648.
- [11] Nisizima, S. and Yoshizawa, A., "Turbulent Channel and Couette Flows Using an Anisotropic  $k-\epsilon$  Model," *AIAA Journal*, vol. 25, No. 3, 1987, pp. 414-420.
- [12] Choi, D.H. and Kang, D.J., "Calculation of Separation Bubbles Using a Partially Parabolized Navier-Stokes Procedure," *AIAA Journal*, Vol. 29, No. 8, 1991, pp. 1266-1272.
- [13] Ghia, K.N., Osswald, G.A., and Ghia, U., "Analysis of Two-Dimensional Incompressible Flow past Airfoils Using Unsteady Navier-Stokes Equations," *Proceeding of a Symposium on the Numerical and Physical Aspects of Aerodynamic Flows III*, 1985, pp. 318-338.
- [14] Coles, D. and Wadcock, A.J., "Flying-hot-wire Study of Two-Dimensional Mean Flow past a NACA 4412 Airfoil at Maximum Lift," *AIAA Journal*, Vol. 17, No. 4, 1979, pp. 321-329.
- [15] Bragg, M.B., "Experimental Aerodynamic Characteristics of an NACA 0012 Airfoil with Simulated Glaze Ice," *Journal of Aircraft*, Vol. 25, No. 9, 1988, pp. 849-854.

# DISCRETE-VORTEX SIMULATION OF PULSATING FLOW ON A TURBULENT LEADING-EDGE SEPARATION BUBBLE

13-15 JANUARY 1992

Hyung Jin Sung and Jae Wook Rhim

*Department of Mechanical Engineering, Korea Advanced Institute of  
Science and Technology, Taejon, KOREA*

and

Masaru Kiya

*Department of Mechanical Engineering, Hokkaido University, Sapporo,  
JAPAN*

## Abstract

Studies are made of the turbulent separation bubble in a two-dimensional semi-infinite blunt plate aligned to a uniform free stream when the oncoming free stream contains a pulsating component. The discrete-vortex method is applied to simulate this flow situations because this approach is effective to represent the unsteady motions of turbulent shear layer and the effect of viscosity near the solid surface. The numerical simulation has fairly reasonable predictions with the experimental results which have already performed. A particular frequency given a minimum reattachment which is related to the drag reduction and the most effective frequency is dependent on the most amplified shedding frequency. The turbulent flow structure is scrutinized, which includes the time-mean and fluctuations of the velocity and the surface pressure, together with correlations between the fluctuating components. A comparison between the pulsating flow and the non-pulsating flow at the particular frequency of the minimum reattachment length of the separation bubble suggests that the large-scale vortical structure is associated with the shedding frequency and the flow instabilities.

## Introduction

An improved understanding of pulsating flow characteristics on the turbulent separation bubble is useful in the design of aerodynamic high-speed vehicles and of pulsating turbomachineries. In this study, the separation bubble is generated by flow separation from a sharp leading-edge of a blunt circular cylinder whose axis is aligned parallel to the approaching main flow. Relevant

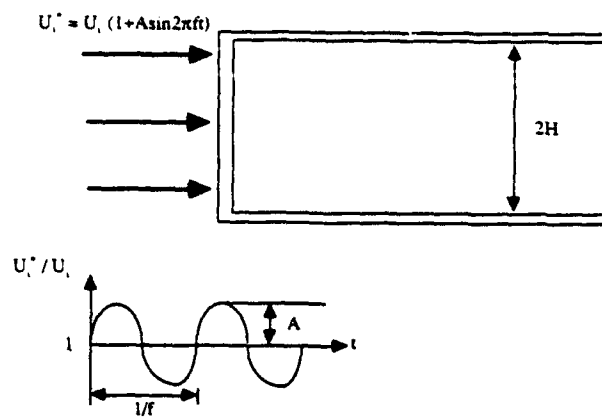
experimental studies have been carried out by Kiya et al.<sup>1</sup> with a view toward the control of a turbulent leading-edge separation bubble.

Control of the separation bubbles by sinusoidal perturbations has been reported by many researchers<sup>2,3</sup>. Roos and Kegelman<sup>2</sup> obtained the reattachment length in a backward-facing step flow as a function of the level and frequency of the perturbation. Sigurdson and Roshko<sup>3</sup> analyzed the structure and control of a turbulent reattaching flow; the reduction of the pressure drag, bubble height and reattachment length were found to depend critically on the forcing frequency.

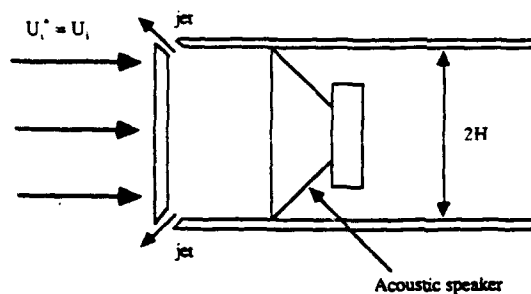
In order to numerically simulate pulsating flow on a turbulent leading-edge separation bubble, the discrete-vortex model is applied. This approach has been demonstrated to be effective in representing the unsteady motions of turbulent separation bubble<sup>4</sup>. The finite-difference simulation of the averaged Navier-Stokes equation with turbulence models has the advantage in computational accuracy and applicability. However, it is currently limited to the ranges of low Reynolds numbers for separated unsteady flows.

The discrete-vortex model is known to be a powerful tool for simulating unsteady separated flows of high Reynolds numbers<sup>4,5</sup>. The separating flow at the leading edge is represented by a combination of an inviscid potential flow and discrete vortices. The effect of viscosity near the solid surface is incorporated in the model. The reduction in the circulation of elemental vortices is also introduced as a function of their ages in order to represent the three-dimensional deformation of vortex filaments. Details regarding the numerical procedures can be found in Ref. 5. The ability of the discrete vortices to adequately represent pulsating





(a) Pulsating flow



(b) Experimental apparatus with acoustic speaker

Fig. 1 Experimental apparatus and numerical analogy

continuous vortex sheets in the separating bubbles has been tested in Ref. 6-7.

In this paper, we consider the specific example of the flow past a two-dimensional flat plate with finite thickness and a blunt leading-edge, which is aligned parallel to a uniform approaching stream. The pulsation was provided by a sinusoidally oscillating jet issued from a thin slit along the separation edge. Therefore, in the numerical simulation, the oncoming free stream was assumed to contain a sinusoidally-varying pulsating component. The entire flow field in the separation bubble is affected mainly by the dynamics near the leading-edge where separation occurs (Fig. 1).

The purpose of this study is to examine the details of the turbulent leading-edge separation bubble by discrete-vortex model. The two key parameters characterizing the free stream are the amplitude of pulsation  $A$ , and the frequency parameter  $St (=fH/U_i)$ . The effects of the separation bubble on the forebody drag, the reattachment length and the lock-on effect between the pulsating frequency and the shedding frequency are investigated. The turbulent flow structure is also scrutinized, which includes the time-mean and fluctuations of the velocity

and the surface pressure, together with the correlations between the fluctuating components. The effect of pulsation on the minimum reattachment length of the separation bubble is examined in detail. This will show that the large scale vortical structure is closely linked with the issues of the shedding frequency and the flow instabilities.

## Discrete-vortex model

The leading-edge separation bubble of a blunt two-dimensional body is considered. This flow geometry is basically the same as the flow configuration of Kiya<sup>5</sup>. Specifics regarding the utilization of discrete-vortex method can be found in their studies. The separation bubble is generated by flow separation from a sharp leading-edge of a blunt two-dimensional body. The dimension of the flat plate is of finite thickness ( $H$ ) and semi-infinite length. The interactions between the two separation bubbles at the corners are assumed to be minimal. Thus, the symmetry condition is applied in this problem. The geometry of the body is given in Fig. 2.

The Schwartz-Christoffel transformation is used to project the exterior region of the body (the physical plane,  $z$ -plane) into an upper half plane (the transformed  $\lambda$ -plane). The transformation is given by

$$z = \frac{H}{\pi} [(\lambda^2 - 1)^{1/2} - \cosh^{-1} \lambda] + iH \quad (1)$$

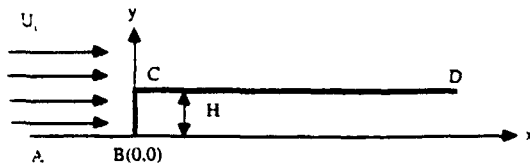
The upstream free stream velocity  $U_i$  contains a pulsating component, therefore,

$$U_i^* = U_i (1 + A \sin 2\pi f t) \quad (2)$$

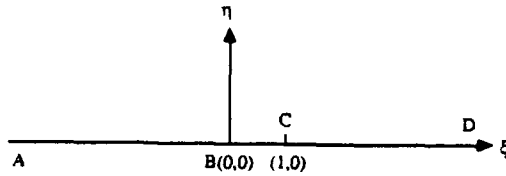
where  $f$  is the pulsating frequency and  $A$  is the amplitude of pulsation. If the flow has no pulsation, i.e.,  $A=0$ ,  $U_i^*$  reverts directly to the constant velocity at upstream infinity  $U_i$ . The complex potential  $w_r$  induced by the discrete vortices is given by

$$w_r = \sum_{j=1}^N \frac{iK_j}{2\pi} \log \frac{\lambda - \lambda_j}{\lambda - \lambda_j^*} \quad (3)$$

where  $N$  is the total number of vortices in the flow field, and  $j$  is the position of the  $j$ th vortex in the transformed plane with its complex conjugate and  $K_j$  denotes its circulation. The complex potential  $w$  for the entire flow field is the sum of  $w_i$  and  $w_r$  by superposition, i.e.,  $w = w_i + w_r$ , where  $w_i$  is the complex potential for the



(a) Physical  $z$  plane



(b) Transformed  $\lambda$  plane

Fig. 2 Geometry of flow

irrotational flow around the body.

The velocity field in the physical plane is given by

$$u - iv = \frac{dw}{dz} = \frac{dw}{d\lambda} \frac{d\lambda}{dz} \quad (4)$$

where  $u$  and  $v$  are the velocity components in the  $x$ - and  $y$ -directions, respectively. The velocity at a vortex point, the  $k$ th vortex, has to be obtained by differentiating with Taylor expansion and the complex invariant,

$$u_k - iv_k = \frac{\frac{U_i}{\pi} + \sum_{j=1}^N \frac{iK_j}{2\pi(\lambda_k - \lambda_j)} - \sum_{j=1}^N \frac{iK_j}{2\pi(\lambda_k - \bar{\lambda}_j)} - \frac{iK_k}{4\pi(\lambda_k^2 - 1)}}{\left(\frac{dz}{d\lambda}\right)_{\lambda_k}} \quad (5)$$

where  $dw/dz$  is deduced from taking the appropriate limit as  $z \rightarrow z_k$ .

The convection of vortices was advanced by a second order scheme with a small time interval, the nascent vortices have to be calculated at a much smaller time interval. Since the velocity at the leading-edge should be finite, the complex potential should satisfy the Kutta condition at the edge

$$(dw/d\lambda)_{\lambda=1}=0. \quad (6)$$

The vortices are shed from the leading-edge into the separation bubble as a result of the separation. The rate of vorticity shedding was determined through the relationship, which was inferred from the experimental results<sup>5</sup>

$$\frac{K_n}{\Delta t_v} = \frac{1}{2} \left( \frac{dw}{dz} \right)^2_{z=i(H+\epsilon)} \quad (7)$$

where  $K_n$  is the initial strength and the position of the nascent vortex is assumed to be  $i(H+0.5\epsilon)$ , and  $\Delta t_v$  is the time interval between the introduction of the nascent vortices. The position of the nascent vortex is assumed to be  $i(H+\epsilon)$ , where  $\epsilon$  is an approximate initial value. The strength and location of the nascent vortices can be adjusted by an appropriate iteration scheme satisfying the Kutta condition<sup>5</sup>.

The reduction of the circulation of every vortex is modelled by<sup>5</sup>

$$\frac{K(t)}{K_n} = 1 - \exp\left(-\frac{a^2 Re}{4U_i/H}\right). \quad (8)$$

where  $K(t)$  is the circulation at time  $t$ ,  $a$  is an adjustable constant, and  $Re$  denotes the Reynolds number  $U_i(H/\nu)$  and  $\nu$  the kinematic viscosity of the fluid. The destruction and coalescence of vortices are assumed to be proportional to the viscous core radius of each vortex. Physically, the removal of potential vortex may be regarded as corresponding to the destruction of vorticity in the shear layer by interaction with the boundary layers along the surface. The decay law (8) was deduced from the exact solution of Navier-Stokes equations for a single rectilinear viscous vortex if  $r$  is replaced by the radial distance from the center of the vortex. After carrying out a number of preliminary calculation, the value of the product  $a^2 Re = 60$  was employed, and this was found to achieve satisfactory agreement with experimental result<sup>5</sup>. It may be noted that an optimum value of  $a^2 Re$  depends on the particular type of flow considered.

The pressure coefficient  $C_p$  can be calculated from the Bernoulli equation,

$$\begin{aligned} C_p &= \frac{P - P_i}{\frac{1}{2}\rho U_i^2} \\ &= 1 - \frac{2}{U_i^2} \frac{\partial \phi}{\partial t} - \frac{1}{U_i^2} \left( \frac{dw}{dz} \right)^2 \end{aligned} \quad (9)$$

where  $p_i$  is the pressure of the free stream,  $\rho$  the density of fluid and  $\phi$  the velocity potential.

In the course of computations, some vortices approach

very closely the wall of the blunt body. Consequently, due to the presence of image vortices, these vortices would have unreasonably large velocities. In order to rectify this computational problem, vortices that approached the wall nearer than the depth of  $0.02H$  were removed from the flow field. Since the transport of momentum and vorticity were negligible in the far field downstream, vortices and their images that were located further than the region  $25H$  were also removed from the computation.

Since a large number of vortices exist with random locations in the flow field, it is probable that some vortices attain small separation and, therefore, produce velocity jumps at each other's positions due to the absence of viscosity. In order to alleviate this difficulty, the concept of the cut-off vortex, which was originally suggested by Chorin<sup>9</sup>, is also employed, i.e.,

$$\begin{aligned}\psi^o &= \frac{K \log r}{2\pi} \quad (r > \sigma) \\ &= \frac{K(r/\sigma)}{2\pi} \quad (r \leq \sigma)\end{aligned}\quad (10)$$

where  $\psi^o$  is the stream function of the vortex and  $\sigma$  the cut-off radius. The numerical value  $\sigma = 0.05H$  was adopted in this simulation. The concept of the cut-off vortices was justified in that the vortex blob in discrete-vortex simulation is basically different from that of potential flow theory, say, the point vortex.

It is noted again that the viscosity of fluid is instrumental in enforcing the no-slip flow condition. Since the discrete-vortex simulation is started from the inviscid flow, an appropriate procedure should be devised to include the viscous effect for the turbulent separation bubble and the shear layer. The viscosity of fluid gives rise to the displacement thickness in the boundary layer and, thereby, transfers momentum to the direction of transverse velocity. For this purpose, an artificial transverse velocity  $V_d (=0.0125U_i)$  was added uniformly to the edge of the shear layer.

It seems that the vortex distributions and wave forms of flow field evolve to be statistically stationary at times  $U_i t/H > 80$ . In this sense, the mean values and fluctuating components were calculated between the interval of  $80 < U_i t/H < 280$ . The non-dimensional time step  $\tau$  for the movement of the vortices was  $0.16H/U_i$  and the time interval  $\Delta t_i$  between the introduction of the nascent vortices was  $0.32H/U_i (=2\Delta\tau)$ .

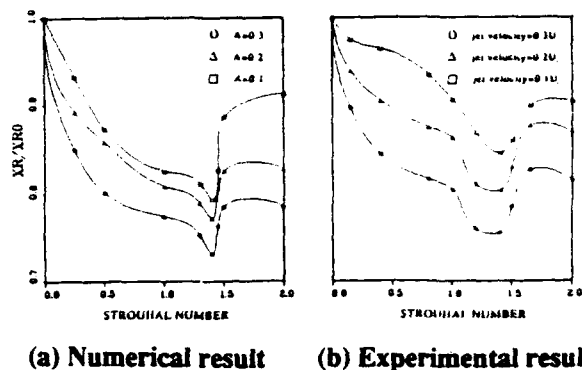


Fig. 3 Comparison of  $X_r/X_{r0}$  between experiment and computation

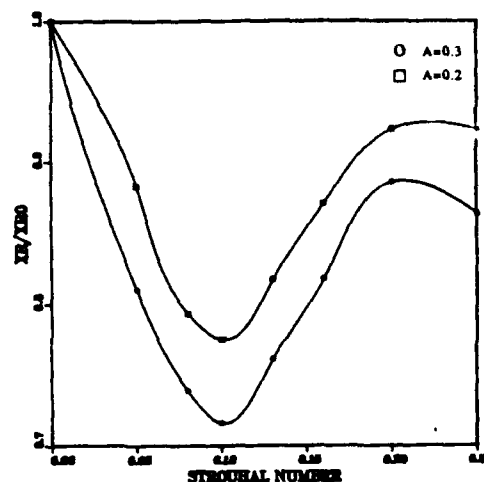


Fig. 4 Reattachment length( $X_r/X_{r0}$ ) with Strouhal number

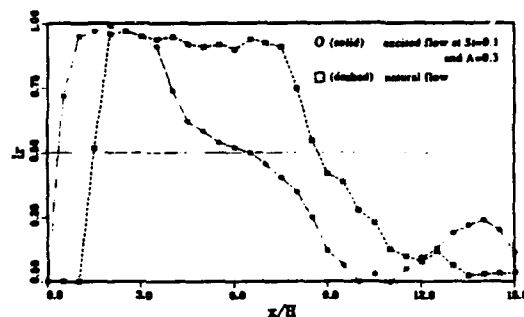


Fig. 5 Reverse flow intermittency distribution

## Results and discussion

It is important to verify the aforementioned analogy between the sinusoidal oscillating jet at the separation edge and the pulsating freestream flows by the present discrete-vortex method. Toward this end, the reattachment length normalized in the form  $X/X_0$  is plotted in Fig.3 against the non-dimensional frequency, i.e., the Strouhal number  $St$  for three different levels of the perturbation. It is noteworthy that the comparison gives a fairly consistent prediction, and this supports the assertion that this analogy seems to be reasonable. The most interesting feature of Fig.3 is that the reattachment length attains a minimum at about  $St=1.4$  for both cases, while the amplitude affects only on the total size of reattachment. This implies that the separation bubble is affected mainly by the frequency of perturbation.

In the present study, the turbulent structures are scrutinized with the comparisons for the non-pulsating flow, natural flow ( $A=0$ ) and for the perturbed flow at  $A=0.3$  and  $St=0.1$ . It should be noted that the condition of flow pulsation was selected such that a maximum reduction of reattachment length for this two-dimensional flow configuration can be realized not for the circular blunt body (Fig. 4). For this two cases, the reverse-flow intermittency is displayed in Fig. 5. The reattachment position is defined as the point where the intermittency,  $I$ , has the value of 0.5. In this figure, it is noticed that the reattachment position ( $X/H=6.5$ ) of perturbed flow is much reduced in comparison to that of non-pulsating flow ( $X/H=9.1$ ). This agrees with the experimental result<sup>3</sup>.

Fig. 6 shows the distribution of surface velocity under the same condition. In a perturbed flow, the position of zero surface velocity is located slightly upstream of the reattachment position while the same position is maintained in natural flow. This means that the reverse flow intensity of perturbed flow is much stronger than that

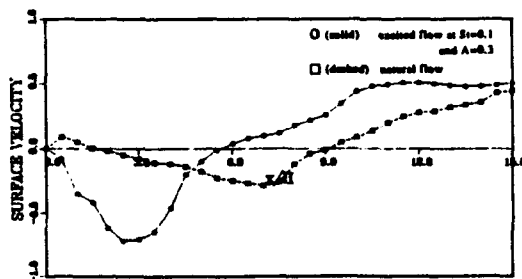


Fig. 6 Surface velocity distribution

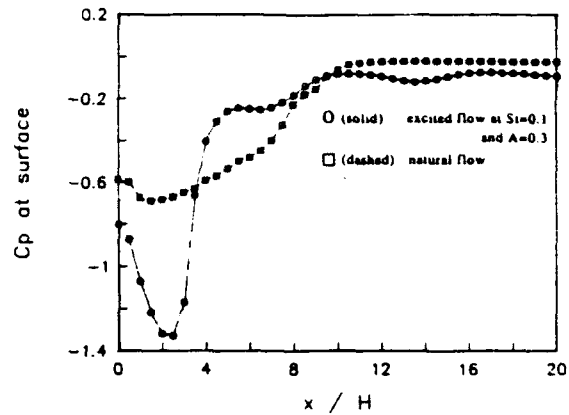


Fig. 7 (a) Time-mean pressure coefficient distribution along the surface

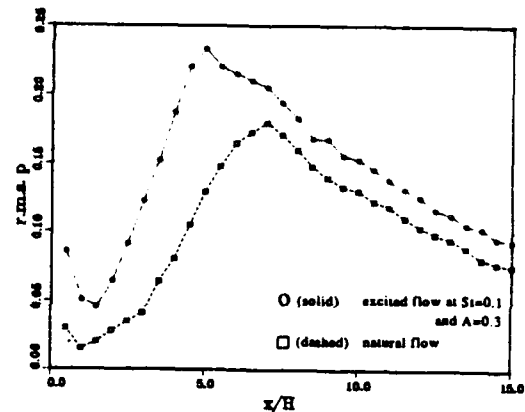


Fig. 7 (b) R.m.s. pressure distribution along the surface

of natural flow, and the feed back of fluid toward upstream of perturbed flow is active.

The distributions of pressure and its fluctuating pressure along the plate surface are shown in Fig. 7. This points to the relation with the flow reattachment for both perturbed and natural flows. It is known that the flow reattachment occurs at near the mean pressure recovery region. It is found that the mean pressure coefficient of perturbed flow at separation line is smaller than that of natural flow (Fig. 7(a)). This implies that the pressure drag is reduced when the flow is perturbed. In the pressure fluctuations of Fig.7(b), this feature of reattachment position can be elucidated more clearly. The r.m.s. of pressure fluctuation is relatively small near the separation region and then it increases along with the downstream and reaches maximum just in front of reattachment position. This region is also the same position of the maximum mean pressure recovery rate. In turbulent shear layer, it is believed that the flow has its own natural

instability and unsteadiness and the flow disturbance can be amplified most effectively at the appropriate pulsation. This is called the most effective frequency,  $St_{max}$ . This effect of amplification is maximized at the flow reattachment region, so the motion of large-scale vortices in this region are the most important elements that can decide the characteristics of the entire flow field.

In passing, it can be found in Fig. 7(a) that the pressure coefficient at separation point ( $C_{ps}$ ) for the pulsating flow is reduced considerably about 30% than that of non-pulsating flow. Reduction of  $C_{ps}$  reproduces the reduction of pressure drag of the body. The maximum reduction of  $C_{ps}$  is also observed at  $St_{max}$ . This agrees well with the experimental result of Sigurdson and Roshko<sup>3</sup>. Koenig<sup>10</sup> studied the relation between  $C_{ps}$  and the drag coefficient ( $C_d$ ) of fluid bodies, and it gives

$$C_{ps} = 0.8 + 0.2C_d \quad (11)$$

From this relation, it can be noticed that the drag of the body ( $C_d$ ) is decreased approximately 6.25% when perturbed, i.e.,  $C_{ps} = 0.68$  for non-pulsating flow while  $C_d = 0.64$  for pulsating flow.

The main reason of drag reduction can be explained in two ways. First, the pulsating perturbation invokes vortex coalescence in the separation bubble and then it causes the enhancement of flow spreading rate. Since the downstream flow rate is increased due to these phenomena, it gives the drag reduction. It means that the enhancement of vortex merging and flow spreading rate is strongly dependent upon the pulsating frequency. This can be analyzed as a preferred mode in Ref. 10. Next, the perturbation increases the entrainment from the outer irrotational flow. This causes the reduction of curvature of the time-mean streamlines near separation line and it deduced the large pressure gradient. Thus it decreases  $C_{ps}$  and  $C_d$ . It is also found that the maximum of entrainment rate is observed at  $St_{max}$ .

Many experimental results reveal that the effect of pulsation on flow structures is observed mostly at the comparatively lower frequency region<sup>23,11,12</sup>. At a particular frequency, the vortex coalescence is surprisingly enhanced. It causes that the reduction of recirculating separation bubble and flow drag of the body.

The distributions of the time-mean velocities  $U$  and  $V$  are displayed in Fig. 8. The difference between non-pulsating flow and pulsating flow is seen to be negligible near the separation line where vortices are just formed out. However, the effect of perturbation is evident in the

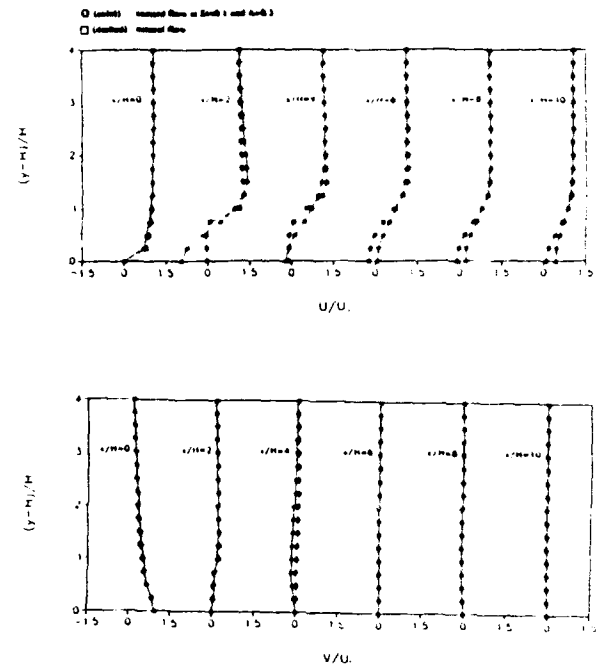


Fig. 8 Distribution of  $U/U_1$  and  $V/U_1$  along the downstream distance

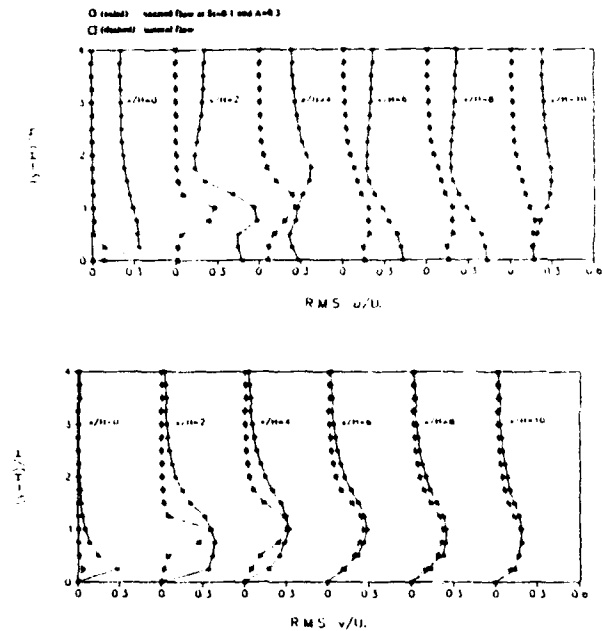


Fig. 9 Distribution of r.m.s.  $u/U_1$  and r.m.s.  $v/U_1$  along the downstream distance

reattachment region. The relatively large value of  $V$  at the separation line is due to the abrupt decrease of the curvatures of streamlines. Fig. 9 shows the r.m.s. of velocity fluctuations. The turbulence level of perturbed flow is found to be considerably higher than that of natural flow.

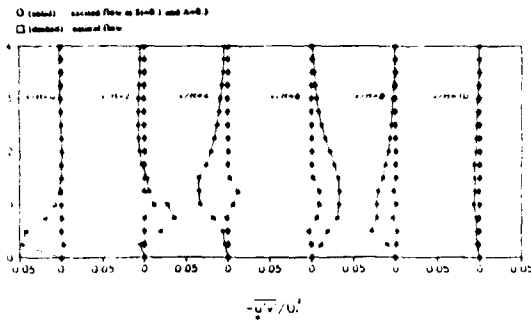


Fig. 10 Distribution of Reynolds shear stress  $-\overline{u'v'}/U_i^2$

The distributions of the Reynolds stress are shown in Fig. 10. In perturbed flow, it is noteworthy that Reynolds stresses have negative values at  $x/H=0.4$  and 8. Hussain<sup>13</sup>, in his study on the coherent structure of turbulent shear layer, proposed that Reynolds shear stress can have negative values of vortical structure in a certain configuration where vortex coalescence process is dominant. Furthermore, since perturbation strengthens the fluctuating components in shear layer, so the mean velocity may be affected by these fluctuating velocities. The characteristic wave length of vortices can be given as follows<sup>12</sup>,

$$\frac{L}{H} = \frac{U_c}{U_i} St^{-1} \quad (12)$$

where  $U_i$  is the convection velocity of vortices and  $St_{max}$  is the most amplified shedding frequency, which will be referred later. Suppose the value of  $U_c/U_i$  was 0.5<sup>14</sup>, then  $L$  has the value of about 5H. This agrees that the locations of negative Reynolds stress are found to be nearly identical to the multiples of  $L$ . This relation reduces that negative Reynolds shear stress are brought about by the enhancement of vortex coalescence by pulsation and the positions are closely related with the characteristic wave length. From this, it can be predicted that the vortex merging is observed at every characteristic wave length in separation bubble.

The patterns discrete-vortices in the separation bubble at a certain time ( $t=288H/U_i$ ) for both cases are plotted in Fig. 11. It may be noted that large-scale vortices are more evident in perturbed flow. In addition, the rolling-up behavior of large-scale vortices, the merging of vortices and the vortex-shedding from separation bubble to downstream are also observed. It is noteworthy that the concentration of discrete-vortices occurs at each multiples of  $L$ . It gives a numerical validation for negative Reynolds shear stresses in separation bubble.

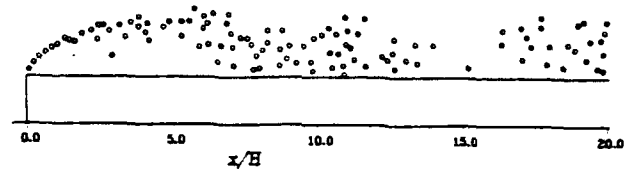


Fig. 11 (a) Distribution of discrete-vortices in unperturbed flow at  $t = 288 H/U_i$

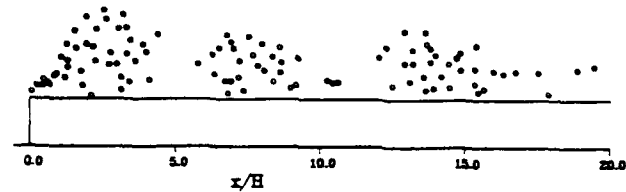


Fig. 11 (b) Distribution of discrete-vortices in perturbed flow at  $t = 288 H/U_i$

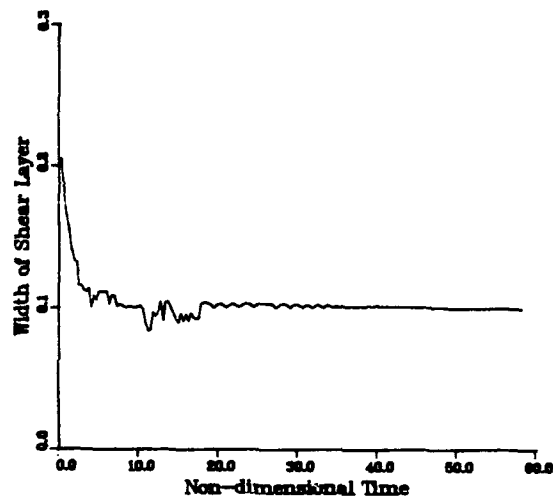


Fig. 12 (a) Width of shear layer with time at leading-edge in natural flow

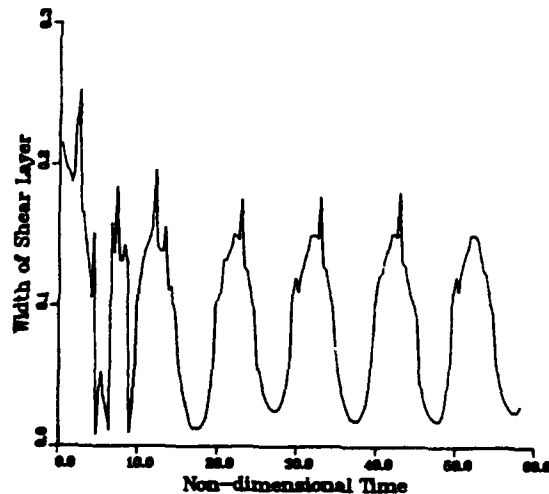


Fig. 12 (b) Width of shear layer with time at leading-edge in excited flow

Fig.12 represents the width of shear at separation as a function of time. Approximately, this width may be regarded as a distance between the core vortex and the wall of body. In non-pulsating flow, as time advances, this width becomes constant. However, in perturbed flow, at  $St_{max}$ , it oscillates with the period of  $10H/U_i$ , which corresponds to the forcing frequency  $St_{max}=0.1$ . In perturbed flow, the nascent vortices interact with the surface from the start of the rolling-up motion, so this is related to the resultant amplification of disturbances.

The power spectra, which as defined as eqn.(13), was obtained at the edge of the shear layer where  $u'/U_i=0.02$  and is shown in Fig.13. As pointed out previously, the power spectra of  $u$  near reattachment region also discloses the broad peak value around  $St=0.1$ . Thus, this

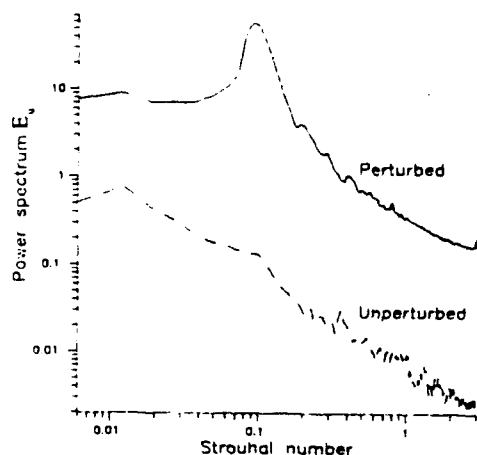


Fig. 13 (a) Power spectrum of  $u'$  ( $=E_u$ ) near separation line at the edge of the shear layer (r.m.s.  $u/U_i \approx 0.02$ )

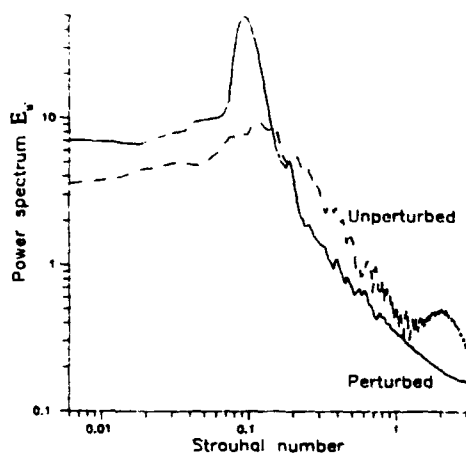


Fig. 13 (b) Power spectrum of  $u'$  ( $=E_u$ ) near reattachment position at the edge of the shear layer (r.m.s.  $u/U_i \approx 0.02$ )

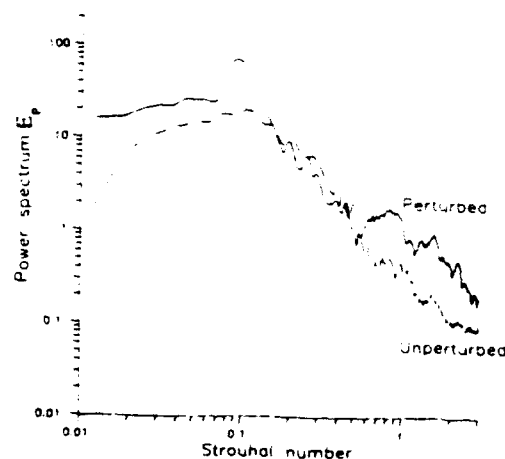


Fig. 14 Power spectrum of  $p'$  ( $=E_p$ ) near reattachment position at the edge of the shear layer (r.m.s.  $u/U_i \approx 0.02$ )

frequency ( $St=0.1$ ) can be considered as the most amplified shedding frequency of large-scale vortices, which is also verified from the power spectra of pressure at the same position (Fig.14).

$$\int_0^\infty (E_u, E_p) d(fH/U_i) = \left( \bar{u}^2/U_i^2, \bar{p}^2/\frac{1}{2}\rho U_i^2 \right) \quad (13)$$

In passing, it is notable that the present result tends to have appreciably the same value as the results of Mabey<sup>15</sup>. It gives the relation of  $St \cdot X_r \approx 0.7$  with almost the same value of the present result. This trend has also been noticed in other experimental results<sup>23</sup>. It is stressed here that the most amplified shedding frequency gives strong effects on the reduction of reattachment length, drag and enhancement of vortex coalescence in the separation bubble.

The power spectra near separation line shows the broad peak at relatively low frequency (Fig.13(a)). This is regarded as an evidence of the flapping motion of separation bubble, which seems to be attributed to unsteadiness<sup>15,16</sup>. Near reattachment region, the low-frequency peak is gradually diminished and the broad peak is centered upon around  $St_{max} \approx 0.1$ . Roshko<sup>3</sup> called this frequency as the shedding-type instability, which is the dominant frequency in separation bubble.

In this study, we assumed that  $St_{shed}$  is identical to  $St_{max}$ . This is attributed to the analogy as follows; If the pulsating frequency is higher than the initial Kelvin-Helmholtz frequency  $St_{KH}$ , there is no instability region. In this sense, the slow disturbance can not be amplified. Thus  $St_{shed}$  becomes dominant around the value of  $St_{max}$ .

The way to estimate  $St_{shed}$  has been tried through a lot

of experiments. Roshko<sup>1</sup> obtained the relation  $fh/U_s=0.08$ , where  $h$  is the asymptotic height,  $U_s$  is the velocity at separation line and  $f$  is the shedding frequency corresponding to  $St_{shed}$ . In the present case, we obtained the value of  $fh/U_s=0.078$ , which is nearly identical to that of Roshko.  $U_s$  can be obtained from the two-dimensional Bernoulli's equation.

$$\frac{U_s}{U_i} = (1 - C_{ps})^{1/2} \quad (14)$$

It should be noted that the flow geometry of Roshko is different from the present experimental configuration, however, the result gives nearly same trends. Roshko's result was obtained from the frequency of von Karman vortex sheet in a blunt circular cylinder. Levi<sup>17</sup> also suggested the Strouhal Law, which defined as  $fd/U_i=0.16$ . In this case, if  $d=2h$  substituted, his law gives the exactly same value of our result. From the aforementioned comparison, the tentative summary can be suggested that  $St_{shed}$  has its origin in the large-scale structures of turbulence, regardless of flow geometries. In this connection, it is believed that  $St_{max}$  is approximated by  $St_{shed}$ . Thus, this forcing frequency enhances the spreading rate of flow and vortex coalescence and minimizes the drag effectively.

## References

- <sup>1</sup>Kiya, M., Mochizuki, O., Tanaka, H., and Tsukasaki, T., "Control of a Turbulent Leading-Edge Separation Bubble," Proceedings of IUTAM Sym. on Separated Flow and Jets (Ed. Kozlov, V. V.), Springer-Verlag, 1991.
- <sup>2</sup>Roos, F. W. and Kegelmann, J. T., "Control of Coherent Structures in Reattaching Laminar and Turbulent Shear Layers," AIAA J., Vol 24, 1986, pp. 1956-1963.
- <sup>3</sup>Sigurdson, L. W. and Roshko, A., "The Structure and Control of a Turbulent Reattaching Flow," Turbulent Management and Relaminarization, Springer-Verlag, 1988, pp. 497-514.
- <sup>4</sup>Sarpkaya, T. and Itasaka, M., "Inviscid Model of Two-Dimensional Vortex-Shedding by a Circular Cylinder," AIAA J., Vol 17, 1979, pp. 1193-1200.
- <sup>5</sup>Kiya, M., Sasaki, K., and Arie, M., "Discrete-Vortex Simulation of a Turbulent Separation Bubble," J. Fluid Mech., Vol 120, 1982, pp. 219-244.
- <sup>6</sup>Aso, S., Hayashi, M., Futatsudera, N., and Fujimoto, A., "Numerical Simulation of Separated Flows around a Wing Section by Discrete Vortex Method," Proceedings of International Sym. on CFD at Nagoya, 1989.
- <sup>7</sup>Clements, R. R., "An Inviscid Model of Two-Dimensional Vortex Shedding," J. Fluid Mech., Vol 57, 1973, pp. 321-336.
- <sup>8</sup>Evans, R. A. and Bloor, M. I. G., "The Starting Mechanism of Wave-Induced Flow through a Sharp-Edged Orifice," J. Fluid Mech., Vol 82, 1977, pp. 115-128.
- <sup>9</sup>Chorin, A. J., "Numerical Study of Slightly Viscous Flow" J. Fluid Mech., Vol 57, 1973, pp. 758-796.
- <sup>10</sup>Koenig, K., "Interference Effects on the Drag of Blunt Bodies in Tandem," Ph. D. Thesis, California Institute of Technology, 1978.
- <sup>11</sup>Hiller, R. and Cherry, N. J., "Pressure Fluctuations under a Turbulent Shear Layer," 3rd Turbulent Shear Flow Symposium, Davis, California, 1981.
- <sup>12</sup>Bhattacharjee, S., Scheelke, B., and Troutt, T. R., "Modification of Vortex Interactions in a Reattaching Separated Flow," AIAA J., Vol 24, 1986, pp. 623-629.
- <sup>13</sup>Hussain, A. K. M. F., "Coherent Structure - Reality and Myth," Phys. Fluids, Vol 26, 1983, pp. 2840-2842.
- <sup>14</sup>Kiya, M. and Sasaki, K., "Structure of a Turbulent Separation Bubble," J. Fluid Mech., Vol 137, 1983, pp. 83-113.
- <sup>15</sup>Mabey, D. G., "Analysis and Correlation of Data on Pressure Fluctuations in Separated Flow," J. Aircraft, Vol 9, 1972, pp. 642-645.
- <sup>16</sup>Eaton, J. K. and Johnston, J. P., "Low Frequency Unsteadiness of a Reattaching Turbulent Shear Layer," Turbulent Shear Flows III (Ed. Bradbury, L. J. S., Durst, F., Launder, B. E., Schmidt, F. W., and Whitelaw, J. H.), Springer-Verlag, 1982, pp. 162-170.
- <sup>17</sup>Levi, E., "Universal Strouhal Law," ASCE J. Engineering Mech., Vol 109, 1983, pp. 718-727.



# **A Unified Approach for Numerical Simulation of Viscous Compressible and Incompressible Flows over**

**Adiabatic and Isothermal Walls**

**M.Hafez, M.Soliman**

**University of California, Davis**

**and**

**S.White**

**NASA Ames Research Center**

## **Abstract**

A new formulation (including the choice of variables, their non-dimensionalization and the form of the artificial viscosity) is proposed for the numerical solution of the full Navier-Stokes equations for compressible and incompressible flows with heat transfer.

With the present approach, the same code can be used for constant as well as variable density flows. The changes of the density due to pressure and temperature variations are identified and it is shown that the low Mach number approximation is a special case. At zero Mach number, the density changes due to the temperature variation is accounted for, mainly through a body force term in the momentum equation. It is also shown that the Boussinesq approximation of the buoyancy effects in an incompressible flow is a special case.

To demonstrate the new capability, three examples are tested. Flows in driven cavities with adiabatic and isothermal walls are simulated with the same code as well as incompressible and supersonic flows over a wall with and without a groove. Finally, viscous flow simulations of an oblique shock reflection from a flat plate are shown to be in good agreement with the solutions available in literature.

## **Introduction**

In a previous work[1], the authors proposed a formulation for both compressible and incompressible viscous flow simulation. First the density is eliminated in terms of the pressure and the temperature via the perfect gas equation of state. This step by itself is not sufficient simply because the equation of state is not valid for incompressible flows. The formulation is completed using the

perturbation of the pressure and the temperature relative to reference values as the dependant variables. It is shown that the density in terms of these new variables approaches a constant as the reference Mach number vanishes. The above formulation is generalized in the present paper to allow for incompressible flows which are not necessarily isothermal.

To obtain a numerical solution, an artificial dissipation is introduced by adding to the governing equations the Laplacians of the pressure and the velocity components. An improved model is also tested which is based on a partial least square procedures. The continuity equation is modified by a Poisson's equation for the pressure similar to that of Harlow and Welch[2], and Harlow and Amsden[3]. The momentum equations are also modified by Poisson's equations of the velocity components. The first modification is obtained by taking the divergence of the momentum equations, while the second modification can be related to a vector identity relating the Laplacian of the velocity vector to the gradient of its divergence and the curl of the vorticity. In both modifications, the evaluation of the nonhomogeneous terms of the Poissons equations are lagged as in the deferred correction procedures.

The energy equation is augmented with second order terms of the total enthalpy obtained via minimizing the squares of the convective terms. This modification is very small in the neighborhood of a solid surface and can be interpreted as an artificial streamline diffusion as in the work of Hughes et al[4].

The present numerical solutions are obtained using a standard Glarkin procedure. The resulting nonlinear system of equations are solved via Newton's method. At each iteration a direct solver based on banded Gaussian elimination is

employed. The use of finite element discretizations and direct solvers are not necessary to obtain numerical solutions based on the present formulations, and other viable alternatives are, for example, finite volumes and iterative procedures.

In the following, the derivation of the governing equations and the applications to some test problems are discussed.

### Governing Equations

For steady compressible viscous flows, the continuity, momentum and energy equations can be written in terms of the primitive variables  $(\rho, p, \vec{q})$  including the effects of a body force as:

$$\begin{aligned}\nabla \cdot \rho \vec{q} &= 0 \\ \nabla \cdot \rho \vec{q} \vec{q} &= \nabla : \tau + \rho \vec{f} \\ \nabla \cdot \rho \vec{q} H &= \nabla \cdot k \nabla T + \nabla \cdot (\tau \cdot \vec{q}) + \rho \vec{f} \cdot \vec{q} \quad (1)\end{aligned}$$

$$\text{where } H = \frac{\gamma}{\gamma-1} \frac{p}{\rho} + \frac{1}{2} (u^2 + v^2)$$

$$\text{and } \tau_{ij} = \lambda (\nabla \cdot \vec{q}) \delta_{ij} + \mu \left( \frac{\partial q_i}{\partial x_j} + \frac{\partial q_j}{\partial x_i} \right)$$

For convenience it is assumed that  $\lambda = -\frac{2}{3}\mu$  and  $p = \rho R T$ . The two constants  $R$  and  $\gamma$  are related to the specific heat constants  $c_p$  and  $c_v$ ;  $R = c_p - c_v$  and  $\gamma = \frac{c_p}{c_v}$ . For the derivation of the above equations, see, for example, Liepman and Roshko [5]

A standard non-dimensional form is obtained using the reference values of  $\rho$  and  $q$  in the far field of external flow problems. The pressure is usually normalized by  $\rho_\infty \frac{q_\infty^2}{2}$  and the temperature by  $\frac{q_\infty^2}{c_p}$ . If  $L$  is a characteristic length, two parameters appear in the equations namely the Reynolds and Peclet numbers, where

$$Re = \frac{\rho_\infty q_\infty L}{\mu_\infty} \quad (2)$$

$$Pe = \frac{\rho_\infty q_\infty L}{k_\infty / c_p} \quad (3)$$

The Peclet number is the product of Prandtl and Reynolds numbers, where

$$Pr = \frac{\mu_\infty}{k_\infty / c_p} \quad (4)$$

Equations (1) becomes

$$\begin{aligned}\nabla \cdot \rho \vec{q} &= 0 \\ \nabla \cdot \rho \vec{q} \vec{q} &= -\nabla p + \frac{1}{Re} \nabla : \tau - \frac{1}{Fr} \rho K \\ \nabla \cdot \rho \vec{q} H &= \frac{1}{Pe} \nabla \cdot k \nabla T + \frac{1}{Re} \nabla \cdot (\tau \cdot \vec{q}) - \frac{1}{Fr} \vec{q} \cdot \rho K\end{aligned} \quad (5)$$

In equations (5), the relative effect of gravity is identified by the Froude number,

$$Fr = \frac{q_\infty^2}{g L} \quad (6)$$

In natural convection problems, the variation of density due to temperature difference  $\Delta T$  creates a buoyancy term in the momentum equation. To first order accuracy, the density variation would be  $\rho = \rho_\infty (1 - \beta \Delta T)$  where  $\beta$  is the thermal expansion coefficient, hence the buoyancy term is given by

$$\frac{\beta \Delta T}{2} \frac{g L}{q_\infty} \frac{\vec{q}}{K} = \frac{Gr}{2} \frac{\vec{q}}{K} \quad (7)$$

where

$$Gr = \frac{\beta \Delta T g L^3}{\mu_\infty} \quad (8)$$

The above formulation is not suitable for incompressible flows since in the limit of zero free stream Mach number, both the normalized pressure and temperature are unbounded. Two new variables were introduced in the previous study to avoid this problem, namely  $p^*$  and  $T^*$  where

$$p^* = p - p_\infty - \frac{1}{\gamma M_\infty^2} \quad (9)$$

and,

$$\bar{T}^* = \bar{T} - \bar{T}_\infty = \bar{T} - \frac{1}{(\gamma-1) M_\infty^2} \quad (10)$$

Hence, the equation of state gives

$$\bar{\rho} = \frac{\gamma M_\infty^2 \bar{p}^* + 1}{(\gamma-1) M_\infty^2 \bar{T}^* + 1} \quad (11)$$

As the Mach number vanishes, the normalized density  $\bar{\rho}$  approaches 1.0, i.e. the reduced incompressible flow is isothermal. To allow for density variations due to temperature changes in the incompressible limit, in cases of adiabatic walls as well as walls with specified temperatures, the variable  $T$  is replaced by

$$\bar{T} = \frac{T}{T_\infty} \quad (12)$$

Equation (11) becomes

$$\bar{\rho} = \frac{\gamma M_\infty^2 \bar{p}^* + 1}{\bar{T}} \quad (13)$$

In the limit of zero Mach number,  $\bar{\rho} \bar{T}$  approaches 1 and the proper general dependence of the density on the temperature is recovered. The isothermal flow is of course a special case of the above relation.

The continuity and the momentum equations are unaltered, the energy equation becomes

$$\bar{\nabla} \cdot \bar{\rho} \bar{q} \bar{H} = \frac{1}{Pe} \bar{\nabla} \cdot \bar{k} \bar{\nabla} \bar{T} + \frac{Ec_w}{Re} \bar{\nabla} \cdot (\bar{\tau} \cdot \bar{q}) - \frac{Ec_w}{Fr} \bar{q} \cdot \bar{\rho} \bar{K} \quad (14)$$

where

$$\bar{H} = \bar{T} + Ec_w \bar{q}^2 / 2$$

and,

$$Ec = \frac{q_\infty^2}{c_p T_\infty} = (\gamma-1) M_\infty^2 \quad (Ec \text{ is the Eckert number})$$

The incompressible limit of Equation (14) is

$$\bar{\nabla} \cdot \bar{\rho} \bar{q} \bar{T} = \frac{1}{Pe} \bar{\nabla} \cdot \bar{k} \bar{\nabla} \bar{T} \quad (15)$$

Here, the temperature ratio  $T_w/T_\infty$ , where  $T_w$  is the average wall specified temperature, enters only through the boundary conditions.

Alternatively, one can choose

$$\bar{T} = \frac{T}{T_\infty} \frac{T_\infty}{T_w} = \bar{T} \frac{T_\infty}{T_w} \quad (12)$$

and, in this case

$$\bar{\rho} = \frac{\gamma M_\infty^2 \bar{p}^* + 1}{\bar{T} \frac{T_w}{T_\infty}} \quad (13)$$

and

$$\bar{\nabla} \cdot \bar{\rho} \bar{q} \bar{H} = \frac{1}{Pe} \bar{\nabla} \cdot \bar{k} \bar{\nabla} \bar{T} + \frac{Ec_w}{Re} \bar{\nabla} \cdot (\bar{\tau} \cdot \bar{q}) - \frac{Ec_w}{Fr} \bar{q} \cdot \bar{\rho} \bar{K} \quad (14)$$

where

$$\bar{H} = \bar{T} + Ec_w \bar{q}^2 / 2$$

and

$$Ec_w = \frac{q_\infty^2}{c_p T_w} = \frac{(\gamma-1) M_\infty^2}{T_w/T_\infty}$$

Thus, the present formulation is valid for compressible and incompressible flows, with adiabatic or specified temperature walls. Moreover, it is clear from equation

(13) or (13') that the low Mach number approximation (see for example Rhem and Baum [6], Majda[7] and Markle[8]) is a special case. The Boussinesq approximation of the buoyancy effects in an incompressible flow is also a special case of the present formulation.

It should be mentioned that the above formulation is not restricted to perfect gases. A more general equation of state can be written in the form

$$\rho = \rho_\infty + \frac{\partial \rho}{\partial T} \Delta T + \frac{\partial \rho}{\partial p} \Delta p \quad (16)$$

or in the non-dimensional form

$$\bar{p} = 1 + \frac{\partial \bar{p}}{\partial T} \bar{\Delta T} + \frac{\partial \bar{p}}{\partial p^*} \Delta p^* \quad (16)$$

The last term of equation (16) always vanishes in the limit of zero Mach number.

### Numerical Method

It is well known that centered schemes permit, in general, odd and even decoupling of the discrete pressure field [9]. To avoid this problem, different interpolations are used for the velocity and the pressure in the standard finite element analysis of incompressible flows [10], [11]. Recently, Pironeau [12] addressed this issue for compressible flows as well.

It is also well known that centered schemes produce oscillatory solutions of convection-diffusion equations with high Reynolds numbers, unless impractical excessively fine meshes are used.

In the present study, artificial dissipation is introduced explicitly in all equations, to eliminate the wiggles and to allow for capturing shocks and contact discontinuities. Two forms of artificial viscosity are considered. In the first method, the governing equations become

$$\begin{aligned} \bar{\nabla} \cdot \bar{\rho} \bar{q} &= \varepsilon_1 \bar{\nabla}^2 \bar{p} \\ \bar{\nabla} \cdot \bar{\rho} \bar{q} \bar{q} + \bar{\nabla} \bar{p} &= \frac{1}{Re} \bar{\nabla} \cdot \bar{\tau} + \frac{1}{Fr} \bar{\rho} K = \varepsilon_2 \bar{\nabla}^2 \bar{q} \\ \bar{\nabla} \cdot \bar{\rho} \bar{q} H &= \frac{1}{Pe} \bar{\nabla} \cdot k \bar{\nabla} T - \frac{Ec}{Re} \bar{\nabla} \cdot (\bar{\tau} \cdot \bar{q}) + \frac{Ec}{Fr} \bar{\rho} f g = \varepsilon_3 \bar{\nabla}^2 H \end{aligned} \quad (17)$$

where  $\varepsilon$ 's are small parameters of the order of the mesh size. A standard Galerkin finite element method is applied to calculate the solution of equations (17). This form has been investigated before for both incompressible and compressible flows with the standard separate formulations. With the present unified approach, the same code is used to calculate compressible and incompressible cases.

In the second method, the Laplacian terms are balanced with nonlinear terms obtained by manipulating the original

equations. For example, the momentum equations can be written in the form

$$\bar{\nabla} \bar{p} = \bar{g} \quad (18)$$

A Poisson's equation is constructed by taking the divergence of equation (18) and allowing a variable (positive) artificial viscosity coefficient, one arrives at

$$\bar{\nabla} \cdot \varepsilon \bar{\nabla} \bar{p} = \bar{\nabla} \cdot \varepsilon \bar{g} \quad (18)$$

Equation (18) can be also obtained from minimizing the functional  $\int \varepsilon (\bar{\nabla} \bar{p} - \bar{g}) \cdot (\bar{\nabla} \bar{p} - \bar{g})$  with respect to  $\bar{p}$ , assuming  $\bar{g}$  is known. The continuity equation is then modified by the Poisson's equation

(18).

Similarly, the Laplacian of the velocity components can be balanced using the vector identity

$$\bar{\nabla}^2 \bar{q} = \bar{\nabla} S - \bar{\nabla} \times \bar{\omega} \quad (19)$$

where

$$S = \bar{\nabla} \cdot \bar{q}$$

$$\bar{\omega} = \bar{\nabla} \times \bar{q}$$

To allow for a variable viscosity coefficients, one can minimize the functional (assuming  $S$  and  $\bar{\omega}$  known)

$$\int \varepsilon (\bar{\nabla} \cdot \bar{q} - S)^2 + \varepsilon (\bar{\nabla} \times \bar{q} - \bar{\omega})^2$$

with respect to  $\bar{q}$  to obtain

$$\bar{\nabla} \cdot \varepsilon \bar{\nabla} \bar{q} = \bar{\nabla} \varepsilon S - \bar{\nabla} \times \varepsilon \bar{\omega} + f(\bar{\nabla} \varepsilon) \quad (19)$$

In equations (18) and (19), the quantities  $\bar{g}$ ,  $S$  and  $\bar{\omega}$  are obtained at each node from their definitions using a standard Galerkin finite element method with the same interpolation used for the other variables. The evaluation of these terms are lagged and their contributions to the Jacobians are neglected.

For the energy equation, the modification is obtained via minimizing

the functional  $\int \varepsilon (\bar{\rho} \bar{q} \cdot \bar{\nabla} H + \pi)$  with respect

to  $H$ . For convenience,  $\pi$  is dropped with the

justification that the artificial dissipation is mostly needed in the inviscid adiabatic part of the flow where the relatively coarse mesh is not capable of resolving the  $\pi$  term. In the neighborhood of a solid surface, a fine mesh is required anyway and there is no need there of artificial viscosity terms. The present modification is very small there since it is scaled with the velocity. The same remark is applicable for the treatment of the momentum equations where the viscous stress terms can be

→  
ignored in the evaluation of the  $g$  term.

The variational formulation of the artificial dissipation terms provides a natural treatment of the numerical boundary conditions. Upon integration by parts, the resulting line integrals are simply ignored.

Because the modification terms, for the continuity, the momentum and the energy equations are obtained separately by adopting a partial least squares procedure for each case the resulting algebraic system of equations are not necessarily symmetric.. A full least squares procedures for all equations coupled together has been successfully used by the first author to introduce dissipative terms for the solution of Euler equations simulating transonic flows with sharp shock waves [13]. In this case, it is possible however to construct a symmetric positive definite system at each Newton's iteration by a proper choice of the coefficients of the artificial terms [Jiang & Povinelli[14]. Unfortunately, such choices result in smearing the discontinuities. For viscous flows, they write the Navier Stokes equations as a system of first order equations in terms of velocity, pressure and vorticity and then a full least squares procedure is applied. The resulting algebraic equations are symmetric positive definite, but the number of unknowns are increased (almost doubled for three dimensional problems).

Needless to say, more work is required to determine the optimal form of the modification terms and the associated solution procedures for the general flow case.

## Numerical Results

Three test problems are solved using the present formulation. The first viscosity method is used for the first two problems. Since the  $Re$  is relatively low, no artificial viscosity in the momentum or the energy equation is needed ( $\epsilon_2 = \epsilon_3 = 0$ ). For the modified continuity equation, a numerical boundary condition,  $\frac{\partial p}{\partial n} = 0$  at the wall is enforced at the wall. The third problem is solved by the two viscosity methods. In the following some preliminary results are presented.

### I. Driven Cavity with Adiabatic and Isothermal Walls

Incompressible ( $M_\infty = 0$ ) and compressible flows ( $M_\infty = 0.4$ ) are simulated for  $Re=100$  with adiabatic walls. The pressure contours of the converged solutions are plotted in figures (I-a) and (I-b) respectively. Next, the temperature at the upper and lower walls are fixed and the calculations are repeated. The pressure contours are plotted in figures (I-c) and (I-d) and the corresponding temperature contours are shown in figures (I-e) and (I-f).

The effects of compressibility and the difference of wall temperatures, are clearly depicted in these figures.

### II- Incompressible and Supersonic Viscous Flows over a Wall with and Without a Groove

A uniform stream of  $Re=1000$  over a flat plate is simulated with the same code. The pressure and velocity profiles at different locations are plotted in figures (II-a) and (II-b) for the case of  $M_\infty=0$ . For supersonic flow with  $M_\infty = 3$ , the pressure, velocity and temperature profiles are shown in figures (II-c), (II-d) and (II-e). The pressure, temperature and density contours are given in figures (II-f), (II-g) and (II-h). As expected, an oblique shock

wave is formed due to the boundary layer displacement effect.

Next, the calculations are repeated for a flat plate with a groove. The pressure profiles for the incompressible flow case is shown in figure (II-i), while the pressure, temperature and density contours of the supersonic case are plotted in figures (II-j), (II-k) and (II-l).

### III- Inviscid and Viscous flow Simulations of Shock Reflection from a flat plate.

First, an inviscid supersonic flow ( $M_\infty=2.0$ ) with a reflected shock is calculated. The results are in agreement with the exact solution. The pressure contours from the two artificial viscosity methods are plotted in figure (III-a) and (III-b). For a viscous supersonic flow at  $Re=296000$  and  $M_\infty=2.0$ , the results are in agreement with those of MacCormack [15] and with experimental data. The velocity profiles before, within and after the separation bubble are plotted in figure (III-c). The skin friction distribution is shown in figure (III-d). The pressure contours from the first and second artificial viscosity methods are compared in figure (III-e) and (III-f).

Cartesian grids and bilinear elements are used for all the problems tested in this paper. Applications to transonic flows over airfoils using unstructured finite elements are reported in a separate paper [16].

### **Conclusions**

A unified approach for a general flow simulation is presented. It is shown that all the normalized variables used in the formulation are always bounded and the proper variation of the density due to changes in pressure and temperature is recovered in the limit of zero Mach number.

Two artificial viscosity methods are applied to obtain numerical results for some test cases. The governing equations are modified by either Laplacian's or Poisson's equations for the pressure, the velocity components and the total enthalpy. Acceptable solutions are

obtained via a standard Galerkin finite element procedure, using equal order interpolations for all normalized variables.

The unified approach offers a convenient formulation which allows, using the same code, the simulation of compressible and incompressible flows where the walls are adiabatic, with specified temperature distributions or of mixed type. In particular, the low Mach number approximation as well as the Boussinesq approximation (of the buoyancy effects) are special cases of the present formulations.

Obviously, it is always possible to have more efficient flow simulations for some special cases. For example, when the speed of sound is finite, explicit schemes can be used to integrate the time dependent gas equations, in contrast to the incompressible flow case where a Poisson's equation of the pressure has to be solved, at each time step, to guarantee the conservation of mass during the time evolution process. Another example is the special case of incompressible (constant density) flow where the energy (temperature) equation decouples and the solution of the continuity and the momentum equations provide the pressure and the velocity components. Therefore, the use of the present unified approach for the above two examples is more costly compared to the use of two separate codes tailored for the specifics of these two cases. It is still necessary however to have a general code for all speeds and all possible boundary conditions to handle the cases of mixed nature.

### **Acknowledgement**

This work has been supported by NASA Ames Research Center.

### **References**

- [1] Hafez, M. and Soliman, M., "Numerical Solution of the Incompressible Navier-Stokes Equations in Primitive Variables on Unstaggered Grids.", AIAA paper 91-1561. see also, Hafez, M. and Ahmed, J., "Vortex Breakdown Simulation, Part III- Compressibility Effects." in Fourth

Symposium on Num. and Phys Aspects of Aerodynamics Flows.", Long Beach, Ca. 1989.

[2] Harlow, F. and Welsh, J. " Numerical Calculations of Time Dependant Viscous Incompressible Flow with Free Surface.", Phys. Fluids, vol.80, pp.2182-2189, 1965.

[3] Harlow, F. and Amseden, A., " A Numerical Fluid Dynamics Calculation Method for All Flow Speeds.", J.of Comp. Phys. vol.8, pp.197-213, 1971.

[4] Hughes, T. and Brooks, A., " A Multidimensional Upwind Scheme With no Crosswind Diffusion.", in ' Finite Element Methods for Convection Dominated Flows.', The American Society of Mechanical Engineers, 1979.

[5] Liepman, H. and Roshko, A., " Elements of Gas Dynamics.", Wiley, 1957.

[6] Rehm, R. and Baum, H., " The Equations of Motion for Thermally Driven Buoyant Flows.", J. Res. Nat. Bur. Stand, vol.83, pp.297-311, 1978.

[7] Majda, A., " Equations for Low Mach Number Combustion.", Report # 112, Center for Pure Appl. Math., Nov. 1982.

[8] Merkle, C. and Choi, Y.H., " Computation of Compressible Flows at Very Low Mach Numbers.", AIAA paper 86-0351.

[9] Peyret, R. and Taylor, T., " Computational Methods for Fluid Flow.", Springer, 1984.

[10] Zienkiewicz, O., Szmlter, J and Peraire, J. " Compressible and Incompressible Flow; An Algorithm for all Seasons.", Comp. Methods Appl. Mech. Eng., vol.78, pp.105-121, 1990.

[11] Hughes, T. and Franca, L., " A New Finite Element Formulation for Computational Fluid Dynamics: VII The Stokes Problem with Various Well-Posed Boundary Conditions : Symmetric Formulations That Converge for All Velocity/Pressure Spaces.", Comp. Methods in Appl. Mech. and Eng., vol.65, pp.85-96. 1987.

[12] Pironneau, O., Proceedings of a Workshops on " Algorithmic Trends in CFD.", Hampton, VA. 1991, to be published by Springer Verlag.

[13] Hafez, M. and Fernandez, C. " Finite Element Simulation of Compressible Flows with Shocks.", AIAA paper 91-1551.

[14] Jiang, B. and Povinelli, L. " Least Squares Finite Element Method for Fluid Dynamics.", NASA TM 102352-ICOMP 89-23.

[15] MacCormack, R., " A Numerical Method for Solving the Equations of Compressible Viscous Flow.", AIAA J., vol.20, no.9, pp.1275-1281, 1982.

[16] Baruzzi, G., Habashi, W. and Hafez, M., " An Improved Finite Element Method for the solution of the Compressible Navier-Stokes Equations", submitted to National Fluid Dynamics Congress, L.A. CA. 1992.

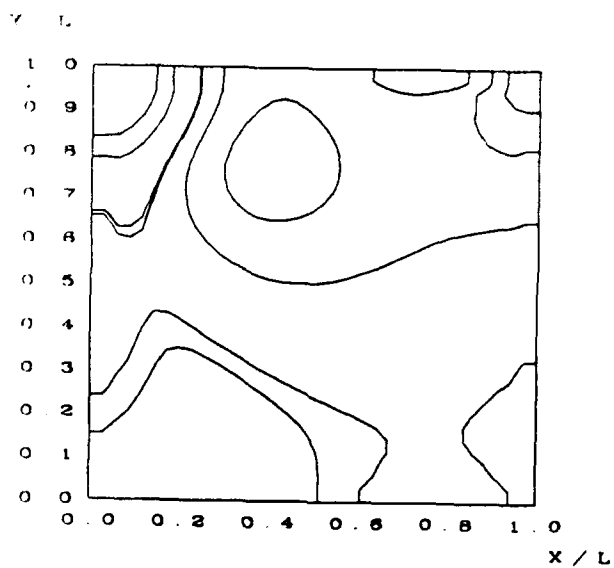


Fig.(I-a) Pressure contours  
Incompressible Flow  
Grid 36x36

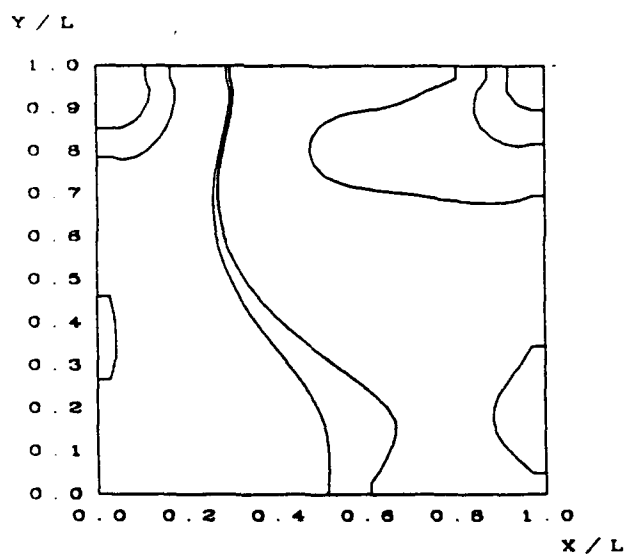


Fig.(I-b) Pressure Contours  
Compressible Flow ( $M_r=0.4$ )  
Grid 36x36



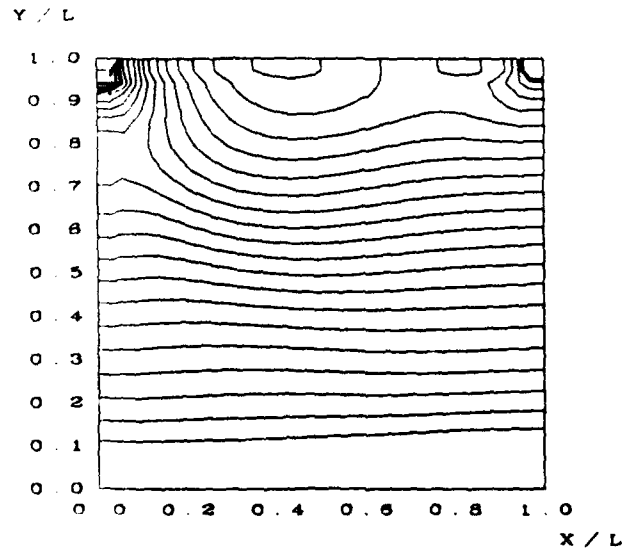


Fig.(I-c) Pressure Contours  
Incompressible Flow  
Grid 36x36  
Upper Wall Temp.= 1.0  
Lower Wall Temp.= 0.5

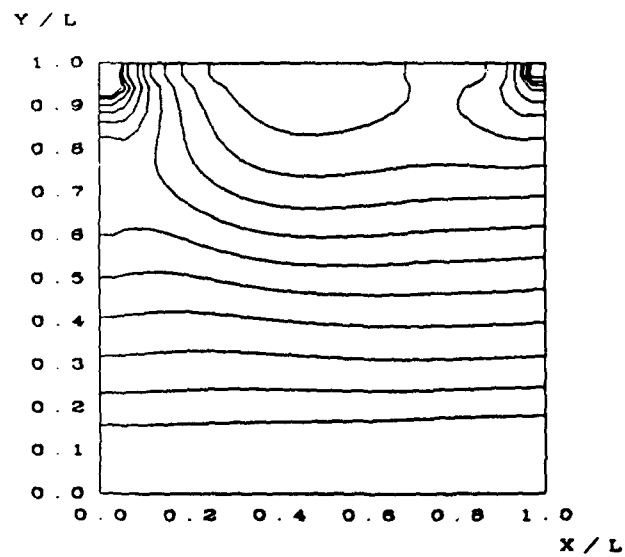


Fig.(I-d) Pressure Contours  
Compressible Flow ( $M_r=0.4$ )  
Grid 36x36  
Upper Wall Temp.= 1.0  
Lower Wall Temp.= 0.5

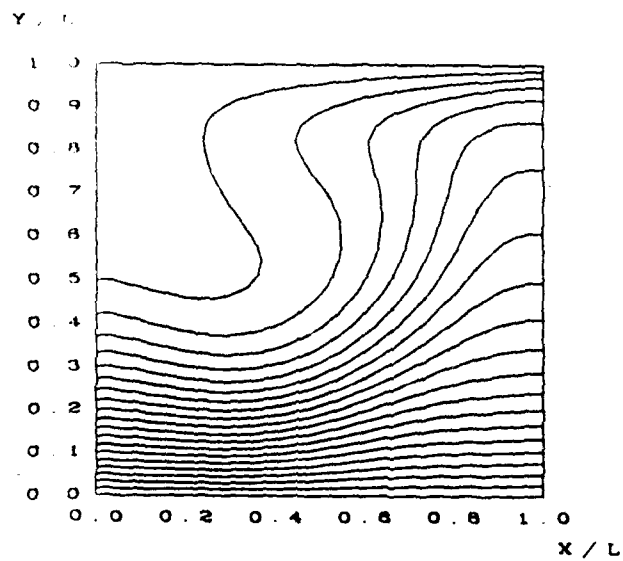


Fig.(I-e) Temperature Contours  
Incompressible Flow  
Grid 36x36  
Upper Wall Temp.= 1.0  
Lower Wall Temp.= 0.5

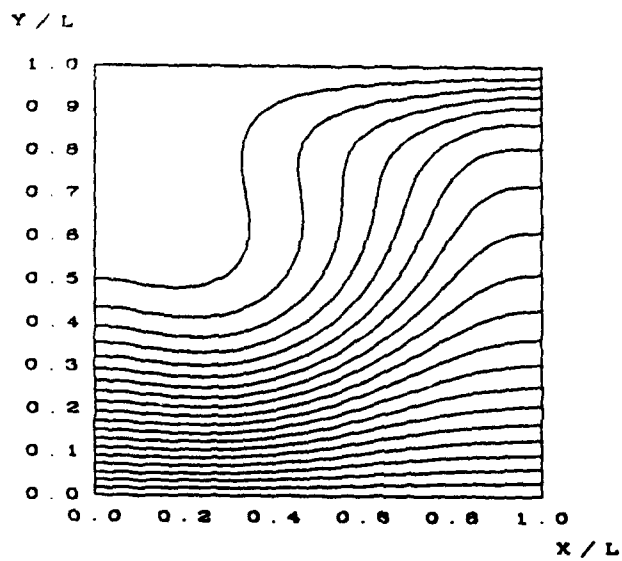


Fig.(I-f) Temperature Contours  
Compressible Flow ( $M_r=0.4$ )  
Grid 36x36  
Upper Wall Temp.= 1.0  
Lower Wall Temp.= 0.5

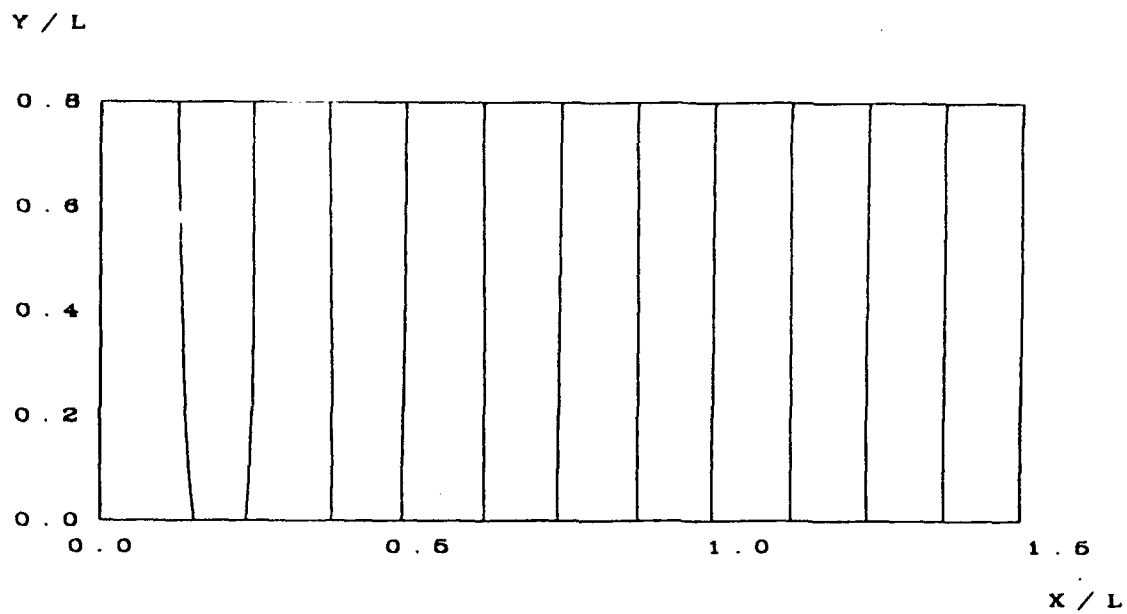


Fig.(II-a) Pressure Profiles  
Incompressible Flow  
Grid 26x31

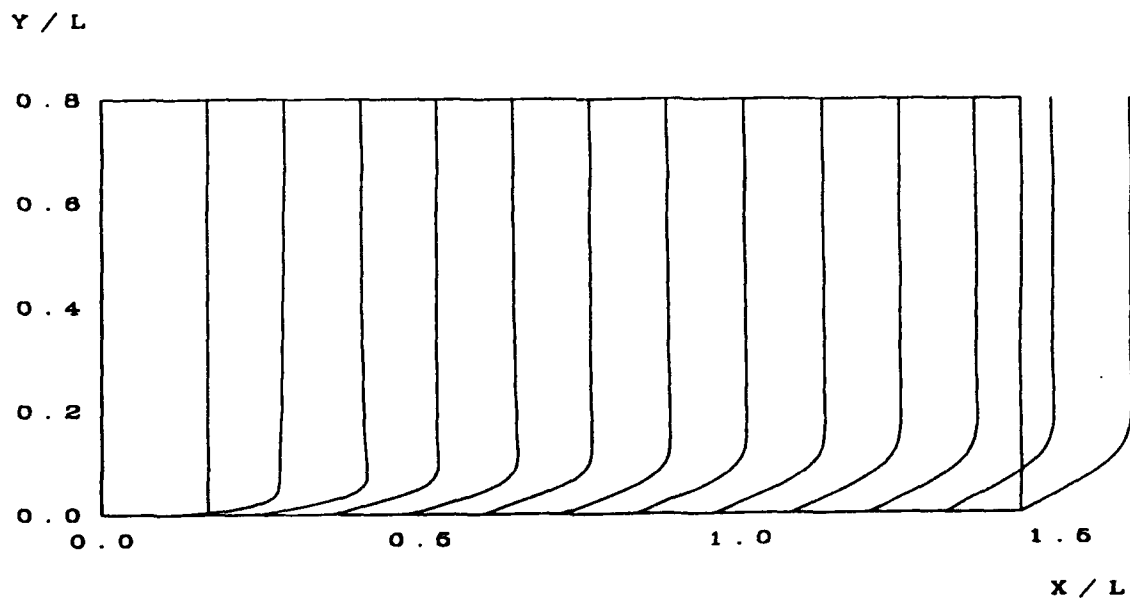


Fig.(II-b) Velocity Profiles  
Incompressible Flow  
Grid 26x31

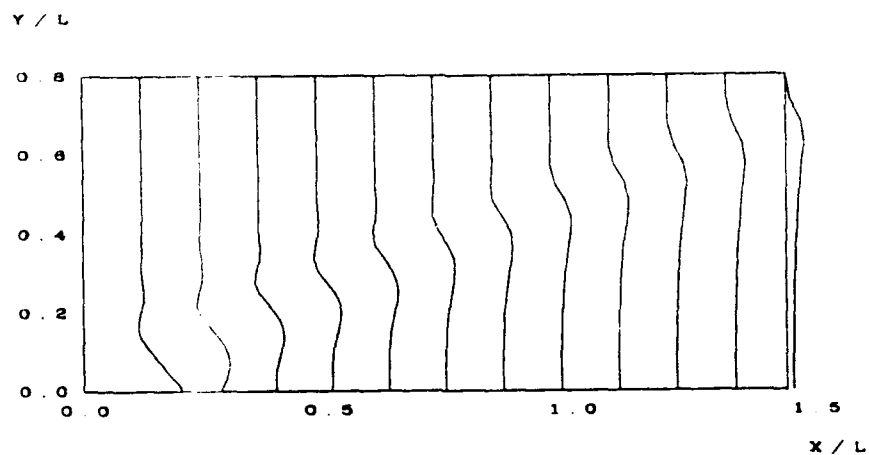


Fig.(II-c) Pressure Profiles  
Supersonic Flow ( $M_{\infty}=3$ )  
Grid 26x31

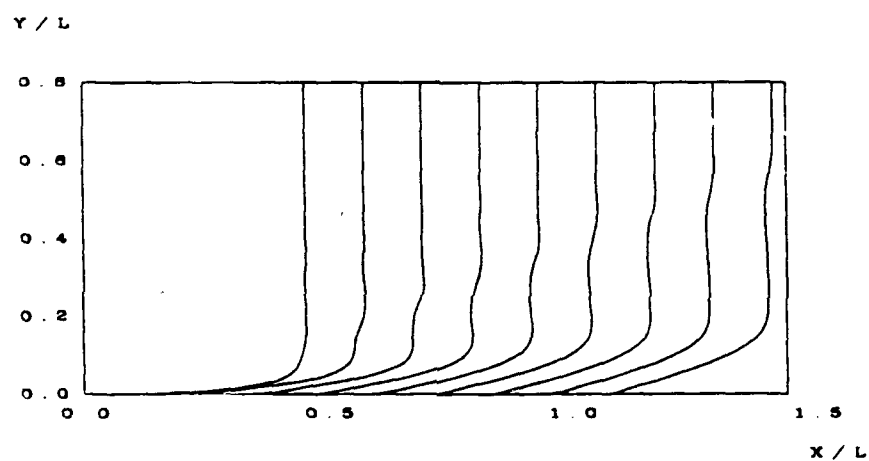


Fig.(II-d) Velocity Profiles  
Supersonic Flow ( $M_{\infty}=3$ )  
Grid 26x31

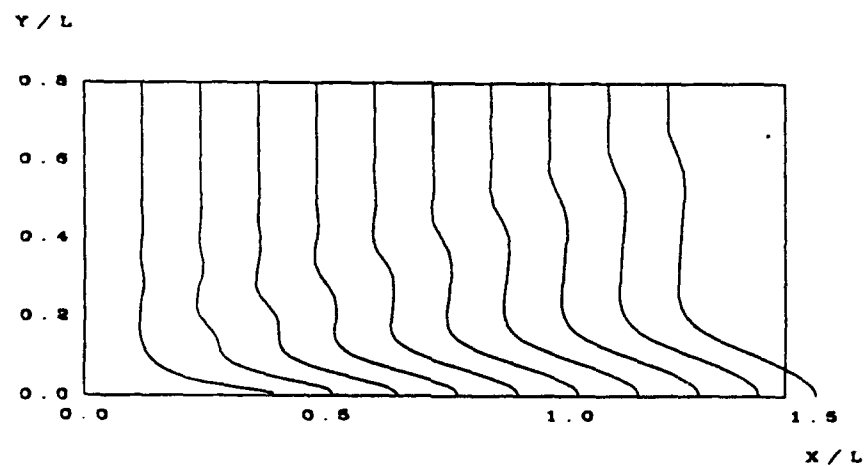


Fig.(II-e) Temperature Profiles  
Supersonic Flow ( $M_{\infty}=3$ )  
Grid 26x31

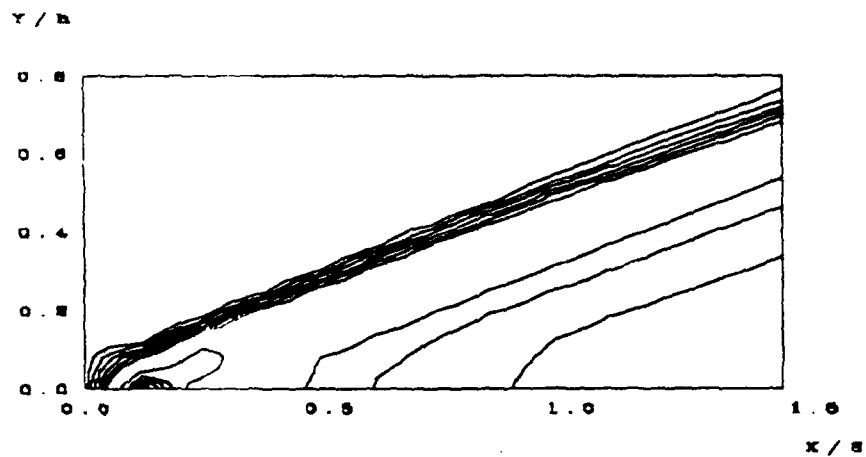


Fig.(II-f) Pressure Contours  
Supersonic Flow ( $M_\infty=3$ )  
Grid 26x31

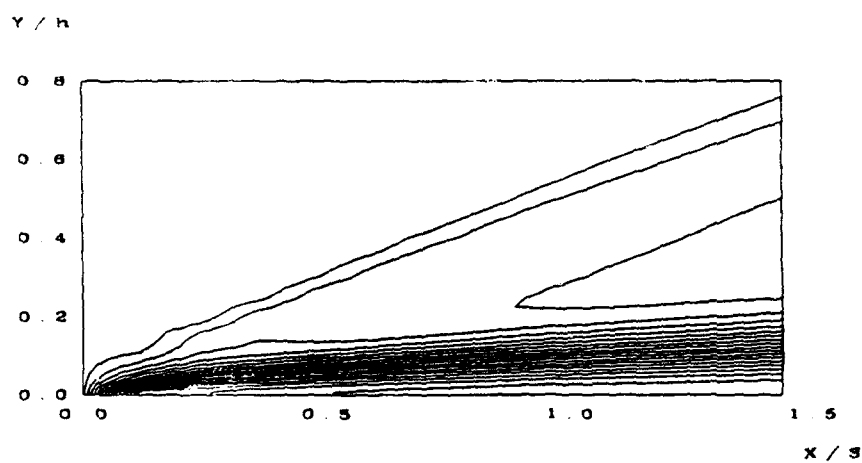


Fig.(II-g) Temperature Contours  
Supersonic Flow ( $M_\infty=3$ )  
Grid 26x31

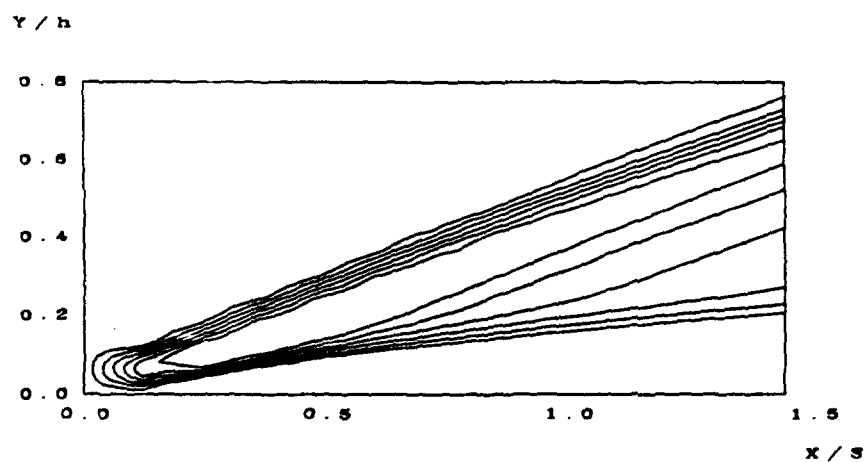


Fig.(II-h) Density Contours  
Supersonic Flow ( $M_\infty=3$ )  
Grid 26x31

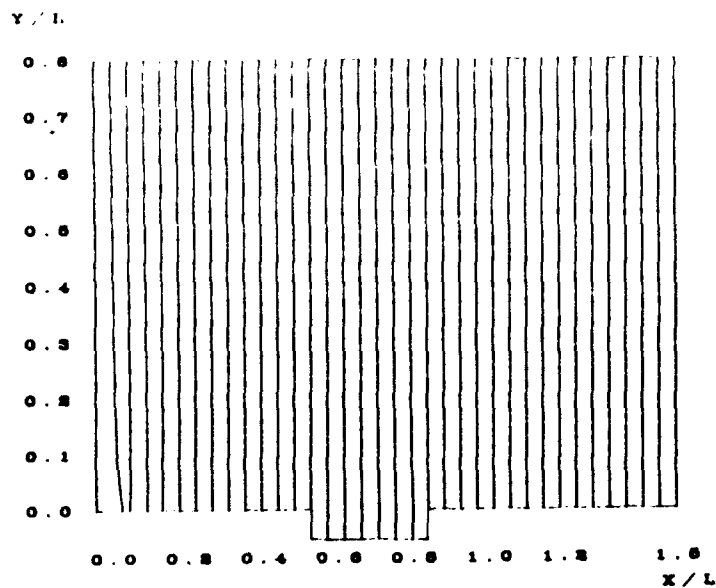


Fig.(II-i) Pressure Profiles  
Supersonic Flow ( $M_\infty = 3$ )  
Grid 36x38

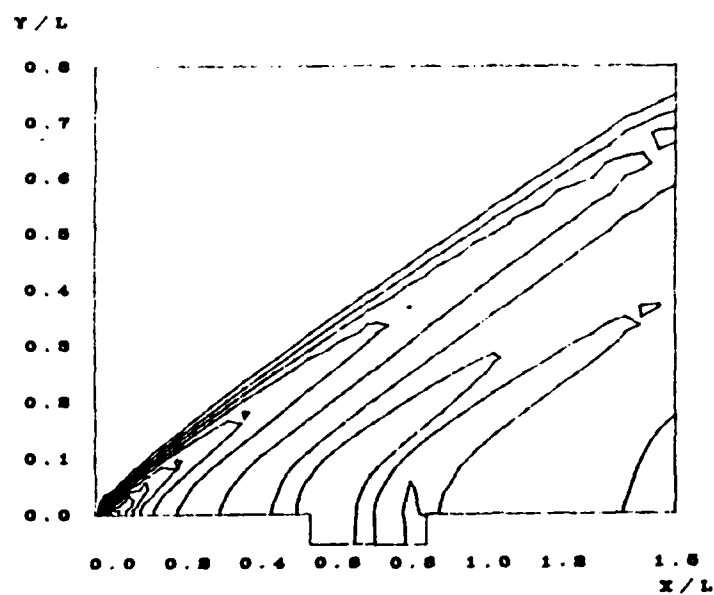


Fig.(II-j) Pressure Contours  
Supersonic Flow ( $M_\infty = 3$ )  
Grid 36x38

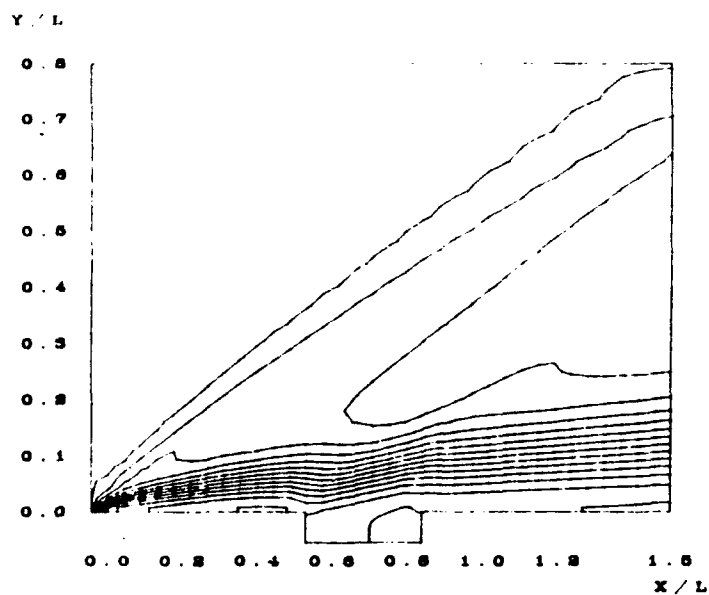


Fig.(II-k) Temperature Contours  
Supersonic Flow ( $M_{\infty}=3$ )  
Grid 36x38

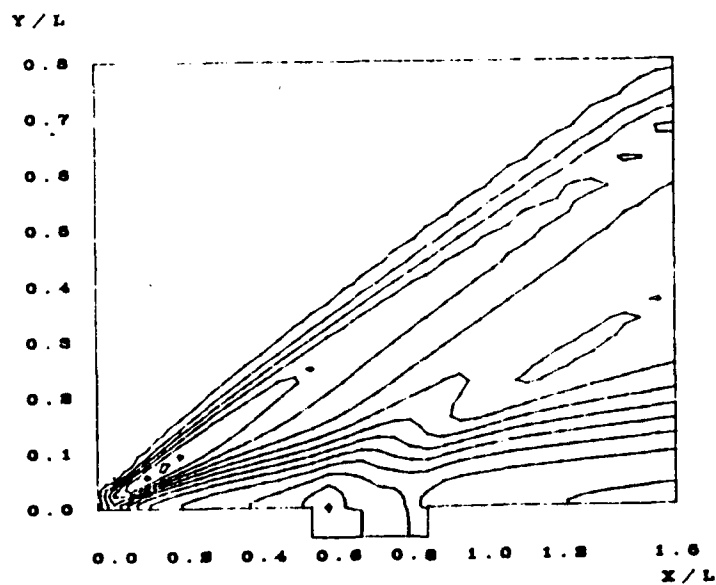
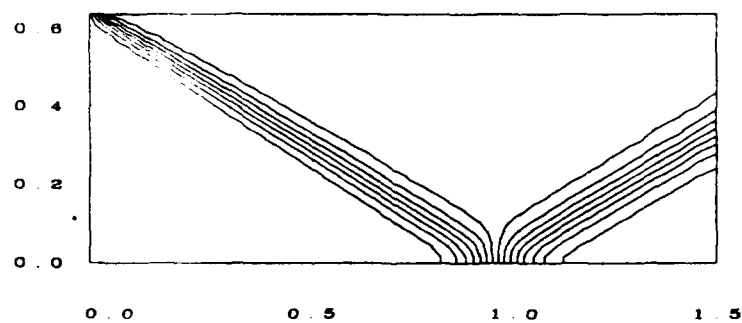


Fig.(II-l) Density Contours  
Supersonic Flow ( $M_{\infty}=3$ )  
Grid 36x38

$y/h$

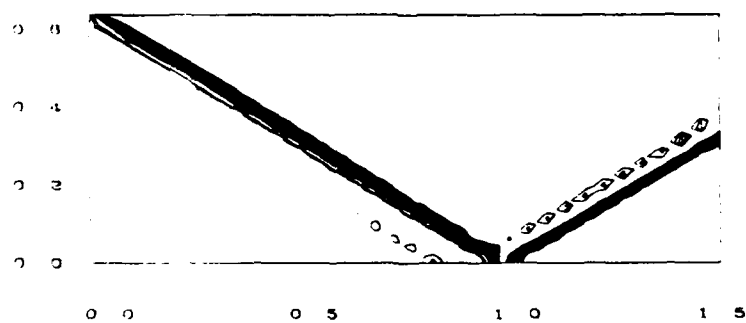


$x/s$

Fig.(III-a) Pressure Contours  
Inviscid Flow ( $M_\infty=2$ )

Grid 34x44  
Viscosity Method #1

$y/L$



$x/L$

Fig.(III-b) Pressure Contours  
Inviscid Flow ( $M_\infty=2$ )

Grid 34x44  
Viscosity Method #2



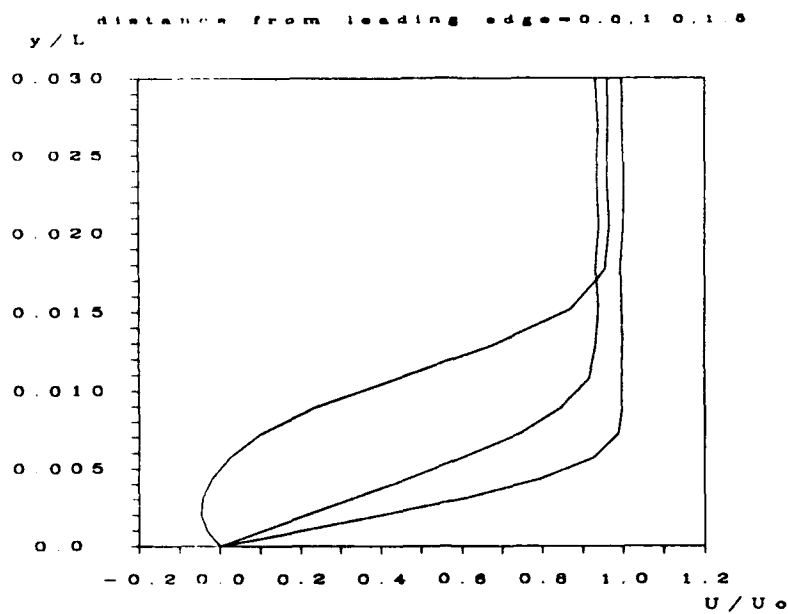


Fig.(III-c) Velocity Profiles  
Viscous Flow ( $M_\infty=2$ )

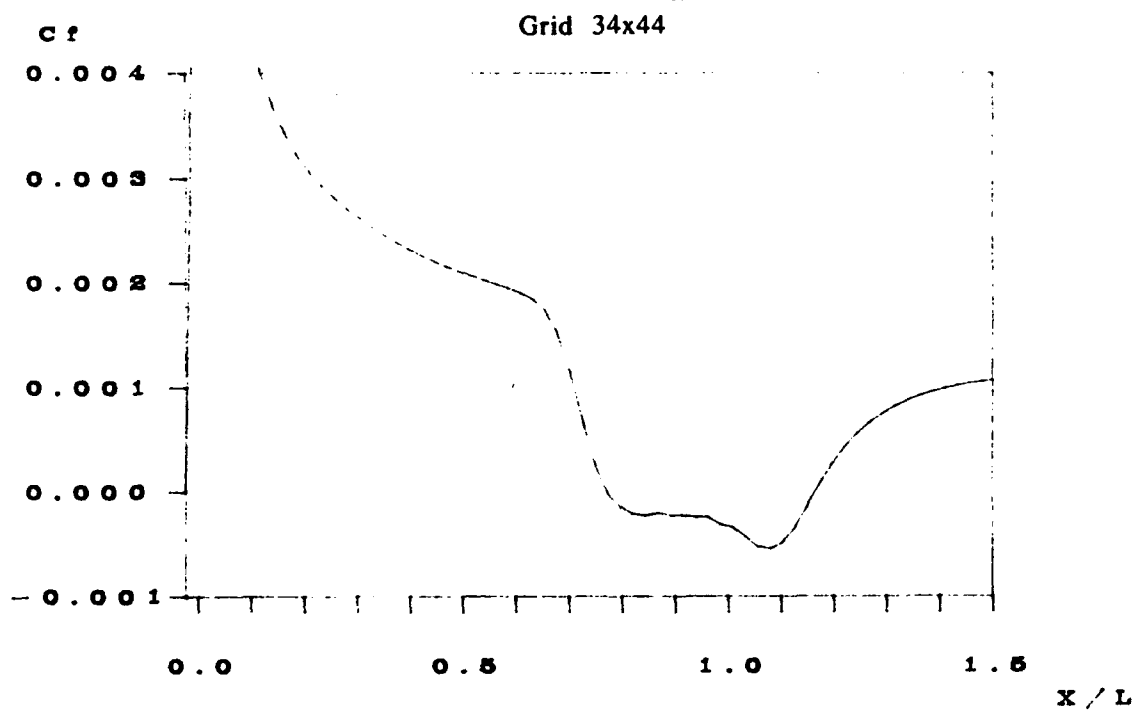
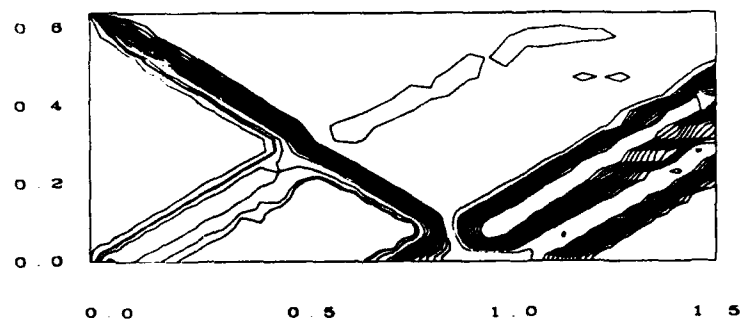


Fig.(III-d) Skin Friction Distribution  
Viscous Flow ( $M_\infty=2$ )  
Grid 56x44

Y / L

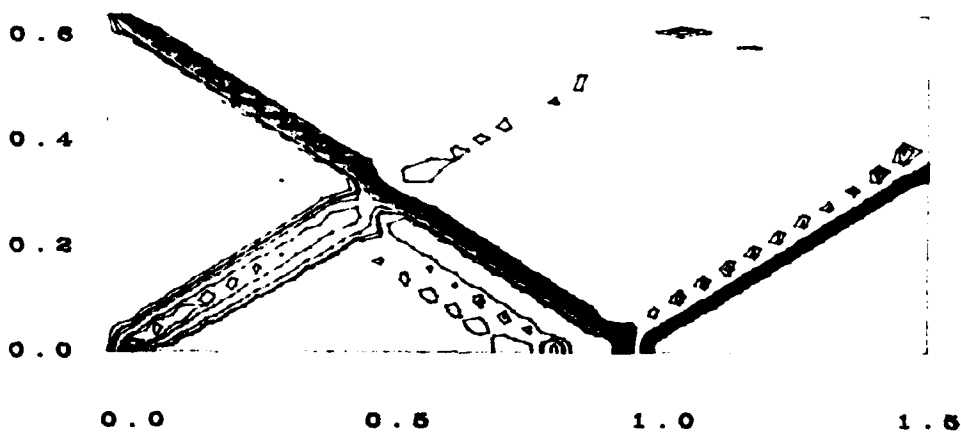


X / L

Fig.(III-e) Pressure Contours  
Viscous Flow ( $M_\infty=2$ )

Grid 34x44  
Viscosity Method #1

Y / L



X / L

Fig.(III-f) Pressure Contours  
Viscous Flow ( $M_\infty=2$ )

Grid 34x44  
Viscosity Method #2

**TWO- AND THREE-DIMENSIONAL FLOWS, 2**  
**SESSION 10**

# PREDICTION OF VORTEX BREAKDOWN ON A DELTA WING

S. Agrawal\*  
B. A. Robinson\*\*  
R. M. Barnett†

McDonnell Aircraft Company  
McDonnell Douglas Corporation  
St. Louis, Missouri 63166

## Abstract

Recent studies of leading-edge vortex flows with computational fluid dynamics codes using Euler or Navier-Stokes formulations have shown fair agreement with experimental data. These studies have concentrated on simulating the flowfields associated with a sharp-edged flat plate  $70^\circ$  delta wing at angles of attack where vortex breakdown or burst is observed over the wing. There are, however, a number of discrepancies between the experimental data and the computed flowfields. The location of vortex breakdown in the computational solutions is seen to differ from the experimental data and to vary with changes in the computational grid and freestream Mach number. There also remain issues as to the validity of steady-state computations for cases which contain regions of unsteady flow, such as in the post-breakdown regions. As a partial response to these questions, a number of laminar Navier-Stokes solutions have been examined for the  $70^\circ$  delta wing. The computed solutions are compared with an experimental database obtained at low subsonic speeds. The convergence of forces, moments and vortex breakdown locations are also analyzed to determine if the computed flowfields actually reach steady-state conditions.

## Introduction

High angle of attack maneuvering has become an integral part of the flight envelopes for current and future fighter aircraft. At such flight conditions vortical flow is a dominant feature of the flowfield. Vortex flows include complex features such as massive flow separation, and breakdown or bursting of vortices, that are not well understood at present and are topics of active research. The bursting of the vortex may result in several adverse effects, such as an abrupt change in pitching moment, loss in lift, and buffet, and can be a serious limitation of its maneuverability. Predicting and understanding such flowfields is, therefore, very important.

Vortex breakdown or burst is characterized by a sudden deceleration of the axial flow in the vortex core, and a decrease in the circumferential velocity associated with the rapid expansion of the vortex core (Ref 1). The vortex burst phenomenon has been the subject of much study, both experimentally (Refs 1,2) and theoretically (Refs 3,4) for more than two decades. A detailed survey

of the research conducted in this subject area is provided in Refs 2-4. The theoretical studies thus far have been for relatively simple cases, such as a vortex confined in a tube, or an isolated vortex. Although many experiments have been performed to help understand breakdown, there is still no general agreement regarding the essential mechanism of vortex breakdown, and no reliable criterion is available to predict vortex breakdown location for a broad range of geometries and flight conditions.

A flat plate delta wing with sharp leading edges presents a simple configuration for the study of vortical flows, including breakdown. Several investigators have analyzed the flowfields past delta wings at high angles of attack, both experimentally (Refs 5-7) and numerically (Refs 8-13). Numerical investigations have been carried out using both Euler and Navier-Stokes formulations. It has been shown that vortex trajectories are predicted quite well, at least in the pre-breakdown regions, using both Euler and Navier-Stokes equations for a sharp-edged delta wing (Ref 12). Breakdown locations are predicted somewhat better using the Navier-Stokes equations, although correlation between the computed and experimental data for breakdown locations is still inadequate.

The majority of studies reported in the literature are based on steady-state calculations, primarily due to the enormous computation time associated with time-accurate solutions. Since the flowfield in the post-breakdown region is inherently unsteady, caution must be exercised in interpreting steady-state results. Flowfields predicted in the vortical flow region are found to be strongly dependent on the grid density. For adequate resolution of the vortical flowfields, a large number of grid points are required, thus increasing the computational time proportionately. Compressibility also plays a role in modifying the structure of the leading-edge vortex, and thereby its breakdown location. These are the issues that are addressed in this paper using computational solutions. Specifically, the effects of compressibility and grid enrichment on vortex breakdown locations are discussed. Although only steady-state solutions of the Navier-Stokes equations are used to characterize flowfields, issues related to unsteady effects are also addressed.

## Grid Topology and Numerical Method

An H-O type grid topology for a half-plane model of the delta wing was used in this study. Figure 1 shows the geometry used in this study. Only cases without sideslip were considered, so a half-plane wing provided the best grid resolution

\* Technical Specialist - Aerodynamics  
\*\* Engineer - Aerodynamics  
† Senior Engineer - Aerodynamics

around the wing for a given number of points. For most calculations, the grid dimensions were 61 (axial), 65 (radial), and 89 (circumferential), with 41 points along the wing in the chordwise direction. This grid will be referred to as the medium grid in this paper. A grid embedding technique was also utilized to refine the medium grid around the leading edge and the upper surface of the wing from the apex to the trailing edge. The extent of embedding in the normal direction was just far enough to include the region where most of the vortical flow phenomena was observed. This refinement of the medium grid yielded an embedded region with dimensions of 81 (axial), 87 (radial), and 133 (circumferential).

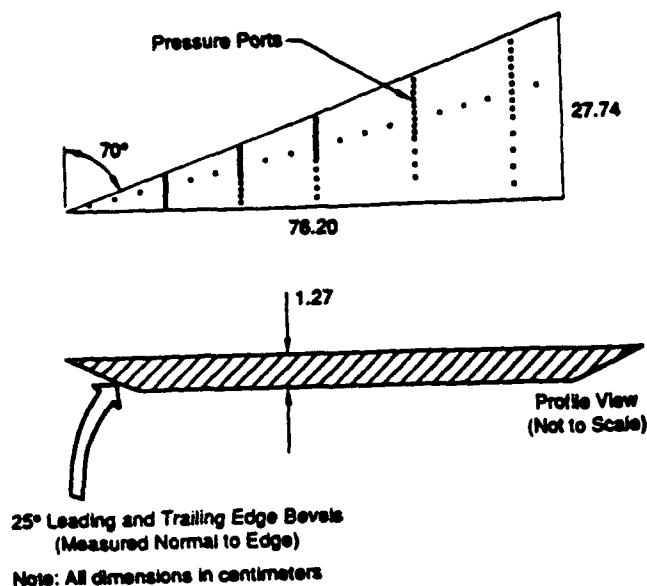


Fig. 1 Flat Plate Semispan Delta Wing Model

The grid was constructed by successive generation of two-dimensional (2-D) grids normal to the wing centerline. These 2-D grids were generated using a method that solves an elliptic system of partial differential equations (Ref 14). This procedure results in a high quality, orthogonal grid, even near difficult areas such as the sharp leading edge of the wing.

The CFL3D Euler/Navier-Stokes code (Ref 15) was used to calculate all of the flowfields in this study. The computational algorithm is based on a thin-layer approximation to the three-dimensional, time-dependent, conservation law form of the compressible Navier-Stokes equations. The code solves the discretized flow equations implicitly using an upwind-biased spatial differencing scheme with either flux difference splitting or flux vector splitting for the convective and pressure terms, and central differencing for the shear stress and heat transfer terms. In this study, the Roe-averaged flux difference splitting is applied for the spatial terms. Flux limiting is also used to alleviate oscillations near high gradient flow regions.

## Rossby Number

As the Rossby number has been used in analyzing the majority of results in this paper, a brief discussion of this number is in order here. It is a parameter which is essentially a ratio of the axial and the circumferential momentum in a vortex. A standard definition (Ref 16) is:

$$Ro = \frac{U}{r \Omega}$$

where  $U$  is the core axial velocity,  $\Omega$  is the rotation rate, and  $r$  is an effective radius of the vortex. For a mathematical model these three quantities may be determined analytically, whereas for experimental and numerical solutions an integral-based approach is used. In this approach, a non-dimensional vorticity ( $\omega$ ) is calculated for each cell using Stokes theorem. An area ( $A$ ) of the primary vortical region is defined by the cells that have  $\omega \geq 1$ . This value of  $\omega$  was chosen empirically. The rotation rate and effective radius are then calculated as

$$\Omega = \frac{\sum \omega dA}{2A}, \quad r = \sqrt{\frac{A}{\pi}}$$

The axial velocity is calculated by integrating the velocity component,  $v'$ , along the vortex axis, over an area defining the vortex core,  $A'$ .

$$U = \frac{\sum v' dA'}{\sum dA'}$$

The area  $A'$  is defined by a circle centered at the centroid of vorticity ( $\omega \geq 1$ ) with some small radius consistent with the size of the vortex. This procedure results in a numerically-determined Rossby number. Through correlations with other methods of determining breakdown and experimental data on the flat plate delta wing, it has been found that Rossby numbers corresponding to burst locations are near 1.0 (Ref 13). In the pre-breakdown regions,  $Ro$  is usually high (above 1.8). In the post-breakdown regions, it is usually small (below 0.9) in which case the vortex will not be stable.

## Results

The numerical results presented here have been obtained using the CFL3D code. Calculations were performed at several angles of attack. Due to similarity of the solutions, results are shown only for an angle of attack of 30°. An earlier investigation focused on the vortex breakdown prediction using Euler and Navier-Stokes (laminar and turbulent) solutions on the delta wing. We observed that the laminar results overall provided the best comparison with the test data (Ref 12). Therefore, only laminar solutions were attempted in this study. The Reynolds number based on the root chord ( $Re$ ) was held constant at one million. Calculations at Mach numbers from 0.1 to 0.4 were performed to address the effects of compressibility on the vortical flow and breakdown position. The pre- and post-breakdown flowfield regions were examined using the Rossby number analysis (Ref 13) to investigate flowfield unsteadiness. Also, grid embedding was used to examine grid enrichment effects on predicted vortex breakdown location. Comparisons between the computed and the wind tunnel test data are shown wherever applicable. The test database consists of surface pressures,

three-component Laser Doppler Velocimetry (LDV) and seven-hole probe flowfield surveys (Ref 17).

### Mach Number Effects

The experimental data used for comparison in this study were obtained at a very low freestream Mach number ( $M_\infty \leq 0.05$ ). It is difficult or sometimes impossible to solve these low speed flows with a compressible CFD code since the solution may converge only after a prohibitively large number of iterations. Therefore, earlier numerical investigations (Ref 12) on this geometry were conducted at a freestream Mach number of 0.3, for efficiency considerations.

Even at a relatively low freestream Mach number, the local Mach number in the vortex core may extend into the compressible range. This is due to the accelerated flow at the core of the vortex which may experience local Mach numbers two to three times the freestream value (Ref 17). To determine if compressibility indeed affects the vortex breakdown location, computed solutions at four different freestream Mach numbers ( $M_\infty = 0.1, 0.2, 0.3$ , and  $0.4$ ) were analyzed on the medium grid. Figure 2 shows the effect of freestream Mach number on the local Mach number in the vortex at 25% root chord. It is apparent that the flow in the core of the vortex shown in Figures 2c-2d, corresponding to  $M_\infty = 0.3$  and  $0.4$ , is well into the compressible range (local Mach number  $\geq 0.7$ ). In fact, for  $M_\infty = 0.4$  it reaches the sonic condition. It is interesting to note that for all cases the local maximum Mach number is about two and a half times the freestream value.

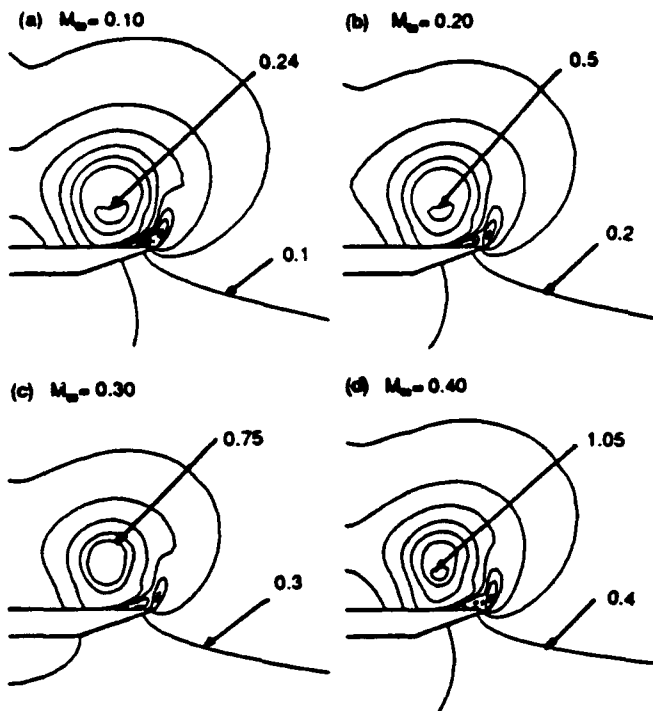


Fig 2. Effect of Freestream Mach Number on Maximum Local Mach Number, Medium Grid,  $\alpha = 30^\circ$ ,  $x/c = 0.25$

The location or trajectory of the leading-edge vortex for the different Mach numbers is shown in Figure 3. Three orthogonal views of the wing are given in this figure to completely define the primary vortex location relative to the wing. Flow visualization data are also shown for comparison. The vortex location from the computed solutions was identified by locating the points of minimum total pressure in the primary vortex at each axial station. The computed vortex trajectories show an insensitivity to compressibility effects as there is good agreement with each other and with experiment in the pre-breakdown region. The figure also indicates that the vortex follows an almost linear path in the pre-breakdown regions, whereas this path becomes random beyond the breakdown. The point of minimum total pressure after breakdown is observed to enter a swirling type motion as it moves downstream. This indicates the spiral-type vortex breakdown that is usually observed on the delta wings. The experimental vortex locations are based on a visual determination of an average vortex center location, and therefore do not exhibit this swirling motion after breakdown.

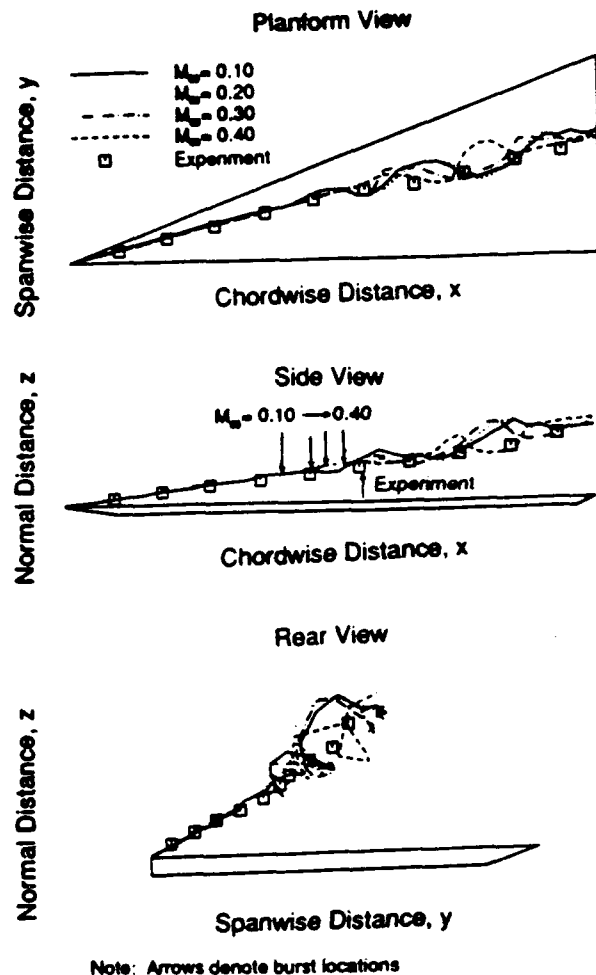


Fig. 3 Comparison of Predicted Vortex Location with Test Data. Medium Grid,  $\alpha = 30^\circ$ ,  $Re = 1 \times 10^6$

Figure 3 also shows that with increased freestream Mach number, the computed breakdown location moves downstream. For the cases analyzed here, the movement is as high as 10% chord. It is postulated that at higher Mach numbers there is a lesser influence of the downstream flowfield on the flowfield upstream of breakdown. Although expected to be the worst prediction of breakdown, the computed location for  $M_\infty = 0.4$  yields the best agreement with the test data. This may be fortuitous, as the test data were obtained at a very low Mach number ( $M_\infty \leq 0.05$ ). However, there are a number of other issues such as wind tunnel wall effects, transition, etc., that may have significant effects on the breakdown locations. No attempt has been made to resolve these issues in this study.

The computational breakdown locations shown in Figure 3 were obtained by examining the axial velocity contours. Ahead of breakdown, the contours usually have a symmetric structure with the maximum axial velocity residing in the well-defined core of the vortex. At axial stations further downstream, however, the core becomes more diffuse. Eventually, the contours become asymmetric with lower axial velocities at the center of the vortex than on the periphery. The breakdown location is thus determined by locating the axial station where this change in the axial velocities is first observed.

This method of determining the breakdown location has been applied successfully for delta wings, and is consistent with experimental observations (Ref 12). This method has also been used to establish a breakdown criterion for delta wings using Rossby number (Ref 13). Figure 4 shows how the Rossby number behaves along the wing chord, for the four different Mach numbers. It has been shown in Ref 13 that when the Rossby number reaches a value on the order of one, breakdown is expected to occur. Although such an observation is based on a very limited amount of experimental and computational results, the present results (Figure 4) also support such a finding. In this figure, the breakdown locations shown in Figure 3 are indicated. As can be observed, the Rossby numbers corresponding to breakdown have values near one.

#### Unsteady Effects

All calculations shown in this study were made using a local time stepping scheme to accelerate convergence. Thus, time-accurate solutions were not obtained. There was evidence, however, of small instabilities in the CFD solutions. These solutions were examined to determine the effects of this unsteadiness on the vortex breakdown location. It should be noted that time-accurate calculations must be performed to obtain data for a true time or frequency response analysis.

Oscillations in the integrated forces and moment histories indicate the presence of inherent flow unsteadiness at high angles of attack. Figure 5 shows typical histories of computed lift, drag, and pitching moment coefficients for  $M_\infty = 0.3$ . Although the solutions appear to be fairly well converged after 1000 iterations, there are oscillations in the forces and moment even after 2400 iterations. The magnitude of the oscillations are, however, on the order of 2% of their mean values. Also, further iterations on the solution did not improve the convergence. The oscillations in forces and moment are indications of inherent flow unsteadiness for such conditions. For improved predictions of vortex breakdown location, it is important to investigate the sensitivity of breakdown location to the flowfield unsteadiness.

Although time-accurate calculations should be used in obtaining the unsteady effects, they require an exorbitant amount of computation time. Therefore, a simpler ad-hoc method was sought for quantifying the effect of unsteady flow on breakdown. The Rossby number has shown promise in predicting flow unsteadiness in the vortical region. Figure 6a shows a typical history of Rossby number at a location (20% root chord) well upstream of breakdown, as the solution is executed for a freestream Mach number of 0.4. Figure 6b shows a similar history at a location (80% root chord) downstream of breakdown. Ahead of breakdown, the Rossby number approaches a nearly constant value (about 1.9) as the solution converges, implying a nearly steady flowfield. On the other hand, downstream of burst, the Rossby number does not converge. This indicates a significant amount of inherent unsteadiness in the post-breakdown region. Such an observation, steady flow upstream of burst and unsteady flow downstream of burst, is also consistent with experimental observations (Ref 17).

The effects of post-breakdown unsteadiness on vortex breakdown location may also be examined using the Rossby number. A breakdown location history determined using a critical Rossby number (assumed to be 1.0, based on Ref 13) for  $M_\infty = 0.4$  is shown in Figure 7. As the solution converges, vortex breakdown first occurs at the trailing edge of the wing and then moves upstream to about 50% root chord. The breakdown location can be observed to be oscillating between chordwise grid planes over approximately 5% root chord after 2000 iterations. Although, the oscillations in burst location shown here are based on computational results using the local maximum time stepping scheme, experimental breakdown location for the 70° delta wing has also been observed to dynamically oscillate about 5% root chord for this angle of attack.

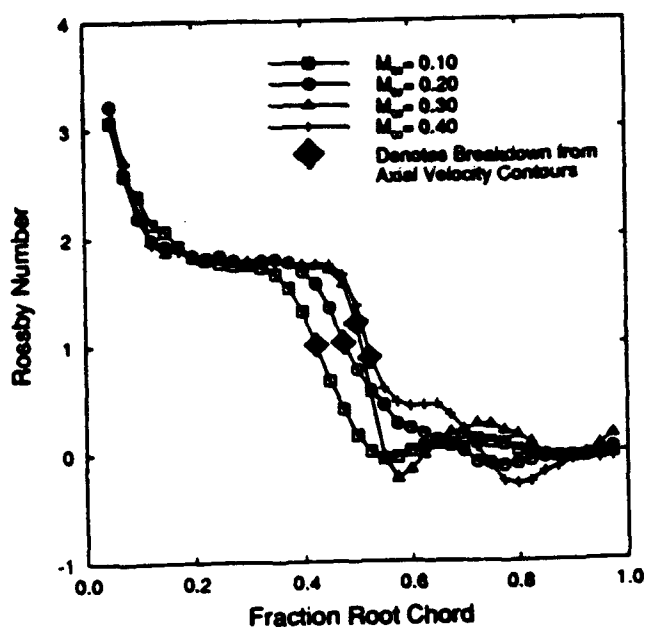


Fig. 4 Effect of Freestream Mach Number on Rossby Number Along the Chord, Medium Grid,  $\alpha = 30^\circ$ ,  $Re = 1 \times 10^6$

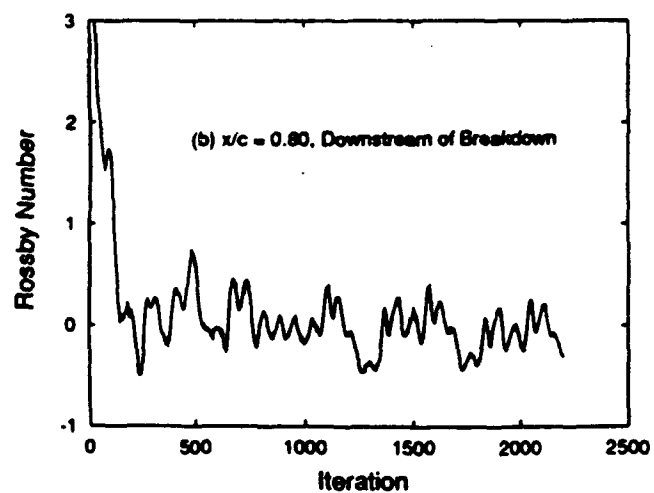
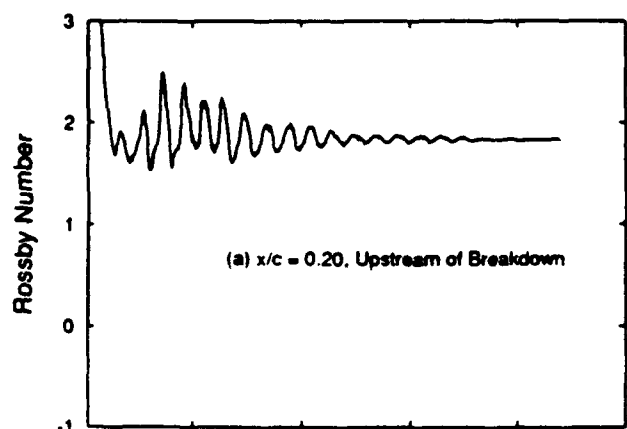


Fig. 6. Typical Rossby Number Histories in Pre- and Post-Breakdown Regions, Medium Grid  $M_\infty = 0.4$ ,  $\alpha = 30^\circ$ ,  $Re = 1 \times 10^6$

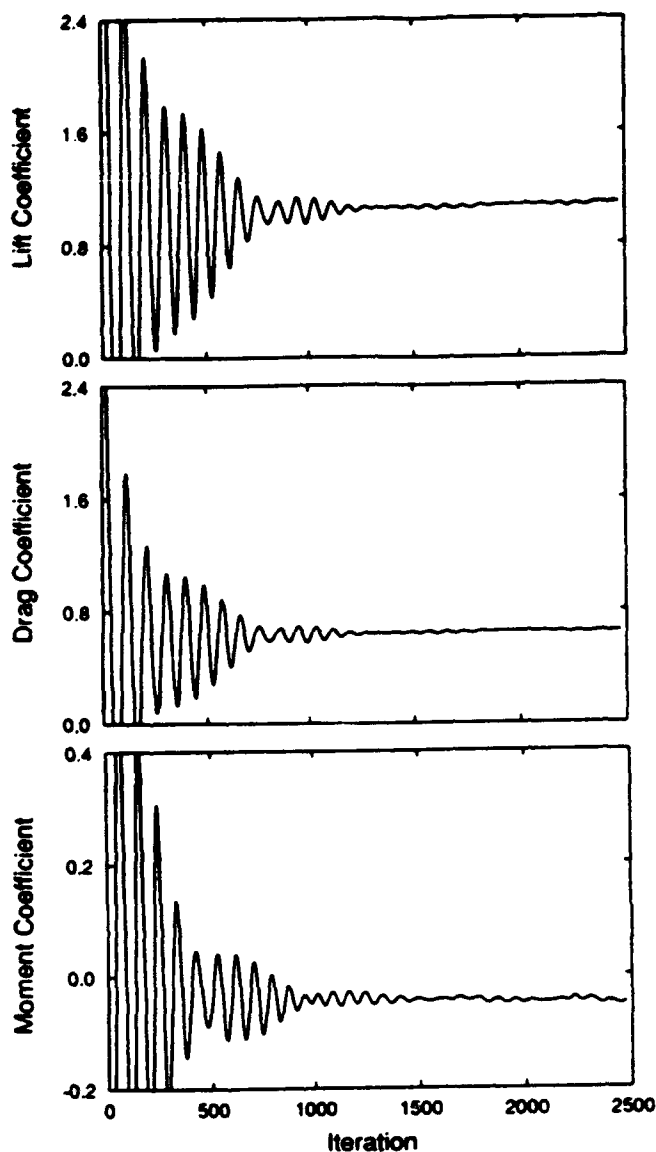


Fig. 5 Force / Moment Histories,  $\alpha = 30^\circ$   
 $M_\infty = 0.30$ ,  $Re = 1 \times 10^6$

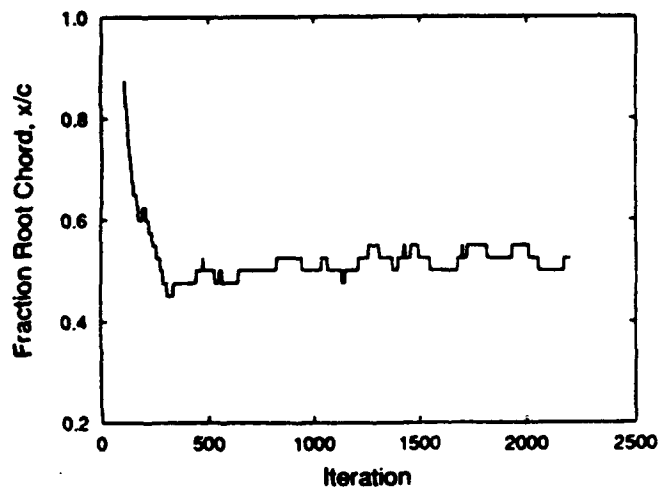


Fig. 7 Vortex Breakdown Location History Corresponding to Rossby Number = 1.0, Medium Grid  $M_\infty = 0.4$ ,  $\alpha = 30^\circ$ ,  $Re = 1 \times 10^6$



## Grid Enrichment Effects

The medium grid used in this study is considered too coarse for adequate resolution of the vortical flowfields. Although only local time stepping was considered for this investigation, adequate spatial resolution of the flowfield is also necessary for time-accurate calculations. To investigate the effect of grid refinement in the vortical flow region, a grid embedding procedure was used in which a subset of the medium grid was enriched equally in all index directions. The grid was enriched over the upper surface of the wing and around the leading edge to better resolve not only the vortical flow region but also the feeding shear layer. The extent of embedding in the normal direction was just far enough to include the region where most of the vortical flow phenomena is observed. This refinement of the medium grid yielded an embedded region with dimensions 81 (axial), 87 (radial), and 133 (circumferential). Figure 8 shows the embedded region in a crossflow plane.

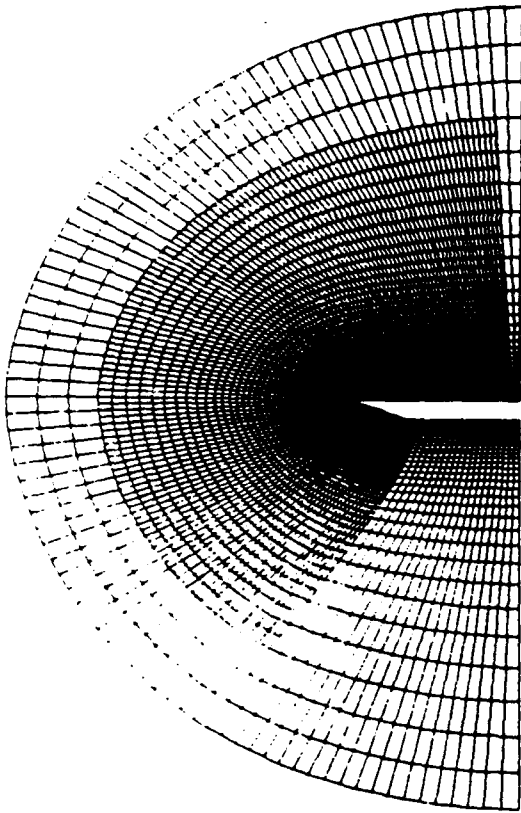


Fig. 8 Cross-Section View of the Embedded Medium Grid  
Grid Dimensions in the Embedded Region: 81 x 87 x 133

The effect of grid refinement on chordwise velocity (normalized by freestream velocity) along a line parallel to the upper surface of the wing is shown in Figure 9. This line was selected to coincide with the maximum chordwise velocity in the LDV data which should be near the center of the primary vortex. Results for both medium and embedded grids are compared with the LDV data. The computed solutions underpredict the velocities compared with experiment, however, grid embedding improves the solution considerably. In general, the shape of the profile is better predicted, although the comparison with the test data is not very good. Without grid embedding, the maximum velocity at the vortex center is only about 2.3 times its freestream value, whereas with grid embedding it is increased to about 3.0, which is closer to the experimental value of about 3.4. Also, outboard of the vortex center location, a slight flattening of the profile is due to the secondary vortex that is predicted better with grid embedding.

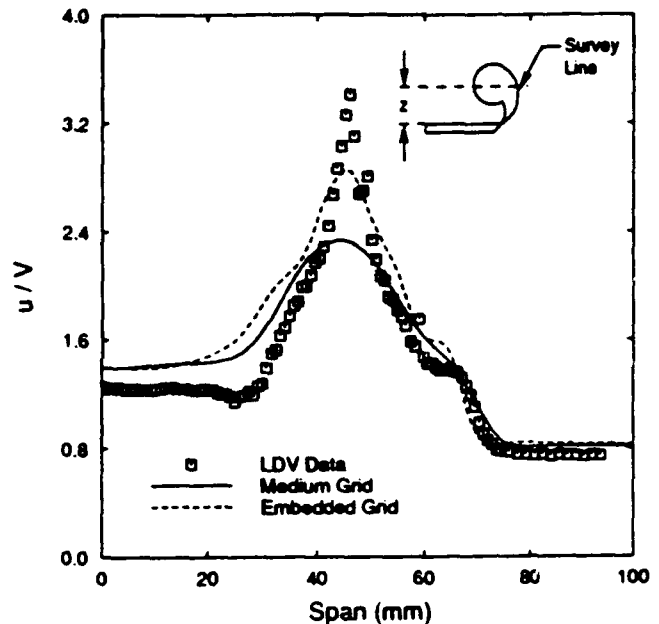


Fig. 9 Comparison of Chordwise Velocity Along a Line  
Parallel to the Wing Upper Surface  
 $M_\infty = 0.3$ ,  $\alpha = 30^\circ$ ,  $Re = 1 \times 10^6$ ,  $x/c = 0.25$ ,  $z = 25$  mm

Improved results with grid embedding can also be seen by analyzing the streamwise vorticity contours (Figure 10). These contours are shown in the pre-breakdown region (25% root chord), for both the medium and embedded grid solutions and also for the experimental data obtained using LDV. Although the computed contour levels are overall very similar to the experimental data, the maximum value of vorticity in the vortex core is nearly 5.5 times greater in the LDV data than in the computed solutions with the medium grid. Much improvement is found with the grid embedding, for which case this ratio is about 3.4. The resolution of vorticity in the secondary vortex region and in the feeding shear layer also is better with the grid embedding.

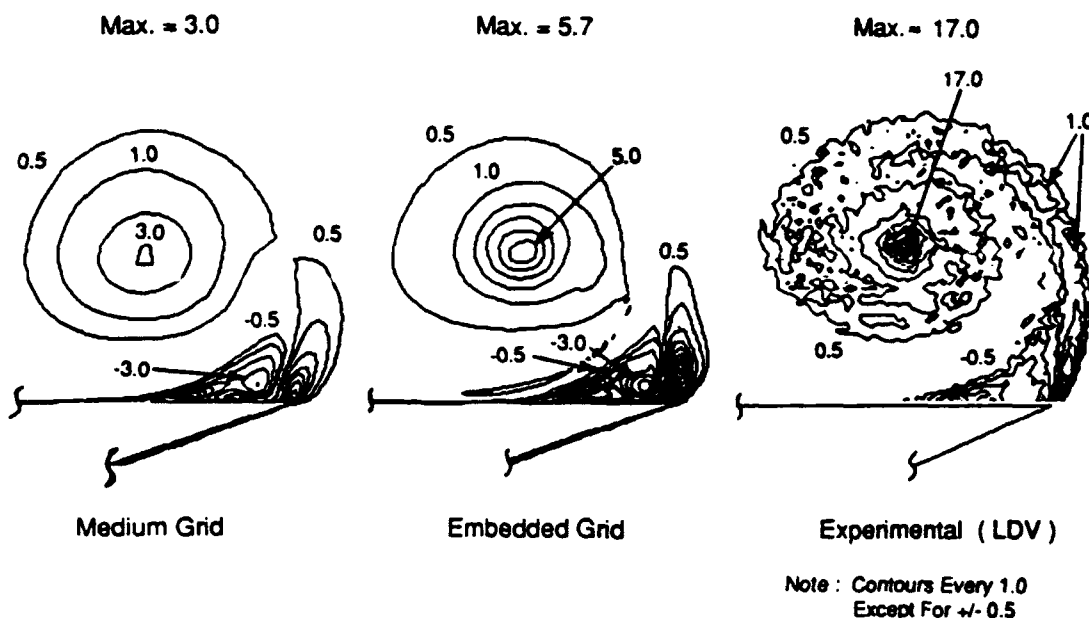


Fig. 10 Comparison of Predicted Vorticity Levels (x-Direction)

Before Burst,  $M_\infty = 0.30$ ,  $\alpha = 30^\circ$ ,  $Re = 1 \times 10^6$ ,  $x/c = 0.25$

Figures 9-10 clearly demonstrate the sensitivity of the grid resolution on flowfield details in the vortical flow regions. The effect of increased grid density on breakdown location, as determined again by the Rossby number of 1.0, is shown in Figure 11. The burst location moves upstream by about 5% root chord with the grid embedding. Unlike the comparisons shown in Figures 9-10, the comparison with the experimental breakdown location has degraded with increased grid density. This discrepancy may be due to not modeling the wind tunnel walls, as the tunnel blockage was approximately 10% at  $40^\circ$  angle of attack.

#### Summary

Effects of Mach number, flowfield unsteadiness, and grid embedding on vortical flow structure and vortex breakdown location were analyzed using Navier-Stokes solutions on a  $70^\circ$  delta wing with sharp leading edge. Analysis was performed for only laminar flow based on previous investigations and in order to eliminate turbulence model effects. The computed results were compared with an experimental database obtained at low subsonic speeds. The computational solutions, in general, showed very good agreement with the test data as far as the vortex trajectories were concerned. However, mixed results were obtained for the streamwise vorticity, velocities near the vortex core, and vortex breakdown locations.

For freestream Mach numbers above 0.3, the computed flow in the core of the vortex was found to be well into the compressible range ( $M_\infty \geq 0.7$ ). In fact, for  $M_\infty = 0.4$  it reached the sonic condition. With the increase in freestream Mach number, the breakdown location moved downstream. The movement was as high as 10% of the root chord for the cases investigated. It is postulated that at higher Mach numbers there is a lesser influence of the downstream flowfield on the flowfield upstream of breakdown.

Oscillations in forces and moment after a few thousand iterations were used as indications of unsteadiness in the flowfield. Although oscillations in forces were less than 2% of their mean values, the breakdown location was found to wander over approximately 5% of the root chord. This was consistent with the test data.

Prediction of the chordwise velocity near the vortex core was improved with grid embedding. Without grid embedding, the maximum velocity at the vortex center was only about 2.3 times its

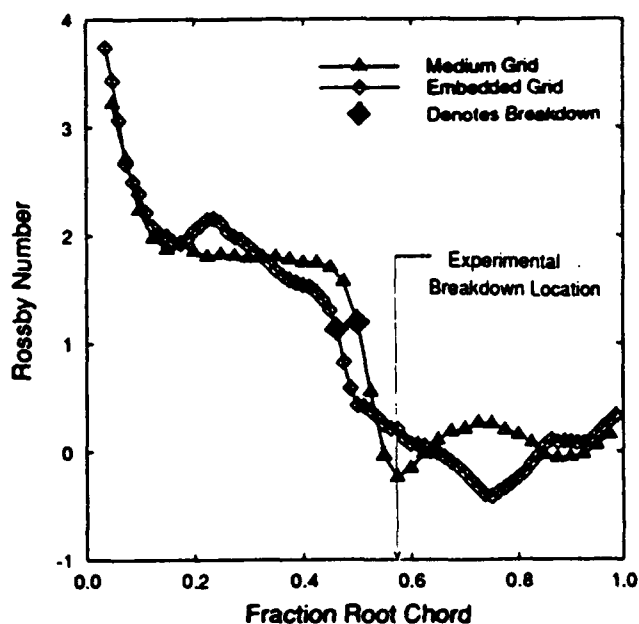


Fig. 11 Effect of Grid Embedding on Rossby Number Along the Chord,  $M_\infty = 0.30$ ,  $\alpha = 30^\circ$ ,  $Re = 1 \times 10^6$

freestream value, whereas with grid embedding it was increased to about 3.0, the experimental value being 3.4. Prediction of streamwise vorticity contour levels was also much improved with the grid embedding. The maximum vorticity contour level increased from 3.0 to 5.0 with the increased grid resolution, experimental value being 17.0. The burst location, however, moved upstream by about 5% root chord, resulting in a degradation in correlation with test data.

The Rossby number value of about 1.0 at vortex breakdown was used in interpreting the majority of results in this study, and provided a useful method for fast determination of vortex breakdown locations. Other issues such as effects of wind tunnel walls, transition, and turbulence modeling still remain unresolved.

#### Acknowledgement

This study was supported by the McDonnell Douglas Independent Research and Development program. Computer resources for this work were provided by the National Aerodynamic Simulation facility as part of a study sponsored by Terry Holst of NASA Ames Research Center. Experimental data was obtained by MCAIR in conjunction with McDonnell Douglas Research Laboratories (MDRL) as part of a United States Navy funded investigation of leading-edge vortex behavior on delta wings.

#### References

1. Lambourne, N.C., and Bryer, D.W., "The Bursting of Leading-Edge Vortices - Some Observations and Discussion of the Phenomenon," A.R.C., R. & M. No. 3282, April 1961.
2. Escudier, M., "Vortex Breakdown: Observations and Explanations," Progress in Aerospace Sciences, Vol. 25, 1988, pp. 189-229.
3. Leibovich, S., "The structure of Vortex Breakdown," Annual Review of Fluid Mechanics, Vol. 10, 1978, pp. 221-246.
4. Leibovich, S., "Vortex Stability and Breakdown: Survey and Extension," AIAA Journal, Vol. 22, No. 9, September 1984, pp. 1192-1206.
5. Wetz, W.H., and Kohlman, P.L., "Wind Tunnel Investigations of Vortex Breakdown on Slender Sharp-Edged Wings," NASA Research Grant NGR-17-002-043, Final Report, November 1968.
6. McKernan, J.F., and Nelson, R.C., "An Investigation of the Breakdown of the Leading Edge Vortices on a Delta Wing at High Angles of Attack," AIAA-83-2114, August 1983.
7. Kegelmann, J.T., and Roos, F.W., "Effects of Leading-Edge Shape and Vortex Burst on the Flowfield of a 70-degree-Sweep Delta Wing," AIAA-89-0086, January 1989.
8. Hitzel, S.M., "Wing Vortex Flows Up Into Vortex Breakdown, A Numerical Simulation," AIAA-88-2518-CP, June 1988, pp. 73-83.

9. O'Neil, P.J., Barnett, R.M., and Louie, C.M., "Numerical Solution of Leading-Edge Vortex Breakdown Using an Euler Code," AIAA-89-2189, July 1989. (also to appear in Journal of Aircraft).
10. Hartwich, P.M., Hsu, C.H., Luckring, J.M., and Liu, C.H., "Numerical Study of the Vortex Burst Phenomenon for Delta Wings," AIAA-88-0505, January 1988.
11. Ekaterinaris, J.A., and Schiff, L.B., "Vortical Flows over Delta Wings and Numerical Prediction of Vortex Breakdown," AIAA-90-0102, January 1990.
12. Agrawal, S., Barnett, R.M., and Robinson, B.A., "Investigation of Vortex Breakdown on a Delta Wing Using the Euler and Navier-Stokes Equations," AGARD-FDP Symposium on Vortex Flow Aerodynamics, AGARD-CP-494, Paper No. 24, July 1991. (also to appear in AIAA Journal).
13. Robinson, B.A., Barnett, R.M., and Agrawal, S., "A Simple Criterion for Vortex Breakdown," AIAA-92-0057, January 1992.
14. Thomson, J.F., Thames, F.C., and Mastin, C.W., "Automatic Numerical Generation of Body-Fitted Curvilinear Coordinate System for Field Containing Any Number of Arbitrary Two-Dimensional Bodies," Journal of Computational Physics, Vol. 15, No. 3, July 1974, pp. 299-319.
15. Thomas, J.L., Taylor, S.L., and Anderson, W.K., "Navier-Stokes Computations of Vortical Flows Over Low Aspect Ratio Wings," AIAA-87-0207, January 1987.
16. Batchelor, G.K., "An Introduction to Fluid Dynamics," Cambridge University Press, 1967.
17. O'Neil, P.J., Roos, F.W., Kegelmann, J.T., Barnett, R.M., and Hawk, J.D., "Investigation of Flow Characteristics of a Developed Vortex," Final Report, NADC-89114-60, May 1989.

PLUME EFFECTS ON THE FLOW AROUND A BLUNTED CONE  
AT HYPERSONIC SPEEDS

P. Atcliffe, D. Kumar & J. L. Stollery  
College of Aeronautics  
Cranfield Institute of Technology  
Cranfield, Bedford, U.K.  
MK43 0AL

**ABSTRACT**

Tests at  $M = 8.2$  show that a simulated rocket plume at the base of a blunted cone can cause large areas of separated flow, with dramatic effects on the heat transfer rate distribution. The plume has been simulated by solid discs of varying sizes or by an annular jet of gas. Flow over the cone without a plume is fully laminar and attached. Using a large disc, the boundary layer is laminar at separation at the test Reynolds number. Transition occurs along the separated shear layer and the boundary layer quickly becomes turbulent. The reduction in heat transfer associated with a laminar separated region is followed by rising values as transition occurs and the heat transfer rates towards the rear of the cone substantially exceed the values obtained without a plume. With the annular jet or a small disc, separation occurs much further aft, so that heat transfer rates at the front of the cone are comparable with those found without a plume. Downstream of separation the shear layer now remains laminar and the heat transfer rates to the surface are significantly lower than the attached flow values.

**INTRODUCTION**

A rocket exhausting from the rear of a vehicle can severely modify the flow in the base region. In particular, exhaust jets can expand so spectacularly at high altitude that flow separation is induced over the rear of the body ahead of the jet plume.

The flow over a blunted cone at  $M_\infty = 8.2$  was studied in the experiments described here. The exhaust plume was simulated initially by attaching one of a number of solid discs of varying sizes to the base of the cone; in later tests, a radial jet of gas (air, helium or argon) was used to more closely model a real plume. Platinum thin film gauges measured the heat transfer rates on the cone surface and schlieren photographs showed the separated flow patterns.

**EXPERIMENTAL DETAILS**

**The Hypersonic Gun Tunnel**

A sketch of the tunnel is shown in figure 1. Measurements of reservoir pressure, made at the end of the barrel, and stagnation pressure in the test section, confirm calibrations made earlier.<sup>1,2</sup>

The test conditions, based on the assumption of perfect gas flow, were:

$$\begin{aligned}M_\infty &= 8.2, R_\infty = 2.37 \times 10^5 \text{ per inch} \\p_\infty &= 0.138 \text{ psia}, P_{0_\infty} = 1580 \text{ psia} \\T_\infty &= 89.3\text{K}, T_{0_\infty} = 1290\text{K}\end{aligned}$$

The useful running time of the tunnel was approximately 25ms.

**The Blunted Cone Model**

A  $7^\circ$  semi-angle blunted cone model was manufactured from "Macor" machinable glass-ceramic and instrumented with nine platinum thin film gauges as shown in Figure 2. The gauges were painted directly onto the cone surface and baked. Conductive paint provided the electrical connection between the gauges and brass contact rods which, as shown in the figure, ran transversely through the model. The rods were connected to leads which were taken away internally and out through the support sting to the data acquisition system. The gauges were calibrated by immersing the model in a heated oil bath and recording the variation of electrical resistance with temperature over a range of approximately  $20^\circ\text{C}$ .

The discs simulating the plume were made from aluminium and mounted flush against the base of the cone. Later tests were made using a plenum chamber fitting mounted on the support sting aft of the model. The exhaust gas (air, argon or helium) was fed to the chamber from an external supply via four tubes attached to the sting, as shown in figure 2b. The large pressure ratios used, typically between 40 and 250, choked the slot between the base and the plenum chamber, so that a radial jet sheet exhausted into the free stream. The width of the slot could be varied between tests.

**Heat Flux Measurement**

The thin film gauges and data acquisition system produced records of electrical signals which were proportional to the temperature variation of each gauge with time. These signals must be integrated to find the heat transfer rates which are of interest. Two methods were used during these tests.

The first method used an analogue network to convert the signal from each gauge into one proportional to the variation of heat transfer rate with time. Such a network is described by Meyer<sup>3</sup>, and his design was adopted with circuit components chosen to suit the running time of the gun tunnel.

The second method involved numerical integration of the temperature signals, which were either stored digitally on floppy discs or plotted out into hard-copy form. Data points taken from either representation were used to calculate heat transfer rates, using the method described by Schultz and Jones<sup>4</sup>.

Both methods were used initially, but the analogue networks began to deteriorate and become unreliable with age, so that most of the results presented below were found using the numerical technique.

## RESULTS AND DISCUSSION

### Blunted Cone

Figure 3 is a schlieren photograph of the flow around the cone when no exhaust plume is present. The boundary layer is laminar and attached along the full length of the model and the contour of the bow shock is smooth and continuous. As will be seen later, a turbulent layer can generate waves of sufficient strength to visibly perturb the shock shape.

Non-dimensional rates of heat transfer to the cone surface, as measured by the thin film gauges, are plotted in the form of Stanton number vs free-stream Reynolds number based on axial distance  $x$ . Figure 4 shows the heat flux distribution found by Sperinck<sup>5</sup> in an earlier series of tests with an identical model in the Cranfield gun tunnel. The theoretical value for the stagnation point Stanton number is 0.029, so the figure shows how rapidly the distribution falls around the nose of the cone: by the first measuring station,  $St$  is less than 10% of the stagnation value. Figure 4 also presents a theoretical estimate of the heat transfer rate distribution on a sharp cone, calculated using the Mangler transformation on theoretical flat plate values, as described by Crabtree, Dommett and Woodley<sup>6</sup>. Over the instrumented region of the model, both curves show the heat transfer dropping as  $Re_x^{-1/2}$ , which confirms the laminar nature of the flow.

### Blunted Cone With Disc

Discs ranging in size from 1.25 to 2.1 times the base diameter of the cone were fitted at the rear of the model to simulate an underexpanded exhaust plume. Schlieren photographs of the flow over the model showed that the presence of the disc caused separation along a large part of the length of the cone. Figures 5 and 6 illustrate the two extremes of the range of disc sizes tested, with  $d/d_b$  values of 1.25 and 2.1 respectively.

With the smallest disc fitted (figure 5), laminar separation occurs at an  $x/L$  value of slightly under 0.6, followed by a laminar shear layer. Towards the rear of the separated zone, the shear layer thickens, the edge becomes ragged and waves can be seen emanating from the boundary of the separated region.

As the size of the disc increases, the separation position moves forward, as shown in figure 7. The shear layer remains laminar initially but soon becomes wavy and appears turbulent. With the largest disc (figure 6), the detached region begins very close to the nose, separation occurring at  $x/L \approx 0.07$ . The photograph indicates a laminar shear layer rapidly becoming transitional and then turbulent over most of the length of the cone.

Heat transfer measurements were made using discs of size  $d/d_b = 1.25, 1.4$  and  $2.1$ . Results from the latter two cases are shown in figure 8 together with the cone-only distribution. Results from the first case are described later. It is expected that heat transfer in a region of detached laminar flow will be reduced by comparison with that in an attached laminar region. This may be seen by comparing the appropriate portions of the heat flux distributions. In the case of the larger disc ( $d/d_b = 2.1$ ), separation has

already occurred ahead of the first thin film gauge, so that the Stanton number at that point is considerably less than that found in the cone-only case. This is followed by a rising heat transfer rate as the free shear layer undergoes transition to turbulent flow, so that the value of  $St$  exceeds that of the attached flow case over more than half the length of the cone.

For the smaller disc ( $d/d_b = 1.4$ ), separation takes place at about  $x/L = 0.3$ . Ahead of this station the Stanton number is comparable with that of the cone-only case. After separation, the detached laminar region exhibits a drop in  $St$ , followed by a sharp increase as the shear layer becomes turbulent.

These trends agree with those obtained by Needham<sup>7</sup> and Holden<sup>8</sup> in their respective studies of (i) flow past a compression corner and (ii) flow over a step on a flat plate. In both cases, significant reductions in heat transfer rate were found in regions of laminar separated flow with a subsequent rapid rise as transition occurs.

The flow past the cone-disc configuration is reminiscent of that over a spiked body where the bow shock ahead of a blunt body interacts with the boundary layer growing along the spike. The shock wave causes separation and the separation point moves to near the tip of the spike, with dramatic changes to the effective shape of the body. In our tests, the blunted cone represents the spike and the disc, the blunt body. Adding a disc effectively changes the body shape from the initial slender blunted cone to a less-slender cone of semi-angle  $\theta$  given approximately by  $\tan \theta = R/L$ .

### Blunted Cone with Radial Jet

Initial tests with the external gas supply examined the effects of slot size and gas pressure. Air jets with total pressures ranging from 1 to 6 atmospheres were used with slot widths between 0.5 and 4.0 mm. For comparison, the static pressure on the surface of the cone for attached flow was calculated to be about 0.025 atmospheres.

The effect of gap size was found to be small over most of the range of widths tried, and a standard slot size of 4 mm (later, 4.5 mm) was adopted for the remainder of the tests. For a given gap width, the extent of the separated region increased with jet total pressure, as expected, and the variation of separation length with jet pressure for one slot size is included in figure 7. The curve shows that for a supply pressure difference above one atmosphere the increase of separated length with pressure is approximately linear. Clearly, a very high jet pressure would be needed to cause separation near the nose as was achieved with discs with values of  $d/d_b$  greater than about 1.6.

Tests were made using helium and argon as the exhaust gas to assess the effects of using a foreign gas and of gases of differing molecular weights. The results were perhaps surprising: compared to an air jet of the same supply pressure, both argon and helium produced slightly larger separated regions. Assuming choked flow with the gas issuing at a Mach number of one, the jet velocity for helium is three times that of air but the density is only 1/7th. Thus, the mass flow rate for helium is lower than for air, but the momentum and energy fluxes are greater.

For argon, the jet speed is less than that of air by some seven percent, but the density is greater by 38 percent, so that the mass, momentum and energy fluxes all exceed those of air. This would appear to imply that the momentum or energy fluxes are of more importance in determining the extent of separation, but a more careful analysis of duct losses and actual exit conditions would be needed to determine the merits of foreign gas injection.

Heat transfer measurements were made for the case of an air jet with a supply pressure of 75 psig (6.10 atmospheres total pressure) exhausting through a 4.5 mm gap. Figure 9 is a Schlieren photograph of the flow past the model and plume. Separation occurs at  $x/L \approx 0.45$ , after which the by-now familiar pattern of an initially laminar shear layer undergoing transition to turbulent flow over the rear of the body may be seen. The flow is very like that seen in figure 5 for the model with a small disc ( $d/d_b = 1.25$ ), and the separation positions are similar.

Nevertheless, a gas jet will entrain flow in a manner which a solid disc of any size cannot emulate. Hence, for a given separation station, one would expect the shape of the conical separated zone to be more acute with jet-induced separation. The experimental data supports this view.

The flow pattern within the separated region is another example of the difference between using a solid disc and a gas jet to simulate an exhaust plume. Figure 10 shows sketches of patterns proposed by the authors for the mean flow in each case. With a solid disc mounted at the rear of the cone, the separated flow re-attaches itself to the surface of the disc, producing a region of contraflow as one might expect. The situation is more complex with the gas jet: the boundary conditions have changed, and the requirement for the flow near the plume boundary to move outwards with the jet gas necessitates the presence of a pair of counter-rotating vortices to satisfy both that requirement and the need for an area of reversed flow.

The similarity between the air jet and small disc cases is also seen in the heat flux distributions shown in figure 11. Since separation does not occur in either case until well back along the cone body, the Stanton numbers found on the first forty percent of the length of the model are comparable to those obtained for the cone alone. For the air jet case, separation occurs just aft of this point and the heat transfer rate drops dramatically in the region of detached laminar flow, before rising slowly over the rear of the cone as the shear layer appears to become turbulent.

The small-disc case exhibits like behaviour, although separation is slightly further to the rear. Thus, the locations at which the heat flux distribution decreases sharply and then rises gently are a short distance behind those found using the air jet.

As noted previously, the heat transfer rate distributions shown in figures 8 and 11 agree with similar measurements made in other investigations. Figure 12 shows the distribution found by Holden<sup>2</sup> when studying the flow past a step on a flat plate at  $M_\infty = 10$ . The step causes laminar separation on the plate and the heat transfer distribution reflects this behaviour. The separated shear layer subsequently

undergoes transition, and the initial drop in Stanton number is followed by a rapid rise as the layer becomes turbulent.

#### General Comments

Flow steadiness is an important factor in any experiment performed in an intermittent facility like a gun tunnel. In the case of these tests, comparison of schlieren photographs of nominally identical tunnel runs produced confidence that the flow could be considered as reasonably steady. There was inevitably some variation between runs, as indicated by the scatter in the heat flux results, but the photographs showed the flow patterns to exhibit satisfactory repeatability.

It is also worthy of note that the flow past the cone and simulated plume was not perfectly axi-symmetric. It was consistently found during examination of Schlieren photographs that separation on the underside of the model occurred slightly further forward than that on the top side. This indicates that there is a three-dimensional nature to the flow, and the locus of separation points around the surface of the cone is not the circular cross-section of the body expected in perfect axi-symmetric flow.

#### CONCLUSIONS

The flow over a slender blunted cone at  $M_\infty = 8.2$  and  $Re_\infty = 2.37 \times 10^5$  per inch was attached and laminar.

Simulating an exhaust plume from the base of the cone, either by fitting a solid disc or by providing a radial gas jet from a choked slot, produces widespread separation. The larger the disc, or the greater the pressure of the gas jet, the further forward the point of separation moves.

The shear layer is laminar at separation but can undergo transition to fully turbulent flow before reaching the base of the cone and the "plume".

The effect of the laminar shear layer is to decrease the heat transfer rate, by comparison with that for the cone alone, over the surface immediately behind the separation point. As the layer becomes turbulent, the heat transfer rate begins to increase and can exceed that of the cone by itself by a considerable margin. Whether the heat flux on the rear of the cone with plume is greater or less than that of just the cone depends on the extent of the separated region: the further forward the separation point, the higher the heat transfer to the rear of the cone.

#### ACKNOWLEDGEMENTS

This work was sponsored by the UK Ministry of Defence under Contract SLS42B/590. The authors would like to thank the contract monitors Dr. A.Holbeche, Mr. J.Woodley and Dr. P.Marriot for continual encouragement and many helpful discussions. However, the views expressed are those of the authors alone.

British Crown Copyright 1991/MOD. Published with the permission of Her Britannic Majesty's Stationery Office.

# NOTATION

$C_p$	specific heat at constant pressure
$d$	disc diameter = $2R$
$d_B$	base diameter of cone
$L$	cone length (fig.2a)
$L_{sep}$	length of separated region on cone
$M_\infty$	Mach number in the test section
$p_\infty$	static pressure in test section
$P_\infty$	reservoir pressure
$Pr$	Prandtl number (taken as 0.72 here)
$\dot{q}$	heat transfer rate
$\dot{q}_{fp}$	$q$ on flat plate
$R$	disc radius (fig.2a)
$Re_\infty$	Reynolds number per unit length $= \rho_\infty u_\infty / \mu_\infty$
$Re_x$	Reynolds number $= \rho_\infty u_\infty x / \mu_\infty$
$r$	recovery factor $= \sqrt{Pr}$
$St$	Stanton number $= \dot{q} / \rho_\infty u_\infty C_p (T_{aw} - T_\infty)$
$T_{aw}$	adiabatic wall temperature $= T_\infty (1 + r \frac{\gamma-1}{2} M_\infty^2)$
$T_\infty$	temperature in test section
$T_\infty$	reservoir temperature
$u_\infty$	velocity in test section
$x$	axial distance
$\gamma$	ratio of specific heats
$\mu_\infty$	viscosity in test section
$\rho_\infty$	density in test section

# REFERENCES

1. Stollery, J.L., Maull, D.J. and Belcher, B.J. "The Imperial College gun tunnel". J.Royal Aeronautical Society, Volume 64, No.589, p24 (1960).
2. Needham, D.A. "Progress report on the Imperial College hypersonic gun tunnel". Aerodynamics Report No. 118, Imperial College, London (1963).
3. Meyer, R.F. "Further comments on analogue networks to obtain heat flux from surface temperature measurements". National Research Council of Canada Aeronautical Report LR-375 (1963).
4. Schultz, D.L. and Jones, T.V. "Heat transfer measurements in short-duration hypersonic facilities". AGARDograph AG-165 (1973).
5. Sperinck, N.P.B. "The simulation of rocket plume effects on a blunted conical body". M.Sc thesis, College of Aeronautics, Cranfield Institute of Technology (1989).
6. Crabtree, L.F., Dommett, R.L., and Woodley, J.G. "Estimation of heat transfer to flat plates, cones and blunt bodies". RAE Technical Report No. 65137 (1965).
7. Needham, D.A. "Laminar separation in hypersonic flow". Ph.D thesis, Imperial College, University of London (1965). See also: "A heat transfer criterion for the detection of incipient separation in hypersonic flow". AIAA Journal, Volume 3, No.4, p781, April 1965.
8. Holden, M.S. "Heat transfer in separated flows". Ph.D thesis, Imperial College, University of London (1963). See also: "Leading-edge bluntness and boundary-layer displacement effects on attached and separated laminar boundary layers in a compression corner". AIAA Paper 68-68, 6th Aerospace Sciences Meeting, New York (1968).

$M_\infty = 8.2$  ,  $Re_\infty = 9.34 \times 10^6$  per metre ,  $T_{0\infty} = 1290^\circ K$  ,  $P_{0\infty} = 108$  Atmospheres  
Running time = 25 msec.

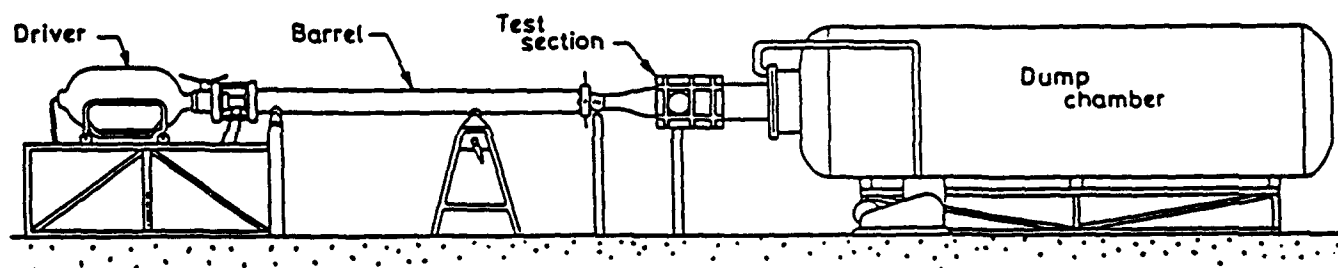


Fig 1. Sketch of the gun tunnel

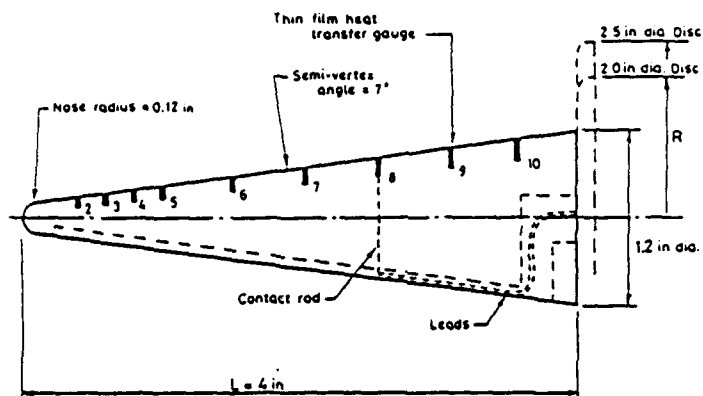


Fig 2a. Blunted cone model showing discs at the base

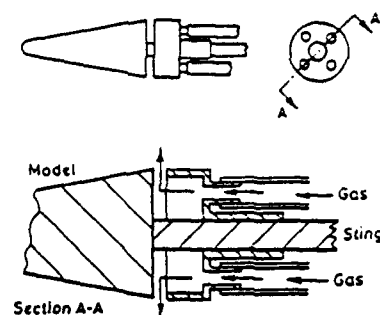


Fig 2b. Same model with adaptor to give a radial jet.



Figure 3. Schlieren photograph of flow past the blunted cone.

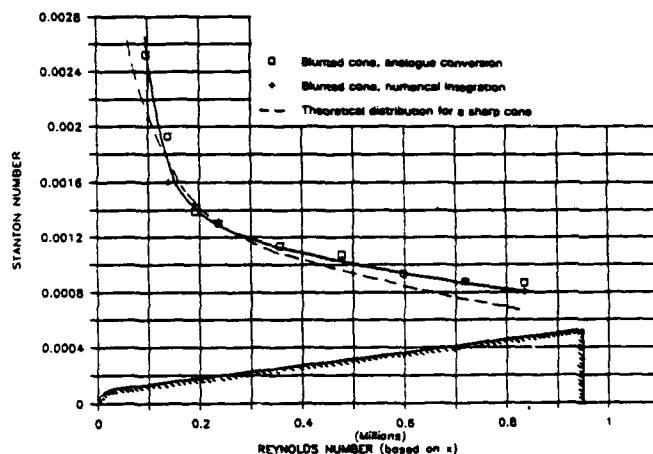


Figure 4. Heat transfer rate distribution on the surface of blunted and sharp cones.

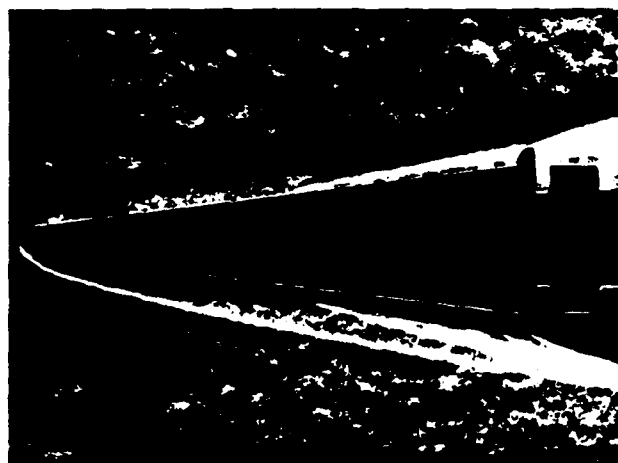


Figure 5. Schlieren photograph of flow past the blunted cone with a small disc ( $d/d_b = 1.25$ ) at its base.

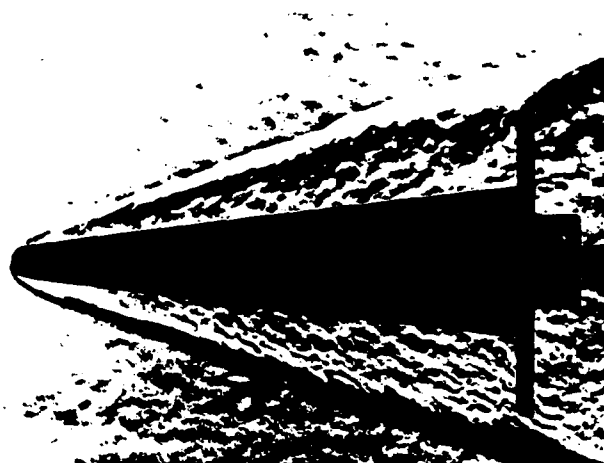


Figure 6. Schlieren photograph of flow past the blunted cone with a large disc ( $d/d_b = 2.1$ ) at its base.



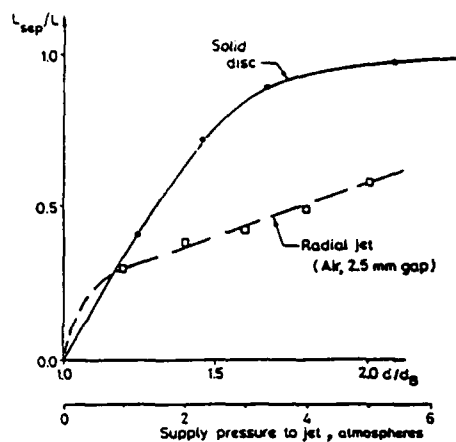


Figure 7. Movement of separation position with disc size and jet pressure.

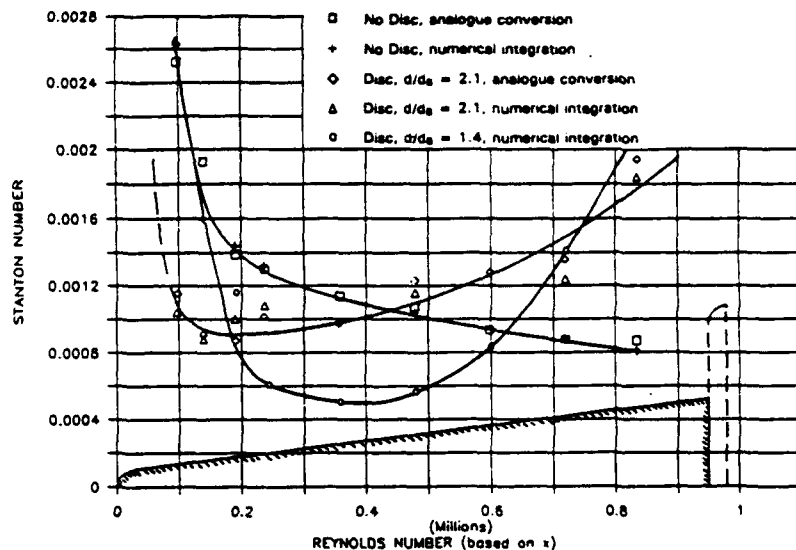


Figure 8. Effect of large- and medium-diameter discs on heat transfer to cone surface.

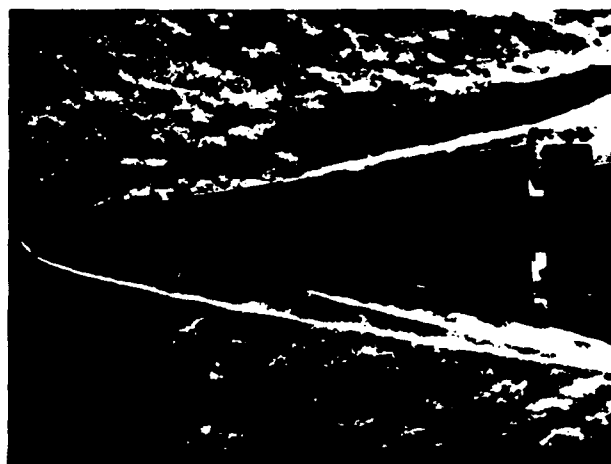


Figure 9. Schlieren photograph of flow past the blunted cone with an annular air jet (6.1 atm total pressure, 4.5 mm gap) at its base.

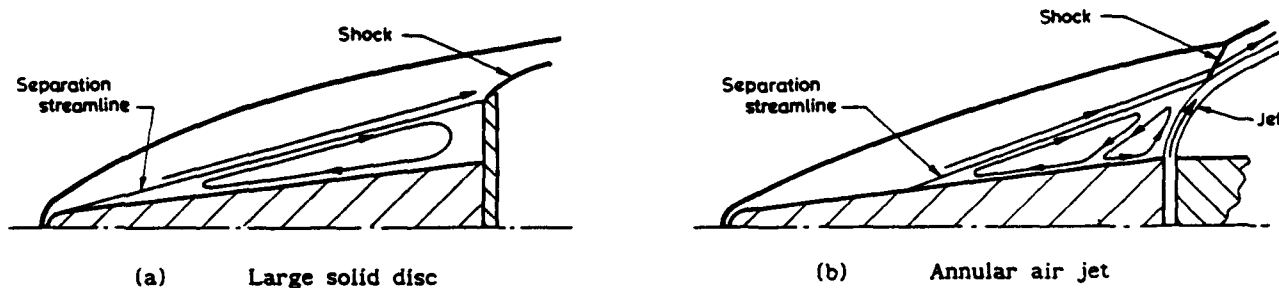


Figure 10. Suggested flow patterns in separated regions.

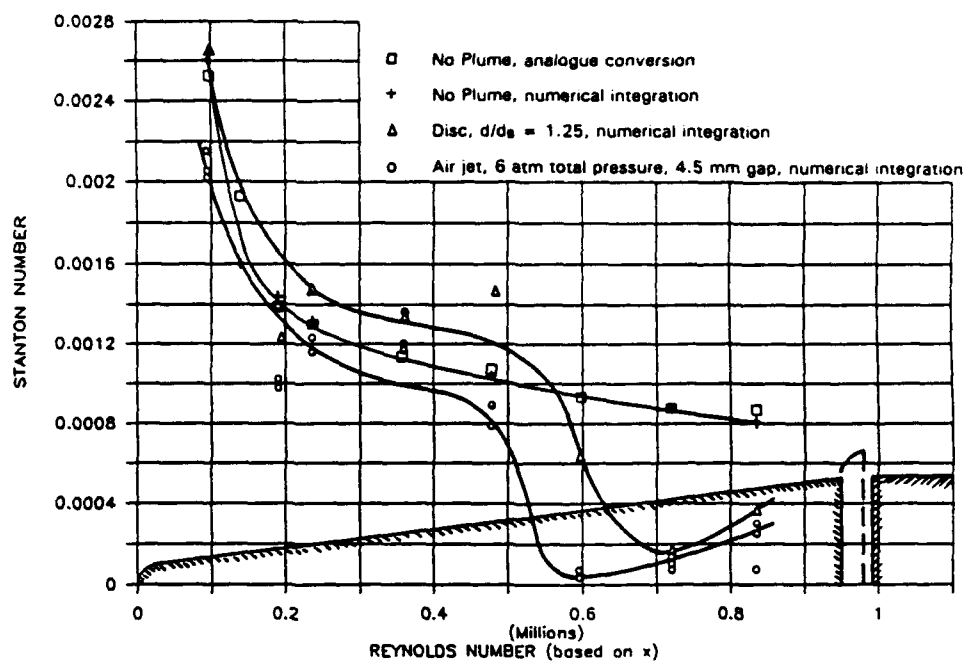


Figure 11. Effect of small-diameter disc and annular air jet on heat transfer to cone surface.

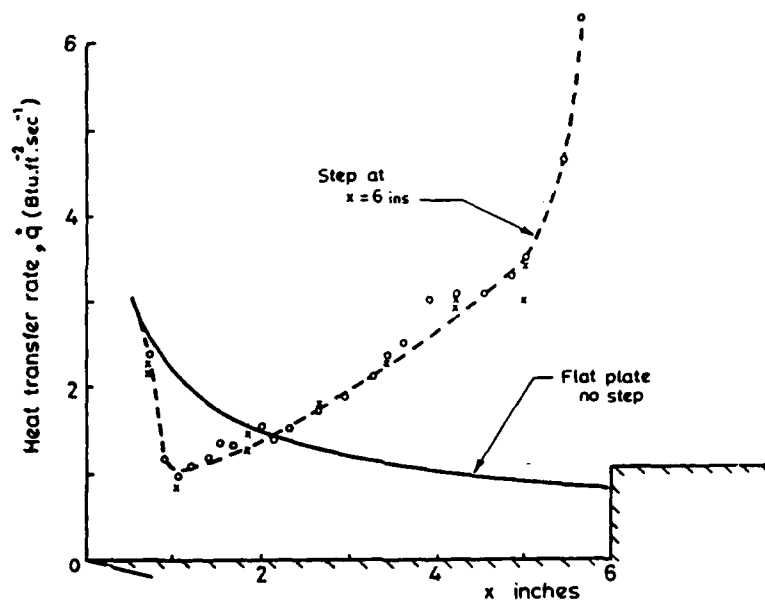


Figure 12. Heat transfer rates in the separated region ahead of a step,  $M_\infty = 10$ .

# COMBINED FORCED AND FREE CONVECTION IN A CURVED DUCT

By

Clement G. Yam and Harry A. Dwyer

University of California, Davis

Department of Mechanical and Aeronautical Engineering

Davis, CA 95616

## Abstract

The purpose of this study is to investigate the flow and heat transfer characteristics of a combined forced and free convection flow in a curved duct. Solutions are obtained by solving the low Mach number model of the Navier-Stokes equation using a control volume method. The finite-volume method has been developed with the use of a predictor-corrector numerical scheme and some new variations of the classical projection method. Solutions indicated that the existence of buoyancy force has changed the entire flow structure inside a curved duct. Reversed flow at both inner and outer bend is observed. For moderate Reynolds number the upstream section of the duct has been significantly influenced by the free convection processes. In general heat transfer is strong at the inner bend of the beginning of the heated section and at the outer bend on the last half of the heated section. The maximum velocity location is strongly influence by the combined effects of buoyancy and centrifugal forces. Strong buoyancy force can reduce the strength of the secondary flow where it plays an important role in mixing.

## 1) Introduction

Steady flow in a curved duct is of practical engineering interest and was first investigated by Dean [1], [2]. The main concern of the fluid mechanics problem is to determine the total pressure drop in the flow since a duct with a bend has a higher pressure drop due to the secondary motion of the fluid. Interest also occurs in this type of flow for the mixing of chemicals by the secondary motion. If the mixing is adequate, then additional pumping is not required.

Combined forced and free convection is of great importance in the design of heat exchangers like the cooling of electronic equipment by Freon-12 where inside the cooling coil the buoyancy force is higher than convection force. Moreover, the effect of secondary flow is of great important as it can enhance the overall heat transfer rate like design of a cooling coil inside a nuclear reactor. Unlike the straight duct flow, which can be solved analytically by using the parallel flow assumption, the flow in the curved section is not parallel and is more complex. Most of the recent research efforts by Masiliyah [3], Soh and Berger [4], [5], and Yao and Berger [6], are limited only to a curved duct because the problem can be written in a toroidal coordinate system. This is the first three dimensional numerical study of a curved duct with straight duct(s) attached where the usage of a non-orthogonal mesh is required.

Numerical solutions are obtained by solving the governing equations in a body fitted, non-orthogonal, coordinate system. A control volume form of the governing equations is used in

this study due to clear physical interpretation of the integral equations. A detail discussion of the initial and boundary conditions for this problem is also included. Solutions are presented in the form of two-dimensional contours and three-dimensional surface contours in order to indicate the local variations. One-dimensional plots are used to show the global results. A detail discussion of the flow structure and local heat transfer rate of the combined forced and free convection flow field and its different with a forced convection flow field is also present in this study.

## 2) Governing Equation:

For internal flow, the dimensionless variables are defined as follows:

$$\bar{\rho} = \frac{\rho}{\rho_{inlet}}; \bar{x} = \frac{x}{L}; \bar{\vec{V}} = \frac{\vec{V}}{U_{ref}}; \bar{P} = \frac{P - P_{ref}}{\rho_{inlet} U_{ref}^2};$$

$$\bar{T} = \frac{T - T_{inlet}}{T_H - T_{inlet}}; \bar{t} = \frac{t U_{ref}}{L}$$

where  $\rho_{inlet}$  is the density at the inlet of the duct,  $L$  is the reference length and is the radius of the duct,  $T_{inlet}$  is the temperature of the inlet fluid,  $T_H$  is the maximum temperature of the system,  $t$  is time,  $U_{ref}$  is the reference velocity scale and is defined by the mean velocity at the inlet which has the following form:

$$U_{ref} = \frac{\iint_A \vec{V}_{inlet} \cdot \vec{n} dA_{inlet}}{\iint_A dA_{inlet}}$$

The resulting dimensionless governing equations (omitting over bars) with the Boussinesq approximation have the following forms:

### 1) Continuity Equation:

$$\frac{\partial}{\partial t} \iiint_V \rho dV + \iint_A \rho \vec{V} \cdot \vec{n} dA = 0$$

where  $t$  is the time,  $\rho$  is the density,  $\vec{V}$  is the velocity vector,  $\vec{n}$  is the unit normal vector pointing out of the control volume,  $dV$  is the finite volume, and  $dA$  is the area on each surface of the finite volume.

## 2) Momentum Equation:

$$\rho \frac{\partial}{\partial t} \iiint_V \vec{V} dV + \rho \iiint_V (\vec{V} \cdot \nabla) \vec{V} dV$$

$$= - \iint_A P \vec{n} dA + \frac{1}{Re} \iint_A \vec{\tau} \cdot \vec{n} dA - \frac{Ra}{Re^2 Pr} \iiint_V \rho T dV$$

## 3) Thermal Energy Equation:

$$\frac{\partial}{\partial t} \iiint_V T dV + \iiint_V (\vec{V} \cdot \nabla) T dV$$

$$= \iint_A \vec{V} T \cdot \vec{n} dA + Ec Pr \iiint_V \phi dV + Ec \left( \frac{\partial}{\partial t} \iiint_V \rho P dV \right.$$

$$\left. + \iint_A \rho P \vec{V} \cdot \vec{n} dA \right)$$

where Rayleigh Number ( $Ra$ ) =  $\frac{g\beta L^3 \Delta T}{\nu \alpha}$  =  $\frac{\text{Buoyancy Force}}{\text{Viscous Force}}$

Prandtl Number ( $Pr$ ) =  $\frac{\nu}{\alpha}$  =  $\frac{\text{Viscous Diffusion}}{\text{Heat Diffusion}}$

Eckert Number ( $Ec$ ) =  $\frac{U^2}{c_p \Delta T}$  =  $\frac{\text{Mechanical Energy}}{\text{Thermal Energy}}$

where  $\beta$  is the coefficient of thermal expansion,  $g$  is the gravitation vector,  $\Delta T$  is temperature difference defined as  $T_H - T_{inlet}$ ,  $U$  is the reference velocity scale defined as the mean inlet velocity, and  $\nu$  is the kinematic viscosity of the fluid.

For subsonic flow (i.e. low Mach number) with a moderate Reynolds number, the Eckert number is much smaller than one. Hence the viscous heating term and the flow work term can be neglected. The dimensionless thermal energy equation has the following form:

$$\frac{\partial}{\partial t} \iiint_V T dV + \iiint_V (\vec{V} \cdot \nabla) T dV = \iint_A \vec{V} T \cdot \vec{n} dA$$

A detail derivation of the low Mach number model equations with the Boussinesq approximation is shown by Yam [7].

## 3) Problem of interest

An experiment with combined forced and free convection in a curved duct has been performed by Cheng and Yeng [8], [9]. In the experiment, a curved duct with a straight long entrance length is fabricated. The straight long entrance length is to ensure a fully developed parabolic velocity profile at the entrance of the heated curved section. (We will later see that this is not always true). A hot water jacker is inserted into the curved section to create the heated section. The heated curved section is then oriented in a vertical upward direction. Room air from a compressor is used as a working fluid inside the assembly. Smoke generated by burning paper straws is injected at the straight duct entrance. Photographs of the secondary flow patterns are taken at the exit of the curved duct where the heated air is discharged directly into the surrounding as jet. A

schematic of the experimental apparatus is shown in Figure 1. The parameters used in this experiment (Reynolds number of 59.92 and 246.69, Rayleigh number of  $2.57 \times 10^4$ , curvature ratio of 1:10.9 and Prandtl number of 0.7) are imported in the current numerical study.

## 4) Numerical Methods

### I) Coordinate System

The problems of interest have geometries that are very difficult to describe using a Cartesian coordinate system. Thus, a coordinate transformation is used to define a body fitted coordinate system. For the problems of internal flow in a curved duct with straight duct attached, a three dimensional boundary fitted, non-orthogonal coordinate is used. Typical grid systems for the surface and sections of the curved duct are shown in Figure 2 through 5.

All derivative terms in the equation of motion are evaluated with the use of the generalized coordinates and this involves a coordinate transformation. A detail derivation of the transformation is shown by Dwyer and Dandy [9] and Yam [7].

### II) Calculations Of Geometry

The control volume equations (integral equations) consist of volume terms and surface terms. The volume and surface area of a control volume can be obtained by the usage of vector operations. For control volumes with cell centers located at a singular point (like those at the axis of the ellipsoid grid), all the dependent variables can become coupled with the adjacent cell through the convection and viscous terms. This leads to difficulty with implicit solvers. A simple solution to this problem is to put the cell surface at the singular point. As shown by the governing equations, the only terms that exist at the control surface are those of the flux and pressure terms. Since they are being multiplied by the surface area of zero, the excessive coupling is removed. The cell center of the control cell however is still coupled to the rest of the system by the remaining five surfaces. A detail discussion of is shown by Yam [7].

### III) Finite Volume Equations

In this study, all the variables are defined at the center of the control cell. When variables are needed at the surface of the cell, averaging is performed, and gradients are evaluated with a second order finite difference with respect to the cell surface. Thus, discretization of the governing equations in generalized coordinates is second order accurate in space. However, for the internal flow, the resulting maximum Reynolds number that we can run to obtain solutions is limited to 200. One way of increasing the Reynolds number is by adding more grid points to the physical domain. This, however, is limited by the capacities of current computers. An alternative is to add artificial dissipation only to the stream wise direction to enhance the stability of the numerical scheme.

This is done by adding  $\frac{1}{2} \frac{\vec{V}_z \cdot \vec{ds}_z}{v}$  to the diffusion coefficient of the stream wise viscous term where  $\vec{V}_z$  is the local stream-wise velocity vector, and  $\vec{ds}_z$  is the local length scale of the control volume in the stream-wise direction:

As shown by Yam [7], the areas on the control cell are defined by the cross product of the two position vectors located on each surface. These two position vectors are determined by linear interpolation between the grid points where the surface is located. For a control volume with plane surfaces this is a good method of determining the surface area, however the resulting surface integral of area is not always equal to zero. This can lead to truncation error in the governing equations where surface integrals are evaluated. A typical and an important example is the pressure force term in the momentum equation. The difficulty can be overcome by correcting the pressure force term as:

$$-\iint_A P \vec{n} dA \Rightarrow -\iint_A P \vec{n} dA + P \iint_A \vec{n} dA$$

Thus any error in the evaluation of the areas is compensated by the second term and the finite volume equations will accept uniform solutions.

#### IV) Numerical Scheme

After the governing equations have been transformed into finite-difference equations, a numerical scheme must be employed to solve the system of equations. An iterative implicit scheme with replacement (Predictor - Corrector - Corrector) is used in this study. This is variation of the alternate line implicit method with replacement. A detail discussion is shown by Yam [7]. The advantage of using this type of iteration scheme is that it has a fast convergence rate compared to other iterative methods [7].

#### V) Pressure Solver

The governing equations consist of the continuity equation, three momentum equations, and energy equation with unknowns of U, V, W, P and T. The velocity field is obtained through the momentum equations, and the temperature field is obtained from the thermal energy equation. However, we do not have an explicit equation for the pressure field. Thus, special treatment must be used in order to obtain the pressure field. The method that was used to obtain pressure for this study is a variation of the method developed by Chorin [8]. A detail discussion is shown by Yam [7].

#### VI) Initial Conditions And Boundary Conditions

Due to the elliptic nature of the governing equations, boundary conditions must be given at all boundaries. Moreover, since all variables are a function of both space and time, initial conditions for all variables must also be given. For mass driven internal flow, the mass flow rate is the only known

quantity. The pressure gradient (pressure drop) is a result from the balancing of the forces on the fluid particles. Thus, velocity and pressure are unknowns everywhere. For the combined forced and free convection flow, it is assumed that the duct has a long straight inlet section such that before the entry of the heated curved section, the flow is fully developed. Thus the velocity field is assumed to be parabolic everywhere. The pressure field is assumed to have a uniform pressure gradient along the duct system. For the temperature field, it is assumed that the temperature is uniform everywhere and is equal to the inlet temperature.

The boundary conditions for the velocity and the pressure fields are more complicated. At the surface of the duct, the no-slip velocity still holds. A zero pressure gradient is applied at the surface. The velocity profile at the inlet is also fixed and is that of the parabolic profile. Hence the velocity correction is specified to be zero. The pressure, however, is to be extrapolated from the pressure at first cell next to the inlet. This will allow the inlet pressure to change in order to satisfy the balance of momentum at the first control cell. At the exit, the velocity field is assumed to be fully developed. Thus, the velocity gradient along a stream line is zero. Again, we extrapolate the pressure for the exit pressure field. For the temperature boundary conditions, the wall temperature at the straight section is equal to zero while the temperature at the curved section is equal to one. The inlet temperature is held constant with a value of zero. At the exit, the temperature field is assumed to be fully developed. Thus, the temperature gradient along a stream line is set to be zero.

As a comparison, a pure forced convection through a 180 degree bend duct with straight ducts attached is included in this study. However, the inlet straight section of this case is relative short. It is reasonable to assume that the flow at the inlet is mainly composed of an inviscid core since the boundary layer has not yet been established. Thus the initial condition for the velocity field is assumed to be an inviscid velocity profile with zero velocity at the wall everywhere. For the temperature, the initial and boundary conditions are the same as the above case with the exception that the straight section is also heated.

A summary of initial and boundary conditions for this case is listed in Table 1.

Table 1  
Initial and Boundary Conditions for Forced and Free Convection (Mass Driven) Internal Flow

	Velocity	Temperature	Pressure
Initial Conditions	$\vec{V} = \vec{V}(\xi, \eta)$	$T = 0$	$P = P(\xi, \eta)$
Body Boundary Conditions	$\vec{V} = 0$	$T = T_{wall}$	$\frac{\partial P}{\partial \eta} = 0$
Far Field Upstream Boundary Conditions	$\vec{V} = \vec{V}(\xi, \eta)$	$T = 0$	$P = \text{Calculated from the flow field.}$

Far Field Down- stream Boundary Conditions	$\frac{\partial \vec{V}}{\partial \vec{s}} = 0$	$\frac{\partial T}{\partial \vec{s}} = 0$	P=Calculated from the flow field.
--	---	---	---

## 5) Discussion Of Results

A primary objective of this study is to determine the surface (normal and shear) stresses, surface heat flux and the internal flow structure inside a straight-curved duct subject to a combined forced and free convection. With the gravity vector parallel to the plane of symmetry of the geometry of this problem, and with the assumption that the flow is symmetric in the cross-section of the duct, only half of the domain needs to be computed. (Hence symmetrical boundary conditions of all gradients equal to zero and the velocity vector tangent to the plane of symmetry are imposed at the plane of symmetry.)

We have placed 15 geometrically stretched (of 11 percent) grid points in the radial ( $\eta$ ) direction, 19 geometrically stretched (of 9 percent) grid points in the circumferential ( $\xi$ ) direction and either 46 or 61 grid points in the stream-wise ( $\zeta$ ) direction. By stretching in the radial direction, we have a grid system that can capture the boundary layer next to the wall. The stretching in the circumferential direction allows us to obtain a more accurate secondary flow in a curved duct. A typical example of the grid system used in the curved duct problem is shown in Figures 2 to 5. A dimensionless time step ( $\Delta t$ ) of 0.1 is used in these calculations. A Prandtl number of 0.7 is used through out this study.

### A) Accuracy

The formulation of the internal flow part of the code is tested by running a series of steady state test cases. Steady state is assumed to be reached when the divergence of the velocity field is dropped to machine zero and the relative change in the velocity field is in the order of  $10^{-4}$ . This generally takes 1200 time steps. The resulting velocity profile of the test case is compared with the exact solution. For the mass driven case with an inviscid inlet velocity being prescribed, the entrance length before the flow becomes fully developed in a straight duct is calculated and is compared with experimental correlations. The resulting pressure drop, and velocity profiles at the fully developed region are compared with the exact solutions. The comparison is good since the errors in velocity and in pressure drop are in the order of discretization error.

Two test cases of mass driven flow in a 180 degrees curved duct, curvature ratio (ratio of curved duct radius  $R_{\text{duct}}$  to the main curved radius  $R_{\text{curve}}$ ) of  $\frac{1}{7}$  with Reynolds number of 242 and 900 are calculated. The resulting speed contour and secondary flow field are then compared with the numerical results obtained by Soh and Berger [4] with excellent agreement. A detail discussion of the solutions and comparison is shown by Yam [7].

For internal flow the mean temperature is defined as

$$T_{\text{mean}} = \frac{\iint T \vec{V} \cdot \vec{n} dA}{\iint \vec{V} \cdot \vec{n} dA}$$

while the local Nusselt Number is defined as

$$Nu = \frac{h R_0}{k} = - \frac{\frac{\partial T}{\partial r}}{T_{\text{mean}} - T_{\text{wall}}}$$

and can be viewed as the ratio of the heat flux due to convection and the heat flux due to conduction. A high Nusselt number means heat transfer is dominated by convection while a low Nusselt number means heat transfer is done mainly by conduction.

To test the evaluation of the local heat transfer rate, a test case of fluid with inlet temperature of 1 and cooled wall temperature of 0 in a straight duct is calculated. The mean temperature and the Nusselt number are calculated and the results are then compared with theoretical values with excellent agreement.

### B) Detail Results

Case I :  $Re = 59.92$ ,  $Ra = 2.57 \times 10^4$ ,  $Pr = 0.7$

We begin the study with a curvature ratio of  $\frac{1}{10.9}$ . Reynolds number of 59.92, Rayleigh number of  $2.57 \times 10^4$  and Prandtl number of 0.7. A total of  $19 \times 15 \times 61$  grid points are used in this study.

At this Reynolds number, the entire flow field is dominated by buoyancy affects. The resulting pressure contour at the plane of symmetry and the pressure contour at the surface of the duct are shown in Figures 6 and 7. It is clear that the pressure distribution has taken the form of hydrostatic.

The pressure at the inner wall, at the center line of the duct and at the outer wall verses the K-station (where K equals 1 is at the inlet, while K equals 61 is at the exit) as shown in Figure 8. The reason for plotting the pressure against the K-station is that there is no obvious physical length scale one can plot the pressure. The number of the K-station can be viewed as the transformed length scale  $\zeta$ . Thus, this is one way of presenting combined results in straight and curved sections in a one-dimensional plot. The unusual reverse of the maximum and minimum value location at the cross-section of the duct is a characteristic of hydrostatic pressure distribution inside a curved duct.

The cross flow velocity field is shown by the velocity vector plot at the symmetry (X-Z) plane (Figure 9). At the inlet, the velocity profile is parabolic as discussed previously. As the fluid particles enter the curved section, heat is added to it. With the combined influence of the buoyancy and inertia

forces, the fluid particles tend to move to the highest portion of each cross section the duct. This is shown by the maximum velocity located at the inner bend of the duct as indicated in Figure 9. In order to satisfy mass balance at each section, those fluid particles at the outer bend where buoyancy force is relative weak (when compare to those at the inner bend) have to flow backwards. This reversed flow at the outer wall travels upstream of the curved section to the straight section due to the low inertia of the fluid particles as indicated in Figure 9. The flow field has this nature until 80 degrees of the bend, when both inertia force and buoyancy force acted in phase to push the fluid particles upwards. The speed contour (Figure 10) at the plane of symmetry clearly shows the reversed flow region at the outer bend of the curved inlet.

As the flow continue to develop, the centrifugal and buoyancy forces act together and continue pushing the fluid particles downstream where a reversed flow at the inner bend is then observed. As the flow continues to develop, the maximum velocity location starts moving towards the outer bend. As the flow reaches the exit, the buoyancy and centrifugal forces act out of phase and the maximum velocity is located near the outer bend. The corresponding surface total shear stress is shown in Figure 11. It is clearly shown that the maximum surface shear stress is located at the inner bend of the curved entrance region due to the high velocity gradient at that location. The minimum shear stress region (with an opposite sign due to the reversed flow) is located at the inner bend immediately downstream of the maximum region. The speed contour at the 80 degree cross section where the reversed flow region exists at the outer bend is shown in Figure 12. A secondary flow is also observed at the exit of the duct as indicated by the velocity vector plot at the exit plane as shown in Figure 13. The center of the secondary flow is located at the top half of the duct due to the strong buoyancy force.

From the temperature contour at the symmetry plane (Figure 14), we can see that thermal boundary layer formed rapidly at the inner bend of the curved section and is confined to a thin layer. At the outer wall, the thermal boundary layer flows backwards to the straight section before convecting downstream. This is due to the reversed flow (shown by the velocity vector plot at the symmetry plane in Figure 9), where fluid particles that have been heated up by hot curved wall have convected backwards to the straight inlet section.

The temperature contour at the exit plane is also shown in Figure 15. We can see that the temperature gradient at the outer wall is at a maximum while the temperature gradient at the inner is at a minimum. Since temperature can be view as a passive scalar, the temperature contour can provided us a view of the flow field. Comparison of the temperature contour at the exit (Figure 15) with the secondary flow smoke pattern (Figure 16) obtained by Cheng and Yuen [8] where the Reynolds number, Rayleigh number and curvature ratio is identical to this case is then made.

From Figure 16, we can see that the buoyancy force is pushing all the smoke towards the outer bend and is confined to the top 30 percent of the cross-sectional area. Since at this Reynolds number, the centrifugal force is relative weak, the flow field is dominated by the buoyancy force. Moreover the secondary

flow is not strong enough to push the smoke from the outer wall back towards the inner wall. This is qualitatively comparable to the temperature contour (Figure 15) where the temperature contour lines do not indicated a downward flow motion next to the wall. (The detection of downward motion is detected by the curvature of the contour lines and will become clear when a higher Reynolds number case is discussed in a later section)

The local Nusselt number at the inner bend, at the top of the duct, and at the outer bend are calculated and are shown in Figure 17. From this local Nusselt number plot, the heat transfer rate at the inner bend of the curved inlet section has increased from a Nusselt number of 6.9 to 8.6 (where the shear stress is at a maximum) then decreased back to 0.7. This is caused by the thermal boundary layer being pressed into the inner wall by the buoyancy force. As this boundary layer lifts off from the inner wall, the resulting heat transfer rate drops to zero. At the outer wall, the reverse of this affect is observed. The Nusselt number remains closed to zero at the beginning of the curved section where reversed flow is observed. At about 80 degrees into the bend, the Nusselt number started to increase up to 6.8 (at 120 degrees ) and remains constant. At the center of the duct, the nusselt number takes on a more convectional form of having a maximum value of 7.0 at the entrance of the heated section and the continues to drop to a constant value of 1.9. This shows that the heat transfer rate in a straight-curved duct is higher than that of a straight duct where the Nusselt number for a fully developed flow base on radius has a value of 1.8.

The mean duct temperature is shown in Figure 18. The mean temperature increases from 0 at the beginning of the duct (at the straight section) and drops back down to zero at the beginning of the heated section. This is due to the reversed flow of the heated fluid flow at the inlet section. As the flow continues to develop, the mean temperature continues to increase to 0.98 at the duct exit.

**Case II :  $Re = 246.69$ ,  $Ra = 2.57 \times 10^4$ ,  $Pr = 0.7$**

The second case presented here is for a Reynolds number of 246.69, Rayleigh number of  $2.57 \times 10^4$  and Prandtl number of 0.7. The curvature ratio and grid density are the same as Case I.

At this Reynolds number, the buoyancy affect dominates the region next to the inner wall at the last half of the duct while the centrifugal force influences the region next to the outer wall of the entire duct system. This is shown by the pressure contour at the plane of symmetry in Figure 19. We can see that the pressure contour has taken the form of hydrostatic (parallel line with respect to the horizon) at the inner wall while centrifugal force (contour lines curved upward) is evident at the outer wall. The pressure at the inner wall, at the center line of the duct and at the outer wall are also presented as the function along the duct in Figure 20. The unusual reverse of the maximum and minimum value which is a characteristic of hydrostatic pressure distribution inside a curved duct occurs near the exit of the duct while the

centrifugal force dominated pressure distribution is observed at the first half of the curved section.

The cross flow field is shown by the velocity vector plot at the symmetry (X-Z) plane (Figure 21). As the fluid particles enter the curved section, heat is added to it. With the combined influence of the buoyancy and inertia forces, the fluid particles tend to move to the highest portion of each cross section of the duct. This is shown by the maximum velocity located at the inner bend of the duct as indicated in Figure 21. In order to satisfy mass balance at each section, those fluid particles at the outer bend where buoyancy force is relative weak (when compare to those at the inner bend) have to flow backwards. However, unlike Case I, the incoming fluid has enough inertia such that reversed flow does not occur at the straight inlet section. The reversed flow at the outer wall continues up to 60 degrees of the bend. At the 55 degree location, both inertia and buoyancy force have accelerated the fluid particles in phase such that a reversed flow at inner bends is observed. (Hence a reversed flow at both the outer and inner bends is detected from 55 to 60 degrees). Moreover, the maximum velocity location has shifted from the region next to the inner bend to the region next to the outer bend. The combined forced and free convection is so strong that the reversed flow at the inner bend continues up to 150 degrees of the curved section. As the flow continues to develop, the maximum velocity location moves towards the outer bend. As the flow reaches the exit, the buoyancy and centrifugal forces act out of phase and the maximum velocity is located near the outer bend due to the centrifugal force. Speed contours at the plane of symmetry are also shown in Figure 22. The reversed flow at the beginning of the outer bend and at the mid-section of the curved duct is clearly shown. The corresponded surface total shear stress is shown in Figure 23. The maximum surface shear stress is located at the outer bend of the curved section due to the high velocity gradient. The minimum shear stress regions (with an opposite sign due to the reversed flow) are located at the outer bend at the beginning of the curved section and at the inner bend of the last half section.

A secondary flow is observed at the 75 degrees station and is shown in Figure 24. The speed contour at the location where the reversed flow at the inner bend is shown in Figure 25. A secondary flow is observed at the exit of the duct as indicated by the velocity vector plot at the exit plane as shown in Figure 26. We can see that the center of the secondary flow is located at the mid section and the strength of the secondary flow is stronger than that of case one due to the strong centrifugal effect. The speed contour at the exit where the high velocity gradient is located next to the outer bend is shown in Figure 27.

From the temperature contour at the symmetry plane (Figure 28), we can see that thermal boundary layer formed rapidly at the inner bend and is confined to a thin layer while the thermal boundary layer at the outer bend grows rapidly due to the buoyancy force. As the duct turned, the combined buoyancy and centrifugal forces have lifted the thermal boundary layer away from the inner bend and pushed it against the outer bend where the thermal boundary layer formed tightly against the outer wall. The temperature contour at the

exit plane is also shown in Figure 29. We can see that the temperature gradient at the outer wall is at maximum while the temperature gradient at the inner is at minimum. Furthermore, the maximum temperature region is closer to the outer bend when compare to the lower Reynolds number case (Figure 15) due to the higher centrifugal force.

From the secondary flow pattern (Figure 30) obtained by Cheng and Yuen [8] with the same Reynolds number, Rayleigh number, Prandtl number and curvature ratio, we can see that the smoke at the outer bend has been convected towards the inner bend by the stronger secondary flow. The smoke has occupied 70 percent of the cross-sectional area. This is qualitative comparable to the temperature contour (Figure 29) where the temperature contour lines shows a concave down shape which indicated that it is being bend by the downward flow at the duct wall region.

From the local Nusselt number plot (Figure 31), the heat transfer rate at the inner bend of the curved inlet section has a Nusselt number of 8.6 and then continue drop to a low value of 0.183 where the thermal boundary layer have lift off the inner bend ( $K=31$ ). The Nusselt number there increases slightly and has a value of 0.45 as the flow exits the duct. At the outer wall, the Nusselt number has a maximum of 3.12 at the beginning of the heated section and then drops back to have a low value of 0.2. This is the location where the thermal boundary layer has lifted off from the outer wall due to the buoyancy effect. At  $K=25$ , the Nusselt number started to increase rapidly to a high value of 13.5. This is due to the reattachment of the thermal boundary layer being pushed to the outer wall by the combined effect of buoyancy and centrifugal forces.

The mean temperature along the duct is shown in Figure 32. The mean temperature has increased from 0 to 0.82 at the duct exit. This shows that even though the Nusselt number reached an asymptotic value, the flow is not thermally fully developed.

### Case III : $Re = 242$ , $Ra = 0$ , $Pr = 0.7$

For comparison, a similar forced convection case without body force is present here. A curvature ratio of  $\frac{1}{7}$ , Reynolds number of 242, Prandtl number of 0.7 is used in this case. A total of  $21 \times 15 \times 46$  grid points are used in this study. The grids in the straight duct section and in the stream-wise direction are expanded geometrically by 10 percent. The resulting grid system is shown in Figures 3, 4 and 5. The flow is driven by an imposed mass flow rate thus the only known quantity is the velocity field at the inlet. The initial and boundary conditions used for this case have already been discussed in the initial and boundary conditions section.

The calculated pressure distribution is presented by plotting, (1) the pressure at the inner bend, (2) the pressure at the center line of the duct, and (3) the pressure at the outer bend verses the K-station as shown in Figure 33. The resulting pressure contour at the plane of symmetry and the pressure contour at the surface of the duct are also shown in Figures 34 and 35. From the pressure profile, Figure 33, the inlet pressure at the center is slightly lower than the pressure at the wall. This is caused by the inlet flow still being mainly composed of an



inviscid core with a boundary layer starting to develop. As the boundary layer grows, the displacement thickness also grows. This increase of the displacement accelerates the main inviscid core in order to maintain the mass balance. By Bernoulli's law, as the velocity increases, the pressure decreases. Thus the pressure is lower at the center. As the fluid enters the curved section, the pressure at the outer bend is higher than the pressure at the inner bend. This is due to the centrifugal force exerted at the duct wall by the fluid particles. Note that at the outer wall of the entrance region of the curved section, the pressure gradient is almost zero. Although there is a slight pressure oscillation at the exit of the curved section, this is due to the lack of resolution of grid points in the stream-wise direction. This problem can be overcome by adding more grids to the stream-wise direction.

From the surface pressure contours, Figure 34, there is a pressure drop along the straight section of the duct, however, the pressure is almost uniform across the duct. We can also see that from Figure 34, not only is there a pressure difference between the inlet and the exit, but also a pressure difference between the inner bend and the outer bend due to the centrifugal force acting by the fluid. At the outer bend of the entrance of the curved section there is a region where the pressure is uniform and it is shown in both pressure contours at the plane of symmetry, Figure 34, and at the surface of the bend duct, Figure 35. This is due to the increase of the pressure by the centrifugal force acting at the curved section. Unlike the combined forced and free convection, here the pressure at the outer bend remains higher than the pressure at the inner bend of the same cross section throughout the curved section.

The velocity profile for this case is significantly different than that of case II. Unlike case II where the maximum velocity location started off at the inner bend and later on moved to the outer bend, the maximum velocity location started off at the region next to the outer bend and remained at the outer bend. A detail description of the flow development is discussed as follows.

The velocity profile (Figure 36) at the inlet is an inviscid one which is explicitly specified. As the flow enters the straight inlet section, the boundary layer started to grow, however due to the shortness of the straight section, the flow is still composed mainly of an inviscid core. As the fluid particles enter the curved section, the velocity profile tends to build up at the outer wall. This is due to the particles coming from the straight section still want to go straight by their momentum. However, because of the existence of the solid curved wall, the fluid particles have no choice but to change their course to follow the curvature of the duct. This leads to a larger buildup of the fluid particles at the outer wall. The existence of an inviscid core (where velocity shows a flat plateau) can still be observed up to the 45 degrees station of the curved section. The developing region exists to about 110 degrees until the flow in the curved section becomes fully developed. (Further study by Yam [7] has indicated the existence of the inviscid does not have major influence in the heat transfer part of the problem). At the fully developed region, the velocity profile has the maximum located close to the outer wall. The speed contour at 90 degrees section of the curved duct is shown in Figure 37. A secondary flow is also observed and is shown by

the secondary flow velocity vector located at the 90 degrees section in Figure 38. As the fluid exits the curved section and enters the straight section, the maximum velocity is still located toward the outer wall. The speed contours at the exit plane is shown in Figure 39. The cross velocity vector at the exit is also shown in Figure 40. The secondary motion is still clearly defined with the center of the secondary flow located at the lower region of the cross section. Without the influence of the buoyancy force, the secondary flow is strong enough to move some of the fluid particles towards the inner bend as indicated by the concave downward shape of the speed contour line. (Without body force, the temperature contours are the same as the speed contours).

The total surface shear stress contour is shown in Figure 41. There is a large area of minimum shear stress located at the inner bend with a large area of maximum shear stress located at the outer bend. This is obvious from the velocity vector plot (Figure 36), we can see that the velocity gradient is higher at the outer bend than at the inner bend. At about 80 degrees from the inner bend, a small region of maximum change in the shear stress is observed in Figure 41. From the secondary flow velocity vector plots (Figure 40), we can see that the center of the secondary flow and the maximum secondary velocity gradient are located at about 80 degrees from the inner bend. This indicates that the region of maximum changes in shear stress at the surface of a curved duct has the same angle that is between the center of the secondary flow and the plane of symmetry.

From the temperature contour at the symmetry plane (Figure 42), we can see that a thermal boundary layer formed rapidly at the outer bend and is confined to a thin layer. At the inner wall, the thermal boundary layer formed at the straight section continues to grow at the curved section and eventually disappears. Unlike the combined forced and free convection case, the thermal boundary layer at the outer bend never lifts off the duct wall. The thermal boundary layer (Figure 42) at the inner wall starts growing rapidly as it enters the curved section while for the combined forced and free convection case (Figure 28), the separation of the thermal boundary layer has delay up to 55 degrees into the curved section.

The mean temperature and the local Nusselt number at the inner bend, at the top of the duct, and at the outer bend are shown in Figures 43 and 44. Unlike the combined forced and free convection cases where the Nusselt number at the inner bend first has a high value and then at outer bend has a high value (Figure 17, Figure 31), the forced convection case has a higher Nusselt number at the outer bend than when compared to the inner bend at all location (Figure 43). From the local Nusselt number plot (Figure 43), the heat transfer rate at the inlet section is decreasing uniformly across the duct. As the flow enters the curved section, the heat transfer rate at the outer bend continues to increase from a Nusselt number of 2.7 to 9.8 towards the end of the curved section while the Nusselt number at the inner bend continues to decrease to a steady value of 0.6. This shows that the heat transfer rate at the outer bend is 5.4 times higher than that of a straight duct (Nusselt number of 1.8). At the inner bend, however, the heat transfer rate is about 3 times lower than that of a straight duct. The heat transfer is about 16 times higher at the outer bend when

compared to the heat transfer at the inner bend. This is reasonable because the fluid particles are convected into the wall at a much higher rate at the outer bend than that at the inner bend. The overall heat transfer rate in a curved duct is also higher than that of a straight duct. This is due to the secondary fluid motion that enhances the heat transfer. As the fluid leaves the curved section to enter the straight section, the Nusselt number at inner bend and at center start to decrease while the Nusselt number at the inner bend starts to increase. If the straight duct section at the exit is long enough, one can expect that the Nusselt number will approach the value of the straight duct (i.e. Nusselt number of 1.8). The resulting surface heat flux contour (Figure 45) shows that the region at the inner bend has a lower heat flux value than the region at the outer bend.

## 6 Conclusion

Solutions for the combined free and forced convection in a curved duct are obtained by solving the low Mach number model of the Navier-Stokes equation using a control volume method. The control volume method has the advantage of clear physical interpretation of the equations. From this study we have concluded the following:

- (1) The maximum velocity is located near the inner bend at the beginning of the curved section and it transfers towards the outer bend as the flow developed. The region where maximum velocity located near the inner bend is buoyancy force dominated while the region where velocity located near the outer bend is a result of the combined buoyancy and centrifugal forces.
- (2) Reversed flow exists at the beginning of the outer bend of the curved duct. This is due to the strong buoyancy force which entrains fluid particles upwards. Fluid with lower momentum have to flow backwards in order to maintain mass balance.
- (3) Reversed flow exists at the inner bend of the last half section of the curved duct. This is due to the strong combined inertia, centrifugal and buoyancy forces that accelerate the fluid particles at the outer bend forward. Again this reversed flow is a necessary condition for the conservation of mass.
- (4) Secondary flow exists in the flow structure. At lower Reynolds number, the strong buoyancy force has reduced the effectiveness in mixing. This was observed by Cheng and Yuen [8] who photographed smoke patterns confined to the upper area of the duct at low Reynolds number. As the Reynolds number increased, the strength of the secondary flow increased and pushed the smoke towards the inner bend.
- (5) A negative Nusselt number is present at the straight section for the lower Reynolds number case. This is due to the backward flow from the heated section. Instead of heat being deposited into the fluid (which yields positive Nusselt number), heat is being deposited back to the duct by the reversed flow of the hot fluid.
- (6) Nusselt number at the inner bend is high at the beginning of the heated section. This is due to the buoyancy force that pushed the thermal boundary layer against the inner bend which lead to a high temperature gradient. As the flow developed, the thermal boundary layer will lift off the inner bend and pressed against the

outer bend thus lead to a high Nusselt number at the outer bend at the last half of the curved section.

When comparing the combined forced and free convection results with the forced convection results, we notice that:

- (1) The maximum velocity location for the forced convection is next to the outer bend due to the centrifugal force in the entire flow field.
- (2) There is no reversed flow exist in the entire flow field for the forced convection.
- (3) The secondary flow is stronger for the forced convection case when compared to the combined forced and free convection case due to the lack of the buoyancy force.
- (4) Heat transfer rate at the outer bend is always stronger than that at the inner bend for the pure forced convection case. This is due to the centrifugal force that pushes the thermal boundary layer closed to the outer wall.

## References

1. Dean, W. R. "Note On The Motion Of Fluid In A Curved Duct", *Phil. Mag.* 20, 208, 1927.
2. Dean, W. R. "The Streamline Motion Of Fluid In A Curved Duct", *Phil. Mag.* 30, 673, 1928.
3. Masliyah, J. H., "on Laminar Flow In Curved Semicircular Ducts", *J. Fluid Mech.* (1980), Vol. 99, part 3, pp.469-479.
4. Soh, W. Y. and Berger, S. A., "Laminar entrance flow in a curved duct", *J. Fluid Mech.* (1984), Vol. 48, pp 109-135.
5. Soh, W. Y. and Berger, S. A., " Fully developed flow in a curved duct of arbitrary curvature ratio", *International Journal For Numerical Methods in Fluid*, Vol. 7, pp. 733-755, 1987.
6. Yao, L. Y. and Berger, S. A., "Flow in heated curved ducts", *J. Fluid Mech.* (1978), Vol. 88, pp. 339-354.
7. Yam, C. "An Investigation of Flow Structure and Heat Transfer Characteristics of Three Dimensional Flows", (1991) Ph.D. Dissertation. University of California, Davis.
8. Cheng, K.C. and Yuen, F. P. "Flow Visualization Experiments on Secondary Flow Patterns in an Isothermally Heated Curved Duct", *Journal of Heat Transfer* (1987), Vol. 109, pp.55-61.
9. Cheng, K.C. and Yuen, F. P. "Flow Visualization Studies on Secondary Flow Patterns in Straight tubes Downstream of a 180 deg Bend and in Isothermally Heated Horizontal Tubes", *Journal of Heat Transfer* (1987), Vol. 109, pp.49-54.

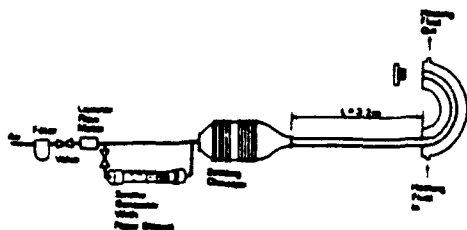


Figure 1  
Schematic Diagram of Experimental  
Apparatus by Cheung and Yuen [8]

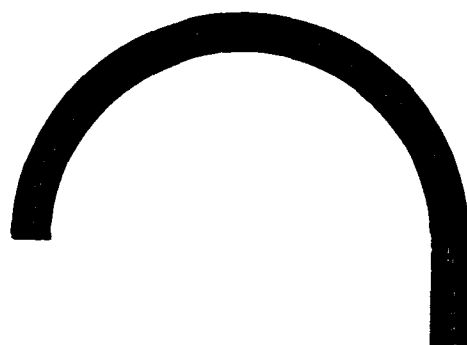


Figure 2  
Grid System For The Straight-Bend Duct  
(X-Z Plane)

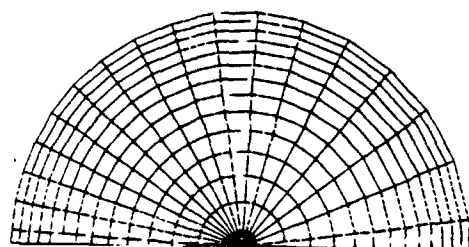


Figure 3  
Internal Grid System

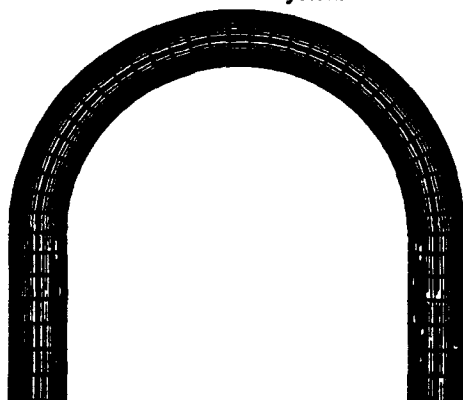


Figure 4  
Grid System For The 180 Degrees Bend  
Duct With Straight Ducts Attached

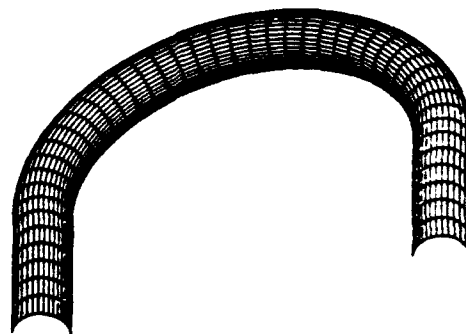


Figure 5  
Surface Grid For The 180 Degrees Bend  
Curved Duct With Straight Ducts Attached

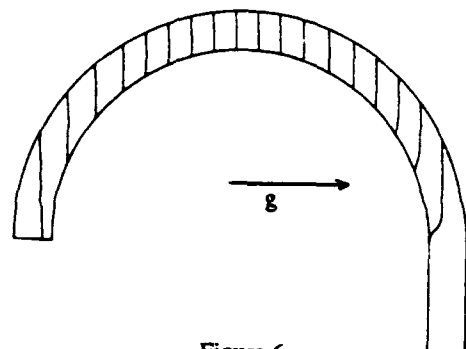


Figure 6  
Pressure Contour At The Plane Of Symmetry  
 $Re = 59.92$ ,  $Ra = 2.57e4$

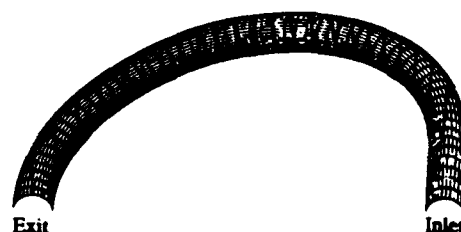


Figure 7  
Surface Pressure Contour  
 $Re = 59.92$ ,  $Ra = 2.57e4$

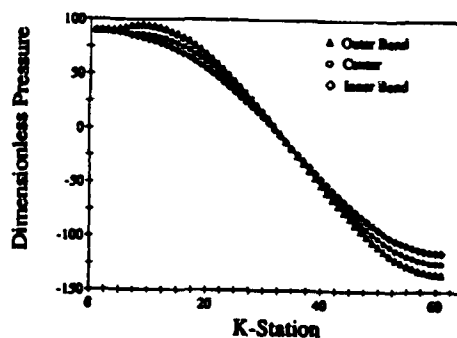


Figure 8  
Pressure Along The Duct  
 $Re = 59.92$ ,  $Ra = 2.57e4$

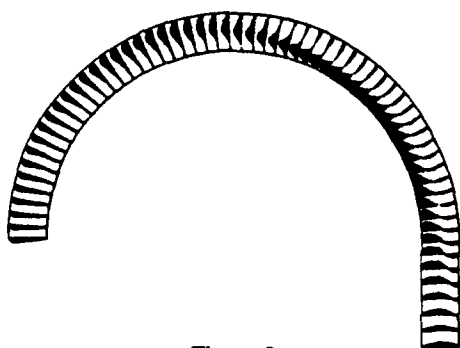


Figure 9  
Velocity Vector At The Plane Of Symmetry  
 $Re = 59.92$ ,  $Ra = 2.57e4$

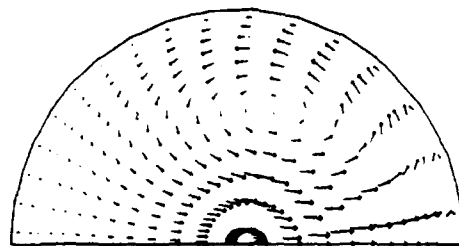


Figure 13  
Secondary Flow At The Exit  
 $Re = 59.92$ ,  $Ra = 2.57e4$



Figure 10  
Speed Contour At The Plane Of Symmetry  
 $Re = 59.92$ ,  $Ra = 2.57e4$

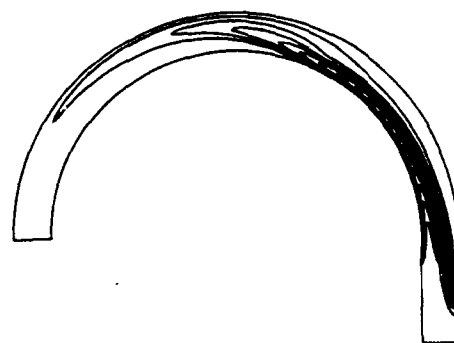


Figure 14  
Temperature Contour At The Plane Of Symmetry

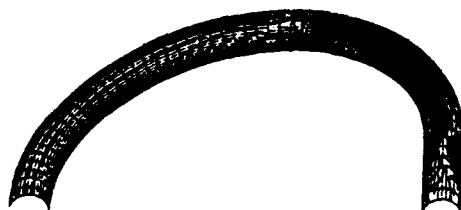


Figure 11  
Total Surface Stresses  
 $Re = 59.92$ ,  $Ra = 2.57e4$

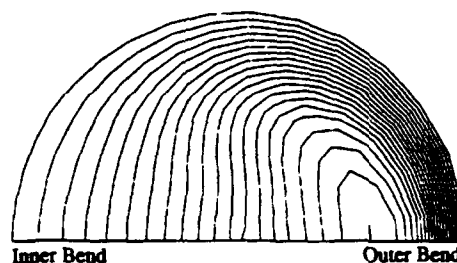


Figure 15  
Temperature At The Exit

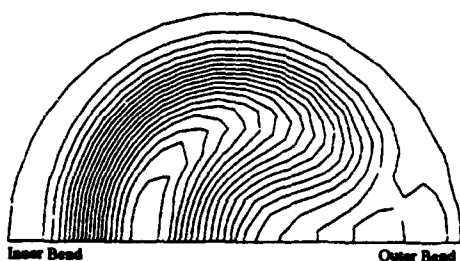


Figure 12  
Speed Contour At The 80 Degrees Location  
 $Re = 59.92$ ,  $Ra = 2.57e4$



Figure 16  
Smoke Pattern At The Exit Obtained By  
Cheng And Yuen [8]

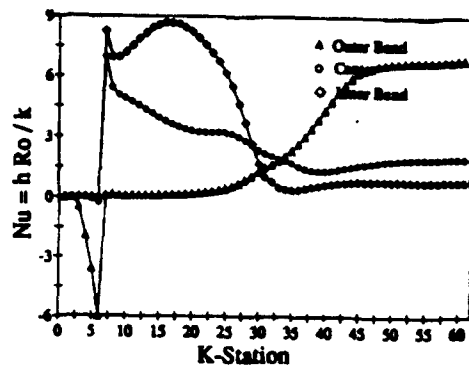


Figure 17  
Nusselt Number Along The Duct  
 $Re = 59.95$   $Ra = 2.57e4$

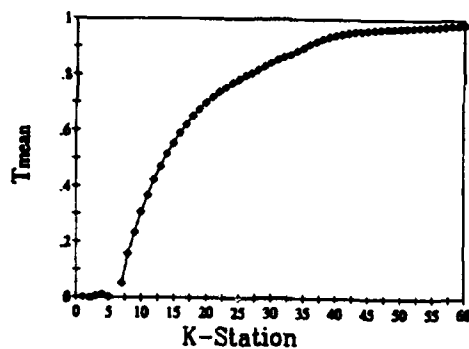


Figure 18  
Mean Temperature Along The Duct  
 $Re = 59.92$   $Ra = 2.57e4$

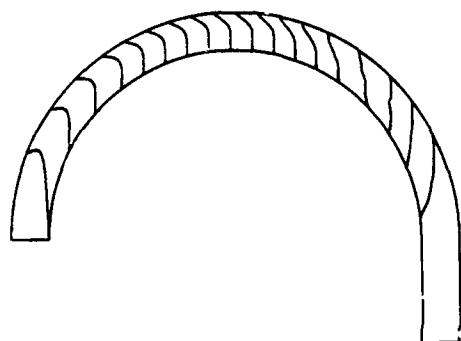


Figure 19  
Pressure At The Plane Of Symmetry  
 $Re = 246.69$   $Ra = 2.57e4$

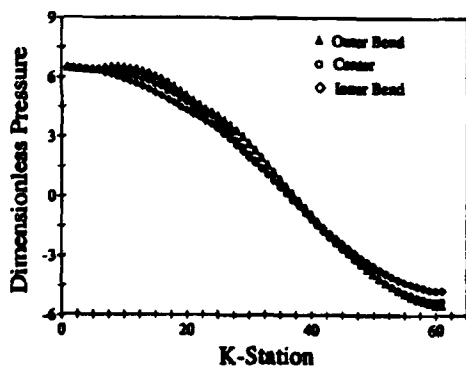


Figure 20  
Pressure Along The Duct  
 $Re = 246.69$   $Ra = 2.57e4$

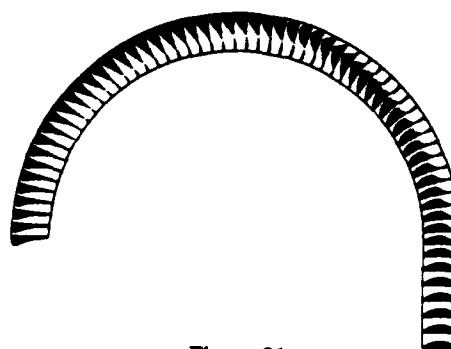


Figure 21  
Velocity Vector At The Plane Of Symmetry  
 $Re = 246.69$   $Ra = 2.57e4$



Figure 22  
Speed Contour At the Plane of Symmetry  
 $Re = 246.69$   $Ra = 2.57e4$

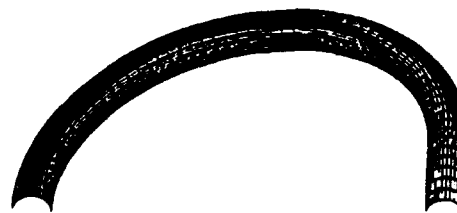


Figure 23  
Total Surface Stresses  
 $Re = 246.69$   $Ra = 2.57e4$

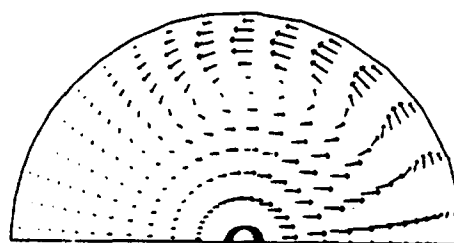


Figure 24  
Secondary Flow At The 75 Degrees Location

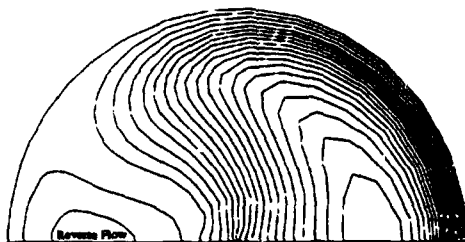


Figure 25  
Speed Contour At the 75 Degrees Location

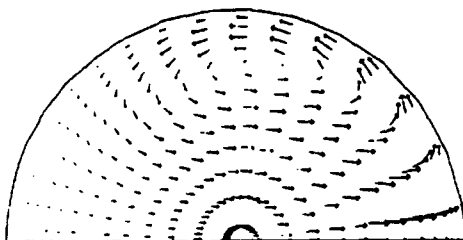


Figure 26  
Secondary Flow At The Exit

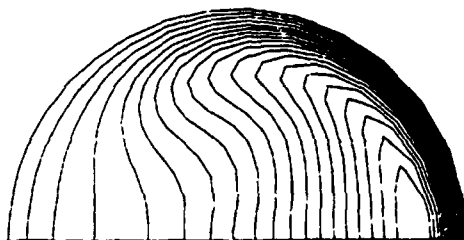


Figure 27  
Speed Contour At The Exit



Figure 28  
Temperature Contour At The Plane Of Symmetry

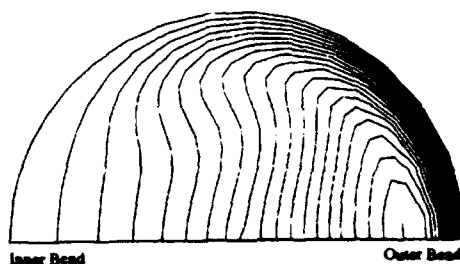


Figure 29  
Temperature Contour At The Exit



Figure 30  
Smoke Pattern At The Exit Obtained By  
Cheng And Yuen [8]

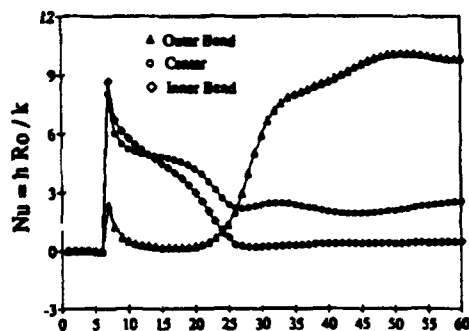


Figure 31  
Local Nusselt Number Along The Duct  
 $Re = 246.69$ ,  $Ra = 2.57e4$

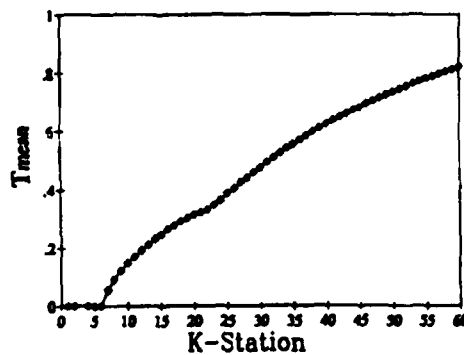


Figure 32  
Mean Temperature Along The Duct  
 $Re = 246.69$ ,  $Ra = 2.57e4$

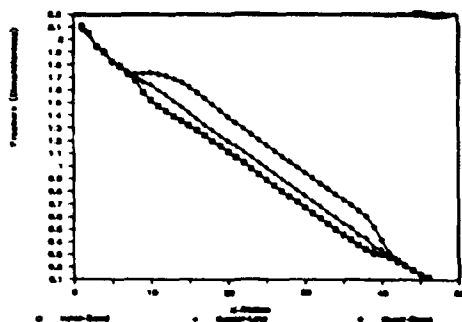


Figure 33  
Pressure Along The Duct  
 $Re = 242, Ra = 0.0$

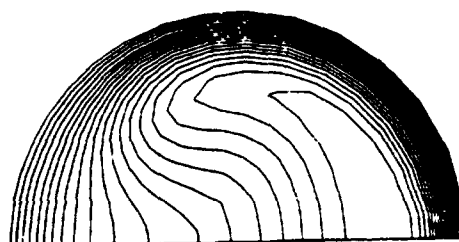


Figure 37  
Speed Contour At the 90 Degrees Location

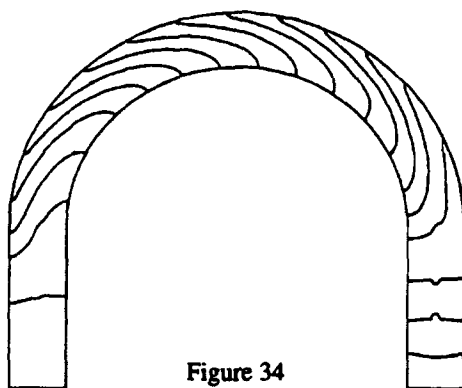


Figure 34  
Pressure At The Plane Of Symmetry  
 $Re = 242, Ra = 0.0$

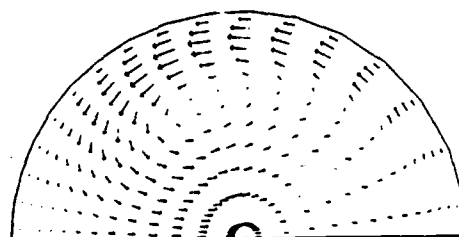


Figure 38  
Secondary Flow At The 90 Degrees Location

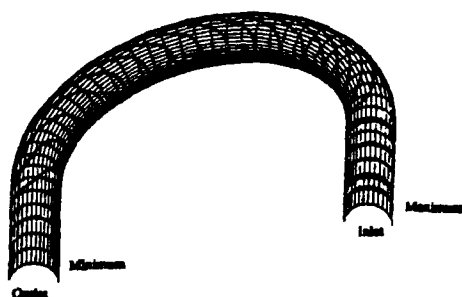


Figure 35  
Surface Pressure Contour  
 $Re = 242, Ra = 0.0$

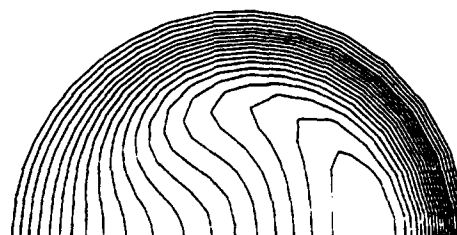


Figure 39  
Speed Contour At The Exit

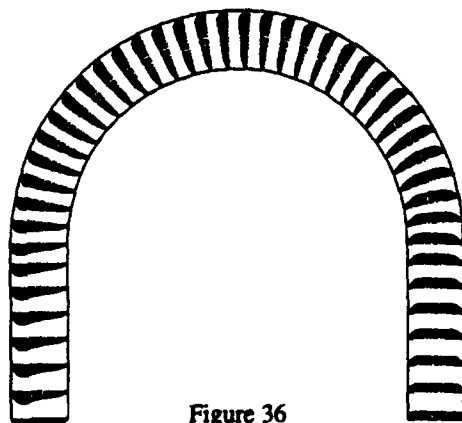


Figure 36  
Velocity Vector At The Plane Of Symmetry  
 $Re = 242, Ra = 0.0$

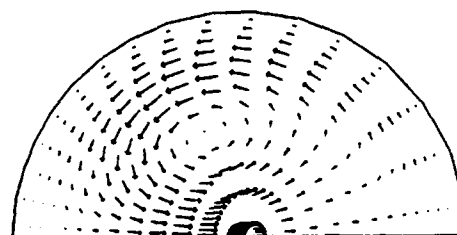


Figure 40  
Secondary Flow At the Exit

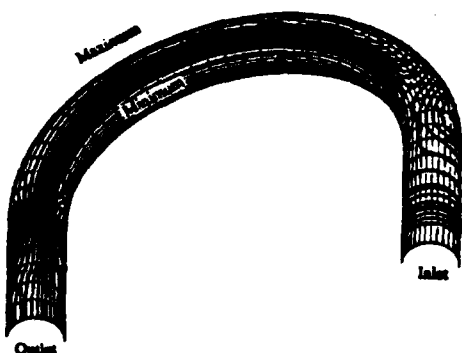


Figure 41  
Total Surface Stresses  
 $Re = 242$ ,  $Ra = 0.0$

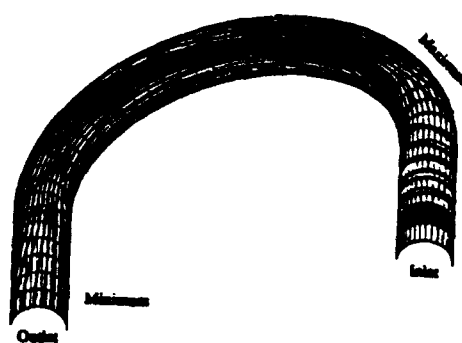


Figure 45  
Surface Heat Flux  
 $Re = 242$ ,  $Ra = 0$

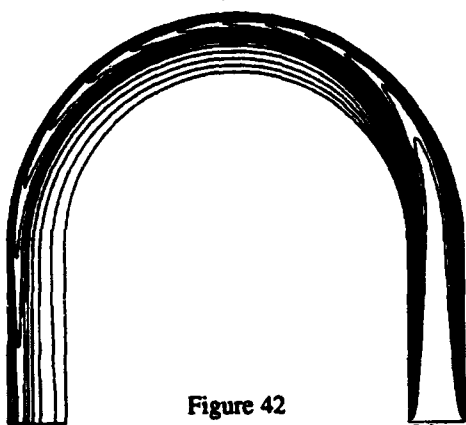


Figure 42  
Temperature Contour At The Plane Of  
Symmetry

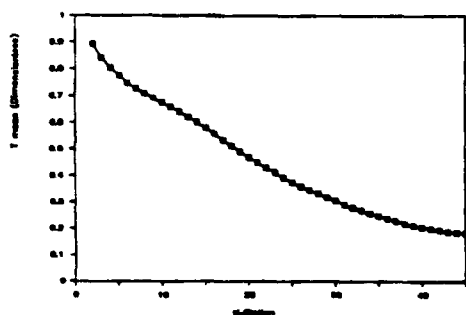


Figure 43  
Mean Temperature Along The Duct

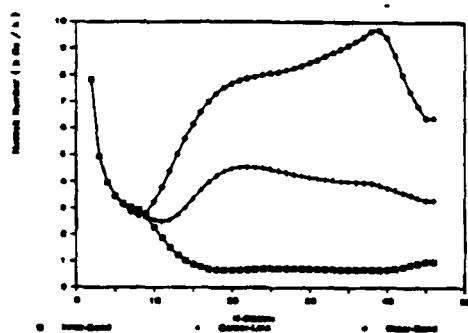


Figure 44  
Local Nusselt Number Along The Duct



# INVESTIGATIONS ON ENTROPY LAYER ALONG HYPERSONIC HYPERBOLOIDS USING A DEFECT BOUNDARY LAYER

J. Ph. Brazier, B. Aupoix and J. Cousteix  
ONERA/CERT - Département Aérodynamique  
2 Avenue E. Belin B.P. 4025  
31055 Toulouse Cedex (France)

## Abstract

A defect approach coupled with matched asymptotic expansions is used to derive a new set of boundary layer equations. This method ensures a smooth matching of the boundary layer with the inviscid solution. These equations are solved to calculate boundary layers over hypersonic blunt bodies, involving the entropy gradient effect. Systematic comparisons are made for both axisymmetric and plane flows in several cases with different Mach and Reynolds numbers. After a brief survey of the entropy layer characteristics, the defect boundary layer results are compared with standard boundary layer and full Navier-Stokes solutions. The entropy gradient effects are found to be more important in the axisymmetric case than in the plane one. The wall temperature has a great influence on the results through the displacement effect. Good predictions can be obtained with the defect approach over a cold wall in the nose region, with a first order solution. However, the defect approach gives less accurate results far from the nose on axisymmetric bodies because of the thinning of the entropy layer.

## Introduction

A blunt body in hypersonic flow is preceded by a bow shock wave, detached in front of the nose. This strong curved shock wave induces an entropy gradient in the shock layer. For an inviscid flow, the entropy gradient is related to the vorticity through Crocco equation :

$$\overrightarrow{\text{curl}} \vec{V} \wedge \vec{V} = - \overrightarrow{\text{grad}} H_t + T \overrightarrow{\text{grad}} S$$

Therefore, velocity and temperature gradients also exist in an inviscid shock layer. The standard boundary layer theory of Prandtl cannot take into account normal gradients outside of the boundary layer. Van Dyke proposed an enlarged theory called higher-order boundary layer theory based on matched asymptotic expansions for high Reynolds numbers [11, 12]. Two expansions corresponding to different approximations of the Navier-Stokes solutions are built. One of them called outer expansion is valid far from the wall, where the viscous effects are negligible. The other one called inner expansion describes the boundary layer where the viscous effects are dominating. The Prandtl boundary layer equations then represent the first term of an expansion in powers of a small parameter. The external flow normal gradients are accounted for in the second order term, which is a small perturbation of the first order solution. Several other second order effects, like the wall curvature, the displacement or the rarefied gas effects are brought into evidence. The main advantage of this systematic method is to give not only the equations but also the matching conditions between the different zones.

For hypersonic reentry flows, the Reynolds number is often moderate at high altitudes, because of the low density of air. The boundary layers are thus thick and can be of the same order of magnitude as the entropy layer, and the inviscid flow quantities can undergo important variations between the wall and the edge of the boundary layer. Because of the hypothesis of Reynolds number tending towards infinity, the boundary layer is assumed to be very thin in Van Dyke's theory and the inviscid flow gradients are represented only by their wall value. So the second order expansion cannot ensure a good matching of the boundary layer with the inviscid flow if the inviscid profiles are not linear, and the influence of the external vorticity on the skin friction and the wall heat flux is not correctly estimated.

## Defect approach

### Decomposition

To ensure a smooth matching at any order whatever the external flow, a defect approach has been used, coupled with asymptotic expansions [3]. In the boundary layer region, the variables are no longer the physical variables, but the difference of them with the external solution (Le Balleur [9]). We consider a steady two-dimensional flow of ideal gas. The variables  $\rho$ ,  $u$ ,  $v$ ,  $p$  and  $T$  stand for the density, tangential and normal component of the velocity, pressure and temperature. The equations are written in a system of orthogonal curvilinear coordinates  $(\xi, \eta)$  where  $\xi$  represents the curvilinear abscissa along the body and  $\eta$  is the distance to the wall. All the variables are made dimensionless by referencing them to the upstream values  $\rho_\infty$  and  $U_\infty$ , the nose radius  $R_0$  and  $T_0 = U_\infty^2 / C_p$ . So we write :

$$\begin{aligned}\rho &= \rho_E + \rho_D \\ u &= u_E + u_D \\ v &= v_E + v_D - v_E(\xi, 0) \\ p &= p_E + p_D \\ T &= T_E + T_D\end{aligned}$$

where the subscript  $E$  stands for the external variables and the defect variables are labelled  $D$ . The term  $v_E(\xi, 0)$  has been added to keep the condition  $v_D(\xi, 0) = 0$  at the wall whatever the value of  $v_E$ .

Expansions are then written using the same small parameter  $\epsilon$  as Van Dyke :

$$\epsilon = \frac{1}{\sqrt{Re}} \quad Re = \frac{\rho_\infty U_\infty R_0}{\mu(T_0)}$$

The external functions depends on the coordinates  $(\xi, \eta)$ . The outer expansions read :

$$\begin{aligned} u_E(\xi, \eta) &= U_1(\xi, \eta) + \varepsilon U_2(\xi, \eta) + \dots \\ v_E(\xi, \eta) &= V_1(\xi, \eta) + \varepsilon V_2(\xi, \eta) + \dots \\ p_E(\xi, \eta) &= P_1(\xi, \eta) + \varepsilon P_2(\xi, \eta) + \dots \\ \rho_E(\xi, \eta) &= R_1(\xi, \eta) + \varepsilon R_2(\xi, \eta) + \dots \\ T_E(\xi, \eta) &= T_1(\xi, \eta) + \varepsilon T_2(\xi, \eta) + \dots \end{aligned}$$

In the inner region, a stretched normal coordinate  $\bar{\eta} = \eta/\varepsilon$  is used for the defect variables :

$$\begin{aligned} u_D(\xi, \eta) &= u_1(\xi, \bar{\eta}) + \varepsilon u_2(\xi, \bar{\eta}) + \dots \\ v_D(\xi, \eta) &= \varepsilon \bar{v}_1(\xi, \bar{\eta}) + \varepsilon^2 \bar{v}_2(\xi, \bar{\eta}) + \dots \\ p_D(\xi, \eta) &= p_1(\xi, \bar{\eta}) + \varepsilon p_2(\xi, \bar{\eta}) + \dots \\ \rho_D(\xi, \eta) &= \rho_1(\xi, \bar{\eta}) + \varepsilon \rho_2(\xi, \bar{\eta}) + \dots \\ T_D(\xi, \eta) &= t_1(\xi, \bar{\eta}) + \varepsilon t_2(\xi, \bar{\eta}) + \dots \end{aligned}$$

The expansion for  $v$  must be shifted to avoid the degeneracy of the continuity equation. These expansions are then brought into the Navier-Stokes equations, and terms of like power of  $\varepsilon$  are equated.

#### Equations

In the outer region, the defect variables are null and the equations for the outer flow are exactly the same as for Van Dyke's theory, i.e. Euler equations. Concerning the inner region, one must first bring the above expansions into the Navier-Stokes equations, then subtract the external equations, and at last equate same powers of  $\varepsilon$ . For practical convenience, the inner equations can then be rewritten in outer coordinates, using  $\eta$  instead of  $\bar{\eta}$ , and replacing  $\bar{v}_1$  and  $\bar{v}_2$  by :

$$v_1(\xi, \eta) = \varepsilon \bar{v}_1(\xi, \bar{\eta}) \quad v_2(\xi, \eta) = \varepsilon \bar{v}_2(\xi, \bar{\eta})$$

Then the following first-order equations are obtained :

- continuity :

$$\frac{\partial}{\partial \xi} [\tau \rho_1 U_1 + \tau (R_1 + \rho_1) u_1] + \frac{\partial}{\partial \eta} [\tau \rho_1 (V_1 + v_1)] + \tau R_1 \frac{\partial v_1}{\partial \eta} = 0$$

-  $\xi$ -momentum :

$$\begin{aligned} (R_1 + \rho_1)(U_1 + u_1) \frac{\partial u_1}{\partial \xi} + [\rho_1 U_1 + (R_1 + \rho_1) u_1] \frac{\partial U_1}{\partial \xi} \\ + (R_1 + \rho_1)(V_1 + v_1) \frac{\partial u_1}{\partial \eta} = - \frac{\partial p_1}{\partial \xi} + \frac{1}{\text{Re}} \frac{\partial}{\partial \eta} \left( \mu_1 \frac{\partial u_1}{\partial \eta} \right) \end{aligned}$$

-  $\eta$ -momentum :

$$0 = - \frac{\partial p_1}{\partial \eta}$$

- energy :

$$\begin{aligned} (R_1 + \rho_1)(U_1 + u_1) \frac{\partial t_1}{\partial \xi} + [\rho_1 U_1 + (R_1 + \rho_1) u_1] \frac{\partial T_1}{\partial \xi} \\ + (R_1 + \rho_1)(V_1 + v_1) \frac{\partial t_1}{\partial \eta} = u_1 \frac{\partial P_1}{\partial \xi} + (U_1 + u_1) \frac{\partial p_1}{\partial \xi} \\ + \frac{\partial}{\partial \eta} \left( \frac{\mu_1}{\text{Pr Re}} \frac{\partial t_1}{\partial \eta} \right) + \frac{\mu_1}{\text{Re}} \left( \frac{\partial u_1}{\partial \eta} \right)^2 \end{aligned}$$

- state :

$$p_1 = \frac{\gamma - 1}{\gamma} [\rho_1 T_1 - (R_1 + \rho_1) t_1]$$

The symbol  $\tau$  represents the distance from the wall to the symmetry axis, with  $j = 0$  for plane and  $j = 1$  for axisymmetric bodies. As in Prandtl equations, the wall curvature appear in the first-order equations only through the transverse curvature radius in the continuity equation. The second-order equations are small-perturbations of the above ones plus source terms due to curvature effects, like in Van Dyke theory.

#### Matching conditions

Each expansion must satisfy the boundary conditions corresponding to its own validity domain. The upstream conditions are to be applied to the outer expansion and the wall conditions to the inner one. The missing conditions are obtained by matching the inner and outer expansions. At the edge of the boundary layer, we can write :

$$\begin{aligned} u &\rightarrow u_E \\ v &\rightarrow v_E \\ \rho &\rightarrow \rho_E \\ p &\rightarrow p_E \\ T &\rightarrow T_E \end{aligned}$$

and so for the defect variables :

$$\begin{aligned} u_D &\rightarrow 0 \\ v_D &\rightarrow v_E(\xi, 0) \\ \rho_D &\rightarrow 0 \\ p_D &\rightarrow 0 \\ T_D &\rightarrow 0 \end{aligned}$$

Thus at first order :

$$\begin{aligned} \lim_{\eta \rightarrow \infty} u_1 &= 0 \\ V_1(\xi, 0) &= 0 \\ \lim_{\eta \rightarrow \infty} p_1 &= 0 \\ \lim_{\eta \rightarrow \infty} t_1 &= 0 \\ \lim_{\eta \rightarrow \infty} \rho_1 &= 0 \end{aligned}$$

The conditions on  $p$ ,  $\rho$  and  $T$  are not independant since they are linked through the state equation. The condition on  $v$  is not a boundary condition for the inner expansion but it gives the wall condition for the outer flow.

The wall conditions for the inner flow are :

$$\begin{aligned} u &= U_1 + u_1 + \varepsilon(U_2 + u_2) = 0 \\ v &= \varepsilon \bar{v}_1 + \varepsilon^2 \bar{v}_2 = 0 \\ T &= T_1 + t_1 + \varepsilon(T_2 + t_2) = T_w \end{aligned}$$

hence :

$$\begin{aligned} u_1(\xi, 0) &= -U_1(\xi, 0) \\ v_1(\xi, 0) &= 0 \\ t_1(\xi, 0) &= T_w - T_1(\xi, 0) \end{aligned}$$

## Discussion

Thanks to the small perturbation approach, the calculations of external flow and boundary layer are uncoupled and can be performed separately provided that a specified sequence is respected. First order external problem must be solved first, then first order internal, second order external, and so on. The defect boundary layer equations are parabolic and can be solved by space marching at a very low cost, like the standard Prandtl equations.

The conditions at the edge of the boundary layer ensure a smooth merging of the boundary layer into the inviscid flow whatever the inviscid profiles. From a theoretical point of view, it can be shown that the defect expansions are consistent with Van Dyke's ones by the fact that at a given order they differ only by terms which are higher-order in Van Dyke's theory.

Using the above conditions, the first order  $\eta$ -momentum equation reduces to

$$p_1 = 0$$

So, the pressure in the first-order boundary layer is everywhere equal to the local inviscid flow pressure, instead of its wall value like in Van Dyke's theory.

## Applications

To experiment the defect approach, several cases have been selected for a blunt body in a hypersonic flow of ideal gas. The general shape of the body is a plane or axisymmetric hyperboloid, defined by the nose radius and the angle of the asymptotes, at zero degree incidence. The numerical data are given by Shinn, Moss and Simmonds [10] for a hyperboloid equivalent to the windward symmetry line of the U.S. space shuttle. Two points of the reentry trajectory of the STS-2 flight are considered here :

Reentry trajectory - Flight STS-2		
Mach $M_\infty$	26.6	23.4
time (s)	250	650
altitude (km)	85.74	71.29
nose radius $R_0$ (m)	1.322	1.253
asymptotes half-angle ( $^\circ$ )	41.7	40.2
pressure $p_\infty$ (Pa)	0.3634	4.0165
temperature $T_\infty$ (K)	199	205
velocity $U_\infty$ (m/s)	7530	6730
density $\rho_\infty$ (kg/m <sup>3</sup> )	$6.35 \cdot 10^{-6}$	$6.80 \cdot 10^{-5}$
reference temperature $T_0$ (K)	56321	44900
Reynolds number $Re = \frac{\rho_\infty U_\infty R_0}{\mu(T_0)}$	183.55	1865.65
small parameter $\epsilon = Re^{-1/2}$	0.074	0.023
Reynolds number $Re_\infty = \frac{\rho_\infty U_\infty R_0}{\mu_\infty}$	4792	42374

The Prandtl number is assumed to be constant and equal to 0.725. The ratio of specific heats  $\gamma$  is 1.4. The wall temperature is fixed and equal to 1500 K. The viscosity law is Sutherland's. No comparison with experimental data is possible since the real gas effects are not yet included. So Navier-Stokes solutions [8] have been taken as reference, to compare

the two Euler + boundary layer methods. Euler calculations are made with a code from ONERA [14]. Standard boundary layer solutions are obtained using a program developed in DERAT [2]. Only first-order boundary layer are presented here since second-order outer flow solutions are not yet available. Several second-order calculations using Van Dyke's theory have been made on a hypersonic blunt body [1, 4, 5, 6, 7].

## Axisymmetric hyperboloid

Past a hyperboloid, the shock wave curvature decrease fastly and the entropy field tends to be uniform, except for the streamlines near the wall, which crossed the strongly curved shock wave at the nose. In this case, the entropy layer is characterized by a non-zero normal gradient at the wall and a decreasing thickness towards the rear, since the mass-flow is constant in the entropy layer and the circumference of the body increases (fig. 1 left). The entropy values at the wall and at the edge of the entropy layer remain constant because the wall is a streamline and outside of the entropy layer the flow is isentropic. So the normal entropy gradient at the wall deeply increases downstream. The shock layer is thinner than in the plane case. Far from the nose, the flow is similar to a flow past a sharp cone except in the entropy layer, whose aspect is quite similar to a viscous boundary layer (fig. 2).

Boundary layer profiles are displayed on figures 4 to 7 for the Mach 23.4 case. Longitudinal velocity profiles are plotted on figure 4 at a distance of nine nose radius from the stagnation point. One can see on this figure the important velocity gradient at the wall in the inviscid flow. This gradient diminishes distinctly between the wall and the boundary layer edge. So even with a second-order expansion, Van Dyke's method could not give a good matching, since it considers only the wall value of the gradient. In this case, it would widely overestimate the skin friction (Adams [1]). Due to the very low wall temperature compared to the inviscid flow one, the displacement effect is quasi-null and the Navier-Stokes solution recasts exactly the inviscid profile in the outer region. In this case, the agreement is quite good with the first-order defect boundary layer. A composite profile has been plotted also, using the additive composite expansion (Van Dyke [13]) constructed with the first order inner and outer expansions. It gives good results for the longitudinal velocity, slightly different of the defect ones.

The corresponding profiles for the temperature are shown on figure 5. The defect profile is in rather good agreement with the Navier-Stokes solution, but in this case the composite expansion written with Van Dyke's first order solutions gives very bad results and does not improve the inner solution. This is due to the negative slope at the wall for the inviscid temperature. Figures 6 and 7 show the velocity and temperature profiles at twenty-one nose radius. The growing boundary layer has overlapped a larger part of the entropy layer. Because of the constant total enthalpy, the positive velocity gradient at the wall induces a negative temperature gradient. In spite of this, the wall heat flux is increased by the vorticity, as well as the skin friction, as can be seen on the figures 8 and 9. But the increase is far more important for the wall friction than for the flux. The defect approach underestimates slightly these quantities but gives better predictions than the standard boundary layer.

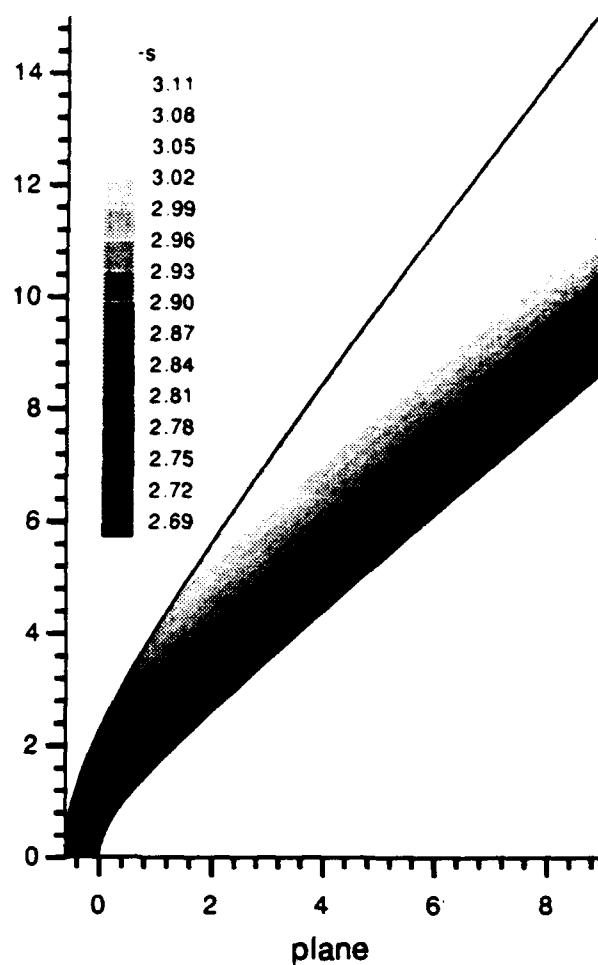
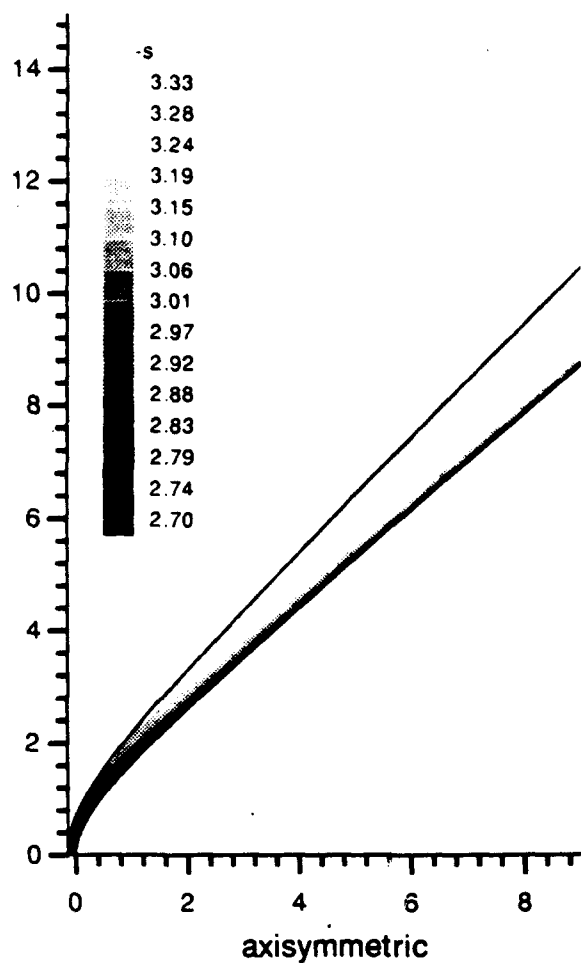


Figure 1: Entropy level in the shock layer - Mach 23.4

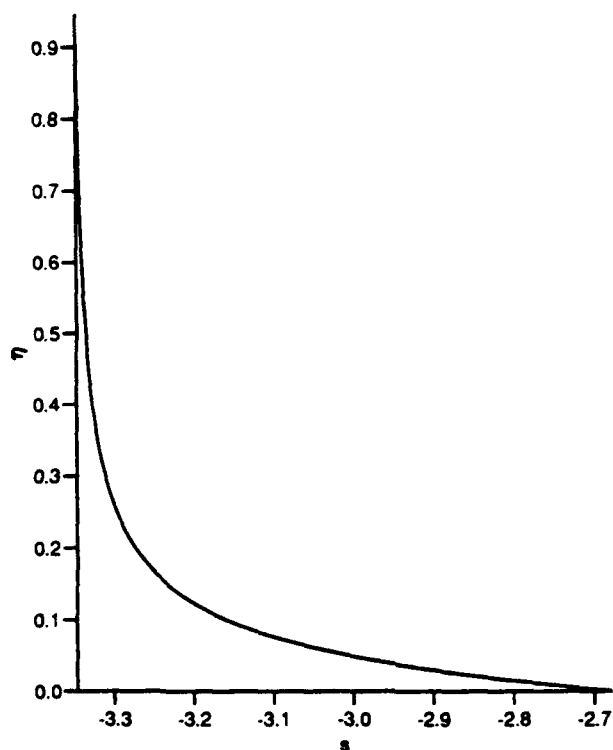


Figure 2: Entropy profile - axisymmetric case  
Mach 23.4,  $\xi = 9$

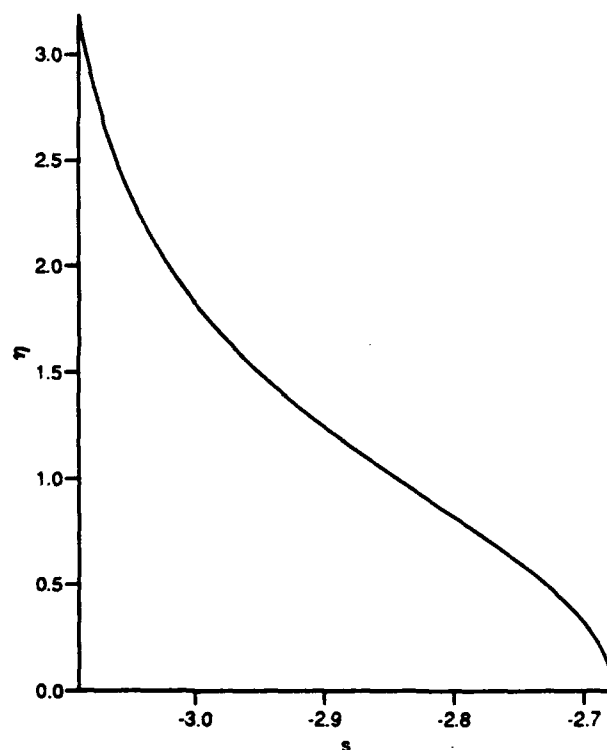


Figure 3: Entropy profile - plane case Mach 23.4,  $\xi = 9$

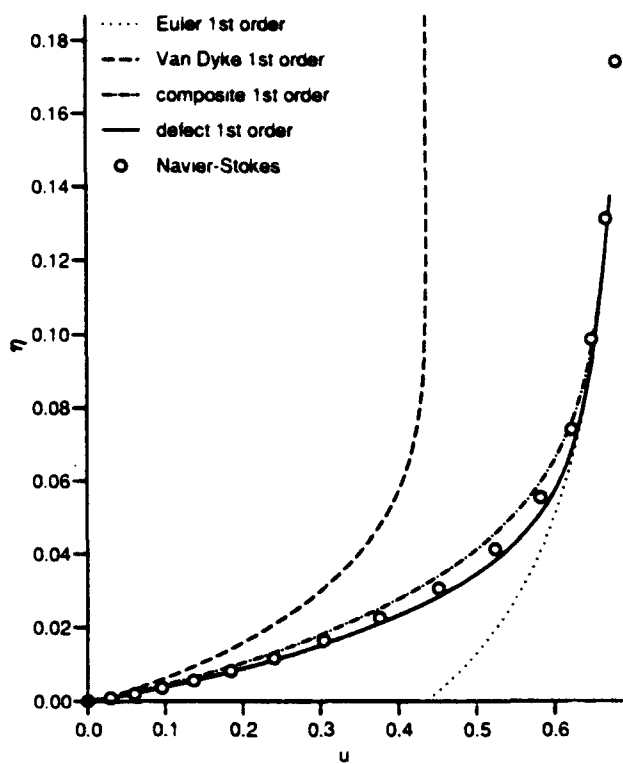


Figure 4: Longitudinal velocity profiles  
Mach 23.4,  $T_w = 1500$  K,  $\xi = 9$

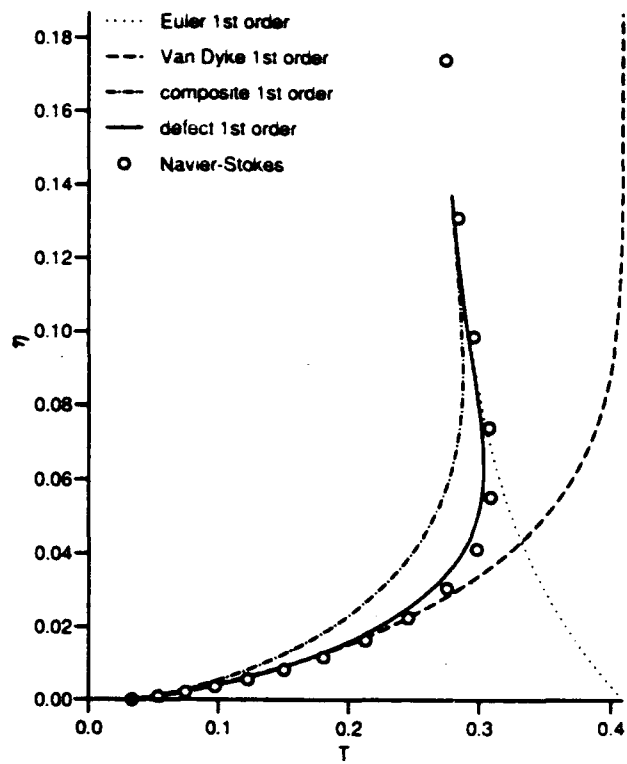


Figure 5: Temperature profiles  
Mach 23.4,  $T_w = 1500$  K,  $\xi = 9$

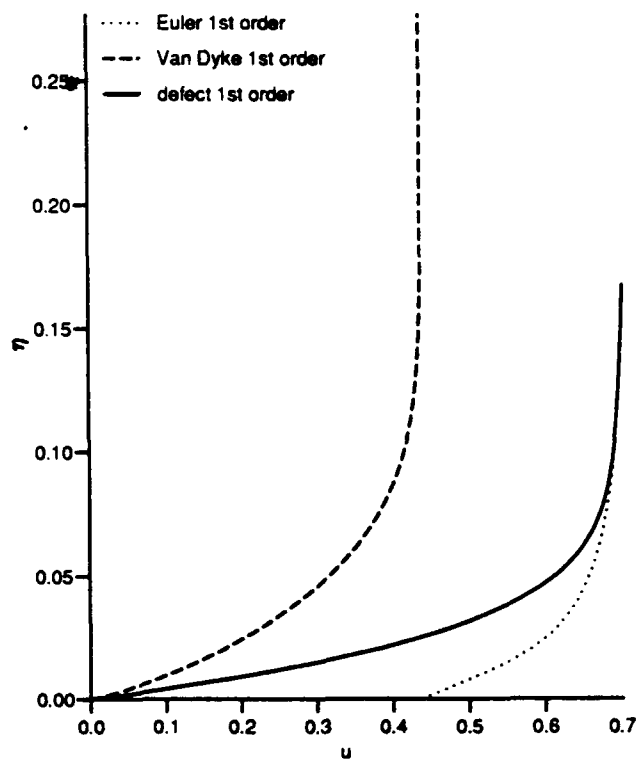


Figure 6: Velocity profiles Mach 23.4,  $T_w = 1500$  K,  $\xi = 21$

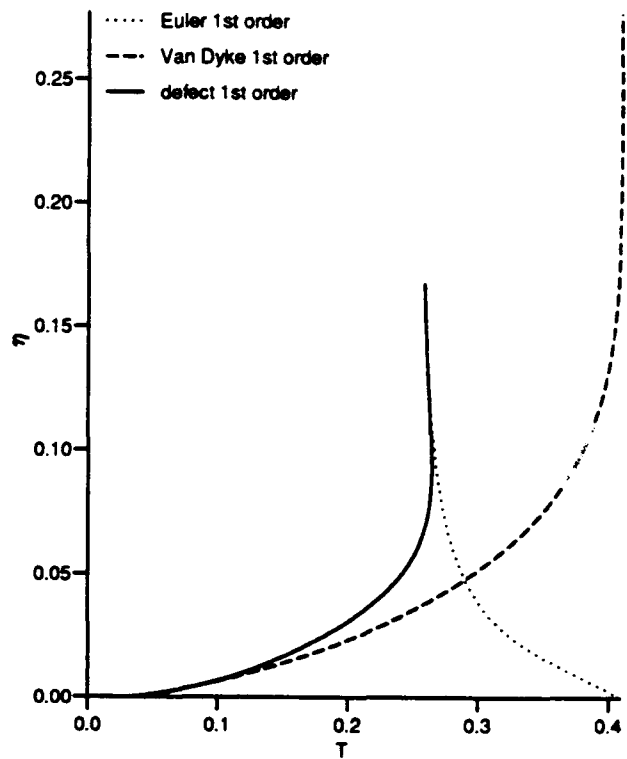


Figure 7: Temperature profiles  
Mach 23.4,  $T_w = 1500$  K,  $\xi = 21$

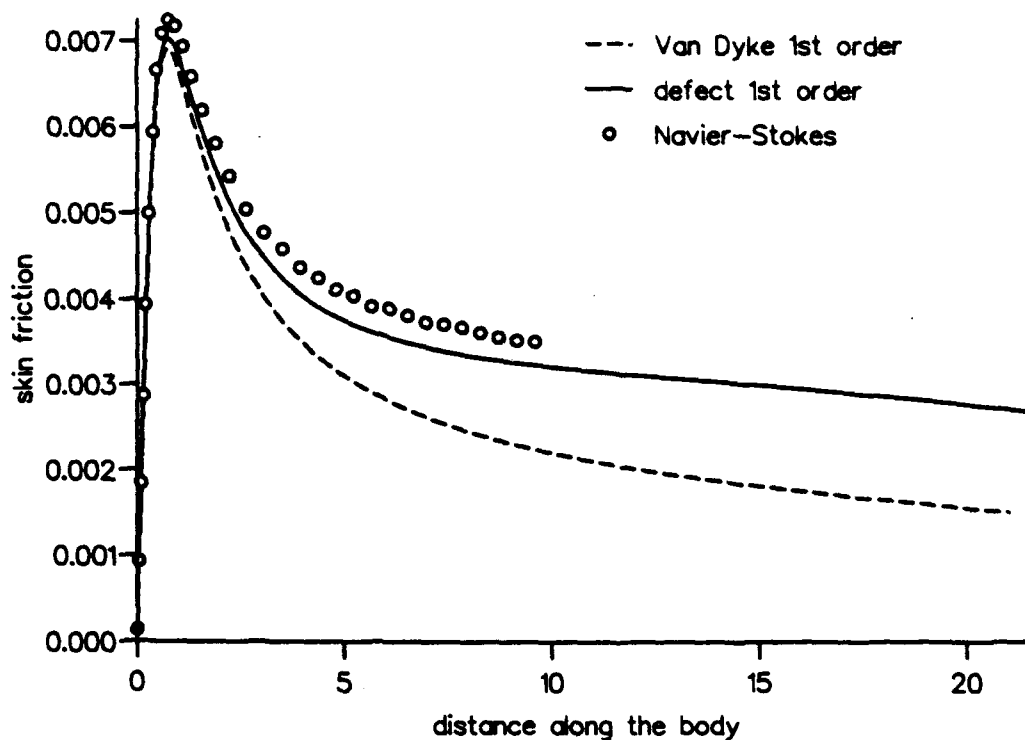


Figure 8: Skin friction on the hyperboloid - Mach 23.4,  $T_w = 1500$  K

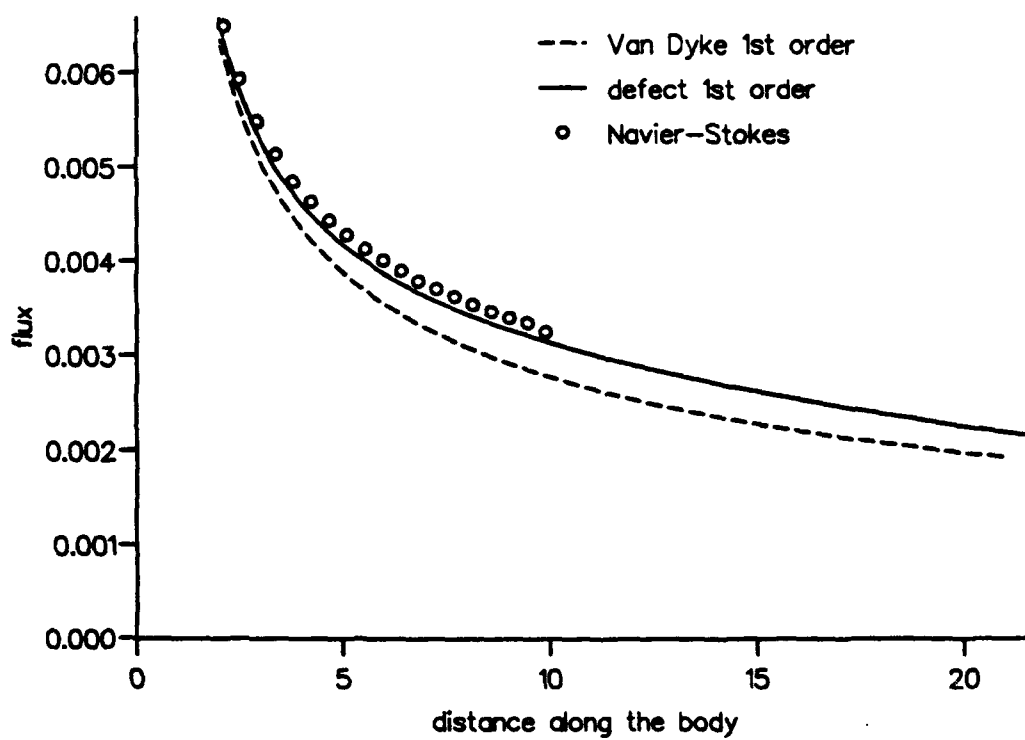


Figure 9: Wall heat flux on the hyperboloid - Mach 23.4,  $T_w = 1500$  K

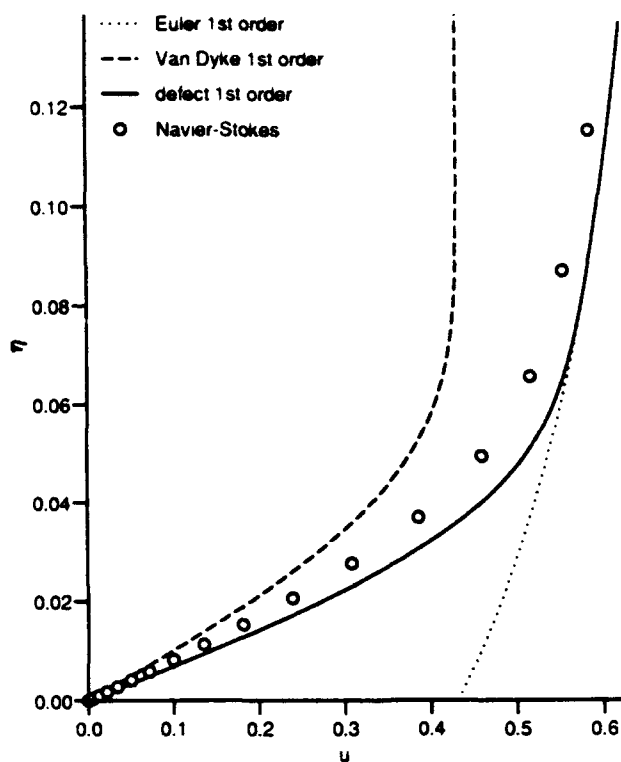


Figure 10: Longitudinal velocity profiles  
Mach 23.4,  $T_w = 15000$  K,  $\xi = 4$

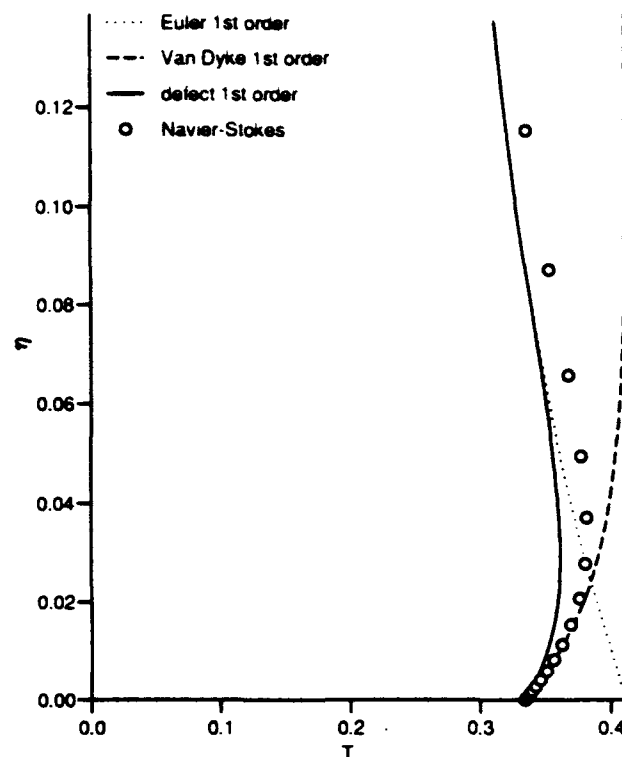


Figure 11: Temperature profiles  
Mach 23.4,  $T_w = 15000$  K,  $\xi = 4$

Figures 10 and 11 show the velocity and temperature profiles with an arbitrary temperature of ten times the temperature of the preceding case. The displacement effect is then far more important and it is obvious on these figures that the Navier-Stokes solution is shifted from the Euler solution in the outer zone. So the first-order boundary layer methods give poor results and a second-order calculation seems to be necessary.

The velocity and temperature profiles at nine nose radius abscissa in the Mach 26.6 case are presented on figures 12 and 13. Because of the lower density, the Reynolds number is small and the boundary layer is about twice as thick as in the Mach 23.4 case. So a large part of the entropy layer is overlapped by the boundary layer. The inviscid velocity and temperature gradients at the edge of the boundary layer are far weaker than their wall values. Due to the high value of the expansion parameter  $\epsilon$ , the second order effects are more important and a slight displacement effect is visible between the Euler and Navier-Stokes profiles outside the boundary layer. The agreement between the Navier-Stokes and defect profiles is rather good, but the shear at the wall is a bit too high for the later one. Note that because of the negative inviscid temperature gradient at the wall, the Van Dyke's composite expansion gives again poor results on the temperature profile.

Figures 14 and 15 show the same quantities at twenty-one nose radius from the nose. The entropy layer is now completely included into the boundary layer, and the gradients in the entropy layer become higher than those of the viscous boundary layer. So the hypothesis of neglecting the viscous effects in the external flow does not hold any longer and the defect boundary layer probably gives overestimated values for

the slope at the wall of the velocity profile. But no Navier-Stokes solution is yet available on such a large domain.

The corresponding skin friction and wall heat flux are shown on figures 16 and 17. As forecast from the velocity profiles, the defect approach improves greatly the standard boundary layer result, but widely overestimates the skin friction on the rear of the body. The predictions concerning the wall heat flux seem to be more reliable.

#### Plane hyperbola

Let us now consider a plane hyperbola in the same conditions of hypersonic flows. On figure 1-right are displayed the entropy levels in the inviscid shock layer. The main difference with the axisymmetric case is that now the entropy gradient is null at the wall (Van Dyke [12]). Figure 3 shows entropy profile across the shock layer. The entropy gradient layer is thus located at a short distance above the wall. So the velocity and temperature gradients in the inviscid flow are null at the wall as well, and their influence will be significant only with a very thick boundary layer. Moreover, far downstream, the flow can be assimilated to a parallel flow and the entropy layer's thickness remains constant whereas in the axisymmetric case the entropy layer gets thinner towards the rear part of the body. Thus the entropy gradient remains bounded. Since it is null at the wall, its influence on the skin friction and the heat flux will now be far less important.

On figures 18 and 19 are plotted the velocity and temperature profiles on the Mach 23.4 hyperbola at nine nose radius abscissa. The inviscid gradients are hardly visible outside the boundary layer and all the methods give the same results.

When the Reynolds number is lower, the matching of the

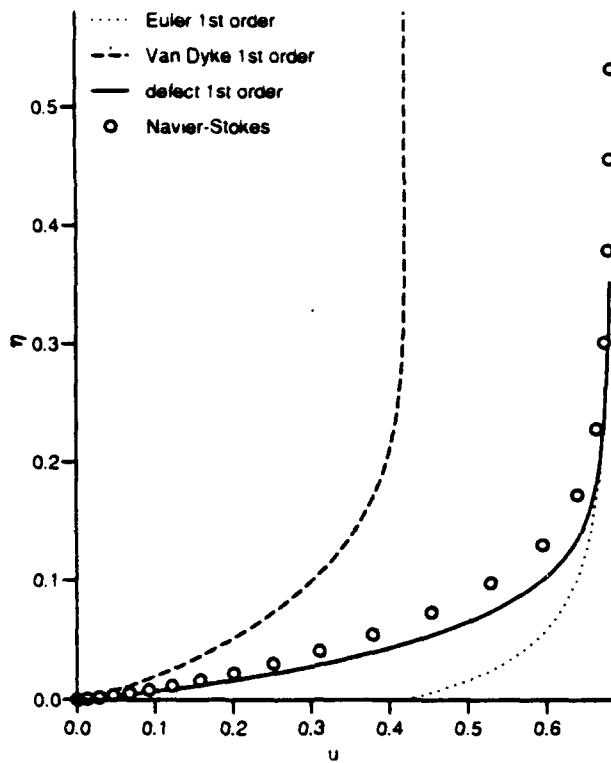


Figure 12: Longitudinal velocity profiles  
Mach 26.6,  $T_w = 1500$  K,  $\xi = 9$

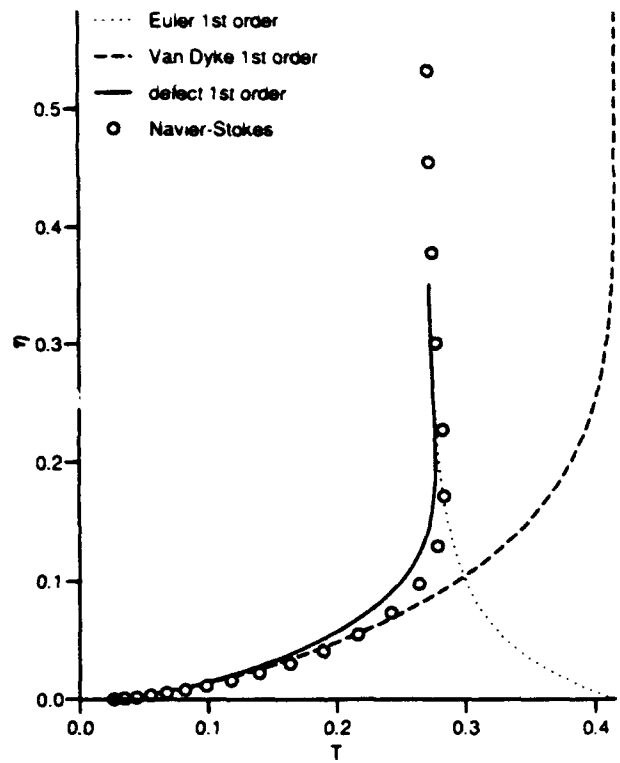


Figure 13: Temperature profiles  
Mach 26.6,  $T_w = 1500$  K,  $\xi = 9$

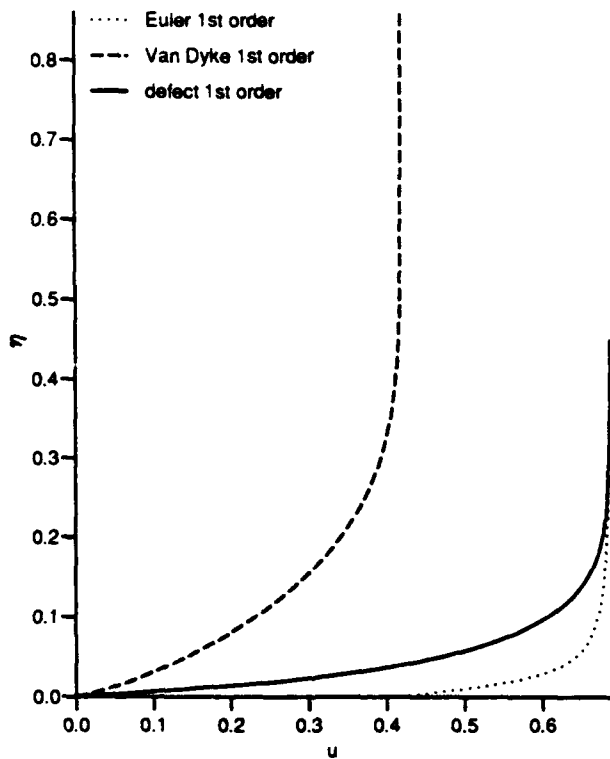


Figure 14: Longitudinal velocity profiles  
Mach 26.6,  $T_w = 1500$  K,  $\xi = 21$

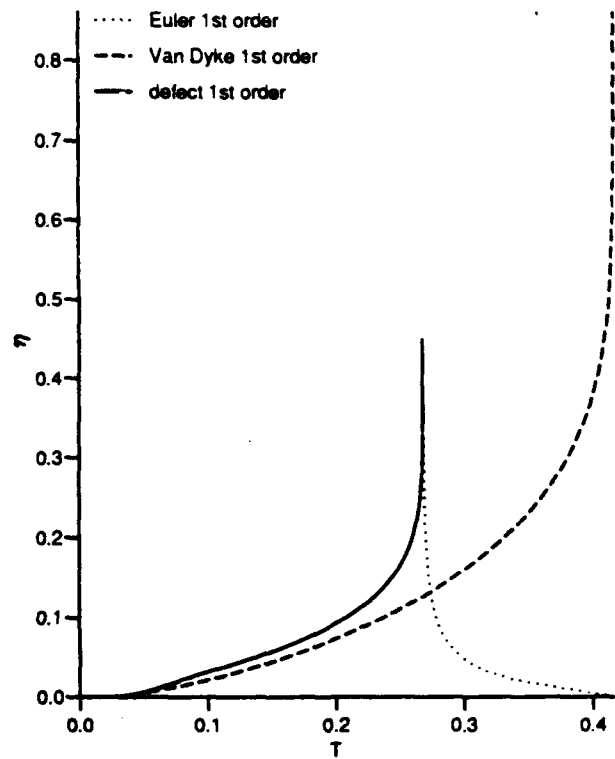


Figure 15: Temperature profiles  
Mach 26.6,  $T_w = 1500$  K,  $\xi = 21$



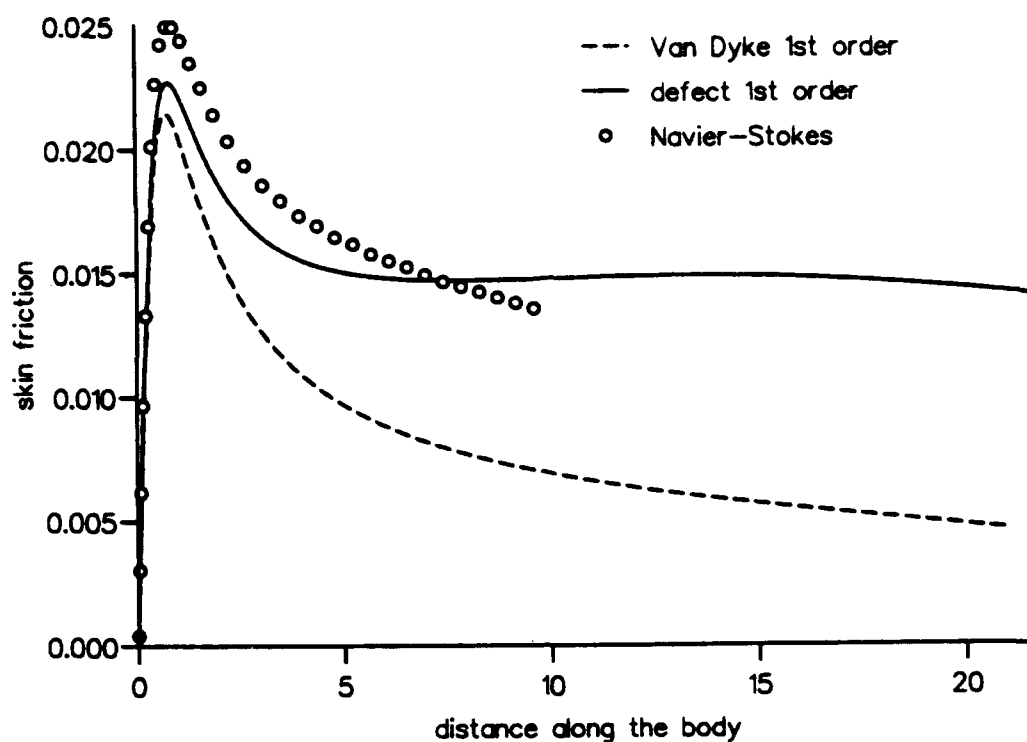


Figure 16: Skin friction on the hyperboloid - Mach 26.6,  $T_w = 1500$  K

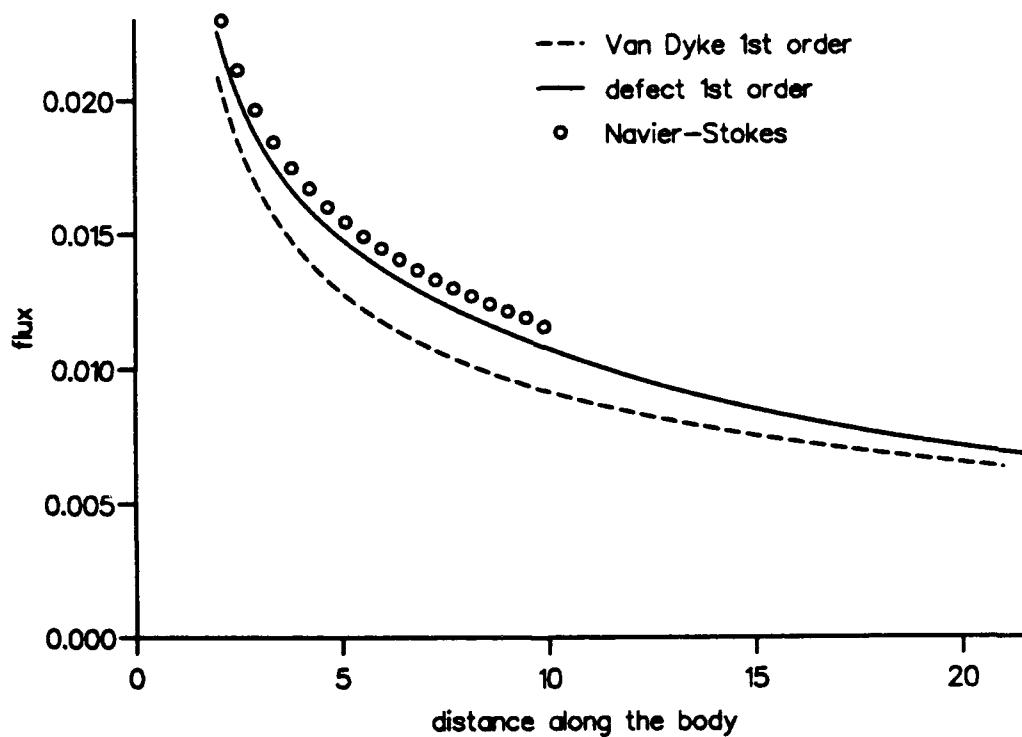


Figure 17: Wall heat flux on the hyperboloid - Mach 26.6,  $T_w = 1500$  K

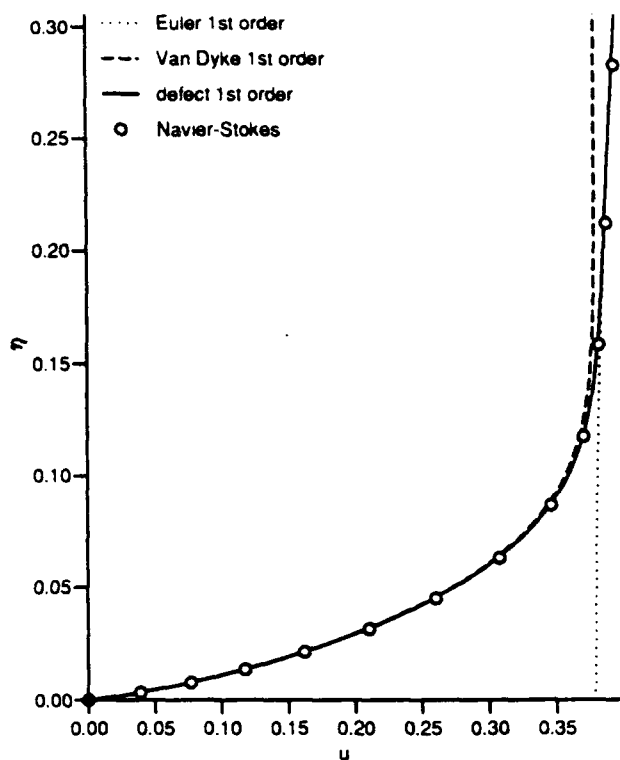


Figure 18: Longitudinal velocity profiles  
Mach 23.4,  $T_w = 1500$  K,  $\xi = 9$

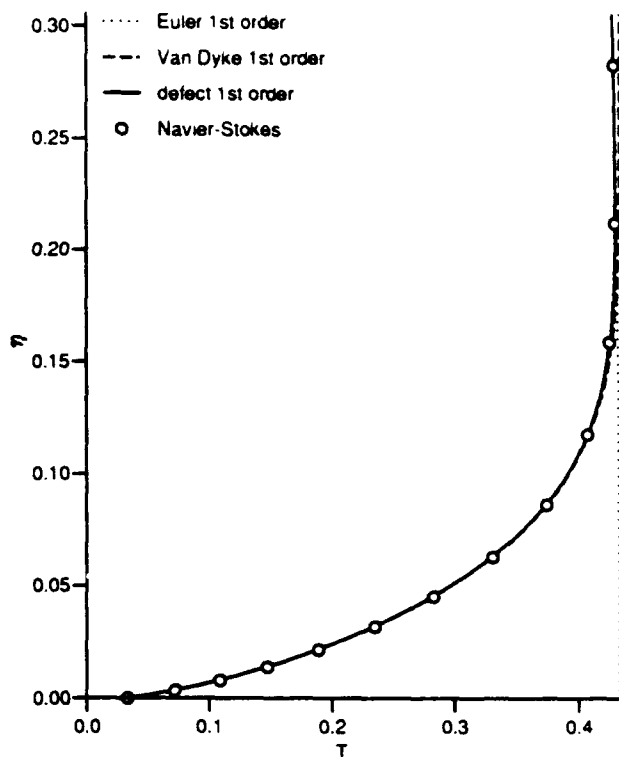


Figure 19: Temperature profiles  
Mach 23.4,  $T_w = 1500$  K,  $\xi = 9$

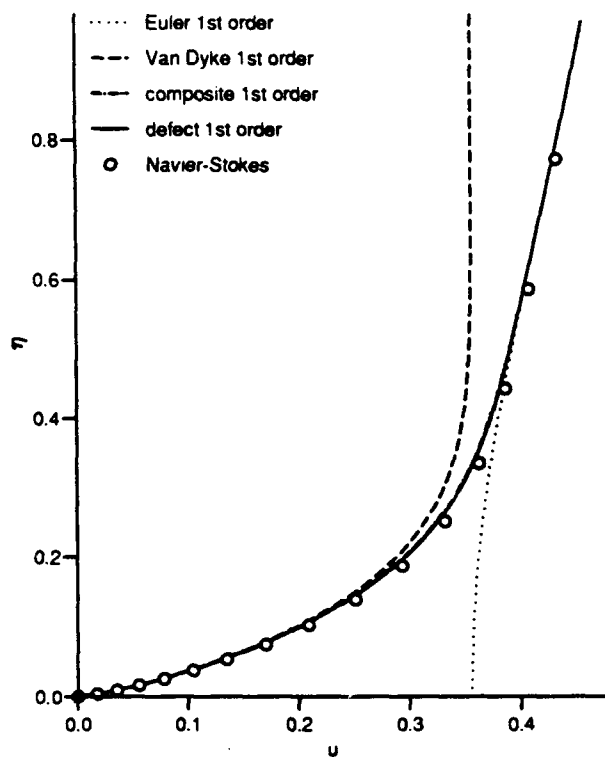


Figure 20: Longitudinal velocity profiles  
Mach 26.6,  $T_w = 1500$  K,  $\xi = 9$

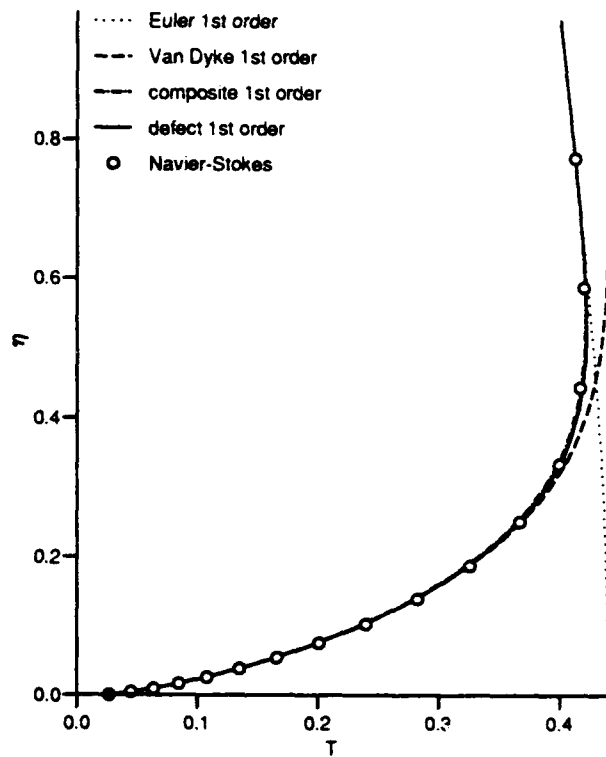


Figure 21: Temperature profiles  
Mach 26.6,  $T_w = 1500$  K,  $\xi = 9$

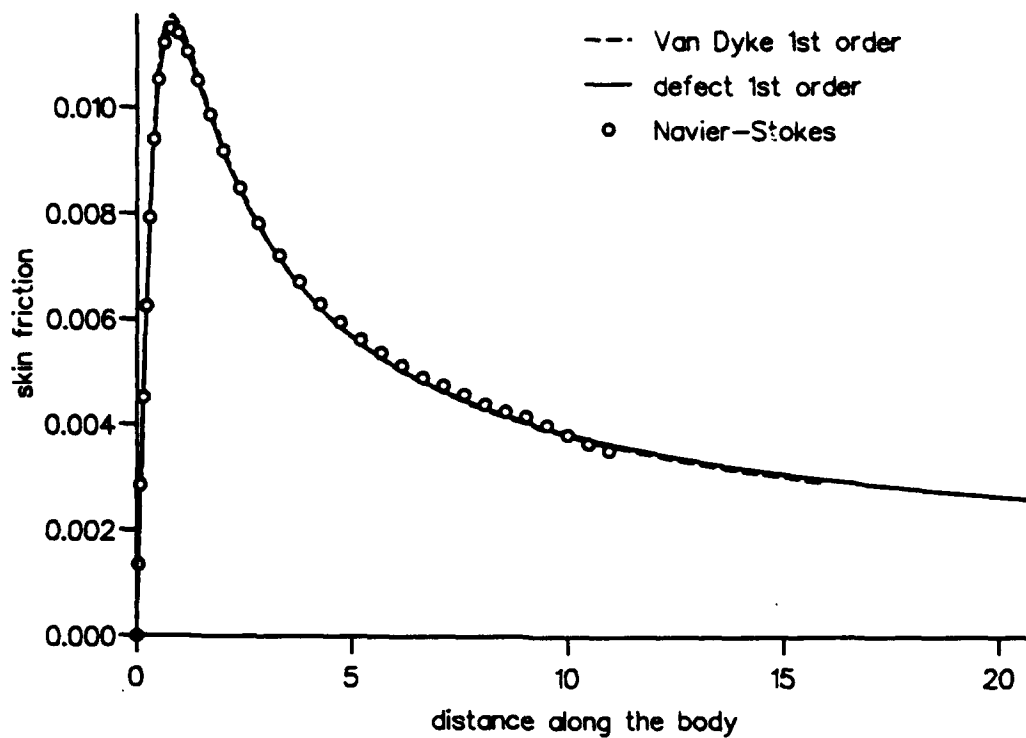


Figure 22: Skin friction on the plane hyperbola - Mach 26.6,  $T_w = 1500$  K

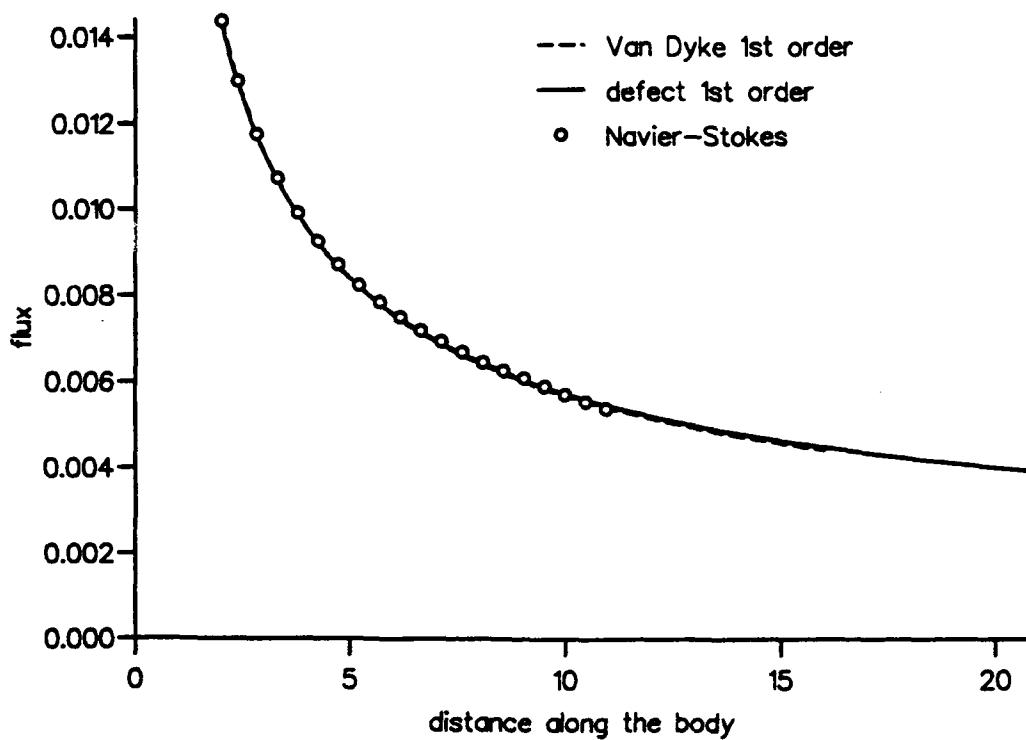


Figure 23: Wall heat flux on the plane hyperbola - Mach 26.6,  $T_w = 1500$  K

boundary layer with the inviscid flow takes place in the gradient region, as can be seen on the figures 20 and 21 for the case Mach 26.6. The defect method gives a good matching and a correct agreement with Navier-Stokes solutions, but the two boundary layer methods give similar results near the wall. Thus no significant difference is visible on the skin friction and the wall heat flux shown on figures 22 and 23.

### Conclusion

Several boundary layer calculations have been performed on various hypersonic bodies, including plane or axisymmetric shapes. The behaviour of the solutions far from the stagnation point has been particularly investigated. The different cases presented here showed both the interest and the limits of boundary layer methods to compute hypersonic flows. Moreover, the importance of taking into account the second order effects when calculating boundary layers at low Reynolds numbers has been brought into evidence. The most important of them are the entropy gradient effect and the displacement effect in the considered cases. They can deeply modify the wall quantities such as the skin friction or the wall heat flux, which are essential to predict the total drag of the vehicle and to design the thermal protection.

Using the matched asymptotic expansions technique, the defect approach allows us to improve the results of the standard higher-order boundary layer theory of Van Dyke, for a similar cost. Particularly, it ensures a smooth matching of the viscous and inviscid flows, even when the inviscid profiles vary significantly through the boundary layer. When the wall temperature is low and thus the displacement effect is negligible, first-order defect calculations can give good results and reproduce Navier-Stokes solutions with a reasonable accuracy at a lower cost, as long as the entropy layer is not too thin compared to the viscous boundary layer. But it gives less accurate results on axisymmetric hyperboloids at low Reynolds number far from the stagnation point, when the inviscid flow normal gradients are higher than those of the boundary layer. The inviscid flow concept seems to be invalid then.

### References

- [1] J.C. Adams *Higher-order boundary-layer effects on analytic bodies of revolution*, Arnold Engineering Development Center, Report AEDC-TR-68-57 (1968)
- [2] B. Aupoix, D. Arnal *CLIC: calcul des couches limites compressibles*, Rapport technique DERAT n° 23/5005.19 (1988)
- [3] B. Aupoix, J.Ph. Brazier, J. Cousteix *An asymptotic defect boundary layer theory applied to hypersonic flows* AIAA 91-0026, 29th Aerospace Sciences Meeting, January 7-10, Reno, Nevada (1991)
- [4] R.T. Davis, I. Flügge-Lotz *The laminar compressible boundary-layer in the stagnation-point region of an axisymmetric blunt body including the second-order effect of vorticity interaction*, International Journal of Heat and Mass Transfer, Vol. 7, pp. 341-370 (1964)
- [5] R.T. Davis, I. Flügge-Lotz *Laminar compressible flow past axisymmetric blunt bodies*, Journal of Fluid Mechanics, Vol. 20, Part 4, pp. 593-623 (1964)
- [6] T.K. Fannelöp, I. Flügge-Lotz *Two-dimensional hypersonic stagnation flow at low Reynolds numbers*, Z. Flugwiss. Vol. 13, n° 8, pp. 282-296 (1965)
- [7] T.K. Fannelöp, I. Flügge-Lotz *Viscous hypersonic flow over simple blunt bodies; comparison of a second-order theory with experimental results*, Journal de Mécanique, Vol. 5, n° 1, pp. 69-100 (1966)
- [8] A. Lafon *Calcul d'écoulements visqueux hypersoniques*, Rapport technique DERAT n° 32/5005.22 (1990)
- [9] J.C. Le Balleur *Calcul des écoulements à forte interaction visqueuse au moyen de méthodes de couplage*, AGARD - CP 291 (1980)
- [10] J.L. Shinn, J.N. Moss, A.L. Simmonds *Viscous shock layer heating analysis for the shuttle windward plane with surface finite catalytic recombination rates*, AIAA Paper n° 82-0842 (1982)
- [11] M. Van Dyke *Higher approximations in boundary layer theory, Part 1: General analysis*, Journal of Fluid Mechanics, vol. 14, pp. 161-177 (1962), *Part 2: Application to leading edges*, Journal of Fluid Mechanics, vol. 14, pp. 481-495 (1962)
- [12] M. Van Dyke *Second-order compressible boundary-layer theory with application to blunt bodies in hypersonic flow*, Hypersonic Flow Research, Vol. 7, pp. 37-76 (1962), F.R. Riddell Editor, Academic Press
- [13] M. Van Dyke *Perturbation methods in fluid mechanics*, Parabolic Press (1975)
- [14] J.P. Veuillot *Calcul de l'écoulement azisymétrique autour d'un corps de rentrée*, Rapport Technique ONERA n° RT 31/1285 AY (Janvier 1989)

**TWO- AND THREE-DIMENSIONAL FLOWS, 3**  
**SESSION 11**

# ADAPTIVE MULTIGRID DOMAIN DECOMPOSITION SOLUTIONS FOR VISCOUS INTERACTING FLOWS

Stanley G. Rubin and Kumar Srinivasan  
Department of Aerospace Engineering and Engineering Mechanics  
University of Cincinnati  
Cincinnati, Ohio

## Abstract

Several viscous incompressible flows with strong pressure interaction and/or axial flow reversal are considered with an adaptive multigrid domain decomposition procedure. Specific examples include the triple deck structure surrounding the trailing edge of a flat plate, the flow recirculation in a trough geometry, and the flow in a rearward facing step channel. For the latter case, there are multiple recirculation zones, of different character, for laminar and turbulent flow conditions. A pressure-based form of flux-vector splitting is applied to the Navier-Stokes equations, which are represented by an implicit lowest-order reduced Navier-Stokes (RNS) system and a purely diffusive, higher-order, deferred-corrector. A trapezoidal or box-like form of discretization insures that all mass conservation properties are satisfied at interfacial and outflow boundaries, even for this primitive-variable non-staggered grid computation.

## Introduction

Viscous interactions are typically associated with turbulent or high Reynolds number ( $Re$ ) laminar flows. These interactions are quite frequently characterized by the appearance of high flow gradients that are most significant in small or 'thin' domains of finite extent, and in one or more directions, e.g., boundary or vortical layers/regions, triple deck structures, shock wave structure. Outside of these regions, the flow is generally more highly diffused or inviscid so that the flow gradients are less severe. However, the flow character in these smoother regions, which generally encompass a major portion of the flow domain, can be significantly influenced by the interaction with the high gradient layers. In order to accurately assess this class of viscous interacting flows with discrete computational methods, (1) local grid refinement is required in the high shear layers, and (2) simple, efficient, adaptive methods, that effectively communicate information between the disparate flow domains, and at the same time maintain all conservation properties, are necessary.

In the present investigation, an adaptive, multigrid, domain decomposition strategy is combined with a pressure-based form of flux vector discretization in order to accomplish these goals<sup>1-4</sup>. The governing Navier-Stokes equations are evaluated through an implicit, lowest-order in  $Re$ , reduced Navier-Stokes (RNS) subsystem<sup>1,2</sup>, that is combined, when necessary, with an explicit purely diffusive deferred-corrector (DC) in viscous layers. Local directional refinement that is driven by specified flow parameters and accuracy limits is achieved by sequentially splitting the overall flow domain into a variety of subdomains. In the present analysis, this domain decomposition strategy is applied, in conjunction with an adaptive multigrid

algorithm, in order to achieve the appropriate level of grid refinement. In this approach, each grid in the multigrid hierarchy, is of equal or lesser extent than all of the coarser predecessors. The subgrids are split into several multidimensional subdomains that are defined by specified directional and global resolution requirements. A similar approach has been presented for cavity and backstep geometries in a recent publication<sup>5</sup>; although, no attempt was made to meet the differing needs for refinement in two or more coordinate directions. In the present investigation<sup>6-8</sup>, this is achieved with a subdomain procedure that allows for segmentally varying grid resolution in two or more directions throughout the flow field. This leads to more optimal grid refinement, and, through the adaptive multigrid procedure, information is very effectively transferred between high and low gradient domains that have distinctly different grid structure. In addition, the equation solver can differ from subdomain to subdomain, e.g., direct solvers can be used in strong interaction domains, line relaxation in moderate interaction domains, etc.

In the present analysis, several two-dimensional, steady, incompressible, large  $Re$  laminar and turbulent flow examples are reviewed and the results are compared with other computations or experiments. The problems to be discussed include, the laminar trailing edge (triple deck) flow past a finite flat plate, the laminar recirculating flow associated with a trough geometry, and the laminar and turbulent flows in a backstep channel. The use of pressure-based flux splitting and a trapezoidal or box-like discretization for the implicit RNS subsystem leads to a precise prescription of the surface normal boundary conditions on the local subdomain boundaries. This ensures that interfacial and global mass conservation requirements are automatically satisfied. This is generally not the case with some characteristic-based Navier-Stokes schemes, where special conditions are required in order to satisfy interfacial and global mass conservation. The primitive variable system considered herein is also directly applicable on non-staggered grids. This differs from many other incompressible primitive variable Navier-Stokes formulations, that require pressure Poisson solver or artificial compressibility concepts.

## Governing Equations and Discretization

The governing Navier-Stokes equations, shown here in sheared cartesian coordinates, is written for incompressible flow in non-conservation form:

$$u_\xi + v_\eta = 0 \quad \text{Continuity. (1a)}$$

$$uu_\xi + uy'_b(v+y'_b u)_\xi + v[(1+y'_b)^2 u_\eta + y'_b v_\eta] + p_\xi = \frac{1}{Re} u_{\eta\eta} + DC \quad \xi\text{-momentum. (1b)}$$

$$u(v+y'_b u)_\xi + v(v+y'_b u)_\eta + p_\eta = DC \quad \eta\text{-momentum. (1c)}$$

where  $\xi = x$ ;  $\eta = y - y_b(x)$ ;  $V = v - y_b' u$  is the contravariant velocity component in the  $\eta$  or normal direction (for  $y_b'(x) \ll 1$ );  $y_b(x)$  is the surface definition and  $(u, v)$  are the cartesian velocities in the  $(x, y)$  directions.

For turbulent computations, the  $k$ - $\epsilon$  model is employed. This introduces two additional equations for  $k$  and  $\epsilon$ . These equations in cartesian coordinates and non-dimensional form are given as:

$$\bar{u} \frac{\partial k}{\partial x} + \bar{v} \frac{\partial k}{\partial y} = 2 C_\mu \frac{K^2}{\epsilon} \left[ \left( \frac{\partial \bar{u}}{\partial x} \right)^2 + \left( \frac{\partial \bar{v}}{\partial y} \right)^2 + \frac{1}{2} \left( \frac{\partial \bar{u}}{\partial y} + \frac{\partial \bar{v}}{\partial x} \right)^2 \right] - \epsilon + \frac{1}{R_\epsilon} \frac{\partial}{\partial y} \left[ \left( 1 + \frac{v_\tau}{\sigma_k} \right) \frac{\partial k}{\partial y} \right]$$

$$\bar{u} \frac{\partial \epsilon}{\partial x} + \bar{v} \frac{\partial \epsilon}{\partial y} = 2 C_\mu C_{\epsilon 1} K \left[ \left( \frac{\partial \bar{u}}{\partial x} \right)^2 + \left( \frac{\partial \bar{v}}{\partial y} \right)^2 + \frac{1}{2} \left( \frac{\partial \bar{u}}{\partial y} + \frac{\partial \bar{v}}{\partial x} \right)^2 \right] - C_{\epsilon 2} \frac{\epsilon^2}{K} + \frac{1}{R_\epsilon} \frac{\partial}{\partial y} \left[ \left( 1 + \frac{v_\tau}{\sigma_\epsilon} \right) \frac{\partial \epsilon}{\partial y} \right]$$

where  $v_\tau = \frac{C_\mu k^2 R_\epsilon}{\epsilon}$  and  $C_\mu$ ,  $C_{\epsilon 1}$ ,  $C_{\epsilon 2}$ ,  $\sigma_k$  and  $\sigma_\epsilon$  are predetermined dimensionless constants which have the values 0.09, 1.44, 1.92, 1.0 and 1.3 respectively. A modified  $k$ - $\epsilon$  model was recommended by Thangam [17] in which the value of the constant  $C_{\epsilon 2}$  is changed from 1.92 to 11/6. This was shown to give much better results for the backstep channel geometry.

A three layer law of the wall is used at the upper and lower walls. This is given as:

$$u^+ = \begin{cases} y^+ & \text{for } y^+ \leq 5 \\ -3.05 + 5 \ln y^+ & \text{for } 5 < y^+ \leq 30 \\ 5.5 + 2.5 \ln y^+ & \text{for } y^+ > 30 \end{cases}$$

where  $y^+ = y u_\tau / \nu$  and  $u^+ = \bar{u} / u_\tau$ .

The RNS approximation is given by the lowest-order system obtained by omitting the purely diffusive deferred-corrector (DC) terms. These terms are retained selectively in some subdomains, when they are important. The RNS system is in effect a composite of the Euler and 2nd order boundary layer equations<sup>1-3</sup>. Trapezoidal or 'box' two point  $(ij \pm 1/2)$  differencing is used for all normal derivatives in the first-order (in  $\eta$ ) RNS equations (1a, 1c), and three point central  $(ij)$  differencing (in  $\eta$ ) is applied for the axial momentum equation (1b). If a shear factor  $\sigma = \mu u_\tau$  is introduced in (1b), a box-scheme can in fact be developed for the entire RNS system (1). All axial ( $\xi$ ) convective and pressure derivatives are upwind differenced with a pressure-based form of flux vector splitting<sup>3</sup>, wherein the  $p_\xi$  term is represented, for compressible flow, by

$$p_\xi = \omega_{1/2} (p_i - p_{i-1}) / \Delta \xi_i + (1 - \omega_{1/2}) (p_{i+1} - p_i) / \Delta \xi_{i+1},$$

and  $\omega_{1/2} = [\gamma M_\xi^2 / (1 + (\gamma - 1) M_\xi^2), 1]_{\min}$ .

Here,  $M_\xi$  is the streamwise Mach number and  $\gamma$  is the ratio of specific heats. This reduces to a simple 'forward'

difference for incompressible flow, so that the elliptic acoustic interaction or upstream influence is introduced through the  $p_\xi = (p_{i+1} - p_i) / (\Delta \xi)_i$  contribution. For reverse flow regions, additional negative eigenvalues or upstream influences appear through the convective terms.

A simple line relaxation procedure is used to solve the system of equations for  $k$  and  $\epsilon$ . The differencing used for the  $k, \epsilon$  equation is consistent with the pressure flux-split discretization. The law of the wall provides the boundary conditions one point away from either wall, which can then be used to implicitly to solve for  $k$  and  $\epsilon$  at any given station. The  $k$ - $\epsilon$  equations are decoupled from the governing RNS equations. Each pressure relaxation sweep is followed by a sweep to solve the  $k, \epsilon$  equations using the latest available values for  $\bar{u}$ ,  $\bar{v}$ . This procedure is convergent.

### Grid Structure

In general, the  $N^{\text{th}}$  multigrid level consists of several subdomains. Each multigrid level has an equal or lesser extent than the coarser grids of the multigrid hierarchy. The first two grid levels cover the entire computational domain. The mesh size is initially quite coarse in the directions in which adaptivity is to be prescribed. Each of the multigrid levels comprise several subdomains, which derive part of their topology from the subdomain pattern of the coarser predecessor. Within each subdomain, of a given multigrid level the refinement is specified independently. Thus, each subdomain of a multigrid level can act as a parent for a subdomain or subdomains at the next finer multigrid level. If at a given multigrid level, a particular subdomain is refined in only one direction, e.g.,  $\eta$ , then on subsequent multigrid levels, further refinement within this subdomain is performed only in the  $\eta$ -direction. A similar strategy is adopted for the  $\xi$ -direction. Only subdomains that result from refinement of a parent subdomain in both the  $\xi$  and  $\eta$  directions require further decomposition according to the direction selective refinement specifications.

### Refinement Strategy

In most adaptive gridding methods, on any grid level, an estimate of the truncation error of the discretized system of equations is used to identify those regions that require finer grid resolution<sup>5</sup>. The overall truncation error estimates, however, do not provide information on the specific direction(s) that require refinement. Therefore for regions requiring higher resolution, the grid is refined in both directions, even though only one coordinate gradient may be significant. In order to achieve directional refinement adaptivity it is necessary to monitor the truncation error of selected gradients or derivatives. For the problems considered herein, the truncation error for the pressure and vorticity gradients, e.g.,  $p_\xi$  and  $u_{,\eta}$ , are monitored in order to define the regions that require refinement in  $\xi$  and  $\eta$ , respectively. Additional gradient parameters can be added when necessary.

The truncation error estimate is obtained from the solution on two successive grids of the multigrid hierarchy. In order to determine the truncation error in a  $\xi$  (and/or

$\eta$ ) derivative, the finer of the two grids must have regions that are refined in the  $\xi$  (and/or  $\eta$ ) direction(s). Although the  $p_t$  and  $u_{\eta\eta}$  terms are the key derivatives for the present analysis, the truncation error of these terms alone will not suffice to ensure that uniform accuracy is achieved throughout the flow domain. The global truncation error for the full discrete system of equations is monitored for this purpose.

Two types of adaptive calculations are performed for the geometries considered herein.

- a. One-dimensional adaptive calculation (semi-coarsening multigrid), with adaptivity in the  $\xi$  direction and with a preset stretched  $\eta$  grid.
- b. Two-dimensional adaptive calculation, in which the refinement is automated in both directions and uniform grids are used in each subdomain. Grid stretching is not applied, except as the grids change discretely from subdomain to subdomain.

The underlying procedure is identical for both methods. The solution is first obtained on a coarse grid, for those direction(s) in which adaptive multigrid refinement is to be considered. For the semi-coarsening adaptive calculation, refinement is performed only in the  $\xi$  direction. The grid is refined over the entire domain, and an improved solution is obtained. From the two full grid solutions, the truncation error of the key derivatives and also of the global discrete system is estimated using Richardson extrapolation. Two types of refinement criteria are used. In one procedure, a tolerance is set for the raw truncation error and, in the other, a tolerance is set for a truncation error normalized with the maximum value. The results obtained with the two methods, i.e., identification of the regions that require refinement in the respective direction(s) are quite similar.

For the one-dimensional (in  $\xi$ ) adaptive calculation only one subdomain results. This decreases in extent as the grid level increases. For the problems considered herein, the significant flow gradients in  $\xi$  are centered around the small region  $|\xi| < \xi_0$ . For more complicated flows, it is possible that disjoint subdomains in  $\xi$  will result. For the two dimensional adaptive calculation, however, the various regions will have different refinement requirements; therefore, it is necessary to define regions that have disparate grid requirements. Subdomains requiring refinement in the  $\eta$  direction, or the  $\xi$  direction, or in both ( $\xi, \eta$ ) directions, are identified. Although different meshes are used in different regions, within each subdomain, a uniform grid is specified. This procedure is applied on the third and higher levels of the multigrid hierarchy. The calculation proceeds with intergrid multigrid transfers. On convergence, the truncation error estimation process is repeated with the  $N^{\text{th}}$  multigrid and the stored  $(N-1)^{\text{th}}$  multigrid level grid solutions.

### Multigrid Implementation

For the RNS system of equations (1), without DC, a semicoarsening multigrid procedure has been presented previously<sup>9,10</sup> to accelerate the convergence of the global pressure relaxation procedure<sup>1,2</sup>. A von Neumann analysis

of the linearized form of the RNS system shows that the rate of convergence of the global procedure is dictated by the maximum eigenvalue  $\lambda$ , as given by

$$\lambda - 1 = c_1 \pi^2 (\Delta \xi)^4 N_t^2 / \eta_M^4,$$

where  $c_1$  is a constant of  $O(1)$ ;  $N_t$  is the number of stations in the  $\xi$  direction;  $\eta_M$  is the normal boundary location, and  $\Delta \xi$  is the axial step size. The convergence rate is significantly improved if the extent of the domain in the two directions is reduced. *The current multigrid domain decomposition procedure, in effect, reduces  $\eta_M$  whenever a fine  $\Delta \xi$  is specified, and thereby achieves comparable 'coarse grid' convergence rates on fine grids.*

In the present application the multigrid method is implemented in a Full Approximation Storage (FAS) mode. The global pressure relaxation procedure considered herein essentially reduces to a block SOR procedure (in  $\xi$ ) for the pressure in attached flows and for the pressure and velocities in reversed flow regions. At each station, an implicit, fully coupled tridiagonal system is inverted. When highly stretched grids are used in  $\eta$  to resolve the boundary layer, the semi-coarsening mode of the multigrid method has been shown to be more effective than the standard full coarsening mode. In this mode, the streamwise grid alone is coarsened when the calculation shifts to coarser grids. The same  $\eta$  grid is retained throughout. Significant gains in the overall effort have been achieved with this approach<sup>9,10</sup>.

A source term (IST), first introduced by Israeli<sup>11</sup>, is required in order to achieve satisfactory performance of the multigrid procedure<sup>10</sup>. The IST acts as a form of under-relaxation or smoother for the pressure field. This leads to much smoother residual fields, which are essential for good representation on the coarser grids. However the IST leads to a slower asymptotic convergence rate on any given grid. The domain decomposition procedure reduces this limitation to a large extent. Since the truncation error in the  $p_t$  term is used to determine regions needing refinement in the  $\xi$  direction, subdomains in which the grid is only refined in the  $\eta$  direction, will generally have a reasonably converged pressure field from the coarser grid. Thus it is possible to perform the multigrid calculation without the IST smoother in these subdomains.

In the present investigation, the one-dimensional adaptive calculation adds an element of sub-domaining to the semi-coarsening analysis<sup>9,10</sup>, so that only portions of the global domain require fine grid resolution in the  $\xi$  direction. For the two-dimensional adaptive calculation, the multigrid algorithm is implemented in the standard full coarsening for domains that require refinement in both directions and the semi-coarsening mode for those domains requiring refinement in only one direction. One fine grid work-unit is comprised of one sweep in each subdomain belonging to a given multigrid level. This also includes the interdomain transfer processes. The decision to move the calculation back to a coarser grid is based on the rate of convergence on each subdomain. If the ratio of the residual norm between two successive global iterations, in any subdomain belonging to that multigrid level, falls below a certain value, typically 0.85-0.95, then the calculation is restricted to the coarser level. The fine grid solution is not



corrected until the residuals in the coarse grid subdomains are all reduced to a value one order-of-magnitude lower than the maximum residual over all subdomains in the finer level. The multigrid components are summarized as follows,

- a. Relaxation:  $u_n^k = S^k u_{n-1}^k$ , where  $S^k$  is the global pressure relaxation operator and  $u^k$  on convergence satisfies  $L^k u^k = f^k$ . Here  $k$  represents the present or finest multigrid level and  $n$  represents the iterate.  $L^k u^k = f^k$  is the discrete approximation of the continuous problem  $Lu = f$
- b. Restriction to coarse grid where the following equations are solved:  $L^{k-1} u^{k-1} = I_k^{k-1} r_n^k + L^{k-1} \hat{I}_k^{k-1} u_n^k$  for points on the coarse grid which lie within the fine grid and  $L^{k-1} u^{k-1} = f^{k-1}$  for points on the coarse grid that lie outside the extent of the fine grid. Here  $r_n^k = f^k - L^k u_n^k$ .  $I_k^{k-1}$  and  $\hat{I}_k^{k-1}$  are fine to coarse grid transfer operators. The full-weighting operator recommended by Brandt<sup>12</sup> is used to transfer the residuals and the solution was restricted by using a simple injection operator.
- c. Prolongation or correction where the fine grid solution is corrected with the solution from the coarse grid modified problem.  
 $u_{n+1}^k = u_n^k + I_k^{k-1} (u^{k-1} - I_k^{k-1} u_n^k)$ , where  $I_k^{k-1}$  is a coarse to fine interpolation operator

It should be noted that in the present calculation, the multigrid transfer operations play a dual role. In addition to accelerating the convergence of the relaxation procedure, they also transmit information from the finer grids to the coarser grids, and thus improve the accuracy of the solution in regions of the coarser grids where refinement was not required. The second term in the multigrid restriction process, acts as a truncation error injection term and improves the discrete approximation on the coarse grid. Thus on the coarser grids, instead of solving  $L^{k-1} u^{k-1} = f^{k-1}$  everywhere, we solve  $L^{k-1} \hat{u} = \tau$  in part of the domain, where  $\tau = L^{k-1} \hat{I}_k^{k-1} u^k$ . This is closer to the continuous problem  $Lu = f$ . Here  $L$  is the continuous counterpart of the discrete operator  $L^k$  and  $u$  is the exact solution for the continuous problem;  $u^{k-1}$  is the exact solution to the discrete problem and  $\hat{u}$  is the improved solution due to the modified right hand side of the discrete approximation.

The deferred-corrector in (1) is input as a prescribed functional form on the right hand side of the fine grid equation. On any given grid level, the calculation is initially considered without the DC term. After a reasonable level of convergence is achieved, e.g.,  $10^{-3}$ , the DC term is evaluated from this known solution. This value is prescribed on the finest grid and added explicitly to the right hand side of the equations. This term is transferred to the coarser grid levels through the standard multigrid procedure. If the DC term is introduced earlier, divergence results. This is due to the fact that the solution is initially quite poor and therefore the prescribed DC term is significantly in error. This distorts the differential equation and induces an instability in the pressure during the relaxation procedure. If the RNS solution is allowed to

converge moderately before introducing the DC term, the overall solution procedure, with the DC addition, exhibits no significant degradation in rate of convergence for the examples considered herein.

For turbulent flow modelling, the eddy viscosity  $\nu_t$  is calculated only on the finest grid. The fine grid values of  $\nu_t$  are injected to the corresponding coarse grid points during the restriction step. The  $\nu_t$  values, at points on the coarse grid, that lie outside of the extent of the fine grid are not updated. This procedure is validated by calculations that do not include any adaptivity. In this case, the fine grid extent is the same as that of the coarse grid. Therefore, the  $\nu_t$  values at all points on the coarse grid will be updated. The results obtained from this full refinement calculation and those from the fully adaptive multigrid calculations are identical.

#### Interdomain Transfer of Boundary Conditions and Conservation at Grid Interfaces

For a given subdomain, the following boundary conditions are to be prescribed:

$$\begin{aligned} u = v = 0 \text{ at } \eta = 0; \quad u = 1, p = 0 \text{ at } \eta = \eta_{\max}; \\ p_{\xi} = 0 \text{ or } p \text{ prescribed at } \xi = \xi_{\max}; \quad u \text{ and } v \text{ are given} \\ \text{by freestream values at } \xi = \xi_0. \end{aligned}$$

For external flows, if a subdomain has its outflow at some  $\xi < \xi_{\max}$  then the boundary condition on pressure changes from Neumann to Dirichlet type. For internal flow, the outflow boundary condition is Dirichlet type for the pressure. Also, if the lower boundary of a subdomain is at some  $\eta > 0$ , then non-zero velocities have to be prescribed. In time-dependent, characteristic-based, Navier-Stokes computations, that use locally embedded grids, boundary conditions are required for all variables, i.e.,  $u$ ,  $v$ , and  $p$ . In addition, special care has to be taken to ensure that mass conservation is not violated locally or globally.

In the pressure-based trapezoidal or 'box' formulation, this difficulty does not occur as the normal velocity  $v$  in  $\eta$ , or  $u$  in  $\xi$ , is not prescribed at the upper or lower, or outflow boundaries. Only the tangential component  $u$  is prescribed at the upper interface or interdomain boundary. The pressure-based box-type differencing allows for the calculation of the normal velocity at the outer boundaries and the pressure at the body surfaces. The normal velocity is computed from the continuity equation and therefore mass conservation is automatically satisfied on all levels, for all subdomains. This eliminates the need for special interpolation formulae to ensure conservation of mass when the boundary conditions are prescribed from the coarse grid solution. Thus weak instabilities, that arise when such methods are applied in Navier-Stokes formulations without satisfying mass conservation, do not appear in the present method. Direct evaluation of the pressure at the inflow or lower boundaries with the trapezoidal or box discretization also eliminates the need for special pressure boundary conditions.

The calculation is performed sequentially rather than in parallel in the various subdomains. As such the boundary conditions at the inflow and outflow stations for

each subdomain are updated with the latest available values. The overlap allowed in the subdomaining process follows the following rules.

- The last station of any subdomain, which is at some  $\xi < \xi_{\max}$  coincides with the first station of the subdomain to its right, (if one exists), where the pressure is computed.
- Similarly, the inflow station of any subdomain, which is at some  $\xi > 0$  coincides with the last station on the subdomain to its left, (if one exists), where the velocities are computed.
- If the inflow station or the outflow station of a given subdomain coincides with the physical boundaries of the global flow field then the boundary conditions discussed previously for inflow, outflow, upper and lower boundaries are used for these subdomains.
- If there are no subdomains to the right, for the cases in a), or if there are no subdomains to the left, for the cases in b), then these boundaries are updated using coarse grid values during the multigrid prolongation process.

In the vertical direction an implicit solver is applied and no overlap is necessary.

If a subdomain has only one of its horizontal boundaries in common with that of another subdomain, then updating the boundary conditions along this edge, after one sweep in all subdomains, leads to iterative divergence on this subdomain. This influence gradually filters through to other subdomains. If these boundaries are updated through the multigrid transfer processes, then the calculation is convergent. This reflects the fact that an update of just one boundary after each sweep, with the other three updated only during the multigrid transfer process, leads to an inconsistency. This constrains the variables from adjusting to changes that occur dynamically, as the solution evolves in the various subdomains. The multigrid transfers provide the correct dynamic response to changes between subdomains.

### Results

All of the calculations presented herein are initiated on the coarsest grid, with uniform flow velocity and pressure. On the finer grids, the interpolated coarse grid solution fields are sequentially applied as initial approximations. Since convergence to the final solution is improved with more accurate initial approximations<sup>5,9,10</sup>, the adaptive multigrid framework introduces this element in a natural and convenient fashion. It is significant that for all of the examples presented herein, Reynolds number continuation is not required in order to obtain a solution for any of the prescribed values of  $Re$ . Even for highly interactive, large  $Re$  flows, the solution is obtained directly with uniform initial values at the designated value of  $Re$ .

#### Example 1: Flow over a finite flat plate: the trailing edge problem<sup>6</sup>.

Figure 1 depicts the grid obtained for a semi-coarsening (in  $\xi$ ) adaptive calculation. The  $\eta$  grid is highly stretched and fixed. Note that the finer grids zoom in

around the trailing edge, which is located at  $\xi = 1.0$  (the figure is scaled by a factor of 2 in the  $\xi$ -direction). Significantly, the extent of the finer grids in the  $\eta$  direction is progressively reduced, even when adaptivity is specified only in the  $\xi$  direction. Although each multigrid level contains only one subdomain (in  $\xi$ ) that requires further refinement on subsequent levels, the  $\eta$  extent of this subdomain is affected.

Figure 2 depicts the composite grid obtained with full two-dimensional adaptivity. Within each subdomain, uniform grids, in both the  $\xi$  and  $\eta$  directions, are prescribed. Figure 2 is an overlay of seven multigrid levels, each of which comprises several subdomains. In each level, it is found that the subdomain, for which refinement in both directions is required, is centered around the trailing edge. The adaptive computations, both semi-coarsening and two-dimensional, are compared with non-adaptive semi-coarsening multigrid calculations. For the latter, a uniform fine grid in  $\xi$  and a highly stretched  $\eta$  grid is prescribed. The grid stretch factor is chosen from the specified minimum and maximum  $\Delta\eta$  values, and the location of  $\eta_{\max}$  that was applied for the two-dimensional adaptive study. The same  $\eta$  grid is employed for the adaptive semi-coarsening calculation. Figure 3 shows a comparison of the pressure coefficient  $C_p$  for the three calculations. There is good agreement in the pressure variation and, in particular, the predicted peak pressures. Table 1 summarizes the computer memory and CPU requirements. These are given as percentages of the non-adaptive, semi-coarsening, calculation. Note that the memory requirement for the one- and two-dimensional adaptive calculations are similar. This signifies that the specified  $\eta$  stretching for the semi-coarsening calculation is reasonable.

Table 1. Summary of Computer Resource Requirements for the finite flat plate calculation

Aspect	Two-D Adaptive	One-D Adaptive	Full Refinement with stretched $\eta$ grid
CPU	18.03%	15.10%	100.0%
Memory	12.90%	13.22%	100.0%

The adaptive grid of Figure 2 defines the extent of the interaction zone surrounding the trailing edge. From large  $Re$  asymptotic triple deck theory, three layers with different length scales have been identified<sup>12</sup>, viz., a lower viscous rotational deck of  $O(Re^{-5/8})$ , a middle inviscid rotational deck of  $O(Re^{-4/8})$ , and an upper inviscid irrotational deck of  $O(Re^{-3/8})$ . Since the vorticity is zero in the upper deck, and since vorticity is the monitored parameter for refinement in the  $\eta$  direction, the adaptive procedure should lead to a grid that does not require  $\eta$  refinement in this 'upper deck' region. The grid obtained from the two-dimensional adaptive calculation displays this result quite clearly. At each multigrid level, there is a region away from the body that is in fact refined only in the  $\xi$  direction. This region, in the finest multigrid level, represents the extent of the upper inviscid irrotational

region. Estimates for the extent of the other two 'decks' are also obtained from the grid structure. In more complicated flows, e.g., turbulent flow past the same geometry, for which analytical methods cannot be easily developed, the appropriate resolution in each distinct region will be automatically captured with the present multigrid adaptive procedure. In this sense, the computation results in a form of discrete asymptotic analysis.

#### Example 2. Flow over a trough<sup>6</sup>.

The second geometry to be considered is the laminar flow over a trough configuration. Both unseparated and reverse flows are computed with the two refinement strategies previously discussed. The trough surface is specified by  $y_0 = -D \text{sech}[4(x-x_0)]$ , where  $D$  represents the maximum depth, which occurs at the location  $x_0$ . The values  $x_0=2.5$  and  $Re = 80000$  are used for the present calculation. The grid obtained from the two-dimensional adaptive procedure, for  $D=0.03$  and with a region of flow reversal, is shown in Figure 4. Note that refinement in the  $\eta$  direction extends to a significantly greater distance than was found for the trailing edge geometry. This is due to the fact that the maximum vorticity now occurs near the outer edge of the separation bubble and not at the surface. Also note the sudden increase in the extent of the region where  $\eta$  refinement is performed. This signifies the increase in boundary layer thickness as a result of flow separation. The reversed flow region is essentially vorticity free; however, the current refinement strategy assumes that regions requiring refinement, in the  $\eta$  direction, will always have a lower boundary at the wall. This condition can be modified to allow for multiple  $\eta$  subdomains in the recirculation region. This was not considered necessary for the current calculations. Figure 5 depicts the pressure variations obtained for the three calculations discussed previously for purely attached flow and  $D=0.015$ . Figure 6 provides comparisons of the skin friction for the separated ( $D=0.03$ ) case. Once again, good agreement is obtained and significant gains in computer resource requirements are found (Table 2). The locations of the

Table 2. Summary of Computer Resource Requirements for the trough geometry

Aspect	Geometry	Two-D Adaptive	One-D Adaptive	Full MG with non uniform $\eta$ grid
CPU	Trough (Sep)	18.03 %	—	100.0 %
	Trough (Unsep)	7.10 %	16.80 %	100.0 %
Memory	Trough (Sep)	16.32 %	—	100.0 %
	Trough (Unsep)	5.10 %	63.4 %	100.0 %

separation and reattachment points computed by the two-dimensional adaptive calculation are at  $\xi=2.31$  and  $\xi=2.54$ , respectively; the values predicted by non-adaptive full multigrid refinement are at  $\xi=2.31$  and  $\xi=2.53$ . This

further confirms the validity of the domain decomposition approach and the advantages of adaptive multigrid over full multigrid. All results presented here are in excellent agreement with all earlier results<sup>1,9</sup> presented for these geometries.

#### Example 3. Internal flow in a back step channel: laminar<sup>7,8</sup> and turbulent flows.

For this flow, which is dominated by rather large recirculation regions, it is still possible to carry out the calculation for all  $Re$  considered herein by prescribing uniform initial flow conditions. This is true even for the relatively difficult, although somewhat artificial two-dimensional calculation with  $Re=800$  (based on channel height). For this  $Re$  value, two separation bubbles, one on each wall are evident. Reynolds number continuation, as applied in many other reported NS solvers<sup>14</sup>, is still not required for the present calculations. Both laminar ( $Re=800$ ) and turbulent results are obtained for the back step geometry. The standard two equation  $k-\epsilon$  model discussed earlier is used for turbulence closure.

For laminar calculation, a step height to channel height ratio of 0.5 is used. The reattachment length ( $X_R$ ) for the primary recirculation zone is compared in Table 3 for a range of laminar Reynolds numbers. Comparisons are given for the present 2-D adaptive method, full refinement with the standard non-adaptive multigrid method, and earlier calculations by Ferziger<sup>5</sup>, Caruso<sup>15</sup> and Sotiropoulos<sup>13</sup>. The calculated reattachment length for the adaptive and non-adaptive procedures is identical to two decimal places; however, the computational effort is considerably less for the former, see Table 4.

Table 3. Comparison of Reattachment Length for Laminar Backstep Channel Flow

Re	Present Calculations		REF [5]	REF [15]	REF [13]
	Adaptive	Non-Adaptive			
133	1.94	1.94	2.0	1.95	1.84
267	3.25	3.25	3.25	3.25	3.17
400	4.32	4.32	4.35	4.40	4.40
600	5.50	5.50	5.35	5.40	5.63

For adaptive refinement in the  $\eta$  direction the truncation error is scanned from the wall towards the outer boundary. For external flow, the vorticity gradient decreases exponentially and a thin layer near the wall, where refinement is maximum, can be identified. This region is specified by fixing the upper boundary at the furthest point, or largest  $\eta$  value taken over all  $\xi$  locations, that satisfies the truncation error tolerance. For internal flows, boundary layers, where refinement in  $\eta$  should be required, exist at both boundaries in the normal or  $\eta$  direction. However, the number of grid points that are necessary to resolve the flow gradients in the  $\eta$  direction is

quite moderate and therefore no attempt was made to adaptively refine in this direction. Instead, the full multigrid procedure is applied in the  $\eta$ -direction for each of the subdomains for which  $\xi$ -refinement is necessary. This allows for different uniform  $\eta$  grids in the different  $\xi$  subdomains.

**Table 4. Summary of Computer Resource Requirements for the Backstep Geometry**

Aspect	Re	Adaptive Multigrid/Full Refinement NonAdaptive Multigrid
CPU	133	35.49 %
	267	36.15 %
	400	46.23 %
	600	50.40 %
Memory	133	30.80 %
	267	37.44 %
	400	41.49 %
	600	47.49 %

Table 4 displays the computer resource requirements for the backstep channel calculation. For each Reynolds number, the CPU and memory requirements are shown as percentages of the corresponding non-adaptive calculations. Note that as the Reynolds number increases from  $Re = 133$  to  $Re = 600$ , the number of grid points required to resolve the flow field increases. This is expected, as the size of the separation bubble increases with Reynolds number. The number of required grid levels, as well as the finest mesh size for all Reynolds numbers up to  $Re = 600$ , is identical in each direction. A total of five multigrid levels are defined for all Reynolds numbers up to  $Re = 600$ . However the subdomain extent for each multigrid level is different for different  $Re$ . The extent of the finer grids is governed by the size of the recirculation zone, which increases as  $Re$  is increased. For the  $Re = 800$  case, six multigrid levels are required, as the change in the solution from level 4 to level 5 is still significant and greater than the specified tolerance.

An increase in computational time and memory requirements is observed as the Reynolds number and associated number of grid points increases. The time required for the full refinement non-adaptive calculation increases only marginally as  $Re$  is increased from 133 to 600. This increase is entirely due to the changing nature of the flowfield, since the same grid is used throughout this  $Re$  range. More specifically, when the degree of velocity relaxation is increased due to the increasing extent of the reversed flow region, the convergence rate degrades and additional iterations are required to achieve the specified tolerances. Furthermore, the percentage gain in adaptive over non-adaptive procedures is reduced as the Reynolds number increases, e.g., to about 50% at  $Re = 600$ .

The effect of location of the outflow boundary and the non-reflectivity of the outflow boundary conditions are important aspects of this study. The adaptive multigrid domain decomposition procedure is initiated on a very coarse grid, and yet, it is possible to place the outflow boundary quite far downstream, e.g., 60 step heights, and still recover very accurate and computer efficient

computations. The solutions at the outflow are in almost perfect agreement with the analytic fully developed flow values. Although the finer grids in  $\xi$  and  $\eta$  occur in subdomains much further upstream, in and near the reverse flow regions, the influence of the outflow boundary conditions is propagated through the multigrid transfers to and from the coarser grids connecting the various subdomains. This allows for efficient transfer of information without excessive grid specification. In addition, as is shown<sup>8</sup>, the RNS pressure flux-splitting procedure allows the outer boundary to be placed very far upstream, e.g., within the upper wall recirculation region, without solution degradation.

For the laminar backstep, the DC terms neglected in the RNS approximation have been included after obtaining a reasonably converged base solution for the RNS system. For this geometry, the vertical wall region near the step corner represents the only portion of the flowfield where the full Navier Stokes terms are of any consequence. Along the vertical wall, the  $v_{xx}$  term represents the vortical or diffusive boundary layer influence. It is found<sup>8</sup> that in this region, although the inclusion of the DC term does not produce a significant quantitative difference, some qualitative difference is observed in the solution. Figures 7a-7d depicts the streamwise velocity profile for  $Re = 400$  at four successive stations near the corner. Note that the effect of the DC diminishes rapidly away from the corner. A significant difference between the two solutions is associated with a small positive axial velocity that is observed near the corner when the DC is included. This represents a counter rotating vortex within the primary separation bubble. The reattachment length remains unchanged even when the DC is included.

The non-reflectivity of the Dirichlet pressure outflow boundary condition was tested for the severe  $Re = 800$  case with calculations on computational domains of three different lengths. It was found that for the cases considered, locating the outflow boundary further upstream did not have a significant effect on any of the solutions. Comparisons of the streamwise velocity profile at the streamwise location  $X = 7$  are given in Figure 8. The outflow boundary was located at  $X = 7$ ,  $X = 15$  and  $X = 30$ ; the results clearly indicate that the effect of the outflow location on the solutions is minimal. Figure 9 shows the comparison of the stream function contours obtained by placing the outflow at  $X = 7$  and  $X = 15$ . The two contour patterns are identical<sup>8</sup>.

A benchmark solution for  $Re = 800$  has been published by Gartling<sup>14</sup>. The present solution, which is obtained with the adaptive multigrid domain decomposition procedure, is compared with these results. In Figure 8, comparison with the benchmark solution of the streamwise velocity profiles at  $X = 7$  is also shown. Note that reverse flow also occurs on the upperwall. The appearance of this upper separation bubble is thought to introduce three-dimensionality into the flow, and for this reason there is some disagreement between the experimental results and all of the numerical solutions. However, the present results, which are totally grid independent, agree quite well with most of the other numerical computations. Due to the very fine meshes that have been prescribed with the

multigrid domain decomposition procedure, the residuals and truncation errors are quite small and therefore these numerical solutions, are considered to be highly accurate. Figure 10 depicts comparison of vorticity profiles. The agreement with the benchmark contours<sup>14</sup> is excellent throughout. Moreover the results are essentially unchanged with the outflow boundary at  $X=30$  or  $X=7$ , which is inside the upper recirculation zone<sup>8</sup> for the  $Re=800$  case.

Figures 11 and 12 show typical grids obtained using the adaptive multigrid procedure for the backstep channel. Figure 11 shows the grid for  $Re=100$  and Figure 12 depicts the grid for  $Re=267$ . Note that the region covered by the finest grid is larger in extent for  $Re=267$ . This is expected as the region of reversed flow is larger in this case. Note that the grid used in the  $y$ -direction is quite coarse far downstream where the flow is fully developed. This reflects the fact that the truncation error is very low in the normal derivatives in this region. Since the fully developed flow profile is parabolic, central differencing will theoretically incur zero truncation error. In streamwise direction, a grid as coarse as  $\Delta x=0.5$  can be used towards the outflow without loss of accuracy. The adaptive multigrid procedure clearly utilizes this fact and provides optimal resolution.

The turbulent flow past the backstep channel is of interest in many engineering applications. For the current study, the  $k-\epsilon$  model has been used to compute the Reynolds stress terms. This model requires that inflow values for  $k$  and  $\epsilon$  be prescribed. For the present calculation these values are generated from a straight channel turbulent flow computation with a step initial profile. The  $k$ ,  $\epsilon$ ,  $u$  and  $v$  profiles obtained at the outflow of the straight duct are used as the inflow conditions for the backstep calculation. This inflow is located at a distance five step heights upstream of the step corner. It is noted that the overall nature of the flow field, including the reattachment length is strongly dependent on the inflow values used for  $k$  and  $\epsilon$ . Different profiles for  $k$  and  $\epsilon$  can be generated by varying the length of the straight duct. This will greatly alter the backstep channel solution. A channel length of 23 step height was used to generate the inflow profile for the present calculation. This ensures that the profiles are quite well developed. The corresponding velocities,  $k$  and  $\epsilon$  profiles are then used for the backstep channel calculation. Once again, the inflow is located five step heights upstream of the step corner. Thangam et al.<sup>16</sup> observed that the predicted reattachment length using the standard isotropic  $k-\epsilon$  model was in error by about 12%, when compared with the experimental value. They showed that a modified  $k-\epsilon$  model which takes anisotropic effects into account provides improved results. In another study by Thangam<sup>17</sup>, it was shown that a modified isotropic  $k-\epsilon$  model can also lead to improved results. This model, which requires only the variation of a single constant, is considered for some of the calculations presented herein.

The step height to channel height ratio used is 1:3 in the present calculations. A reattachment length ( $x/H$ ) of 7.04 was obtained for a  $Re=132000$  based on channel height. This is in very good agreement with the experimental value of 7.1. Figure 13 shows the streamfunction contours for the same flow. Note that there is a secondary counter rotating vortex within the primary

separation bubble. This was also observed by Thangam et al.<sup>16</sup>. The calculation was also performed by modifying the value of  $c_{\epsilon 2}$  to 11/6 as suggested<sup>17</sup>. The reattachment length increased, in this case, to 7.66. This was also the trend observed<sup>17</sup>. Although in their case, the standard  $k-\epsilon$  model was underpredicting the reattachment length and modifying the constant produced acceptable results.

### Summary

An adaptive multigrid domain decomposition method has been used to efficiently compute incompressible laminar and turbulent flows with regions of recirculation and strong pressure interaction. A low order RNS system of equations, a fully consistent primitive variable non-staggered grid solver, accurate mass conservation at subdomain interfaces and global boundaries, non-reflective outflow boundary conditions and a pressure-based flux-split discretization are the key features of the procedure. The adaptive multigrid domain decomposition procedures allows for efficient grid definition consistent with asymptotic theory and for effective transfer of information to and from fine grid high gradient regions to coarse grid 'inviscid' regions.

Significant gains in computer resources have been achieved when compared to standard non-adaptive methods. Good agreement is obtained between the present solutions, standard non-adaptive full refinement computations and other published results. The computational cost is several times smaller than that required by most other NS methods<sup>14</sup>. For example, the CPU required for the backstep channel calculations, with Reynolds numbers in the range 100-600, varies between 5-10 minutes on an IBM 320 RISC/6000 workstation. For the  $Re=800$  case, an additional multigrid level is added to ensure grid independence and the CPU required is increased to approximately 30 minutes on the same workstation. All solutions are initiated with uniform flow approximations and Reynolds number continuation is not required, even for the relatively complex  $Re=800$  case. Grid convergence has been established efficiently through an adaptive multigrid procedure. The outflow boundary condition has been shown to be non-reflective. In addition, it has been shown that the procedure is not very sensitive to the location of the outflow, i.e. far downstream or somewhat closer to the inflow. The flux-split discretization allows for direct computation of the normal velocity and therefore mass conservation at grid interfaces and subdomain boundaries is achieved in a simple fashion.

### Acknowledgement

This research was supported in part by the NASA Lewis Research Center (J. Adamczyk, Technical Monitor), Grant No. NAG-397 and by the AFOSR (L. Sakell, Technical Monitor), Grant No. 90-0096. The Cray Y-MP at the Ohio Supercomputer was used for these computations.

### References

1. Rubin, S.G. and Reddy, D.R., "Analysis of Global Pressure Relaxation for Flows With Strong

- Interaction and Separation", *Computers and Fluids*, **11**, pp. 281-306, 1983.
2. Rubin, S.G., "Incompressible Navier-Stokes and Parabolized Navier-Stokes Formulations and Computational Techniques", *Computational Methods in Viscous Flows*, Vol. 3, W. Habashi, Ed., Pineridge Press, pp. 53-99, 1984.
3. Rubin, S.G., "RNS/Euler Pressure Relaxation and Flux Vector Splitting", *Computers and Fluids*, **16**, pp. 485-490, 1988.
4. Fuchs, L., "A Local Mid-Refinement Technique for Incompressible Flows", *Computer and Fluids*, **14**, pp. 69-81, 1986.
5. Thompson, M.C. and Ferziger, J.H., "An Adaptive Multigrid Technique for the Incompressible Navier-Stokes Equations", *J. of Comp. Physics*, **82**, pp. 94-121, 1989.
6. Srinivasan, K. and Rubin, S.G., "Adaptive Multigrid Domain Decomposition Solutions of the Reduced Navier-Stokes Equations", *Proceedings of Fifth SIAM Conference on Domain Decomposition Methods for Partial Differential Equations*, Norfolk, VA., May 1991.
7. Srinivasan, K. and Rubin, S.G., "Flow Over a Backward Facing Step Using the Reduced Navier-Stokes Equations", *Proceedings of the Minisymposium on Outflow Boundary Conditions*, Stanford University, July 1991.
8. Srinivasan, K. and Rubin, S.G., "Adaptive Multigrid Domain Decomposition Solutions for Incompressible Viscous Flows", submitted to *Int'l J. Num. Methods in Fluids*.
9. Himansu, A. and Rubin, S.G., "Multigrid Acceleration of a Relaxation Procedure for the Reduced Navier-Stokes Equations", *AIAA J.*, **26**, pp. 1044-1051, 1988.
10. Rubin, S.G. and Himansu, A., "Convergence Properties of High Reynolds Number Separated Flow Calculations", *Int'l J. Num. Methods in Fluids*, **2**, pp. 1395-1411, 1989.
11. Rosenfeld, M. and Israeli, M., "Numerical Solution of Incompressible Flows by a Marching Multigrid Nonlinear Method", *AIAA J.*, **25**, pp. 641-47, 1987.
12. Brandt, A., "Multi-level Adaptive Solutions to Boundary Value Problems", *Mathematics of Computation*, **31**, pp. 333-390, 1977.
13. Sotiropoulos, F., "A Primitive Variable Method for the Solution of External and Internal Incompressible Flow Fields", Ph.D Dissertation, University of Cincinnati, 1991.
14. Gartling, D.K., "A Test Problem for Outflow Boundary Condition - Flow Over Backward Facing Step", *Int'l Journal of Num. Meth. in Fluids*, **11**, pp. 953-967, 1990.
15. Caruso, S., "Adaptive Grid Techniques for Fluid Flow Problems", Ph.D Thesis, Thermosciences Division, Department of Mechanical Engineering, Stanford University, California, 1985.
16. Thangam, S. and Spezial, C.G., "Turbulent Separated Flow Past a Backward Facing Step: A Critical Evaluation of Two-Equation Turbulence Models, ICASE Report No. 91-23, February 1991.
17. Thangam, S., "Analysis of Two-Equation Turbulence Models for Recirculating Flows", ICASE Report No. 91-61, July 1991.

18. Eaton, J. and Johnston, J.P., "Turbulent Flow Reattachment: An Experimental Study of the Flow and Structure Behind a Backward Facing Step", Technical Report MD-39, Stanford University, California, 1980.

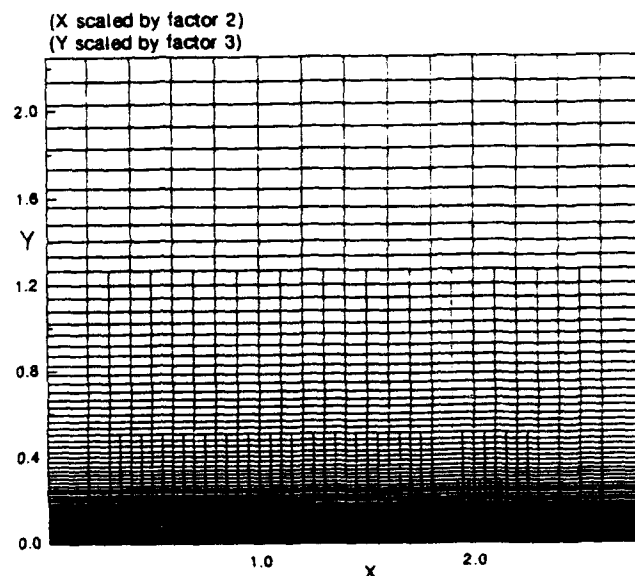


Figure 1. Multigrid levels (one-dimensional adaptivity); trailing edge flow ( $Re=10^5$ )

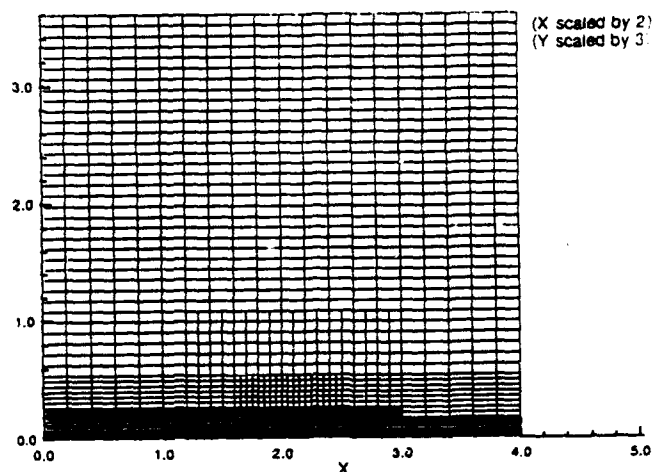


Figure 2. Multigrid levels (two-dimensional adaptivity); trailing edge flow ( $Re=10^5$ )

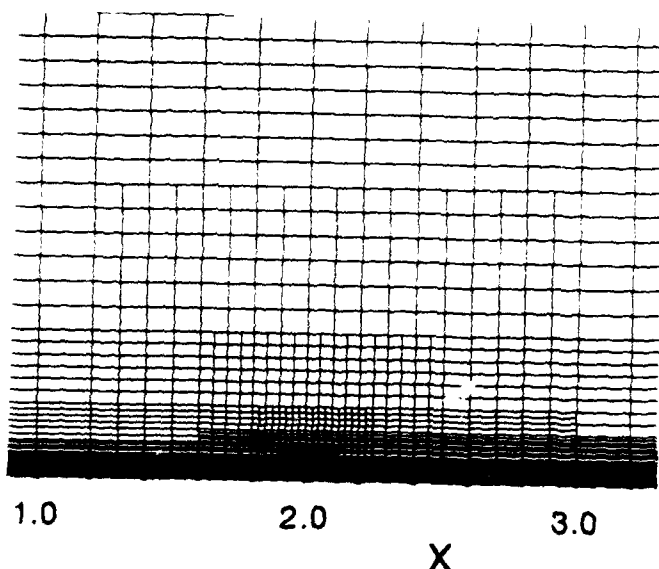


Figure 2a. Enlargement of the fine grid region in Figure 2.

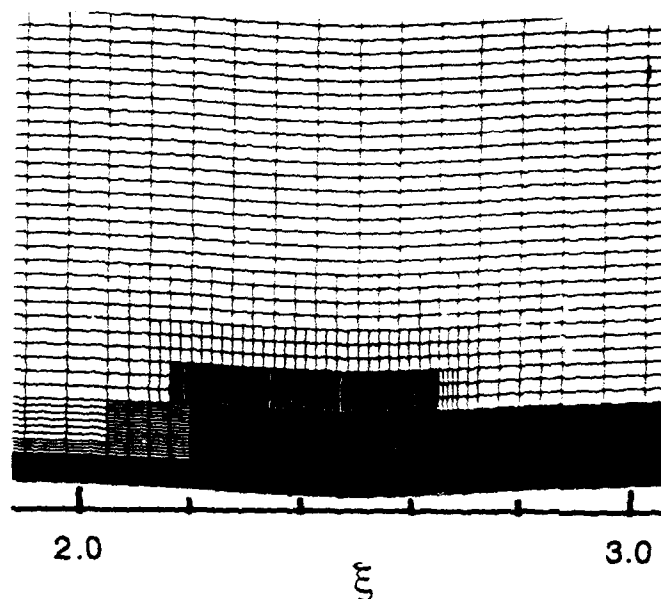


Figure 4a. Enlargement of the fine grid region in Figure 4.

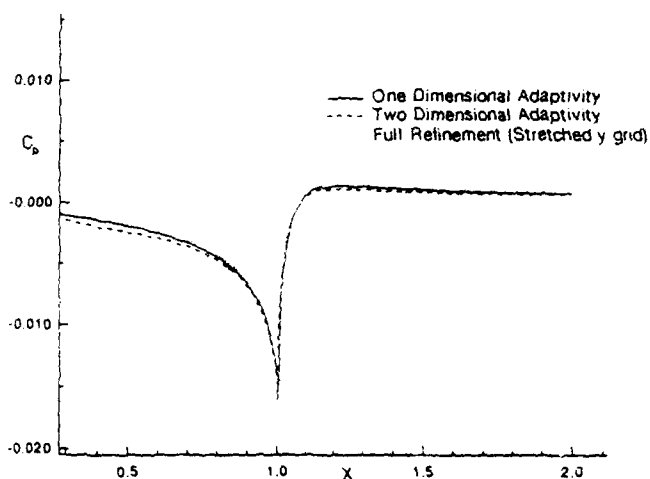


Figure 3. Comparison of  $c_p$  variation; trailing edge flow ( $Re=10^5$ )

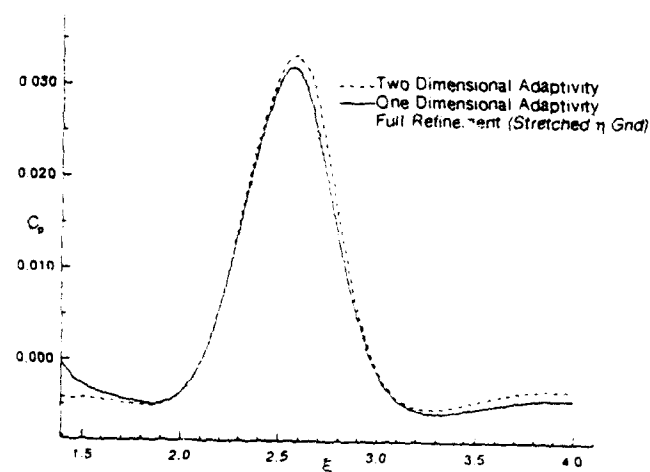


Figure 5. Comparison of  $c_p$  variation; unseparated flow past trough ( $D=0.015$ ,  $Re=80000$ )

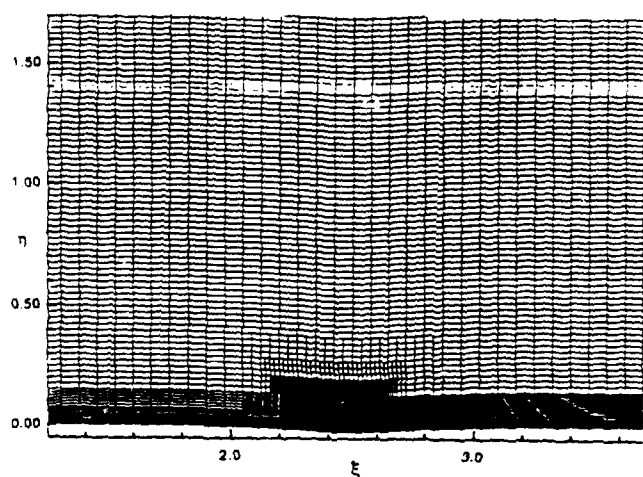


Figure 4. Multigrid levels (two-dimensional adaptivity) separated flow past trough ( $D=0.03$ ,  $Re=80000$ )

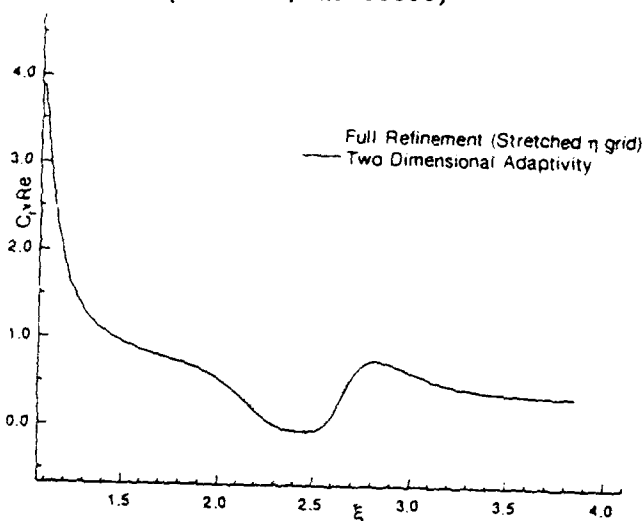


Figure 6. Comparison of skin friction parameter; separated flow past trough ( $D=0.03$ ,  $Re=80000$ )

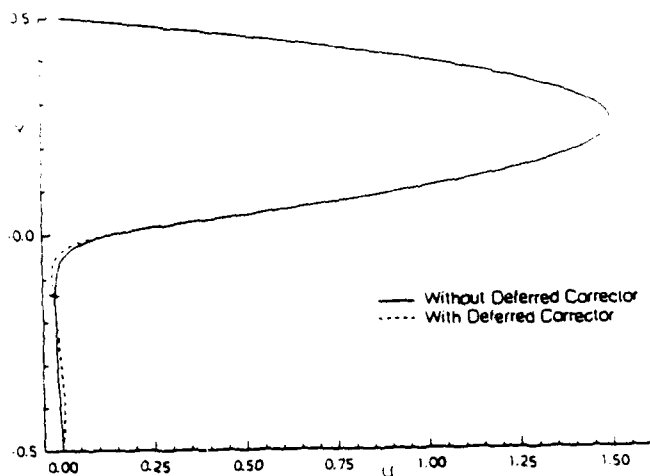


Figure 7a. Comparison of streamwise velocity profile at  $x=0.0625$ ; Backward facing step ( $Re=400$ )

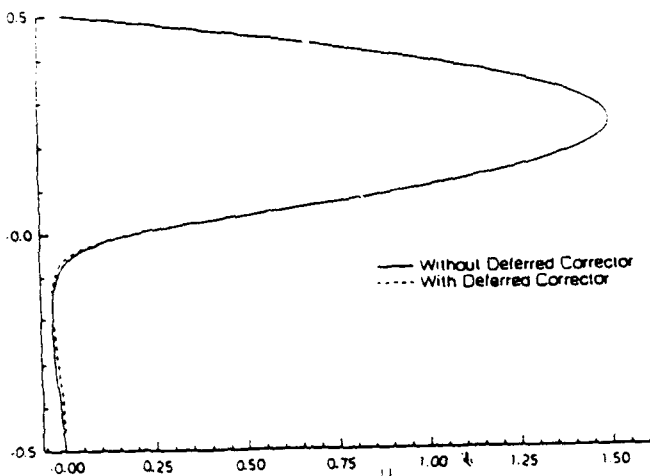


Figure 7b. Comparison of streamwise velocity profile at  $x=0.125$ ; Backward facing step ( $Re=400$ )

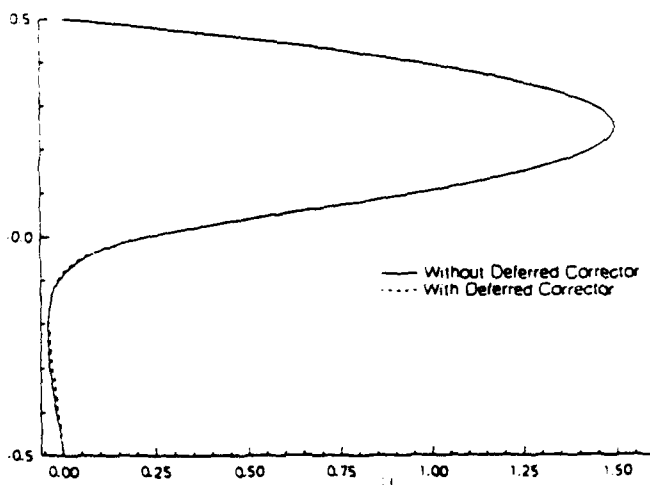


Figure 7c. Comparison of streamwise velocity profile at  $x=0.1875$ ; Backward facing step ( $Re=400$ )

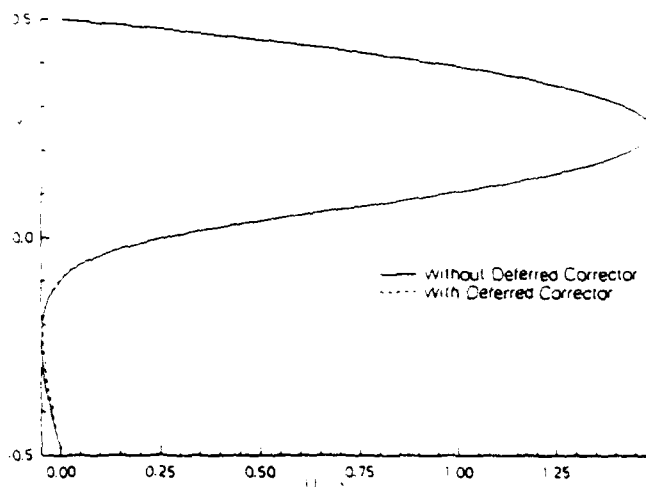


Figure 7d. Comparison of streamwise velocity profile at  $x=0.25$ ; Backward facing step ( $Re=400$ )

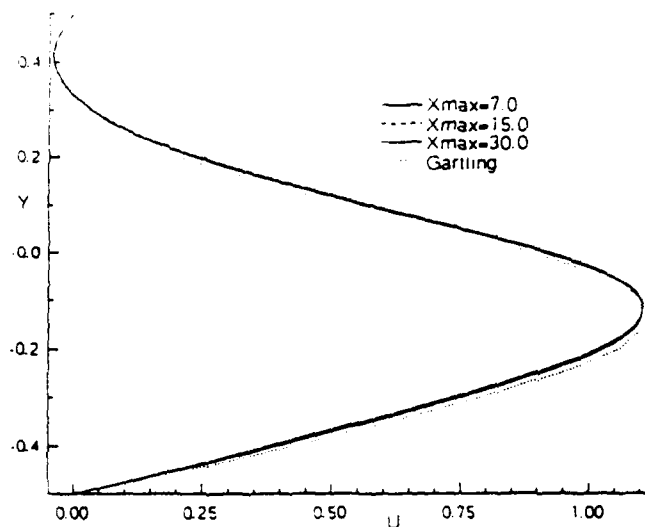


Figure 8. Comparison of streamwise velocity profile at  $x=7$ ; Effect of location of outflow boundary; Backward facing step ( $Re=800$ )

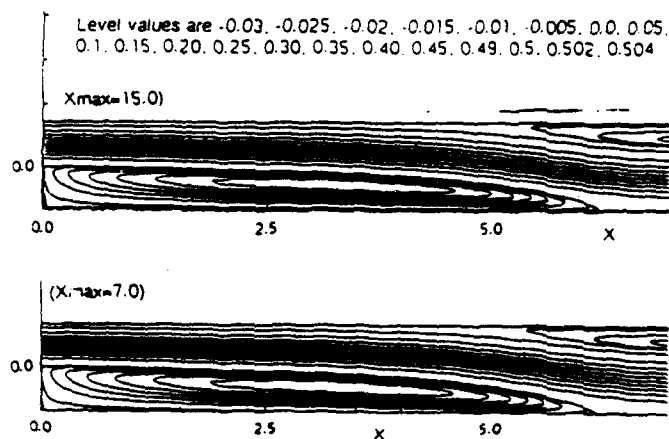


Figure 9. Comparison of streamfunction contours; effect of location of outflow boundary; Backward facing step ( $Re=800$ )



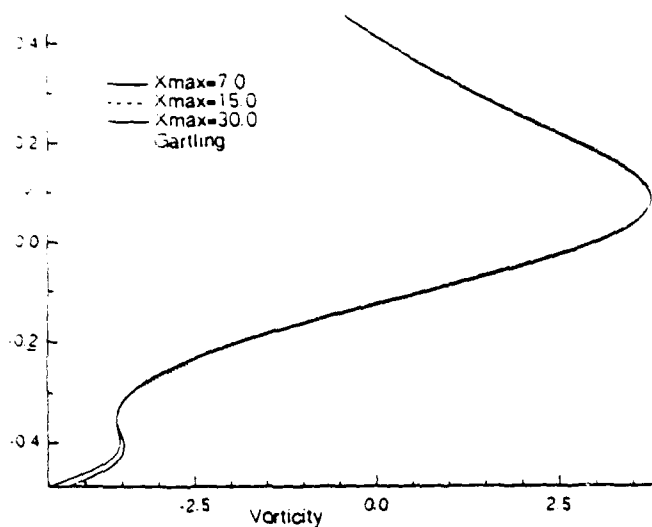


Figure 10. Comparison of vorticity profiles at  $x=7.0$ ; Backward facing step ( $Re=800$ )

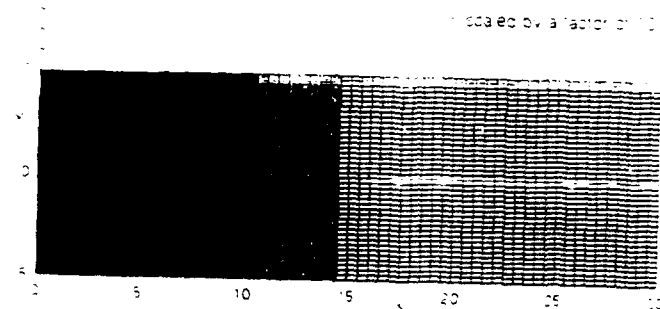


Figure 12. Multigrid levels; Backward facing step ( $Re=267$ )

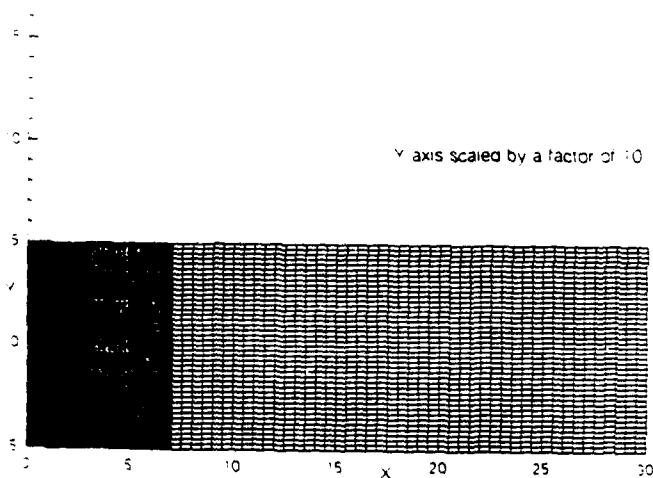


Figure 11. Multigrid levels; Backward facing step ( $Re=100$ )

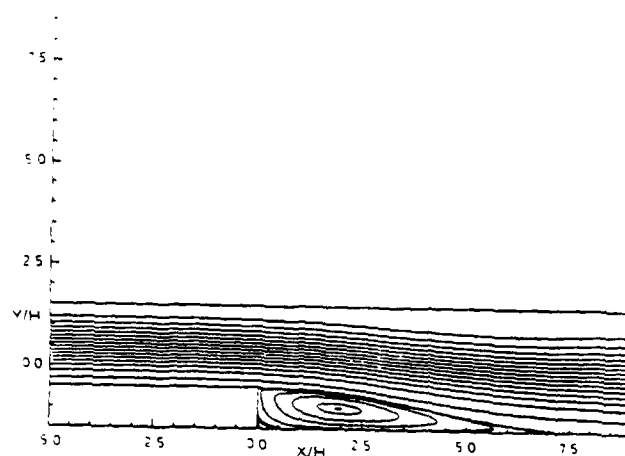


Figure 13. Streamfunction contours; Backward facing step ( $Re=132000$ )

$$d_i = [(x_{i+1} - x_j)^2 + (y_{i+1} - y_j)^2 + (z_{i+1} - z_j)^2]^{\frac{1}{2}} \quad (12a)$$

The normalized rate at which grid spacing changes (ARCL) is then

$$(ARCL)_i = \frac{d_i - d_{i-1}}{\frac{1}{2}(d_i + d_{i-1})} \quad (12b)$$

### error estimations

The objective of this section is to present heuristic error estimates which give order of magnitude approximations for the truncation error and the solution error in the numerical solution of the Euler equations for compressible flow and other systems of conservation laws. Any conservation law can be written in a general form as

$$u_t + f_x + g_y + h_z = 0 \quad (13a)$$

The transformation of this system to an arbitrary curvilinear coordinate system is

$$U_t + F_{\xi^1} + G_{\xi^2} + H_{\xi^3} = 0 \quad (13b)$$

where  $\sqrt{g}$  is the Jacobian of the transformation and

$$F = \sqrt{g} (\xi^1 f + \xi^2 g + \xi^3 h)$$

$$G = \sqrt{g} (\xi^1 f + \xi^2 g + \xi^3 h)$$

Let  $h$  be the spacing of the fine grid, and  $nh$  be the spacing of the coarse grid. Let  $L_h$  be the difference approximation operator on the fine grid, and  $L_{nh}$  be the difference approximation operator on the coarse grid. Then the finite difference approximation of the PDE can be represented on the fine grid as

$$u_t + f_x + g_y + h_z = L_h(F, G, H) + T(h)^p \quad (13c)$$

and on the coarse grid as

$$u_t + f_x + g_y + h_z = L_{nh}(F, G, H) + T(nh)^p \quad (13d)$$

where  $n$  is an integer.

From (13c) and (13d), the estimate of the truncation error on the fine grid can be computed as

$$T(h)^p = \frac{L_{nh} - L_h}{(1 - n^p)} \quad (14)$$

A similar procedure can be used to compute the error in the numerical solution. Such a procedure has long been used in the numerical solution of ordinary differential equations and is referred to as Richardson extrapolation. Even though numerical solutions must be computed on both fine and coarse grids, the error estimates which result do not have the large peaks at solution singularities which can be encountered with the truncation error computed from difference approximation of higher derivatives. Thus the solution error estimates may sometimes be more useful in the construction of adaptive grids.

Assume that there are two numerical solutions of order  $p$  accuracy for (13b) that have been computed on a fine grid and on a coarse grid, with grid spacing  $h$  and  $nh$ , respectively, in each coordinate direction. Assuming that the same  $p$ th order method is used in both cases, then the relation between the two numerical solutions and the actual solution  $u$  of the PDE can be established as

$$u = U_h + R(h)^p \quad (15a)$$

and

$$u = U_{nh} + R(nh)^p \quad (15b)$$

From these equations, an extrapolated value of  $u$  can be computed as

$$u = \frac{n^p U_h - U_{nh}}{(n^p - 1)} \quad (15c)$$

Thus the estimate of the error in the numerical solution computed on the  $h$  grid is:

$$u - U_h = \frac{U_h - U_{nh}}{(n^p - 1)} \quad (15d)$$

## RESULTS AND DISCUSSION

The adaptive grid generation system based on the control function approach as described in the previous chapters has been used to generate static and multiple adaptive grids for several geometries (Ref. 11). Some of these results are presented in this section. The static adaptive grids were obtained by adapting the initial grids to either grid quality measure variables or to existing flow solution variables. The multiple adaptive procedure was tested on several different configurations with the adaptive MISSE Euler flow code (Ref. 12) for transonic and supersonic flow cases, and with the adaptive INS3D flow code (Ref. 13) for incompressible flow.

### Adaptation to Quality Measures

Some examples of the grid quality adaptation are shown in Figure 1 for adaptation to various quality measures. (In Ref. 11, color contour plots of the quality measures and the other adaptive features are given.) Figures 2a-d shows the difference of the average skew angle between the initial and adaptive grids. The same number of total adaptive iterations were run in each case. The control functions were updated based on the geometry of the previous grid, rather than the initial grid, at each adaptation.

Comparison of Figure 1b with Figure 1a shows that adaptation to the skewness is effective in reducing the skewness in one region, while increasing the skewness in other regions of the grid. A small improvement in aspect ratio occurs, but the smoothness of the grid is decreased.

Comparison of Figure 1c with Figure 1a indicates that adaptation to aspect ratio does improve both aspect ratio and smoothness of the grid; the skewness is increased, however. Comparison of Figure 1d with Figure 1a shows that adaptation to smoothness improves the skewness and aspect ratio of the grid effectively, but the adaptive grid is not as smooth as the initial elliptic grid.

Figure 1e shows the beneficial effect of including adaptation to aspect ratio, arc length, and smoothness, with adaptation to skewness: the skewness is reduced more by the combination than with skewness adaptation alone. A little improvement occurs in aspect ratio; the smoothness of the grid does, however, decrease.

Results from these examples show that the adaptation to the combination of all grid quality measures, or to each individually, can improve some grid properties while damaging others. For example the adaptation to the Laplacian of this particular grid can reduce the skewness, but the resulting adaptive grid is not as smooth as the initial grid. The choice of the adaptive variable for the adaptation very much depends on what property of the grid needs to be improved and the configurations of the grids.

### Multiple Adaptation

Results of multiple adaptation performed with the adaptive MISSE Euler flow code are shown in Figures 3-8. In all these plots, NTT is the total number of time steps, INT indicates the number of time steps at which the first adaptation is performed, NCL is the number of time steps between each adaptation, and MAXINT indicates the number of time steps at which the last adaptation is performed. Values of weight functions ( $AWT_1$ ,  $AWT_2$ ), weight coefficients ( $C_1$ ,  $C_2$ ), adaptive variables density ( $RHO_1$ ,  $RHO_2$ ), pressure ( $PRES_1$ ,  $PRES_2$ ) are given for the  $\xi^1$  and the  $\xi^2$  directions, respectively. For example,  $AWT = GRAD$ ,  $CURV$ ,  $C_1 = 0.5$ ,  $C_2 = 0.3$ ,  $RHO = 1.0$ ,  $PRES = 0.1$  and  $\alpha = 1$ ,  $\beta = 1$ , can be interpreted as adaptation to the density gradient in the  $\xi^1$  direction with  $C_1 = 0.5$ , and to the curvature of the pressure in the  $\xi^2$  direction with  $C_2 = 0.3$  with coefficients of gradient and curvature  $\alpha = 1$ ,  $\beta = 1$ , respectively.

#### double wedge (supersonic Euler)

Results obtained from a supersonic flow at Mach = 2 over fine (121 x 41) and coarse (81 x 31) double-wedge grids are shown in Figures 3-7. Figure 3 shows the pressure contours obtained from 300 time steps on the initial and adaptive grids (121 x 41). The grid was adapted to the density gradient in the flow direction ( $RHO = 1.0$ ) with  $C_1 = 0.7$  and to the pressure gradient in the normal direction with  $C_2 = 0.5$ . A total of 4 adaptations was used for this case, with control functions updated from the previous grid.

Figure 4 shows the pressure coefficients on the lower wall, and convergence histories of the two solutions are shown in Figure 5. In Figure 5, the high peaks at each adaptation are due to the use of the previous solution on the new adapted grid without integration onto the new grid. From these figures, clearly the adaptive grid gives a much better representation of the shock regions as well as the expansion regions. Shocks are much sharper for the solution obtained on the adaptive grid. A record of the CPU time on an IRIS 4D/440VGX machine shows that the total CPU time for the initial grid (121 x 41) without adaptation was 1481.51 CPU seconds and for the adaptive grid (121 x 41) was 1599.02 CPU seconds, an 8% increase.

Contour plots on the pressure of the initial fine grid (121 x 41), the initial coarse grid (81 x 31), and the adaptive grid (81 x 31) are shown in Figure 6. The coarse grid was adapted to the combination of density and pressure in  $\xi^1$  direction, with weight coefficient  $C_1 = 0.5$ , and to the gradient of this combination in  $\xi^2$  direction with weight coefficient  $C_2 = 0.5$ , ( $AWT = VAR$ ,  $GRAD$ ,  $RHO = 1.1$ ,  $PRES = 1.1$ ).

Different adaptive mechanisms applied to the coarse grid in the multiple adaptation process are shown in Figure 7. Figure 7b shows the pressure contours obtained on the adaptive grid of Figure 7a. The initial grid was adapted to the curvature of the combination of density and pressure in both directions ( $AWT = CURV$ ,  $CURV$ ,  $RHO = 1.1$ ,  $PRES = 1.1$ ). The total number of adaptations was 4 with  $C_1 = 0.7$ ,  $C_2 = 0.7$ . The coefficients of the gradient and curvature were  $\alpha = 1$  and  $\beta = 0.5$ , respectively, and the updates were from the original control functions.

Figure 7d shows the pressure contours obtained on the adaptive grid of Figure 7c. The adaptive mechanism for this case was pressure gradient in both directions with  $C_1 = 0.7$ ,  $C_2 = 0.7$  and total number of adaptations was 4, ( $AWT = GRAD$ ,  $GRAD$ ,  $RHO = 0.0$ ,  $PRES = 1.1$ ).

The initial grid, adapted to the gradient of the combination of density and pressure in the  $\xi^1$  direction only is shown in Figure 7e. Total number of adaptations was 5 with  $C_1 = 0$ ,  $C_2 = 0.9$ , and updates were applied to the previous control functions. Pressure contours obtained from this adaptive grid are shown in Figure 7f.

From these figures, the representation of the shocks on the adapted coarse grid is much sharper and closer to the fine grid solution than the nonadaptive coarse grid. The total CPU time for obtaining 300 time steps solution for the adaptive grid was approximately 800 seconds for each adaptive mechanism, nearly 50% saving time compared to that of the fine grid.

The adaptation to the combination of density and pressure in  $\xi^1$  direction and to the gradient of this combination in  $\xi^2$  direction of Figure 6 gives a smoother behavior of the pressure coefficient behind the shock than the adaptation to the gradient of pressure alone of Figures 7c and 7d. The adaptation to the curvature of Figures 7a and 7b gives a better result, however with a little over prediction of the pressure coefficient right behind the shock. The adaptation to the gradient of the combination of the density and pressure in  $\xi^2$  direction only in Figures 7e and 7f gives the closest solution to the fine grid solution.

From these results, clearly multiple adaptive grids produce a better representation of the shock regions, as well as the expansion regions, than that of the same nonadaptive grid. Among these adaptive mechanisms, the use of the better results than the use of single variable. Another advantage that should be mentioned here is the controlling of the direction in which adaptation is applied. As shown above, the adaptation in only one direction ( $\xi^1$ ) gives the closest solution to the fine grid solution. Moreover, the grid in this adaptive mechanism is not being disturbed as much as by the adaptation in both directions. The minimum skew angle for this case is higher compared to those of adaptation in both directions. Of course, this is true only for a certain number of adaptations and a particular value of weight coefficients.

#### wind tunnel (supersonic Euler)

Results from the supersonic flow at Mach = 2 in a wind tunnel are shown in Figure 8. These results were also obtained in 300 time steps. Figure 8a is the initial grid, Figure 8b is the adaptive grid adapted to the error estimation in both directions, and Figure 8c is the adaptive grid adapted to gradient of the combination of density and pressure in both directions. The number of adaptations was 5 for both cases, with  $C_1 = 0.6$ ,  $C_2 = 0.55$  for the adaptation to gradient of the combination. Shocks are much sharper for solutions obtained on the adaptive grids than on the nonadaptive grids for this configuration in supersonic flow as well.

Results from these examples show that multiple adaptive grids captured very well major features of the flow field in supersonic flow for these particular configurations. The adaptations to the combination of the grid quality measures, such as skewness of the grid and the flow solution, for these particular grids not only make the grid more skewed but also resulted in poor resolution of the major features of the flow field. On the other hand the adaptation to the error estimation and the use of the weighted average in weight functions computed from several flow variables does, in fact, improve the solutions.

The computation of the weight functions and the choice of the adaptive solution variable are independent from one direction to another thus enabling the users to have more freedom in choosing suitable adaptive mechanism for each kind of flow. For example, in the case of boundary layers and shocks occurring in the same flow field, the users may choose to adapt the grid to the velocity magnitude gradient in the normal direction to capture the boundary layer regions and to the pressure gradient in the flow direction to capture the shocks.

#### backward facing step (incompressible Navier-Stokes)

Results of multiple adaptation performed with the adaptive INS3D incompressible flow code are shown in Figures 9-12. These results are obtained for incompressible laminar flow for a

2-block backward facing step, (grid size for the first block is  $(21 \times 35)$  and  $(81 \times 41)$  for the second block). The Reynolds number used in this investigation for the backward facing step was 183.32 for comparison with experimental data.

The grid constructed for the backward facing step considered in this case is the same as the geometry of the experiment. However, the step length downstream of the grid is only 30 times the length of the step height, while the step length for the experiment was much larger. Figure 9c shows the velocity magnitude contours obtained from 5000 time steps on the initial grid of Figure 9a. Velocity vectors are shown in Figure 9b. Figure 10 shows the velocity magnitude, vorticity contours and velocity vectors obtained from 5000 time steps on the adaptive grid. The initial grid was adapted at 500 and 1000 time steps to the vorticity magnitude in the direction normal to the walls with  $C_1 = 0$ ,  $C_2 = 1$ , ( $AWT = VAR$ ,  $VAR$ ,  $VORR = 0.1$ ). Total number of adaptations was 2 for this case, and updates were applied to the initial control functions.

Skin friction coefficients on the lower and upper walls (beginning at the step) obtained from initial and adaptive grids are plotted in Figure 11. Velocity profiles at the step and several locations downstream (nearest to the experimental data) along with digitized experimental data are shown in Figure 12.

Results from these figures show that the velocity profiles obtained from the adaptive grid are closer to the experimental data than for the nonadaptive grid. However, there are some wiggles of the skin friction coefficient obtained from the adaptive grid occurring at the separation region of the lower wall. This may be due to the redistribution of grid spacings in this region. Digitized values of the reattachment length from Figure 11 are approximately 7.67 for both solutions, while the experimental value was 7.9 for this particular Reynolds number. The difference of these values may be due to the difference of the step length of the experiment and the grid downstream.

A record of the CPU time on a Cray 2 machine shows that the total CPU time for the initial grid without adaptation was 25956.26 CPU seconds and for the adaptive grid was 26363.74 CPU seconds. Since there is only 2 adaptive iterations the increase in time for this case is 1.2%.

#### 180 degree turn around duct (incompressible Navier-Stokes)

Most flow solvers for incompressible flow require grid lines which are packed closely to the walls in order to resolve the boundary layer regions. This results in a large number of grid points and hence long computer times. The multiple adaptation can be used to reduce the cost of computer time by allowing the use of a coarser grid. In the present investigation, a fine grid  $(111 \times 51)$  with spacing off the walls of 0.002 and a coarse grid  $(111 \times 31)$  with spacing 0.004 off the walls are considered for the turn around duct. The result of the adaptation on the coarse grid is compared with the nonadaptive fine grid solution, while the Reynolds number for the turn around duct was 500. Results obtained from 6000 time steps on fine, coarse and adaptive grids for turn around duct are shown in Figures 9-18.

Figure 13 shows the velocity magnitude contours obtained on the initial and adaptive grids. The initial coarse grid was adapted to the velocity magnitude gradient at 1000, 1500, 2000 and 2500 time steps, in the direction normal to the flow direction, ( $AWT = GRAD$ ,  $GRAD$ ,  $VOMA = 0.1$ ). Total number of adaptations was 4 with  $C_1 = 0.1$ ,  $C_2 = 0.5$ , and the updates were applied to the initial control functions. Figures 14 and 15 show the skin friction and pressure coefficients of the inner and outer walls obtained from coarse, fine and adaptive coarse grids.

Figure 14 shows that the behavior of the skin friction coefficients for the adaptive grid are much closer to the fine grid solution than the nonadaptive coarse grid. Figure 15 shows that the adaptation for this case did not help significantly in the improvement of the pressure coefficients, however.

Figure 16 shows the velocity magnitude contours obtained on the initial and another adaptive grid. The initial coarse grid was adapted to the combination of vorticity and quality measure aspect ratio of the grid in the direction normal to the flow direction, ( $AWT = VAR$ ,  $VAR$ ,  $VORR = 0.1$ ,  $ASPE = 1$ ). Here  $C_1 = 0.3$ ,  $C_2 = 0.5$ . Figures 17 and 18 show the skin friction and pressure coefficients of the inner and outer walls obtained from coarse, fine and adaptive coarse grids.

Figure 17 shows that the behavior of the skin friction coefficient of the outer wall is almost identical to that of the fine grid. The representation of the skin friction of the inner wall is smoother than that of the nonadaptive grid but with a large change after the separation region toward the outlet of the duct. Figure 18, again indicates that the adaptation did not help in the improvement of the pressure coefficients for this case either.

A record of the CPU time on an IRIS 4D/440VGX machine shows that the total CPU time for the initial grid  $(111 \times 51)$  was 23870.61 CPU seconds and for the adaptive grid  $(111 \times 31)$  was approximately 13800 CPU seconds for each adaptive mechanism. From Figures 13 and 16, it can be seen that in both adaptations the grids get finer at the turn. Correspondingly the skin friction coefficients obtained from adaptive grids have higher peak at the turn and capture separation region well, as shown in Figures 14 and 17. Moreover, the reattachment point obtained from adaptive grid of Figure 14 is closer to that of the fine grid than the adaptation of Figure 17 and the non-adaptive grid.

## CONCLUSIONS

The widely-used EAGLE grid generation system (Ref. 14) has been extended and enhanced so that it can be readily coupled with existing PDE solvers which operate on structured grids to provide a flexible adaptive grid capability. The adaptive EAGLE grid code can be used for generating not only algebraic grids and elliptic grids but static adaptive grids as well. In the static adaptation, the grid can be adapted to an existing PDE solution or to grid quality measures or to a combination of both. The test cases show that some grid properties can be improved by the static adaptation to grid quality measures.

In this study, the weight functions can be formulated as weighted average of weight functions from several flow variables or several quality measures or the combination of both. Different weight functions and adaptive variables can be applied in each direction. These operations are controlled through the input parameters in static as well as multiple adaptation mode.

There are several successful incorporations of the adaptive EAGLE packed subroutines into flow codes, including INS3D from NASA Ames and the MISSE Euler solver developed at Mississippi State University. Several configurations are considered for each of these adaptive flow codes for the investigation of the new weight functions formulations and grid quality measures in the multiple adaptation.

Results obtained from the adaptive MISSE Euler flow code show considerable success as measured by improvements in shock resolution on coarse grids in the compressible flows. Some success has been made in capturing separation regions on coarse grids of the adaptive INS3D flow code in incompressible flows. For further study, the interpolation of the previous solutions to the new adapted grids would be recommended, especially for the adaptive INS3D flow code and the implementation of arbitrary block adaptation in multi-block configurations.

## ACKNOWLEDGEMENT

This work was supported in part by Grant F08635-89-C-0209 from the Air Force Armament Directorate, Eglin AFB, (Dr. Lawrence Lijewski, monitor) and in part by Contract NAS8-36949 from NASA Marshall Space Flight Center (Dr. Paul McConnaughey, monitor).

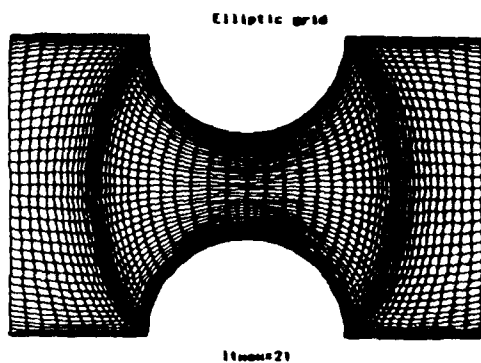


Figure 1a. Elliptic Grid

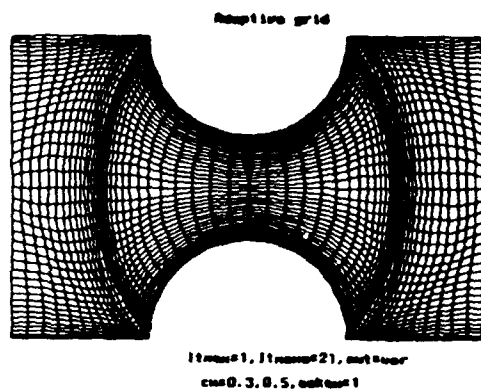


Figure 1b. Adaptation to skewness.

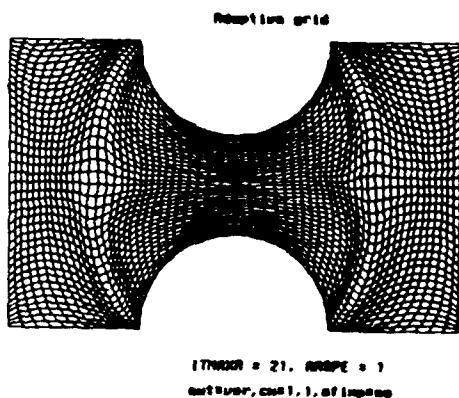


Figure 1c. Adaptation to aspect ratio.

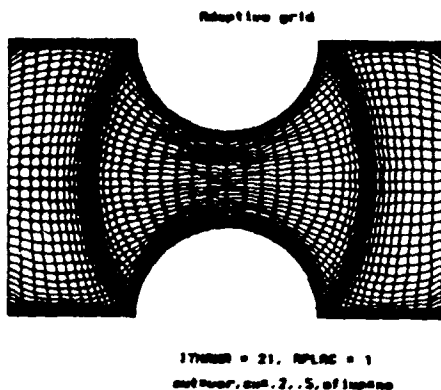


Figure 1d. Adaptation to Laplacian.

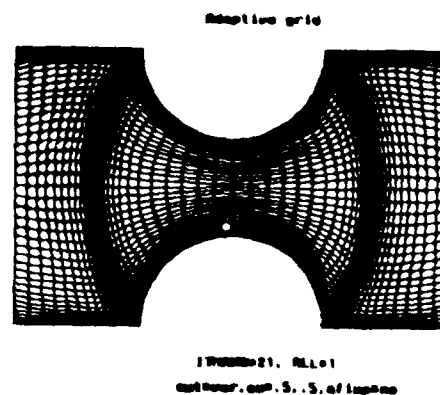


Figure 1e. Adaptation to skewness, aspect ratio, and Laplacian.

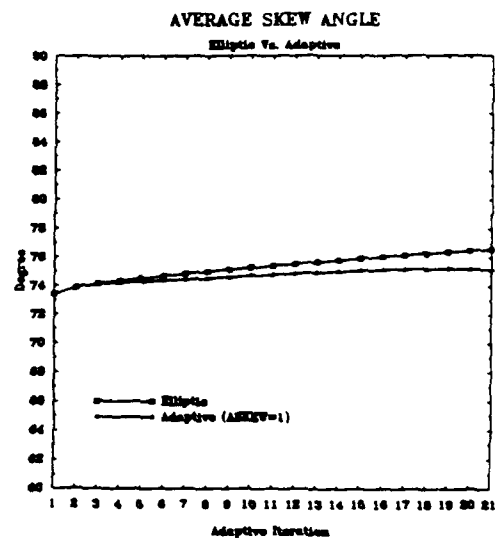


Figure 2a. The difference of average skew angle between initial and adaptive grids.

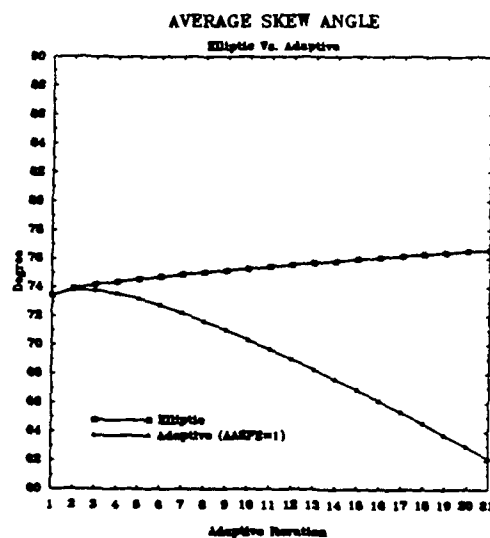


Figure 2b. The decreasing of average skew angle in the adaptation to aspect ratio.

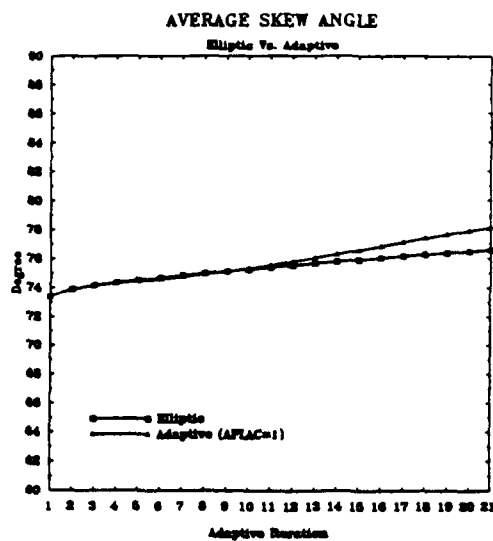


Figure 2c. The increasing of average skew angle in the adaptation to Laplacian of the grid.

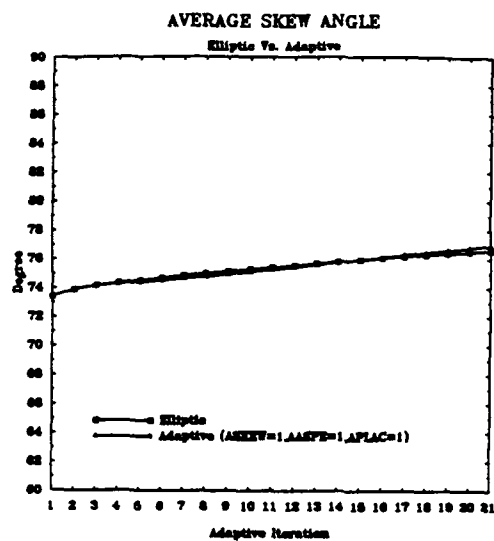


Figure 2d. Average skew angle in the adaptation to all grid quality measures.

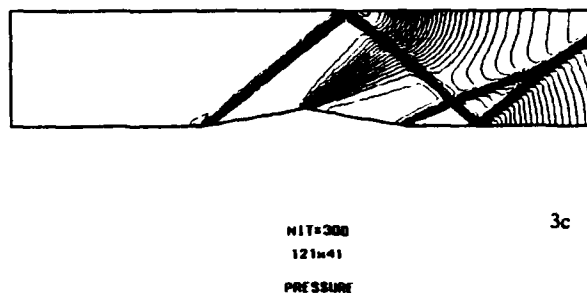
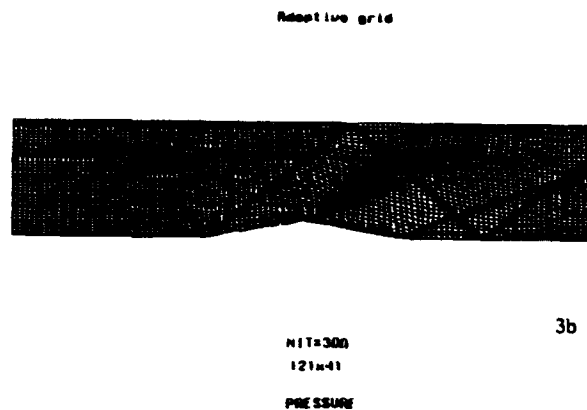
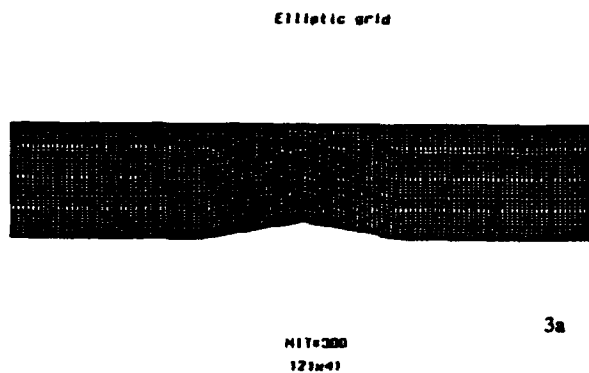


Figure 3. Contour plots of pressure on initial and adaptive grids.

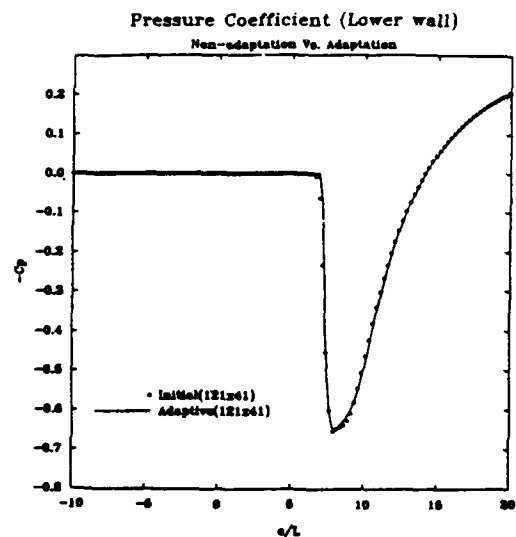


Figure 4. Adaptation with  $swt = grad, grad, PRES = 1,1$ ,  $cw = 0.7, 0.7$ .

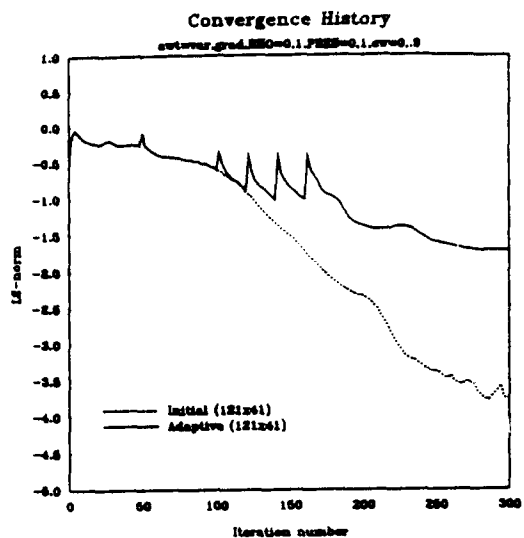


Figure 5. Convergence history of the initial and adaptive grid solutions.

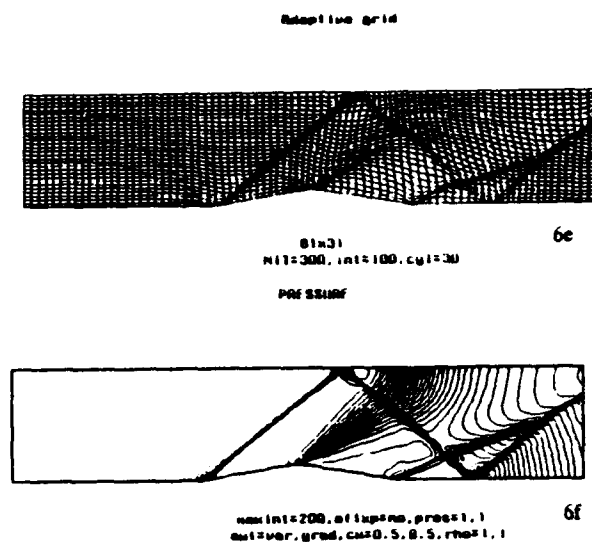
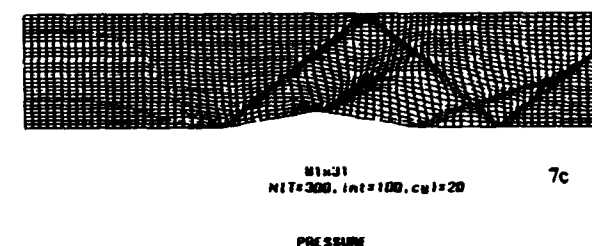
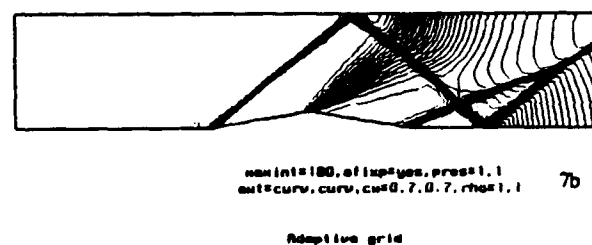
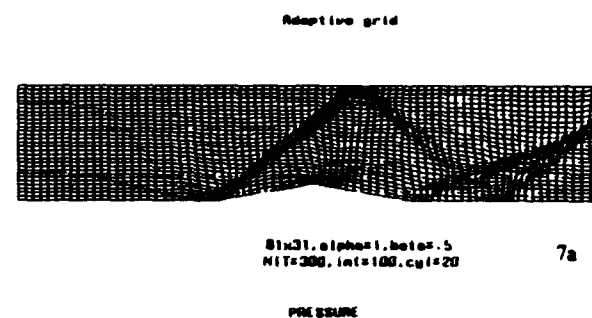
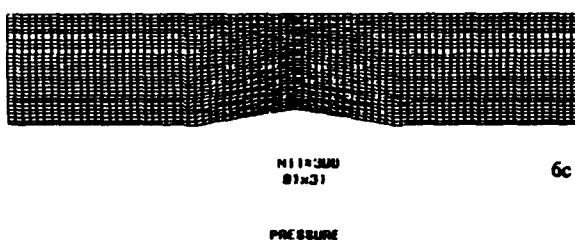
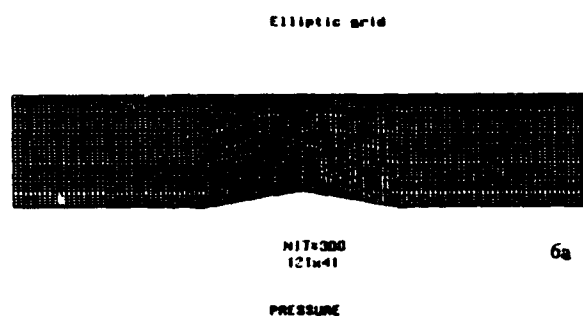


Figure 6. Contour plots of the pressure on fine, coarse and adaptive grids.



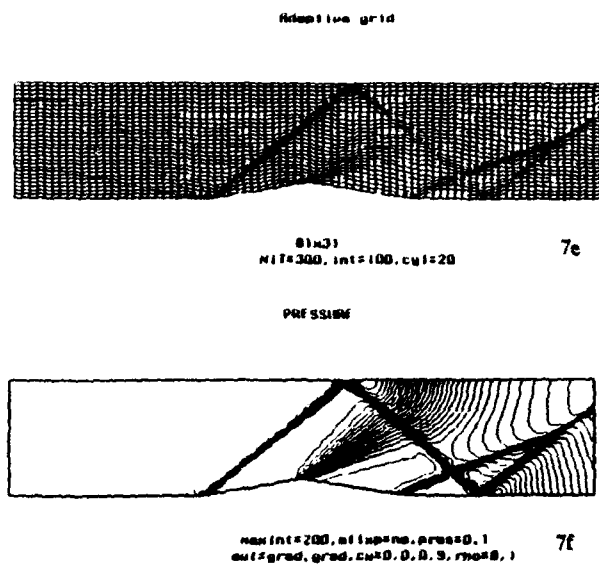


Figure 7. Contour plots of pressure on adaptive grids.

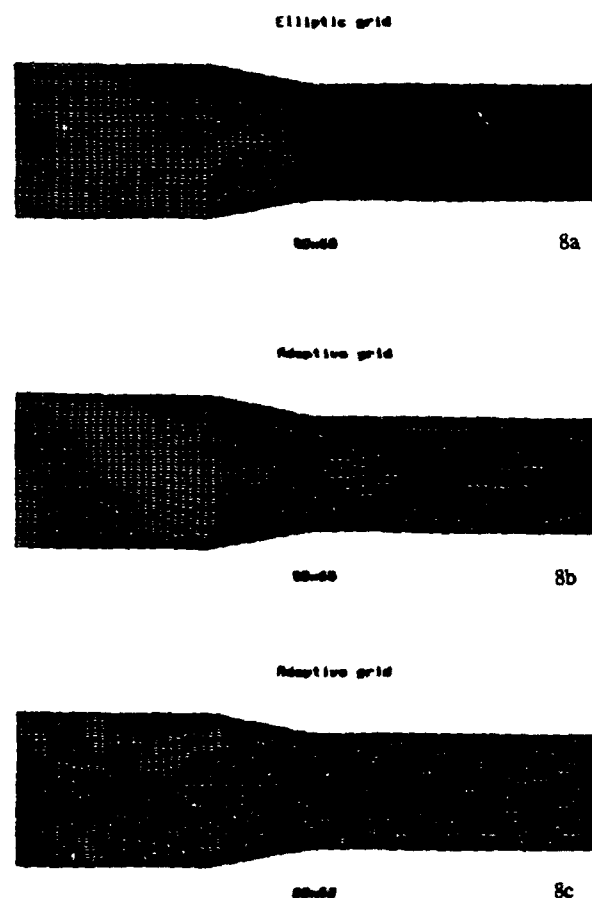


Figure 8. Contour plots of pressure on initial and adaptive grids.

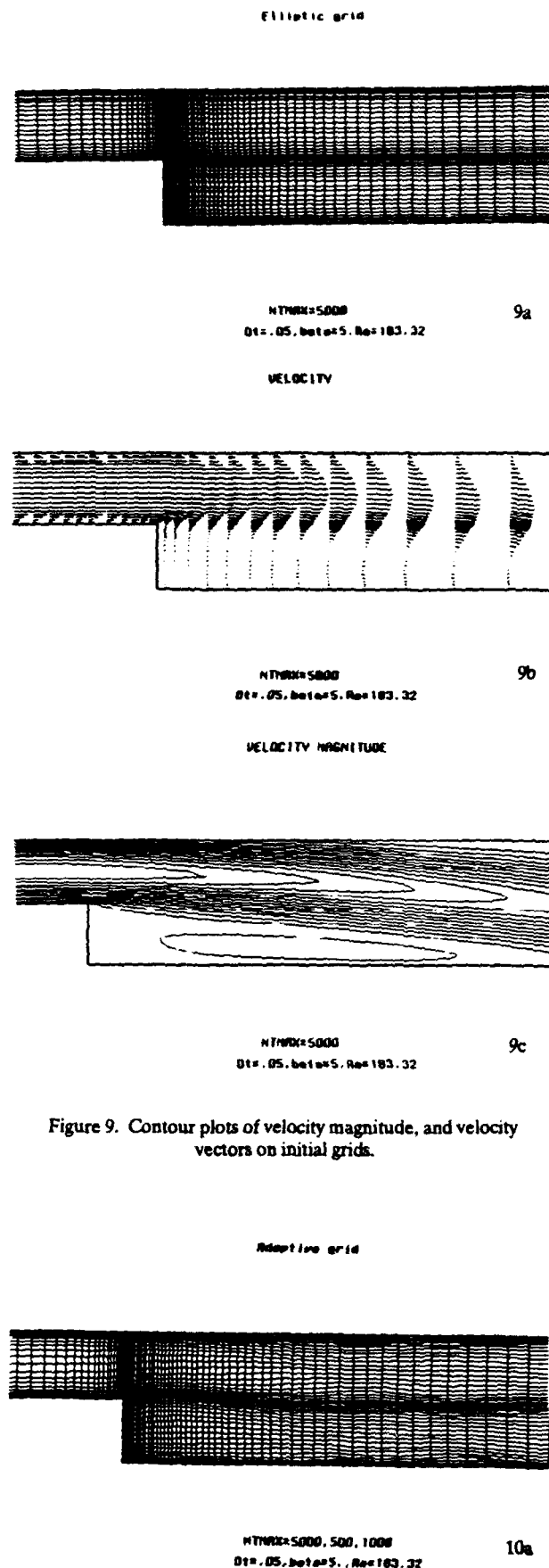
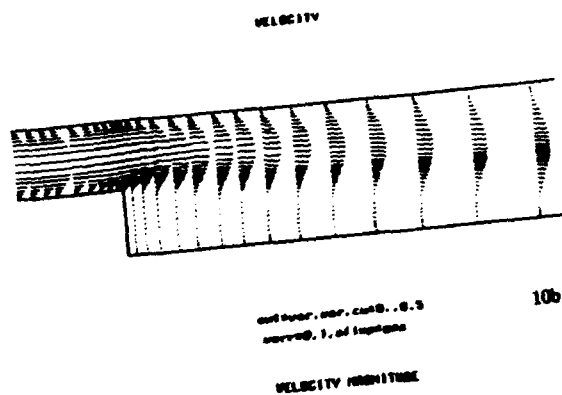
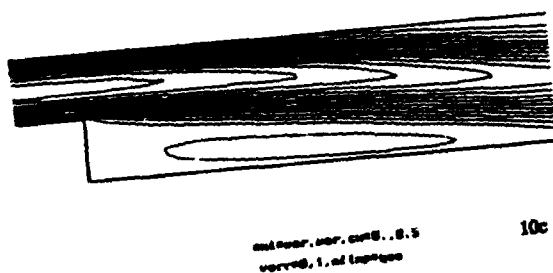


Figure 9. Contour plots of velocity magnitude, and velocity vectors on initial grids.



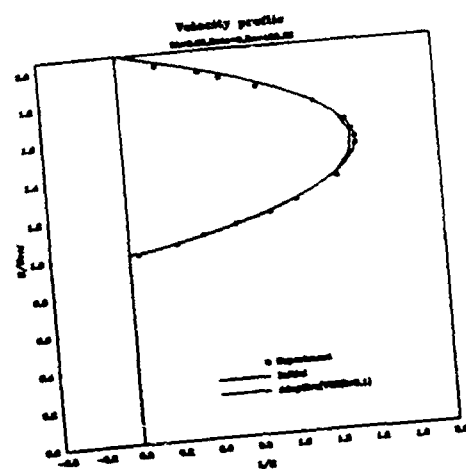


10b

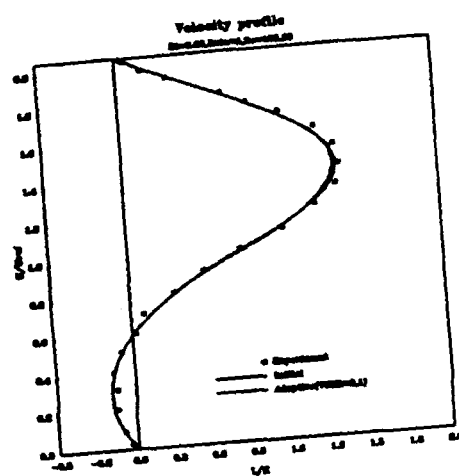


10c

Figure 10. Contour plots of velocity magnitude and velocity vectors on adaptive grid.



12a



12b

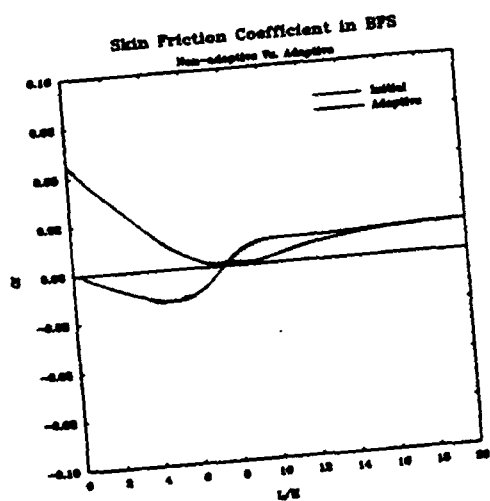
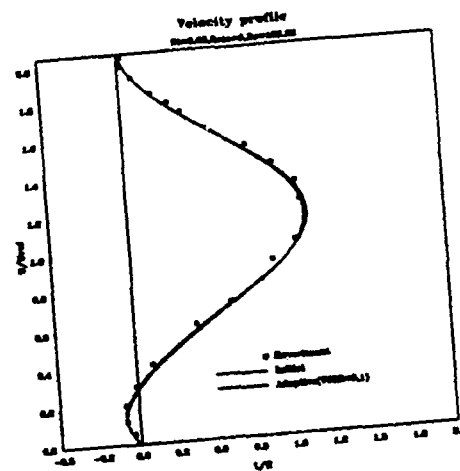


Figure 11. Skin friction of the lower and upper walls obtained from initial and adaptive grids.



12c

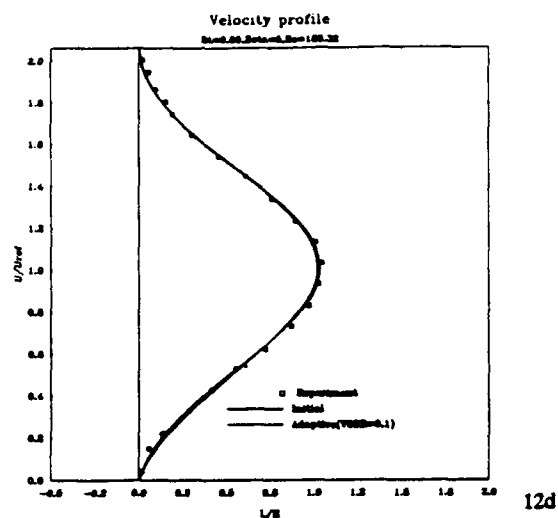


Figure 12. Velocity profile at the step  $x = 2.77, x = 6.27$ , and  $x = 8.128$ .

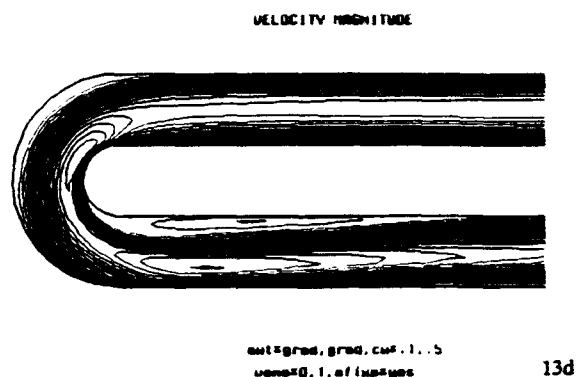
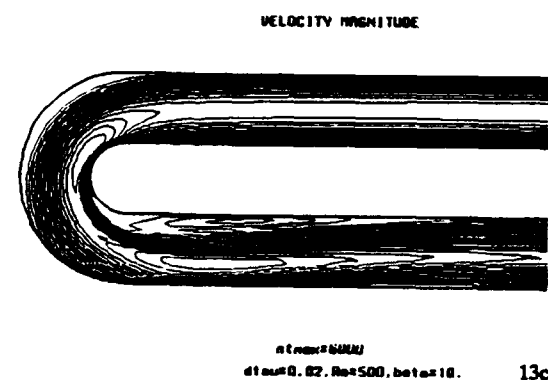
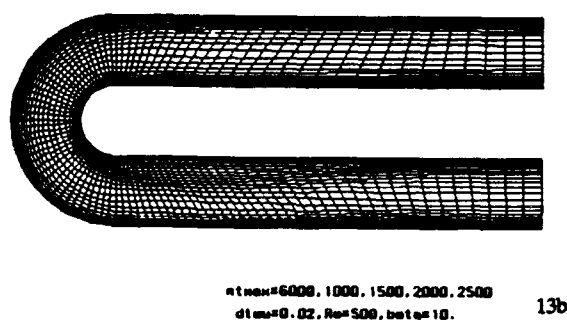
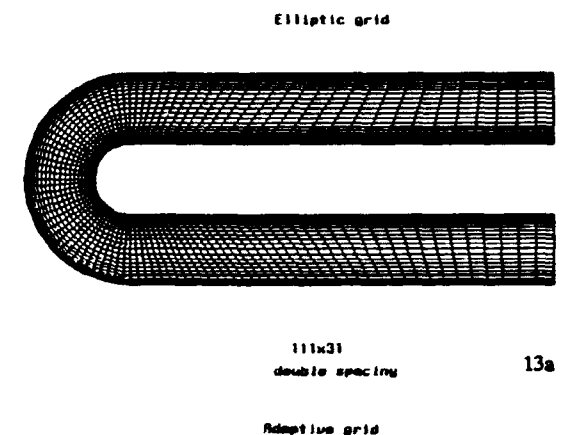


Figure 13. Contour plots of velocity magnitude on initial coarse grid and adaptive coarse grid with  $awt = grad, grad$ ,  $VOMA = 0.1, cw = 0.1, 0.5$ .

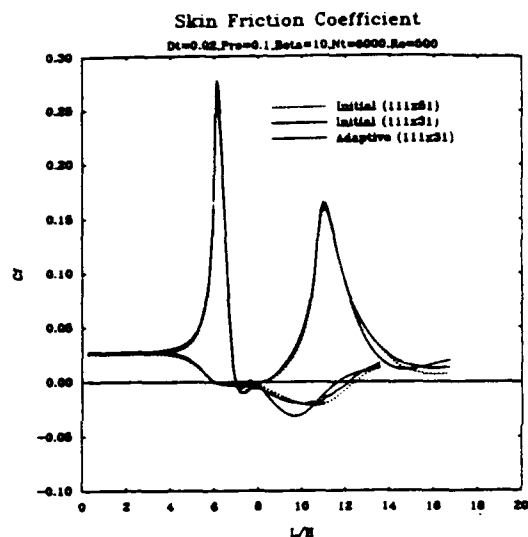


Figure 14. Skin friction coefficients of the inner and outer walls obtained from initial fine, coarse and adaptive grids with  $awt = grad, grad$ ,  $VOMA = 0.1, cw = 0.1, 0.5$ .

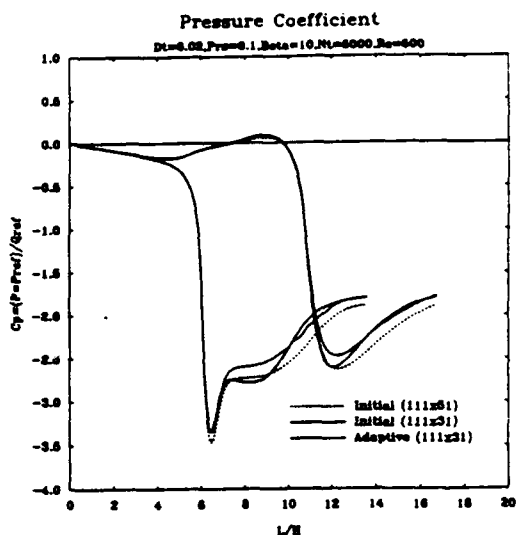


Figure 15. Pressure coefficients of the inner and outer walls obtained from initial fine, coarse and adaptive coarse grids with  $awt = grad, grad$ ,  $VOMA = 0.1, cw = 0.1, 0.5$ .

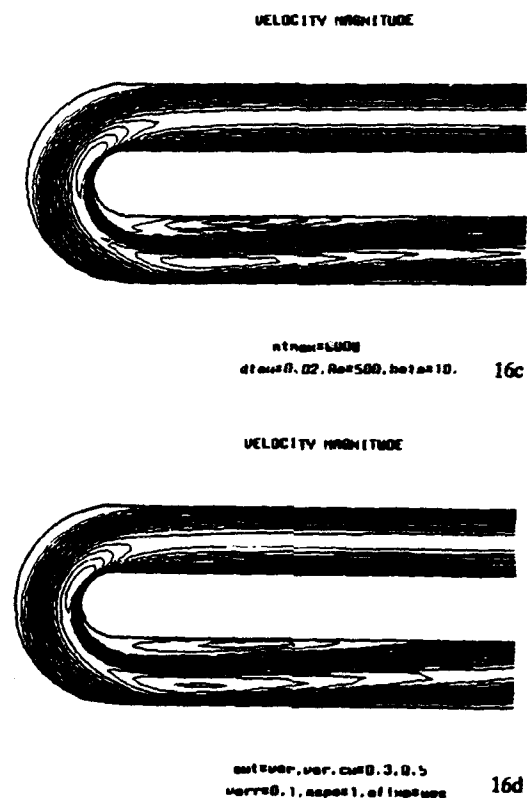
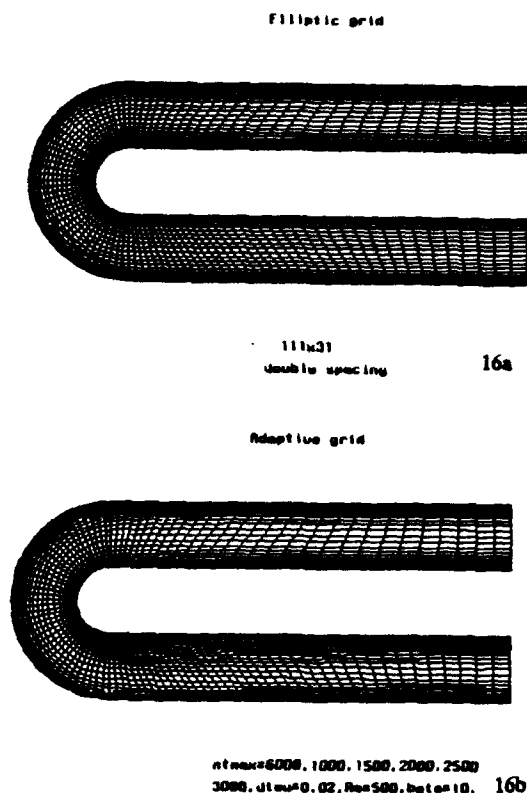


Figure 16. Contour plots of velocity magnitude on initial coarse grid and adaptive coarse grid with  $awt = var, var, VORR = 0.1, ASPE = 1, cw = 0.1, 0.5$ .

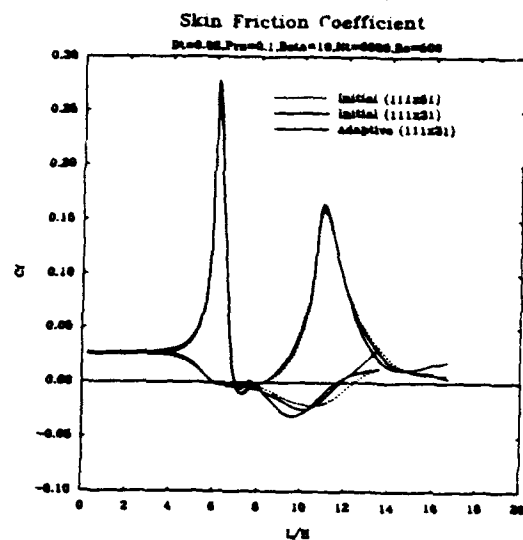


Figure 17. Skin friction coefficients of the inner and outer walls obtained from initial fine, coarse and adaptive coarse grids with  $awt = var, var, VORR = 0.1, ASPE = 1, cw = 0.1, 0.5$ .

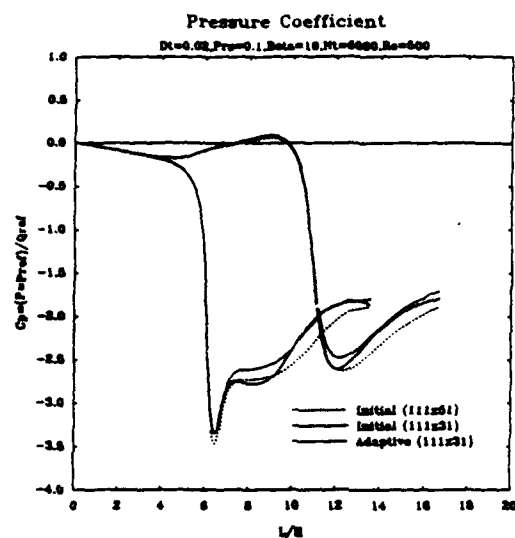


Figure 18. Pressure coefficients of the inner and outer walls obtained from initial fine, coarse and adaptive coarse grids with  $awt = var, var, VORR = 0.1, ASPE = 1, cw = 0.1, 0.5$ .

## REFERENCES

1. J. F. Thompson "A Survey of Dynamically-Adaptive Grids in the Numerical Solution of PDE", *Journal of Applied Numerical Mathematics*, Vol. 1, pp. 3-27, North-Holland, 1985.
2. H. J. Kim and J. F. Thompson, "Three Dimensional Adaptive Grid Generation on a Composite Block Grid", *ALAA 88-0311, ALAA 26th Aerospace Sciences Meeting*, Reno, Nevada, 1988.
3. J. Tu and J. F. Thompson, "Three Dimensional Solution-Adaptive Grid Generation on Composite Configurations", *ALAA 90-0329, ALAA 28th Aerospace Sciences Meeting*, Reno, Nevada, 1990.
4. D. A. Anderson, "Equidistribution Schemes, Poisson Generators, and Adaptive Grids", *Applied Mathematics and Computation*, Vol. 24, p. 211, 1987.
5. D. A. Anderson, "Generating Adaptive Grids with Conventional Grid Scheme", *ALAA 86-0427, ALAA 24th Aerospace Science Meeting*, Reno, Nevada, 1986.
6. B. F. Johnson and J. F. Thompson, "Discussion of a Depth-Dependant Adaptive Grid Generator for Use in Computational Hydraulics", *Numerical Grid Generation in Computational Fluid Mechanics*, J. Hauser and C. Taylor, Ed., Pineridge Press, 1986.
7. P. R. Eiseman, "Adaptive Grid Generation", *Computer Methods in Applied Mechanics and Engineering*, Vol. 64, p. 321, 1987.
8. G. D. Kerlick and G. H. Klopfer, "Assessing the Quality of Curvilinear Coordinate Meshes by Decomposing the Jacobian Matrix", *Numerical Grid Generation*, J. F. Thompson, Ed., pp. 787-796, North-Holland, 1982.
9. B. Gatlin, et al., "Extensions to the EAGLE Grid Code for Quality Control and Efficiency", *ALAA 90-0148, ALAA 29th Aerospace Sciences Meeting*, Reno, Nevada, 1991.
10. C. W. Mastin, "Error Estimates and Adaptive Grids for the Numerical Solution of Conservation Laws", *Proceedings of the First International Conference on Computation Physics*, pp. 73-76, Boulder, CO, June, 1990.
11. Phu Luong, "Analysis and Control of Grid Quality in Computational Simulation", PhD Dissertation, Mississippi State University, December, 1991.
12. D. L. Whitfield, "Implicit Upwind Finite Volume Scheme for the 3D Euler Equations", Mississippi State University, MSSU-EIRS-ASE-85-1, September, 1985.
13. S. E. Rogers, D. Kwak and J. L. Chang, "INS3D - An Incompressible Navier-Stokes Code in Generalized 3D Coordinates", NASA Technical Memorandum 100012, NASA Ames Research Center, November, 1987.
14. J. F. Thompson, "A Composite Grid Generation Code for General 3D Region - the EAGLE Code", *ALAA Journal*, Vol. 26, No. 3, p. 271, 1988.

A ROBUST QUASI-SIMULTANEOUS INTERACTION METHOD FOR  
A FULL POTENTIAL FLOW WITH A BOUNDARY LAYER WITH  
APPLICATION TO WING/BODY CONFIGURATIONS<sup>\*)</sup>

A.J. van der Wees<sup>\*\*) and J. van Muijden<sup>\*\*\*)</sup></sup>

National Aerospace Laboratory NLR  
P.O. Box 90502; 1006 BM Amsterdam  
The Netherlands  
Tel: (020)5113113; Fax: (020)5113210

**Abstract**

The MATRICS flow solver calculates the inviscid transonic potential flow about a wing/body semi-configuration. At present, work is in progress to extend MATRICS to take viscous effects into account through coupling with a boundary layer solver. This solver, MATRICS-V, is based on robust calculation methods for the boundary layer, the outer wing flow and their interaction. MATRICS-V is intended for (inverse) design purposes. The boundary layer and wake are based on an integral formulation of the unsteady first order boundary layer equations, the inviscid method is the existing MATRICS potential flow solver and the interaction algorithm is of the quasi-simultaneous type.

The paper gives a progress report on the coupled potential-flow boundary-layer method for transonic wing/body configurations.

**1. Introduction**

Computation methods for three-dimensional transonic potential flow are an important component in design systems for civil aircraft wing/body configurations. Accurate performance prediction under these conditions (e.g. lift-drag analysis) requires that the transonic potential flow solver is coupled with a boundary layer solver to account for the viscous effects on the wing pressure distribution in a sufficiently accurate way. For some years NLR has available its own developed system MATRICS (Multi-component Aircraft Transonic Inviscid Computation System) for the calculation of the three-dimensional inviscid transonic potential flow about wing/body configurations (Ref. 1). The MATRICS-derivative MATRICS-V -now under development- will calculate the interaction of the inviscid potential outer flow and a viscous boundary layer on the wing of a transonic transport wing/body configuration. The ultimate objective of the development of MATRICS-V will be the embedding of this system in a wing design system, also currently under development at NLR.

This paper gives a progress report on the development of MATRICS-V. Firstly, a description will be given of the MATRICS three-dimensional transonic potential flow solver, being the starting point for the development of MATRICS-V. Secondly, the requirements for the development of the viscous-inviscid interaction solver will be

formulated. Robustness of the interaction algorithm has been formulated as the main requirement. Next, the basic concepts of the viscous-inviscid interaction solver will be given. Subsequently, a short system overview will be given of the MATRICS-V flow solver, followed by an analysis of the boundary layer equation system and on the interaction law. Finally, some preliminary computational results will be presented.

**2. Starting position for the development of MATRICS-V**

The MATRICS-V viscous-inviscid interaction solver is a follow-up to the MATRICS three-dimensional inviscid transonic potential flow solver. This flow solver solves the full potential equation in strong conservation form on a grid of C-H or C-O topology. This grid is generated using the MATGRID grid generator (Tysell and Hedman, Ref. 2). The solver uses a fully conservative finite volume discretization and a multigrid solution method. The discretization scheme is second order accurate in the mesh size in subsonic parts of the flow, and first order accurate in supersonic parts of the flow. For the capture of supersonic/subsonic shock waves a Godunov-type shock operator is used. Options for fully-conservative as well as non-conservative shock-capture are available. Details on the MATRICS flow solver can be found in references 3, 4. MATRICS provides data for a lift-drag-diving-moment analysis. Substantial research has been performed on the reliable prediction of drag by the MATRICS flow solver. Findings of this research have been reported in reference 5.

The development of MATRICS-V is partly based on experience at NLR with the modelling of two-dimensional strong viscous-inviscid interaction on airfoils (Refs. 6, 7).

**3. Requirements**

MATRICS-V is designed to calculate the influence of the wing boundary layer and wake on the inviscid potential outer flow about a given transport-type wing/body configuration from subsonic up to and including transonic cruise conditions. Laminar as well as turbulent boundary layers should be calculated, where the turbulent boundary layer is allowed to be mildly separated. The MATRICS-V method should be robust; a guaranteed converged solution should be obtained for realistic flow conditions. The method should also be about ten times faster than a three-dimensional Reynolds-averaged Navier-Stokes solver, to enable wing design applications.

**4. Basic concepts**

The coupling of an inviscid outer flow with a viscous boundary layer flow will be done using an

<sup>\*)</sup> This research has been performed under contract with the Netherlands Agency for Aerospace Programs (NIVR 01802N)

<sup>\*\*) Research scientist, Num. Math. and Appl. Prog. Dep., Informatics Division</sup>

<sup>\*\*\*)</sup> Research Scientist, Theoretical Aerodynamics Dep., Fluid Dynamics Division

integral method formulation of the boundary layer equations. With integral methods there is no explicit formulation of a turbulence model, but the system of equations is supplemented by suitable empirical closure relations. The integral method is reasonably easy to implement, because in the integral method the three-dimensional flow problem is formulated as a two-dimensional problem on the wing surface and the wake center-surface. This is a great advantage in code development.

Until a few years ago, the boundary layer equations have always been used in their steady form to compute a steady boundary layer flow. The main advantage of this formulation over an unsteady formulation has always been its lower computation time. However, using the boundary layer equations in their unsteady formulation, integrating them towards a steady solution, the boundary layer method is particularly well suited for vectorization and hence for implementation on today's supercomputers, see Van Dalsem and Steger (Ref. 8), Swafford and Whitfield (Ref. 9). An even more important advantage of using the unsteady boundary layer equations for solving steady boundary layer flow is the robustness of this approach. With the unsteady formulation a simple time-integration scheme will in any case produce an unsteady answer. With the steady formulation a space-marching scheme has to be used and the specification of initial data proves to be more difficult in a space-marching scheme than in a time-integration scheme. Also in case the steady boundary layer solution is non-unique or non-existent, the solution produced by an unsteady formulation is probably more useful than the solution produced by a steady formulation.

Two candidate interaction algorithms have been considered, namely the semi-inverse and quasi-simultaneous algorithm. (The more sophisticated simultaneous algorithm is too expensive to implement in MATRICS because of the fully implicit relaxation algorithm employed in the existing inviscid potential outer flow solver). Experience by Ashill e.a. (Ref. 10), pp. 35, and Cebeci, Chen e.a. (Ref. 11) indicates that the semi-inverse algorithm lacks robustness in difficult flow cases. Therefore the quasi-simultaneous interaction algorithm is used, being the best available interaction algorithm that can be implemented in interaction with the inviscid potential outer flow solution algorithm.

In the inviscid potential outer flow solver the "blowing velocity approach" is used to account for the boundary layer effects on the inviscid outer flow, which means that a source strength is specified at the body surface and a jump in source strength at the wake. This approach is reasonably standard, while experience by Chen, Li e.a. (Ref. 12) reports that this approach is more reliable than the boundary layer displacement approach.

Experience by Chow (Ref. 13) indicates that it is mandatory to prescribe the pressure jump across the wake as a boundary condition to the outer inviscid flow. The latter jump influences the Kutta condition prescription in the outer inviscid flow, and this is essential in order to compute realistic lift values for the wing. The pressure jump across the boundary layer is computed as in Chow (Ref. 13) and Lock and Williams (Ref. 14).

## 5. Description of the calculation method

### 5.1 Inviscid method

The full potential equation

$$\frac{\partial}{\partial x^1} (\rho u^1) = 0, \quad (1)$$

$$u^1 = u_\infty^1 + \frac{\partial \varphi}{\partial x^1}, \quad (2)$$

$$q^2 = (u^1)^2 + (u^2)^2 + (u^3)^2, \quad (3)$$

$$\rho = \left\{ 1 + \frac{\gamma-1}{2} M_\infty^2 (1 - q^2) \right\}^{\frac{1}{\gamma-1}}, \quad (4)$$

is solved using a finite volume discretization formulated on a curvilinear coordinate system and a multigrid method employing ILU/SIP smoothing. At present only semi-configurations can be considered.

The boundary conditions are:

- on wetted surfaces  $u_n = qS$ ; (5)
- for the inviscid flow solver, the source strength  $S = 0$  on the body, else  $S$  is computed by the boundary layer solver;
- in the symmetry plane  $u_n = 0$ , (6)
- in the far-field, except downstream,  $\varphi = 0$ , (7)
- in the far-field downstream (Trefftz-plane)

$$\frac{\partial^2 \varphi}{(\partial \xi^1)^2} = 0, \quad (8)$$

where  $\xi^1$  is the chordwise (wrap-around) grid coordinate.

- across the prescribed vortex sheet

$$\begin{cases} [q] = q^+ - q^-, \\ [\rho q S] = (\rho q S)^+ - (\rho q S)^-; \end{cases} \quad (9)$$

for the inviscid flow solver the jump across the wake,  $(.)^+ - (.)^-$ , is computed by the boundary layer solver,

- across the C-0 topology branch cut that extends from the tip section to the far-field lateral boundary

$$[\varphi] = 0, [\rho u_n] = 0. \quad (10)$$

### 5.2 Viscous method

The steady first order boundary layer equations, describing conservation of mass and momentum in a general right-handed coordinate system, can be found in Myring (Ref. 15). Adding time-dependent terms and using first order integral thicknesses, the boundary layer equations can be integrated with respect to  $z$  (normal to the wing surface or wake centerline), using the momentum equation in  $z$ -direction to eliminate the pressure. Then the integral equations are obtained in the form

$x$ -momentum:

$$\frac{1}{q} \frac{\partial \delta_1}{\partial t} - \frac{\bar{u}}{q^2} \frac{\partial \delta_p}{\partial t} + \left\{ \frac{1}{q^2} (1 - \bar{M}^2) \delta_1 + \frac{\bar{u}}{q^3} \bar{M}^2 \delta_p \right\} \frac{\partial \bar{q}}{\partial t} +$$

$$\frac{1}{h_1} \frac{\partial \theta_{11}}{\partial x} + \theta_{11} \left\{ \frac{2-\bar{M}^2}{h_1} \frac{1}{q} \frac{\partial \bar{q}}{\partial x} + \frac{1}{J} \frac{\partial}{\partial x} \left( \frac{J}{h_1} \right) + k_1 \right\} + \quad (11)$$

$$+ \frac{1}{h_2} \frac{\partial \theta_{12}}{\partial y} + \theta_{12} \left\{ \frac{2-\bar{M}^2}{h_2} \frac{1}{q} \frac{\partial \bar{q}}{\partial y} + \frac{1}{J} \frac{\partial}{\partial y} \left( \frac{J}{h_2} \right) + k_3 \right\} +$$

$$\delta_1 \left\{ \frac{1}{h_1} \frac{1}{q} \frac{\partial \bar{u}}{\partial x} + k_1 \frac{\bar{u}}{q} \right\} + \delta_2 \left\{ \frac{1}{h_2} \frac{1}{q} \frac{\partial \bar{u}}{\partial y} + k_2 \frac{\bar{v}}{q} + k_3 \frac{\bar{u}}{q} \right\}$$

$$+ \theta_{22} k_2 = \frac{1}{2} C_{x1};$$

y-momentum:

$$\frac{1}{q} \frac{\partial \delta_2}{\partial t} - \frac{\bar{v}}{q^2} \frac{\partial \delta_p}{\partial t} + \left\{ \frac{1}{q^2} (1-\bar{M}^2) \delta_2 + \frac{\bar{v}}{q^3} \bar{M}^2 \delta_p \right\} \frac{\partial \bar{q}}{\partial t} +$$

$$\frac{1}{h_1} \frac{\partial \theta_{21}}{\partial x} + \theta_{21} \left\{ \frac{2-\bar{M}^2}{h_1} \frac{1}{q} \frac{\partial \bar{q}}{\partial x} + \frac{1}{J} \frac{\partial}{\partial x} \left( \frac{J}{h_1} \right) + l_1 \right\} + \quad (12)$$

$$+ \frac{1}{h_2} \frac{\partial \theta_{22}}{\partial y} + \theta_{22} \left\{ \frac{2-\bar{M}^2}{h_2} \frac{1}{q} \frac{\partial \bar{q}}{\partial y} + \frac{1}{J} \frac{\partial}{\partial y} \left( \frac{J}{h_2} \right) + l_2 \right\} +$$

$$\delta_1 \left\{ \frac{1}{h_1} \frac{1}{q} \frac{\partial \bar{v}}{\partial x} + l_1 \frac{\bar{u}}{q} + l_3 \frac{\bar{v}}{q} \right\} + \delta_2 \left\{ \frac{1}{h_2} \frac{1}{q} \frac{\partial \bar{v}}{\partial y} + l_2 \frac{\bar{v}}{q} \right\}$$

$$+ \theta_{11} l_1 = \frac{1}{2} C_{x2};$$

entrainment:

$$\frac{1}{\rho q J} \left\{ \rho J \frac{\partial}{\partial t} (\delta - \delta_p) - J \frac{\bar{p}}{q} \bar{M}^2 (\delta - \delta_p) \frac{\partial \bar{q}}{\partial t} + \frac{\partial}{\partial x} \left( \frac{\rho J}{h_1} (\bar{u} \delta - \bar{q} \delta_1) \right) + \right.$$

$$\left. \frac{\partial}{\partial y} \left( \frac{\rho J}{h_2} (\bar{v} \delta - \bar{q} \delta_2) \right) \right\} = \frac{1}{q} \left\{ \frac{\bar{u}}{h_1} \frac{\partial \delta}{\partial x} + \frac{\bar{v}}{h_2} \frac{\partial \delta}{\partial y} - \bar{w} + \frac{\partial \delta}{\partial t} \right\} = C_x.$$

(13)

where  $q$  is the velocity,  $J$  is the Jacobien of the transformation from physical to computational space, and overbars denote boundary layer edge values. The density thickness  $\delta_p$  is the integral of  $(\bar{\rho} - \rho)/\rho$  over the boundary layer.

In the latter equation (13) the instationary entrainment coefficient is an extension of the unsteady two-dimensional definition as used by Houwink (Ref. 16).

Subsequently an expression is needed for the calculation of the non-dimensional mass flux  $S$  through the surface of the wing and wake, representing the displacement effect of the boundary layer on the inviscid outer flow. Assuming an inviscid flow between the stream surface  $z = 0$  and the displacement surface  $\delta^*$ , which is a stream surface for the inviscid flow, the following expression can be obtained from (13) by setting

$$\delta = 0:$$

$$S = \frac{1}{\rho q J} \left\{ \rho J \frac{\partial \delta_p}{\partial t} - J \frac{\bar{p}}{q} \bar{M}^2 \delta_p \frac{\partial \bar{q}}{\partial t} + \frac{\partial}{\partial x} \left( \frac{\rho J}{h_1} \bar{q} \delta_1 \right) + \frac{\partial}{\partial y} \left( \frac{\rho J}{h_2} \bar{q} \delta_2 \right) \right\}; \quad (14)$$

this is equivalent to  $S = \bar{w}/q$ , yielding the usual interpretation of  $S$  in steady inviscid flow.

In the used body-conforming non-orthogonal coordinate system the  $y$ -axis is in the spanwise direction of the wing, while the  $x$ -axis is in chordwise direction wrapping around the wing and the wake.

Next, a streamline coordinate system is adopted, in which the variables (now denoted with tildes) reduce to their familiar form, see Myring (Ref. 15). Transformation to and from the streamline coordinate system is done whenever necessary. Thus it is possible to derive equations using the well-known integral parameters in streamline coordinates and in the curvilinear system.

The equations (11) to (14) are thus written in the basic variables  $\bar{\theta}_{11}$ , ...,  $\bar{q}$  and  $C$ , where the cross-flow parameter  $C$  is defined as

$$C = \frac{\text{sign}(\beta_w) \sqrt{-\bar{\theta}_{22}}}{\delta_1} \quad (15)$$

Reduction of the number of unknowns to the four basic variables is established by prescribing a set of turbulent velocity profiles in the streamline coordinate system, while the density thickness  $\delta_p$  is eliminated using the Crocco relation, prescribing a parabolic distribution between velocity and temperature (Ref. 17). For the time being no velocity profiles are used, but proven closure relations taken from accepted two-dimensional methods for attached as well as separated flow (Ref. 16, 18, 19) have been implemented in a first version of the code. In a next version, more physical closure relations and velocity profile families will be used.

Initial conditions for the turbulent boundary layer calculation are generated by the BOLA-2D solver (Ref. 20), which calculates the laminar quasi-two-dimensional flow in the leading edge region of the wing.

Boundary conditions are set at the wing root, where derivatives in spanwise direction are assumed to be zero, and the wing tip, where zero lateral derivatives in local sweep direction are prescribed, see Cross (Ref. 21). Far downstream, a zero gradient condition in chordwise direction is specified for all quantities.

The system of equations (11) to (13) is solved in combination with an interaction law (to be discussed in the next section). The complete set of equations can be written symbolically as

$$\frac{E}{q} u_t = Au_x + Bu_y + Du = f, \quad (16)$$

where  $u = [\bar{\theta}_{11}, \bar{H}, \bar{q}, C]$ .

The system (16) appears to be hyperbolic in practice. Discretization is done according to the directions of the characteristics in  $(x, t)$  and  $(y, t)$ -space, using a matrix-split procedure (Ref. 22). Thus equation (16) is discretized as

$$\frac{E}{q} u_t + A^+ \bar{\partial}_x u + A^- \bar{\partial}_x u + B^+ \bar{\partial}_y u + B^- \bar{\partial}_y u + Du = f. \quad (17)$$

In smooth parts of the flow second order accurate differencing will be obtained using a scheme as for example in Spekrijse (Ref. 23).

The system of equations (17) is solved using the fully implicit backward Euler time-integration scheme proposed by Steger and Warming (Ref. 24) and Yee (Ref. 25).

### 5.3 Interaction law

In order to avoid a breakdown of the boundary layer formulation in separated flow regions an extra equation is needed which modifies the inviscid flow boundary layer edge velocity  $\bar{q}$ . Usually a highly linearized form of the inviscid outer potential flow is taken, for example the two-dimensional Hilbert-integral formulation as used by Veldman (Ref. 26). An even more simplified form is given by Williams (Ref. 27). In this paper the latter form is slightly modified, but still derived from the linearized potential equation. This will be discussed in more detail in section 6.2. In its simplest form the interaction law can be written as

$$\frac{\partial \bar{q}}{\partial s} - \frac{\bar{q}\pi}{\beta \Delta x} s = \left( \frac{\partial \bar{q}}{\partial s} \right)^* - \frac{\bar{q}^* \pi}{\beta^* \Delta x} s^*. \quad (18)$$

Time-dependent terms are obtained from the instationary form of  $S$  (equation (4)), paying special attention to the limiting case for  $M \rightarrow 0$ . Two remarks are made:

1. Equation (18) is written along streamlines, which implies that the streamline directions are known from the inviscid flow solver and are kept fixed during a viscous calculation.
2. Equation (18) is a law in correction form, indicating that it will not influence the converged solution. In this way the interaction law can be shown to be essential to avoid breakdown of the boundary layer formulation, but once convergence is obtained it does not affect the final solution.

### 5.4 Viscous-inviscid interaction algorithm

The leading edge part of the boundary layer will be calculated in direct mode using the program BOLA-2D (Ref. 20). This presupposes that the flow does not separate in this part of the boundary layer. The inviscid flow computation in this part is done in direct mode with a source strength  $S$

specified on the wing. Further downstream, a quasi-simultaneous interaction algorithm is used. In this formulation the inviscid flow calculation is done in direct mode with a prescribed source strength  $S$  on the wing and the wake and a prescribed velocity jump across the wake. The viscous calculation is done in quasi-simultaneous mode with a prescribed inviscid wall velocity, which has been corrected for boundary layer curvature effects. Thus the boundary layer is computed effectively with a prescribed edge velocity instead of the inviscid wall velocity. Cebeci, Clark e.a. (Ref. 28) have shown that such an approach avoids the initiation of undesirable pressure fluctuations in the trailing-edge region at reasonably large angles of attack. The boundary layer computation computes a new source strength  $S$  and velocity jump  $\Delta q$ , which are used as the subsequent input for the interactive calculations.

## 6. Analysis of the system of equations

### 6.1 Analysis of boundary layer equation system

To analyze the properties of the boundary layer equations formulated in chapter 5 (Eqs. (1), (2), (3), (18)) we assume the following simplifying conditions:

- orthonormal coordinate system, i.e.  $h_1=h_2=1$ ,  $g=0$ ;  $k_1=k_2=k_3=0$ ;  $l_1=l_2=l_3=0$ ;
- outer streamline aligned with the  $x$ -axis, i.e.  $u/q=1$ ,  $v/q=0$ ;
- closure conditions as in Cousteix and Houdeville (Ref. 20), i.e.

$$\bar{\theta}_{12} = C(\bar{\delta}_1 - \bar{\theta}_{11}), \quad \bar{\theta}_{21} = -C\bar{\theta}_{11},$$

$$\bar{\theta}_{22} = -C^2(\bar{\delta}_1 - \bar{\theta}_{11}), \quad \bar{\delta}_2 = -C\bar{\delta}_1. \quad (19)$$

With  $H = \bar{\delta}_1 / \bar{\theta}_{11}$  and  $H_1 = (\bar{\delta} - \bar{\theta}_1) / \bar{\theta}_{11}$  we obtain an equation system

$$\frac{E}{q} u_t + Au_x + Bu_y = f, \quad u = [\ln \bar{\theta}_{11}, \bar{H}, \ln \bar{q}, \ln C],$$

where

$$E = \begin{bmatrix} H \cdot \bar{H}(\bar{H}+1)\delta_r & 1 & -H(\bar{H}^2-1) + \bar{H}^2\delta_r(\bar{H}+1) & 0 \\ H + H_1 \cdot \delta_r(\bar{H}+1) & H_1' + 1 & -\bar{H}^2(H+H_1-\delta_r(\bar{H}+1)) & 0 \\ -K_1(\delta_r+\epsilon)(\bar{H}+1) & -K_1(\epsilon+\delta_r) & -(\bar{H}+1)(2\epsilon K_1 + \bar{H}_q \delta_r K_1 - \bar{H}^2\delta_r K_d) & 0 \\ H & \delta_r + 1 & H(1-\bar{H}^2) + \bar{H}_q \delta_r(\bar{H}+1) & H \end{bmatrix}, \quad (20)$$

$$A = \begin{bmatrix} 1 & 0 & H+2-\bar{H}^2 & 0 \\ H_1 & H_1' & H_1(1-\bar{H}^2) & 0 \\ -HK_1 & -K_1(\delta_r+1) & K_d - K_1\bar{H}_q\delta_r(\bar{H}+1) & 0 \\ 1 & 0 & 2-\bar{H}^2 & 1 \end{bmatrix}, \quad (21)$$

$$B = \begin{bmatrix} H-1 & \delta_r+1 & (1-\bar{H}^2)H + (\bar{H}+1)\bar{H}_q\delta_r\bar{H}^2-2 & H-1 \\ H & \delta_r+1 & (1-\bar{H}^2)H + (\bar{H}+1)\bar{H}_q\delta_r & H \\ 0 & 0 & 0 & 0 \\ C(H-1) & C(\delta_r+1) & C((H-1)(2-\bar{H}^2) + (\bar{H}+1)\bar{H}_q\delta_r) & 2C(H-1) \end{bmatrix}; \quad (22)$$



the parameter  $\epsilon=0$  at  $\bar{M}=0$  and

$$\delta_r = \frac{\gamma-1}{2} \bar{M}^2, \quad (23a)$$

$$\bar{M}_q = 2 + (\gamma-1) \bar{M}^2, \quad (23b)$$

$$H = (\bar{H}+1)(1+\delta_r) - 1, \quad (23c)$$

$$H'_1 = dH_1/dH. \quad (23d)$$

Setting  $K_d=1$  and  $K_1=\pi/(\beta\Delta x)$  in the third row of eqs. (20)–(22) reproduces eq. (18).

Following Myring, reference 16, the characteristics of an equation

$$Eu_t + Au_x + f = 0, \quad u = [u_1 \dots u_n]$$

can be obtained from

$$\det(E-\lambda A) = 0, \quad \lambda = \frac{dt}{dx}. \quad (24)$$

We first consider the quasi two-dimensional flow case ( $\partial/\partial y=0$ ) where no interaction law is used, i.e.  $K_1=0$ ,  $K_d=1$ . This way we find the following expressions for the characteristic directions  $\lambda$ :

$$\lambda = H, \quad (25a)$$

$$\lambda = \bar{M}_q \delta_r (\bar{H}+1), \quad (25b)$$

$$-H'_1 \lambda^2 + ((H+1)H'_1 - H_1 + 1 - (\bar{H}+1)\delta_r H'_1) \lambda +$$

$$-HH'_1 + H_1 + (\bar{H}+1)\delta_r H'_1 = 0. \quad (25c)$$

For realistic  $H_1(H)$ -functions, viz. with  $H'_1 - H_1/\bar{H}$  the roots of the latter quadratic equation are real. Consequently, the equation system is fully hyperbolic. If  $H'_1 < 0$  the values for  $\lambda$  are greater than zero. At separation, that is at  $H'_1=0$ , in the minimum of the  $H_1(\bar{H})$  curve, one eigenvalue  $\lambda$  passes through zero, which means that the characteristic direction changes from upwind to downwind there. Consequently, the equation system models the corresponding physical behaviour.

We continue the analysis for the quasi two-dimensional case ( $\partial/\partial y=0$ ), but now for the case where an interaction law is used to solve for  $\ln q$ , i.e.  $K_1 \neq 0$ ,  $K_d=1$ . In case  $K_1=1$ ,  $\bar{M}^2=0$  and  $\epsilon=0$  we find the following expressions for  $\lambda$ :

$$\lambda = 0, \quad (26a)$$

$$\lambda = H, \quad (26b)$$

$$((H+1)^2 H'_1 - (H+1)H_1) \lambda^2 + (-H'_1(2H+1)(H+1) + H_1(2H+3) - 1) \lambda + (H+1)(HH'_1 - H_1) = 0. \quad (26c)$$

For realistic  $H_1(\bar{H})$ -functions, namely with  $(H+1)H'_1 - H_1 < 0$  and  $HH'_1 - H_1 < 0$  three values for  $\lambda$  are positive, one is negative. For small  $\epsilon < 0$  it can be shown that

all values for  $\lambda$  are positive for all  $H$ , so that now all characteristics originate from the upwind direction.

For the case  $\partial/\partial y \neq 0$  we find the following characteristic directions in the  $x, y$ -plane ( $\lambda = dy/dx$ ):

- No interaction law ( $K_1=0$ ,  $K_d=1$ ):

$$\lambda = 0, \quad (27a)$$

$$\lambda = H-1, \quad (27b)$$

$$H'_1 \lambda^2 + ((H-1)H'_1 - H_1(1+\delta_r) + 1 + \delta_r) \lambda + 1 + \delta_r = 0; \quad (27c)$$

as in the  $x, t$ -plane a characteristic direction changes from upwind to downwind at separation (i.e. at  $H'_1=0$ ).

- With interaction law ( $K_1 \neq 0$ ,  $K_d=1$ ) in case  $K_1=1$ ,  $\bar{M}^2=0$ ,  $\epsilon=0$ :

$$\lambda = 0, \quad (28a)$$

$$(-(H+1)^2 H'_1 + (H+1)H_1) \lambda^3 + ((2H^3 + H^2 - 2H - 2)H'_1 + (-2H^2 + 1)H_1 + H^2 + H + 1) \lambda^2 + ((H^2 - 1)H'_1 + H^2 + H + 2) \lambda + 1 = 0; \quad (28b)$$

two positive and one negative value for  $\lambda$  are found in case of realistic  $H_1(H)$ -functions.

The characteristics in the  $x, t$ -plane for the more general case with an interaction law ( $K_1 \neq 0$ ) and without the additional settings  $K_1=1$ ,  $\bar{M}^2=0$  and  $\epsilon=0$  can only be analyzed numerically. We find the following expressions for the characteristic directions:

$$\lambda = H, \quad (29a)$$

$$a_3 \lambda^3 + a_2 \lambda^2 + a_1 \lambda + a_0 = 0, \quad (29b)$$

where  $a_3 = \det A$  and  $a_0 = \det E$ .

A well-defined interaction law has the property that  $a_3 \neq 0$  for all  $\bar{H}$ . This gives the following relation between  $K_1$  and  $K_d$ :

$$K_1 > \frac{-H'_1}{(HH'_1 - H_1)(H+1) - \delta_r \bar{M}_q H'_1 (\bar{H}+1) + HH'_1 (1 - \bar{M}^2) - H_1 \delta_r (H+1)} K_d. \quad (30)$$

if  $H'_1 < 0$  the value  $K_1=0$  may be chosen (direct mode). If  $H'_1 < 0$  the value  $K_1=0.01K_d$  is suitable for all  $\bar{M}^2$  and all  $\bar{H}$ , in the sense that numerical computation of  $\lambda$  indicates that then for  $0 < \bar{M}^2 < 1.7$  all values for  $\lambda$  are real and positive, while in some rare cases complex values are found with a positive real part. The boundary layer equation system (and interaction law) have consequently favourable properties for use in the transonic flow regime at cruise conditions. Because all characteristic directions generally originate from upstream, initial conditions for  $\bar{\theta}_{11}$ ,  $\bar{H}$ ,  $\bar{q}$  and  $C$  have to be

specified upstream, while downstream no initial conditions need be specified.

## 6.2 Properties of interaction law

Following Lock and Williams (Ref. 14), we consider a source strength  $S$  approximately normal to the surface, a velocity  $q$  approximately parallel to the surface, and define a perturbation potential  $\phi$  as

$$\frac{\Delta q}{q} = \phi_s, \Delta S = \phi_s. \quad (31)$$

The outer potential flow can be described by the linearized perturbation potential equation

$$(1-M^2) \phi_{ss} + \phi_{zz} = 0, \quad (32)$$

with  $\phi_s = \Delta S$  at  $z = 0$ .

In the context of the definition of an interaction law we will interpret  $\Delta q/q$  and  $\Delta S$  as corrections with respect to a starting solution, i.e.

$$\frac{\Delta q}{q} = \frac{q-q^k}{q}, \Delta S = S-S^k, \quad (33)$$

where  $q^k$  is given by the preceding outer flow computation and  $S^k$  by the preceding viscous flow calculation. A solution to (32) in subsonic flow in Fourier space is given by

$$\phi = C e^{i \nu s} e^{-\beta \nu z}, \beta = \sqrt{|1-M^2|}. \quad (34)$$

Algebraic manipulation of (31), (32) and (34), using the derivative of  $\Delta q/q$  with respect to  $s$  in order to obtain non-imaginary quantities, then leads to a law in Fourier space of the form

$$\beta \left( \frac{1}{q} \frac{\partial q}{\partial s} - \frac{1}{q^k} \frac{\partial q^k}{\partial s} \right) = \nu (S-S^k). \quad (35)$$

In physical space we may consider (35) as the leading term in an integral form of an interaction law and use it in this simplified form. In supersonic flow only the right-running wave is considered,

$$\phi = C e^{i \nu s} e^{-i \beta \nu z}. \quad (36)$$

Manipulation now yields a non-imaginary interaction law of the form

$$\beta \frac{q-q^k}{q} = - (S-S^k). \quad (37)$$

Considering eq. (37) as the leading term of an integral form of an interaction in physical space, we now have a form of interaction law that couples  $S$  to  $q$  instead of  $\partial q/\partial s$ , which cannot be incorporated in the system of boundary layer equations in a simple way. The subsonic law (35) appears however to produce useful results both in subsonic and supersonic flow, which is mainly due to the fact that strong interaction occurs in subsonic parts of the flow (at supersonic-subsonic shock waves and at trailing edges). This relaxes the need for an explicit supersonic law, also considering the findings described in section 5.1. We will therefore use eq. (35) both in supersonic and subsonic flow.

Parameters are now introduced for the direct and inverse parts of eq. (35):

$$K_d \beta \left( \frac{1}{q} \frac{\partial q}{\partial s} - \frac{1}{q^k} \frac{\partial q^k}{\partial s} \right) = \nu K_i (S-S^k). \quad (38)$$

The parameters  $K_i$  and  $K_d$  can be used to perform direct, inverse and quasi-simultaneous computations as follows:

$$\text{direct} : K_i = 0, K_d = 1, \quad (39a)$$

$$\text{inverse} : K_i = 1, K_d = 0, \quad (39b)$$

$$\text{quasi-simultaneous: } K_i > 0, K_d = 1. \quad (39c)$$

With quasi-simultaneous computations, inspection of equation (3.8) shows that the inviscid outer flow solution is modified locally at places where  $S$  differs much from the previous solution  $S^k$ . In the first few iterations between inner and outer solver this will lead to non-physical velocity distributions in the boundary layer, especially at the wake where a velocity difference will occur between upper and lower side for lifting cases, showing the deficiency of not modelling the circulation in the interaction law. The inviscid flow solver will therefore have to compute this circulation effect on its own.

Considering the two-dimensional steady form of  $S$  and using the property of mass conservation along streamlines in the outer flow, we will use in eq. (38):

$$S = \frac{\partial \delta^*}{\partial s}. \quad (40)$$

It can now be observed that with  $K_i > 0$  and  $K_d > 0$  in equation (38)  $\partial q/\partial s$  has a positive correlation with  $\partial \delta^*/\partial s$ , which is a desired property in subsonic flow.

## 7. Preliminary computational results

The MATRICS inviscid flow solver has been tested extensively and appears to be a robust method (Ref. 3, 4). In this section attention will be given to the boundary layer solver with interaction law and its robustness. Finally a fully converged solution of the whole viscous-inviscid interaction computation will be shown. Starting with an inviscid velocity distribution provided by the MATRICS outer solver, some calculations have been made to obtain a converged boundary layer solution only. Initial values for the boundary layer parameters were obtained from a two-dimensional flat plate solution. These calculations, without any interaction with the inviscid outer solver, show the changes made by the interaction law.

The first case is a NACA-0012 straight wing at a Mach number of 0.70, zero angle of attack and Reynolds number of 9 million. Only the root section of the wing will be shown, because this section is a symmetry plane with a two-dimensional flow by definition, and therefore allows comparison with two-dimensional methods. In figure 1a the inviscid velocity distribution at the root section is given. It can be shown that the trailing edge stagnation behaviour causes a severe boundary layer growth, leading to separation if no interaction law is used to adapt the velocity distribution. Figures 1b, c, d show the resulting velocity, momentum thickness and shape factor  $H$  at Reynolds number of 9 million,

calculated with interaction factor  $K_i=0.05$ . The resulting velocity distribution shows smaller decelerating velocity gradients and a less severe stagnation behaviour at the trailing edge. In order to obtain a physically relevant viscous solution, the outflow, computed from this very first boundary layer solution, can be added to the full inviscid flow solver for an adjustment of the inviscid flow to the boundary layer effect. A fully converged viscous-inviscid solution requires a number of such interactions between the inviscid flow solver and the boundary layer/interaction law computation.

The second case is the same straight wing at Mach number of 0.799, angle of attack of 2.26 degrees, and a Reynolds number of 9 million. The inviscid velocity distribution at the root section (Fig. 2a) will certainly cause separation on the upper side of the wing. Starting from a very simple flat plate momentum thickness distribution, large changes must be expected in the velocity gradients. In this case, the resulting momentum thickness at the trailing edge is much below the viscous-inviscid converged value, due to the changes in velocity distribution, while the shape factor  $H$  is only showing separation just behind the shock wave (Fig. 2b, c, d). In the viscous-inviscid converged solution separation will probably occur from shock to trailing edge (Ref. 29). The non-physical velocity jump across the wake (Fig. 2b) is due to the asymmetry of the computed flow and the simplicity of the interaction law. In the iterative process between the full inviscid flow solver and the boundary layer/interaction law, however, the errors due to the simplicity of the interaction law should disappear, resulting in a converged solution and an inactive interaction law.

Figures 3a and 3b show the convergence histories of the residuals of the x-momentum equation, entrainment equation and interaction law of the boundary layer equation system for the testcases presented in figures 1 and 2. Using the same computational parameters, both convergence histories show a robust convergence, which means that a converged solution can be computed even when the inviscid flow velocity distribution and the starting solution for the boundary layer flow do not at all fit together.

At the time of writing of the paper, work on the interaction algorithm was making good progress. A first fully converged interacting solution has been obtained for the attached flow around the NACA-0012 wing at a Mach number of 0.70, angle of attack of 1.49 degrees, and a Reynolds number of 9 million. The boundary layer is computed with an increasing part of the inviscid flow velocity in the first few iterations, while underrelaxation is applied to the source strength that is used as input to the outer solver. No boundary layer curvature effects have yet been accounted for. Using this procedure the inner and outer flow are smoothly adapted to each other.

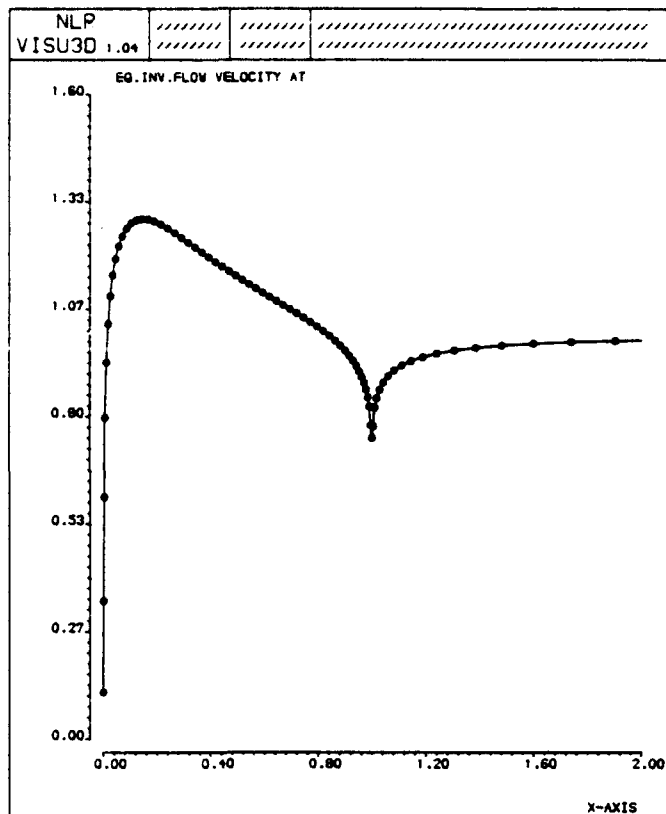
In figure 4 the initial inviscid velocity distribution (viz. without a boundary layer effect) is shown, together with the final viscous velocity distribution and the corresponding boundary layer variables. The difference between the inviscid and viscous velocity is small, except at the trailing edge, where the boundary layer displacement effect is appreciable. This testcase has been calculated with thirteen viscous-inviscid iterations in order to obtain a converged lift value. The convergence

history is shown in figure 5a. Finally, in figure 5b the convergence history of the residuals in the MATRICS outer flow solver are given as a function of the number of smoothings. A reduction in both maximum and mean value residual of 2.5 orders of magnitude has been obtained, which is promising for further development of the interaction algorithm.

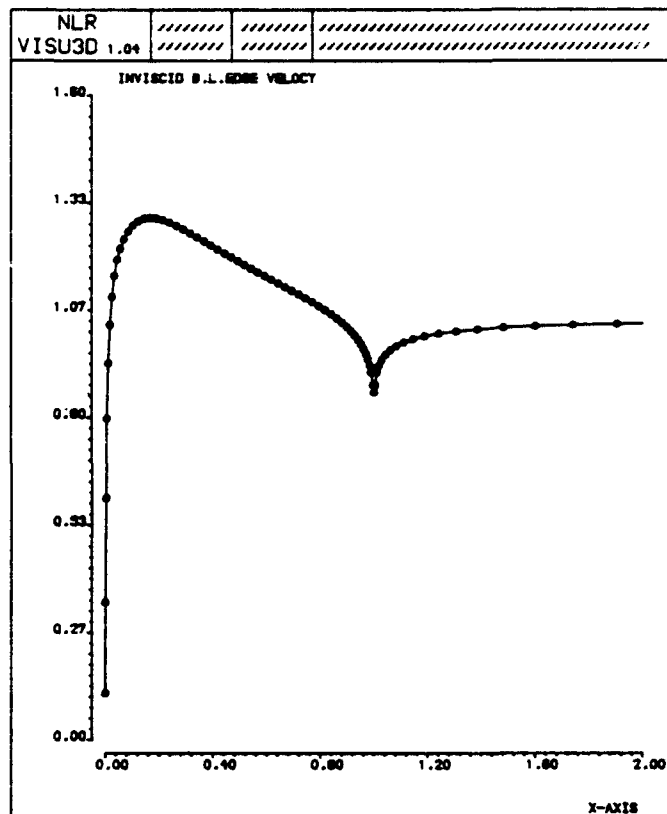
## 8. References

1. Vooren, J. van der, Wees, A.J. van der, Meelker, J.H., MATRICS, Transonic Potential Flow Calculations About Transport Aircraft. In: AGARD Conf. Proc. No. 412, 1986
2. Tysell, L.G., Hedman, S.G., Towards a General Three-Dimensional Grid Generation System. ICAS-88-4.7.4, 1988
3. Wees, A.J. van der, A Nonlinear Multigrid Method for Three-Dimensional Transonic Potential Flow. Ph. D. thesis, University of Technology Delft, The Netherlands, 1988
4. Wees, A.J. van der, Impact of Multigrid Smoothing Analysis on Three-Dimensional Potential Flow Calculations. In: Mandel, J., e.a. (eds.), Proc. 4th Copper Mountain Conf. on Multigrid Methods, SIAM Proceedings, ISBN 0-89871-248-3, 1989
5. Vooren, J. van der, Wees, A.J. van der, Inviscid Drag Prediction for Transonic Transport Wings Using a Full-Potential Method, AIAA-90-0576, January 1990 (accepted for publication in AIAA Journal)
6. Veldman, A.E.P., Lindhout, J.P.F., Boer, E. de, Somers, M.A.M., VISTRAFS, a Simulation Method for Strongly-Interacting Viscous Transonic Flow. NLR MP 88061 U, 1988
7. Houwink, R., Veldman, A.E.P., Steady and Unsteady Separated Flow Computations for Transonic Airfoils. NLR MP 84028 U, 1984
8. Dalsem, William R. van, Steger, Joseph L., Efficient Simulation of Separated Three-Dimensional Viscous Flows using the Boundary-Layer Equations, AIAA Journal Vol. 25, No. 3, 1987
9. Swafford, T.W., Whitfield, D.L., Time-Dependent Solution of Three-Dimensional Compressible Turbulent Integral Boundary-Layer Equations, AIAA Journal Vol. 23, No. 7, July 1985
10. Ashill, P.R., Wood, R.F., Weeks, D.J., An Improved, Semi-Inverse Version of the Viscous Garabedian and Korn Method (VGK), RAE Techn. Report 87002, 1987
11. Cebeci, T., Chen, L.T., Chang, K.C., Peavey, C.C., An Interactive Scheme for Three-Dimensional Transonic Flows, Proc. 3rd Symp. on Num. and Phys. Aspects of Aerodyn. Flows, pp. 11-39 - 11-49, 1985
12. Chen, L.T., Li, S., Chen, H., Calculation of Transonic Airfoil Flows by Interaction of Euler and Boundary-Layer Equations, AIAA-87-0521, 1987
13. Chow, R., Solution of Viscous Transonic Flow over Wings, Computers & Fluids Vol. 13, No. 3, pp. 285-317, 1985
14. Lock, R.C., Williams, B.R., Viscous-Inviscid Interactions in External Aerodynamics, Prog. Aerospace Sci. Vol. 24, pp. 51-171, 1987
15. Myring, D.F., An Integral Prediction Method for Threedimensional Turbulent Boundary Layers in Incompressible Flow, RAE Techn. Report 70147, 1970
16. Houwink, R., Veldman, A.E.P., Steady and Unsteady Separated Flow Computations for

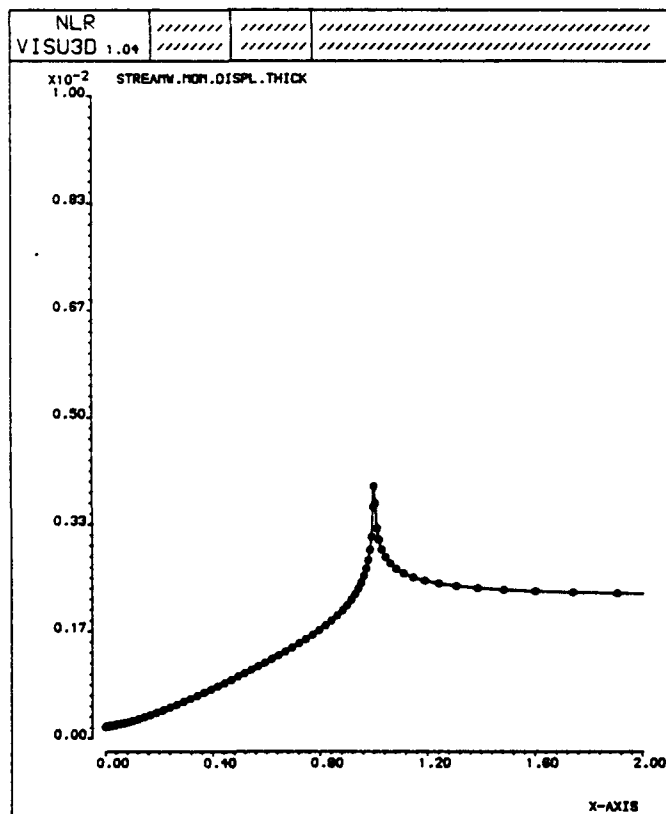
- Transonic Airfoils, AIAA-84-1618, 1984
17. Cebeci, T., Smith, A.M.O., Analysis of Turbulent Boundary Layers. Academic Press, 1974
  18. Green, J.E., Weeks, D.G., Brooman, J.W.F., Prediction of Turbulent Boundary Layers and Wakes in Compressible Flow by a Lag-Entrainment Method, ARC R&M 3791, 1973
  19. Cousteix, J., Houdeville, R., Singularities in Three-Dimensional Turbulent Boundary-Layer Calculations and Separation Phenomena, AIAA Journal, Vol. 19, No. 8, pp. 976-985, 1981
  20. Bruin, A.C. de, Boer, E. de, Users Guide of BOLA-2D, the NLR-method for the Calculation of (Quasi) Two-dimensional Boundary Layers, NLR memorandum AI-82-014 U, 1982
  21. Cross, A.G.T., Calculation of Compressible Three-Dimensional Turbulent Boundary layers with Particular Reference to Wings and Bodies, YAD Note 3379, November 1979
  22. Hartwich, P.M., Split Coefficient Matrix (SCM) Method with Floating Shock Fitting for Transonic Airfoils. Proc. Int. Conf. on Num. Meth. in Fluid dynamics, Oxford, July 1990
  23. Spekrijse, S., Multigrid Solution of Monotone Second-order Discretizations of Hyperbolic Conservation Laws, Math. Comp. Vol. 49, No. 179, pp. 135-155, July 1987
  24. Steger, J.L., Warming, R.F., Flux Vector Splitting of the Inviscid Gasdynamic Equations With Application to Finite Difference Methods, NASA-TM-78605, 1979
  25. Yee, H.C., Upwind and Symmetric Shock-Capturing Schemes, NASA-TM-89464, 1987
  26. Veldman, A.E.P., A new Quasi-Simultaneous Method to Calculate Interacting Boundary Layers. AIAA J, Vol. 19, pp. 79-85, 1981
  27. Williams, B.R., Coupling Procedures for Viscous-Inviscid Interaction in External Aerodynamics. In: Proc. 4th Symp. on Num. and Phys. Aspects of Aerodyn. Flows, Long Beach, CA, January 1989
  28. Cebeci, T., Clark, R.W., Chang, K.C., Halsey, N.D., Lee, K., Airfoils with Separation and the Resulting Wakes, Proc. 3rd Symp. on Num. and Phys. Aspects of Aerodyn. Flows, pp. 2-13 - 2-26, 1985
  29. Holst, T.L., Viscous Transonic Airfoil Workshop Compendium of Results. AIAA-87-1460, 1987



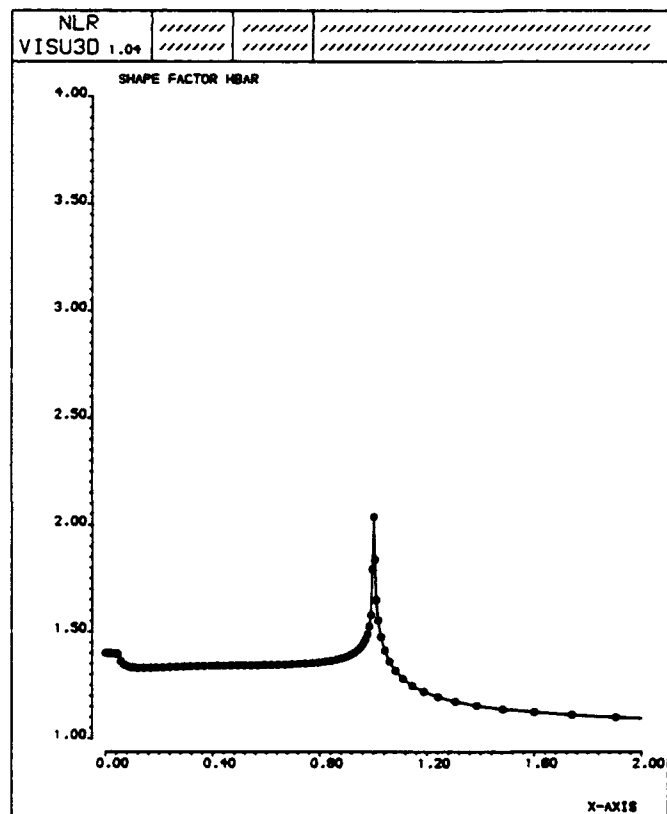
a) Inviscid flow velocity distribution



b) Boundary layer inviscid edge velocity

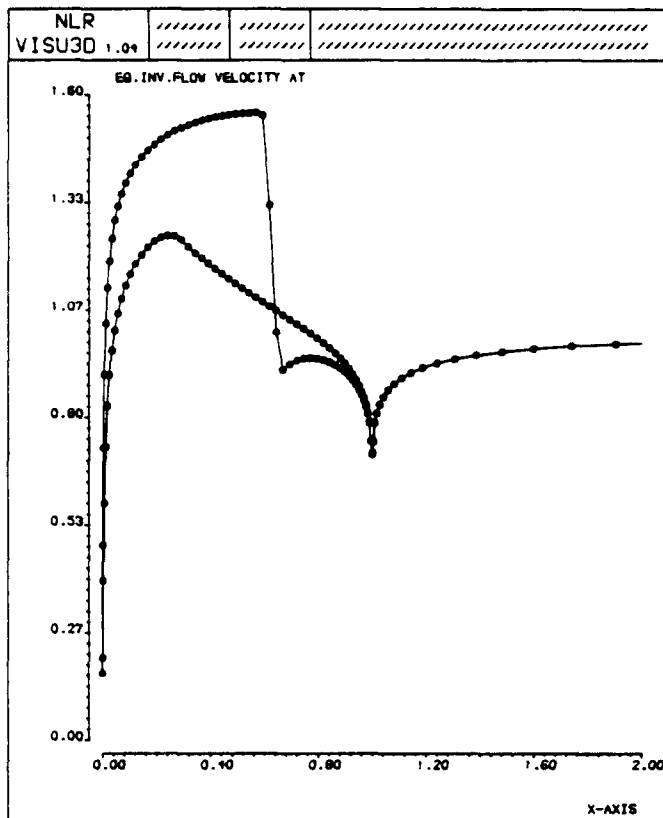


c) Boundary layer streamwise momentum thickness

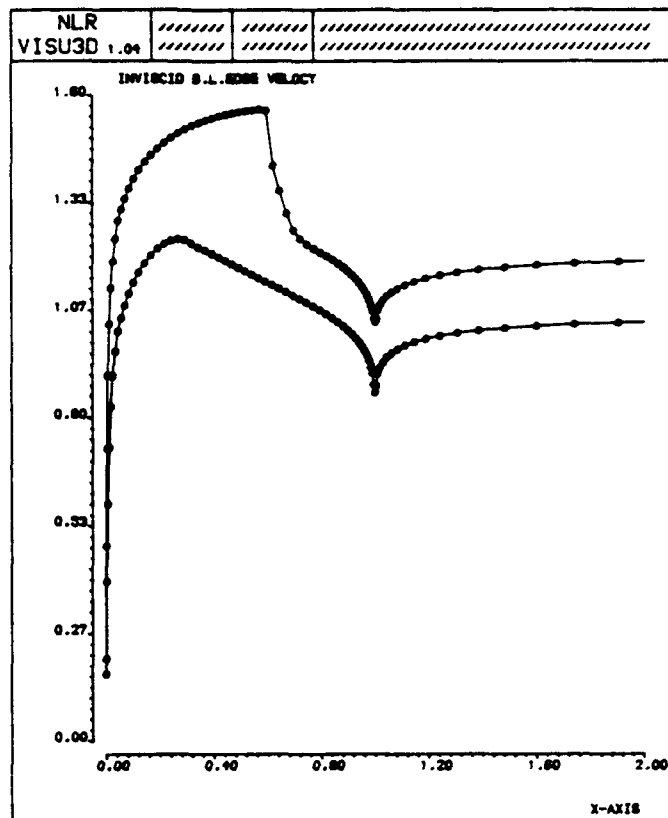


d) Boundary layer shape factor  $\bar{H}$

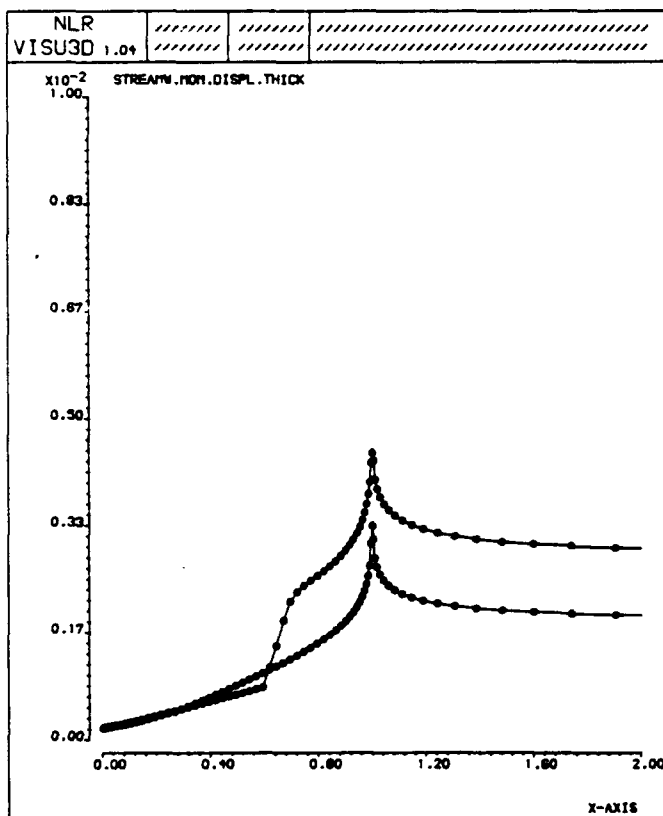
Fig. 1 Boundary layer results for root section of a NACA-0012 straight wing at  $M_\infty = 0.70$ ,  $\alpha = 0$ ,  $Re = 9 \times 10^6$



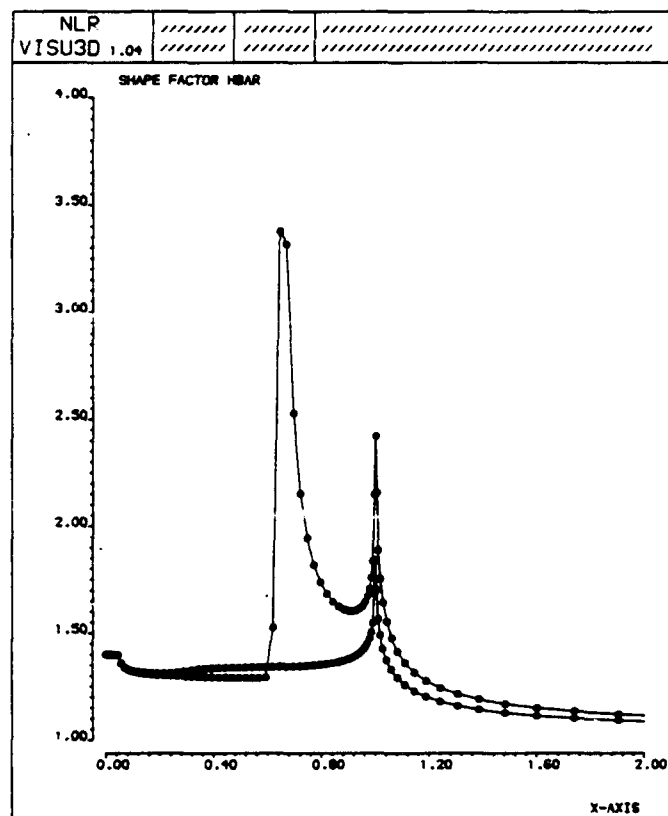
a) Inviscid flow velocity distribution



b) Boundary layer inviscid edge velocity

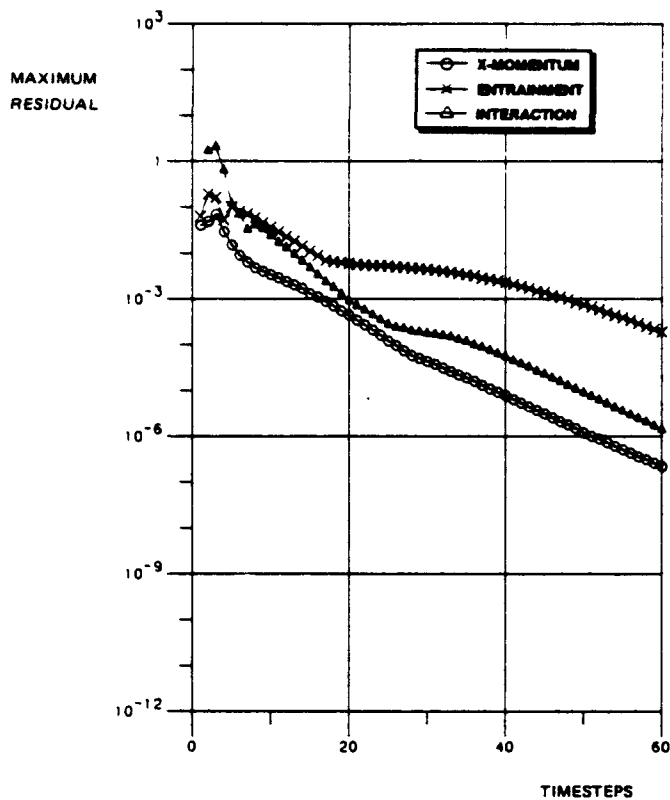


c) Boundary layer streamwise momentum thickness

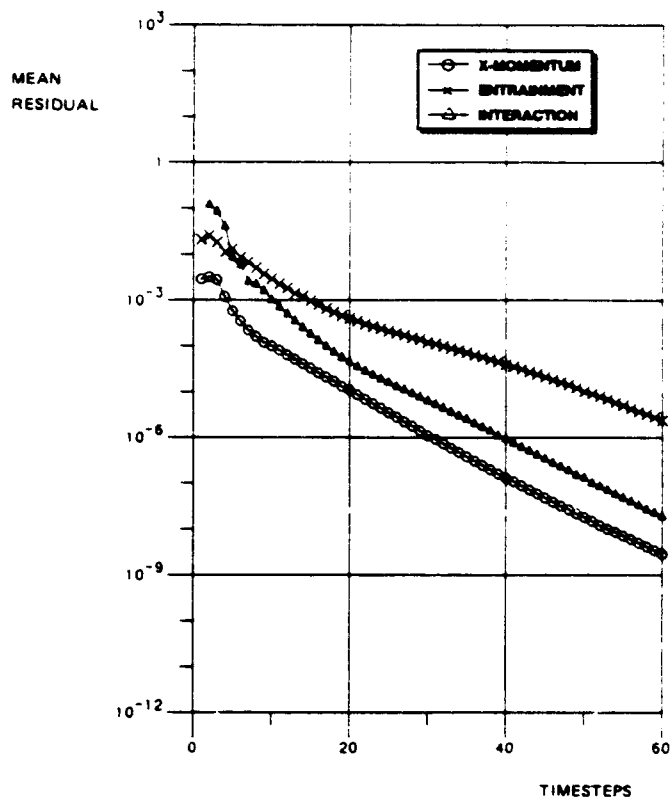


d) Boundary layer shape factor  $\bar{H}$

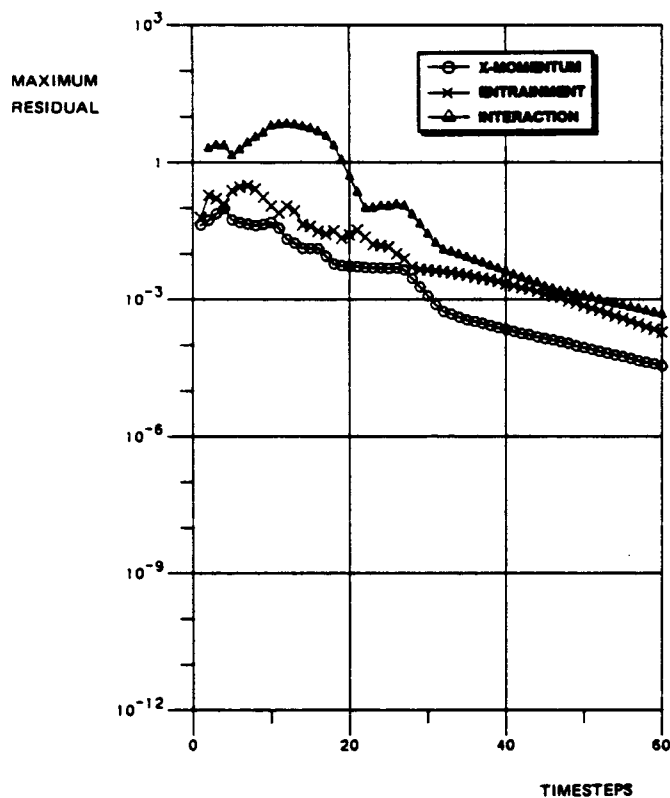
Fig. 2 Boundary layer results for root section of a NACA-0012 straight wing at  $M_\infty = 0.799$ ,  $\alpha = 2.26^\circ$ ,  $Re = 9 \times 10^6$



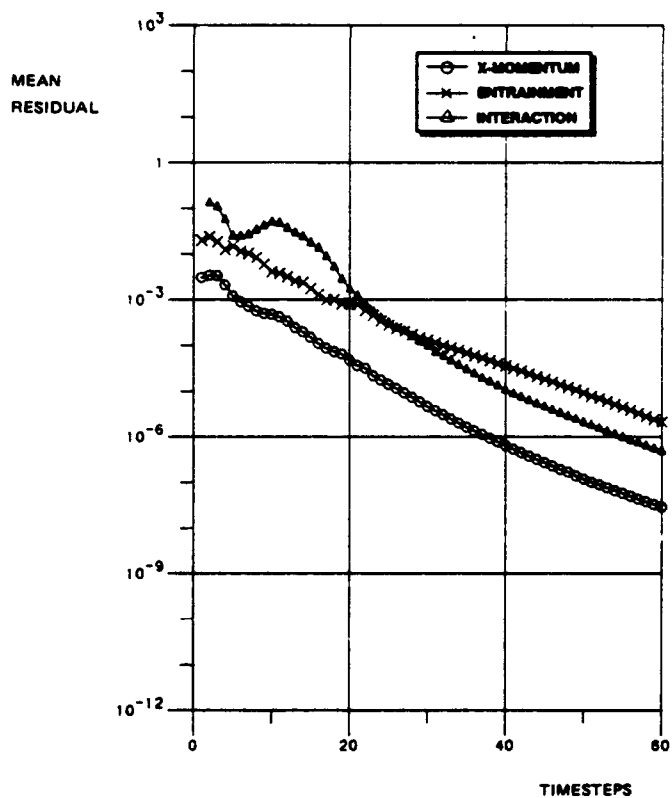
a) Maximum residual vs. timesteps  
 $M_\infty = 0.70$ ,  $\alpha = 0$ ,  $Re = 9 \times 10^6$



b) Mean residual vs. timesteps  
 $M_\infty = 0.70$ ,  $\alpha = 0$ ,  $Re = 9 \times 10^6$

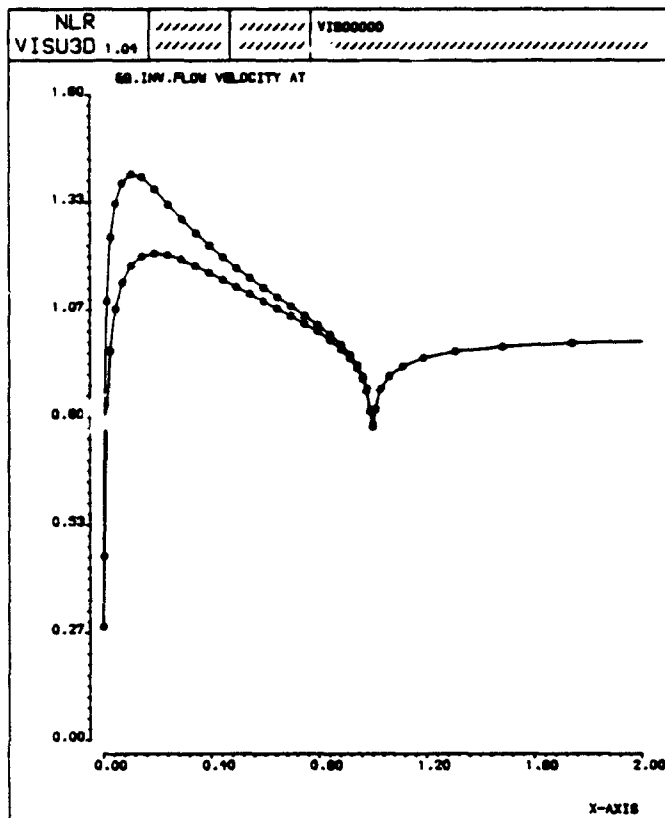


c) Maximum residual vs. timesteps  
 $M_\infty = 0.799$ ,  $\alpha = 2.26$ ,  $Re = 9 \times 10^6$

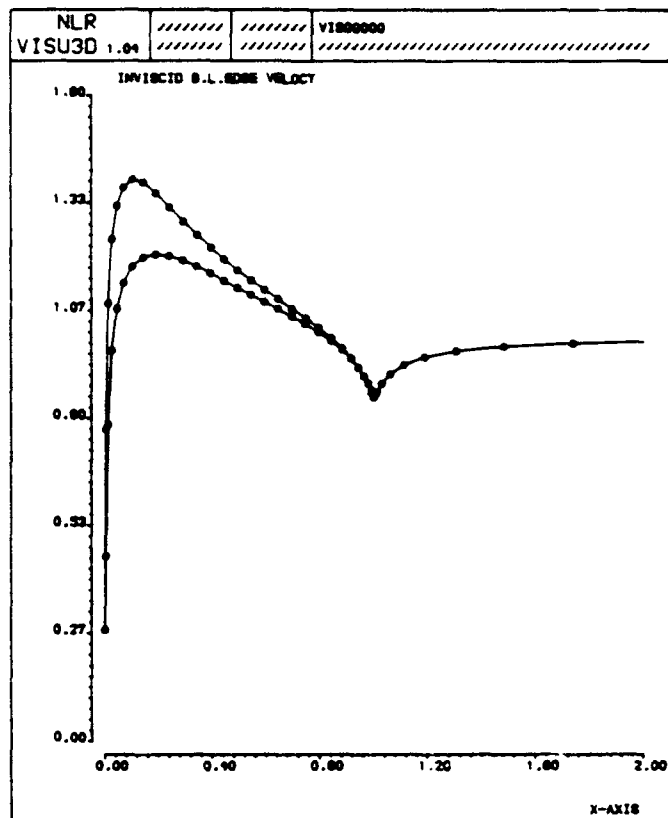


d) Mean residual vs. timesteps  
 $M_\infty = 0.799$ ,  $\alpha = 2.26$ ,  $Re = 9 \times 10^6$

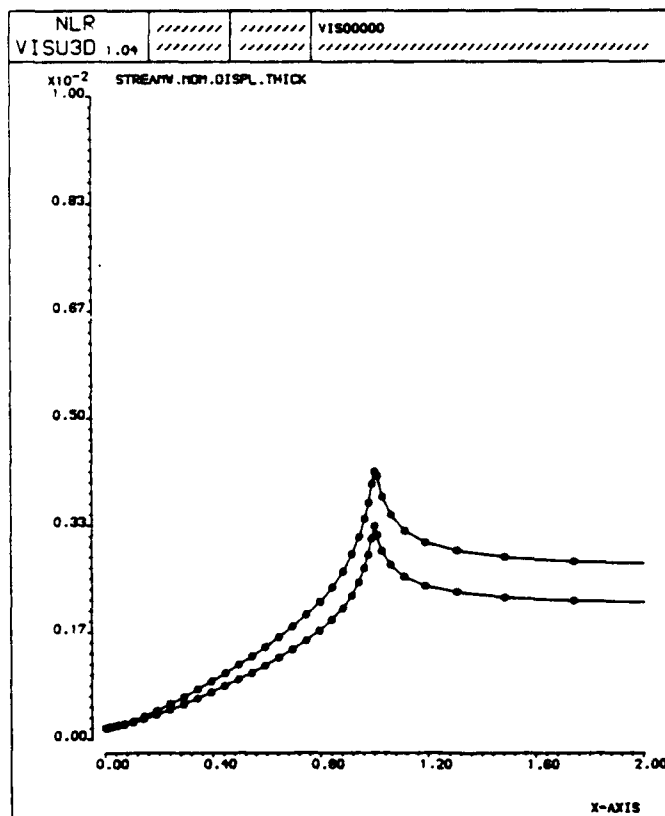
Fig. 3 Convergence histories for boundary layer computation on a NACA-0012 straight wing



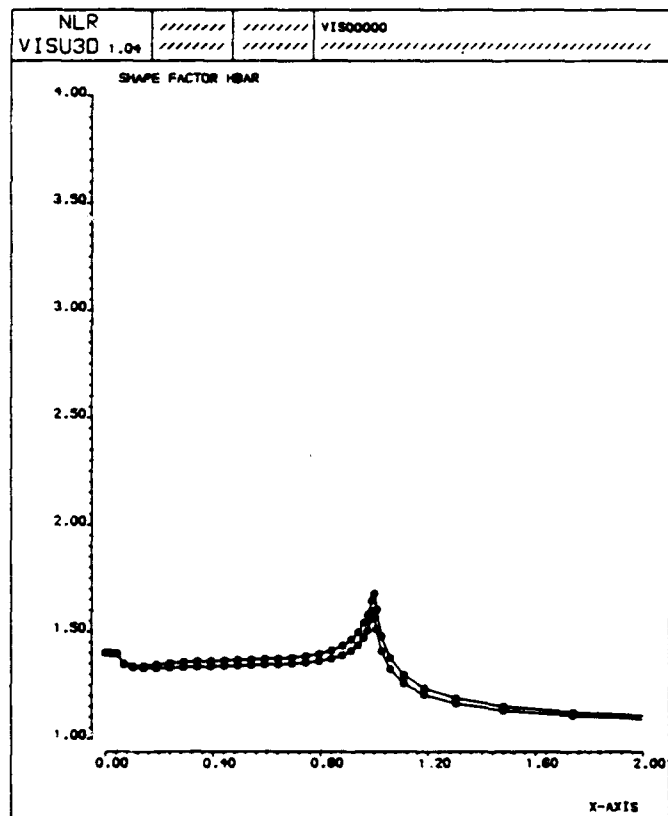
a) Inviscid flow velocity distribution



b) Viscous flow velocity distribution



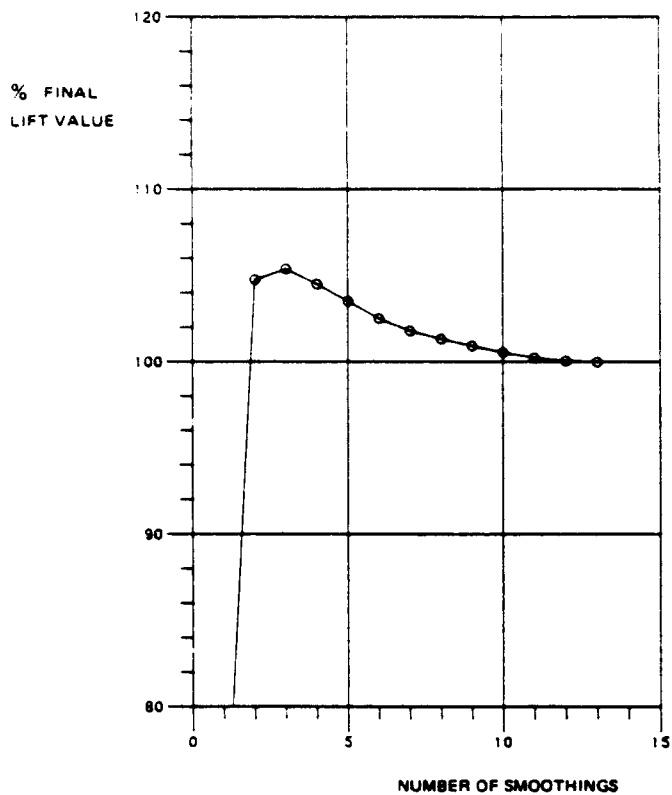
c) Boundary layer streamwise momentum thickness



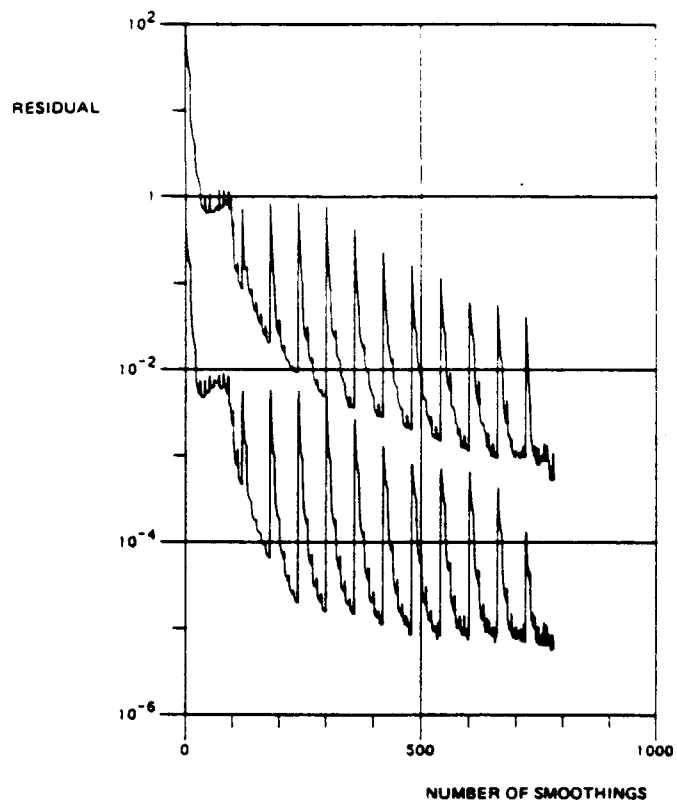
d) Boundary layer shape factor  $\bar{H}$

Fig. 4 Viscous-inviscid interaction results for root section of a NACA-0012 straight wing at  $M_\infty = 0.70$ ,  $\alpha = 1.49$ ,  $Re = 9 \times 10^6$





a) Lift coefficient of wing



b) Maximum and mean residual

Fig. 5 Convergence histories for viscous-inviscid interaction computation on a NACA-0012 straight wing at  $M_\infty = 0.70$ ,  $\alpha = 1.49$ ,  $Re = 9 \cdot 10^6$

**TWO- AND THREE-DIMENSIONAL FLOWS, 4**  
**SESSION 12**



SHIP VISCOUS FLOW  
A REPORT ON THE 1990 SSPA-CTH-IIHR Workshop

Virendra C. Patel  
Iowa Institute of Hydraulic Research  
Iowa City, Iowa

Lars Larsson  
Chalmers University of Technology and  
FLOWTECH International AB  
Gothenburg, Sweden

**Abstract**

To assess the state of the art in ship viscous flow computation a Workshop was organized in 1990 by three organizations: SSPA Maritime Consulting AB, Chalmers University of Technology and Iowa Institute of Hydraulic Research. Two test cases were specified by the organizers and sent out to all interested research groups, which were asked to submit results in a prescribed format. In September 1990 a meeting was held at Chalmers University of Technology. All results had then been collected and presented in a common format, and the theories behind the methods compiled in a table based on responses to a questionnaire sent out earlier. During the meeting, each research group was first given the opportunity to briefly introduce their method and results. Thereafter, a considerable time was spent on general discussions on the performance of the different methods considering the differences in the underlying theories. Specific items that were addressed were grid generation, governing equations, boundary conditions, turbulence modelling and numerical method. Practical aspects on the results, for instance from the point of view of propeller design, were also discussed. The Workshop Proceedings contain a description of the participating methods and the results of both test cases. In the present paper a summary of the Workshop and its results is presented.

**Introduction**

Although viscosity is present in the entire flow around a ship it has a significant effect only in the boundary layer around the ship and the wake behind it. The present paper deals with the flow in these two regions, which are limited in size, but very important from at least two points of view. Frictional forces within the boundary layer give rise to a viscous resistance of the ship, in most cases the dominant resistance component, and the velocity distribution in the near wake determines the design and performance of the propeller.

Despite its obvious importance the first serious attempts to compute the viscous flow were made relatively recently, about twenty years ago. This is in contrast to the long term research in the inviscid flow area, where wave resistance research has been under way during the entire twentieth century. The reason for the difference

is that the complicated viscous flow equations, i.e. the Navier-Stokes equations and approximations thereof, are less amenable to analytical treatment than the inviscid equations, normally based on potential flow theory. Therefore it was not until computers had become powerful enough to handle three-dimensional boundary layer theory numerically that research on viscous flow computations was started.

During the 1970's a number of methods for predicting ship boundary layers were developed, and in 1980 it was considered appropriate to assess the state of the art in this area. To accomplish this, an international Workshop on ship boundary layers was organized by SSPA, the Swedish State Shipbuilding Experimental Tank, in cooperation with the International Towing Tank Conference, ITTC<sup>1</sup>. The purpose was to bring together specialists on ship boundary layer calculations from all over the world, and to let them apply their techniques and methods to two test cases, specified in detail by the organizers. In June of 1980 a meeting was held in Gothenburg. The results of 17 methods had then been collected and presented in a uniform format. During the meeting the various components of the methods were discussed in the light of the results produced. The general finding was that most methods were able to predict the thin boundary layer over the major part of the hull with an accuracy sufficient for engineering purposes, while all of the methods failed completely in predicting the flow near the stern and in the wake.

In the 1980's development accelerated, and the focus was changed from the thin boundary layer to the stern/wake flow. As evidenced by the 1980 Workshop a new class of methods with less restrictive approximations was required. The interest of researchers was soon focused on the Reynolds Averaged Navier-Stokes (RANS) equations, and a number of such methods was proposed during the 1980's. Towards the end of the decade it was considered timely to organize a second Workshop to investigate the progress made. This task was undertaken by three organizations: SSPA Maritime Consulting and Chalmers University of Technology (CTH) in Sweden and Iowa Institute of Hydraulic Research (IIHR) in the USA.

As in the first Workshop, the purpose of the new event was twofold:

- o to assess the state of the art in ship viscous flow calculations
- o to analyze the results of the different methods in light of the underlying theories, thereby obtaining information on the most promising ways to achieve further improvement

The 1980 Workshop had been successful in achieving these goals, so the new Workshop was organized in a similar way. Two test cases were selected. The so-called HSVA tanker<sup>2</sup> was again chosen, as being the best documented test case available, see for instance Hoffmann<sup>3</sup> and Wieghardt and Kux<sup>4</sup>. Even though measurement data have been obtained only at model Reynolds numbers, the participants were asked, as an optional exercise, to carry out calculations also for a full scale Reynolds number. This was to shed some light on the difficulties encountered at this larger scale, for which calculations have been very rare, so far. The second test case was designed to produce a significantly different stern flow with a minimum change of geometry. More information about the design philosophy is given in the next section. A very important feature of the second case (the "Mystery case") was that no measurement data were available when the calculations were carried out.

As in the first Workshop, attention was confined to double models, in which wave effects are absent and the free surface may be considered as a plane of symmetry. Also, only the flow on the bare hull, without appendages and propulsors, was considered.

The first announcement of the "1990 SSPA-CTH-IIHR Workshop on Ship Viscous Flow" was distributed in late 1988, together with a questionnaire to be returned by 15 May 1989 by all researchers interested in taking part in the Workshop calculations. Efforts were made to invite participation by originators of commercial CFD codes. No less than 21 computers indicated their interest in participating, and in August the data and instructions for the first test case were sent out. Similar information for the second case was distributed in December. In the early summer of 1990 results from 19 methods had been received, and the difficult task of condensing all the information into a uniform format was started at CTH. By the time of the Workshop meeting, which was held at CTH 12-14 September 1990, all results had been plotted in a way such that comparison between the different methods could be easily made. Further, the replies to the questionnaire had been compiled at IIHR and condensed into a table, useful for quick reference to the theory behind each method.

In the present paper a brief summary of the Workshop is given. The two test cases are described next, followed by an overview of the methods. Thereafter, some important results are discussed and finally some conclusions are drawn. For a full ac-

count of the Workshop, reference should be made to the Proceedings<sup>5</sup>.

### Test cases

#### HSVA Tanker, Case I

A body plan of the first test case, the HSVA tanker is shown in Fig. 1. The boundary layer measurements by Hoffmann<sup>3</sup>, and the subsequent stern-flow measurements by Wieghardt, Kux and Knaack<sup>4</sup>, were made on a double model of this hull in a 1.2 m diameter, slotted-wall wind tunnel, in which the turbulence level was of the order of 1 percent. Different types of pressure probes were used. The model was supported in the tunnel by means of wires and a sting at the stern. The nominal length of the model was 2.74 m but for reference length we have used the length between perpendiculars,  $L = 2.664$  m, which gives a Reynolds number of  $5 \cdot 10^6$ . Neither the tunnel nor the support were modeled by any of the computers.

#### Mystery hull, Case II

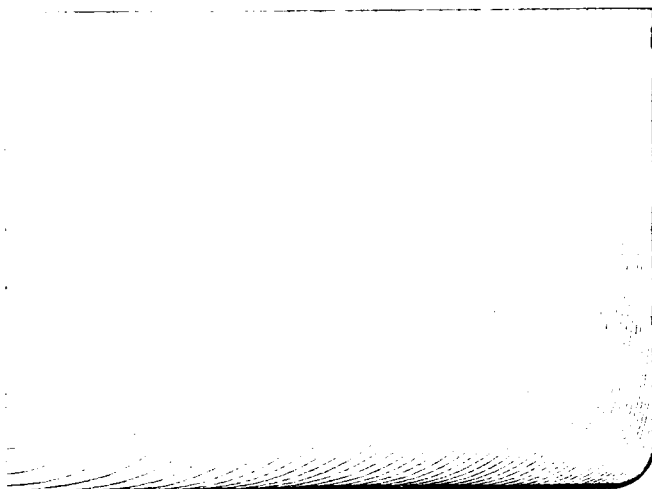
The second test case, for which no measured data were available by the time of the meeting, was designed by Prof G. Dyne at Chalmers and Mr L.G. Jonsson at SSPA. The purpose was to create a significantly different wake pattern with a minimum of geometry change as compared to the first case. Thus, only the stern sections were modified. By making them more U-shaped stronger longitudinal vortices could be expected behind the hull, creating a more distorted wake field, see Dyne<sup>6</sup>. A body plan is shown in Fig. 2.

Velocity measurements using Laser-Doppler Velocimetry were carried out at the University of Hamburg after the Workshop<sup>7</sup>, but the results are analyzed and included in the Proceedings<sup>5</sup>.

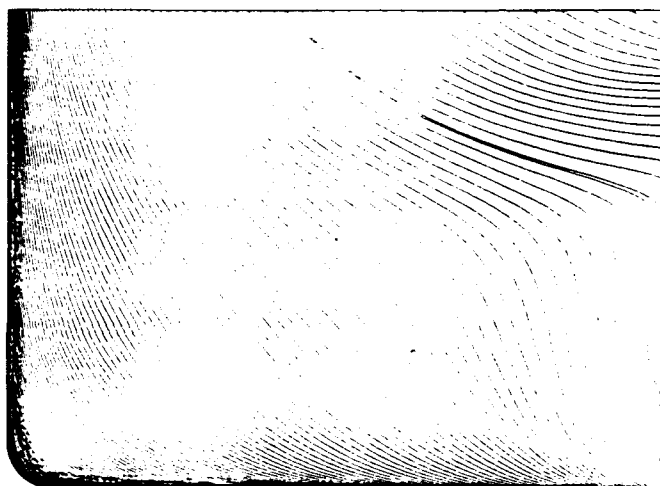
### Overview of methods

Some 19 organizations from 12 countries participated in the Workshop. A summary of the important characteristics of the methods is presented in Table 1 (at the end of the paper). This table was prepared on the basis of information supplied by the participants in a questionnaire that was distributed at the beginning and again at the end of the Workshop. Effort was made to obtain as much and as accurate information as possible on each method. The following is a review of some of the similarities and differences among the methods.

The overall strategy summarized in item A indicates that 12 participants restricted their calculations to the stern and wake flow (S) while 7 treated the complete hull (H), including the bow. Both global (G) and zonal (Z) methods are represented but the most common combination is a global method applied to the stern flow (S,G). The 5 zonal approaches employ an inviscid-flow method. In three of these,

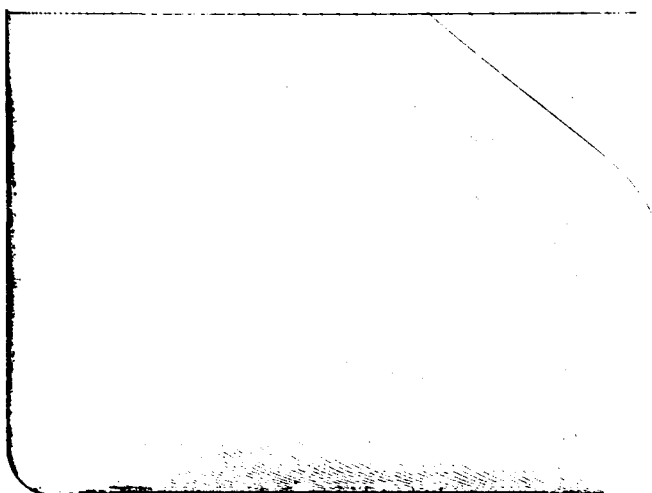


Forebody



Afterbody

# 1. Body plan, HSVA Tanker



# 2. Body plan, Mystery Hull (Forebody as HSVA Tanker)

the viscous and inviscid solutions are matched at a specified boundary outside the viscous layer. One participant group (CT) made both global and zonal calculations. However, only the results from their global calculations are presented here. It is significant to note that none of the zonal approaches performed iterations between the viscous and inviscid flows to allow for interaction although in some cases the match boundary between the two zones was placed rather close to the hull.

Section B of Table 1 summarizes the equations and variables. One method employs integral equations and therefore provides a link to the earlier ship boundary layer Workshop<sup>1</sup>. It is clear that much of the information sought through the questionnaire is not relevant to the integral approach and therefore there are very few entries for that method. Among the differential methods, a vast majority solves the Reynolds-Averaged Navier-Stokes equations, while four adopt reduced forms (P, Ra) of these equations. One method uses large-eddy simulation along with a subgrid turbulence model. In all cases, the equations are solved in the so-called primitive variables, i.e., velocity and pressure. Thus, for example, methods that use vorticity or stream functions are not represented. There is a great deal of variability in the choice of the velocity components, ranging from simple, orthogonal ones to covariant components and grid-oriented nonorthogonal components. This choice impacts on the complexity of the codes and storage requirements for the geometrical quantities associated with the grid. Most methods employ nonorthogonal coordinates in all planes, but a few retain orthogonality in one (usually transverse) plane. This particular feature is related to the manner in which the grid is generated.

With the exception of the integral approach, all methods require a model for turbulence. These are summarized in section C. It is seen that 4 methods use algebraic models of eddy viscosity or mixing length (AL) and 13 employ the k- $\epsilon$  model. The large-eddy simulation method uses the Smagorinsky eddy-viscosity model along with the van Driest damping function for the subgrid scales. Of the 4 methods that employ algebraic, zero-equation models, three use the Baldwin-Lomax model and one (H) uses the mixing-length model. As far as can be ascertained, all users of the two-equation k- $\epsilon$  model retain the same constants, ( $C_\mu$ ,  $C_{\mu 1}$ ,  $C_{\mu 2}$ ,  $G_k$ ,  $G_\epsilon$ ) = (0.09, 1.44, 1.92, 1.0, 1.3). In two cases (HC, PV), however, the basic k- $\epsilon$  model is combined with a one-equation model for the near-wall region, while others employ the wall function approach. These two, and the methods employing algebraic models, integrate the flow equations up to the wall, where the no-slip condition is applied. This approach requires many more grid points in the near-wall region to resolve the large gradients of velocity and eddy viscosity. Methods using the wall-function approach,

On the other hand, satisfy the law of the wall and related conditions at one or more grid points away from the wall, and do not explicitly solve the flow equations in the near-wall layer.

Section D of Table 1 provides an overview of the boundary and initial conditions employed in the various calculations. As all methods approach the solution either by a time marching or an iterative process, all require initial conditions (time = 0). In this respect, three methods start the solution from rest, 7 use uniform flow, one uses boundary layer solutions, another uses a potential flow solution, while 5 indicate some other procedure. Among the last category are methods in which a parabolic march is made through the solution domain with an assumed initial pressure field. There is also considerable variation among methods in the quantities that are determined or prescribed at the start of the calculations. The initial conditions presumably influence the number of iterations or time steps required to obtain the steady state solutions that are sought.

The upstream boundary conditions depend upon whether the solution is obtained for the entire hull or only the stern and wake flow. In the case of the calculations for the entire hull, two types of treatment have been made. In five of the seven such calculations, the upstream boundary is placed about one-half ship length ahead of the bow, and quite simple boundary conditions are prescribed in the uniform flow there. In the remaining two (IL and Ka0), the boundary layer over the bow is calculated. It appears that none of these calculations takes any account of the initial region of laminar flow or of the transition that was provoked artificially in the experiments. In the 12 calculations that were restricted to the stern and wake flow, there are differences in the location where the calculations were started as well as in the parameters that are prescribed. Three participants started the calculations at a check station,  $X/L = 0.646$ , where the integral parameters of the boundary layer were supplied from experiment. (The X-axis is along the hull, with the origin at the bow.) Others started the calculations somewhat ahead of this section, using, in some cases, the data at the check station as a guide. In all such calculations, however, the detailed velocity and turbulence parameter distributions required by the methods had to be generated by the participants. In this regard, most appear to have used two-dimensional boundary layer correlations, with the three dimensionality neglected. In one case (PJL), however, a special updating scheme was devised to obtain a set of initial conditions that is consistent with the equations being solved. The differences in the initial conditions are likely to be observed most clearly in the results at the check station.

There is also considerable variation in the location of the downstream boundary

where the solutions terminate, and the conditions applied at that boundary. In most cases the solutions are taken far enough from the stern to assume a negligible upstream influence and for the parabolic or extrapolated conditions to be valid.

The boundary conditions at the hull surface were discussed above in connection with the turbulence model. For completeness, however, we note that the no-slip conditions are applied explicitly in some methods whereas they are satisfied indirectly in methods that rely on the wall-functions approach.

All of the calculations presented at the Workshop have exploited the geometric symmetry about the ship centerplane and calculated only one half of the hull. Also, all participants assumed a double body and applied symmetry conditions along the water plane.

The location of the solution boundary in the "farfield" some distance from the ship axis, and the conditions specified along that boundary, also show considerable differences. With respect to the location, the five zonal calculations performed with viscous and inviscid methods use a boundary that varies from 0.08 of a ship length in one case (H) to 0.7 in another (Ka0). Recall that this is the boundary at which the two solutions are matched and, as noted earlier, none of the calculations accounted for the interactions between the two regions. In these zonal calculations, the inviscid solutions provided the boundary conditions for the viscous solutions. In the remaining, global approaches, the location of the farfield boundary ranged from 0.1 of a ship length (T) to 1.5 (HC) with many using a value of one ship length. However, those who have used boundaries rather close to the hull (SZC and T) have provided boundary conditions from inviscid flow. In this respect, these methods, characterized as global by their originators, could also be regarded as zonal. Methods that have placed the boundary at larger distances from the hull have tended to prescribe uniform-flow conditions in the far field. Some differences are observed, however, in these cases in the particular variables or conditions that are specified or satisfied; see, for example, codes C and A in the table.

Section E of Table 1 pertains to the generation and control of the numerical grid. For the Workshop calculations, all participants employed a single block grid although one (GCHM) indicated that their method can accommodate a multi-block grid. Fully nonorthogonal grids as well as grids that are orthogonal in some planes (typically in the transverse sections) or at boundaries (usually at the hull) are represented in the calculations. The most popular method for generating the grid appears to be numerical, although some participants have employed analytic and algebraic methods, and even combinations of methods.

Among the numerical approaches, elliptic methods for the entire three-dimensional solution domain are the most common. Several methods use post-generation smoothing of the grid. Control of the grid is exercised most commonly from the boundaries although some indicate that it is done from inside the solution domain.

The numerical features of the various methods are summarized in section F. First of all, we note that there is no participation from the finite-element community and therefore items in the questionnaire that were designed specifically to obtain information on such methods are deleted in the table. Of the methods represented at the Workshop, there are four finite-difference methods, 10 finite-volume methods, and, for lack of a better term, four are classified as mixed methods. To these must be added the one based on integral equations which are also solved by finite-difference methods. It should be pointed out that not all of the methods in each of these categories are generically different. In other words, there are groups of methods in each class which share a great deal in common and, from a numerical perspective, may be classified as a single method. Be that as it may, we shall note the most significant features of the methods represented here.

First, discretization in both staggered and regular (colocated) grids is used in finite-difference as well as finite-volume methods. There is some correlation between the type of grid used and the method employed to solve for the pressure (or establish the pressure-velocity coupling) for this incompressible flow. Differencing of the convective terms is made by a variety of means, including upwinding, central differences, hybrid combinations and use of analytic solutions (FA). The responses to the questions on formal order of accuracy and formally conserved quantities are rather surprising. Most methods claim first or second-order accuracy but two consider their methods to be accurate up to the third order. The response to the second question seems to be correlated with the equations that are solved rather than any formal attempt in the methods to conserve mass, momentum, and total energy.

For the pressure, four methods use fully-coupled solutions. Two of these (GCHM and K) employ artificial compressibility, one (AS) uses a discretized continuity equation, another (H) uses the normal momentum equation. Most of the remaining methods employ segregated pressure-velocity coupling algorithms, SIMPLE being the most common.

In the execution of the solutions, most methods employ iterative techniques with under-relaxation or variable time steps. Explicit as well as implicit methods are represented. The solutions of the discretized algebraic equations are obtained using different tactics, including point substitution, line substitution, LU decomposition of matrices, and ADI methods.

Section G of Table 1 concerns the computations performed by the participants. As the two test cases are not substantially different with respect to the computational effort involved, the numbers in this section are typical of both cases. First of all, it is quite significant that calculations have been performed not only on state-of-the-art supercomputers (designated by S) but also on smaller machines (designated by M), such as workstations. The total number of grid points employed shows a great deal of variation, ranging from a low of 8,000 to a high of 253,000. It is interesting to note that the higher numbers are not necessarily correlated with the use of supercomputers, nor are they correlated with the use of near-wall turbulence models or calculations made for the entire hull including the bow.

The number of time steps or iterations performed to obtain the solutions presented here varied widely, ranging from only 40 (BZLS and SZC) to 20,000 (ZM), although, in the latter case, the large-eddy simulation should never realize a steady state as defined for the other methods. It should be noted that a variety of convergence criteria were adopted to declare that a steady state had been obtained. The storage requirements and computer run times also varied over very wide limits. This is not surprising in view of the differences in the number of grid points and machines employed, but it is interesting to note that run times ranging from several hours to 5 days were reported by users of the smaller machines. The differences in the machines are also reflected in the cpu time per iteration per grid point. The fastest times were of course reported by users of supercomputers.

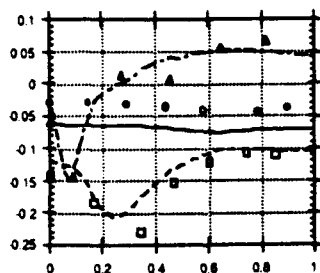
## Results and Discussion

Results were requested from the participants at a Reynolds number of  $5 \cdot 10^6$  for both hulls. As an optional exercise the computers were also asked to submit full scale results corresponding to a Reynolds number of  $2 \cdot 10^9$  for case I. All but one delivered the model scale predictions but only three had computed the high Reynolds number case.

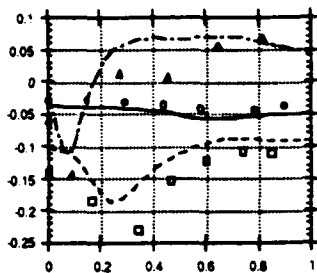
Pressure and friction distributions were reported at the waterline and keel and along three section girths on the hull, while velocity distributions in the form of iso-velocity contours and, in some cases, cross-flow vectors were given at four sections. For the most interesting section, the propeller plane, the pressure and (if computed) the turbulent kinetic energy were also reported.

The complete results may be found in the Proceedings<sup>5</sup>, but in the present paper only a few representative examples will be given. These include the pressure distribution along three section girths and the velocity distribution (iso-velocities and

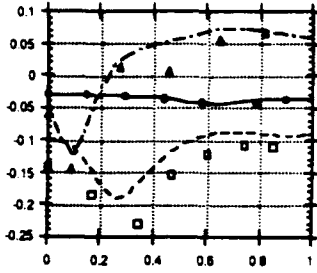
Abdallah &amp; Sotiropoulos



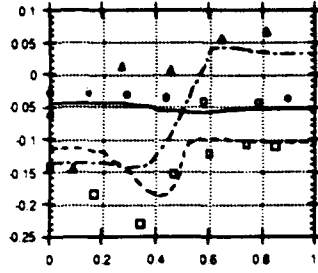
Broberg, Zhang, Larsson &amp; Schöön



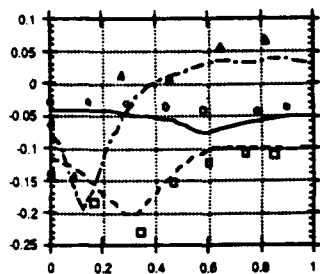
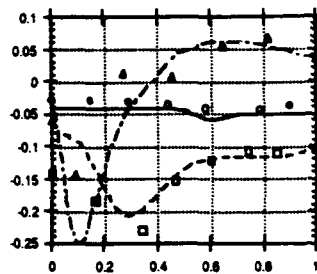
## Bull, Watson & Musker



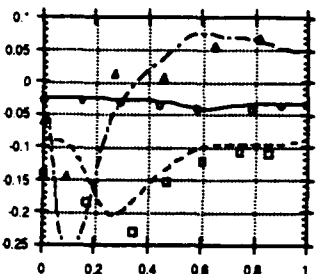
Caprino &amp; Traverso



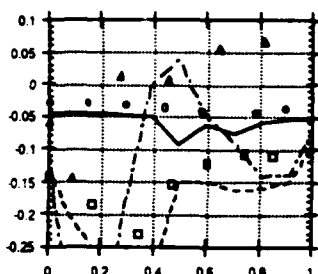
**Gorski, Coleman, Hausling & Miller**

**Hoekstra**

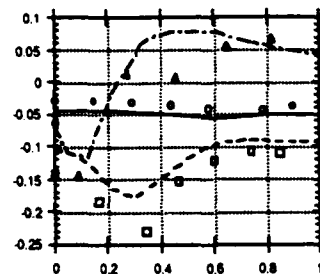
Hoffman &amp; Chan



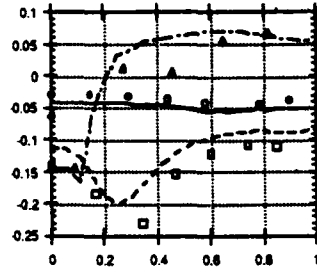
Ikehata &amp; Liu



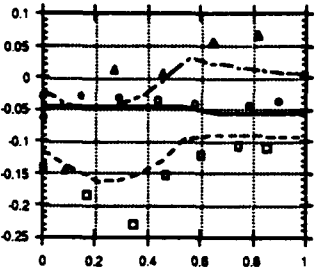
Kang &amp; Oh



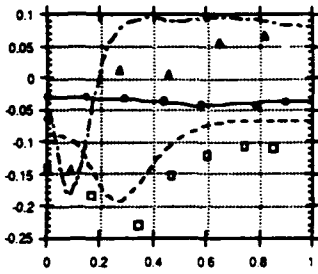
**Kodama**



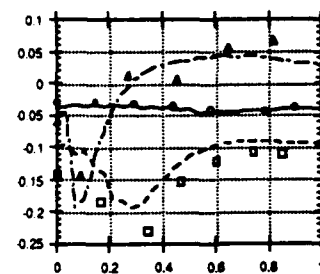
Kanevsky &amp; Orlov



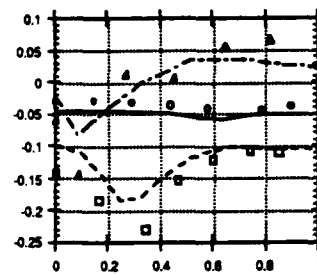
Majumdar, Zhu &amp; Rodi



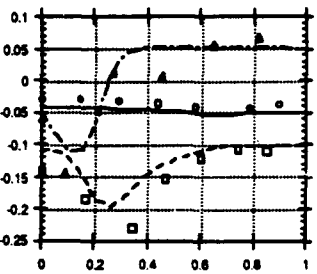
Masuko, Shirosé &amp; Abe



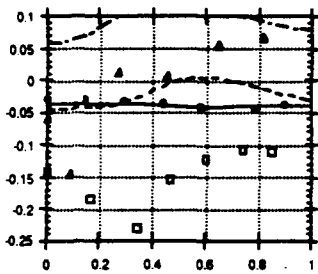
Patel, Ju &amp; Low



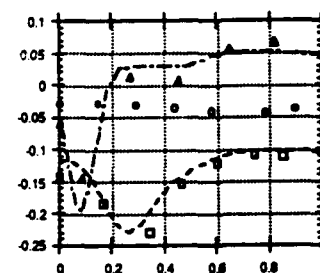
**Piquet & Visonneau**



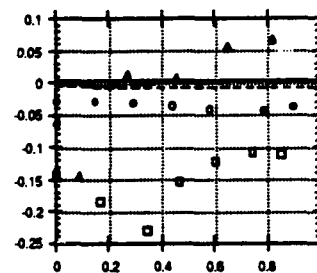
Shen, Zhang &amp; Cai



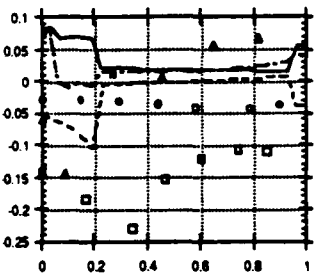
## Tzabiras



Zhou &amp; Gao



Zhu &amp; Miyata



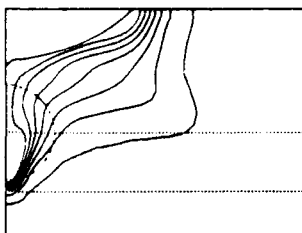
**Legend:**

exp	calc	
○	—	$c_p$ at $x/L=0.646$
□	- - -	$c_p$ at $x/L=0.875$
△	- -	$c_p$ at $x/L=0.942$

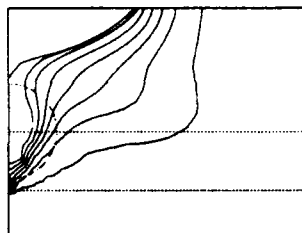
### 3. Pressure distribution at three sections



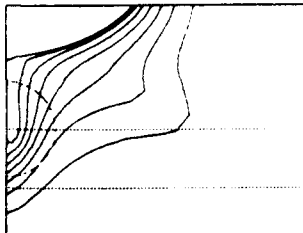
Abdallah & Sotiropoulos



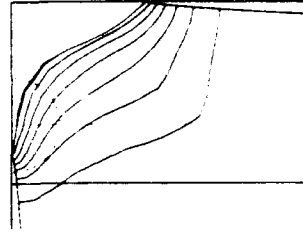
Broberg, Zhang, Larsson & Schön



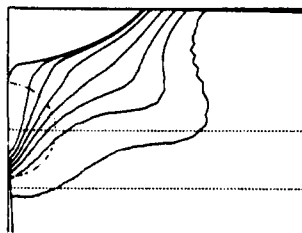
Bull, Watson & Musker



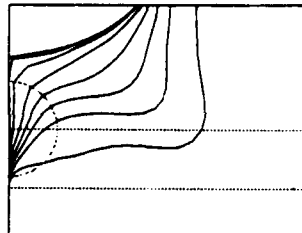
Caprino & Traverso



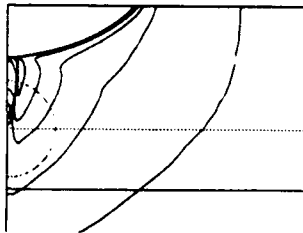
Gorski, Coleman, Haussling & Miller



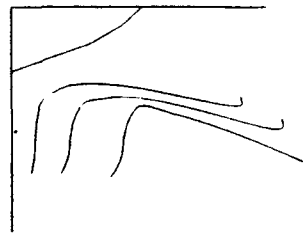
Hoekstra



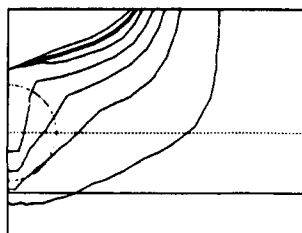
Hoffman & Chan



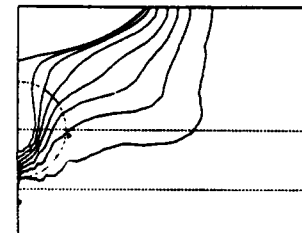
Ikehata & Liu



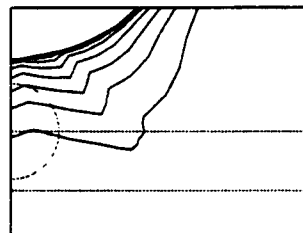
Kang & Oh



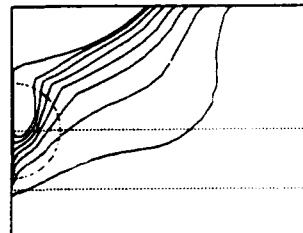
Kodama



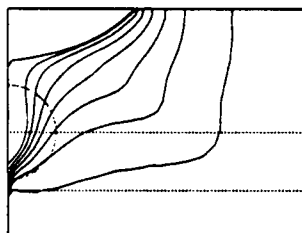
Kanevsky & Orlov



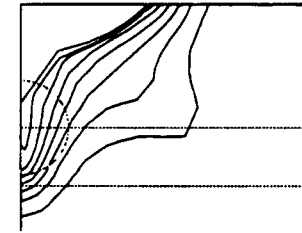
Majumdar, Zhu & Rodi



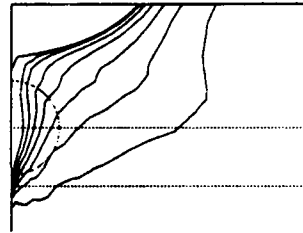
Masuko, Shirose & Abe



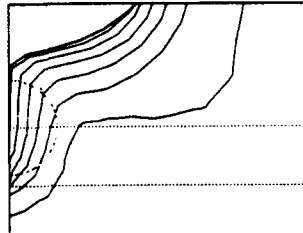
Patel, Ju & Law



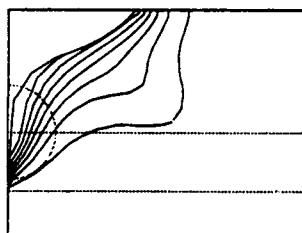
Piquet & Visonneau



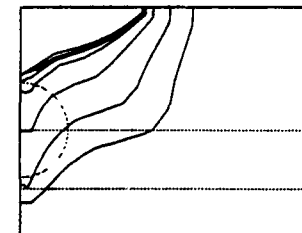
Shen, Zhang & Cai



Tzabiras



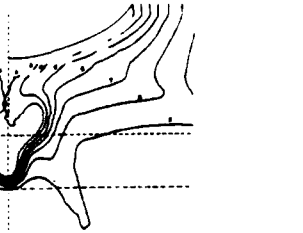
Zhou & Gao



Zhu & Miyata

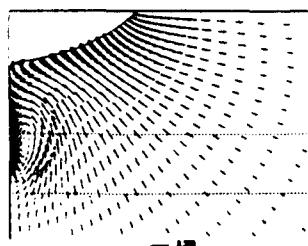


Experiment

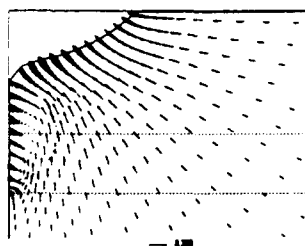


4. Axial velocity contours at the propeller plane  $X/L = 0.976$  ( $U/U_\infty = 0.3, 0.4, 0.5, 0.6, 0.7, 0.8, 0.9$ )

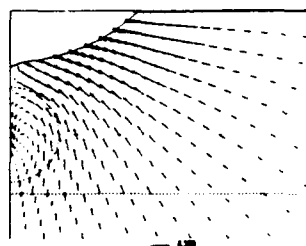
Abdallah & Sotiropoulos



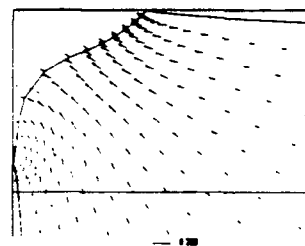
Broberg, Zhang, Larsson & Schön



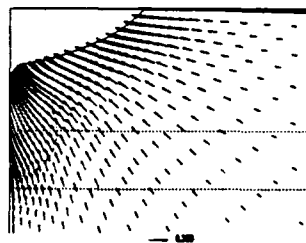
Bull, Watson & Musker



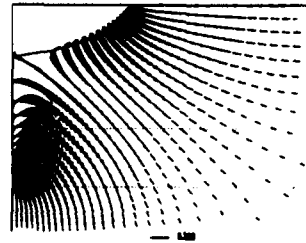
Caprino & Traverso



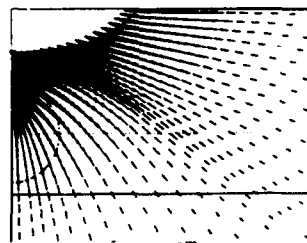
Gorski, Coleman, Haussling & Miller



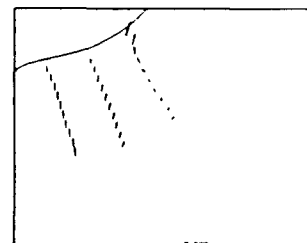
Hoekstra



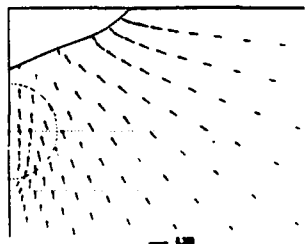
Hoffman & Chan



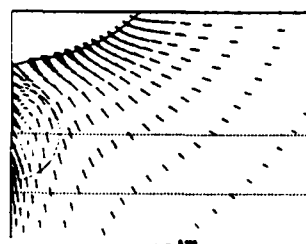
Ikehata & Liu



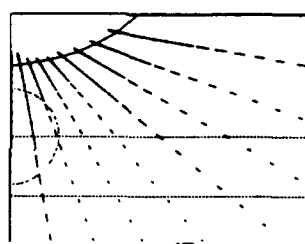
Kang & Oh



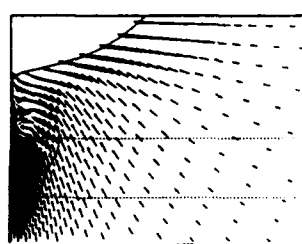
Kodama



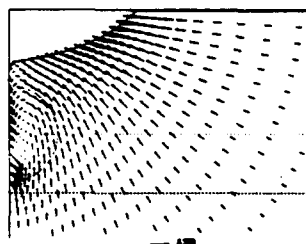
Kanevsky & Orlov



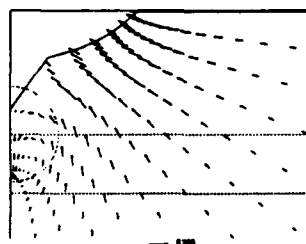
Majumdar, Zhu & Rodi



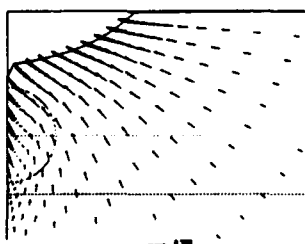
Masuko, Shirosé & Abe



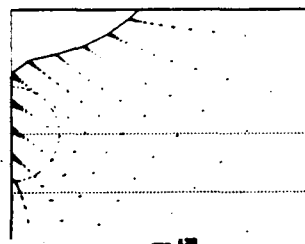
Patel, Ju & Law



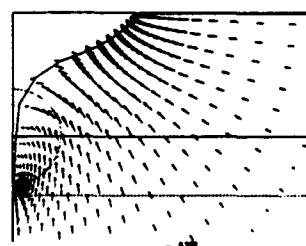
Piquet & Visonneau



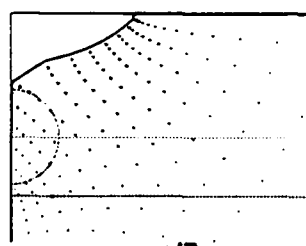
Shen, Zhang & Cai



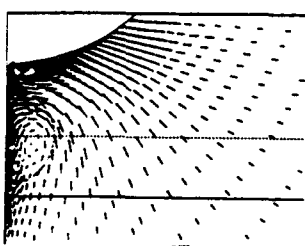
Tzabiras



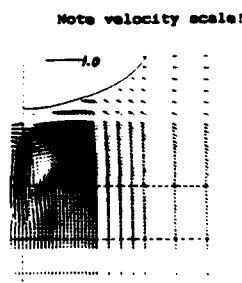
Zhou & Gao



Zhu & Miyata



Experiment



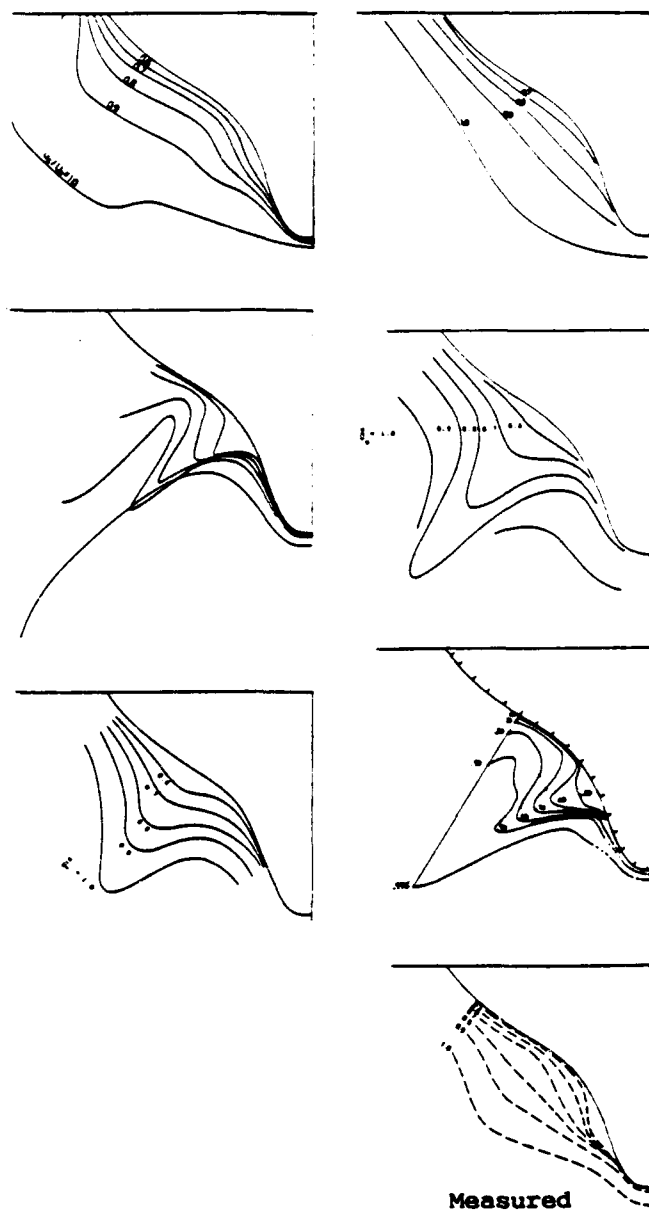
5. Cross-flow velocity vectors at the propeller plane  $X/L = 0.976$

cross-flow vectors) at the propeller plane of Case I, see Figs. 3, 4 and 5. In these Figures the results of all 19 methods are included. Measured data are represented by symbols in Fig. 3, while the computed results are given as lines. In Fig. 4 iso-velocity contours corresponding to 0.3, 0.4, 0.5, 0.6, 0.7, 0.8 and 0.9 times the undisturbed velocity are given. For comparison the experimental data are shown in the lower right corner. Note the different scales for the computed and experimental cross-flow vectors in Fig. 5.

Before embarking on a more detailed analysis a comparison of the results presented at this Workshop with those obtained a decade ago for the SSPA-ITTC Workshop on Ship Boundary Layers<sup>1</sup> is quite revealing. Fig. 6 shows the axial velocity contours for the HSVA Tanker at  $X/L=0.942$  presented at the previous Workshop. A comparison of these with the results shown in Fig. 4 provides an overview of the achievements of the past decade. It is clear that the earlier boundary layer methods have given way to those based on the Navier-Stokes equations. Only one such method was represented in 1980. At the present Workshop, only one boundary layer method was represented. The question is whether or not real progress has been achieved in the prediction of the flow. If the contours of axial velocity at the stern are used as the only measure of success, then we may conclude that progress has indeed been made. But, consider the following observation. Most calculations methods of the past did rather well at prediction of the boundary layer over the hull and failed only at the stern. Among the present methods, few, if any, predict the boundary layers with the same level of accuracy but continue to provide results for the flow over the stern and into the wake.

The girthwise pressure distributions of Fig. 3, will be considered section by section. First of all, we note that there are significant differences in the way different methods obtained the results at the check station,  $X/L = 0.646$ . As indicated in item A of Table 1 (Code H), seven methods performed calculations for the entire hull, starting upstream of it. Although the manner in which this was accomplished differed, their results at the check station reflect, to some extent, their resolution of the flow over the bow. Of the remaining methods, three started the calculations at the check station itself (see item D, Table 1) using the integral parameter information provided there. Note that no information on the crossflow at the check station was provided. The remaining methods started the solutions on the hull somewhere upstream of the check station and may have used the information provided to guide the selection of the upstream conditions. These differences among the methods must be taken into consideration when examining the results at the check station as well as further downstream.

In view of the foregoing, the results of four of the seven methods that calcula-



6. Axial velocity contours at  $X/L = 0.942$ , predicted in the 1980 Workshop<sup>1</sup>.

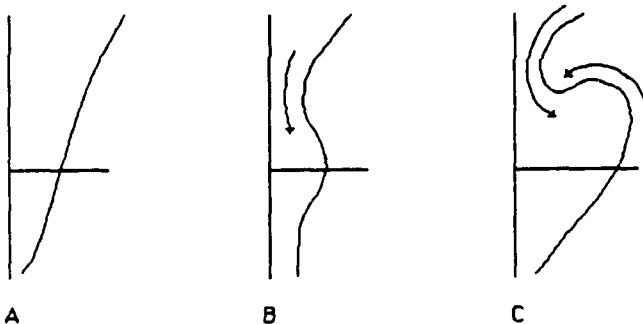
ted the flow over the entire hull are in remarkably good agreement with the data with respect to the girthwise pressure distribution at the first station. In fact, their predictions are as good as those of some of the methods that started the solutions on the hull. Methods that started the calculations on the hull show varying levels of agreement in the pressure distribution at the check station. The disagreement at the check station of methods that started at that station, or just upstream, are rather surprising. The reasons for this are not clear. Be that as it may, these differences should be borne in mind as comparisons are made further downstream.

At the next downstream section,  $X/L = 0.875$ , we see that the measured pressure distribution shows a decrease from the

keel, with a minimum  $c_p$  of about -0.24 around 30 percent of the girth, an increase up to about 70 percent of girth, followed by a near constant value of -0.11 around the waterline. It is clear from Fig. 3 that many methods reproduce this trend but, with one possible exception, fail to predict either the magnitude or the location of the pressure minimum.

At the last section,  $X/L = 0.942$ , the measurements indicate minimum  $c_p$  at around 8 percent girth, much closer to the keel than at the previous station, and an increase followed by a constant pressure around the waterline. The calculations generally predict higher pressures throughout and all fail to capture the dip in pressure around 45 percent girth. The methods that did poorly at the previous station continue to yield poor results at this station also.

From the point of view of propeller design the most interesting results are those at the propeller plane, reported in Figs. 4 and 5. The propeller disk is indicated in these Figures, and it is seen that particularly in this area the results vary considerably between the different methods. For classification purposes it is possible to distinguish between three types of results, see Fig. 7.



7. Different types of axial velocity contours at the propeller plane.

- A. V-shaped contours
- B. Contours with a bulge at or below the propeller center, indicating that part of the ship boundary layer has been displaced downwards by the longitudinal vortex hitting the propeller plane slightly above the propeller center (see Fig. 5).
- C. Contours with a pronounced "hook" due to the action of a stronger vortex.

Obviously the measured wake is of type C with quite distinct hooks in the 0.3 and 0.4 contour curves.

Investigating the contours of Fig. 5 it is seen that only one method produced a wake of type C, but the results of this method outside the propeller disk, particularly near the waterline, look quite unre-

alistic. Four or five methods predicted a wake of type B, while the remaining ones produced A type wakes.

For a propeller designer this situation is unsatisfactory, since the wake distribution determines the variation in loading during one turn of the propeller, i.e. the vibratory forces. On the other hand, as was shown by one of the authors (Larsson) at a continued Workshop in Osaka in the fall of 1991, the mean value around the circle at all radii may still be well predicted, as may the mean value of the velocity in the entire propeller disk. This means that the pitch and its distribution on the blades might be reasonably well predicted using the calculated wakes of the 4-5 best methods.

The reason for the failure to predict hook-like velocity contours was discussed extensively during the Workshop. To structure the discussion it was divided into four main themes: grid generation, equations and boundary conditions, turbulence models and numerical method.

There appeared to be a general consensus that grid resolution was not a major cause of the differences between, on the one hand the methods themselves, and on the other hand the measurements. This opinion was substantiated by the fact that several computers had carried out grid independence studies with very small changes in the results. There was however a general feeling that the resolution of the transverse pressure gradient was too low near the bilge (region of high transverse curvature) on the afterbody. Since this is where the longitudinal vortex is generated, the lack of resolution could explain the too-weak vorticity in the wake predicted by most methods. An impression of the grids used can be obtained from Fig 5, although, for clarity, not all the grid points are shown for some methods.

As for the governing equations, a difference not reported in the questionnaire turned out to be the way in which the turbulence terms are considered. It became clear that only a few methods include all of the terms. Another difference in the governing equations (appearing from Table I) is that some methods use the partially-parabolic approximation, while others are fully elliptic. This difference was discussed, and it was concluded that no correlation could be found between the approximation level in this respect and the performance of the method, as judged by the results reported. Some participants had in fact computed Case I using both types of equations and found very small differences.

Different inlet boundary conditions are required depending on whether the computational domain starts on the hull or upstream of it, but in all cases the participants were free to match their solution to the measured data at  $X/L = 0.646$ . Large differences are, however, seen at this sta-

tion, indicating that this possibility was not exploited by most of the computers. Instead, the boundary layer at the inlet station, if on the hull, seems to have been estimated from flat-plate correlations. The methods starting upstream use uniform inlet flow. To avoid numerical problems a nonzero value of the eddy viscosity had to be applied right from the start. Values of 50 to 100 times the laminar viscosity were mentioned. No attempt was made to consider transition. The general feeling was that the inlet conditions did not significantly influence the results at the stations on the afterbody and in the wake. This conclusion had in fact been verified by some participants.

Some discussers expressed the opinion that the only way to resolve details of the flow close to the wall (such as limiting streamlines) is to abandon the wall law. The general opinion was, however, that it is difficult to see a large difference in performance between the methods using the wall law and the others. A better prediction of the wake contours would have been expected, and this was achieved by some of the non-wall law methods but not all. It was pointed out also that virtually the only way to compute the full scale case is to employ the wall law, since otherwise the innermost grid points have to be positioned extremely close to the surface, giving rise to problems with the cell aspect ratios (the non-dimensional distance from the surface,  $y/L$ , is about 250 times smaller for the full scale case for a given value of  $y$ ). The other boundary conditions were considered relatively unimportant for the problems at hand.

Different opinions on the general importance of turbulence modeling were expressed. It was argued that as experiments have indicated that the Reynolds stresses are very small in the major part of the viscous region near the stern, even an inviscid calculation might produce a reasonable result. Some participants reported on earlier computations for axisymmetric and three-dimensional bodies, where this approach had been tested with relatively good results. Obviously the inviscid region had to be restricted to the neighborhood of the stern.

A possible explanation for the failure to predict the correct wake contours might be the inability of the methods to resolve the pressure field accurately, i.e. to predict the transverse pressure gradients that are believed to produce the vortical flow structure. In this case, a number of numerical issues are involved, including the grid arrangement used (staggered versus regular) and the manner in which the pressure is calculated.

### Conclusions

The Workshop clearly showed that great progress has been made during the 1980's in the development of methods for predicting

the flow around the stern and in the near wake of ships. The boundary layer based approaches of the 1980 Workshop have given way to methods based on the Reynolds-Averaged Navier-Stokes equations, albeit using relatively simple turbulence models. While the former methods either broke down before, or predicted completely unrealistic results in the propeller plane, the new methods in general capture the gross features of the wake, such as the thin shear layer in the lower part and the piling-up of boundary layer low speed flow around half draught. In fact, the best methods of the Workshop predict the shape and location of the velocity contours in most of the propeller plane with reasonable accuracy. The results are however less satisfactory in the central part of the wake, i.e. inside the propeller disk. The bilge vortex, although weak, redistributes the low speed flow from the boundary layer in such a way that very uneven hook shaped velocity contours are created. This feature is missed to varying degrees by the different methods. Various reasons for this were discussed during the Workshop, but no definite answer could be given. One possible explanation is that the large velocity and pressure gradients in the bilge region are too inaccurately resolved in the grids employed.

There are no general differences in performance between methods based on zero equation turbulence models as compared to the two equation models. The disadvantages of the simpler models may be outweighed by the advantages of computing the flow all the way down to the surface. Two equation models are usually employed in combination with the wall law.

Although the new methods are superior to the old ones in predicting the wake, results from calculations starting upstream of the hull, or in front of the check station, indicate that the ability to predict the thin boundary layer has not been improved, rather the contrary. The likely reason for this is grid resolution. To save computer time very few grid points are located in the thin boundary layer on the forebody, where the much faster boundary layer methods may use grids with a very high resolution. This suggests a zonal approach where the expensive Navier-Stokes method is used in the stern and wake region while an efficient boundary layer method is used for the rest of the hull.

A final point to note is that most methods predicted, at least qualitatively, the differences between the two test cases. The computed cross flow for the second case is considerably larger in the propeller disk than for the first case, as the measurements have indicated, and the change in the contours of axial velocity also shows the right trend.

### Acknowledgements

The authors are grateful to Dr J Kux and his group at the University of Hamburg for releasing their unpublished data for the second test case. Thanks are also extended to Professors G. Dyne, J. Piquet and W. Rodi, Mr M. Hoekstra and Mr D Humphreys for important technical discussions and advice, and to Mr B. Regnström for preparing all the graphs presented in the Proceedings.

The Workshop participation by V.C. Patel and IIHR was made possible by support from the Applied Hydromechanics Research program of the US Office of Naval Research under Grant N00014-89-J-1670, technically monitored by Mr J.A. Fein. The work at SSPA/FLOWTECH and CTH was sponsored by the Swedish National Board for Technical Development.

### References

- 1 Larsson, L., (ed.) "SSPA-ITTC Workshop on Ship Boundary Layers 1980: Proceedings," SSPA, Goteborg, Sweden, Report No. 90, 1981.
- 2 Collatz, G., "Geosim Tests with a Model of Large Fullness," (in German) Forschungszentrum des Deutschen Schiffbaus, Report 28, Hamburg, 1972.
- 3 Hoffmann, H.P., "Investigation of the Three-Dimensional Turbulent Boundary Layer on a Double Model of a Ship in a Wind Tunnel," (in German) Inst. Schiffbau, Uni. Hamburg, Report 343, 1976.
- 4 Wieghardt, K. and Kux, J., "Nominal Wakes Based on Wind Tunnel Tests," (in German) Jahrbuch der Schiffbautechnischen Gesellschaft (STG), 1980, Springer-Verlag, pp. 303-318.
- 5 Larsson, L., Patel, V.C. and Dyne, G., (ed.) "Ship Viscous Flow - Proceedings of the 1990 SSPA-CTH-IIHR Workshop", FLOWTECH, Gothenburg, Sweden, Research Report No 2, 1991.
- 6 Dyne, G., "A Study on the Scale Effect of Wake, Propeller Cavitation and Vibratory Pressure at the Hull of Two Tanker Models", Trans SNAME, 1974
- 7 Denker, J., Knaack, T. and Kux, J. "Experiments and Numerical Investigation of the HSVA2 Tanker (Second Test Case of the 1990 SSPA-CTH-IIHR Workshop), Inst. Schiffbau, Uni. Hamburg, Report 516, 1991.

Table I is found on the following 3 pages.

Table 1

# SUMMARY OF COMPUTATION METHODS INFORMATION FROM RESPONSES TO QUESTIONNAIRE

A. OVERALL STRATEGY		Authors >>	AS	BZ LS	BW M	CT	GC IDM	H	HC	IL	KO	K	KO	KO	KO	MS A	MZ R	PJL	PV	SZ C	T	ZG	ZM
INDICATE whether you calculate the complete hull (by H), or only the stern and wake flow (by S)			S	S	S	H	S	S	S	H	S	H	S	H	S	S	H	S	S	S	S	S	H
GLOBAL (single method is used for entire flow) (G)			G	---	G	G	G	---	G	---	G	G	---	G	G	G	G	G	G	G	G	G	G
ZONAL (separate methods are used in different regions; matched or patched) (Z) : (* indicates combinations)			---	Z	---	Z*	---	Z	---	Z	---	Z	---	Z	---	Z	---	---	---	---	---	---	---
Note: If ZONAL, complete the remainder for each viscous-flow region, carefully denoting the region to which the description applies. If a VISCIOUS-INVISCID interaction method is used, indicate INTERACTION LAW: Displacement thickness (D); Surface and wake blowing or suction (S); Matching along a specified boundary outside the viscous layer (P); INVISCID METHOD used (I)			---	P,I	---	P,I*	---	P,I	---	P,I	---	?	I	---	---	---	---	---	---	---	---	---	---
B. EQUATIONS SOLVED			R	R	R	R	R	P	R	I	R	R	R	R	R	R	R	R	R	R	R	P	L
A PRIORI or DE FACTO APPROXIMATIONS None: Direct Simulation: no turbulence model (N); Large Eddy Simulation: NS equations with sub-grid model (L); Reynolds-averaged NS equations (R); RANS with grid-related approximations (e.g., nonorthogonal viscous terms neglected) (R-); Partially-parabolic RANS (longitudinal diffusion neglected; RANS with FLARE etc) (P); Thin-Layer RANS (only wall normal diffusion retained) (T); Boundary-layer equations (D: differential; I: integral)																							
VARIABLES Velocity and pressure (VP); Velocity and vorticity (VV); Stream function and vorticity (SV) Choice of components of vector quantities (indicate by number(s)) Cartesian (1), cylindrical (2), other orthogonal (3), contravariant (4), covariant (5), grid-line oriented physical (6), mixed (M), other (7)			VP	VP	VP	VP	VP	VP	VP	I	VP	VP	VP	VP	VP	VP	VP	VP	VP	VP	VP	VP	VP
COORDINATES (see also GRID) Nonorthogonal in all planes (3); Nonorthogonal in two planes (2); Nonorthogonal in one plane (1); Orthogonal in all planes (0); Other (finite elements, etc.) (A)			3	3	3	3	3	2	3	0	3	3	3	3	3	3	3	3	3	3	3	3	3
C. TURBULENCE MODEL			AL	k ε	k ε	k ε	AL	AL	k ε	I	k ε	AL	k ε	k ε	k ε	k ε	k ε	k ε	k ε	k ε	k ε	k ε	SG
None (N); Sub-grid (SG); Algebraic eddy-viscosity or mixing-length (AL); One-equation (e.g., k); Two-equation (-, ε, k, ε); Algebraic stress equations (AS); Reynolds stress equations (RS); Other (e.g., integral equations, I) Note: combinations indicated by two symbols (e.g., k ε, k)			NS	WP	WP	W	NS	NS	---	---	W	NS	?	W	W	WP	NS	W	W	W	W	W	NS
Near-wall treatment: No-slip (NS); Law of the wall: with pressure-gradient (WP), without (W) Number of turbulence-model equations solved			0	2	2	2	0	0	2	0	2	0	2	2	2	2	2	2	2	2	2	2	0
D. BOUNDARY AND INITIAL CONDITIONS																							
INITIAL (time = 0) From rest (O), uniform flow (1), potential flow (2), boundary layer solutions (4), other (5)			0	5	5	2	1	5	0	---	1	1	7	1	1	1	5	1	5	4	1	0	0
Variables determined in the above manner: Code - 0: p; 1: p, V; 2: V, k, ε; 3: p, V, k, ε			1	2	3	3	1	0	3	---	3	7	7	2	3	2	3	1	7	0	7	7	7
UPSTREAM Location (x = 0 is bow, x = L is stern), x/L =			.5	.5	.3	.2	.646	.646	.5	.05	.5	.5	.1	.51	.5	.3	.5	.5	.646	.5	.5	.5	.5
Variables specified (e.g., C <sub>f</sub> , δ, u, v, w, p, k, ε, v <sub>0</sub> , ...) Code - 0: p; 1: integral parameters; 2: V; 3: V, k, ε			2	1,3	2,3	0,3	0,2	2	0,2	1	1,3	0,2	1	2,3	0,2	1	1	0,2	1	1	0,2	1	0,2
Conditions specified (e.g., uniform stream, 2D b.l. flow, ...) Code - 0: uniform stream; 1: inviscid flow; 2: 2DBL; 3: 3DBL			2	1,2	0,2	0	2	---	4	2	2	0	2,3	0	0	(3)	3	1,3	3	2	2	2	2
DOWNSTREAM Location, x/L =			1.8	2.0	5	3.92	1.4	1.35	1.5	1.5	2	1.5	<1	1.6	2	4.5	2	2.5	1.25	1.8	2	2	2
Conditions specified Code - A: p <sub>0</sub> , q <sub>0</sub> = 0; A1: p <sub>0</sub> = 0; B: p <sub>0</sub> , q <sub>0</sub> = 0; C: V <sub>infinity</sub> ; D: Pressure;			B	B	B	A	D	E	A	A	---	A	?	---	A	B	A	A	E	A	A	?	?

WALL: No-slip (NS); wall function (WF)

# WAKE CENTER

Conditions Specified: Code - S: Symmetry ( $U_n = 0, \partial(U, U_p, p, \dots)/\partial n = 0$ )

# FREE SURFACE

Double body, plane of symmetry (S), exact with fixed grid (O).

exact with boundary-fitted grid (B), approximate (A, describe)

Conditions specified exact with boundary-fitted grid (B),

approximate (A, describe)

# FAR FIELD

Location, R/L (or equivalent distance from axis) =

Tunnel/rank wall (T), uniform stream (U), inviscid flow (I)

Parameters specified: Code - B: ( $p, U^1, U^2$ )<sub>boundary</sub>;  $C_0: U^1 = 1, \partial U^2/\partial n = 0$

$C_1: U^1 = 1, U^2 = 0, p = 0; C_2: U^1, U^2, p;$

Conditions specified: Code - A:  $p_\infty = 0, \partial^2 U/\partial n^2 = 0; A_2: \partial(p, U^1)/\partial n = 0;$

$K_1: \partial(\xi, \epsilon)/\partial n = 0; K_2: (\xi, \epsilon) = 0; S: symmetry$

# E. GRID

## TYPE

Single block (SB) or multi-block (MB)?

Nonorthogonal everywhere (N), orthogonal in planes (P), orthogonal at some

boundaries (B), orthogonal everywhere (O)

## GENERATION METHOD

Analytic (A), numerical (N), algebraic (L)

Elliptic (E), hyperbolic (H), parabolic (P), transfinite (T), conformal (C), geometrical (G)

3D (3), 2D plane by plane (2), other (1)

Post-generation smoothing? yes (Y), no (N)

## CONTROL

Adaptive? yes (Y), no (N)

Control from boundaries (B), from inside the domain (D)

## F. NUMERICAL METHOD

### GENERAL CLASSIFICATION

Finite-element (FE), finite-difference (FD), finite-volume (FV),

Spectral (S), Integral (I), mixed (M), Other (O)

## DISCRETIZATION

Finite-difference, regular or collocated grid (R); finite-difference, staggered grid (T);

finite volume, regular grid (V); finite-volume, staggered grid (S); finite element (L);

hybrid (H) & other (O), specify

### DIFFERENCING OF CONVECTIVE TERMS

Centered (C); upwind, standard (U); upwind, skewed (K); rotated (A); explicit artificial viscosity (D);

hybrid, specify (H); other, specify (O) Code - finite-analytic (FA)

FORMAL ORDER OF ACCURACY (Convective terms)

First (1); second (2); third (3); fourth (4); mixed (M); other (O)

### FORMALLY CONSERVED QUANTITIES

Mass (Q); mass and momentum (M); mass, momentum, kinetic energy (I); mass, momentum,

total energy (W); other (O) Note: There is some confusion here about conserved quantities

LINEARIZATION: Picard (P); Newton (N); Quasi-Newton (Q); Other (O)

### PRESSURE-VELOCITY COUPLING

Pully-coupled solutions: direct method (D); penalty method (P); compressible-flow code

used at low Mach number (C); artificial compressibility (A); other (O)

NS	WF	WF	WF	NS	NS	NS	WF	WF	WF	WF	NS	WF	WF	WF	NS
S	S	S	S	?	S	S	---	S	S	---	S	S	S	S	S
S	S	S	S	S	S	S	G	S	S	S	S	S	S	S	S
S	S	S	S	S	S	S	---	S	S	S	S	S	S	S	S
.5	.3	1.	1.	.375	.08	1.5	>.5	1.	1.	.7	.51	.5	1.	1.	.15
U	I	U	U	U	I	U	I	U	U	I	U	U	U	I	?
---	B	C <sub>1</sub>	C <sub>2</sub>	C <sub>2</sub>	B	?	B	C <sub>1</sub>	C <sub>1</sub>	B	S	C <sub>1</sub>	C <sub>1</sub>	C <sub>0</sub>	B
A <sub>1</sub>	K <sub>1</sub>	K <sub>1</sub>	A <sub>2</sub>	---	---	---	---	K <sub>2</sub>	---	---	S	---	K <sub>1</sub>	K <sub>1</sub>	A <sub>2</sub>

SB	SB	SB	SB	MB	SB	SB	---	SB	SB	SB	SB	SB	SB	SB	SB
N	B	N	P	N	P	N	---	N	N	N	N	B	N	P	B
N	N	N	N	L	A,N	A,L	---	N	N	N	N,L	N	N	L	A
B	E	B	E	T	C	C,T	---	E	Q	?	T	E	E	G	C
2	3	2	3	3	2	2	---	3	3	3	3	3	3	3	3
N	N	N	Y	N	N	N	---	N	Y	N	N	Y	N	Y	N
N	N	N	N	N	N	N	---	N	N	---	N	---	N	N	N
B	B	B	D	B	---	---	---	B	---	---	D	---	D	B	B,D

FD	M	M	FV	FV	FD	FV	I	FV	FD	FV	FV	M	M	FV	FD
----	---	---	----	----	----	----	---	----	----	----	----	---	---	----	----

NO FINITE-ELEMENT METHOD REPRESENTED

R	S	S	S	V	R	R	---	S	R	V	R,V	S	S	S	T
---	---	---	---	---	---	---	-----	---	---	---	-----	---	---	---	---

U	FA	FA	U	U	O	U,D	---	C,U	C,D	O	H	C,U	FA	O	H
---	----	----	---	---	---	-----	-----	-----	-----	---	---	-----	----	---	---

2	M	M	M	3	2	2	---	M	2	1	1	1,2	1,2	M	1,2
---	---	---	---	---	---	---	-----	---	---	---	---	-----	-----	---	-----

M	Q	J	J	M	M	M	J	M	M	M	M	J	Q	M	J
---	---	---	---	---	---	---	---	---	---	---	---	---	---	---	---

---	---	P	---	N	N	N	---	O	N	P	P	---	O	Q	---
-----	-----	---	-----	---	---	---	-----	---	---	---	---	-----	---	---	-----

O	---	---	---	A	O	---	---	A	---	---	---	---	---	---	---
---	-----	-----	-----	---	---	-----	-----	---	-----	-----	-----	-----	-----	-----	-----



Segregated: Poisson equation, e.g., capacitance techniques (P); pressure-correction technique, e.g., SIMPLE, SIMPLER, SIMPLEX, PISO, saddle-point method, preconditioning (C, list); other (e.g., boundary-layer type code) describe (O)  
Code - S<sub>1</sub>: SIMPLE; S<sub>2</sub>: SIMPLER; S<sub>3</sub>: SIMPLER; S<sub>4</sub>: SIMPLEX; P: PISO

#### ACCELERATION OF ITERATIVE SOLUTIONS

If you distinguish more than one iteration process in your method, classify them and specify the following for each of them: Under-relaxation (U); over-relaxation (R); grid sequencing (G); (U) on p only; multi-grid (M); additive terms (e.g., quasi-time dependent, fixed or variable time step) (A); conjugate gradient methods (C); other, describe (O)

#### STRATEGY

Explicit (E); implicit (I); semi-implicit (S); fractional step (F); other (e.g., optimal control, Newton-Raphson), describe (O)

#### TACTICS

Point substitution (P); line substitution (L); direct matrix inversion (M); Split (ADI-like); incomplete LU decomposition (D); other, describe (O)

#### G. COMPUTATIONS

Computer used, list

Code - S<sub>1</sub>: CRAY YMP; S<sub>2</sub>: CRAY XMP; S<sub>3</sub>: CRAY 2; S<sub>4</sub>: FACOM VP400; S<sub>5</sub>: FACOM VP50  
M<sub>1</sub>: DEC 2100; M<sub>2</sub>: FPS 264; M<sub>3</sub>: MICROVAX 3800; M<sub>4</sub>: Apollo 10000; M<sub>5</sub>: SUN 4WS;  
M<sub>6</sub>: STELLAS WS; M<sub>7</sub>: BESM6; M<sub>8</sub>: IBM 3031; M<sub>9</sub>: SPARC 330; (Note: S for super; M for other)

Number of grid points used in axial and transverse directions:

Total number of grid points, thousands (K)

For above grid, storage utilized (MW: megawords  
MB: megabytes)

For above grid, cpu time: m: min; h: hour; d: days

For above grid, number of iterations or time steps required for convergence, in thousands (K)

Convergence criteria employed

Code - NE: no explicit criterion; O: other

	A		B		C	
	1	2	3	4	5	6
1	$\Delta p < 5 \cdot 10^{-3}$	$ES < 10^{-3}$	$\Delta u < 10^{-4}$			
2	$5 \cdot 10^{-4}$	$5 \cdot 10^{-4}$				
3	$10^{-4}$	$10^{-5}$				
4		$5 \cdot 10^{-5}$				

Approximate cpu per iteration per grid point, in  $10^{-5}$  secs

Maximum grid that can be accommodated on the computer in thousands (K)

Number of grid points used in the region

$0.63 < X/L < 1.0$ ,  $n^* > 100$ ,  $n/L < 0.1$

axial  
radial  
girth

Total number of grid points in the above region, thousands (K)

#### AUTHORS CODE

AS: Sotiropoulos & Abdallah, Uni. Cincinnati, USA  
EZLS: Broberg, Zhang, Larsson & Schöon, Flowtech, Sweden  
BWM: Bull, Watson & Mueker, ARE-Heller, U.K.  
CT: Caprino & Traverso, CETENA, Italy  
GCHM: Gorski, Coleman, Hausling & Miller, DTRC, USA  
H: Hochstra, MARIN, The Netherlands  
HC: Hoffman & Chan, ARL, Penn State Uni. & Rockwell, USA  
IL: Ikebata & Ito, Yokohama Nat. Uni., Japan  
KO: Kang & Oh, Seoul Nat. Uni. & Kyungnam Uni., Korea  
K: Kodama, Ship Res. Inst., Japan

KaO: Kanevsky & Orlov, Krylov, USSR  
MZR: Majumdar, Zhu & Rodi, NAL, India & Uni. Karlsruhe, Germany  
MSA: Masuko, Shirosu & Abe, IHI, Japan  
PIL: Patel, Ju & Lew, IHR, Uni. Iowa, USA & Daewoo, Korea  
PV: Piquet & Vismoreau, ENSM Nantes, France  
SZC: Shen, Zhang & Cai, MARIC, China  
T: Tzabaras, Nat. Tech. Uni., Greece  
ZO: Zhou & Qiao, CSSRC, China  
ZM: Zhu & Miyata, Uni. Tokyo, Japan

--- S<sub>2</sub> S<sub>3</sub> --- P --- S<sub>1</sub> --- S<sub>1</sub> S<sub>1</sub> S<sub>1</sub> S<sub>2</sub> P S<sub>1</sub> S<sub>1</sub> S<sub>4</sub> ?

U A R U O A C --- U --- U U A A U U U U

E I S --- I I S --- I I I I I I I I I I S E.S

P L L O D P.D D --- L Split L D P L D L P.L L P

S<sub>7</sub> M<sub>6</sub> M<sub>7</sub> M<sub>8</sub> S<sub>1</sub> S<sub>2</sub> M<sub>9</sub> --- M<sub>6</sub> M<sub>6</sub> M<sub>6</sub> S<sub>2</sub> S<sub>2</sub> S<sub>7</sub> S<sub>2</sub> M<sub>6</sub> M<sub>7</sub> M<sub>8</sub> M<sub>9</sub>

57 60 93 63 65 113 92 58 81 50 124 133 50 80 36 45 80 120  
41 33 40 16 33 55 86 25 27 10 44 25 30 40 20 29 15 30  
33 25 21 25 49 35 32 16 31 20 32 29 15 21 12 62 20 30

79 49 78 25 105 218 253 23 68 10 175 96 23 67 8 81 24 108

MW 2.4

MB --- 6 24 11 --- 8 20 --- 0.2 --- 0.4 56

90m 2h 30h 10h 9h 80m 20h --- 3h 50h 30h 11m 2h 10m 4h --- 5h 5d

4 .04 1.6 3 2.5 .035 1. --- .13 5. --- .1 4 .16 .3 .04 .06 20.

A<sub>3</sub>C NE --- NE NE A<sub>1</sub> B<sub>1</sub> --- B<sub>1</sub> NE --- B<sub>2</sub> B<sub>4</sub> NE A<sub>3</sub>C C B<sub>3</sub> A<sub>2</sub> A<sub>3</sub>

2 500 92 --- 11.4 --- 29 --- 388 50 --- 3.9 13 16 50 2780 615 625 20  
--- 300 --- 120 --- --- --- 123 --- 705 500 112 1000 --- 32 110

33

20

25

16.5

30

20

21

12.6

# THREE-DIMENSIONAL BOUNDARY LAYER CALCULATION BY A CHARACTERISTIC METHOD

R. Houdeville  
O N E R A - C E R T  
2 avenue Edouard Belin  
31055 TOULOUSE Cedex  
FRANCE

## Summary

A numerical method for solving the three-dimensional boundary layer equations for bodies of arbitrary shape is presented. In laminar flows, the application domain extends from incompressible to hypersonic flows with the assumption of chemical equilibrium. For turbulent boundary layers, the application domain is limited by the validity of the mixing length model used. In order to respect the hyperbolic nature of the equations reduced to first order partial derivative terms, the momentum equations are discretized along the local streamlines using of the osculator tangent plane at each node of the body fitted coordinate system. With this original approach, it is possible to overcome the use of the generalized coordinates and therefore it is not necessary to impose an extra hypothesis about the regularity of the mesh in which the boundary conditions are given. By doing so, it is possible to limit, and sometimes to suppress, the pre-treatment of the data coming from an inviscid calculation. Although the proposed scheme is only semi-implicit, the method remains numerically very efficient.

## 1 INTRODUCTION

A great number of three-dimensional boundary layer calculation methods have been developed in the last two decades. Some of them are presented in the synthetic papers of Smith<sup>33</sup>, Cousteix<sup>14</sup> and, more recently, Humphreys and Lindhout<sup>17</sup>. Although the amount of work done to solve the Prandtl equations is substantial, some difficulties remain when the crossflow direction changes in the calculation domain. As it has been shown by Wang<sup>35</sup> and Krause<sup>21</sup> this problem comes from the nature of the set of the boundary layer equations which imposes a *CFL* type condition to the discretization scheme (Cebeci et al<sup>9</sup>). To fulfil this condition, at least two solutions may be proposed: i) to choose a simple numerical scheme as, for example, an explicit upwind discretization of the crosswise derivatives; ii) to use an implicit discretization of the crosswise derivatives at the unknown station.

With the first solution, the advancement of the integration at a given station always goes in the same crosswise direction and the changes of the crossflow, which appear on bodies at incidence, cannot be completely calculated, as shown by Cebeci<sup>9 19 25</sup>, unless a change of the discretization scheme across the boundary layer thickness is allowed

(Lindhout-Moek<sup>25</sup>). In the second case, the calculation effort is much more important, and therefore reduces the interest in using the Prandtl equations (Patel-Baek<sup>31</sup>, Johnston<sup>20</sup>). In practice, a third strategy exists to conciliate the respect of the *CFL* condition with the efficiency of the numerical scheme. Considering only the finite difference methods, Cebeci<sup>9</sup> uses the standard "Keller Box" method everywhere it is possible and the "zig-zag" scheme where the crossflow direction changes. In this latest scheme, the crosswise advection terms are partly written at the calculation station, and partly at the upstream station. To overcome some limitations of this method, Cebeci<sup>9 10 11</sup> proposes the "Characteristic Box Scheme" which takes into account the existence of characteristic directions in the boundary layer equations to limit the streamwise integration step in the region where the crossflow changes sign in the boundary layer thickness. This leads to an extra iteration step at each calculation station.

The numerical scheme which is presented in this paper integrates the Prandtl equations along the local streamlines, which are sub-characteristic lines. By doing so, the integration proceeds always in the same direction whatever the crossflow direction, and the *CFL* condition is fulfilled, providing that the marching step is small enough. As the diffusion terms are expressed at the unknown station, the proposed method belongs to the semi-explicit type.

The main originality of the proposed method comes from the choice of the space in which the equations are integrated. Most methods use generalized coordinates in a body fitted coordinate system. This needs the calculation of the Christoffel coefficients which introduces an extra hypothesis dealing with the regularity of the mesh, while the boundary layer assumptions impose only the regularity of the body surface. To avoid this extra limitation, the discretization of the equations at a given station can be done in the tangent plane to the surface at this point instead of the actual surface. To respect the metric properties of the surface and express the covariant derivatives of the velocity, the tangent plane must be provided with a particular metric. This is simply done by orthogonally projecting the body fitted coordinate system and the velocity field on the tangent plane at the considered points.

## 2 Boundary layer equations

### Body fitted coordinate system

To set up the boundary layer equations, it is convenient to use a body fitted coordinate system (see, for example, Hirschel-Kordulla<sup>16</sup>). Let  $x^i$  be the cartesian coordinates of a surface point. This point is known by the two parameters  $X^1$  and  $X^2$ . With  $\vec{e}_i$  the cartesian base vector, the vectors defined by

$$\vec{a}_\alpha = \frac{\partial x^i}{\partial X^\alpha} \vec{e}_i \quad \alpha = 1, 2 \quad i = 1, 2, 3 \quad (1)$$

are tangent to the body fitted coordinate system.

The surface base reference frame is obtained by adding the unity vector  $\vec{a}_3$  perpendicular to  $\vec{a}_1$  and  $\vec{a}_2$ . The reference frame  $(\vec{e}_1, \vec{e}_2, \vec{e}_3)$  in the vicinity of the surface is built as shown in figure 1. Introducing the thin layer assumption, the metric elements  $g_{ij} = \vec{e}_i \cdot \vec{e}_j$  become independent of the  $X^3$  coordinate.

The boundary layer equations are obtained by applying the Prandtl hypothesis to the Navier-Stokes equations written in the curvilinear coordinates  $(X^i, i = 1, 2, 3)$ .

For an incompressible laminar flow, the boundary layer equations read :

$$\nabla_i U^i = 0 \quad i = 1, 2, 3 \quad (2a)$$

$$\rho U^i \nabla_i U^\alpha = -\nabla_\alpha P + \frac{\partial}{\partial X^3} \left( \mu \frac{\partial U^\alpha}{\partial X^3} \right) \quad \alpha = 1, 2 \quad (2b)$$

The covariant derivatives of the velocity are expressed using the Christoffel coefficients:

$$\nabla_i U^\alpha = \frac{\partial U^\alpha}{\partial X^i} + \Gamma_{ij}^\alpha U^j \quad (3)$$

In the equations 2a and 2b, the pressure field is known. It is, for example, the wall pressure given by an inviscid calculation. The boundary conditions are the no-slip condition at the wall and the velocity components  $U_\alpha^e$ , (with  $\alpha = 1, 2$ ) at the outer edge of the boundary layer. The latter can be obtained from the pressure field by integrating the Euler equations at the wall.

### Nature of the set of equations

From the theory of quasi linear differential equations, the boundary layer equations 2a and 2b are parabolic because of the diffusion terms. It has been shown by Wang<sup>35</sup> and Krause<sup>21</sup> that the particular influence of the advection terms could be studied from the characteristic surfaces of the subset of equations made of the first order derivatives. They have shown that the surfaces made of the straight lines perpendicular to the wall and the stream surfaces are sub-characteristic surfaces. This means that the influence domain of a particular station is limited by the two surfaces, formed of perpendicular lines to the wall, which are tangent to the two most deviated streamlines.

## 3 Numerical method

A great number of calculation methods have been developed to integrate the boundary layer equations in direct mode, i.e. with a prescribed external velocity field. Some reviews of these methods can be found in Smith<sup>33</sup>, Cousteix<sup>14</sup> and Humphreys-Lindhout<sup>17</sup>. Most of these methods are space-marching, with an upstream discretization of the advection terms.

Lindhout-Boer<sup>24</sup> made a semi-implicit method in which the crosswise derivatives along  $X^2$  are explicitly discretized in the upstream direction, the other derivatives being written implicitly. This allows a change of the crossflow direction to be taken into account very simply. The calculation step in the streamwise direction is limited by a CFL condition. To avoid this constraint, it is necessary to express implicitly the  $X^2$ -derivatives. This can be done simply if the dependence domains remain in a given side of the mesh lines  $X^1$  in the whole calculation domain (fig. 2a). For such flows, for example flows over infinite swept wings, the calculation advances everywhere in the same direction along the  $X^1$  lines. Jelliti<sup>19</sup> and Barberis<sup>6</sup> used this technique. For more complex boundary layer flows, such methods do not allow accessibility to the domains for which the crossflow does not remain in the marching direction along the  $X^1$  lines.

Lindhout *et al.*<sup>25</sup> have developed a technique in which the choice of the numerical scheme for the crosswise derivatives in the  $X^2$  direction and the marching sense along these lines depend on the most deviated streamlines throughout the boundary layer at the calculation station. This allows a certain optimization of the calculation effort by choosing in each region the most suitable discretization.

Other methods have been considered. An efficient scheme of the "predictor-corrector" type is used by Matsuno<sup>27</sup>. Wang<sup>36</sup> has proposed a "zig-zag" scheme in order to take into account the dependence domains for the discretization of the velocity along the  $X^2$  direction. These terms are written partly at the known upstream station and partly at the unknown calculation station, on both sides of the corresponding  $X^1$  line. The stability of this scheme is discussed by Krause<sup>21</sup>. A similar scheme has been used also by Iyer *et al.*<sup>18</sup> and Cebeci<sup>9</sup>. This author prefers a modified version of the "Keller box scheme", called the "characteristic box scheme" which takes into account the dependence domains by using the direction of the local streamline in the discretization formulation. This leads to an extra iteration step at each station and a limitation of the marching step in the  $X^1$  direction<sup>11</sup>.

Fully implicit techniques in which the  $X^2$ -derivatives are written in the unknown plane  $X^1 = Cste$  (fig. 2a) can be considered. Patel-Baek<sup>31</sup> and Tassa *et al.*<sup>34</sup> use the alternated direction procedure to solve the equations in a whole plane  $X^1 = Cste$ . Johnston<sup>20</sup> prefers to sweep only in the  $X^2$  direction, which leads to iterative inversion of tridiagonal matrices; the unknown quantities being taken at the previous iteration.

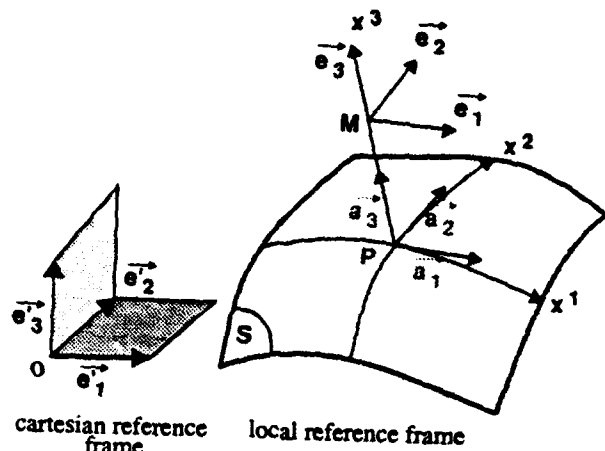


Figure 1 : Body fitted coordinate system and wall reference frame.

### Equations along the local streamlines

In order to respect the physical dependence domains at each point of the boundary layer while keeping a single marching direction along the  $X^2$ -lines, the momentum and energy equations will be discretized along the local streamlines. This also allows the use of a unique scheme in the whole calculation domain.

As is usually done in boundary layer calculations, a reference length  $L(X^1, X^2)$  is introduced to adapt the grid perpendicular to the wall to the boundary layer thickness. With the normal coordinate  $\eta = X^3/L(X^1, X^2)$ , the boundary layer equations along the local streamlines read

$$\begin{aligned} \nabla_i \rho U^i + \frac{\partial \rho \bar{U}^3}{L \partial \eta} &= -\frac{\rho}{L} U^i \frac{\partial L}{\partial X^i} \quad i = 1, 2 \quad (4a) \\ \rho \left| \bar{U} \right| \frac{\nabla U^a}{ds(\eta)} + \rho \bar{U}^3 \frac{\partial U^a}{L \partial \eta} &= \rho_e \left| \bar{U}_e \right| \frac{\nabla U_e^a}{ds(\delta)} + \frac{\partial}{L^2 \partial \eta} \\ &\quad \left( \mu_{eff} \frac{\partial U^a}{\partial \eta} \right) \quad \alpha = 1, 2 \quad (4b) \end{aligned}$$

with

$$\bar{U}^3 = U^3 - \eta U^i \frac{\partial L}{\partial X^i} \quad i = 1, 2 \quad (5)$$

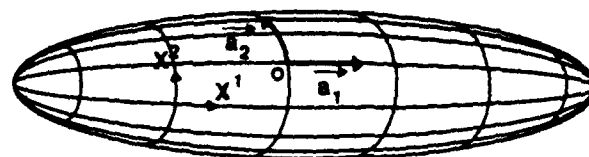
$dX^1$  being the step size in the main marching direction,  $ds(\eta)$  is calculated using the metric coefficients

$$ds(\eta) = (g_{ij} dX^i dX^j)^{1/2} \quad i, j = 1, 2 \quad (6)$$

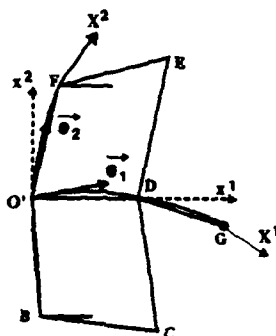
where  $dX^2_\eta$  is a function of  $\eta$  obtained from the definition of the local streamline parallel to the wall

$$\frac{dX^1_\eta}{U^1} = \frac{dX^2_\eta}{U^2} \quad (7)$$

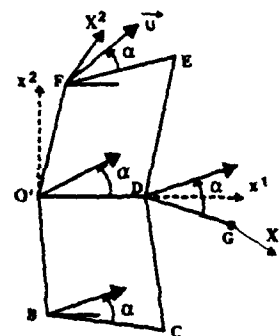
$\nabla U^i$  is the total variation of the velocity component  $U^i$  along the streamline



a) body fitted coordinate system



b) reference frame in the tangent plane



c) velocity field in the tangent plane

Figure 2 : Building of the calculation mesh and velocity field in the tangent osculator plane.

$$\nabla U^a = \left( \frac{\partial U^a}{\partial X^i} + \Gamma^a_{ij} U^j \right) dX^i_\eta \quad i, \alpha = 1, 2 \quad (8)$$

### Osculator tangent plane

The use of generalized coordinates introduces an extra hypothesis concerning the regularity of the body fitted coordinate system which must be regular enough to allow the calculation of the Christoffel coefficients. Moreover, as the calculation method is of semi-implicit type, the respect of the CFL condition leads to the use of a subgrid for the integration in the  $X^1$ -direction. The calculations can be done more rapidly if the equations are written in a cartesian coordinate system. Due to the local character of the boundary layer problem, confined to the vicinity of the body surface, it is not the global cartesian frame used to define the surface which will be considered, but a local cartesian frame linked to a mesh of the body fitted coordinate system in which the boundary conditions are given.

To build the osculator tangent plane, it will be assumed that the Christoffel symbols are defined, in order to show that the new approach is identical to the classic one, but this assumption is not necessary.

Let  $O$  be the node  $(X^1_i, X^2_j)$  of the mesh in which the boundary conditions are given. The local reference frame at this point is  $\vec{e}_i$ ,  $i = 1, 2, 3$ . To integrate the boundary layer equations to the next station  $(X^1_{i+1}, X^2_j)$ , it is necessary to represent in a cartesian space the neighbouring nodes with respect to point  $O$  as well as the velocity vectors (fig 3). To this end, at the point  $O$  of the surface (S) is associated a

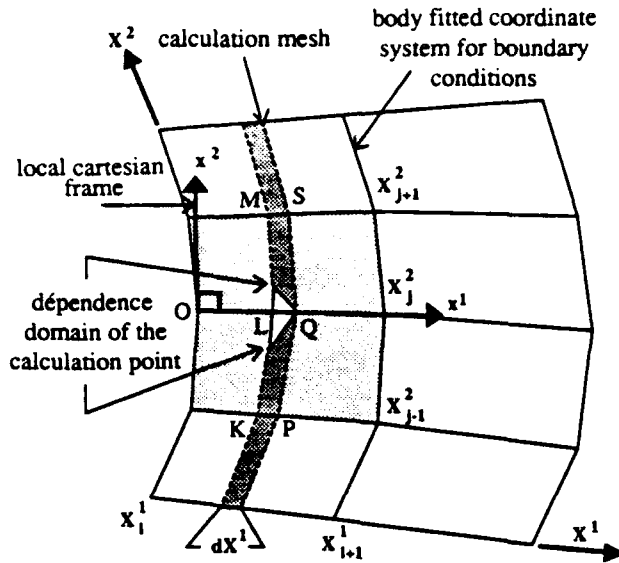


Figure 3 : Sub-calculation mesh with respect to the representation of the body fitted coordinate system in the tangent plane.

point  $O'$  of an euclidian space (E). The reference frame  $(\vec{e}_i)$ ,  $i = 1, 2$  at this point is such that

$$\vec{e}_i)_{O'} = \vec{e}_i)_O \quad (9)$$

This leads to the equality for the metric elements

$$g_{ij})_{O'} = g_{ij})_O \quad (10)$$

It can be noted that if the points  $O$  and  $O'$  are identical, the euclidian space (E) which has been built is simply the tangent plane to the surface at  $O$ . In order to give to (E) the metric properties that represent the vicinity of point  $O$  of (S), we impose

$$\Gamma_{ij}^k)_{O'} = \Gamma_{ij}^k)_O \quad (11)$$

This allows to represent the body fitted coordinate system in the vicinity of point  $O$  by a curvilinear coordinate system in the tangent plane while respecting the distances to the second order (fig. 2-b). For this reason, the tangent plane is called osculator plane. With the condition (11), the image  $P'$  in (E) of a point  $P$  in (S) near the point  $O$  is given by

$$\vec{O'P'} = (\vec{e}_i)_O \left[ dx^i + \frac{1}{2} (\Gamma_{jk}^i)_O dx^j dx^k \right] \quad (12)$$

After the construction of the mesh in the neighbourhood of  $O$  in the tangent plane, the representation of the velocity field is simply done: the velocity vectors are known, for example, by their modulus and directions with respect to the lines  $X^1$  on the surface. The directions with respect to the curvilinear mesh in the tangent plane are assumed to be the same (fig. 2-c). Knowing the geometry of the mesh and the velocity at the nodes, the calculation of the covariant derivatives of the velocity is straightforward. With the

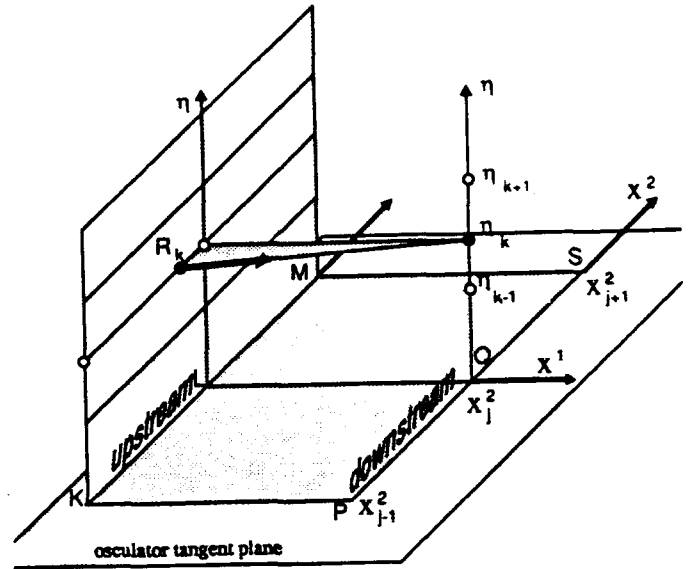


Figure 4 : Discretization of the momentum and energy equations.

representation which has been adopted, the precision of this calculation is of first order.

The covariant derivative of a vector is an intrinsic quantity which does not depend on the reference mesh. This quantity exists even if discontinuities of the slope of the coordinate lines are present. In this case, the Christoffel coefficients are not defined and the velocity components are discontinuous. Such a configuration can be dealt with if the osculator tangent plane is built without using the Christoffel coefficients. It can be shown that the construction which has been described is equivalent to the orthogonal projection of the body fitted coordinate system, and the velocity field, in the tangent plane at a given point. This transformation respects the lengths and the angles to the second order, which allows to express the covariant derivatives to the first order.

## Basic equation

It has been shown that the integration of the boundary layer equations could be done in the tangent plane instead of using the generalized coordinates. For this reason, the equations can be written in cartesian coordinates. For a compressible turbulent boundary layer, equations (2a), (4a) and the energy equation become

$$\frac{\partial \rho u^i}{L \partial x^i} + \frac{\partial \rho \bar{u}^3}{L \partial \eta} = -\frac{\rho u^i}{L} \frac{\partial L}{\partial X^i} \quad i = 1, 2 \quad (13a)$$

$$\rho |\vec{u}| \frac{du^a}{ds(\eta)} + \rho \bar{u}^3 \frac{\partial u^a}{L \partial \eta} = \rho_e |\vec{u}_e| \frac{du_e^a}{ds(\delta)} + \frac{\partial}{L^2 \partial \eta} \left( \mu_{eff} \frac{\partial u^a}{\partial \eta} \right) \quad \alpha = 1, 2 \quad (13b)$$

$$\rho |\vec{u}| \frac{dh_s}{ds(\eta)} + \rho \vec{u}^3 \frac{\partial h_s}{L \partial \eta} = \frac{\partial}{L^2 \partial \eta} \left[ \frac{\lambda_{eff}}{C_p} \frac{\partial h_s}{\partial \eta} + \left( \mu_{eff} - \frac{\lambda_{eff}}{C_p} \right) \frac{\partial}{2L \partial \eta} ((u^1)^2 + (u^2)^2) \right] \quad (13c)$$

with

$$\vec{u}^3 = u^3 - \eta \left( u^1 \frac{\partial L}{\partial x^1} + u^2 \frac{\partial L}{\partial x^2} \right) \quad (14)$$

and the equation of the streamline parallel to the wall

$$\frac{dx^1}{u^1} = \frac{dx^2}{u^2} \quad (15)$$

$dx^1$  is given by the marching step along the  $x^1$ -lines, roughly in the general direction of the flow.  $du^a$  is the variation of the  $u^a$ -component of the velocity over the distance  $ds$  along a streamline. The energy equation (13c) is written for the total enthalpy  $h_s$

$$h_s = C_p T + \frac{|\vec{U}|^2}{2} \quad (16a)$$

and the effective viscosity coefficient is expressed as follows

$$\mu_{eff} = \mu + \gamma \mu_t \quad (17a)$$

where  $\mu$  is the dynamic viscosity coefficient given by the law of Sutherland,  $\mu_t$  the eddy viscosity coefficient and  $\gamma$  the intermittency function which is equal to 0 for laminar flow and 1 in turbulent boundary layer. In the transition region,  $\gamma$  depends on the thickening of the boundary layer represented by the ratio of the momentum thickness to the momentum thickness at the beginning of the transition region,  $\theta/\theta_T^4$ .

Since the first objective of this study is the validation of the numerical technique, including the discretization scheme and the use of the osculator tangent plane, a simple turbulence model is used. The model is a direct extension of the mixing length formulation commonly used in two-dimensional flows<sup>12</sup>, with the damping function proposed by Cebeci<sup>8</sup>

$$\tau_{x^1} = \mu \frac{\partial u^1}{\partial x^3} - \overline{\rho u^1 u^3} = (\mu + \mu_t) \frac{\partial u^1}{\partial x^3} \quad (18a)$$

$$\tau_{x^2} = \mu \frac{\partial u^2}{\partial x^3} - \overline{\rho u^2 u^3} = (\mu + \mu_t) \frac{\partial u^2}{\partial x^3} \quad (18b)$$

$$\mu_t = \rho l^2 F^2 \sqrt{\left( \frac{\partial u^1}{\partial x^3} \right)^2 + \left( \frac{\partial u^2}{\partial x^3} \right)^2} \quad (18c)$$

$$\frac{l}{\delta} = 0,085 \tanh \left( \frac{0,41}{0,085} \frac{x^3}{\delta} \right) \quad (18d)$$

with

$$F = 1 - \exp \left( -\frac{y^+}{A} \right) \quad y^+ = \frac{y u_\tau}{\nu} \quad (19a)$$

$$A = \frac{26}{N} \frac{\nu}{u_\tau} \sqrt{\frac{\rho}{\rho_w}} \quad u_\tau = \sqrt{\tau_w / \rho} \quad (19b)$$

$$N = \sqrt{1 - 11,8 \frac{\mu_w}{\mu_e} \left( \frac{\rho_e}{\rho_w} \right) \left( \frac{\nu_e u_e}{u_\tau^3} \frac{du_e}{ds_e} \right)} \quad (19c)$$

In these relations, only applicable in a cartesian reference frame,  $u_e$  is the modulus of the external velocity and the friction velocity.

## Laminar-turbulent transition

### Longitudinal instability mode

Two criteria are used to predict the onset of transition. Both are based on stability calculations for the self-similar Falkner-Skan velocity profiles and on the relation proposed by Mack<sup>26</sup> to link the total amplification coefficient  $n$  of the most unstable instability waves, at the point of transition, to the turbulence level of the external flow

$$n_T = -2.4 \ln T_u - 8.43 \quad (20)$$

In a first criterion proposed by Arnal *et al.*<sup>1</sup>, the velocity profile is characterized by the mean value of the Pohlhausen parameter  $\bar{\Lambda}_2$ , and  $n$  is represented as a function of  $(R_{\theta_{11}} - R_{\theta_{11cr}})$  and  $\bar{\Lambda}_2$

$$R_{\theta_{11}} - R_{\theta_{11cr}} = -206 \exp(25.7 \bar{\Lambda}_{2T}) [\ln(16.8 T_u) - 2.77 \bar{\Lambda}_{2T}] \quad (21a)$$

$$\bar{\Lambda}_2 = \frac{1}{x - x_{cr}} \int_{x_{cr}}^x \frac{\theta_{11}^2}{\nu} \frac{du_e}{dx} dx \quad (21b)$$

To determine the critical value of the momentum thickness  $\theta_{11cr}$  corresponding to the point  $x_{cr}$ , the calculated value of  $\theta_{11}$  is compared to the corresponding value of  $\theta_{11cr}$ , given by the stability diagrams and represented by the correlation

$$\theta_{11cr} = \exp \left( \frac{52}{H_i} - 14.8 \right) \quad H_i = \frac{\delta_{11}^2}{\theta_{11}} \quad (22)$$

As soon as  $R_{\theta_{11}}$  becomes equal to  $R_{\theta_{11cr}}$ , the instability waves become amplified and  $x_{cr}$  is reached.

The second longitudinal criterion, proposed by Arnal<sup>4</sup>, is a parametric type method. For a given velocity profile, characterized by the shape parameter  $H_i$ , the local amplification coefficient  $\sigma$ , corresponding to the frequency  $F$ , is represented as a function of  $R_{\theta_{11}}$  in the form of two half-parabols. This allows a simplified representation of the stability diagrams with a minimum number of parameters. Knowing the evolution of the shape parameter  $H$  along an external streamline, the total amplification coefficient is calculated and equation (20) is used to determine the onset of transition.

### Streamwise instability mode

To predict this mode of transition particular to three-dimensional flows, two criteria can be used. The first one is an extension made by Coustols<sup>15</sup> of a criterion originally proposed by Beasley<sup>7</sup>. The transition occurs when the Reynolds number based on the streamwise displacement thickness  $\delta_1$  becomes larger than a critical value which is a function of the

longitudinal incompressible shape parameter. More precisely, this criterion reads

$$R_{\delta_2 T} = 95.5 \arctan \left( \frac{0.106}{(H_1 - 2.3)^{2.052}} \right) \quad 2.3 < H_1 < 2.7 \quad (23a)$$

$$R_{\delta_2 T} = 150 \quad H_1 < 2.3 \quad (23b)$$

With this criterion, the influence of the turbulence level of the external flow is not taken into account.

The second criterion, also developed by Coustols and Arnal<sup>4,3</sup> requires a more important numerical effort and cannot be detailed here. At each calculation station, the most unstable direction  $\epsilon$  of the velocity profiles in the vicinity of the crossflow direction must be determined. The transition occurs when the Reynolds number defined with the displacement thickness in the  $\epsilon$  direction becomes larger than a given value which is a function of the turbulence level of the external flow. The number and location of the inflection points of the velocity profile in the  $\epsilon$  direction are also taken into account in order to represent the results of stability calculations for three-dimensional boundary layers.

## Numerical scheme

The momentum and energy equations (13b) (13c) are discretized in the tangent plane according to the scheme presented in figure 4. At the unknown station  $Q$ , the diffusion terms are written at 3 points and the advection term is taken between the points  $R_k$  and  $\eta_k$ .  $R_k$  is the origin at the upstream station of the streamline going through the point  $\eta_k$ . At this stage, all the quantities are known.  $R_k$  is calculated according equation (15) assuming a linear variation of the velocity components at the upstream stations. This discretization scheme leads, after linearization, to three tridiagonal matrices which can be inverted independently to give the two velocity components  $u^1$  and  $u^2$  and the total enthalpy  $h_t$ . The scheme is stable whatever the location of points  $R_k$  may be. In practice, the marching step along  $X^1$  is limited in order that  $R_k$  remains between the two adjacent stations  $K$  and  $M$  of the calculation point (fig.4). This constraint is identical to the CFL condition of a semi-explicit scheme.

To complete the integration, the normal velocity component  $u^3$  is calculated using the continuity equation (13a).

The  $x^1$ -derivatives are taken between the points  $L$  and  $Q$  and the  $x^2$ -derivatives are deduced from the relation

$$(\rho u^2)_M - (\rho u^2)_K = \left( \frac{\partial \rho u^1}{\partial x^1} \right)_L (x_M - x_K) + \left( \frac{\partial \rho u^2}{\partial x^2} \right)_L (z_M - z_K) \quad (24a)$$

with  $x^1$  and  $x^2$  the cartesian coordinates in the tangent plane defined in figure 3.

At each station  $X^1$ , the boundary layer parameters are calculated for all the points in the  $X^2$  direction. This is always done in the direction of the increasing values of  $X^2$ ,

whatever the crossflow direction may be, because the calculation at a particular station is independent of the neighbouring points. The process is repeated in the subgrid calculation in the  $X^1$  direction up to the station  $X_{i+1}^1$  of the body fitted coordinate system in which the boundary conditions are given. At this point, the change of direction  $\alpha$  of the coordinate system must be taken into account. Since it is imposed that the calculation subgrid coincides with the station  $X_{i+1}^1$ ,  $\alpha$  does not have to be necessarily small. This means that slope discontinuities of the reference mesh can be correctly treated. A new osculator tangent plane is calculated at each node  $X_j^2$  of the station  $X_{i+1}^1$  and the calculation process continues.

## 4 APPLICATION TO A PROLATE SPHEROID

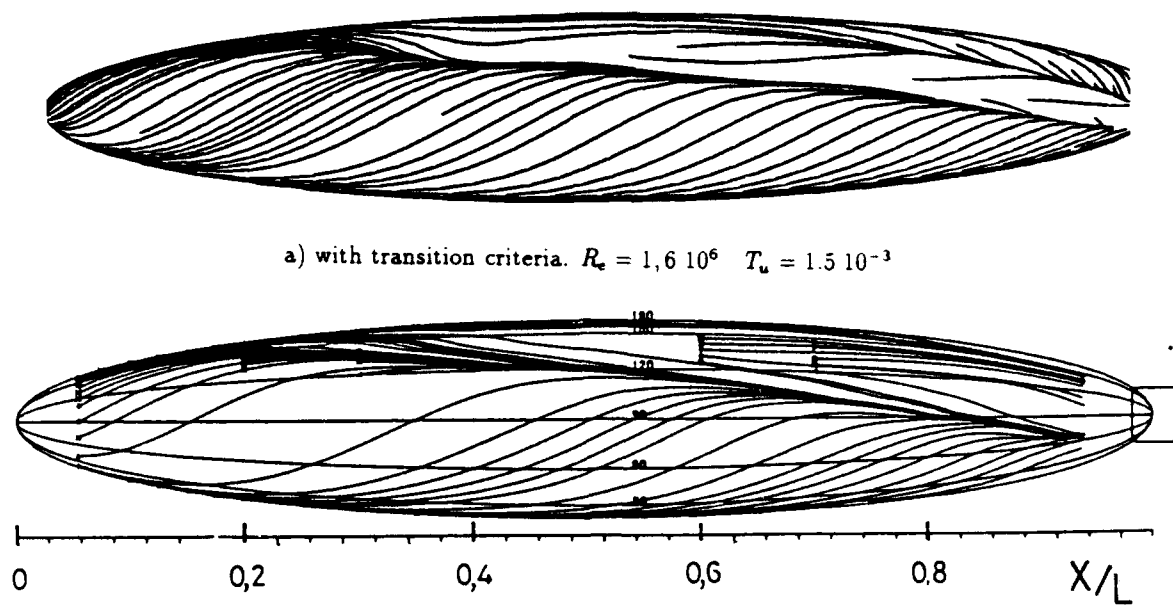
To illustrate some capabilities of the method to predict complex three-dimensional boundary layers, we will consider the prolate spheroid with an aspect ratio equal to 6 at a  $10^\circ$  incidence. A number of experimental studies have been devoted to this case, in particular at the DLR<sup>28,29,30</sup>. At the chosen incidence, the experimental pressure field remains close to the analytical inviscid pressure field. Moreover, the stagnation point is sufficiently close to the nose of the body to use the simple body fitted coordinate system made of ellipses passing through the two poles and circles included in planes perpendicular to the symmetry axis of the body.

In figure 5-c, the light lines show the inviscid streamlines at the wall and the thickest lines represent the friction lines for a fully laminar boundary layer. The friction lines converge to form the separatrix line<sup>23,32</sup>. Along it, a strong

thickening of the boundary layer occurs, leading to the abandon of the corresponding calculation line after  $X/L = 0.8$ . Figure 5-a shows the wall friction lines obtained by taking into account the transition phenomenon. With  $R_L = 1.6 \cdot 10^6$  and a turbulence level equal to  $1.5 \cdot 10^{-3}$ , the boundary layer remains laminar in the windward side up to the separation line, and turbulent in the leeward side. In the latter side, the accumulation of the friction lines for  $X/L > 0.7$  can be interpreted as a secondary separation. In figure 5-b are plotted the friction lines calculated by Meier *et al.*<sup>29,30</sup> from measurements of the skin friction. At a  $10^\circ$  incidence, the influence of the flow separation on the pressure field remains small which explains the good agreement concerning the location of the separation line in figures 5-b and 5-a. The comparison of figures 5-a and 5-c shows the great influence of the transition phenomenon.

The same results are presented in figure 6 at a higher Reynolds number of  $7.2 \cdot 10^6$ . The transition to turbulence occurs sooner, which leads to the displacement of the separation line towards the leeward region and suppresses the secondary separation.

In figure 7 are plotted the longitudinal and streamwise displacement thicknesses  $\delta_1$  and  $\delta_2$  as well as the shape parameter. They are compared to experimental results obtained by Meier *et al.* at  $X/L = 0.64$  and  $0.71$ . The development of separation is characterized by a thickening of  $\delta_1$  and

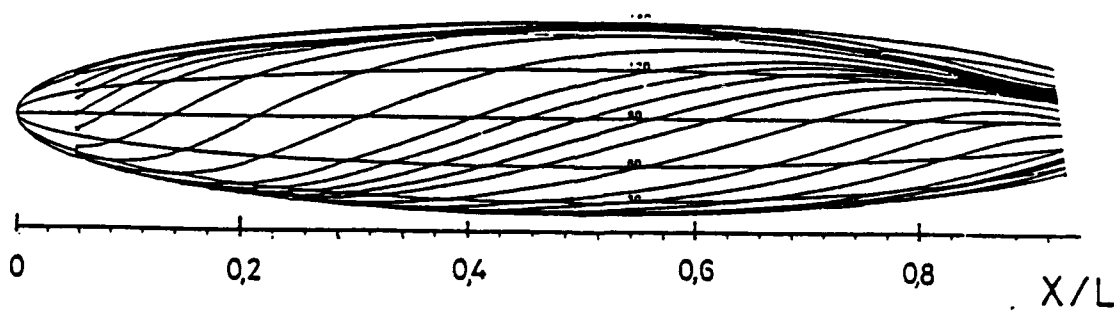


b) experimental results from *DLR*<sup>30</sup>



c) laminar calculation

Figure 5 : Ellipsoide at 10° incidence.



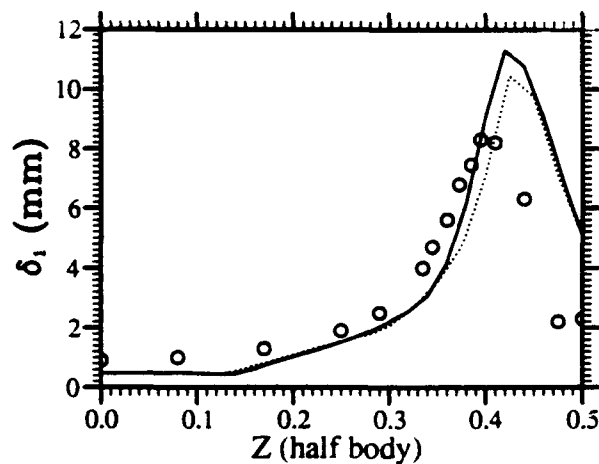
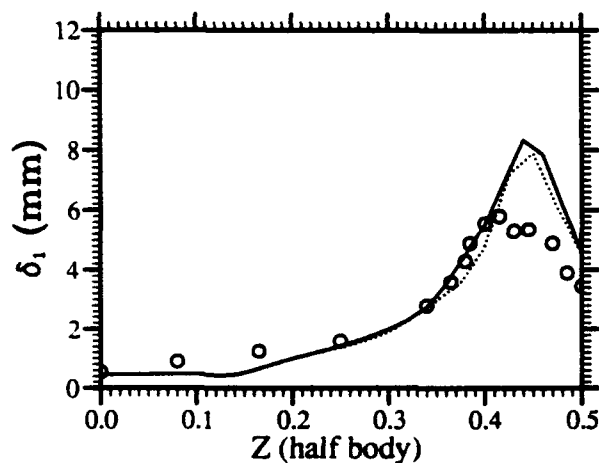
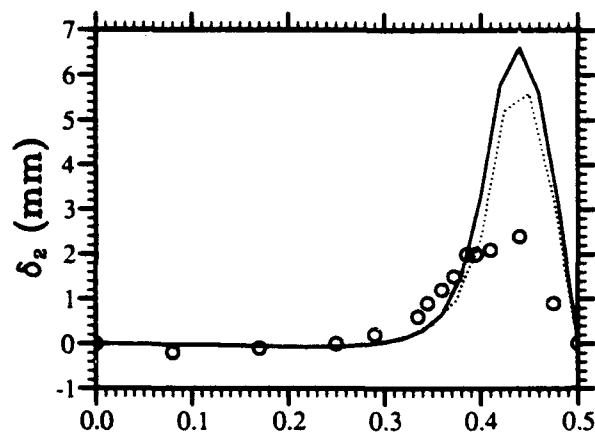
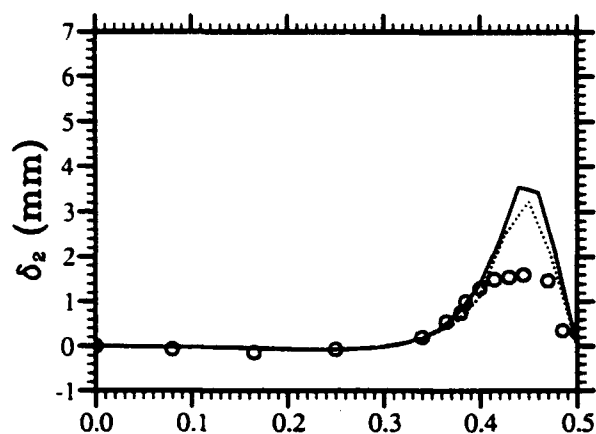
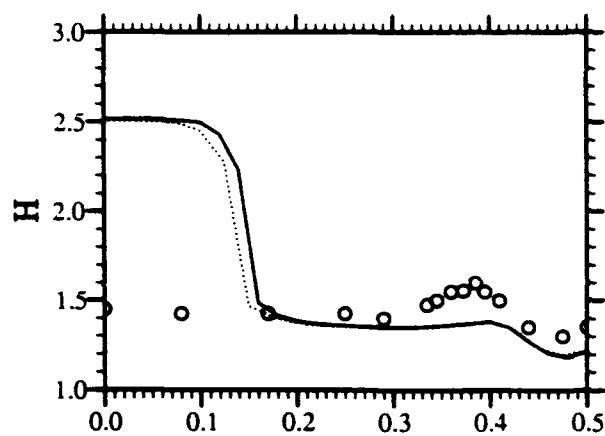
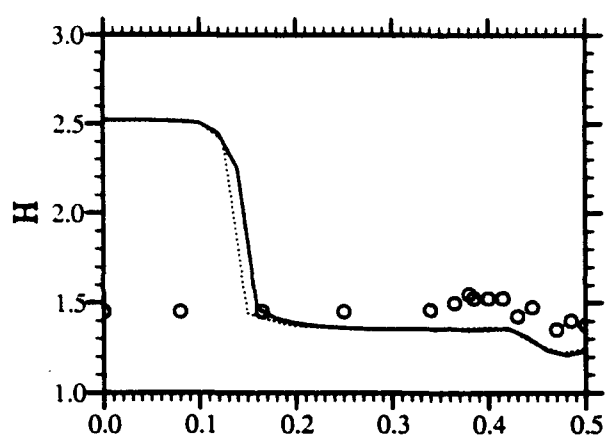
a) experimental results from *DLR*<sup>30</sup>



b) wall friction lines.  
 $R_e = 7,2 \cdot 10^6$   $T_u = 1,5 \cdot 10^{-3}$ .

Figure 6 : Ellipsoide at 10° incidence.





$X/L = 0,64$

$X/L = 0,71$

— with theoretical external velocity  
 ..... with experimental pressure field  
 ○ experiment

$R_e = 7,2 \cdot 10^6 \quad T_u = 1,5 \cdot 10^{-3}$

Figure 7 : Ellipsoide at  $10^\circ$  incidence.

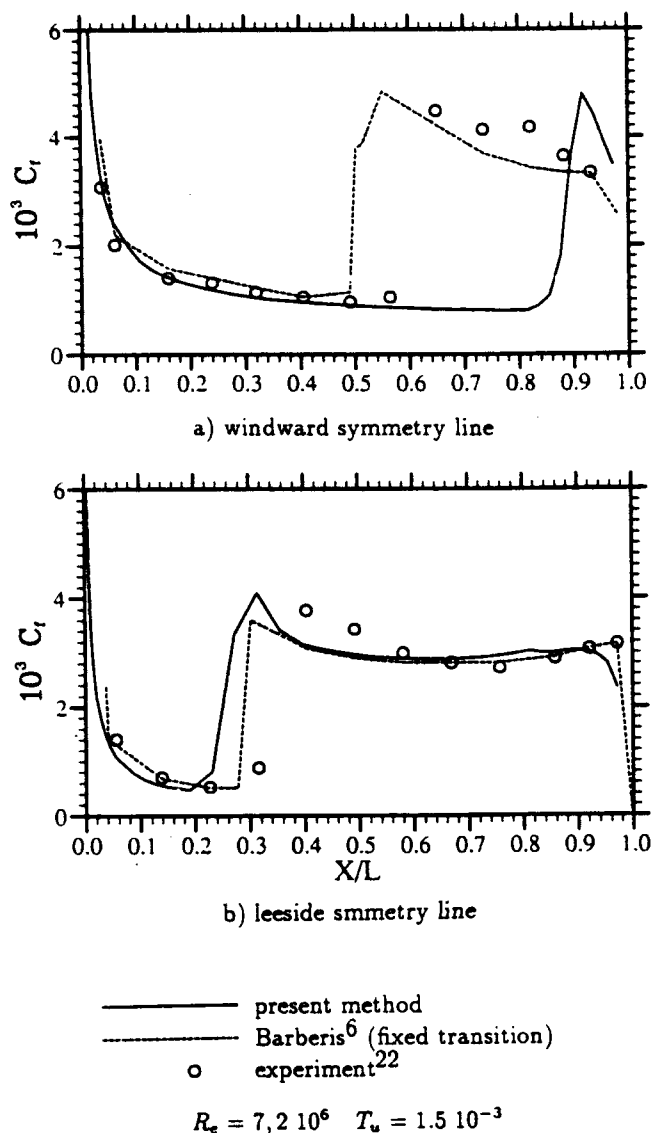


Figure 8 : Ellipsoïde at  $10^\circ$  incidence.

$\delta_2$ , particularly important at  $X/L = 0.71$ . The evolution of the longitudinal shape parameter  $H$  is mainly sensitive to the nature of the boundary layer. To perform the calculation with the present method, the analytical inviscid flow field has been used as well as the experimental pressure field. The influence on the results remains small. The most critical point concerns the prediction of the transition. The external turbulence level is equal to  $1.5 \cdot 10^{-3}$ , as in the experiments. With the present calculation methods all the transition criteria have been set active and the first one to predict transition is retained. As it can be seen in the evolution of  $H$  in figure 7, the location of the onset of the transition near the windward plane of symmetry is not correctly predicted. This is difficult to explain because the transition occurs along this line by amplification of the longitudinal instability waves which are calculated by the second criterion<sup>5</sup>. Maybe the use of the linear instability theory along a symmetry line with a divergent flow from this line must be questioned. Figure 7, showing the skin friction evolution along the windward and leeward lines in the symmetry

plane, indicates that the calculated transition point is located at  $X/L = 0.85$  with a turbulence level equal to  $1.5 \cdot 10^{-3}$ . This turbulence level gives the correct location of the transition line in the lee side region of the body. Its experimental value is estimated between 1 and  $2 \cdot 10^{-3}$ . By taking the largest value of turbulence level, the transition occurs at  $X/L = 0.73$  on the windward symmetry line, instead of 0.65 experimentally, but it reaches 0.17 on the upper symmetry line.

### Calculation time

In the present method, the marching step in the  $X^1$  direction is limited by the most deviated streamline at a given section. This step is also limited with respect to the boundary layer thickness  $\delta$ . For the prolate spheroid, the marching step was limited to be in the range  $0.6\delta_{\min}$  and  $2\delta_{\max}$ , the minimum and maximum values being taken in every section  $X^1$ . With this condition, roughly 1000 calculation steps are needed in the  $X^1$  direction. With 26 lines in the azimuthal direction (for a half-body), this corresponds on a CRAY XMP to 10 s for a fully laminar boundary layer and 30 s with all the transition criteria.

## 5 CONCLUSION

The three-dimensional boundary layer calculation method which has been presented is of semi-implicit type. The advection terms are discretized along the local streamlines. The dependence domains are thereby satisfied with a simple numerical scheme. The counterpart is a limitation on the size of the marching integration step. Despite this limitation, the efficiency of the method remains good due to the reduced amount of calculation at each step. This is partly a consequence of the use of local cartesian coordinates. The discretization of the equations in the osculator tangent plane allows the existence of slope discontinuities in the body fitted coordinate system in which the boundary conditions are given. It also often reduces or suppresses the pre-treatment phase of the data for a calculation.

Although the application cases which have been presented only deal with the prolate spheroid at incidence in incompressible flow, the application range of the code is very large. It extends from subsonic to hypersonic flows.

For turbulent boundary layers, the mixing length model which is used up to now is restrictive. The introduction of transport equation model is being done. It has also been tested that the present method can run in the inverse mode with only minor modifications.

## Références

- [1] D. Arnal : *Laminar-turbulent transition problems in supersonic and hypersonic flows*. AGARD/FDP/VKI Special Course "Aerothermodynamics of Hypersonic Vehicles", Rhode-Saint-Genèse, 30 may-3 june 1988
- [2] D. Arnal : *Transition prediction in transonic flow* IUTAM Symposium Transsonicum III DFVLR-AVA Göttingen 1988

- [3] D. Arnal, E. Coustols : *Application de critères bi- et tridimensionnels au calcul de la transition et de la couche limite d'ailes en flèche* Symposium AGARD "Improvement of aerodynamic performance through boundary layer control and high lift systems" Bruxelles may 1984
- [4] D. Arnal, E. Coustols, J.C. Juillen : *Transition sur une aile en flèche infinie*. La Recherche Aéronautique 1984-4 (1984)
- [5] D. Arnal, M. Habiballah, E. Coustols : *Laminar instability theory and transition criteria in two and three-dimensional flows*. La Recherche Aéronautique 1984-2 (1984) p. 45-63
- [6] D. Barberis : *Calcul de la couche limite tridimensionnelle en modes direct ou inverse sur des obstacles quelconques*. La Recherche Aéronautique, 1986-3 p.169-195
- [7] J.A. Beasley : *Calculation of the laminar boundary layer and the prediction of the transition on a sheared wing*. ARC R&M 3787 1973
- [8] T. Cebeci, A.M.O Smith : *Analysis of turbulent boundary layers*. Academic Press 1974
- [9] T. Cebeci, A. K. Khattab, K. Stewartson : *Three-dimensional laminar boundary layers and the effect of accessibility*. J. Fluid Mech. (1981), Vol.107, pp. 57-87
- [10] T. Cebeci : *Problems and opportunities with three-dimensional boundary layers*. AGARD May 1984
- [11] T. Cebeci : *An approach to practical aerodynamic configurations*. V.K.I Lecture Series, 14-18 april 1986
- [12] J. Cousteix, C. Quemard, R. Michel : *Application d'un schéma amélioré de longueur de mélange à l'étude des couches limites turbulentes tridimensionnelles*. AGARD CP N°93 on "Turbulent Shear Flows" (1971)
- [13] J. Cousteix : *Analyse théorique et moyens de prévision de la couche limite turbulente tridimensionnelle*. T.P. ONERA 157, 1974
- [14] J. Cousteix : *Three-dimensional boundary layers. Introduction to calculation methods* AGARD REPORT N°741
- [15] E. Coustols : *Stabilité et transition en écoulement tridimensionnel : cas des ailes en flèche*. Thèse de Docteur-Ingénieur ENSAE (Juin 1983)
- [16] E. H. Hirschel, W Kordulla : *Shear flow in surface-oriented coordinates*. Notes on numerical fluid mechanics, Vol 4, Vieweg, 1981.
- [17] D. A. Humphreys, J. P. F. Lindhout : *Calculation methods for 3D turbulent boundary layers*. Prog. Aerospace Sci. 25, 107-129 (1988)
- [18] V. Iyer, J. Harris : *Three-dimensional compressible boundary layer calculations to fourth order accuracy on wings and fuselages*. 27th Aerospace Sciences Meeting, January 9-12, 1989/Reno, Nevada AIAA 89-0130
- [19] M. Jelliti : *Transition du régime laminaire au régime turbulent : effets de la tridimensionnalité et de la compressibilité*. Thèse de l'ENSAE (1986)
- [20] L. J. Johnston : *An upwind scheme for the three-dimensional boundary layer equations*. International Journal for Numerical Methods in Fluids, Vol 11, 1043-1073 (1990)
- [21] E. Krause : *Numerical treatment of boundary layer problems*. AGARD Lectures Series 64 in Advances in Numerical Fluid Dynamics (1973)
- [22] H. P. Kreplin, H. Vollmers, H. U. Meier : *Experimental determination of wall shear stress vectors on an inclined prolate spheroid*. Proc. 5th US/FRG DEA meeting AFFDL-TR-80-3088, (1980), p. 315-332. Numerical Fluid Dynamics (1973)
- [23] R. Legendre : *Lignes de courant d'un écoulement permanent. Décollement et séparation*. La Rech. Aéro. Nov.-déc. 1977
- [24] J. P. F. Lindhout, E. Boer : *A program for the computation of a compressible turbulent boundary layer under infinite swept wing conditions*. NLR TR 75090 U (1975)
- [25] J. P. F. Lindhout, G. Moek : *A method for the calculation of 3D boundary layers on practical wing configurations*. NLR MP 79003 U (1979)
- [26] L. M. Mack : *Transition prediction and linear stability theory*. AGARD Conference Proceedings 224, NATO, PARIS (1977)
- [27] K. Matsuno : *A vector-oriented finite difference scheme for calculating three-dimensional compressible laminar and turbulent boundary layers on practical wing configurations*. AIAA paper 81-1020
- [28] H. U. Meier, H. P. Kreplin : *Experimental investigation of the boundary layer transition and separation on a body of revolution*. 2<sup>nd</sup> Symposium on Turbulent Shear Flows. London Jul. 1979
- [29] H. U. Meier, H. P. Kreplin, H. Vollmers : *Development of boundary layer and separation patterns on a body of revolution at incidence*. 2<sup>nd</sup> Symposium on Numerical and Physical Aspects of Aerodynamic Flows, Long Beach, Jan. 1983
- [30] H. U. Meier, H. P. Kreplin, A. Landhausser, D. Baumgarten : *Boundary layers developing on a 1:6 prolate spheroid with natural transition*. Rapport interne DFVLR IB 222-84 A10 1984

- [31] V. C. Patel, J. H. Baek : *Calculation of three-dimensional boundary layers on bodies at incidence*. Iowa Inst. of Hydraulic Research Rept. No 256 (1982)
- [32] D. J. Peake, M. Tobak : *Three-dimensional interactions and vortical flows with emphasis on high speed*. NASA TM-81169 AGARDograph 252, July 1980.
- [33] P. D. Smith : *The numerical computation of three-dimensional turbulent boundary layers*. In: IUTAM Symposium on Three Dimensional Turbulent Boundary Layers. Springer Verlag, 1982, 265-185
- [34] A. Tassa, E. H. Atta, L.A. Lemmerman : *A new three-dimensional boundary layer calculation method*. AIAA Paper 82-0224
- [35] K. C. Wang : *On the determination of the zones of influence and dependence for three-dimensional boundary layer equations*. J. Fluid Mech., Vol.48, Part 2, pp. 397-404
- [36] K. C. Wang : *Boundary layer over a blunt body at low incidence with circumferencial reverse flow*. J. Fluid Mech., Vol.72, Part 1, pp. 49-65

# Towards Industrial-Strength Navier-Stokes Codes

Wen-Huei Jou, Laurence B. Wigton, Steven R. Allmaras,

Philippe R. Spalart, N. Jong Yu

Boeing Commercial Airplane Group

P.O. Box 3707, MS 7H-96

Seattle, WA 98124-2207

## Abstract

In this paper we discuss our experiences with Navier-Stokes (NS) codes using central differencing (CD) and scalar artificial dissipation (SAD). NS-CDSAD codes have been developed by Jameson, Martinelli, Swanson, and Vatsa among others. Our results confirm that for typical commercial transport wing and wing/body configurations flying at transonic conditions with all turbulent boundary layers, NS-CDSAD codes, when used with the Johnson-King turbulence model, are capable of computing pressure distributions in excellent agreement with experimental data. However, results are not as good when laminar boundary layers are present. Exhaustive 2-D grid refinement studies supported by detailed analysis suggest that the numerical errors associated with SAD severely contaminate the solution in the laminar portion of the boundary layer. It is left as a challenge to the CFD community to find and fix the problems with Navier-Stokes codes and to produce a NS code which converges reliably and properly captures the laminar portion of the boundary layer on a reasonable grid.

## Introduction

Boeing's recent acquisition of a CRAY Y-MP has enabled us to perform definitive grid-refinement studies with NS codes. We will focus attention on Jameson-technology (JT) codes developed by, among others, Jameson [1], Martinelli [2], Swanson [3], and Vatsa [4]. JT-NS codes employ central differences (CD) with scalar artificial dissipation (SAD). From the point of view of accuracy in a Navier-Stokes calculation, CDSAD is thought by some not to be as good as other available methods. Indeed, van Leer [5] boldly states that there is no hope for the flux formula of the Jameson type. Nonetheless, the combination of CDSAD with Runge-Kutta time marching, augmented with implicit residual smoothing and multigrid, have given JT codes a well deserved reputation of being fast and reliable compared

to other available methodologies. Thus JT-NS codes have achieved a wide following in the CFD community.

In this paper we will present some applications of JT-NS codes to 3-D and 2-D problems of aerodynamic interest, including wing/body, nacelle, airfoil and multi-element airfoil configurations.

We will begin our discussion with an account of the relative success of JT-NS codes applied to 3-D wing/body configurations with turbulent flow. We will follow with a somewhat sadder tale for 2-D airfoils involving runs of laminar flow. Our attempts to locate the problems with 2-D JT-NS have included detailed grid refinement studies which indicate numerical problems particularly in the laminar portion of the boundary layer. These numerical problems are discussed at length. The inability of JT-NS codes to properly capture the laminar portion of the boundary layer (on a reasonable grid) prevents us from including a stability analysis needed to predict the onset of transition. We give examples where transition prediction is very important, including flow around a high-lift multi-element airfoil configuration and for around a nacelle.

## Wing and Wing/Body Analysis and Design

In this section we will compare the capabilities of the JT-NS code TLNS3D developed at NASA Langley [4], using the Johnson-King turbulence model [6], with our traditional viscous/inviscid coupled code A488.

In figure (1) we show a comparison, for a supercritical wing near design conditions, between experimental data, TLNS3D, and A488. The TLNS3D solution matches well with test data, whereas the A488 solution places the shock too far back. For the many test cases, TLNS3D has proven to be consistently more accurate than A488 [7, 8].

Another advantage TLNS3D enjoys over A488 is the ability to predict flows at off-design conditions involving

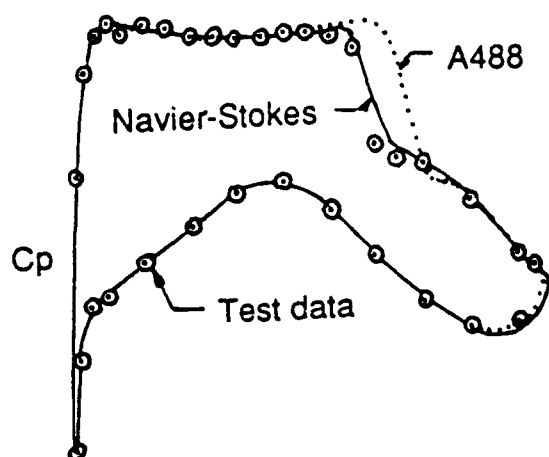


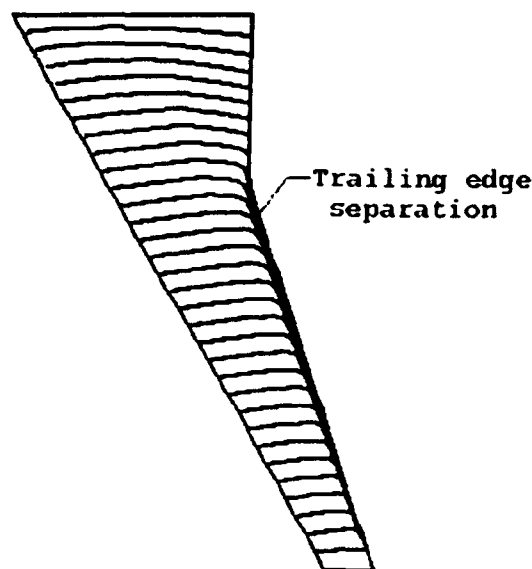
Figure 1: 3-D Navier-Stokes versus A488

flow separation. Figure (2) shows wing upper surface streamlines and pressure distributions at 65% semispan station. TLNS3D properly predicts the trailing edge separation and detailed surface pressures.

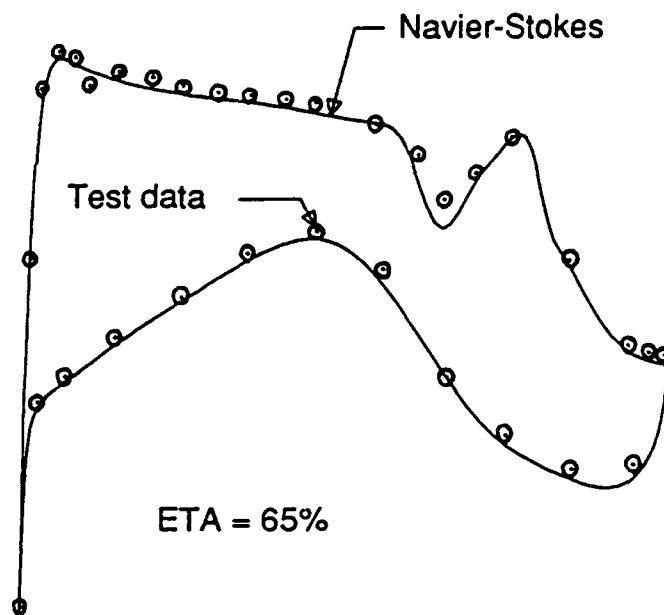
Encouraged by these successful analysis runs using TLNS3D, work has begun on design. An iterative design method that allows the designer to prescribe desired pressure distributions together with geometry constraints, such as thickness and trailing edge closure is under development. Preliminary results based on this method are shown in figure (3). Here the target geometry is the ONERA M6 wing, and the pressure distributions are given. Beginning with a NACA 0012 wing section as an input geometry, the target geometry is accurately recovered within 20 design cycles. A more detailed description of the design method is under preparation [9].

#### Practical CFD Assessment for Wing/Body

Generally speaking, the ability of TLNS3D to properly predict the pressures at both cruise and slightly off-design conditions is good. The main problems are laminar flow predictions and accurate drag predictions. Accurate drag predictions are crucial to design/optimization. Indeed, one of the design goals is to maximize the lift-to-drag ratio (under constraints). The designer will make a considerable effort to reduce drag by even as little as 1%. It is estimated that a 1% drag reduction, for a long-range airplane such as the Boeing 777, will save the airlines 6 billion dollars, based on a 2,000 airplane fleet operating over a 20 year service life [10]. Customer airlines require that tight performance guarantees be offered years before the airplane is actually built. In this tough commercial environment, the accuracy and reliability requirements must be very high if CFD is to be depended on to help fine tune final



a. Upper surface streamlines



b. Pressure distributions

Figure 2: 3-D Navier-Stokes Streamlines and Pressures at 65% semispan

## INVERSE DESIGN WITH NAVIER STOKES

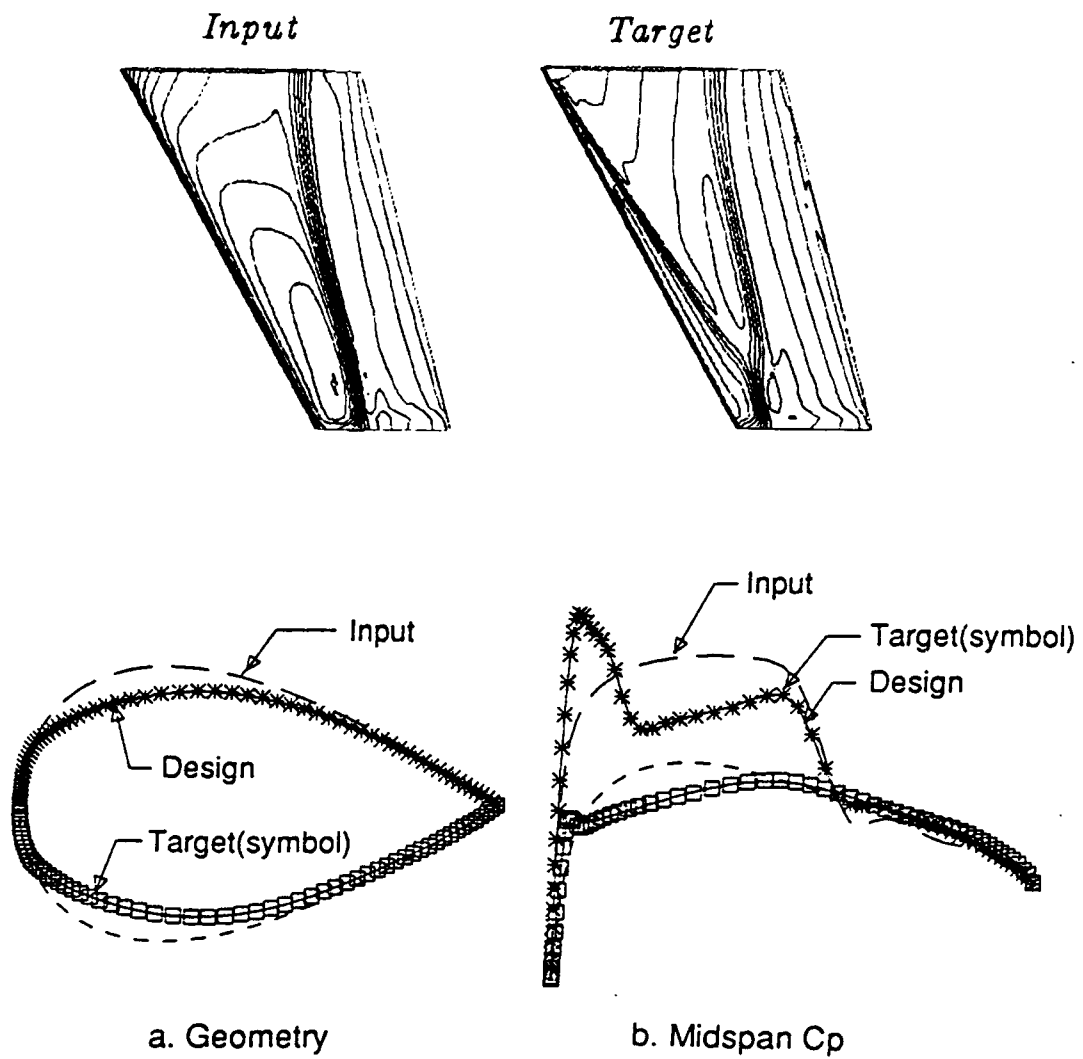


Figure 3: 3-D Navier-Stokes Design

designs and to establish meaningful performance guarantees.

## 2-D Airfoil Studies

The most direct 2-D equivalent to TLNS3D is the JT-NS code FLOMGE developed by Swanson [3] which also incorporates the Johnson-King turbulence model. For some flow situations, FLOMGE gives reasonable results. An example involving RAE 2822 case 6 is shown in figure (4).

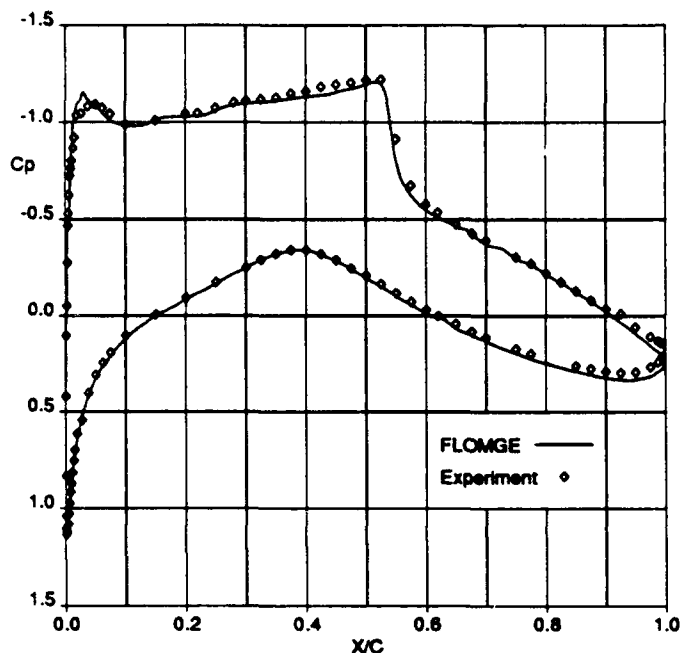


Figure 4: RAE 2822 Case 6 Surface Pressures; Comparison of FLOMGE with Johnson-King Model and Experiment [15]

There are, however, data cases which stress the credibility of all currently available 2-D airfoil codes. An apparently innocuous example is provided by the NACA 0012 airfoil at zero incidence. This condition removes the angle of attack as a "Fudge Factor". In figures (5) and (6) we compare experimental data [15] with results computed by FLOMGE and ISES (viscous/inviscid coupled code developed by Giles and Drela [13]) at two different Mach numbers. The solutions computed by FLOMGE and ISES agree well with each other at the lower Mach number, but the computed shock locations are too far back on the airfoil. At the higher Mach number, the ISES result is a little better than the FLOMGE solution, but again the shocks are too far back. The transition point for these calculations was placed at 3% of chord, but changing the transition point location drastically, say to 40% of chord, changes the shock location very little. These poor test/theory comparisons are present not only for ISES and FLOMGE but for all

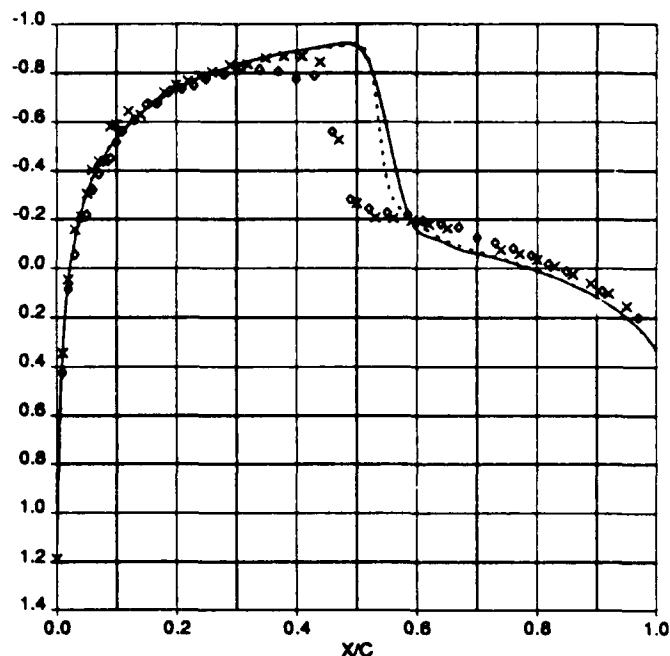


Figure 5: NACA 0012, experiment (Symbols) versus FLOMGE (Solid Line) and ISES (Dashed Line) at  $M = 0.814$ ,  $Re = 24.7 \times 10^6$ ,  $\alpha = 0^\circ$

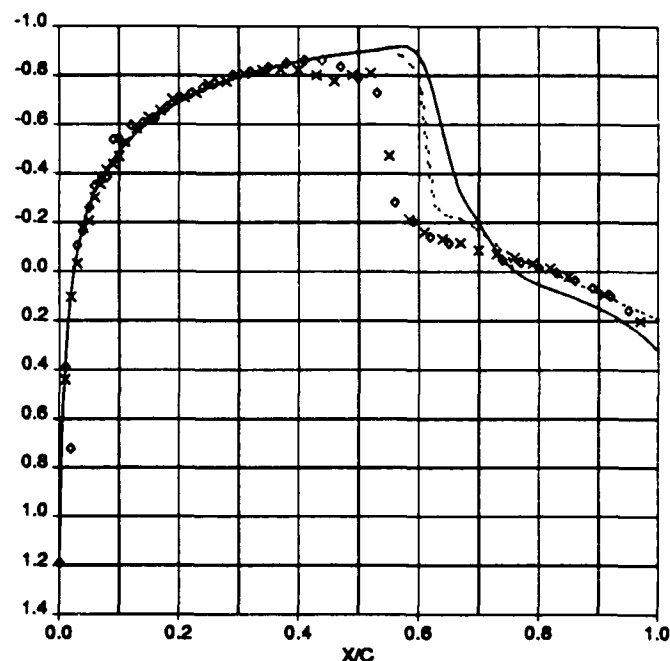


Figure 6: NACA 0012, experiment (Symbols) versus FLOMGE (Solid Line) and ISES (Dashed Line) at  $M = 0.835$ ,  $Re = 24.7 \times 10^6$ ,  $\alpha = 0^\circ$



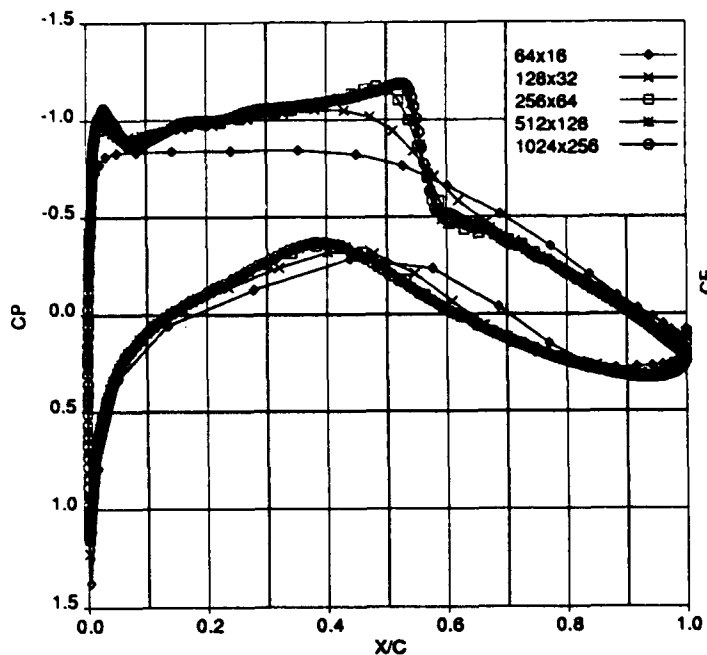


Figure 7: Pressure Distributions Computed on a Sequence of Grids ( $64 \times 16$ ) through ( $1024 \times 256$ ) for RAE 2822 Case 7.

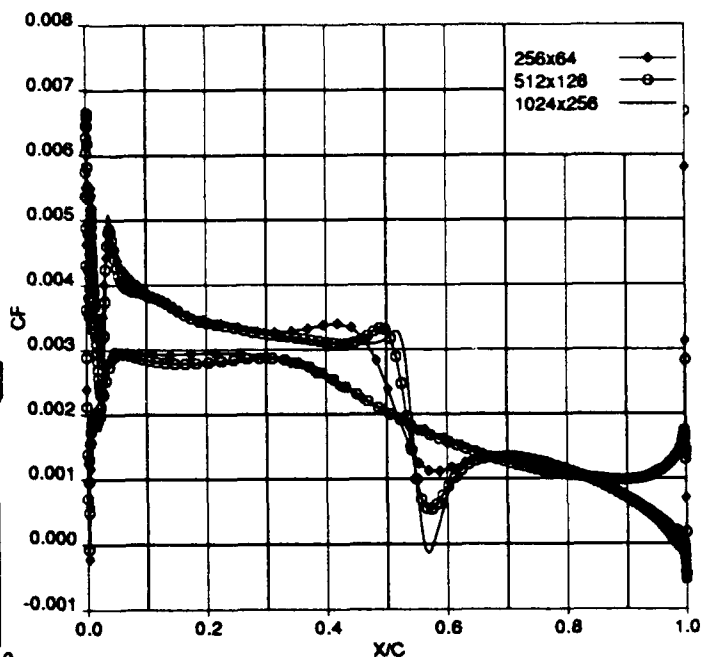


Figure 9: Skin Friction Computed on ( $256 \times 64$ ) through ( $1024 \times 256$ ) Grids for RAE 2822 Case 7.

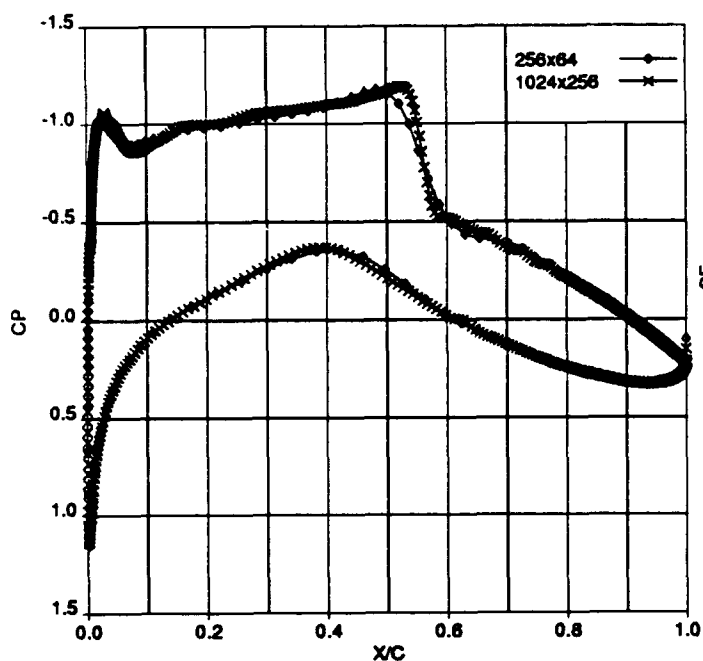


Figure 8: Pressure Distributions Computed on ( $256 \times 64$ ) and ( $1024 \times 256$ ) Grids for RAE 2822 Case 7.

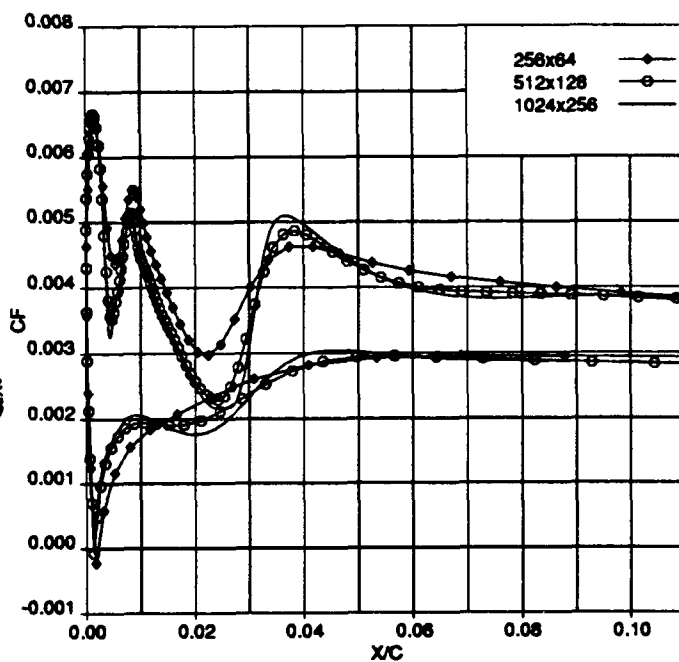


Figure 10: Skin Friction Computed on ( $256 \times 64$ ) through ( $1024 \times 256$ ) Grids for RAE 2822 Case 7 (Focus Near Leading Edge).

Navier-Stokes codes we have tried and for all turbulence models.

We realize that one must properly account for wind tunnel effects, especially for 2-D flows. However in the NACA 0012 test case it would require a Mach number reduction of more than 0.02 to produce a reasonable test/theory comparison. The large number of comparisons we have made between experimental data, ISES, and available 2-D Navier-Stokes codes suggest that there really is something wrong with the Navier-Stokes codes and/or the wind tunnel data which must be corrected.

## 2-D Grid Refinement Studies

As part of our program to find out if something is ailing the 2-D Navier-Stokes codes, we have taken advantage of the large memory afforded by our CRAY Y-MP to make exhaustive grid convergence studies. We have conducted such studies using the central-difference scheme of Martinelli and Jameson [2]. A grid refinement study for RAE 2822 case 7 is shown in figures (7) through (10). The flow conditions for this calculation were taken to be  $M_\infty = 0.73$ ,  $\alpha = 2.0^\circ$  and  $Re = 6.5 \times 10^6$  (based on chord). Transition was set at 3% of chord.

## Trailing Edge Glitches

Glitches in the solution at the trailing edge are quite apparent. These glitches are characteristic of JT-NS codes for airfoils with a finite trailing-edge angle. The glitches do not go away with grid refinement. If anything, they tend to increase in amplitude. We have not found a satisfactory cure for these glitches but they can be ameliorated by turning off the fourth order artificial dissipation near the trailing edge.

## Martinelli Compromise

On the 512 by 128 mesh (10), the transition from laminar to turbulent flow takes place over about 10 grid points. This spreading out of transition is caused by the "Martinelli Compromise" in the artificial dissipation, which has become common practice in JT-NS codes. The "Martinelli Compromise" is introduced to enhance convergence on grids with high-aspect ratio cells characteristic of a Navier-Stokes calculation [2]. Since JT codes depend on explicit time marching, the local time step they are permitted to use depends on how long it takes information to traverse the cell in the short direction. For a high aspect ratio cell this does not provide time for information to traverse the cell in the long direction. To ensure convergence, Martinelli dissipates the information traveling in the long direction by augmenting the artificial dissipation in this direction. The

factor by which the artificial dissipation is augmented is proportional to the cell aspect ratio raised to the 2/3's power. Thus in the case of a 1000-to-1 aspect-ratio cell, the artificial dissipation in the long direction is multiplied by 100.

The "Martinelli Compromise" does serve to improve the speed and reliability of convergence, but as can be seen clearly at the transition point, the quality of the solution is indeed compromised. In some JT codes the ill effects of augmenting the artificial dissipation are diminished by reducing the 2/3's power to something smaller like 1/2 or even 0.3. The artificial dissipation in ARC2D [16] is essentially the same as that present in JT codes, except that no compromise is introduced. As a result, transition in ARC2D typically takes place over 3 points. On the other hand it has been our experience that ARC2D does not converge as reliably or as fast as JT codes.

## Laminar Flow Convergence

In looking at figures (7) through (10) one notices that, as grid density is increased, the airfoil surface pressure distribution first begins to lock onto its grid converged values (with the exception of the immediate shock region), next the turbulent skin friction distribution locks in (but not at the shock), and finally (on unacceptably fine grids) the laminar skin friction distribution begins to lock in. We find it disturbing that a Navier-Stokes code would have so much trouble with laminar flow, particularly when compared to the resolution requirements for accurate solutions in boundary-layer codes.

For typical airfoils, the boundary layer is laminar for only a few percent of chord, and poorly resolved laminar regions often have little impact on the lift and drag calculations. However, we are also concerned with situations where laminar flow and transition prediction are important; hybrid laminar flow control and high-lift devices are two examples. For these flow fields, accurate prediction of laminar boundary layers on reasonable grids is crucial. The behavior at the shock (skin-friction reversal only on the 1024 by 256 grid) could also have an impact on the pressure drag.

## SAD Laminar Flow Test Case

The poor performance of methods using scalar artificial dissipation (SAD) for high Reynolds number laminar flows can be demonstrated by considering flow over a flat plate at zero incidence. We present results for a laminar flat plate at a Reynolds number of  $Re = 500,000$  and free stream Mach number of  $M_\infty = 0.3$ . More detailed results for this test case will be presented elsewhere.

Two numerical schemes are employed to solve this

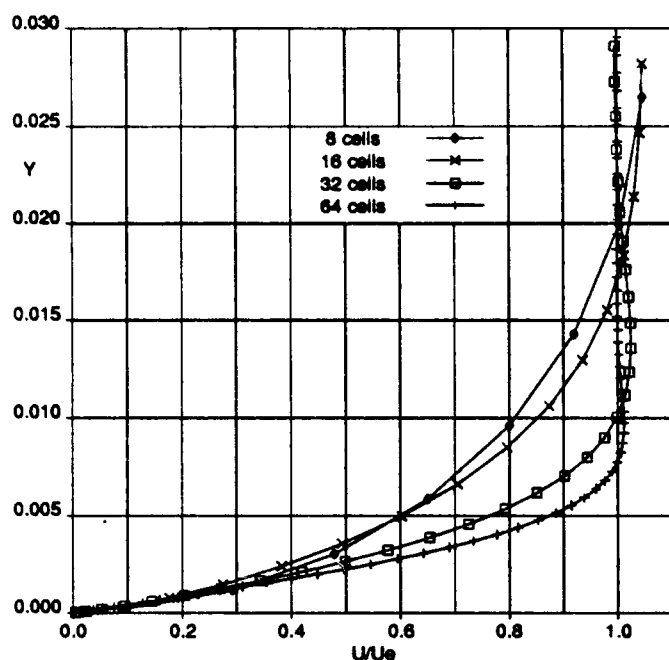


Figure 11: Grid Convergence of Velocity Profiles at  $x = 1$  for Central Difference with Scalar Artificial Dissipation

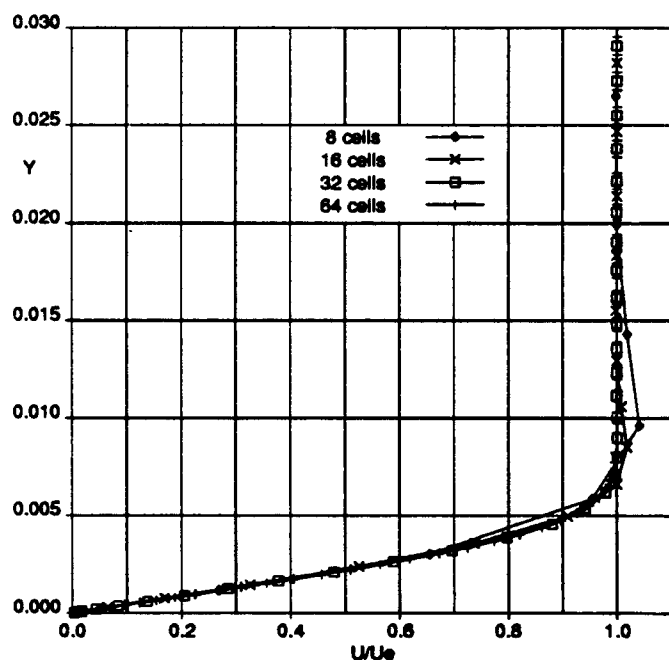


Figure 12: Grid Convergence of Velocity Profiles at  $x = 1$  for Second-Order Upwind

Table 1: Central-Difference Boundary Layer Parameters at  $x = 1$

grid	$C_f$ ( $\times 1000$ )	$\delta^*$ ( $\times 1000$ )	$\theta$ ( $\times 1000$ )	$C_f Re_\theta$
$16 \times 8$	1.683	6.240	3.514	2.956
$32 \times 16$	1.693	5.343	2.741	2.321
$64 \times 32$	1.124	2.977	1.158	0.651
$128 \times 64$	0.965	2.564	1.009	0.487
Blasius	0.9390	2.434	0.9390	0.4409

Table 2: Upwind Boundary Layer Parameters at  $x = 1$

grid	$C_f$ ( $\times 1000$ )	$\delta^*$ ( $\times 1000$ )	$\theta$ ( $\times 1000$ )	$C_f Re_\theta$
$16 \times 8$	1.006	2.435	1.096	0.5512
$32 \times 16$	0.901	2.509	0.994	0.4481
$64 \times 32$	0.919	2.465	0.956	0.4392
$128 \times 64$	0.9318	2.450	0.9471	0.4413
Blasius	0.9390	2.434	0.9390	0.4409

flow. The first utilizes Jameson technology—central differencing with scalar artificial dissipation—to discretize the inviscid fluxes. The second scheme discretizes the inviscid fluxes using Roe's flux-difference splitting with second order upwind extrapolation of cell-centered states to cell faces [19]. Both schemes discretize the viscous fluxes using central differencing.

Figures (11) and (12) show velocity profiles at  $x = 1$  unit downstream of the plate leading edge computed using the two numerical schemes. The profiles are computed on a sequence of four grids obtained by deleting every other grid line from the finest grid in the typical multigrid fashion. The finest grid contains 64 cells normal to the plate with the upper boundary at approximately three boundary layer thicknesses; the grid is parabolically stretched away from the plate. The grid is also parabolically stretched away from the leading edge in  $x$  with a grid spacing of approximately  $\Delta x = 0.03$  at  $x = 1$ .

Figures (11) and (12) show much faster grid convergence for the profiles computed with the upwind scheme. The central-difference results are characterized by an overshoot in the velocity near the edge of the boundary layer and a significant thickening of the boundary layer. The two coarsest upwind profiles also show an overshoot, but that for the 16-cell grid is no worse than the result for the central difference scheme on the 64-cell

finest grid.

The disparity in accuracy between the central-difference and upwind solutions is further shown in Tables 1 and 2, where skin friction, displacement and momentum thicknesses are compared with the Blasius profile parameters at  $x = 1$ . Table 1 shows a quite rapid reduction in errors for the central-difference scheme with increased grid density (better than second order), but coarse grid errors are enormous compared to the upwind scheme results. For the 32-cell grid, the upwind solution contains approximately 18 cells within the boundary layer and gives 2% errors in the predicted parameters. This is consistent with our experience on resolution requirements for boundary layer solvers. In comparison, the central-difference results are still in error by 20% on this same grid.

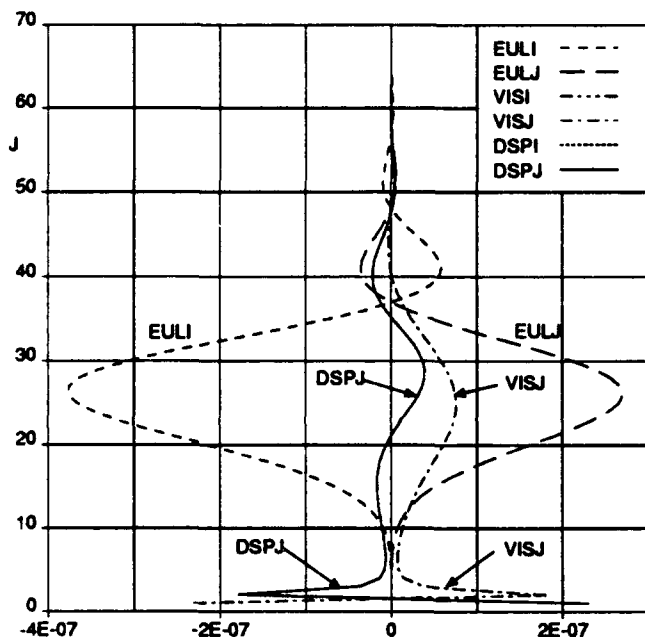


Figure 13:  $x$ -Momentum Equation Budget at  $x = 1$  for Central Difference Scheme (64-cell grid)

We have identified the culprit for the relatively poor performance of the central-difference scheme; it is the scalar fourth-difference artificial dissipation in the normal direction; it is not related to the "Martinelli Compromise". Specifically, contamination results from excessive dissipation normal to the boundary layer in the  $x$ -momentum equation. This occurs because the artificial dissipation is scaled by the flux Jacobian spectral radius  $|v| + c$ , whereas a properly formulated matrix dissipation or upwind scheme (e.g. Roe's flux-splitting) scales the normal dissipation by  $|v|$ . It is easily shown that with the  $|v| + c$  scaling, the normal artificial dissipation in the  $x$ -momentum equation is proportional to  $(\Delta y/\delta)^3 \sqrt{Re}/M$  based on edge conditions. Therefore, as the Reynolds number is increased, more grid resolution (i.e. more grid points across the boundary layer thickness  $\delta$ ) is required to achieve a given level of accu-

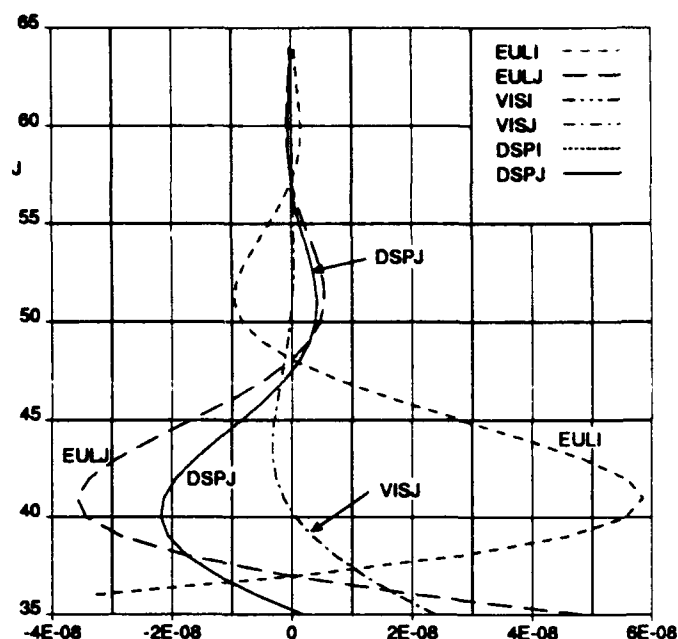


Figure 14:  $x$ -Momentum Equation Budget at  $x = 1$  for Central Difference Scheme (64-cell grid) Blow-up of Boundary-Layer Edge

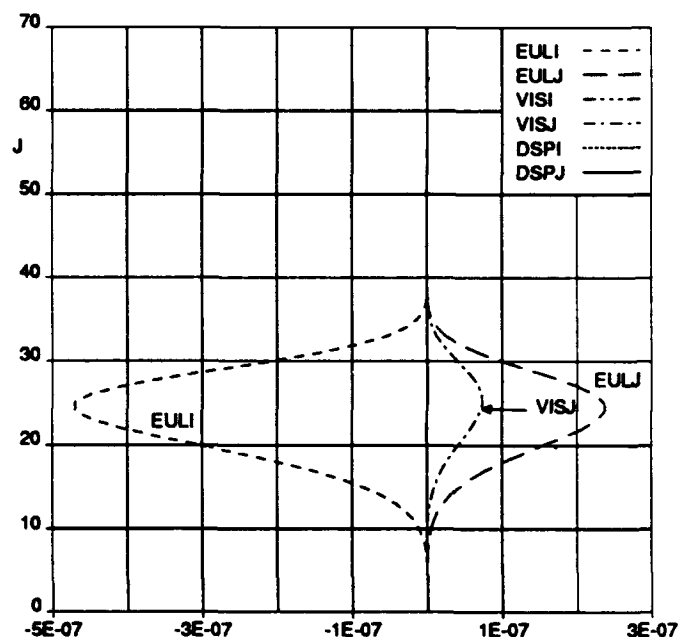


Figure 15:  $x$ -Momentum Equation Budget at  $x = 1$  for Upwind Scheme (64-cell grid)

racy. This also explains why similar poor performance of scalar dissipation methods is not seen in low Reynolds number flows.

To illustrate the contamination, the budget for the  $x$ -momentum equation for the profile of cells at  $x = 1$  is plotted in Figures (13), (14) and (15) for the central-difference and upwind schemes on the finest grid. In the figures, EULI, VISI and DSPI represent the difference in inviscid, viscous, and artificial dissipation fluxes, respectively, through the vertical faces of each cell (i.e. streamwise fluxes). EULJ, VISJ and DSPJ represent the analogous flux differences through horizontal faces (i.e. normal fluxes). For the upwind scheme, DSPI and DSPJ are taken as the difference of the split-fluxes and the face-averaged fluxes; hence, EULI and EULJ are consistently defined between the upwind and central-difference schemes.

Figures (13) and (14) reveal that the normal artificial dissipation (DSPJ) is large *everywhere* in the profile, even outside the boundary layer. Near the wall, the momentum balance is completely nonphysical with artificial dissipation (DSPJ) balancing viscous diffusion (VISJ). The budget for the upwind scheme is more physical; artificial dissipation is small everywhere, and the dominant terms are EULI, EULJ, and VISJ.

Some previous researchers have introduced ad hoc scaling reductions of the artificial dissipation through the boundary layer as an attempt to eliminate contamination. We have also applied some of these "fixes" with disappointing results, and know of no ad hoc scaling that will reduce the artificial dissipation across the entire profile to a point where the results are comparable to a properly formulated upwind scheme.

We wish to emphasize that these problems with high Reynolds number laminar flows are not inherent to central-difference schemes, but to central-difference schemes that use *scalar* artificial dissipation (CDSAD). This leads us to conclude that any scheme using scalar artificial dissipation or any scheme that is highly dissipative for low Mach number flows (e.g. van Leer's flux-splitting, see Ref. [5]), should be suspect for calculating laminar flows.

Our current research is directed towards improving the convergence rates of upwind schemes to steady-state. It is well known that reducing the spatial dissipation in a scheme usually results in slower convergence to steady-state.

## 2-D High-Lift Configurations

High-lift flow provides a significant challenge to CFD technology. For instance, the CFD code must have the ability to accurately predict the laminar boundary-layer profile ahead of the transition point so that a transi-

tion prediction method can be applied. The confluent boundary layer on the main element and the separated flows in the cove and on the flap must be modeled. There are free-shear layers in many parts of the flow-field where the spatial length scales of the flow characteristics are non-isotropic. The free-shear flows interact with the boundary layer on the flap to sometimes cause dramatic and unexpected flow behavior (e.g. Reynolds number reversal effects described in [8]). Simple boundary-layer approximations may not be adequate for such complex flows. Navier-Stokes methods seem to be the natural choice, but even here turbulence models remain a major issue.

We have written a code called A610 described in [17] that uses viscous/inviscid coupling to calculate flows around multi-element airfoil configurations. We will compare A610 with the Mavriplis unstructured grid NS code [18] for a Douglas 3 element configuration tested at LTPT. Comparisons between experiment, A610 and the Mavriplis code for 8, 20, and 23 degrees angle of attack are shown figures (16), (17), and (18). In order to run with A610, the coves on the lower surfaces of the leading edge slat and near the rear of the main element had to be smoothed. The effects of this smoothing are particularly noticeable in the A610 results at 8°. At all angles of attack A610 seems to predict  $C_p$  peaks that are a little too high. The overall test/theory comparisons seem to favor A610 at 20° and the Mavriplis code at 23°. At 8° A610 properly predicts separation for the trailing edge of the flap while the Mavriplis code does not. The inability to predict this flow separation seems to be a failing of the Chimera based Navier-Stokes codes as well.

## Practical CFD assessment for High-Lift

Given these results there does not appear to be any strong reason for us to favor the Navier-Stokes code. All the more so since we know that being a NS-CDSAD code, the Mavriplis code is not able to properly calculate the laminar portions of the boundary layer and thus can not give us a transition prediction capability. The importance of transition, shown in figure (19), is computed using A610. When the Navier-Stokes codes come closer to achieving their theoretical potential, we will use them in earnest.

Also, while the preliminary capability in 2-D is being developed by many researchers, we badly need a 3-D code. In three dimensions, high-lift flow can be even more complex than in two dimensions. The edge vortices, gap flows, and embedded longitudinal vortices in the boundary layer all have strong effects on the overall performance of the high-lift system.

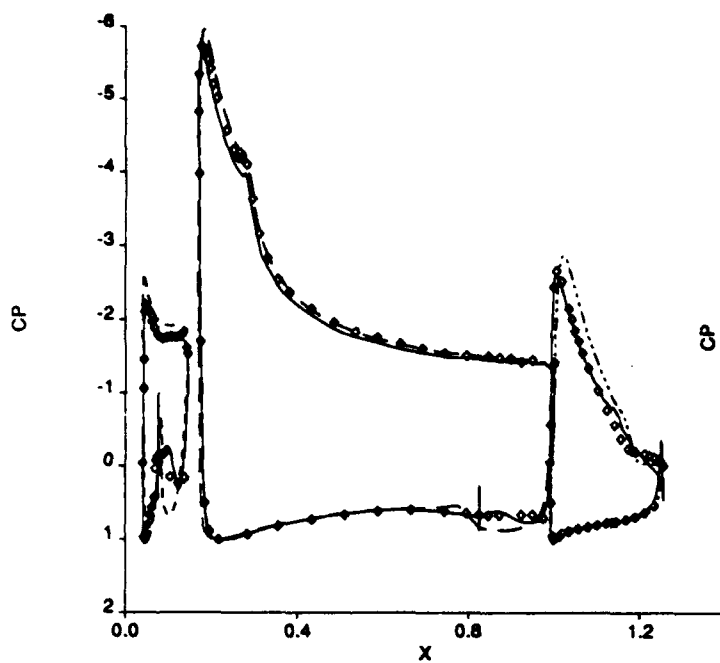


Figure 16: "High lift Olympics" 8° angle of attack. Experiment (Symbols) vs. Mavriplis (Lines) and A610 (Dashed-Lines)

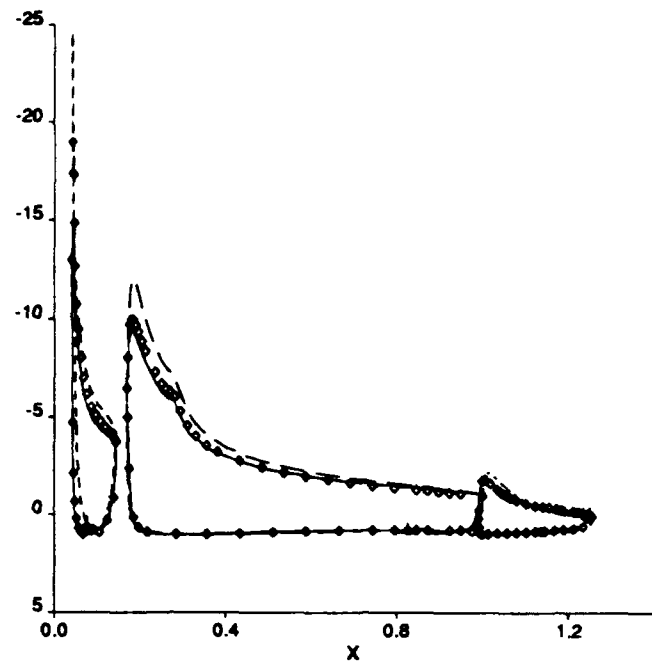


Figure 18: "High lift Olympics" 23° angle of attack. Experiment (Symbols) vs. Mavriplis (Lines) and A610 (Dashed-Lines)

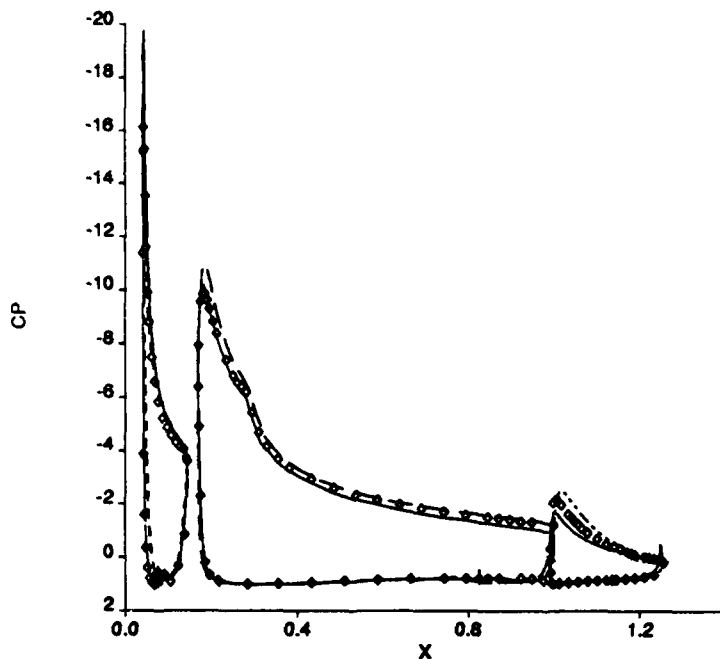


Figure 17: "High lift Olympics" 20° angle of attack. Experiment (Symbols) vs. Mavriplis (Lines) and A610 (Dashed-Lines)

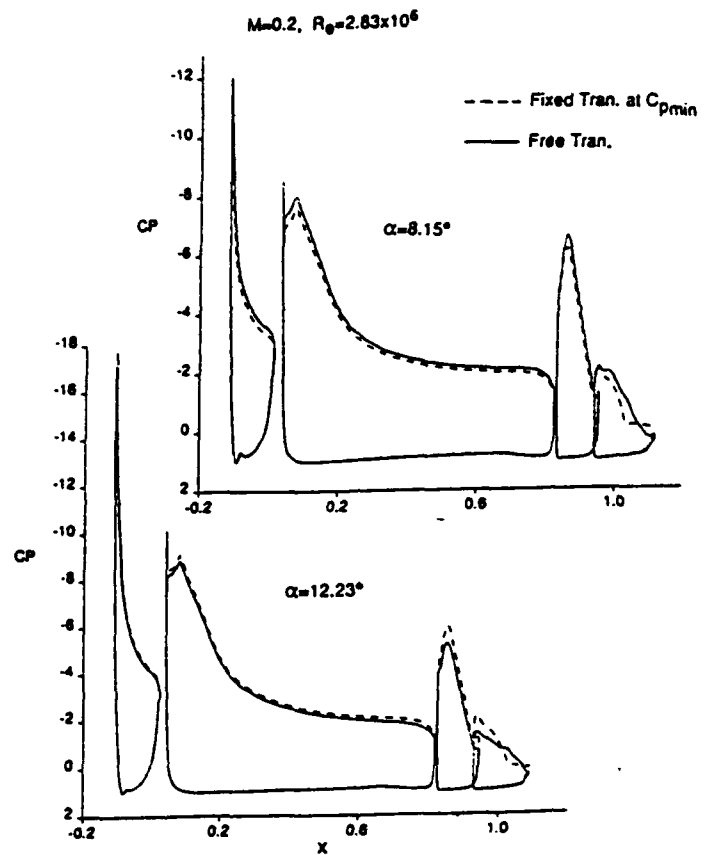


Figure 19: High lift, importance of transition

# ADAPTIVE EAGLE DYNAMIC SOLUTION ADAPTATION AND GRID QUALITY ENHANCEMENT

Phu Vinh Luong  
Naval Oceanographic Office  
Stennis Space Center, MS 39529

J. F. Thompson, B. Gatlin, C. W. Mastin, H. J. Kim  
NSF Engineering Research Center for Computational Field Simulation  
Mississippi State University  
Mississippi State, MS 39762

## ABSTRACT

In the effort described here, the elliptic grid generation procedure in the EAGLE grid code has been separated from the main code into a subroutine, and a new subroutine which evaluates several grid quality measures at each grid point has been added. The elliptic grid routine can now be called, either by a CFD code to generate a new adaptive grid based on flow variables and quality measures through multiple adaptation, or by the EAGLE main code to generate a grid based on quality measure variables through static adaptation. Arrays of flow variables can be read into the EAGLE grid code for use in static adaptation as well. These major changes in the EAGLE adaptive grid system make it easier to convert any CFD code that operates on a block-structured grid (or single-block grid) into a multiple adaptive code.

## INTRODUCTION

The requirements of accuracy and efficiency for obtaining solutions to PDE's have always been a conflict in numerical methods for solving field problems. On the one hand, it is well known that increasing the number of grid points implies decreasing the local truncation error. This, however, results in long computation time due to large numbers of grid points. On the other hand, shorter computation time can be achieved by decreasing the number of grid points, but the result is a less accurate solution.

Adaptive grid generation techniques are a means for resolving this conflict. For many practical problems, the initial grid may not be the best suited for a particular physical problem. For example, the location of flow features, such as shocks, boundary and shear layers, and wake regions, are not known before the grid is generated. In multiple adaptive grid generation, grid points are moved continually to respond to these features in the flow field as they develop. This adaptation can reduce the oscillations associated with inadequate resolution of large gradients, allowing sharper shocks and better representation of boundary layers. Thus it is possible to achieve both efficiency and high accuracy for numerical solutions of PDE's. Several basic techniques involved in adaptive grid generation are discussed in Ref. (1).

In the earlier form of the adaptive EAGLE system (2, 3), the coupling of the adaptive grid system with a CFD code required the encapsulation of both the entire grid code and the CFD flow code into separate subroutines, and the construction of a driver to call each. This was inefficient that it included some unnecessary parts of the grid code and required significant modification, and perhaps restructuring, of the CFD code. In particular, the flow code arrays and/or the grid code arrays had to be modified to be compatible in structure.

The conversion procedure is accomplished by adding the elliptic grid generation subroutine, and certain other subroutines from the EAGLE grid system that are involved in the elliptic grid generation process, to the flow code. The CFD code may then call the elliptic grid generation routine at each time step when a new

grid is desired. The CFD code passes its current solution to this EAGLE routine via a scratch file. This structure eliminates the need for compatibility between CFD and grid arrays. One restriction is that the initial grid must be generated by the EAGLE system, or be processed through that system. This provides the necessary parameters and structural information to be read from files by the adaptive EAGLE routine.

In the present work, the control function approach is used as the basic mechanism for the adaptive grid generation. The static and multiple adaptive grid generation techniques are investigated by formulating the control functions in terms of either grid quality measures, the flow solution, or both.

Previous work (2, 3) with the adaptive EAGLE system allowed the grid to only adapt to the gradient of a variable. The work described here has extended this adaptive mechanism to also allow adaptation to the curvature of a variable or to the variable itself. The system provides for different weight functions in each coordinate direction. In addition, the mechanism now includes the ability to calculate the weight functions as weighted averages of weight functions from several flow variables and/or quality measures. This allows the adaptation to take into account the effect of many of the flow variables instead of just one. The construction of the weighted average of flow variables and quality measures, and the choice of adaptation to gradient, curvature, or variable, are all controlled in each coordinate directions through input parameters. The quality measures now available in the EAGLE grid system are skewness, aspect ratio, arc length, and smoothness of the grid. These grid quality measures, and the resulting control and weight function values, can be output for graphical contouring.

## ADAPTIVE MECHANISM

### Control Function Approach

The control function approach to adaptation is developed by noting the correspondence between the 1D form of the system,

$$x_{\eta\eta} + Px_{\xi} = 0 \quad (1)$$

and the differential form of the equidistribution principle,  $Wx_{\xi} = \text{constant}$ ,

$$Wx_{\eta\eta} + W_{\xi}x_{\xi} = 0 \quad (2)$$

where  $P$  is the function to control the coordinate line spacing, and  $W$  is the weight function.

From (1) and (2) the control function can be defined in terms of the weight function and its derivative as

$$P = \frac{W_i}{W} \quad (3)$$

This equation can be extended in a general 3D form as

$$P_i = \frac{W_{\xi^i}}{W} \quad (4)$$

This approach was suggested by Anderson (Ref. 4, 5), and has been applied with success for 2D configurations by Johnson and Thompson (Ref. 6) and for 3D configurations by Kim and Thompson (Ref. 2) and by Tu and Thompson (Ref. 3).

The complete generalization of (4) was proposed by Eiseman (Ref. 7) as

$$P_i = \sum_{j=1}^3 \frac{g^{ij}}{g^{jj}} \frac{(W)_{\xi^j}}{W_i} \quad (5)$$

where  $W_i$  is the weight function chosen for the  $\xi^i$  direction. This definition of the control functions provides a convenient means to specify three separate control functions, with one in each coordinate direction.

In order to preserve the geometrical characteristics of the existing grid, it is practical to construct the control functions in such a manner that the control functions defined by (5) are added to the initial set of control functions obtained from the geometry, i.e.,

$$P_i = (P)_g + C_i(P)_w \quad i = 1, 2, 3 \quad (6)$$

where

$(P)_g$  : control function based on geometry

$(P)_w$  : control function based on weight function

In these equations the weight function  $W$  can be computed by different formulas for different adaptive mechanisms:

Adaptation to

Variable :  $W = 1 + |V|$

Gradient :  $W = 1 + |\nabla V|$

Curvature :  $W = (1 + \beta |K|) \sqrt{1 + \alpha |\nabla V|^2}$  (7)

where  $V$  can be either a flow solution variable or a grid quality measure. Here  $\alpha$  and  $\beta$  are on the range 0-1, and

$$K = \frac{\nabla^2 V}{(1 + |\nabla V|^2)^{3/2}} \quad (8)$$

is the curvature of the variable  $V$ .

Using these definitions of the control function, the elliptic generation system becomes an adaptive grid generation system. This system is then solved iteratively in adaptive EAGLE by the point SOR method to generate the adaptive grid.

## Grid Quality Measures

The objective of this part of the investigation was to develop a means of evaluating grids through the computation of certain grid properties that are related to grid quality and to develop techniques for estimating the truncation error. Following Kerlick and Klopfer (Ref. 8), and Gatlin, et. al. (Ref. 9), the grid quality measures are taken as skew angle, aspect ratio, grid Laplacian, and arc length. Techniques for estimating the truncation error due to the work of Mastin (Ref. 10) are also included. At each grid point in a general 3D grid, each property can have three values associated with the three directions. The approach taken in this investigation is to treat each surface of constant  $\xi^i$  separately for ease in graphical interpretation.

### skew angle

The minimum skew angle between intersecting grid lines is one of the most important measurable grid properties. This angle can be expressed in terms of the covariant metric elements as

$$\theta_{ij} = \cos^{-1} \left\{ \frac{g_{ij}}{\sqrt{g_{ii} g_{jj}}} \right\} \quad (9)$$

Since  $g_{12} = g_{21}$ ,  $g_{13} = g_{31}$  and  $g_{23} = g_{32}$ , the three skew angles associated with each grid point in a 3D grid are  $\theta_{12}$ ,  $\theta_{23}$  and  $\theta_{31}$ .

### aspect ratio

Since aspect ratio is the ratio of the length of the sides of a grid cell, it can be defined in two different ways. For example, on a surface of constant  $\xi^i$ , this ratio can be expressed in terms of metric elements  $g_x$  and  $g_y$  as

$$AR_y = \sqrt{\frac{g_{xx}}{g_{yy}}} \quad (10a)$$

or

$$AR_x = \sqrt{\frac{g_{yy}}{g_{xx}}} \quad (10b)$$

Large changes in aspect ratio of grids from one part of the field to another may inhibit the convergence of viscous flow solutions to a steady state.

### Laplacian

A useful measure of the smoothness of a grid is the Laplacian of the curvilinear system,  $\nabla^2 \xi^i$ ,  $i = 1, 2, 3$ , which is simply the rate of change of grid point density in the grid. For a perfectly uniform grid, the grid Laplacian would vanish everywhere, but exceedingly large values may arise in highly stretched grids. The mathematical representation of the grid Laplacian is defined in terms of the contravariant metric elements  $g^{ij}$ , the contravariant base vectors  $\alpha^i$  and the position vector  $r$  as

$$\nabla^2 \xi^i = - \sum_{j=1}^3 \sum_{k=1}^3 g^{ij} \alpha^k \cdot r_{\xi^j \xi^k} \quad i = 1, 2, 3 \quad (11)$$

### arc length

Another important measure of the grid quality is the local rate at which grid spacing changes. On a coordinate surface of constant  $\xi^3$ , and along a coordinate line of constant  $\xi^2$ , the grid spacing can be defined as



## Nacelle-Flow Analysis

Nacelle analysis and design is an integral part of the airplane design process. In advanced aircraft, propulsion systems are closely coupled with the airframe, and proper engine installation is essential in order to improve the overall performance of the aircraft. Inviscid methods (panel and full-potential) have been very useful, but viscous effects are also of interest especially for off-design conditions on large twin-engine airplanes.

It is relatively easy to analyze an isolated flow-through nacelle using a code written to treat wings. We have adapted the TLNS3D Navier-Stokes code. The nacelle is treated as a ring wing, with periodic boundary conditions. To simulate a powered nacelle one can either specify inlet and exhaust boundary conditions, or use a center body with variable geometry to control the mass flux through in the engine. At cruise condition, the Navier-Stokes code provides accurate results, similar to that of wing or wing/body analysis. Problems are encountered in nacelle analysis with low-speed takeoff conditions, and with high-speed engine-out conditions.

At takeoff, the effective angle of attack for the nacelle is high. The flow is highly three-dimensional, and a laminar separation bubble may form at the nacelle highlight region. The marginal accuracy of the available Navier-Stokes codes in the laminar flow region was mentioned above. In the long run we must arrive at a reliable 3-D boundary-layer transition-prediction capability, as well as a plausible behavior in the transition region, before we can capture the laminar separation bubble. This bubble has dramatic effects on the overall flow field. Figure (20) compares the results of nacelle analysis, first treating the flow as fully turbulent (turbulence model active in the whole domain), and then assuming transition at 5% from the leading edge (turbulence model active only downstream of that line). The results are drastically different, and neither agree well with experiment. The flow pattern with transition at 5% is however similar to the experimental pattern.

At a high-speed, engine-out condition the large amount of spillage around the nacelle results in a strong shock on the exterior surface of the fan cowl, which may cause severe shock-induced separation. Present Navier-Stokes technology is capable of handling mild shock-induced separation. However, none of the turbulence models tested gives reliable solution for strong shock-induced separation.

In summary, attempts at nacelle analysis and engine-airframe integration by Navier-Stokes solutions raise the same issues as wing design. These are: gridding difficulties when other components are included; numerical accuracy particularly in the boundary layers; and turbulence-modeling accuracy particularly at shock interactions. In addition, because of lower Reynolds num-

Effects of trip location on nacelle lip separation  
(High alpha, low Reynolds No.)

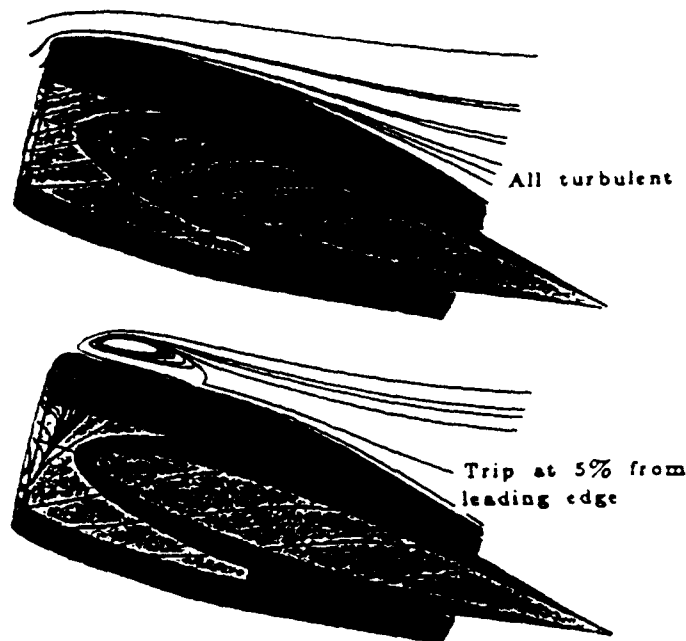


Figure 20: Nacelle with transition at 5% versus all turbulent flow

bers and extreme velocity peaks at the lips, laminar regions may exist in the boundary layers and exert much control over the global flow field. In the long run we need a reliable and, as much as possible, automatic 3-D boundary-layer transition-prediction capability. For this, two key ingredients are—presumably—a stability analysis with sufficient robustness and generality to handle steep three-dimensional pressure gradients, and accurate velocity profiles directly out of the Navier-Stokes solver. Neither ingredient is at hand. The turbulence models also need improvement to handle moderate or massive separation, whether encountered at low-speed takeoff conditions or at high-speed, engine-out conditions.

## Conclusion

The 3-D Wing/Body calculations show that Navier-Stokes codes hold much promise. However, our test/theory comparisons in 2-D and for nacelles, as well as our detailed 2-D grid refinement studies, are sobering. It is apparent that much work remains to be done in numerics and physical modeling of transition and turbulence before we can say that we have an "Industrial-Strength" Navier-Stokes code in hand.

## Acknowledgements

We wish to thank Steve Robinson (NASA Langley), Daryl Bonhaus (NASA Langley), Dimitri Mavriplis (NASA Langley), Frank Lynch (Douglas Aircraft Company), and Paul Meridith (Boeing) for helping us collect the data and computed results for the "High Lift Olympics" held at NASA Ames on May 2, 1991. Thanks to Wendy Wilkinson (Boeing) for rearranging the data and computed results so that they could (for the first time!) be plotted together and directly compared. Thanks also to Kevin Moschetti (Boeing) and Bill Newbold (Boeing) for providing ISES code results.

## References

- [1] Antony Jameson, "Successes and Challenges in Computational Aerodynamics," AIAA-87-1184, 1987.
- [2] Luigi Martinelli, "Calculations of Viscous Flows with a Multigrid Method", Ph.D Thesis, Department of Mechanical and Aerospace Engineering, Princeton University, October, 1987.
- [3] Swanson, R. C. and Turkel, E., "Artificial Dissipation and Central Difference Schemes for the Euler and Navier-Stokes Equations," AIAA-87-1107, 1987.
- [4] Vatsa, V. N., and Wedan, B. W., "Development of an Efficient Multigrid Code for 3-D Navier-Stokes Equations," AIAA-89-1791, 1989
- [5] Bram van Leer, James L. Thomas, Philip L. Roe, and Richard W. Newsome, "A Comparison of Numerical Flux Formulas for the Euler and Navier-Stokes Equations", AIAA-87-1104, 1987.
- [6] Johnson, D. A., and Coakley, T. J., "Improvements to a Nonequilibrium Algebraic Turbulence Model," AIAA J., Vol. 28, No. 11, Nov., 1990
- [7] Yu, N. J., Allmaras, S. R., and Moschetti, K. G., "Navier-Stokes Calculations for Attached and Separated Flows Using Different Turbulence Models," AIAA-91-1791, 1991
- [8] Garner, P.L., Meridith, P.T., and Stoner, R.C., "Areas for Future CFD Development as Illustrated by Transport Aircraft Applications", AIAA-91-1527-CP, 1991.
- [9] Yu, N. J., and Campbell, R. L., "Transonic Airfoil and Wing Design Using Navier-Stokes Codes," paper in preparation.
- [10] Bengelink and Rubbert, "The Impact of CFD on the Airplane Design Process: Today and Tomorrow", iPAC International Pacific Air & Space Technology Conference and 29th Aircraft Symposium, Gifu, Japan, 1991.
- [11] Bieterman, M. B., Bussoletti, J. E., Hilmes, C. L., Johnson, F. T., Melvin, R. G., Samant, S. S., and Young, D. P., "Solution Adaptive Local Rectangular Grid Refinement for Transonic Aerodynamic Flow Problems," Proceedings of the Eighth GAMM Conference on Numerical Methods in Fluid Mechanics, 1990, pages 22-31.
- [12] Hafez, M. M., and Lovell, D., "Entropy and Vorticity Corrections for Transonic Flows," AIAA-83-1926, July 1983.
- [13] Michael Giles and Mark Drela, "A Two-Dimensional Transonic Aerodynamic Design Method," AIAA-86-1793, 1986.
- [14] Cook, P. H., McDonald, M. A., and Firmin, M. C. P., "Aerofoil RAE 2822 - Pressure Distributions, and Boundary Layer and Wake Measurements," AGARD-AR-138, pp. A6-1 through A6-77, May 1979.
- [15] Thibert, J.J, Grandjacques M., and Ohman L. H., "NACA 0012 Airfoil," AGARD-AR-138, pages A1-1 through A1-36, May 1979.
- [16] Thomas H. Pulliam, "Euler and Thin Layer Navier-Stokes Codes: ARC2D, ARC3D," Computational Fluid Dynamics Workshop held at the University of Tennessee Space Institute, Tullahoma, Tennessee, March 12-16, 1984, pages 15.1 through 15.85.
- [17] Kusonose, K., Wigton, L., and Meredith, P., "A Rapidly Converging Viscous/Inviscid Coupling Code for Multi-Element Airfoil Configurations," AIAA-91-0177, January 1991.
- [18] Dimitri Mavriplis, "Turbulent Flow Calculations Using Unstructured and Adaptive Meshes," ICASE Report No. 90-61, September 1990.
- [19] Roe, P. L., "Approximate Riemann Solvers, Parametric Vectors, and Difference Schemes," Journal of Computational Physics, Vol. 43, 1981, pp. 357-372.